Transactions of the ASME®

Transactions of the ASME, Journal of Heat Transfer (ISSN 0022-1481) is published quarterly (Feb., May, Aug., Nov.) for $165.00 per year by The American Society of Mechanical Engineers, 345 East 47th Street, New York, NY 10017. Second class postage paid at New York, NY and additional mailing offices. POSTMASTER: Send address changes to Transactions of the ASME, Journal of Heat Transfer, c/o THE AMERICAN SOCIETY OF MECHANICAL ENGINEERS, 22 Law Drive, Box 2300, Fairfield, NJ 07007-2300.
CHANGES OF ADDRESS must be received at Society headquarters seven weeks before they are to be effective. Please send old label and new address.
PRICES: To members, $40.00, annually: to nonmembers, $165.00.
Add $24.00 for postage to countries outside the United States and Canada.
STATEMENT from By-Laws. The Society shall not be responsible for statements or opinions advanced in papers or . . . printed in its publications (B7.1, para. 3).

INDEXED by Applied Mechanics Reviews and Engineering Information, Inc.
Canadian Goods & Services Tax Registration #126148048.

Journal of Heat Transfer

Published Quarterly by The American Society of Mechanical Engineers

VOLUME 115 • NUMBER 4 • NOVEMBER 1993

ANNOUNCEMENTS

TECHNICAL PAPERS

Heat Conduction

Forced Convection

Natural Convection

Boiling and Condensation

(Contents continued)

Radiative Transfer

Solid/Liquid Phase Change

TECHNICAL NOTES

The 1991 Max Jakob Memorial Award Lecture

Image-Forming Optical Techniques in Heat Transfer: Revival by Computer-Aided Data Processing

F. Mayinger
Lehrstuhl A für Thermodynamik,
Technische Universität,
Arcisstr. 21
8000 Munich 2,
Federal Republic of Germany

Increasing possibilities of computer-aided data processing have fostered a revival of image-forming optical techniques in heat and mass transfer as well as in fluid dynamics. Optical measuring techniques can provide comprehensive and detailed information on the formation of phase interfaces, particle movement, or the size distribution of droplet swarms. Holographic interferograms contain full information, not only about boundary layers restricting transport processes, but also on local coefficients of heat and mass transfer. Laser-induced fluorescence promotes a better understanding of combustion processes by conveying insights into the concentration and the temperature in and around a flame. For describing complicated phenomena in fluid dynamics or in heat transfer by computer programs, global experimental information is not sufficient. Optical techniques provide local data without disturbing the process and with a high temporal resolution. By using the results of optical measuring techniques, it is possible to improve computer programs that describe physical processes. Optical techniques are also very sensitive touchstones for checking the quality of such programs.

1 Holography

1.1 Experimental Method and Optical Setup. Optical methods use changes of light waves as sensoric signals, which are due to interaction between the light and the material. Such changes and interaction consequences include, for example, attenuation, scattering, deflection or reflection and phase shift. Generally one can distinguish between image-forming and non-image-forming methods. Here only the first type shall be discussed.

Recently a new image-forming technique, holography, came into use in studying fluid dynamic processes, and holographic interferometry became a new recording mode for studying temperature fields in boundary layers during heat and mass transfer processes.

The Greek word holography comes from the ability of the method to record the totality (holos) of the light information, respectively of the wave front, namely the amplitude (as brightness), the wavelength (as color), and the phase position of the light. Holography demands a source emitting coherent light. For the general theory of holography, reference is made to the literature (Kiemle and Röss, 1969, Smith, 1969; Caufield and Lu, 1971). Here only some principles necessary for understanding the holographic measurement techniques are mentioned. In Fig. 1 the holographic two-step image-forming process of recording and reconstructing an arbitrary wave front is illustrated.

The object is illuminated by a monochromatic light source and the reflected or scattered light falls directly onto a photographic plate. This object wave usually has a very complicated wavefront. According to the principle of Huygens, one can, however, regard it to be the superposition of many elementary spherical waves. In order to simplify the matter, only one wave is drawn in Fig. 1. A second wave, called "reference wave" is superimposed on the first. If the waves are mutually coherent, they form a stable interference pattern when they meet on the photographic plate. This system of fringes can be recorded on the photographic emulsion. After the chemical processing of the plate, it is called "hologram." The amplitude is recorded in the form of different contrast of the fringes and the phase in the spatial variations of the pattern.

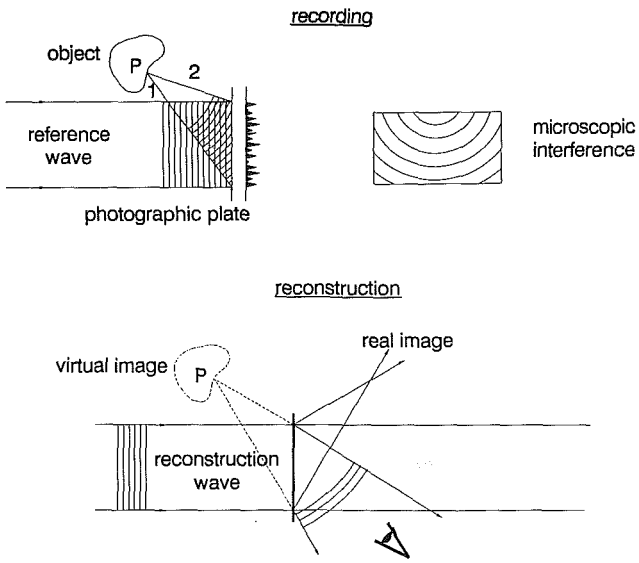

Fig. 1 Principle of holographic two-step image-forming process

If the plate is subsequently illuminated by a light beam similar to the original reference wave, the microscopic pattern acts like a defraction grating with variable grating constant. The light transmitted consists of a zero-order wave, traveling

Contributed by the Heat Transfer Division and presented at the ASME National Heat Transfer Conference, San Diego, California, August 9–12, 1992. Manuscript received by the Heat Transfer Division April 1993; revision received August 1993. Keywords: Flow Visualization, Measurement Techniques. Technical Editor: R. Viskanta.

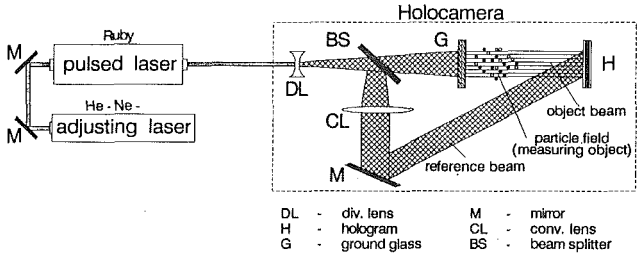

Fig. 2 Holographic setup for ultrashort time exposures with a pulsed laser

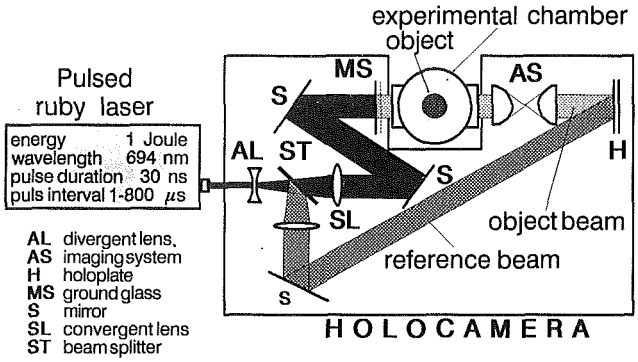

Fig. 3 Holographic interferometer for spray analysis

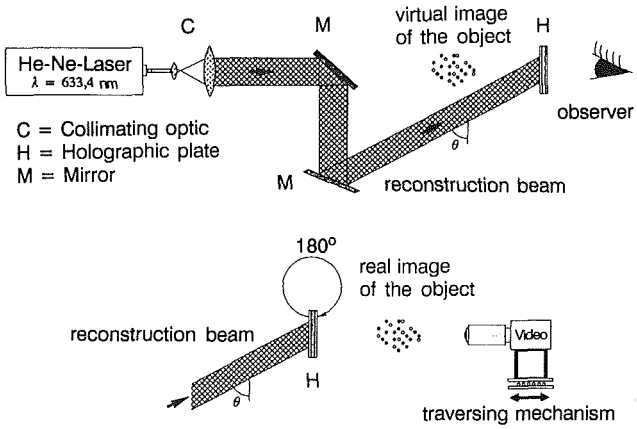

Fig. 4 Optical arrangement for the reconstruction of pulsed laser holograms

in the direction of the reconstructing beam, plus two first-order waves. One of these first-order waves travels in the same direction as the original object wave and has the same amplitude and phase distribution. The first-order wave produces a virtual image in front of the holographic plate, seen from the side of the incoming reference beam. The other wave goes in the opposite direction and creates a real image of the object behind the photographic plate. This real image can be studied with various reconstruction devices, such as a microscope.

For conventional applications of holography, one can use lasers emitting continuous light, for which adjustment of the holographic plate is a trivial task. The recording of very fast moving or changing objects needs ultrashort exposure times, which can be achieved by using a pulsed laser, for example, a ruby laser with pulse durations of 20–30 ns. A holographic setup using a pulsed laser is shown in Fig. 2. For adjusting such a holographic setup with a pulsed laser, one needs a second laser emitting continuous light to adjust the holographic arrangement and the photographic plate. With a ruby laser as a light source, one can use the special feature of the ruby crystal to transmit red light. The beam of a helium-neon-continuous laser can be arranged in such a way that it travels through the ruby of the pulsed laser. The holographic setup shown in Fig. 2 is a special arrangement for studying particle flow or phase distribution in multiphase mixtures. It presents a very suitable nonintrusive method to visualize dispersed flow with particles or droplets not smaller than 10 λ where λ is the wavelength of the laser light.

A more sophisticated arrangement for recording pulsed laser holograms is shown in Fig. 3. In this arrangement the light emitted by the pulsed ruby laser travels through a lens and mirror system, where it is expanded, divided, and guided through the measuring object and onto the holographic plate. The laser beam is first expanded in the lens AL and then divided in the beam splitter ST to produce the object beam and the reference beam. The object beam travels via a collecting lens, two mirrors, and a screen through the object, and after the object passes an imaging lens before it falls onto the holographic plate. There it is superimposed by the reference wave, which is split off by the beam splitter ST and falls via the collecting lens SL and a mirror onto the holographic plate, bypassing the object. An instantaneous picture of the situation in the spray can be registered. If the electronic system of the ruby laser emits more than one laser pulse within a very short period of time, sequences of the spray behavior can be stored on the photographic emulsion of the holographic plate, from which the velocity of the droplets as well as their changes in the size and geometric form can be evaluated. The evaluation, however, needs a very sophisticated and computerized procedure, which will be briefly described later.

For evaluating the hologram, it first has to be reconstructed as demonstrated in Fig. 4. As an example, the formation of a droplet spray leaving a nozzle is studied in this reconstructing procedure. After chemical processing, the holographic plate is replaced in the old position and then illuminated by a continuously light-emitting helium–neon laser. The new beam produced by this laser is now called a reconstruction beam. If the holographic plate is replaced in the same orientation it had when the exposure was made, one can look at it with the naked eye and see a virtual image of the droplet spray exactly at the place where it was produced previously. For a quantitative evaluation one needs a closer examination via an enlarging lens or a microscope and by a camera, perferably a video camera. To do this, the holographic plate has to be turned by 180 deg, when positioning to the old place. By illuminating with the reconstruction beam, a real image of the spray is now produced, which has a three-dimensional extension. The arrangement of the video camera is shown in Fig. 5. For technical evaluation, the camera is focused to the midplane of the spray image. The camera is moved forward or backward with a fixed focus of the lens so that the spray cloud can be evaluated plane by plane.

1.2 Computer-Aided Evaluation. The quantitative evaluation via the video camera works with a computer system. The main components of this system are a digitizer, a graphic monitor, and a PC. The video camera is scanning the real image of the reconstructed hologram O and sends its information to the digitizer D. It changes the electrical signal from an analog character to a digital one, and stores it in a frame memory. Now the computer C can use the digitalized information for performing the image reprocessing.

The processing of images obtained from holograms involves:

- separation of the droplet images from the background.
- identification of sharply focused droplets.
- measuring of their projected areas.
- evaluation of their equivalent diameters and center points.

By applying an average filter, the noisy background can be suppressed. Afterward the sharply focused parts of the image have to be identified. This can be realized by contouring the parts of the image. It is obvious that sharply focused contours deliver a strong grey gradient and out-of-focus images have a

smooth transition of grey values. To identify the well-focused contours, many so-called auto-focus-algorithms have been developed (Lighthart and Groen, 1982). The gradient of the grey values represents a criterion to separate sharply focused parts of an image from unsharply focused ones. This can be done by using a Sobel operator. Strong gradients are enhanced while weak ones tend to disappear. The last step is to eliminate all particles that are not well focused. This can be done by allowing only pixels to remain in the image, which have a grey gradient to their neighbors above a certain value. For details, reference is made to the work by Chavez and Mayinger (1990). By this procedure a "picture" is electronically produced containing only contours, which are within a very narrow tolerance of the focusing plane.

It may happen that the contours of some parts—for example, droplets—do not have a closed and continuous outline, because pixels may have been extinguished spotwise during the gradient checking procedure. Therefore, a next step has to follow, in which the open contours are filled with color to produce closed outlines of the particle reproductions. In order not to create new spots by this process, the situation after the contouring is compared with that which existed before the out-of-focus particles were eliminated. A "particle" in the new picture is only accepted if it existed already in the original picture. Finally, the remaining particle reproductions are filled with color and now the evaluation with respect to particle size, form, and concentration can go on.

After this plane in the hologram has been evaluated, the video camera is moved slightly and the whole procedure starts again. So the picture can be evaluated plane by plane and a three-dimensional picture can be reconstructed.

An example of a computerized reproduction of the veil and the droplet swarm originating from a nozzle is shown in Fig. 6 (Chavez and Mayinger, 1990, 1992). It conveys a good impression of how the information of a hologram can be improved by computerized evaluation. While the photograph and the left-hand side of this figure show only the shape of the veil, the computerized picture on the right-hand side clearly presents the thickness of the liquid film of the veil and also shows its wavy nature. In addition, the droplets separating from the lower end of the veil are clearly defined.

A sequence of reproduced "pictures" by this computer-aided image processing is shown in Fig. 7. The upper row in this figure shows the region of a spray near the nozzle and the lower one a region further downstream where the veil already is disintegrated into a droplet swarm.

1.3 Double Exposure Technique. If two exposures of a droplet spray are illuminated onto the same holographic plate within a short time, the velocity of the droplets can also be determined from such a hologram (Chavez and Mayinger, 1992). To evaluate such a double-exposed hologram, first the

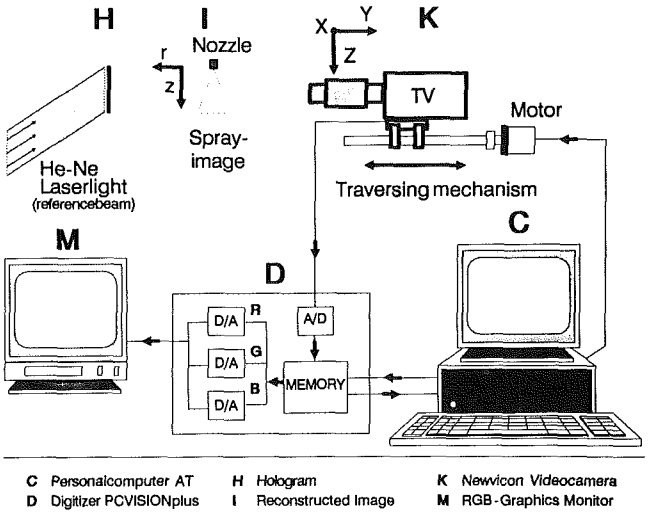

Fig. 5 Digital image processing system for the evaluation of pulsed laser holograms

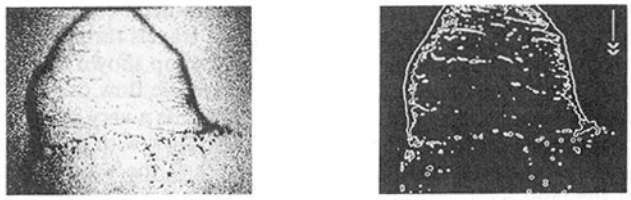

Fig. 6 Veil and spray flow behind a nozzle: left side: photographic view, right side: evaluation of a hologram

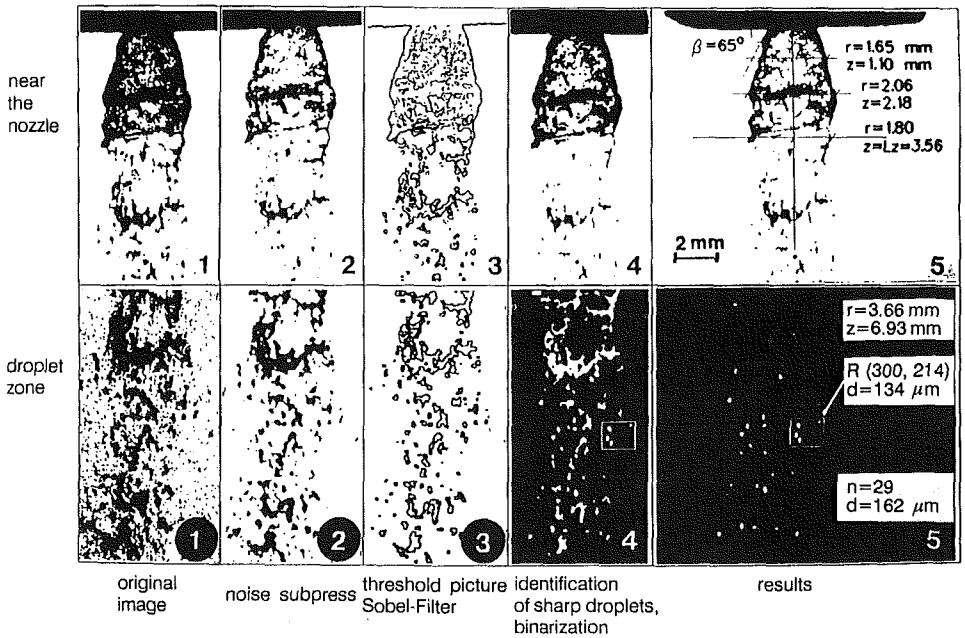

Fig. 7 Steps of image-processing of a hologram: upper row: spray near the nozzle; lower row: spray downstream of the nozzle

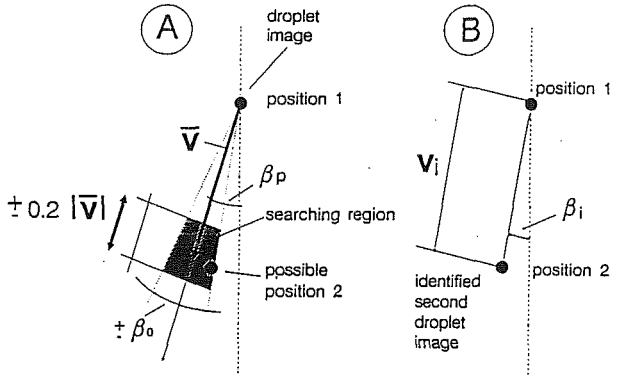

Fig. 8 Method for evaluating particle velocity from double pulse holograms; definition of the search area

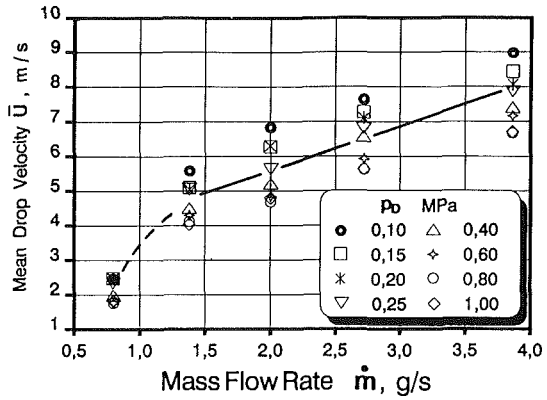

Fig. 9 Mean droplet velocity in a spray as a function of flow rate at different ambient pressures

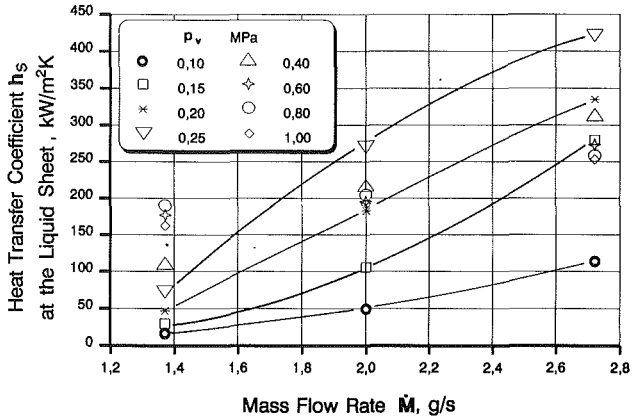

Fig. 10 Heat transfer coefficient during condensation at the phase interface of liquid droplets and vapor

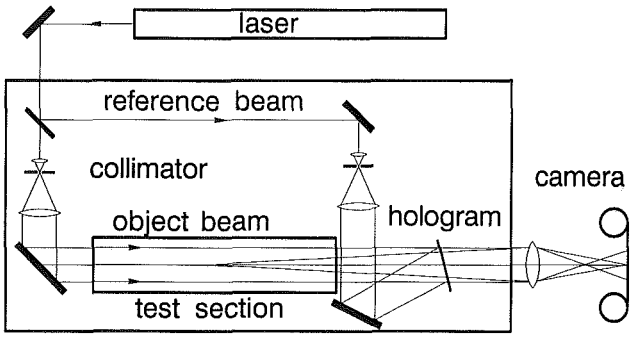

Fig. 11 Optical setup for holographic interferometry

same procedure has to be performed as briefly discussed before. After that the center point of each droplet has to be defined by the computer, which is the basis for determining the distance between the two images of the same droplet, and for evaluating the velocities and trajectories of the droplets. In the next step, the computer draws connection lines between all portrayed particles, regardless of whether they originate from the first or the second exposure. These connecting lines are evaluated with respect to direction and length via a Fourier analysis. This Fourier analysis converts the spatial distribution into a normalized frequency distribution with the maximum F_{max} used as a norm. With this information a second Fourier transformation with the distance as the independent variable is carried out. The preferential angle and the preferential distance appear as peaks in the Fourier diagram, showing the main direction and the mean velocity of the droplets.

In the next step, the computer defines a searching area in a spatial distance from each particle portrayed with this information as briefly sketched in Fig. 8. If it finds the image of a particle within this searching area, it defines it as the second exposure of the particle at position 1, and it calculates the real velocity V_i and the direction β_i of the droplet. If it does not find a particle image within this searching area, it cancels the input of position 1, assuming that the particle moved out of the focused plane before the second exposure was done. In a more sophisticated way, this searching procedure can be also performed between two or more focus planes. This step, however, is very time consuming on the computer.

The data produced by this opto-electronic process are of high accuracy, as Fig. 9 demonstrates. The suspicion that the computerized processing of the double exposure hologram produces a large scattering in the velocity data is misproved by this figure. Even the influence of the pressure of the atmosphere, in which the droplets are traveling, is clearly brought out.

If the droplets are moving in a vapor atmosphere of the same substance as the liquid, and if the temperature of the liquid is below the saturation temperature, condensation occurs at the phase interface, which makes the volume of the droplet grow. This increase in diameter can also be depicted from double-exposure holograms and evaluated by the computer. By using a simple energy balance, the condensation heat transfer can be calculated from this growth of volume versus time. The accuracy and the reproducibility of the described opto-electronic measuring technique are good enough to determine the heat transfer coefficients at the veil and at the droplet cloud, as Fig. 10 demonstrates. The heat transfer data are averaged values from all droplets being reproduced in a hologram.

2 Holographic Interferometry

2.1 Principal Arrangement of Optical Components. By using the recording capabilities of holography, different waves—even those shifted in time—can be stored on the same holographic plate. By illuminating the developed holographic plate with the reference wave, all object waves are reconstructed simultaneously. Where they differ only slightly from each other, they can interfere with each other. These are the fundamentals of holographic interferometry.

In heat and mass transfer, the temperature and the concentration distribution in a fluid are of special interest. To investigate such processes, a so-called through light method is used, where the object wave is irradiating through a volume, in which heat or mass transport takes place.

An exemplary arrangement for holographic investigations is shown in Fig. 11. A beam splitter divides the laser beam in an object wave and in a reference wave, which is also called

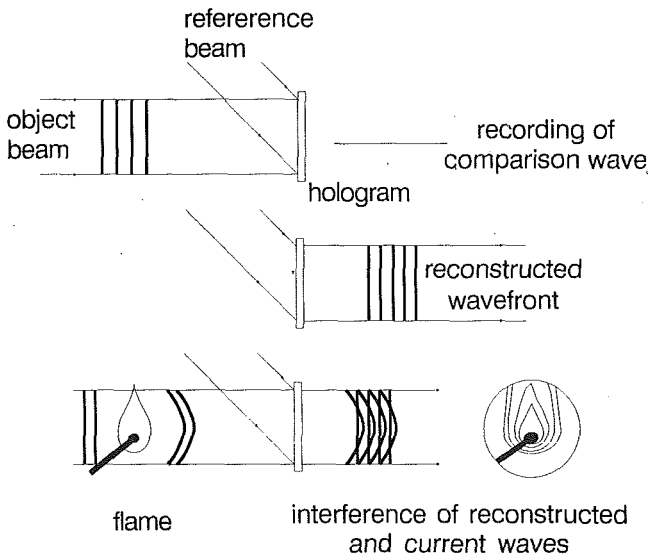

Fig. 12 Real-time method for holographic interferometry

a comparison wave. Both waves are expanded to parallel wave bundles behind the beam splitter via lenses, usually consisting of an arrangement of a microscope lens and a collecting lens. The expanded and parallel organized object wave travels through the space with the research object of interest—called a test section—in which the distribution of temperature or concentration may be measured. The reference wave bypasses the test section and falls directly onto the photographic plate.

To obtain a well-focused picture of a hologram, the interference pattern between the object and the reference wave must be completely stable. With longer exposure times, by using a continuous laser, the optical components have to be mounted on vibration-free tables. On the other hand, there is no need for a high optical quality of the optical components—as it is the case in conventional interferometry—because only relative changes of the object wave are recorded, and optical errors are automatically compensated by the interferometric method. In many cases, only a two-dimensional temperature distribution over a test object is of interest, and it is then good enough to record the change of the refractive index only in a two-dimensional way. For such cases object waves with parallel light provide pictures of high quality. There are many possibilities for arranging the optical setups to form a holographic interferometer, which cannot be discussed here in detail. Reference is, therefore, made to the literature (Mayinger and Panknin, 1974; Mayinger, 1991).

Several procedures exist to produce interferograms; here only one method will be explained, which can also be used in connection with high-speed cinematography. It is called a "real-time-method," because it observes a process to be investigated in real time and continuously. The method is illustrated in Fig. 12.

After the first exposure, by which the comparison wave is recorded and during which no heat transfer is going on in the test section, the hologram is developed and fixed. Remaining at its place or repositioned accurately, the comparison wave is reconstructed continuously by illuminating the hologram with the reference wave. This reconstructed wave can now be superimposed onto the momentary object wave. If the object wave is not changed, compared to the situation before the chemical developing process, and if the hologram is precisely repositioned, no interference fringes will be seen on the hologram.

Now the heat transfer process and boiling or condensation for two-phase flow can be started. Due to the heat transport, a temperature field is formed in the fluid, and the object wave receives an additional phase shift, when passing through this temperature field. Behind the hologram, both waves interfere with each other, and the changes of the interference pattern can be continuously observed or photographed.

The real-time method demands an accurate reconstruction of the comparison wave. Therefore, the hologram must be repositioned precisely at its original place. This can be done by using an adjustable plate holder, which can be purchased from the market. It is recommended to use a plate holder, where the final adjustment can be done via remote control, for example, with quartz crystals. The adjustment of the repositioned holographic plate gets its feedback control signals on an optical basis, because the adjustment has to be done in such a way that the interference fringes—at first visible due to nonprecise position of the plate—disappear during this procedure. This, certainly, has to be done without the heat transfer process having started. However, the same pressure and temperature exist in the fluid, under which the system is operated during the experiments.

A series of holographic interferograms taken with this method is illustrated in Fig. 13, where the boundary layer and the bubble formation at a heated horizontal surface, immersed in water, flowing slowly from the right to the left, was studied. The bulk temperature of the water was slightly below the saturation temperature and, therefore, the bubble is condensing after penetrating the superheated boundary layer near the wall. The black and white fringes in Fig. 13 represent lines of constant temperature in a first approximation. From this figure we can also learn something about the limitation, with which this and all other interferometric methods are afflicted. The temperature field in the fluid near the heated wall is not only shifting the phase of the light wave, it is also deflecting the light beam when traveling through it. This deflection has the consequence that with very high temperature gradients at the wall—as is the case in subcooled boiling—the zone immediately adjacent to the wall cannot be seen. With lower heat fluxes, this deflection is not a problem in interferometry.

The evaluation of the interference fringes and the derivation of the temperature field from the interference pattern as well as the calculation of the local heat transfer coefficients or the Nusselt numbers is the same as with the conventional interferometry, for example, the Mach-Zehnder-interferometry, and is well described in the literature (Hauf and Grigull, 1970; Hauf 1991). Therefore, the optical rules and the mathematical procedure are not presented here. Also the evaluation of spherical and cylindrical temperature fields by using the Abel correction can be found in the literature (Hauf and Grigull, 1970; Chen, 1985).

Evaluating a holographic interferogram by hand, as was done until a short time ago, was a very time consuming and tedious task. Today computerized evaluation is available, which reduces the time needed for deducing the local Nusselt numbers out of an interferogram from several hours down to a few seconds. For computerized evaluation one needs the same components as described in the chapter before, namely a video camera, a digitizer, a graphic monitor, and a PC. In the first step the procedure is very similar to that explained in Section 1. Also searching the gradients of greyness is similar, as briefly mentioned before. Then, however, a special algorithm has to be used to enhance the contrast of the grey steps to find the maximum of the greyness and to formulate the contour of the heat transferring wall in a digital way on the computer. Knowing the greyness maxima of the interference fringes and the digitized contour of the wall, one can determine the exact distances of the interference fringes—and by this of the isotherms—in the boundary layer near the wall. Isotherms usually run normal to the heat flux, and so knowing the position of the isotherms, one gets the temperature gradient orthogonal to the wall. By assuming sticking conditions at the wall, one can derive the local heat transfer coefficient from this tem-

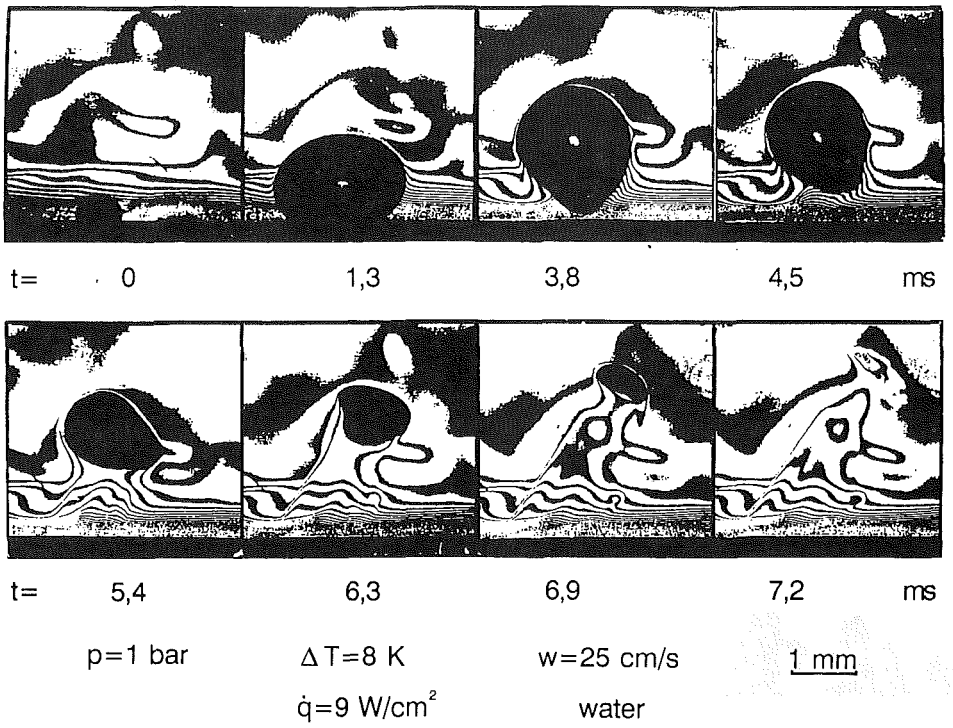

Fig. 13 Interferograms of subcooled boiling on a heated wall

perature gradient. For studying these various algorithmic procedures in detail, reference is made to a thesis by Klas (1993).

Here only the result of such a computerized evaluation will be briefly discussed as an example. Figure 14 shows the interference fringes and the local Nusselt numbers around an element of a compact heat exchanger designed for application in aviation at high altitudes with low atmospheric density. The computer automatically draws lines perpendicular to the surface of the heat transfer element and also lines of constant Nusselt numbers parallel to the surface of the heat transfer element. From the interference fringes it then calculates the local Nusselt numbers at each position of the element.

With very high heat transfer coefficients, the boundary layer at the wall usually becomes very thin, down to a few hundredths of a millimeter. In this case, it is difficult to evaluate the interference pattern if it is registered with the procedure described up to now. A slightly altered method, the so-called "finite fringe method," offers some benefits. In this method, after the reference hologram was produced, a pattern of parallel interference fringes is created by tilting the mirror in the reference wave of Fig. 15, or by moving the holographic plate there within a few wavelengths. The direction of the pattern can be selected as one likes, and it is only depending on the direction of the movement of the mirror or of the holographic plate.

This pattern of parallel interference fringes is then distorted by the temperature field due to the heat transfer process. The distortion or deflection of each fringe from its original parallel directions is a measure from the temperature gradient at this place and allows us to deduce the heat flux and by this the heat transfer coefficient.

Figure 16 demonstrates the possibilities of using these techniques in a flow with a bubble condensing in a liquid. By combining this method with high-speed cinematography, it allows an inertia-less and precise evaluation of the heat transfer coefficient at the phase interface of the condensing bubble. Holographic interferometry, certainly, can only be used if the flow situation is not too complicated and if the bubble population is not too numerous so that individual bubbles can be identified. It is not possible to look inside the bubbles, because the light is totally reflected at the phase interface.

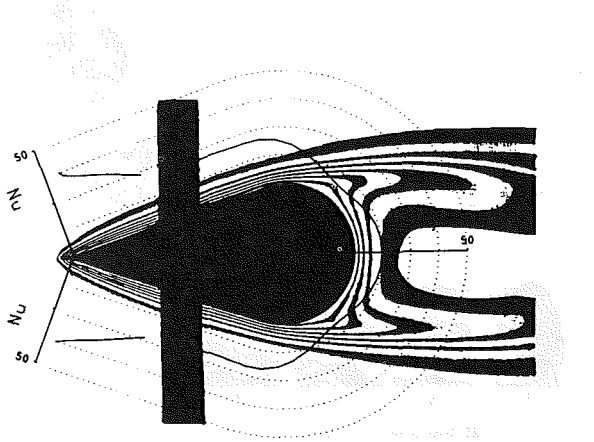

Fig. 14 Interferogram and local Nusselt numbers around a heat transfer element of a compact heat exchanger

2.2 Two-Wavelengths Method. The phase shift of the light wave when traveling through a gas or liquid is a function of the change in the density of the fluid. In pure substances the density depends only on temperature and pressure. In multicomponent systems the concentration also influences the density. Conventional interferometry, whether according Mach-Zehnder or on a holographic basis, works on the assumption that the alteration of the density is affected by a temperature change only. If variations in the refractive index are caused not only by a temperature, but also by a concentration change, this simple evaluation method is no longer possible. There is, however, a method to determine simultaneously the temperature and the concentration field by optical means, which was first proposed by El-Wakil et al. (1966), and which was further developed by Panknin (1977) and Panknin and Mayinger (1978) to the so-called "two-wavelengths holographic interferometry." It is performed by applying the dependence of the refractive index on the wavelength of the light. The problem

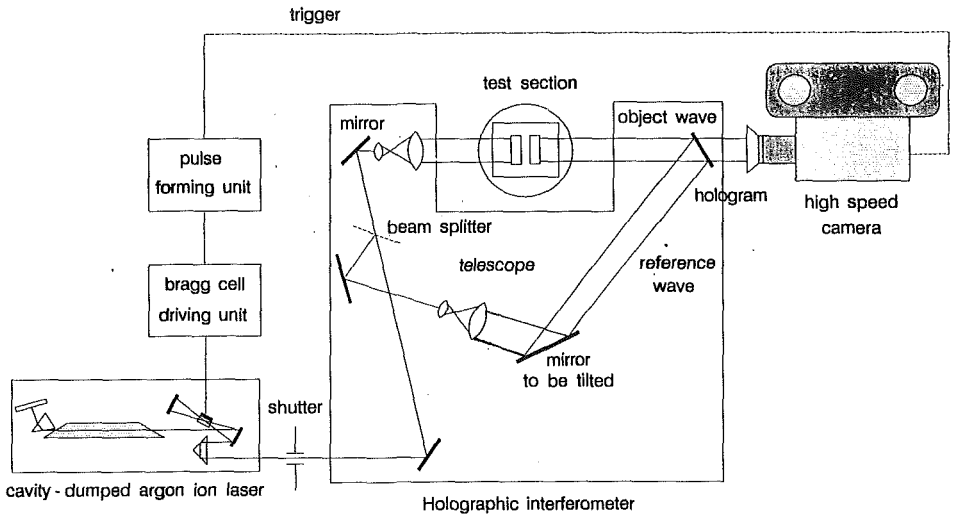

Fig. 15 Finite fringe method for holographic interferometry

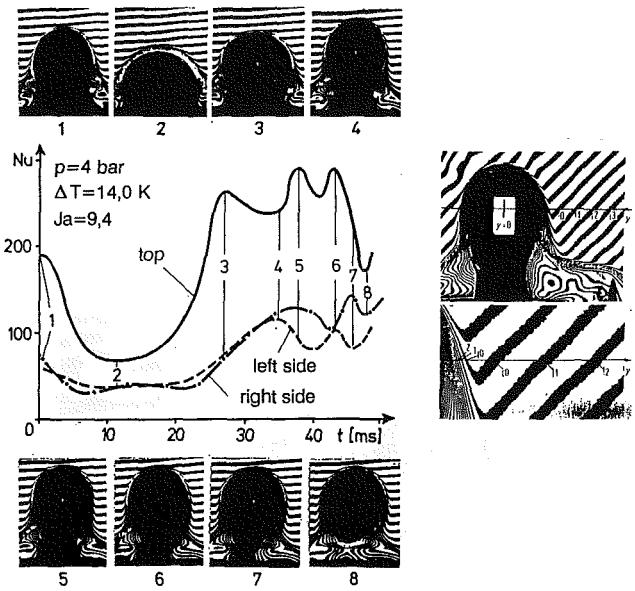

Fig. 16 Heat transfer at the phase interface of a vapor bubble condensing in a subcooled liquid, deduced from a sequence of interferograms

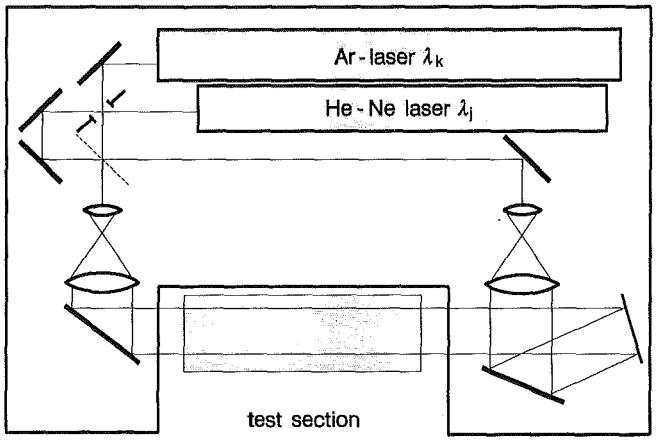

Fig. 17 Optical arrangement for holographic two-wavelength interferometry

with this two-wavelengths interferometry is that the two interferograms originating from these two beams of different wavelength have to be superimposed very accurately. Here, the peculiarity of the holography allowing the recording of different interference pattern on one and the same plate is a great help to overcome these difficulties. A simple setup for the holographic two-wavelength interferometry is shown in Fig. 17. It resembles very much the arrangement of Fig. 11, and actually the only difference is that two lasers are used as light sources, a He-Ne laser emitting red light, and an argon laser emitting green light. The two beams intersect, and at the position of this intersection a shutter is placed, which guarantees equal exposure times for both waves. The beams are then superimposed by means of a beam splitter, which results in two object and two reference waves at different wavelengths.

For the evaluation of the interferograms, some simple equations shall be presented. For a more detailed study, reference is made to the work by Panknin (1977). In an ideal gas, the Boyle-Mariott law is valid and the relation between fringe shift and temperature and concentration distribution can be easily formulated by

$$S(x, y)\lambda = \frac{3pl}{2R} N_m \left[\frac{1}{T(x, y)} - \frac{1}{T_\infty} \right] \tag{1}$$

In this equation S is the multiple of a wavelength, and l is the length of the test section, in which the refractive index is varied. R and p stand for the gas constant and the absolute pressure, respectively. The molar refractivity N_m of a mixture of two gaseous components is given by

$$N_m = N_a C_a + N_b C_b; \text{ with } C_a + B_b = 1 \tag{2}$$

where N_a and N_b are the molar refractivities of the components and C is the concentration of the component in the mixture. During recording of the comparison wave, the temperature distribution T in the test section is constant, and there are only two components of the mixture.

Combining Eqs. (1) and (2), we obtain for each wavelength

$$S(x, y)\lambda = \frac{3pl}{2R} \left[\frac{1}{T(x, y)} \left(N_a + C_b(x, y)\right)\left(N_b - N_a\right) - \frac{N_a}{T_\infty} \right] \tag{3}$$

Eliminating $C_b(x, y)$, the temperature $T(x, y)$ can be calculated by using information from both wave-lengths λ_j and λ_k

$$S_j(x, y) \frac{\lambda_j}{N_{bj} - N_{aj}} - S_k(x,y) \frac{\lambda_k}{N_{bk} - N_{ak}} = \frac{3pl}{2R} \left[\frac{1}{T(x, y)} - \frac{1}{T_\infty} \right] \left[\frac{N_{aj}}{N_{bj} - N_{aj}} - \frac{N_{ak}}{N_{bk} - N_{ak}} \right] \tag{4}$$

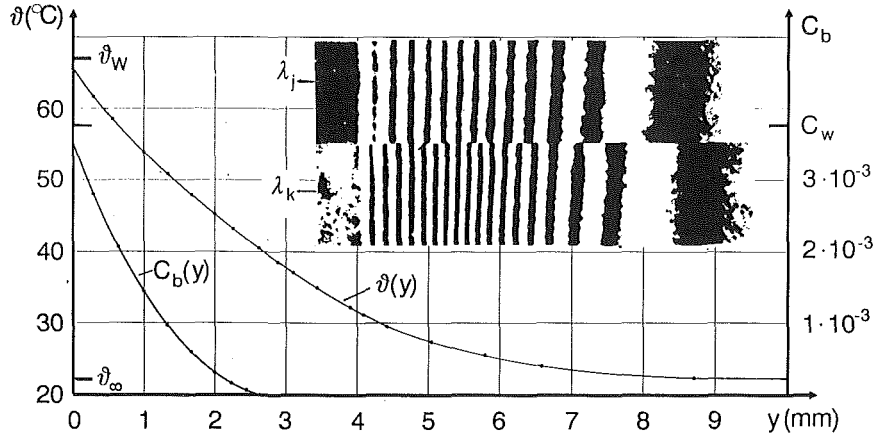

Fig. 18 Two-wavelength interferogram of combined heat and mass transfer by free convection from a vertical plate

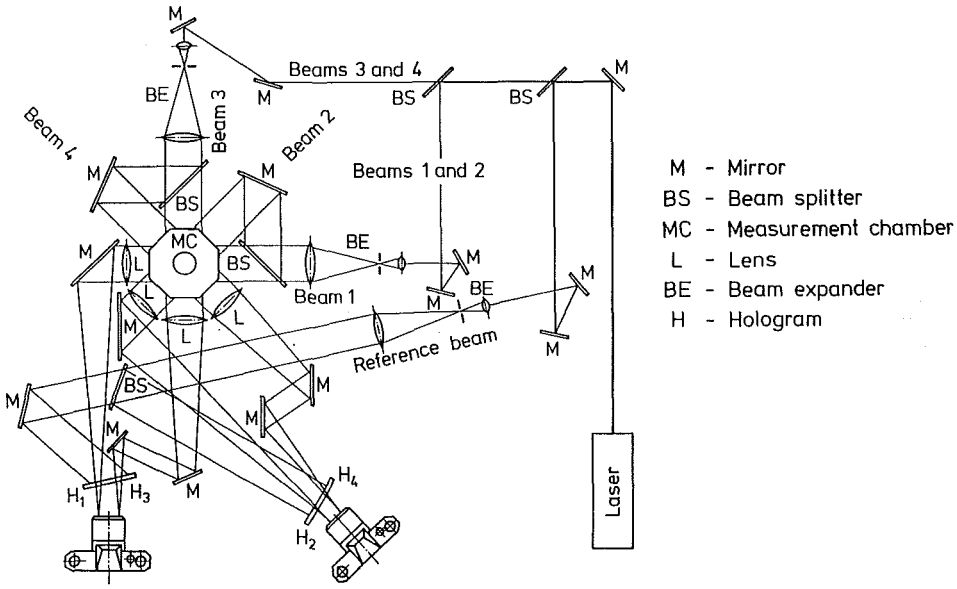

Fig. 19 Optical arrangement for holographic interferometry on a tomographic basis

After determining the temperature distribution, only one interferogram is needed to calculate the concentration profile.

Equation (4) shows that it is the difference between the phase shifts of the two wavelengths that is used for evaluating the temperature. This difference is usually very small. Therefore, the two wavelengths used should be as far apart as possible. The fact that the wavelengths have to be in or near the visible range of light limits the applicability of the method.

A simple example of application for the two-wavelength technique is shown in Fig. 18. A vertical plate was paved with naphthalene and heated. The heat and mass transfer were generated by a natural convective upward air-flow. In order to demonstrate the differences in the phase shift, only the upper and lower halves of each interferogram are shown, and the evaluation is made at the intersection of these two interferograms.

Heat and mass transfer experiments can also be performed in a burning flame as Panknin (1977) demonstrated.

2.3 Interferometric Tomography. The holographic-interferometric methods discussed up to now do not allow us to evaluate a three-dimensional temperature field of complicated local structure, because each beam traveling through the temperature field is integrating all local situations on its way. For a multidimensional information, the volume of interest has to be irradiated from various directions, and a tomographic method can be used to evaluate the various interference patterns and integrate them to a three-dimensional picture.

Figure 19 presents an example of a holographic setup for multidimensional irradiation (Mayinger and Lübbe, 1984; Lübbe, 1982; Ostendorf et al., 1986). The vessel with its volume to be investigated is irradiated via four different object waves spanning an angle of 135 deg. To avoid deflection of the light at curved surfaces of the glass vessel, the outer surrounding of the vessel is arranged in an octagonal form so that each of the beams hits a plain surface in the orthogonal direction. Only the inner vessel is of cylindrical shape. To avoid a deflection of the light at the surface of this inner vessel, a liquid is filled in the annular space between the outer and the inner vessel, which has exactly the same refractive index as the glass of these vessels. After hitting the mirror M, the light of the laser travels to two adjustable beam splitters BS. The first beam splitter fades out the reference wave, and the second beam splitter produces four different object waves, which are expanded via microlenses. A prefocusing of the object waves is produced by four lenses. The arrangement is organized in such a way that it is possible to store two interferograms of high quality on one holographic plate. By proper arrangement of the mir-

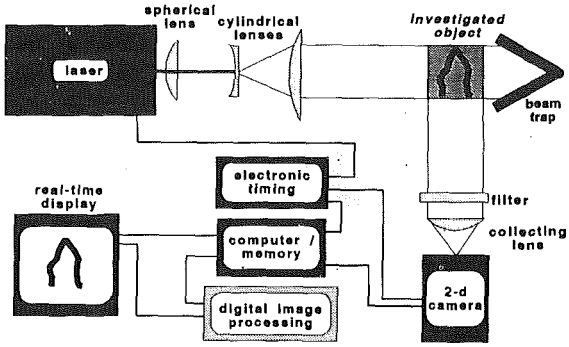

Fig. 20 Experimental arrangement for planar laser-induced fluorescence

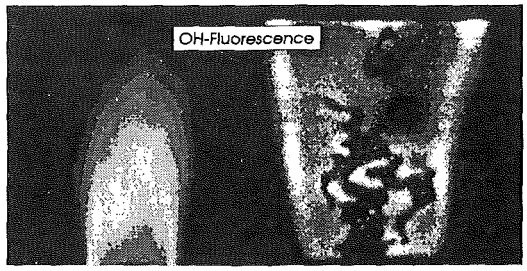

Fig. 21 Laser-induced fluorescence (right-hand side) and self-induced fluorescence (left-hand side) from a Bunsen flame

rors, lenses, and beam splitters, it is possible to make the length of the optical paths of the reference waves and of the objects waves almost equal so the demand on the coherence length of the laser can be moderate. The procedure can be combined with real-time holography, and cinematographic recording is also possible.

3 Laser-Induced Fluorescence

Light is comprised of much information and not only the phase shift can be used to get information about the distribution of temperature or concentration in a gas or fluid. Besides the phase shift, the effect of scattering is most commonly used to get information about the chemical and physical conditions of a substance. Raman scattering is a method, which allows us to measure the variety of substances present in a mixture, the concentration of each species, and under certain circumstances also the temperature. Rayleigh scattering can be used as a nonintrusive method for measuring the temperature, and the fluorescence indicates the kind and the density of atoms and molecules and also allows us to deduce the temperature. Of course, there are also other scattering methods, like Mie scattering used in phase-Doppler velocimetry, Bragg scattering for detecting density fluctuations and for investigating the structure of crystals, and Brillouin scattering for measuring sound velocity and sound absorption. Here only the fluorescence used together with a light-sheet method will be discussed, because it is an image-forming process.

The laser-induced fluorescence is based on the fact that when the molecule under investigation is absorbing a photon of the incoming light, the molecule is transferred to a state of higher energy for a short period and falls back to its original energy level when light is emitted. The fluorescence signal determines the type of species via the wavelength, and the intensity of the fluorescence can be used for determining the concentration. Also the temperature of the gas under investigation can be obtained by different techniques, which are based on temperature-dependent equilibrium distribution of the population among the energy levels. This can be done by either exciting different transitions and observing the total light emission or by spectral analysis of the emitted light after broadband excitation. Besides the standard Laser-Induced-Fluorescence (LIF), there has also recently been proposed a slightly altered method in the literature, the Laser-Induced-Predissociation-Fluorescence (LIPF) (Andresen et al., 1988).

The theory about fluorescence is very comprehensive and cannot be discussed in detail here. Therefore, reference is made to the literature (Hanson, 1986, 1990). Here only the experimental setup and the measuring procedure are briefly discussed.

Figure 20 shows an example of a setup for planar fluorescence (LIF) measurements. The laser beam of circular cross section is transformed into a thin light sheet by cylindrical lenses. The thickness of the light sheet determines the spatial resolution and is usually on the order of 100 m. The height of the light sheet depends on the power of the laser and on the format of the camera to be used for observation. A usual value is 50 mm. The light sheet travels through the volume to be investigated. Orthogonal to the light sheet a CCD camera is arranged, which registers the fluorescence induced by the light sheet via a filter and a collecting lens. By using the filter, only the fluorescence signal is observed by the detector in the camera. Usually the solid-state camera is equipped with a gateable image intensifier. The intensity data of the two-dimensional image are transferred from the camera to a data acquisition system, where they are evaluated by a computer. The data are stored in grey scale values, and the resolution capacity depends on the dynamic range of the camera and the intensity of the emitted light. The processed image is finally displayed in false color pictures, where a certain color is associated with a distinct intensity range.

Modern developments in laser and camera technology as well as the modern standard of digital image-processing have led to several LIF applications. Here only one application is presented, namely the investigation of flames, and this example is restricted to hydrogen combustion. To make understanding easier, the flame of a Bunsen burner is investigated. For a better impression, the fluorescence image is compared with a photograph of the glowing flame. The photograph of the left-hand side of Fig. 21 shows only the conical form of the flame and in reality it represents the total fluorescence of the gas produced by the high temperature in the reaction zone. This can be called self-fluorescence. On the right-hand side of Fig. 21, the fluorescence induced by an Excimer laser is registered selectively, monitoring the fluorescence of the OH molecules only, which are emitting light at 308 nm. The laser beam is irradiating a very thin sheet of the flame only, and, therefore, a two-dimensional picture results. The presence of OH indicates the zone of highest reactivity characterizing the center of the flame. The centers of highest reaction are represented by the light zones and spots in the LIF image. The main reaction takes place in a narrow zone near the outer surface of the jet. Due to strong mixing turbulence produced by a flame holder in the center of the mouth of the burner, there are also some high reaction spots in the center of the jet. For a complete, three-dimensional investigation of the flame, the light sheet has to be moved stepwise forward and backward to record the flame layer by layer.

Finally one can combine various optical methods, for example, holographic interferometry and fluorescence to study combustion processes (Mayinger and Haibel, 1992). Figures 22 and 23 present an example of such a combination. The combustion zone of a hydrogen flame was studied in this example, however, under the condition of very high air velocities. The combustion process is controlled by two phenomena, namely the heat and mass transfer and the reaction kinetics. In a diffusion flame, the mass transport usually dominates the combustion. Therefore, this mass transport is of interest at first. It was investigated in a modeling experiment where in-

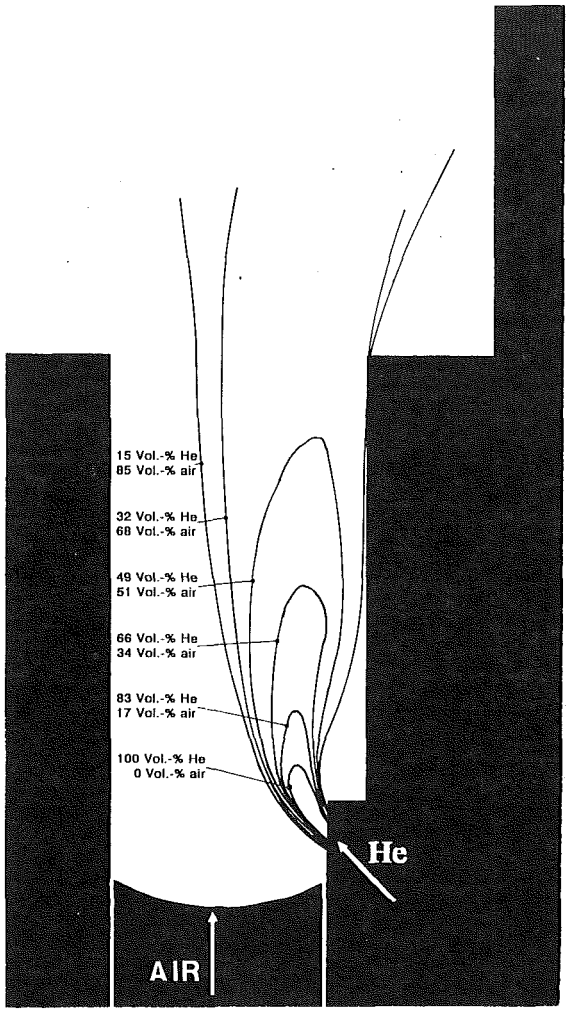

Fig. 22 Concentration distribution in the mixing zone of a high velocity flame; cold experiment with helium as modeling fluid

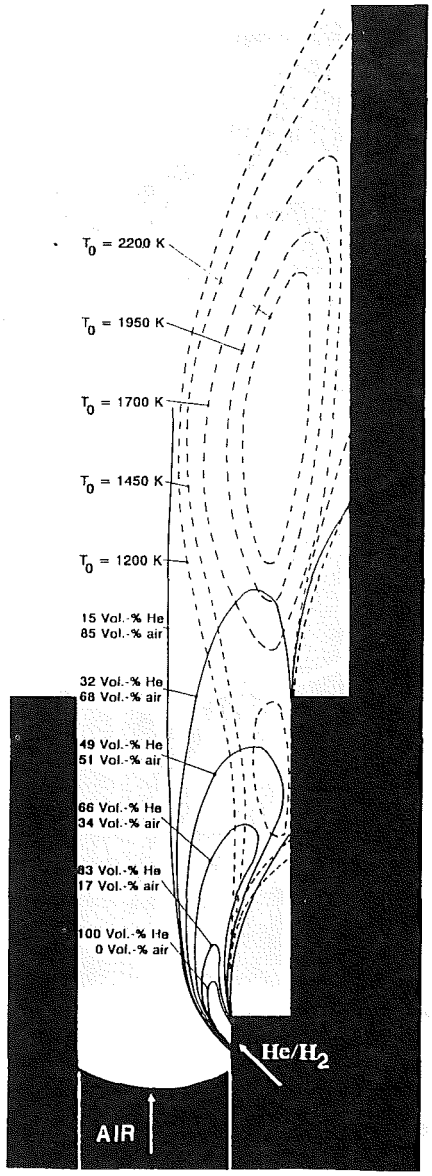

Fig. 23 Readings of the helium mixing experiments superimposed on the isotherms of the burning flame

stead of hydrogen, helium was injected into a high-velocity channel through a tiny nozzle. The concentration of the helium in the channel behind the injection spot was measured by holographic interferometry. The intention was to get a clear insight into the mixing process at first, and, therefore, nonflammable helium was used, having a similar high sound velocity to hydrogen. Figure 22 clearly shows the concentration distribution of the helium in the high velocity air stream.

For a high-speed, high-turbulence flame, the minimum concentration of the fuel must not be too low in order to avoid that the turbulent mixing extinguishing the flame instead of agitating it. One can assume that for a hydrogen flame, a fuel concentration of 10–15 volumetric percent may be a minimum for flame acceleration. Therefore, in Fig. 22 the line of 15 volumetric percent helium can be roughly regarded as the outer border where a high-speed flame can exist.

In Fig. 23 the readings of the helium-mixing experiments are superimposed by isotherms of the burning flame—with hydrogen as fuel—which result from a combined measuring technique of holographic interferometry and a self-induced fluorescence method. The figure clearly conveys the information that the ignition starts in the recirculation zone behind the step in the channel where the air concentration is rather low, but good enough for a first reaction to form radicals like OH. The main combustion takes place far downstream of the spot where the hydrogen was injected, namely in the area where the hydrogen concentration in the air is between 10 and 15 volumetric percent. The superposition of information gained by holographic interferometry and fluorescence proves a good agreement concerning the mixing and the reaction process.

Finally in Fig. 24 it is demonstrated that holographic interferometry not only can register heat and mass transfer processes—like mixing of fuel and air—but also is good for detecting shock fronts in a supersonic flow. In the same channel, as discussed in Figs. 22 and 23, again helium is injected into air, which, however, is now flowing with supersonic velocity upstream of the injection spot. The injection of the fuel not only disturbs the boundary layer, but also displaces the air flow, which finally results in a diagonal compression shock, starting at the boundary between mixing zone and undisturbed air flow downstream of the injection spot. In Fig. 24 the finite fringe method was used, and, therefore, parallel oriented fringes indicate none or weakly influenced air flow.

4 Concluding Remarks

Optical methods are expected to experience a powerful revival due to three reasons:

Sophisticated theoretical treatment of heat and mass transfer processes with large computer codes needs very detailed in-

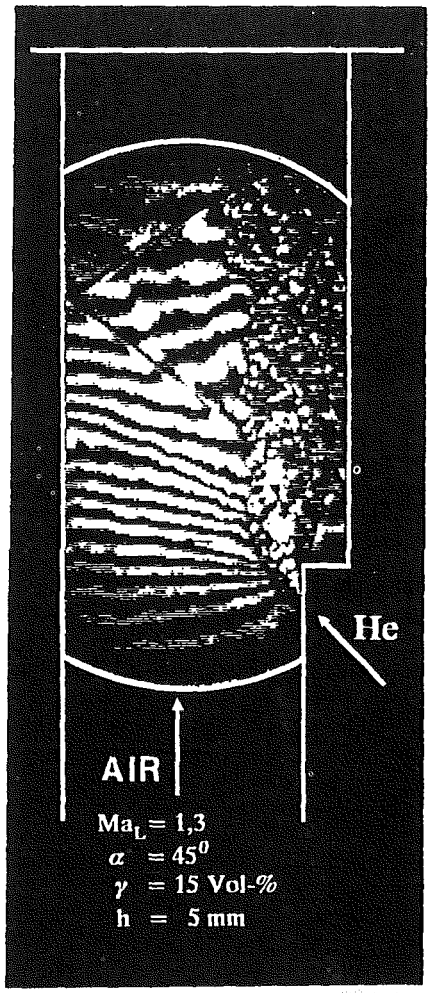

Fig. 24 Interferogram of mixing jet with a shock front in a Laval nozzle

formation about temperature and concentration fields in the area of interest for accessing and improving the physical models used in codes and for verifying such codes. An optically determined pattern of isotherms is a very stringent touchstone for the reliability and accuracy of a code.

Modern developments in power and process engineering make transient situations more and more interesting, especially for controlling procedures and safety deliberations. Optical measuring techniques work inertia-less and nonintrusively.

A former drawback of the image-forming optical measuring techniques, the laborious and time-consuming evaluation, does not exist anymore. Even a personal computer is good enough for evaluating a hologram or an interferogram within a few seconds, a process that took several hours in the past. The costs of such an evaluating equipment are relatively moderate.

A new symbiosis could come into being between theorists and experimentalists, working in heat and mass transfer.

References

Andresen, P., Bath, A., Gröger, W., Lülf, H. W., Meijer, G., and ter Meulen, J. J., 1988, "Laser-Induced Fluorescence With Tunable Excimer Lasers as a Possible Method for Instantaneous Temperature Field Measurements at High Pressures: Check With an Atmospheric Flame," *Appl. Optics*, Vol. 27(2), p. 365.

Caulfield, H. J., and Lu, Sun, 1971, *The Applications of Holography*, Wiley Interscience, New York.

Chavez, A., and Mayinger, F., 1990, "Evaluation of Pulsed Laser Holograms of Spray Droplets by Applying Image Processing," *9th International Conference on Heat Transfer*, p. 187.

Chavez, A. A., 1991, "Holografische Untersuchung an Einspritzstrahlen—Fluiddynamik und Wärmeübertragung durch Kondensation," Diss. Techn. Univ. München, Federal Republic of Germany.

Chavez, A., and Mayinger, F., 1992, "Measurement of Direct-Contact Condensation of Pure Saturated Vapour on an Injection Spray by Applying Pulsed Laser Holography," *Int. J. Heat Mass Transfer*, Vol. 35, No. 3, pp. 691–702.

Chen, Y. M., 1985, "Wärmeübertragung an der Phasengrenze kondensierender Blasen," Diss. Techn. Univ. München, Federal Republic of Germany.

El-Wakil, X. X., Myers, G. E., and Schilling, R. J., 1966, "An Interferometric Study of Mass Transfer From a Vertical Plate at Low Reynolds Numbers," ASME JOURNAL OF HEAT TRANSFER, Vol. 88, pp. 399–406.

Hanson, R. K., 1986, "Combustion Diagnostics: Planar Imaging Techniques, *18th Symp. (Intl.) on Combustion*, The Combustion Institute, Pittsburgh, PA.

Hanson, R. K., Seitzmann, J. M., and Paul, P. H., 1990, "Planar Fluorescence Imaging of Gases," *Applied Physics*, Vol. B50, pp. 441–454.

Hauf, W., and Grigull, U., 1970, "Optical Methods in Heat Transfer," *Advances in Heat Transfer*, Vol. 6, p. 133.

Hauf, W., 1991, "Das Mach-Zehnder-Interferometer," in: *Optische Meßverfahren in der Wärme- und Stoffübertragung*, U. Grigull, ed., Springer-Verlag, Berlin, pp. 70–130.

Kiemle, H., and Röss, D., 1969, *Einführung in die Technik der Holographie*, Akademische Verlagsgesellschaft, Frankfurt, Federal Republic of Germany.

Klas, J., 1993, "Wärmeübertragung in Strömungskanälen ohne und mit Turbulenzpromotoren," Diss. Techn. Univ. München, Federal Republic of Germany.

Lighthart, G., and Groen, C. A., 1982, "A Comparison of Different Autofocus Algorithms," *IEEE Trans.*, Vol. XX, pp. 597–604.

Lübbe, D., 1982, "Ein Messverfahren für instationäre dreidimensionale Verteilungen und seine Anwendung auf Mischvorgänge," Diss. Universität Hannover, Federal Republic of Germany.

Mayinger, F., and Panknin, W., 1974, "Holography in Heat and Mass Transfer," *5th Int. Heat Transfer Conference*, Tokyo, Vol. VI, p. 28.

Mayinger, F., and Lübbe, D., 1984, "Ein tomographisches Messverfahren und seine Anwendung auf Mischvorgänge und Stoffaustausch. 2," *Wärme- und Stoffübertragung*, Vol. 18, pp. 49–59.

Mayinger, F., 1991, "Holographie und holographische Interferometrie in Optische Meßverfahren in der Wärme- und Stoffübertragung," U. Grigill, ed., Springer-Verlag, Berlin, pp. 194–225.

Mayinger, F., and Haibel, M., 1992, "Turbulenz-gestützte Gemischbildung und Stabilisierung von sub- und supersonischen Wasserstoff-Luft-Flammen," *DGLR-Jahrbuch*, Bremen, Federal Republic of Germany.

Ostendorf, W., Mewes, D., and Mayinger, F., 1986, "A Tomographical Method Using Holographic Interferometry for the Registration of Three-Dimensional Unsteady Temperature Profiles in Laminar and Turbulent Flow," *Heat Transfer 1986, Proc. of the 8th Int. Heat Transfer Conference*, C. L. Tiens, et al., eds., Hemisphere Publ. Corp., New York, Vol. 2, pp. 519–524.

Panknin, W., 1977, "Eine holographische Zweiwellenlängen-Interferometrie zur Messung überlagerter Temperatur- und Konzentrationsgrenzschichten," Ph.D. thesis, Techn. Universität Hannover, Federal Republic of Germany.

Panknin, W., and Mayinger, F., 1978, "Anwendung der holographischen Zweiwellenlängen-interferometrie zur Messung überlagerter Temperatur- und Konzentrationsgrenzschichten," *Verfahrenstechnik*, Vol. 12, No. 9, pp. 582–589.

Smith, H. M., 1969, *Principles of Holography*, Wiley, New York.

Heat Transfer Mechanisms During Short-Pulse Laser Heating of Metals

T. Q. Qiu
Postdoctoral Fellow.

C. L. Tien
A. Martin Berlin Professor,
Fellow ASME

Department of Mechanical Engineering,
University of California,
Berkeley, CA 94720

This work studies heat transfer mechanisms during ultrafast laser heating of metals from a microscopic point of view. The heating process is composed of three processes: the deposition of radiation energy on electrons, the transport of energy by electrons, and the heating of the material lattice through electron-lattice interactions. The Boltzmann transport equation is used to model the transport of electrons and electron-lattice interactions. The scattering term of the Boltzmann equation is evaluated from quantum mechanical considerations, which shows the different contributions of the elastic and inelastic electron-lattice scattering processes on energy transport. By solving the Boltzmann equation, a hyperbolic two-step radiation heating model is rigorously established. It reveals the hyperbolic nature of energy flux carried by electrons and the nonequilibrium between electrons and the lattice during fast heating processes. Predictions from the current model agree with available experimental data during subpicosecond laser heating.

Introduction

Short-pulse lasers with pulse duration ranging from nanoseconds to femtoseconds have developed rapidly since the 1980s. To date, the shortest achievable laser pulse has reached six femtoseconds (6×10^{-15} s). Due to the ability to control the location and depth of heating precisely and to realize high heating/cooling rates, new technologies based on short-pulse laser heating have made tremendous impacts in microelectronics processing and material processing, as well as fundamental scientific studies. These abundant applications of short-pulse lasers require a better understanding of radiation heating mechanisms.

Laser heating of metals involves three general steps: the deposition of radiation energy on electrons, the energy exchange between electrons and the lattice, and the propagation of energy through media. There exist two characteristic times for these processes: the thermalization time and the relaxation time. The thermalization time is the typical time for electrons and the lattice to reach thermal equilibrium. It represents the finite time needed to convert radiation energy to internal energy of the lattice. The relaxation time is the mean time for electrons to change their states. It characterizes whether the transport of electrons is diffusive or ballistic. During a relatively slow heating process, the deposition of radiation energy can be assumed to be instantaneous and the propagation of energy can be modeled by the Fourier conduction model. For very short laser-pulse heating, these assumptions are subject to question. More general and rigorous models are needed to include effects of electron-lattice interactions and non-Fourier transport.

The energy exchange between electrons and the lattice was first evaluated theoretically by Kaganov et al. (1957) and was observed by many researchers recently (e.g., see Eesley, 1983; Brorson et al., 1987). Anisimov et al. (1974) proposed a phenomenological two-step model to describe the electron temperature and the lattice temperature during short-pulse laser heating of metals. This model, however, has not been rigorously derived. Furthermore, it predicts an infinite speed of energy transport, which is contradictory to the observed finite speed of energy propagation (Brorson et al., 1987).

Contributed by the Heat Transfer Division and presented at the ASME National Heat Transfer Conference, San Diego, California, August 10–12, 1992. Manuscript received by the Heat Transfer Division July 1992; revision received March 1993. Keywords: Laser Processing, Materials Processing and Manufacturing Processes, Radiation Interactions. Technical Editor: R. Viskanta.

Non-Fourier heat conduction models have long been proposed to remove the problems associated with the Fourier model, e.g., its failure to predict second sound in solids and finite speeds of energy propagation (Joseph and Preziosi, 1989). For example, Maurer (1969) derived a hyperbolic heat conduction model for metals. Its predictions are significantly different from those predicted from the parabolic Fourier model (e.g., see Özişik and Vick, 1984; Tzou, 1992). Since non-Fourier models neglect the energy exchange between electrons and the lattice, their applicability to short-pulse laser heating of metals is questionable.

The purpose of this paper is to present a more general and rigorous model to describe energy transport during short-pulse laser heating of metals. The model is derived from the Boltzmann transport equation for electrons. Its predictions agree with reported subpicosecond laser heating experiments. Under different conditions the current model can be simplified to either the two-step model of Anisimov et al. (1974) or to Maurer's hyperbolic heat conduction model (1969).

Microscopic Energy Deposition and Transport

From the microscopic point of view, energy deposits into materials in different ways, depending on the nature of heating methods and the structure of materials. For example, it can deposit simultaneously on all energy carriers through contact heating at surfaces, e.g., electrons and phonons (vibrations of the lattice), or selectively on a particular group of carriers by radiation heating. Radiation heating excites free/bound electrons in metals, but excites valence electrons or optical phonons in semiconductors, depending on the radiation wavelength. These different mechanisms of heating become important when the time scale of interest is comparable with the characteristic time for different energy carriers to communicate with each other. In this case, the energy transport by each group of carriers and the interactions among them need to be considered.

The transport of energy carriers can be treated, under a quasi-classical particle framework, by the Boltzmann transport equation,

$$\frac{\partial f}{\partial t} + V_x \frac{\partial f}{\partial x} + \frac{F_x}{m} \frac{\partial f}{\partial V_x} = \left[\frac{\partial f}{\partial t}\right]_s \tag{1}$$

It expresses the total rate of change of the particle distribution function $f(\mathbf{r}, \mathbf{V}, t)$ as the result of diffusion, external field

driving, and scattering, respectively. The scattering term describes the change of particle numbers at an energy state due to collisions. To make the problem more tractable, the following three assumptions are made: (1) Electron-phonon interaction is the dominant scattering process for electrons; (2) the conduction of heat by phonons is negligible; and (3) phonons and electrons have temperatures T_l and T_e, respectively.

Assumptions 1 and 2 are justified for most pure metals. Only for metals containing a large amount of impurities, or for some very particular metals, like bismuth, does the lattice thermal conduction become important (Makinson, 1938). Fann et al. (1992) have shown that after the initial period of laser heating (a few hundred femtoseconds) the electron subsystem is well thermalized and the electron temperature is well defined. During the initial heating period, the electron subsystem is slightly away from thermal equilibrium and can be approximately characterized by an effective electron temperature. The phonon subsystem is commonly assumed to be in thermal equilibrium and is described by the phonon temperature (Allen, 1987; Fann et al., 1992; Groeneveld et al., 1992; Juhasz et al., 1992).

Solution Aproaches. The conventional approaches to solve the Boltzmann equation use three basic approximations: (1) the relaxation time approximation, (2) the steady-state approximation, and (3) the near-equilibrium approximation (Bube, 1974). Based on these approximations, the scattering term can be expressed explicitly in terms of the relaxation time, and the total rate of change of the distribution function can be neglected. The solution leads to the classical Fourier law. However, these approximations are subject to question in short-time-scale processes. For instance, it has not yet been proven that the scattering term can be generally expressed by an equivalent relaxation time when different energy carriers have different temperatures. Even if the relaxation time approximation is still valid, it is not clear which temperature the relaxation time should be based on. The validity of the second approximation can be checked roughly by comparing the relative importance of the total rate of change term with the diffusion term

$$\frac{\dfrac{\partial f}{\partial t}}{V_x \dfrac{\partial f}{\partial x}} = \frac{\dfrac{\partial f_{eq}}{\partial T}\dfrac{\partial T}{\partial t}}{V_F \dfrac{\partial f_{eq}}{\partial T}\dfrac{\partial T}{\partial x}} \sim \frac{\dfrac{\Delta T}{t_p}}{V_F \dfrac{\Delta T}{\delta}} = \frac{\delta}{V_F t_p} \tag{2}$$

in which V_F is the speed of electrons of the Fermi energy, δ is the radiation penetration depth, and t_p is the pulse duration. For typical metals, δ is about 10^{-8} m and V_F is about 10^6 m/s. When t_p is of order of 10^{-14} s, the total rate of change term is comparable with the diffusion term and the steady-state assumption may break down. The third assumption is valid as long as the states are not far from equilibrium. This study eliminates the relaxation time approximation and the steady-state approximation and solves the Boltzmann equation only with the near-equilibrium approximation. It will first evaluate the scattering term of the Boltzmann equation and then find the electron distribution function. Integrating all the energy carried by free electrons will lead to the heat flux.

Electron-Phonon Scattering. Electron-phonon scattering processes redistribute the number of electrons among energy states. During the scattering processes, electrons can be forced into or ejected from a certain energy state, $\mathbf{k}$, by either emitting or absorbing phonons. The electron wavevector $\mathbf{k}$ correlates to the electron velocity $\mathbf{V}$ through its momentum,

$$m\mathbf{V} = h\mathbf{k}/2\pi \tag{3}$$

where h is Planck's constant. The transition probability of electrons from a $\mathbf{k}'$ state to the $\mathbf{k}$ state by emitting a phonon is proportional to $f'(1-f)(N+1)$, where f' is the probability of finding an electron at the $\mathbf{k}'$ state, $1-f$ is the probability of finding an unoccupied space in the $\mathbf{k}$ state, N is the average number of phonons with a wavevector $\mathbf{q}$, and $N+1$ represents phonon emission probability, which, like photon emission, includes the stimulated emission and the spontaneous emission processes. The transition satisfies both the conservation of energy,

$$E_{\mathbf{k}} - E_{\mathbf{k}'} + h\nu = 0 \tag{4}$$

and the conservation of momentum,

$$\mathbf{k} - \mathbf{k}' + \mathbf{q} = 0 \tag{5}$$

where E is the electron energy and $h\nu$ is the energy of the emitted phonon. The transition probability from the $\mathbf{k}$ state to the $\mathbf{k}'$ state by absorbing a phonon is proportinal to $f(1-f')N$. In a similar way the probabilities of transitions from $\mathbf{k}'$ to $\mathbf{k}$ states by absorbing a phonon and from $\mathbf{k}$ to $\mathbf{k}'$ states by emitting a phonon are proportional to $f'(1-f)N$ and $f(1-f')(N+1)$, respectively. The total change rate of

Nomenclature

B = constant defined in Eq. (6*b*)
C = heat capacity, $\mathrm{Jm^{-3}\,K^{-1}}$
D = density of states, $\mathrm{m^{-3}\,J^{-1}}$
e = electron charge, C
E = electron energy, J
f = distribution function of electrons
F = laser energy flux, $\mathrm{Jm^{-2}}$
F_x = external driving force, N
G = electron-phonon coupling factor, $\mathrm{Wm^{-3}\,K^{-1}}$
h = Planck's constant, Js
I = laser intensity, $\mathrm{Wm^{-2}}$
J = electrical current, amp
$\mathbf{k}$ = electron wave vector, $\mathrm{m^{-1}}$
K = integral defined in Eq. (20*c*)
k_B = Boltzmann constant, $\mathrm{JK^{-1}}$
L = film thickness, m
m = effective mass of electrons, kg
M = atomic mass, kg
n = electron number density, $\mathrm{m^{-3}}$
N = distribution function of phonons
$\mathcal{P}$ = transient matrix element
$\mathbf{q}$ = phonon wave vector, $\mathrm{m^{-1}}$
Q = heat flux, $\mathrm{Wm^{-2}}$
R = metal surface reflectivity
S = source term, $\mathrm{Wm^{-3}}$
t = time, s
t_c = electron-phonon thermalization time = C_{eo}/G, s
t_p = laser pulse duration, s
T = temperature, K
T_D = Debye temperature, K
u = speed of sound, $\mathrm{ms^{-1}}$
U = energy exchange rate between electrons and phonons, $\mathrm{Wm^{-3}}$
V = speed of electrons, $\mathrm{ms^{-1}}$
x = spatial coordinate, m
α = radiation absorption coefficient, $\mathrm{m^{-1}}$
δ = radiation penetration depth, m
Δ = volume of the unit cell, $\mathrm{m^3}$
ϵ = electrical field intensity, $\mathrm{Vm^{-1}}$
γ = electron heat capacity constant, $\mathrm{Jm^{-3}\,K^{-2}}$
κ = thermal conductivity, $\mathrm{Wm^{-1}\,K^{-1}}$
Λ = constant defined in Eq. (12*c*)
ν = phonon frequency, $\mathrm{s^{-1}}$
τ = electron mean free time between collisions, s
ϕ = a function defined in Eq. (10)
Ω = delta function defined in Eq. (6*c*)

Subscripts

0 = reference temperature
e = electron
eq = equilibrium
F = Fermi surface
l = lattice

electron numbers in the **k** state due to electron-phonon scattering is then the sum of the above transitions (Wilson, 1953)

$$\left[\frac{\partial f}{\partial t}\right]_s = B\int \frac{|\mathbf{q}|^2}{\nu}\{[f'(1-f)(N+1)-f(1-f')N]\cdot\Omega^+ + [f'(1-f)N-f(1-f')(N+1)]\cdot\Omega^-\}d\mathbf{q} \quad (6a)$$

$$B=\frac{\mathcal{P}^2\Delta}{8\pi^3 Mh} \quad (6b)$$

$$\Omega^+=\delta(E_{\mathbf{k}}-E_{\mathbf{k}'}+h\nu); \quad \Omega^-=\delta(E_{\mathbf{k}}-E_{\mathbf{k}'}-h\nu) \quad (6c)$$

where $\mathcal{P}$ is the transition matrix element, Δ is the volume of the unit cell, and M is the atomic mass. The delta function, δ, represents the requirement of the energy conservation on electronic transitions. The integration is performed in the three-dimensional **q** space, using the notation

$$d\mathbf{q}=dq_x dq_y dq_z = q^2\sin\theta dq d\theta d\varphi \quad (7)$$

At equilibrium, f and N are the Fermi–Dirac distribution function and the Bose–Einstein distribution function, respectively, given as

$$f_{eq}=\frac{1}{1+\exp((E-E_F)/k_B T_e)} \quad (8)$$

$$N=\frac{1}{\exp(h\nu/k_B T_l)-1} \quad (9)$$

where E_F is the Fermi energy.

Due to the heating effects, the electron distribution function can be written as the sum of f_{eq} and a small perturbation,

$$f=f_{eq}-\phi\frac{\partial f_{eq}}{\partial E}=f_{eq}(1+\phi(1-f_{eq})/k_B T_e) \quad (10)$$

Substituting Eqs. (8)–(10) into Eq. (6) yields

$$\left[\frac{\partial f}{\partial t}\right]_s=\left[\frac{\partial f}{\partial t}\right]_{s1}+\left[\frac{\partial f}{\partial t}\right]_{s2} \quad (11a)$$

$$\left[\frac{\partial f}{\partial t}\right]_{s1}=Bf_{eq}(1-f_{eq})\int\frac{|\mathbf{q}|^2}{\nu}\frac{f'_{eq}}{f_{eq}} \times N[(e^z-e^{z_e})\Omega^+ + (1-e^{z-z_e})\Omega^-]d\mathbf{q} \quad (11b)$$

$$\left[\frac{\partial f}{\partial t}\right]_{s2}=\frac{B}{k_B T_e}\int\frac{|\mathbf{q}|^2}{\nu}f'_{eq}(1-f_{eq})N\{[-\phi f_{eq}+\phi'(1-f_{eq})] \cdot(e^z\Omega^+ +\Omega^-)-[\phi(1-f_{eq})-\phi' f'_{eq}]\cdot(e^{z_e}\Omega^+ + e^{z-z_e}\Omega^-)\}d\mathbf{q} \quad (11c)$$

$$z=h\nu/k_B T_l; \quad z_e=h\nu/k_B T_e \quad (11d)$$

The scattering term is separated into two parts. The first part, expressed in Eq. (11b), becomes zero when the electron temperature is equal to the phonon temperature. The second part, expressed in Eq. (11c), becomes zero when electrons are in thermal equilibrium. By assuming that ϕ is proportional to the electron wavevector in the direction of temperature gradient (Makinson, 1938), integrals (11b) and (11c) can be evaluated.

When the electron and lattice temperatures are higher than the Debye temperature of the material, T_D, the scattering term can be solved in closed form,

$$\left[\frac{\partial f}{\partial t}\right]_{s1}=\frac{1}{2}\Lambda f_{eq}(1-f_{eq})\left(f_{eq}-\frac{1}{2}\right)\left(1-\frac{T_l}{T_e}\right)\frac{T_D}{T_e}E^{-1/2} \quad (12a)$$

$$\left[\frac{\partial f}{\partial t}\right]_{s2}=\frac{1}{2^{4/3}}\Lambda(f_{eq}-f)\frac{T_l}{T_D}E_{F_0}E^{-3/2} \quad (12b)$$

$$\Lambda=\frac{3\pi^2\mathcal{P}^2(m/2)^{1/2}}{Mk_B T_D}\left(\frac{3}{4\pi\Delta}\right)^{1/3} \quad (12c)$$

Even though the above results are derived rigorously for the high-temperature case, they are expected to be valid as long as the lattice temperature is not much lower than the Debye temperature. This is indicated by the similar situation of the Wiedemann–Franz law. Strictly speaking, the Wiedemann–Franz law, which compares the thermal conductivity with the electrical conductivity, can be derived only when the lattice temperature is much larger than the Debye temperature, but it agrees well with experimental measurements even when the lattice temperature is lower than the Debye temperature (Kittel, 1986).

Equation (12) provides very interesting physical insights into the electron-phonon scattering processes. The first scattering process, $[\partial f/\partial t]_{s1}$, causes the energy exchange between electrons and lattice. Since $0.5 < f_{eq} < 1$ when $E < E_F$, $0 < f_{eq} < 0.5$ when $E > E_F$, and $f_{eq} = 0.5$ when $E = E_F$ (i.e., at the Fermi surface), $[\partial f/\partial t]_{s1}$ changes signs for $E > E_F$ and $E < E_F$. For the case $T_e > T_l$, $[\partial f/\partial t]_{s1}$ is negative for the states above the Fermi surface and is positive for the states below the Fermi surface, indicating an inelastic scattering process that removes electrons from high-energy states to low-energy states and transports a net energy from the electrons to the lattice. On the other hand for the case $T_e < T_l$, energy is transported from lattice to electrons, raising electrons from low-energy states to high-energy states. This inelastic scattering process becomes important when there is a large difference between the electron and lattice temperatures.

The second scattering process, $[\partial f/\partial t]_{s2}$, does not cause a net energy exchange between electrons and the lattice. This elastic scattering process restores spatial homogeneity for electrons. The relaxation time can be uniquely defined for this process as

$$\left[\frac{\partial f}{\partial t}\right]_{s2}=\frac{f_{eq}-f}{\tau} \quad (13a)$$

$$\tau=2^{4/3}\Lambda^{-1}\frac{T_D}{T_l}E_{F_0}^{-1}E^{3/2}=\tau_{eq}(T_l) \quad (13b)$$

where E_{F_0} is the Fermi energy at $T_e = 0$ K and τ_{eq} (T_l) is the relaxation time when electrons are in thermal equilibrium with the lattice ($T_e = T_l$). Equation (13) shows that the relaxation time depends on the electron energy and the lattice temperature but not the electron temperature. This is consistent with the nature of electron–phonon interactions, since the thermal vibration of the lattice, which causes the scattering of electrons, is determined by the lattice temperature. Equation (13a) also shows that in the short-time-scale regime the relaxation time approximation is only valid for part of the scattering processes and is not valid for the inelastic scattering process, as described by Eq. (12a).

Solution of the Boltzmann Equation. Since electrons are near equilibrium, the diffusion term and the external field driving term in Eq. (1) can be linearized as

$$V_x\frac{\partial f}{\partial x}\approx V_x\frac{\partial f_{eq}}{\partial x} \quad (14a)$$

$$\frac{F_x}{m}\frac{\partial f}{\partial V_x}\approx\frac{F_x}{m}\frac{\partial f_{eq}}{\partial V_x} \quad (14b)$$

Using the relations

$$\frac{\partial f_{eq}}{\partial x}=\frac{\partial f_{eq}}{\partial T_e}\frac{\partial T_e}{\partial x}=-\left[\frac{E}{T_e}+T_e\frac{d}{dT_e}\left(\frac{E_F}{T_e}\right)\right]\frac{\partial f_{eq}}{\partial E}\frac{\partial T_e}{\partial x} \quad (15a)$$

$$\frac{\partial f_{eq}}{\partial V_x}=\frac{\partial f_{eq}}{\partial E}\frac{\partial E}{\partial V_x}=mV_x\frac{\partial f_{eq}}{\partial E} \tag{15b}$$

$$F_x=-e\epsilon_x \tag{15c}$$

and the solution of the scattering term yields the implicit solution of the Boltzmann equation, Eq. (1),

$$f(E)=f_{eq}(E)+\tau V_x\left[\frac{E}{T_e}+T_e\frac{d}{dT_e}\left(\frac{E_F}{T_e}\right)\right]\frac{\partial f_{eq}}{\partial E}\frac{\partial T_e}{\partial x}+\tau e\epsilon_x V_x-\tau\frac{\partial f}{\partial t}+\tau\left[\frac{\partial f}{\partial t}\right]_{s1} \tag{16}$$

where ϵ_x is the electric field induced by the temperature gradient in the x direction.

Macroscopic Formulations

Heat Flux Relation. The electric and heat currents in the x direction carried by electrons are

$$J=-\iiint eV_xD(\mathbf{V})f(\mathbf{V})dV_xdV_ydV_z \tag{17a}$$

$$Q=\iiint EV_xD(\mathbf{V})f(\mathbf{V})dV_xdV_ydV_z \tag{17b}$$

where $D(\mathbf{V})$ is the density of states. Inserting the solution of $f(\mathbf{V})$ gives transport equations for the electricity and energy.

Because f_{eq} and $[\partial f/\partial t]_{s1}$ are symmetric about the surface $V_x = 0$,

$$f_{eq}(-V_x)=f_{eq}(V_x) \tag{18}$$

and V_x is antisymmetric about the surface $V_x = 0$, the contributions of f_{eq} and $[\partial f/\partial t]_{s1}$ to the net electric current and heat current are zero. Since the scattering terms, $[\partial f/\partial t]_{s1}$ and $[\partial f/\partial t]_{s2}$, the diffusion term, and the electrical-force-driving term are nonzero only in a very narrow regime around the Fermi surface (Bube, 1974), $\partial f/\partial t$, determined by Eq. (1), is a delta-like function at $E = E_F$. Therefore, the contribution of the $\tau(\partial f/\partial t)$ term to the electric and heat current can be reasonably approximated as

$$\iiint -eV_xD(\mathbf{V})\tau(\mathbf{V})\frac{\partial f}{\partial t}dV_xdV_ydV_z\approx\tau_F\frac{\partial J}{\partial t} \tag{19a}$$

$$\iiint EV_xD(\mathbf{V})\tau(\mathbf{V})\frac{\partial f}{\partial t}dV_xdV_ydV_z\approx\tau_F\frac{\partial Q}{\partial t} \tag{19b}$$

where τ_F is the relaxation time evaluated at the Fermi surface. By using the above relations, the transport equations become

$$J=-\tau_F\frac{\partial J}{\partial t}+eK_1\left[e\epsilon_x+T_e\frac{d}{dT_e}\left(\frac{E_F}{T_e}\right)\frac{\partial T_e}{\partial x}\right]+\frac{e}{T_e}K_2\frac{\partial T_e}{\partial x} \tag{20a}$$

$$Q=-\tau_F\frac{\partial Q}{\partial t}-eK_2\epsilon_x-\left[\frac{K_3}{T_e}+K_2T_e\frac{d}{dT}\left(\frac{E_F}{T_e}\right)\right]\frac{\partial T_e}{\partial x} \tag{20b}$$

$$K_n=-\frac{2}{3m}\int_0^\infty\tau(E)D(E)E^n\frac{\partial f_{eq}}{\partial E}dE \tag{20c}$$

Since there is no electrical current during laser heating, it follows that $J = 0$ and $\partial J/\partial t = 0$. Combining Eqs. (20$a$) and (20$b$) yields the macroscopic heat flux equation,

$$Q=-\kappa\frac{\partial T_e}{\partial x}-\tau_F\frac{\partial Q}{\partial t} \tag{21a}$$

$$\kappa=(K_1K_3-K_2^2)/K_1T_e \tag{21b}$$

Equation (21a) reveals the hyperbolic nature of energy transport by electrons in metals: The heat flux relies on both its rate of change and the temperature gradient. Even though the form of the current model is similar to that of generalized Fourier models (Joseph and Preziosi, 1989), it has different physical meanings: First energy is transported by electrons and second the effective thermal conductivity depends not only on T_l but also T_e.

Effective Thermal Conductivity. The effective thermal conductivity during short-time-scale heating can be evaluated from Eq. (21b) as

$$\kappa=\left(\frac{T_e}{T_l}\right)\kappa_{eq}(T_l) \tag{22}$$

where κ_{eq} is the conventional thermal conductivity measured at a slow heating rate during which electrons and phonons are in thermal equilibrium. Equation (22) shows that during the short-pulse laser heating the thermal conductivity is modified by the local electron and lattice temperatures. Qualitatively this correction on κ can be derived through simple physical reasoning. From the kinetic theory of gases, the thermal conductivity can be expressed as (Kittel, 1986)

$$\kappa=\frac{1}{3}C_eV_F^2\tau_F \tag{23}$$

The electron heat capacity C_e is proportional to T_e (as long as $k_B T_e \ll E_F$), the relaxation time is proportional to T_l^{-1}, and the Fermi speed V_F is relatively constant. Therefore, when the electron temperature is not equal to the lattice temperature, the ratio of κ to κ_{eq} is proportional to T_e/T_l. This result indicates that during the short-pulse laser heating the thermal conductivity depends on processing parameters, such as the laser pulse duration and intensity.

Heat Transfer Equations. Laser pulses deposit energy on electrons. The excited electrons transport energy and heat the metal lattice through the electron-phonon interaction. The rate of energy exchange, U, between electrons and phonons can be evaluated by integrating the rate of energy changes of all transitions. This was done by Kaganov et al. (1957), and later, expressed in terms of the thermal conductivity by Qiu and Tien (1992),

$$U=G(T_e-T_l) \tag{24a}$$

$$G=\frac{\pi^4}{18}\frac{(n_euk_B)^2}{\kappa_{eq}} \tag{24b}$$

Energy conservation equations for both electrons and phonons and the heat flux equation (21a) form the hyperbolic two-step radiation heating model (HTS):

$$C_e(T_e)\frac{\partial T_e}{\partial t}=-\frac{\partial Q}{\partial x}-G(T_e-T_l)+S \tag{25a}$$

$$C_l(T_l)\frac{\partial T_l}{\partial t}=G(T_e-T_l) \tag{25b}$$

$$\tau_F\frac{\partial Q}{\partial t}+\kappa\frac{\partial T_e}{\partial x}+Q=0 \tag{25c}$$

$$C_e(T_e)=\gamma T_e;\quad \kappa=\kappa_{eq}T_e/T_l \tag{25c}$$

where S is the radiation heating source term.

From Eq. (25), if the temperature dependence of thermal properties and the term $\partial Q/\partial t$ are neglected, the electron and phonon temperature difference after a laser pulse ($S = 0$) becomes

$$\frac{\partial(T_e-T_l)}{\partial t}=-\left(\frac{G}{C_{eo}}+\frac{G}{C_l}\right)(T_e-T_l) \tag{26a}$$

As can be seen, the characteristic time for electrons and phonons to reach equilibrium, i.e., the thermalization time, is

$$t_c=C_{eo}C_l/(C_{eo}+C_l)G\approx C_{eo}/G \tag{26b}$$

Table 1 Relaxation time and thermalization time at 300 K (in ps)

Metal	τ_F	t_c	Metal	τ_F	t_c
Cu	0.03	0.6	V	0.002	0.06
Ag	0.04	0.6	Nb	0.004	0.05
Au	0.04	0.8	Ti	0.001	0.05
Cr	0.003	0.1	Pb	0.005	0.4
W	0.01	0.2			

Table 2 Physical constants of gold used in calculations

Reflectivity (R)	0.93[a]
Radiation penetration depth (d)	15.3 nm[a]
Thermal conductivity (κ_{eq})	315 W/mK[b]
Initial temperature (T_0)	300 K
Lattice heat capacity (C_l)	2.5×10^6 J/m^{3}K[b]
Electron heat capacity (C_{eo})	2.1×10^4 J/m^{3}K[c]
Relaxation time (τ_F)	0.04 ps (Table 1)
Electron-Phonon coupling factor (G)	2.6×10^{16} W/m^{3}K[d]

[a] Typical value for visible light, see b.

[b] American Institute of Physics Handbook, 3rd ed. (MaGraw-Hill, New York,1972).

[c] Kittel, 1986.

[d] Qiu and Tien, 1992

When the laser pulse duration is shorter than τ_F, the hyperbolic transport effect on the electron temperature becomes important, and when it is shorter than t_c, the mechanism of energy deposition becomes important. Table 1 lists τ_F and t_c for common metals. The relaxation time τ_F is evaluated from Eq. (13*b*) and t_c is deducted from the measured value of G compiled by Qiu and Tien (1992). All the physical constants used in this calculation are taken from Kittel (1986).

At room temperature τ_F is about one order of magnitude smaller than t_c. Therefore, the mechanisms of energy deposition are expected to play much more important roles during short-pulse-laser heating of metals than the effects of hyperbolic transport.

Fast Radiation Heating of a Metal Film

Existing Radiation-Heating Models. Short-pulse laser heating of metal films can be modeled as a one-dimensional problem (Fig. 1), since the beam diameter is much larger than the heat penetration depth. The spatial distribution of laser intensity is assumed to be uniform, and the temporal shape of the laser pulse is assumed to be Gaussian with a FWHM (full width at half maximum) pulse duration t_p. Furthermore, heat losses from the film surface are neglected during the short heating period.

Neglecting the temperature dependence of the optical properties, the laser heating source term is

$$S=(1-R)I\alpha\exp[-\alpha x-2.77(t/t_p)^2] \tag{27}$$

This assumption is reasonable if the laser wavelength is in the visible light range (Scouler, 1967; Pells and Shiga, 1969).

The initial and boundary conditions are

$$T_e(x,\,-2t_p)=T_l(x,\,-2t_p)=T_o;\quad Q(x,\,-2t_p)=0 \tag{28a}$$

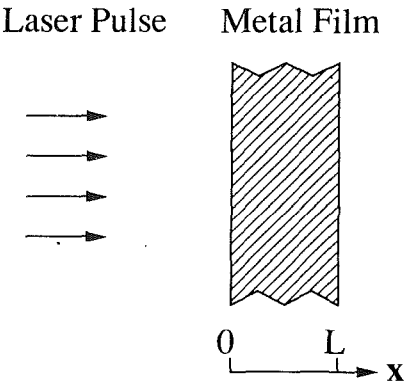

Fig. 1 Schematic diagram for laser heating of a metal film

$$\left.\frac{\partial T_e}{\partial x}\right|_{x=0}=\left.\frac{\partial T_e}{\partial x}\right|_{x=L}=\left.\frac{\partial T_l}{\partial x}\right|_{x=0}=\left.\frac{\partial T_l}{\partial x}\right|_{x=L}=0 \tag{28b}$$

$$Q(0,\,t)=Q(L,\,t)=0 \tag{28c}$$

Different radiation heating models are solved numerically under the same initial and boundary conditions. The material simulated is gold and its physical constants are listed in Table 2. The models include the parabolic one-step radiation-heating model (POS),

$$C\frac{\partial T}{\partial t}=\frac{\partial}{\partial x}\left(\kappa_{eq}\frac{\partial T}{\partial x}\right)+S \tag{29}$$

the hyperbolic one-step radiation-heating model (HOS, Maurer, 1969),

$$\tau\frac{\partial Q}{\partial t}+\kappa_{eq}\frac{\partial T}{\partial x}+Q=0 \tag{30a}$$

$$C\frac{\partial T}{\partial t}+\frac{\partial Q}{\partial x}-S=0 \tag{30b}$$

the parabolic two-step radiation heating-model (PTS, Anisimov et al., 1974),

$$C_e(T_e)\frac{\partial T_e}{\partial t}=\frac{\partial}{\partial x}\left(\kappa\frac{\partial T_e}{\partial t}\right)-G(T_e-T_l)+S \tag{31a}$$

$$C_l\frac{\partial T_l}{\partial t}=G(T_e-T_l) \tag{31b}$$

and the hyperbolic two-step radiation-heating model (HTS) described in Eq. (25). These three existing models (POS, HOS, and PTS) are special cases of the current HTS model. When the laser pulse duration is much longer than the relaxation time, the HTS becomes the PTS model. On the other hand, when the laser pulse duration is much longer than the thermalization time, it reduces to the HOS model. The POS model is the special case when laser pulse duration is much longer than both the relaxation time and the thermalization time.

The hyperbolic models (HOS and HTS) are solved numerically using the MacCormack scheme (Glass et al., 1985). A uniform grid system is used with 400 grid points. The total increase in the electron energy and phonon energy is calculated at certain times and compared with the absorbed radiation energy. The difference is within 10^{-4}. Furthermore, different time steps and grid spacings are used to check the consistency of the numerical solutions. The parabolic models (POS and PTS) are solved by the Crank-Nicholson scheme with a nonuniform grid system. The electron and lattice temperatures are iterated for each time step until the convergence criteria are satisfied ($\Delta T_e/T_{e0} < 10^{-4}$ and $\Delta T_l/T_{l0} < 10^{-5}$).

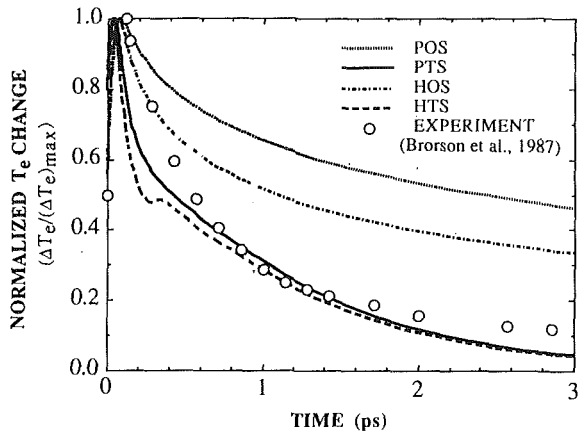

Fig. 2 Comparison of predicted electron-temperature changes with experimental data at the front surface [t_p = 96 fs, L = 0.1 μm, F = 10 J/m^2]

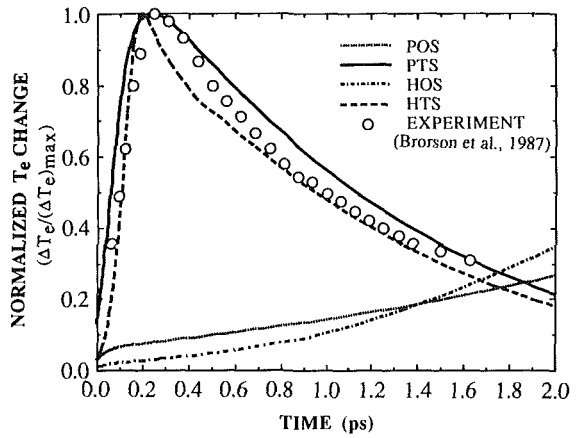

Fig. 3 Comparison of predicted electron-temperature changes with experimental data at the rear surface [t_p = 96 fs, L = 0.1 μm, F = 10 J/m^2]

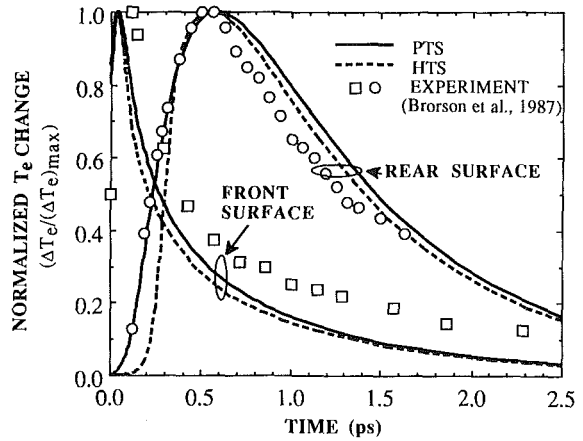

Fig. 4 Comparison of predicted electron-temperature changes from the two-step models with experimental data [t_p = 96 fs, L = 0.2 μm, F = 10 J/m^2]

Experimental and Numerical Comparison. Figures 2–4 show the comparison of the normalized electron temperature changes, $(T_e - T_{eo})/(T_e - T_{eo})_{max}$, predicted from different models, with experimental data during subpicosecond laser pulse heating (Brorson et al., 1987). The experiment measures the transient reflectivity changes, ΔR. The probe laser excites electrons from the completely filled valence d band to the states near the Fermi level in the conduction band. The increase of the electron temperature changes the electron occupation probability, which in turn modulates the reflectivity. For example, the increase of the electron numbers in the final state of the transition decreases the transition probability, and thus decreases the radiation absorption and results in an increase of reflectivity. Therefore, the reflectivity change is a measure of the electron temperature. Previous study has shown that ΔR is proportional to ΔT_e in the laser-intensity range of experiment of Brorson et al. (Qiu and Tien, 1992). Juhasz et al. (1992) also showed that ΔR is proportional to ΔT_e near room temperature. Therefore, the normalized electron temperature changes can be deduced from the measured normalized reflectivity changes as $\Delta T_e/(\Delta T_e)_{max} = \Delta R/(\Delta R)_{max}$.

At the front surface (Fig. 2), after the exposure to the laser pulse, the absorbed radiation energy is removed from the excited electrons quickly by the electron transport and the electron–phonon interaction. This gives rise to a rapid decrease of the electron temperature. Since both the POS model and the HOS model neglect the microscopic energy transfer between electrons and phonons, the predicted decrease of the electron temperature is much slower than the measured one. The predictions from the two-step models (PTS and HTS) agree well with the experimental results and the difference between them is small.

At the rear surface (Fig. 3), the electron temperature increases due to the energy transport by the hot electrons and then decreases due to the electron–phonon interactions. The two-step models predict the correct temperature response, but the one-step models fail even to predict the correct trend. The PTS and HTS models, however, predict totally different speeds of energy propagation. Due to the diffusion nature of the PTS model, it predicts an infinite speed. On the other hand, the hyperbolic heat flux model predicts a finite speed of heat propagation as $(\kappa/C_e\tau_F)^{1/2} = V_F/3^{1/2}$ (Joseph and Preziosi, 1989). Using $V_F = 1.4 \times 10^6$ m/s (Kittel, 1986), the predicted heat propagation velocity in gold is 8.1×10^5 m/s, which agrees with the measured result, 8.4×10^5 m/s (Brorson et al., 1987).

Figure 4 shows the comparison of the two-step models with experimental data at a different film thickness. Again, the two-step models give good predictions.

Figures 5–7 provide the temperature profiles in a 0.1 μm gold film during 0.1 ps laser pulse heating. The predictions from the two-step models and the one-step models are totally different. The two-step models predict much higher electron temperature, much lower lattice temperature, and much larger heat-affected regions than the one-step models. At the end of the laser pulse, the absorbed energy, predicted from the one-step models, is confined mainly within the radiation penetration depth, but spreads quite uniformly in the material lattice for the case of the two-step models. This indicates that the absorbed radiation energy is not converted into the lattice energy where it is absorbed during the short-pulse laser heating.

For both the one-step models and the two-step models, the effect of the hyperbolic heat transport on the whole heating process is small. It lowers the peak temperature for the one-step models. For the two-step models, it increases the peak electron temperature and has negligible effects on the lattice temperature response. By comparing the times required to remove the energy out of the radiation absorption region by different transport mechanisms, these effects become clear. The required transport times for the HOS, POS, HTS, and PTS models are $\pi\delta/(\kappa/\tau_F C_l)^{1/2} = 8 \times 10^{-13}$ s, $\delta^2 C_l/\kappa = 2 \times 10^{-12}$ s, $\pi\delta/(\kappa/\tau_F C_e)^{1/2} = 8 \times 10^{-14}$ s, and $\delta^2 C_e/\kappa = 1 \times 10^{-14}$ s, respectively. Therefore, the hyperbolic transport process is slightly faster than the diffusion process for the one-step models and slower for the two-step models.

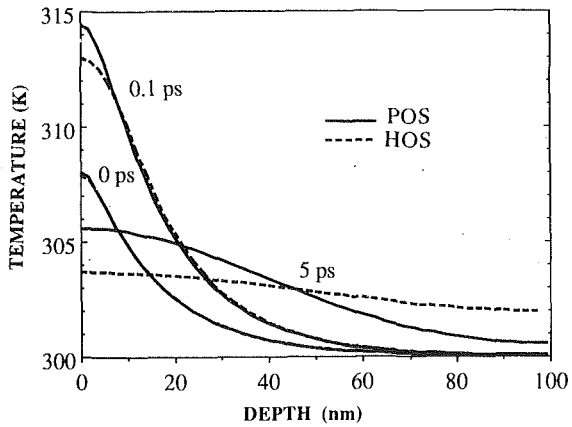

Fig. 5 Predicted electron and lattice temperature profiles from the one-step models during a 0.1 ps laser heating [L = 0.1 μm, F = 10 J/m^2]

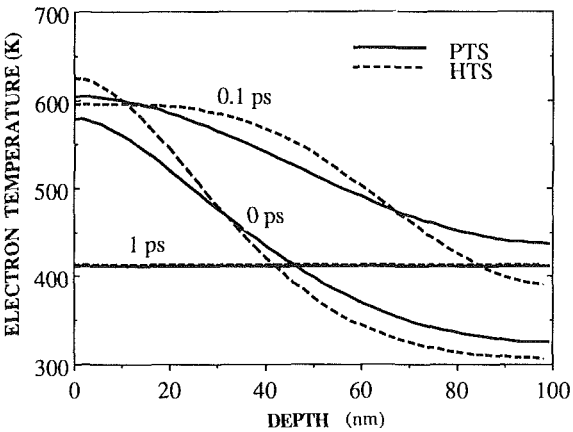

Fig. 6 Predicted electron-temperature profiles from the two-step models during a 0.1 ps laser heating [L = 0.1 μm, F = 10 J/m^2]

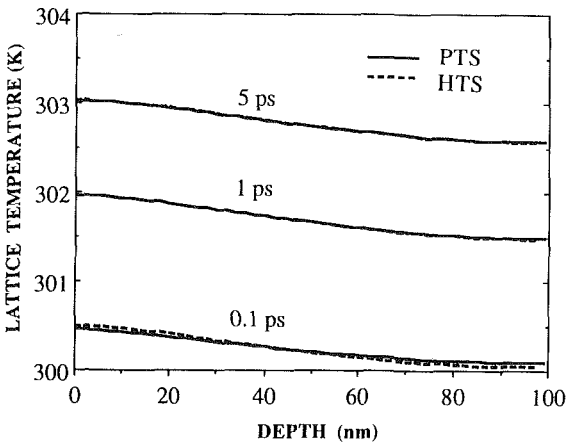

Fig. 7 Predicted lattice-temperature profiles from the two-step models during a 0.1 ps laser heating [L = 0.1 μm, F = 10 J/m^2]

Conclusions

The microscopic heat transfer mechanisms during the short-pulse laser heating on metals have been studied theoretically. The rigorous solution of the scattering term in the Boltzmann transport equation shows that the electron-phonon scattering processes are composed of two parts. One part brings electrons and phonons to equilibrium, and the other part keeps electrons in local thermal equilibrium. The former cannot be approximated by a relaxation time, but the latter can. This relaxation time depends on the lattice temperature but not the electron temperature. The solution of the Boltzmann equation leads to a hyperbolic heat flux equation for electrons and provides a physical basis for the applicability of the thermal conductivity in the short-time-scale regime. During a fast heating process, the thermal conductivity is predicted to be different from that for a relatively slow heating process.

The hyperbolic heat flux equation of electrons and energy conservation equations for electrons and phonons form a hyperbolic two-step radiation heating model. This model can be simplified to the existing radiation models under different conditions of laser pulse durations. Predictions of these models are compared with subpicosecond laser heating experiments. The current model agrees well with experimental data. The previous parabolic two-step model predicts the general temperature response, but it fails to predict a finite speed of energy propagation. The conventional one-step models are not applicable for subpicosecond laser heating of metals.

Acknowledgments

The authors gratefully acknowledge the financial support for this research from the U.S. National Science Foundation, the U.S. Department of Energy, and the K. C. Wong Education Foundation.

References

Allen, P. B., 1987, "Theory of Thermal Relaxation of Electrons in Metals," *Phys. Rev. Lett.*, Vol. 59, pp. 1460–1463.

Anisimov, S. I., Kapeliovich, B. L., and Perel'man, T. L., 1974, "Electron Emission From Metal Surfaces Exposed to Ultrashort Laser Pulses," *Sov. Phys. JETP*, Vol. 39, pp. 375–377.

Brorson, S. D., Fujimoto, J. G., and Ippen, E. P., 1987, "Femtosecond Electronic Heat-Transfer Dynamics in Thin Gold Film," *Phys. Rev. Lett.*, Vol. 59, pp. 1962–1965.

Bube, R. H., 1974, *Electronic Properties of Crystalline Solids*, Academic Press, New York.

Eesley, G. L., 1983, "Observation of Non-equilibrium Electron Heating in Copper," *Phys. Rev. Lett.*, Vol. 51, pp. 2140–2143.

Fann, W. S., Storz, R., Tom, H. W. K., and Bokor, J., 1992, "Direct Measurement of Nonequilibrium Electron-Energy Distributions in Subpicosecond Laser-Heated Gold Films," *Phys. Rev. Lett.*, Vol. 68, pp. 2834–2837.

Glass, D. E., Özisik, M. N., McRae, D. S., and Vick, B., 1985, "On the Numerical Solution of Hyperbolic Heat Conduction," *Numerical Heat Transfer*, Vol. 8, pp. 497–504.

Groeneveld, R. H. M., Sprik, R., Wittebrood, M., and Lagendijk, A., 1992, "Effect of a Nonthermal Electron Distribution on the Electron-Phonon Energy Relaxation Process in Noble Metals," *Phys. Rev. B*, Vol. 45, pp. 5079–5082.

Joseph, E. E., and Preziosi, L., 1989, "Heat Waves," *Rev. Modern Phys.*, Vol. 61, pp. 41–73.

Juhasz, T., Elsayed-Ali, H. E., Hu, X. H., and Bron, W. E., 1992, "Time-Resolved Thermoreflectivity of Thin Gold Films and Its Dependence on the Ambient Temperature," *Phys. Rev. B*, Vol. 45, pp. 13819–13822.

Kaganov, M. I., Lifshitz, I. M., and Tanatarov, L. V., 1957, "Relaxation Between Electrons and Crystalline Lattices," *Sov. Phys. JETP*, Vol. 4, pp. 173–178.

Kittel, C., 1986, *Introduction to Solid State Physics*, 6th ed., Wiley, New York.

Makinson, R. E. B., 1938, "The Thermal Conductivity of Metals," *Proc. Camb. Phil. Soc.*, Vol. 34, pp. 474–497.

Maurer, M. J., 1969, "Relaxation Model for Heat Conduction in Metals," *J. Appl. Phys.*, Vol. 40, pp. 5123–5130.

Özisik, M. N., and Vick, B., 1984, "Propagation and Reflection of Thermal Waves in a Finite Medium," *Int. J. Heat Mass Transfer*, Vol. 35, pp. 719–726.

Pells, G. P., and Shiga, M., 1969, "The Optical Properties of Copper and Gold as a Function of Temperature," *J. Phys. C*, Vol. 2, pp. 1835–1846.

Qiu, T. Q., and Tien, C. L., 1992, "Short-Pulse Laser Heating on Metals," *Int. J. Heat Mass Transfer*, Vol. 35, pp. 719–726.

Scouler, W. J., 1967, "Temperature-Modulated Reflectance of Gold From 2 to 10 eV," *Phys. Rev. Lett.*, Vol. 18, pp. 445–448.

Tzou, D. Y., 1992, "Thermal Shock Phenomena Under High Rate Response in Solids," *Annual Review of Heat Transfer*, C. L. Tien, ed., Hemisphere Publishing Corporation, Washington, Vol. IV, pp. 111–185.

Wilson, A. H., 1953, *The Theory of Metals*, 2nd ed., Cambridge University Press, New York.

Size Effects on Nonequilibrium Laser Heating of Metal Films

T. Q. Qiu
Graduate Student Researcher.

C. L. Tien
A. Martin Berlin Professor.

Department of Mechanical Engineering,
University of California,
Berkeley, CA 94720

Picosecond and sub-picosecond lasers have become important tools in the fabrication and study of microstructures. When the laser pulse duration becomes comparable with or less than the characteristic time of energy exchange among microscopic energy carriers, the excited carriers are no longer in thermal equilibrium with the other carriers, creating a nonequilibrium heating situation. The presence of interfaces in metals provides additional scattering processes for electrons, which in turn affects the nonequilibrium heating process. This work studies size effects, due to both surface scattering and grain-boundary scattering, on the thermal conductivity and the energy exchange between electrons and the material lattice. A simple formula is established to predict the influence of film thickness, grain size, interface scattering parameters, and the electron and lattice temperatures on the effective thermal conductivity of metal thin films. Predictions of the analysis agree with the available experimental data. A three-energy-level model is developed to characterize the energy exchange between electrons and the lattice. This study shows that the size effect reduces the effective thermal conductivity and increases the electron-phonon energy exchange rate. The results are useful for improving processing quality, interpreting diagnostic results, and preventing thermal damage of thin films during short-pulse laser heating.

Introduction

Energy transport during fast laser heating of solids has become a very active research area due to the tremendous applications of short-pulse lasers in the fabrication of sophisticated microstructures (Chlipala et al., 1989), syntheses of advanced materials (Simon, 1991; Narayan et al., 1991), measurement of thin-film properties (Eesley, 1990), and diagnostics of material's structure transformation (Reitze et al., 1989; Saeta et al., 1991). Two fundamental problems of particular importance are the mechanism of energy transport and the material's thermal properties during rapid laser heating.

There exist basically two different models describing the mechanism of energy transport during short-pulse laser heating (SPLH). One is based on the hyperbolic heat conduction model (e.g., Kim et al., 1990; Tzou, 1992), which was first postulated for gases by Maxwell (1867). The other one is based on the thermal nonequilibrium concept of microscopic energy carriers, i.e., electrons and phonons having different temperatures during the heating process (Kaganov et al., 1957; Anisimov et al., 1974; Qiu and Tien, 1992a). Qiu and Tien (1992b) rigorously developed the hyperbolic two-step radiation heating model by modeling the interaction and transport of electrons and phonons. The results reveal the origins of nonequilibrium heating and hyperbolic transport and show that the nonequilibrium heating effect is dominant during SPLH of metals.

Two important properties during nonequilibrium laser heating of metals are the thermal conductivity and the electron-phonon coupling factor, which governs the energy exchange rate between electrons and the material lattice. Since many applications of short-pulse lasers involve interactions with microstructures, it is necessary to investigate size effects on these properties, i.e., laser trimming of thin film resistors (Schultze and Fischer, 1989) and laser damage of thin films (Guenther and McIver, 1989). This paper presents a theoretical study of the size effects, due to both surface and grain boundary scattering, on the thermal conductivity and the electron-phonon coupling factor during nonequilibrium laser heating of metals.

Contributed by the Heat Transfer Division and presented at the ASME Winter Annual Meeting, Anaheim, California, November 8-13, 1992. Manuscript received by the Heat Transfer Division October 1992; revision received January 1993. Keywords: Conduction, Thermophysical Properties. Technical Editor: R. Viskanta.

Nonequilibrium Laser Heating

Laser heating of metals consists of two major steps of microscopic energy transfer. Electrons in metals absorb radiation energy first and then subsequently transmit energy to the lattice through inelastic electron-phonon scattering processes. It takes about $0.1 \sim 1$ ps for electrons and the lattice to reach thermal equilibrium for typical metals. When the laser pulse duration is comparable with or less than this thermalization time, t_c, electrons and the lattice are not in thermal equilibrium. This nonequilibrium heating process (i.e., electron temperature $\neq$ lattice temperature) can be described by the hyperbolic two-step model that can be further simplified, for most cases, to the parabolic two-step radiation heating model (Anisimov et al., 1974; Qiu and Tien, 1992b) as

$$C_e(T_e)\frac{\partial T_e}{\partial t} = \nabla \cdot (\kappa \nabla T_e) - G(T_e - T_l) + S \qquad (1a)$$

$$C_l(T_l)\frac{\partial T_l}{\partial t} = G(T_e - T_l) \qquad (1b)$$

$$C_e(T_e) = \frac{\pi^2}{2}\frac{nk^2 T_e}{E_F} \qquad (1c)$$

where T_e and T_l are the electron and lattice temperatures, respectively, C_e and C_l are the electron and lattice heat capacities, respectively, n is the number density of electrons, and E_F is the Fermi energy. In Eq. (1*b*) heat conduction by the lattice is neglected since for pure metals energy is mainly carried by electrons.

The electron-phonon coupling factor, G, governs the characteristic time for electrons and the lattice to reach thermal equilibrium. By assuming uniform electron and lattice temperatures and neglecting the temperature dependence of thermal properties, the solution of Eq. (1) is

$$T_e - T_l = (T_{eo} - T_{lo})\exp(-t/t_c) \qquad (2a)$$

$$t_c = \left(\frac{G}{C_e} + \frac{G}{C_l}\right)^{-1} \qquad (2b)$$

where T_{eo} and T_{lo} are the initial electron and lattice temperatures, respectively. This is similar to the case of delta-function laser-pulse heating if thermal diffusion is neglected. By further using the fact that C_l is typically two orders of magnitude

larger than C_e at room temperature, the dependence of the thermalization time, t_c, on G becomes

$$t_c = C_e/G \tag{2c}$$

The material's thermal response depends on κ and G during nonequilibrium SPLH. The lattice temperature can be roughly estimated from the absorbed radiation energy and the energy penetration depth. For laser pulses durations shorter than t_c, the heat penetration depth in the lattice is determined by t_c as $(\kappa t_c/C_e)^{1/2}$. For a typical metal, $\kappa = 100$ W/mK, $t_c = 1$ ps, $C_e = 2\times 10^4$ J/m^{3}K, the heat penetration depth is about 700 Å, which is much larger than the radiation penetration depth (around 150 Å). Therefore the maximum lattice-temperature rise due to a laser pulse irradiation is roughly

$$(\Delta T_l)_{\max} = \frac{Q}{C_l\sqrt{\kappa t_c/C_e}} = \frac{Q}{C_l}\sqrt{\frac{G}{\kappa}} \tag{3}$$

where Q is the absorbed energy. Factors that increase κ enhance energy transport, which in turn reduce the maximum lattice temperature rise during SPLH; and factors that increase G reduce the electron-lattice thermalization time, resulting in an increase of the peak lattice-temperature rise. For short-pulse laser processing, a small κ and large G are desired to reduce the size of the heated region. On the other hand, for prevention of laser damage, a large κ and small G are preferred to increase the damage threshold (the maximum laser intensity allowed). Therefore it is necessary to have a better understanding of the dependence of κ and G on the material's microstructure.

Effect of Size on the Thermal Conductivity

In pure metals heat is carried primarily by electrons at all temperatures. From kinetic theory, the thermal conductivity of metals is related to the electron mean-free-path, Λ, as (Tien and Lienhard, 1979)

$$\kappa_{eq}(T_l) = \frac{1}{3}C_e(T_l)v_F\Lambda(T_l) = \frac{\pi^2 nk^2}{3mv_F}T_l\Lambda(T_l) \tag{4}$$

where v_F is the speed of those electrons possessing the Fermi energy and is of the order of 10^6 m/s. During nonequilibrium heating ($T_e > T_l$), electrons carry much more energy than they do in the equilibrium case, and therefore $\kappa(T_e, T_l)$ is larger than $\kappa_{eq}(T_l)$. From Eq. (4), the ratio of the thin-film thermal conductivity, $\kappa_f(T_e, T_l)$, to the bulk value in equilibrium is

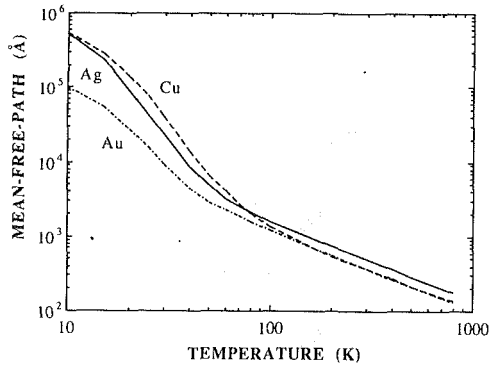

Fig. 1 Electron mean free path

$$\frac{\kappa_f(T_e,T_l)}{\kappa_{eq,b}(T_l)} = \frac{C_e(T_e)}{C_e(T_l)}\cdot\frac{\Lambda_f(T_l)}{\Lambda_b(T_l)} = \frac{T_e}{T_l}\cdot\frac{\Lambda_f(T_l)}{\Lambda_b(T_l)} \tag{5}$$

Here the fact that Λ does not depend on the electron temperature is used (Qiu and Tien, 1992b).

When the characteristic length of materials, i.e., the film thickness and the grain diameter, is comparable with or less than Λ_b, the additional scattering processes of electrons at interfaces become also important compared with the background electron-lattice scattering, which in turn reduce κ, known as the size effect. Figure 1 shows Λ_b in the bulk materials of copper (Cu), silver (Ag), and gold (Au) from 10 K to 800 K, estimated from Eq. (4). The thermal conductivity data are from Powell and Ho (1968) and the other physical constants are from Kittel (1986). At room temperature, Λ_b is around 400 Å for Cu, Ag, and Au.

The size effect due to surface scattering of energy carriers has been studied recently for different materials, including high-temperature superconducting thin-films (Flik and Tien, 1990), dielectric thin films (Majumdar, 1991), gallium arsenide based quantum well structures (Chen and Tien, 1992) and metal thin films (Kumar and Vradis, 1991). The applicability of these models to polycrystalline thin films, however, is subject to question, since these studies neglect the size effect due to grain boundary scattering. In polycrystalline metal thin films, the presence of grain boundaries (Fig. 2) introduces additional scattering processes for electrons. Since the grain size is often of the same order as the film thickness, the size effect due to grain boundary scattering may also become important.

Nomenclature

C = volumetric heat capacity, Jm^{-3}K^{-1}
D = average grain diameter, m
d = film thickness, m
E = electron energy, J
e = electron charge, C
f = distribution function of electrons
G = electron-phonon coupling factor, Wm^{-3}K^{-1}
h = Planck constant, Js
k = Boltzmann constant, JK^{-1}
m = effective mass of electrons, kg
n = electron number density, m^{-3}
n_{e-l} = effective number of electrons during collisions
N = distribution function of phonons
P = specular reflection parameter at surfaces
P_a = probability of absorbing a phonon
P_e = probability of emitting a phonon
Q = absorbed radiation energy, Jm^{-2}
R = reflectivity of electrons at grain boundaries
S = source term, Wm^{-3}
T = temperature, K
$\mathfrak{I}$ = transition probability between energy levels
T_D = Debye temperature, K
t = time, s
t_c = characteristic electron-phonon thermalization time $= C_e/G$, s
U = lattice energy, Jm^{-3}
v_F = speed of electrons, ms^{-1}
x = spatial coordinate, m
α = grain diameter parameter $= R\Lambda_b/(1-R)/D$
β = film thickness parameter $= d/\Lambda_b$
κ = thermal conductivity, Wm^{-1}k^{-1}
Λ = electron mean-free-path, m
ν = phonon frequency, s^{-1}
σ = electrical conductivity, Ω^{-1}m^{-1}

Subscripts

b = bulk material
e = electrical condition
eq = equilibrium
f = film
F = Fermi surface
l = lattice
o = initial condition

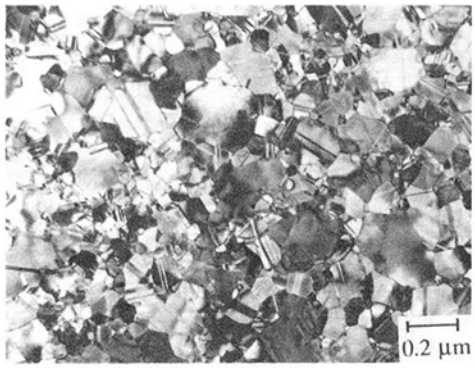

Fig. 2 Microstructures in a polycrystalline gold film (taken with TEM at 100 kV)

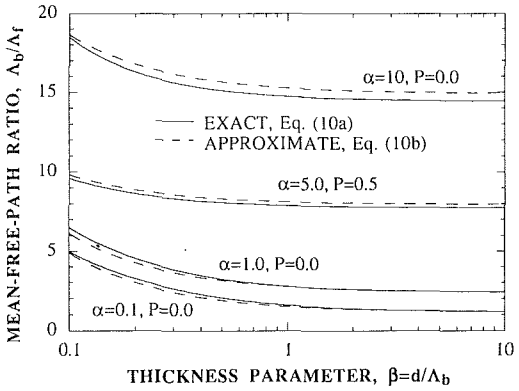

Fig. 3 Comparison between exact and approximate expressions of Λ

Table 1 Grain boundary reflection coefficient, R

Metal	R
Al	0.15[a], 0.17[a], 0.23[b], 0.19[c]
Fe	0.983-0.996[d]
Ni	0.19[e]
Cu	0.24[a], 0.32-0.34[d], 0.23[f]
Mo	0.4-0.75[d]
Ag	0.24[b], 0.25[c]
Sn	0.61-0.71[g]
Au	0.17[b], 0.17[e]
Pb	0.72-0.85[g]

[a]Mayadas & Shatzkes (1970); [b]De Vries (1988)
[c]Tochitskii & Belyavskii (1980); [d]Kwapulinski et al. (1988)
[e]De Vries (1987a,b); [f]Islamgaliev et al. (1990)
[g]Kumar et al. (1987).

Mayadas and Shatzkes (1970) analyzed the effects of both grain boundary scattering and film surface scattering on the electrical conductivity of thin films, σ, yielding

$$\frac{\sigma_f}{\sigma_b}=1-\frac{3}{2}\alpha+3\alpha^2-3\alpha^3\ln\left(1+\frac{1}{\alpha}\right)-\frac{6(1-P)}{\pi\beta}\times\int_0^{\pi}d\theta\int_0^1\frac{\cos^2\theta}{H^2}(u-u^3)\cdot\frac{1-\exp(-\beta H/u)}{1-P\exp(-\beta H/u)}du \quad (6a)$$

$$H=1+\frac{\alpha}{\sqrt{1-u^2\cos\theta}},\quad \alpha=\frac{R}{1-R}\frac{\Lambda_{e,b}}{D},\quad \beta=\frac{d}{\Lambda_{e,b}} \quad (6b)$$

where $\Lambda_{e,b}$ is the electron mean-free-path during electrical conduction in bulk materials, R is the electron reflection coefficient at grain boundaries (Table 1), P is the specular reflection parameter of electrons at film surfaces, d is the film thickness, and D is the averaged grain diameter. The parameter P depends on the relative film roughness compared with the wavelength of electrons.

The thermal conductivity is related to the electrical conductivity through the Wiedemann-Franz law at relatively high temperatures (compared to the Debye temperature) by

$$\frac{\kappa_{eq}}{\sigma_{eq}T}=\frac{\pi^2k^2}{3e^2} \quad (7)$$

By further using Eq. (4) and the relation

$$\sigma_{eq}=\frac{ne^2\Lambda_e}{mv_F} \quad (8)$$

the Wiedemann-Franz law yields

$$\Lambda=\Lambda_e \quad (9)$$

indicating that the electron mean-free-path in the transport of energy is identical to that in the transport of electricity. Therefore, combining Eqs. (6), (8), and (9) yields the effective Λ_f for heat conduction, which accounts for both surface scattering and grain boundary scattering,

$$\frac{\Lambda_f}{\Lambda_b}=1-\frac{3}{2}\alpha+3\alpha^2-3\alpha^3\ln\left(1+\frac{1}{\alpha}\right)-\frac{6(1-P)}{\pi\beta}\int_0^{\pi}d\theta\int_0^1\times\frac{\cos^2\theta}{H^2}(u-u^3)\cdot\frac{1-\exp(-\beta H/u)}{1-P\exp(-\beta H/u)}du \quad (10a)$$

which can be further approximated by

$$\frac{\Lambda_b}{\Lambda_f}=1+\frac{3}{8\beta}(1-P)+\frac{7}{5}\alpha \quad (10b)$$

within 9 percent error when the film thickness and the grain diameter are not too small compared with Λ_b, i.e., $\alpha<10$ and $\beta>0.1$ (Fig. 3).

Inserting Eq. (10*b*) into Eq. (5) gives rise to the thermal conductivity of thin films during nonequilibrium heating,

$$\frac{\kappa_f(T_e,T_l)}{\kappa_{eq,b}(T_l)}=\frac{T_e}{T_l}\left[1+\frac{3}{8\beta}(1-P)+\frac{7}{5}\alpha\right]^{-1} \quad (11)$$

It is clearly shown that the effect of interface scattering reduces κ and the effect of nonequilibrium heating increases κ. If $T_e=T_l$ and $D\to\infty$, Eq. (11) describes the size effect due to surface scattering only for the equilibrium case and is identical, to first order, to the previous model (Tien et al., 1969; Kumar and Vradis, 1991),

$$\frac{\kappa_{eq,f}}{\kappa_{eq,b}}=1-\frac{3}{8\beta}-\frac{3}{4}\left(\beta-\frac{1}{12}\beta^3\right)Ei(-\beta)-e^{-\beta}\left(\frac{5}{8}+\frac{1}{16}\beta-\frac{1}{16}\beta^2-\frac{3}{8\beta}\right) \quad (12)$$

where Ei is the exponential integral function. The current formula, however, is more general, because it includes the effects of both grain boundary scattering and nonequilibrium heating.

Figure 4 shows the comparison of the predicted size effect on $\kappa_{eq,f}$ with experimental data (Nath and Chopra, 1974; Kelemen, 1976). The averaged grain diameter depends on conditions of film deposition, including the chamber pressure, the substrate temperature, and the evaporation rate. The mean grain diameter typically increases with the increase of the substrate temperature and is often proportional to the film thickness for films thinner than 1 μm (Mayadas and Shatzkes, 1970; Hoffmann et al., 1985; Kumar et al., 1987; De Vries, 1988). De Vries (1988) found that D/d is about 0.2 for nickel, cobalt, and palladium films deposited at 295 K onto a silicon substrate covered with 0.4 μm SiO_2. Therefore, D/d is chosen as 0.2 here for model simulation. Since the electron wavelength is extremely small, about 10 Å, the reflection of electrons at film

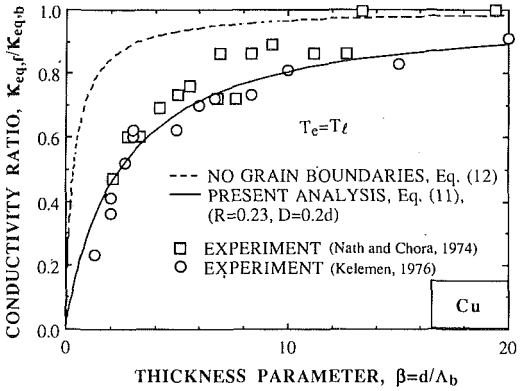

Fig. 4 Comparison of predicted size effect on thermal conductivity with experimental data

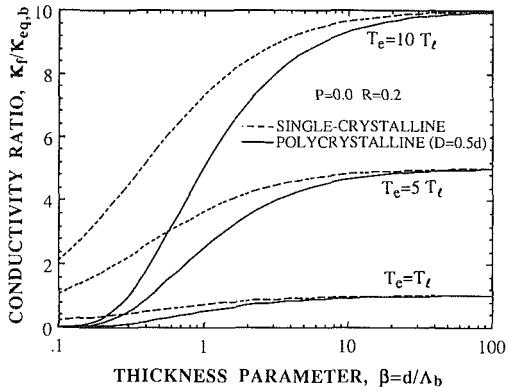

Fig. 5 Effects of size and nonequilibrium heating on the thermal conductivity

surfaces is diffusive for most film surfaces. Therefore, P is taken to be zero. The reflectivity of electrons at grain boundaries is $R=0.23$ for Cu (Table 1) and the bulk Λ used in the model predictions is from Fig. 1. The comparison shows that the current model (Eq. (11)) agrees well with the experimental results, and the previous model (Eq. (12)), which does not consider grain boundary scattering, underpredicts the size effect. When the film thickness is around or smaller than the mean-free-path, e.g., $\beta=1$, the film thermal conductivity is significantly reduced because of surface and grain boundary scattering.

Figure 5 shows the effects of size and nonequilibrium heating on the thermal conductivity of single-crystalline and polycrystalline films. The grain diameter is assumed to be proportional to the film thickness, e.g., $D=0.5d$, and the scattering parameters are chosen as $P=0$ and $R=0.2$. The results show that in the regime $\beta>10$, the size effect is small and the nonequilibrium effect increases κ significantly. In the region $\beta<10$, however, the size effect becomes important, reducing κ greatly, and is further enhanced in the polycrystalline films due to grain boundary scattering.

Effect of Size on Electron-Phonon Coupling Factor

Electrons collide with the material lattice due to the thermal vibration of atoms, imperfections, and surfaces. When electrons and the lattice are not in thermal equilibrium, there is a net energy exchange between electrons and the lattice, described by G (Eq. (1)). Even though quantum-mechanics evaluation of G has been done for single crystals (Kaganov et al., 1957), its extension to polycrystalline films is very difficult since the potentials at surfaces and grain boundaries needed for the quantum mechanical calculation are not known. Therefore this work develops a simple thermodynamics approach to evaluate G.

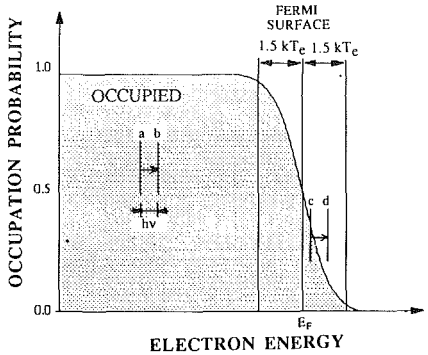

Fig. 6 Electron occupation probability

The procedure is to estimate (1) the effective number of electrons contributing to the energy exchange between electrons and the lattice, and (2) the averaged energy exchange per collision. Then the total energy exchange per unit time per unit volume is the product of the number of the active electrons, the average energy change per collision, and the collision frequency. The size effect increases G by increasing the electron collision frequency, since variations of atomic spacing and structures at surfaces and grain boundaries cause additional collisions for electrons.

Electrons Contributing to Energy Exchange. Electrons obey Fermi-Dirac statistics

$$f=\frac{1}{1+\exp\left((E-E_F)/kT_e\right)} \tag{13}$$

Near room temperature, they occupy almost all the states below the Fermi surface and leave almost all the states empty above the Fermi surface except a very narrow region around the Fermi surface (Fig. 6). The width of this narrow region is about $3kT_e$ (about 50 meV) and is much smaller than the Fermi energy E_F (e.g., for gold, $E_F=5.5$ eV). During electron-lattice interactions, electrons gain or lose the energy of a phonon. In the Debye model for phonons, the maximum energy of a phonon is

$$h\nu_D=kT_D \tag{14}$$

where T_D is the Debye temperature and is in the range of 100–400 K for typical metals. Therefore the phonon energy, about 20 meV, is also very small compared to the Fermi energy, and the energy states of electrons before and after transitions are very close. Due to the restriction of the Pauli exclusion principle, electronic transitions cannot take place between occupied states, e.g., $a\rightarrow b$ (Fig. 6). The transitions can only occur in the very narrow region around the Fermi surface, e.g., $c\rightarrow d$ (Fig. 6). The number of electrons in this region is roughly

$$n_{e-l}=f(E_F)\cdot D(E_F)\cdot 3kT_e=\frac{9}{4}\frac{kT_e}{E_F}n \tag{15a}$$

where $D(E_F)$ is the density of states at the Fermi surface,

$$D(E_F)=\frac{3}{2}\frac{n}{E_F} \tag{15b}$$

Only about 1 percent of the total free electrons contribute to the energy exchange with the lattice during collisions.

Energy Exchange During Collisions. This work develops a simple three-energy-level model to characterize the energy exchange between free electrons and the lattice. Electrons collide with the lattice whenever iron cores are not in perfectly periodic positions. For a polycrystalline thin-film, the iron cores are away from the perfect positions due to thermal vi-

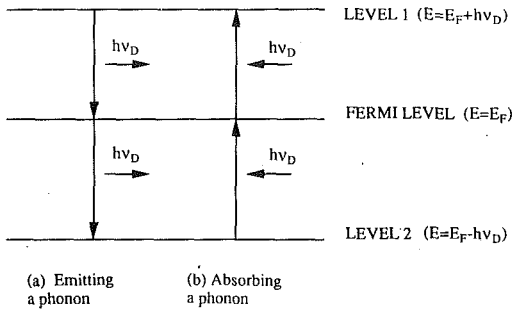

Fig. 7 Schematic diagram of electronic transitions between three energy levels

bration, structure change at grain boundaries, and structure change at surfaces. During collisions, electrons can either lose energy to the lattice by emitting phonons or gain energy from the lattice by absorbing phonons. When electrons and the lattice are not in thermal equilibrium, there is a net energy exchange between electrons and the lattice, which can be evaluated from phonon energy and phonon emission/absorption probabilities. Two approximations are made to simplify the evaluation procedure: (1) all the phonons emitted or absorbed during electronic transitions have the fixed energy $h\nu_D$, and (2) electronic transitions take place only between three energy levels, $E_F - h\nu_D$, E_F, and $E_F + h\nu_D$. The first approximation is reasonable when the lattice temperature is much higher than the Debye temperature. The second approximation makes the evaluation extremely simple compared with the standard quantum-mechanical approach.

Figure 7 is a schematic diagram showing the electronic transition processes. The transition probability from level 1 to the Fermi level by emitting a phonon is

$$\Im_{1\to F} = f(E_F + h\nu_D)[1 - f(E_F)]P_e = \frac{1}{2}\cdot\frac{P_e}{1+\exp(h\nu_D/kT_e)} \quad (16a)$$

where $f(E_F + h\nu_D)$ is the probability of finding an electron at the initial level, $1 - f(E_F)$ is the probability of having an empty state at the final level, and P_e is the probability of emitting a phonon. In a similar way, the transition probability from the Fermi level to level 1 by absorbing a phonon is

$$\Im_{F\to 1} = f(E_F)[1 - f(E_F + h\nu_D)]P_a = \frac{1}{2}\cdot\frac{P_a \exp(h\nu_D/kT_e)}{1+\exp(h\nu_D/kT_e)} \quad (16b)$$

where P_a is the probability of absorbing a phonon and is proportional to the averaged number of phonons of frequency ν_D,

$$P_a \propto N(\nu_D) = \frac{1}{\exp(h\nu_D/kT_l) - 1} \quad (17a)$$

Phonon emission is analogous to photon emission, consisting of both spontaneous emission and stimulated emission processes. Therefore, P_e is proportional to $1 + N(\nu_D)$,

$$P_e \propto 1 + N(\nu_D) = \frac{\exp(h\nu_D/kT_l)}{\exp(h\nu_D/kT_l) - 1} \quad (17b)$$

Thermal equilibrium considerations can lead to further expressions for P_a and P_e. When electrons and the lattice are in thermal equilibrium, i.e., $T_e = T_l$, the transition probabilities $\Im_{1\to F}$ and $\Im_{F\to 1}$ should be equal. Therefore, the proportion constants in Eqs. (17*a*) and (17*b*) are equal. By further using the condition, $P_a + P_e = 1$, P_a and P_e can be evaluated as

$$P_a = \frac{1}{\exp(T_D/T_l) + 1}, \quad P_e = \frac{\exp(T_D/T_l)}{\exp(T_D/T_l) + 1} \quad (18)$$

At relatively high temperature (T_e, $T_l > T_D$), expanding Eqs. (16) and (18) yields approximate expressions for transition probabilities between level 1 and the Fermi level,

$$\Im_{1\to F} = \frac{1}{8}\left(1 + \frac{1}{2}\frac{T_D}{T_l} - \frac{1}{2}\frac{T_D}{T_e} - \frac{1}{4}\frac{T_D^2}{T_eT_l}\right),$$
$$\Im_{F\to 1} = \frac{1}{8}\left(1 - \frac{1}{2}\frac{T_D}{T_l} + \frac{1}{2}\frac{T_D}{T_e} - \frac{1}{4}\frac{T_D^2}{T_eT_l}\right) \quad (19a)$$

At temperatures $T_e = T_D$ and $T_l = T_D$, the error of the above expressions is 5 percent. At higher electron and lattice temperatures, these approximations are much more accurate.

Equation (19*a*) provides very interesting insights about the transition processes. When the electron and the lattice temperatures are equal, the transition probability from level 1 to the Fermi level and that from the Fermi level to level 1 are equal. When $T_e > T_l$, however, the number of transitions from level 1 to the Fermi level is more than that in the reverse direction, resulting in a net flow of electrons from the high energy level to the low energy level and a net energy flux to the lattice.

The transition probabilities between level 2 and the Fermi level can be evaluated in the same way:

$$\Im_{F\to 2} = \frac{1}{8}\left(1 + \frac{1}{2}\frac{T_D}{T_l} - \frac{1}{2}\frac{T_D}{T_e} - \frac{1}{4}\frac{T_D^2}{T_eT_l}\right),$$
$$\Im_{2\to F} = \frac{1}{8}\left(1 - \frac{1}{2}\frac{T_D}{T_l} + \frac{1}{2}\frac{T_D}{T_e} - \frac{1}{4}\frac{T_D^2}{T_eT_l}\right) \quad (19b)$$

The net energy exchange between electrons and the lattice per unit time and per unit volume is then the product of the effective collision frequency, the effective number density of electrons, and the averaged energy exchange per collision, as

$$\frac{dU}{dt} = \frac{v_F}{\Lambda(T_l)} n_{e-l} h\nu_D (\Im_{1\to F} - \Im_{F\to 1} + \Im_{F\to 2} - \Im_{2\to F}) = G(T_e - T_l) \quad (20a)$$

$$G = \frac{9}{16}\frac{nk^2T_D^2v_F}{\Lambda(T_l)T_lE_F} \quad (20b)$$

This simple thermodynamics approach gives the same form of G as that from a quantum-mechanics approach (Kaganov et al., 1957) except for the different meaning of $\Lambda(T_l)$ used in the expressions. The $\Lambda(T_l)$ here is the effective electron mean-free-path in polycrystalline thin films, and in the work of Kaganov et al. $\Lambda(T_l)$ is for single-crystalline bulk materials.

Side Effect. The electron-phonon coupling factor of thin films is readily found from Eq. (20) and Eq. (10*b*) as

$$\frac{G_f}{G_b} = \frac{\Lambda_b}{\Lambda_f} = 1 + \frac{3}{8\beta}(1-P) + \frac{7}{5}\alpha \quad (21)$$

The effect of grain-boundary scattering on G has been observed in 200 Å gold films (Elsayed-Ali et al., 1991). The factor G of single-crystalline films and polycrystalline films deduced from measurements is 3.4×10^{16} W/m^{3}K and 4.0×10^{16} W/m^{3}K, respectively. On the other hand the calculated G for 200 Å single-crystalline and polycrystalline gold films is 4.1×10^{16} W/m^{3}K and 5.7×10^{16} W/m^{3}K, respectively, using published data, $n = 5.9\times10^{28}$ m^3, $T_D = 165$ K, $v_F = 1.39\times10^6$ m/s, $E_F = 8.82\times10^{-19}$ J (Kittel, 1986), Λ_b (300 K) = 390 Å (Fig. 1), and film parameters, $P = 0$, $R = 0.17$ (Table 1) and $D = 160$ Å (Elsayed-Ali, 1992). The model predicts the right trend of the size effects on G. Quantitative agreement between predicted G and measured G is within 42 percent.

Figure 8 shows the effect of size on G. In the region $\beta > 10$, the size effect is negligible; and in the region $\beta < 1$, the size effect increases G significantly. This result indicates that stresses and scratches in thin metal films, which produce small grains, may increase G, which in turn decrease their thermal damage threshold to short laser pulses.

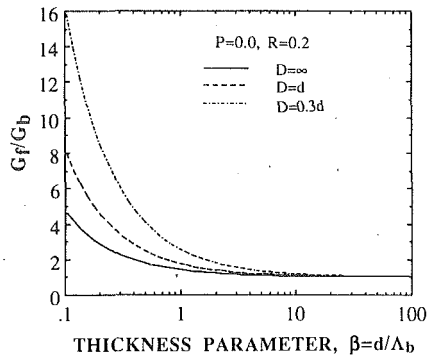

Fig. 8 Size effects on electron-phonon coupling factor

Conclusions

A better understanding of energy transport mechanisms and properties during fast laser heating is important for applications of short-pulse lasers and for prevention of laser damage. This paper presents a theoretical study on the effects of electron scattering at grain and film boundaries on the thermal conductivity and the electron-phonon coupling factor during the nonequilibrium heating of metals.

The effective thermal conductivity of metal thin films is determined considering the size effects due to both surface scattering and grain boundary scattering and the nonequilibrium heating effect. The predictions of the current model agree with experimental data.

A simple three-energy-level model is developed to evaluate the electron-phonon coupling factor and to estimate the size effects on it. The size effects increase this factor and the prediction is consistent with experimental results.

Acknowledgments

The authors gratefully acknowledge financial support for this research from the U.S. National Science Foundation and the K.C. Wong Education Foundation.

References

Anisimov, S. I., Kapeliovich, B. L., and Perel'man, T. L., 1974, "Electron Emission From Metal Surfaces Exposed to Ultrashort Laser Pulses," *Sov. Phys. JETP*, Vol. 39, pp. 375–377.

Chen, G., and Tien, C. L., 1993, "Thermal Conductivity of Quantum Well Structures," *AIAA Journal of Thermophysics and Heat Transfer*, Vol. 7, pp. 311–318.

Chlipala, J. D., Scarfone, L. M., and Lu, C. Y., 1989, "Computer-Simulated Explosion of Poly-Silicide Links in Laser-Programmable Redundancy for VLSI Memory Repair," *IEEE Transactions on Electron Devices*, Vol. 36, pp. 2433–2439.

De Vries, J. W. C., 1987a, "Temperature-Dependent Resistivity Measurements on Polycrystalline SiO_2-Covered Thin Gold Films," *Thin Solid Films*, Vol. 150, pp. 201–208.

De Vries, J. W. C., 1987b, "Temperature-Dependent Resistivity Measurements on Polycrystalline SiO_2-Covered Thin Nickel Films," *Thin Solid Films*, Vol. 150, pp. 209–215.

De Vries, J. W. C., 1988, "Temperature and Thickness Dependence of the Resistivity of Thin Polycrystalline Aluminum, Cobalt, Nickel, Palladium, Silver and Gold Films," *Thin Solid Films*, Vol. 167, pp. 25–32.

Eesley, G. L., 1990, "Picosecond Dynamics of Thermal and Acoustic Transport in Metal Films," *Int. J. Thermophysics*, Vol. 11, pp. 811–817.

Elsayed-Ali, H. E., Juhasz, T., Smith, G. O., and Bron, W. E., 1991, "Femtosecond Thermoreflectivity and Thermotransmissivity of Polycrystalline and Single-Crystalline Gold Films," *Phys. Rev. B*, Vol. 43, pp. 4488–4491.

Elsayed-Ali, H. E., 1992, Private Communication, University of Rochester, Rochester, NY.

Flik, M. I., and Tien, C. L., 1990, "Size Effect on the Thermal Conductivity of High-T_c Thin-Film Superconductors," ASME JOURNAL OF HEAT TRANSFER, Vol. 112, pp. 872–881.

Guenther, A. H., and McIver, J. K., 1989, "The Pulsed Laser Damage Sensitivity of Optical Thin Films—Thermal Conductivity," *Laser and Particle Beams*, Vol. 7, pp. 433–441.

Hoffmann, H., Vancea, J., and Jacob, U., 1985, "Surface Scattering of Electrons in Metals," *Thin Solid Films*, Vol. 129, pp. 181–193.

Islamgaliev, R. K., Akhmadeev, N. A., Mulyukov, R. R., and Valiev, R. Z., 1990, "Grain Boundary Influence on the Electrical Resistance of Submicron Grained Copper," *Physica Status Solid A*, Vol. 118, pp. K27–K29.

Kaganov, M. I., Lifshitz, I. M., and Tanatarov, L. V., 1957, "Relaxation Between Electrons and Crystalline Lattices," *Sov. Phys. JETP*, Vol. 4, pp. 173–178.

Kelemen, P. G., 1976, "Pulse Method for the Measurement of the Thermal Conductivity of Thin Films," *Thin Solid Films*, Vol. 36, pp. 199–203.

Kim, W. S., Hector, L. G., Jr., and Özişik, M. N., 1990, "Hyperbolic Heat Conduction Due to Axisymmetric Continuous or Pulsed Surface Heat Sources," *J. Appl. Phys.*, Vol. 68, pp. 5478–5485.

Kittel, C., 1986, *Introduction to Solid State Physics*, 6th ed., Wiley, New York.

Kumar, A., Chandra, G., and Katyal, O. P., 1987, "The Effect of Grain Boundary Scattering on the Electrical Resistivity of Polycrystalline Lead, Tin, and Tin–Lead Alloy Films," *Physica Status Solid A*, Vol. 100, pp. 169–175.

Kumar, S., and Vradis, G. C., 1991, "Thermal Conduction by Electrons Along Thin Films: Effects of Thickness According to Boltzmann Transport Theory," *Micromechanical Sensors, Actuators, and Systems*, D. Cho et al., eds., ASME DSC-Vol. 32, pp. 89–101.

Kwapulinski, P., Rasek, J., and Gierak, Z., 1988, "Scattering of Conductivity Electrons on Grain Boundaries in Metals," *Physica Status Solid A*, Vol. 107, pp. 299–304.

Majumdar, A., 1991, "Microscale Heat Conduction in Dielectric Thin Films," in: *Thin Film Heat Transfer: Properties and Processing*, ASME HTD-Vol. 184, pp. 33–42.

Mayadas, A. F., and Shatzkes, M., 1970, "Electrical-Resistivity Model for Polycrystalline Films: the Case of Arbitrary Reflection at External Surfaces," *Phys. Rev. B*, Vol. 1, pp. 1382–1389.

Maxwell, J. C., 1867, "On the Dynamical Theory of Gases," *Philos. Trans. Soc. London*, Vol. 157, pp. 49–88.

Narayan, J., Godbole, V. P., and White, G. W., 1991, "Laser Method for Synthesis and Processing of Continuous Diamond Films on Nondiamond Substrates," *Science*, Vol. 52, pp. 416–418.

Nath, P., and Chopra, K. L., 1974, "Thermal Conductivity of Copper Films," *Thin Solid Films*, Vol. 20, pp. 53–62.

Powell, R. W., and Ho, C. Y., 1968, "The State of Knowledge Regarding the Thermal Conductivity of the Metallic Elements," *Proceedings of Seventh Thermal Conductivity Conference*, D. R. Flynn et al., eds., National Bureau of Standards Special Publication 302, pp. 1–32.

Qiu, T. Q., and Tien, C. L., 1992a, "Short-Pulse Laser Heating on Metals," *Int. J. Heat Mass Transfer*, Vol. 35, pp. 719–726.

Qiu, T. Q., and Tien, C. L., 1992b, "Heat Transfer Mechanisms During Short-Pulse Laser Heating on Metals," in: *Transport Phenomena in Materials Processing and Manufacturing*, M. Charmchi et al., eds., ASME HTD-Vol. 196, pp. 41–49.

Reitze, D. H., Wang, X., Ahn, H., and Downer, M. C., 1989, "Femtosecond Laser Melting of Graphite," *Phys. Rev. B*, Vol. 40, pp. 11986–11989.

Saeta, P., Wang, J. K., Siegal, Y., Bloembergen, N., and Mazur, E., 1991, "Ultrafast Electronic Disordering During Femtosecond Laser Melting of GaAs," *Physical Review Letters*, Vol. 67, pp. 1023–1026.

Schultze, V., and Fischer, A., 1989, "Laser Trimming of NiCr Thin Film Resistors, I. Thin Film Resistors Without a Protective Layer," *Thin Solid Films*, Vol. 18, pp. 23–33.

Simon, R., 1991, "High-T_c Thin Films and Electronic Devices," *Physics Today*, Vol. 44, pp. 64–70.

Tien, C. L., Armaly, B. F., and Jagannathan, P. S., 1969, "Thermal Conductivity of Thin Metallic Films and Wires at Cryogenic Temperature," *Proceedings of Eighth Thermal Conductivity Conference*, C. Y. Ho and R. E. Taylor, eds., Plenum Press, pp. 13–20.

Tien, C. L., and Lienhard, J. H., 1979, *Statistical Thermodynamics*, Hemisphere, Washington, DC.

Tochitskii, E. I., and Belyavskii, N. M., 1980, "Grain-Boundary Electron Scattering Effect on Metal Film Resistivity," *Physica Status Solid A*, Vol. 61, pp. K21–K24.

Tzou, D. Y., 1992, "Thermal Shock Phenomena Under High Rate Response in Solids," *Annual Review of Heat Transfer*, C. L. Tien, ed., Hemisphere, Washington, DC, Vol. 4, pp. 111–185.

Three-Dimensional Analytical Temperature Field Around the Welding Cavity Produced by a Moving Distributed High-Intensity Beam

P. S. Wei
Professor.
Mem. ASME

M. D. Shian
Graduate Student.

Institute of Mechanical Engineering,
National Sun Yat-Sen University,
Kaohsiung, 80424 Taiwan

An analytical solution for the three-dimensional temperature field in the liquid and heat-affected zones around a welding cavity produced by a moving distributed low- or high-power-density-beam is provided. The incident energy rate distribution is assumed to be Gaussian and the cavity is idealized by a paraboloid of revolution in workpieces of infinite, semi-infinite, or finite thicknesses. The present study finds that temperature fields can be described by the Laguerre and confluent hypergeometric functions. By satisfying a momentum balance at the cavity base and utilizing a consequence of the second law of thermodynamics, the depth of penetration is uniquely determined. The results show that the predicted depths and temperatures of the cavity agree with available experimental data. Some crucial factors affecting the transition from low- to high-power-density-beam welding are presented.

Introduction

Temperature fields are required to predict welding processes, microstructures, residual stresses, and distortions of workpieces (Wei and Lii, 1990; David and Vitek, 1989; Masubuchi, 1980). Therefore, finding analytical and simple thermal solutions is strongly desired. In arc or low-power-density-beam welding, which has energy densities greater than a critical value (Elmer et al., 1990), a high temperature is produced near the center of the surface area heated by the incident fluxes. Incident energy fluxes have been assumed to be generated by a point source at the surface in order to simplify the model and obtain an analytical solution (Rosenthal, 1941). On the other hand, a line-source model (Rosenthal, 1941) is applicable for high-power-density-beam welding (Elmer et al., 1990), which is characterized by the formation of a deep and narrow cavity in the molten pool. Recently, Wei et al. (1993b) numerically simulated the development of the cavity in the molten pool by accounting for convection and phase changes between the solid and liquid. The deep cavity results from upward and outward flows induced by vapor pressure and surface tension gradients, as proposed by Wei and Chiou (1988).

It has been more than fifty years since Rosenthal (1941) applied solutions for the moving point- and line-heat sources (see Eqs. (27) and (26), respectively) in welding and cutting. These models have been the basis for most subsequent studies of heat flow in metals processing. The results were first successfully used by Adams (1958) to predict cooling rates and hardness of workpieces. Christensen et al. (1965) nondimensionalized the point-source model and confirmed the solution by observing fusion zones over a wide range of arc welding parameters. Swift-Hook and Gick (1973) utilized the line-source model to calculate consistent shapes of the laser- and electron-beam welds, provided the energy absorbed by the workpiece is known.

Although they are attractive, the point and line-source solutions in their pristine forms have certain defects. They are: (1) infinite temperatures occurred near the sources; (2) the distribution of incident flux was not taken into account. Giedt and Tallerico (1988) and Wei et al. (1990) found that the distribution of incident fluxes is the most important factor affecting the depth of penetration. Measurements of a transition between a distribution, point and line-sources for electron beam welding (Elmer et al., 1990) therefore are important; (3) vertical heat transport was neglected in the line-source model. Since energies primarily irradiate at the cavity base where the maximum temperature and energy losses around 40–50 percent of beam power occur (Wei and Ho, 1990), an ignorance of vertical energy transport can induce significant errors; (4) momentum balance was not taken into account; and (5) the thermal fields in the liquid region cannot be relevantly accounted for and the effect of convection was ignored.

Good agreement between point and line-source models and experimental results can be due to compensating effects between these uncertain factors. In order to avoid weaknesses and obtain additional valuable results, the point and line-source models have been extended. The point-source was integrated by Cline and Anthony (1977) over the workpiece surface to yield finite temperatures induced by a low-energy-density laser beam with a Gaussian distribution. Eagar and Tsai (1983) found that the distribution parameter of the Gaussian profile significantly affects shapes of fusion zones. Nunes (1983) expanded the point and line-source solutions in multipolar forms by introducing empirical dipole and quadrupole moments. Effects of phase change and circulation in the weld pool were presumably expected. The line-source solution was also applied by Giedt and Tallerico (1988) to calculate depths of conically shaped fusion zones. Steen et al. (1988) added point-source near the top and bottom of a line-source input to simulate a nail-head weld.

The cavity produced by a high-intensity beam is finite in size. An approximate three-dimensional heat-conduction model by satisfying interfacial energy and momentum balances at the cavity was therefore proposed by Wei et al. (1990) and Wei and Chow (1992). In these studies, the local two-dimensional

Contributed by the Heat Transfer Division for publication in the JOURNAL OF HEAT TRANSFER. Manuscript received by the Heat Transfer Division May 1992; revision received March 1993. Keywords: Conduction, Laser Processing, Materials Processing and Manufacturing Processes. Associate Technical Editor: Y. Bayazitoglu.

analytical solution of a moving circular cylinder of a constant temperature (Carslaw and Jaeger, 1959; Tong and Giedt, 1971) was used and an iteration technique was applied. Although prediction of fusion zones fails in a region where the radius of the cavity approaches zero, this model first exclusively and successfully demonstrated effects of beam focusing characteristics such as the convergence angle, spot size, focal location, and volatile elements on temperatures and shapes of the cavity. Using the moving cavity model therefore is a relevant way to investigate general features of welding and cutting.

In this study, three-dimensional temperature fields around the welding cavity produced by a moving energy beam of a Gaussian distribution are provided. For simplicity, the cavity is idealized by a paraboloid of revolution. By using the separation-of-variables method in parabolic orthogonal coordinates, analytical solutions can be found. The result will show additional important factors such as the effects of convection and dimensionless cavity opening radius (i.e., the cavity opening radius-to-energy distribution parameter ratio) on penetration depth. Factors affecting the transition between the low- and high-power-density-beam welds are also treated. Advantages of the present work are revealed by comparing with the point and line-source solutions.

System Model and Analysis

A workpiece is moved with a constant speed relative to the energy beam, as illustrated in Fig. 1. As the base material reaches the energy beam location, it is melted and flows in a thin layer around a vapor-supported cavity to the rear where it cools and solidifies. To simplify the analysis, the following assumptions are made:

1 A quasi-steady state is assumed for a sufficient welding length or time.

2 The incident energy flux on any horizontal cross section

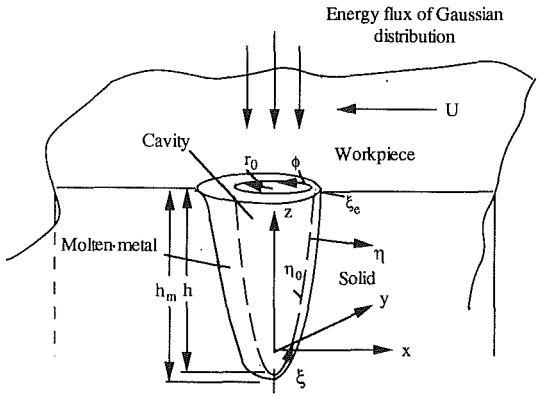

Fig. 1 Physical model and coordinate system

of the beam is a Gaussian distribution. This was confirmed by Hicken et al. (1991) by measuring distributions of incident fluxes at vertical distances that deviated from the focal spot of an electron beam. As for a laser beam, the distribution is relevant for the spatially coherent TEM_{00} model (Nippes, 1983) while incident fluxes of a multimode caused by the transverse electric and magnetic fields cannot be treated.

3 The radiative absorptivity of the cavity wall is assumed to be unity so that energies absorbed are simply related to the Gaussian distribution. In reality, the cavity is a specular and diffuse reflector. Wang and Wei (1992) are the first to use a Monte Carlo method to calculate energy absorption by a cavity of paraboloid of revolution irradiated by an incident beam of uniform top-hat and Gaussian distributions. Energies absorbed were found to be similar to a Gaussian distribution for a cavity depth-to-opening radius ratio greater than 5.

4 Incident energies are a surface heat source. This is because

Nomenclature

g, g^* = dimensionless workpiece thickness, $g = \hat{g}/\hat{\sigma}$, $g^* = U\hat{g}/2\alpha$

h = dimensionless cavity depth $= \hat{h}/\hat{\sigma}$

H = $h_{lg}/R(T_m - T_\infty)$

h_{lg} = latent heat of evaporation

$\hat{h}_m$ = dimensional maximum weld pool depth

K = conductivity ratio $= k_s/k_l$

k_l, k_s = liquid and solid thermal conductivity

L_p^m = Laguerre function

p = pressure

P = $\hat{p}_b\hat{\sigma}/\gamma_m$

Pe = Peclet number $= U\hat{\sigma}/\alpha$

q, Q = incident energy flux and power

Q^* = dimensionless beam power $= \hat{Q}/k_l\hat{\sigma}(T_m - T_\infty)$

r = radial coordinate $= \hat{r}/\hat{\sigma}$

R = gas constant

r_0 = dimensionless cavity opening radius $= \hat{r}_0/\hat{\sigma}$

S = parameter approximating convection $= \alpha/\alpha_z$

T, T_∞ = dimensional temperature and ambient temperature

U = dimensional welding speed

v = transformed dimensionless temperature

x, y, z = Cartesian coordinates as shown in Fig. 1, $x = \hat{x}/\hat{\sigma}$, $y = \hat{y}/\hat{\sigma}$, $z = \hat{z}/\hat{\sigma}$

x^*, y^*, z^* = dimensionless Cartesian coordinates, defined in Eq. (3)

α, α_s = liquid and solid diffusivity

α_z = enhanced diffusivity in vertical direction

γ = surface tension or Euler's constant

Γ = gamma function

η, η_0 = parabolic coordinate and coordinate on cavity surface, as shown in Fig. 1

θ = dimensionless temperature $= (T - T_\infty)/(T_m - T_\infty)$

θ_∞ = $T_\infty/(T_m - T_\infty)$

Λ = α/α_s

ξ, ξ_e = parabolic coordinate and coordinate at cavity opening, as shown in Fig. 1

$\hat{\sigma}$ = dimensional energy distribution parameter, dimensionless energy distribution parameter $\sigma = 1$

Y = $(T_m - T_\infty)(d\gamma/dT)/\gamma_m$ where $d\gamma/dT$ is a constant

ϕ = parabolic coordinate, as shown in Fig. 1

Φ = Kummer's function

ψ = di-gamma function

Ψ = confluent hypergeometric function of the second kind

Superscripts

m = index

$\hat{}$ = dimensional quantity

$', ''$ = image coordinates creating adiabatic top and bottom surfaces, respectively, as shown in Fig. 4

Subscripts

b = boiling

B = cavity base

m = melting

p = index

energy incident on the side wall is low due to a large incident angle and the radiative absorptivity, that is a reciprocal of absorption length, is as large as 10^7 m^{-1} for most metals and alloys (Wei et al., 1993a).

5 The cavity is idealized by a paraboloid of revolution. Hence, a curvilinear orthogonal parabolic coordinate $\xi\eta\phi$ system (Morse and Feshbach, 1978) can be used effectively. In fact, the shapes of the cavity can be a cone, paraboloid of revolution, and other irregular geometries (Tong and Giedt, 1969). For welding with a moving heat source the geometry becomes slightly asymmetric (Wei et al., 1990). The cavity, however, can be roughly observed to be a paraboloid of revolution near the cavity base (Schauer and Giedt, 1978), especially for a deep and narrow cavity.

6 Thermal diffusivity is nonisotropic in order to account for convection. Since the flow of liquid enhances energy transport, the diffusivity in the flow direction is increased by a constant multiple of around five (e.g., Gau and Viskanta, 1984; Giedt et al., 1984). This assumption is used for a rough approximation. A further study of the enhanced diffusivity is definitely required.

7 Local thermodynamic equilibrium is assumed at the base of the cavity. The vapor in the cavity behaves like a neutral deal gas. Vapor pressure therefore can be estimated from the Clausius–Clapeyron equation (e.g., Giedt, 1971). Surface tension as a function of temperature and concentrations of solutes for stainless steel SS 304 is simulated to be that of an Fe–S binary alloy (Sahoo et al. 1988), as proposed by Zacharia et al. (1989) and also used by Choo and Szekely (1991). This seems relevant because sulfur is the surface active solute. This model works well for predicting transient weld pools during arc and low-power-density laser beam welding.

8 Energy losses due to evaporation can be neglected by comparison with incident beam energy and heat conduction loss to the workpiece. This has been quantitatively confirmed by Wei and Ho (1990).

9 Average thermal, physical properties of the workpiece within the temperature range considered are chosen.

Governing Equations and Boundary Conditions. With the above assumptions, the heat conduction equation becomes

$$-U\frac{\partial T}{\partial \hat{x}}=\alpha\left(\frac{\partial^2 T}{\partial \hat{x}^2}+\frac{\partial^2 T}{\partial \hat{y}^2}\right)+\alpha_z\frac{\partial^2 T}{\partial \hat{z}^2} \tag{1}$$

where the quantity α_z is the enhanced diffusivity in the flow or approximately vertical direction. In dimensionless form Eq. (1) becomes

$$-2\frac{\partial\theta}{\partial x^*}=\nabla^2\theta \tag{2}$$

where the dependent variable, θ, represents the dimensionless temperature of liquid, the independent variables are

$$x^*=\frac{U\hat{x}}{2\alpha},\quad y^*=\frac{U\hat{y}}{2\alpha},\quad z^*=\frac{U\hat{z}}{2\alpha_z\sqrt{S}} \tag{3}$$

In eq. (3) the parameter approximating convection $S\equiv\alpha/\alpha_z$. Convection becomes significant as the parameter approximating convection is much less than unity. Introducing a new dependent variable defined as $v\equiv\theta\exp(\sqrt{\xi\eta}\cos\phi)$ (Carslaw and Jaeger, 1959; Miyazaki and Giedt, 1982; Miyazaki et al., 1991) in the parabolic coordinate system, Eq. (2) becomes

$$\frac{4}{\xi+\eta}\left[\frac{\partial}{\partial\xi}\left(\xi\frac{\partial v}{\partial\xi}\right)+\frac{\partial}{\partial\eta}\left(\eta\frac{\partial v}{\partial\eta}\right)+\frac{1}{4}\left(\frac{1}{\xi}+\frac{1}{\eta}\right)\frac{\partial^2 v}{\partial\phi^2}\right]=v \tag{4}$$

where the Cartesian and parabolic orthogonal coordinates are related by

$$x^*=\sqrt{\xi\eta}\cos\phi,\quad y^*=\sqrt{\xi\eta}\sin\phi,\quad z^*=\frac{1}{2}(\xi-\eta) \tag{5}$$

The Gaussian distribution of the incident energy flux across the cavity opening is

$$\hat{q}=\frac{3\hat{Q}}{\pi\hat{\sigma}^2}\exp\left(-\frac{3\hat{r}^2}{\hat{\sigma}^2}\right) \tag{6}$$

where $\hat{\sigma}$ is a dimensional energy flux distribution parameter that defines the region in which 95 percent of the total heat is deposited. An energy balance at the cavity wall then yields

$$\frac{\partial v}{\partial\eta}-\frac{v}{2\eta_0}\sqrt{\xi\eta_0}\cos\phi=-\frac{3Q^*\sqrt{S}}{\pi\mathrm{Pe}}\exp\left(\sqrt{\xi\eta_0}\cos\phi-\frac{12}{\mathrm{Pe}^2}\xi\eta_0\right) \tag{7}$$

where the second term on the left-hand side is ignored in the present work because no error occurs at a location of either an angle of 90 deg or the cavity base where the incident flux is the highest. Although errors increase as the workpiece surface is approached, temperatures predicted are still acceptable. The reason for this is that energies impinging on this region have a large incident angle so that the intensity is reduced. A momentum balance between the vapor pressure and pressure due to surface tension at the cavity base is required to determine the coordinate η_0 of the cavity surface (Wei and Chow, 1992). This yields

$$\eta_0=\frac{\mathrm{Pe}[1+Y(\theta_B-1)]}{P\sqrt{S}}\exp\left[\frac{H(\theta_b-\theta_B)}{(\theta_B+\theta_\infty)(\theta_b+\theta_\infty)}\right] \tag{8}$$

where vapor pressure is evaluated by the Clausius–Clapeyron equation; surface tension is assumed to be a linearly decreasing function of temperature. For a workpiece of SS 304 vapor pressure is found to be (Kim, 1975; Zacharia et al., 1991)

$$\hat{p}=1.01\times10^5\exp\left(14.09-\frac{43371.5}{T}\right) \tag{9}$$

Surface tension yields (Zacharia et al., 1989)

$$\gamma=1.872-4.3\times10^{-4}(T-1725)-1.33\times10^{-8}\times RT\ln\left[1+0.00318\,a_i\exp\left(\frac{1.88\times10^8}{RT}\right)\right] \tag{10}$$

where the quantity a_i is the activity of sulfur in bulk liquid phase. In the present work the activity $a_i=0.022$ wt% as chosen by Zacharia et al. (1989). The depth of the cavity and the coordinate of the cavity surface are related by

$$h=r_0^2\frac{\mathrm{Pe}}{4\eta_0\sqrt{S}} \tag{11}$$

where the dimensionless cavity opening radius, r_0, is around 0.75–0.95 for a surface-focused high-power-density-beam weld (Wei et al., 1990; Wei and Chow, 1992). This indicates that approximately 80–90 percent of the beam power flows into the cavity.

Analytical Solution for an Infinite Workpiece. Using the separation-of-variables method and assuming the dependent variable $v(\xi,\eta,\phi)=L(\xi)M(\eta)\Theta(\phi)$, Eq. (4) reduces to three ordinary differential equations

$$\frac{d^2L}{d\xi^2}+\frac{1}{\xi}\frac{dL}{d\xi}+\left(-\frac{m^2}{4\xi^2}+\frac{n}{\xi}-\frac{1}{4}\right)L=0 \tag{12}$$

$$\frac{d^2M}{d\eta^2}+\frac{1}{\eta}\frac{dM}{d\eta}+\left(-\frac{m^2}{4\eta^2}-\frac{n}{\eta}-\frac{1}{4}\right)M=0 \tag{13}$$

$$\frac{d^2\Theta}{d\phi^2}+m^2\Theta=0 \tag{14}$$

where Eq. (14) gives $\Theta\sim\cos(m\phi)$ with the eigenvalues $m=0,1,..,\infty$, in order to satisfy the symmetric condition at the weld centerline. The last term on the right-hand side of Eq. (A3) becomes infinity at the cavity base ($\xi=0$) for a nonnegative

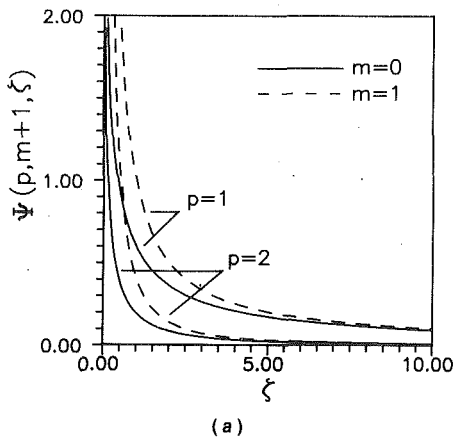

Fig. 2 Values for (*a*) confluent hypergeometric function of the second kind; (*b*) Kummer's function or Laguerre function ($m=0$)

integer $a=(1+m)/2-n \equiv 1-p$, as shown in Fig. 2(*a*). Dropping this term and using Eq. (A5) a solution of Eq. (12) yields

$$L \sim \xi^{\frac{m}{2}} e^{-\frac{\xi}{2}} L_{p-1}^{m}(\xi) \tag{15}$$

where the orthogonal Laguerre function L_{p-1}^{m} is defined by Eq. (A5). On the other hand, the first term representing the Kummer's function on the right-hand side of Eq. (A3) approaches infinity when $\eta \to \infty$, as shown in Fig. 2(*b*). By dropping the Kummer's function in Eq. (A3) to assure a finite value far from the cavity, a solution of Eq. (13) yields

$$M \sim \eta^{\frac{m}{2}} e^{-\frac{\eta}{2}} \Psi(m+p,\ m+1,\ \eta) \tag{16}$$

where the confluent hypergeometric function of the second kind, Ψ, is defined by Eq. (A6). Combining Eqs. (15), (16), and the result of Eq. (14) gives the dimensionless temperature

$$\theta = \frac{3Q^*\sqrt{S}}{\pi \mathrm{Pe}} \exp\left(-\sqrt{\xi\eta}\cos\phi - \frac{\eta+\xi}{2}\right) \sum_{m=0}^{\infty}\sum_{p=1}^{\infty} A_{m,p}(\xi\eta)^{\frac{m}{2}} L_{p-1}^{m}(\xi)\Psi(m+p,\ m+1,\ \eta)\cos(m\phi) \quad \eta \geq \eta_0 \tag{17}$$

where the coefficient $A_{m,p}$ is found from Eq. (A14), δ_{m0} is the Kronecker delta function, which is defined as $\delta_{m0}=1$ if $m=0$; $\delta_{m0}=0$ if $m\neq 0$. The truncation error using the first p terms for $m=0$ is examined and presented in Fig. 3. Evidently, a partial sum of the first eight terms reaches 98 percent of the converged solution, which is obtained by using the first 20 terms including both $m=0$ and 1. Computations also show that the truncation error using the first 13 terms for $m=0$ is the order of 0.3 percent at the base and 3 percent at the cavity opening. Equation (17) therefore can be reduced to

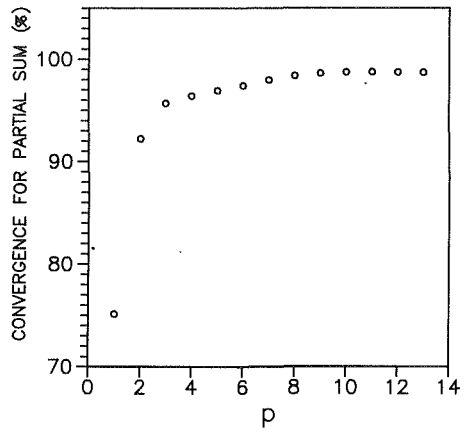

Fig. 3 Test of convergence for partial sum of the first p terms ($m=0$)

$$\theta = \frac{3Q^*\sqrt{S}}{\pi \mathrm{Pe}} \exp\left(-\sqrt{\xi\eta}\cos\phi - \frac{\eta+\xi}{2}\right) \sum_{p=1}^{\infty} A_{0,p} L_{p-1}^{0}(\xi)\Psi(p,\ 1,\ \eta) \quad \eta \geq \eta_0 \tag{18}$$

where the coefficients $A_{0,p}$ are

$$A_{0,p} = \left(\frac{12\eta_0}{\mathrm{Pe}^2}+\frac{1}{2}\right)^{-p}\left(\frac{12\eta_0}{\mathrm{Pe}^2}-\frac{1}{2}\right)^{p-1} L_{p-1}^{0}\left[\frac{\eta_0}{4}\left(\frac{144\eta_0^2}{\mathrm{Pe}^4}-\frac{1}{4}\right)^{-1}\right] \times \exp\left[\frac{\eta_0}{2}+\frac{\eta_0}{4}\left(\frac{12\eta_0}{\mathrm{Pe}^2}+\frac{1}{2}\right)^{-1}\right] \Big/ \left[\frac{1}{2}\Psi(p,\ 1,\ \eta_0) + p\Psi(p+1,\ 2,\ \eta_0)\right] \tag{19}$$

Nondimensionalizing lengths by the energy-beam distribution parameter is more convenient than the diffusivity-to-welding speed ratio. Hence, Eq. (5) is rewritten as

$$\xi = \frac{\mathrm{Pe}}{2}(z\sqrt{S}+\sqrt{x^2+y^2+Sz^2}),$$
$$\eta = \frac{\mathrm{Pe}}{2}(-z\sqrt{S}+\sqrt{x^2+y^2+Sz^2}),\ \phi = \tan^{-1}\left(\frac{y}{x}\right) \tag{20}$$

Equation (18) associated with Eqs. (19) and (20) is the analytical description of three-dimensional temperatures in the liquid and heat-affected zones around the welding cavity in an infinite workpiece.

Asymptotic Expression. Equations (18) and (19) can be simplified if the coordinate of the cavity surface $\eta_0 \ll 1$ or the parameter Pe $r_0(r_0/h)$ is much smaller than unity, as can be seen from Eq. (11). This is generally valid for a low or high-power-density-beam weld having a small Peclet number and dimensionless cavity opening radius of the order of 1 (Elmer et al., 1990; Wei and Chow, 1992). Equations (18) and (19) therefore are simplified to

$$\theta = \frac{3Q^*\sqrt{S\eta_0}}{\pi \mathrm{Pe}} \exp\left(-\sqrt{\xi\eta}\cos\phi - \frac{\eta+\xi}{2}\right) \sum_{p=1}^{\infty} \Gamma(p)\left(\frac{12\eta_0}{\mathrm{Pe}^2}+\frac{1}{2}\right)^{-p} \times \left(\frac{12\eta_0}{\mathrm{Pe}^2}-\frac{1}{2}\right)^{p-1} L_{p-1}^{0}(\xi)\Psi(p,\ 1,\ \eta) \quad \eta \geq \eta_0 \tag{21}$$

Even though the confluent hypergeometric function of the second kind in Eq. (21) is infinite (see Eq. (A10)) near the heat source, temperatures remain finite when multiplied by a small value of η_0, which is less than η. A dimensionless cavity opening radius much smaller than unity will underestimate the heating effects. This is because energy incident on the top surface is ignored in the present model.

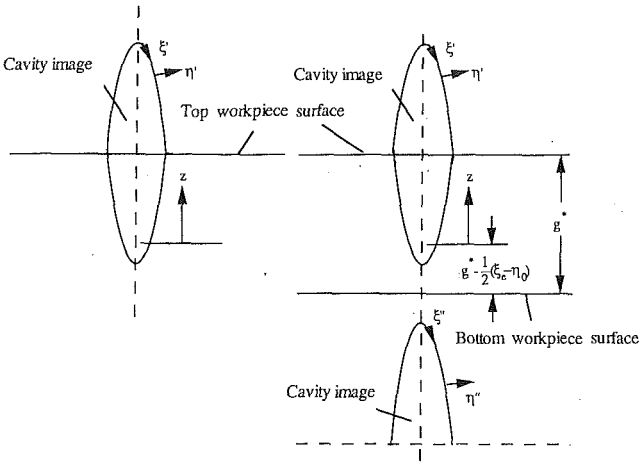

Fig. 4 Description of coordinates of image: (*a*) Image 1: top surface is adiabatic; (*b*) Image 2: top and bottom surface are adiabatic

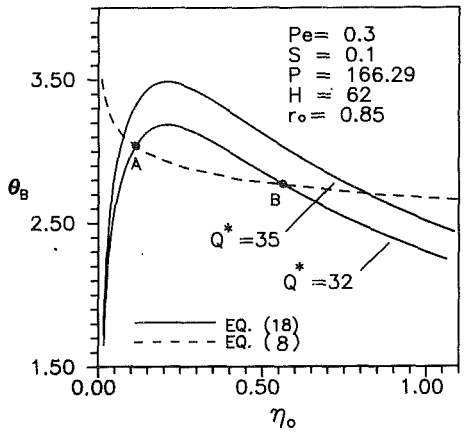

Fig. 5 Uniqueness of cavity depth; points *A* and *B* are two solutions satisfying conservation of energy and interfacial momentum

Approximate Solutions for Workpieces of Semi-infinite and Finite Thicknesses. In reality, energy losses to the surroundings at surfaces of workpieces are small. Assuming the temperature gradients $\partial\theta/\theta z \approx 0$ at surfaces, approximate temperature fields can be found by using an image method (Rosenthal, 1941). As illustrated in Fig. 4(*a*), temperature fields in a semi-infinite workpiece having an adiabatic top surface are found to be

$$\theta'(\xi, \eta, \phi) = \theta(\xi, \eta, \phi) + \theta(\xi', \eta, \phi) \tag{22}$$

where the first term on the right-hand side is calculated from Eq. (18), the second term is obtained by replacing the ξ coordinate in Eq. (18) by a coordinate of the image $\xi' \equiv 2(\xi_e - \eta_0 + \eta) - \xi$. For a workpiece of finite thickness with adiabatic surfaces, the predicted temperatures are

$$\theta''(\xi, \eta, \phi) = \theta'(\xi, \eta, \phi) + \theta'(\xi'', \eta'', \phi) \tag{23}$$

where the first and second terms on the right-hand side are determined by using Eq. (22) and introducing coordinates of the second image, as illustrated in Fig. 4(*b*). Relationships between parabolic coordinates and coordinates of the second image are

$$\eta'' = 2g^* + \frac{1}{2}(\xi - \eta) - (\xi_e - \eta_0) + \left\{\left[2g^* + \frac{1}{2}(\xi - \eta) - (\xi_e - \eta_0)\right]^2 + \xi\eta\right\}^{\frac{1}{2}} \tag{24}$$

$$\xi'' = \frac{\xi\eta}{\eta''} \tag{25}$$

Solution Procedure. An iterative procedure to obtain temperature fields is described as follows:

1 The dimensionless beam power, cavity opening radius, Peclet number, parameter approximating convection, and workpiece are specified.

2 An initial coordinate of cavity surface η_0 is guessed.

3 Coefficients $A_{0,p}$ are evaluated from Eq. (19).

4 Temperature at the cavity base is determined from Eq. (18).

5 An improved η_0 is calculated by using interfacial momentum Eq. (8).

6 Steps 3–5 are repeated until η_0 converges.

7 The uniqueness of η_0 is determined from a consequence of the second law of thermodynamics.

8 The final cavity depth, h, is found from Eq. (11).

9 The depth of the weld pool h_m is determined from the location where the dimensionless temperature $\theta = 1$.

The significance of step 7 is illustrated in Fig. 5. Temperatures at the cavity base obtained from Eq. (18) and the interfacial momentum Eq. (8) are plotted. The intersections, *A* and *B*, are two solutions that simultaneously satisfy conservation of energy and interfacial momentum. In order to obtain a unique depth, the dimensionless beam power is assumed to increase from 32 to 35 while other conditions remain the same. Since an increase in the base temperature is expected, point *A* is the desired solution.

Results and Discussion

The independent parameters governing the temperature distribution in the liquid and heat-affected zones around the welding cavity are: the dimensionless beam power (Q^*), cavity opening radius (r_0), Peclet number (Pe), parameter approximating convection (S), workpiece thickness (g), boiling pressure (P) and temperature (θ_b), latent heat of evaporation (H), capillary number (Y), and ambient temperature (θ_∞). The validity of the results is established by comparison with the line and point-source solutions (Rosenthal, 1941). The line-source solution expressed in dimensionless form yields

$$\theta = \frac{Q^*}{4\pi Kg} \exp\left(-\frac{\mathrm{Pe}\Lambda x}{2}\right) K_0\left(\frac{\mathrm{Pe}\Lambda}{2}\sqrt{x^2+y^2}\right) \tag{26}$$

where K_0 is the modified Bessel function of the second kind and order zero. Two independent parameters Q^*/kg and PeΛ need to be specified. Ratios of conductivities and diffusivities of the liquid and solid appear because thermal properties in the Rosenthal's models were chosen for the solid. Interestingly, Eq. (26) describing a workpiece of thickness g (equal to the cavity depth h for a full penetration) is similar to Eq. (21). The similarities include: (*i*) a reciprocal of the penetration depth appears by replacing the parameter $S^{1/2}\eta_0/\mathrm{Pe}$ in Eq. (21) from Eq. (11); (*ii*) the radial coordinate $\eta = \mathrm{Pe}\,(x^2+y^2)^{1/2}/2$ as $S \to 0$; and (*iii*) the confluent hypergeometric function $\Psi(p, 1, \eta) \sim K_0(\eta)$ when $\eta \to 0$. In Fig. 6, it can be seen that temperatures predicted by Eq. (26) become infinite as the argument of the modified Bessel function approaches zero. In contrast, the maximum temperature predicted by this work gives a dimensionless temperature of 3.25, which agrees with a realistic temperature of 2070°C at the cavity base for welding aluminum (Schauer and Giedt, 1978; Schauer et al., 1978).

In the case of a low-power-density beam welding temperatures can be determined by the point-source solution (Rosenthal, 1941)

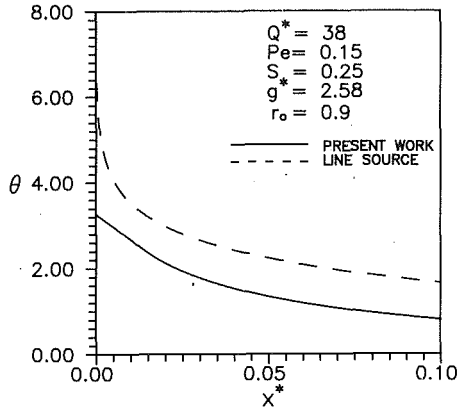

Fig. 6 Comparison of dimensionless temperatures in liquid and heat-affected zones predicted by the present work and line-source model

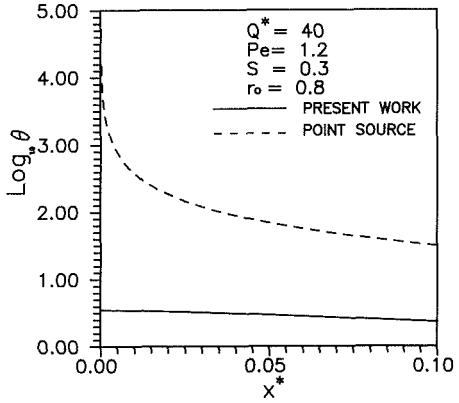

Fig. 7 Comparison of dimensionless temperatures in liquid and heat-affected zones predicted by the present work and point-source model

$$\theta = \frac{Q^*}{2\pi K\sqrt{x^2+y^2+z^2}} \exp\left(-\frac{\mathrm{Pe}\Lambda x}{2} - \frac{\mathrm{Pe}\Lambda}{2}\sqrt{x^2+y^2+z^2}\right) \quad (27)$$

where the control parameters are Q^*/K and PeΛ. Equation (27) is analogous to Eq. (18) or (21) if the parameter approximating convection $S=1$. However, the former leads to infinity near the source, as shown in Fig. 7. The maximum temperature predicted by the present work is 3.55, which corresponds to 2250°C for welding aluminum. This temperature is slightly above the experimental result of 2000°C for electron beam welds (Schauer and Giedt, 1978). Block-Bolten and Eagar (1984) predicted the evaporation rate of alloying elements in arc welding. The temperatures determined from the evaporation rates by using the kinetic theory agreed with temperatures measured by Schauer and Giedt (1978) for electron beam welding. Referring to Figs. 6 and 7 indicates that using the conventional point and line-source solutions to investigate arc or high-intensity beam welding is not accurate.

Cavity temperatures predicted by Eqs. (18), (22), and (23) are shown in Fig. 8. These equations are referred to workpieces of infinite, semi-infinite, and finite thicknesses, respectively. Equation (18) gives the lowest values because of significant energy losses to the region of large ξ. A decrease in thickness increases cavity temperatures. As the dimensionless thickness g^*, become greater than 0.4, a variation of thickness only induces temperature differences within 5 percent. In this case, the complicated Eq. (23) can be replaced by Eq. (22). As asymptotic result obtained by Eq. (21) is also plotted. For a

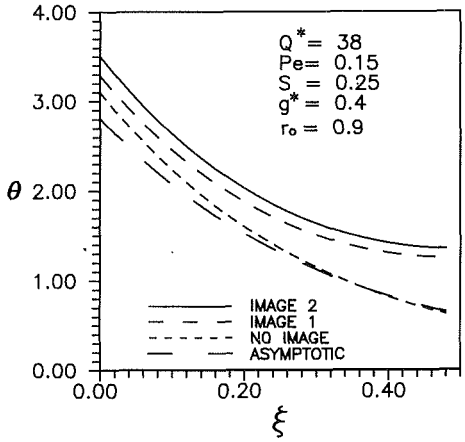

Fig. 8 Comparison of dimensionless cavity temperatures for workpieces of infinite, semi-infinite, and finite thicknesses. The asymptotic result from Eq. (21) is also presented.

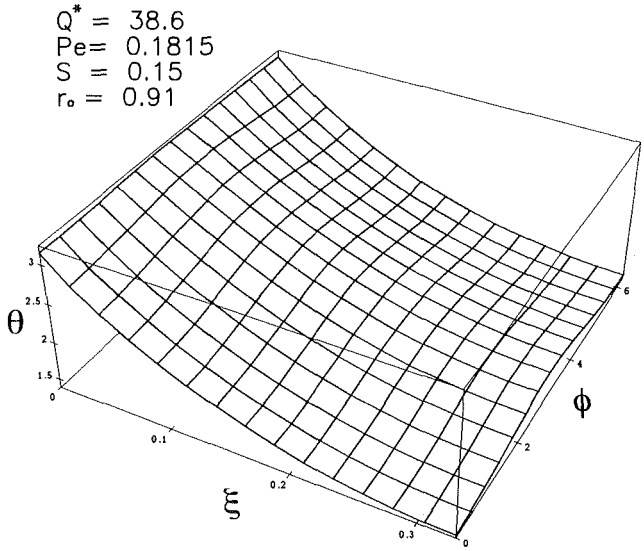

Fig. 9 Three-dimensional dimensionless cavity temperatures

workpiece of infinite thickness, temperatures predicted by Eqs. (21) and (18) are close.

Three-dimensional dimensionless cavity temperatures are shown in Fig. 9. The maximum and minimum temperatures of around 3.4 and 1.2 occur at the base and opening of the cavity, respectively. For a given depth the highest temperature is at the rear (Wei et al., 1993a) where energy is released from the cavity temperature to the ambient temperature. Cavity temperatures are approximately axisymmetric. The difference in temperatures between the front and the rear of the cavity is around 0.1, which is in accord with 70 K predicted by Wei and Giedt (1985) for welding aluminum. A slight asymmetry of base temperatures results from the approximate image method.

As shown in Fig. 10, the base temperature for welding aluminum is found to be around 2000°C, which agrees with experimental work conducted by Schauer et al. (1978) and Schauer and Giedt (1978), and theoretical predictions by Wei et al. (1990). However, the relative discrepancy between the experimental data and present study can be 30 percent. One possibility for this error results from the idealized shape of the cavity. Wei et al. (1990) found that temperature gradients near the cavity opening are around 10^6 K/m. Hence, a slight deviation of the wall from a paraboloid of revolution by 0.5 mm

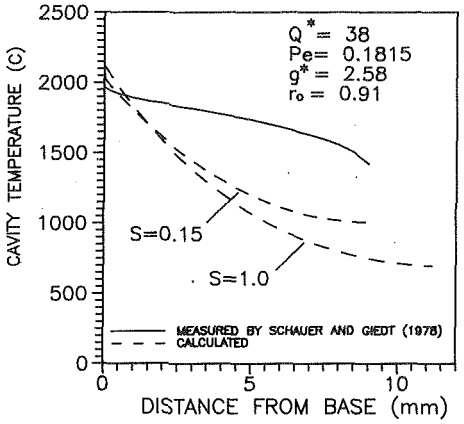

Fig. 10 Comparison of the predicted and measured cavity temperatures from the cavity base to opening for welding Al 1100

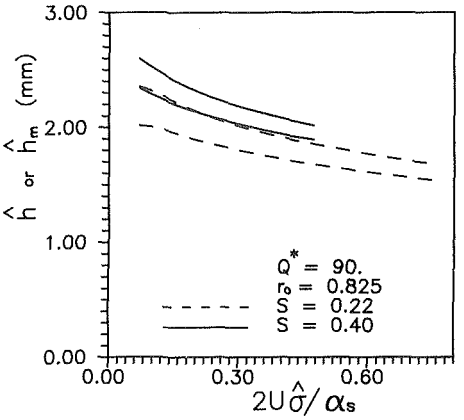

Fig. 11 Depths of cavity and weld pool produced as a function of solid Peclet number for different values of the parameter approximating convection by using a high-power-density beam

induces an increase of the cavity temperature of 500 K, which is approximately the maximum deviation. Other factors affecting the discrepancy might be redistributions of the incident energy flux resulting from specular and diffuse reflections on the cavity wall, more realistic prediction of convection heat transport, variations of properties with temperature, and complicated phenomena near the free surface such as the existence of a Knudsen layer (Knight, 1982; Mundra and DeBroy, 1993), and dissocations and ionizations of the evaporating atoms. A quantitative investigation is still lacking at the present time. The parameter approximating convection equal to or less than 1 indicates that pure conduction or convection takes place, respectively. Hence, convection reduces the base temperature and depth of the cavity.

Depths of the cavity and weld pool for a high-power-density beam welding are shown in Fig. 11. The depth of the weld pool is determined by the location where the dimensionless temperature is unity. The difference between depths of the cavity and weld pool indicates the thickness of the weld pool at the cavity base. It can be seen that the thickness of the molten metal in a thin layer is around 0.25 mm, which agrees with the prediction made by Chan and Mazumder (1987), Wei and Chiou (1988), and Wei and Ho (1990). On the other hand, the thickness of the molten metal at the cavity base increases to 30 percent of the depth of the molten region for low-power-density-beam welds, as shown in Fig. 12.

In Fig. 13, the predicted beam power per unit of penetration versus solid Peclet number for welding workpieces of SS 304 by selecting $Q^* = 110$ shows agreement with experimental results obtained by Hicken et al. (1991). It can be seen that

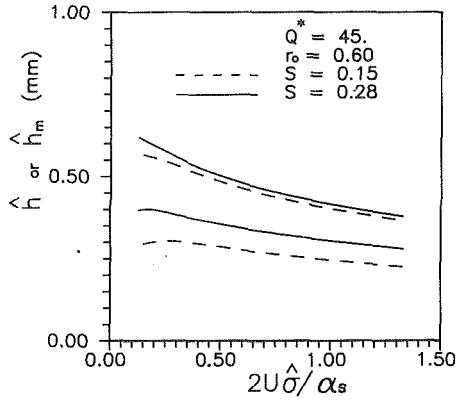

Fig. 12 Depths of cavity and weld pool produced as a function of solid Peclet number for different values of the parameter approximating convection by using a low-power-density beam

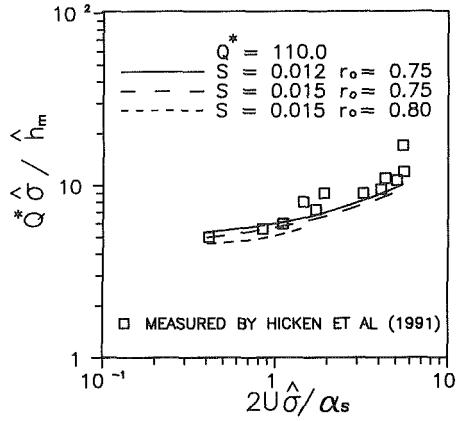

Fig. 13 Comparison of the predicted and measured power per unit of penetration as a function of solid Peclet number for different values of parameter approximating convection and cavity opening radii in welding SS 304

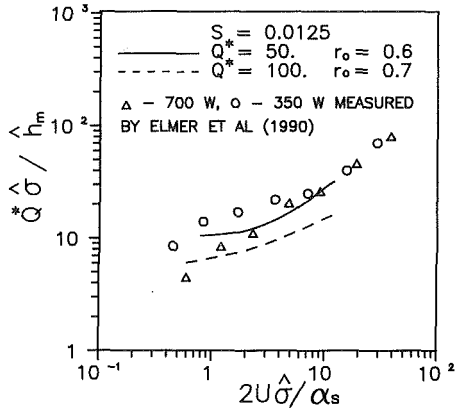

Fig. 14 Comparison of the predicted and measured power per unit of penetration as a function of solid Peclet number for different dimensionless beam powers in welding SS 304

decreasing either the dimensionless cavity opening radius or the parameter approximating convection increases the power per unit of penetration. It is surprising that the parameter approximating convection is much smaller than that of Al 1100. which has a greater thermal diffusivity. The present model also found that the effect of the dimensionless workpiece thickness on the power per unit of penetration is insignificant. In Fig. 14, the predicted result indicating that an increase of

the dimensionless beam power results in a decrease of the power per unit of penetration agrees with measurements conducted by Elmer et al. (1990). Unfortunately, an intersection of the predicted powers per unit of penetration between different dimensionless beam powers is impossible. Since important factors, as mentioned previously, aren't accounted for in this model, an interpretation for the transition from the low to high-power-density-beam welds is difficult. Referring to Figs. 13 and 14 does indicate that more relevant values of the dimensionless beam power, cavity opening radius, and parameter approximating convection are sufficiently required for a reliable prediction of the transition.

Conclusions

The following conclusions are drawn:

1 Realistic three-dimensional analytical descriptions of temperature fields in the liquid and heat-affected zones around a welding cavity are provided. The control parameters include the dimensionless beam power, cavity opening radius, Peclet number, workpiece thickness, parameter approximating thermal convection, and properties of the workpiece. This new approach developed is not subject to the five limiting assumptions of the conventional line and point-source solutions.

2 An asymptotic expression, Eq. (21), for temperature around a cavity in a workpiece having a Peclet number much less than unity is provided. This is generally valid for low and high-power-density-beam welding.

3 The depth of penetration is uniquely determined by simultaneously satisfying the interfacial momentum and a consequence of the second law of thermodynamics. The second law requires that the base temperature increases with increasing beam power.

4 The power per unit of penetration is found to increase with decreasing dimensionless cavity opening radius, and increasing convection and workpiece thickness. Relevant choices of the dimensionless beam power, cavity opening radius, and parameter approximating convection will be required for a reliable determination of the transition between low and high-power-density-beam welds. A theoretical prediction and interpretation for this transition, unfortunately, is still difficult at the present time.

5 The maximum deviation of cavity temperatures between the theoretical prediction and experimental measurement can be 30 percent. The error induced by an idealized shape of the cavity can be of the same magnitude of this discrepancy.

Acknowledgments

The authors acknowledge the interest and guidance of Professor W. H. Giedt during the preparation of this manuscript. This work supported in part by the National Science Council, Taiwan, the Republic of China, through Grant number NSC81-0401-E-110-03 is appreciated.

References

Adams, C. M., Jr. 1958, "Cooling Rates and Peak Temperatures in Fusion Welding," *Welding Journal*, Vol. 37, pp. 210-s–215-s.

Block-Bolten, A., and Eagar, T. W., 1984, "Metal Vaporization From Weld Pools," *Metallurgical Transactions B*, Vol. 15B, pp. 461–469.

Carslaw, H. C., and Jaeger, J. C., 1959, *Conduction of Heat in Solids*, Clarendon Press, Oxford, p. 390.

Chan, C. L., and Mazumder, J., 1987, "One-Dimensional Steady-State Model for Damage by Vaporization and Liquid Expulsion Due to Laser-Material Interaction," *Journal of Applied Physics*, Vol. 62, pp. 4579–4586.

Choo, R. T. C., and Szekely, J., 1991, "The Effect of Gas Shear Stress on Marangoni Flows in Arc Welding," *Welding Journal*, Vol. 70, pp. 223-s–233-s.

Christensen, N., Davies, V. de L., and Gjermundsen, K., 1965, "Distribution of Temperatures in Arc Welding," *British Welding Journal*, Vol. 12, pp. 54–75.

Cline, H. E., and Anthony, T. R., 1977, "Heat Treating and Melting Material With a Scanning Laser or Electron Beam," *Journal of Applied Physics*, Vol. 48, pp. 3895–3900.

David, S. A., and Vitek, J. M., 1989, "Correlation Between Solidification Parameters and Weld Microstructures," *International Materials Reviews*, Vol. 34, pp. 213–245.

Eager, T. W., and Tsai, N. S., 1983, "Temperature Fields Produced by Traveling Distributed Heat Sources," *Welding Journal*, Vol. 62, pp. 346-s–355-s.

Elmer, J. W., Giedt, W. H., and Eagar, T. W., 1990, "The Transition From Shallow to Deep Penetration During Electron Beam Welding," *Welding Journal*, Vol. 69, pp. 167-s–176-s.

Erde'lyi, A., ed., 1953, *Higher Transcendental Functions*, Vol. 1, McGraw-Hill, New York, Chap. VI.

Gau, C., and Viskanta, R., 1984, "Melting and Solidification of a Metal System in a Rectangular Cavity," *International Journal of Heat and Mass Transfer*, Vol. 27, pp. 113–123.

Giedt, W. H., 1971, *Thermophysics*, Van Nostrand Reinhold, New York, pp. 387–388.

Giedt, W. H., Wei, X.-C., and Wei, S.-R., 1984, "Effect of Surface Convection on Stationary GTA Weld Zone Temperatures," *Welding Journal*, Vol. 63, pp. 376-s–383-s.

Giedt, W. H., and Tallerico, L. N., 1988, "Prediction of Electron Beam Depth of Penetration," *Welding Journal*, Vol. 67, pp. 299-s to 305-s.

Gradshteyn, I. S., and Ryzhik, I. M., 1980, *Table of Integrals, Series, and Products*, A. Jeffrey, ed.; translated from the Russian by Scripta Technica, Inc., England; pp. 482, p. 847, p. 1037.

Hicken, G. K., Giedt, W. H., and Bentley, A. E., 1991, "Correlation of Joint Penetration With Electron Beam Current Distribution," *Welding Journal*, Vol. 70, pp. 69-s–75-s.

Kim, C. S., 1975, *Thermophysical Properties of Stainless Steels*, Argonne National Laboratory, Argonne, IL, Report No. ANL-75-55.

Knight, C. J., 1982, "Transient Vaporization From a Surface Into Vacuum," *AIAA Journal*, Vol. 20, pp. 950–954.

Masubuchi, K., 1980, *Analysis of Welded Structures*, Pergamon Press, New York, Chap. 3.

Miyazaki, T., and Giedt, W. H., 1982, "Heat Transfer From an Elliptical Cylinder Moving Through an Infinite Plate Applied to Electron Beam Welding," *International Journal of Heat and Mass Transfer*, Vol. 25, pp. 807–814.

Miyazaki, T., Kimura, T., and Giedt, W. H., 1991, "Temperature Distribution Around a Sphere Moving Through an Infinite Solid and Its Application to Plasma Arc Surface Treatment," *Proc. ASME/JSME Thermal Engineering Joint Conference*, Reno, NV, Mar. 17–22, pp. 365–372.

Morse, P. M., and Feshbach, H., 1978, *Methods of Theoretical Physics*, McGraw-Hill, New York, Part I, p. 660; Part II, p. 1664.

Mundra, K., and DeBroy, T., 1993, "Toward Understanding Alloying Element Vaporization During Laser Beam Welding of Stainless Steel," *Welding Journal*, Vol. 72, pp. 1-s–9-s.

Nippes, E. F., coordinator, 1983, *Metals Handbook*, 9th ed., ASM, Metals Park, OH, Vol. 6, pp. 649–651.

Nunes, A. C., Jr., 1983, "An Extended Rosenthal Weld Model," *Welding Journal*, Vol. 62, pp. 165-s–170-s.

Rosenthal, D., 1941, "Mathematical Theory of Heat Distribution During Welding and Cutting," *Welding Journal*, Vol. 20, pp. 220-s–234-s.

Sahoo, P., DeBroy, T., and McNallan, M. J., 1988, "Surface Tension of Binary Metal-Surface Active Solute Systems Under Conditions Relevant to Welding Metallurgy," *Metallurgical Transactions B*, Vol. 19B, pp. 483–491.

Schauer, D. A., and Giedt, W. H., 1978, "Prediction of Electron Beam Welding Spiking Tendency," *Welding Journal*, Vol. 57, pp. 189-s–195-s.

Schauer, D. A., Giedt, W. H., and Shintaku, S. M., 1978, "Electron Beam Welding Cavity Temperature Distributions in Pure Metals and Alloys," *Welding Journal*, Vol. 57, pp. 127-s–133-s.

Steen, W. M., Dowden, J., Davis, M., and Kapadia, P., 1988, "A Point and Line Source Model of Laser Keyhole Welding," *Journal of Physics D: Applied Physics*, Vol. 21, pp. 1255–1260.

Swift-Hook, D. T., and Gick, A. E. F., 1973, "Penetration Welding With Lasers," *Welding Journal*, Vol. 52, pp. 492-s–499-s.

Tong, H., and Giedt, W. H., 1969, "Radiographs of the Electron Beam Welding Cavity," *Review of Scientific Instruments*, Vol. 40, pp. 1283–1285.

Tong, H., and Giedt, W. H., 1971, "Depth of Penetration During Electron Beam Welding," ASME JOURNAL OF HEAT TRANSFER, Vol. 93, pp. 155–163.

Wang, S. C., and Wei, P. S., 1992, "Energy-Beam Redistribution and Absorption in a Drilling or Welding Cavity," *Metallurgical Transactions B*, Vol. 23B, pp. 505–511.

Wei, P. S., and Giedt, W. H., 1985, "Surface Tension Gradient-Driven Flow Around an Electron Beam Welding Cavity," *Welding Journal*, Vol. 64, pp. 251-s–259-s.

Wei, P. S., and Chiou, L. R., 1988, "Molten Metal Flow Around the Base of a Cavity During a High-Energy Beam Penetrating Process," ASME JOURNAL OF HEAT TRANSFER, Vol. 110, pp. 918–923.

Wei, P. S., and Ho, J. Y., 1990, "Energy Considerations in High-Energy Beam Drilling," *International Journal of Heat and Mass Transfer*, Vol. 33, pp. 2207–2217.

Wei, P. S., and Lii, T. W., 1990, "Electron Beam Deflection When Welding Dissimilar Metals," ASME JOURNAL OF HEAT TRANSFER, Vol. 112, pp. 714–720.

Wei, P. S., Wu, T. H., and Chow, Y. T., 1990, "Investigation of High-Intensity Beam Characteristics on Welding Cavity Shape and Temperature Distribution," ASME JOURNAL OF HEAT TRANSFER, Vol. 112, pp. 163–169.

Wei, P. S., and Chow, Y. T., 1992, "Beam Focusing Characteristics and

Alloying Element Effects on High-Intensity Electron Beam Welding," *Metallurgical Transactions B*, Vol. 23B, pp. 81-90.

Wei, P. S., Hwang, J. H., and Lai, S. J., 1993a, "Solidification of High-Intensity Beam Welding," submitted to *Metallurgical Transactions*.

Wei, P. S., Lee, J. D., Yang, W. J., and Lai, S. J., 1993b, "Development of Cavity Produced by a High-Intensity Beam," submitted to ASME JOURNAL OF HEAT TRANSFER.

Zacharia, T., David, S. A., Vitek, J. M., and DeBroy, T., 1989, "Weld Pool Development during GTA and Laser Beam Welding of Type 304 Stainless Steel, Part I—Theoretical Analysis," *Welding Journal*, Vol. 68, pp. 499-s-509-s.

Zacharia, T., David, S. A., Vitek, J. M., 1991, "Effect of Evaporation and Temperature-Dependent Material Properties on Weld Pool Development," *Metallurgical Transactions B*, Vol. 22B, pp. 233-241.

APPENDIX

(A) General Solutions of Eqs. (12) and (13). Equations (12) and (13) are special cases of the following equation (Morse and Feshbach, 1978):

$$\frac{d^2f}{d\zeta^2}+\left(\frac{c-2b}{\zeta}\right)\frac{df}{d\zeta}+\left[\frac{b(b-c+1)}{\zeta^2}+\frac{-2a+c}{2\zeta}-\frac{1}{4}\right]f=0 \quad \text{(A1)}$$

where a, b, c are constants. Equation (A1) can be derived from Kummer's equation by using the transformation $\omega=\zeta^{-b}e^{\zeta/2}f$:

$$\zeta\frac{d^2\omega}{d\zeta^2}+(c-\zeta)\frac{d\omega}{d\zeta}-a\omega=0 \quad \text{(A2)}$$

General solutions of Eq. (A2) are (Erde'lyi, 1953)

$$\omega=c_1\Phi(a, c, \zeta)+c_2\Psi(a, c, \zeta) \quad \text{(A3)}$$

where Kummer's function Φ is defined as

$$\Phi(a, c, \zeta)=\sum_{n=0}^{\infty}\frac{\Gamma(a+n)\,\Gamma(c)\,\zeta^n}{\Gamma(a)\,\Gamma(c+n)\Gamma\,(n+1)} \quad \text{(A4)}$$

The Laguerre and Kummer functions are related by (Erde'lyi, 1953; Gradshteyn and Ryzhik, 1980)

$$L_p^m(\zeta)=\frac{\Gamma(m+p+1)}{\Gamma(m+1)\Gamma(p+1)}\Phi(-p, m+1, \zeta)$$
$$=\sum_{n=0}^{p}(-1)^n\frac{\Gamma(m+p+1)\,\zeta^n}{\Gamma(p-n+1)\Gamma(m+n+1)\Gamma(n+1)} \quad \text{(A5)}$$

where m is a nonnegative integer. The confluent hypergeometric function of the second kind Ψ in Eq. (A3) is defined as (Erde'lyi, 1953)

$$\Psi(a, n+1, \zeta)=\frac{(-1)^{n-1}}{\Gamma(n+1)\Gamma(a-n)}\left\{\Phi(a, n+1, \zeta)\ln\zeta\right.$$
$$+\sum_{m=0}^{\infty}\frac{\Gamma(a+m)\,\Gamma(n+1)}{\Gamma(a)\,\Gamma(n+m+1)}[\psi(a+m)-\psi(1+m)-\psi(1+n+m)]$$
$$\left.\frac{\zeta^m}{\Gamma(m+1)}\right\}+\frac{\Gamma(n)}{\Gamma(a)}\sum_{m=0}^{n-1}\frac{\Gamma(a-n+m)\,\Gamma(1-n)}{\Gamma(a-n)\,\Gamma(1-n+m)}\frac{\zeta^{m-n}}{\Gamma(m+1)} \quad \text{(A6)}$$

where $a>1$, $n=0, 1,\ldots$ and the last term on the right-hand side of Eq. (A6) vanishes for $n=0$; the di-gamma function ψ is defined as

$$\psi(1+n)=-\gamma+\sum_{m=1}^{n}\frac{1}{m},\ \psi(1)=-\gamma, \text{ for } n=1, 2, \ldots \quad \text{(A7)}$$

where $\gamma=0.5772156649$ is Euler's constant.

(B) The Asymptotic Expressions

As $\zeta\to 0$ the confluent hypergeometric functions of the second kind become

$$\Psi(a, c, \zeta)=\frac{\Gamma(c-1)}{\Gamma(a)}\zeta^{1-c}+O(\zeta^{c-2}) \text{ for } c>2 \quad \text{(A8)}$$

$$\Psi(a, c, \zeta)=\frac{\Gamma(c-1)}{\Gamma(a)}\zeta^{1-c}+O(\ln\zeta) \text{ for } c=2 \quad \text{(A9)}$$

$$\Psi(a, c, \zeta)=-\frac{1}{\Gamma(a)}[\ln\zeta+\psi(a)+2\gamma]$$
$$+O(\zeta\ln\zeta) \text{ for } c=1 \quad \text{(A10)}$$

(C) Determination of Coefficients $A_{m,p}$ of Eq. (17)

A substitution of Eq. (17) into Eq. (7) gives

$$-\exp\left(\sqrt{\xi\eta_0}\cos\phi-\frac{12}{\mathrm{Pe}^2}\xi\eta_0\right)$$
$$=\sum_{m=0}^{\infty}\sum_{p=1}^{\infty}A_{m,p}(\xi\eta_0)^{\frac{m}{2}}\exp\left(-\frac{\xi+\eta_0}{2}\right)$$
$$\cdot\left[\left(\frac{-1}{2}+\frac{m}{2\eta_0}\right)\Psi(m+p, m+1, \eta_0)\right.$$
$$\left.+\frac{d\Psi(m+p, m+1, \eta)}{d\eta}_{\eta=\eta_0}\right]L_{p-1}^m(\xi)\cos(m\phi) \quad \text{(A11)}$$

where the cosine functions $\cos(m\phi)$ and Laguerre functions $L_{p-1}^m(\xi)$ form orthogonal sets, respectively. The orthogonality of Laguerre functions requires that

$$\int_0^{\infty}\xi^m e^{-\xi}L_u^m(\xi)L_v^m(\xi)d\xi=\delta_{uv}\frac{\Gamma(m+u+1)}{\Gamma(u+1)} \quad \text{(A12)}$$

where δ_{uv} is the Kronecker delta function. By satisfying the orthogonality of the cosine and Laguerre functions, the coefficients $A_{m,p}$ of Eq. (A11) are found to be

$$A_{m,p}=\int_0^{\infty}\xi^{\frac{m}{2}}\exp\left[-\left(\frac{1}{2}+\frac{12\,\eta_0}{\mathrm{Pe}^2}\right)\xi\right]L_{p-1}^m(\xi)\int_0^{\pi}\cos(m\phi)$$
$$\exp(\sqrt{\xi\eta_0}\cos\phi)d\phi d\xi\cdot\frac{2\Gamma(p)}{\pi\Gamma(m+p)}\Big/\left\{\eta_0^{\frac{m}{2}}\exp\left(-\frac{\eta_0}{2}\right)\left[\left(\frac{1}{2}-\frac{m}{2\eta_0}\right)\right.\right.$$
$$\left.\left.\Psi(m+p, m+1, \eta_0)+(m+p)\Psi(m+p+1, m+2, \eta_0)\right]\right\} \quad \text{(A13)}$$

where an identity $d\Psi(m+p, m+1, \eta)/d\eta=-(m+p)\,\Psi(m+p+1, m+2, \eta)$ is used. Equation (A13) can be integrated to give (Gradshteyn and Ryzhik, 1980)

$$A_{m,p}=\left(\frac{1}{2}\right)^{\delta_{m0}}\frac{\Gamma(p)2^{1-m}}{\Gamma(m+p)}\left(\frac{12\eta_0}{\mathrm{Pe}^2}+\frac{1}{2}\right)^{-m-p}\left(\frac{12\eta_0}{\mathrm{Pe}^2}-\frac{1}{2}\right)^{p-1}$$
$$L_{p-1}^m\left[\frac{\eta_0}{4}\left(\frac{144\eta_0^2}{\mathrm{Pe}^4}-\frac{1}{4}\right)^{-1}\right]$$
$$\cdot\exp\left[\frac{\eta_0}{2}+\frac{\eta_0}{4}\left(\frac{12\eta_0}{\mathrm{Pe}^2}+\frac{1}{2}\right)^{-1}\right]\Big/$$
$$\left[\frac{1}{2}\left(1-\frac{m}{\eta_0}\right)\Psi(m+p, m+1, \eta_0)\right.$$
$$\left.+(m+p)\Psi(m+p+1, m+2, \eta_0)\right] \quad \text{(A14)}$$

where the argument of the Laguerre function can even be negative.

Thermal Response of Rolling Components Under Mixed Boundary Conditions: An Analytical Approach

P. Ulysse

M. M. Khonsari

Department of Mechanical Engineering,
University of Pittsburgh,
Pittsburgh, PA 15261

An analytical solution for the steady-state temperature distribution in a cylinder undergoing uniform heating and nonuniform cooling is presented. The method of solution is a Fourier integral transform technique. The analysis shows that the Neumann series resulting from an integral equation can be well represented by a first-order approximation when the Peclet number is large. Furthermore, it is shown that the ratio of the Biot number to the square root of the Peclet number of the cooling zones is found to play an important role in governing the thermal response of the cylinder surface. The predicted results for the circumferential temperature distribution are compared to published experimental measurements for hot rolling and also existing analytical solutions for special cases. The agreement is found to be very good. By an appropriate superposition technique, the analysis presented may be easily extended to various heat sources and convective cooling zones at different locations of the cylinder surface.

Introduction

The volume of published research dealing with the behavior of rotating cylinders subject to a heat source demonstrates the growing interest in obtaining models sufficiently accurate to predict the performance of cylindrical rolling components.

Rolling elements such as those in roller bearings, shafts in journal bearings, and steel rolls in rolling mills are subject to one or more heat sources due to rubbing of surfaces. In the case of steel workrolls in hot rolling mills, the heat source is mainly the combination of an external heating from strips rolling and the heat generated by friction at the interface of the strip and the roll. As rolling components normally operate at relatively high speed, external cooling is required to avoid overheating and reduce thermal stresses that cause their surfaces to deteriorate and consequently shorten their lifespan.

A literature survey revealed that considerable attention has been devoted to the cooling and heating of rolling elements. The following is a brief account of the pertinent published work. Jaeger (1944) used a theory of moving heat sources to develop an analytical transient solution for an adiabatic cylinder subject on its surface to a rotating continuous heat source. Cerni (1961) applied Jaeger's theory on line sources to the problem of strip rolling and Hogshead (1967) considerably simplified Cerni's work. DesRuisseaux and Zerkle (1970) extended Jaeger's solution by including a uniform convective cooling on the cylinder surface. Using a quasi-steady-state approach, Ling (1970) expressed the temperature solution for a cylinder subject to cooling and heating. Patula (1981) provided an innovative approach of a cylinder cooled and heated on parts of its surface but insulated on the rest. This was in an attempt to simulate the boundary conditions of steel roll in rolling mills. To provide a more realistic solution of Patula's problem, Yuen (1984) extended the boundary condition formulation to nonuniform cooling and heating. However, no evaluations of the nonuniform cooling case were presented. Also, Gecim and Winer (1984) used Ling's approach for tribocontact applications. In that study the circumferential temperature variation was assumed to be negligible.

The solution of the problem of a cylinder subject to nonuniform cooling and heating is indeed very complex. The relatively simple analytical solution given by Patula (1981) resulted in the solution of a large number of equations that must be solved simultaneously. This drawback is stressed by Yuen (1984) who indicates that to obtain a 1 percent accuracy solution in the roll gap, over 500 terms in the infinite temperature series must be evaluated. Consequently a 1001×1001 matrix must be manipulated to determine two sets of coefficients of the temperature solution. This is costly and time-consuming and any extensive parametric study becomes unpractical. As pointed out by Tseng (1984), numerical solutions are also complicated by the fact that the temperature variations are localized in a thin layer near the surface and thus require a very fine mesh. This also results in an expensive numerical simulation.

In this paper, an analytical solution for the temperature distribution in a cylinder subject to surface heating and nonuniform cooling is presented. While the present approach may be applied to more heat sources and convective cooling zones, only one heat source and two different convective regions are adopted here. This nonuniform heat removal is simulated by a uniform cooling around the cylinder surface over which a specified convective cooling is superimposed. The temperature distribution is obtained by a Fourier transform technique and expressed as simple infinite sums, which can be effectively handled by a personal computer. Also, the results obtained are compared to published experimental temperature measurements and existing analytical solutions for the special case of a uniform cooling around the cylinder periphery.

Theoretical Analysis

A long rotating cylinder, subjected to heating and nonuniform convective cooling at arbitrary angles along the circumference, is shown in Fig. 1. This situation is typical in rolling mills where significant heat is generated at the roll-strip interface. External cooling is assumed to be provided by means of spray cooling in the interval $(\psi - \alpha)$ (where the impingement region is located) while coolant running on the cylinder surface

Contributed by the Heat Transfer Division for publication in the JOURNAL OF HEAT TRANSFER. Manuscript received by the Heat Transfer Division April 1992; revision received December 1992. Keyword: Conduction. Associate Technical Editor: Y. Bayazitoglu.

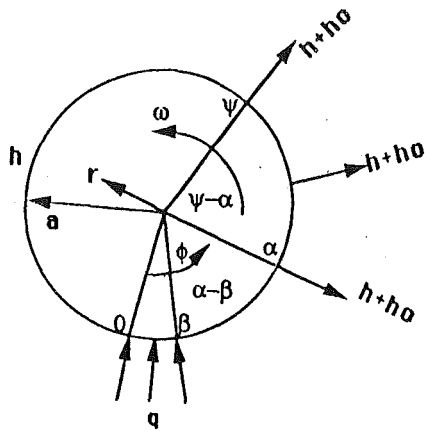

Fig. 1 Geometry and boundary conditions

cools the region $0 \le \phi \le \alpha$ and $\psi \le \phi \le 2\pi$. We seek to determine the cyclically steady-state temperature distribution in the cylinder based on the following assumptions:

1 Since the cylinder is long, axial conduction is neglected.
2 The cylinder rotates around its axis with constant angular velocity.
3 The thermal properties of the cylinder are independent of the temperature and remain uniform.

Adopting a fixed Eulerian reference frame, the steady-state heat conduction equation governing the problem is:

$$\frac{\partial^2 T}{\partial r^2}+\frac{1}{r}\frac{\partial T}{\partial r}+\frac{1}{r^2}\frac{\partial^2 T}{\partial \phi^2}=\frac{\omega}{\kappa}\frac{\partial T}{\partial \phi}, \tag{1}$$

where T represents the excess of coolant or ambient temperature.

The boundary conditions at $r = a$ are:

$$\begin{aligned} k\frac{\partial T}{\partial r}&=q && 0\le\phi\le\beta\\ k\frac{\partial T}{\partial r}&=-hT && \beta\le\phi\le\alpha\\ k\frac{\partial T}{\partial r}&=-hT-h_0T && \alpha\le\phi\le\psi\\ k\frac{\partial T}{\partial r}&=-hT && \psi\le\phi\le 2\pi. \end{aligned} \tag{2}$$

The use of the following dimensionless variables:

$$u=\frac{\pi h_0 T}{q};\quad \rho=\frac{r}{a};\quad \mathrm{Bi}_0=\frac{h_0 a}{k};\quad \mathrm{Bi}=\frac{ha}{k};\quad \mathrm{Pe}=\frac{\omega a^2}{\alpha},$$

transforms the heat conduction equation into:

$$\frac{\partial^2 u}{\partial \rho^2}+\frac{1}{\rho}\frac{\partial u}{\partial \rho}+\frac{1}{\rho^2}\frac{\partial u^2}{\partial \phi^2}=\mathrm{Pe}\frac{\partial u}{\partial \phi}. \tag{3}$$

The corresponding boundary conditions at $\rho = 1$ are:

$$\begin{aligned} \frac{\partial u}{\partial \rho}&=\pi\mathrm{Bi}_0 && 0\le\phi\le\beta\\ \frac{\partial u}{\partial \rho}&=-\mathrm{Bi}u && \beta\le\phi\le\alpha\\ \frac{\partial u}{\partial \rho}&=-u(\mathrm{Bi}+\mathrm{Bi}_0) && \alpha\le\phi\le\psi\\ \frac{\partial u}{\partial \rho}&=-\mathrm{Bi}u && \psi\le\phi\le 2\pi. \end{aligned} \tag{4}$$

Additional boundary conditions are that u is periodic over the interval $[0, 2\pi]$ and at $\rho = 0$, u is finite.

Applying the following finite Fourier transform:

$$\bar{u}=\frac{1}{2\pi}\int_0^{2\pi} u e^{-im\phi}d\phi, \tag{5}$$

Eq. (3) becomes:

$$\rho^2\frac{\partial^2 \bar{u}}{\partial \rho^2}+\rho\frac{\partial \bar{u}}{\partial \rho}-\bar{u}(m^2+im\rho^2\mathrm{Pe})=0. \tag{6}$$

The boundary condition at $\rho = 1$ becomes

$$\frac{\partial \bar{u}}{\partial \rho}=\frac{\mathrm{Bi}_0}{2}\int_0^{\beta} e^{-im\phi}d\phi-\frac{1}{2\pi}\int_{\beta}^{2\pi}u\mathrm{Bi}e^{-im\phi}d\phi -\frac{1}{2\pi}\int_{\alpha}^{\psi}u\mathrm{Bi}_0 e^{-im\phi}d\phi.$$

In order to apply the transformation given in Eq.(5), the second term on the righthand side of the above equation is decomposed into two terms as shown below:

$$-\frac{1}{2\pi}\int_{\beta}^{2\pi}u\mathrm{Bi}e^{-im\phi}d\phi=-\frac{1}{2\pi}\int_0^{2\pi}u\mathrm{Bi}e^{-im\phi}d\phi +\frac{1}{2\pi}\int_0^{\beta}u\mathrm{Bi}e^{-im\phi}d\phi.$$

In the above operation, the convective cooling over $\beta \le \phi \le 2\pi$ is decomposed into a uniform cooling over the entire pe-

Nomenclature

a = cylinder radius
Bi_0 = Biot number of one cooling zone = h_0a/k
Bi = Biot number for both cooling zones = ha/k
BP_0 = parameter for main cooling zone = $(\mathrm{Bi}_0/\sqrt{\mathrm{Pe}})$
BP = parameter for both cooling zones = $(\mathrm{Bi}/\sqrt{\mathrm{Pe}})$
ber_m = real part of Bessel function of order m with imaginary argument
bei_m = imaginary part of Bessel function of order m with imaginary argument
ber'_m = derivative of ber_m
bei'_m = derivative of bei_m
h = convection heat transfer coefficient in both cooling zones, $\mathrm{Wm}^{-2}\,^{\circ}\mathrm{C}^{-1}$
h_0 = convection heat transfer coefficient in main zone, $\mathrm{Wm}^{-2}\,^{\circ}\mathrm{C}^{-1}$
I_m = Bessel function of order m
I'_m = derivative of I_m
i = $\sqrt{-1}$
k = thermal conductivity, $\mathrm{Wm}^{-1}\,^{\circ}\mathrm{C}^{-1}$
m = index in summations
Pe = Peclet number = $\omega a^2/\alpha$
q = heat source strength
r = radial coordinate
Re = real part of
t = temperature, °C
T = excess of coolant or ambient temperature = $t - T_c$, °C
T_c = coolant temperature, °C
u = dimensionless temperature = $(\pi h_0 T/q)$
U = normalized u = $(h_0T/q\beta)$
$\bar{u}$ = transformed u
α = location of superimposed convective cooling, rad
β = location of heat source, rad
κ = thermal diffusivity, $\mathrm{m}^2\,\mathrm{s}^{-1}$
ρ = dimensionless radius = r/a
ϕ = angular location, rad
ψ = end location of superimposed convective cooling
ω = angular speed, rad s^{-1}
$\bar{\omega}_m$ = dimensionless parameter = $\sqrt{m\mathrm{Pe}}$

riphery of the cylinder and an additional term, which cancels the "convective cooling in the heating zone." Therefore, the boundary condition at $\rho = 1$ becomes

$$\frac{\partial \bar{u}}{\partial \rho} = -\mathrm{Bi}\bar{u} + \frac{1}{2\pi}\int_0^{\beta} u\mathrm{Bi}e^{-im\phi}d\phi + \frac{\mathrm{Bi}_0}{2}\int_0^{\beta} e^{-im\phi}d\phi - \frac{1}{2\pi}\int_{\alpha}^{\psi} u\mathrm{Bi}_0 e^{-im\phi}d\phi, \quad (7)$$

after making use of $u(0) = u(2\pi)$.

Equation (6) is a Bessel's equation with the general solution of

$$\bar{u} = A_1 I_m(\sqrt{im\mathrm{Pe}}\rho), \quad (8)$$

where A_1 is a constant.

Evaluating A_1 using Eq. (7), and substituting into Eq. (8) yields,

$$\bar{u} = \frac{\left(\frac{1}{2\pi}\int_0^{\beta} \mathrm{Bi}ue^{-im\phi}d\phi + \frac{\mathrm{Bi}_0}{2}\int_0^{\beta} e^{-im\phi}d\phi - \frac{\mathrm{Bi}_0}{2\pi}\int_{\alpha}^{\psi} ue^{-im\phi}d\phi\right) I_m(\sqrt{im\mathrm{Pe}}\rho)}{(\sqrt{im\mathrm{Pe}}I_m'(\sqrt{im\mathrm{Pe}}) + \mathrm{Bi}I_m(\sqrt{im\mathrm{Pe}}))}.$$

The first term of the numerator of $\bar{u}$ is due to the convective cooling from h in the heating zone $0 \le \phi \le \beta$. The heat removal in the heating zone is negligible whenever β is small: It becomes a small fraction of the overall convective cooling on the cylinder periphery. In fact, this was shown to be true by Gecim and Winer (1984) who solved the problem of a rotating cylinder under uniform cooling and heating. As a consequence of the above, the first term of the numerator of $\bar{u}$ will not be taken into consideration in the subsequent derivations.

Hence,

$$\bar{u} = \frac{\left(\frac{\mathrm{Bi}_0}{2}\int_0^{\beta} e^{-im\phi}d\phi - \frac{\mathrm{Bi}_0}{2\pi}\int_{\alpha}^{\psi} ue^{-im\phi}d\phi\right) I_m(\sqrt{im\mathrm{Pe}}\rho)}{(\sqrt{im\mathrm{Pe}}I_m'(\sqrt{im\mathrm{Pe}}) + \mathrm{Bi}I_m(\sqrt{im\mathrm{Pe}}))}. \quad (9)$$

Now with the inverse Fourier transform of the form

$$u(\rho, \phi) = \mathrm{Re}\sum_{m=-\infty}^{m=+\infty} e^{im\phi}\,\bar{u}(\rho, m), \quad (10)$$

we have

$$u(\rho, \phi) = \mathrm{Re}\sum_{m=-\infty}^{m=+\infty}\left\{\frac{\left(\frac{\mathrm{Bi}_0}{2}\int_0^{\beta} e^{-im(\phi'-\phi)}d\phi' - \frac{\mathrm{Bi}_0}{2\pi}\int_{\alpha}^{\psi} u(1, \phi')e^{-im(\phi'-\phi)}d\phi'\right) I_m(\sqrt{im\mathrm{Pe}}\rho)}{(\sqrt{im\mathrm{Pe}}I_m'(\sqrt{im\mathrm{Pe}}) + \mathrm{Bi}I_m(\sqrt{im\mathrm{Pe}}))}\right\}, \quad (11)$$

or

$$u(\rho, \phi) = \frac{\mathrm{Bi}_0}{2\mathrm{Bi}}\beta - \frac{\mathrm{Bi}_0}{2\pi\mathrm{Bi}}\int_{\alpha}^{\psi} u(1, \phi')d\phi' + 2\mathrm{Re}\sum_{m=1}^{\infty}\left\{\left(\frac{\mathrm{Bi}_0}{2}\int_0^{\beta} e^{-im(\phi'-\phi)}d\phi' - \frac{\mathrm{Bi}_0}{2\pi}\int_{\alpha}^{\psi} u(1, \phi')e^{-im(\phi'-\phi)}d\phi'\right)\right.$$
$$\left.\cdot I_m(\sqrt{im\mathrm{Pe}}\rho)/(\sqrt{im\mathrm{Pe}}I_m'(\sqrt{im\mathrm{Pe}}) + \mathrm{Bi}I_m(\sqrt{im\mathrm{Pe}}))\right\}. \quad (12)$$

The solution $u(\rho, \phi)$ is then the superposition of two terms independent of location and another one function of the circumferential variable ϕ and the dimensionless radius ρ. The temperature at the center of the cylinder $\rho = 0$ corresponds to the first two terms of Eq. (12):

$$u(0, \phi) = \frac{\mathrm{Bi}_0}{2\mathrm{Bi}}\beta - \frac{\mathrm{Bi}_0}{2\pi\mathrm{Bi}}\int_{\alpha}^{\psi} u(1, \phi')d\phi'. \quad (13)$$

The above centerline temperature is coupled to the unknown surface cylinder temperature $u(1, \phi')$. Patula (1981) showed that for the case of a cylinder with convective cooling and insulated regions around its periphery, the bulk temperature provides a good representation for the centerline temperature of the cylinder since at high speeds the centerline temperature becomes insensitive to cooling and heating locations. This holds whenever the ratio $\mathrm{Bi}_0/\sqrt{\mathrm{Pe}}$ or BP_0 is small, usually lower than 0•1. The bulk temperature, by definition, neglects all internal temperature gradients. Hence, by applying a global energy balance to satisfy the condition that at steady state the heat input must be equal to the heat output by convective cooling, we obtain the following approximation for the centerline temperature:

$$u(0) = \frac{\beta}{2\left(\frac{(\psi-\alpha)}{2\pi} + \frac{\mathrm{Bi}}{\mathrm{Bi}_0}\right)}. \quad (14)$$

When $\mathrm{Bi}/\mathrm{Bi}_0$ is very small, it can be readily shown that $u(0)$ reduces identically to Patula's expression for the bulk temperature with $\mathrm{Bi} \to 0$.

Therefore Eq. (12) becomes:

$$u(\rho, \phi) = \frac{\beta}{2\left(\frac{(\psi-\alpha)}{2\pi} + \frac{\mathrm{Bi}}{\mathrm{Bi}_0}\right)} + 2\mathrm{Re}\sum_{m=1}^{\infty}\left\{\left(\frac{\mathrm{Bi}_0}{2}\int_0^{\beta} e^{-im(\phi'-\phi)}d\phi' - \frac{\mathrm{Bi}_0}{2\pi}\int_{\alpha}^{\psi} u(1, \phi')\right.\right.$$
$$\left.\left.\times e^{-im(\phi'-\phi)}d\phi'\right) I_m(\sqrt{im\mathrm{Pe}}\rho)/(\sqrt{im\mathrm{Pe}}I_m'(\sqrt{im\mathrm{Pe}}) + \mathrm{Bi}I_m(\sqrt{im\mathrm{Pe}}))\right\}. \quad (15)$$

Letting $\bar{\omega}_m = \sqrt{m\mathrm{Pe}}$, the term involving summation becomes:

$$u_0(\rho, \phi) = \sum_{m=1}^{\infty}\left\{\left(\frac{\mathrm{Bi}_0}{2}\int_0^{\beta} e^{-im(\phi'-\phi)}d\phi' - \frac{\mathrm{Bi}_0}{2\pi}\int_{\alpha}^{\psi} u(1, \phi')e^{-im(\phi'-\phi)}d\phi'\right)\right.$$
$$\left.\cdot (I_m(i^{1/2}\bar{\omega}_m\rho))/(i^{1/2}\bar{\omega}_m I_m'(i^{1/2}\bar{\omega}_m) + \mathrm{Bi}I_m(i^{1/2}\bar{\omega}_m))\right\} + \text{conjugate}. \quad (16)$$

The above expression may be simplified using the real and imaginary parts of the Bessel's functions $I_m'(i^{1/2}\bar{\omega}_m)$, $I_m(i^{1/2}\bar{\omega}_m)$ and $I_m(i^{1/2}\bar{\omega}_m\rho)$ also known as $\mathrm{ber}_m(\,)$ and $\mathrm{bei}_m(\,)$ functions. Now, using the modulus and phase notation defined below:

$$M_1 = (\mathrm{ber}_m^2(\bar{\omega}_m\rho) + \mathrm{bei}_m^2(\bar{\omega}_m\rho))^{1/2},$$

$$\phi_1 = \tan^{-1}\left(\frac{\mathrm{bei}_m(\bar{\omega}_m\rho)}{\mathrm{ber}_m(\bar{\omega}_m\rho)}\right),$$

$$M_2=(\mathrm{ber}_m'^2(\bar{\omega}_m)+\mathrm{bei}_m'^2(\bar{\omega}_m))^{1/2},$$

$$\phi_2=\tan^{-1}\left(\frac{\mathrm{bei}_m'(\bar{\omega}_m)}{\mathrm{ber}_m'(\bar{\omega}_m)}\right),$$

$$M_3=(\mathrm{ber}_m^2(\bar{\omega}_m)+\mathrm{bei}_m^2(\bar{\omega}_m))^{1/2},$$

$$\phi_3=\tan^{-1}\left(\frac{\mathrm{bei}_m(\bar{\omega}_m)}{\mathrm{ber}_m(\bar{\omega}_m)}\right), \tag{17}$$

after some trigonometric manipulations, the temperature solution $u(\rho, \phi)$ reduces to the following:

$$u(\rho,\phi)=\frac{\beta}{2\left(\frac{(\psi-\alpha)}{2\pi}+\frac{\mathrm{Bi}}{\mathrm{Bi}_0}\right)}+2\mathrm{Bi}_0\sum_{m=1}^{\infty}\frac{M_1}{m}\sin m\left(\frac{\beta}{2}\right)$$
$$\times\left[\bar{\omega}_m M_2\cos\left(\phi_1-\phi_2+m\phi-\frac{m\beta}{2}\right)+\mathrm{Bi}M_3\cos\left(\phi_1-\phi_3+m\phi-\frac{m\beta}{2}\right)\right]\Bigg/$$
$$[\bar{\omega}_m^2M_2^2+\mathrm{Bi}^2M_3^2+2\bar{\omega}_mM_2\mathrm{Bi}M_3\cos(\phi_2-\phi_3)]$$
$$-\frac{\mathrm{Bi}_0}{\pi}\sum_{m=1}^{\infty}\left\{\int_{\alpha}^{\psi}M_1u(1,\phi')[\bar{\omega}_mM_2\cos(m(\phi-\phi')+\phi_1-\phi_2)+\mathrm{Bi}M_3\cos(m(\phi-\phi')+\phi_1-\phi_3)]/[\bar{\omega}_m^2M_2^2+\mathrm{Bi}^2M_3^2+2\bar{\omega}_mM_2\mathrm{Bi}M_3\cos(\phi_2-\phi_3)]\right\}d\phi'. \tag{18}$$

The functions M_1, M_2, M_3, ϕ_1, ϕ_2, and ϕ_3 all involve infinite series and are, therefore, difficult to compute when their arguments reach large values (cf. Abramowitz and Stegun, 1964). Hence, any evaluation of the terms in $u(\rho, \phi)$ would require a significant amount of computational time. Therefore, when the arguments of the moduli and phases are large, the asymptotic expansions of the functions are used. We note that a large $\bar{\omega}_m\rho$, provided $\rho \neq 0$, implies that the Pe number is large. This is indeed the case in most practical applications. As a consequence of the above, after some simplifications involving the asymptotic expansions of the Bessel's functions, Eq. (18) reduces to the following:

$$u(\rho,\phi)=\frac{\beta}{2\left(\frac{(\psi-\alpha)}{2\pi}+\frac{\mathrm{Bi}}{\mathrm{Bi}_0}\right)}+\frac{2\mathrm{Bi}_0}{\sqrt{\rho}\sqrt{\mathrm{Pe}}}\sum_{m=1}^{\infty}\frac{e^{-\frac{\bar{\omega}_m(1-\rho)}{\sqrt{2}}}}{m}$$
$$\times\sin\frac{m\beta}{2}\left\{\left(\frac{\bar{\omega}_m}{\mathrm{Bi}}\right)\cos\left(m\phi-\frac{m\beta}{2}-\frac{\bar{\omega}_m}{\sqrt{2}}(1-\rho)-\frac{\pi}{4}\right)+\cos\left(m\phi-\frac{m\beta}{2}-\frac{\bar{\omega}_m}{\sqrt{2}}(1-\rho)\right)\right\}\Bigg/\left[\left(\left(\frac{\bar{\omega}_m}{\mathrm{Bi}}\right)+\left(\frac{\mathrm{Bi}}{\bar{\omega}_m}\right)+\sqrt{2}\right)\sqrt{m}\right]-\frac{\mathrm{Bi}_0}{\pi\sqrt{\rho}\sqrt{\mathrm{Pe}}}\sum_{m=1}^{\infty}\int_{\alpha}^{\psi}\left\{e^{-\frac{\bar{\omega}_m(1-\rho)}{\sqrt{2}}}u(1,\phi')\right.$$
$$\times\left[\frac{\bar{\omega}_m}{\mathrm{Bi}}\cos\left(m\phi-m\phi'-\frac{\pi}{4}-\frac{\bar{\omega}_m(1-\rho)}{\sqrt{2}}\right)+\cos\left(m\phi-\frac{\bar{\omega}_m}{\sqrt{2}}(1-\rho)-m\phi'\right)\right]\Bigg/$$
$$\left.\left[\left(\left(\frac{\bar{\omega}_m}{\mathrm{Bi}}\right)+\left(\frac{\mathrm{Bi}}{\bar{\omega}_m}\right)+\sqrt{2}\right)\sqrt{m}\right]\right\}d\phi'. \tag{19}$$

Equation (19) is a Fredholm integral equation of the second kind and is nonhomogeneous.

For $\rho = 1$, Eq. (19) takes on the form:

$$u(\phi)=f(\phi)+\lambda\int_{\alpha}^{\psi}k(\phi,\phi')u(\phi')d\phi'. \tag{20}$$

This integral equation is solved in Appendix A. The solution is:

$$u(\rho,\phi)=\frac{\beta}{2\left(\frac{(\psi-\alpha)}{2\pi}+\frac{\mathrm{Bi}}{\mathrm{Bi}_0}\right)}+\frac{2\mathrm{Bi}_0}{\sqrt{\rho}\sqrt{\mathrm{Pe}}}\sum_{m=1}^{\infty}\frac{e^{-\frac{\bar{\omega}_m(1-\rho)}{\sqrt{2}}}}{m}$$
$$\times\sin\frac{m\beta}{2}\left\{\left(\frac{\bar{\omega}_m}{\mathrm{Bi}}\right)\cos\left(m\phi-\frac{m\beta}{2}-\frac{\bar{\omega}_m}{\sqrt{2}}(1-\rho)-\frac{\pi}{4}\right)+\cos\left(m\phi-\frac{m\beta}{2}-\frac{\bar{\omega}_m}{\sqrt{2}}(1-\rho)\right)\right\}\Bigg/\left[\left(\left(\frac{\bar{\omega}_m}{\mathrm{Bi}}\right)+\left(\frac{\mathrm{Bi}}{\bar{\omega}_m}\right)+\sqrt{2}\right)\sqrt{m}\right]-\frac{\beta}{\left(\frac{(\psi-\alpha)}{2\pi}+\frac{\mathrm{Bi}}{\mathrm{Bi}_0}\right)}\frac{\mathrm{Bi}_0}{\pi\sqrt{\mathrm{Pe}}\sqrt{\rho}}\sum_{m=1}^{\infty}\frac{e^{-\frac{\bar{\omega}_m(1-\rho)}{\sqrt{2}}}}{m}\sin m$$
$$\times\left(\frac{(\psi-\alpha)}{2}\right)\left\{\left(\frac{\bar{\omega}_m}{\mathrm{Bi}}\right)\cos\left(m\phi-\frac{\pi}{4}-\frac{m(\psi+\alpha)}{2}-\frac{\bar{\omega}_m(1-\rho)}{\sqrt{2}}\right)+\cos\left(m\phi-\frac{m(\psi+\alpha)}{2}-\frac{\bar{\omega}_m(1-\rho)}{\sqrt{2}}\right)\right\}\Bigg/$$
$$\left[\left(\left(\frac{\bar{\omega}_m}{\mathrm{Bi}}\right)+\left(\frac{\mathrm{Bi}}{\bar{\omega}_m}\right)+\sqrt{2}\right)\sqrt{m}\right]. \tag{21}$$

Equation (21) consists of three terms. The first two terms arise in the problem of a cylinder with a heat source and convective cooling throughout the surface. They are similar to Des-Ruisseaux and Zerkle's results (1970) derived from a totally different approach, using the method of instantaneous heat sources ($\psi - \alpha = 0$, $\mathrm{Bi} = \mathrm{Bi}_0$). Note that the same centerline temperature (see Eq. (14)) would be obtained if the bulk temperature is used as a zero-order approximation in Eq. (13). The third term is representative of the cooling effect over the angle ($\psi - \alpha$). The temperature distribution given by Eq. (21) represents a first-order approximation of Eq. (19). Note that for surface temperatures it depends only on the parameters BP and BP_0.

Results and Discussion

The dimensionless temperature is normalized by defining $U = u/\pi\beta$. Unless stated otherwise, this new dimensionless variable is used in all the figures to be discussed below.

As mentioned before, the first two terms of Eq. (20) (for the case of $\psi - \alpha = 0$ and $\mathrm{Bi} = \mathrm{Bi}_0$) belong to the problem of a cylinder with a heat source and uniform cooling all around the periphery. Therefore, by setting $\psi - \alpha = 0$ and $\mathrm{Bi} = \mathrm{Bi}_0$, it is expected to reproduce Gecim and Winer's (1984) results.

Figure 2 is a comparison of the dimensionless surface temperature from Gecim and Winer's solution (1984) and the present result. Results are presented for temperature distributions over a certain angular interval for various values of the parameter $\mathrm{Bi}_0/\sqrt{\mathrm{Pe}}$ called BP_0. It is noticed that the differences in the solutions are almost indistinguishable. It is recalled that the present result includes the circumferential conduction term, while the paper referenced above neglects this term. Close agreement stems from the fact that for speeds

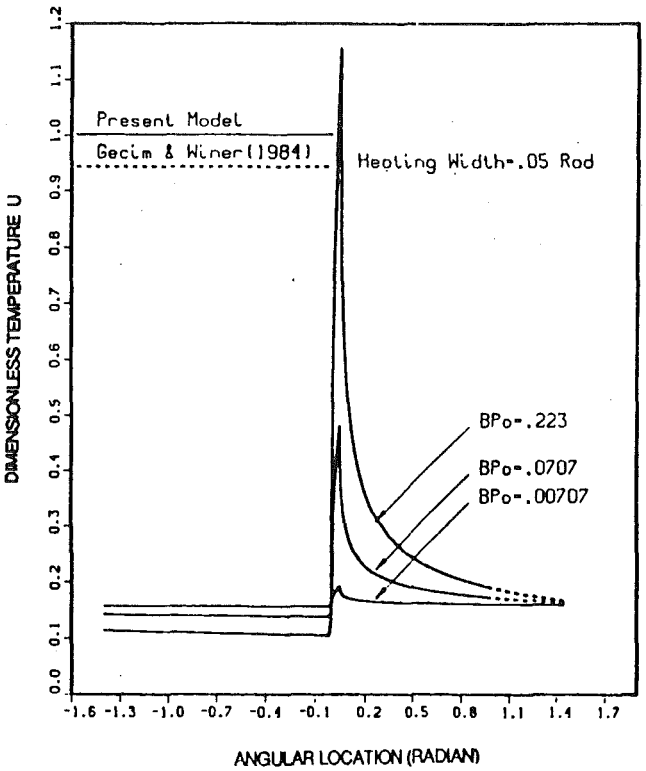

Fig. 2 Dimensionless surface temperature

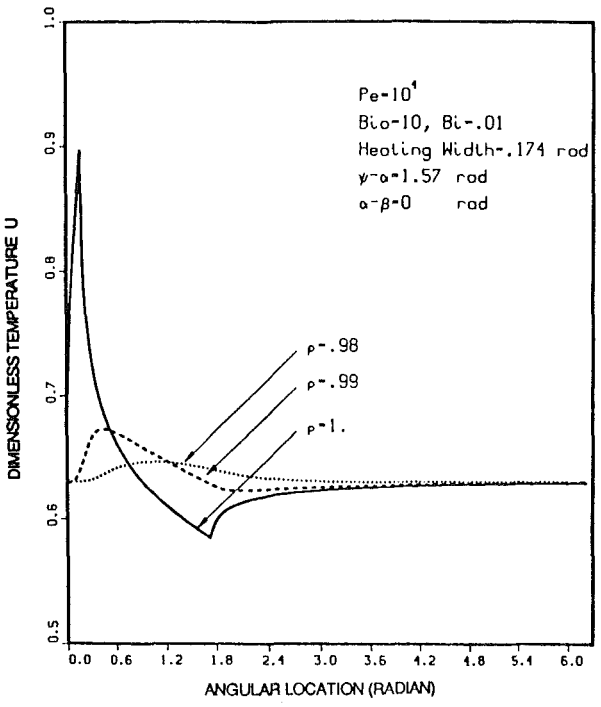

Fig. 3 Circumferential temperature variation for $\alpha - \beta = 0$

or Pe number as high as those presented in Fig. 2, the conduction term in the circumferential direction becomes insignificant compared to the convection term in the same direction. The data presented in Fig. 2 correspond to a heat source width of 0.05 rad and BP values ranging from 0.01 to 0.316. It is recalled that the dimensionless surface temperature depends only on the parameter BP_0.

Convective Cooling Location. From Fig. 1, it is seen that the cylinder is subjected to a convective cooling zone over a specified width ($\psi - \alpha$). This case is very common in spray

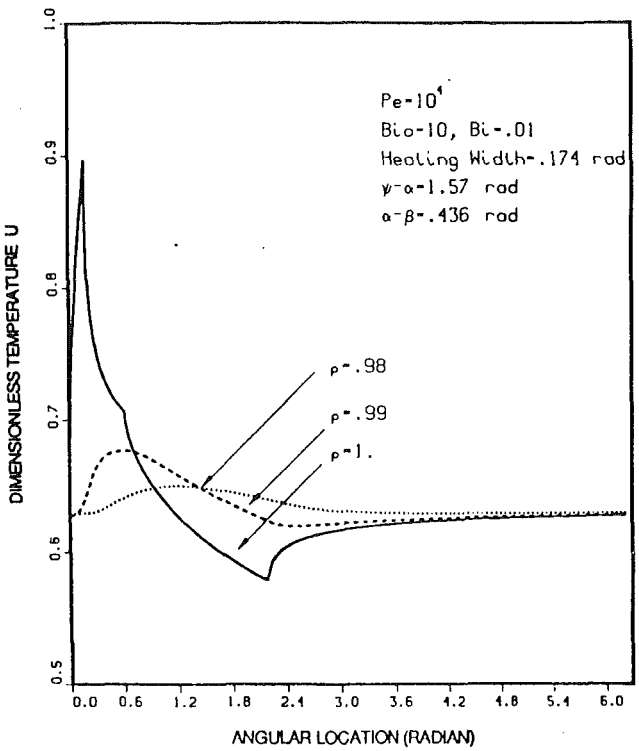

Fig. 4 Circumferential temperature variation for $\alpha - \beta = 0.436$

cooling where most of the heat removal occurs over a certain portion of the circumference, while a large portion of the cylinder surface ($0 \le \phi \le \alpha$ and $\psi \le \phi \le 2\pi$) has a much smaller convection coefficient. Figures 3–7 show the effect of varying the location of the main cooling region when $Bi_0 = 10$, $Bi = 0.01$, $\beta = 0.174$, $Pe = 10^4$. In Fig. 3, the circumferential dimensionless temperature distribution is shown for $\alpha - \beta = 0$. This means that the main cooling region has its trailing edge at the location β. As in the case of uniform cooling throughout the cylinder surface, the maximum temperature occurs at the end of the heating zone.

The thermal history of a point can be easily followed from Fig. 3. A point uniformly heated by the heat source increases its temperature significantly to reach a maximum at the end of the heating width. This point is then cooled as the result of convective cooling as well as circumferential and radial heat conduction. A cusp is created at the end of the main cooling zone where the minimum temperature occurs. The temperature then slowly increases due to the heat conducted from the inner layers to the surface of the cylinder and eventually levels off.

Points inside the cylinder are less affected by the cooling and heating. From the work of Jaeger (1944), DesRuisseaux and Zerkle (1970), and Gecim and Winer (1984), it is well established that, for this cyclically steady-state problem, due to the length of time needed for the heat to be conducted into the inner layers, the maximum temperatures at interior locations are always shifted in the direction of rotation. The same effect is observed for the minimum temperatures but for the opposite reason. This is due to the length of time that it takes for the heat to be conducted to the outer layers of the cylinder. An interior point reaches its minimum temperature, only after the corresponding point on the surface at the same angular location partially recovers its heat loss.

Figure 4 presents the temperature profile for the case where the main cooling zone occurs at 0.436 rad (25 deg) away from the end of the heat input region. Two cusps are created, defining the main cooling area: one at the beginning and the other at the end of the cooling zone. A similar phenomenon is also observed at interior layers of the cylinder but at a much reduced magnitude.

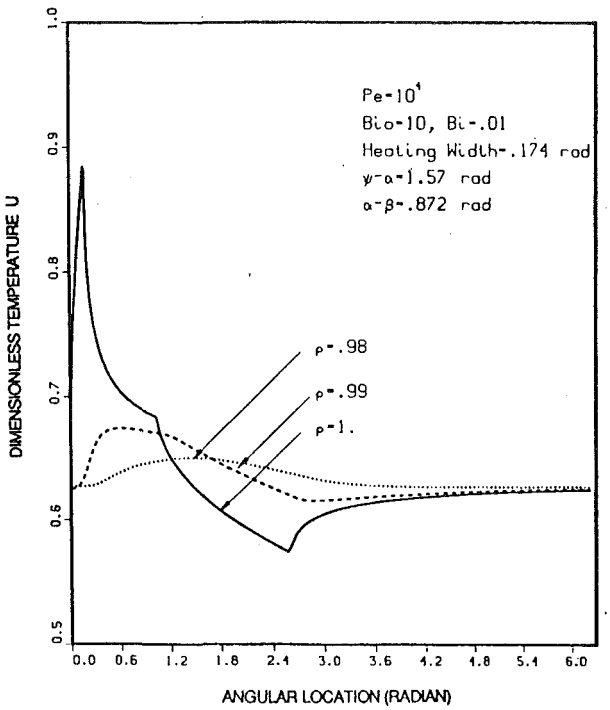

Fig. 5 Circumferential temperature variation for $\alpha - \beta = 0.872$

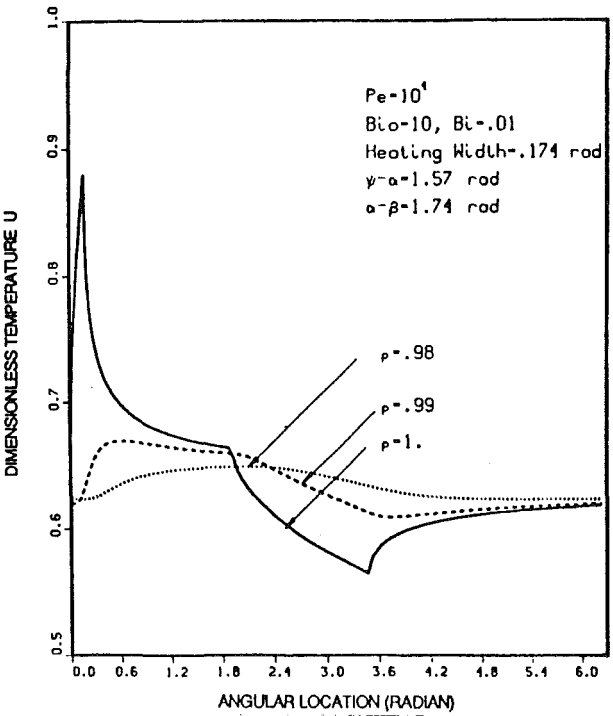

Fig. 6 Circumferential temperature variation for $\alpha - \beta = 1.74$

One notices that the maximum temperature in Fig. 4 is slightly lower than its counterpart in Fig. 3. This can be explained by examining the thermal history of a material element. A point leaving the heating zone immediately loses heat by conduction and convective cooling at the surface. Therefore when it encounters the main cooling zone, its temperature is already reduced to a certain degree because of the 0.436 rad separation zone. After being further cooled in the main cooling zone, its temperature as it enters the heating zone is lower than in the case of Fig. 3.

Increasing the separation zone by 0.436 rad or 25 deg was found not to cause great variations from the situation just described (see Fig. 5). In Fig. 6, for a separation zone of 1.74 rad (100 deg), the same pattern is observed. But, clearly, the temperature of the surface and interior points do not level off as before to the same temperature at locations very far from the source.

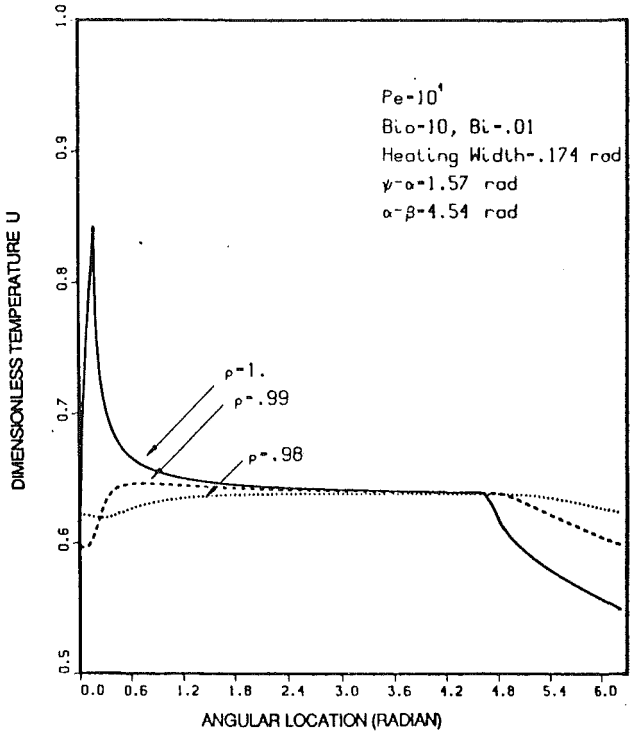

Fig. 7 Circumferential temperature variation for $\alpha - \beta = 4.54$

Figure 7 is the case of a main cooling zone located near the entry of the heating region with the separation zone of 4.54 rad (260 deg). A large portion of the cylinder surface is at near-uniform temperature and the cusps are created as before at the beginning and the end of the main cooling area. Clearly, the temperature profile in this case is quite different from the one of Fig. 3, where the trailing edge of the main cooling zone is located at the end of the heating region. The maximum temperature is much lower for the reasons given above for the thermal history of a material element.

Sensitivity of Bi. The purpose of this section is to investigate how the temperature profile is affected when Bi is increased, leaving Bi_0 constant. The average value of the heat transfer coefficient for the larger portion of the circumference depends on many considerations, such as cylinder speed, type of lubricant, etc. The data presented in Fig. 8 are the same as those in Fig. 3, except that $Bi_0 = 20$ and Bi varies from 3 to 9. From Bi = 3–9, the peak temperature is decreased to about 20 percent of its initial value while the minimum temperature (not necessarily at the cusp when Bi = 9) is reduced to about 45 percent. Hence, tripling Bi in this particular case significantly influences the temperature distribution away from the heating zone. This can be attributed to the fact that the temperature away from the source is severely affected by a change in the bulk temperature.

Peak Surface Temperature. One of the essential design parameters is the peak surface temperature, which needs to be monitored to avoid overheating. Figure 9 shows that variation of the maximum temperature as a function of the BP_0 and BP parameters.

From the figure, it is seen that the peak temperature increases almost linearly when the Pe number or the speed decreases. This is because more time is allowed for the heat source to penetrate into the heating region. The effect of increasing Bi_0

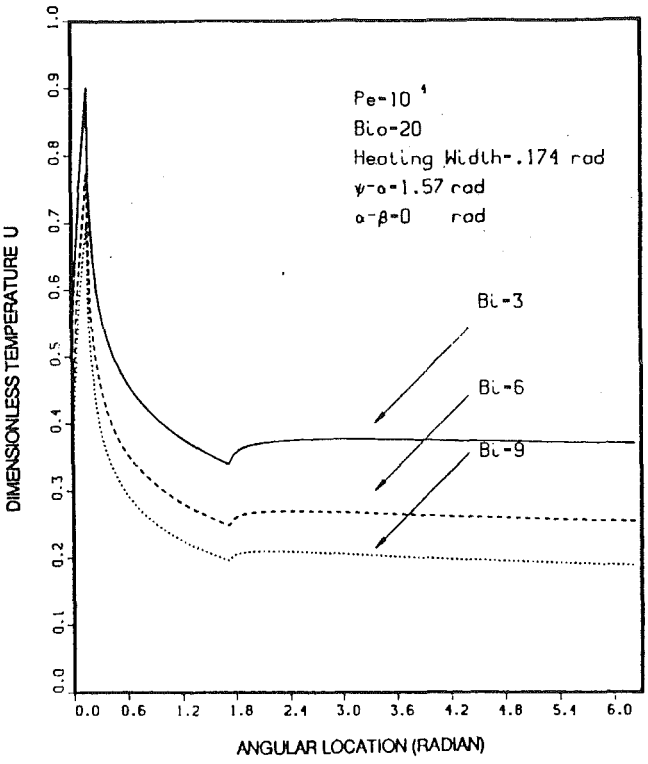

Fig. 8 Variation of surface temperature with Bi

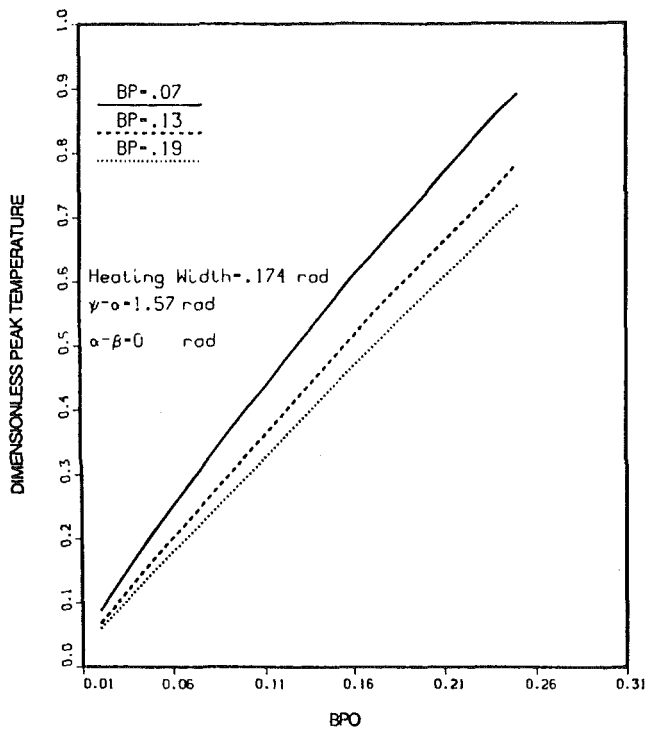

Fig. 9 Variation of surface peak temperature

is to lower the peak temperature since h_0 is in the normalized variable U. If BP is increased, the maximum temperature decreases because more heat is removed in the other cooling zone.

Validation of Model. To validate the present model, a comparison with experimental values measured by Stevens et al. (1971) for the case of hot steel rolling in a roughing stand is presented. An instrumented workroll with thermocouples at the surface and different depths of the roll is described in the

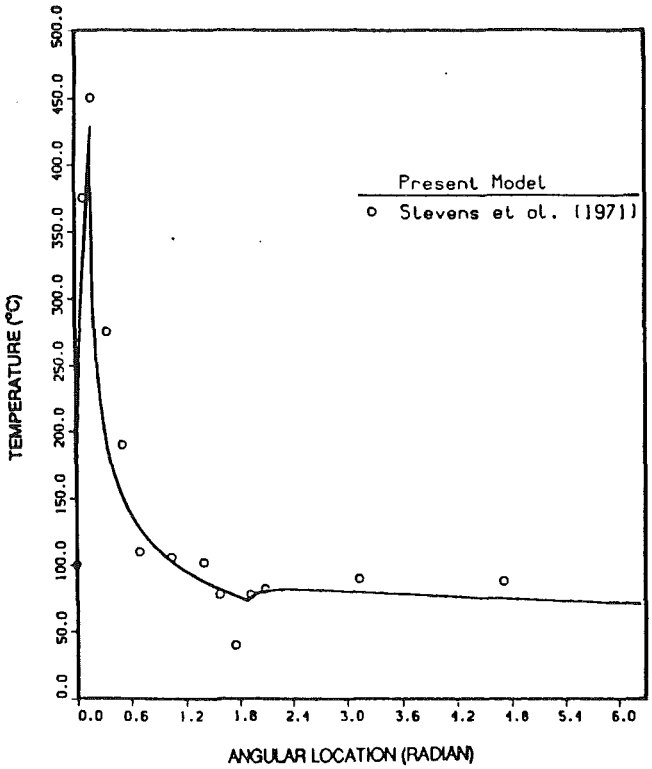

Fig. 10 Comparison of model with measured surface temperature

paper referenced above. In the experiment the following operating conditions were used:

(*a*) Roll speed, ω = 1.34 rad/s
(*b*) ψ = approximately 110 deg
(*c*) Spray configuration: 11 Watson 45 deg V-jets, with 0.95 cm (3.8 in.) bore, at 5.08 cm (2 in.) spacing and a supply pressure of 34.47 kPa (5 lb/in.^{2}).

Stevens et al. (1971) also provide a rough estimate of the heat transfer coefficient at the interface of the roll and strip.

Using the operating conditions provided in the above paper, the workroll thermal response is predicted in Fig. 10. The predicted values are shown to be in good agreement with measured experimental surface temperatures. The greatest discrepancy is noted at the impingement region of the spray where the amount of water coolant is greater than at other areas. One explanation is that the measured surface temperature at this location might have been affected by the water coolant.

Error Analysis. In this section, we present an analysis for estimating the compounded error from a number of possible sources that may be presented in the results. These are:

1 Approximation of the Bessel's functions for large arguments using asymptotic expansion.
2 First-order approximation of the integral equation solved in Appendix A.
3 Truncation of the infinite series by using a finite number of terms.
4 Approximation of the centerline temperature as the bulk temperature.

For a systematic evaluation of the overall error, a heat balance at steady-state conditions is computed at the cylinder surface. Details are provided in Appendix B. The difference between the output and input heat is normalized with the latter and expressed as a percentage of error.

In Fig. 11 the heat balance error percentage is shown as a function of the parameters BP and BP_0 for the particular case

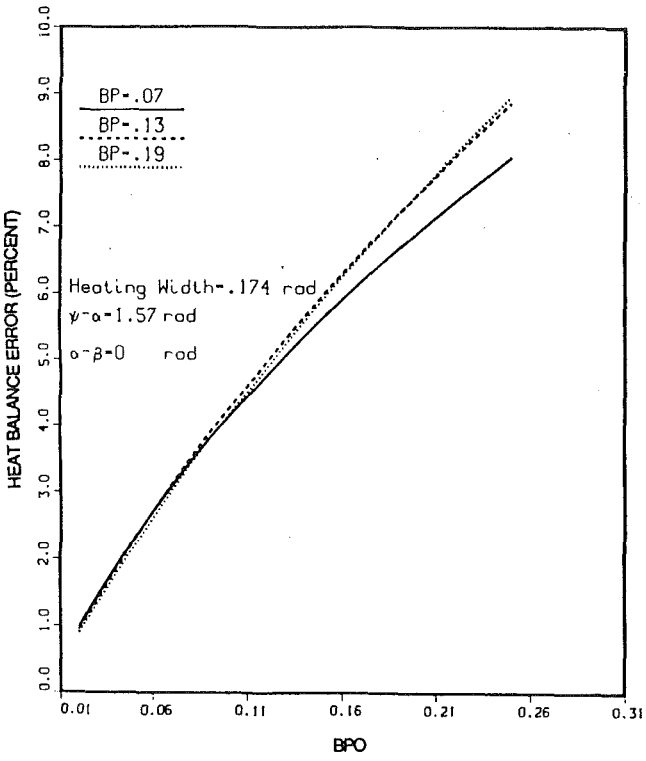

Fig. 11 Heat balance error at steady state

described in the figure. It is clear that the error increases with BP_0. This is due to the elimination of terms containing BP_0 to the second order or higher. However, the error is still acceptable for values of BP_0 slightly above 0.3. Also, increasing BP results in an increase in the overall error. The same magnitude of errors are found in somewhat simpler models such as the one given by Tseng (1984).

Conclusions

An analytical solution, obtained using a finite Fourier integral method, is presented for the temperature distribution of a rotating cylinder subjected to nonuniform cooling and uniform heating.

The following conclusions are drawn from the results presented in this paper. First, the analysis confirms that at high rotational speeds, i.e., large Peclet numbers, the circumferential conduction term may be neglected compared to convection heat transfer in the same direction.

It is shown that the cooling pattern of the cylinder changes considerably with locations of the main cooling zone relative to the heating zone. In addition, the peak temperature is seen to increase almost linearly with BP_0 but decrease when the parameter BP is increased. Therefore, the ratio of the Biot number to the square root of the Peclet number of the cooling zones is found to play an important role on the surface temperature distribution of the cylinder.

Also, the analytical prediction of the model is compared with experimentally measured circumferential temperature distribution for the case of a hot steel rolling. The agreement between the predicted with the measured temperature profile is considered to be excellent.

An analysis is presented to determine the compounded error involved. It is shown that even for BP_0 values slightly greater than 0.3, the error is small.

Finally, the present analysis offers a relatively simple and computationally attractive approach that may be useful in the evaluation of cooling practices in rolling mills.

References

Abramowitz, M., and Stegun, I. A., 1964, *Handbook of Mathematical Functions*, Applied Mathematics Series No. 55, National Bureau of Standards, Washington, DC.

Cerni, S., 1961, "The Temperature and Thermal Stresses in the Rolling of Metal Strip," Ph.D. Thesis, Carnegie Mellon University, Pittsburgh, PA.

DesRuisseaux, N. R., and Zerkle, R. D., 1970, "Temperature in Semi-infinite and Cylindrical Bodies Subjected to Moving Heat Sources and Surface Cooling," ASME JOURNAL OF HEAT TRANSFER, Vol. 92, pp. 456–464.

Gecim, B., and Winer, W. O., 1984, "Steady Temperature in a Rotating Cylinder Subject to Surface Heating and Convective Cooling," ASME *Journal of Tribology*, Vol. 106, pp.120–127.

Hogshead, T. H., 1967, "Temperature Distribution in the Rolling of Metal Strip," Ph.D. Thesis, Carnegie Mellon University, Pittsburgh, PA.

Jaeger, J. C., 1944, "Some Problems Involving Line Sources in Conduction of Heat," *Philosophical Magazine*, Series 7, Vol. 35, p. 169.

Ling, F. F., 1970, *Surface Mechanics*, Wiley Interscience, New York.

Patula, E. H., 1981, "Steady-State Temperature Distribution in a Rotating Roll Subject to Surface Heat Fluxes and Convective Cooling," ASME JOURNAL OF HEAT TRANSFER, Vol. 103, pp. 36–41.

Stevens, P. G., Ivens, K. P., and Harper, P., 1971, "Increasing Work-Roll Life by Improved Roll-Cooling Practice," *J. Iron Steel Inst. London*, Vol. 209, pp. 1–11.

Tseng, A. A., 1984, "Finite-Difference Solutions for Heat Transfer in a Roll Rotating at High Speed," *Numerical Heat Transfer*, Vol. 7, pp. 113–125.

Yuen, W. Y. D., 1984, "On the Steady-State Temperature Distribution in a Rotating Cylinder Subject to Heating and Cooling Over Its Surface," ASME JOURNAL OF HEAT TRANSFER, Vol. 106, pp. 578–585.

APPENDIX A

Equation (19) is a Fredholm equation of the second kind and nonhomogeneous of the form, when $\rho = 1$:

$$u(\phi) = f(\phi) + \lambda \int_{\alpha}^{\psi} k(\phi, \phi')u(\phi')d\phi'$$

where

$$f(\phi) = \frac{\beta}{2\left(\frac{(\psi-\alpha)}{2\pi} + \frac{\mathrm{Bi}}{\mathrm{Bi}_0}\right)} + \frac{2\mathrm{Bi}_0}{\sqrt{\mathrm{Pe}}} \sum_{m=1}^{\infty} \frac{1}{m} \times \sin\frac{m\beta}{2} \left\{ \left(\frac{\bar{\omega}_m}{\mathrm{Bi}}\right) \cos\left(m\phi - \frac{m\beta}{2} - \frac{\pi}{4}\right) + \cos\left(m\phi - \frac{m\beta}{2}\right) \right\} \Bigg/ \left[\left(\left(\frac{\bar{\omega}_m}{\mathrm{Bi}}\right) + \left(\frac{\mathrm{Bi}}{\bar{\omega}_m}\right) + \sqrt{2} \right) \sqrt{m} \right]$$

and

$$\lambda = \frac{-\mathrm{Bi}_0}{\pi\sqrt{\mathrm{Pe}}}$$

and the kernel

$$k(\phi, \phi') = \sum_{m=1}^{\infty} \left[\frac{\bar{\omega}_m}{\mathrm{Bi}} \cos\left(m\phi - m\phi' - \frac{\pi}{4}\right) + \cos(m\phi - m\phi') \right] \Bigg/ \left[\left(\left(\frac{\bar{\omega}_m}{\mathrm{Bi}}\right) + \left(\frac{\mathrm{Bi}}{\bar{\omega}_m}\right) + \sqrt{2} \right) \sqrt{m} \right].$$

The integral equation may be solved by an iterative scheme, making use of the resolvent kernel:

$$\Gamma(\phi, \phi'; \lambda) = \sum_{m=1}^{\infty} \lambda^{m-1} k_m(\phi, \phi') = k(\phi, \phi') + \lambda k_2(\phi, \phi') + \lambda^2 k_3(\phi, \phi') + \ldots$$

If the zero-order approximation to $u(\phi)$ is taken as the bulk temperature, then by use of the Neumann series:

$$u(\phi)=f(\phi)+\int_{\alpha}^{\psi}[\lambda k(\phi,\phi')+\lambda^2 k_2(\phi,\phi')+\lambda^3 k_3(\phi,\phi')+\ldots]\times\frac{\beta}{2\left(\frac{(\psi-\alpha)}{2\pi}+\frac{\mathrm{Bi}}{\mathrm{Bi}_0}\right)}d\phi'$$

where

$$k_2(\phi,\phi')=\int_{\alpha}^{\psi}k(\phi,\phi'')k(\phi'',\phi')d\phi''$$

$$k_3(\phi,\phi')=\int_{\alpha}^{\psi}k_2(\phi,\phi'')k(\phi'',\phi')d\phi''.$$

For small values of λ, a first-order approximation is adopted. The acceptable limit for λ is discussed in the heat balance error section. Therefore:

$$u(\phi)=f(\phi)+\frac{\beta}{2\left(\frac{(\psi-\alpha)}{2\pi}+\frac{\mathrm{Bi}}{\mathrm{Bi}_0}\right)}\int_{\alpha}^{\psi}[\lambda k(\phi,\phi')]d\phi'.$$

The surface temperature is obtained by integrating the kernel $k(\phi,\phi')$:

$$u(\phi)=f(\phi)-\frac{\beta}{\left(\frac{(\psi-\alpha)}{2\pi}+\frac{\mathrm{Bi}}{\mathrm{Bi}_0}\right)}\frac{\mathrm{Bi}_0}{\pi\sqrt{\mathrm{Pe}}}\sum_{m=1}^{\infty}\frac{1}{mD_{m1}}\times\sin\frac{m(\psi-\alpha)}{2}\left[\frac{\bar{\omega}_m}{\mathrm{Bi}}\cos\left(m\phi-\frac{\pi}{4}-\frac{m(\psi+\alpha)}{2}\right)+\cos\left(m\phi-\frac{(\psi+\alpha)}{2}\right)\right],\quad(A1)$$

where

$$D_{m1}=\left(\frac{\bar{\omega}_m}{\mathrm{Bi}}+\frac{\mathrm{Bi}}{\bar{\omega}_m}+\sqrt{2}\right)\sqrt{m}.$$

Once the surface temperature is inserted in Eq. (19) of the text, new terms involving the coefficients

$$\frac{\beta}{\left(\frac{(\psi-\alpha)}{2\pi}+\frac{\mathrm{Bi}}{\mathrm{Bi}_0}\right)}\left(\frac{\mathrm{Bi}_0}{\pi\sqrt{\mathrm{Pe}}}\right)^2\quad\text{and}\quad\frac{2}{\pi}\left(\frac{\mathrm{Bi}_0}{\sqrt{\mathrm{Pe}}}\right)^2$$

are found but neglected because λ is a small number. In fact the accuracy of the solution will depend not only on the parameter $\mathrm{Bi}_0/\sqrt{\mathrm{Pe}}$ but also on $\mathrm{Bi}/\sqrt{\mathrm{Pe}}$. The final solution is Eq. (21) in the text.

APPENDIX B

This appendix provides the expression for evaluating the error involved in the present analytical model. The heat balance equation at steady-state conditions is:

$$-h_0\int_{\alpha}^{\psi}aTd\phi-h\int_{0}^{2\pi}Td\phi a=-q_0\beta a.\quad(A2)$$

The above equation in dimensionless form is:

$$\int_{\alpha}^{\psi}ud\phi+\frac{\mathrm{Bi}}{\mathrm{Bi}_0}\int_{0}^{2\pi}ud\phi=\pi\beta,\quad(A3)$$

where u is Eq. (21) of the text at the surface ($\rho = 1$).

Now normalizing with $\pi\beta$, we obtain the following:

$$\int_{\alpha}^{\psi}Ud\phi+\frac{\mathrm{Bi}}{\mathrm{Bi}_0}\int_{0}^{2\pi}Ud\phi=1.\quad(A4)$$

Effective Thermal Conductivity of a Composite Material: A Numerical Approach

D. Veyret

S. Cioulachtjian

L. Tadrist

J. Pantaloni

Institut Universitaire des Systèmes Thermiques Industriels, Université de Provence, Marseille, France

The purpose of this paper is to characterize conductive heat transfer through composite, granular, or fibrous materials. A numerical approach was used to determine the effective thermal conductivity of the diphasic media. The media are composed of a solid continuous matrix containing similar particles. The configuration studied was a cubic lattice array with cylindrical inclusions. Behavior laws were established according to particle geometry, concentration, and the type of contact between particles. The effective thermal conductivity of the material was determined using the Laplace equation, as were the temperature and flux fields within the cell. A finite-element formulation was therefore used in this study. Calculation is carried out on two and three-dimensional geometric spaces. The results obtained from this calculation were compared to theoretical results found in prior literature.

1 Introduction

Composite materials have gained significant importance in the design of new systems. The physical properties of the different media must be thoroughly understood in order to predict their behavior and thus to optimize their use in real-life applications. Determining the thermal conductivity of composite, multiphase, porous, or fibrous materials is crucial in a number of industrial processes. These include thermal insulation, drying of moist porous materials, and heat transfer problems (e.g., heat pipes). The temperature fields in catalytic reactors, porous beds, and composite materials cannot be determined unless the thermal conductivities of the media are known. Despite the fundamental importance of this parameter and the considerable number of studies that have been carried out, the determination of effective thermal conductivity is only partially understood. The effective thermal conductivity of a composite material is a complex function of the thermal conductivity of the different phases, their geometry, distribution within the medium, and contact between the particles. Numerous theoretical and experimental approaches have been developed to determine the precise value of this parameter. A review of the different approaches is presented by Azizi (1988).

Maxwell (1881) was the first to study the effective thermal conductivity of heterogenous materials. By solving Laplace's equation, he determined the effective conductivity of a random suspension of spheres within a continuous medium. The model developed by Maxwell assumes that the particles are sufficiently far apart that the potential around each sphere will not be influenced by the presence of other particles. Rayleigh (1892) extended Maxwell's work to larger particle concentrations in cubic lattice arrays, whereas McPhedran and McKenzie (1978) have studied centered and face-centered cubic lattice arrays and DeVries (1972) has studied ellipsoidal particles. Rayleigh analyzed the effect of 248 spheres on the potential at the surface of a nearby sphere. Rayleigh's results were extended by Robert et al. (1969) to include larger concentrations. Jeffrey (1973) continued along the lines set out by Maxwell. Batchelor and O'Brien (1977) analyzed the conduction in a cubic array of spheres that were in contact at a single point. These authors developed a solution for the case in which the conductivity of the particles was high compared to that of the continuous phase. Bruggeman (1953) proposed a theory based on a model of average effective medium.

In real composite material, the isothermal surfaces present a very complex shape and cannot be analytically determined. The models used to calculate thermal conductivities are thus highly simplified models of the real media. The calculation of thermal conductivity is carried out using a parallel juxtaposition of elementary series models or by associating a series of elementary parallel models (Woodside, 1958; Russel, 1935). A great number of models can be obtained according to how the cell is divided. The results fall between a lower boundary (the "series model") and an upper boundary (the "parallel model"). In the case of isotropic media, Hashin and Shtrikman (1962) give more restrictive boundaries. Yet with high thermal conductivity ratios, the values obtained using the series-parallel models are slightly different.

Deissler and Boegli (1958) carried out the numerical studies. Using a relaxation method, they proposed a solution to Laplace's equation for a cubic array of spheres presenting a single point of contact and similar diameters ($p=\pi/6$). Deissler's works were extended by Wakao and Kato (1968) for a cubic ($p=\pi/6$) or orthorhombic ($p=7\pi/12$) array of uniform spheres in contact. Shonnard and Whitaker (1989) have investigated the influence of contacts on two-dimensional models. They have developed a global equation with an integral method for heat transfer in the medium.

The present study aims at evaluating the variations of effective thermal conductivity of periodic, diphasic, and homogeneous media. To accomplish this, two- and three-dimensional numerical analysis was carried out for the conductive heat transfer in an elementary cell. A systematic study was carried out for the different phase conductivity ratios (1 to 10,000), for the different phase quantities and for the geometry of the medium. This study focuses on the influence of contacts between the phases.

2 Methodology

The temperature field in the elementary cell was defined by solving Laplace's equation numerically using a finite element (Dhatt and Touzot, 1984) formulation. Three systems, each consisting of cubic lattice array, were developed into models to study the influence of the previously mentioned parameters. The two-dimensional systems analyzed in this study consisted of infinite parallel cylinders or parallelepipeds ($0<p<\pi/4$).

Contributed by the Heat Transfer Division for publication in the JOURNAL OF HEAT TRANSFER. Manuscript received by the Heat Transfer Division June 1992; revision received March 1993. Keywords: Conduction, Thermophysical Properties. Technical Editor: R. Viskanta.

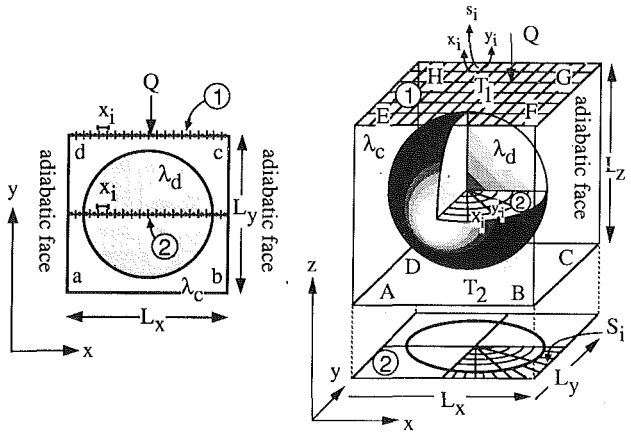

(a) (b)

Fig. 1 Determination of the effective thermal conductivity on an elementary cell at an isothermal side ① or at the central plane ②: (*a*) two-dimensional models; (*b*) three-dimensional model

Spheres ($0<p<\pi/6$) formed the three-dimensional system. The Laplace's equation ($\Delta T=0$) was then solved by imposing the following boundary conditions:

- The horizontal sides perpendicular to the direction of the heat flow are isothermal at the entrance to and the exit from the cell (Fig. 1*a*: sides *ab* and *cd*, Fig. 1*b*: surfaces *ABCD* and *EFGH*).
- The vertical sides parallel to the direction of the heat flow are adiabatic (Fig. 1*a*: sides *ad* and *bc*, Fig. 1*b*: surfaces: *ADHE*, *BCGF*, *ABFE*, and *DCGH*).

3 Results

3.1 Two-Dimensional Systems. The following section deals with the results relating to heat transfer and thermal conductivity of cubic lattice arrays composed of infinite cylinders or parallelepipeds ($0<p<\pi/6$). Figure 2 indicates meshes that were used in the computations. In the case of a cylinder situated inside a square, the reference elements were triangular three-node linear elements. A quarter of the cell was divided into 238 elements with 140 for the inclusions (a quadrant) and 98 for the continuous phase. In the case of a square situated inside another square, the reference elements were four-node bilinear quadrilateral elements. The mesh of the cell is regular. Figure 3 shows the temperature fields obtained respectively with a cylinder and a parallelepiped of λ_d conductivity contained within a continuous matrix of λ_c conductivity. The thermal conductivity ratio was 10,000 and the particle concentration was 64 percent. When the thermal conductivity ratio is equal to 1, the isothermal curves are plane and parallel. There is a linear decrease of the temperature in the cell. When the thermal conductivity of the discontinuous phase is relatively high, the temperature field is greatly deformed owing to the high conductivity ratio and the resulting modifications in flux lines. With cylindrical particles, the flux lines are directed toward inclusions of higher thermal conductivity. The heat flow moving into or out of the cell reaches its peak at the center of the isothermal faces. For an elementary two-dimensional cell with the dimensions of L_x (along the x axis) and L_y (along the y axis), the thermal conductivity is determined using the following relation (Fig. 1*a*):

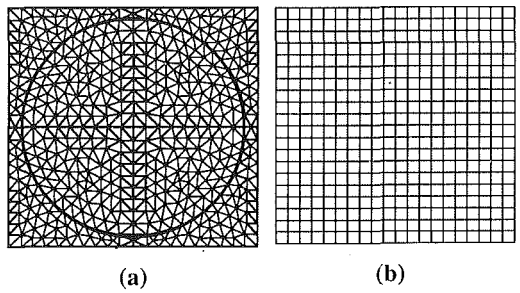

(a) (b)

Fig. 2 Mesh of two-dimensional cells: (*a*) square lattice array of infinite cylinders; (*b*) square lattice array of infinite parallelepipeds

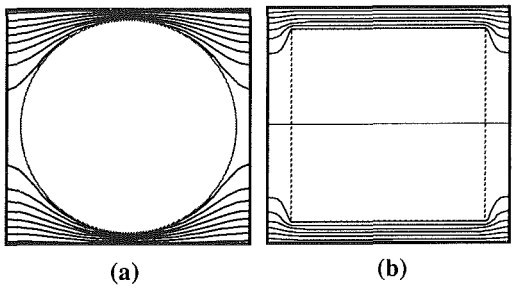

(a) (b)

Fig. 3 Representation of isothermal curves in two-dimensional elementary cells: (*a*) square lattice array of infinite cylinders; (*b*) square lattice array of infinite parallelepipeds; the conductivities ratio λ_d/λ_c is equal to 10,000

$$\lambda_e \frac{\Delta T_{\text{cell}}}{L_y} = \frac{1}{L_x} \sum_i \lambda_i x_i \left(\frac{\partial T_i}{\partial y}\right)$$

with

$$\sum_i x_i = L_x$$

and

$$\lambda_i = \begin{Bmatrix} \lambda_c \text{ in the continuous phase} \\ \lambda_d \text{ in the inclusions} \end{Bmatrix}$$

The calculation is carried out in a plane parallel to the isothermal boundaries. Figure 4 shows the effective thermal conductivity variations for square-in-square and circle-in-square systems for different conductivity ratio λ_d/λ_c and concentration. Similar behavior can be noted for both types of media. With large λ_d/λ_c values, a horizontal asymptote was observed.

Nomenclature

L_x = elementary cell size along the x axis
L_y = elementary cell size along the y axis
p = concentration of the inclusions
Q = heat flux per unit area
S = surface
$s_{i,j}$ = surface of the i,j element
T = temperature
x_i = length of the ith element along the x axis
x, y, z = space coordinates
Δ = Laplacian operator
λ = thermal conductivity
$\bar{\lambda}$ = thermal conductivity ratio $=\lambda/\lambda_c$

Subscripts

b = thermal bridge
c = continuous phase
d = discontinuous phase
e = effective

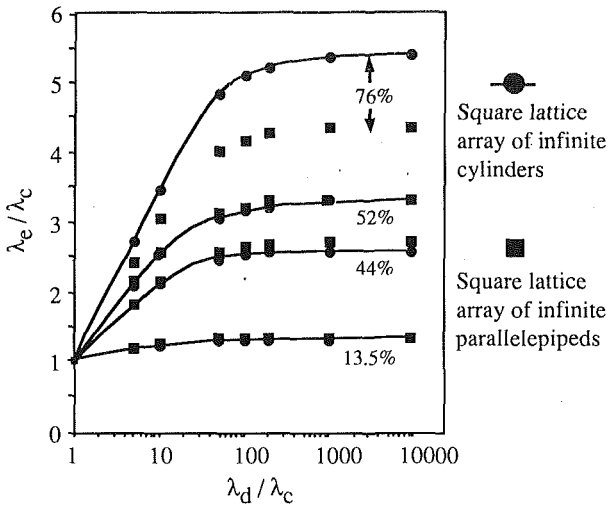

Fig. 4 Variation of the thermal conductivity obtained from the numerical simulation according to the ratio λ_d/λ_c for various particle concentrations

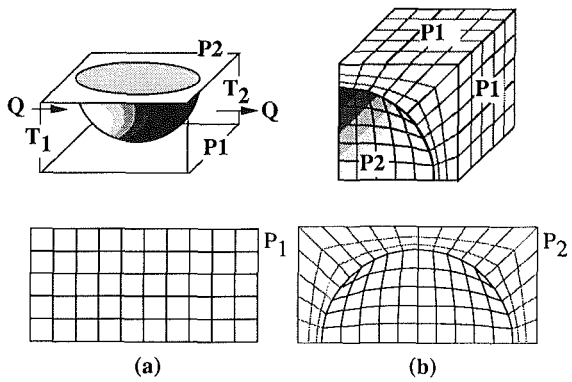

Fig. 5 Mesh of three-dimensional cells in the case of cubic lattice array of spheres: (*a*) mesh of the faces of the cell; (*b*) mesh of the centered plane of the cell perpendicular to isothermal faces

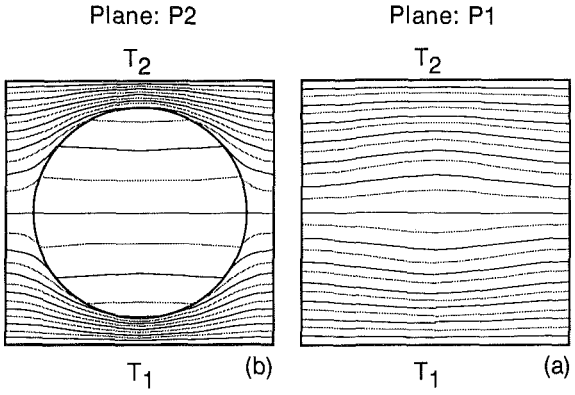

Fig. 6 Representation of isothermal curves in a three-dimensional elementary cell. Sphere array in a cube: (*a*) adiabatic faces of the cell; (*b*) centered plane of the cell perpendicular to isothermal faces.

In all cases, the effective thermal conductivity remains rather low compared to the thermal conductivity of the inclusions. The conductivity of a cubic array of circle particles is higher than that of a cubic array of parallelepiped particles when the particle concentration exceeds 54 percent. The comparison of the cylinder and parallelepiped configurations shows that the

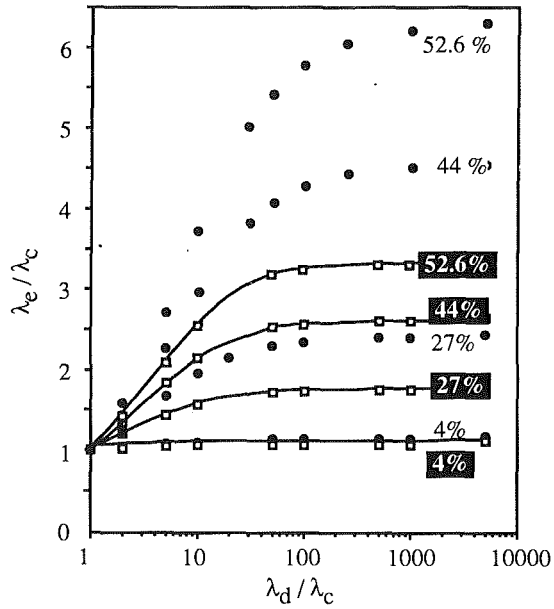

Fig. 7 Variation of thermal conductivity obtained from the numerical simulation on the basis of the ratio λ_d/λ_c for various particle concentrations: ⊟ square lattice array of infinite cylinders; ● cubic lattice array of spheres

effective thermal conductivity depends on the geometry of the inclusion.

3.2 Three-Dimensional System. The results presented below relate to heat transfer and thermal conductivity for a cubic lattice array of spheres. Figure 5 (*a*, *b*) describes the mesh of the cells. The reference elements were four-node three linear parallelepipeds. One-eighth of the cell was divided into 230 elements with 175 for the inclusions (i.e., 1/8th of the sphere) and 55 for the continuous phase. Figure 6 shows the temperature field for a thermal conductivity ratio λ_d/λ_c of 10,000 and a particle concentration of 27 percent. In the centered plane of the cell parallel to the direction of the average heat flow, the isothermal curves present shapes similar to those found with infinite cylinder systems. The isothermal curves on the adiabatic surfaces are nearly plane and parallel. The thermal conductivity was calculated using the following relation (Fig. 1*b*):

$$\lambda_e \frac{\Delta T_{\text{cell}}}{L_z} = \frac{1}{S} \sum_i \sum_j \lambda_{i,j} x_i y_j \left(\frac{\partial T_{i,j}}{\partial z}\right)$$

$$Q$$

with

$$s_{i,j} = x_i y_j$$

and

$$\sum_i \sum_j s_{i,j} = S$$

and

$$\lambda_{i,j} = \begin{Bmatrix} \lambda_c \text{ in the continuous phase} \\ \lambda_d \text{ in the inclusions} \end{Bmatrix}$$

The results obtained from the isothermal boundaries were compared to those obtained from the center plane of the cell and the difference did not exceed 2 percent. Figure 7 shows the variation in thermal conductivity according to the thermal conductivity ratio of the phases for the various concentrations of the inclusions. The shape of the curves that were obtained resembles that found with the square lattice array of cylinders.

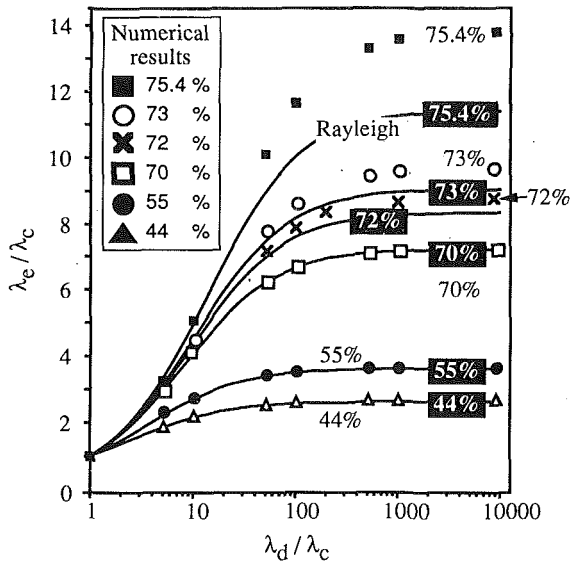

Fig. 8 Variation of thermal conductivity according to the ratio λ_d / λ_c for various particle concentrations. Case of a square lattice array of parallel cylinders. Results obtained through Rayleigh's models for particle concentration equal to *x*.

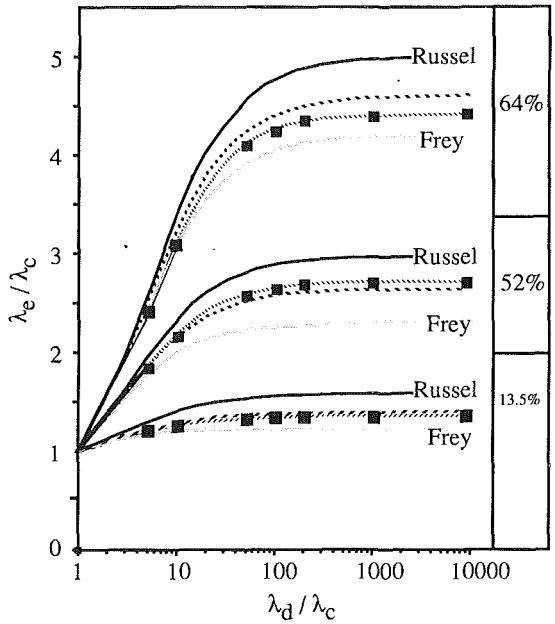

Fig. 9 Square lattice array of infinite parallelepipeds. Variation of thermal conductivity according to λ_d / λ_c for various particle concentrations. Comparison of our numerical results with those obtained from Russel's and Frey's *series—parallel models:*
results of our numerical simulation; —— Russel's model; Frey's model; ····· results of the combination (Frey + Russel)/2

In the same conditions, the effective thermal conductivity of the three-dimensional system exceeded that of the two-dimensional system.

4 Analysis and Interpretation of the Results

The following section offers a comparison of the numerical results for effective thermal conductivity with those obtained using a number of different approaches. Comparison with the results from this study indicates that the models closest to numerical simulation are those based on the analytical solution of Laplace's equation.

Cylinder. Figure 8 describes the thermal conductivity variations according to the thermal conductivity ratio of the numerical simulation and to Rayleigh's model. Rayleigh's model is in good agreement with the results of the simulation when the cylinder concentration does not exceed 70 percent. This corresponds to a cylinder-diameter/cell-side ratio of 0.95. The numerical results from the present study are also in good agreement with the numerical results of Perrins et al. (1979) for a cubic lattice array of cylinders. With higher concentrations ($0.7 < p < \pi/4$), the results derived from this numerical simulation are higher than those found in Rayleigh's model. The difference increases in proportion to the concentration of the inclusions. When the concentration is high, the flux lines between the inclusions are greatly deformed.

Square Case. In Fig. 9, the numerical results are compared with analytical results calculated from models similar to those of Russel (1935) and Frey (1932) but established with a two-dimensional cell:

$$\overline{\lambda_e} = \left[1 - \sqrt{1-p} + \frac{\sqrt{1-p}}{\sqrt{1-p}\,\overline{\lambda_d} + (1-\sqrt{1-p})} \right]^{-1}$$

"Russel formula"

$$\overline{\lambda_e} = 1 - \sqrt{1-p} + \frac{\sqrt{1-p}}{(1-\sqrt{1-p}) + \dfrac{\sqrt{1-p}}{\overline{\lambda_d}}}$$

"Frey formula"

Russel's model is based on a division "into parallel isotherms," whereas Frey's model is based on a division "into flux tubes." The results from the present study consistently varied between those of Russel (i.e., the upper boundary for effective thermal conductivity), and those of Frey (i.e., the lower boundary). The results presented here correspond closely to the arithmetic mean of these two models, and also to Shonnard and Whitaker's numerical results (1989).

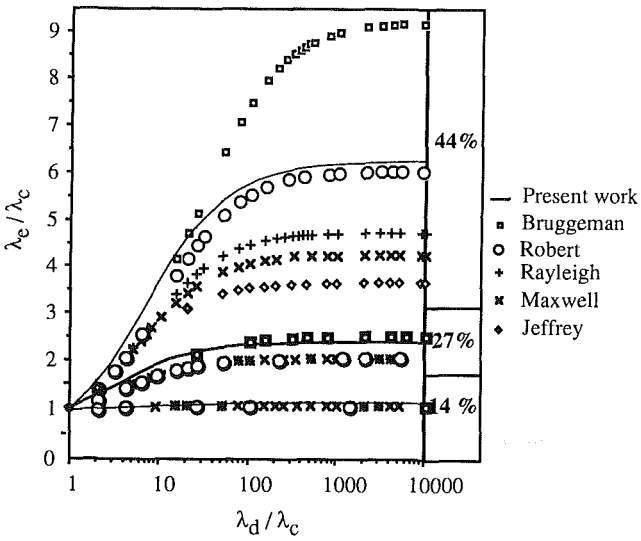

Fig. 10 Cubic lattice array of spherical particles. Variation of thermal conductivity on the basis of λ_d / λ_c for various particle concentrations. Comparison of our numerical results with those of Maxwell's and Rayleigh's models.

Spherical Case. Figure 10 shows a comparison of the simulation results with the models developed by Rayleigh (modified by Runge, 1925), Maxwell (1881), Bruggeman (1953), Jeffrey (1973), and Robert et al. (1969) for a variety of sphere concentrations. It was noted that all models with the exception of Bruggeman's gave results that were lower than the simulation results. The model of Robert et al. was in good agreement with the simulation results for a particles concentration equal

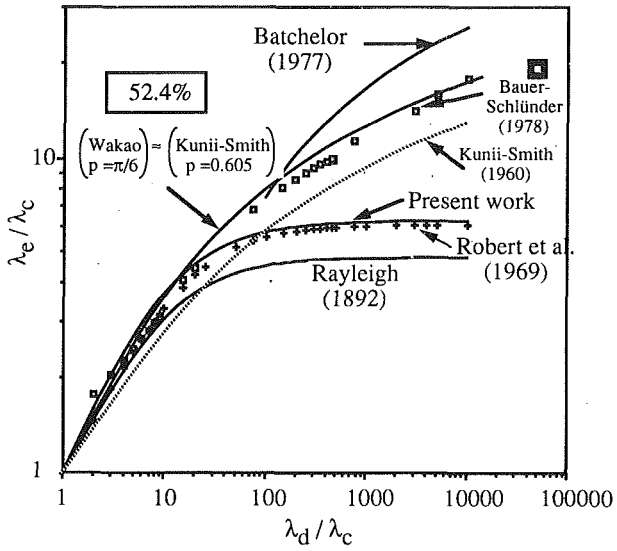

Fig. 11 Cubic lattice array of spherical particles. Variation of thermal conductivity according to λ_d/λ_c for a sphere concentration equal to $\pi/6$. Comparison of our numerical results with those of the literature.

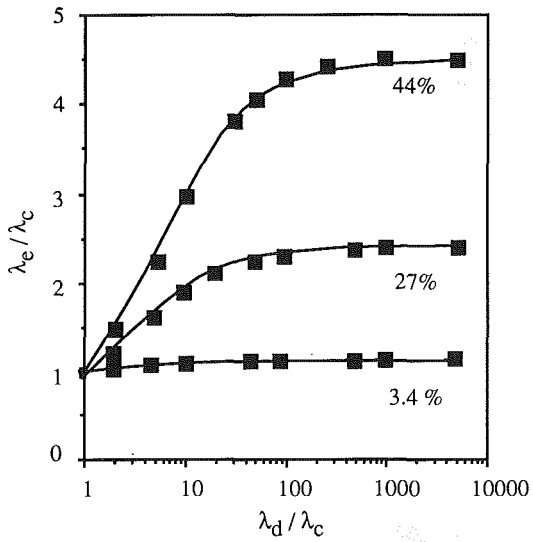

Fig. 12 Cubic lattice array of spherical particles. Variation of thermal conductivity according to λ_d/λ_c for various particle concentrations. Comparison of our numerical results with those from the correlation.

to $\pi/6$ (case of point contact spheres—Fig. 11). But this model diverges from the simulation for the other concentration values. Figure 11 shows a comparison of the simulation results with Batchelor and O'Brien's (1977) analytical results and Wakao and Kato's (1968) numerical results. The results in the present study fell below those in Batchelor's model and they were smaller than those in Wakao's model when λ_d/λ_c is higher than 13. This difference between numerical results can be attributed to the cell mesh. These authors use a regular square grid that is unsuitable for a sphere curve. The appearance of the curve is clearly similar to those of Maxwell's and Rayleigh's analytical models. A correlation can thus be proposed from the numerical results, starting from Rayleigh's expression and including an empirical function:

$$\overline{\lambda_e} = [1 + 0.6\, p\, (1 - (\overline{\lambda_s})^{-(1-p)})] * \mathrm{Ray}(\overline{\lambda_s}, p)$$

where Ray $(\overline{\lambda_s}, p)$ is Rayleigh's law as modified by Runge (1925). The relative error between this correlation and numerical results does not exceed 3 percent for any concentration values (Fig. 12).

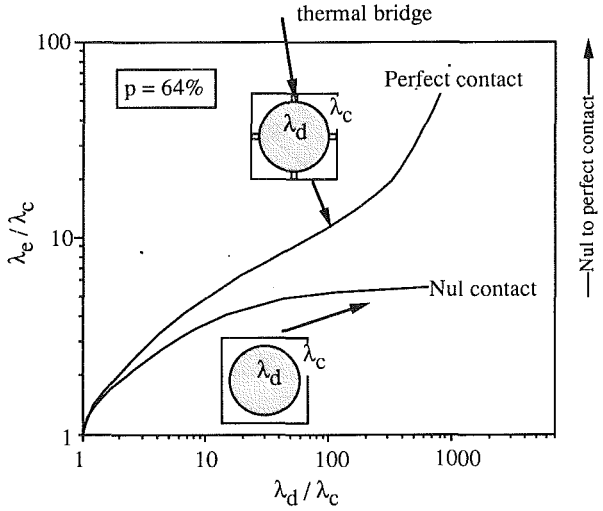

Fig. 13 Influence of thermal contact resistances for cylinders

5 The Influence of the Contacts Between the Inclusions

It is often difficult to take into account the contact effects between particles, as this depends on their geometry and surface state (e.g., oxidation, cleanliness...). They can be studied numerically on the roughness scale, or on a larger scale by introducing the contact resistance scheme. In this scheme, the thickness of this area is neglected and a temperature discontinuity is introduced on either side of the interface. A very thin contact zone is always characterized by a drop in the effective thermal conductivity. In order to study the effect of contact thermal resistances on the thermal conductivity of the medium, "thermal bridges" are introduced, and these have thermal conductivities λ_p that fall between those of the continuous and discontinuous phases (Fig. 13). These bridges are relatively small and narrow so that they do not modify the phase concentration in the cell and they can represent at best the contacts for cylinder or sphere cases. This approach is analogous to that of Shonnard and Whitaker (1989). There is no contact when the thermal conductivity of the bridge λ_b is equal to that of the continuous phase. A model of perfect contact is obtained by using a thermal conductivity equal to that of the discontinuous phase:

$$\text{No contact:} \quad \lambda_b = \lambda_c$$

$$\text{Good contact:} \quad \lambda_b = \lambda_d$$

Figure 13 shows the variations in thermal conductivity for a cubic lattice array of cylinders according to the ratio λ_d/λ_c, the inclusion concentration was 64 percent. The results shown in Fig. 13 were obtained with rather little contact surface (i.e., the width of the thermal bridge over the width of the cell equals 0.01) thus indicating the considerable influence of this parameter on the effective thermal conductivity of the medium. Major differences in the thermal conductivity values and in the variation of this parameter relative to the thermal conductivity ratio of both phases are to be noted. When there is no contact, the effective thermal conductivity of the medium remains relatively low. The curve has a horizontal asymptote. When the contact is good, however, the thermal conductivity increases regularly with that of the discontinuous phase, reaching quite high values. When the particles have contact points, the effective thermal conductivity of the medium depends on the nature of the contacts. Contact effects are all the more important as the conductivity ratio of both phases is quite high, and the number of contacts and their surfaces are high. In a porous medium consisting of similar-sized spherical particles, the average number of contact points per particle shows a linear

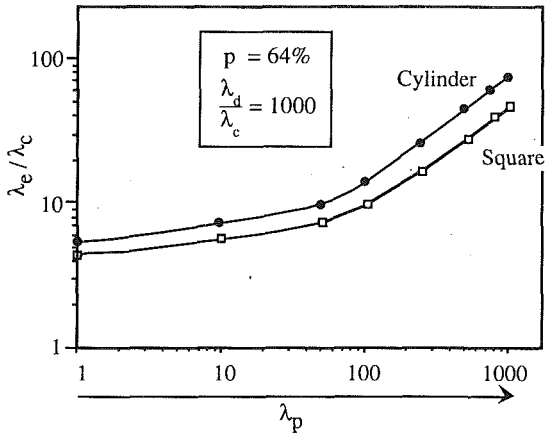

Fig. 14 Variation of effective thermal conductivity according to the contact resistance value. Comparison of the square and cylinder cases. Thermal conductivity ratio of both phases: 1000. Inclusion concentration: 64 percent.

variation from 4 to 12, with a variation in sphere concentration from 53 to 73 percent (Beveridge and Haughey, 1971). The case of parallelepiped inclusions has also been studied (Fig. 14), and the same type of behavior was observed.

6 Conclusion

Using a numerical method, the effective thermal conductivity of a composite material was determined for square, cylindrical, or spherical particles at the base of a cubic lattice array. When there are no contact points between the particle, the particle inclusion, of which the thermal conductivity is quite high compared to that of the continuous phase, does not allow the thermal conductivity of the composite material to be raised significantly. In two-dimensional systems, the results obtained for cylinders are in perfect agreement with those from Rayleigh's analytical model if the cylinder concentration remained below 70 percent. For larger concentrations the agreement is no longer satisfactory. The values of the numerical simulation exceed those of Rayleigh's model. With parallelepiped inclusions, the results indicate that the effective thermal conductivity is best approximated by Russel's model as an upper boundary and Frey's model as a lower boundary. The effective thermal conductivity of a square lattice array of parallelepipeds is higher than that of an array of cylinders when the particle concentration is lower than 54 percent, and that this reversed when it exceeds 54 percent. In three-dimensional systems, the variation curves of thermal conductivity obtained for spheres are analogous to those obtained with cylinders. The thermal conductivity of a sphere array, however, is always higher than that of cylinder arrays of the same concentration. The results from Rayleigh's and Maxwell's models are lower than those found in this simulation. The aspect of the variation curve is nevertheless similar. A model was developed to analyze the influence of contact thermal resistances. The effective thermal conductivity of the two-phase media were found to depend essentially on the value of this contact resistance.

References

Azizi, S., 1988, "Conductivité Thermique des Matériaux Poreux Humides. Mesure par Méthode Flash et Interprétation," Thèse, l'Institut National Polytechnique de Lorraine, Nancy, France.

Batchelor, G. K., and O'Brien, R. W., 1977, "Thermal and Electrical Conduction Through a Granular Material," *Proc. R. Soc. Lond. A.*, Vol. 355, pp. 313-333.

Beveridge, G. S. G., and Haughey, D. P., 1971, "Axial Heat Transfer in Packed Beds. Stagnant Beds Between 20 and 750°C," *Int. J. Heat Mass Transfer*, Vol. 14, pp. 1093-1113.

Bruggeman, D. A. G., 1953, "Dielectric Constant and Conductivity of Mixtures of Isotropic Materials," *Ann. Phys.*, Vol. 24, pp. 636-679.

Deissler, R. G., and Boegli, J. S., 1958, "Investigation of Effective Thermal Conductivities of Powders in Various Gases," *Trans. ASME*, Vol. 80, pp. 1417-1425.

DeVries, D. A., 1972, "Heat Transfer in Soils," in: *Heat and Mass Transfer in the Biosphere.* Wiley, New York.

Dhatt, G., and Touzot, G., 1984, "Une Présentation de la Méthode des Eléments Finis," Collection Université de Compiègne, 2nd ed., S. A. Maloine, ed., Paris.

Frey, S., 1932, "Uber die Elektrische Leitfäbrigkeit Binäer Aggregate," *Z. Electrochem.*, Vol. 38, No. 5, pp. 260-274.

Hashin, Z., and Shtrikman, S., 1962, "A Variational Method of the Theory of Effective Magnetic Permeability of Multiphase Materials," *J. App. Phys.*, Vol. 33, pp. 3125-3131.

Kunii, D., and Smith, J. M., 1960, "Heat Transfer of Porous Rocks," *AIChE J.*, Vol. 6, No. 1, pp. 71-78.

Jeffrey, D. J., 1973, "Conduction Through a Random Suspension of Spheres," *Proc. R. Soc. Lond. A.*, Vol. 335, pp. 355-367.

Maxwell, J. C., 1881, "A Treatise on Electricity and Magnetism," 3rd ed., Vol. 1, p. 440, Clarendon Press, Oxford, United Kingdom.

McPhedran, R. C., and McKenzie, D. R., 1978, "The Conductivity of Spheres. Part I: The Simple Cubic Lattice," *Proc. R. Soc. Lond. A.*, Vol. 359, pp. 45-63.

McPhedran, R. C., McKenzie, D. R., and Derrick, G. H., 1978, "The Conductivity of Spheres. Part II: The Body Centered and Face Centered Cubic Lattice," *Proc. R. Soc. Lond. A.*, Vol. 362, pp. 211-232.

Perrins W. T., McKenzie, D. R., and McPhedran, R. C., 1979, "Transport Properties of Regular Arrays of Cylinders," *Proc. R. Soc. Lond. A.*, Vol. 369, pp. 207-225.

Rayleigh, L., 1892, "On the Influence of the Obstacles in Rectangular Order Upon the Properties of a Medium," *Phil. Mag.*, Vol. 34, pp. 481-502.

Robert, E., Meredith, X., and Tobias, W., 1969, "Resistance to Potentiel Flow Through a Cubic Arrangement of Sphères," *J. App. Phys.*, Vol. 37, No. 7, pp. 1270-1273.

Rogeon, P., 1990, "Analyse et Modélisation des Transferts de Chaleur dans une Liaison Hélicoïdale type Vis-écrou," Thèse, l'Université de Nantes, ISITEM, France.

Runge, I., 1925, "On the Electrical Conductivity of Metallic Aggregates," *Z. Tech. Physik*, Vol. 6, p. 61.

Russel, H. W., 1935, "Principles of Heat Flow in Porous Insolators," *J. Am. Ceram. Society*, Vol. 18, pp. 1-5.

Shonnard, D. R., and Whitaker, S., 1989, "The Effective Thermal Conductivity for a Point-Contact Porous Medium: an Experimental Study," *Int. J. Heat Mass Transfer*, Vol. 32, No. 3, pp. 503-512.

Wakao, N., and Kato, K., 1968, "Effective Thermal Conductivity of Packed Beds," *Journal of Chemical Engineering of Japan*, Vol. 2, No. 1, pp. 24-33.

Woodside, W., 1958, "Calculation of the Thermal Conductivity of Porous Media," *Canadian Journal of Physics*, Vol. 36, pp. 815-823.

Forced Convection Heat Transfer From Microstructures

S. W. Ma

F. M. Gerner

Department of Mechanical, Industrial, and Nuclear Engineering, University of Cincinnati, Cincinnati, OH 45221-0072

For many microstructures, which utilize forced convection cooling, the average thickness of the thermal boundary layer is of the same order as the length of the heated element. For these cases, thermal boundary layer theory is invalid. The elliptic energy equation for steady, two-dimensional incompressible flow over a finite flat plate with insulated starting and ending lengths is analyzed utilizing matched asymptotic expansions. A conventional Blasius technique transforms the energy equation into an elliptic-to-parabolic equation. A new technique is used that treats the boundary layer solution as the outer expansion of the elliptic-to-parabolic equation. The inner expansion, or leading-edge equation, is found by stretching to independent variables simultaneously. Trailing-edge effects are considered using superposition methods. A first-order composite formula is constructed based on the outer and inner expansions, which is uniformly valid over the entire surface of the plate. With the aid of statistics, a correlation is developed for the average Nusselt number

$$\overline{\mathrm{Nu}}_l = 0.6626\mathrm{Pr}^{1/3}\mathrm{Re}_{x_0+l}^{1/2}\left[1-\left(\frac{x_0}{x_0+l}\right)^{3/4}\right]^{2/3}\left[1+\frac{0.3981(x_0/l)^{0.5987}}{\mathrm{Pr}^{0.3068}\mathrm{Re}_{x_0}^{0.4675}}\right]$$

for $0.5 \le \mathrm{Pr} \le 100$, $x_0/l \le 50$, *and* $\mathrm{Re}_{x_0} \ge 100$

where x_0 and l represent the lengths of the insulated starting section and the heated element, respectively. This correlation is accurate to within 2 percent as compared with the entire composite solution.

1 Introduction

Microstructures, such as micro-integrated flow sensors (Van Oudheusden and Huijsing, 1988, Henderson and Hsieh, 1989), and micro-Wheatstone bridges (Van Putten, 1988) subject to forced convection cooling have two typical characteristics. First, the heated surfaces are extremely small: Typical they are of order 10^{-4}–10^{-5} m. The small structure lies on a flat plate, which is of order 10^{-3} m. Second, the fluid velocity is relatively small, of order 1–10 m/s. This leads to Reynolds numbers, based on the entire length of the plate, of about 10^2–10^3. For these cases, leading and trailing-edge effects become important. In other words, axial conduction (which is neglected in conventional boundary layer theory) must be considered. In the process of designing microstructures, however, either the shear flow model (Van Oudheusden, 1989, 1991) or the model from the Pohlhausen–von Kàrmàn integral methods (Van Putten, 1988; Moffat and Ortega, 1988) is extensively used.

Van Oudheusden (1989, 1991) employed the shear flow model to investigate heat transfer from microflow sensors. Based on the approximation that the upstream velocity profile is linear in the y direction, this model simplifies the entire two-dimensional energy equation to

$$\theta_{xx} + \theta_{yy} = \mathrm{Pe}\ y\ \theta_x \tag{1}$$

where Pe is the Péclet number, θ is a dimensionless temperature, and the subscripts stand for partial differentiation with respect to the variable indicated. This equation was first derived by Lévêque (1928). Under the assumption that Pe is very large, Lévêque neglected axial diffusion, namely the term θ_{xx}. The equation then degenerates into a parabolic equation and he obtained an exact solution. Springer and Pedley (1973) and Springer (1974) included the term omitted by Lévêque in the leading and trailing-edge regions of a semi-infinite heated plate. Finite heated films were investigated by Ackerberg et al. (1978) who obtained a perturbation solution for very small Pe. The solution of the shear flow model is accurate if the fluid velocity is linear, such as that generated by the movement of parallel plates. The solution is asymptotic for hydrodynamically fully developed flow in a channel with a very large Prandtl (or Schmidt, for mass transfer) number fluid. The model is therefore useful in problems such as monitoring blood flow in arteries (Ackerberg et al., 1978) and some electrochemical systems (Newman, 1973). Although very close to the plate the velocity field may be linear in a local x regime for external convection over microstructures, the momentum boundary layer thickness is a function of x. Therefore it is obvious that the shear flow model is inaccurate for general external forced convection over microstructures.

Moffat and Ortega (1988) and Van Putten (1988) investigated microstructures with an unheated starting length using integral methods. If the flow is steady incompressible and two dimensional, the local Nusselt number from the integral solution can be expressed by

$$\mathrm{Nu}_{x_0+x} = 0.33129\ \mathrm{Re}_{x_0+x}^{1/2}\mathrm{Pr}^{1/3}\left[1-\left(\frac{x_0}{x_0+x}\right)^{3/4}\right]^{-1/3} \tag{2}$$

where Re_{x_0+x} and Pr stand for the local Reynolds number and Prandtl number, respectively. The integral correlation is the approximate solution of the nonsimilar boundary layer equation, which is the left-hand side of the following energy equation in terms of the variables x and η:

$$\theta_{\eta\eta} + f\ \mathrm{Pr}\ \theta_\eta - 2(x+x_0)\mathrm{Pr}\ f_n\ \theta_x = -\epsilon^2\left[2\theta_{xx}(x+x_0) + \frac{\eta^2\theta_{\eta\eta}}{2(x+x_0)} + \frac{3\eta\theta_\eta}{2(x+x_0)} - 2\eta\theta_{\eta x}\right] \tag{3}$$

Unfortunately, the integral solution of this equation leaves a

Contributed by the Heat Transfer Division and presented at the National Heat Transfer Conference, San Diego, California, August 9–12, 1992. Manuscript received by the Heat Transfer Division April 1992; revision received March 1993. Keywords: Forced Convection. Associate Technical Editor: R. J. Simoneau.

number of questions unanswered, specifically for the application of microstructures. Solution (2) converges to a similarity solution that is almost exact as $x_0/x \to 0$. However, the accuracy of the integral methods in other locations was not previously known. Some researchers (Cebeci and Bradshaw, 1984) argue that integral methods are less successful for predicting heat transfer in cases where the temperature profiles are strongly nonsimilar because the wall temperature changes rapidly with x. In general, integral methods assume that the temperature field varies as a polynomial in terms of y. If this assumption is inaccurate, the solution cannot be substituted into the right-hand side of the differential Eq. (3) to develop higher-order approximations. On the other hand, if the Reynolds number at the leading edge of the heated element is not large, the integral method yields large inaccuracies due to neglecting the right-hand side of Eq. (3). Another source of error from the integral method is that the boundary condition near the leading and trailing edges of the heated section of a plate is subject to a sudden change along the x direction, so that the rate of change of heat transfer in the same direction, θ_{xx}, is very large. It can be shown that these regions still exist even with very large Reynolds numbers, although they decrease in size as Re increases. This implies that the boundary layer approximations are invalid near these points. In macroscale heat transfer, these local errors do not greatly affect the average heat transfer coefficient. For many microstructures, which utilize forced convection cooling, the average thickness of the thermal boundary layer is of the same order as the length of the heated element. The local inaccuracy does affect the average heat transfer coefficient. Naturally, in such cases higher-order approximations of Eq. (3) should be developed.

Recently the closed-form solution of the nonsimilar boundary layer equation was found by Ma et al. (1992) and the accuracy of the integral method was examined. Also the concept of an internal boundary layer was proposed for solving this type of elliptic-to-parabolic Eq. (3). With the generalized principle of least degeneracy developed in that paper, the boundary layer equation is treated as an outer expansion of Eq. (3). Two different scales, $x = \epsilon^{\alpha} X$, and $\eta = \epsilon^{\beta} Y$, for stretching two independent variables are applied in the inner expansion of Eq. (3), which leads to two algebraic equations for determining the indices α and β of ϵ. It is very interesting to note that Eq. (1) resembles the first-order inner expansion of Eq. (3) in a transformed plane. This means that the first-order approximation for velocity in the energy equation is linear at the leading and trailing edges. However, the problem solved in the earlier work concentrated on a semi-infinite flat plate with an unheated, constant temperature, starting length, and a constant temperature heated element. The temperature distribution at the plate was expressed in terms of a discontinuous function. The local Nusselt numbers were of order $1/x$ and were therefore nonintegrable. In other words, the average heat transfer coefficient approached infinity. Obviously, it is impractical for a real application to have an infinite average heat transfer coefficient. The reason shown by Ma et al. (1992) is that the singularity results from the discontinuous boundary condition in temperature. This difficulty does not arise in conventional boundary layer theory since the axial diffusion is neglected.

The boundary conditions used in the present paper are that the unheated starting and ending lengths are insulated and the heated element is at a constant temperature. These boundary conditions allow for a continuous temperature distribution along the plate, and are also physically more realistic than the discontinuous boundary condition in temperature. In the process of microstructure design, most heated elements are installed on the flat plate with insulated materials or are isolated by other techniques. For example, the thermal insulation of a Wheatstone bridge between the heated chip and the ceramic substrate is achieved by insertion of a small piece of glass (Van Putten, 1988). Or for microflow sensors, a silicon wafer is attached to a silicon dioxide pad. Then a chemical etching technique is applied to isolate the wafer and the pad (Henderson and Hsieh, 1989). However, since the original Dirichlet problem investigated by Ma et al. (1992) is changed into a mixed boundary-value problem along the plate, it is mathematically more complicated. It will be shown later that, although it is still singular, the local Nusselt number is of order

Nomenclature

Ai = airy function
D = coefficient of the trailing-edge solution, Eq. (48)
f = solution of the Blasius equation
h_x = local heat transfer coefficient, W/m^2K
$\bar{h}$ = average heat transfer coefficient, W/m^2K
K_ν = modified Bessel function of the second kind with parts ν
k = thermal conductivity, W/mK
l = length of the heated section, m
Nu_x = local Nusselt number = $h_x x/k$
$\overline{Nu}_l$ = average Nusselt number = $\bar{h}l/k$
O = order symbol
Pr = Prandtl number = ν/α
$Q_1(x)$ = integral function defined by Eq. (19)
Re = Reynolds number on unit length = U_∞/ν
Re_x = local Reynolds number = $U_\infty x/\nu$
T = temperature, K
T_w = temperature of the heated element, K
T_∞ = temperature of upstream, K
x, y = Cartesian coordinates, outer variables for elliptic equations
x_0 = length of the insulated part, m
X, Y = inner variables for elliptic-to-parabolic equations
U_∞ = velocity of upstream, m/s
α = thermal diffusivity m^2/s
ϵ = small parameter in differential equations = $1/Re^{1/2}$
η = inner variable for elliptic equations and outer variable for elliptic-to-parabolic equations
$\theta, \Theta, \hat{\Theta}$ = dimensionless temperature defined by $(T - T_\infty)/(T_w - T_\infty)$
θ = outer expansion for elliptic equations
Θ = inner expansion for elliptic equations and outer expansion for elliptic-to-parabolic equations
$\hat{\Theta}$ = inner expansion for elliptic-to-parabolic equations
ν = kinematic viscosity, m^2/s

Superscripts

c = composite expansion
err = error of average Nusselt numbers
i = inner expansion
o = outer expansion

Subscripts

$+$ = upper function
$-$ = lower function
L = leading edge
T = trailing edge

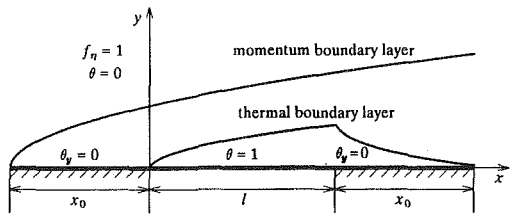

Fig. 1 A heated element mounted flush on a plate with insulating material

$x^{-1/2}$ and is therefore integrable. This paper consists of three parts. The mathematical formulation and the generalized principle of least degeneracy are introduced in the next section. Since the energy equation and boundary equations are linear, the problem can be split into two parts using the principle of superposition. One is a uniformly heated semi-infinite plate with an insulated starting length. The other is a semi-infinite plate with a specified surface heat flux and an unheated starting length. Their solutions will be derived in Section 3. Section 4 will present composite formulas and numerical results for the problem.

2 Mathematical Formulation and the Generalized Principle of Least Degeneracy

The problem considered here is external forced convection over a tiny heated microstructure of length l. This small structure lies flush on an insulated plate with length $2x_0 + l$ in the rectangular Cartesian coordinate system (x, y) (Fig. 1). The origin of the x axis is defined by the leading edge of the heated section. The entire structure is subject to a steady incompressible two-dimensional flow. The upstream has a constant velocity and temperature. When the velocity of the upstream is large enough, momentum and thermal boundaries start at $x = -x_0$ and $x = 0$, respectively. At the trailing edge of the heated microstructure ($x \geq l$), the thermal boundary layer has a sudden change, which may be mathematically described using the principle of superposition (Bejan, 1984). The components of dimensionless velocity are

$$u = f_\eta, \quad v = \epsilon(\eta f_\eta - f)/[2(x+x_0)]^{1/2} \tag{4}$$

in which f is the solution of the familiar Blasius equation, $f_{\eta\eta\eta} + f f_{\eta\eta} = 0$, where the Blasius similarity transformation is defined by $\eta = y/\epsilon[2(x + x_0)]^{1/2}$. Introducing no-slip conditions on the plate and a uniform upstream condition, the solution of the Blasius equation can be written as Weyl's expansion (Jones and Watson, 1963)

$$f = \sum_{n=0}^{\infty} (-1)^n D_n \eta^{3n+2} \tag{5a}$$

where D_n satisfies the expressions

$$(3n+2)(3n+1)3nD_n = \sum_{i=0}^{n-1} (3i+2)(3i+1)D_i D_{n-1-i}$$

$$2D_0 = 0.469600 \tag{5b}$$

The dimensionless energy equation for small Mach number flow past a flat plate is (Bejan, 1984)

$$\mathrm{Pr}\ u\ \theta_x + \mathrm{Pr}\ v\ \theta_y = \epsilon^2(\theta_{yy} + \theta_{xx}) \tag{6}$$

where the small parameter $\epsilon = 1/\mathrm{Re}^{1/2}$. The symbol $\mathrm{Re} = U_\infty/\nu$ denotes Reynolds number based on a unit length. Since the governing equation is elliptic, we need to consider four boundary conditions. Viewing Fig. 1, it is not difficult to see that the appropriate boundary conditions are

$$\theta_y(x, 0), = 0, \quad x < 0, \text{ or } x < l; \quad \theta(x, 0) = 1, \quad 0 < x < l; \tag{7}$$

$$\theta(x, \infty) = 0; \tag{8}$$

$$\theta(-\infty, y) = 0; \tag{9}$$

$$\theta(\infty, y) = 0. \tag{10}$$

Since Eq. (6) is a linear elliptic equation with nonconstant coefficients, it appears difficult to find an exact solution. Notice, however, that coefficients in front of the highest derivatives are very small. Therefore it is possible to develop an approximate solution that satisfies the governing equation and boundary conditions using the method of matched asymptotic expansions. The first-order outer expansion of the elliptic Eq. (6) can be obtained by neglecting the terms containing the small parameter,

$$u\ \theta_x + v\ \theta_y = 0. \tag{11}$$

Equation (11) is homogeneous. With a constant temperature in the upstream, its solution was proven to be zero, $\theta = 0$, by Van Dyke (1962). Because the highest derivatives are lost in the outer expansion (11), the solution is invalid near the plate. In other words, boundary condition (7) is not satisfied. In order to obtain a uniformly valid solution near the plate, the independent variable y must be enlarged using the boundary layer theory. Introducing the Blasius transformation and the velocity expression (4) into Eq. (6), Eq. (6) can be changed into an elliptic-to-parabolic equation in terms of the new independent variables, x and η

$$\Theta_{\eta\eta} + f\ \mathrm{Pr}\ \Theta_\eta - 2(x+x_0)\mathrm{Pr}\ f_\eta\ \Theta_x = -\epsilon^2\left[2\Theta_{xx}(x+x_0) + \frac{\eta^2\Theta_{\eta\eta}}{2(x+x_0)} + \frac{3\eta\Theta_\eta}{2(x+x_0)} - 2\eta\Theta_{\eta x}\right] \tag{12}$$

where $\Theta = \Theta(x, \eta)$. It is obvious that by neglecting the terms in Eq. (12) that include the small parameter ϵ, it will degenerate into a nonsimilar boundary layer equation

$$\Theta_{\eta\eta} + f\ \mathrm{Pr}\ \Theta_\eta - 2(x+x_0)\mathrm{Pr}\ f_\eta\ \Theta_x = 0; \tag{13}$$

Equation (13) can be viewed as the first-order inner expansion corresponding to the original Eq. (6). Since this parabolic equation is one order higher than the first-order partial differential equation, Eq. (11), its solution can satisfy one more boundary condition. However, there is still one boundary condition, among the conditions (7)–(10), which cannot be satisfied. It has been shown by Ma et al. (1992) that the solution of Eq. (13) is invalid near the leading edge $x = 0$ and trailing edge $x = l$. The physical reason is that the heat diffusion along the x direction might be very large at locations where the boundary conditions suddenly change. Mathematically, the original energy Eq. (6) is elliptic and has four boundary conditions. Equation (13) is parabolic, which only satisfies three boundary conditions.

A new generalized principle of least degeneracy (Ma et al., 1992) was developed for solving Eq. (12), which states that both of the highest derivatives with respect to η and x as well as at least another term in the elliptic-to-parabolic Eq. (12) should be kept in the inner expansion. By using this principle, an internal boundary layer equation, which controls the leading and trailing edges, is derived by Ma et al. (1992):

$$\hat{\Theta}_{XX} + \hat{\Theta}_{YY} - b\ Y\ \hat{\Theta}_X = 0 \tag{14}$$

where $b = 0.66411\ x_0^{1/2}\ \mathrm{Pr}$ and relations between x, y and X, Y are

$$x = \epsilon^{3/2} X(2x_0)^{1/2}; \quad y = \epsilon^{3/2}\ Y[2(x_0+x)]^{1/2}. \tag{15}$$

The neglected terms in Eq. (14) are of order $\epsilon^{3/2}$. Notice that the derivation of Eq. (14) is independent of the location. Therefore, the equation is suitable whenever the boundary conditions are subject to a sudden change including both the leading and trailing edges under the same transformation of the coordinates. It is well known that the boundary layer Eq. (13) is the inner expansion of the elliptic Eq. (6). However, the same equation is the outer expansion of the elliptic-to-parabolic Eq.

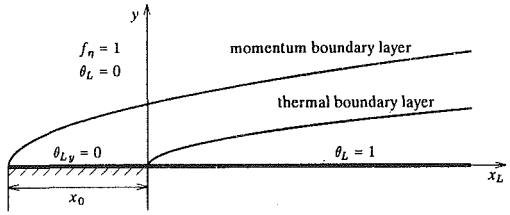

Fig. 2(*a*) A semi-infinite plate with an insulated starting length

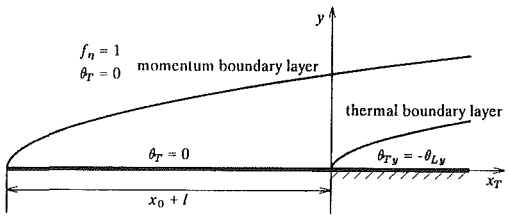

Fig. 2(*b*) A semi-infinite plate with an unheated starting length

Fig. 2 The application of the principle of superposition

(12) where the inner expansion is Eq. (14). This relation was first revealed by Ma et al. (1992). Since the governing Eq. (6) and basic boundary conditions (7)–(10) are linear, the principle of superposition will be used to simplify the problem. For this purpose, the equation and boundary conditions can be divided into two different mixed boundary-value problems: problem (*a*) the leading-edge problem, or a semi-infinite plate with an insulated starting length x_0 subject to forced convection; problem (*b*) the trailing-edge problem, or a semi-infinite plate with an unheated starting length $x_0 + l$ as shown in Fig. 2. Now let the dimensionless temperature consist of two problems, $\theta = \theta_L + \theta_T$, where the subscripts L and T denote problem (*a*) and problem (*b*), respectively. Thus the original problem can be split into two sets of independent mixed boundary-value problems if the summation of their solutions satisfies the boundary conditions (7)–(10). A detailed description of the solutions will be presented in the next section.

3 Derivation of Analytical Solutions

Problem (*a*). The coordinate system in this problem is the same as the global system, $x_L = x$ as shown in Fig. 2(*a*). Outer expansion of the elliptic-to-parabolic equation for the problem is Eq. (13) as well as suitable boundary conditions transformed from the boundary conditions (7)–(10). The closed-form solution for this boundary-valued problem was found by Ma et al. (1992). Since it has been shown in the paper that integral methods are more than 98 percent accurate in the range $0.5 \le \mathrm{Pr} \le 100$, they will be introduced directly instead of using the closed-form solution, which leads to the following Nusselt number (Holman, 1986), Nu[1]:

$$\mathrm{Nu}^o_{x_0+x} = -(x_0+x)\Theta_{Ly}|_{y=0}$$

$$= 0.33129\ \mathrm{Re}^{1/2}_{x_0+x}\ \mathrm{Pr}^{1/3}\left[1-\left(\frac{x_0}{x_0+x}\right)^{3/4}\right]^{-1/3} \quad (16)$$

where the superscript o stands for the outer expansion of the elliptic-to-parabolic Eq. (12). The Nusselt number from Eq. (16) is invalid near the leading edge of the heated section. Therefore it is necessary to solve the internal boundary layer Eq. (14). By using Van Dyke's matching principle, it is easy to find that all boundary conditions corresponding to Eq. (14) are homogeneous except the mixed boundary condition (7). Thus the boundary-value problem resembles those investigated by Springer and Pedley (1973) except for the additional constant, b. Their equation is different because they considered the energy equation with a shear flow model. With the aid of the Wiener–Hopf method, the details for solving the mixed boundary-value problem have been carried out by Springer and Pedley (1973). The solution is

$$\hat{\Theta}_{LY}|_{Y=0} = -\frac{9b^{1/2}}{(2\pi)^2}\int_0^\infty \left\{\frac{\prod_{n=1}^{\infty}\left(\frac{1+r/a_n}{1+r/d_n}\right)\exp(-b^{1/2}rX)}{r^2[J^2_{-1/3}(\xi)-J_{-1/3}(\xi)J_{1/3}(\xi)+J^2_{1/3}(\xi)]}\right\} dr \quad (17)$$

where $\xi = 2r^{2/3}$, a_n and d_n in the infinite product satisfy the relations $Ai(-a^{4/3}_n) = 0$, and $Ai'(-d^{4/3}_n) = 0$ in which Ai and Ai' are the Airy function and its differentiation, respectively (Abramowitz and Stegun, 1972). The local Nusselt number can be found from the definition

$$\mathrm{Nu}^i_{x_0+x} = -(x_0+x)\,Y_y\,\hat{\Theta}_{LY}|_{Y=0}$$

$$= 0.13137\ \mathrm{Re}^{1/2}_{x_0+x}\ \mathrm{Re}^{1/4}_{x_0}\ \mathrm{Pr}^{1/2}\ Q_1(x) \quad (18)$$

where the superscript i stands for the inner expansion of the elliptic-to-parabolic Eq. (14) and the integral function is defined by

$$Q_1(x) = \int_0^\infty \left\{\frac{\prod_{n=1}^{\infty}\left(\frac{1+r/a_n}{1+r/d_n}\right)\exp(-0.57624\ \mathrm{Pr}^{1/2}\ \mathrm{Re}^{3/4}\ rx/x_0^{1/4})}{r^2[J^2_{-1/3}(\xi)-J_{-1/3}(\xi)J_{1/3}(\xi)+J^2_{1/3}(\xi)]}\right\} dr \quad (19)$$

Springer and Pedley (1973) have found that the singularity of Eq. (18) is of order $1/x^{1/2}$ as $x \to 0$. This means that the local Nusselt number will approach infinity at the leading edge. However, if the integration is carried out along the x direction, which leads to an average Nusselt number, the result is finite. Note that the expansions (16) and (18) have a common region of validity. It is quite easy to construct a single uniformly valid expansion using the concept of composite expansions (Van Dyke, 1975). The rule of the additive composition is used, which states that the first-order composite expansion of temperature, θ^c_L, is equal to the sum of the first-order inner and outer expansions corrected by subtracting the inner expansion of the outer expansion, Θ^i_L:

$$\theta^c_L = \hat{\Theta}_L + \Theta_L - \Theta^i_L \quad (20)$$

From the definition of the Nusselt number and Eq. (20) it is clear that

$$\mathrm{Nu}^c_L = \mathrm{Nu}^i_L + \mathrm{Nu}^o_L - \mathrm{Nu}^i_{Lo} \quad (21)$$

where Nu^i_L is expressed by Eq. (18), Nu^o_L is the integral solution (16), and Nu^i_{Lo} is the first term of the Taylor expansion of Eq. (16) in terms of ascending power of x. The final result of the local Nusselt number is

$$\mathrm{Nu}^c_{Lx_0+x} = 0.13137\ \mathrm{Re}^{1/2}_{x_0+x}\mathrm{Re}^{1/4}_{x_0}\ \mathrm{Pr}^{1/2}Q_1(x) + 0.33129\ \mathrm{Re}^{1/2}_{x_0+x}\mathrm{Pr}^{1/3}\left\{\left[1-\left(\frac{x_0}{x_0+x}\right)^{3/4}\right]^{-1/3} - \left(\frac{3x}{4x_0}\right)^{-1/3}\right\} \quad (22)$$

When x is very small, the Nusselt number in Eq. (22) will be

[1]The coefficient, $0.33129 = 1.5(14/13)^{1/3}(13/280)^{1/2}$, is derived following the process of Holman (1986), which is a little different from some references, such as 0.332 (Kays and Crawford, 1980; Holman, 1986) and 0.323 (Bejan, 1984). The exact value, 0.332057, can be obtained by the Runge–Kutta algorithm for similarity flow.

dominated by the integral term since the summation of the other two terms will approach zero. When x is very large, the Nusselt number will degenerate into the boundary layer solution since the integration in Eq. (22) converges as the last term. The conclusion is that Eq. (22) is a uniformly valid expression on the plate without trailing-edge effects. However, for a finite heated section it is necessary to investigate the effects of the trailing edge. Thus the following paragraph will be devoted to problem (b).

Problem (b). The coordinates in this problem are plotted in Fig. 2(*b*). The solution of this problem for $x_T < 0$ will be superposed on solution (22). However, the contribution from the boundary layer is equal to zero in this region. Thus, concentration will focus on the internal boundary layer Eq. (14). By means of the relation $x_T = x - l$, and x_0, which should be substituted by $x_0 + l$, the inner variables of this problem can be expressed, using Eq. (15), in terms of the global variables

$$X=(x-l)\mathrm{Re}^{3/4}/[2(x_0+l)]^{1/2}\quad Y=y\mathrm{Re}^{3/4}/[2(x_0+x)]^{1/2} \tag{23}$$

Under the coordinate transformation (23), it is obvious that the governing equation of the internal boundary layer is the inner expansion (14)

$$\hat{\Theta}_{TXX}+\hat{\Theta}_{TYY}-bY\hat{\Theta}_{TX}=0 \tag{24}$$

where $b = 0.66411\,[x_0+l]^{1/2}\,\mathrm{Pr}$. The boundary conditions can be found by the matching principle. As $Y \to \infty$ or $X \to \infty$, the boundary conditions should match the upstream solutions

$$\hat{\Theta}_T(X, \infty)=\theta_T(x, 0)=0. \tag{25}$$

$$\hat{\Theta}_T(-\infty, Y)=0. \tag{26}$$

The other two boundaries depend on the solutions of the boundary layer equation. Since the integral method approximates the closed-form solution very well in problem (*a*), it will be applied in problem (*b*), although no closed-form solution for arbitrary surface heat flux is available to prove this. Using the integral method, the temperature distribution on the surface can be found (Kays and Crawford, 1980):

$$\Theta_T(x_T, 0)=-0.623\,\mathrm{Pr}^{-1/3}\,\mathrm{Re}_{x_T+x_0+l}^{-1/2}\,x_T \times\int_0^1(1-t^{3/4})^{-2/3}\,\Theta_{Ty}[t(x_T+x_0+l), 0]\,dt. \tag{27}$$

In order to have the insulated boundary condition satisfied, $-\Theta_{Ly}$ must be applied instead of Θ_{Ty} in Eq. (27) as shown in Fig. 2(*b*). Since the limitation of $\Theta_{Ly}[t(x_T+x_0+l), 0]$ is finite as $x_T \to 0$ so that the integration in Eq. (27) is finite, it is clear that $\Theta_T(x_T, 0)$ approaches zero in Eq. (27) as $x_T \to 0$. For the situation $\eta \neq 0$, it is difficult to get the same result analytically. However, it has been found from boundary layer theory that the dimensionless temperature is zero when x_T is less than zero no matter whether the problem concerns arbitrarily specified temperature or the problem of specified heat flux. Since the temperature field is always continuous, $\Theta_T(x_T, \eta)$ should be zero as $x_T \to 0$. The guess for the situation of a heated section with specified temperature and unheated starting length has been proved by Ma et al. (1992). If the conclusion is also valid for problem (*b*), by virtue of the asymptotic matching principle it is natural to derive the following condition:

$$\hat{\Theta}_T(\infty, Y)=\Theta_T(0, \eta)=0. \tag{28}$$

The remaining is a mixed boundary condition. It is easy to see that the dimensionless temperature is equal to zero when X is less than zero as shown in Fig. 2(*b*). On the other hand, Eq. (22) can be expressed in terms of x_T

$$\Theta_{LY}(x_T, 0)=-0.18578\,x_0^{1/4}\,\mathrm{Pr}^{1/2}Q_1(x_T+l)-0.46815\,\mathrm{Pr}^{1/3} \times\mathrm{Re}^{-1/4}\left\{\left[1-\left(\frac{x_0}{x_T+x_0+l}\right)^{3/4}\right]^{-1/3}-\left[\frac{3(x_T+l)}{4x_0}\right]^{-1/3}\right\} \tag{29}$$

Applying the asymptotic matched principle, the one-item inner expansion (of the one-term outer expansion) is equal to the one-term outer expansion (of the one-term inner expansion), leading to the boundary condition

$$\hat{\Theta}_{TY}(X, 0)=\Theta_{LY}(0, 0);\quad X>0,\quad \hat{\Theta}_T(X, 0)=0;\quad X<0 \tag{30}$$

When he investigated the trailing-edge effects of the shear flow model, Springer (1974) utilized the whole boundary layer solution, corresponding to Eq. (29) in this paper, as the boundary condition in Eq. (30). However, it is unnecessary from the point of view of the perturbation technique. Physically, the boundary layer equation governs the whole positive x_T axis except for the leading edge. The internal boundary layer equation governs the region of the leading edge. At their interfaces where x_T is quite small, the higher-order terms of x_T can be neglected without larger errors. Mathematically, the terms dropped from Eq. (29) are the higher-order small terms of $\epsilon^{3/2}$ if the equation is expanded in terms of X. It should be stressed that Eq. (29) is derived from the composite expansion (22) rather than the integral solution (16). Its physical significance can be realized from the discussion of Eq. (22).

The governing Eq. (24) with boundary conditions (25), (26), (28), and (30) can be solved using the Wiener–Hopf technique. This method was first introduced by Springer and Pedley (1973) to account for the leading-edge effect for the shear flow model. Their solution has been presented in problem (*a*). When he investigated the trailing-edge approximation in the same model, Springer (1974) modified their method in order to compare their solution to the trailing-edge effect from the momentum equations due to Stewartson (1968). In the present paper, the trailing-edge problem will be solved following the technique of Springer and Pedley (1973). In order to apply their method, the following coordinate transformation is introduced

$$u=b^{1/2}X,\quad v=b^{1/2}Y \tag{31}$$

the governing Eq. (24) is expressed in terms of u and v

$$\hat{\Theta}_{Tuu}+\hat{\Theta}_{Tvv}-v\hat{\Theta}_{Tu}=0 \tag{32}$$

and nonhomogeneous condition (30) is changed into

$$\hat{\Theta}_{Tv}=\Theta_{LY}(0, 0)b^{1/2};\quad u>0,\quad \hat{\Theta}_T=0;\quad u<0. \tag{33}$$

The other homogeneous boundary conditions (25), (26), and (28) keep their original forms in the u–v plane. Defining the generalized Fourier transform pair

$$\psi(\alpha, v)=\int_{-\infty}^{\infty}\hat{\Theta}_T(u, v)\exp(i\alpha u)du;$$

$$\hat{\Theta}_T(u, v)=\frac{1}{2\pi}\int_{-\infty+i\tau}^{\infty+i\tau}\psi(\alpha, v)\exp(-i\alpha u)d\alpha \tag{34}$$

where $\alpha = \sigma + i\tau$. In order to ensure the existence of the Fourier transforms of the governing equation and boundary conditions, the first expression in Eq. (33) can be written

$$\hat{\Theta}_{Tv}=\Theta_{LY}(0, 0)\exp(\tau_- u)/b^{1/2},\quad u>0, \tag{35}$$

and the original function, $\hat{\Theta}_T$, must have the form $\hat{\Theta}_T=\mathrm{O}(\exp(\tau_- u))$ as $u \to \infty$; $\hat{\Theta}_T = \mathrm{O}(\exp(\tau_+ u))$ as $u \to -\infty$ where τ_+ and τ_- are unknown constants, which may be determined later. Under the condition $\tau_- < \tau < \tau_+$, the Fourier transform of Eq. (32) with respect to u, which has satisfied the boundary conditions (26) and (28) in terms of u and v, is

$$\psi_{ss}-s\psi=0\quad \text{where } s=\exp(-i\pi/6)\alpha^{1/3}(v+i\alpha) \tag{36}$$

The solution of the Airy Eq. (36), which satisfies the boundary condition (25), can be found from (Abramowitz and Stegun, 1972)

$$\psi=H(\alpha)Ai(s) \tag{37}$$

where the unknown function $H(\alpha)$ will be determined from the mixed boundary condition (33). Defining

$$\psi_+(\alpha, v)=\int_0^\infty \hat{\Theta}_T(u, v)\exp(i\alpha u)du;$$

$$\psi_-(\alpha, v)=\int_{-\infty}^0 \hat{\Theta}_T(u, v)\exp(i\alpha u)du \quad (38)$$

so that $\psi = \psi_+ + \psi_-$. Taking the derivative of solution (37) with respect to v, a set of algebraic equations can be found as $v = 0$

$$\psi_+(\alpha, 0)+\psi_-(\alpha, 0)=H(\alpha)Ai[\exp(i\pi/3)\alpha^{4/3}]$$

$$\psi_+'(\alpha, 0)+\psi'^-(\alpha, 0)=H(\alpha)Ai'[\exp(i\pi/3)\alpha^{4/3}]\alpha^{1/3}\exp(-i\pi/6) \quad (39)$$

where primes denote differentiation with respect to v. The Fourier transform of the boundary condition (33) under condition (35) is

$$\psi_+'(\alpha, 0)=\frac{\Theta_{LY}(0, 0)i}{(\alpha+i\tau_-)b^{1/2}}, \quad \psi_-(\alpha, 0)=0. \quad (40)$$

Comparing the original Eq. (33) and condition (35), it can immediately be seen that $\tau_- = 0$. Inserting the results into Eq. (39) and eliminating the unknown function $H(\alpha)$, Eq. (39) becomes

$$\psi_-'-\frac{Ai'[\exp(i\pi/3)\alpha^{4/3}]}{Ai[\exp(i\pi/3)\alpha^{4/3}]}\alpha^{1/3}\exp(-i\pi/6)\psi_+ + \frac{i\Theta_{LY}(0, 0)}{\alpha b^{1/2}}=0, \quad (41)$$

There are two unknown functions in Eq. (41). By means of the Wiener–Hopf technique, the equation can be solved. For this purpose, we introduce the infinite product

$$\chi(\alpha)=\prod_{n=1}^\infty \frac{ia_n-\alpha}{id_n-\alpha}\exp[-(\alpha_n-d_n)/d_n] \quad (42)$$

where a_n and d_n have been defined in Eq. (17). $\chi(\alpha)$ is a so-called lower function, that is analytical, nonzero in the region $\tau<\min(a_n, d_n)$. On the other hand, from the existing condition $\tau<\tau_+$ of the generalized Fourier transform it is easy to find $\tau_+ = d_1$. Multiplying $\chi(\alpha)$ by Eq. (41) and utilizing the identity

$$Ai'(z)/Ai(z) = -z^{1/2}K_{2/3}(2z^{3/2}/3)/K_{1/3}(2z^{3/2}/3) \quad (43)$$

Eq. (41) reduces to

$$\psi'-\chi(\alpha)+\frac{i\Theta_{LY}(0, 0)}{\alpha b^{1/2}}[\chi(\alpha)-\chi(0)]= -\chi(\alpha)\frac{\alpha K_{2/3}(2\exp(i\pi/2)\alpha^2/3)}{K_{1/3}(2\exp(i\pi/2)\alpha^2)/3}\psi_+ - \frac{i\Theta_{LY}(0, 0)}{\alpha b^{1/2}}\chi(0) \quad (44)$$

where $K_\nu(z)$ is the modified Bessel function of the second kind of order ν. It is not difficult to show that all terms on the left side of Eq. (44) are lower functions, all terms on the right side are upper functions, which are analytical, nonzero as $\tau > 0$. According to the theory of complex variables (Noble, 1958), the two sides should be zero, respectively. From the inversion in Eq. (34), the left side of Eq. (44) yields in the plane of X and Y

$$\hat{\Theta}_{TY}(X, 0)=\frac{i\Theta_{LY}(0, 0)}{2\pi} \times\int_{-\infty+i\tau}^{\infty+i\tau}\frac{1}{\alpha}\left[\frac{\chi(0)}{\chi(\alpha)}-1\right]\exp(-i\alpha b^{1/2}X)d\alpha \quad (45)$$

The integration can be calculated with the Cauchy residue theorem if the contour is expanded into the upper half-plane where $\tau > 0$. The integral is replaced by the sum of the residues at the infinite number of poles on the positive imaginary axis

$$\hat{\Theta}_{TY}(X, 0) = \Theta_{LY}(0, 0)\sum_{m=1}^\infty \frac{a_m-d_m}{a_m d_m}\prod_{n=1}^\infty \left(\frac{1-a_m/d_n}{1-a_m/a_n}\right)\exp(a_m b^{1/2}X) \quad (46)$$

where $n \neq m$. Substituting expressions (23) of X and Y as well as the expression for b in Eq. (24) into Eq. (46), the local Nusselt number may be found

$$\mathrm{Nu}_{Tx_0+x}=\mathrm{Re}_{x_0+x}^{1/2}D\sum_{m=1}^\infty \frac{a_m-d_m}{a_m d_m}\prod_{n=1}^\infty \times\left(\frac{1-a_m/d_n}{1-a_m/a_n}\right)\exp[0.57624\ a_m\ \mathrm{Pr}^{1/2}\mathrm{Re}_{x_0+L}^{3/4}(x-l)/(x_0+l)] \quad (47)$$

where $n \neq m$ and D is defined by

$$D=0.13137\ \mathrm{Re}_{x_0}^{1/4}\ \mathrm{Pr}^{1/2}\ Q_1(l)+0.33129\ \mathrm{Pr}^{1/3} \times\left\{\left[1-\left(\frac{x_0}{x_0+l}\right)^{3/4}\right]^{-1/3}-\left(\frac{3l}{4x_0}\right)^{-1/3}\right\} \quad (48)$$

Note that Nusselt number in Eq. (47) approaches infinity with order $1/(l - x)^{1/2}$ as $x \to l$. The detailed description is given by Springer (1974). The singularity of the square root at the leading and trailing edge also can be found in other mixed boundary-value problems, such as fracture mechanics (Ma and Zhang, 1991), as well as fluid dynamics (Sneddon, 1951).

4 Numerical Results and Discussions

Taking the summation of Eq. (47) and the composite expansion (22), the local Nusselt number, which is valid on the entire heated section, may be obtained immediately:

$$\mathrm{Nu}_{x_0+x}\mathrm{Re}_{x_0+x}^{-1/2}=D\sum_{m=1}^\infty \frac{a_m-d_m}{a_m d_m}\prod_{n=1}^\infty \times\frac{1-a_m/d_n}{1-a_m/a_n}\exp[0.57624\ a_m\mathrm{Pr}^{1/2}\mathrm{Re}_{x_0+L}^{3/4}(x-l)/(x_0+l)] -0.33129\ \mathrm{Pr}^{1/3}\left(\frac{4x_0}{3x}\right)^{1/3}+0.13137\ \mathrm{Re}_{x_0}^{1/4}\ \mathrm{Pr}^{1/2}Q_1(x) +0.33129\ \mathrm{Pr}^{1/3}\left[1-\left(\frac{x_0}{x_0+x}\right)^{3/4}\right]^{-1/3} \quad (49)$$

where $n \neq m$. Figures 3–5 plot the function $\mathrm{Nu}_{x_0+y}\mathrm{Re}_{x_0+x}^{-1/2}$ versus the local coordinate, x/l, for various x_0/l ratios and a Prandtl number of 1. The results show that the Nusselt number has an exponential decay along the x direction at both edges. The solution for Reynolds number at the leading edge, Re_{x_0}, of 1000 is consistent with predictions from boundary layer theory except for tiny regions at the two edges. However, the error for boundary layer theory increases as the Reynolds number decreases. Note that the error also is proportional to the ratio x_0/l. In other words, decreasing the length of the heated section leads to larger inconsistencies. Notice in Figs. 3–5 that if at least one point of the curves is tangent to the integral solution, there is at least one point of the heated section that the prediction from the boundary layer theory is valid. However, the two curves for $\mathrm{Re}_{x_0} = 100$ in Figs. 4 and 5 as well as the curve $\mathrm{Re}_{x_0} = 500$ in Fig. 5 have entirely left the integral solution. This specifies that the boundary layer theory breaks down in the whole heated region. Although the present solutions are obtained by taking the boundary layer solution as

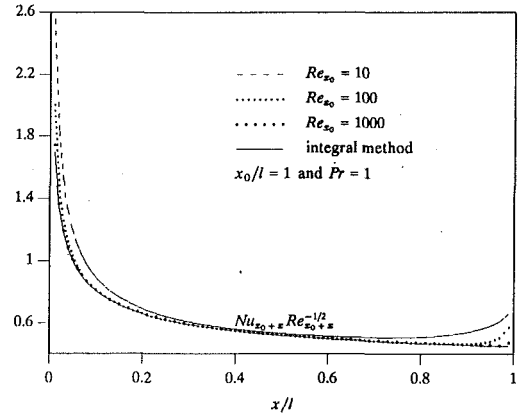

Fig. 3 Local Nusselt numbers from present work (49) and integral methods (16)

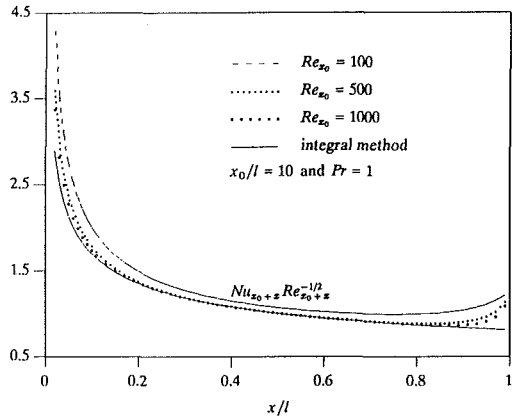

Fig. 4 Local Nusselt numbers from present work (49) and integral methods (16)

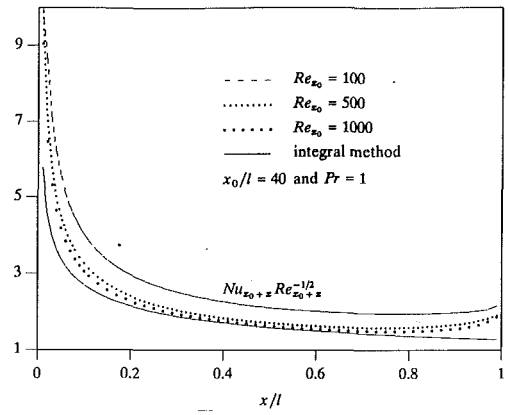

Fig. 5 Local Nusselt numbers from present work (49) and integral methods (16)

Table 1 Ratio of $\overline{Nu}_l Re_{x_0+l}^{-1/2}$ between the present work (54) and integral method (53) for Pr = 0.72

Re_{x_0}	80	100	200	300	500	700	1000	integral (53)
x_0/l								
1	1.053	1.048	1.038	1.033	1.029	1.027	1.026	0.3253
2	1.079	1.071	1.052	1.045	1.037	1.034	1.031	0.2433
3	1.102	1.091	1.066	1.055	1.045	1.040	1.036	0.1991
5	1.143	1.127	1.090	1.074	1.059	1.051	1.045	0.1507
7	1.178	1.160	1.112	1.091	1.072	1.062	1.053	0.1239
10	1.225	1.202	1.143	1.116	1.090	1.076	1.065	0.0999
20	1.334	1.312	1.126	1.185	1.143	1.120	1.101	0.0647
30	1.431	1.394	1.292	1.242	1.188	1.159	1.132	0.0498
40	1.499	1.459	1.346	1.289	1.227	1.192	1.161	0.0413

outer expansions, it can be shown from the principle of superposition that they are still valid since the composite expansion (29) has been applied in problem (*b*), where the expansion will degenerate into the leading-edge solution automatically if l is very small. An important supplement is that the boundary condition (30) of problem (*b*) is $\hat{\Theta}_T = \theta_T = 0$ as $x_T < 0$ (Fig. 2(*b*)). If l is large, the condition automatically satisfies $\theta_{Ty} = 0$. However, if l is very small, the y gradient at the plate is not equal to zero. The reason is that if the heated section is small enough, energy is diffused upstream from the trailing edge to the leading edge. In other words, although the trailing-edge solutions decay exponentially, they still have small effects on the leading edge if the heated section is very small. More strictly, instead of the boundary condition $\theta_T = 0$ in Fig. 2(*b*), the following condition should be applied:

$$\theta_{Ty}=0; \quad x_T<-l \quad \text{and} \quad \theta_T=0; \quad -l<x_T<0. \tag{50}$$

which will lead to a triple integral equation in the trailing edge. It seems impossible to get a closed-form solution. On the other hand, it is unnecessary to consider condition (50) since the error can be improved by other ways based on perturbation methods. One is to solve the internal boundary layer equation iteratively under the extra condition, that is, take the result of Eq. (47) at $x < 0$ as the new boundary condition and solve Eq. (14) again. The second method is to consider the additional heat flux in the higher-order approximations. A simpler method which evaluates the error from the average Nusselt number, will be presented in the next paragraph.

Since the average Nusselt number over the heated section is by definition (Holman, 1986)

$$\overline{\mathrm{Nu}}_l=\frac{\bar{h}l}{k}=\int_0^l \frac{h_{x_0+x}}{k}\,dx=\int_0^l \frac{\mathrm{Nu}_{x_0+x}}{x_0+x}\,dx \tag{51}$$

the average heat transfer in the insulated section before the leading edge can be found by integration of Eq. (47) with respect to x from $-x_0$ to 0 and dividing by x_0. A simple calculation yields

$$\overline{\mathrm{Nu}}_l^{\mathrm{err}}\,\mathrm{Re}_{x_0+l}^{-1/2}=\frac{2Dl}{x_0(1+l/x_0)^{1/2}}\sum_{m=1}^{\infty}\frac{a_m-d_m}{a_m d_m}\prod_{n=1}^{\infty}\left(\frac{1-a_m/d_n}{1-a_m/a_n}\right)$$

$$\times\int_0^1 \exp[0.57624\,a_m\,\mathrm{Pr}^{1/2}\mathrm{Re}_{x_0}^{3/4}(x^2-1-l/x_0)/(1+l/x_0)^{1/4}]dx \tag{52}$$

where $n \neq m$ and the superscript err of $\overline{\mathrm{Nu}}_l$ denotes the error from the actual noninsulated boundary before the leading edge. The magnitude of the error depends on x_0/l, Pr, Re_{x_0}. Assuming the heat transfer from Eq. (52) acts directly on the heated section, it leads to the maximum error. A practical comparison can be evaluated after the average Nusselt number is obtained. Substituting the integral solution (16) into Eq. (51) yields the average Nusselt number from boundary layer theory

$$\overline{\mathrm{Nu}}_l\mathrm{Re}_{x_0+l}^{-1/2}=0.66258\,\mathrm{Pr}^{1/3}\left[1-\left(\frac{x_0}{x_0+l}\right)^{3/4}\right]^{2/3} \tag{53}$$

If the ratio $x_0/l \ll 1$, Eq. (53) degenerates into $\overline{\mathrm{Nu}}_l \sim 0.66258\,\mathrm{Re}_l^{1/2}\,\mathrm{Pr}^{1/3}$, which is the result of the plate heated over its entire length (Holman, 1986). This denotes that the effects of the insulated or unheated starting lengths can be neglected for average Nusselt numbers if their relative magnitude is very small. Following the definition (51) the average Nusselt number including the leading- and trailing-edge effects also can be obtained by integrating Eq. (49) over the length of the heated section

$$\overline{\mathrm{Nu}}_l \mathrm{Re}_{x_0+l}^{-1/2} = 0.26274\ \mathrm{Re}_{x_0}^{1/4}\left(\frac{\mathrm{Pr}x_0}{x_0+l}\right)^{1/2}$$

$$\int_0^\infty \left\{ \frac{\prod_{m=1}^{\infty}\left(\frac{1+r/a_m}{1+r/d_m}\right)\int_0^{\left(\frac{x_0+l}{x_0}\right)^{1/2}-1}\exp[-0.57624\ \mathrm{Pr}^{1/2}\mathrm{Re}_{x_0}^{3/4}\, r(x^2+2x)]dx}{r^2[J^2_{-1/3}(\xi)-J_{-1/3}(\xi)J_{1/3}(\xi)+J^2_{1/3}(\xi)]} \right\} dr$$

$$+0.66258\ \mathrm{Pr}^{1/3}\left[1-\left(\frac{x_0}{x_0+l}\right)^{3/4}\right]^{2/3} - 1.0939\ \mathrm{Pr}^{1/3}\left(\frac{x_0}{x_0+l}\right)^{1/2}\int_0^{(l/x_0)^{1/3}}\frac{x}{(1+x^3)^{1/2}}\,dx$$

$$+2D\sum_{m=1}^{\infty}\frac{a_m-d_m}{a_m d_m}\prod_{n=1}^{\infty}\frac{1-a_m/d_n}{1-a_m/a_n}\int_0^{\left(\frac{x_0+2l}{x_0+l}\right)^{1/2}-1}\exp[-0.57624\ a_m\mathrm{Pr}^{1/2}\mathrm{Re}_{x_0+l}^{3/4}(x^2+2x)]dx \qquad \text{where } n\neq m. \quad (54)$$

Some numerical results for air have been listed in Table 1. For example, if the ratio $x_0/l = 3$, from the integral solution (53) it can be found that $\overline{\mathrm{Nu}}_l \mathrm{Re}_{x_0+l}^{-1/2} = 0.1991$. When $\mathrm{Re}_{x_0} = 300$, the Nusselt number of the present work can be calculated directly for $\overline{\mathrm{Nu}}_l \mathrm{Re}_{x_0+l}^{-1/2} = 0.2101$ by taking the product of the ratio, 1.055, and the integral solution. It has been shown from the table that the ratio between the present work and conventional boundary layer theory increases as x_0/l increases and Pr decreases, respectively. The former is, just as analyzed before, characteristic of microstructures. In the case $\mathrm{Re}_{x_0} = 1000$, where it is unnecessary to consider the higher-order approximation of momentum equations (Van Dyke, 1975), the increasing ratio is 1.161. This means that heat transfer from conventional boundary layer theory is inaccurate for large ratio x_0/l. Finally, according to Eq. (52), the maximum error can be calculated. However, comparing the average Nusselt numbers, the error is so small that it can be neglected without greatly affecting these results. For example, under the worst condition in Table 1, where $x_0/l = 40$ and $\mathrm{Re}_{x_0} = 80$, the $\overline{\mathrm{Nu}}_l^{\mathrm{err}}$ is below 0.2 percent of the present average Nusselt number. This indicates that the boundary condition (30) is valid in these regions.

The complexity of Eq. (54) inhibits its general applicability. It is, however, possible to develop a closed-form correlation. It only takes ten seconds to get a numerical result from Eq. (54) on the Vax 6350 computer. Then with the aid of the procedure NLIN in the software SAS (SAS/STAT, 1988), the correlation can be obtained as

$$\overline{\mathrm{Nu}}_l = 0.6626\ \mathrm{Pr}^{1/3}\mathrm{Re}_{x_0+l}^{1/2}\left[1-\left(\frac{x_0}{x_0+l}\right)^{3/4}\right]^{2/3} \times\left[1+\frac{0.3981(x_0/l)^{0.5987}}{\mathrm{Pr}^{0.3068}\mathrm{Re}_{x_0}^{0.4675}}\right] \quad (55)$$

$$\text{for } 0.5 \le \mathrm{Pr} \le 100,\ x_0/l \le 50, \text{ and } \mathrm{Re}_{x_0} \ge 100$$

The term including 0.3981 is obtained from the present work. The error for this correlation is less than 2 percent as compared with the original solution (54). From the previous derivation, it is evident that Eq. (55) is valid for $\mathrm{Re}_{x_0} \ge 100$ if the higher-order approximation of the velocity components is neglected.

5 Conclusion

The internal boundary layer Eq. (14), which is suitable for the leading and trailing edges, is proposed with the aid of the generalized principle of least degeneracy. It is interesting to note that these equations, in the transformed plane, resemble shear flow. In other words, the first-order approximation of velocity in the internal boundary layer of the energy equation is linear. The solution of the internal boundary layer equation has been performed through the use of the Wiener–Hopf technique.

For practical application, the main result is Eq. (55). The significance of Eq. (55) is to expand the boundary layer solution into the regime for moderate Reynolds number and larger length ratio. Equation (55) is uniformly valid for higher and moderate Reynolds number in the sense of laminar flow. In other words, if Reynolds number is very large and the length ratio x_0/l is small, Eq. (55) reduces to the boundary layer solution (53). Otherwise, the error from boundary layer theory can be directly calculated from Eq. (55). For example, air flow with $\mathrm{Pr} = 0.72$ passes over a heated element with $x_0/l = 40$ and $\mathrm{Re}_{x_0} = 100$. The average Nusselt number from boundary layer theory (53) is

$$\overline{\mathrm{Nu}}_l = 0.6626\ \mathrm{Pr}^{1/3}\mathrm{Re}_{x_0+l}^{-1/2} \times\left[1-\left(\frac{x_0}{x_0+l}\right)^{3/4}\right]^{2/3} = 0.04131\ \mathrm{Re}_{x_0+l}^{1/2}$$

The straightforward calculation of Eq. (55) from current theory gives

$$\overline{\mathrm{Nu}}_l = 0.6626\ \mathrm{Pr}^{1/3}\mathrm{Re}_{x_0+l}^{1/2}\left[1-\left(\frac{x_0}{x_0+l}\right)^{3/4}\right]^{2/3} \times\left[1+\frac{0.3981(x_0/l)^{0.5987}}{\mathrm{Pr}^{0.3068}\mathrm{Re}_{x_0}^{0.4675}}\right] = 0.06054\ \mathrm{Re}_{x_0+l}^{1/2}$$

The ratio of these results is 1.465. A more accurate result from the numerical results (see Table 1) yields 1.459. This specifies that boundary layer theory underestimates heat transfer by approximately 50 percent. The reason is that boundary layer theory does not include the effect of the axial diffusion. In summary, the boundary layer solutions might lead to larger inaccuracy for microstructures being built.

References

Abramowitz, M., and Stegun, I. A., 1972, *Handbook of Mathematical Functions*, Dover, New York.

Ackerberg, R. C., Patel, R. D., and Gupta, S. K., 1978, "The Heat/Mass Transfer to a Finite Strip at Small Péclet Numbers," *Journal of Fluid Mechanics*, Vol. 86, pp. 49–65.

Bejan, A., 1984, *Convection Heat Transfer*, Wiley, New York.

Bender, C. M., and Orszag, S. A., 1984, *Advanced Mathematical Methods for Scientists and Engineers*, McGraw-Hill, New York.

Cebeci, T., and Bradshaw, P., 1984, *Physical and Computational Aspects of Convective Heat Transfer*, Springer-Verlag, New York.

Henderson, H. T., and Hsieh, W., 1989, "A Miniature Anemometer for Ultrafast Response," *Sensors*, Vol. 22, pp. 22–26.

Holman, J. P., 1986, *Heat Transfer*, McGraw-Hill, New York.

Jones, C. W., and Watson, E. J., 1963, "Two-Dimensional Boundary Lay-

ers," in: *Laminar Boundary Layers*, L. Rosehead, ed., Oxford University Press, London.

Kays, W. M., and Crawford, M. E., 1980, *Convective Heat and Mass Transfer*, McGraw-Hill, New York.

Lévêque, M. A., 1928, "Les lois de la Transmission de la Chaleur par Convection," *Annales de Mines*, Vol. 13, pp. 201–239.

Ma, S. W., and Zhang, L. X., 1991, "A New Solution of an Eccentric Crack off the Center Line of a Rectangular Sheet for Mode-III," *Engineering Fracture Mechanics*, Vol. 40, pp. 1–7.

Ma, S. W., Gerner, F. M., and Tsuei, Y. G., 1992, "Composite Expansions on Forced Convection Over a Flat Plate With an Unheated Starting Length," *International Journal of Heat and Mass Transfer*, Vol. 35, pp. 3275–3289.

Moffat, R. J., and Ortega, A., 1988, "Direct Air-Cooling of Electronic Components," in *Advances in Thermal Modeling of Electronic Components and Systems*, Vol. 1, A. Bar-Cohen and A. D. Kraus, eds., Hemisphere Pub. Corp.

Newman, J., 1973, "The Fundamental Principles of Current Distribution and Mass Transport in Electrochemical Cells," in: *Electroanalytical Chemistry*, Vol. 6, A. J. Bard, ed., Marcel Dekker, New York, pp. 187–352.

Noble, B., 1958, *Methods Based on the Wiener–Hopf Technique for the Solution of Partial Differential Equations*, Pergamon Press, New York, NY, pp. 36–38.

SAS/STAT, 1988, "SAS/STAT User's Guide, Release 6.03 Edition," SAS Institute Inc., Cray, NC.

Sneddon, I. N., 1951, *Fourier Transforms*, McGraw-Hill, New York.

Springer, S. G., and Pedley, T. J., 1973, "The Solution of Heat Transfer Problems by the Wiener–Hopf Technique. I. Leading Edge of a Hot Film," *Proceedings of the Royal Society of London*, Series A, Vol. 333, pp. 347–362.

Springer, S. G., 1974, "The Solution of Heat Transfer Problems by the Wiener–Hopf Technique. II. Trailing Edge of a Hot Film," *Proceedings of the Royal Society of London*, Series A, Vol. 337, pp. 395–412.

Stewartson, K., 1968, "On the Flow Near the Trailing Edge of a Flat Plate," *Proceedings of the Royal Society of London*, Series A, Vol. 306, pp. 275–290.

Van Dyke, 1962, "Higher Approximation on Boundary-Layer Theory," *Journal of Fluid Mechanics*, Vol. 14, pp. 161–177.

Van Dyke, M., 1975; *Perturbation Methods in Fluid Mechanics*, Parabolic, Stanford, CA.

Van Oudheusden, B. W., and Huijsing, J. H., 1988, "Integrated Flow Friction Sensor," *Sensors and Actuators*, Vol. 15, pp. 135–144.

Van Oudheusden, B. W., 1989, "The Behavior of a Thermal-Gradient Sensor in Laminar and Turbulent Shear Flow," *Journal of Physics E: Scientific Instruments*, Vol. 22, pp. 490–498.

Van Oudheusden, B. W., 1991, "The Thermal Modeling of a Flow Sensor Based on Differential Convective Heat Transfer," *Sensors and Actuators A*, Vol. 29, pp. 93–106.

Van Putten, A. F. P., 1988, "A Constant Voltage Constant Current Wheatstone Bridge Configuration," *Sensors and Actuators*, Vol. 13, pp. 103–115.

Heat Transfer and Pressure Drop Correlations for Twisted-Tape Inserts in Isothermal Tubes: Part I—Laminar Flows

R. M. Manglik[1]
Mem. ASME

A. E. Bergles
Fellow ASME

Heat Transfer Laboratory,
Rensselaer Polytechnic Institute,
Troy, NY 12180-3590

Laminar flow correlations for f *and* Nu_m *are developed based on experimental data for water and ethylene glycol, with tape inserts of three different twist ratios. The uniform wall temperature condition is considered, which typifies practical heat exchangers in the chemical and process industry. These and other available data are analyzed to devise flow regime maps that characterize twisted-tape effects in terms of the dominant enhancement mechanisms. Depending upon flow rates and tape geometry, the enhancement in heat transfer is due to the tube partitioning and flow blockage, longer flow path, and secondary fluid circulation; fin effects are found to be negligible in snug- to loose-fitting tapes. The onset of swirl flow and its intensity is determined by a swirl parameter,* $\mathrm{Sw} = Re_{sw}/\sqrt{\mathrm{y}}$, *that defines the interaction between viscous, convective inertia, and centrifugal forces. Buoyancy-driven free convection that comes into play at low flow rates with large* y *and* ΔT_w *is shown to scale as* $Gr/\mathrm{Sw}^2 \gg 1$. *These parameters, along with numerical baseline solutions for laminar flows with* $\mathrm{y} = \infty$, *are incorporated into correlations for* f *and* Nu_m *by matching the appropriate asymptotic behavior. The correlations describe the experimental data within* ±10 *to 15 percent, and their generalized applicability is verified by the comparison of predictions with previously published data.*

Introduction

The need for reliable correlations to predict heat transfer and pressure drop in forced convective, viscous fluid flows in tubes with twisted-tape inserts cannot be overstated. Given the vast numbers of heat exchangers used in the process industry for viscous fluids, substantial capital and operating cost savings can be achieved by employing twisted tapes to improve their heat transfer performance. Tape inserts are inexpensive to manufacture, and they can be readily used to retrofit existing shell-and-tube heat exchangers in order to upgrade their tube-side thermal performance. Also, for a given heat load, smaller heat exchangers can be made, thereby reducing capital investments. Twisted tapes will significantly reduce the dominant thermal resistance of the viscous stream, which dictates the required heat transfer surface area. There is, of course, a trade-off between the thermal improvements and the increased pressure drops associated with their usage. However, the net benefits of enhanced heat transfer can be incorporated effectively in practical heat exchangers only if accurate and generalized design criteria are available.

For almost a century, heat transfer enhancement by means of twisted-tape inserts has been considered in the literature (Whitham, 1896; Manglik, 1991). Most of the early work was concerned with turbulent flows of air and water (Royds, 1921; Koch, 1958; Smithberg and Landis, 1964; Lopina and Bergles, 1969). Date and Singham (1972), Date (1974), and Hong and Bergles (1976) were the first to investigate heat transfer enhancement in laminar, viscous liquid flows in tubes with uniform heat flux (UHF). In the numerical solutions of Date and Singham (1972) and Date (1974), the flow conditions were idealized for zero tape thickness but the tape twist and fin effects were included. Hong and Bergles (1976) have reported a correlation for predicting Nusselt numbers in fully developed swirl flows, based on their experimental data for water and ethylene glycol in electrically heated tubes. Additional data for UHF conditions have been reported for laminar flows of air (Watanabe et al., 1983), oil (Bandyopadhyay et al., 1991), and non-Newtonian liquids (Manglik et al., 1988).

However, in typical practical applications, in the chemical and process industry, steam heating or turbulent flow liquid heating/cooling of viscous liquids is encountered. These conditions are more closely simulated by the uniform wall temperature (UWT) or isothermal tube boundary. Marner and Bergles (1978, 1989) have reported the first set of experimental data for laminar flows of ethylene glycol and polybutene 20 with a twisted-tape insert ($y = 5.39$) in an isothermal tube. The polybutene 20 data ($1000 < \mathrm{Pr} < 7000$) suggest that in very viscous liquid flows, swirl flows do not set in and the heat transfer enhancement is simply due to the duct partitioning. Also, for both liquids, temperature-dependent viscosity variations in the flow cross section are significant. This, along with the lack of agreement with the Hong and Bergles (1976) correlation, is contrary to previously held contentions that entrance effects, fluid property variations, and boundary conditions have little effect in twisted-tape flows. Based on these data and a numerical baseline solution, an earlier attempt at developing a generalized Nusselt number correlation is given by Manglik and Bergles (1987). Lecjaks et al. (1984a,b) have reported experimental data for water and water–glycerol solutions; they have also devised a correlation for f and a design nomogram for Nu. DuPlessis and Kröger (1984, 1987) have presented correlations for f and Nu that are based on their numerical solutions for constant-property, laminar flows. Experimental data for non-Newtonian liquids have been reported by Dasmahapatra and Raja Rao (1991).

Geometrically, a twisted-tape insert is characterized by the

[1] Present address: Department of Mechanical, Industrial, and Nuclear Engineering, University of Cincinnati, Cincinnati, OH 45221-0072.

Contributed by the Heat Transfer Division and presented at the National Heat Transfer Conference, San Diego, California, August 9–12, 1992. Manuscript received by the Heat Transfer Division July 1992; revision received March 1993. Keywords: Augmentation and Enhancement, Forced Convection, Heat Exchangers. Associate Technical Editor: T. W. Simon.

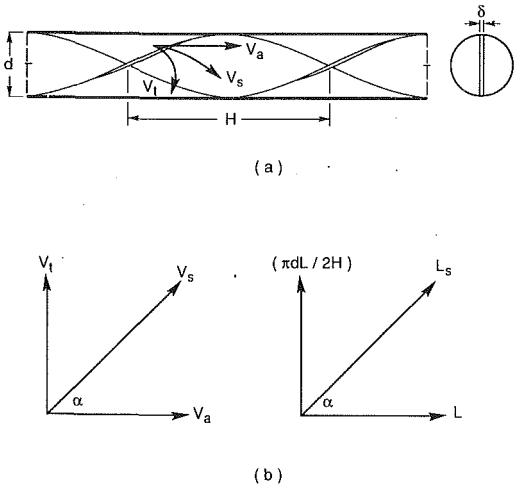

Fig. 1 A twisted-tape insert: (*a*) geometrical characteristics, and (*b*) resolution of fluid swirl velocity and flow length into its axial and tangential components

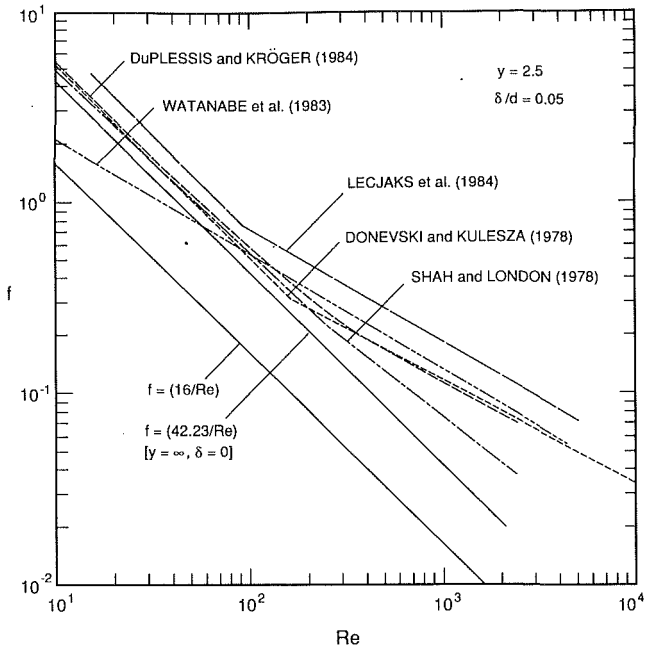

Fig. 2 Comparison of isothermal friction factor correlations for laminar flows in circular tubes with twisted-tape inserts

features shown in Fig. 1(*a*). The severity of the helical twist is usually designated by a dimensionless twist ratio, $y = H/d$. Depending upon the application, tube diameter, and tape material, inserts of very small twist ratios can be employed; the smaller the twist ratio, the greater the heat transfer enhancement (Bergles, 1985). A lower limit is described by $y = \infty$, or a straight tape insert that partitions the tube into two circular segments. In general, the heat transfer enhancement is attributed to several mechanisms: swirl flow mixing, increased flow velocity and flow length, and tape fin effects. From an extensive literature review (Manglik, 1991), it is observed that the few attempts at developing laminar flow correlations for f and Nu with UWT conditions have accounted for these effects over a very limited parametric range. The strategies have included equations based on empirical data, semi-empirical theoretical considerations, and numerical solutions.

A comparison of isothermal friction factor correlations reported in the literature is presented in Fig. 2 for a twisted tape with $y = 2.5$. The results for laminar flows in circular and semicircular tubes are also given in this figure for reference. The considerable disagreement between the various predictions is clearly evident. Almost all predictions significantly differ from each other, except those obtained by the Donevski and Kulesza (1978), and DuPlessis and Kröger (1984) correlations. The Shah and London (1978) predictions agree with these for $Re < 200$, but underpredict substantially at higher Re. Watanabe et al. (1983) underpredict the low Re asymptotic behavior; for $Re < 60$, their results are less than those for a semicircular duct. On the other hand, the Lecjaks et al. (1984a) predictions are consistently higher than all others. In almost all cases, the twist-ratio effects have been incorporated differently: Shah

Nomenclature

A = heat transfer area, m^2
A_c = axial flow cross-sectional area $= (\pi d^2/4) - \delta d$, m^2
A_0 = empty tube flow cross-sectional area $= \pi d^2/4$, m^2
c_p = specific heat at constant pressure, J/kg•K
d = tube inside diameter, m
d_h = hydraulic diameter $= 4A_c/P_w$, m
f = Fanning friction factor
f_{sw} = swirl flow friction factor, Eq. (5)
g = gravitational acceleration, m/s^2
Gr = Grashof number $= g\rho^2 d^3 \beta \Delta T_w/\mu^2$
Gz = Graetz number $= \dot{m}c_p/kL$
h = heat transfer coefficient, W/m^2•K
H = 180 deg twist pitch, m
k = fluid thermal conductivity, W/m•K
L = axial length, m
L_s = maximum helical flow length, Eq. (4), m
$\dot{m}$ = mass flow rate, kg/s
Nu = Nusselt number based on tube inside dimensions $= hd/k$
Δp = pressure drop, N/m^2
P_w = wetted perimeter, m
Pr = Prandtl number $= \mu c_p/k$
Ra = Rayleigh number = Gr•Pr
Re = Reynolds number based on empty tube diameter $= \rho V_0 d/\mu$
Re_{ax} = Reynolds number based on axial velocity $= \rho V_a d/\mu$
Re_{sw} = Reynolds number based on swirl velocity $= \rho V_s d/\mu$
Sw = dimensionless swirl parameter $= Re_{sw}/\sqrt{y}$, Eq. (3)
ΔT_w = wall-to-bulk fluid temperature difference, K
V_a = mean axial velocity $= \dot{m}/\rho A_c$, m/s
V_0 = mean velocity based on empty tube diameter $= \dot{m}/\rho A_0$, m/s
V_s = actual swirl velocity at tube wall, Eq. (2), m/s
V_t = tangential velocity at tube wall, Eq. (2), m/s
y = twist ratio $= H/d$
β = coefficient of isobaric thermal expansion $= -(\partial\rho/\partial T)_p/\rho$, K^{-1}
δ = thickness of twisted tape, m
μ = fluid dynamic viscosity, kg/m•s
ρ = fluid density, kg/m^3

Subscripts

ax = at axial flow conditions
b = at bulk fluid temperature
h = based on the hydraulic diameter, d_h
m = mean or average
sw = at swirl flow conditions
w = at tube wall temperature
∞ = at fully developed flow conditions

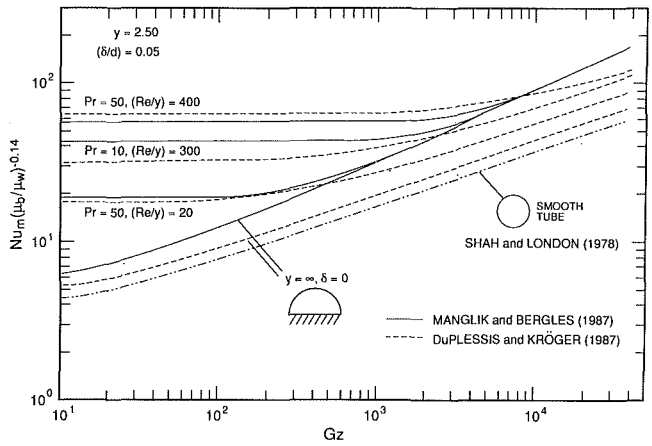

Fig. 3 Comparison of heat transfer correlations for laminar flow in circular tubes with a twisted-tape insert ($y = 2.5$, $\delta/d = 0.05$) and uniform wall temperature

and London (1978) use Re/y, Donevski and Kulesza (1978) use $1/(y\mathrm{Re})^2$ and $1/(\mathrm{Re}^n y^{0.04})$, Watanabe et al. (1983) use the effective curvature at the wall, Lecjaks et al. (1984b) employ $1/(y\mathrm{Re})$ and $\mathrm{Re}^{-1/y}$, and DuPlessis and Kröger (1984) use $\mathrm{Re}/y^{1.3}$ [see Manglik (1991) for details of respective equations and further discussion]. These differences are primarily due to the curve-fitting strategies adopted by the investigators.

The two correlations for Nu_m in laminar flows with twisted-tape inserts in UWT tubes due to Manglik and Bergles (1987), and DuPlessis and Kröger (1987) are presented in Fig. 3 in the form $\mathrm{Nu}_m(\mu_b/\mu_w)^{-0.14}$ versus Gz for $y = 2.5$. There is little agreement between the two, either in the thermal entrance or the fully developed swirl-flow regions. The most significant difference is for the limiting case of $y = \infty$, $\delta = 0$; DuPlessis and Kröger (1987) underpredict the performance considerably. Even though the correlation is based on their numerical results, an arbitrarily extrapolated and incorrect value for the fully developed asymptote has been used. In fact, this correlation inadequately describes their own experimental data for oil (Manglik and Bergles, 1987). On the other hand, the Manglik and Bergles (1987) equation incorporates the more accurate solution for the $y = \infty$, $\delta = 0$, asymptote, but is based on very limited experimental data for the swirl flow region—that reported by Marner and Bergles (1978) for ethylene glycol with $y = 5.39$.

From the foregoing it is evident that previously reported correlations for f and Nu lack general applicability and are, at best, useful only in the limited ranges of their databases. One limiting factor has been the difficulty in accounting for all the different phenomena associated with twisted tapes; the thermal-hydraulic performance depends upon the fluid and geometrical characteristics of the duct, as well as a variety of mechanisms that influence the flow field. Consequently, empirically derived correlations require a very large database that covers a wide range of variation of the independent parameters. The alternative approach of computational and/or theoretical analysis also has limitations; the very complex flow field is often simplified considerably in order to render the governing differential equations more tractable for obtaining convergent solutions. In some instances, empirical information is needed to verify the computational results. [The error of a factor of 2 in numerical results reported by Date (1974), which was discovered after the experimental investigation of Hong and Bergles (1976), is a case in point.]

Perhaps a more general approach would be to analyze the flow field mechanistically, and to use the empirical and numerical databases to quantify the identified phenomena. Such an attempt has been made in this study by combining numerical baseline solutions with experimental data, and introducing correlating parameters that are derived from a theoretical analysis of the phenomenological attributes of flows with twisted-tape inserts. First, the various effects twisted tapes have on the flow field are identified and flow regime maps are defined. Next, parameters that describe these effects are devised on the basis of force balances and scale analysis. Finally, predictive equations for f and Nu are developed, and their generalized applicability verified by comparing the predictions with previously published data.

Furthermore, recognizing the need for a larger database, experiments were conducted to obtain data for isothermal f and Nu under UWT conditions. Water ($3.5 < \mathrm{Pr} < 6.5$) and ethylene glycol ($68 < \mathrm{Pr} < 100$) were used as test fluids, because they represent a broad spectrum of viscous, industrial process liquids. Twisted-tape inserts of three different twist ratios ($y = 3.0$, 4.5, and 6.0) were tested, and data obtained for both heating and cooling over a wide range of flow rates corresponding to $300 \le \mathrm{Re} \le 3 \times 10^4$; these flows describe the laminar, transition, and turbulent regimes in smooth tube flows. The test section consisted of a heated/cooled segment, $L/d = 144$ ($d = 21.18$ mm), preceded by a calming section, $L/d = 72$, to ensure hydrodynamically developed flows. Full-length twisted-tape inserts were used that covered the entire test section ($L/d = 216$). The details of the test apparatus, data acquisition and reduction, and experimental uncertainties can be found from Manglik (1991). The average uncertainties in Re, q, Nu, Gr, and f were ± 1.32, ± 2.33, ± 4.1, ± 3.5, and ± 4.5 percent, respectively. Also, the energy balances for more than 80 percent of the data were within ± 5 percent, with a maximum of ± 10 percent. Only laminar flow data are considered here, and the analysis for transition and turbulent flows with twisted-tape inserts is given in the companion paper (Manglik and Bergles, 1993). A comparison of these data with existing correlations further substantiates the inadequacy of the correlations, and the need for more reliable equations; see Manglik (1991) for details.

Phenomenological Flow Regimes

Twisted tapes are generally classified as swirl-flow devices and are a part of the general area of confined swirl flows (Bergles, 1985). Phenomenologically, the heat transfer enhancement is ascribed to a variety of effects: (1) the partitioning and blockage of the tube flow cross section by the tape, which results in higher flow velocities, (2) the hydraulic diameter is reduced, which in effect increases the heat transfer coefficient, (3) the helically twisting fluid motion has an effectively longer flow path, (4) secondary fluid motion is generated by the tape twist, and the resulting swirl mixing improves the convective coefficient, and (5) the metallic tape, if in "good" contact with the tube walls, acts as a fin; the effective heat transfer area is increased, which allows higher heat fluxes to be sustained. The first four are a consequence of the tape geometry, i.e., thickness, δ, and pitch of 180 deg twist, H. The fin effect depends primarily on the tape material and the tape-to-tube fit.

From hydrodynamic considerations, the flow field is significantly influenced by the tube blockage, increased flow path, and the secondary fluid circulation. The tape insert increases the wetted perimeter, reduces the flow cross-sectional area, and, because the fluid has to follow a partitioned, twisting path, it increases the flow length. Furthermore, due to the helically rotating fluid flow, a centrifugal force is superimposed over the longitudinal flow, which produces secondary motion. The net effect is that higher pressure drops and heat transfer coefficients are obtained in comparison with those for equivalent smooth tube flows.

The secondary circulation, which causes a transverse fluid transport across the partitioned duct cross section, is

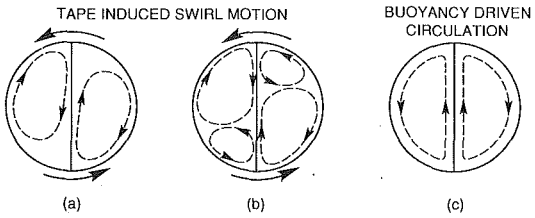

Fig. 4 Secondary flow due to (*a*) tape twist at low Re or moderate twist ratios, (*b*) tape twist at high Re or small twist ratios, and (*c*) buoyancy driven free convection

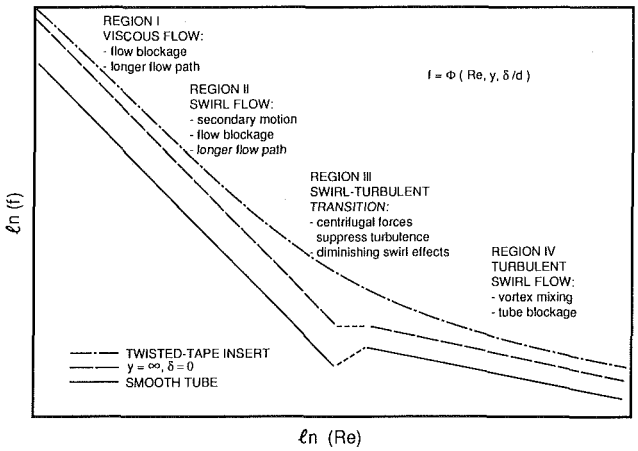

Fig. 5 Flow regime map for isothermal friction factors in tube flows with twisted-tape inserts

qualitatively[2] shown in Fig. 4(*a*) for low Reynolds number flow with a tape of moderate twist pitch. For a smaller twist pitch, or a higher velocity, this circulation breaks up into two nonsymmetric, counterrotating vortices, as shown in Fig. 4(*b*). However, at very low flow rates, swirl may not set in and the fluid simply follows a twisted path. In such situations, the flow resistance increases due to the tape thickness and longer flow path. In the limit when either $\dot{m} \to 0$, or $y \to \infty$, the duct geometry effectively becomes partitioned into two circular segments and there is no secondary circulation, and undisturbed streamline fluid motion prevails. This limiting model has been theoretically considered by Manglik (1991).

On the basis of the foregoing, a flow regime map is proposed in Fig. 5 to describe the isothermal friction factor behavior in tubes with twisted-tape inserts. Four distinct regions are identified where the interplay of viscous, convective inertia, and centrifugal forces, and those due to turbulent pulsations influences the flow resistance. These regions can be described in terms of the dominant flow characteristics and enhancement mechanisms as follows:

Region I — Viscous flow; balance of convective inertia and viscous forces; tube blockage and longer effective flow path.

Region II — Swirl flow superimposed over the axial flow; balance of convective inertia, centrifugal and viscous forces; tube blockage, longer flow path, and tape-twist induced secondary fluid motion.

Region III — Swirl-turbulent transition; competing effects of swirl flow and onset of turbulent fluctuations; centrifugal forces suppress turbulent bursts and "laminarize" the flow; diminishing influence of secondary flow.

Region IV — Turbulent swirl flow; fluctuating velocities and centrifugal forces affect the flow field; tube blockage and swirl-induced vortex mixing.

[2]The qualitative assessment is based on the reported findings of Date (1974) and Penney (1965); however, none of these investigators have explicitly presented stream function profiles to show the exact nature of the secondary motion. For high Re flows, Fig. 4(*b*) is consistent with swirl flow actually observed by Seymour (1966). A double vortex has also been reported by Cheng et al. (1983) for curved semicircular duct flows.

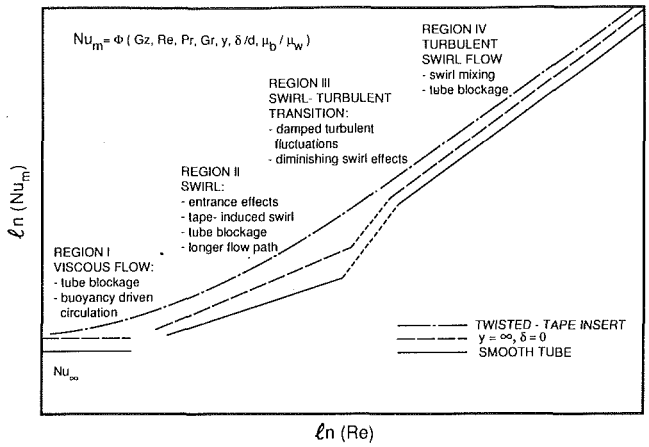

Fig. 6 Flow regime map for Nusselt numbers in tube flows with twisted-tape inserts

A somewhat similar characterization is given by Donevski and Kulesza (1978). The effects of hydrodynamically developing flows have been ignored here because, for most viscous liquids, the hydrodynamic entry length is usually quite short and is not likely to be a significant factor.

Likewise, the heat transfer characteristics are mapped in Fig. 6 where, once again, the thermal behavior is qualitatively illustrated for the four flow regimes. The phenomenological descriptions for each flow regime are as follows:

Region I — Viscous flow; thermally developing boundary layer with superimposed buoyancy-driven secondary flows in the presence of large wall-to-bulk ΔT; tube flow blockage.

Region II — Thermally developed swirl flow; centrifugal forces due to the tape twist wipe out free convection effects; tape induced secondary motion, longer flow path, and tube blockage.

Region III — Swirl-turbulent transition; competing effects of centrifugal forces and turbulent pulsations, with the former tending to dampen the latter instability; diminishing swirl flow effects.

Region IV — Fully developed turbulent swirl flow; increased flow velocity due to tube blockage and swirl mixing.

In Region I, with the absence of strong swirl motion, free convection effects may be present in situations where there are large wall-to-bulk temperature differences. Bandyopadhyay et al. (1991) have reported results that also reflect this phenomenon in the case of tubes with UHF. The parameters that influence the interplay between swirl and buoyant motion are considered in the next section, and their relative scales are identified.

Theoretical Assessment of Enhancement Mechanisms

In all previously reported studies, the swirl flow effects have been correlated by the parameter Re/*y*; it has been suggested that this parameter is similar to the Dean number in curved pipe flow, and it accounts for the centrifugal force effects (Date and Singham, 1972; Hong and Bergles, 1976; Shah and London, 1978; Manglik and Bergles, 1987). This appears to

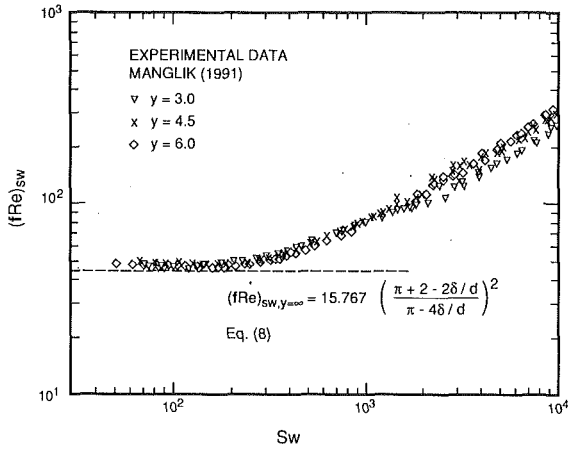

Fig. 7 Variation of isothermal friction factor with the swirl parameter, *Sw*

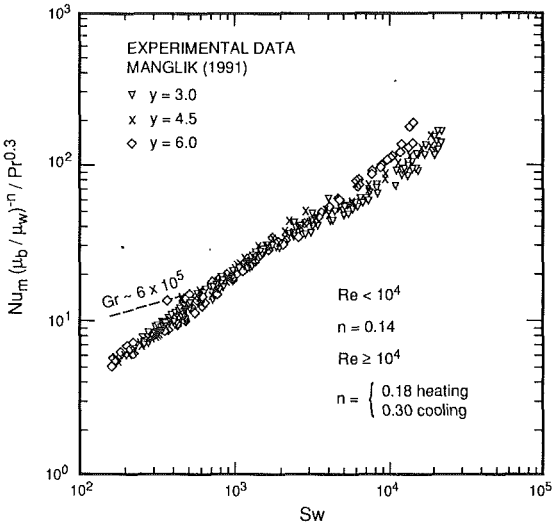

Fig. 8 Variation of Nusselt number with the swirl parameter, *Sw*

be an erroneous contention, because the Dean number represents a balance of centrifugal, convective inertia, and viscous forces, whereas the parameter Re/y represents the centrifugal-to-viscous force ratio. In twisted-tape flows, the centrifugal force due to the helically swirling flow and the convective inertia of the bulk axial flow is balanced by the viscous force, and the appropriate force ratio[3] is

$$\frac{(\text{centrifugal force})(\text{convective inertia force})}{(\text{viscous force})^2}$$

Thus, a swirl parameter that describes the intensity of the tape-twist induced secondary motion can be defined as

$$\text{Swirl parameter} = \frac{(\rho V^2/H)\,(\rho V^2/d)}{(\mu V/d^2)^2} = \mathrm{Re}^2/y \qquad (1)$$

where V is some reference duct-flow velocity. The resulting parameter is Re^2/y instead of Re/y used previously.

The reference velocity can be considered as the *actual swirl flow velocity at the tube wall*, which directly influences the shear stress. On the basis of solid-body rotation, the swirl velocity, V_s, can be represented by its axial and tangential velocity components, as shown in Fig. 1(*b*). This is in concurrence with the forced-vortex flow considerations of Smithberg and Landis (1964), and Gutstein et al. (1970). These velocities are related to the mass flow rate and the tape geometry as follows:

$$V_a = \dot{m}/\rho A_c, \quad V_t = \pi V_a/2y, \quad V_s = V_a[1 + (\pi/2y)^2]^{1/2} \qquad (2)$$

Furthermore, because the square of Reynolds number becomes very large in magnitude, the swirl parameter, *Sw*, can be redefined as

$$Sw = \mathrm{Re}_{sw}/\sqrt{y} = (\mathrm{Re}/\sqrt{y})\left(\frac{\pi}{\pi - 4\delta/d}\right)(1 + (\pi/2y)^2)^{1/2} \qquad (3)$$

where Re_{sw} is based on V_s and d. This parameter accounts for the tape thickness, its twist ratio, and the increased helically twisting flow velocity.

The increased flow path is reflected in the actual, maximum length, L_s, of the helically twisting streamline. From Fig. 1(*b*), the swirl flow length is given by

$$L_s = L(1 + (\pi/2y)^2)^{1/2} \qquad (4)$$

Thus, the Fanning friction factor can be expressed in terms of swirl parameters as

$$f_{sw} = \Delta p d/(2\rho V_s^2 L_s) = f(L/L_s)\,(V_o/V_s)^2 \qquad (5)$$

[3] For flow in curved tubes, this force ratio will yield the Dean number. Also, if the centrifugal force is replaced by the buoyancy force, then the Grashof number is obtained.

From these definitions it follows that

$$(f\mathrm{Re})_{sw} = (f\mathrm{Re})\left(\frac{\pi - 4\delta/d}{\pi}\right)(1 + (\pi/2y)^2)^{-1} \qquad (6)$$

where $(f\mathrm{Re})$ is based on the envelope, or empty tube, dimensions.

The validity of the foregoing analysis is amply demonstrated in Fig. 7, where the isothermal friction factor behavior is adequately described by *Sw*, except at high flow rates (Region IV). This behavior is very similar to that in curved tube flows, where the Dean number is the correlating parameter for laminar flows but not for turbulent flows. [The data presented here, and in the subsequent figure, have been reported by Manglik and Bergles (1992), along with experimental details.] A similar pattern is observed in the heat transfer performance given in Fig. 8; Nu_m is correlated by *Sw* in the laminar and transition flow region, and not in turbulent flow. The transition to turbulent flow, as seen from Figs. 7 and 8, appears to occur when $1400 \le Sw \le 3000$, depending upon the twist ratio, y. For the purpose of developing correlations, laminar swirl flow can be identified by $Sw \le 1400$, and fully developed turbulent swirl flow can be considered when $\mathrm{Re} \ge 10^4$. This is a rather arbitrary demarcation, and an accurate assessment can perhaps be made from a controlled flow visualization experiment. However, as shown in the companion paper (Manglik and Bergles, 1993), the exact identification of the transition point is not crucial to the present analysis, and a conservative approach suffices.

An interesting feature of Fig. 8 is the deviation of high Gr data, for a given magnitude of *Sw*. This supports the earlier contention that in flows with high Gr (or, more appropriately, high Ra) and weak swirl flow effects, buoyancy-driven free convection will appear. However, as seen qualitatively in Fig. 4, the secondary motions due to centrifugal forces and buoyancy forces are not complementary, and they tend to negate each other. Consequently, the relative magnitude of the force balance

$$\frac{(\text{buoyancy force})}{(\text{centrifugal force})} = \frac{g\Delta\rho}{\rho V_s^2/H} = \frac{\mathrm{Gr}}{Sw^2} \qquad (7)$$

determines the dominant flow phenomenon. When $\mathrm{Gr} \gg Sw^2$, free convection effects dominate, and when $\mathrm{Gr} \ll Sw^2$, pure swirl flow exists; this is analogous to the familiar $\mathrm{Gr} \gg \mathrm{Re}^2$ scale for forced and free convection in smooth tube flows. For a given flow rate, the swirl intensity is determined by the tape-twist pitch, H, i.e., with small H, the centrifugal force dominates and the resulting swirl motion suppresses free convective

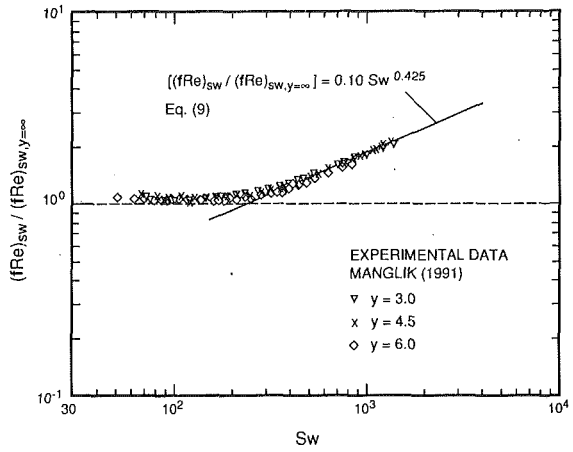

Fig. 9 Asymptotic behavior of isothermal friction factors in fully developed, laminar swirl flows

circulation, and as $H \to \infty$, swirl motion diminishes and free convective effects dominate.

Laminar Flow Correlations

Although it is difficult to identify precisely the transition to turbulent flow from the present data, a critical value of $Sw \simeq 1400$ should provide a reasonable estimate (see Figs. 7 and 8). This is a conservative approach, and it should be recognized that the correct identifying scale will be a function of both flow rate and twist ratio.

Isothermal Friction Factor. In Fig. 7, an asymptotic condition is approached when $Sw \to 0$, which is identified by the limit $H \to \infty$, i.e., a straight tape insert, and is represented by hydrodynamically fully developed laminar flow in a circular-segment duct. Numerical and analytical results for friction factors in ducts of different segment shapes are presented by Manglik (1991). For most practical applications, the tape thickness is usually in the range $0 < (\delta/d) < 0.1$. In this range, isothermal friction factors are virtually constant and can be calculated from

$$(f\mathrm{Re})_{sw,y=\infty} = 15.767\left(\frac{\pi + 2 - 2\delta/d}{\pi - 4\delta/d}\right)^2 \qquad (8)$$

with 1 percent accuracy. Here $(f\mathrm{Re})_h = 15.767$ is the analytical solution for fully developed, laminar flow in a semicircular duct ($y = \infty$, $\delta = 0$).

The normalized friction factor data, $(f\mathrm{Re})_{sw}/(f\mathrm{Re})_{sw,y=\infty}$, are graphed against Sw in Fig. 9. The asymptotic behavior of fully developed laminar swirl flows, $300 \le Sw \le 1400$, can be correlated by the log-linear regression fit

$$(f\mathrm{Re})_{sw} = 0.10\, Sw^{0.425} (f\mathrm{Re})_{sw,y=\infty} \qquad (9)$$

which describes the data with a correlation coefficient of 0.986. Thus, the two limiting asymptotes of Eq. (8) for $Sw \to 0$ and Eq. (9) for $Sw \to \infty$ can be combined by the method outlined by Churchill (1983) to yield

$$(f\mathrm{Re})_{sw} = 15.767\left(\frac{\pi + 2 - 2\delta/d}{\pi - 4\delta/d}\right)^2 (1 + 10^{-6} Sw^{2.55})^{1/6} \qquad (10)$$

where the exponent 1/6 is derived from the best fit to the present study's data. Equation (10) predicts isothermal friction factors[4] for laminar swirl-flows within ±10 percent, as is evident from the comparison with experimental data in Fig. 10.

[4] Only adiabatic f is considered in this study. However, diabatic friction factors can be predicted reasonably well by using $(f/f_{\text{isothermal}}) = (\mu_b/\mu_w)^m$ or $(T_b/T_w)^m$, for liquids and gases, respectively, with the exponent m being the same as that for smooth tube flows.

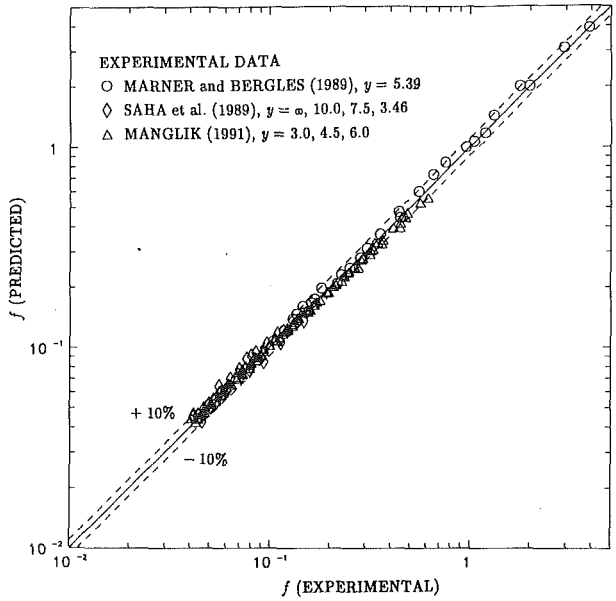

Fig. 10 Comparison of isothermal friction factor predictions of Eq. (10) with experimental data

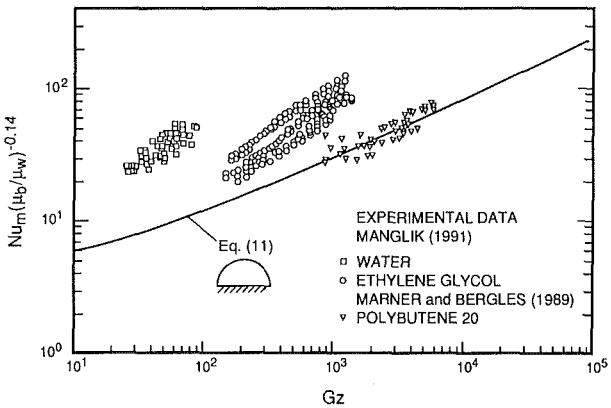

Fig. 11 Experimental results for laminar flow heat transfer in circular tubes with twisted-tape inserts and uniform wall temperature

Mean Nusselt Number. As in the previous case, the thermal behavior for the limiting condition of $y \to \infty$ is described by the heat transfer to laminar flow in circular-segment ducts; the segment shape is determined by the thickness of the tape. Also, for large y and/or high Pr flows, a developing thermal boundary layer will prevail over a significant length of the tube. Furthermore, there are negligible fin effects in snug- to loose-fitting tapes, as has been verified in several experimental studies (Manglik and Bergles, 1987; Marner and Bergles, 1989; Manglik, 1991). Based on the numerical results for such conditions (Manglik, 1991), and tape thicknesses in the range $0 < (\delta/d) < 0.1$, Nu_m can be obtained from

$$\mathrm{Nu}_m = 4.612(1 + 0.0951\,\mathrm{Gz}^{0.894})^{0.5}\left(\frac{\mu_b}{\mu_w}\right)^{0.14} \qquad (11)$$

This equation predicts all of the numerical data within −2 percent and +3 percent; $\mathrm{Nu} = 4.612$ is the fully developed flow asymptote. It provides the reference baseline solution as shown in Fig. 11, where the present study's data represent fully developed swirl flows and exhibit no thermal entrance effects. However, the polybutene 20 data ($1000 < \mathrm{Pr} < 7000$) reported by Marner and Bergles (1985) exhibit primarily an entrance effect; in highly viscous liquids, tape-induced secondary motion does not occur, and the enhancement is simply due to the

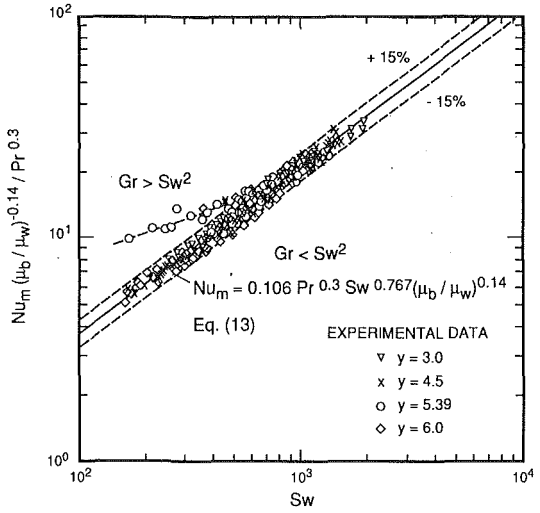

Fig. 12 Laminar swirl flow heat transfer results [the data for $y = 5.39$ are from Marner and Bergles (1978), and the rest from Manglik (1991)]

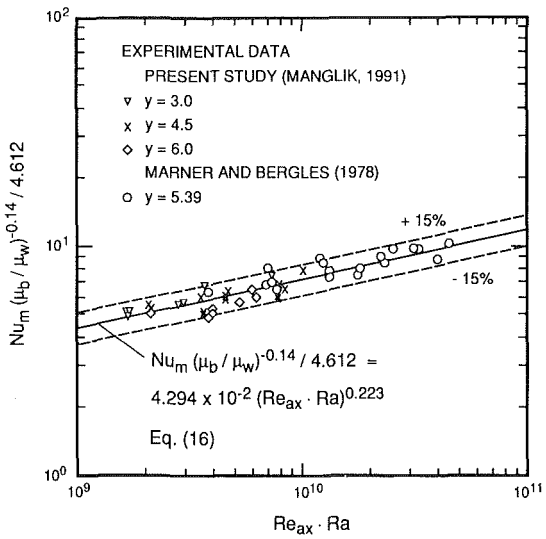

Fig. 13 Correlation of free convection effects in laminar flow heat transfer in tubes with twisted-tape inserts

tube partitioning. The classical viscosity ratio correction factor, $(\mu_b/\mu_w)^{-0.14}$, was needed to account for large viscosity variations in the data and to normalize heating and cooling effects (Manglik, 1991). Thus, the heat transfer data for twisted-tape inserts can be functionally correlated as

$$\mathrm{Nu}_m = \phi(\mathrm{Gz},\ Sw,\ \mathrm{Pr},\ \mathrm{Ra},\ \mu_b/\mu_w) \tag{12}$$

Fully developed swirl flow is characterized by $\mathrm{Nu}_m = \phi(Sw, \mathrm{Pr}, \mu_b/\mu_w)$ and $\mathrm{Gr} < Sw^2$; when $\mathrm{Gr} > Sw^2$, free convection effects will dominate rather than the secondary motion due to the twisted tape. This is seen in Fig. 12, where all of the data with $\mathrm{Gr} < Sw^2$ can be correlated by

$$\mathrm{Nu}_m = 0.106\,\mathrm{Pr}^{0.3} Sw^{0.767} (\mu_b/\mu_w)^{0.14} \tag{13}$$

within ±15 percent, and the regression fit through the present study's data has a correlation coefficient of 0.99. The fully developed flow asymptote, $Sw \to 0$, is $\mathrm{Nu}_m = 4.612$, which can be combined with Eq. (13) as per the method of Churchill (1983) on the basis of the present study's data, to yield

$$\mathrm{Nu}_m = 4.612 \left(\frac{\mu_b}{\mu_w}\right)^{0.14} (1 + 6.413 \times 10^{-9} (Sw \cdot \mathrm{Pr}^{0.391})^{3.835})^{0.2} \tag{14}$$

Equation (14), which represents the swirl flow asymptote for the limit $Sw \to \infty$, $\mathrm{Gz} \to 0$, can be combined with Eq. (11), which embodies thermal entrance effects when $Sw \to 0$, $\mathrm{Gz} \to \infty$, to give the following correlation:

$$\mathrm{Nu}_m = 4.612 \left(\frac{\mu_b}{\mu_w}\right)^{0.14} ((1 + 0.0951\,\mathrm{Gz}^{0.894})^{2.5} + 6.413 \times 10^{-9} (Sw \cdot \mathrm{Pr}^{0.391})^{3.835})^{0.2} \tag{15}$$

Experimental data that scale as $\mathrm{Gr} > Sw^2$ have dominant free convective effects, and these results are plotted against $\mathrm{Re}_{ax} \cdot \mathrm{Ra}$ in Fig. 13. For laminar mixed convection in smooth tube flows, the grouping (Re•Ra) describes the strength of buoyancy effects (Morton, 1959) and it represents the following balance between fluid flow and heat transfer:

$$\mathrm{Re} \cdot \mathrm{Ra} = \frac{(\text{convective inertia})(\text{buoyancy force})(\text{thermal convection})}{(\text{viscous force})^2(\text{thermal conduction})}$$

In twisted-tape flows, the presence of buoyancy driven secondary motion reflects the diminishing effect of the twist ratio, y, and $\mathrm{Re}_{sw} \to \mathrm{Re}_{ax}$, where Re_{ax} is based on the axial velocity, V_a, given by Eq. (2). The Re•Ra grouping has been used in other confined swirl flow situations to correlate free convective effects, for example, curved tube flows (Prusa and Yao, 1982) and rotating pipe flows (Mori and Nakayama, 1967). In the present case, the log-linear regression fit

$$\frac{\mathrm{Nu}_m (\mu_b/\mu_w)^{-0.14}}{4.612} = 4.294 \times 10^{-2} (\mathrm{Re}_{ax} \cdot \mathrm{Ra})^{0.223} \tag{16}$$

describes the data within ±15 percent (see Fig. 13), and has a correlation coefficient of 0.92.

Finally, for the functional relationship of Eq. (12), the following two asymptotic conditions can be identified: (1) swirl flow asymptote, $\mathrm{Ra} \to 0$, described by Eq. (15), and (2) buoyancy effects, $\mathrm{Ra} \to \infty$, represented by Eq. (16). These two equations can be combined by the asymptotic matching technique of Churchill (1983), based on the present study's data, to yield

$$\mathrm{Nu}_m = 4.612(\{(1 + 0.0951\,\mathrm{Gz}^{0.894})^{2.5} + 6.413 \times 10^{-9} (Sw \cdot \mathrm{Pr}^{0.391})^{3.835}\}^{2.0} + 2.132 \times 10^{-14} (\mathrm{Re}_{ax} \cdot \mathrm{Ra})^{2.23})^{0.1} \left(\frac{\mu_b}{\mu_w}\right)^{0.14} \tag{17}$$

Equation (17) gives the final correlation for laminar flow heat transfer in circular tubes with uniform wall temperature and twisted-tape inserts. This is a composite equation that accounts for thermal entrance effects, Eq. (11), fully developed swirl flows, Eq. (14), and combined forced and free convection, Eq. (16), and it describes the experimental data very well as evident from Figs. 14 and 15. Figure 14 illustrates the interplay of free convective and swirl flow effects, while Fig. 15 shows the thermal entrance effects and the subsequent swirl flow development. The scatter plot of Fig. 16 lends additional validity to Eq. (17), where the predictions are within ±15 percent of the experimental data for both heating and cooling conditions.

Concluding Remarks

Laminar flows in horizontal, circular tubes with twisted-tape inserts and UWT conditions are considered. New predictive equations have been developed on the basis of experimental data, and numerical baseline solutions for the limiting case of a straight tape insert ($y = \infty$). Experimental data for water and ethylene glycol with $y = 3.0$, 4.5, and 6.0, along with those reported in the literature, were analyzed. The flow field was examined mechanistically and mapped according to the dominant phenomenological attributes of twisted tapes. A theoretical analysis of the balance of viscous, convective inertia, and centrifugal forces resulted in the development of a swirl

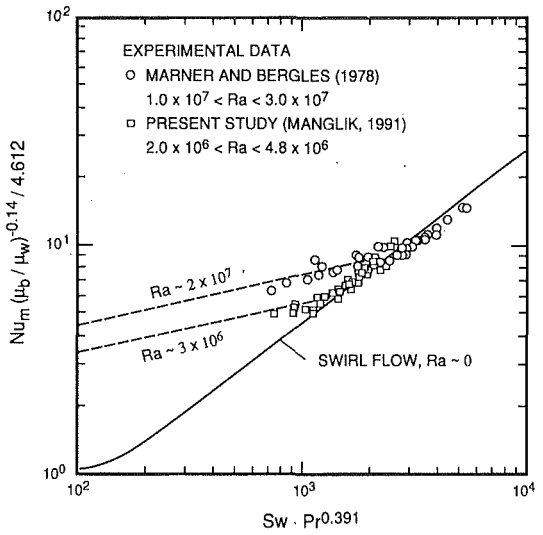

Fig. 14 Effect of Ra on the heat transfer in laminar, fully developed swirl flows in tubes with twisted-tape inserts as predicted by Eq. (17)

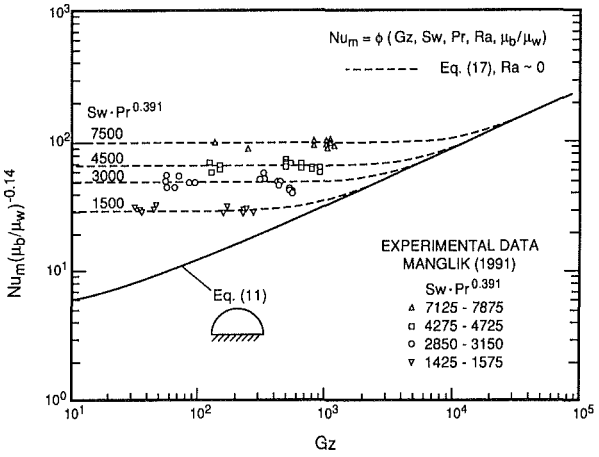

Fig. 15 Effect of $Sw \cdot Pr^{0.391}$ as a parameter on the variation of Nu_m with Gz

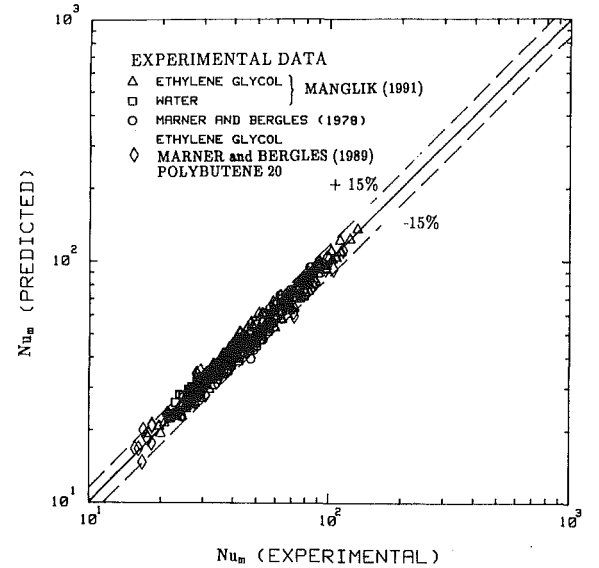

Fig. 16 Comparison of experimental data with the predictions of Eq. (17) for laminar flow heat transfer

parameter, $Sw = Re_{sw}/\sqrt{y}$, that describes tape-induced swirl flows in laminar conditions. Furthermore, buoyancy-driven free convection effects that come into play at low flow rates with large y and ΔT_w, are shown to scale as $Gr/Sw^2 \gg 1$; with $Gr > Sw^2$, buoyancy forces dominate, and with $Gr < Sw^2$, pure swirl flow prevails. These parameters along with numerical solutions for flows in circular-segment ducts ($y = \infty$, $\delta \neq 0$) are incorporated in correlations for f and Nu_m, given by Eqs. (10) and (17), respectively. These equations describe the data in the present study and those reported in the literature very well, over a broad range of tape geometry and fluid flow conditions.

It may be noted that limited data were available for $Gr > Sw^2$, and it would be desirable to test the predictions of Eq. (17) for this asymptotic condition with additional experimental data. Results obtained with large y and ΔT_w will be very helpful in this context. Nevertheless, Eqs. (10) and (17) are useful predictive tools that have generalized applicability for the thermal-hydraulic design of process heat exchangers for viscous liquids.

Acknowledgments

This study was supported in part by Brown Fintube Co., Houston, TX, and the advice of Mr. R. Shilling is acknowledged.

References

Bandyopadhyay, P. S., Gaitonde, U. N.,and Sukhatme, S. P., 1991, "Influence of Free Convection on Heat Transfer During Laminar Flow in Tubes With Twisted Tapes," *Experimental Thermal and Fluid Science*, Vol. 4, pp. 577–586.

Bergles, A. E., 1985, "Techniques to Augment Heat Transfer," *Handbook of Heat Transfer Applications*, 2nd ed., W. M. Rohsenow et al., eds., McGraw-Hill, New York, Chap. 3.

Cheng, K. C., Inaba, T., and Akiyama, M., 1983, "Flow Visualization Studies of Secondary Flow Patterns and Centrifugal Instability in Curved Circular and Semicircular Pipes," *Flow Visualization III*, Proc. Third International Symposium on Flow Visualization, Ann Arbor, MI, pp. 531–536.

Churchill, S. W., and Usagi, R., 1974, "A Standardized Procedure for the Production of Correlations in the Form of a Common Empirical Equation," *Industrial and Engineering Chemistry, Fundamentals*, Vol. 13, pp. 39–44.

Churchill, S. W., 1983, "The Development of Theoretically Based Correlations for Heat and Mass Transfer," *Latin American Journal of Heat and Mass Transfer*, Vol. 7, pp. 207–229.

Dasmahapatra, J. K., and Raja Rao, M., 1991, "Augmentation of Tube Side Heat Transfer to Power Law Fluids in Laminar Flow by Means of Twisted Tape Inserts," *Experimental Heat Transfer, Fluid Mechanics, and Thermodynamics 1991*, J. F. Keffer et al., eds., Elsevier Science Publishing, New York, pp. 661–667.

Date, A. W., and Singham, J. R., 1972, "Numerical Prediction of Friction and Heat Transfer Characteristics of Fully Developed Laminar Flow in Tubes Containing Twisted Tapes," ASME Paper No. 72-HT-17.

Date, A. W., 1974, "Prediction of Fully-Developed Flow in a Tube Containing a Twisted-Tape," *International Journal of Heat and Mass Transfer*, Vol. 17, pp. 845–859.

Donevski, B., and Kulesza, J., 1978, "Resistance Coefficients for Laminar and Turbulent Flow in Swirling Ducts," *Archiwum Termodynamiki i Spalania*, Vol. 9, No. 3, pp. 497–506.

Donevski, B., Plocek, M., Kulesza, J., and Sasic, M., 1990, "Analysis of Tubeside Laminar and Turbulent Flow Heat Transfer With Twisted Tape Inserts," *Heat Transfer Enhancement and Energy Conservation*, S.-J. Deng et al., eds., Hemisphere Pubishing, New York, pp. 175–185.

DuPlessis, J. P., and Kröger, D. G., 1984, "Friction Factor Prediction for Fully Developed Laminar Twisted-Tape Flow," *International Journal of Heat and Mass Transfer*, Vol. 27, pp. 2095–2100.

DuPlessis, J. P., and Kröger, D. G., 1987, "Heat Transfer Correlation for Thermally Developing Laminar Flow in a Smooth Tube With a Twisted-Tape Insert," *International Journal of Heat and Mass Transfer*, Vol. 30, pp. 509–515.

Gutstein, M. U., Converse, G. L., and Peterson, J. R., 1970, "Theoretical Analysis and Measurement of Single-Phase Pressure Losses and Heat Transfer for Helical Flow in a Tube," NASA Technical Note D-6097, National Aeronautics and Space Administration, Washington, DC.

Hong, S. W., and Bergles, A. E., 1976, "Augmentation of Laminar Flow Heat Transfer in Tubes by Means of Twisted-Tape Inserts," ASME JOURNAL OF HEAT TRANSFER, Vol. 98, pp. 251–256.

Koch, R., 1958, "Druckverlust und Wärmeübergang bei Verwirbelter Strömung," *VDI-Forschungsheft 469*, Series B, Vol. 24, pp. 1–44.

Lecjaks, Z., Machač, I., and Šir, J., 1984a, "Druckverlust bei der Strömung einer Flüssigkeit durch ein Rohr mit Schraubeneinbauten," *Chemical Engineering and Processing*, Vol. 18, pp. 67–72; also see English translation as "Pressure Loss in Fluids Flowing in Pipes Equipped With Helical Screws," *International Chemical Engineering*, Vol. 27, 1987, pp. 205–209.

Lecjaks, Z., Machač, I., and Šir, J., 1984b, "Wärmeübertragung bei der Strömung Newton'scher Flüssigkeiten in Rohren mit Schraubeneinheiten," *Chemical Engineering and Processing*, Vol. 18, pp. 129–136; also see English translation as "Heat Transfer to a Newtonian Liquid Flowing Through a Tube With an Internal Helical Element," *International Chemical Engineering*, Vol. 27, 1987, pp. 210–217.

Lopina, R. F., and Bergles, A. E., 1969, "Heat Transfer and Pressure Drop in Tape Generated Swirl Flow of Single-Phase Water," ASME JOURNAL OF HEAT TRANSFER, Vol. 91, pp. 434–442.

Manglik, R. M., and Bergles, A. E., 1987, "A Correlation for Laminar Flow Enhanced Heat Transfer in Uniform Wall Temperature Circular Tubes With Twisted-Tape Inserts," *Advances in Enhanced Heat Transfer—1987*, ASME HTD-Vol. 68, New York, pp. 19–25.

Manglik, R. M., Bergles, A. E., and Joshi, S. D., 1988, "Augmentation of Heat Transfer to Laminar Flow of Non-Newtonian Fluids in Uniformly Heated Tubes With Twisted-Tape Inserts," *Experimental Heat Transfer, Fluid Mechanics and Thermodynamics 1988*, R. K. Shah et al., eds., Elsevier Science Publishing, New York, pp. 676–684.

Manglik, R. M., 1991, "Heat Transfer "Heat Transfer Enhancement of Intube Flows in Process Heat Exchangers by Means of Twisted-Tape Inserts," Ph.D. thesis, Department of Mechanical Engineering, Aeronautical Engineering and Mechanics, Rensselaer Polytechnic Institute, Troy, NY.

Manglik, R. M., and Bergles, A. E., 1992, "Heat Transfer Enhancement and Pressure Drop in Viscous Liquid Flows in Isothermal Tubes With Twisted-Tape Inserts," *Wärme- und Stoffübertragung*, Vol. 27, pp. 249–257.

Manglik, R. M., and Bergles, A. E., 1993, "Heat Transfer and Pressure Drop Correlations for Twisted-Tape Inserts in Isothermal Tubes: Part II—Transition and Turbulent Flows," ASME JOURNAL OF HEAT TRANSFER, Vol. 115, this issue, pp. 890–896.

Marner, W. J., and Bergles, A. E., 1978, "Augmentation of Tubeside Laminar Flow Heat Transfer by Means of Twisted-Tape Inserts, Static-Mixer Inserts, and Internally Finned Tubes," *Heat Transfer 1978*, Hemisphere Publishing, Washington, DC, Vol. 2, pp. 583–588.

Marner, W. J., and Bergles, A. E., 1989, "Augmentation of Highly Viscous Laminar Heat Transfer Inside Tubes With Constant Wall Temperature," *Experimental Thermal and Fluid Sciences*, Vol. 2, pp. 252–267.

Mori, Y., and Nakayama, W., 1967, "Forced Convective Heat Transfer in a Straight Pipe Rotating Around a Parallel Axis (1st Report, Laminar Region)," *International Journal of Heat and Mass Transfer*, Vol. 10, pp. 1179–1194.

Morton, B. R., 1959, "Laminar Convection in Uniformly Heated Horizontal Pipes at Low Rayleigh Numbers," *Quarterly Journal of Mechanics and Applied Mathematics*, Vol. 12, pp. 410–420.

Penney, W. R., 1965, "The Spiralator—Initial Tests and Correlations," AIChE Paper No. 16 for Eighth National Heat Transfer Conference, Los Angeles, CA.

Prusa, J., and Yao, L. S., 1982, "Numerical Solution for Fully Developed Flow in Heated Curved Tubes," *Journal of Fluid Mechanics*, Vol. 123, pp. 503–522.

Royds, R., 1921, *Heat Transmission by Radiation, Conduction, and Convection*, 1st ed., Constable and Co., London, United Kingdom, pp. 191–201.

Saha, S. K., Gaitonde, U. N., and Date, A. W., 1989, "Heat Transfer and Pressure Drop Characteristics of Laminar Flow in Circular Tube Fitted With Regularly Spaced Twisted-Tape Elements," *Experimental Thermal and Fluid Science*, Vol. 2, pp. 310–322.

Seymour, E. V., 1966, "Fluid Flow Through Tubes Containing Twisted Tapes," *The Engineer*, Vol. 222, pp. 634–642.

Shah, R. K., and London, A. L., 1978, *Laminar Flow Forced Convection in Ducts*, Supplement 1, Advances in Heat Transfer, Academic Press, New York.

Smithberg, E., and Landis, F., 1964, "Friction and Forced Convection Heat Transfer Characteristics in Tubes With Twisted Tape Swirl Generators," ASME JOURNAL OF HEAT TRANSFER, Vol. 86, pp. 39–49.

Watanabe, K., Taira, T., and Mori, Y., 1983, "Heat Transfer Augmentation in Tubular Flow by Twisted Tapes at High Temperatures and Optimum Performance," *Heat Transfer—Japanese Research*, Vol. 12, No. 3, pp. 1–31.

Whitham, J. M., 1896, "The Effect of Retarders in Fire Tubes of Steam Boilers," *Street Railway Journal*, Vol. 12, No. 6, p. 374.

Heat Transfer and Pressure Drop Correlations for Twisted-Tape Inserts in Isothermal Tubes: Part II—Transition and Turbulent Flows

R. M. Manglik[1]
Mem. ASME

A. E. Bergles
Fellow ASME

Heat Transfer Laboratory,
Rensselaer Polytechnic Institute,
Troy, NY 12180-3590

Thermal-hydraulic design correlations are developed to predict isothermal f *and Nu for in-tube, turbulent flows with twisted-tape inserts. Experimental data taken for water and ethylene glycol, with* $y = 3.0$, *4.5, and 6.0, are analyzed, and various mechanisms attributed to twisted tapes are identified. Tube blockage and tape-induced vortex mixing are the dominant phenomena that result in increased heat transfer and pressure drop; for loose- to snug-fitting tapes, the fin effects are insignificant. The limiting case of a straight tape insert correlates with the hydraulic-diameter-based smooth tube equation. Tape twist effects are thus isolated by normalizing the data with the asymptotic predictions for* $y = \infty$, *and the swirl effects are found to correlate with Re and 1/y. The validity of the final correlations is verified by comparing the predictions with previously published data, which include both gases and liquids, under heating and cooling conditions and a wide range of tape geometries, thereby establishing a very generalized applicability. Finally, correlations for laminar (presented in the companion Part I paper) and turbulent flows are combined into single, continuous equations. For isothermal* f, *the correlation describes most of the available data for laminar-transition-turbulent flows within* ± 10 *percent. For Nu, however, a family of curves is needed due to the nonunique nature of laminar–turbulent transition.*

Introduction

For almost a century, twisted-tape inserts have been used to enhance heat transfer. With their early beginnings as "retarders"—a name perhaps due to the increased pressure drop, and, hence, flow-retarding characteristics—used in the flueways of fire-tube boilers, today they find many applications. These range from hot-gas flow waste-heat recovery systems, to domestic water heaters, to exchangers for heating/cooling of viscous process liquids. Also, because of the ease with which twisted tapes can be inserted in and removed from tube bundles, they are particularly attractive for retrofit and fouling duties. In recent times, the focus on energy conservation and abatement of environmental degradation has generated renewed interest in the use of twisted tapes as passive enhancement devices. However, to exploit their potential industrial usage fully, reliable and generalized equations for predicting heat transfer coefficients and friction factors are warranted.

Most of the early research on twisted-tape usage was conducted with turbulent flows of air and water (for example, Royds, 1921; Kirov, 1949; Koch, 1958; Gambill and Bundy, 1963; Smithberg and Landis, 1964; Lopina and Bergles, 1969; Watanabe et al., 1983). The gas flow work was primarily targeted at fire-tube boiler and hot-water heater applications; water flow investigations were intended to provide single-phase baseline data for the study of flow boiling enhancement. With renewed interest in waste-heat recovery, particularly in corrosive high-temperature environments, the use of twisted-tape inserts in hot gas flows has been investigated (Armstrong and Bergles, 1990; Bergles et al., 1991). In an extensive literature review (Manglik, 1991), more than 30 citations have been identified on twisted-tape inserts in turbulent flows. Also, several correlations for f and Nu have been reported in the literature for such flows (Manglik, 1991). Despite this effort, the reliable prediction of heat transfer and pressure drop characteristics remains a difficult and restrictive process.

The comparison between the various turbulent flow correlations for isothermal f reported in the literature is given in Fig. 1. A twisted tape with $y = 2.5$ and $(\delta/d) = 0.05$ is considered, which is representative of the more severe twist ratio and tape thickness used in practical applications. All parameters are based on empty tube dimensions, as per the recommendations of Marner et al. (1983). As is evident, a very wide envelope represents the predicted isothermal friction factors. The results of Seymour (1966) and Ibragimov et al. (1961), respectively, describe the upper and lower ends of the performance envelope. There is fair agreement between the Lopina and Bergles (1969), and Donevski and Kulesza (1978) correlations, but all others differ significantly.

Friction factors for turbulent flows in ducts with straight tape inserts ($y = \infty$) can be predicted by circular tube correlations, when the parameters are based on the hydraulic diameter. By and large two different equations have been used in the literature: one from Blasius (1913)

$$f_h = 0.0791/\mathrm{Re}_h^{0.25}$$

and one from McAdams (1954)

$$f_h = 0.046/\mathrm{Re}_h^{0.2}$$

These two correlations are also graphed in Fig. 1 to represent the results for circular and semicircular ($y = \infty$, $\delta = 0$) tubes. It

[1]Present address: Department of Mechanical, Industrial, and Nuclear Engineering, University of Cincinnati, Cincinnati, OH 45221-0072.

Contributed by the Heat Transfer Division and presented at the National Heat Transfer Conference, San Diego, California, August 9–12, 1992. Manuscript received by the Heat Transfer Division July 1992; revision received March 1993. Keywords: Augmentation and Enhancement, Forced Convection, Heat Exchangers. Associate Technical Editor: T. W. Simon.

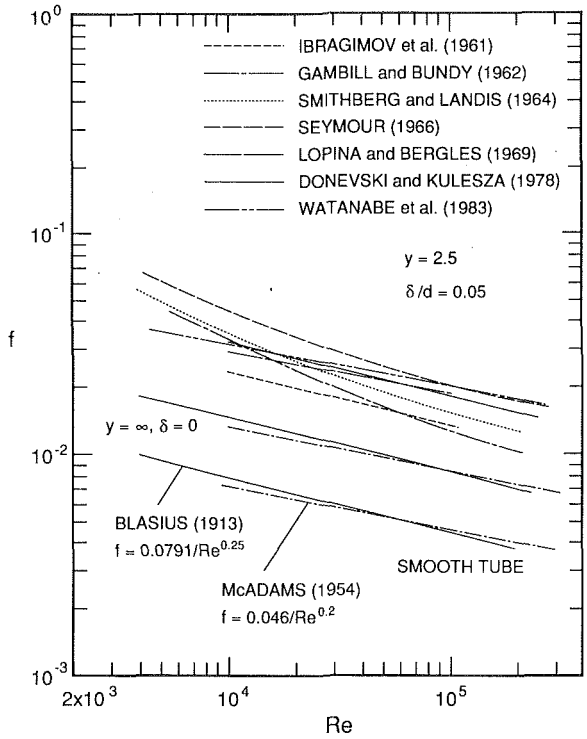

Fig. 1 Comparison of isothermal friction factor correlations for turbulent flows in circular tubes with twisted-tape inserts

is evident that considerably higher friction factors are obtained with a twisted-tape insert having $y = 2.5$, $(\delta/d) = 0.05$; in general, as y decreases, the friction factor increases for a given flow rate. To account for this behavior, various investigators have devised different strategies but there is no consensus among them. As in the case of laminar flows (Manglik and Bergles, 1993), varying expressions of y have been used to correlate the swirl flow effects, namely, $1/y^{0.406}$, $1/y$, $1/y^{1.31}$, $1/y^{1.61}$, $1/y^4$, and the wall curvature, K_c; in most instances, these forms are the results of multiple-variable, regression-analysis, curve fits. The exceptions are the implicit, semi-analytical equations of Smithberg and Landis (1964), Migai (1966), and Donevski and Kulesza (1980).

A large number of correlations for Nusselt numbers in turbulent flows with twisted-tape inserts have been reported in the literature (Manglik, 1991). Because additional parameters are involved in this case, the various correlations are compared on the basis of the following:

$$y = 2.5,\ (\delta/d) = 0.05,\ (L/d) = 150$$

$$\text{Water: } \mathrm{Pr} = 5.2,\ \beta\Delta T_w = 0.02$$

$$\text{Air: } \mathrm{Pr} = 0.71,\ \beta\Delta T_w = 0.20$$

For these conditions, which represent typical operating conditions, the predicted heat transfer performances are graphically presented in Figs. 2 and 3, respectively, for water and air. It is seen from Fig. 2 that there is fair agreement between the results of Smithberg and Landis (1964), Lopina and Bergles (1969), Dižius et al. (1980), and Donevski et al. (1990), while the Ibragimov et al. (1961) correlation underpredicts the performance considerably. For air flows, however, a relatively wider performance envelope is seen in Fig. 3. While there is some agreement among the Smithberg and Landis (1964), Watanabe et al. (1983), and Donevski et al. (1990) correlations, the equation given by Kidd (1969) overpredicts the performance for most flow rates.

In their efforts to develop mechanistic models, Thorsen and Landis (1968) and Lopina and Bergles (1969) have included a "thermal centrifugal convection" term in their correlations, in addition to a term accounting for twist ratio effects; Gambill and Bundy (1963) have proposed that the centrifugal convection term alone is sufficient to correlate turbulent swirl-flow contribution. This term is devised by replacing the acceleration due to gravity, g, in the Grashof number with the centrifugal acceleration, a_c, due to the tape-induced swirl flow

$$a_c = (\pi^2/2d)\,(V_a/y)^2 \tag{1}$$

where V_a is the axial velocity. The resulting expression for swirl Grashof number, Gr_s, is given by

$$\mathrm{Gr}_s = 0.5\pi^2(\beta_f \Delta T_w)(\mathrm{Re}_h/y)^2(d_h/d) \tag{2}$$

Nomenclature

a_c = centrifugal acceleration, Eq. (1), m/s^2
A_c = axial flow cross-sectional area $= (\pi d^2/4) - \delta d$, m^2
A_o = empty tube flow cross-sectional area $= \pi d^2/4$, m^2
c_p = specific heat at constant pressure, J/kg•K
d = tube inside diameter, m
d_h = hydraulic diameter $= 4A_c/P_w$, m
f = Fanning friction factor
f_{sw} = swirl flow friction factor $= f(L/L_s)\,(V_o/V_s)^2$
g = gravitational acceleration, m/s^2
Gr = Grashof number $= g\rho^2 d^3 \beta \Delta T_w/\mu^2$
Gr_s = Grashof number based on swirl acceleration, Eq. (2)
h = heat transfer coefficient, W/m^2•K
H = 180 deg twist pitch, m
k = fluid thermal conductivity, W/m•K
K_c = dimensionless wall curvature, Eq. (3)
L = axial length, m
L_s = maximum helical flow length $= L[1 + (\pi/2y)^2]^{1/2}$, m
$\dot{m}$ = mass flow rate, kg/s
Nu = length averaged mean Nusselt number $= hd/k$
P_w = wetted perimeter, m
Pr = Prandtl number $= \mu c_p/k$
Ra = Rayleigh number $= \mathrm{Gr}\cdot\mathrm{Pr}$
Re = Reynolds number based on empty tube dimensions $= \rho V_o d/\mu$
Re_{sw} = Reynolds number based on swirl velocity $= \rho V_s d/\mu$
Sw = dimensionless swirl parameter $= \mathrm{Re}_{sw}/\sqrt{y}$
T = fluid temperature, °C or K
ΔT_w = wall-to-bulk fluid temperature difference, K
V_a = mean axial velocity $= \dot{m}/\rho A_c$, m/s
V_o = mean velocity based on empty tube diameter $= \dot{m}/\rho A_o$, m/s
V_s = actual swirl velocity at tube wall $= V_a[1 + (\pi/2y)^2]^{1/2}$, m/s
y = twist ratio $= H/d$
β = coefficient of isobaric thermal expansion $= -(\partial\rho/\partial T)_p/\rho$, K^{-1}
δ = thickness of twisted tape, m
μ = fluid dynamic viscosity, kg/m•s
ρ = fluid density, kg/m^3

Subscripts

b = at bulk fluid temperature
cp = at constant fluid properties
cr = critical value
f = at mean film temperature; $T_f = (T_w + T_b)/2$
h = based on hydraulic diameter and mean axial flow velocity
m = mean or average
sw = at swirl flow conditions
w = tube wall

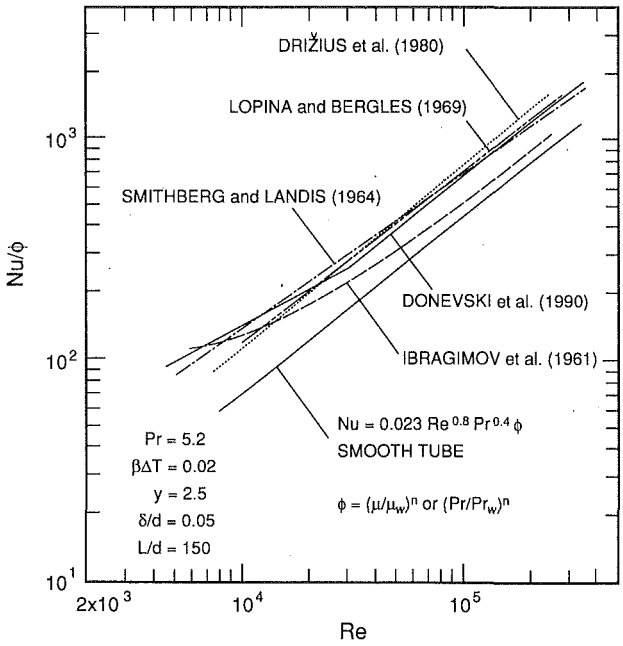

Fig. 2 Heat transfer in tubeside turbulent flows of water with a twisted-tape insert

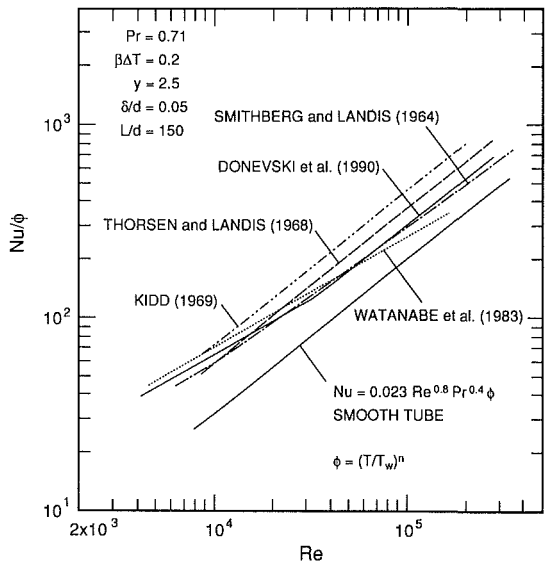

Fig. 3 Heat transfer in tubeside turbulent flows of air with a twisted-tape insert

where β_f is evaluated at the film temperature. The contention here is that the buoyancy force is augmented by the swirl acceleration. However, in forced convective smooth tube flows, buoyancy-driven circulation has an effect only when $(Gr/Re^2) \gg 1$. If this scale is extended to twisted-tape flows, it follows that $Gr_s \gg Re_h^2$ should hold good for any significant centrifugal convection. In fact, Thorsen and Landis (1968) have correlated these effects by the term $(1 \pm 0.25\sqrt{Gr_s}/Re_h)$. However, for $y = 2.5$ and typical water flow conditions (as per Fig. 11 in the Lopina and Bergles paper),

$$(Gr_s/Re_h^2) = 0.5\beta\Delta T_w(\pi/y)^2(d_h/d) = 0.01$$

which suggests that centrifugal convection does not significantly influence the heat transfer. The correlation term of Thorsen and Landis (1968), $(1 + 0.25\sqrt{Gr_s}/Re_h) = 1.025$, accounts for only 2.5 percent of the total enhanced heat transfer due to twisted-tape inserts under typical heating conditions. In the case of Lopina and Bergles (1969), $Pr \cdot Gr_s$ was used as

Table 1 Fluid property correction factor for turbulent flow heat transfer with twisted-tape inserts: liquids: $(Nu / Nu_{cp}) = (\mu_b / \mu_w)^n$ or $(Pr_b / Pr_w)^n$; gases: $(Nu / Nu_{cp}) = (T_b / T_w)^m$

Investigator(s)	n	m	Flow conditions
Ibragimov et al. (1961)†	0.25	–	water heating
Smithberg and Landis (1964)‡	0.36	0.575	heating of water and air
Kidd (1968)	–	0.70	heating of Nitrogen
Thorsen and Landis (1968)	–	0.32	air heating
	–	0.10	air cooling
Drižius et al. (1980)	0.06	–	heating of water
Watanabe et al. (1983)	–	0.50	air heating
Junkhan et al. (1985)*	–	0.45	cooling of air
Armstrong and Bergles (1990)*	–	0.45	heating of air

†suggest using Prandtl number ratio instead of viscosity ratio.
‡based on the recommendations of Kays and London (1955).
*use smooth tube correction factor given by Gnielinski (1976).

the correlating parameter and it accounted for roughly 10 percent of the enhancement; for cooling, this was completely excluded. Clearly, swirl flow effects have not been adequately accounted for in these correlations, and Gr_s is an inappropriate parameter.

Another prominent feature of the heat transfer correlations for turbulent flows is the lack of consensus on the variable property correction ratio. Generally, the viscosity ratio, $(\mu_b/\mu_w)^n$, is used for liquids and a temperature ratio, $(T_b/T_w)^m$, for gases. Many different values for the exponents n and m have been used in the literature, and these are tabulated in Table 1. This is not surprising, given the complexity of the flow situation and considering that there is no unanimity in the literature regarding these exponents for turbulent flows in smooth tubes (Manglik, 1991). In most cases, they are somewhat arbitrarily chosen, and few experiments have been performed with both heating and cooling of the test fluid, with other conditions being the same, to support the recommended correction factor. Also, as seen from Table 1, many investigators have simply used the prevailing correction factor at that time for smooth tube flows. In the absence of any definitive recommendations, such a strategy would be adequate for most practical design purposes.

Furthermore, as in the case of turbulent flow friction factors, the heat transfer for a straight tape insert, $y = \infty$, can be predicted by smooth tube correlations of the form: $Nu_h = CRe_h^a Pr^b$. However, even though the Re number exponent has been taken as $a = 0.8$ in many instances in the literature, several different values for C and the Prandtl number exponent b have been used; $C = 0.021$, 0.023, and 0.024, and $b = 1/3$, 0.4, and 0.43. A detailed evaluation and a listing of turbulent flow correlations for twisted-tape inserts are given by Manglik (1991). In any event, the differences are not significant and any such log-linear form of smooth tube correlation, based on the hydraulic diameter of the tube with a straight tape insert, would suffice.

It is evident that the correlations reported in the literature present a very wide performance envelope for the predictions for any given flow condition and tape geometry. The majority of them can only be applied to the restricted range of the databases on which they have been developed. The comparison with additional data acquired in the present study (see Manglik, 1991, for details) further demonstrates the inadequacy of these equations. In most instances, curve fits of simple relationships through sparse empirical data have been used. Practical applications, however, require generalized correlations that can be used to design heat exchangers for different fluids, tape geometries, and flow conditions. The development of such thermal-hydraulic tools has been addressed in the present study.

Based on the identification of the different enhancement mechanisms, correlations for predicting f and Nu in turbulent flows with twisted-tape inserts are devised. Their generalized applicability is verified by comparing the predictions with previously published data for both heating and cooling conditions. Finally, the turbulent flow equations are combined with the laminar flow correlations, given in the companion paper (Manglik and Bergles, 1993), to provide design guidelines that cover a wide range of flows corresponding to the laminar, transition, and turbulent regimes. The data for the present study have been reported by Manglik and Bergles (1992) along with experimental details and error analysis.

Turbulent Flow Correlations

The transition to turbulent flow is generally characterized by fluctuating velocities and flow instabilities. However, in the case of twisted-tape inserts, the presence of centrifugal forces due to the swirl motion tends to suppress this. In fact, there is a competing effect where the secondary circulation dampens the turbulent pulsations, thereby delaying transition (Manglik and Bergles, 1993); with higher flow rates, however, swirl effects diminish. Seymour (1966), Donevski and Kulesza (1978), Watanabe et al. (1983), and Nair (1986) have also reported delayed transition to turbulent flows with twisted-tape inserts. Watanabe et al. (1983) and Donevski and Kulesza (1978) have given correlations to predict the critical Reynolds number. However, there is no agreement between the two, and the predictions differ by an order of magnitude for typical conditions; for $y=3.0$ and $(\delta/d)=0.023$, Watanabe et al. (1983) predict $\mathrm{Re}_{cr}=6.36\times10^3$ whereas Donevski and Kulesza (1978) give $\mathrm{Re}_{cr}=3.43\times10^4$. In both cases, Re_{cr} is simply the intersection of their respective laminar and turbulent flow correlations, and it is not based on any fundamental assessment of the flow characteristics. Nevertheless, on the basis of the phenomenological flow regime maps given in the companion paper (Manglik and Bergles, 1993), flow rates with $\mathrm{Re}\geq10^4$ can be considered to be in the fully developed, turbulent flow regime (Region IV of the flow regime maps). Even though in some instances, depending upon the twist ratio, turbulent conditions might exist at lower values of Re, this cutoff value is reasonable and adequate for the conditions in the present study. Furthermore, as shown later, the precise estimation of Re_{cr} is not necessary.

Isothermal Friction Factor. The influence of the twist ratio, y, on turbulent flow friction factors is quite different from that in laminar, swirl flow situations, described by Manglik and Bergles (1993); the swirl parameter, Sw, does not appear to be applicable in the turbulent regime. In some previous studies (Thorsen and Landis, 1968; Watanabe et al., 1983), an attempt has been made to correlate the pressure drop with the curvature of the helical flow path near the tube wall. The wall curvature in twisted-tape flows can be expressed in dimensionless form as

$$K_c=(\overline{K}_c d/2)=(1+(2y/\pi)^2)^{-1} \tag{3}$$

where $\overline{K}_c$ is the dimensional curvature expressed in m^{-1}. The inadequacy of such a scheme is apparent in Fig. 4, where the average friction factor ratio, $(f/f_{y=\infty})$, is plotted against K_c. Included in the figure are the available data of other investigators, and a correlation proposed by Watanabe et al. (1983). A nonlinear regression fit to the data acquired in the present study (see Manglik and Bergles, 1992, for experimental details) gives

$$(f/f_{y=\infty})=1+2.06(1+(2y/\pi)^2)^{-0.74} \tag{4}$$

where

$$f_{y=\infty}=0.0791\ \mathrm{Re}^{-0.25}\left(\frac{\pi}{\pi-4\delta/d}\right)^{1.75}\left(\frac{\pi+2-2\delta/d}{\pi-4\delta/d}\right)^{1.25} \tag{5}$$

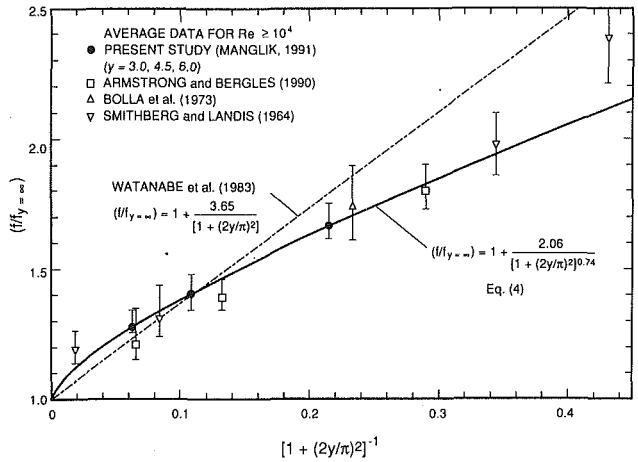

Fig. 4 Effect of the wall curvature of the helical path on turbulent flow friction factor

As seen in Fig. 4, there is considerable disagreement between the predictions of Eq. (4), the Watanabe et al. (1983) correlation, and the experimental data reported by other investigators, particularly for very small wall curvature (large y) and very large curvature (small y) cases. Conceptually, in the limit $y\to0$, the pressure drop is such that $f\to\infty$; however, the two equations give finite values.

An alternative scheme is to correlate $(f/f_{y=\infty})$ with $(1/y)$, as shown in Fig. 5. Employing a nonlinear regression fit to the present study's data (Manglik, 1991), the following equation is obtained:

$$(f/f_{y=\infty})=1+2.752/y^{1.29} \tag{6}$$

This has a correlation coefficient of 0.97 and it can be rewritten as

$$f=\frac{0.0791}{\mathrm{Re}^{0.25}}\left(\frac{\pi}{\pi-4\delta/d}\right)^{1.75}\left(\frac{\pi+2-2\delta/d}{\pi-4\delta/d}\right)^{1.25}\left(1+\frac{2.752}{y^{1.29}}\right) \tag{7}$$

It is seen from Fig. 5 that Eq. (7) describes within ±5 percent most of the available data in the literature. Also given in this figure are the predictions from the correlations reported by Lopina and Bergles (1969), Donevski and Kulesza (1978), and Watanabe et al. (1983). For the primary range of twist ratios employed by these investigators, Eq. (7) is in very good agreement with their predictions. Clearly, Eq. (7) is a more generalized correlation, which covers a broad database of available empirical data and, as such, is recommended for design purposes.[2]

Mean Nusselt Number. To devise a generalized correlation for turbulent flow heat transfer with twisted-tape inserts, a strategy similar to that used for friction factor was employed. This is consistent with the fundamental premise of the heat and momentum transfer analogy. In Fig. 6, the average Nusselt number ratios, $(\mathrm{Nu}/\mathrm{Nu}_{y=\infty})$, for $\mathrm{Re}\geq10^4$ are graphed with $(1/y)$. In this case, a linear regression analysis of the present study's data (Manglik, 1991) gives the straight-line fit

$$(\mathrm{Nu}/\mathrm{Nu}_{y=\infty})=[1+0.769/y] \tag{8}$$

The Nusselt number for a straight tape insert ($y=\infty$) is given by

$$\mathrm{Nu}_{y=\infty}=0.023\ \mathrm{Re}^{0.8}\mathrm{Pr}^{0.4}\left(\frac{\pi}{\pi-4\delta/d}\right)^{0.8}\left(\frac{\pi+2-2\delta/d}{\pi-4\delta/d}\right)^{0.2}\phi \tag{9}$$

[2] In the case of diabatic friction factors, though not considered here, reasonable design estimates may be made for heating/cooling by using the viscosity (or temperature) ratio correction for smooth tube flows along with the isothermal predictions of Eq. (6).

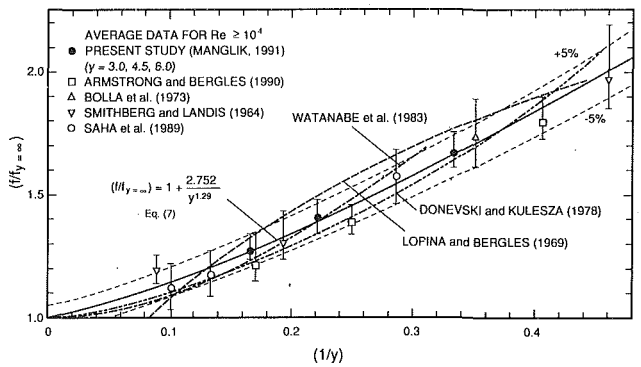

Fig. 5 Correlation of turbulent flow isothermal friction factors in tubes with twisted-tape inserts

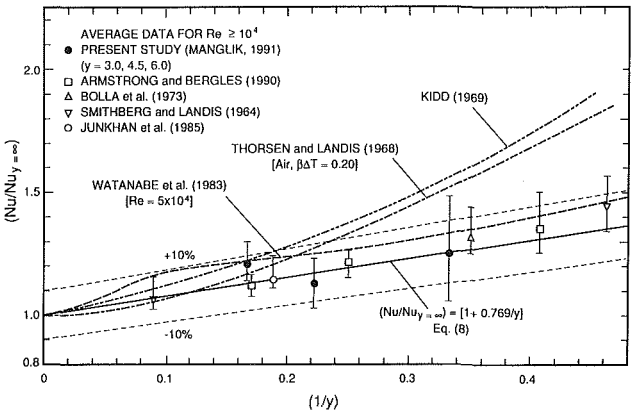

Fig. 6 Correlation of turbulent flow Nusselt numbers in tubes with twisted-tape inserts

where

$$\phi = (\mu_b/\mu_w)^n \text{ or } (T_b/T_w)^m$$

$$n = \begin{cases} 0.18 \text{ for liquid heating} \\ 0.30 \text{ for liquid cooling} \end{cases} \text{ and } m = \begin{cases} 0.45 \text{ for gas heating} \\ 0.15 \text{ for gas cooling} \end{cases}$$

Here the viscosity ratio exponent is the same as that in the ESDU (1967, 1968) correlation for smooth tube flows; such a correction factor normalizes heating and cooling effects rather well in the present study's data (Manglik, 1991). In the case of temperature ratio for gas flows, the exponents have been chosen as the consensus values based on previous results for smooth tube flows (Kays and London, 1955; Petukhov, 1970; Mizushina et al., 1977; Ibrahim and Thomas, 1986). As can be seen from Fig. 6, Eq. (8) predicts the data in this study as well as those of other investigators within ± 10 percent.

In Fig. 6 correlations from Watanabe et al. (1983), Kidd (1969), and Thorsen and Landis (1968) are also graphed. While there is fair agreement with the results of Watanabe et al. (1983), the correlations given by Thorsen and Landis (1968) and Kidd (1969) deviate considerably for small values of y. Donevski et al. (1990) have proposed a correlation that is virtually the same as Eq. (8). In their correlation, the constant in the right-hand-side term in parentheses is 0.761 instead of 0.769 in the present case, and the predicted values are indistinguishable from those of Eq. (8). However, they have proposed a very high Re cutoff for the application of their equation; $\text{Re} \geq 3.43 \times 10^4$ is obtained for the tape with $y = 3.0$ used in the present study, which appears to be a very conservative value. Also, the correlation they give for $\text{Re} \leq 3.43 \times 10^4$ significantly overpredicts the present data (Manglik, 1991). It is, therefore, evident that Eq. (8) gives the more generalized correlation for heat transfer in turbulent swirl flows ($\text{Re} \geq 10^4$).

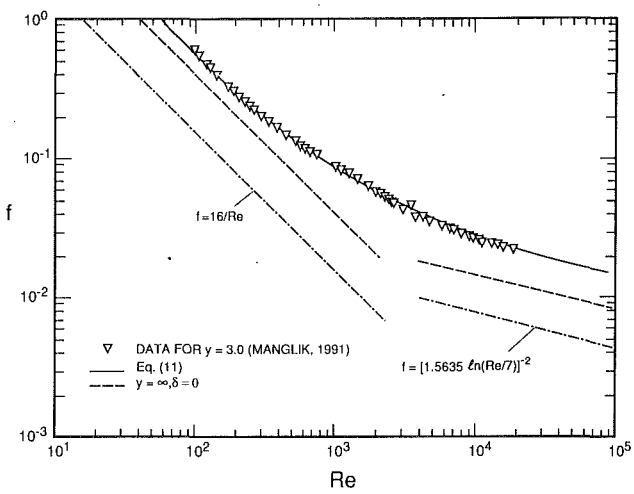

Fig. 7 Comparison of Eq. (11) with isothermal friction factor data for $y = 3.0$

Generalized Correlations for Laminar-Transition-Turbulent Flows

An attempt has been made to combine the correlations for laminar and turbulent flows into single continuous equations, which describe the thermal-hydraulic performance of twisted-tape inserts. This is motivated by the observation that friction factor results in the present study do not exhibit the characteristic discontinuity of the transition region in smooth tube flows. This feature can also be seen in the data reported by Seymour (1966) for a much larger range of twist ratios. In principle, laminar flow represents the asymptote for $\text{Re} \to 0$ and turbulent flow describes the condition when $\text{Re} \to \infty$, and, in the absence of any discontinuity in the intermediate region, the two can be represented by a single curve (or a family of curves, as the case may be).

Isothermal Friction Factor. For the pressure drop characteristics of twisted tapes, the laminar flow asymptote, which represents the limit $\text{Re} \to 0$, is given by the following correlation (see Manglik and Bergles, 1993, for details):

Laminar flow, $\text{Re} \to 0$

$$f_l = \frac{15.767}{\text{Re}} (1 + 10^{-6} Sw^{2.55})^{1/6} (1 + (\pi/2y)^2) \times \left(\frac{\pi + 2 - 2\delta/d}{\pi - 4\delta/d}\right)^2 \left(\frac{\pi}{\pi - 4\delta/d}\right) \quad (10)$$

For the turbulent flow limit, $\text{Re} \to \infty$, the friction factor f_t is described by Eq. (7). Thus, the asymptotic matching of these two limits with the method of Churchill (1983) results in

$$f = (f_l^{10} + f_t^{10})^{0.1} \quad (11)$$

based on the present study's data. This equation, where f_l and f_t are given by Eqs. (10) and (7), respectively, gives a single expression for predicting isothermal friction factors for all flow rates with $\text{Re} > 0$.

The validity of Eq. (11) is verified by Fig. 7, where it is graphed along with the data for $y = 3.0$; the data are described very well by the continuous curve of the correlation. Furthermore, as seen in the scatter plot of Fig. 8, the predictions are within ± 10 percent of experimental data. Besides its precision, this correlation is a very useful design equation as it obviates the need to identify the flow regime. This is an important feature for practical heat exchanger applications, where off-design performance ratings are often required; a single, continuous predictive equation provides the ease of making such calculations.

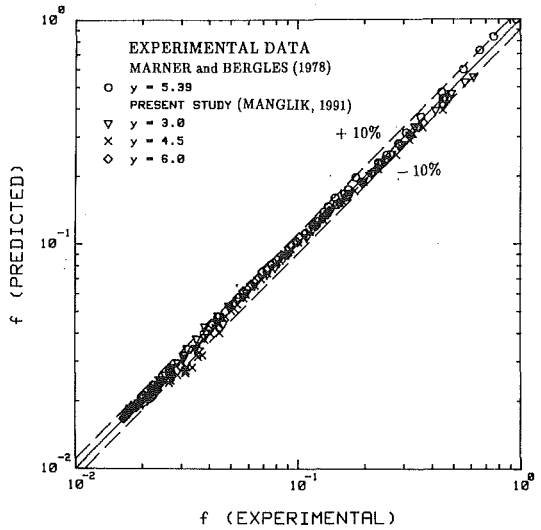

Fig. 8 Comparison of isothermal friction factor predictions from Eq. (11) with experimental data in the laminar, transition, and turbulent flow regimes

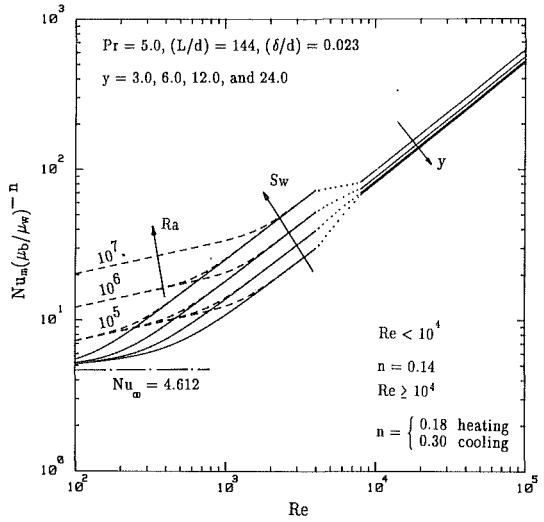

Fig. 9 Heat transfer characteristics in laminar, transition, and turbulent flows in circular tubes with twisted-tape inserts

Mean Nusselt Number. The heat transfer behavior of in-tube flows with twisted-tape inserts appears to be rather complex and different from the hydrodynamic performance. Even though the transition from laminar to turbulent flow is smooth, its effect on the data is influenced by the twist ratio. For example, with $y = 12.0$ the transition is imperceptible and the data follow a continuous, log-linear line; with $y = 3.0$, however, there is a "dip" in the data as turbulent conditions are attained (Manglik, 1991). This behavior is further exemplified in Fig. 9, where Eq. (8) and the laminar flow correlation [see Eq. (17) in the companion paper, Manglik and Bergles (1993), for details] are presented for typical conditions with $y = 3.0$, 6.0, 12.0, and 24.0. It is obvious that instead of a single expression, a family of curves will have to be obtained to represent the results in a continuous manner.

Nair (1986) had encountered a similar situation with heat transfer data for water in an electrically heated tube and tapes having $y = 3.3$ and 4.8. In this case, an attempt was made to derive a single equation for the data with $y = 3.3$. However, the methodology could not be generalized because different forms of expressions are required for each tape; both y and Re have a role in describing the transition behavior. To resolve this problem, a qualitative and quantitative assessment of laminar-turbulent transition needs to be made. This is beyond the scope of the present investigation.

Nevertheless, for design purposes it is recommended that a linear fit can be employed between the laminar and turbulent flow estimates for $Sw > 1400$ and $\mathrm{Re} < 10^4$, respectively. The critical value, $Sw \sim 1400$, for the start of the transition regime is an arbitrary but conservative criterion based on the present study's data; for some twist ratios, laminar swirl flow conditions might prevail for Reynolds number beyond this cutoff. However, despite the ambiguity in identifying the transition behavior, the linear interpolation in the region $Sw > 1400$ and $\mathrm{Re} < 10^4$ will not entail large errors.

Concluding Remarks

The majority of previously reported correlations for predicting isothermal f and Nu in turbulent flows with twisted tapes give a rather wide performance envelope for typical conditions. Also, there is considerable disagreement in the literature on the manner in which the various enhancement mechanisms can be correlated, and curve-fits to sparse data have usually been employed. In order to develop more generalized correlations, experimental data for isothermal f and Nu in turbulent flows of water and ethylene glycol, obtained with twisted-tape inserts having $y = 3.0$, 4.5, and 6.0 in tubes with UWT, are analyzed. Additional data for gas and water flows reported in the literature are also considered.

The increase in heat transfer coefficients, and the concomitant pressure drops, with twisted-tape inserts is found to be strongly influenced by tape-induced vortex motion and higher flow velocity due to the tube blockage. Tape fin effects are negligible for the case of snug- to loose-fitting inserts. Furthermore, there is delayed transition in the presence of swirl flows and the laminar-turbulent transition region is characterized by the turbulent fluctuations being initially suppressed by the centrifugal forces; with higher flow rates, however, turbulent flows with superimposed secondary circulation prevail. For the case of straight tape inserts ($y = \infty$), correlations for smooth tubes can be employed with f, Nu, and Re based on the hydraulic diameter of the partitioned duct. Consequently, tape twist effects are modeled by the functional relationships of the form $(f/f_{y=\infty})$ and $(\mathrm{Nu}/\mathrm{Nu}_{y=\infty}) = \phi(1/y)$, and the final correlations are given in Eqs. (7) and (8), respectively. There is excellent agreement between the predictions of these equations and the data in the present study, as well as those reported in the literature for gases and liquids. This verifies their applicability over a very broad range of operating conditions, covering different fluids and tape-twist ratios.

Finally, in the case of friction factors, the laminar and turbulent flow equations are combined into a single generalized correlation, given by Eq. (11), to predict continuously the performance for laminar, transition, and turbulent flow conditions. However, in the case of heat transfer, a family of curves, rather than a single expression, is needed to describe the transition flow behavior; in this region, the heat transfer characteristics are influenced by both Re and y. A linear interpolation between the predictions of the laminar flow correlation (presented in the companion paper, Manglik and Bergles, 1993) and Eq. (8), in the region $Sw > 1400 - \mathrm{Re} < 10^4$, can be used with reasonable accuracy. These correlations and design guidelines are of considerable importance to practical heat exchanger applications; they obviate the need of identifying the flow regime and readily lend themselves to off-design performance ratings and the optimization of thermal-hydraulic characteristics of twisted-tape inserts.

Acknowledgments

This study was supported in part by Brown Fintube Co., Houston, TX, and the advice of Mr. R. Shilling is much appreciated.

References

Armstrong, R. D., and Bergles, A. E., 1990, "A Study of Enhanced Ceramic Tubes for High Temperature Waste Heat Recovery," *Heat Transfer 1990*, Vol. 4, Hemisphere Publishing, New York, pp. 21–26.

Bergles, A. E., Jensen, M. K., Somerscales, E. F. C., and Manglik, R. M., 1991, "Literature Review of Heat Transfer Enhancement Technology for Heat Exchangers in Gas-Fired Applications," Topical Technical Report No. GRI 91-0146, Gas Research Institute, Chicago, IL.

Blasius, H., 1913, "Das Ähnlichkeitsgesetz bei Reibungsvorgängen in Flussigkeiten," *Forschg. Arb. Ing.-Wes.*, No. 131, Berlin.

Bolla, G., De Giorgio, G., and Pedrocchi, E., 1973, "Heat Transfer and Pressure Drop Comparison in Tubes With Transverse Ribs and With Twisted Tapes," *Energia Nucleare*, Vol. 20, pp. 604–613.

Churchill, S. W., 1983, "The Development of Theoretically Based Correlations for Heat and Mass Transfer," *Latin American Journal of Heat and Mass Transfer*, Vol. 7, pp. 207–229.

Donevski, B., and Kulesza, J., 1978, "Resistance Coefficients for Laminar and Turbulent Flow in Swirling Ducts," *Archiwum Termodynamiki i Spalania*, Vol. 9, No. 3, pp. 497–506 [in Polish].

Donevski, B., and Kulesza, J., 1980, "Friction in Isothermal Turbulent Flow in Tubes With Twisted Tapes," *Zeszyty Naukowe Politechniki Lodzkiej*, Mechanika, Vol. 58, No. 358, pp. 5–25 [in Polish].

Donevski, B., Plocek, M., Kulesza, J., and Sasic, M., 1990, "Analysis of Tubeside Laminar and Turbulent Flow Heat Transfer With Twisted Tape Inserts," *Heat Transfer Enhancement and Energy Conservation*, S.-J. Deng et al., eds., Hemisphere Publishing, New York, pp. 175–185.

Dižius, M.-R. M., Shkema, R. K., and Shlančiauskas, A. A., 1980, "Heat Transfer in a Twisted Stream of Water in a Tube," *International Chemical Engineering*, Vol. 20, pp. 486–489.

ESDU, 1967, "Forced Convection Heat Transfer in Circular Tubes, Part I: Correlations for Fully-Developed Turbulent Flow—Their Scope and Limitations," Data Item No. 67016, ESDU International, London, United Kingdom (formerly Engineering Science Data Unit).

ESDU, 1968, "Forced Convection Heat Transfer in Circular Tubes, Part III: Further Data for Turbulent Flow," Data Item No. 68007, ESDU International, London, United Kingdom.

Gambill, W. R., and Bundy R. D., 1962, "An Evaluation of the Present Status of Swirl Flow Heat Transfer," ASME Paper No. 62-HT-42.

Gambill, W. R., and Bundy R. D., 1963, "High-Flux Heat Transfer Characteristics of Pure Ethylene Glycol in Axial and Swirl Flow," *AIChE Journal*, Vol. 9, pp. 55–59.

Gnielinski, V., 1976, "New Equations for Heat and Mass Transfer in Turbulent Pipe and Channel Flow," *International Chemical Engineering*, Vol. 16, No. 2, pp. 359–368; originally in *Forschung im Ingenieurwesen*, Vol. 41, No. 1, 1975, pp. 8–16 [in German].

Ibragimov, M. H., Nomofelov, E. V., and Subbotin, V. I., 1961, "Heat Transfer and Hydraulic Resistance With Swirl-Type Motion of Liquid in Pipes," *Teploenergetika*, Vol. 8, No. 7, pp. 57–60.

Ibrahim, M. B., and Thomas, L. C., 1986, "Turbulent Variable Property Gas Flows," *Chemical Engineering Communications*, Vol. 42, pp. 315–332.

Junkhan, G. H., Bergles, A. E., Nirmalan, V., and Ravigururajan, T., 1985, "Investigation of Turbulators for Fire Tube Boilers," ASME JOURNAL OF HEAT TRANSFER, Vol. 107, pp. 354–360.

Kays, W. M., and London, A. L., 1955, *Compact Heat Exchangers: A Summary of Basic Heat Transfer and Flow Friction Design Data*, National Press, Palo Alto, CA.

Kidd, G. J., Jr., 1969, "Heat Transfer and Pressure Drop for Nitrogen Flowing in Tubes Containing Twisted Tapes," *AIChE Journal*, Vol. 15, pp. 581–585.

Kirov, N. Y., 1949, "Turbulence Promoters in Boiler Smoke Tubes," *Journal of the Institute of Fuel*, Vol. 22, pp. 192–196.

Koch, R., 1958, "Druckverlust und Wärmeübergang bei Verwirbelter Strömung," *VDI-Forschungsheft 469*, Series B, Vol. 24, pp. 1–44.

Lopina, R. F., and Bergles, A. E., 1969, "Heat Transfer and Pressure Drop in Tape Generated Swirl Flow of Single-Phase Water," ASME JOURNAL OF HEAT TRANSFER, Vol. 91, pp. 434–442.

McAdams, W. H., 1954, *Heat Transmission*, 3rd ed., McGraw-Hill, New York.

Manglik, R. M., 1991, "Heat Transfer Enhancement of Intube Flows in Process Heat Exchangers by Means of Twisted-Tape Inserts," Ph.D. thesis, Department of Mechanical Engineering, Aeronautical Engineering and Mechanics, Rensselaer Polytechnic Institute, Troy, NY.

Manglik, R. M., and Bergles, A. E., 1992, "Heat Transfer Enhancement and Pressure Drop in Viscous Liquid Flows in Isothermal Tubes With Twisted-Tape Inserts," *Wärme- und Stoffübertragung*, Vol. 27, pp. 249–257.

Manglik, R. M., and Bergles, A. E., 1993, "Heat Transfer and Pressure Drop Correlations for Twisted-Tape Inserts in Isothermal Tubes: Part I—Laminar Flows," ASME JOURNAL OF HEAT TRANSFER, Vol. 115, this issue, pp. 881–889.

Marner, W. J., and Bergles, A. E., 1989, "Augmentation of Highly Viscous Laminar Heat Transfer Inside Tubes With Constant Wall Temperature," *Experimental Thermal and Fluid Science*, Vol. 2, pp. 252–267.

Marner, W. J., Bergles, A. E., and Chenoweth, J. M., 1983, "On the Presentation of Performance Data for Enhanced Tubes Used in Shell-and-Tube Heat Exchangers," ASME JOURNAL OF HEAT TRANSFER, Vol. 105, pp. 358–365.

Migai, V. K., 1966, "Friction and Heat Transfer in Twisted Flow Inside a Tube," *Isvestia Akademii Nauk SSSR, Energetika I Transport*, No. 5, pp. 143–151 [in Russian].

Mizushina, G. T., Matsumoto, T., and Yoneda, S., 1977, "The Effect of Large Temperature Difference in the Turbulent Heat and Momentum Transfer in an Air Flow Inside a Circular Tube," *Heat and Mass Transfer Source Book*, Proc. 5th All-Union Conference, Minsk, pp. 34–46.

Nair, R. K., 1986, "Performance of Twisted-Tape Inserts in Laminar and Turbulent Flow," M. S. Thesis, Dept. of Mechanical Engineering, Iowa State University, Ames, IA.

Petukhov, B. S., 1970, "Heat Transfer and Friction in Turbulent Pipe Flow With Variable Physical Properties," *Advances in Heat Transfer*, Vol. 6, Academic Press, New York, pp. 503–564.

Royds, R., 1921, *Heat Transmission by Radiation, Conduction, and Convection*, 1st ed., Constable and Co., London, United Kingdom, pp. 191–201.

Saha, S. K., Gaitondi, U. N., and Date, A. W., 1989, "Heat Transfer and Pressure Drop Characteristics of Laminar Flow in a Circular Tube Fitted With Regularly Spaced Twisted-Tape Elements," *Experimental Thermal and Fluid Science*, Vol. 2, pp. 310–322.

Seymour, E. V., 1966, "Fluid Flow Through Tubes Containing Twisted Tapes," *The Engineer*, Vol. 222, pp. 634–642.

Smithberg, E., and Landis, F., 1964, "Friction and Forced Convection Heat Transfer Characteristics in Tubes With Twisted Tape Swirl Generators," ASME JOURNAL OF HEAT TRANSFER, Vol. 86, pp. 39–49.

Thorsen, R. S., and Landis, F., 1968, "Friction and Heat Transfer Characteristics in Turbulent Swirl Flow Subjected to Large Transverse Temperature Gradients," ASME JOURNAL OF HEAT TRANSFER, Vol. 90, pp. 87–98.

Watanabe, K., Taira, T., and Mori, Y., 1983, "Heat Transfer Augmentation in Tubular Flow by Twisted Tapes at High Temperatures and Optimum Performance," *Heat Transfer—Japanese Research*, Vol. 12, No. 3, pp. 1–31.

The Investigation of Developing Flow and Heat Transfer in a Long Converging Duct

K. R. Mutama

H. Iacovides

Department of Mechanical Engineering, University of Manchester Institute of Science and Technology, Manchester, M60 1QD United Kingdom

The hydrodynamic and thermal development of turbulent boundary layers subjected to streamwise acceleration has been investigated. This was accomplished by obtaining detailed flow and temperature measurements over 52 entrance heights of a converging channel (with one wall heated) and with uniform velocity and temperature profiles at entry. Results are presented for three Reynolds numbers of 4000, 16,000, and 21,000 corresponding to acceleration parameter k levels of 2.31×10^{-6}, 5.78×10^{-7}, and 4.47×10^{-7}, respectively. At acceleration parameter levels of 2.3×10^{-6} the flow behaves in a laminarlike fashion in all respects. Even at an acceleration parameter level of 4.5×10^{-7} the skin friction coefficients and Stanton number values are well below those encountered in parallel channel flow at corresponding Reynolds numbers. The entry region behavior is further complicated by the combined effects of thin inlet boundary layers and streamwise acceleration. These entry effects are perhaps more obvious in the Stanton number development. The well-defined entry conditions make these detailed measurements suitable for turbulence model validation and refinement.

1 Introduction

This work examines the effects of streamwise acceleration on the development of two-dimensional hydrodynamic and thermal boundary layers. Such flows have a broad range of engineering applications. Design criteria for cooled rocket engine thrust chambers, gas turbine blade cascade design, and air intake ducts of high-performance fighter jet aircraft are representative examples.

Early studies of turbulent boundary layers under acceleration were carried out by Launder (1964) who performed boundary layer traverses and determined friction coefficients. Launder observed that toward the end of acceleration the shape factor (H) rose suddenly and the friction coefficient (C_f) decreased. Later investigations included Patel and Head's study (1968), which provided information on axial pressure and velocity profile variation. A significant conclusion was that the distribution of shear stress in the wall region rather than the overall Reynolds number is the important parameter in initiating reverse transition. Morretti and Kays (1965) and Kays et al. (1970) investigated the variation of the heat transfer rate and expressed their results in terms of the Stanton number. Stanton numbers obtained under accelerating conditions were lower than those expected in fully developed thermal turbulent boundary layers. Launder and Lockwood (1969) and subsequently Jones and Launder (1971) carried out theoretical predictions using a two-equation turbulence model. An important finding of these studies was that after the initial stages of rapid development, the thermal boundary layer penetrates progressively farther beyond the velocity boundary layer, causing the Stanton number to decrease significantly. Recently Tanaka et al. (1982) accelerated a fully developed thermal and hydrodynamic boundary layer at Reynolds numbers ranging from 5000 to 14,000. Nusselt numbers measured in the accelerating portion of the flow were lower than without acceleration, suggesting laminarization.

The above studies have shown that turbulent boundary layers subjected to flow acceleration laminarize, and under such conditions the heat transfer characteristics begin to deviate from those usually associated with turbulent flow. This phenomenon is more pronounced at lower Reynolds numbers. The determining parameter proposed by Launder is known as the acceleration parameter k. It is defined as

$$k=\frac{\nu}{U_\infty^2}\frac{dU_\infty}{dx} \tag{1}$$

For a two-dimensional converging duct of angle α, the above definition can be reduced to:

$$k=\frac{\tan\alpha}{\mathrm{Re}} \tag{2}$$

In this case the local bulk velocity is increasing axially because of the reduction in cross-sectional area of the channel and is inversely proportional to the local channel height. Consequently, the Reynolds number, Re, remains constant. According to Launder (1964), when the acceleration parameter value is greater than 2.3×10^{-6}, a two-dimensional boundary layer will eventually revert to laminar conditions.

Boundary layer acceleration affects wall shear stress and wall heat flux rates, in convective heat transfer situations. In order to achieve an improved understanding of flow acceleration effects on wall heat transfer rates, a simultaneous investigation of their hydrodynamic and thermal aspects is necessary.

The present work is an attempt to investigate flow and convective heat transfer development in a long two-dimensional converging channel with uniform entry conditions. This is done by obtaining detailed mappings of both the hydrodynamic and thermal fields for the same flow conditions. Measurements of wall shear stress and wall heat flux rates have also been obtained. The results provide a clearer picture of convective heat transfer in accelerated flows. The study creates a useful set of test data for the validation and further refinement of mathematical models of near-wall turbulence, because the entry conditions are well defined.

2 Experimental Apparatus

The apparatus used in this study was developed originally

Contributed by the Heat Transfer Division for publication in the JOURNAL OF HEAT TRANSFER. Manuscript received by the Heat Transfer Division March 1992; revision received March 1993. Keywords: Flow Transition, Forced Convection, Turbulence. Associate Technical Editor: T. W. Simon.

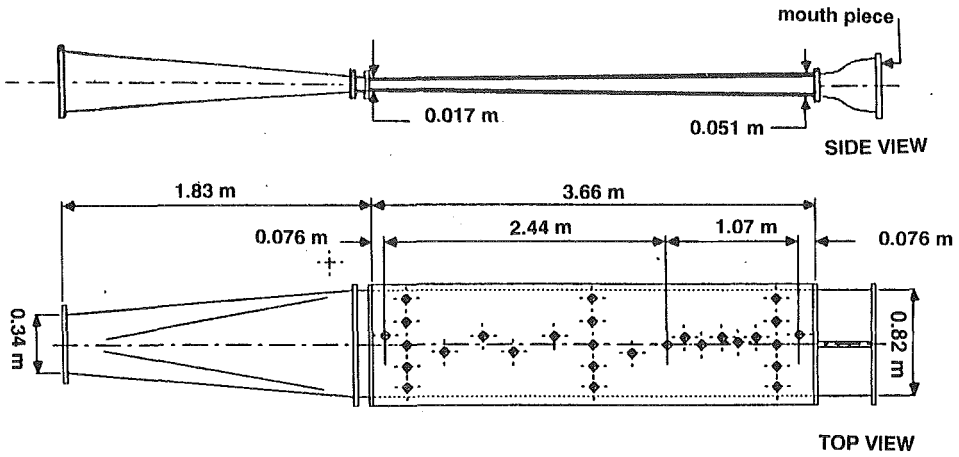

Fig. 1 General arrangement of the duct

by Marriot (1969) for the investigation of flow and heat transfer through a diverging channel. The same apparatus was subsequently used by Ince (1981) among others for the examination of flow and heat transfer in a parallel channel. For this work, the channel was modified into a converging one, as shown in Fig. 1. Over a length of 3.66 m, the channel height, D, is reduced from 51 mm at inlet to 17 mm at exit. The resulting angle of convergence is thus 0.53 deg. In order to ensure that the flow was two-dimensional, the channel is 0.82 m wide compared to its entry height of 0.051 m giving an entry aspect ratio of 1:16. Uniform entry conditions were produced by using a bell-shaped inlet piece of 6:1 contraction ratio and a honeycomb mesh. At the channel exit, a centrifugal single-stage fan was used to draw air through the channel and create the required flow conditions.

Over the first 2.64 m of the channel, the bottom wall was covered with a thin copper layer, which was connected to an electrical power supply. Uniform wall heating could thus be provided to the flow from the lower channel surface.

The upper channel plate had 16 access holes uniformly spaced along the centerline. They served both as static pressure taps and as traversing ports for hot wire and thermocouple probes. Some of these holes were offset with respect to the centerline to minimize flow disturbances arising from irregularities around the holes. As shown in Fig. 1, three extra sets of holes were drilled across the upper channel wall, one set near the inlet, the next set at the middle, and the last near the channel exit. These extra traversing holes were used to check the two dimensionality of the flow.

A layout of the heating element is given in Fig. 2. The heating element, which is a 0.38-mm-thick copper foil, is backed by a 2.2-mm-thick layer of plastic. The foil has been etched to provide an electrical current path 20 mm wide. The copper foil temperature was monitored by a set of 28 thermocouples

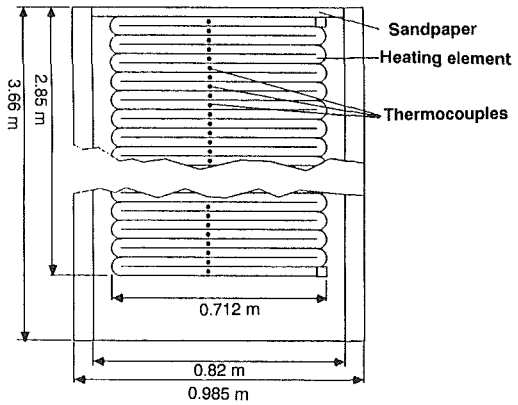

Fig. 2 Duct heating element

soldered along the copper foil's centerline. These thermocouples were connected to a multiswitch box. The electrical resistance of the copper foil, R, was determined by Marriot (1969) as a function of the heating element surface temperature, T_w, to be:

$$R = 1.416(1 + 0.00428(T_w - 23)) \tag{3}$$

3 Instrumentation

Mean and fluctuating velocity measurements were obtained using a 90 deg tungsten DISA probe of 5 μm diameter. The probe signals were processed using a CTA standard anemometer bridge and a linearizer. A Solatron data transfer unit (DTU) transmitted the information to a microcomputer for statistical processing. Velocity traverses were carried out at 12

Nomenclature

U = local velocity
U_B = local bulk velocity
y, Y = distance from bottom plate of channel
y^+ = nondimensional distance = yu_τ/ν
D_x = local channel height
D = entrance channel height
X = axial distance in mm or m
u^+ = nondimensional velocity = u/u_τ
v_τ = frictional velocity = $(\tau_w/\rho)^{1/2}$
τ_w = wall shear stress
ρ = air density
C_p = specific heat capacity at constant pressure
C_f = skin friction coefficient
k = acceleration parameter = $(\nu/U_\infty^2)(dU_\infty/dx)$
ν = kinematic viscosity
Re = Reynolds number = U_BD/ν
T_a = ambient air
T_b = bulk air temperature
T_w = wall temperature
I = electrical current
R = electrical resistance
Q = wall heat flux
St = Stanton number
P_s = static pressure
α = channel angle of convergence

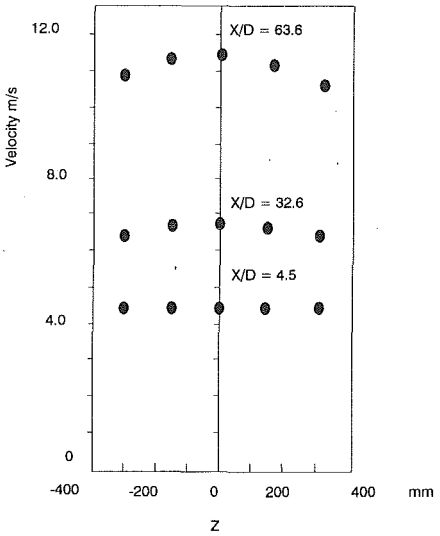

Fig. 3 Velocity profiles across the duct at Re = 14,500

streamwise locations starting from a distance of 1.5 channel entry heights from inlet and going as far as 51.9 entry heights downstream. The probe was traversed using a micrometric traverse mechanism accurate to within 0.01 mm.

The voltage output from the wall thermocouples was monitored by a Schlumberger A 200, connected to a multiswitch box. Temperature traverses were performed using a thermocouple probe. The probe thermocouple output was also monitored in the same manner as the wall thermocouples' output.

4 Experimental Procedure

Before the start of the main investigation, a number of preliminary tests were carried out to assess the two dimensionality of the flow and the heat losses from the apparatus to the surroundings.

Figure 3 presents spanwise velocity profiles along the line halfway between the top and bottom walls, at the three different streamwise locations. It can be seen that the flow changes relatively little in the third direction. Over the middle part of the channel, velocity gradients in the third direction are negligible and the assumption that the side walls do not exert any significant influence on the middle part of the channel is a reasonable one, at least over the first 32 entry heights of the channel.

In a second test of the flow two dimensionality, the streamwise variation of the centerline mass flow rate was examined. The mass flow rate was calculated numerically by integrating the relevant measured mean velocity profiles. These comparisons revealed that the flow rate varied by at most 6 percent from entry to exit. This variation in flowrate is due to experimental uncertainty and is also caused by small deviations from two dimensionality. The same numerical integration technique was also employed to determine the bulk velocity and the Reynolds number.

The heat loss from the apparatus was determined by blocking the channel entrance, applying different heating rates to the copper foil, and then monitoring the resulting steady-state temperatures. This process gave the following heat loss equation:

$$Q_L = 4.31(T_w - T_a)\ W/m^2 \tag{4}$$

Hydrodynamic and thermal measurements were carried out in separate tests but at nominally the same flow rates. The normal calibration procedures were followed for the hot-wire and thermocouple measurements. The wall shear stress τ_w was determined by two different methods. In the first method the mean velocity gradient du/dy at the wall was obtained by differentiating the measured near-wall velocity profiles, which were corrected according to the method of Bhatia et al. (1982).

Table 1 Uncertainty estimates in derived and measured quantities

Parameter	Symbol	Error estimate, percent
Velocity	U	2.0
Turbulence (rms) level	u'	< 3.0
Static pressure	P_s	6.0
Temperature	T	5.6
Diameter	D_x	< 2.9
Reynolds number	Re	< 5.0
Friction coefficient	C_f	<12.9
Stanton number	St	< 9.5

The second technique involved the integration of a simplified version of the streamwise momentum equation and the use of the static pressure measurements. Numerical differentiation of the static pressure measurements gave the streamwise distribution of the streamwise pressure gradient, dp/dx. The convective term of the streamwise momentum equation was evaluated by replacing the streamwise velocity with the local bulk velocity, thereby assuming a fully developed profile. The U momentum equation was thus simplified to:

$$\frac{\partial(\rho U_B^2)}{\partial X} = -\frac{dP}{dX} + \mu \frac{\partial^2 U}{\partial y^2} \tag{5}$$

The equation above is not applicable in the entry region. For a channel of known geometry, the streamwise bulk velocity variation can be easily obtained provided the flowrate is known. Integration of Eq. (5) in the y direction (between the top and bottom wall) can then provide the wall shear stress τ_w.

The determination of the local wall heat flux coefficient requires the knowledge of the local wall heat flux rate, Q, and of the local wall and bulk temperatures, T_w and T_b, respectively. Of these three quantities, only T_w is directly measured. The local heat transfer rate is obtained by deducting the local heat loss rate, Q_L, given by Eq. (4), from the total electrical power input, Q_T, given by

$$Q_T = I^2 R\ W/m^2 \tag{6}$$

where R is the electrical resistance per unit area of the copper foil.

The local bulk temperature, T_b, is calculated from the overall energy balance. Mutama (1989) shows that the application of the overall energy balance leads to

$$T_b = T_{\text{inlet}} + \int \frac{Q dX}{\rho U_B C_p D_x} \tag{7}$$

where D_x is the local channel height. Numerical integration is used to evaluate Eq. (7).

A detailed error analysis has been carried out by Mutama (1989). The results of this error analysis are summarized in Table 1. The errors quoted in the table represent the highest possible in all measured quantities where the "less than" sign (<) is indicated. Temperature measurement for example involved checking the accuracy of thermocouples against known temperatures and noting the uncertainties. A large sample of readings was obtained, and the arithmetic mean and the percentage deviation were calculated.

Results and Discussion

(a) Flow Measurements. The complete set of measurements

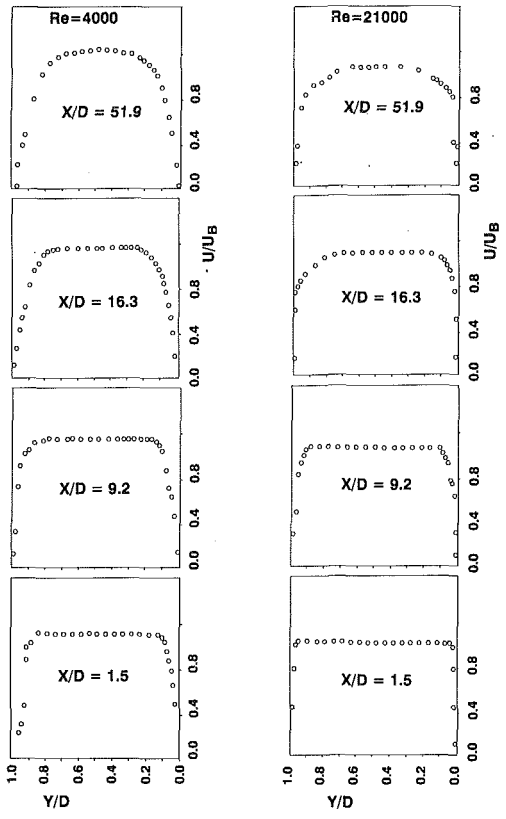

Fig. 4 Mean velocity field development

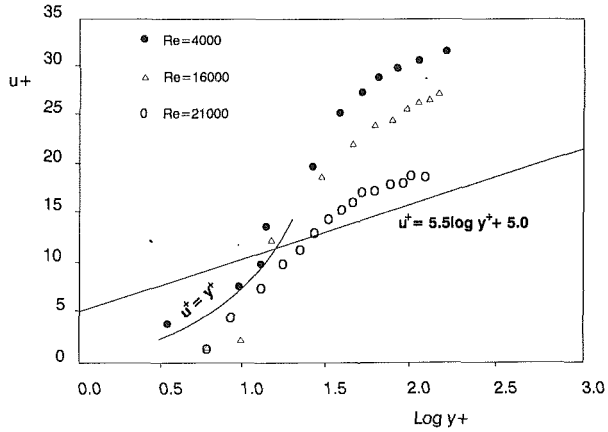

Fig. 5 Mean velocity profiles in wall coordinates at $X/D = 39.4$

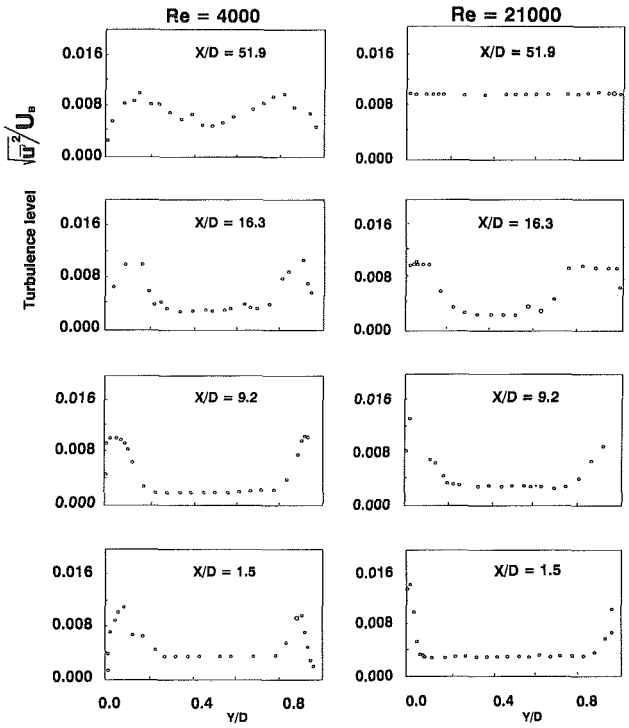

Fig. 6 Turbulence level profiles

obtained in this study is presented by Mutama (1989). This section is confined to the presentation and discussion of the most significant characteristic features of the flow.

The mean velocity profiles of Fig. 4 present an overall picture of the flow development at Reynolds numbers of 4000 and 21,000. These Reynolds numbers correspond to acceleration parameters of 2.31×10^{-6} and 4.47×10^{-7}, respectively. Local velocities and cross channel distances are normalized with the values of the local bulk velocity, U_{Bx}, and channel height, D_x, respectively.

At the entry region, in both cases, velocity profiles are flat across the channel with thin boundary layers. Entry boundary layers are thinner at the higher Reynolds numbers. As the flow progresses downstream, the normalized boundary layers become thicker. In both cases the inviscid middle core is still present after 16.3 entry channel heights of flow development ($X/D = 16.3$) and disappears by the time the flow reaches X/D of 51.9. At the lower Reynolds number of 4000, the boundary layers are considerably thicker and, at the fully developed stage, the velocity profiles assume a laminarlike structure. In contrast to the lower Reynolds number behavior, at the higher Reynolds numbers (and lower k values) the velocity profiles retain their turbulent character. In a similar study of parallel channel flow, Ince (1981) found that the velocity profiles exhibited a purely turbulent structure at similar low Reynolds numbers. The strong acceleration effect is able to modify the structure of the turbulent boundary layer at this k level.

The mean velocity development at the higher Reynolds number is similar to those presented by Patel and Head (1968), and Back et al. (1970) for accelerating flow in axisymmetric nozzles. It thus becomes clear that at k levels of around 2.0×10^{-6} boundary layer acceleration effects are strong enough to alter the turbulent character of the boundary layer.

The above view is also confirmed by Fig. 5 in which the fully developed velocity profiles are presented in wall coordinates. For the highest k level (Re = 4000) the plot indicates that the boundary layer is completely laminar. At lower k values, the measurements are closer to the fully turbulent semilogarithmic form. Even for the case with the lowest k level, acceleration effects are still clearly present. These observations are consistent with earlier studies of accelerating flows and at variance to those of Ince's (1981) study of parallel channel flow.

Further evidence of the streamwise acceleration effects on the flow structure is provided by the turbulence intensity profile plots of Fig. 6. As in Fig. 4 the turbulence intensity levels u' are normalized with the local bulk velocity, U_B, and the cross channel distance y with the local channel height D_x. Figure 6 reveals significant differences between the turbulent structures at Re = 4000 and at Re = 21,000. At both Reynolds numbers, turbulence levels are initially high at the near-wall regions and uniformly low (0.4 percent) at the inviscid core.

For the high Reynolds number case at the downstream locations, high turbulence levels gradually begin to spread from

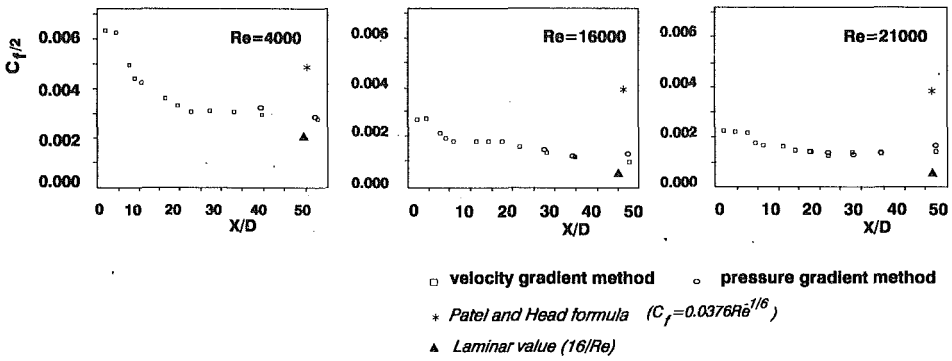

Fig. 7 Streamwise development of friction coefficients

the near-wall regions to the channels center. After the first 50 channel entry heights, the turbulence intensity levels become uniformly high at around 1 percent. At the lowest Reynolds number case ($k = 2.31 \times 10^{-6}$) near-wall levels appear to be considerably lower. Even at the entry region, the turbulence intensity profiles do not exhibit the monotonic increase from the low core levels to the high near-wall values seen at the higher Reynolds number plots. The low inviscid core turbulence levels do begin to rise within the outer region of the boundary layer, but a maximum is soon reached, and across a significant part of the boundary layer region nearer to the wall, turbulence levels are gradually reduced to zero. At the downstream locations, the maximum turbulence levels move farther away from the channel walls. The stronger streamwise acceleration therefore leads to a substantial suppression of near-wall turbulence throughout the converging channel. The turbulence levels measured in this study are similar to those reported by Tanaka et al. (1982) for similar k levels and lower than the ones reported by Ince (1981) for parallel channel flow.

Figure 7 shows plots of the two different experimental estimates of the friction coefficient. The C_f estimates obtained from the pressure gradient method over the first entry heights of the entry region of the channel are not included since the fully developed flow assumption does not apply. Downstream of the entry region, the different sets of experimental C_f estimates converge to the same levels. The fact that both methods produce the same C_f values for the fully developed region enhances confidence in the accuracy of the experimentally obtained C_f values for the fully developed region. Because of the developing nature of the flow, C_f levels are high at the entrance region of the channel and then gradually fall to the fully developed levels. At higher Reynolds numbers, the fully developed condition is reached over a shorter length of flow development.

Fully developed friction coefficients from the present studies are well below those obtained from the Blasius friction law and Patel and Head's formula for turbulent flow through constant area passages. They are not, however, as low as the laminar pipe flow values. Acceleration effects, therefore, appear to be important even at k values less than 5.0×10^{-7} and at k values of 2.31×10^{-6} the flow is still not completely laminar.

(b) Thermal Measurements. Figure 8 gives the normalized temperature plots obtained. At Re = 4000 the normalized thermal boundary layer grows relatively slowly over the first 16 channel entry heights. Downstream of this entry region the rate of growth of the normalized thermal boundary layer increases and within 40 entry heights of thermal development, the uniform temperature core disappears. At Re = 21,000 the opposite thermal development trends are apparent. Initial thermal boundary layer growth is fast, relative to that at Re = 4000,

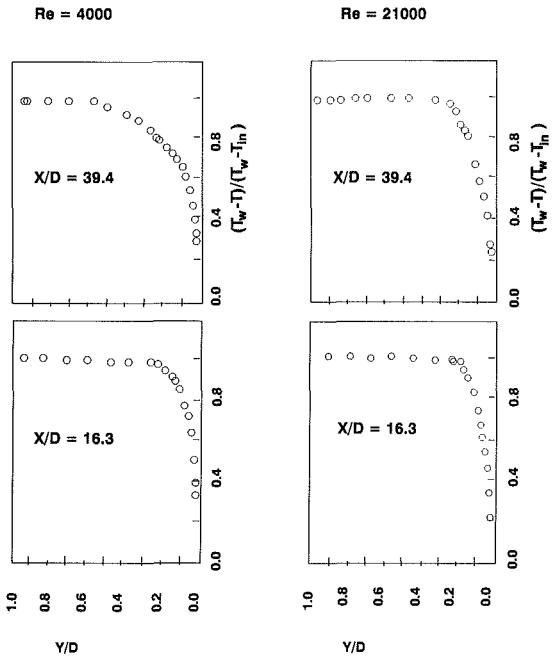

Fig. 8 Mean temperature profiles

and over the rest of the channel it becomes substantially slower. Even after 40 channel entry heights there is a relatively large uniform temperature core region.

The streamwise development of the dimensionless measured wall heat flux rate is plotted in Fig. 9 in the form of Stanton number. These plots indicate that the thermal behavior at the lower Reynolds number is markedly different from that at the other two Reynolds numbers. At Re = 4000, the high entry Stanton number level is monotonically reduced to the fully developed value of 0.0013. Fully developed St values in parallel channel flow and heat transfer at similar Re levels (Ince, 1981) are around four times higher than the ones obtained in this study. At the higher Reynolds numbers the Stanton number reaches a minimum level of 0.0013 approximately 10 entry heights into the channel and then recovers to a fully developed value of 0.0019. This behavior is consistent with the temperature field shown in Fig. 8. At the lower Reynolds number, as a result of severe suppression of the near-wall turbulence levels, wall heat transfer is inhibited, leading to almost laminar Stanton number levels. At higher Reynolds numbers the Stanton number plots of Fig. 9 (as well as the temperature profile plots of Fig. 8) indicate that acceleration effects are stronger within the entrance region. This phenomenon is probably caused by the combined effects of reduction in area in the

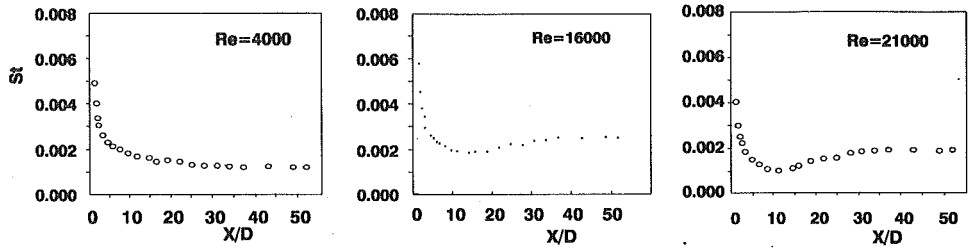

Fig. 9 Stanton number development

streamwise direction and rapid boundary layer development at entry. The sudden imposition of a favorable pressure gradient on a thin boundary layer suppresses turbulence over the entry region. The Stanton number is thus reduced to its minimum level within the first 10 entry heights of flow development.

Once the boundary layers are established, acceleration effects appear to weaken and allow the downstream recovery of St to take place. An alternative explanation for the Stanton number developments is provided by the plots of the turbulence intensity of Fig. 10. At high Re, the centerline turbulence levels are suppressed over the first 20 entry heights. Farther downstream, by which point the boundary layers are reasonably thick in comparison to the local channel height, centerline turbulence levels begin to rise for the high Reynolds number case. At the lower Reynolds number where the entry boundary layers are thicker and the acceleration parameter high, centerline turbulence intensity develops in a different way compared to the higher Reynolds number case. Over the first five entry heights turbulence levels increase, and then the stronger acceleration effects cause a severe suppression of free-stream turbulence, which is sustained over the first 30 entry heights and is then followed by a weak recovery. A recent publication by Maciejewski and Moffat (1992) shows that free-stream turbulence levels have a direct effect on wall heat transfer rates. In this case the variation of centerline turbulence also mirrors that of Stanton number. To our knowledge this pattern of heat flux coefficient development has not been reported in previous converging channel flow investigations. Similar Stanton numbers have also been reported by Morretti and Kays (1965) for similar k values and with fully developed flow conditions at entry.

It must be concluded that the observed undershoots in the Stanton number developments are only formed in converging channel flows with thin inlet boundary layers.

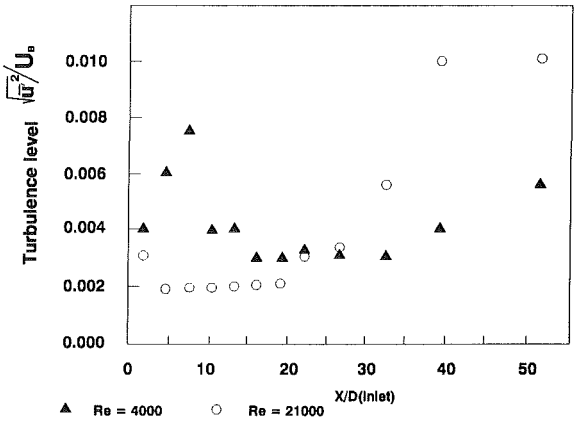

Fig. 10 Variation of free-stream turbulence with axial distance

7 Conclusions

A detailed experimental investigation of the hydrodynamic and thermal aspects of developing flow in a converging channel has been presented for acceleration parameter values between 2.3×10^{-6} and 4.5×10^{-7}. The resulting measurements improve overall understanding of developing flow behavior under the influence of streamwise acceleration. At acceleration parameter levels of 2.3×10^{-6} and Reynolds number values of 4000, the hydrodynamic and thermal boundary layer become almost laminar. Near-wall turbulence levels are severely suppressed leading to wall friction and heat transfer coefficients, which are close to those for laminar parallel channel flows.

At the lower k level of 4.5×10^{-7}, acceleration effects appear to be stronger over the entry region of the converging channel, than farther downstream. These entry acceleration effects cause a rapid reduction in heat transfer coefficients to a minimum level within the first 10 entry heights. Downstream of the entry region, even though the hydrodynamic and thermal boundary layers are of a turbulent nature, friction and heat flux coefficient levels are still well below those for turbulent parallel channel flow.

Because of the well-defined entry conditions of the flows investigated in this study, the comprehensive and detailed measurements presented in this paper are also very useful for the validation and further refinement of near-wall turbulence models.

Acknowledgments

The authors would like to thank the British Council for their financial support during the course of this work. Thanks are also due to the following people for their technical support and advice: Professor B. E. Launder, Professor M. Leschziner, Dr. A. J. Yule, Mr. D. Cooper, and Dr. N. Ince of the Department of Mechanical Engineering, U.M.I.S.T.

References

Back, L. H., Cuffel, R. H., and Massier, P. F. 1970, "Laminarization of Turbulent Boundary Layer in Nozzle Flow-Boundary and Heat Transfer Measurements With Wall Cooling," ASME JOURNAL OF HEAT TRANSFER, Vol. 92, pp. 333-334.

Bhatia, J. C., Durst, F., and Jovanic, J., 1982, "Corrections of Hot Wire Measurements Near Walls," *J. Fluid Mech.*, Vol. 122, pp. 411-431.

Bruun, H. H., Khan, M. A., Al-Kayiem, H. H., and Farad, A. A. 1988, "Velocity Calibration Relationships for Hot Wire Anemometry," *J. Phys. E. Sci. Instrum.*, Vol. 21, pp. 225-232.

Hanjalic, K., and Launder, B. E., 1972, "Fully Developed Asymmetric Flow in a Plane Channel," *J. Fluid Mech.*, Vol. 55, pt. 2, pp. 301-335.

Ince, N. A., 1981, "Low Reynolds Number Turbulent and Transitional Flow With Heat Transfer in Parallel Wall Duct," M.Sc. Thesis, University of Manchester, Faculty of Technology, United Kingdom.

Jones, W. P., and Launder, B. E., 1971, "The Prediction of Laminarization With a Two Equation Model of Turbulence," *Int. J. Heat Mass Transfer*, Vol. 15, pp. 301-314.

Jones, W. P., and Launder, B. E., 1972, "Some Properties of Sink-Flow Turbulent Boundary Layers," *J. Fluid Mech.*, Vol. 56, Pt. 2, pp. 377-351.

Kays, W. M., Moffat, R. J., and Thielbahr, W. H., 1970, "Heat Transfer to the Highly Accelerated Turbulent Boundary Layer With and Without Mass Addition," ASME JOURNAL OF HEAT TRANSFER, Vol. 92.

Launder, B. E., 1964, "Laminarization of the Turbulent Boundary Layer in

a Severe Pressure Gradient," ASME *Journal of Applied Mechanics*, Vol. 31, pp. 707–708.

Launder, B. E., and Lockwood, F. C., 1969, "An Aspect of Heat Transfer in Accelerating Turbulent Boundary Layers," ASME JOURNAL OF HEAT TRANSFER, Vol. 91, pp. 229–234.

Maciejewski, P. K., and Moffat, R. J., 1992, "Heat Transfer With Very High Free-Stream Turbulence," ASME JOURNAL OF HEAT TRANSFER, Vol. 114, Part I, pp. 827–833, and Part II, pp. 834–839.

Marriott, P. G., 1969, "Heat Transfer in the Entrance Region of Parallel Duct," M.Sc. Thesis, University of Manchester, Institute of Science and Technology, United Kingdom.

Morretti, P. M., and Kays, W. M., 1965, "Heat Transfer to a Turbulent Boundary Layer With Varying Free-Stream Velocity and Varying Surface Temperature—An Experimental Study," *Int. J. Heat Mass Transfer*, Vol. 8, pp. 1182–1202.

Mutama, K. R., 1989, "The Investigation of Fluid Flow and Heat Transfer in a Converging Duct," M.Sc. Thesis, University of Manchester, Faculty of Technology, United Kingdom.

Patel, V. C., and Head, M. R., 1968, "Reversion of Turbulent to Laminar Flow," *J. Fluid Mech.*, Vol. 34, Pt. 2, pp. 371–392.

Susec, J., and Lu, Y., 1990, "Heat Transfer Across Turbulent Boundary Layers With Pressure Gradients," ASME JOURNAL OF HEAT TRANSFER, Vol. 112, pp. 906–912.

Tanaka, H., and Shimizu, J., 1977, "Laminarization in Low Reynolds Number Turbulent Duct Flows," ASME JOURNAL OF HEAT TRANSFER, Vol. 99, pp. 682–684.

Tanaka, H., Kawamura, H., Tateno, A., and Hatamaya, S., 1982, "Effects of Laminarization and Retransition on Heat Transfer for Low Reynolds Number Flow Through a Converging to a Constant Area Duct," ASME JOURNAL OF HEAT TRANSFER, Vol. 104, pp. 363–370.

Wilson, D. G., and Pope, J. A., 1954, "Convective Heat Transfer to Gas Turbine Blade Surfaces," *Trans. IMechE*, Vol. 168, pp. 861–874.

Influence of Unsteady Wake on Heat Transfer Coefficient From a Gas Turbine Blade

J.-C. Han
HTRI Professor.
Fellow ASME

L. Zhang[1]
Research Assistant.

S. Ou[2]
Research Associate.

Turbine Heat Transfer Laboratory,
Department of Mechanical Engineering,
Texas A&M University,
College Station, TX 77843

The effect of unsteady wake on surface heat transfer coefficients of a gas turbine blade was experimentally determined using a spoked wheel type wake generator. The experiments were performed with a five-airfoil linear cascade in a low-speed wind tunnel facility. The cascade inlet Reynolds number based on the blade chord was varied from 1 to 3 × 10^5. The wake Strouhal number was varied between 0 and 1.6 by changing the rotating wake passing frequency (rod speed and rod number), rod diameter, and cascade inlet velocity. A hot-wire anemometer system was located at the cascade inlet to detect the instantaneous velocity, phase-averaged mean velocity, and turbulence intensity induced by the passing wake. A thin foil thermocouple instrumented blade was used to determine the surface heat transfer coefficients. The results show that the unsteady passing wake promotes earlier and broader boundary layer transition and causes much higher heat transfer coefficients on the suction surface, whereas the passing wake also significantly enhances heat transfer coefficients on the pressure surface. The blade heat transfer coefficients for a given Reynolds number flow increase with the wake Strouhal number by increasing the rod speed, rod number, or rod diameter. For a given wake passing frequency and rod diameter, the blade heat transfer coefficients decrease with decreasing Reynolds number, although the corresponding wake Strouhal number is increased. The results suggest that both the Reynolds and Strouhal numbers are important parameters in determining the blade heat transfer coefficients in unsteady wake flow conditions.

Introduction

The trend in advanced aeroengine design for high thermal efficiency and high power density is toward high entry gas temperature. Highly sophisticated cooling techniques such as film cooling and augmented internal cooling have to be employed in order to maintain acceptable life and safety requirements under such extreme operating conditions. In order to provide a better cooling design it is necessary to understand the convective heat transfer characteristics between a high-temperature gas stream and turbine airfoil. This investigation focuses on the measurement of the surface heat transfer coefficient distributions on a model turbine blade under incident unsteady wake conditions.

There have been many studies on the effect of unsteady wake caused by the passing of the upstream blade row on the surface heat transfer coefficient of the downstream blade row. Many published results investigate the interaction between the wake flow and the boundary layer on the suction side of a turbine blade. It is well known that the unsteady wake impact causes an increased stagnation region heat transfer and an early laminar–turbulent boundary layer transition. This wake-induced earlier transition covers a longer streamwise length on the suction surface of a turbine blade. These zones of transition form a higher heat transfer and a growing region of turbulent flow. Experiments have been conducted in turbines (Dunn, 1986; Dunn et al., 1986, 1989, 1994; Blair et al., 1989; Blair, 1994; Abhari et al., 1992) or in laboratory simulations (Doorly et al., 1988; Priddy and Bayley, 1988; O'Brien and Capp, 1989; Wittig et al., 1987, 1988; Liu and Rodi, 1989, 1992; Dullenkopf et al., 1991; Dullenkopf and Mayle, 1994). A squirrel cage type wake generator was used in laboratory simulations by Priddy and Bayley (1988) and Liu and Rodi (1989, 1992); however, a spoked wheel type wake generator was employed by Doorly et al. (1988), O'Brien and Capp (1989), Wittig et al. (1987, 1988), and Dullenkopf et al. (1991). Some investigators (Dunn et al., Doorly et al., and Abhari et al.) used fast response sensors to detect the real time variation on the blade surface heat transfer induced by unsteady wake, while other researchers (Dullenkopf et al., Wittig et al., Liu and Rodi, and Blair et al.) employed the standard method to obtain the mean (time-averaged) heat transfer on an airfoil in unsteady wake conditions. Mayle and Dullenkopf (1990) and Mayle (1991) recently developed a theory to incorporate the unsteady effect into a steady-flow analysis by introducing a time-averaged intermittency factor. They showed that the time-averaged heat transfer distribution on the airfoil surface can be obtained from the predicted time-averaged intermittency factor and the laminar and turbulent heat transfer distributions as calculated from steady-flow conditions. They also found that the theory agrees with the measurement of the time-averaged heat transfer coefficient on the suction surface of a turbine blade in a spoked wheel generated wake flow condition.

It is well known that the turbine blade heat transfer coefficient varies with the wake Strouhal number. The wake Strouhal number is defined as the relative strength of the wake tangential velocity to the mainstream axial velocity, while the wake tangential velocity is proportional to the rotating rod rotational speed, the rotating rod number, and the rotating rod diameter. This means that the wake Strouhal number is composed of four variables: the rotating rod speed, rod number, rod diameter, and mainstream velocity. This study focuses on the effect of the wake Strouhal number on turbine blade heat transfer. The wake Strouhal number can be varied by changing one of the four variables while keeping the other three variables constant. It is of interest to determine whether or not the heat transfer coefficient increases with an increased

[1]Current address: Solar Turbines, San Diego, CA 92186-5376.
[2]Current address: Aero Propulsion and Power Laboratory, Wright Patterson AFB, OH 45433.

Contributed by the Heat Transfer Division for publication in the JOURNAL OF HEAT TRANSFER. Manuscript received by the Heat Transfer Division July 1992; revision received May 1993. Keywords: Flow Transition, Turbines, Wakes. Associate Technical Editor: R. J. Simoneau.

Strouhal number by respectively changing each of the four variables. The other question to be answered is whether or not the same Strouhal number causes the same impact on heat transfer coefficient distributions on the turbine blade. The same Strouhal number can be obtained by combining the decreasing rotating rod speed with an increasing rod number or diameter, or by increasing rotating rod speed with an increasing mainstream velocity. The objectives of this study are: (1) to determine the effect of rotating rod speed, rod number, rod diameter, or mainstream velocity, respectively, on the blade heat transfer coefficient distributions, (2) to determine the combined effect of rotating rod speed with rod number, rod diameter, or mainstream velocity, respectively, on the blade heat transfer coefficient distributions, and (3) to determine the combined effect of wake Strouhal number and mainstream Reynolds number on the blade heat transfer coefficient distributions. For this study, a five-bladed cascade (including an instrumented blade) was installed in a low-speed wind tunnel at the Turbine Heat Transfer Laboratory of Texas A&M University. The upstream unsteady wake is produced by a spoked wheel type wake generator similar to those used by O'Brien and Capp, Dullenkopf et al., and Wittig et al. The standard thin foil–thermocouple technique is used to determine the mean (time-averaged) heat transfer coefficient on the blade. This thin foil–thermocouple method has also been employed to determine the leading edge and flat plate heat transfer coefficient distributions under high mainstream turbulence conditions (Mehendale et al., 1991; Young et al., 1992).

Test Apparatus

Low-Speed Wind Tunnel. Figures 1 and 2 show the cascade setup and instrumentation layout. The wind tunnel consists of an inlet nozzle, a wake generator, a test section, an exhaust duct, and a suction blower. The wind tunnel has been modified to accommodate the 107.49 deg turning in the cascade. A five-airfoil cascade is installed inside the test section downstream of the wake generator. A casing has been installed around the rotating spoke wheel to prevent leakage flow and to protect the system.

Cascade Design and Analysis. The cascade is designed to accommodate the low-speed wind tunnel facility with an inlet air velocity ranging from 7 to 21 m/s. The airfoil configuration will produce a velocity ratio distribution similar to that inside a typical advanced high-pressure turbine blade row. The computer software used in the airfoil design and analysis was provided by General Electric Company-Aircraft Engines. A 5× scaled up model was used to simulate the engine Reynolds number. The selected blade has a 107.49 deg turning with relative flow angles of 35 and −72.49 deg at the blade inlet and exit, respectively. The cascade is made of high-quality model wood and has a chord length of 22.68 cm, a radial span of 25.2 cm, and a blade spacing of 17.01 cm. The center blade

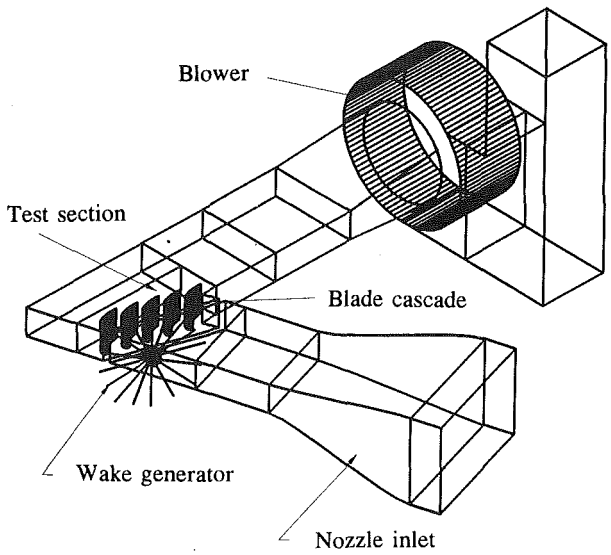

Fig. 1 Schematic of the linear turbine cascade with rotating wake generator

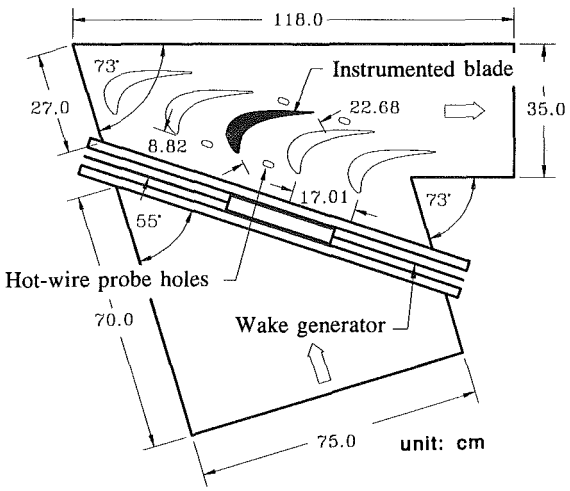

Fig. 2 Test section and instrumentation layout (unit: cm)

is instrumented and can be replaced for pressure or heat transfer experiments. Two slots are located near the blade leading edge and in the middle of flow passages to measure flow velocities, wake profiles, turbulence fluctuations, and to check the flow periodicity between two adjacent flow passages. The distance between the rotating rod and blade inlet is 8.82 cm.

Rotating Wake Simulation. The wake simulation was accomplished by means of the rotating spoked wheel shown in

Nomenclature

C = airfoil chord
d = rotating rod diameter
h = heat transfer coefficient
k = thermal conductivity of air
n = rotating rod number
N = rotating rod speed, rpm
Nu = Nusselt number based on blade chord = hC/k
q'' = net surface convection heat flux
q''_{gen} = foil-generated surface heat flux
q''_{loss} = surface heat flux loss
Re = Reynolds number based on blade chord = V_1C/ν
r_m = distance between the wake generator shaft center and the cascade midspan
S = Strouhal number = $2\pi Ndn/(60V_1)$
T_w = blade surface temperature
T_{aw} = adiabatic blade surface temperature
T_∞ = mainstream air flow temperature at the inlet of the cascade
Tu = local turbulence intensity
U_r = rotational velocity at the cascade midspan
V = local mainstream velocity in the cascade
V_1 = mainstream velocity at the inlet of the cascade
V_2 = mainstream velocity at the exit of the cascade
X = blade surface coordinate in streamwise direction
ν = kinematic viscosity of air

Fig. 3. The wake Strouhal number (S) is used to simulate the unsteady wake flow characteristics of modern gas turbines (O'Brien and Capp, 1989) and is defined as

$$S = \frac{2\pi Ndn}{60\ V_1} \tag{1}$$

where N is the rod rotational speed (rpm), d is the rod diameter (m), n is the number of rods, and V_1 is the mainstream flow velocity at the inlet of the cascade (m/s). A wider range of Strouhal numbers can be tested in this program by varying the rod rotational speed, rod number, rod diameter, and flow inlet velocity. In this paper, as shown in Table 1, the Strouhal number ranges from 0.05 to 1.6 by varying the rod rotating speed (N = 64 to 765 rpm), the rotating rod diameter (d = 0.315 to 0.945 cm), the rotating rod number (n = 8 to 32), and flow inlet velocity (V_1 = 7 to 21 m/s), respectively. The flow coefficients, $V_1/U_r = dn/(r_m S)$ (O'Brien and Capp, 1989), varies from 0.35 to 11.4. The Reynolds number (Re) is defined as

$$\mathrm{Re} = \frac{V_1 C}{\nu} \tag{2}$$

where V_1 is the mainstream flow velocity at the inlet of the cascade, C is the airfoil chord, and ν is air kinematic viscosity. In this paper, the flow inlet velocity (V_1) ranges from 7 to 21 m/s and the airfoil chord (C) is kept at a constant value of 22.68 cm (9 in.). Therefore, the Reynolds number (Re) varies from 1×10^5 to 3×10^5.

Instrumentation and Data Analysis

Hot-Wire Instrumentation. A calibrated single hot-wire anemometer TSI IFA 100 is used to measure the unsteady (instantaneous) velocity profile of the passing wake. The hot-wire anemometer is connected to an IBM PC through a 100 kHz A/D converter in order to get sufficient sampling data for analysis. The anemometer also is connected to a NICOLET 446A Spectrum Analyzer that displays the instantaneous wake profile and frequency distribution. The hot-wire sensor is located at 8.82 cm downstream of the rotating rod. Figure 4 shows the conceptual view of the effect of unsteady wake on the heat transfer blade model. The mean velocity and turbulent intensity are time dependent and periodic and, because of the periodic nature of the wake passing and shedding, the analysis of the unsteady random signal indicates that its behavior cannot be characterized by the time mean average only. In order to get the time-dependent periodic mean velocity and turbulent intensity of the wake flow, the phase-averaged (or ensemble-averaged) method suggested by O'Brien and Capp (1989) and Dullenkopf et al. (1991) is adapted. The phase-averaged mean velocity is obtained by dividing each rod-passing period into a certain number of bins and entering data from a number of the period into each bin. The phase-averaged mean velocity for each bin is then simply the sum of all the entering data for that bin divided by the number of the period. The phase-averaged turbulent intensity of the wake flow is obtained in a similar way. In this paper, digital sampling rates up to 100 kHz are obtained depending on rod-passing frequency such that approximately 100 rod-passing periods and 150 samples per period are included in each digital record.

Pressure Tap Blade Instrumentation. The blade containing pressure taps is made of high-quality model wood with a smooth surface by the numerical controlled machine. The blade is then coated with paints. There are 26 pressure taps located at the midspan of the blade: 1 on the geometric stagnation point, 11 on the pressure side, and 14 on the suction side. The taps are connected to the inclined manometer through flexible tubings for the blade surface static pressure measurements.

Heat Transfer Blade Instrumentation. Figure 5 shows a sketch of the instrumented blade used for heat transfer meas-

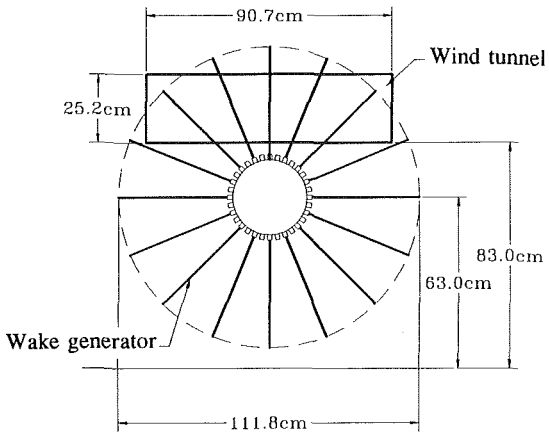

Fig. 3 Wake flow generator

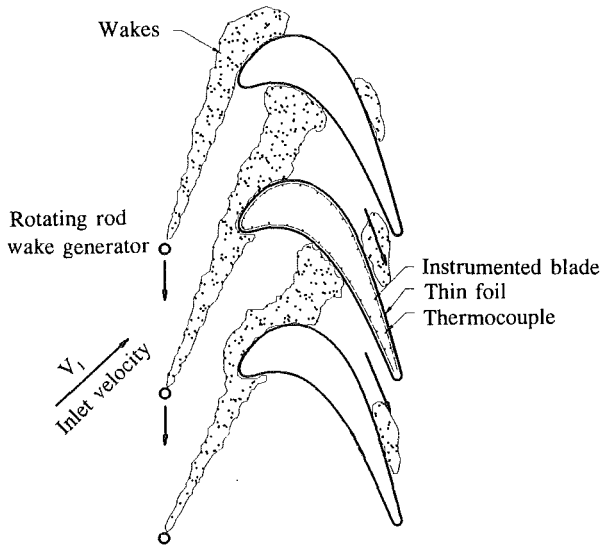

Fig. 4 Conceptual view of effect of unsteady wake on the heat transfer blade model

Table 1 Test conditions for wake Strouhal number

Re	V_1 (m/s)	d (cm)	n	N (rpm)	S	V_1/U_r
300,000	21	0.630	32, 16, 8	96–765	0.05–0.4	1.4–11.4
		0.945	32	128–510	0.2–0.8	1.1–4.3
200,000	14	0.315	32	128–510	0.1–0.4	0.7–2.9
		0.630	32, 16, 8	64–765	0.05–0.8	0.7–11.4
		0.945	32	170–340	0.4–0.8	1.1–2.2
100,000	7	0.315	32	64–510	0.1–0.8	0.35–2.9
		0.630	32, 16, 8	64–765	0.1–1.2	0.48–5.7
		0.945	32	170–340	0.8–1.6	0.53–1.1

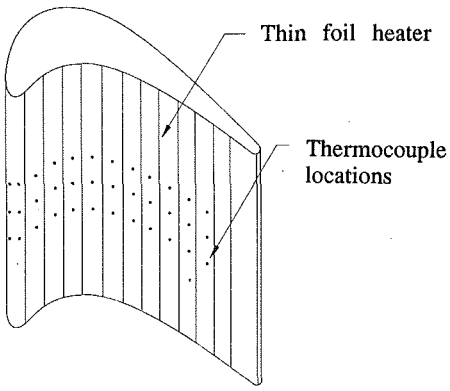

Fig. 5 Heat transfer instrumentation blade

urement. The blade is made of high-quality model wood with a smooth surface by the numerical controlled machine. Twenty-six foil strips are vertically cemented on the outer surface of the test model. Each strip of foil is 25.4 cm long, 2 cm wide, and 0.00378 cm thick. A gap of 0.8 mm separates any two foils. These gaps are filled with wood filler and made flush with the foil surface for electrical insulation. These wood-filled gaps provide a smooth surface. All foils are connected in series by copper bus bars. The heated foils produce a nearly constant heat flux for the heat transfer test. The 36 gage copper-constantan thermocouples are soldered on the underside of the foils with 11 rows on the pressure side and 15 rows on the suction side. Each row has 3 thermocouples around the 7.6 cm midspan region of the blade. All thermocouples are connected to a Fluke 2280A data logger interface with an IBM PC. The voltage and current input through the foils are measured by digital multimeters. The local heat transfer coefficient (h) is calculated as

$$h = \frac{q''}{T_w - T_\infty} = \frac{q''_{\text{gen}} - q''_{\text{loss}}}{T_w - T_{aw}} \tag{3}$$

where q'' is the net convective heat flux from the foil surface, q''_{gen} is the generated surface heat flux from voltage-current measurements, q''_{loss} is the heat loss, T_w is the local steady foil temperature, T_∞ is the mainstream inlet temperature, and T_{aw} is the local adiabatic wall temperature. Heat loss tests were performed to determine the heat losses from the blade model for a no-flow condition. Several different power input levels at steady state were used to obtain the heat loss relationships for each foil wall as a function of the wall temperature. T_w was about 40–50°C and T_{aw} about 25°C (room temperature) for the heat transfer test. The heat loss was less than 10 percent of the foil-generated heat. The conduction and radiation heat losses were 4 and 6 percent, respectively, of the heat generated. Heat loss through the tiny thermocouple wires was less than 0.1 percent, and axial and lateral conduction through the thin foil was found to be negligible. The local heat transfer coefficient was then converted into the local Nusselt number (Nu = hC/k) based on the blade chord (C) and air thermal conductivity (k).

An uncertainty analysis based on the method of Kline and McClintock (1953) was carried out for the heat transfer coefficient. The uncertainty of the heat transfer coefficient is less than 5 percent. Note that the abovementioned thin foil thermocouple technique is the same as that used by Mehendale et al. (1991) and Young et al. (1992).

Results and Discussions

Aerodynamics Test. The periodicity of velocity profiles between adjacent flow paths has been measured and confirmed. The velocity profiles in the radial direction for three

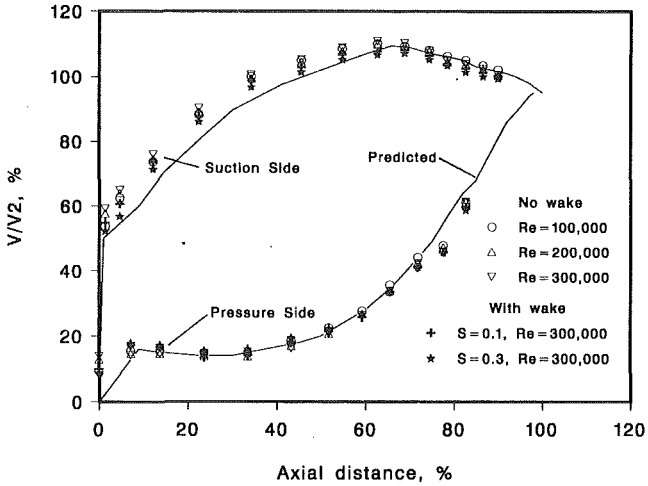

Fig. 6 Velocity distribution on the pressure tap blade model with and without wake condition

Reynolds numbers (Re = 1, 2, and 3 × 10^5) at the inlet (and outlet) of the central flow path and at the inlet (and outlet) of an adjacent flow path have been obtained. The results indicate that the inlet (and outlet) velocity profile is essentially uniform between a 25 and 75 percent span. The periodicity of velocity profile between adjacent flow paths is excellent. Also, the flow direction at the inlet and outlet of both flow paths was uniform. The pressure tap airfoil provided the distribution of surface static pressures, which were used to calculate the velocity distribution around the airfoil. Figure 6 shows the distribution of velocity ratio (V/V_2) between local and exit velocity for the three studied Reynolds numbers. The solid line in Fig. 6 is the pretest prediction based on Re = 2 × 10^5. The velocity on the pressure side surface is an excellent match. The measured velocity on the suction side surface is higher than the predicted value. The results also indicated that the unsteady wake does not change the distribution of surface static pressures.

Wake Flow Measurement. The hot-wire probe was located near the blade leading edge and in the middle of flow passages to measure the instantaneous velocities in unsteady wake flow conditions. Figure 7 shows typical instantaneous profiles and Fig. 8 shows typical phase-averaged mean velocity profiles, and phase-averaged turbulent intensity profiles for S = 0.1, 0.2, and 0.4, respectively. The Strouhal number (S) is varied by increasing the rotating rod speed (N) for a given rod diameter (d = 0.63 cm), rod number (n = 16), and cascade inlet velocity (V_1 = 21 m/s or Re = 3 × 10^5). The instantaneous velocity profile shows the periodic unsteady fluctuations caused by the upstream passing wake, whereas the periodic fluctuations increase with the Strouhal number (rotating rod speed). Note that the incident angle and wake propagation length are not constant when increasing the Strouhal number by changing the rotational speed. The phase-averaged profile shows the time-dependent mean velocity defect caused by the upstream passing wake, whereas the wake width increases with the Strouhal number. The phase-averaged turbulent intensity reaches 20 percent inside the wake, while the wake-induced higher turbulence becomes broader for higher Strouhal numbers. This is because the higher rotating rod speed produces a larger amount of unsteady wake. The time-averaged turbulence intensity is about 8, 10, and 15 percent, respectively for S = 0.1, 0.2, and 0.4. The background turbulence intensity is only about 0.75 percent for the case of no rotating rods in the wind tunnel. From the results of instantaneous velocity, phase-averaged mean velocity, and turbulence intensity profiles, it is expected that the unsteady wake with higher Strouhal numbers will produce a larger impact on the downstream blade

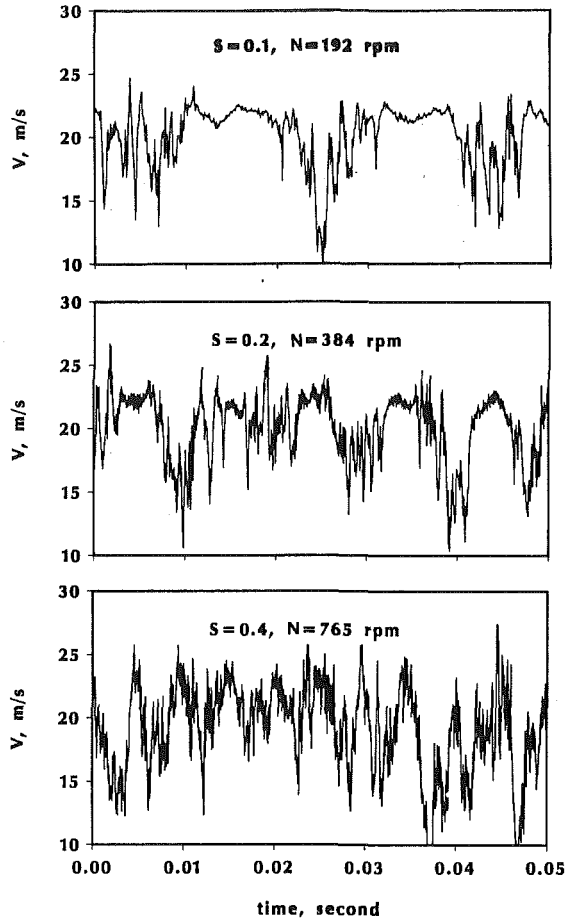

Fig. 7 Instantaneous velocity profile under different unsteady wake conditions for Re = 300,000, d = 0.63 cm, and n = 16

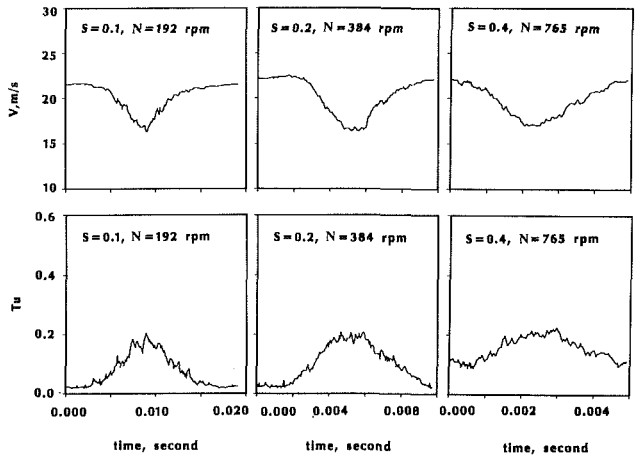

Fig. 8 Phase-averaged turbulence distribution under different unsteady wake conditions for Re = 300,000, d = 0.63 cm, n = 16

heat transfer for a given flow Reynolds number. Note that using nonlinear rotating rods with a linear blade cascade causes the wakes at the top of the cascade to pass by the blades faster than the wakes at the bottom of the cascade. However, heat transfer tests indicate that the spanwise thermocouple readings in the 7.6 cm midspan region were off only about ±0.5 percent. Therefore, the error was small.

Heat Transfer Test. Figure 9 shows the effect of Strouhal numbers by varying the rotating rod speed, N, on the spanwise-averaged Nusselt number (Nu = hC/k) distributions on the

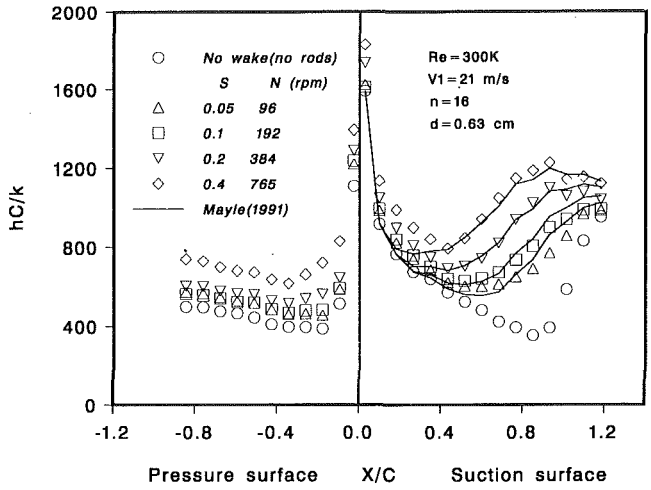

Fig. 9 Effect of Strouhal number by varying N on the local heat transfer coefficient distributions

blade surface. The conditions are: Re = 3×10^5, V_1 = 21 m/s, n = 16, d = 0.63 cm, S = 0.05, 0.1, 0.2, and 0.4 (corresponding to N = 96, 192, 384, and 765 rpm). Test results for the steady mainstream flow condition (i.e., with no rotating rods, turbulence intensity Tu = 0.75 percent) are also included for comparison. The results for the no-wake flow case (rods removed) show that the suction surface Nusselt number decreases monotonically with increasing streamwise distance from the blade stagnation line, and then increases sharply due to transition in the turbulent flow at 80 percent blade chord distance (x/C = 0.8). The pressure surface Nusselt number decreases sharply with increasing streamwise distance from the leading edge of the blade and, due to strong acceleration, starts to increase gradually at about 20 percent blade chord distance. The general trends of the results for the wake flow case are: (1) The Nusselt number on both the suction and pressure surfaces increases with an increasing Strouhal number due to higher wake passing frequency, (2) the passing wake has more impact on the suction surface heat transfer than on the pressure surface heat transfer, i.e., the suction surface Nusselt number increments are higher than those of the pressure surface in wake flow conditions, (3) the suction surface boundary layer transition starts earlier but requires a longer distance to become turbulent under wake flow conditions, (4) the wake not only effects the suction surface boundary layer transition but also disturbs the laminar type boundary layer from the blade leading edge to transition, as well as enhancing its heat transfer, (5) the suction side Nusselt number increases about 15 percent at the blade leading edge and about 3 times at 80 percent blade chord length when the wake passing Strouhal number changes from zero (no wake) to 0.4 (strong wake), and (6) the pressure side Nusselt number increases somewhere between 30–100 percent, with the smallest increment (30 percent) near the blade leading edge and the largest increment (100 percent) near 20 percent blade chord length, when wake Strouhal number varies from 0 to 0.4. The general observations of the passing wake impact on the blade surface heat transfer, as shown in Fig. 9, agree with those presented and discussed in the previous investigations (Dullenkopf et al., 1991). Figure 9 also shows that Mayle's theory (1991) predicts the present data reasonably well, except that the theory underpredicts the data before transition for the high Strouhal number flows (S = 0.2 and 0.4).

Figure 10 shows the effect of Strouhal number (by varying the inlet velocity V_1) on the spanwise-averaged Nusselt number distributions on the blade surface. The test conditions are: N = 765 rpm, n = 16, d = 0.63, cm, S = 0.4, 0.6, and 1.2 (corresponding to V_1 = 21, 14, and 7 m/s or Re = 3, 2, and 1×10^5, respectively). The results show that the heat transfer

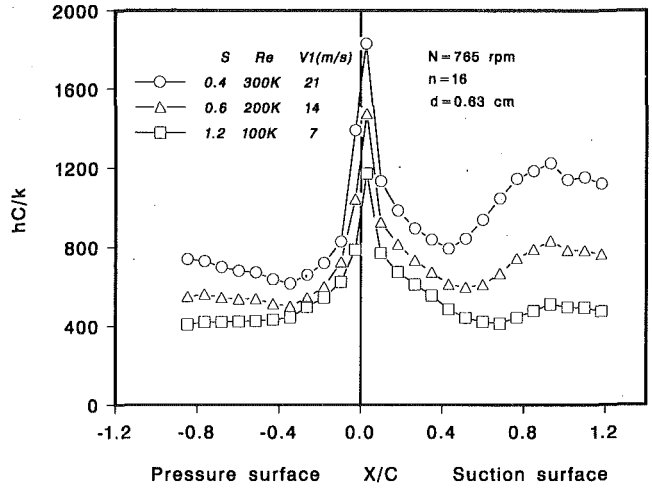

Fig. 10 Effect of Strouhal number by varying V_1 on the local heat transfer coefficient distributions

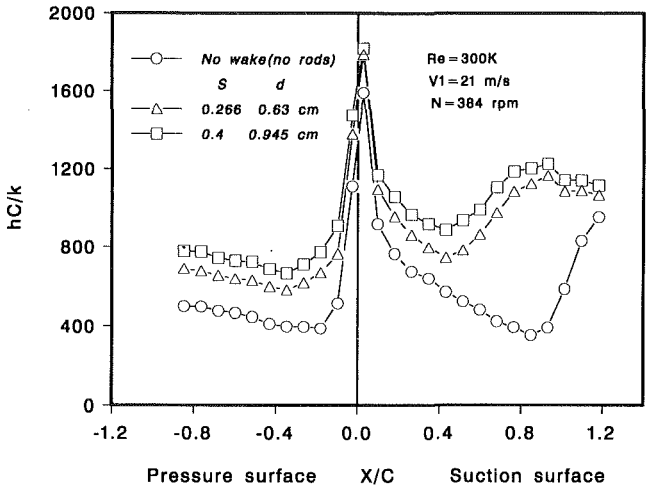

Fig. 12 Effect of Strouhal number by varying d on the local heat transfer coefficient distributions

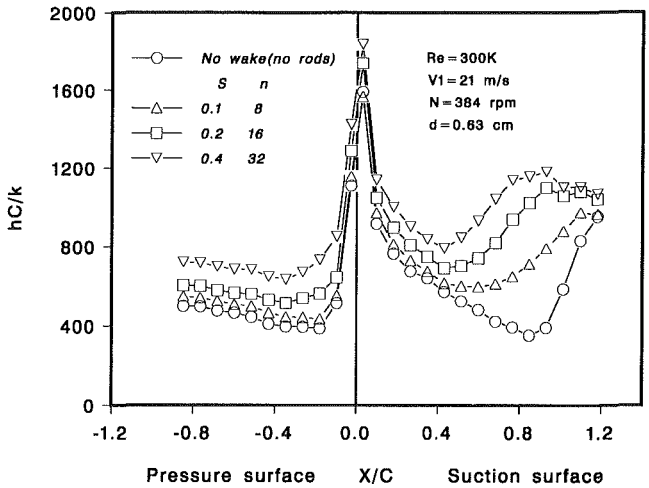

Fig. 11 Effect of Strouhal number by varying n on the local heat transfer coefficient distributions

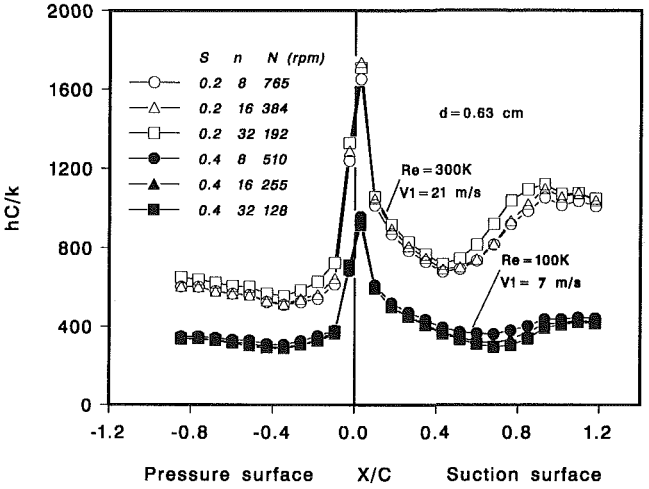

Fig. 13 Effect of Strouhal number by varying Nn on the local heat transfer coefficient distributions

coefficient increases with a decreasing, instead of increasing, Strouhal number (by increasing inlet velocity with a constant value of rotating rod diameter, number and speed). This is because the higher Reynolds number flow (higher inlet velocity) creates the faster moving wake and produces the thinner boundary layer on the blade surface. Therefore, the higher Reynolds number flow for the same rotating rod passing frequency (same rod speed, diameter, and number) causes an earlier boundary layer transition and a higher heat transfer coefficient distribution on the blade than those of the lower Reynolds numbers. By definition, however, the lower Reynolds number case has a greater Strouhal number value for the same rotating rod passing frequency. This implies that the faster moving wake has more impact on the thinner boundary layer than the slower moving wake on the thicker boundary layer flow. It also implies that the Strouhal number effect is valid (meaningful) only under the same Reynolds number condition.

Figure 11 shows the effect of Strouhal number (by varying the rotating rod number, n) on the spanwise-averaged Nusselt number distributions on the blade surface. The test conditions are: N = 384 rpm, d = 0.63 cm, V_1 = 21 m/s, Re = 3 × 10^5, S = 0.1, 0.2, and 0.4 (corresponding to n = 8, 16 and 32). The results show that the greater the number of rotating rods, the earlier boundary layer transition occurs resulting in a higher heat transfer coefficient distribution on the blade surface. This set of data clearly indicates that the Nusselt number can be increased by increasing the rod number (increasing wake passing frequency) and holding the rod diameter, rod speed, and inlet velocity constant. Similarly, Fig. 12 shows a plot for the effect of the rotating rod diameter by holding rod speed, rod number, and inlet velocity constant. The results show that the blade surface heat transfer coefficient distribution increases with an increasing Strouhal number due to the increase in rod diameter. This is because the larger diameter rod causes a wider wake-induced velocity defect for the given rod speed, rod number and inlet velocity.

Figure 13 shows the combined effect of rotational rod speed and rod number on the blade heat transfer for two Reynolds numbers. The Strouhal number can be a constant value by increasing rod number and decreasing rod speed for a given rod diameter and inlet velocity. The results show that the blade heat transfer coefficient distribution is about the same for the same product of rotating rod speed and rod number (i.e., the same wake passing frequency or Strouhal number) for a given rod diameter and inlet velocity. This is because the same product of rotational speed and rod number creates the same amount of unsteady wake, which moves at a similar velocity toward the blade for a given Reynolds number flow. This implies that the wake impact on the blade heat transfer depends on the Strouhal number as long as the product of rotating rod speed

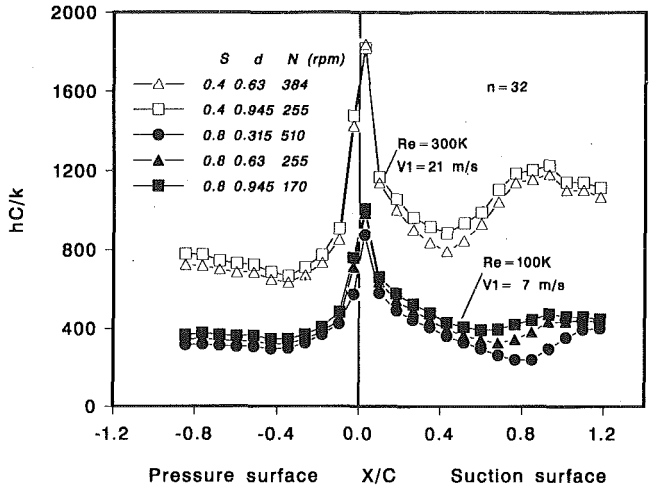

Fig. 14 Effect of Strouhal number by varying *Nd* on the local heat transfer coefficient distributions

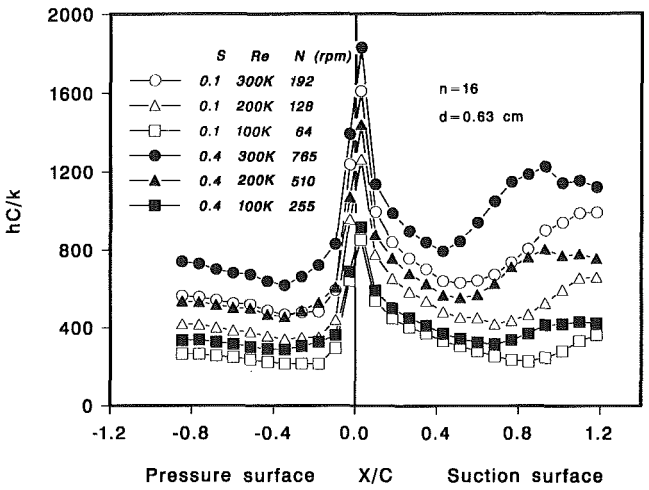

Fig. 15 Effect of Strouhal number by varying NV_1 on the local heat transfer coefficient distributions

and rod number (i.e., wake passing frequency) stays the same for a given rod diameter and inlet velocity. This is true for two studied Reynolds numbers, although, as discussed above, the higher Reynolds number flow causes the higher blade heat transfer due to its faster moving wake and thinner boundary layer. Figure 14 shows the combined effect of the rotating rod speed and rod diameter on the blade heat transfer for two Reynolds numbers. The results show that the larger diameter rod (d = 0.945 cm) tends to produce a slightly higher heat transfer than the smaller diameter rod (d = 0.63 cm) for the same Strouhal number at the same rod number and inlet velocity. This is true for two studied Reynolds numbers, while the higher Reynolds produces the higher blade heat transfer as mentioned above.

Figure 15 shows the combined effect of the rotational speed and the inlet velocity (Reynolds number) on the blade heat transfer for a given rod diameter and rod number. The results clearly indicate that, for the same Strouhal number (S = 0.1 or 0.4), the passing wake with higher Reynolds number and higher rod speed (Re = 3×10^5 and N = 192 rpm for S = 0.1 or Re = 3×10^5 and N = 765 rpm for S = 0.4) has a much stronger impact on the blade heat transfer than the passing wake with lower Reynolds number and lower rod speed (Re = 1×10^5 and N = 64 rpm for S = 0.1, or Re = 1×10^5 and N = 255 rpm for S = 0.4). This is because the higher rod speed and higher Reynolds number produce more and faster moving wake toward the blade thinner boundary layer, while the lower rod speed and lower Reynolds number has less and slower moving wake toward the thicker boundary layer. This implies that for the same Strouhal number (S = 0.1 or 0.4), the blade heat transfer distribution is sensitive to the inlet velocity and the wake passing frequency. Thus, the blade heat transfer coefficient distribution depends strongly on both the inlet Reynolds number and the wake Strouhal number. The Strouhal number is the sole important parameter in determining the unsteady wake effect on the blade heat transfer for a given fixed Reynolds number. However, the Reynolds number has an even stronger effect on the blade heat transfer under unsteady wake conditions.

Concluding Remarks

The influence of upstream passing wake on the surface heat transfer coefficient distributions has been performed in a linear blade cascade by using the spoked wheel type rotating rods as wake generators. The wake Strouhal number was varied from 0.05 to 1.6 by changing the rotating rod speed (N = 64 to 765 rpm), rod number (n = 8, 16, and 32), rod diameter (d = 0.315, 0.63, and 0.945 cm), and cascade inlet velocity (V_1 = 7, 14, and 21 m/s or Re = 1, 2, and 3×10^5). The main findings are:

1 For a given Reynolds number flow, the higher wake Strouhal number (the higher wake passing frequency) causes more frequent instantaneous velocity fluctuations, more broad velocity defect profiles, and more higher level turbulence intensities induced by the passing wake.

2 The unsteady wake promotes a much earlier and wider boundary layer transition on the suction surface and greatly enhances its surface heat transfer coefficient distribution. The strong wake also significantly increases the pressure surface heat transfer coefficient depending on the wake Strouhal number (wake passing frequency). This confirms the observations of previous investigators.

3 The blade surface heat transfer coefficient distribution for a given Reynolds number flow increases with wake Strouhal number by increasing either rotating rod speed, rod number, or rod diameter.

4 For a given wake passing frequency (rod speed and number) and rod diameter, the lower Reynolds number flow that corresponds to a higher Strouhal number has a smaller impact on the blade heat transfer coefficient distribution. This is because the slower moving wake has less effect on the thicker boundary layer created by the lower Reynolds number flow. This implies that the Strouhal number effect is meaningful only under the same Reynolds number condition.

5 The blade surface heat transfer coefficient distribution for a given Reynolds number flow seems to depend only on the wake Strouhal number, regardless of whether the number is produced by the combination of a higher rotating rod speed with less rod numbers or with a smaller rod diameter, or the combination of a lower rotating speed with more rod numbers or larger rod diameter.

6 The cascade inlet velocity (or Reynolds number) has the biggest effect on the blade heat transfer coefficient. For the same wake Strouhal number, the wake with higher flow velocity and higher rod speed has a much bigger impact on the blade heat transfer coefficient than that with lower flow velocity and lower rod speed. The implication is that the Reynolds and Strouhal numbers are important parameters in determining the blade heat transfer coefficient distribution under unsteady wake flow conditions.

Acknowledgments

The project was sponsored by the U.S. Naval Air Warfare Center through General Electric Aircraft Engines. The authors

are indebted to Dr. C. Pang Lee, project manager for General Electric Aircraft Engines, for his performance of the cascade analysis and design, as well as his helpful discussions throughout the project investigation.

The project was also supported by the Texas Higher Education Coordinating Board—Advanced Technology Program under grant number 999903-104.

References

Abhari, R. S., Guenette, G. R., Epstein, A. H., and Giles, M. B., 1992, "Comparison of Time-Resolved Measurements and Numerical Calculations," ASME *Journal of Turbomachinery*, Vol. 114, pp. 818–827.

Blair, M. F., Dring, R. P., and Joslyn, H. D., 1989, "The Effects of Turbulence and Stator/Rotor Interactions on Turbine Heat Transfer: Parts I and II," ASME *Journal of Turbomachinery*, Vol. 111, pp. 87–103.

Blair, M. F., 1994, "An Experimental Study of Heat Transfer in a Large-Scale Turbine Rotor Passage," ASME *Journal of Turbomachinery*, in press.

Doorly, D. J., 1988, "Modeling the Unsteady Flow in a Turbine Rotor Passage," ASME *Journal of Turbomachinery*, Vol. 110, pp. 27–37.

Dullenkopf, K., Schulz, A., and Wittig, S., 1991, "The Effect of Incident Wake on the Mean Heat Transfer of an Airfoil," ASME *Journal of Turbomachinery*, Vol. 113, pp. 412–418.

Dullenkopf, K., and Mayle, R. E., 1994, "The Effect of Incident Turbulence and Moving Wakes on Laminar Heat Transfer in Gas Turbines," ASME *Journal of Turbomachinery*, in press.

Dunn, M. G., 1986, "Heat Flux Measurements for the Rotor of a Full-Stage Turbine: Part I— Time Averaged Results," ASME *Journal of Turbomachinery*, Vol. 108, pp. 90–97.

Dunn, M. G., George, W. K., Rae, W. J., Woodward, S. H., Moller, J. C., and Seymour, J. P., 1986, "Heat Flux Measurements for the Rotor of a Full-Stage Turbine: Part II—Description of Analysis Technique and Typical Time-Resolved Measurements," ASME *Journal of Turbomachinery*, Vol. 108, pp. 98–107.

Dunn, M. G., Seymour, P. J., Woodward, S. H., George, W. K., and Chupp, R. E., 1989, "Phase-Resolved Heat Flux Measurements on the Blade of a Full-Scale Rotating Turbine," ASME *Journal of Turbomachinery*, Vol. 111, pp. 8–19.

Dunn, M. G., Kim, J., Civinskas, K. C., and Boyle, R. J., 1994, "Time Averaged Heat Transfer and Pressure Measurements and Comparison With Prediction for a Two-Stage Turbine," ASME *Journal of Turbomachinery*, in press.

Kline, S. J., and McClintock, F. A., 1953, "Describing Uncertainties in Single-Sample Experiments," *Mechanical Engineering*, Vol. 75, Jan., pp. 3–8.

Liu, X., and Rodi, W., 1989, "Measurements of Unsteady Flow Over and Heat Transfer From a Flat Plate," ASME Paper No. 89-GT-2.

Liu, X., and Rodi, W., 1992, "Measurements of Unsteady Flow and Heat Transfer in a Linear Turbine Cascade," ASME Paper No. 92-GT-323.

Mayle, R. E., and Dullenkopf, K., 1990, "A Theory for Wake-Induced Transition," ASME *Journal of Turbomachinery*, Vol. 112, pp. 188–195.

Mayle, R. E., 1991, "The Role of Laminar-Turbulent Transition in Gas Turbine Engines," ASME *Journal of Turbomachinery*, Vol. 113, pp. 509–537.

Mehendale, A. B., Han, J. C., and Ou, S., 1991, "Influence of High Mainstream Turbulence on Leading Edge Heat Transfer," ASME JOURNAL OF HEAT TRANSFER, Vol. 113, pp. 843–850.

O'Brien, J. E., and Capp, S. P., 1989, "Two-Component Phase-Averaged Turbulence Statistics Downstream of a Rotating Spoked-Wheel Wake Generator," ASME *Journal of Turbomachinery*, Vol. 111, pp. 475–482.

Priddy, W. J., and Bayley, F. J., 1988, "Turbulence Measurements in Turbine Blade Passages and Implications for Heat Transfer," ASME *Journal of Turbomachinery*, Vol. 110, pp. 73–79.

Wittig, S., Dullenkopf, K., Schulz, A., and Hestermann, R., 1987, "Laser-Doppler Studies of the Wake-Effected Flow Field in a Turbine Cascade," ASME *Journal of Turbomachinery*, Vol. 109, pp. 170–176.

Wittig, S., Schulz, A., Dullenkopf, K., and Fairbank, J., 1988, "Effects of Free-Stream Turbulence and Wake Characteristics on the Heat Transfer Along a Cooled Gas Turbine Blade," ASME Paper No. 88-GT-179.

Young, C. D., Han, J. C., Huang, Y., and Rivir, R. B., 1992, "Influence of Jet-Grid Turbulence on Flat Plate Turbulent Boundary Layer Flow and Heat Transfer," ASME JOURNAL OF HEAT TRANSFER, Vol. 114, pp. 65–72.

Uneven Wall Temperature Effect on Local Heat Transfer in a Rotating Two-Pass Square Channel With Smooth Walls

J.-C. Han
HTRI Professor.
Fellow ASME

Y.-M. Zhang
Research Associate.
Mem. ASME

Kathrin Kalkuehler[1]

Turbine Heat Transfer Laboratory,
Department of Mechanical Engineering,
Texas A&M University,
College Station, TX 77843-3123

The influence of uneven wall temperature on the local heat transfer coefficient in a rotating, two-pass, square channel with smooth walls is investigated for rotation numbers from 0.0352 to 0.352 by varying Reynolds numbers from 25,000 to 2500. The two-pass square channel, composed of 12 isolated copper sections, has a length-to-hydraulic diameter ratio of 12. The mean rotating radius to the channel hydraulic diameter ratio is kept at a constant value of 30. Three cases of thermal boundary conditions are studied: (A) four walls at the same temperature, (B) four walls at the same heat flux, and (C) trailing wall hotter than leading with side walls unheated and insulated. The results for case A of four walls at the same temperature show that the first channel (radial outward flow) heat transfer coefficients on the leading surface are much lower than that of the trailing surface due to the combined effect of Coriolis and buoyancy forces. The second channel (radial inward flow) heat transfer coefficients on the leading surface are higher than that of the trailing surface. The difference between the heat transfer coefficients for the leading and trailing surface in the second channel is smaller than that in the first channel due to the opposite effect of Coriolis and buoyancy forces in the second channel. However, the heat transfer coefficients on each wall in each channel for cases B and C are higher than case A because of interactions between rotation-induced secondary flows and uneven wall temperatures in cases B and C. The results suggest that the effect of uneven wall temperatures on local heat transfer coefficients in the second channel is greater than that in the first channel.

Introduction

Advanced gas turbine engines require combined cooling technologies such as blade surface film cooling and blade internal convective cooling. This investigation considers blade internal convective cooling with rotation. Since heat is transferred from both the blade pressure and suction surfaces, rib turbulators (turbulence promoters) are often cast on two opposite walls of the blade internal coolant passages (i.e., inner walls of the pressure-trailing and suction-leading surface) to enhance heat transfer to the cooling air. A typical blade internal coolant passage can be modeled as a single pass or multipass rectangular channel with four smooth walls or two opposite rib-roughened walls. This paper models the blade internal coolant passage as a two-pass square channel with four smooth walls (see Fig. 1) and focuses particularly on the effect of uneven surface temperature on local heat transfer coefficient distributions in a rotating two-pass square channel with four smooth walls.

Most available data/correlations in the literature on turbine blade internal cooling are from tests performed with nonrotation flow conditions (e.g., Han, 1984, 1988; Han and Zhang, 1991). Heat transfer data are difficult and expensive to obtain under rotation; therefore, only limited amounts of data are available in the open literature. Mori et al. (1971) studied the mean convective heat transfer in a rotating radial circular pipe. Clifford et al. (1984) reported the local and mean transfer in a triangular-sectioned duct rotating in the orthogonal model. Harasgama and Morris (1988), Morris and Ghavami-Nasr (1991), and Morris and Salemi (1992) studied the effect of rotation on heat transfer characteristics of circular, triangular, rectangular, and square-sectioned coolant passages of gas turbine rotor blades. Guidez (1989) presented the study of convective heat transfer in a rotating rectangular channel. Taslim et al. (1991a, 1991b) studied heat transfer coefficients in a rotating channel with ribbed walls. Wagner et al. (1991a, 1991b, 1992) investigated local heat transfer in rotating serpentine passages with smooth walls and with two opposite ribbed walls. With the exception of Taslim et al. (1991a, 1991b), Wagner et al. (1992) and Clifford et al. (1984), all of the abovementioned work was conducted with smooth wall models, and with the exception of Wagner et al. (1991a, 1991b, 1992), the aforementioned studies were tested for straight channels. Some investigators found that large increases and decreases in trailing and leading surface heat transfer occur under certain conditions of rotation, while other investigators found lesser effects. Some inconsistencies exist between investigators due to differences in measurement techniques, models, and test conditions.

Wagner et al. (1991a, 1991b) performed the most thorough investigation of the effects of Coriolis and buoyancy forces on local heat transfer coefficient distributions of a multipass square channel with smooth walls. Wagner et al. (1991a, 1991b) found that the difference in heat transfer between rotating and nonrotating flow conditions is primarily due to secondary flows associated with Coriolis and centrifugal buoynacy forces (see Fig. 1). The trailing surface heat transfer coefficient with rotation of the first coolant passage (radial outward flow) can be increased up to 3.5 times the fully developed circular tube value without rotation while the leading surface heat transfer coefficient can be decreased 40 percent of the fully developed circular tube values. The local heat transfer coefficient on the

[1]Current address: Fakultät für Maschineubau, Ruhr-Universität, Bochum, Federal Republic of Germany.

Contributed by the Heat Transfer Division for publication in the JOURNAL OF HEAT TRANSFER. Manuscript received by the Heat Transfer Division August 1992; revision received May 1993. Keywords: Forced Convection, Rotating Flows, Turbines. Associate Technical Editor: R. J. Simoneau.

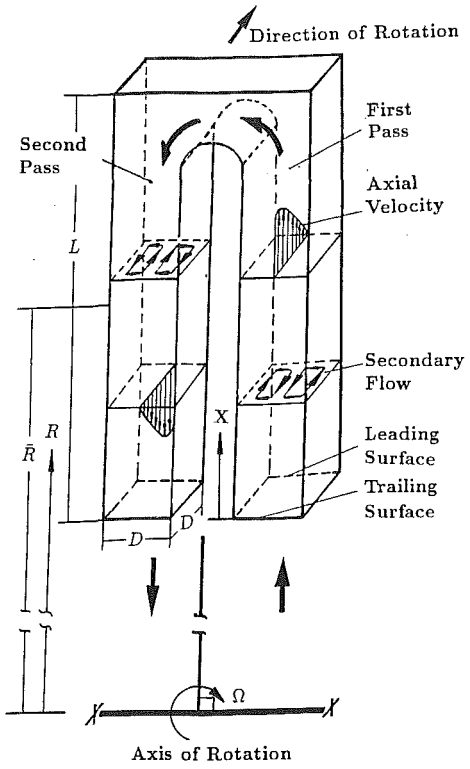

Fig. 1 Conceptual view of the velocity distribution in a rotating, two-pass channel

trailing (pressure) surface of the first coolant passage (radial outward flow) increases with increasing rotational speed and wall-to-coolant temperature difference. However, the local heat transfer coefficient on the leading (suction) surface decreases with increasing rotational speed but increases with wall-to-coolant temperature differences. The effect of rotation on the heat transfer coefficient in the second coolant passage (radial inward flow) is significantly different when compared to the first coolant passage (radial outward flow). The heat transfer coefficient for the inward flowing passage increases on the leading surface and decreases on the trailing surface, which is the opposite of the effect in the outward flowing passage. The heat transfer coefficient for the inward flowing passage increases only 10–20 percent on the leading surface compared to the stationary result while the heat transfer coefficient on the trailing surface decreases about 5–30 percent compared to the stationary values. Therefore, the difference between the rotation effect on the heat transfer coefficient of the leading and trailing surfaces in the second coolant passage is greatly reduced compared to that in the first coolant passage.

The previously mentioned studies (Wagner et al., 1991a, 1991b) were limited to uniform wall temperatures of the multipass square channel. However, the heat flux or temperature of the leading surface is quite different from that of the trailing surface and sidewalls (i.e., uneven wall temperature) in advanced gas turbine blades (Han et al., 1992). Han and Zhang (1992) reported the influence of uneven wall temperature on the local heat transfer coefficient in a rotating square channel with smooth walls and radial outward flow. They confirm the previous investigator's results (Wagner et al., 1991a) in that the difference between the leading and trailing heat transfer coefficient in the outward flow passage can be up to six times for the case of four walls with uniform temperature. However, they found that the trailing surface heat transfer coefficients for the case of uneven wall temperature are slightly higher than for uniform surface temperature and the leading surface heat transfer coefficients for the uneven surface temperature are much higher than for the uniform surface temperature. This implies that the difference between the leading and trailing heat transfer coefficient with uneven wall temperature becomes smaller (only up to three times) compared to the uniform wall temperature case. The results suggest that the uneven wall temperature creates local buoyancy forces that change the effect of the rotation. Therefore, the local heat transfer coefficients on the leading and trailing surfaces are altered by the uneven wall temperature.

It is of interest to determine whether or not the effect of uneven wall temperature on the leading and trailing surface heat transfer coefficient in the first coolant passage (radial outward flow, Han and Zhang, 1992) can be applied to that in the second coolant passage (radial inward flow). This investigation is a continuation of the work of Han and Zhang (1992). The objective is to investigate the effect of wall heating condition on the local heat transfer coefficient in a rotating, two-pass, square channel with smooth walls. Three surface heating conditions are tested: (A) four walls at the same temperature (a baseline test to compare the data of Wagner et al., 1991b), (B) four walls at the same heat flux (an uneven wall temperature test to compare the data of four walls at the same

Nomenclature

A = heat transfer surface area
D = hydraulic diameter; square channel width or height
h = heat transfer coefficient
k = thermal conductivity of coolant (air)
L = heated channel length (each path)
Nu = Nusselt number = hD/k
Nu_o = Nusselt number in fully developed tube flow
Pr = Prandtl number
q_{net} = net heat transfer rate, W
q'' = net heat transfer flux, W/m^2
R = rotating radius
$\bar{R}$ = mean rotating radius
Re = Reynolds number = $\rho DV/\mu$
Ro = rotation number = $\Omega D/V$
T_b = local bulk mean coolant temperature, °C or K
T_{bi} = inlet bulk mean coolant temperature, °C or K
T_w = local wall temperature, °C or K
T_{wA} = local wall temperature of side A surface, °C or K
T_{wB} = local wall temperature of side B surface, °C or K
T_{wL} = local wall temperature of leading surface, °C or K
T_{wT} = local wall temperature of trailing surface, °C or K
V = mean coolant velocity
X = axial distance from heated channel inlet
$\Delta\rho/\rho$ = coolant-to-wall density ratio based on local bulk mean coolant temperature = $(\rho_b - \rho_w)/\rho_b = (T_w - T_b)/T_w$
$(\Delta\rho/\rho)_i$ = coolant-to-wall density ratio based on inlet bulk mean coolant temperature = $(\rho_{bi} - \rho_w)/\rho_{bi} = (T_w - T_{bi})/T_w$
μ = coolant dynamic viscosity
ρ = coolant density
ρ_b = coolant density based on local bulk mean coolant temperature
ρ_{bi} = coolant density based on inlet bulk mean coolant temperature
ρ_w = coolant density based on local wall temperature
Ω = rotational speed, rpm

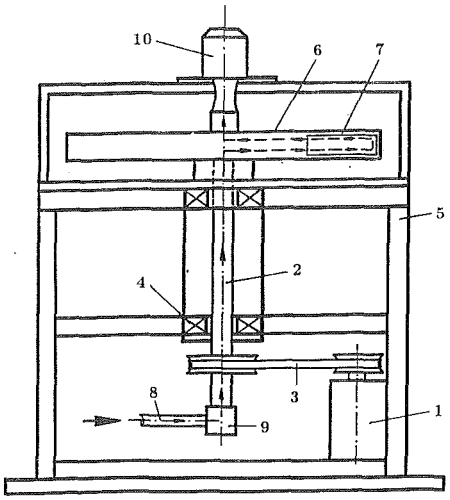

1. Electric Motor with Controller
2. Rotating Shaft
3. Belt Drive Pully System
4. Bearing Support System
5. Steel Table
6. Rotating Arm
7. Test Section
8. Compressor Air
9. Rotary Seal
10. Slip Ring

Fig. 2 Schematic of the rotating rig

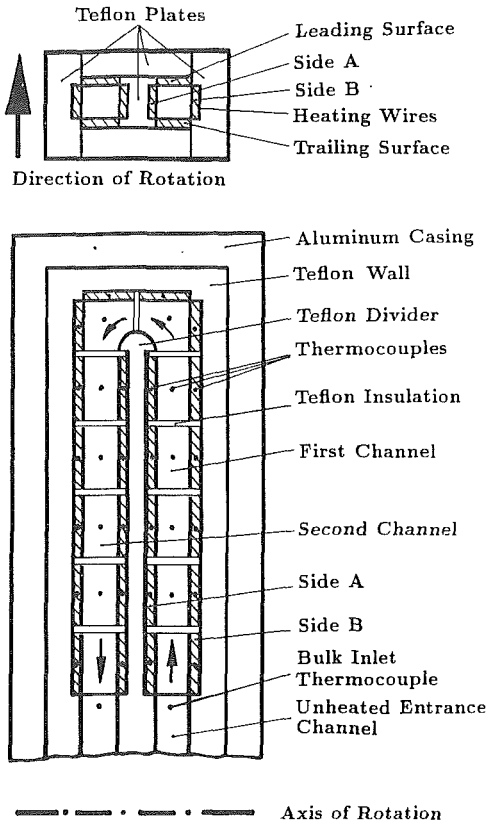

Fig. 3 Schematic of the two-pass heat transfer test model

temperature. The absolute temperature ratio of the first channel leading surface (or second channel trailing surface) and first channel trailing surface (or second channel leading surface) to the side wall is 1.05 and 0.95, respectively), and (C) trailing wall hotter than leading but two side walls unheated and insulated (an uneven wall temperature test to simulate the actual turbine operating conditions. The absolute temperature ratio of the trailing and leading surfaces to the side wall is 1.10 and 1.05, respectively).

Experimental Facility

Figure 2 shows a schematic of the rotating rig. The regulated compressor air is routed through an orifice meter, which measures the coolant flow rate to the hollow rotating shaft, hollow rotating arm, and test model (two-pass channel) and is then exhausted into the atmosphere at the exit (top) of the rotating shaft. The model pressure is about one atmosphere. A 100 contact slip ring transfer outputs from thermocouples attached to the rotating channel to a 100 point data logger interfaced to an IBM computer. A second 32 contact slip ring transfers outputs from heaters attached to the rotating channels to a 32 point variac connected with digital multimeters. The local surface temperature and heat flux can be measured through these slip ring systems. The rotating speed is measured by a digital photo tachometer.

It is better to have a test section that can determine the regionally averaged heat transfer coefficients in the duct streamwise flow direction in order to obtain true, regionally averaged heat transfer coefficients for turbine cooling design. The two-pass square duct is divided into 12 short copper sections as shown in Fig. 3. Each copper section is composed of four copper plates and has an inner crosssection of 1.27 cm by 1.27 cm (1/2 in. by 1/2 in.). Thin Teflon strips are machined along the periphery contact surface between copper sections as insulation to prevent possible heat conduction. The length-to-hydraulic diameter ratio (L/D) of the square test duct is 12. The ratio of the mean rotating arm radius to the channel hydraulic diameter ($\overline{R}/D$) is 30. Figure 3 also shows the cross section of the test duct. The resistance heaters are uniformly cemented between the copper plate backface grooves and the Teflon wall to insure good contact. Each of the four duct walls has its own heater with each heater independently controlled by a variac transformer. Each heater provides a controllable heat flux for each duct wall. The side walls are isolated from the leading and trailing walls to eliminate heat conduction. The entire heated test duct is insulated by Teflon material. The local wall temperature of the test duct is measured by 48 copper-constantan thermocouples distributed along the length and across the circumference of the copper duct. Two more thermocouples measure the inlet and outlet bulk temperature. There is an unheated Teflon entrance duct (not shown in Fig. 3) that has the same cross section and length as that of the test duct. This entrance duct serves to establish hydrodynamically fully developed flow at the entrance to the test duct. The inlet velocity profiles were not measured.

Data Reduction

The local heat transfer coefficient is calculated from the local net heat transfer rate per unit surface area to the cooling air, the local wall temperature on each copper plate, and the local bulk mean air temperature as:

$$h = (q_{\text{net}})/[A\,(T_w - T_b)] \tag{1}$$

Equation (1) is used for the local leading, trailing, and side surface heat transfer coefficient calculations. The local net heat transfer rate (q_{net}) is the electrical power generated from the heaters minus the heat loss outside the test section. The electrical power generated from the heater is determined from the measured heater resistance and voltage on each wall of the test duct. The effect of the local wall temperature variation on the local heater resistance is estimated to be less than 2 percent but is included in the data reduction. The effect of axial wall conduction between copper sections on the local net heat transfer rate is less than 2 percent but is also included in the data analysis. Heat loss tests were performed to determine the total

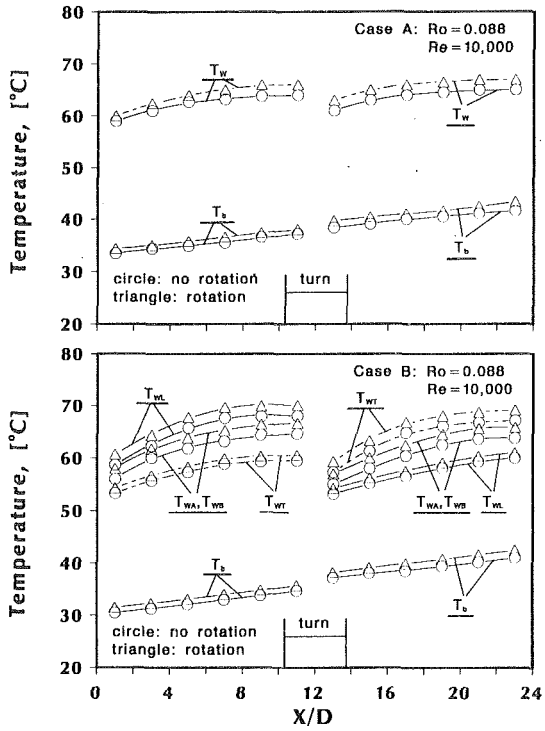

Fig. 4 Variation of the surface and coolant temperature with axial location for cases A and B

heat loss from each of the test model walls for a no-flow condition (with rotation but without coolant flow). The heat loss test is performed by supplying electrical power to the test section until the steady-state condition is achieved. This is done for several different power inputs to obtain the relation between the total heat loss from each surface and the corresponding surface temperature. The heat loss test (without air flow) is performed for three different surface heating conditions (cases A, B, and C) and with and without rotation, respectively. The average heat loss of case A is 10–20 percent of the heat input for Reynolds numbers greater than 10,000, while the average heat loss for cases B and C are slightly lower than that for case A.

The local wall temperatures used in Eq. (1) are read from the thermocouple output of each copper plate. The local bulk mean air temperature used in Eq. (1) is calculated from the local net heat input to the coolant flow through each set of four heated surfaces. The local bulk mean temperature is determined by marching along the test duct and calculating the temperature rise from the local net heat input to the coolant. The calculation is started at the inlet of the heated test duct where the coolant temperature is measured by a single thermocouple (about 30°C). The local bulk mean air temperature for each heated surface is determined by averaging the inlet and exit calculated bulk mean air temperatures for each set of four heated walls. Figure 4 shows the typical variations of local wall to bulk mean air temperature along the two-pass test duct for two different surface heating conditions (cases A and B) at rotation numbers of 0.0 and 0.088 (0.0 and 800 rpm at Re = 10,000). The local heat transfer coefficient calculated from Eq. (1) is converted to the dimensionless Nusselt number for a given flow Reynolds number. The properties in the Nusselt and Reynolds numbers are evaluated at the average of the inlet and outlet bulk mean coolant temperatures. To reduce the influence of flow Reynolds number on the heat transfer coefficient with rotation, the local Nusselt number of the present study is normalized by the Nusselt number for fully developed turbulent flow in smooth circular tubes with no rotation correlated by Dittus-Boelter/McAdams (Rohsenow and Choi, 1961) as:

$$\mathrm{Nu}/\mathrm{Nu}_0 = (hD/k)/[0.023\ \mathrm{Re}^{0.8}\mathrm{Pr}^{0.4}] \qquad (2)$$

with Pr = 0.72. The uncertainty of the local heat transfer coefficient is affected by the local wall-to-coolant temperature difference and the net heat input to the coolant flow from each heated copper plate. The uncertainty of the local heat transfer coefficient increases when decreasing the local wall-to-coolant temperature difference ($T_w - T_b$) and the net heat input. Based on the method described by Kline and McClintock (1953), the typical uncertainty in the Nusselt number was estimated to be less than 8 percent for Reynolds number larger than 10,000. However, the maximum uncertainty could be 20–25 percent higher for the lower heat transfer coefficient at the lowest Reynolds number tested.

Experimental Results and Discussion

According to Wagner et al. (1991b), the Nusselt number in a rotating passage is a function of rotating radius to channel hydraulic diameter ratio, streamwise distance to channel hydraulic diameter ratio, Reynolds number, Prandtl number, rotation number, wall-to-coolant temperature (density) difference ratio, and flow direction (radial outward flow or radial inward flow), respectively. The function relationship between Nusselt numbers and these parameters can be written as:

$$\mathrm{Nu} = f(\overline{R}/D,\ X/D,\ \mathrm{Re},\ \mathrm{Pr},\ Ro,\ \Delta\rho/\rho,\ \text{flow direction}) \qquad (3)$$

where Pr = 0.72 and $\overline{R}/D$ = 30 in the present study. The tests are performed for four Reynolds numbers (Re = 2500, 5000, 10,000 and 25,000) and two rotational speeds (Ω = 0 and 800 rpm). Five rotation numbers (Ro = 0.0, 0.0352, 0.088, 0.176, and 0.352) are obtained. Three surface heating conditions are tested: (A) four walls at the same temperature (T_w = 60–65°C and $(\Delta\rho/\rho)_i$ = 0.1), (B) four walls at the same heat flux (T_w = 60–65°C, 50–55°C, 55–60°C, respectively, for the first channel leading, trailing, and sidewalls, and $(\Delta\rho/\rho)_i$ = 0.1, 0.07, 0.08, respectively, for the first channel leading, trailing, and sidewalls. The reverse is true in the second channel leading and trailing), and (C) trailing wall hotter than leading but with sidewalls unheated and insulated (T_w = 60–65°C, 55–60°C, 45–50°C, respectively, for trailing, leading, and sidewalls, and $(\Delta\rho/\rho)_i$ = 0.1, 0.08, 0.05, respectively, for trailing, leading, and sidewalls). Coolant inlet temperature (T_{bi}) is about 30°C for cases A, B, and C. The results of all tests are evaluated on a local basis (i.e., on the leading and trailing surfaces along the X/D streamwise direction in the first and second coolant passage) by varying each parameter while holding the remaining parameters constant. The effect of each parameter on the local heat transfer coefficients is presented in the following order: effect of uneven wall temperature (i.e., effect of each surface's $(\Delta\rho/\rho)_i$), effect of rotation number, and effect of buoyancy parameter.

Effect of Rotation and Uneven Wall Temperature

Radial Outward Flow. The local (regionally averaged) heat transfer results are presented as the axial distributions of a normalized Nusselt number ratio ($\mathrm{Nu}/\mathrm{Nu}_o$ versus X/D). Figures 5 and 6 show the effect of surface heating condition (cases A, B, and C) on the leading and trailing surface Nusselt number ratios for Ro = 0.352, 0.176, 0.088, and 0.0352, respectively. Note that the test results for the Nusselt number ratios on the leading and trailing surface with no rotation for all three cases of surface heating conditions are about the same within 5 percent. Therefore, the Nusselt number ratios with no rotation are presented as a single curve and included in Figs. 5 and 6 (read legend +) for comparison with the rotating data.

For case A of four walls at the same temperature (T_w = 60–65°C and $(\Delta\rho/\rho)_i$ = 0.1), as previously discussed by Wagner

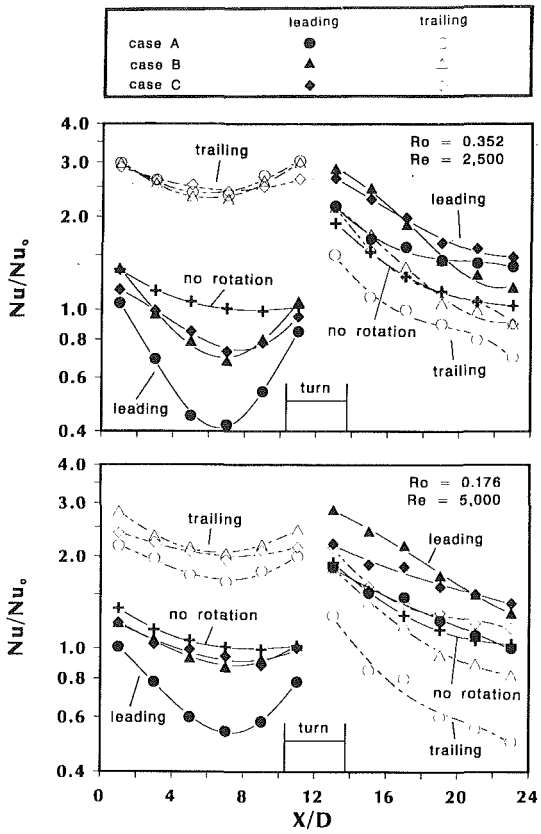

Fig. 5 Effect of surface heating condition on Nusselt number ratio variation for cases A, B, and C at rotation numbers of 0.352 and 0.176

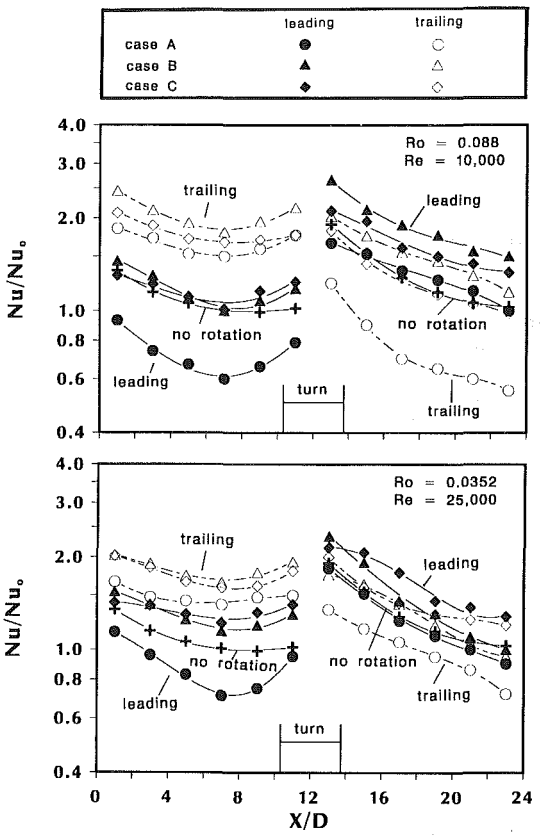

Fig. 6 Effect of surface heating condition on Nusselt number ratio variation for cases A, B, and C at rotation numbers of 0.088 and 0.0352

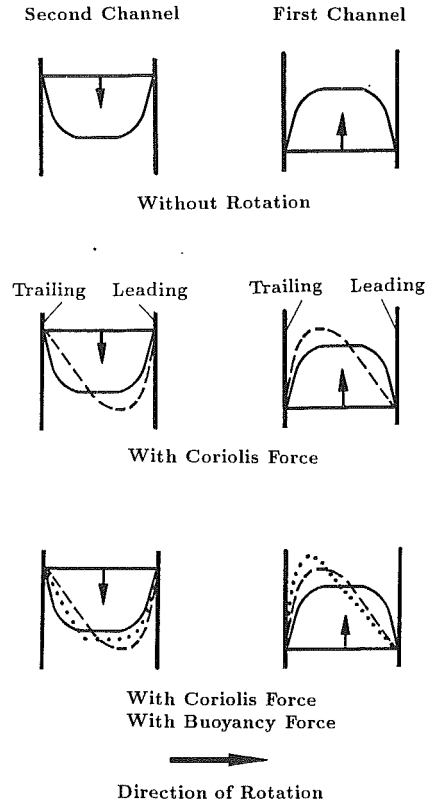

Fig. 7 Conceptual view of the effect of inertia, Coriolis, and buoyancy forces on outward and inward flow velocity and temperature profiles

et al (1991a) and Han and Zhang (1992), the heat transfer coefficient difference on the leading and trailing surfaces between rotating and nonrotating conditions is attributed to the increasing strength of the secondary cross-stream flow vortices due to the Coriolis force (Johnston et al., 1972) and the centrifugal buoyancy. The results presented in Figs. 5 and 6 can be explained in the conceptual view of the velocity and temperature profiles in the two-pass, rotating channel shown in Fig. 7. The higher heat transfer coefficients on the trailing surface are caused by (1) the coolant impingement (due to rotation) on the trailing surface creating a thinner boundary layer, and (2) the velocity profile distortion (due to rotation) inducing a stronger centrifugal buoyancy that further thins the trailing surface boundary layer. Decreases in heat transfer coefficients near the inlet of the channel on the leading surfaces are due to a thicker stabilized boundary layer. The subsequent increases in heat transfer coefficients near the end of the channel are attributed to the stronger centrifugal buoyancy-induced, destabilized wall turbulence boundary layer. These are the typical combined effects of Coriolis and buoyancy forces due to rotation on the leading and trailing surfaces of a square channel with four walls at the same temperature and with radially outward flow (see Fig. 7).

For case B of four walls at the same heat flux (q'' = 1005, 1682, 2916, and 6172 W/m^2 for Ro = 0.352, 0.176, 0.088, and 0.0352, respectively), the trailing surface temperature (T_w = 50–55°C and $(\Delta\rho/\rho)_i$ = 0.07) being lower than the leading (T_w = 60–65°C and $(\Delta\rho/\rho)_i$ = 0.1) and sidewall (T_w = 55–60°C and $(\Delta\rho/\rho)_i$ = 0.08) surface can result in more cooler fluid near the trailing surface. It is conjectured that the cooler fluid is accelerated due to centrifugal buoyancy and so a thinner boundary layer (steeper velocity and temperature slope) is created near the trailing surface. Meanwhile, the secondary cross-stream flow carries the cooler fluid from trailing and sidewalls back to the leading surface due to the Coriolis force. This cooler fluid causes a steeper temperature profile (compare to

case A of four walls at the same temperature) near the leading surface due to the centrifugal buoyancy force. Figures 5 and 6 therefore show higher trailing surface heat transfer coefficients for case B than case A and much higher leading surface heat transfer coefficients for case B than case A. The difference in heat transfer coefficients between the trailing and leading surface becomes smaller for case B. Similarly, for case C with trailing hotter than leading surfaces (T_w = 60–65°C and $(\Delta\rho/\rho)_i$ = 0.1 for trailing; T_w = 55–60°C and $(\Delta\rho/\rho)_i$ = 0.08 for leading) but two cold side surfaces (T_w = 45–50°C and $(\Delta\rho/\rho)_i$ = 0.05), the secondary cross-stream flow carriers the cooler fluid from the side walls back to the leading surface due to rotation. Figures 5 and 6 therefore show slightly higher trailing surface heat transfer coefficients for case C than case A and much higher leading surface heat transfer coefficients for case C than case A.

Radial Inward Flow. Figures 5 and 6 also show the effect of surface heating condition on leading and trailing surface Nusselt number ratios in the second coolant passage (radial inward flow). Note that the test results for the nonrotating Nusselt number ratios on the leading and trailing surface for the three cases of wall heating conditions are about the same within 5 percent. A single curve along the streamwise location is presented in Figs. 5 and 6 (read legend +) for comparison with the rotating data. The nonrotating heat transfer ratio decreases monotonically from 1.5 near the thermal entrance of the first passage to about 1.0 near the downstream (X/D = 9) before flow enters the sharp 180 deg turn. The nonrotating heat transfer ratio reaches the highest value of 2.0 right after the sharp 180 deg turn (X/D = 13) due to the strong turbulent flow turning effect. The Nusselt number ratio approaches the fully developed turbulent flow value of 1.0 near the outlet region of the second channel (X/D = 23). The nonrotating results agree with the previous study of local heat transfer ratios in a typical multipass coolant passage with smooth walls (Han and Zhang, 1991).

For case A with four walls at the same temperature, the effect of rotation on Nusselt number ratios for the second channel leading and trailing surfaces is not as strong as that in the first channel. The rotation in the second coolant passage (radial inward flow) causes an increase of the leading surface heat transfer ratio and a decrease of the trailing surface heat transfer ratio, which is opposite of that in the first channel (radial outward flow). The reason can be explained as follows. The coolant flows radially inward in the second passage while the Coriolis force acts in the opposite direction to that in the first passage, which shifts the symmetric velocity profile toward the leading surface (see Fig. 7). This results in the fluid moving faster near the leading surface and slower near the trailing surface. The heat transfer coefficient on the leading surface is expected to be higher than that on the trailing surface; however, the buoyancy force acts in the radially outward flow direction, which is opposite to the coolant inward flow direction and reduces the Coriolis force effect. Since the cooler fluid is near the leading surface, the buoyancy force pushes the Coriolis distorted profile back to the symmetric velocity/temperature profile (as shown in Fig. 7). We may conclude that the Coriolis and buoyancy forces in the outward flow channel act in the same direction (see Fig. 7), which results in a much higher heat transfer coefficient on the trailing surface and a very low heat transfer coefficient on the leading surface (see Figs. 5 and 6). The Coriolis and buoyancy forces in the inward flow channel act in the opposite direction (see Fig. 7), which results in a slightly higher heat transfer coefficient on the leading surface and a fairly lower heat transfer coefficient on the trailing surface (see Figs. 5 and 6). Therefore, the difference in the trailing and leading surface heat transfer coefficient in the inward flow channel is smaller than that in the outward flow channel.

For case B with four walls at the same heat flux (q'' = 1005, 1682, 2916, and 6172 W/m^2 for Ro = 0.352, 0.176, 0.088, and 0.0352, respectively), the leading surface temperature (T_w = 50–55°C and $(\Delta\rho/\rho)_i$ = 0.07) is lower than the trailing (T_w = 60–65°C and $(\Delta\rho/\rho)_i$ = 0.1) and sidewall (T_w = 55–60°C and $(\Delta\rho/\rho)_i$ = 0.08) surface and can result in more cooler fluid near the leading surface. Meanwhile, due to the Coriolis force the secondary cross-stream flow carries the cooler fluid from leading and side walls back to the trailing surface. This implies that the cooler fluid is closer to the leading surface while the Coriolis force drives the cooler fluid toward the trailing surface, which produces a greater velocity/temperature gradient (compared to case A) near both the leading and trailing surfaces, respectively). Therefore, the colder leading surface and hotter trailing surface (case B) eventually enhances the effect of rotation on the leading surface but reduces the effect of rotation on the trailing surface heat transfer coefficient in the second channel (inward flow direction). The leading and trailing surface heat transfer coefficients for case B are much higher than case A. Similarly, for case C with trailing hotter than leading surfaces (T_w = 60–65°C and $(\Delta\rho/\rho)_i$ = 0.1 for trailing, T_w = 55–65°C and $(\Delta\rho/\rho)_i$ = 0.08 for leading) but two cold side walls (T_w = 45–50°C and $(\Delta\rho/\rho)_i$ = 0.05), the secondary cross-stream flow carries the cooler fluid from the leading and side walls back to the trailing surface due to rotation. Figures 5 and 6 show that the trailing and leading surface heat transfer coefficients for case C are higher than case A.

Effect of Rotation Number and Uneven Wall Temperature. As previously discussed, the convective heat transfer coefficients on the leading and trailing surface of a rotating two-pass square channel with smooth walls can be affected by the Coriolis force (rotation number) and the surface heating condition (bulk or local buoyancy force). Figure 8 shows the variation of Nusselt number ratio with rotation number at selected axial locations for the three studied surface heating conditions. The experimental results of Wagner et al. (1991b) for the case of uniform wall temperature also are included for comparison. Note that the Wagner et al. results are based on the following conditions and axial locations: Ro calculated at Re = 25,000 and varying rotational speed, $(\Delta\rho/\rho)_i$ = 0.13, $\bar{R}/D$ = 49, and X/D = 4.7, 8.5, and 12.4, respectively. The present data for the case of four walls at the same temperature (case A) are based on: Ro calculated at Ω = 800 rpm and varying Re between 2500 and 25,000, $(\Delta\rho/\rho)_i$ = 0.10, $\bar{R}/D$ = 30, and X/D = 5, 9, and 11, respectively. The results show that the present Nusselt number ratio on the trailing and leading surface for case A of four walls at the same temperature (Fig. 8–circular symbols) agrees with those of Wagner et al. (Fig. 8—broken lines) except that X/D = 5. This confirms that the trailing surface Nusselt number ratio (in the first channel) increases with an increasing rotation number, whereas the leading surface Nusselt number ratio (in the first channel) decreases and then increases with an increasing rotation number for the case of uniform wall temperature condition. This also confirms that the difference between the leading and trailing surface heat transfer coefficients in the second channel is not as significant as that in the first channel. The leading and trailing heat transfer coefficients in the second channel are relatively insensitive to the rotation number compared to that in the first channel. The leading surface Nusselt number ratios of this study are much lower at X/D = 5 than that of Wagner et al. The difference may be caused by the flow inlet condition used in each study: a fully developed flow entrance for this study versus a sharp developing flow entrance for Wagner et al. The fully developed flow profile with a thicker boundary layer can be easily affected by the Coriolis force than the developing accelerating flow with a thinner boundary layer. The flow pattern at the test section entrance in the present study may

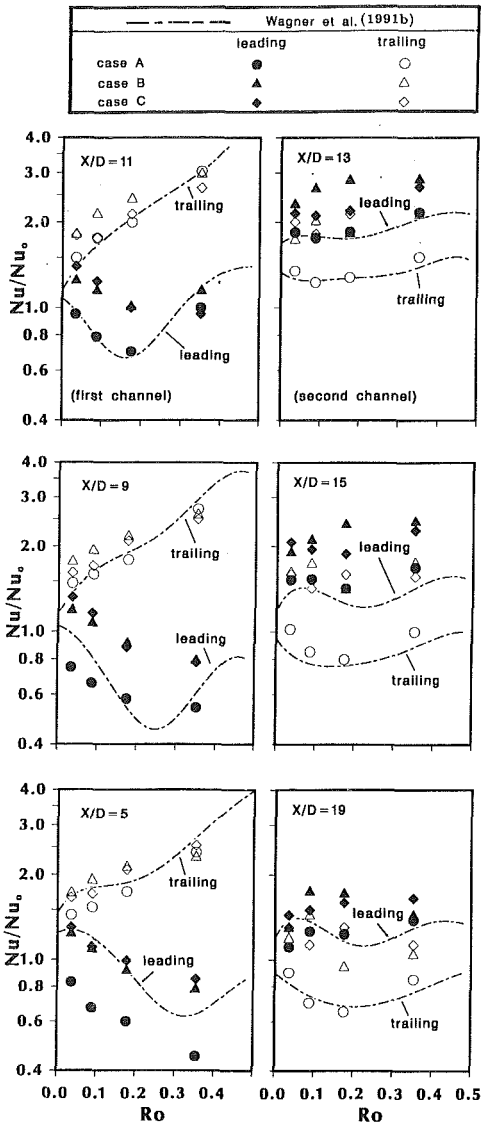

Fig. 8 Effect of rotation number on Nusselt number ratio variation at selected axial locations for cases A, B, and C and comparison with the previous results

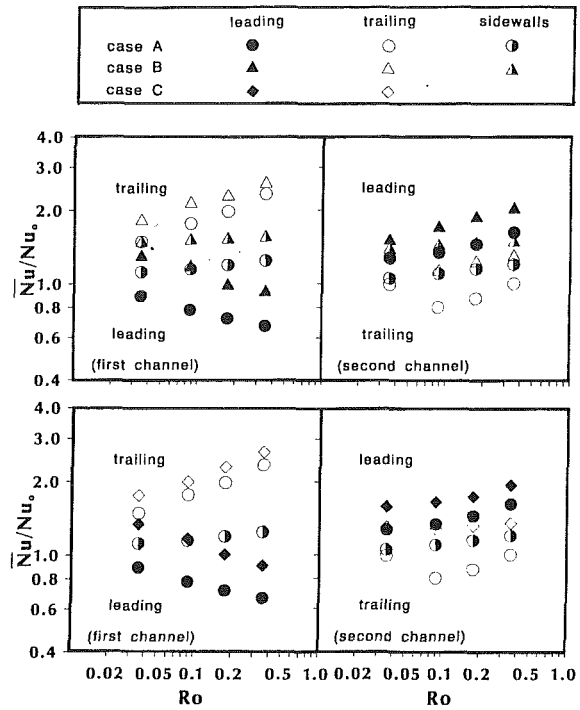

Fig. 9 Effect of rotation number on channel-average Nusselt number ratio variation for cases A, B, and C

have a stronger cross-stream flow and thicker boundary layer on the leading surface. Therefore, the leading surface Nusselt number ratios of this study are much lower. We may conclude that, except for the first channel entrance region effect, the present two-pass results on both leading and trailing surfaces agree with those of Wagner et al. for case A with four walls at the same temperature.

As previously mentioned, the uneven surface temperature on both the leading and trailing surfaces create unequal local buoyancy forces that alter the heat transfer coefficients. Figure 8 shows that the trailing surface Nusselt number ratios in the first channel for case B are about 20 percent higher than that for case A (except at $Ro = 0.352$). The leading surface Nusselt number ratios for case B (triangular symbols) are 40–80 percent higher than that for case A. The trailing surface Nusselt number ratios for case C are also slightly higher than case A but the leading surface Nusselt number ratios for case C (diamond symbols) are 40–80 percent higher than for case A. Figure 8 also shows the leading surface Nusselt number ratios in the second channel for case B are 30–70 percent higher than for case A, whereas the trailing surface Nusselt number ratios for case B are 80–100 percent higher than case A. The leading surface Nusselt number ratios for case C are 20–30 percent higher, while the trailing surface Nusselt number ratios for case C are 40–60 percent higher than case A. We may conclude that the uneven wall temperature enhances both the trailing and leading surface heat transfer coefficients of the two-pass rotating channel. The uneven wall temperature effect in the second channel is particularly more significant than that in the first channel.

Figure 9 shows the variation of the channel-averaged Nusselt number ratio with rotation number for cases A, B, and C. The channel-averaged Nusselt number ($\overline{Nu}$) on the leading surface (or trailing surface, side walls) is the average value of the entire leading surface (or trailing surface, side walls) local Nusselt number (Nu) from $X/D = 1$ to $X/D = 11$ for the first channel and from $X/D = 13$ to $X/D = 23$ for the second channel. The data are from four sets of rotation numbers for cases A, B, and C: $Ro = 0.352$, 0.176. 0.088, and 0.035 (based on $\Omega = 800$ rpm and Re = 2500, 5000, 10,000 and 25,000). The results show that in the first channel for case A with four walls at the same temperature, the channel-averaged Nusselt number ratio on the trailing surface increases from 1.5 to 2.5 when the rotation number change from 0.0176 to 0.352. However, the corresponding channel-averaged Nusselt number ratio of the leading surface decreases from 0.9 to 0.6, and the channel-averaged Nusselt number ratio on the side walls is about or equal to 1.2 to 1.3 over the range of studied rotation numbers. Again, the effect of uneven wall temperature in the first channel is to: (1) increase the leading surface average heat transfer coefficients for cases B and C (compared to case A); (2) increase the trailing surface heat transfer coefficients for cases B and C and (3) increase the side wall heat transfer coefficients for case B (compared to case A). Figure 9 also shows similar results of the channel-averaged Nusselt number ratio on the leading and trailing surface in the second channel for cases A, B, and C, except that the trailing surface Nusselt number ratio in the second channel for case A decreases with the rotation number and then increases again with further increasing rotation number. The uneven wall temperature (cases B and C) provides a much higher Nusselt number ratio on all surfaces over the range of studied rotation numbers.

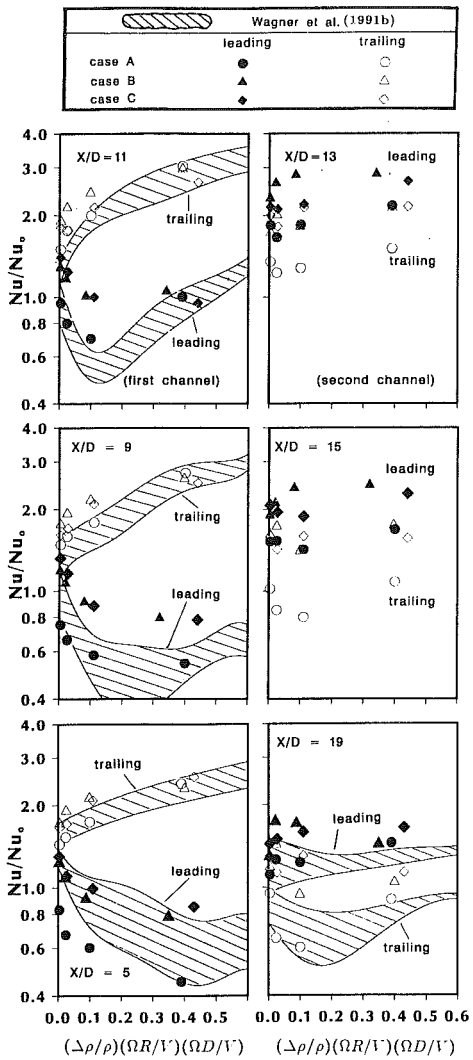

Fig. 10 Effect of buoyancy parameter on Nusselt number ratio variation at selected axial locations for cases A, B, and C and comparison with the previous results

Effect of Buoyancy Parameter and Uneven Wall Temperature. A buoyancy parameter $(\Delta\rho/\rho)\ (R/D)\ (Ro)^2$ was used by Wagner et al. (1991b) to consider the combined effects of Coriolis and buoyancy forces on heat transfer. The buoyancy parameter includes the effects of axial coolant-to-wall density ratio ($\Delta\rho/\rho = (T_w - T_b)/T_w$, related to buoyancy force), secondary cross-stream flow (Coriolis force, R_o), and rotating radius to hydraulic diameter ratio (R/D, related to buoyancy force). Figure 10 shows the variation of the Nusselt number ratio with the buoyancy parameter at selected axial locations for the three studied surface heating conditions. The experimental results from Wagner et al. (1991b) for the case of four walls at the same temperature are also included for comparison. The shaded area shown in Fig. 10 represents the data from Wagner from two sets of mean rotating radius $\overline{R}/D = 49$ and 33) and Ro between 0.0 and 0.48 (Wagner's plots are not available in the second channel at $X/D = 13$ and 15). Note that the $\overline{R}/D$ ratio of the present study is 30 and R_o is between 0.0 and 0.352. Wagner et al. (1991b) indicated that the Nusselt number ratio variation for a given buoynacy parameter is primarily due to the range of studied rotation numbers. Figure 10 shows that the present Nusselt number ratios on the trailing and leading surface for the case of uniform wall temperature (case A) are in the range of Wagner's data variation (except that, as discussed above, the leading surface Nusselt number ratios are much lower at $X/D = 5$). Again, the results show that the effect of uneven surface temperature is to: (1) increase the leading surface heat transfer coefficients in the first channel for cases B and C at a given buoyancy parameter condition, (2) increase the trailing surface heat transfer coefficients in the first channel for cases B and C except for the larger buoyancy parameter of 0.4, (3) increase the leading surface heat transfer coefficients in the second channel for cases B and C, and (4) increase the trailing surface heat transfer coefficients in the second channel for cases B and C (compared to case A).

Concluding Remarks

The influence of uneven wall temperature on the local heat transfer coefficients in a rotating, two-pass, square channel with smooth walls has been performed for rotating numbers from 0.0352 to 0.352 by varying the Reynolds number from 25,000 to 2,500. The main findings are:

1 The general trend of the effect of rotation on heat transfer is that the Nusselt number ratio for the first channel trailing surface (or second channel leading surface) increases while the Nusselt number ratio for the first channel leading surface (or second channel trailing surface) decreases and then increases with increasing rotation numbers (or buoyancy parameters). The increased (or decreased) heat transfer coefficients on the first channel trailing (or leading) surface are due to the combined effect of Coriolis and buoyancy forces from rotation. However, the leading and trailing surface heat transfer coefficient difference in the second channel is smaller than that in the first channel due to the opposite effects of Coriolis and buoyancy forces in the second channel. The Nusselt number ratio for the first channel trailing surface (or second channel leading surface) can be as high as 2.5–3.0 (or 1.5–2.0); however, the Nusselt number ratio for the first channel leading surface (or second channel trailing surface) can be as low as 0.4 (or 0.6) for case A with four walls at the same temperature at $(\Delta\rho/\rho)_i = 0.10$ and $Ro = 0.352$. This confirms the previous investigator's results (Wagner et al., 1991b).

2 The effect of uneven wall temperature enhances the heat transfer coefficients in a rotating channel compared to the uniform wall temperature. This is because of the interactions between rotation-induced secondary flows and uneven wall temperatures. The heat transfer coefficients for any surface in a two-pass, rotating channel are higher for cases B and C (uneven wall temperature) than for case A (uniform wall temperature). The uneven wall temperature effect on local heat transfer in the second channel is greater than that in the first channel.

3 The Nusselt number ratios for the first channel trailing and second channel leading surfaces for case B with uneven surface temperature are 20 percent and 30–70 percent higher, respectively, than for case A. The Nusselt number ratios for the first channel leading and second channel trailing surfaces for case B are 40–80 percent 80–100 percent higher, respectively, than for case A at a given buoyancy parameter or rotation number. Similarly, the Nusselt number ratios for the first channel trailing and second channel leading surfaces for case C are a few and 20–30 percent higher, respectively, than case A. However, the Nusselt number ratios for the first channel leading and second channel trailing surfaces for case C are 40–80 percent and 40–60 percent higher, respectively, than case A.

4 The Nusselt number ratios for the sidewalls in case A are about 20–30 percent higher than the nonrotating results, whereas the Nusselt number ratios for the sidewalls in case B are about 20–50 percent higher than case A.

5 It should be noted that the present results are based on the rotating channel with a long length entrance and a low rotating radius to channel diameter ratio ($\overline{R}/D = 30$). However, typical coolant channels in modern aircraft gas turbine

engines have a sharp entrance and a higher rotating radius to channel diameter ratio.

Acknowledgments

This investigation was supported by the Texas Higher Education Coordinating Board (Energy Research in Application Programs, TEES 70730) and by NASA Center for Space Power (RF2500020). Sincere appreciation goes to Ms. Pam Hoestenbach for her technical writing assistance.

References

Clifford, R. J., Morris, W. D., and Harasgama, S. P., 1984, "An Experimental Study of Local and Mean Heat Transfer in a Triangular-Sectioned Duct Rotating the Orthogonal Mode," ASME *Journal of Engineering for Gas Turbines and Power*, Vol. 106, pp. 661–667.

Guidez, J., 1989, "Study of the Convective Heat Transfer in Rotating Coolant Channels," ASME *Journal of Turbomachinery*, Vol. 111, pp. 43–50.

Han, J. C., 1984, "Heat Transfer and Friction in Channels With Two Opposite Rib-Roughened Walls," ASME JOURNAL OF HEAT TRANSFER, Vol. 106, pp. 774–781.

Han, J. C., 1988, "Heat Transfer and Friction Characteristics in Rectangular Channels With Rib Turbulators," ASME JOURNAL OF HEAT TRANSFER, Vol. 110, pp. 321–328.

Han, J. C., Zhang, P., 1991, "Effect of Rib-Angle Orientation on Local Mass Transfer Distribution in a Three-Pass Rib-Roughened Channel," ASME *Journal of Turbomachinery*, Vol. 113, pp. 123–130.

Han, J. C., Zhang, Y. M., and Lee, C. P., 1992, "Influence of Surface Heat Flux Ratio on Heat Transfer Augmentation in Square Channels With Parallel, Crossed, and V-Shaped Angled Ribs," ASME *Journal of Turbomachinery*, Vol. 114, pp. 872–880.

Han, J. C., and Zhang, Y. M., 1992, "Effect of Uneven Wall Temperatures on Local Heat Transfer in a Rotating Square Channel With Smooth Walls and Radial Outward Flow," ASME JOURNAL OF HEAT TRANSFER, Vol. 114, pp. 850–858.

Harasgama, S. P., and Morris, W. D., 1988, "The Influence of Rotation on the Heat Transfer Characteristics of Circular Triangular, and Square-Sectional Coolant Passages of Gas Turbine Rotor Blades," ASME *Journal of Turbomachinery*, Vol. 110, pp. 44–50.

Johnston, J. P., Halleen, R. M., and Lezius, D. K., 1972, "Effect of Spanwise Rotation on the Structure of Two-Dimensional Fully Developed Turbulent Channel Flow," *Journal of Fluid Mechanics*, Vol. 56, part 3, pp. 533–557.

Kline, S. J., and McClintock, F. A., 1953, "Describing Uncertainties in Single-Sample Experiments," *Mechanical Engineering*, Jan., pp. 3–8.

Mori, Y., Fukada, T., and Nakayama, W., 1971, "Convective Heat Transfer in a Rotating Radial Circular Pipe (2nd Report)," *International Journal of Heat and Mass Transfer*, Vol. 14, pp. 1807–1824.

Morris, W. D., and Ghavami-Nasr, G., 1991, "Heat Transfer Measurements in Rectangular Channels With Orthogonal Mode Rotation," ASME *Journal of Turbomachinery*, Vol. 113, pp. 339–345.

Morris, W. D., and Salemi, R., 1992, "An Attempt to Experimentally Uncouple the Effect of Coriolis and Buoyancy Forces on Heat Transfer in Smooth Circular Tubes Which Rotate in the Orthogonal Mode," ASME *Journal of Turbomachinery*, Vol. 114, pp. 858–864.

Rohsenow, W. M., and Choi, H., 1961, *Heat, Mass and Momentum Transfer*, Prentice-Hall, New Jersey, pp. 192–193.

Taslim, M. E., Rahman, A., and Spring, S. D., 1991a, "An Experimental Investigation of Heat Transfer Coefficients in a Spanwise Rotating Channel With Two Opposite Rib-Roughened Walls," ASME *Journal of Turbomachinery*, Vol. 113, pp. 74–82.

Taslim, M. E., Bondi, L. A., and Kercher, D. M., 1991b, "An Experimental Investigation of Heat Transfer in an Orthogonally Rotating Channel Roughened With 45 Degree Criss-Cross Ribs on Two Opposite Walls," ASME *Journal of Turbomachinery*, Vol. 113, pp. 346–353.

Wagner, J. H., Johnson, B. V., and Hajeck, T. J., 1991a, "Heat Transfer in Rotating Passages With Smooth Walls and Radial Outward Flow," ASME *Journal of Turbomachinery*, Vol. 113, pp. 42–51.

Wagner, J. H., Johnson, B. V., and Kopper, F. C., 1991b, "Heat Transfer in Rotating Serpentine Passages With Smooth Walls," ASME *Journal of Turbomachinery*, Vol. 113, pp. 321–330.

Wagner, J. H., Johnson, B. V., Graziani, R. A., and Yeh, F. C., 1992, "Heat Transfer in Rotating Serpentine Passages With Trips Normal to the Flow," ASME *Journal of Turbomachinery*, Vol. 114, pp. 847–857.

Improved Hybrid Lumped-Differential Formulation for Double-Pipe Heat Exchanger Analysis

F. Scofano Neto[1]

R. M. Cotta

Mechanical Engineering Department—EE/COPPE,
Universidade Federal do Rio de Janeiro—UFRJ,
CP 68503 Cidade Universitaria,
Rio de Janeiro—RJ—21945970—Brasil

Based on recent developments in the so-called Coupled Integral Equation Approach for the approximate solution of heat and mass diffusion problems, the classical lumped-differential formulation for double-pipe heat exchangers is extended and significantly improved in terms of overall accuracy. The energy equation for the outer annular channel is formally integrated and temperature gradients approximately taken into account, in contrast to the conventional lumped system analysis. The resulting partial differential equation for the inner stream, involving a more general type of boundary condition, is analytically handled through the generalized integral transform technique. A critical accuracy analysis is then performed in order to demonstrate the improvement over the plain lumped-differential formulation.

Introduction

Double-pipe heat exchangers are frequently employed in process heat transfer and for this reason considerable effort has been devoted to the analysis of such devices within the last few decades. Since the early work of Stein (1965a, 1965b), various contributions followed (Nunge and Gill, 1966; Gill et al., 1968; Mikhailov and Shishedjiev, 1976, 1981; Cotta and Özişik, 1986a) directed toward the analytical solution of the partial differential system that governs the temperature distributions within the two fluid streams. Due to the inherent difficulties in dealing with the associated eigenvalue problem coupled through the interface conditions, such developments were mainly on laminar concurrent fully developed flow situations, except for the countercurrent asymptotic solutions (Nunge and Gill, 1966). In parallel to these attempts in solving the complete fully differential coupled system, an alternative approach was advanced (Stein and Sastri, 1972) based on radially lumping the temperature distribution in the outer channel, by neglecting the temperature gradients across the annulus, and solving the resulting single partial differential equation for the inner stream with the more general boundary condition, involving the bulk temperature variation of the outer fluid along the exchanger length. Approximate solutions were then obtained through the Laplace transform technique (Sastri and Mastanaiah, 1973; Mastanaiah and Sastri, 1974), for both parallel-plate and double-pipe heat exchangers. More recently (Scofano Neto and Cotta, 1992), the ideas in the generalized integral transform technique (Cotta and Özişik, 1986b, 1987; Aparecido and Cotta, 1990a; Cotta, 1989, 1990; Guedes et al., 1991) were extended, allowing for an exact solution to this hybrid lumped-differential formulation, for both concurrent and counterflow situations. Also, in Scofano Neto and Cotta (1992), a critical inspection of the relative accuracy behind the classical lumping procedure was conducted, and applicability limits for this simplified approach were established, in terms of the governing dimensionless parameters. Due to space limitations, the analytical approach in Scofano Neto and Cotta (1992) is only briefly described and the presentation of numerical results is drastically reduced.

The present contribution brings a significant improvement to the simple lumped-differential model of double-pipe heat exchangers (Scofano Neto and Cotta, 1992), by taking into account, though approximately, the effects of nonnegligible temperature gradients in the outer stream. To accomplish this goal, the ideas in the coupled integral equation approach (Mennig and Özişik, 1985; Cotta et al., 1990; Aparecido and Cotta, 1990b), for the approximate analysis of diffusion problems, are here employed. The energy equation for the annular region is integrated over the cross section and the related integrals approximated through two-point Hermite formulae (Mennig et al., 1983) involving temperature and heat fluxes at the boundaries. The resulting expression is incorporated into the interfacial wall condition, which becomes a more general boundary condition for the inner fluid energy equation. The formulation here proposed is as simple as the plain lumped-differential model, and the analytical approach based on the generalized integral transform technique is described in detail. The accuracy improvement achieved is demonstrated by critical comparisons against benchmark results in the thermal entrance region for concurrent flow situation (Cotta and Özişik, 1986) and a limited number of asymptotic results for countercurrent configuration (Nunge and Gill, 1966), under different combinations of the governing dimensionless parameters. The classical lumped-differential formulation (Scofano Neto and Cotta, 1992) is, in fact, a special case of the more general model here advanced, and the relative thermal resistance of the fluids, which cancels out in the classical approach, appears as an important parameter in the improved version and limits the application range for such models. Numerical results for quantities of practical interest such as fluid bulk temperatures, Nusselt numbers, and exchanger effectiveness, are obtained under different parameter combinations, in order to establish these application ranges and report some additional information concerning the physical behavior of double-pipe heat exchangers for certain parameter variations.

Analysis

Although more general flow situations could be here considered, for the sake of illustrating the procedure to be proposed and comparing against the quite limited benchmark results available, we focus on hydrodynamically fully developed laminar flow conditions on both streams, either in cocurrent or counterflow arrangements. Viscous dissipation, axial conduction, and natural convection effects are neglected, and fluid properties are assumed to be constant. The fully differential model for the temperature distributions in both shell and tube sides, according to the geometry and coordinate sys-

[1]Permanent address: Seção de Engenharia Mecânica e de Materiais, Instituto Militar de Engenharia—IME, Rio de Janeiro—RJ—Brasil.

Contributed by the Heat Transfer Division for publication in the JOURNAL OF HEAT TRANSFER. Manuscript received by the Heat Transfer Division December 1990; revision received October 1992. Keywords: Forced Convection, Heat Exchangers, Numerical Methods. Associate Technical Editor: J. H. Kim.

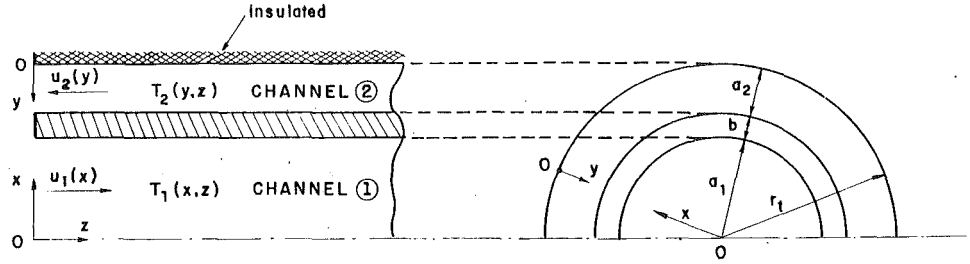

Fig. 1 Geometry and coordinate system for double-pipe heat exchanger

tem in Fig. 1, is given in dimensionless form as (Cotta and Özişik, 1986a; Stein and Sastri, 1972; Sastri and Mastanaiah, 1973; Mastanaiah and Sastri, 1974; Scofano Neto and Cotta, 1992):

Tube Side

$$RU_1(R)\frac{\partial\theta_1(R,Z)}{\partial Z}=\frac{\partial}{\partial R}\left[R\frac{\partial\theta_1(R,Z)}{\partial R}\right],\quad 0<R<1,\quad 0<Z<L \tag{1a}$$

Shell Side

$$(-1)^p\frac{KH}{2}[1-R(1-R^*)]U_2(R)\frac{\partial\theta_2(R,Z)}{\partial Z}=\frac{\partial}{\partial R}\left[(1-R(1-R^*))\frac{\partial\theta_2(R,Z)}{\partial R}\right],\quad 0<R<1,\quad 0<Z<L \tag{1b}$$

where p denotes the flow arrangement

$$p=\begin{cases}0, & \text{cocurrent flow}\\ 1, & \text{countercurrent flow}\end{cases}$$

with inlet conditions

$$\theta_1(R,0)=0,\quad \theta_2(R,pL)=1,\quad 0\le R\le 1 \tag{1c, d}$$

and boundary conditions

$$\frac{\partial\theta_1(0,Z)}{\partial R}=0,\quad \frac{\partial\theta_2(0,Z)}{\partial R}=0,\quad 0\le Z\le L \tag{1e, f}$$

$$K\frac{\partial\theta_1(1,Z)}{\partial R}+\frac{\partial\theta_2(1,Z)}{\partial R}=0,\quad 0\le Z\le L \tag{1g}$$

$$K_w\frac{\partial\theta_1(1,Z)}{\partial R}+\theta_1(1,Z)-\theta_2(1,Z)=0,\quad 0\le Z\le L \tag{1h}$$

where the dimensionless groups are given by

$R = x/a_1$ or y/a_2, dimensionless transverse coordinate
$Z = \alpha_1 z/(\bar{u}_1 a_1^2)$, dimensionless axial coordinate
$U_i(R) = u_i/\bar{u}_i$, $i = 1, 2$, dimensionless velocity profiles
$L = \alpha_1 L^*/(\bar{u}_1 a_1^2)$, dimensionless exchanger length
$\theta_i(R, Z) = (T_i - T_{e_1})/(T_{e_2} - T_{e_1})$, $i = 1, 2$, dimensionless temperature profiles

$$R^* = (a_1 + b)/(a_1 + b + a_2),\ \text{aspect ratio} \tag{2}$$

$K = (k_1/k_2)(a_1/(a_1 + b))(a_2/a_1)$, relative thermal resistance of fluids
$K_w = (k_1/k_w)\ln(1 + b/a_1)$, relative thermal resistance of wall
$H = \dot{m}_2 C_2/\dot{m}_1 C_1 = 2(\rho_2 c_2 \bar{u}_2)/(\rho_1 c_1 \bar{u}_1) \cdot (a_2/a_1) \cdot ((a_1+b)/a_1)$, heat capacity flow rate ratio for the limiting case of $R^* \to 1$, while the dimensionless velocity profiles are obtained from

$$U_1(R)=2(1-R^2) \tag{3a}$$

and

$$U_2(R)=\frac{2}{1+R^{*2}-2R_M^2}[1-(1-R(1-R^*))^2+2R_M^2\ln(1-R(1-R^*))] \tag{3b}$$

where

$$R_M=\left[\frac{1-R^*}{2\ln(1/R^*)}\right]^{1/2} \tag{3c}$$

The energy equation for the outer fluid stream is now integrated over the annulus cross section and the interface condition, Eq. (1g), utilized to yield:

$$\frac{d\theta_{2,\text{avg}}(Z)}{dZ}+(-1)^p\frac{2}{H^*}\frac{\partial\theta_1(1,Z)}{\partial R}=0,\quad 0<Z<L \tag{4a}$$

where the actual heat capacity flow rate ratio is given by

$$H^*=\frac{\dot{m}_2 C_2}{\dot{m}_1 C_1}=H\left[1+\frac{1-R}{2R^*}\right] \tag{4b}$$

with the inlet condition

$$\theta_{2,\text{avg}}(pL)=1 \tag{4c}$$

and the bulk temperature of the outer fluid is defined as

$$\theta_{2,\text{avg}}(Z)=\frac{1}{C_2^*}\int_0^1[1-R(1-R^*)]U_2(R)\theta_2(R,Z)dR \tag{4d}$$

where

Nomenclature

a_k = inner and outer tube radii, $k = 1, 2$
b = interfacial wall thickness
c_k = specific heats of inner and outer fluids, $k = 1, 2$
k_k = thermal conductivities of inner and outer fluids, $k = 1, 2$
L^* = exchanger length
$\dot{m}_k$ = mass flow rates, $k = 1, 2$
R = dimensionless radial coordinate
T_k = temperature distributions, $k = 1, 2$
u_k = velocity profiles, $k = 1, 2$
$\bar{u}_k$ = average velocities, $k = 1, 2$
$U_k(R)$ = dimensionless velocity profiles, $k = 1, 2$
x or y = transverse coordinate
z = axial coordinate
Z = dimensionless axial coordinate
α_k = thermal diffusivities, $k = 1, 2$
$\theta_k(R, Z)$ = temperature distributions, $k = 1, 2$
$\theta_{\text{avg},k}(Z)$ = bulk temperatures, $k = 1, 2$
μ = eigenvalues of Sturm-Liouville problem, Eq. (7)
ρ_k = densities, $k = 1, 2$

$$C_2^* = \int_0^1 [1 - R(1-R^*)] U_2(R) dR \quad (4e)$$

The conventional lumping procedure would now proceed by letting $\theta_2(1, Z) \cong \theta_{2,\text{avg}}(Z)$, therefore neglecting radial temperature gradients in the shell side, and providing a simple coupling between the two fluid streams through the interface condition, Eq. (1*h*), as presented in Scofano Neto and Cotta (1992). Here, we seek a more involved relation between $\theta_2(1, Z)$ and $\theta_{2,\text{avg}}(Z)$ that at least approximately accounts for the transverse temperature gradients and carries some information about parameters that would, otherwise, vanish in the plain lumping procedure, namely, aspect ratio, R^*, relative thermal resistance of fluids, K, and velocity profile of the outer fluid, $U_2(R)$. Following the ideas in the so-called coupled integral equation approach (Mennig and Özişik, 1985; Cotta et al., 1990; Aparecido and Cotta, 1990b), the integral that defines the average outer fluid temperature, Eq. (4*d*), is approximated through a two-point Hermite formula (Mennig et al., 1983) that utilizes the values of the integrand and its derivative at the extreme points. This $H_{1,1}$ formula is equivalent to the corrected trapezoidal rule and is given by:

$$H_{1,1}: \int_a^b y(\chi) d\chi = \frac{b-a}{2} [y(a) + y(b)] + \frac{(b-a)^2}{12} [y'(a) - y'(b)] + \frac{1}{720} y^{(\text{IV})}(\xi)(b-a)^5 \quad (5a)$$

where $a \le \xi \le b$, which when applied to Eq. 4(*d*) yields

$$\theta_{2,\text{avg}}(Z) \cong \frac{1}{12C_2^*} [U_2'(0)\theta_2(0, Z) - (R^* - U_2'(1))\theta_2(1, Z)], \quad (5b)$$

and prime denotes differentiation with respect to R.

The variable introduced, $\theta_2(0, Z)$, is eliminated by approximating the integral over the cross section of the temperature derivative, i.e.,

$$\int_0^1 \frac{\partial \theta_2(R, Z)}{\partial R} dR = \theta_2(1, Z) - \theta_2(0, Z) \quad (5c)$$

and the $H_{0,0}$ formula, which is equivalent to the trapezoidal rule, is employed for this purpose:

$$H_{0,0}: \int_a^b y(\chi) d\chi = \frac{b-a}{2} [y(a) + y(b)] + \frac{y''(\xi)}{12} (b-a)^3 \quad (5d)$$

where $a \le \xi \le b$, which provides:

$$\theta_2(0, Z) \simeq \theta_2(1, Z) - \frac{1}{2} \frac{\partial \theta_2(1, Z)}{\partial R} \quad (5e)$$

Utilizing Eq. (1*g*), the final relation between the bulk temperature, $\theta_{\text{avg},2}(Z)$, and the interfacial wall temperature, $\theta_2(1, Z)$, becomes:

$$\theta_2(1, Z) = \frac{12C_2^*}{U_2'(0) - R^* U_2'(1)} \theta_{2,\text{avg}}(Z) - \frac{KU_2'(0)}{2[U_2'(0) - R^* U_2'(1)]} \frac{\partial \theta_1(1, Z)}{\partial R} \quad (5f)$$

The hybrid lumped-differential formulation then becomes:

$$RU_1 \frac{\partial \theta_1(R, Z)}{\partial Z} = \frac{\partial}{\partial R} \left[R \frac{\partial \theta_1(R, Z)}{\partial R} \right], \quad 0 < R < 1, \quad 0 < Z < L \quad (6a)$$

$$\frac{d\theta_{2,\text{avg}}(Z)}{dZ} + (-1)^p \frac{2}{H^*} \frac{\partial \theta_1(1, Z)}{\partial R} = 0, \quad 0 < Z < L \quad (6b)$$

with inlet conditions

$$\theta_1(R, 0) = 0; \quad \theta_{2,\text{avg}}(pL) = 1, \quad 0 \le R \le 1 \quad (6c, d)$$

and boundary conditions

$$\frac{\partial \theta_1(0, Z)}{\partial R} = 0, \quad 0 \le Z \le L \quad (6e)$$

$$\left[K_w + \frac{KU_2'(0)}{2(U_2'(0) - R^* U_2'(1))} \right] \frac{\partial \theta_1(1, Z)}{\partial R} + \theta_1(1, Z) = C_1^* \theta_{2,\text{avg}}(Z), \quad 0 \le Z \le L \quad (6f)$$

where

$$C_1^* = \frac{12C_2^*}{U_2'(0) - R^* U_2'(1)} \quad (6g)$$

The formulation described by Eq. (6) is mathematically equivalent to the conventional lumped-differential model in Scofano Neto and Cotta (1992), but includes local information from the annular channel that appears in the coupling wall condition, Eq. (6*f*). Higher order two-point Hermite approximations (Mennig et al., 1983) can be employed in estimating the integrals of Eqs. (4*d*) and (5*c*), but the complexity of the resulting model might increase significantly, with a not necessarily significant gain in terms of precision.

Following the ideas in Scofano Neto and Cotta (1992), the generalized integral transform technique is applied to system (6), providing a reliable analytical solution as now described. The appropriate auxiliary eigenvalue problem is chosen as:

$$\frac{d}{dR} \left[R \frac{d\psi_i(R)}{dR} \right] + \mu_i^2 R U_1(R) \psi_i(R) = 0, \quad 0 < R < 1 \quad (7a)$$

$$\frac{d\psi_i(0)}{dR} = 0, \quad K_w^* \frac{d\psi_i(1)}{dR} + \psi_i(1) = 0 \quad (7b, c)$$

where

$$K_w^* = K_w + \frac{KU_2'(0)}{2(U_2'(0) - R^* U_2'(1))} \quad (7d)$$

which allows definition of the following integral transform pair:

$$\bar{\theta}_{1,i}(Z) = \frac{1}{N_i^{1/2}} \int_0^1 R U_1(R) \psi_i(R) \theta_1(R, Z) dR, \quad \text{transform} \quad (8a)$$

$$\theta_1(R, Z) = \sum_{i=1}^{\infty} \frac{1}{N_i^{1/2}} \psi_i(R) \bar{\theta}_{1,i}(Z), \quad \text{inversion} \quad (8b)$$

Equation (6*a*) is operated on with $\int_0^1 \psi_i(R)/N_i^{1/2} dR$ and the boundary conditions, Eqs. (6*f*) and (7*c*) are manipulated to yield the following equation for the transformed potential:

$$\frac{d\bar{\theta}_{1,i}(Z)}{dZ} + \mu_i^2 \bar{\theta}_{1,i}(Z) = -\frac{1}{N_i^{1/2}} C_1^* \psi_i'(1) \theta_{2,\text{avg}}(Z), \quad 0 < Z < L \quad (9a)$$

with the transformed inlet conditions

$$\bar{\theta}_{1,i}(0) = 0, \quad i = 1, 2, \ldots \quad (9b)$$

Equation (6*b*) for the outer fluid bulk temperature is to be solved simultaneously with Eq. (9*a*) for the transformed temperatures of the inner stream, provided the derivative at the wall in Eq. (6*b*) is rewritten in terms of the transformed potentials. Therefore, Eq. (6*a*) is integrated over the inner tube cross section and the inversion formula (8*b*) recalled, to yield:

$$\frac{\partial \theta_1(1, Z)}{\partial R} = \sum_{j=1}^{\infty} \bar{f}_j \frac{d\bar{\theta}_{1,j}(Z)}{dZ} \tag{10a}$$

where

$$\bar{f}_j = \frac{1}{N_j^{1/2}} \int_0^1 RU_1(R)\psi_j(R)dR \tag{10b}$$

Equation (6*b*) can then be rewritten as:

$$\frac{d\theta_{2,\text{avg}}(Z)}{dZ} + (-1)^{p+1} \frac{2C_1^*}{H^*} \left(\sum_{j=1}^{\infty} \frac{\bar{f}_j}{N_j^{1/2}} \psi_j'(1) \right) \times \theta_{2,\text{avg}}(Z)$$

$$= (-1)^p \frac{2}{H^*} \sum_{j=1}^{\infty} \mu_j^2 \bar{f}_j \bar{\theta}_{1,j}(Z), \quad 0 < Z < L \tag{11a}$$

with the inlet condition

$$\theta_{2,\text{avg}}(pL) = 0 \tag{11b}$$

It has been pointed out by a reviewer that Eqs. (9*a*) and (11*a*) could have also been obtained through the method of variation of parameters. Equations (9) together with Eqs. (11) form an infinite system of ordinary differential equations with constant coefficients, for the transformed inner fluid temperatures and outer fluid bulk temperature. For computational purposes, the infinite sums in Eq. (11*a*) are truncated to a sufficiently large finite order, N, and the resulting finite system of $(N + 1)$ O.D.E.'s is rewritten in matrix form as:

$$\mathbf{y}'(Z) = A\mathbf{y}(Z) \tag{12a}$$

$$y_i(0) = 0, \quad i = 1, 2, \ldots, N \tag{12b}$$

$$y_{N+1}(pL) = 1 \tag{12c}$$

where the solution vector $\mathbf{y}(Z)$ is given by

$$\mathbf{y}(Z) = \{\bar{\theta}_{1,1}, \bar{\theta}_{1,2}, \ldots, \bar{\theta}_{1,N}, \theta_{2,\text{avg}}(Z)\}^T \tag{12d}$$

and the coefficient matrix $A = \{a_{ij}\}$ is computed from

$$a_{ij} = \begin{cases} -\delta_{ij}\mu_i^2, & \text{for } i, j \le N \\ -\dfrac{C_1^*}{N_i^{1/2}} \psi_i'(1), & \text{for } i \le N, j = N+1 \\ (-1)^p \dfrac{2}{H^*} \mu_j^2 \bar{f}_j, & \text{for } i = N+1, j \le N \\ (-1)^p \dfrac{2}{H^*} \displaystyle\sum_{j=1}^{N} \mu_j^2 \bar{f}_j, & \text{for } i = N+1, j = N+1 \end{cases} \tag{12e}$$

System (12) is readily solved analytically through the associated matrix eigensystem analysis, in the form:

$$\mathbf{y}(Z) = \sum_{i=1}^{N+1} c_i^* \xi^{(i)} e^{\lambda_i Z} \tag{13a}$$

where the related matrix eigenvalues, λ_i's, and eigenvectors, $\xi^{(i)}$, are evaluated from the algebraic problem

$$(A - \lambda I)\xi = 0 \tag{13b}$$

and the constants c_i^* are computed by restricting the solution (13*a*) to satisfy the inlet conditions, Eqs. (12*b*, *c*), or

$$\sum_{j=1}^{N+1} c_j^* \xi_i^{(j)} = 0, \qquad i = 1, 2, \ldots, N$$

$$\sum_{j=1}^{N+1} c_j^* \xi_{N+1}^{(j)} e^{\lambda_j pL} = 1, \quad i = N+1 \tag{13c}$$

Problems (13*b*, *c*) are automatically and accurately handled through well-established subroutines for matrix eigenvalue problems and algebraic linear systems, readily available in scientific subroutines packages, such as the IMSL library (1987). The inversion formula (8*b*) is then recalled to provide the original temperature field within the tube side.

Quantities of practical interest can be computed from their definitions (Cotta and Özişik, 1986), such as:

Average Fluid Temperature

$$\theta_{1,\text{avg}}(Z) = \frac{\displaystyle\int_0^1 RU_1(R)\theta_1(R, Z)dR}{\displaystyle\int_0^1 RU_1(R)dR} \tag{14a}$$

Local Nusselt Number

$$\text{Nu}_1(Z) = \frac{2\dfrac{\partial \theta_1(1, Z)}{\partial R}}{\theta_1(1, Z) - \theta_{1,\text{avg}}(Z)} \tag{14b}$$

Overall Nusselt Number

$$\text{Nu}_0(Z) = \frac{2\dfrac{\partial \theta_1(1, Z)}{\partial R}}{\theta_{2,\text{avg}}(Z) - \theta_{1,\text{avg}}(Z)} \tag{14c}$$

Heat Exchanger Effectiveness

$$\epsilon(Z) = \frac{Q(Z)}{Q_{\max}} = \frac{\theta_{1,\text{avg}}(Z)}{H^*/(1 + H^*)}, \quad \text{for } p = 0 \tag{14d}$$

or

$$\epsilon(Z) = \theta_{1,\text{avg}}(Z), \quad \text{for } p = 1 \text{ and } H^* \ge 1 \tag{14e}$$

and

$$\epsilon(Z) = \frac{\theta_{1,\text{avg}}(Z)}{H^*}, \quad \text{for } p = 1 \text{ and } H^* < 1 \tag{14f}$$

where average fluid temperatures are related by

$$\theta_{2,\text{avg}}(Z) = 1 - \frac{\theta_{1,\text{avg}}(Z)}{H^*}, \quad \text{for } p = 0 \tag{14g}$$

$$\theta_{2,\text{avg}}(Z) = 1 + \frac{1}{H^*} \left[\theta_{1,\text{avg}}(Z) - \theta_{1,\text{avg}}(L) \right], \quad \text{for } p = 1 \tag{14h}$$

The conventional lumped-differential formulation is readily recovered from the present more general model by letting $K_w^* = K_w$ and $c_1^* = 1$.

Results and Discussion

Numerical results were obtained for all the quantities defined in Eqs. (14), for various combinations of the related parameters (p, K, H^*, K_w, R^*, L). Due to space limitations, only a few of such findings are here reported. The associated eigenvalue problem, Eq. (7), is readily solved by the Sign-Count method for Sturm–Liouville type problems, as introduced in Mikhailov and Özişik (1984). This finite-analytic procedure provides a safe and error-controlled computation of eigenvalues, and explicit expressions for eigenfunction and related quantities.

First, in Tables 1 and 2, numerical results for the asymptotic overall Nusselt numbers from both the conventional and improved lumped-differential formulations are compared, with $R^* = 1$ and $K_w = 0$. For a cocurrent flow arrangement, Table 1, benchmark results in both the asymptotic and thermal entrance regions are readily available (Cotta and Özişik, 1986a), allowing for a rather complete inspection of the relative accuracy of the two approximate models in terms of relative thermal resistance of the fluids, K, and heat capacity flow rate ratio, H^*. For increasing values of K, which correspond to increasing thermal resistance in the outer stream, the temper-

Table 1 Comparison of asymptotic overall Nusselt numbers for cocurrent flow double-pipe heat exchangers ($R^* = 1$; $K_w = 0$)

H^*	K	0.01	0.05	0.1	0.2	0.5	1.0
		1.0267*	1.0256	1.0242	1.0214	1.0121	0.9942
0.1		0.10%**	0.20	0.34	0.62	1.54	3.37
		0.09%***	0.10	0.15	0.19	0.50	1.24
		2.5631	2.5383	2.5070	2.4435	2.2498	1.9380
0.5		0.30%	1.28	2.54	5.21	14.3	32.6
		0.13%	0.43	0.85	1.74	4.91	11.2
		3.0419	2.9974	2.9419	2.8318	2.5161	2.0664
1.0		0.39%	1.88	3.80	7.84	21.4	47.8
		0.14%	0.62	1.26	2.60	7.17	15.4
		3.3252	3.2651	3.1906	3.0444	2.6370	2.0904
2.0		0.45%	2.30	4.69	9.72	26.7	59.8
		0.15%	0.76	1.56	3.27	9.09	19.6
		3.5722	3.4939	3.3929	3.1813	2.5106	1.6494
10.0		0.53%	2.78	5.84	12.9	43.6	117.7
		0.17%	0.96	2.13	5.18	20.4	57.0

*Exact $Nu_0(\infty)$ results from fully differential model (Cotta and Özisik, 1986a)
**Percentage error of lumped-differential model (Scofano Neto and Cotta, 1992)
***Percentage error of improved model (present)

Table 2 Comparison of asymptotic overall Nusselt numbers for countercurrent flow double-pipe heat exchangers ($R^* = 1$; $K_w = 0$; $H^* = 1$)

K	Lumped*	Improved**	Nunge and Gill***	Percent error (lumped)	Percent error (improved)
0.01	4.3636	4.3214	4.32	1.01	0.03
0.05	4.3636	4.2386	4.18	4.39	1.40
0.1	4.3636	4.1248	4.03	8.28	2.35
0.2	4.3636	3.9328	3.77	15.7	4.32
0.6	4.3636	3.2874	2.93	48.9	12.2
1.0	4.3636	2.8232	2.68	62.8	5.34

*Conventional lumped-differential model (Scofano Neto and Cotta, 1992)
**Present improved lumped-differential model
***Approximate asymptotic results for fully differential model (Nunge and Gill, 1966)

ature gradients in the annular region become more significant and the assumption of negligible gradients, implicit in the conventional lumping procedure, makes such results increasingly inaccurate. The more complete relation defined by Eq. (5*f*) approximately accounts for the steeper wall gradients, and provides a significant correction over all the range of K presented. Similarly, for increasing H^*, the convective heat transfer between the two streams is enhanced and, consequently, temperature gradients are markedly affected. Again, over the entire range of H^* here illustrated, the improved model provides a significant correction to the asymptotic region results. It should be noted that the value of $H^* = 10$, although not practical, is presented in order to illustrate the correction characteristics.

For a counterflow arrangement, a very limited number of studies on the fully differential model are readily available, due to the inherent difficulties in accurately solving the more involved nonclassical eigenvalue problem. The results of Nunge and Gill (1966) for the asymptotic overall Nusselt number are reproduced in Table 2 as benchmark results, obtained from an approximate solution of the associated eigenvalue problem, with $R^* = 1$, $K_w = 0$, and $H^* = 1$. The plain lumping procedure, for which the dependence on K cancels out, is essentially limited for K around 0.1 with relative errors of the order of 10 percent, while the improved version extends such limits to K around 1.0. The result for $K = 0.6$ seems to indicate nonmonotonic behavior of the error associated with the proposed model and/or a degree of uncertainty in the early and approximate computations of Nunge and Gill (1966). Several runs with intermediate values of K were made and always, as expected, satisfying the overall heat balance to at least five significant digits. Since situations of $K > 1.0$ are not frequently encountered in practice, the present simpler formulation can be, in most cases, an alternative to the more complex fully differential model of double-pipe heat exchangers, which is particularly interesting in the involved problems of counterflow configuration and turbulent regime. Although not so markedly in the simpler parabolic system of concurrent flow, the present approach saves analytical and computational effort, especially in the more involved elliptic counterflow problem. In this situation, the associated eigenvalue problem involves both a positive and negative spectrum of difficult evaluation, and purely numerical solutions to the original partial differential system require costly iterative procedures.

Figures 2–5 illustrate the behavior of the lumped-differential models within the thermal entrance region for different combinations of the related parameters (K, H^*, K_w, and R^*) in cocurrent flow exchangers. Figures 2 and 4 correspond to the local Nusselt number at the tube side, $Nu_1(Z)$, which requires the evaluation of radial temperature derivatives at the interface, while Figs. 3 and 5 correspond to the exchanger effectiveness, which is directly related to the average fluid temperature, evaluated through integration of the approximate temperature field over the tube cross section. For both quantities, the agreement between the improved model and the exact results (Cotta and Özişik, 1986b) is indeed better than with respect to the plain lumped-differential model (Scofano Neto and Cotta, 1992), for all the parameter combinations selected. Figures 2 and 3 illustrate a marked variation in the heat capacity flow rate ratio, $H^* = 0.5$ and 2.0, respectively, while Figs. 4 and 5 represent an extreme aspect ratio of $R^* = 0.6$, when the ordinary lumped procedure is even less reliable. In both cases, the improved formulation retains its excellent approximation characteristics, offering higher precision at essentially no extra cost with respect to the conventional lumped-differential model.

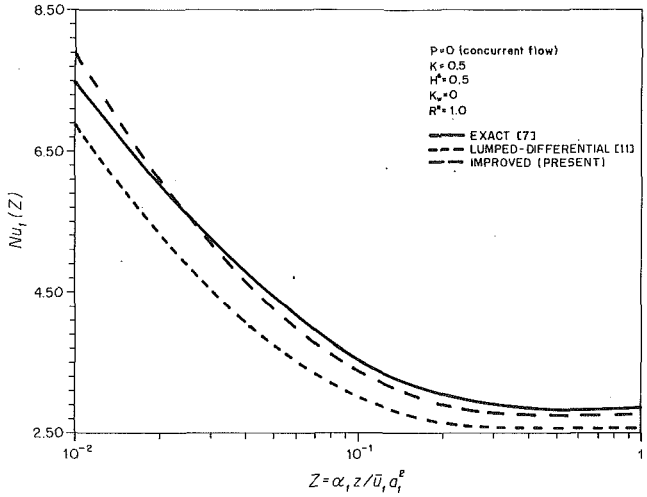

Fig. 2 Comparison of improved and plain lumped-differential models for local Nusselt number within the thermal entrance region ($p = 0$; $K = 0.5$; $H^* = 0.5$; $K_w = 0$; $R^* = 1.0$)

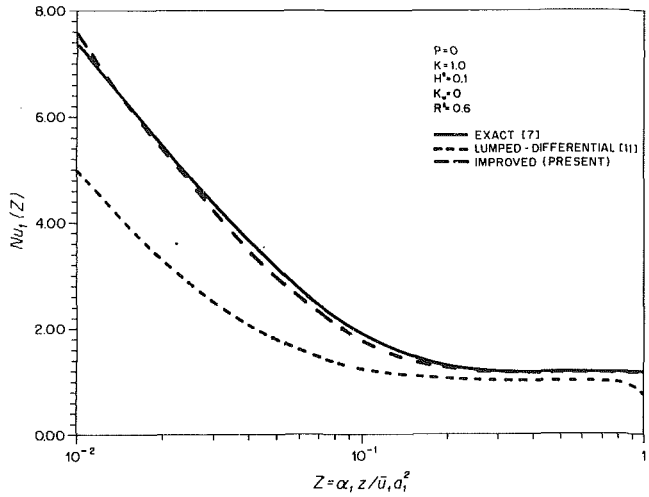

Fig. 4 Comparison of improved and plain lumped-differential models for local Nusselt number within the thermal entrance region ($p = 0$; $K = 1.0$; $H^* = 0.1$; $K_w = 0$; $R^* = 0.6$)

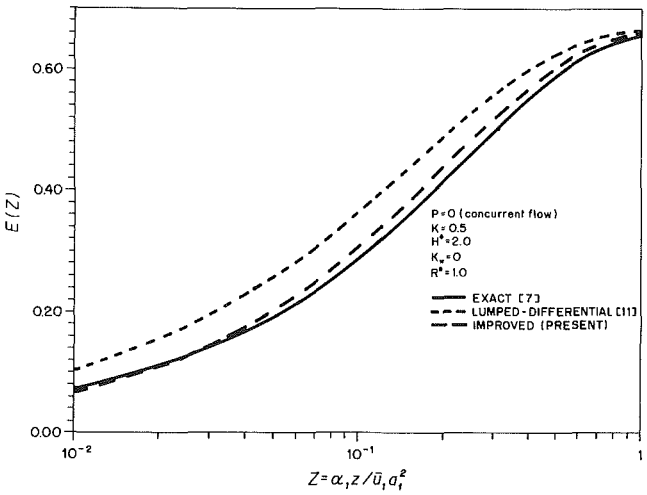

Fig. 3 Comparison of improved and plain lumped-differential models for exchanger effectiveness versus exchanger length ($p = 0$; $K = 0.5$; $H^* = 2.0$; $K_w = 0$; $R^* = 1.0$)

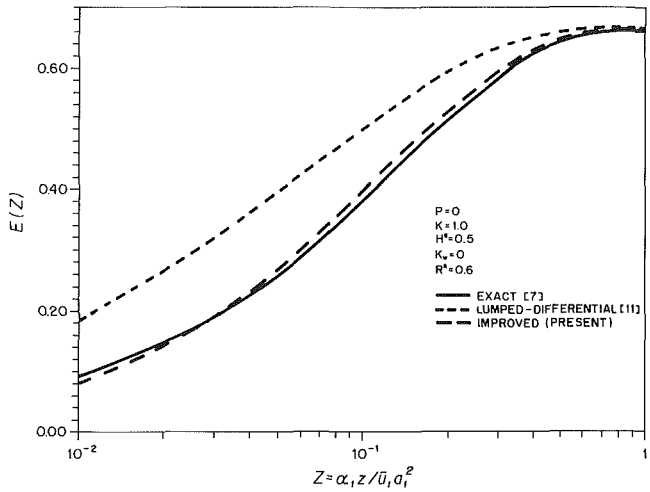

Fig. 5 Comparison of improved and plain lumped-differential models for exchanger effectiveness versus exchanger length ($p = 0$; $K = 1.0$; $H^* = 0.5$; $K_w = 0$; $R^* = 0.6$)

It should be recognized that the present approach is potentially an attractive alternative to various coupled problems in heat and mass transfer.

References

Aparecido, J. B., and Cotta, R. M., 1990a, "Thermally Developing Laminar Flow Inside Rectangular Ducts," *Int. J. Heat Mass Transfer*, Vol. 3, pp. 341–347.

Aparecido, J. B., and Cotta, R. M., 1990b, "Improved One-Dimensional Fin Solutions," *Heat Transfer Eng.*, Vol. 11, No. 1, pp. 49–59.

Cotta, R. M., and Özişik, M. N., 1986a, "Thermally Developing Concurrent Flow Circular Double Pipe Heat Exchanger Analysis," *8th Int. Heat Transfer Conference*, San Francisco, pp. 2805–2810.

Cotta, R. M., and Özişik, M. N., 1986b, "Laminar Forced Convection in Ducts With Periodic Variation of Inlet Temperature," *Int. J. Heat Mass Transfer*, Vol. 24, No. 10, pp. 1495–1501.

Cotta, R. M., and Özişik, M. N., 1987, "Diffusion Problems With General Time-Dependent Coefficients," *J. Braz. Assoc. Mech. Sciences, RBCM*, Vol. 9, No. 4, pp. 269–292.

Cotta, R. M., 1993, *Integral Transforms in Computational Heat and Fluid Flow*, CRC Press, Boca Raton, FL.

Cotta, R. M., 1990, "Hybrid Numerical-Analytical Approach to Nonlinear Diffusion Problems," *Num. Heat Transfer, Part B—Fundamentals*, Vol. 17, pp. 217–226.

Cotta, R. M., Özişik, M. N., and Mennig, J., 1990, "Coupled Integral Equation Approach for Solving Phase-Change Problem in a Finite Slab," *J. Franklin Inst.*, Vol. 327, No. 2, pp. 225–234.

Gill, W. N., Porta, E. M., and Nunge, R. J., 1968, "Heat Transfer in Thermal Entrance Region of Concurrent Flow Heat Exchangers With Fully Developed Laminar Flow," *Int. J. Heat Mass Transfer*, Vol. 11, pp. 1408–1412.

Guedes, R. O. C., Cotta, R. M., and Brum, N. C. L., 1991, "Heat Transfer in Laminar Tube Flow With Wall Axial Conduction Effects," *J. Thermophys. Heat Transfer*, Vol. 5, No. 4, pp. 508–513.

IMSL Library, 1987, MATH/LIB, Houston, TX.

Mastanaiah, K., and Sastri, V. M. K., 1974, "Surface Temperature Distributions in Double-Pipe Heat Exchangers," *Can. J. Chem. Eng.*, Vol. 52, pp. 838–840.

Mennig, J., Auerbach, T., and Hälg, W., 1983, "Two Point Hermite Approximations for the Solution of Linear Initial Value and Boundary Value Problems," *Comp. Meth. Appl. Mech. Eng.*, Vol. 39, pp. 199–224.

Mennig, J., and Özişik, M. N., 1985, "Coupled Integral Equation Approach for Solving Melting or Solidification," *Int. J. Heat Mass Transfer*, Vol. 28, pp. 1481–1485.

Mikhailov, M. D., and Shishedjiev, B. K., 1976, "Coupled at Boundary Mass or Heat Transfer in Entrance Concurrent Flow," *Int. J. Heat Mass Transfer*, Vol. 19, pp. 553–557.

Mikhailov, M. D., and Shishedjiev, B. K., 1981, "Heat Transfer in Concurrent Flow Double Pipe Heat Exchangers," in: *Heat Exchangers—Thermalhydraulics Fundamentals and Design*, S. Kakaç, A. E. Bergles, and F. Mayinger, eds., Hemisphere Publishing Corporation, New York.

Mikhailov, M. D., and M. N. Özişik, 1984, *Unified Analysis and Solutions of Heat and Mass Diffusion*, Wiley, New York.

Nunge, R. J., and Gill, W. N., 1966, "An Analytical Study of Laminar Counterflow Double Pipe Heat Exchangers," *AIChE Journal*, Vol. 12, pp. 279–289.

Sastri, V. M. K., and Mastanaiah, K., 1973, "Heat Transfer Parameters of a Parallel Plate Heat Exchanger," *Int. J. Heat Mass Transfer*, Vol. 16, pp. 857–861.

Scofano Neto, F., and Cotta, R. M., 1992, "Lumped-Differential Analysis of Concurrent Flow Double-Pipe Heat Exchangers," *Can. J. Chem. Eng.*, Vol. 70, pp. 592–595.

Stein, R. P., 1965a, "Heat Transfer Coefficient in Liquid Metal Councurrent Flow Double Pipe Heat Exchangers," *Chem. Engng. Progr. Symp. Series*, Vol. 59, pp. 64–75.

Stein, R. P., 1965b, "The Graetz Problem in Concurrent Flow Double Pipe Heat Exchangers," *Chem. Engng. Progr. Symp. Series*, Vol. 59, pp. 78–87.

Stein, R. P., and Sastri, V. M. K., 1972, "A Heat Transfer Analysis of Heat Exchangers With Laminar Tube-Side Turbulent Shell-Side Flows—A New Heat Exchanger Graetz Problem," *AIChE Symp. Series*, Vol. 68, pp. 81–89.

D. M. McEligot[1]
Fellow ASME

C. M. Stoots

W. A. Christenson

D. C. Mecham
Mem. ASME

W. G. Lussie[2]

Idaho National Engineering
Laboratory/EG&G Idaho,
Idaho Falls, ID 83415-3895

Turbulent Natural Convection From a Vertical Cylinder to an Array of Cooled Tubes

In order to determine whether available correlations are adequate to treat a complicated, turbulent natural convection problem encountered in industrial practice, experiments were conducted by resistively heating a slender, vertical cylinder centered inside a concentric perforated tube, which was, in turn, surrounded by an array of three larger-diameter cooled tubes. The ratio of the test section temperature to the cooling tube temperature was varied up to 2.6; and the Rayleigh number, based on tube diameter and properties evaluated at the cooling tube temperature, ranged from 2.9×10^4 *to* 9.2×10^5. *Results indicate that the convective heat transfer parameters for the perforated tube are about 15 percent higher than for the smooth bare tube centered in the same position relative to the array. The Nusselt number for convective heat transfer across the annulus between the heated test section and the perforated tube corresponded approximately to parallel laminar flow (i.e.,* $Nu_s \approx 1$).

1 Introduction

A recent industrial application, to nuclear reactors moderated with heavy water outside vertical tubes (Butcher et al., 1990; Leonard et al., 1990; Mochizuki and Ishii, 1992), revealed a need for basic information on gaseous natural convection from one heated circular tube in a closely packed array to surrounding tubes that are cooled. In the event of a loss-of-moderator incident, the core may be partially filled with air. In this scenario a control rod or safety rod may be heated by absorption of an incident gamma flux from fission product decay after the reactor is shut down, while water flow through cooling tubes holds the surroundings at a lower temperature. The thermal energy evolving in the rod must then be transferred by a combination of natural convection, thermal radiation, and thermal conduction to avoid exceeding material limits. In a typical case, the rod may also be immediately surrounded by a perforated guide tube, which could either enhance or inhibit thermal exchange.

Figure 1 demonstrates a cross section of an experimental model of the situation with the key features and Fig. 2 provides details of the central assembly. The generic solutions involved would be applicable to other industrial cases, such as a vertical tube in a heated array where it has a higher heating rate than its neighbors, protective safety shields around individual heated tubes, and high-temperature exhaust tubes in proximity to other surfaces. In general, the sizes and temperature difference are large so that the buoyant flow regime is turbulent, gas properties vary, and the tubes are slender in terms of aspect ratio.

For this situation, a number of questions arise concerning the transport via natural convection:

1 How should one predict heat transfer from the central tube to the surrounding array if the central tube is smooth?

2 Is there an increase or decrease in convective heat transfer parameters if the surface is interrupted by perforations?

3 How should one predict heat transfer from the smooth central tube to the surrounding perforated tube?

One of the *purposes* of the present work is to determine the correctness or inadequacy of available approaches to answer these questions; in the process we have provided new basic measurements of engineering value, and we have identified needs for further research beyond the present scope as well.

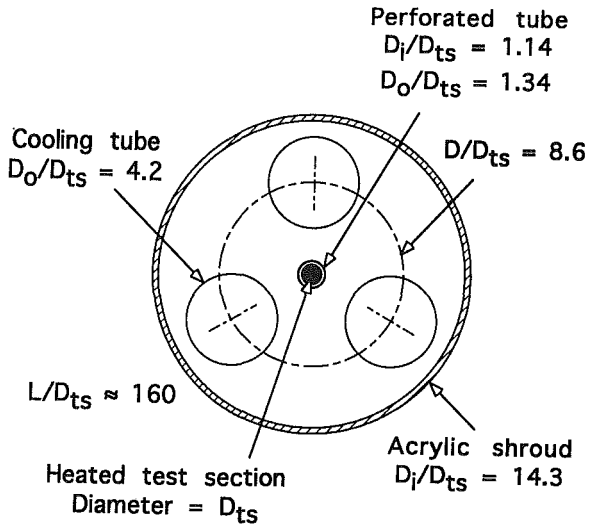

Fig. 1 Scale drawing of cross section of experimental model (in application the triangular pattern extends to additional concentric rings of cylinders)

For a typical application, the length-to-diameter ratios of individual tubes fall in the range of 30 to 300. If the temperature range is taken to be from room temperature to the melting point of aluminum, the length Rayleigh number will be greater than 10^{10}, so that the induced flow can be expected to be turbulent above a half meter from the bottom of the heated tube (Hama and Recesso, 1958).

It is evident that the generic configuration cannot reasonably be considered to be an isolated single tube in infinite surroundings. Essentially, the cylinder and its surrounding array form an enclosure, possibly described as an annulus with an irregular and/or extended outer surface consisting of the other tubes. Possible logical thermal boundary conditions for this natural convection problem are the specification of temperatures on the surfaces of the cylinder and of the surrounding array, plus appropriate conditions on the axial end surfaces. The dependent variables or desired results for this case include the convective heat flux from the cylinder, an appropriately defined convective heat transfer coefficient, and any undefined

[1] Also Professor Emeritus, Aero. Mech. Engr. Dept., University of Arizona, Tucson, AZ 85721.

[2] Also Visiting Professor, University of Idaho, Idaho Falls, ID 83415-2301.

Contributed by the Heat Transfer Division for publication in the JOURNAL OF HEAT TRANSFER. Manuscript received by the Heat Transfer Division September 9, 1992; revision received March 23, 1993. Keywords: Enclosure Flows, Natural Convection, Turbulence. Associate Technical Editor: J. R. Lloyd.

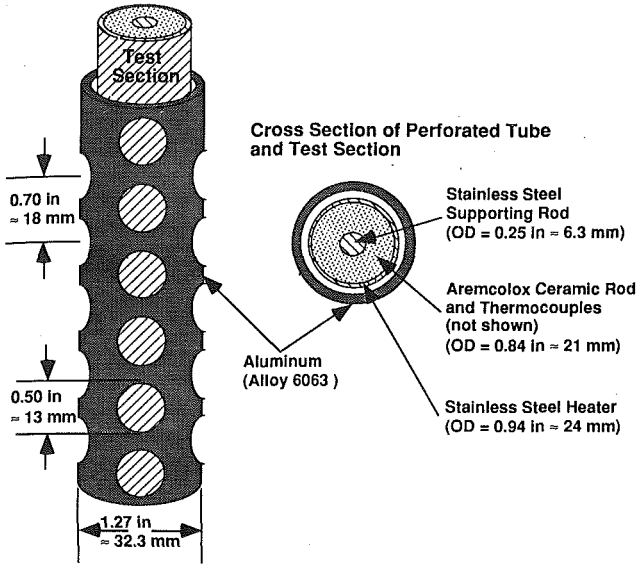

Fig. 2 Schematic diagram of experimental model with perforated tube surrounding heated tube

surface temperatures. It should be recognized that the gas temperature field and velocity distributions are also dependent variables, rather than controlled parameters.

For the assembly of a circular tube surrounded concentrically with a perforated cylinder, several effects have been postulated that could either improve or decrease its heat transfer performance relative to a single tube: area augmentation, thermal radiation shielding, induced turbulent mixing, interrupted or rough surfaces and thermosiphon behavior via the annular gap. The net result, augmentation or inhibition of heat transfer, will depend on the balance between these and possibly other effects—and cannot now be predicted in advance.

Directly related *previous work* is limited. A number of useful surveys and texts have been published on the general topic of natural convection in the past few decades (e.g., Ostrach, 1958; Gebhart, 1971; Jaluria, 1980; Raithby and Hollands, 1985). Flow over cylinders has been summarized by Morgan (1975) and natural convection in enclosures has been emphasized by Catton (1978). The reader is referred to these summaries for a general background on the topic.

A search of the literature, including examination of the reviews mentioned above, revealed no work on the present topic: turbulent natural convection from a vertical cylinder to a surrounding array. No published data were found for *turbulent* natural convection in an annular enclosure. However, Keyhani and colleagues (Keyhani and Kulacki, 1985; Keyhani et al., 1983, 1985) have presented data, nominally for the laminar boundary layer regime, that show evidence of transition at their highest Rayleigh numbers. Almost no results were even available for *turbulent* natural convection from isolated, slender, vertical cylinders of aspect ratios pertinent to the present study. Morgan (1975) does report such data from Carne (1937) and Eigenson (1940). In a related study Steimke (1991) also measured convective parameters for an isolated assembly of a heated tube inside a perforated tube in large surroundings with temperatures to about 150°C on the perforated tube.

For natural convection between two smooth, vertical, concentric circular cylinders, Eckert and Drake (1959) recommend applying results from enclosures formed by infinitely wide parallel flat plates. Predictions for *laminar* flow and its stability have been developed for tall annuli by Korpela and his colleagues (e.g., Choi and Korpela, 1980) and Shaaban and Ozisik (1982). For an application having some features of the present study, Bejan and co-workers examined natural convection in a vertical enclosure with an internal permeable screen numerically, but the assumptions included laminar flow and constant properties (Zhang et al., 1991). Lacking *turbulent* data for the geometry considered, the designer is forced to extrapolate from

Nomenclature

A = surface (or apparent surface) area, m^2; A_{solid}, for solid surface only of perforated tube rather than total envelope of tube
b = exponent in power-law approximation of temperature dependence of thermal conductivity
C = coefficient in correlation
c_p = specific heat at constant pressure, kJ/(kg•K)
D = tube diameter, m
F = geometric radiative view factor; e.g., $F_{h\to\infty}$, geometric radiative view factor from edge of a hole to its fictitious outer surface (then to outer surroundings)
G' = thermal energy generation rate per unit length, W/m
g = acceleration of gravity, m/s^2
h = convective heat transfer coefficient, $W/(m^2•K)$
k = thermal conductivity, W/(m•K)
L = characteristic length, x, D, etc., m; length of heated section
N_h' = number of holes per unit tube length, m^{-1}
q' = heat transfer rate per unit length, W/m; e.g., $q'_{r,h\to\infty}$, radiative heat transfer per unit tube length from edges of holes to outside surroundings
r = radius, m
s = spacing between surfaces forming annular gap, m
T = absolute temperature, K
x = axial location, measured upward from start of heating, m
Nu = Nusselt number = hD/k; Nu_s, based on gap spacing s
Gr = Grashof number = $\rho^2 g\beta D^3(T_{pt}-T_{ct})/\mu^2$
Pr = Prandtl number = $c_p\mu/k$
Ra = Rayleigh number = Gr Pr
β = volumetric coefficient of expansion, 1/T, 1/K
ϵ = thermal emissivity
μ = absolute viscosity, Pa•s
ρ = density, kg/m^3
σ = Stefan-Boltzmann constant = 5.670×10^{-8} W/m^2K^4

Subscripts

air = evaluated at air temperature
c = convective; cooler surface
ct = cooling tube
D = based on diameter D as characteristic dimension
gap = based on annular gap spacing s as characteristic dimension
h = hot; warmer surface; hole
i = inner
m = mean, evaluated at mean diameter
o = outer
pt = perforated tube
r = radiative
s = based on annular gap spacing
ts = test section (usually bare tube)
w = evaluated at heated wall or surface, outer surface of smooth tube or of perforated tube, as appropriate
x = based on axial distance x as characteristic dimension
∞ = "infinity," large distance, surroundings

information for an isolated cylinder or for a rectangular enclosure.

2 Apparatus and Procedures

The experimental configuration was chosen to approximate a vertical triangular array with a central cylindrical assembly and three surrounding cooling tubes in near full scale (for a reactor). Figure 1 is a scale drawing of a cross section of the overall test assembly.

Atmospheric air serves as the primary working fluid. Applied thermal boundary conditions approximate uniform wall heat flux along the test section and uniform wall temperature along the cooling tubes. The lower end plate was designed to provide a uniform temperature. The upper end is insulated to approach an adiabatic boundary condition. An acrylic shroud surrounds this apparatus radially to serve as a convection shield, avoiding drafts in the bay where the experiment was mounted, as well as providing a weak simulation of the effects of the next ring of tubes that would be at a larger radius in an array. Small openings in the lower end plate maintain the air pressure inside the enclosure at the local atmospheric pressure, approximately 0.84 atm. The dominant natural convective path is from the test section and/or perforated tube to the nearby cooling tubes.

The test section is heated electrically. Overall height is about 6 m. Direct current is employed and shunts measure the current flow. A voltmeter measures the voltage drop from electrode to electrode in order to check the test section electrical resistance and the total power generation.

Three aluminum cooling tubes of about 10 cm diameter surround the test section to remove the thermal energy from the test apparatus so steady-state conditions may be approached. Water flows upward through the cooling tubes at flow rates sufficient to keep these tubes nearly isothermal at the water inlet temperature, which is near room temperature. (Maintaining this boundary condition inhibits the application of an energy balance to check the relative heat transfer rates, since the water temperature rise is of the same order as its experimental uncertainty.) The thermal resistance from the inside surface of the acrylic shroud to the room is about ten to twenty times the thermal resistance through the cooling tubes to the cooling water, so the thermal path through the shroud has only a slight effect on the air temperature and surface temperatures inside the enclosure.

The *test section* is fabricated from seamless stainless steel tubing, type 304 per ASTM 269, with an outside diameter of 2.40 cm (actual measurements ranged from 0.944 to 0.946 in. with 0.9443 in. taken as the average). Copper electrodes of approximately the same diameter are brazed at each end. Heated length is about 160 diameters. The test section is supported at the top and allowed to expand freely through the bottom end plate, which serves as a guide.

Inner wall temperatures were measured with standard-grade, sheathed Type K (chromel/alumel) thermocouples inside the tube at about 30 cm intervals. Near the copper electrodes at the ends of the test section, the spacing is closer. These thermocouples are mounted in an Aremcolox ceramic assembly, which fills the test section.

The surrounding *perforated tube* was constructed from Aluminum Alloy 6063 tubing with outside diameter taken as about 3.233 cm and inner as about 2.743 cm (actual measurements were 1.270 in. and 1.080 in., respectively). It is perforated by holes of 13 mm diameter spaced vertically on 18 mm centers. Four rows of holes are distributed circumferentially, displaced by 90 deg from each other, as shown in Fig. 2. Small, short Macor ceramic screws are threaded through this tube to serve as spacers, prohibiting electrical contact between the perforated tube and the stainless steel test section, which has direct current passing along it. Sheathed Type K thermocouples of about 1 mm diameter are submerged in grooves in the outer surface of the perforated tube.

The *primary measurements* are the temperatures and test section power. Most temperatures are measured via standard-grade, Type K thermocouples. The thermocouples are connected to Type K extension wire, which runs to a reference oven held at about 65.5°C (150°F).

Measurement of the normal, band thermal emissivity of the test section for the wavelength range from 8 to 14 μm is accomplished manually with an Omega infrared pyrometer (model OS-2104 L) with a measurement spot size of six mm. Approximately three meters above the level where the heated section starts, a 15 cm viewing port was cut into the acrylic shroud in order to provide direct visual access to the test section during a heated experiment.

As part of the design calculations the thermal response of the test section and the axial thermal conduction were estimated. The time constant was estimated to be about one half-hour, indicating that manual control and data recording would be feasible and that one would expect two to three hours to be required to reach an approximate steady state. The characteristic length for axial conduction along the stainless steel tube was estimated to be about 8 cm, so end effects would become negligible about 30 cm from either electrode.

Since the heat transfer rate by *thermal radiation* is often of the same order of magnitude as that by natural convection to gases, it is desirable to minimize the thermal radiation and to measure the radiative properties in order to deduce the convective heat transfer parameters accurately. As indicated in Section 3, the convective heat transfer rates in an experimental run are deduced by subtraction of the estimated radiation heat transfer rates from the total energy generation rate. Therefore, the experimental uncertainties of the convection results are sensitive to the magnitude of the thermal radiation and to the uncertainties in the radiative properties of the surfaces involved.

O'Brien (1991) developed our technique for deducing the emissivities and conducted measurements before the experiment was operated. Essentially, the Omega infrared pyrometer is employed to deduce a normal band emissivity for the range 8 to 14 μm by comparison between the instrument indication and the surface temperature measured by thermocouples. He measured values as functions of temperature for samples cut from the same tubing that was used to fabricate the experiment. Using approaches suggested by Siegel and Howell (1972), O'Brien applied these data as the bases for estimates of the total, hemispherical emissivities, which were required for the data reduction.

Linear approximations of the measurements are used to estimate the *total hemispherical emissivities* of the surfaces. The specific relations are

Test section

$$\epsilon_{ts,t,h} = 0.165 + 0.0001667\ (T - 300) \tag{1a}$$

Perforated tube

$$\epsilon_{pt,t,h} = 0.112 + 0.00008333\ (T - 300) \tag{1b}$$

Cooling tubes

$$\epsilon_{ct,t,h} = 0.087 + 0.000030\ (T - 300) \tag{1c}$$

with T in degrees Kelvin.

Procedures for the *experimental runs* were straightforward. Actual runs involved mainly setting the electrical current to the desired constant level, then monitoring appropriate signals until an apparent steady state was reached. Shortly after initiating the transient, we recorded "instantaneous" values of the test section voltage, current, and temperature to check that the overall resistance-to-temperature relation had not changed since the previous run. Once it was determined that an apparent

steady-state condition had been reached, a final scan of the electronic signals was recorded and manual observations were written in the experiment log.

Two phases of experiments were conducted. The first utilized the bare, smooth test section alone as the central assembly, while in the second it was surrounded by the perforated tube as shown in Figs. 1 and 2.

If the radiative properties of the test section and/or the perforated tube had changed significantly due to "aging" during the experiment, the total heat transfer rate and deduced convective heat transfer rate would also change. Therefore, the test section emissivity was monitored. The perforated tube was oriented so that one row of 13 mm perforations faced the removable port opening. Since the diameter of the focused observation spot of the pyrometer is about 6 mm, the test section surface could be observed directly. After steady-state measurements had been recorded, the port could be opened and the normal band emissivity of the test section could be checked. Throughout the range of experiments conducted, there was no evidence of a change in the emissivity-versus-temperature relationship of the stainless steel. (This conclusion was also checked by repeating runs and examining the deduced convective parameters.)

Additional details of the experiment design and instrumentation, along with the tabulated measurements, are provided in a more detailed report by McEligot and co-workers (1992).

3 Data Reduction

In deducing the experimental results, one must consider the question of how best to define the parameters in a fashion useful to the thermal design engineer. Since no correlations were found for the complicated annular enclosure studied, definitions were selected so that—in the limiting case of large outer radii for the enclosure—they would correspond to correlations for isolated, vertical, slender cylinders. These correlations typically employ the diameter as the characteristic dimension. For our bare tube runs the diameter of the stainless steel test section is used, and for those with the perforated tube the definitions are based on its outside diameter ($D_{pt,o}$).

While treatment of the convective heat transfer from the bare tube is essentially straightforward, when it is surrounded by the perforated tube a choice must be made concerning the surface area to use in defining the convective heat transfer coefficient. We follow a standard approach for enhanced surfaces (Webb et al., 1971; Bergles, 1988; Rabas, 1992) where it is defined in terms of the base area of the unmodified surface (i.e., without holes in our case). Parameters are calculated in the present work in terms of the envelope of the perforated tube, e.g.,

$$q_c' = h\Pi D_{pt,o}(T_{pt} - T_{ct}) \tag{2}$$

for convection from its outer surface. Thus, apparent convection from the perforated tube includes both the contributions from the solid surface and from the fictitious surface of each hole.

Since the gas temperature in an enclosure is a consequence (dependent variable) rather than a boundary condition, the driving temperature difference is defined in terms of the primary surface temperatures in the convective heat transfer situation, i.e., the temperatures of the outer surface of the cylinder and of the cooling tubes. In the limiting case of a large enclosure, this value would approach the temperature difference between the cylinder surface and the ambient air at "infinite" distance. Since an equivalent mean air temperature is not available for the enclosure, it is not a useful design parameter.

The *local thermal energy generation rate* was calculated from the measured electrical current, the measured cross section of the stainless steel test section, the local measured temperature, and values of the electrical resistivity versus temperature taken from the literature. Data presented by Touloukian (1967) were approximated by a linear relation for $T < 650$ K and adjusted for the nonlinearity in his figure above 650 K. The calculated value of the resistivity was checked approximately by comparing the predicted resistance per unit length to a value deduced from the measurements of current and overall voltage. These comparisons agreed to within 1.7 percent over the range of data presented herein.

For the bare test section the energy loss by *thermal radiation* was calculated as for a small grey body in large surroundings (Incropera and deWitt, 1981). Calculations with a five body description, following the approach of Gebhart (1971), agreed within 2–5 percent for this radiation contribution (the discrepancy decreased as the temperature increased and radiation became more important).

The geometry of the perforated tube complicated the treatment of its thermal radiation transfer compared to the heated test section alone. Radiation was approximated by three terms: (1) from the test section through the holes, (2) from the outer surface of the perforated tube, and (3) from the edges of the holes outward. These terms are believed to be the major contributions, but the estimates of experimental uncertainties for each are increased to account for the lack of a more exact treatment. Since these terms are key to applying the present results, details of their calculation are included in an Appendix.

Local convective heat transfer rates were determined at the location about 3 m above the lower electrode, via energy balances for steady state, from the difference between the thermal energy generation rate and the net thermal radiation rate. The fraction of the total energy rate that was transferred as thermal radiation is estimated to have been from 16 to 48 percent for the base tube runs and 17 to 37 percent for the data with the perforated tube.

Air properties were evaluated from the work of Hilsenrath et al. (1960). As a consequence of the large range of temperature differences in the study, the question arises concerning *evaluation of gas properties* in calculating the nondimensional parameters. Lacking data on turbulent natural convection in comparable geometries in general, one has no direct guidance on how to account for the *effects of temperature-dependent transport properties* in this specific situation. For internal, turbulent forced convection, typical approaches are to employ a film/reference temperature to evaluate properties or to use the gas bulk temperature and a temperature-ratio multiplier (with an exponent of about 0.5) (McEligot et al., 1965; Kays and Crawford, 1980). Since different phenomena are involved in natural convection, different values may be necessary with comparable approaches. For natural convection on a vertical flat plate of large dimensions (hence high Rayleigh numbers also) with a turbulent boundary layer, Siebers et al. (1985) reviewed the available literature and found conflicting recommendations, which gave significant differences when there are large temperature ratios. They indicated that "recent works point to a reference temperature weighted toward T_∞ with β evaluated to T_∞."

Siebers et al. conducted measurements on a vertical plate with temperature ratios T_w/T_∞ to 2.7, approximately the same range as in the present study. When they attempted to correlate their data with T_∞ as the reference and $\beta = 1/T_\infty$, they found a slight systematic variation and accounted for it by a temperature ratio method. We have chosen an approximately equivalent approach, e.g.,

$$\mathrm{Nu}\,(T_w/T_{ct})^{0.14} \sim fn\{\mathrm{Ra}\} \tag{3}$$

with our air properties evaluated at the cooling tube surface temperature (and at 0.84 atm) and we adopted the exponent of Siebers et al. (1985) (i.e., 0.14). The volumetric coefficient of thermal expansion is calculated in the same manner, $\beta = 1/T_{ct}$. In the limit of constant properties the temperature ratio approaches unity, and such variable properties correlations be-

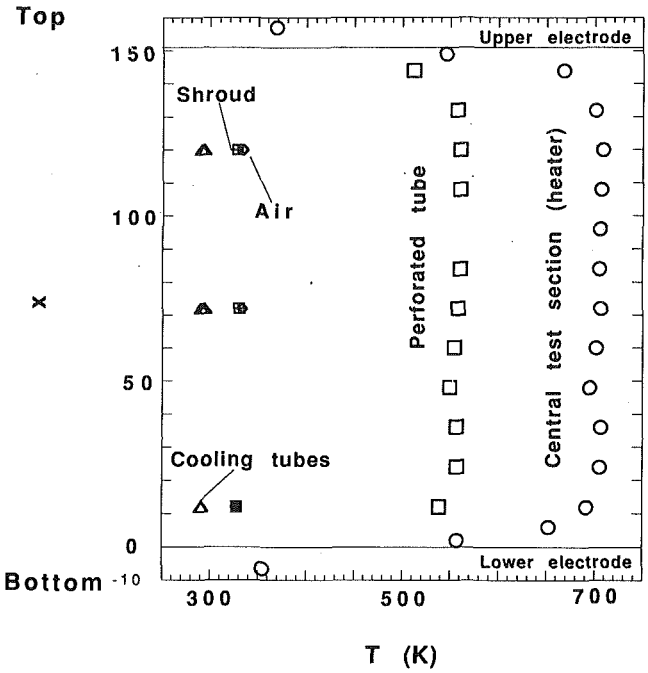

Fig. 3 Measured axial temperature distributions along test section and perforated tube for typical experiment (axial distance nondimensionalized by dividing by reference length of 25.4 mm)

come equivalent to the appropriate constant property correlations.

The primary contributors to the *experimental uncertainties of the results* reported here are those in the thermocouple measurements and the thermal emissivities. The estimation of the resulting uncertainties is handled in the standard manner (e.g., as by Kline and McClintock, 1953). The standard-grade thermocouples with their connectors and reference junctions yielded estimates of uncertainties of *temperature differences* ranging from 4.5–5.5°C, depending on the test section temperature. Estimates for the emissivity data range from 10 to 14 percent, for the range of emissivity measurements, and are slightly higher at low temperatures. The uncertainty in thermal energy generation rate is dominated by a 2½ percent uncertainty in test section thickness.

In general, the uncertainty in temperature measurement dominates the results at low temperature. Then as the fraction of energy transferred as thermal radiation grows, the uncertainty in q_r' becomes more important. The result of these trends is that the uncertainty in convective heat transfer parameters is greatest at the extremes—lowest and highest power—and is minimized at intermediate levels (see Figs. 4, 5, and 6 later). Consequently, typical estimates of the uncertainties of the deduced Nusselt numbers for the bare tube experiments become about 18, 5, and 13 percent for low, medium, and high temperature runs, respectively. For the perforated tube data, the comparable uncertainties are about 8, 6½, and 18 percent.

4 Results and Discussion

4.1 Typical Conditions. Eight sets of data were obtained with the smooth test section alone as the central assembly and ten sets were measured with the perforated tube surrounding it. Typical temperature distributions, measured for a moderate temperature run with the combined assembly, are shown in Fig. 3. These axial profiles are representative of all 18 runs.

The temperatures on the heater and on the perforated tube are essentially uniform above the first half meter and away from the axial conduction at the ends. Consequently, the temperature difference between the two was near constant in this region. Likewise, the cooling tube surface temperatures are seen to be nearly isothermal, as intended. The air temperatures are pointwise values, taken between the cooling tubes, and are near the cooling tube temperatures but slightly higher (of the order of 15 percent of the temperature difference, $T_{pt} - T_{ct}$). At the lower end of the test assembly the boundary layer could be laminar, but the perforations may be expected to act as "tripping" roughness elements, which could cause early transition to turbulent flow (Schlichting, 1968). The effect of axial conduction at the upper end appears negligible beyond 50 cm from the upper electrode (our local measurements were concentrated about 80 cm away).

For this particular run, convection from the envelope of the perforated tube accounted for about 70 percent of the total heat transfer, with radiation to the surroundings being 30 percent. Also, radiation across the gap accounted for about 30 percent of the heat transfer from the test section to the perforated tube. Thus, both convection and radiation resistances were significant in determining the resulting axial profiles. These observations imply that (1) the energy generation was uniform, (2) the thermal emissivities were relatively uniform, and (3) the two convection paths were uniform for the upper part of the tube. Since the pertinent temperature differences appear near constant, the local convective heat transfer coefficients do not vary significantly with position, so $Nu_x \sim Ra_x^{1/3}$ along the tube. These consequences [and $Ra_x > 10^{10}$ (Hama and Recesso, 1958)], in turn imply that turbulent and/or fully established conditions existed axially along the perforated tube.

The air temperature distribution and the acrylic shroud temperatures are dependent variables determined by the balance of thermal energy flows significant within the test configuration, rather than being controlled boundary conditions as in other configurations. (This situation is one reason a mean or bulk air temperature was not used to evaluate the gas properties.) Air temperature was measured at three axial locations above one another. If the air was reasonably well mixed, these data *may* be representative of the so-called equilibrium air temperature, which is used in some code calculations for this geometry. Shroud temperatures were obtained at the same levels. The air temperature data and the maximum values of the shroud readings are also plotted on Fig. 3. Their axial uniformity is evident.

The effects of the electrical power on the nondimensional air and (maximum) shroud temperatures, defined as $(T - T_{ct})/(T_{pt} - T_{ct})$, were examined in terms of the diameter Rayleigh number (McEligot et al., 1992). With the exception of the lowest power run, the nondimensional internal air temperatures fell in the range of 0.13 to 0.17 while the shroud temperature increased from about 0.05 to 0.16 as the incident thermal radiation increased. The warmer shroud temperatures apparently contributed to a slight increase in the air temperatures. Also monitored were the temperatures of the laboratory room air; they fell from -0.01 to $+0.04$ in nondimensional terms, i.e., close to the cooling tube temperatures. As noted earlier, the thermal resistance from the inside surface of the shroud to the room is estimated to be over ten times the thermal resistance through the cooling tubes to the cooling water; therefore, the shroud acts mainly as an insulator relative to the total thermal system of the test assembly.

A number of investigators have attempted to include the slenderness or aspect ratio in their correlations and analyses for vertical cylinders with large values of the aspect ratio, L/D. Hama et al. (1959) and Nagendra et al. (1969, 1970) conducted *laminar* analyses plus experiments to confirm them. Morgan (1975) summarized the available data for vertical cylinders and showed most for high aspect ratios to be from fine wires or small, short cylinders. Results are usually presented in terms of Rayleigh number divided by the aspect ratio, $Ra_D/(L/D)$, as evolves from the laminar analyses.

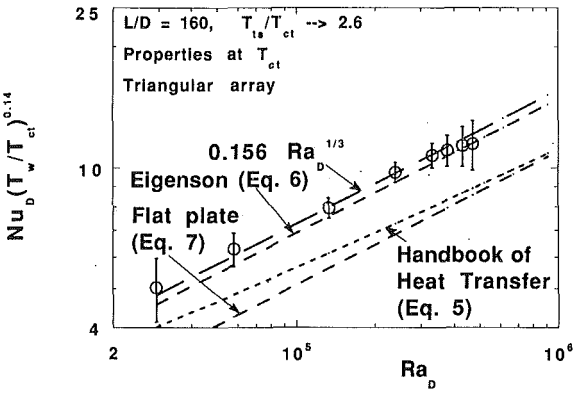

Fig. 4 Data for turbulent natural convection from a smooth tube in an irregular annular enclosure

The results of Nagendra et al. (1969, 1970) are presented as

$$Nu_D = 1.37[Ra_D\ (D/L)]^{0.16} \tag{4}$$

for the range $0.05 < Ra_D D/L < 10^4$ with constant-property conditions. Their comparisons to data are mostly near the ends of this region. Our data span the range $180 < Ra_D D/L < 7700$.

With the variable property "correction" from Siebers et al. (1985) applied, our data were compared to the relation of Nagendra et al., Eq. (4) above (McEligot et al., 1992). The main conclusion was that both the bare and perforated tube data are about twice as high as the predictions based on laminar analyses (and confirmatory experiments), providing a further indication that the present data represent a turbulent flow. Comparable correlations accounted for the effects of aspect ratio do not appear to be available for turbulent flow. Obviously, the *laminar correlation* of Nagendra et al. is not applicable for the present "large-scale" geometry, which apparently gives *turbulent* conditions in this range of $Ra_D D/L$.

4.2 Smooth, Bare Tube Experiments. Data were obtained for conditions ranging from near room temperature to maximum test section temperatures near 800 K (1000°F). The temperature ratio, T_{ts}/T_{ct}, varied from about 1.1 to 2.6 over this range. Local measurements are presented mainly for a height of $x/D = 127$ and at that location the Rayleigh number, Ra_D, varied from about 2.9×10^4 to 4.6×10^5. Using predictions from isolated flat plate analyses as a guide, one can estimate the order-of-magnitude for the boundary-layer-thickness at this level on the heated tube to be about 3 cm if it were laminar (Özisik, 1985) or 16 cm if turbulent (Eckert and Jackson, 1951; Rohsenow and Choi, 1961); the former would approach the cooling tubes and the latter would engulf them. Rayleigh numbers based on heated length were in the range of $1.2 \times 10^{11} < Ra_L < 1.9 \times 10^{12}$. Cooling tube surface temperatures were maintained between 286 K and 296 K, essentially near room temperature.

Results of our measurements are presented in Fig. 4 in terms of parameters based on test section diameter and cooling tube temperature as defined earlier. Data and correlations for *turbulent* flow from slender cylinders (i.e., tall cylinders) are sparse. Our literature survey found none for annular enclosures with regular or irregular outer surfaces. For an isolated slender cylinder, the *Handbook of Heat Transfer* (Raithby and Hollands, 1985) suggests a method to extrapolate predictions from the better explored vertical flat plate. Recommendations on its page 6-24 can be rearranged to the form

$$Nu_D = 1.8[\ln\{1 + (17.48/Ra_D^{1/3})\}]^{-1} \tag{5}$$

If the cylinder is tilted, the plume that they assume to envelop it would no longer be centered, giving the result that the heat transfer would be higher; the effect is particularly sensitive near vertical (Raithby, 1992). One would expect that the close proximity of the bounding surfaces in our enclosure would have comparable effects and improve the convective heat transfer. This equation has been plotted also on Fig. 4 and it does appear that our measurements are indeed higher (even accounting for the differences in definitions).

Morgan (1975) suggested a relation of the form

$$Nu = 0.148\,Ra^{1/3} \tag{6}$$

to correlate the data of Eigenson (1940) for an isolated cylinder. In this case the heat transfer coefficient is defined in terms of the temperature difference from the heated cylinder to the undisturbed air at a distance. This relation is plotted on Fig. 4 along with equations that correspond to the correlations suggested by Siebers et al. (1985) for a flat plate,

$$Nu_x(T_w/T_\infty)^{0.14} = 0.098\,Gr_x^{1/3} \tag{7}$$

and by Raithby and Hollands. Since these correlations are based on definitions that differ from ours, it must be emphasized that we are not making comparisons to the correlations directly.

For our irregular annular enclosure with an outer surface formed by the three cooling tubes plus shroud and with our definitions, our data can be approximated by

$$Nu_D(T_{ts}/T_{ct})^{0.14} = 0.156\,Ra_D^{1/3} \tag{8}$$

reasonably well for the range $3 \times 10^4 < Ra_D < 5 \times 10^5$. Another way of viewing this result is that by adopting the temperature ratio method and the same exponent of Siebers et al. (1985) we were able to correlate our data with $Ra_D^{1/3}$-dependence (within the range of experimental uncertainties) despite significant air property variation.

A preliminary comparison to correlation (6) of Bushan et al. (1983) for annuli showed *approximate* agreement *could* be reached for our range of Ra_D although their data were ostensibly for the laminar boundary layer regime (as noted earlier, some of their data showed evidence of transition). Since their correlation accounts for dependence on a radius ratio and an aspect ratio, it is necessary to select a basis for defining an equivalent outer radius, r_o. Use of the circle determined by the centers of the cooling tubes (identified as D/D_{ts} in Fig. 1) gave this agreement for our data at low heating rates. In their correlation a mean temperature, $T_m = (T_o + T_i)/2$, is used for evaluating properties. At high heating rates (high T_w/T_{ct}), this reference temperature did not quite collapse our data to the correlation since use of T_m systematically gave multiple values of the measured Nusselt number at the same Rayleigh number. At the highest heating rate the correlation underpredicted the measurement by about ten percent; this difference was within the experimental uncertainty at that data point and would be acceptable in many applications.

Though appearing close to the Eigenson relation in Fig. 4, our result is not a confirmation that the cylinder can be considered to be isolated. In our technical report (McEligot et al., 1992) it is shown that, by converting to alternate definitions with this information, one can derive an equivalent correlation in terms of properties evaluated at the air temperature between the cooling tubes,

$$\frac{Nu_{air}}{C\,Ra_{air}^{1/3}} = \left(\frac{T_{ct}}{T_{air}}\right)^{-0.53}\left[\frac{T_{ts} - T_{ct}}{T_{ts} - T_{air}}\right]^{4/3} \tag{9}$$

where C is the coefficient of the initial correlation, our 0.156 for properties based on cooling tube temperature. The right-hand side of this correlation is estimated to vary from about 1.24 to 1.37 for our range of data. Thus, this estimate could be interpreted to imply that the data for the bare tube in our enclosure configuration might be represented by

$$Nu_{D,air} = (0.193 \rightarrow 0.214)Ra_{D,air}^{1/3} \tag{10}$$

which is about 40 percent higher than the Eigenson correlation

(Morgan, 1975) for an isolated tube, with equivalent definitions.

4.3 Convection From Smooth Tube to Perforated Tube. In order to conduct the thermal design of a vertical cylindrical heater surrounded by a perforated tube, one must account for the thermal resistance between the two due to radiation and convection. The contribution of thermal radiation will depend on the materials employed and their thermal emissivities, so it will differ from application to application (and from experiment to application). Accordingly, the present study concentrates on examining the treatment of the convective contribution.

The two tubes form an annulus between them with a rough/"porous" outer surface. Considering the present configuration relative to an annulus between two smooth impermeable tubes of comparable radius ratio and boundary conditions, one could reasonably expect either an increase or a decrease of convective heat transfer parameters.

For the annulus of smooth impermeable tubes, the heat transfer via the fluid in the gap will be by molecular conduction if (1) the fluid is stagnant or (2) any fluid flow is laminar and parallel to the walls. The latter case is comparable to fully established, forced flow in an annulus as analyzed by Shumway (1969; Shumway and McEligot, 1971) for gases with transport property variation. Eckert and Drake (1959), citing the earlier work of Kraussold, suggest approximating the annular gap as equivalent to two parallel plates by evaluating the heat flux at the mean diameter of the annulus and using the spacing as the characteristic dimension in the pertinent parameters. Groeber et al. (1961) indicate that a logarithmic mean should be used, but in the present work the difference is only 0.2 percent. If the Rayleigh number based on gap spacing is less than 10^3, the suggestion of Eckert and Drake predicts a Nusselt number (based on gap spacing) of unity as for parallel plates (Catton, 1978; el Sherbiny et al., 1982).

The present data for the annular gap were analyzed in terms of the suggestion of Eckert and Drake. A steady-state energy balance was employed to estimate the *local convective heat transfer rate from the test section to the perforated tube* by subtracting, from the thermal energy generation rate, estimates of the thermal radiation rates through the holes and across the gap. The details of these calculations are presented in the technical report by McEligot et al. (1992). In forming the nondimensional parameters, gas properties were evaluated at the mean temperature in the annulus, $T_m = (T_{ts} + T_{pt})/2$, and the gap spacing was taken as the characteristic length. The convective heat transfer coefficient is defined by

$$q'_{c,ts\to pt} = h\pi D_m (T_{ts} - T_{pt}) \tag{11}$$

This definition of the convective heat transfer coefficient includes nonradiative transport both to the inner surface of the perforated tube and to the fictitious inner surfaces of the holes; i.e, it is the energy transfer from the air in the annulus to the inner "envelope" of the perforated tube.

The data for the annular gap fell in the range $1.1 < \mathrm{Ra}_{\mathrm{gap}} < 4.6$, with the higher heating rates corresponding to the lower Rayleigh numbers. These values correspond to the laminar conduction regime for vertical slots (Catton, 1978), where one would expect a Nusselt number of unity for smooth parallel surfaces. If one accounts for variation of thermal conductivity by approximating it as $k \sim T^b$, then the relation for parallel plates can be written as

$$\mathrm{Nu}_{\mathrm{gap}} = \frac{2^b}{b+1} \cdot \frac{\left[\left(\frac{T_h}{T_c}\right)^{b+1} - 1\right]}{\left(\frac{T_h}{T_c} - 1\right)\left(\frac{T_h}{T_c} + 1\right)^b} \tag{12}$$

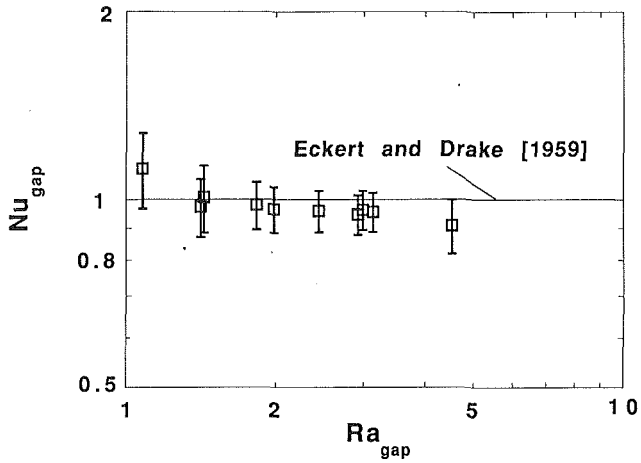

Fig. 5 Natural convection across annular space between heated test section and perforated tube with parameters based on mean diameter and properties at mean temperature

where T_h and T_c represent the temperatures of the warmer and cooler surfaces, respectively. However, for $b = 0.8$ and T_h/T_c less than 10, this relation gives a value within 2 percent of unity!

For the present geometric configuration, the radius ratio is about 0.87, i.e., near the parallel plate limit. The fraction of energy transferred as radiation varied from 0.12 to 0.35 as the temperatures increased. The maximum temperature ratio T_{ts}/T_{pt} was about 1.3 across the annulus. As with the other convective data, estimated experimental uncertainties are dominated by radiation at high temperatures and by small temperature differences at the lower end with the best data being at intermediate temperatures (and Rayleigh numbers). At the highest temperature ($\mathrm{Ra}_{\mathrm{gap}} \approx 1.1$) the estimated uncertainty in Nusselt number is about 15 percent.

The results are presented in Fig. 5. Heating rate and temperature level *decrease* from left to right as a consequence of the variation of the property grouping in the definition of the Rayleigh number. The general conclusion is that the data for the annulus formed by the perforated tube and the smooth test section agree reasonably well with the predictions for annuli formed between two smooth, impermeable concentric cylinders, when treated as in the present work.

4.4 Convection From Perforated Tube to Array. The measurements with the perforated aluminum tube were obtained at test section temperatures from near room temperature to about 860 K (1090°F). The local measurements were concentrated at a height of $x/D_{pt} = 95$ (i.e., $x \approx 3$ m = same vertical location as for bare tube). Partly as a consequence of low values of the thermal emissivities, the temperature differences between the test section and perforated tube were large; so the perforated tube temperature ranged only to approximately 670 K (750°F), yielding temperature ratios, T_{pt}/T_{ct}, to 2.3 for this range. The larger diameter, compared to the bare test section, gives a smaller aspect ratio and higher Rayleigh numbers (Ra_D). This Rayleigh number varied from 2.3×10^5 to 9.2×10^5, based on properties at the cooling tube temperature; corresponding length-based Rayleigh numbers were in the range $3.4 \times 10^{11} < \mathrm{Ra}_L < 1.6 \times 10^{12}$. Cooling water flow rates were kept high enough to approach isothermal flow with tube surface temperatures between 291 K and 295 K at the point of interest. Ten experimental runs were conducted at six power levels, with four runs being reproducibility checks.

In Fig. 6 our local measurements are plotted with relations for turbulent natural convection from isolated vertical cylinders from section 4.2. Our data are adjusted for the large gas property variation across the thermal boundary layer via the

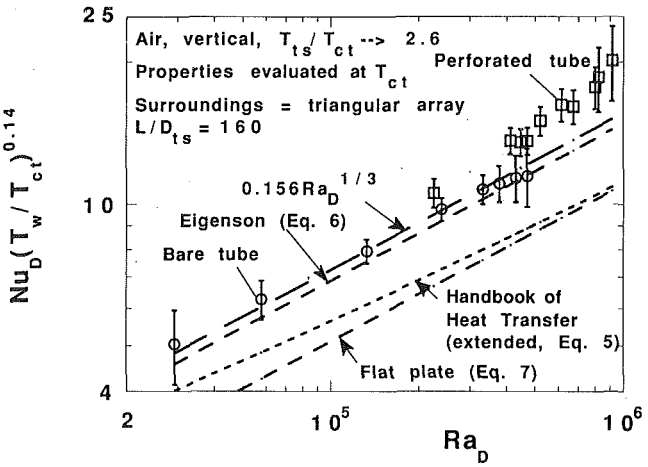

Fig. 6 Data for turbulent natural convection in an irregular annular enclosure (with parameters based on gas properties at cooling tube surface temperatures) and empirical correlations corresponding to limiting case of isolated cylinder

approach of Siebers et al. (1985). The reader is again cautioned that these correlations are not directly comparable to our geometry except in the limit of large outer radius where $T_{\text{air},\infty}$ becomes equivalent to T_{ct}.

Agreement of the reproducibility checks was good except for the last one at $Ra_D \approx 8\times10^5$, which was the last run and was the next one after the run at the highest Rayleigh number. The test section emissivity was usually measured after reaching and recording steady-state values for each run; no significant change was observed during the experiments. After the last run the emissivity of the perforated aluminum tube was found to have an apparent increase. This increase is believed to have occurred during the run at $Ra_D \approx 9\times10^5$, which was at the highest temperatures of the experiment. Estimated experimental uncertainties for the radiation calculations were increased for the runs at the two highest Rayleigh numbers to account for this apparent change. Reproducibility checks at $Ra_D \le 6\times10^5$ showed no evidence of any change in the radiation characteristics.

The data for the smooth bare tube and their correlation, Eq. (8), are also plotted on Fig. 6. One might expect the results for the larger-diameter, perforated tube to be lower at equal Rayleigh numbers, as suggested by considering the correlating parameter for slender (smooth) tubes, $Ra_D D/L$.

Our results show the perforated tube data *may* be considered to have "enhanced" convective heat transfer parameters relative to the extrapolation of the smooth tube data. That is, they are higher despite the larger diameter of the perforated tube. (The slope also may be slightly greater than the 1/3-power of the bare smooth tube relation, but the range of experimental uncertainty estimates would allow variation as $Ra^{1/3}$.) Three explanations for higher heat transfer parameters come to mind. The most obvious is the "rough" shape of the surface of the perforated tube. Secondly, as a consequence of its larger diameter, the spacing between it and the nearby cooling tubes is less, possibly permitting greater interaction through turbulent mixing. Finally (for now), at a given Rayleigh number the temperature ratio T_w/T_{ct} differs for the two tubes; if the correction for the effects of gas property variation is not adequate, the results would differ. Examining which explanation, if any, is the cause of the difference would require different experiments and is beyond the scope of the present study.

The main conclusion from the present results is that the perforated tube shows an increase of about 15 percent in $Nu_D(Ra_D)$ when centered in the same surrounding array as the smooth, smaller tube.

4.5 Application. The present experimental results correspond to a unique nuclear reactor geometry but, probably, would provide conservative bounding estimates of the convective heat transfer coefficients in cases where the distance to the cooling tubes is closer (in nondimensional terms). In a safety analysis for a reactor, the thermal emissivities of the actual surfaces must be estimated to predict the contribution by thermal radiation; since we attempted to keep the emissivities low for accuracy in deducing the convective contribution, we would expect more energy transfer by thermal radiation in some actual applications than in our experiment. (During the initial transient from operating temperature natural convection will dominate. Depending on materials employed, radiation may or may not become the larger contribution later in the transient but convection is not expected to be negligible in estimating structural integrity.) The present correlations can be applied to estimate the convective contribution. The data may also be used to verify or refute numerical predictions that claim to cover the situation.

This study demonstrates that available correlations were not adequate to predict natural convection from a vertical cylinder to an array in close promixity. Further fundamental measurements are needed on several topics. Only the heating rate was varied significantly in the experiment, so the effect of property variation has been adopted from the data of Siebers et al. (1985) rather than tested by varying temperature ratio independently from Rayleigh number. Likewise, the geometric ratios (e.g., spacing) have not been varied. Other geometric patterns for the surrounding array may change the behavior slightly, and there is probably an infinite variety of "augmentation surfaces," which could be examined looking for optimization in some sense. Generalizing relations for the complicated thermal radiation problem, with the perforated surface interposed between the smooth tube and its irregular surroundings, would help. However, lacking the necessary experiments, one probably could reasonably expect that results for larger radius ratios (between the test section and the nearest cooling tube surface) would be bracketed by the present measurements and the Eigenson correlation for an isolated tube.

5 Concluding Remarks

The general result of the present work is the observation that available correlations for single vertical cylinders do not predict closely the local behavior of turbulent natural convection from a small cylinder to a surrounding array of cylinders. (The nondimensional geometric parameters are presented in Fig. 1.) The present local results are approximately uniform above about 60 cm or less. The questions posed in the Introduction may be answered as follows:

1 For the bare tube geometry, the correlation

$$Nu_D(T_{ts}/T_{ct})^{0.14} = 0.156\,Ra_D^{1/3} \tag{8}$$

is recommended for the ranges

$$4\times10^4 < Ra_D < 5\times10^5,\ T_{ts}/T_{ct} < 2.6,\ Pr \approx 0.7$$

provided (1) the gas properties are evaluated at the cooling tube temperature, (2) the parameters are calculated as defined above, and (3) $Ra_x > \sim 10^{10}$ (i.e., turbulent).

2 Measurements with a perforated tube surrounding the heated test section covered the ranges

$$2.3\times10^5 < Ra_D < 9.2\times10^5,\ T_{pt}/T_{ct} < 2.3,\ Pr \approx 0.7$$

with properties evaluated in the same manner. The net result of the perforations was an increase in convective heat transfer parameters. It was found that the nondimensional parameters (with heat transfer coefficients based on the outside envelope

area of the perforated tube) were about 15 percent higher than the bare tube data and their extrapolation.

3 In these experiments the Rayleigh number for the annulus between the heated test section and the perforated tube, Ra_{gap}, fell between 1.1 and 4.6 based on spacing and quantities evaluated at the mean radius. Despite the interrupted or rough surface of the outer cylinder (the perforated tube), for this range the data agreed reasonably well with the prediction for annuli formed between smooth, impermeable cylinders (i.e., $Nu_{gap} \approx 1$). This prediction implies either stagnant conditions or parallel, axial laminar flow within the annulus.

Acknowledgments

The work reported was supported by the U.S. Department of Energy, Assistant Secretary for Defense Programs under DOE Idaho Field Office, Contract DE-AC07-76ID01570, to whom we are grateful. We appreciate the guidance and interest of Dr. Fred E. Witmer and Ms. Sharon L. Zeigler, DOE, who helped as technical program monitors.

References

Bergles, A. E., 1988, "Some Perspectives on Enhanced Heat Transfer—Second Generation Heat Transfer Technology," ASME JOURNAL OF HEAT TRANSFER, Vol. 110, pp. 1082–1096.

Bhushan, R., Keyhani, M., Christensen, R. N., and Kulacki, F. A., 1983, "Correlations for Convective Heat Transfer in Vertical Annular Gas Layers With Constant Heat Flux on the Inner Wall," ASME JOURNAL OF HEAT TRANSFER, Vol. 105, pp. 910–912.

Butcher, P., Debenham, A. A., and Holloway, N. J., 1990, "PRA-Based Accident Management for the Winfrith Prototype Steam Generating Heavy Water Reactor," *Proceedings, International Topical Meeting on the Safety, Status and Future of the Non-commercial Reactors and Irradiation Facilities*, Boise, Idaho Section, American Nuclear Society, pp. 273–277.

Carne, E. B., 1937, "Heat Loss by Natural Convection From Vertical Cylinders," *Phil. Mag.*, Vol. 24, pp. 635–653.

Catton, I., 1978, "Natural Convection in Enclosures," *Proceedings, 6th International Heat Transfer Conference*, Toronto, Vol. 6, pp. 13–31.

Choi, I. G., and Korpela, S. A., 1980, "Stability of the Conduction Regime of Natural Convection in a Tall Vertical Annulus," *Journal of Fluid Mechanics*, Vol. 99, pp. 725–738.

Eckert, E. R. G., and Jackson, T. W., 1951, "Analysis of Turbulent Free Convection Boundary Layer on a Flat Plate," NACA Report 1015.

Eckert, E. R. G., and Drake, R. M., 1959, *Analysis of Heat and Mass Transfer*, McGraw-Hill, New York.

Eigenson, L. S., 1940, "Les lois gouvernant la transmission de la chaleur aux gaz biatomiques par les parois des cylindres verticaux dans le cas de convection naturelle," *Dokl. Akad. Nauk SSSR*, Vol. 26, pp. 440–444.

el Sherbiny, S. M., Raithby, G. D., and Hollands, K. G. T., 1982, "Heat Transfer by Natural Convection Across Vertical and Inclined Air Layers," ASME JOURNAL OF HEAT TRANSFER, Vol. 104, pp. 96–102.

Gebhart, B., 1971, *Heat Transfer*, McGraw-Hill, New York.

Groeber, H., Erk, S., and Grigull, U., 1961, *Fundamentals of Heat Transfer*, McGraw-Hill, New York.

Hama, F. R., and Recesso, J. V., 1958, "The Axisymmetric Free-Convection Temperature Field Along a Vertical Thin Cylinder," Tech. note BN-116, Inst. Fluid Dynamics Appl. Math., Univ. Maryland; ASTIA AD-148 064.

Hama, F. R., Recesso, J. V., and Christiaens, J., 1959, "The Axisymmetric Free-Convection Temperature Field Along a Vertical Thin Cylinder," *Journal of the Aerospace Sciences*, Vol. 26, pp. 335–342.

Hilsenrath, J., Hoge, H. J., Beckett, C. W., Masi, J. F., Benedict, W. S., Nuttall, R. L., Fano, L., Touloukian, Y. S., and Woolley, H. W., 1960, *Tables of Thermodynamic and Transport Properties*, Pergamon, Oxford; originally *Tables of Thermal Properties of Gases*, NBS circular 564, Washington: Govt. Printing Off., 1955.

Incropera, F. P., and deWitt, D. P., 1981, *Fundamentals of Heat Transfer*, Wiley, New York.

Jaluria, Y., 1980, *Natural Convection Heat and Mass Transfer*, Pergamon, Oxford, United Kingdom.

Kays, W. M., and Crawford, M. E., 1980, *Convective Heat and Mass Transfer*, 2nd ed., McGraw-Hill, New York, Chap. 14.

Keyhani, M., Kulacki, F. A., and Christensen, R. N., 1983, "Free Convection in a Vertical Annulus With Constant Heat Flux on the Inner Wall," ASME JOURNAL OF HEAT TRANSFER, Vol. 105, pp. 454–459.

Keyhani, M., and Kulacki, F. A., 1985, "Natural Convection in Enclosures Containing Tube Bundles," *Natural Convection, Fundamentals and Applications*, S. Kakac, W. Aung, and R. Viskanta, eds., Hemisphere, Washington, DC, pp. 330–380.

Keyhani, M., Kulacki, F. A., and Christensen, R. N., 1985, "Experimental Investigation of Free Convection in a Vertical Rod Bundle—A General Correlation for Nusselt Numbers," ASME JOURNAL OF HEAT TRANSFER, Vol. 107, pp. 611–623.

Kline, S. J., and McClintock, F. J., 1953, "Describing Uncertainties in Single-Sample Experiments," *Mechanical Engineering*, Vol. 75, No. 1, pp. 3–8.

Leonard, M. T., Williams, K. A., and Church, J. P., 1990, "Modifications to MELCOR for the Analysis of Heavy-Water Moderated, U-Al Fuel Reactors," *Proceedings, International Topical Meeting on the Safety, Status and Future of Noncommercial Reactors and Irradiation Facilities*, Boise, Idaho Section, American Nuclear Society, pp. 104–111.

McEligot, D. M., Magee, P. M., and Leppert, G., 1965, "Effect of Large Temperature Gradients on Convective Heat Transfer: The Downstream Region," ASME JOURNAL OF HEAT TRANSFER, Vol. 87, pp. 67–76.

McEligot, D. M., Stoots, C. M., Christenson, W. A., O'Brien, J. E., Larson, T. K., Mecham, D. C., and Lussie, W. G., 1992, "Turbulent Natural Convection in an Enclosure Formed by an Array of Vertical Cylinders," Tech. Report EG&G-NE-10237, Idaho Nat. Engrg. Lab.; available through OSTI, Oak Ridge.

Mochizuki, H., and Ishii, Y., 1992, "Study of Thermalhydraulics Relevant to Natural Circulation in ATR," *Proceedings, 5th International Topical Meeting on Reactor Thermal Hydraulics*, Salt Lake City, Idaho Section, American Nuclear Society, pp. 127–134.

Morgan, V. T., 1975, "The Overall Convective Heat Transfer From Smooth Circular Cylinders," *Adv. Heat Transfer*, Vol. 11, pp. 199–264.

Nagendra, H. R., Tirunarayanan, M. A., and Ramachandran, A., 1969, "Free Convection Heat Transfer From Vertical Cylinders and Wires," *Chem. Engr. Sci.*, Vol. 24, pp. 1491–1495.

Nagendra, H. R., Tirunarayanan, M. A., and Ramachandran, A., 1970, "Laminar Free Convection From Vertical Cylinders With Uniform Heat Flux," ASME JOURNAL OF HEAT TRANSFER, Vol. 92, pp. 191–194.

O'Brien, J. E., 1991, "Emissivity Measurements in Support of Experiments on Natural Convection Between a Vertical Cylinder and a Surrounding Array," Tech. report EG&G-NE-10083, Idaho Nat. Engrg. Lab.; available through OSTI, Oak Ridge.

Ostrach, S., 1958, "Internal Viscous Flows With Body Forces," *Boundary Layer Research*, H. Goertler, ed., Springer, Berlin, pp. 185–209.

Özişik, M. N., 1985, *Heat Transfer*, McGraw-Hill, New York

Rabas, T., 1992, personal communication, Argonne Nat. Lab., 24 March.

Raithby, G. D., and Hollands, K. G. T., 1985, "Natural Convection," *Handbook of Heat Transfer Fundamentals*, 2nd ed., W. M. Rohsenow, J. P. Hartnett, and E. N. Ganic, eds., McGraw-Hill, New York, pp. 6-1 to 6-94.

Raithby, G. D., 1992, personal communication, Univ. Waterloo.

Rohsenow, W. M., and Choi, H. Y., 1961, *Heat, Mass and Momentum Transfer*, Prentice-Hall, Englewood Cliffs, NJ.

Schlichting, H., 1968, *Boundary-Layer Theory*, 6th ed., McGraw-Hill, New York, p. 509 et seq.

Shaaban, A. H., and Özişik, M. N., 1982, "Effect of Curvature on the Thermal Stability of a Fluid Between Two Long Vertical Coaxial Cylinders," *Proceedings, 7th International Heat Transfer Conference*, Paper No. NC27, Vol. 2, pp. 281–286.

Shumway, R. W., 1969, "Variable Properties Laminar Gas Flow Heat Transfer and Pressure Drop in Annuli," Ph.D. thesis, University of Arizona; ASTIA AD-696 458.

Shumway, R. W., and McEligot, D. M., 1971, "Heated Laminar Gas Flow in Annuli With Temperature-Dependent Transport Properties," *Nuc. Sci. Engrg.*, Vol. 46, pp. 394–407.

Siebers, D. L., Moffat, R. J., and Schwind, R. G., 1985, "Experimental, Variable Properties Natural Convection From a Large, Vertical, Flat Surface," ASME JOURNAL OF HEAT TRANSFER, Vol. 107, pp. 124–132.

Siegel, R., and Howell, J. R., 1972, *Thermal Radiation Heat Transfer*, McGraw-Hill, New York.

Steimke, J. L., 1991, "Heat Transfer for Safety Rod and Thimble," Tech. report WSRC-TR-91-600, Savannah River Lab.

Touloukian, Y. S., ed., 1967, *Thermophysical Properties of High Temperature Solid Materials. Vol. 3: Ferrous Alloys*, MacMillan, New York.

Webb, R. L., Eckert, E. R. G., and Goldstein, R. J., 1971, "Heat Transfer and Friction in Tubes With Repeated-Rib Roughness," *International Journal of Heat and Mass Transfer*, Vol. 14, pp. 601–617.

Zhang, Z., Bejan, A., and Lage, J. L., 1991, "Natural Convection in a Vertical Enclosure With Internal Permeable Screen," ASME JOURNAL OF HEAT TRANSFER, Vol. 113, pp. 377–383.

APPENDIX

Treatment of Energy Flow Rates

A key to applying the results of this experiment is an understanding of the approaches used in calculating the convective and radiative terms to account for the holes in the perforated tube. A few more details are available in our technical report, but this appendix is provided to give an overview.

The geometry of the perforated tube complicated the treatment of the thermal radiation transfer, compared to the heated test section alone. Radiation was approximated by three con-

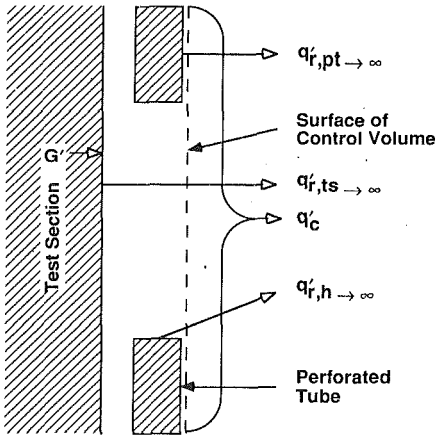

Fig. A-1 Energy flows for control volume analysis to determine convective heat transfer from perforated tube to surroundings (geometry in scale)

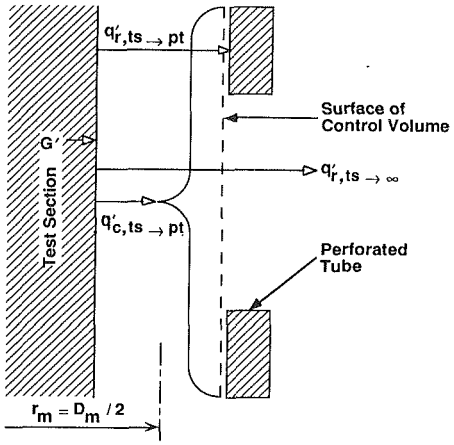

Fig. A-2 Energy flows for control volume analysis to determine convective heat transfer across annular gap from test section to perforated tube (gap spacing exaggerated)

tributions: (1) from the test section through the holes, (2) from the outer surface of the perforated tube and (3) from the edges of its holes outwards. Figure A-1 demonstrates the definitions and use of these energy flows for determining the convective heat transfer rate from the outer envelope of the perforated tube to its surroundings. These are believed to be the major contributions, but the estimates of experimental uncertainties are increased for each radiation term to account for the lack of a more exact treatment.

The estimate of radiation from the test section through the holes is based on the assumption that any radiation falling on the fictitious inner surface of a hole, coming from the test section, would pass out to the surrounding environment (either indirectly by reflection from the low emissivity edge of the hole or directly). The view factor from the test section to the holes is taken as the area ratio (hole/total) on the inner diameter of the thimble. These approximations lead to representation of this term as

$$q'_{r,ts\to\infty} = \epsilon_{ts}(A_h/A_{pt,i})\pi D_{ts}\sigma(T_{ts}^4 - T_{ct}^4) \tag{A1}$$

Radiation from the outer surface of the perforated tube is represented as from a small surface (which does not view itself) to large surroundings (Incropera and deWitt, 1981),

$$q'_{r,pt\to\infty} = \epsilon_{pt}(A_{\text{solid}}/A_{pt,o})\pi D_{pt,o}\sigma(T_{pt}^4 - T_{ct}^4) \tag{A2}$$

An additional contribution is the radiation between the edges of the holes and the outer surroundings. This contribution is about 10 percent of that for the outside of the perforated tube and is represented as

$$q'_{r,h\to\infty} = N'_h\epsilon_{pt}F_{h\to\infty}A_h\sigma(T_{pt}^4 - T_{ct}^4) \tag{A3}$$

Here N'_h is the number of holes per unit length and the view factor $F_{h\to\infty}$ is approximated following Siegel and Howell (1972, example 27, p. 789).

The local convective heat transfer *from the perforated tube to its surroundings* is deduced from the energy balance on a control volume defined by the outer envelope of the perforated tube (as shown in Fig. A-1),

$$q'_c = G' - q'_{r,ts\to\infty} - q'_{r,pt\to\infty} - q'_{r,h\to\infty} \tag{A4}$$

For the *annular gap*, a steady-state energy balance was employed to estimate the local convective heat transfer rate from the test section to the perforated tube,

$$q'_{c,ts\to pt} = q'_{\text{total},ts\to pt} - q'_{r,ts\to pt} = (G' - q'_{r,ts\to\infty}) - q'_{r,ts\to pt} \tag{A5}$$

as demonstrated in Fig. A-2. The radiation from the test section through the holes was calculated as above. For the fraction of the test section covered by the solid surface of the perforated aluminum tube, the radiation exchange between the two ($q'_{r,ts\to pt}$) was approximated as a two-surface enclosure (e.g., Eq. 13.25 of Incropera and deWitt, 1981) with geometric view factor $F_{ts\to pt}$ of unity and emissivities determined from the temperature measurements. In forming the nondimensional parameters, properties were evaluated at the mean temperature in the annulus, $T_m = (T_{ts} + T_{pt})/2$. The convective heat transfer coefficient is defined by

$$q'_{c,ts\to pt} = h\pi D_m(T_{ts} - T_{pt}) \tag{A6}$$

and the nondimensional parameters are based on s_{gap}, the spacing across the annulus.

Natural Convection Heat Transfer From a Staggered Vertical Plate Array

G. Tanda
Researcher,
Department of Energy Engineering,
University of Genoa,
I-16145 Genova, Italy

An experimental study was performed to evaluate the natural convection heat transfer characteristics of an array of four staggered vertical plates. The thermal input at each plate was the same or differed from plate to plate depending on various heating modes. The effects of the interplate spacing and the plate-to-ambient temperature difference were investigated. The experiments were performed in air. Convective interactions among the plates were identified by examining the per-plate heat transfer coefficients and the local heat transfer coefficients along the vertical sides of plates. Local heat transfer results were obtained by means of the schlieren quantitative technique. Comparison of local heat transfer coefficients along the plate assembly with those of a continuous vertical plate (having the same height) showed enhancements up to a factor of two. Comparison of average heat transfer results with those for a parallel plate channel having the same exchanger size showed only little reductions in heat transfer rate, despite a 28 percent reduction in heat transfer area, with enhancements, in terms of specific heat flux, up to 30 percent.

Introduction

Natural convection heat transfer from surfaces has important applications in the cooling of electronic components and small energy conversion devices. There is, therefore, a clear motivation to examine the efficacy of enhancement techniques in the field of free convection. However, while a large number of studies have been performed on single and two-phase forced convection enhancement (as well as on pool boiling and condensation), there are only a few papers dealing with natural convection heat transfer enhancement. In a natural convection system no energy costs are needed to pump the mass flow rate of the cooling fluid. Therefore, the evaluation of an enhancement technique should be based on heat transfer performance, by simply comparing the heat transfer rates of the enhanced and reference (unenhanced) systems under given constraints, for instance at the same heat transfer surface area (or exchanger size) and temperature difference.

An example of a natural convection enhanced system, proposed by Sobel et al. (1966) and numerically analyzed by Prakash and Sparrow (1980), consists of a staggered array of vertical discrete-plate segments as the heat transfer surface in lieu of an array of uninterrupted surfaces. The numerical simulations performed by Prakash and Sparrow (1980) indicated that natural convection heat transfer enhancement, relative to an array of parallel plates having the same heat transfer area and wall-to-ambient temperature difference, can be achieved up to 80–90 percent.

While Prakash and Sparrow (1980) analyzed a two-dimensional problem with zero plate thickness, a more practical situation, involving an array of vertical staggered segments of finite length and thickness (connected to an isothermal baseplate) was experimentally investigated by Guglielmini et al. (1987), and by Guglielmini and Tanda (1989). A general correlation for natural convection heat transfer was developed and enhancements, with respect to an array of vertical continuous parallel plates, were found in the range 0–20 percent, with the exchanger size (instead of the heat transfer surface area) constrained to be the same.

Contributed by the Heat Transfer Division for publication in the JOURNAL OF HEAT TRANSFER. Manuscript received by the Heat Transfer Division September 1992; revision received February 1993. Keywords: Flow Visualization, Heat Exchangers, Natural Convection. Associate Technical Editor: J. R. Lloyd.

The studies mentioned reported overall performance of free convection heat transfer of the considered surface configurations, without information about the local characteristics. In this paper the natural convection heat transfer for a system consisting of a staggered array of four vertical plates was experimentally investigated. Special attention has been devoted to the local heat transfer behavior and to comparisons with the thermal performance of natural convection reference systems. The configuration here considered can be encountered in gas-side heat exchangers, radiators for room air heating, and finned surfaces. Alternatively, each plate of the array may be a model of an energy dissipating device (such as an electronic panel), thus allowing the system to simulate an electronic packaging configuration.

The Experiments

Apparatus. The experimental apparatus consists of the test section (the plate assembly), the power supply system, a schlieren visualization system, and instrumentation for measuring temperature, electrical power, and pressure. A schematic view of the test section is presented in Fig. 1. The four vertical plates, suspended by nylon lines, were affixed at three different levels in the vertical coordinate. Designations A, B, and C were assigned to denote plates respectively located at the lower, middle, and upper stages. The experimental setup was designed to be operated with the plates set at different spacings, and to supply a controlled amount of heating power to each plate.

Each vertical plate consisted of two aluminum sheets with an electrical plane resistor sandwiched between them, dissipating thermal power by Joule effect (Fig. 2). The dimensions of each plate were the following: thickness $D = 8$ mm, height $H = 6.5$ cm, and length $L = 30$ cm. Both the plates and the surroundings were instrumented with fine-gage, chromel-alumel thermocouples, calibrated to ± 0.1 K. Thermocouples were embedded in the wall of each plate through ten 0.5-mm-dia holes drilled into the inner faces of the two aluminum sheets (see details in Fig. 2). Care was taken to drill the holes as close to the exposed surfaces as possible. The ambient air temperature was measured by five shielded thermocouples situated just below the plate array.

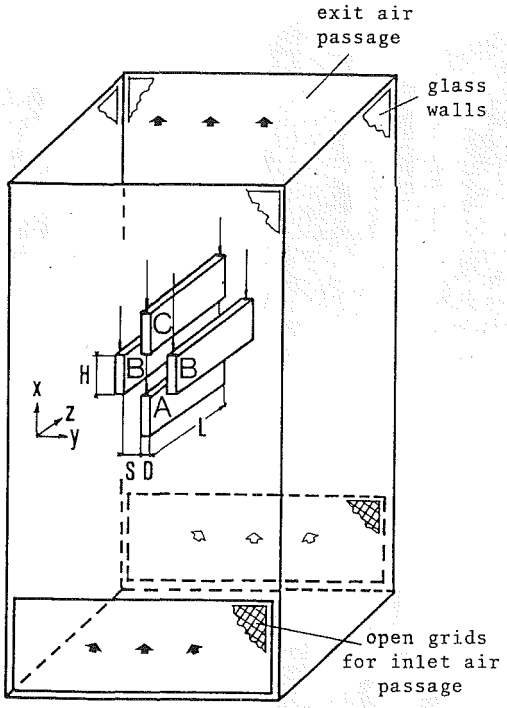

Fig. 1 Schematic view of the test section

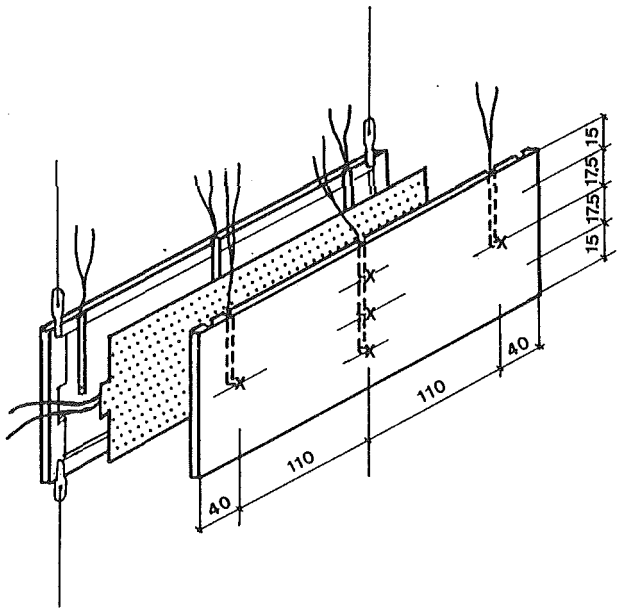

Fig. 2 Detail of the housing of electrical heater and thermocouples (*X*) in the plate (all dimensions are in mm)

The power input supplied to each plate was transferred to the surroundings by natural convection and radiation. Since the thermal resistance of the plate material was very small, owing to the high thermal conductivity of aluminum, each plate was expected to be virtually isothermal. The surface temperature uniformity was checked by means of an infrared thermographic system in a preliminary experiment. The wall temperature field on a single heated plate (previously black-anodized to increase thermography sensitivity) was analyzed. The maximum temperature nonuniformities, based on the mean plate-to-ambient temperature difference, turned out to be 1 percent in the vertical direction and 4 percent in the transverse direction. In particular, a 2 percent temperature drop was found in the proximity of the transverse extremities of the plate (within 2 cm of the edges, approximately), due to limited three-dimensional effects. The same wall temperature behavior was expected in the experiments on the plate assembly, for which the maximum variations in temperature over each plate (recorded by thermocouples) were generally less than 2 percent of the mean plate-to-ambient temperature difference. Hence, each plate of the assembly was assumed to attain a different uniform temperature, the value of which depended on the

Nomenclature

A = heat transfer surface area
AH, BH, MH, CH = heating of: plate A, one of plates B, both plates B, and plate C, respectively
D = plate thickness
F = angle factor
f_2 = focal distance of mirror M_2 in the schlieren apparatus of Fig. 3
g = acceleration of gravity
H = plate height
h = local natural convection heat transfer coefficient
h_o = natural convection heat transfer coefficient averaged on the vertical sides of the plate
h_{av} = per-plate natural convection heat transfer coefficient
J = radiosity
K = Gladstone–Dale constant
k = thermal conductivity
L = plate length
Nu_{av} = per-plate Nusselt number
n = refractive index
n_o = refractive index of air at reference conditions
P = pressure
Pr = Prandtl number
Q_c = natural convection heat transfer
Q_r = radiation heat transfer
Q_t = electrical power input
R = ideal gas constant
Ra = Rayleigh number
S = spacing parameter (see Figs. 1 and 5)
S' = spacing parameter in the modified staggering arrangement (see Fig. 5*b*)
T = absolute temperature
UH, NUH = all the plates heated by the same power input, and all the plates heated by different power inputs, respectively
x, y, z = spatial coordinates
α = light ray angular deflection
β = coefficient of thermal expansion
Δ = light ray displacement
ϵ = thermal emittance
μ = dynamic viscosity
ρ = density
σ = Stefan–Boltzmann constant

Subscripts

i, j, k = surface indexes
w = wall
∞ = ambient air

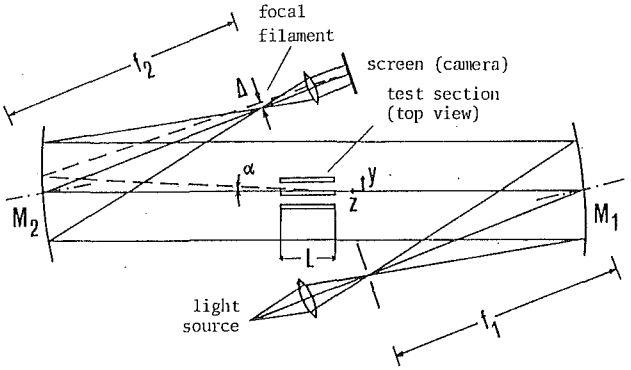

Fig. 3 Schlieren apparatus for local heat transfer coefficient measurements

characteristics of the buoyancy-induced flow and on the amount of heating power to be transferred to the surroundings.

The radiation heat transfer was reduced to a small value (8 to 14 percent of the total power input) because of the low thermal emittance ϵ of the polished aluminum surfaces, measured by a radiometric apparatus (described by Ruffino and Pisoni, 1976) to be 0.1 ± 0.02 in the temperature range of interest. As will be further described, the radiation heat transfer from each plate was determined by calculation and subtracted from the total power input, thereby yielding the per-plate natural convection heat transfer rate. This last quantity was only slightly affected (no more than 3 percent) by the uncertainty in emittance.

The plate assembly was confined on four sides by glass walls having open grids at the bottom (see Fig. 1). Runs conducted without the side walls revealed negligible effects on heat transfer performance, but their presence was necessary to minimize extraneous air-current effects that might disturb schlieren visualizations. The experiments were carried out in a large isolated room. All instrumentation (scanning thermometer, barometer, voltmeters, and ammeters) as well as the power supply system were set far away from the plate assembly.

A schlieren optical system was used to perform measurements of local heat transfer coefficients. The schlieren system employed is schematically shown in Fig. 3. The light beam of a slit source, collimated by a concave mirror M_1 (38 cm diameter), enters the test section. Light rays, initially parallel to the length of the plates, undergo angular deflections α owing to the refractive index gradients of air near the test section. The deflected beam is then collected by a second concave mirror M_2 (38 cm diameter), and projected onto a screen or a camera. A technique for establishing curves of equal angle of deflection consists in setting a vertical opaque filament in the focal plane of the mirror M_2 (Vasil'ev, 1971). When no heating power is supplied, the air refractive index is constant and the light beam is not deflected. Under such conditions, if the illuminating slit is projected on the middle of the filament, the light is stopped and the screen appears uniformly dark. When the plate assembly is heated, light rays passing through regions of fluids with variable refractive index will be deflected. Therefore, the projected image of these regions on the screen will appear lighted, as shown in Fig. 4(*a*). Moving the filament in the direction of deflections allows one to visualize on the screen (or camera) the regions of fluid deflecting light rays through an angle α equal to Δ/f_2, where Δ is the displacement of the filament and f_2 is the focal length of mirror M_2 (equal to 1.9 m). The light rays deflected through the angle α are stopped by the focal filament, and the corresponding areas of the fluid appear dark. The quantity Δ can be easily determined by direct measurement. The images of the test section recorded on the camera after successive shifts of the filament are reported in Figs. 4(*b*) and 4(*c*). Collimating the centerline of the filament

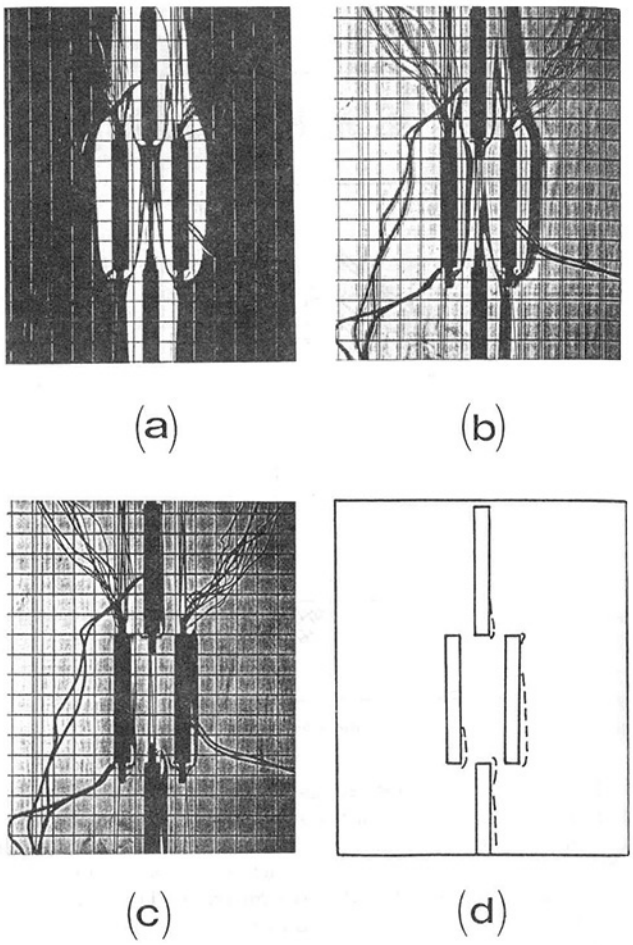

Fig. 4 Test section images recorded by schlieren apparatus: (*a*) light beam projected on the middle of focal filament; (*b*) and (*c*) the focal filament is progressively shifted in the direction of light deflections; (*d*) locus of points at equal light deflection after the image processing: the intersection of the filament shadow centerline with vertical surface profile allows α_w measurement

shadow (projected onto the screen) on a given point of the vertical surface profile allows one to evaluate deflection α_w of light ray passing in the vicinity of the wall, as schematically shown in Fig. 4(*d*). This quantity is related to the local convective heat transfer coefficients. The relation between deflection angle α_w and the local heat transfer coefficient will be outlined in the Data Reduction section.

Operating Procedure. Two different arrangements of plates were investigated, as depicted in Figs. 5. In the main body of experiments, the vertical plates were symmetrically staggered, with the two plates at the middle stage (labeled *B*) equally spaced with respect to the remaining plates (labeled *A* and *C*), as depicted in Fig. 5(*a*). Three different spacings (i.e., three values of the distance *S*) were set, namely $S = 1.95$ cm, 1.3 cm, and 0.65 cm, respectively (with an expected accuracy of ± 0.25 mm). Values of *S* were chosen in order to obtain values of the ratio *S/H* equal to 0.3, 0.2, and 0.1. Supplementary experiments were performed with a modified staggered arrangement (Fig. 5*b*). In particular, the spacing between the two middle plates was kept fixed (with *S/H* equal to 0.3 or 0.2), while the upper plate was slightly shifted. This last situation, in which symmetry is eliminated, was considered in order to assess whether the adverse effect of the wake generated by plate *A* on heat transfer performance of plate *C* may be reduced. With reference to Fig. 5(*b*), the distance *S* was varied between 1.95 cm and 1.3 cm with the distance S' ranging from 1.3 cm to 0.65 cm.

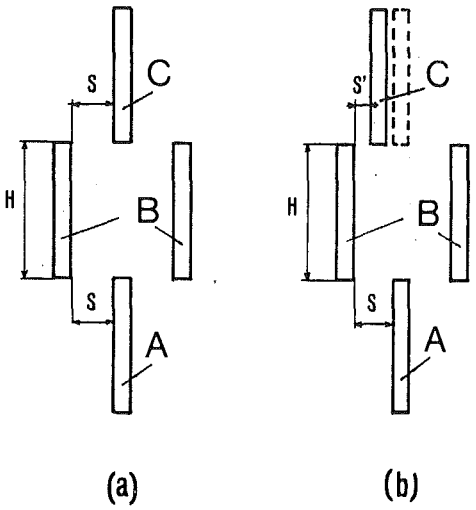

Fig. 5 Schematic of plate assembly: (*a*) symmetric staggered arrangement; (*b*) modified staggered arrangement

In addition to the different arrangements of the plate assembly, alternative heating conditions were considered. The case in which each plate dissipates the same thermal power is designated by the label *UH*. In a different case (designated by label *NUH*) the upper and lower plates (*C* and *A*, respectively) are heated by four times as much power as that supplied to each of plates *B*. The case in which only the middle plates *B* are equally heated is labeled by *MH*. Finally, labels *AH*, *BH*, and *CH* respectively denote the cases in which only the lower plate *A*, or one of the two middle plates *B*, or the upper plate *C* is heated. In the modified staggered arrangements investigated (Fig. 5*b*), the *UH* heating mode only was applied.

Each experimental run consisted of the heating of the plate array (under a given heating mode, namely *UH*, *NUH*, *MH*, *AH*, *BH*, *CH*) by delivering a known amount of electrical power to the heaters embedded in the plates. From 12 to 24 hours were allowed for the attainment of steady-state conditions after a power input change.

Data Reduction

The main purpose of the experimental investigation was to determine the natural convection heat transfer characteristics of each plate under the spacing and heating mode considered. Attention was devoted not only to per-plate heat transfer behavior but also to local characteristics along the vertical surfaces of the plate assembly. Overall and local heat transfer characteristics were analyzed by two different procedures.

Per-Plate Heat Transfer Characteristics. For each plate the energy balance leads to

$$Q_t = Q_c + Q_r \tag{1}$$

where Q_t, Q_c, and Q_r, respectively, denote the electrical power input, the convective heat transfer, and the radiant heat transfer.

An analytical scheme for determining the net radiation heat transfer from each plate to the environment was developed. Each plate is decomposed into a number N of plane surfaces having different orientations. For each surface of index i, assumed isothermal, gray and diffuse, the following relationship is applied:

$$(\sigma T_i^4 - J_i)\,\frac{\epsilon}{1-\epsilon} = J_i - \sum_{j=1}^{M} J_j\, F_{i-j} \tag{2}$$

In this equation, T_i and J_i, respectively, are the absolute temperature and radiosity of the generic i-surface and F_{i-j} is the angle factor between the i-surface and the generic j-surface, with radiosity J_j, exposed to i-surface radiation. All the angle factors included in the summation can be readily computed by using the appropriate parallel and perpendicular plate formulae reported in radiation textbooks. If a fictitious boxlike envelope is supposed to confine the plate assembly, M accounts for all plate surfaces viewed by the generic i-surface and for the envelope, assumed nonreflecting and at the temperature T_∞ of ambient air, so that its radiosity is σT_∞^4.

As relation (2) can be written for each plane surface of plates, a system of equations with the radiosities J_i as unknowns can be obtained. The algebraic system can be solved by using surface and ambient temperatures given by experiments in order to evaluate the net radiation exchanged between each plate and surroundings (ambient and viewed plates) as follows:

$$Q_r = \frac{\epsilon}{1-\epsilon} \sum_{k=1}^{N} A_k\,(\sigma T_w^4 - J_k) \tag{3}$$

where T_w is the surface temperature of the plate and A_k and J_k represent surface area and radiosity of each of the N plane surfaces of the plate. As previously noted, calculated Q_r values were only 8 to 14 percent of the input power Q_t to the plate. Only little variations of Q_r values from plate to plate (up to 12 percent) were found, depending on the specific position in the assembly.

Returning now to Eq. (1), Q_c can be determined by using the measured value of Q_t and the calculated value of Q_r. The average per-plate heat transfer coefficient was evaluated from:

$$h_{\text{av}} = Q_c / A(T_w - T_\infty) \tag{4}$$

In the above equation A is the plate surface area, T_w is the surface temperature, and T_∞ is the ambient air temperature. The surface temperature T_w of each plate was evaluated by averaging the readings of the thermocouples embedded in the wall. Similarly, the ambient temperature T_∞ was obtained by averaging the readings of the thermocouples deployed below the plate assembly.

For a dimensionless presentation, Nusselt and Rayleigh numbers were introduced

$$\text{Nu}_{\text{av}} = h_{\text{av}} H/k \tag{5}$$

$$\text{Ra} = g\beta\rho^2 (T_w - T_\infty) H^3 \text{Pr}/\mu^2 \tag{6}$$

The thermophysical properties appearing in Eqs. (5) and (6) were evaluated at the film temperature $(T_w + T_\infty)/2$.

Local Heat Transfer Characteristics. Heat transfer coefficients along the vertical surfaces of the plates were evaluated by using the previously described schlieren apparatus. With reference to Fig. 3, the experimental setup allows one to record the light ray shift Δ related to the angular deflection α in the y direction (orthogonal to the vertical surfaces of the plates). The relation between the angular deflection and the refractive index gradient of fluid $\partial n/\partial y$ is

$$\alpha = \frac{1}{n_o}\frac{\partial n}{\partial y} L \tag{7}$$

where n_o is the refractive index of air at reference conditions and L is the plate length. Use of Eq. (7) implies that the thermal field should be two dimensional (i.e., independent of a z coordinate). This condition is assumed to be well verified, because of the low temperature nonuniformities of each plate and the large ratio of the plate length to the plate spacing. By introducing the Gladstone-Dale formula ($n = K\rho + 1$) and state equation of ideal gas ($\rho = P/RT$), one obtains

$$\alpha = -\left(\frac{K\,P\,L}{R\,n_o}\right)\frac{1}{T^2}\,(\partial T/\partial y) \tag{8}$$

where K is the Gladstone-Dale constant of air, P the pressure (whose variations near the test section are assumed to be neg-

ligible), and R the constant of air. Since the measured light ray shift Δ is equal to $f_2 \cdot \alpha$, it follows that

$$\Delta = -f_2 \left(\frac{K\,L}{R\,n_o}\right) \frac{P}{T^2}\,(\partial T/\partial y) = -C\,\frac{P}{T^2}\,(\partial T/\partial y) \qquad (9)$$

in which the constant C is equal to 0.45×10^{-6} m^{2}K/Pa in the present experiment (with Δ expressed in m).

The definition of local convective heat transfer coefficient is now introduced:

$$h = \frac{-k_w(\partial T/\partial y)_w}{(T_w - T_\infty)} \qquad (10)$$

where k is the thermal conductivity of the fluid and the subscript w denotes quantities evaluated at the wall conditions. Taking into account Eq. (9), it follows that

$$h = \frac{k_w T_w^2 \Delta_w}{C\,P\,(T_w - T_\infty)} \qquad (11)$$

The absolute value of deviation Δ_w should be considered for the vertical surfaces whose normal is oriented toward negative values of the y axis. Equation (11) directly relates the local convective heat transfer coefficients to deviations of light rays passing in the vicinity of heated vertical surfaces (no correction for radiation is needed). When local measurements were conducted, only a limited number of sites along the vertical surfaces of plates were chosen (7–8 positions for each vertical surface, ranging between 5 mm from the leading edge and the top edge).

By means of the numerical integration of measured coefficients h along the two vertical faces, one obtains a mean value h_o for each plate. After runs, this quantity turned out to be only slightly different (0 to 15 percent) from the coefficient h_{av} introduced in the previous paragraph. The difference can be ascribed both to the experimental uncertainty of the two different evaluations and to the role played by the horizontal surfaces (for which a local measurement was not possible), h_o being averaged only on the vertical surfaces.

Experimental Uncertainty. The uncertainty in the results (at 95 percent confidence level) was evaluated by using a root-square combination of the effects of each individual measurement, according to the procedures outlined by Moffat (1988). The uncertainty in each variable was estimated by evaluating the fixed error and the random error observed during running trials (33 observations with the apparatus at steady state). Uncertainties in the Rayleigh number Ra and the Nusselt number Nu_{av} turned out to be 5 and 7 percent, respectively. The uncertainty in the local heat transfer coefficient h as measured by the schlieren method is generally sensitive to the circumstances involved (dimensions of optical components and their alignment, dimensions of test section, etc). Therefore the error analysis performed is strictly valid for the apparatus employed (whose optical parameters were previously described) and for a perturbed optical path of 30 cm. The uncertainty in the light deviation Δ_w readings was found to be the major source of error in the h measurements. Since the accuracy in Δ_w readings improves with increasing Δ_w, the uncertainty in h values turned out to be inversely proportional to the recorded Δ_w values. That is, in the field of Δ_w values between 2 and 9 mm (in which measurements were performed), the uncertainty in h values was estimated to range from 12 to 8 percent. Comparison of h values measured in the case of an isothermal single vertical plate with predictions of Ostrach (1953) revealed only a maximum deviation of 10 percent in the range of Ra values between 5×10^5 and 10^6. Comparison of h values measured between two isothermal vertical plates with numerical results of Naylor et al. (1991) showed a maximum deviation of 9 percent (Ra = 10^6, spacing-to-height ratio = 1/12).

Results and Discussion

Per-Plate Heat Transfer Characteristics. Attention is first focused on the per-plate heat transfer characteristics. The results for the cases in which only one (*AH, BH, CH*) or two (*MH*) plates of the array are heated are plotted in Fig. 6, in terms of per-plate Nusselt number Nu_{av} as a function of the Rayleigh number. A specific data symbol is used to identify each heating condition and the position of the plates considered. Comparisons are made between present results and those for a single, isolated, two-dimensional, isothermal plate. For this purpose, standard correlations reported in the literature (McAdams, 1954) were employed to evaluate an average heat transfer coefficient (taking into account both vertical and horizontal exposed surfaces) and to obtain, via Eq. (5), the Nusselt number plotted by the continuous line. It appears that measured data tend to fall on the single plate line or slightly below. In the *CH* case (only plate *C* is heated) the unheated plates *A* and *B* probably tend to obstruct the buoyant flow, slightly reducing heat transfer from plate *C*.

Figures 7, 8, and 9 refer to results obtained after the heating of all plates of the assembly, at different spacings *S/H*. The thermal behavior of plates *A*, *B*, and *C* is seen separately. As expected, Nusselt numbers of lowest plate *A* (Fig. 7) are practically independent of the heating condition (*UH* or *NUH* cases) and of the spacing *S/H* considered. Inspection of the figure also shows good agreement among experimental data and the single plate correlation.

Now attention is turned to the middle plates *B* (Fig. 8). Owing to the symmetry of the assembly, results for the two plates are obviously coincident, so that one symbol for both

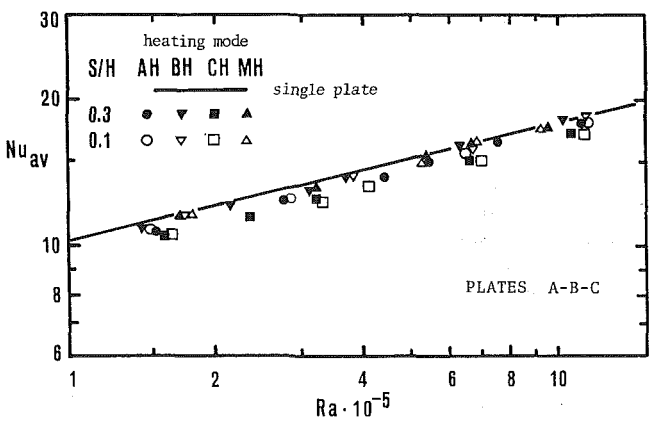

Fig. 6 Per-plate Nusselt numbers when *A*, *B*, or *C* plates are alternately heated

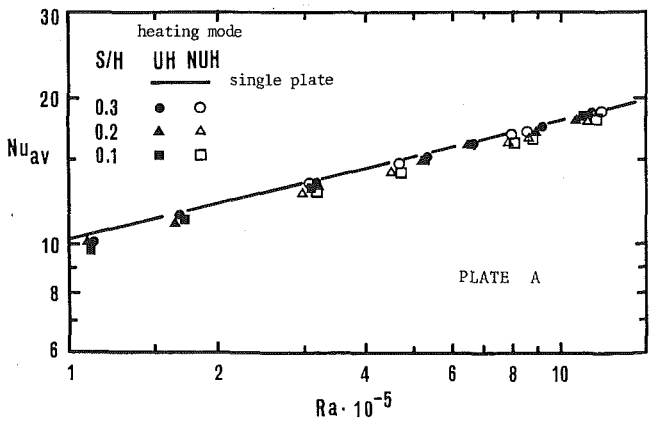

Fig. 7 Nusselt numbers of plate *A* at different interplate spacings and heating modes

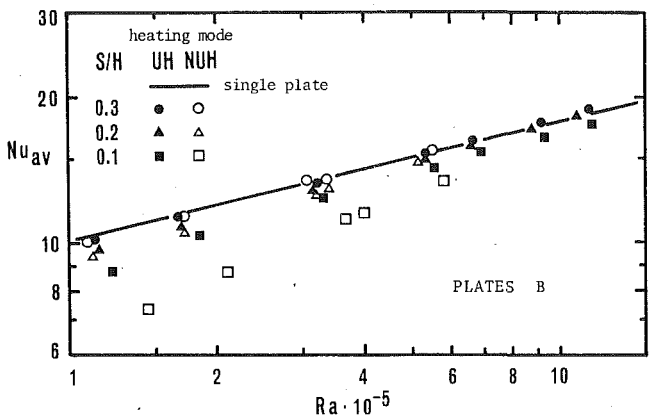

Fig. 8 Nusselt numbers of plates *B* at different interplate spacings and heating modes

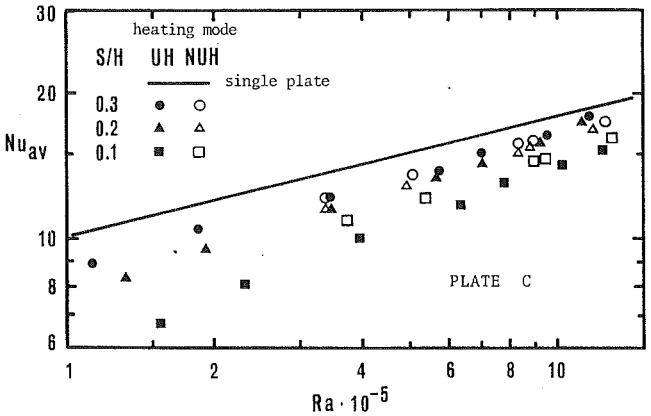

Fig. 9 Nusselt numbers of plate *C* at different interplate spacings and heating modes

plates is plotted. Various degrees of deviation from the single plate line are in evidence in the figure, depending on the spacing parameter, the Rayleigh number, and the heating condition. It is expected that the plume rising from the lower plate *A* may interact with boundary layers growing along facing surfaces of plates *B*. If the interspacing between plates *B* is large (i.e., $S/H = 0.3$) the convective interaction is low, while this effect becomes significant as the interspacing is reduced ($S/H = 0.1$). An important role is played by the type of heating employed. When plates provide the same rate of thermal power (*UH* case), and the interspacing $S/H = 0.1$ is set, the extreme reductions in the per-plate Nusselt number (as compared with the single plate line) are of about 15 percent, for the lowest Rayleigh number investigated. In the case of *NUH* heating mode, power input supplied to plate *A* (and plate *C*) is four times that delivered to each plate *B*, so that a larger amount of preheated air mass is expected to impinge on plates *B*. This expectation is fulfilled at the lowest interplate spacing ($S/H = 0.1$) for which the reductions of the Nusselt number vary from 14 to 32 percent as the Rayleigh number decreases.

The Nusselt number data for plate *C* are reported in Fig. 9. Inspection of the figure shows that downside deviations from the single plate line are present in all cases, with any spacing and heating mode. It should be noted that the heat transfer performance is affected by two factors: the submersion in the thermal wake from plate *A*, and the interaction between the thermal boundary layer growing along plate *C* and wakes from side plates *B*. For the highest values of S/H investigated (0.3 and 0.2), the data in the range of intermediate and high Rayleigh numbers (say $Ra > 6 \times 10^5$) tend to fall in a tight band below the single plate line. In these conditions the interactions with side plates *B* are negligible, and the slight reduction (5–10 percent) of heat transfer from plate *C* is mainly due to the preheating of the impinging buoyant upflow induced by plate *A*. For the abovementioned ranges of parameters (S/H, Ra), experimental data are in agreement with the numerical results obtained by Sparrow and Faghri (1980) for the natural convection heat transfer from a colinear, separated pair of vertical plates. At low Rayleigh numbers, the thermal boundary layer along plate *C* and wakes from plates *B* are likely to interfere, with further heat transfer degradation. The two effects mentioned are active in the case of the smallest interspacing ($S/H = 0.1$) and equal heat input at plates (*UH* case), for which the largest heat transfer deviations from the single plate line are found (from 15 to 40 percent). Conversely, when plates *B* dissipate a smaller amount of thermal power than plates *A* and *C* (*NUH* case), the preheating of air downstream of the side plates has a minor effect. This accounts for the slight improvement in the thermal performance of plate *C* for $S/H = 0.1$.

Per-plate Nusselt number results have been presented for various interplate spacings and heating modes in a symmetric staggered array. Experiments were performed for a different staggering arrangement, in which upper plate *C* is shifted away from the symmetry axis, as shown in Fig. 5(*b*). The aim is to reduce the adverse effect on heat transfer by the wake from the upstream plate *A*. As shown in a previous study performed on mixed convection by Kurosaki et al. (1988), this modified arrangement can lead to improved thermal performance with increases in the heat transfer coefficients of the shifted plates up to 10 percent, as compared with the regularly spaced plate assembly. Starting from the symmetric staggered arrangement (Fig. 5*a*) with $S/H = 0.3$, plate *C* was displaced in order to vary S'/H from 0.1 to 0.2. In the case of the symmetric staggering with $S/H = 0.2$, only one value of S'/H was set ($S'/H = 0.1$). Finally, the small interplate distance corresponding to the arrangement of Fig. 5(*a*) with $S/H = 0.1$ did not allow any staggering modification. The *UH* heating mode was considered. For all the described asymmetric arrangements, Nusselt number variations for plate *C* (with respect to the symmetric staggering) were confined in the ±4 percent range. It was found that shifting the upper plate *C* reduces the effect on heat transfer due to the wake from lower plate *A* but, on the other hand, tends to increase the convective interaction with the closest plate at the middle stage *B*. This conflict of effects yields to heat transfer coefficients that are practically unchanged when compared with those of the regular staggered arrangement. This result is not in contrast with that of Kurosaki et al. (1988) since the dimensionless interplate spacing S/H set in the above paper was higher than those considered here, thus preventing the displaced plate from interfering with the thermal wakes of the lower row of plates.

Local Heat Transfer Characteristics. Further insight into the heat transfer behavior can be obtained by examining the variation of the local heat transfer coefficients along the vertical surfaces of the plates. The range of the Rayleigh number for which local measurements were performed was 5×10^5–10^6. The results are presented in dimensionless form by plotting the ratio h/h_o, where h_o is the per-plate heat transfer coefficient averaged on the vertical surfaces, against the quantity x/H, where the vertical coordinate x starts from the leading edge of each plate.

It has been established that the thermal performance of the lower plate *A* is not influenced by the presence of the plates situated above it. In the same manner, local heat transfer coefficients are close to the single-plate ones and their presentation is without interest. In Fig. 10 the normalized local heat transfer coefficient is plotted for plates *B*, in the case of equal input at the plates (*UH* heating mode) and different S/H values. Open and blackened symbols refer to the inner

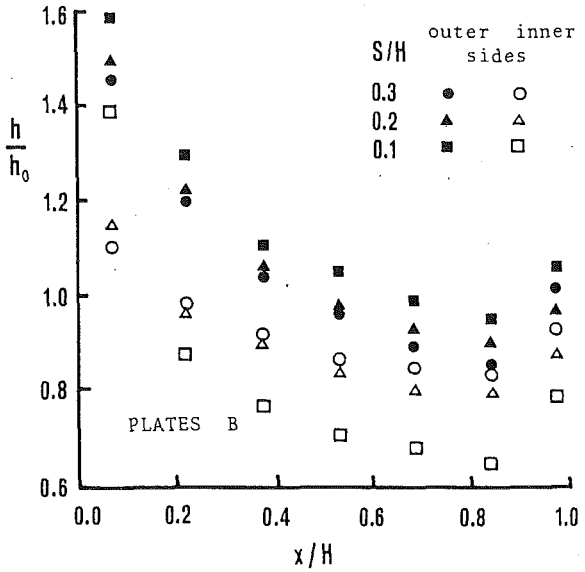

Fig. 10 Variation of local heat transfer coefficient along the vertical sides of plates *B* (normalized by the value averaged on vertical sides). Heating of the whole plate assembly (*UH* heating mode). Ra $\approx 7 \times 10^5$.

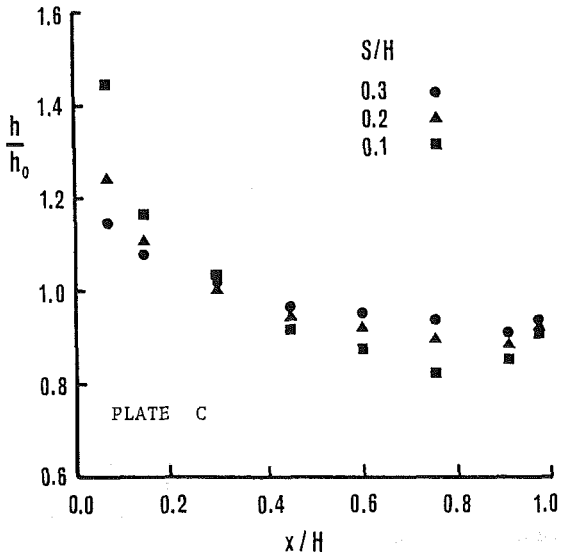

Fig. 11 Variation of local heat transfer coefficient along the vertical sides of plate *C* (normalized by the value averaged on vertical sides). Heating of the whole plate assembly (*UH* heating mode). Ra $\approx 7 \times 10^5$.

sides of plates *B* and to the outer sides, respectively. Comparisons between local thermal characteristics are performed approximately at the same Rayleigh number (Ra about 7×10^5). In all cases h/h_o values are higher than unity near the leading edge and then decay with increasing x/H until very close to the trailing edge, where the changes in flow direction contribute to increase the heat transfer coefficient. Differences in the local behavior of inner and outer vertical sides are found. In fact, the thermal boundary layers growing along the two facing sides may not only interfere with each other but also blend with the thermal wake of the lower plate *A*, with degradation of local heat transfer. Conversely, the outer vertical sides are free of natural convection interactions and their local performance remains high. It can be observed that in the cases of interspacing $S/H = 0.3$ and 0.2, the heat transfer degradation of inner faces tends to lessen as x/H is increased. When S/H is small ($S/H = 0.1$), the flow acceleration caused by the blockage effect of the plates contributes to increase the heat transfer coefficient at the leading edge of inner surfaces, with differences among the values on the two sides (at the same level) confined within 15 percent. As x/H is increased, differences between the thermal behavior of the two sides become stronger, with inside local coefficients reduced by about 30 percent as compared with the outside ones at the same level x/H.

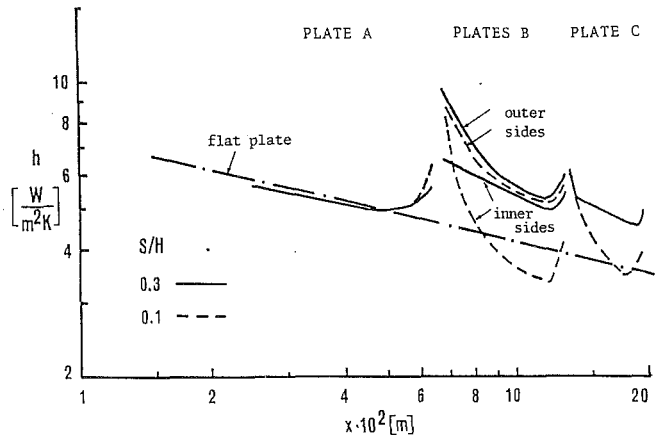

Fig. 12 Local heat transfer coefficients along the staggered vertical assembly ($S/H = 0.3$ and 0.1) compared with the ones along a vertical isothermal continuous plate

The local characteristics of plate *C* are reported in Fig. 11 (*UH* heating mode, Ra $\approx 7 \times 10^5$). At intermediate and large S/H values (for which thermal interactions are limited to the colinear plates *A* and *C*) the heat transfer coefficient has a gradual decay along the vertical coordinate. For the smallest interplate spacing, the normalized heat transfer coefficient starts with a value well in excess of unity at small x/H (owing to the contraction of the flow passage area), and then drops sharply with increasing x/H because of interactions with plates *B*. In all cases, the previously observed rise near $x/H = 1$ is still present.

Comparisons With Natural Convection Reference System. For comparison purposes, the local heat transfer coefficients measured along the vertical sides of the discrete-plate array (*UH* heating mode) and those predicted along a vertical isothermal continuous plate (Ostrach, 1953) are reported in Fig. 12. The experimental data for the staggered plate array correspond to plate-to-ambient temperature differences ranging from 21.5 to 27 K (Ra $\approx 5 \times 10^5$–6×10^5) while the flat plate correlation is used for a 25 K temperature drop. Two values of the spacing parameter of the discrete-plate array are considered, namely $S/H = 0.3$ and 0.1. The vertical coordinate x starts at the leading edge of the lowest plate *A* for the discrete-plate array and at the leading edge of the continuous plate. Heat transfer augmentation provided by the discrete-plate arrangement (as compared with the continuous plate) is clearly shown, for both S/H values. In particular, the local heat transfer coefficient is enhanced at most by a factor of two near the leading edge of plate *B* (external side) and on average by 44 percent (plates *B*, $S/H = 0.3$), 27 percent (plates *B*, $S/H = 0.1$), 39 percent (plate *C*, $S/H = 0.3$), and 16 percent (plate *C*, $S/H = 0.1$). For the lowest interplate spacing ($S/H = 0.1$) the degree of enhancement is reduced, but the compactness of the heat exchanger is increased (the exchanger size is less than half as compared with the $S/H = 0.3$ case).

It is worthwhile also to compare the thermal characteristics of the discrete plate system (under *UH* heating conditions) with those predicted for a reference system, consisting of two parallel isothermal continuous plates, as depicted in Fig. 13. The comparison is performed in terms of overall heat transfer,

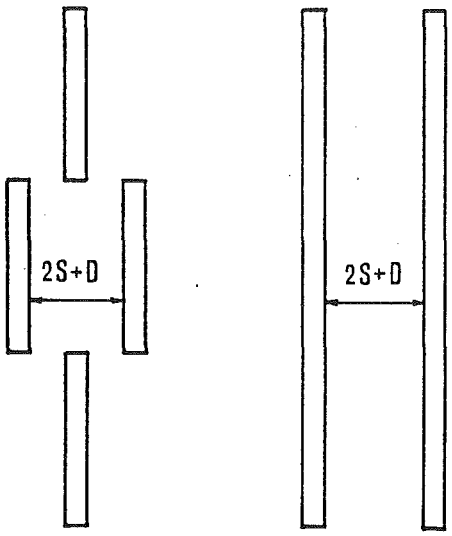

Fig. 13 Staggered discrete-plate and parallel continuous-plate exchangers; the volume of the two systems is constrained to be the same

keeping the exchanger size fixed (i.e., the volume $(2S + 3D) \cdot 3H$ is equal for both systems) and at the same mean plate-to-ambient temperature difference. Correlations for isothermal parallel plates (Elenbaas, 1942) and for isothermal flat plate (McAdams, 1954) are used for the inner and outer sides of the reference system. Under the constraint considered, the discrete-plate heat exchanger has 72 percent of the heat transfer surface area and 67 percent of the weight with respect to the continuous-plate heat exchanger. In the variation range of the mean plate-to-ambient temperature difference between 5 and 65 K (Ra values between 10^5 and 10^6) and for interplate spacing of the discrete-plate array corresponding to $S/H = 0.3$, the discrete-plate system provides 85–93 percent of the heat transfer exchanged by the continuous-plate system, despite the 28 percent reduction in heat transfer surface area. This result leads to an enhancement in the 18–30 percent range, in terms of specific heat flux. If the S/H parameter is reduced, the enhancement of the specific heat flux varies between 11 and 26 percent ($S/H = 0.2$) and between 3 and 18 percent ($S/H = 0.1$), in the same range of the plate-to-ambient temperature drop. It is apparent that the degradation of heat transfer occurring in the discrete-plate array with reducing the interplate spacing is more pronounced than that of the corresponding continuous-plate system. Besides, the enhancement obtained by the discrete-plate array increases with the temperature difference between plates and ambient air.

Concluding Remarks

Experiments were performed to investigate natural convection heat transfer for an array of four staggered vertical plates. Convective interactions among the plates were identified by examining the per-plate heat transfer coefficients and the local heat transfer coefficients along the vertical sides of plates. It was shown that the wakes generated by the lower plates can have an adverse effect on heat transfer from the upper plates. The extent of this effect was found to depend on the interplate spacing and on the Rayleigh number. At the lowest interplate distance, heat transfer performance of middle and upper plates was affected by changing the heating mode (from *UH* to *NUH*), with enhancement or degradation depending on the specific position in the array. In spite of convective interaction effects, it was observed that local heat transfer coefficients along the vertical sides of the staggered plates were markedly higher (up to a factor of two) than those of a corresponding continuous vertical plate. The staggered plate assembly, compared with a parallel plate channel having the same exchanger size, showed only little reductions in heat transfer rate, in a large field of the mean-to-ambient temperature difference, despite a 28 percent reduction in heat transfer area, with enhancements, in terms of specific heat flux, up to 30 percent.

References

Elenbaas, W., 1942, "Heat Dissipation of Parallel Plates by Free Convection," *Physica*, Vol. 9, pp. 1–28.

Guglielmini, G., Nannei, E., and Tanda, G., 1987, "Natural Convection and Radiation Heat Transfer From Staggered Vertical Fins," *International Journal of Heat and Mass Transfer*, Vol. 30, pp. 1941–1948.

Guglielmini, G., and Tanda, G., 1989, "Sulla Convezione Naturale da Superfici Alettate a Segmenti Rettangolari Sfalsati: Calcolo del Flusso Termico e Criterio di Dimensionamento," *Proceedings, VII U.I.T. (Italian Union of Thermo-fluid-dynamics) National Heat Transfer Conference*, pp. 203–214.

Kurosaki, Y., Kashiwagi, T., Kobayashi, H., Uzuhashi, H., and Tang, S.-C., 1988, "Experimental Study on Heat Transfer From Parallel Louvered Fins by Laser Holographic Interferometry," *Experimental Thermal and Fluid Science*, Vol. 1, pp. 59–67.

McAdams, W. H., 1954, *Heat Transmission*, McGraw-Hill, New York.

Moffat, R. J., 1988, "Describing the Uncertainties in Experimental Results," *Experimental Thermal and Fluid Science*, Vol. 1, pp. 3–17.

Naylor, D., Floryan, J. M., and Tarasuk, J. D., 1991, "A Numerical Study of Developing Free Convection Between Isothermal Vertical Plates," ASME JOURNAL OF HEAT TRANSFER, Vol. 113, pp. 620–626.

Ostrach, S., 1953, "An Analysis of Laminar Free-Convection Flow and Heat Transfer About a Flat Plate Parallel to the Direction of the Generating Body Force," National Advisory Committee for Aeronautics Report No. 1111.

Prakash, C., and Sparrow, E. M., 1980, "Natural Convection Heat Transfer Performance Evaluations for Discrete- (In-Line or Staggered) and Continuous-Plate Arrays," *Numerical Heat Transfer*, Vol. 3, pp. 89–105.

Ruffino, G., and Pisoni, C., 1976, "An Apparatus for Emissivity Measurements," *High Temperatures — High Pressures*, Vol. 8, pp. 419–424.

Sobel, N., Landis, F., and Mueller, W. K., 1966, "Natural Convection Heat Transfer in Short Vertical Channels Including the Effect of Stagger," *Proceedings, III International Heat Transfer Conference*, Vol. II, pp. 121–125.

Sparrow, E. M., and Faghri, M., 1980, "Natural Convection Heat Transfer From the Upper Plate of a Colinear, Separated Pair of Vertical Plates," ASME JOURNAL OF HEAT TRANSFER, Vol. 102, pp. 623–629.

Vasil'ev, L. A., 1971, *Schlieren Methods*, Keter Inc., New York.

Simulation of Transient Natural Convection Around an Enclosed Vertical Channel

W. Shyy

M. M. Rao

Department of Aerospace Engineering, Mechanics, and Engineering Science, University of Florida, Gainesville, FL 32611

Accurate numerical calculations have been conducted for buoyancy-driven two-dimensional flow of air between two vertical parallel isothermal plates, of aspect ratio 1, placed inside a rectangular enclosure. The Grashof number based on the channel half width is 10^5. Insights have been obtained regarding the structure of the transient flow and thermal fields in a configuration of particular interest to electronics cooling. In the early stages of the transient the flowfield was found to be highly vortical and the net volume flow rate in the channel displayed an oscillatory behavior, periodically reversing its direction. However, the velocity profile adjacent to the heated plates maintained the same direction throughout the process, and hence the Nusselt number was relatively insensitive to the periodic flow reversal in the channel. Detailed studies of the transient flow field and the heat transfer results are presented.

1 Introduction

Buoyancy-induced flows play an important role in many engineering applications, such as thermal control of electronic devices, emergency cooling of nuclear reactors, solar collection systems, etc. This is mostly due to the inherent reliability, simplicity, and cost effectiveness associated with natural convection heat transfer. In the literature, two generic problem types have been extensively investigated: the enclosure and the open cavity. Flows within enclosures are bounded on all sides by walls, whereas open cavities, such as vertical parallel plate channels or tubes, have their ends open to the ambient. An extensive discussion of important heat transfer results pertaining to such configurations has been presented by Raithby and Hollands (1985), Gebhart et al. (1988), and Peterson and Ortega (1990).

The first experimental investigation of natural convection of air in isothermal, parallel-plate channels was carried out by Elenbaas (1942). By analyzing a simplified set of equations, and fitting experimental results, a correlation for the Nusselt number was obtained against Ra^* where $Ra^* = Ra\, d/L$ is the Elenbaas Rayleigh number, Ra is the Rayleigh number based on channel half width, d is the half-width of the channel, and L is its height. The experiments spanned the range $0.1 < Ra^* < 10^5$. Subsequent investigations by Sparrow and Bahrami (1980) showed inaccuracies in the data of Elenbaas at low values of Ra^* and they observed that the corrections employed by Elenbaas for extraneous heat losses, like radiation, exceeded the actual natural convection heat transfer; they and Martin et al. (1991) have improved Elenbaas's correlation for the isothermal parallel plate channel.

Isothermal, asymmetrically heated, vertical parallel-plate channels have been investigated by Sparrow et al. (1984). In this study, one wall was isothermal while the other was unheated. The experiments, carried out in water, with Pr = 5, revealed a pocket of recirculating flow adjacent to the unheated wall, close to the downstream end of the channel. In spite of this recirculating zone, the Nusselt number correlated well with the parameter $(2d/L)$ Ra where $2d$ is the interwall spacing. They also complemented the experimental results with numerical solutions based on parabolic equations, derived by neglecting the streamwise second derivatives. Thus, they concluded that the Nusselt number is relatively insensitive to the backflow. Sparrow and Azevedo (1985) followed up this study by investigations over a greater range of interwall spacing. They were able to obtain a correlation for the Nusselt number against $(2d/L)$ Ra over a wide range spanning the fully developed limit and the flat plate limit. They found that the flat plate limit does not form an upper bound on the heat transfer results. They also concluded that the Nusselt number is insensitive to three-dimensional effects.

Experiments have also been performed for iso-heat-flux plates by Wirth and Stutzman (1982) for the symmetrically heated case and by Webb and Hill (1989) for the asymmetrically heated plates. Correlations were presented for the average Nusselt number, local Nusselt number, and the maximum temperature on the plates, as a function of the Rayleigh number. The results were in reasonable agreement with the previous numerical work of Aung (1972), for the limit of fully developed flow, and Aung et al. (1972) for developing flow.

Theoretical investigation of free convection between parallel plates was first undertaken by Bodoia and Osterle (1962). They solved the finite difference form of the parabolic equations, and obtained good agreement with the data of Elenbaas except at low values of the Grashof number, which they attributed to side leakage effects. However, they confined their analysis to the slot region, neglecting the effects of inflow and outflow boundaries.

In order to resolve the flow profile at the inlet, Kettleborough (1972) solved the laminar, two-dimensional Boussinesq equations for air with Pr = 0.7, Gr = 12.5, 1250, and on a domain with an aspect ratio AR of 5 that included an upstream entrance region. He, however, imposed fully developed conditions at the channel exit, which is a restrictive assumption. A similar analysis was carried out by Nakamura et al. (1982) with the difference that the wall boundary condition for the streamfunction was obtained by consideration of the pressure drop along the channel wall. Their results were significantly different from those of Kettleborough, especially at higher Grashof number. Also, they could not capture the reverse flow region predicted by Kettleborough.

Chang and Lin (1989) performed a transient analysis, which ultimately ended in steady state. Calculations were carried out for Pr = 0.7, $10^3 < Ra < 10^6$, and AR = 5, 10. The inlet and exit domains were considered in the analysis. However, they replaced the 180 deg turn at the slot inlet and exit with

Contributed by the Heat Transfer Division for publication in the JOURNAL OF HEAT TRANSFER. Manuscript received by the Heat Transfer Division April 1992; revision received April 1993. Keywords: Enclosure Flows, Natural Convection, Transient and Unsteady Heat Transfer. Associate Technical Editor: J. R. Lloyd.

an artificial 90 deg adiabatic corner. They presented the time evolution of the flow and thermal fields and also a correlation for the Nusselt number as a function of the Rayleigh number and the channel aspect ratio, for air. At the free surfaces they prescribed the following boundary conditions: normal gradient of all velocities were zero at the free surfaces, normal gradient of temperature was zero if, locally, the fluid flowed out of the domain, otherwise, the temperature was set equal to the ambient temperature.

Naylor et al. (1991) have solved the steady two-dimensional Navier–Stokes equations with consideration of the inlet domain. They also replaced the 180 deg turn at the inlet and outlet with an artificial 90 deg adiabatic corner. The inflow boundary was a semicircle and the boundary conditions were obtained from considerations of Jeffrey–Hamel flow, which is a similarity solution of isothermal flow due to a sink at the point of intersection of two walls. Fully developed flow conditions were imposed at the slot exit. They also, for comparison purposes, solved the parabolic equations. Their solutions are in closer qualitative agreement with those of Nakamura et al. (1982) than with Kettleborough (1972), but the overall quantitative agreement with either is quite poor. Reverse flow predicted by Kettleborough was not obtained.

Shyy et al. (1992) carried out calculations modeling both the inflow and the outflow domains. The inflow domain had an upstream boundary condition amounting to that generated by a virtual line mass source located at the centerline of the inlet, and whose side boundaries were modeled by side entrainment boundary conditions. For the outflow region, the downstream boundary corresponded to the plume solution generated by a virtual line heat source located at the inlet centerline. The source/sink strengths were determined by matching the total convective energy transported across each boundary with the thermal energy conducted from the plates to the fluid. For the side entrainment boundaries, the normal derivatives of the velocity components were set to zero and the normal derivative of the temperature was set to zero, if the fluid flowed out of the domain; otherwise, the temperature was set equal to the ambient temperature. Calculations were carried out for Gr = 10^3, 10^4, 10^5 and for AR = 1, 2. For channel aspect ratio of unity, and at the Grashof numbers studied, a recirculation zone was observed in the slot.

Ramanathan and Kumar (1991) tried to circumvent the problem of artificial outflow and inflow boundary conditions by putting the slot within a large, isothermal enclosure. Iso-heat-flux boundary conditions were applied to the side of the heated plates facing the interior of the channel. The sides facing the enclosure were insulated. The problem is difficult to solve parametrically; apart from the usual Ra, Pr, and channel AR, there are five more geometric parameters. They found that their results were sensitive to the relative location of the slot in the vertical direction. In order to extrapolate their results to the limit of infinitely large enclosures, the temperatures within the slot were offset by the entry temperature at the inlet centerline. The steady two-dimensional Navier–Stokes equations, incorporating the Boussinesq approximation, were employed for the computations. They obtained good agreement with the experimental results of Wirth and Stutzman (1982) for Ra = 18.8, 191, 2414. Correlations were presented for maximum temperature on the plates and for the average Nusselt number against the Rayleigh number and channel aspect ratio, for air. They also found that for fluids with Pr > 0.7, the hydrodynamic development length is smaller than the thermal development length up to Ra = 400 and for Pr < 0.1, the opposite holds. They concluded that vertical diffusion of energy cannot be neglected, especially for low Pr and short AR channels.

Thus it is seen that various investigators, in an attempt to compute natural convection heat transfer between two vertical plates, have formulated various boundary conditions to deal with the artificial boundaries of a finite computational domain. The results are also as varied. The heat transfer results seem to correlate well with parameters obtained by neglecting streamwise diffusion, yet, in terms of the velocity field, recirculating flows have been found within the slot, which is incompatible with the boundary layer assumption. Attempts have been made to solve the full elliptic equations with the fully developed boundary conditions at the channel exit, which is

Nomenclature

L = channel height
d = channel half width
X_{max}, Y_{max} = enclosure dimensions
L_1, L_2 = horizontal and vertical location of the heated plate, respectively
AR = channel aspect ratio = $L/2d$
τ = physical time
x, y = nondimensional Cartesian coordinate
X,Y = physical Cartesian coordinate
U, V = dimensional velocities
u, v = nondimensional velocities
P_s = dimensional static pressure
P_m = dimensional motion pressure
Θ = dimensional temperature
Θ_c = enclosure side-wall temperature
Θ_p = channel wall temperature
g = acceleration due to gravity
ρ = density
μ = dynamic viscosity
k = thermal conductivity
C_p = heat capacity
β = thermal expansion coefficient
α = thermal diffusivity = $k/\rho\, C_p$
L_r = reference length = d
U_r = reference velocity = a/d
τ_r = reference time = d^2/a
P_r = reference pressure = ρU_r^2
t = nondimensional time = τ/τ_r
x, y = nondimensional coordinates
p = nondimensional motion pressure
T = dimensionless temperature = $(\Theta - \Theta_c)/(\Theta_p - \Theta_c)$
Pr = Prandtl number = ν/α
Gr = Grashof number = $g\beta d^3(\Theta_p - \Theta_c)/\nu^2$
Ra = Rayleigh number = Gr Pr
Q = dimensionless volume flow rate
Nu_p = Nusselt number – dimensionless heat transfer coefficient from channel wall to the fluid
Nu_c = dimensionless heat transfer coefficient from fluid to enclosure wall
Nu^+ = local heat transfer coefficient on side of plate facing channel interior
Nu^- = local heat transfer coefficient on side of plate facing enclosure
Nu = local heat transfer coefficient on enclosure wall

Subscripts

p, c = for quantities located on hot plates and cold enclosure walls, respectively

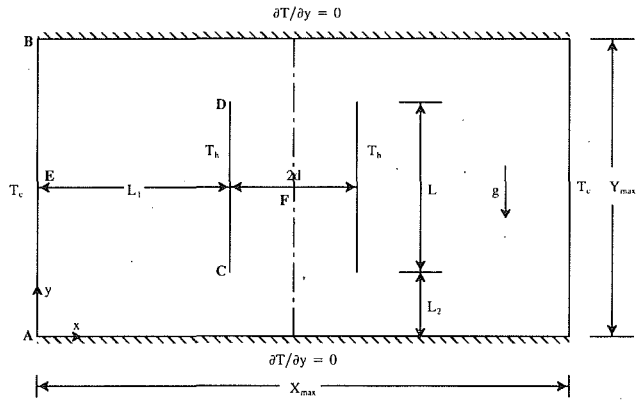

Fig. 1 Schematic of present problem with a heated vertical channel inside a cold rectangular enclosure. The hatched lines indicate adiabatic walls. The domain is symmetric about the vertical centerline. The side walls of the enclosure and the channel walls are isothermal. The letters A, B indicate the vertical extent of the enclosure wall. Similarly, the letters C, D designate the vertical extent of the channel wall.

restrictive and has been found unsatisfactory by other investigators.

Despite the fact that most investigators have dealt with the flow between two parallel plates in an open domain, yet many practical applications, especially in the electronics industry, have geometric configurations similar to the one in this study, as shown in Fig. 1. For example, as discussed by Gingrich et al. (1992), an electronics cooling cabinet often adopts such a generic design where hot plates are placed in the middle of the enclosing cabinet. Such geometries, however, involve several independent geometric parameters and it may not be feasible to conduct parametric investigations over the entire range of possible values, especially if the transient effects are of interest. Recently, interest has arisen in the use of non-Newtonian fluids in electronics cooling applications (Gingrich et al., 1992), which, however, is outside the scope of the current study.

A discussion of the present contribution relative to the previous efforts is in order. In Shyy et al. (1992), not only were the computations conducted for an open channel, but most importantly, there was a major issue in terms of prescribing the boundary conditions for that configuration. As discussed in that paper, there is a fundamental difficulty in determining the overall incoming and outgoing mass fluxes and their distributions, for an open channel flow, unless some simplifications are made in the problem formulation. That is the rationale behind deriving the line-source and the plume solutions for the inlet and outlet conditions respectively. A detailed account of this issue can be found in Shyy et al. (1992). There is a need to understand the way of extending the theoretical framework from a confined enclosure to that of an open domain, and the correct approach has yet to be identified. The configuration chosen here represents a more realistic case in the area of electronics cooling. Furthermore, the present work is a simulation of transient heat transfer, whereas the work of Shyy et al. (1992) is a steady-state formulation.

The current study consists of two isothermal vertical parallel plates placed within a rectangular enclosure. The top and bottom walls of the enclosure are insulated, whereas the side walls are isothermal, as shown in Fig. 1. The geometric parameters are held constant and have the values $X_{max}/2d = 4$, $Y_{max}/2d = 3$, $L_1/2d = 1.5$ and $L_2/2d = 1$. Initially there is no convection and uniform temperature prevails. At time $t = 0$, the plates experience a step change in the temperature. A Grashof number of 10^5, typical of electronic devices, is considered in our work. The present study attempts to accurately capture the detailed flow and thermal structures of the transient, two-dimensional buoyancy-induced flowfield and associated heat transfer results. Thus, care has been taken to ensure adequate numerical accuracy in both time and space. Also reasonable for the Navier–Stokes flow fields is the Boussinesq approximation, which has been employed here. The main motivation of the work is to utilize a set of accurate transient simulations to facilitate a detailed scrutiny of the development of the flow and heat transfer characteristics, yielding improved insights in important practical problems.

2 Formulation and Solution Procedure

The nondimensionalized, unsteady, two-dimensional, Navier–Stokes equations incorporating the Boussinesq approximation can be written as:

Continuity:

$$\frac{\partial u}{\partial x}+\frac{\partial v}{\partial y}=0 \tag{1}$$

x-Momentum:

$$\frac{\partial u}{\partial t}+\frac{\partial u^2}{\partial x}+\frac{\partial uv}{\partial y}=-\frac{\partial p}{\partial x}+\mathrm{Pr}\left(\frac{\partial^2 u}{\partial x^2}+\frac{\partial^2 u}{\partial y^2}\right) \tag{2}$$

y-Momentum:

$$\frac{\partial v}{\partial t}+\frac{\partial uv}{\partial x}+\frac{\partial v^2}{\partial y}=-\frac{\partial p}{\partial y}+\mathrm{Pr}\left(\frac{\partial^2 v}{\partial x^2}+\frac{\partial^2 v}{\partial y^2}\right)+\mathrm{Ra}\ \mathrm{Pr}\ T \tag{3}$$

Energy:

$$\frac{\partial T}{\partial t}+\frac{\partial uT}{\partial x}+\frac{\partial vT}{\partial y}=\frac{\partial^2 T}{\partial x^2}+\frac{\partial^2 T}{\partial y^2} \tag{4}$$

The dimensionless variables are defined as: $t = \tau/\tau_r$, $x = X/d$, $y = Y/d$, $u = U/U_r$, $v = V/V_r$, and $T = (\Theta - \Theta_c)/(\Theta_p - \Theta_c)$, where the reference scales are d, the half channel width, the velocity scale $U_r = \alpha/d$, α is the thermal diffusivity, and the time scale $\tau_r = d^2/\alpha$. The Boussinesq approximation involves the assumption that density variations are small enough to be neglected everywhere except in the buoyancy source term in the y-momentum equation. All other fluid properties such as viscosity, thermal conductivity, and specific heat are assumed constant.

The solution methodology involved the use of the second-order central differences for discretization of all spatial derivatives, including the convection terms, and the first-order, implicit, backward Euler scheme for the time derivatives. The resulting algebraic equations were iterated until a desired accuracy was achieved. The SIMPLE algorithm (Patankar, 1980), which is a semi-implicit pressure correction based approach, was used for the iteration procedure at each time step. The following quantities were monitored at each time step: (*i*) heat flux from the heated plates, (*ii*) heat flux out of the enclosure wall, and (*iii*) volume flux through the channel. These quantities were nondimensionalized as:

$$\mathrm{Nu}_c=\frac{d}{2L}\int_{L_2/d}^{(L_2+L)/d}\left[\left.\frac{\partial T}{\partial x}\right|_{x=xp_+}+\left.\frac{\partial T}{\partial x}\right|_{x=xp_-}\right]dy \tag{5}$$

where $xp = L_1/d$ is the nondimensional x location of the heated plate under consideration

$$\mathrm{Nu}_c=\frac{d}{Y_{\max}}\int_0^{Y_{\max}/d}\left.\frac{\partial T}{\partial x}\right|_{x=0}dy \tag{6}$$

where $x = 0$ defines the cold enclosure wall, and

$$Q=\int_{L_1/d}^{(L_1+L)/d} v|_{y=y_k}\,dx, \qquad L_2/d\le y_k\le (L_2+L)/d \tag{7}$$

where y_k is any y location within the channel region.

The temperature gradients at the walls were evaluated by one-sided finite differences at the walls. The integrals were evaluated by assuming a piecewise constant distribution of the dependent variables within each control volume, which is con-

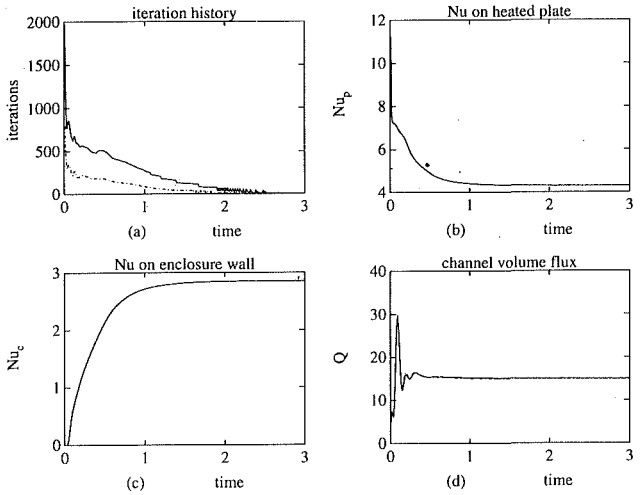

Fig. 2 Comparison of calculations on the 61 × 61 grid versus the 91 × 91 grid. $\Delta t = 10^{-2}$ for both cases. (*a*) Number of iterations for convergence at each time step. (*b*) Nusselt number, Nu_p, based on heat flux through channel wall. (*c*) Nusselt number, Nu_c, based on heat flux through enclosure wall. (*d*) Nondimensional volume flux through channel, *Q*. Key: ———91 × 91 grid. - - - - - 61 × 61 grid.

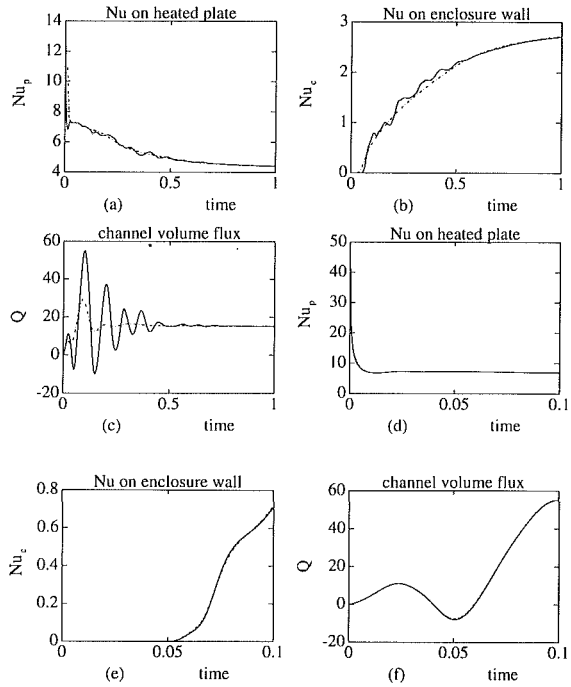

Fig. 3 Comparison of calculations with (*a*)-(*c*) $\Delta t = 10^{-2}$ and $\Delta t = 10^{-4}$ on the 91 × 91 grid. Key: ———$\Delta t = 10^{-4}$, - - - - - $\Delta t = 10^{-2}$. (*a*) Nusselt number, Nu_p, based on heat flux through channel wall. (*b*) Nusselt number, Nu_c, based on heat flux through enclosure wall. (*c*) Nondimensional volume flux through channel, *Q*; and with (*d*)-(*f*) $\Delta t = 10^{-4}$ and $\Delta t = 10^{-5}$ on the 91 × 91 grid. Key: ———$\Delta t = 10^{-5}$, - - - - - $\Delta t = 10^{-4}$. (*d*) Nusselt number, Nu_p, based on heat flux through channel wall. (*e*) Nusselt number, Nu_c, based on heat flux through enclosure wall. (*f*) Nondimensional volume flux through channel *Q*.

sistent with the discretization procedure. The heat flux distribution on the isothermal walls can be described as a local Nusselt number:

$$\mathrm{Nu}^+ = \left.\frac{\partial T(y)}{\partial x}\right|_{x=xp^+} \qquad \mathrm{Nu}^- = \left.\frac{\partial T(y)}{\partial x}\right|_{x=xp^-}$$

$$\mathrm{Nu} = \left.\frac{\partial T(y)}{\partial x}\right|_{x=0^+} \tag{8}$$

where xp is the x location of the heated plate, and $x = 0$ defines the cold enclosure wall. Calculations were carried out for a Grashof number, $\mathrm{Gr} = 10^5$, and channel aspect ratio, $AR = 1$. Other geometric parameters were also held constant.

Although some of the more elaborate techniques in discretization schemes, gridding and solver, such as those discussed in Shyy (1993), are not employed, a systematic effort is made to ensure that the solutions presented are grid independent in time as well as in space. Initial computations were carried out on a coarse grid of 60 × 60 control volumes and a fine grid of 90 × 90 control volumes, with a time step (nondimensional) $\Delta t = 10^{-2}$. The grid spacing was adjusted by a cubic polynomial, with the grid spacing specified at the two ends. The coarse grid had 30 control volumes between the enclosure wall and the channel wall, in the x direction, with $\Delta X/2d = 10^{-3}$ at the channel wall and 10^{-2} at the enclosure wall and 30 control volumes between the channel wall and the channel centerline. In the y direction, there were 15 control volumes between the bottom enclosure wall and the channel inlet, 20 control volumes in the channel region, and 25 control volumes between the channel outlet and the enclosure top wall. The grid spacing was $\Delta Y/2d = 10^{-3}$ at the channel inlet and outlet and 10^{-2} at the enclosure wall. The corresponding parameters for the fine grid were $\Delta X/2d = 5 \times 10^{-4}$ at the channel wall and 5×10^{-3} at the enclosure wall, with 50 control volumes in the x direction between the enclosure side walls and the channel walls, and 40 control volumes between the channel wall and the channel centerline. In the y direction, the parameters were $\Delta Y/2d = 5 \times 10^{-4}$ at the channel inlet and outlet, and 5×10^{-3} at the enclosure top and bottom walls. There were 20 control volumes in the region between the bottom enclosure wall and the channel inlet, 30 control volumes in the channel region, and 40 control volumes in the region between the channel outlet and the top enclosure wall. Symmetry boundary conditions:

$$u = 0, \qquad \frac{\partial v}{\partial x} = 0, \qquad \frac{\partial T}{\partial x} = 0 \tag{9}$$

were applied at the channel centerline and the calculations were carried out for half the domain, thereby achieving good spatial resolution along with economy of storage and CPU time. At each time step, the algebraic equations were iterated until the normalized residuals obtained by summing, over the whole domain, the absolute values of the mass, momentum, and energy flux imbalances within each cell, were within 10^{-3}.

3 Results and Discussion

Initially, a time step, $\Delta t = 10^{-2}$ was chosen and the calculations advanced up to 300 time steps. At that point, the calculations converged in less than three iterations per time step. At that time instant, the heat balance within the domain was within 0.6 percent for the coarse grid and 0.4 percent for the fine grid, yielding a difference of less than 0.2 percent between the two solutions. The iterative calculation procedure at a given time step was terminated when the normalized residual, for each dependent variable, was less than 10^{-3}. The residual for any given dependent variable is computed by summing over the absolute values of the relevant flux imbalances in each control volume over the entire computational domain. The residuals are then normalized with respect to characteristic quantities obtained from the reference scales defined in section 2. For example, the mass imbalance in the domain is nondimensionalized with respect to the total mass in the enclosure. From Fig. 2 it can be observed that the above comparisons hold true over the entire time history. It was clear that grid independence had been achieved. However, to maintain adequate computational accuracy, the *fine* grid was used for all further calculations.

To verify the time step dependence of the solution, a com-

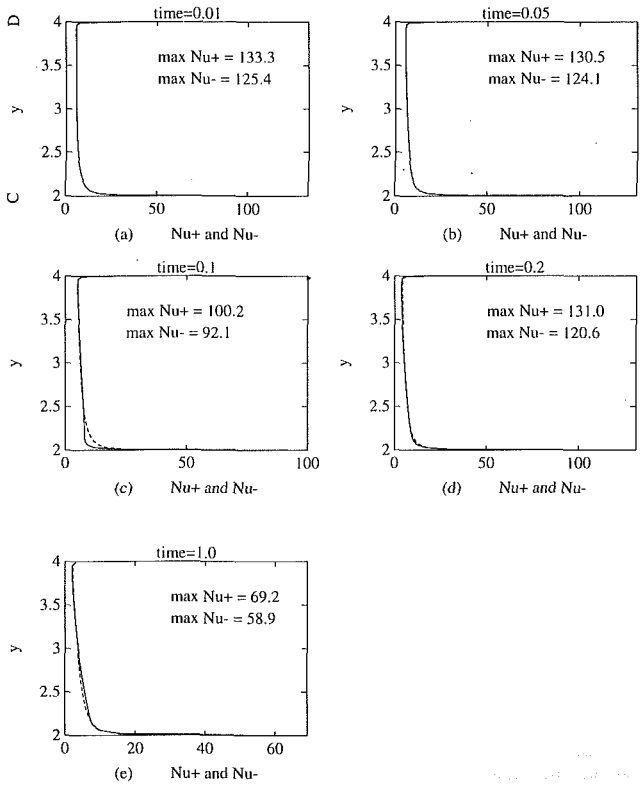

Fig. 4 Time evolution of Nusselt number distribution on the inner (Nu^+) and outer (Nu^-) channel wall as defined in Eq. (8). The letters C and D designate the channel wall at $2d \le Y \le 4d$, $X = 1.5d$, as shown in Fig. 1. Key: ——— Nu^+, based on heat flux to channel interior; - - - - - Nu^-, based on heat flux to the open side.

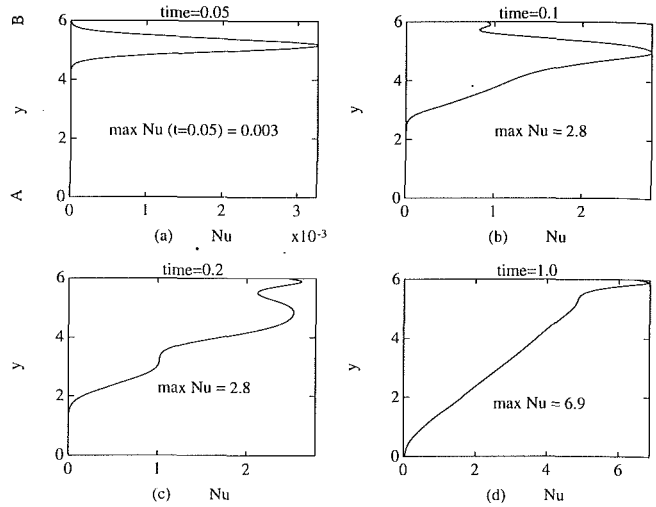

Fig. 5 Time evolution of the Nusselt number distribution on the enclosure wall, Nu as defined in Eq. (8). The letters A and B refer to the vertical extent of the enclosure wall at $0 \le Y \le 6d$, $X = 0$, as shown in Fig. 1.

putation was conducted for $\Delta t = 10^{-4}$ and marched up to 10^4 time steps. Figure 3 summarizes some of the key findings in terms of the monitored quantities. At time $t = 1.0$, the differences between the two solutions are within 0.2 percent for the heat flux from the heated plates, 0.3 percent for the heat flux out of the enclosure walls, and 0.1 percent for the volume flux through the channel. However, at intermediate time, i.e., $0.01 < t < 0.6$, there are significant differences between the solutions. For the Nusselt number based on heat flux from the channel wall, Nu_p, the differences are negligible throughout the time history, but for the Nusselt number based on heat flux out of the enclosure walls, Nu_c, there are noticeable quantitative and qualitative differences. For the volume flux, Q, the solutions corresponding to each of the two time steps are profoundly different. The solution corresponding to $\Delta t = 10^{-2}$ shows a highly damped oscillatory trend, extending up to $t \sim 0.3$, but does not show net mass flow reversal through the channel. But the solution corresponding to $\Delta t = 10^{-4}$ shows oscillations of much larger amplitude showing net mass flow reversal through the channel. The amplitude reaches a maximum at about $t \sim 0.1$ and the oscillations are damped to their steady-state value at about $t \sim 0.6$. The peak-to-peak average also displays an oscillatory tendency. The solutions also differ in phase. As an explanation, it is recalled that the backward Euler is first order in time and prone to numerical damping. As a check on the solution accuracy, a computation was initiated with $\Delta t = 10^{-4}$ and advanced to 10^4 time steps. Figure 3 shows no discernible differences in the solutions corresponding to $\Delta t = 10^{-4}$ and $\Delta t = 10^{-5}$, indicating that the solution is independent of the value of Δt.

It is noted that the solution corresponding to $\Delta t = 10^{-4}$ was marched up to 10^4 time steps, i.e., $t = 1.0$. From a comparison with the steady-state solution obtained with $\Delta t = 10^{-2}$, it is seen that steady state cannot be achieved at $t = 1.0$. But the differences, in terms of the monitored quantities are quite small, less than 2.6 percent for Nu_p, 5 percent for Nu_c, and 1 percent for Q. The fine time step calculations are expensive in terms of computer time. The solution corresponding to $\Delta t = 10^{-4}$ and 10^4 time steps took about 1.5 *days* of CPU time on a DEC station 5000. Since the steady-state solution can be obtained by using $\Delta t = 10^{-2}$ or higher, the calculations were terminated at this stage. All further discussion applies to the transient solution corresponding to $\Delta t = 10^{-4}$.

Figure 4 shows the distribution of the local Nusselt number on the heated channel walls. The solid line shows the Nusselt number, Nu^+, based on the heat flux from the plates to the interior of the channel and the broken line the Nusselt number, Nu^-, based on the heat flux from the heated plates to the exterior of the channel. The quantities Nu^+ and Nu^- are defined in Eq. (8). These are established early in time and do not vary significantly thereafter. Notably, these are relatively insensitive to the oscillations in the net volume flux through the channel, Q, as will be discussed later in connection with the detailed analysis of the flow and thermal structures in the slot.

Figure 5 shows the local Nusselt number distribution, Nu, as defined in Eq. (8), on the enclosure walls. Initially, there is a spikelike distribution established near the top, as the heated fluid reaches that location. Gradually, it broadens as the convection field develops and increases in magnitude and at large time, it has a triangular distribution resulting from the fact that the convection field moves toward the top part of the enclosure side-wall and moves away from its bottom part.

Figure 6 shows the streamlines, isotherms, and contours of motion pressure at $t = 0.01$, 0.05, 0.1, 0.15, 0.2, and 1.0. Physically, at the early stages of the transient process, heat transfer from the heated plates to the fluid amounts to a conduction process (Gebhart et al., 1988); buoyancy-induced motion arises, but convective effects on the heat transfer process are absent. This phenomenon is, however, present only for a short time during the startup of the transient. At any location, the conduction effect ends with the arrival of the leading edge effect. Thereafter, the process is multidimensional and the transient process continues toward a steady state. Thus it is evident, from the streamlines and the isotherms, that time $t = 0.01$ depicts the end of the one-dimensional conduction process. The flow adjacent to the channel walls consists of a thin layer of heated fluid moving upward and has a structure qualitatively similar to a buoyancy-driven boundary layer on a single isothermal vertical flat plate as can be observed from

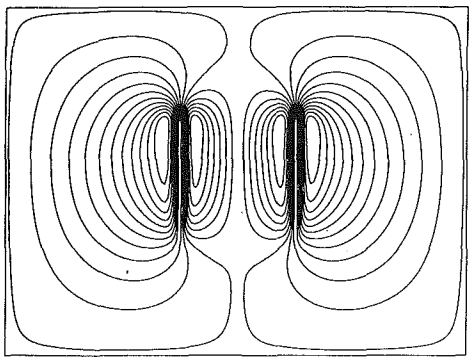

(a) streamlines. min: -12.13 max: 21.15 int: 1.664

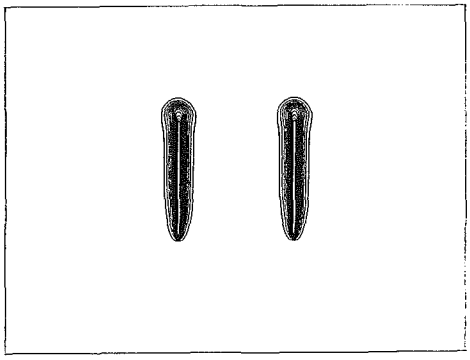

(b) isotherms. min: 0.0 max: 0.997183 ΔT: 0.0665

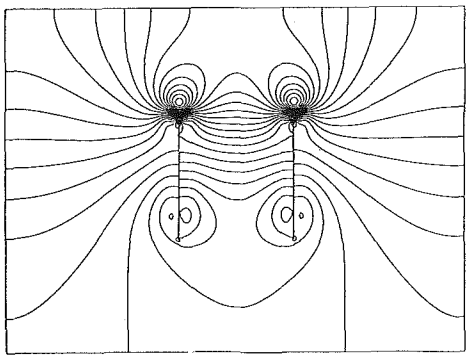

(c) isobars. Δp: 421

Fig. 6(i) $t = 0.01$

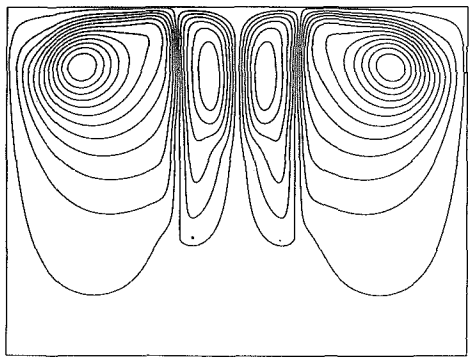

(a) streamlines. min: -63.55 max: 113.5 int: 8.85

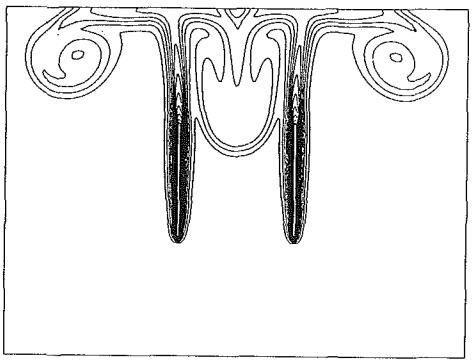

(b) isotherms. min: 0.0 max: 0.997255 ΔT: 0.0665

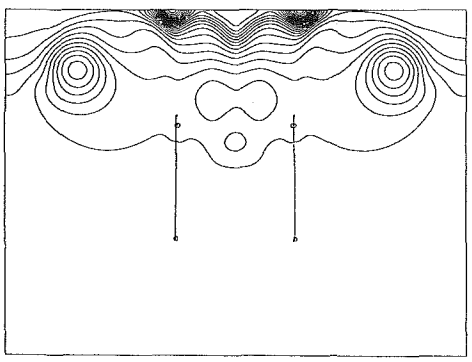

(c) isobars: Δp: 2339

Fig. 6(ii) $t = 0.05$

the v-velocity profiles across the middle of the channel, depicted in Fig. 7. It is evident from Fig. 7 that in the course of the transient evolution while the v-velocity reverses in sign in the regions away from the heated plates, adjacent to the plates it exhibits only modest variations in magnitude and maintains its direction. Thus the flow structure near the channel walls is qualitatively insensitive to the flow in the rest of the channel. This particular flow feature, established early in the transient stages, persists till steady state, and shields the wall heat transfer process from the effects of the flow in the central region of the channel. This explains the relative insensitivity of the plate Nusselt number to the oscillating volume flux within the slot. At $t = 0.05$ large vortical structures can be seen both inside and outside the slot. The net volume flow rate in the channel, Q, is in the negative y direction. The isotherms show distorted shapes corresponding to the convection field in the vicinity of the recirculating flow structures.

At $t = 0.1$ there are many pockets of recirculating flow close to the enclosure walls and near its top. The net volume flux, Q, is directed upward and attains its global maximum value. It is noted that vorticity generation occurs in the flow field as explained by the fact that the equation of vorticity transport has a source term proportional to $\partial T/\partial x$, the physical origin of which lies in the baroclinicity of the flowfield. The isotherms in the channel show a strong tendency to become horizontal and the temperature increases in the positive y direction.

At $t = 0.15$, there is a net downward volume flux, Q, in the channel. Many recirculating flow structures persist, although the tendency to decay by viscous action is evident. The isotherms in the center of the slot are horizontal and increasing in the positive y direction. It is observed that the motion pressure contours are normal to the plates and to the sidewalls of the enclosure, i.e., $\partial P/\partial x$ is negligible in the slot and near the sidewalls of the enclosure. At $t = 0.2$, the net volume flux is upward, and attains a local maximum, but the other trends described for the previous case continue. At $t = 1.0$ the solution approaches the steady-state solution. At this time, viscous action results in the decay of several of the vortices and many of the recirculating flow structures coalesce. There are two counterrotating vortices near the top wall of the enclosure and these extend downward into the slot region. It is also noted that the motion pressure variation in the x direction is negligible.

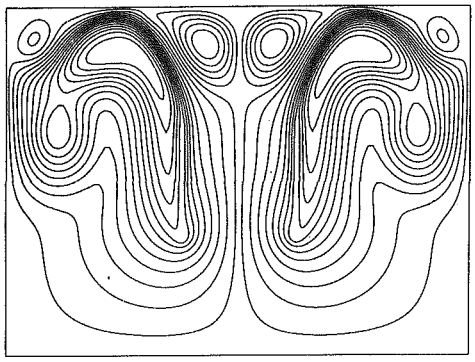

(a) streamlines. min: -37.92 max: 90.25 int: 6.41

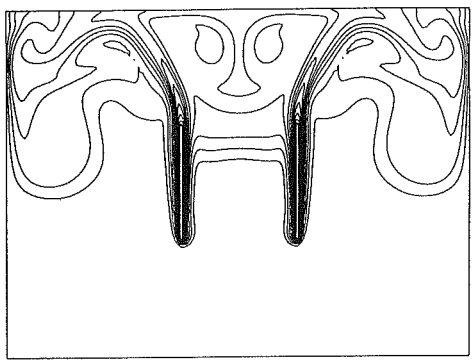

(b) isotherms. min: -0.00182 max: 0.997488 ΔT: 0.0665

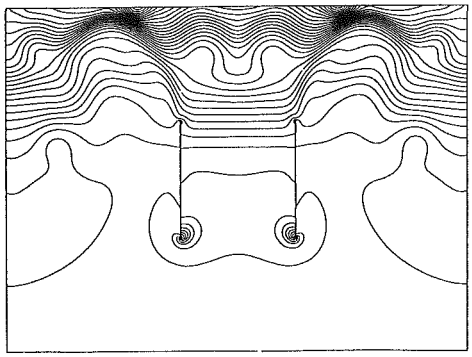

(c) isobars. Δp: 1564

Fig. 6(iii) t = 0.1

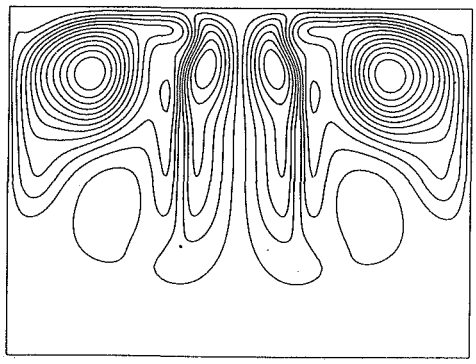

(a) streamlines. min: -52.53 max: 99.1 int: 7.58

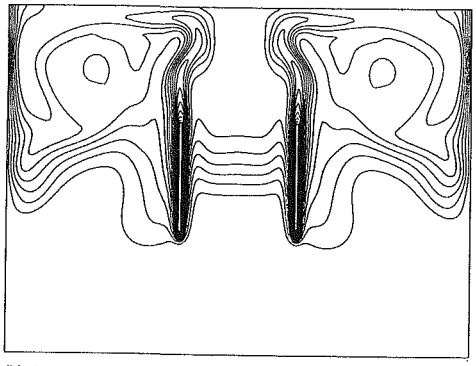

(b) isotherms. min: 0.0 max: 0.99786 ΔT: 0.0499

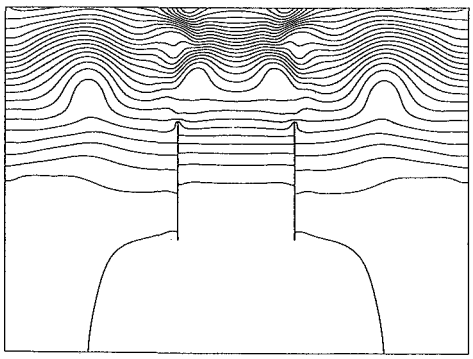

(c) isobars: Δp: 2090

Fig. 6(iv) t = 0.15

A qualitative comparison of the current results can be made against the results of Chang and Lin (1989). They have presented detailed studies of the flow and thermal structures for the case of Pr = 0.7, Ra = 10^4, AR = 5. A monotonic variation of the flow characteristics up to steady state, especially the recirculating cells in the early stages of the transient, was obtained, as opposed to the current results, where an oscillatory volume flux decaying to steady state can be observed. However, in the heat transfer results, notably the Nusselt number, they recorded an undershoot in the time evolution of the Nusselt number. In the current calculations, the Nusselt number decays monotonically to steady state and no undershoot can be observed. Also, Chang and Lin (1989) did not obtain recirculating flow in the channel at steady state, probably due to the higher aspect ratio channel used in their calculations. The recirculating flow observed at steady state, in the present case, is qualitatively consistent with the results obtained by Shyy et al. (1992) for their case of Pr = 0.71, Gr = 10^5, AR = 1. Low Ra cases have been presented by Ramanathan and Kumar (1991), where no backflow was found. They have also presented a case for Ra = 10^5, for which they have not presented the complete details of the flow and thermal fields. However, they show that the temperature distribution along the channel walls were qualitatively consistent with the similarity solution of Sparrow and Gregg (1956). This agreement with a theoretical prediction based on the parabolic equations implies the absence of recirculating flow in the channel, in their case.

4 Conclusions

Calculations have been conducted for transient natural convection around a vertical isothermally heated, two-dimensional channel placed inside a rectangular enclosure, for the case of Prandtl number 0.71, Grashof number 10^5, and channel aspect ratio of 1. We have presented a systematic assessment to substantiate the numerical accuracy of the solutions, subject to the Boussinesq approximation. Steady state was obtained. The results show several interesting features such as an oscillating volume flux in the channel preceding decay to the steady state, back flow in the central region of the channel even at steady state, and most importantly, insensitivity of the heat transfer results to the presence of the periodic reversal of flow in the channel during the transient stage. The latter is due to the shielding effect of a thin layer of upward moving heated fluid,

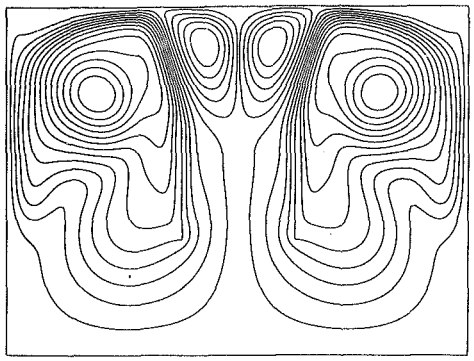

(a) streamlines. min: -41.49 max: 107.1 int: 7.43

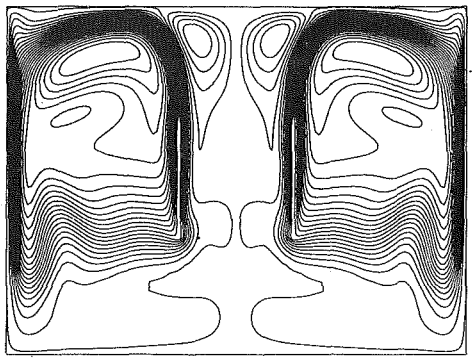

(a) streamlines. min: -8.49 max: 41.64 int: 1.671

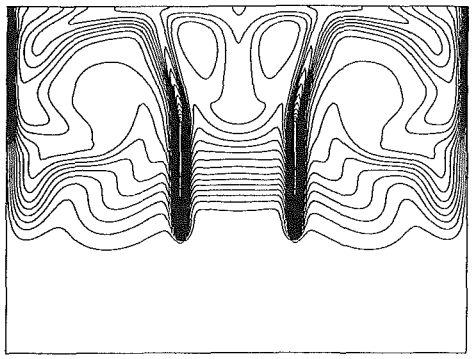

(b) isotherms. min: 0.0 max: 0.998157 ΔT: 0.0333

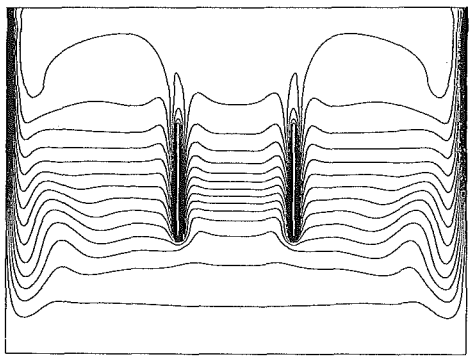

(b) isotherms. min: 0.0 max: 0.998983 ΔT: 0.0499

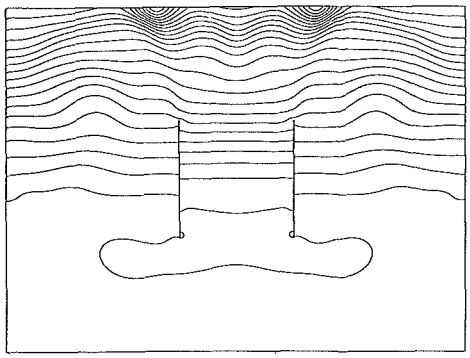

(c) isobars. Δp: 3229

Fig. 6(v) $t = 0.2$

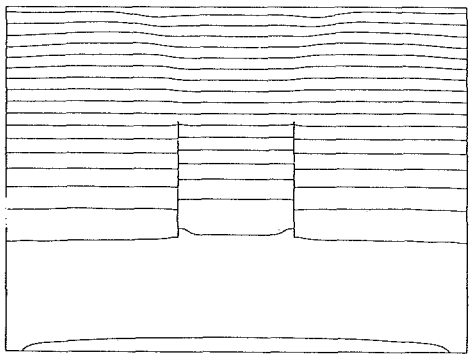

(c) isobars: Δp: 6824

Fig. 6(vi) $t = 1.0$

Fig. 6 Contour plots of the solution

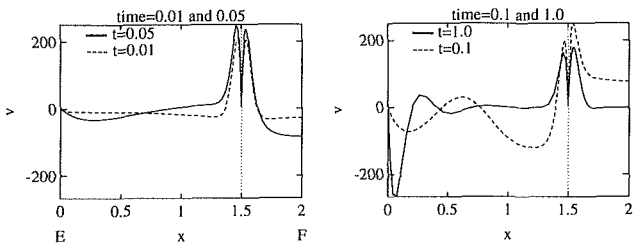

Fig. 7 *v*-velocity profiles along a horizontal line at the center of the domain, i.e., along $y = 1.5$. The dotted line, - - - - -, shows the location of the heated plate. Only the left half of the domain is shown. The profiles clearly show the existence of a thin wall layer adjacent to the heated channel walls. The letters E and F correspond to the physical locations shown in Fig. 1.

which qualitatively resembles a buoyancy-driven boundary layer, adjacent to the vertical surfaces. This thin layer, which comes into being at the initial stages of the transient process, is completely responsible for maintaining the wall temperature gradient and consequently the heat transfer at the wall, irrespective of the transient flow structures in the channel. It is also clear that predictions based on solution of the boundary layer equations would be qualitatively incorrect, especially for short aspect ratio channels, even at high Grashof numbers.

References

Aung, W., 1972, "Fully Developed Laminar Free Convection Between Vertical Plates Heated Asymmetrically," *Int. J. Heat Mass Transfer*, Vol. 15, pp. 1577–1580.

Aung, W., Fletcher, L. S., and Sernas, V., 1972, "Developing Laminar Free Convection Between Vertical Plates and Asymmetric Heating," *Int. J. Heat Mass Transfer*, Vol. 16, pp. 2293–2308.

Bodoia, J. R., and Osterle, J. F., 1962, "The Development of Free Convection Between Heated Vertical Plates," ASME JOURNAL OF HEAT TRANSFER, Vol. 84, pp. 40–43.

Chang, T. S., and Lin, T. F., 1989, "Transient Buoyancy-Induced Flow Through a Heated, Vertical Channel of Finite Height," *Num. Heat Transfer*, Vol. 16A, pp. 15–35.

Elenbaas, W., 1942, "Heat Dissipation of Parallel Plates by Free Convection," *Physica*, Amsterdam, Vol. IX, No. 1, pp. 1–28.

Gebhart, B., Jaluria, Y., Mahajan, R. L., and Sammakia, B., 1988, *Buoyancy Induced Flows and Transport*, Hemisphere, Washington, DC.

Gingrich, W. K., Cho, Y. I., and Shyy, W., 1992, "Effect of Shear Thinning on Laminar Heat Transfer Behavior in a Rectangular Duct," *Int. J. Heat Mass Transfer*, Vol. 35, pp. 2823–2836.

Kettleborough, C. F., 1972, "Transient Laminar Free Convection Between Heated Vertical Plates Including Entrance Effects," *Int. J. Heat Mass Transfer*, Vol. 15, pp. 883–896.

Martin, L., Raithby, G. D., and Yovanovich, M. M., 1991, "On the Low Rayleigh Number Asymptote for Natural Convection Through an Isothermal Parallel-Plate Channel," ASME JOURNAL OF HEAT TRANSFER, Vol. 113, pp. 899–905.

Nakamura, H., Asako, Y., and Naitou, T., 1982, "Heat Transfer by Free Convection Between Two Parallel Plates," *Numer. Heat Transfer*, Vol. 5, pp. 95–106.

Naylor, D., Floryan, J. M., and Tarasuk, J. D., 1991, "A Numerical Study of Developing Free Convection Between Isothermal Vertical Plates," ASME JOURNAL OF HEAT TRANSFER, Vol. 113, pp. 620–626.

Patankar, S. V., 1980, *Numerical Heat Transfer and Fluid Flow*, Hemisphere, Washington, DC.

Peterson, G. P., and Ortega, A., 1990, "Thermal Control of Electronic Equipment and Devices," in: *Advances in Heat Transfer*, Vol. 20, Academic Press, pp. 181–314.

Raithby, G. D., and Hollands, K. G. T., 1985, "Natural Convection," in: *Handbook of Heat Transfer*, W. M. Rohsenow, J. P. Hartnett, and E. N. Ganic, eds., McGraw-Hill, New York, pp. 6.1–6.93.

Ramanathan, S., and Kumar, R., 1991, "Correlations for Natural Convection Between Heated Vertical Plates," ASME JOURNAL OF HEAT TRANSFER, Vol. 113, pp. 97–107.

Shyy, W., Gingrich, W. K., and Gebhart, B., 1992, "Adaptive Grid Solution for Buoyancy Induced Flow in Vertical Slots," *Num. Heat Transfer*, Vol. 22A, pp. 51–70.

Shyy, W., 1993, *Computational Modeling for Fluid Flow and Interfacial Transport*, Elsevier, Amsterdam, The Netherlands.

Sparrow, E. M., and Gregg, J. L., 1956, "Laminar Free Flow Convection From a Vertical Plate With Uniform Surface Heat Flux," ASME JOURNAL OF HEAT TRANSFER, Vol. 78, pp. 435–440.

Sparrow, E. M., and Bahrami, P. A., 1980, "Experiments on Natural Convection From Heated Vertical Parallel Plates With Either Open or Closed Edges," ASME JOURNAL OF HEAT TRANSFER, Vol. 102, pp. 221–227.

Sparrow, E. M., Chrysler, G. M., and Azevedo, L. F., 1984, "Observed Flow Reversals and Measured-Predicted Nusselt Numbers for Natural Convection in a One-Sided Heated Vertical Channel," ASME JOURNAL OF HEAT TRANSFER, Vol. 106, pp. 325–332.

Sparrow, E. M., and Azevedo, L. F., 1985, "Vertical-Channel Natural Convection Spanning Between the Fully Developed Limit and the Single-Plate Boundary-Layer-Limit," *Int. J. Heat Mass Transfer*, Vol. 28, No. 10, pp. 1847–1857.

Webb, B. W., and Hill, D. P., 1989, "High Rayleigh Number Laminar Natural Convection in an Asymmetrically Heated Vertical Channel," ASME JOURNAL OF HEAT TRANSFER, Vol. 111, pp. 649–656.

Wirth, R. A., and Stutzman, R. A., 1982, "Experiments on Free Convection Between Vertical Plates With Symmetric Heating," ASME JOURNAL OF HEAT TRANSFER, Vol. 104, pp. 501–507.

Interaction of the Nucleation Processes Occurring at Adjacent Nucleation Sites

R. L. Judd
Mem. ASME

A. Chopra
Student Mem. ASME

Department of Mechanical Engineering,
McMaster University,
Hamilton, Ontario, L8S 4L7
Canada

An experimental investigation to explore the interaction between bubbles forming at adjacent nucleation sites is presented. The results obtained are consistent with the results of Calka's and Knowles' experimental investigations and confirm that nucleation site activation/deactivation, whereby a bubble growing at a nucleation site is able to promote/hinder the formation of a bubble at an adjacent nucleation site by depositing/displacing a vapor nucleus in the nucleation cavity, is instrumental in determining how a bubble forming at a nucleation site influences the nucleation of the subsequent bubble at an adjacent nucleation site.

Introduction

In situations where the cooling of high energy generation systems is involved, nucleate boiling, the process by which energy is transported from a heat transfer surface by the action of bubbles, is often used to achieve the high rate of heat transfer required. Numerous predictive relationships have been developed over the years in which the rate of heat transfer by nucleate boiling has been equated to the product of the heat transported from the surface by the bubbles departing from a single nucleation site, the average nucleation site density, and the average bubble emission frequency. It has been assumed implicitly that the formation of bubbles at adjacent nucleation sites was independent, implying that the formation of a bubble at one nucleation site would have no effect on the formation of a bubble at a neighboring nucleation site. However, it is becoming apparent that this view of the nucleate boiling process is not correct and that interaction does occur between bubbles forming at adjacent nucleation sites.

Assuming that the number of bubbles produced per unit area per unit time is in some way governed by the interactions that occur in the formation of bubbles at adjacent nucleation sites, then the predictive relationships to which reference is made above, which are based upon the assumption that the bubble flux density is simply the product of the active site density and the average frequency of bubble emission, must be in error. Obviously, there is a need to have a better understanding of the bubble formation process in order to improve the predictive relationships. The purpose of this paper is to review the literature relating to the interaction of bubbles forming at adjacent nucleation sites and to present some new experimental evidence that enables the underlying mechanism to be identified.

Literature Review

As noted above, nucleate boiling is associated with the formation of bubbles at discrete nucleation sites on the heated surface. Corty and Foust (1955) published a paper that indicated that rougher surfaces were capable of forming greater numbers of bubbles per unit area per unit time than smoother surfaces. Subsequently, Bankoff (1958) postulated that the locations of the nucleation sites were actually the grooves, cavities, and scratches typically found in a rough surface. Clark et al. (1959) confirmed Bankoff's (1958) theory through the use of high-speed motion and still photography.

Contributed by the Heat Transfer Division for publication in the JOURNAL OF HEAT TRANSFER. Manuscript received by the Heat Transfer Division July 1992; revision received March 1993. Keywords: Boiling, Measurement Techniques. Associate Technical Editor: L. C. Witte.

Corty and Foust (1955) postulated that a vapor residue trapped in a surface cavity would act as the nucleus for the next bubble to be formed at the same location. Bankoff (1957) demonstrated that the initiation and continuation of bubble formation always proceeds from a small quantity of vapor or gas trapped within the cavities on the surface. Cole (1974) reviewed the literature related to bubble nucleation and proved the necessity of a vapor residue for continuous bubble formation theoretically.

The existence of a small volume of vapor trapped in a nucleation cavity is the necessary condition for the formation of a bubble at a nucleation site when appropriate thermodynamic conditions have been established. Griffith and Wallis (1960) performed an experiment that established that bubble formation occurs at a nucleation site when the size of the nucleus exceeds that imposed by thermodynamic equilibrium. This concept has formed the basis of all the theories of bubble nucleation under boiling conditions.

Bubble departure, which usually results in the entrapment of a residue of vapor in the nucleation cavity to enable subsequent bubble formation, follows bubble nucleation and growth. The departure of a bubble induces the fluid surrounding it to move to fill the void left by it and causes the fluid to sweep across the nucleation site. If the nucleation cavity is relatively shallow, the motion of the fluid can displace a nucleus that might already have been in it, in which case bubble formation is terminated until the nucleation cavity obtains a nucleus once again. The fluid replacing the departing bubble has a better chance of displacing a nucleus from a shallow nucleation cavity than a deep nucleation cavity.

It has generally been assumed that the trapping of a vapor residue occurs continually each time a bubble departs, independent of the formation of bubbles at adjacent nucleation sites. In the formulation of their bubble nucleation theories, Hsu (1962) and Han and Griffith (1965) implicitly assumed that nuclei would be continually deposited upon the departure of the preceding bubble so that all that would be required for the formation of a subsequent bubble was for the thermodynamic equilibrium between the vapor in the nucleus and the fluid surrounding it to be upset.

In a study performed by Eddington and Kenning (1978), the assumption above was tested by pressurizing the liquid in a boiling vessel in order to cause the gas dissolved in the liquid to form nuclei in cavities within a selected range of sizes. The theory was found to be unable to explain the behavior observed at a number of nucleation sites. Some cavities that should have contained a nucleus and should have been active did not form bubbles when boiling conditions were established, whereas

other cavities that should not have been active because they should not have contained a nucleus did form bubbles when boiling conditions were established. As an explanation for the inconsistent behavior that occurred at these nucleation sites, Eddington and Kenning (1978) hypothesized thermal interference at adjacent nucleation sites to explain their observations.

The interaction process has actually been observed. Using the results of an experiment conducted by Judd and Hwang (1976) to investigate the behavior of dichloromethane boiling on a heated glass surface using laser interferometry and high-speed motion picture photography, Judd and Lavdas (1980) explored the nature of the interactions occurring during bubble formation. Both the activation of an inactive nucleation site and the deactivation of an active nucleation site were observed in the motion picture films. Activation resulted from the growth of a bubble, which formed at an adjacent nucleation site and covered an inactive nucleation site, where it was assumed that a vapor residue that later formed a bubble had been deposited. Deactivation occurred when a bubble growing at an adjacent site approached a previously active site, where it was assumed that it had displaced or absorbed the nucleus deposited in it.

Chekanov (1977) applied two pointed heaters to the underside of a strip of foil to produce a stream of bubbles in water at atmospheric pressure wherever contact was made in order to investigate the interaction of bubbles forming at adjacent nucleation sites. The separation distance between the active nucleation sites underlying the bubbles could be varied arbitrarily. For each separation distance, probability distributions $p(\tau)$ of the time τ elapsed between the start of bubble formation at one nucleation site and the start of bubble formation at the other nucleation site were measured.

According to the theory of pulse processes, one form of the distribution of the elapsed time that occurs between two interacting pulses is given by the relationship

$$p(\tau) = [(\tau^{\nu-1}/\bar{\tau}^{\nu})/\Gamma(\nu)]e^{-\tau/\bar{\tau}}$$

where $p(\tau)$ is the probability of an event, such as the formation of a bubble at one nucleation site, occurring in a time interval τ after the occurrence of another event, such as the formation of a bubble at an adjacent nucleation site. In the equation, $\bar{\tau}$ is the elapsed time in the absence of any interaction between the events and ν is the shape parameter.

The probability density relationship above is known as the gamma distribution. When $\nu > 1$, the probability of occurrence of elapsed time τ between the formation of the bubbles is greater than in the case $\nu = 1$. Conversely, when $\nu < 1$, the probability of occurrence of elapsed time τ between the formation of the bubbles is less than in the case $\nu = 1$. For the case $\nu = 1$, the gamma distribution degenerates to the exponential distribution, from which we infer that the elapsed time values τ are completely random and implies that there is no correlation between the events. Events for which $\nu > 1$ are said to be "promotive" because the formation of a bubble at a nucleation site increases the probability of the formation of a bubble at an adjacent nucleation site whereas events for which $\nu < 1$ are said to be "inhibitive" because the formation of a bubble at a nucleation site decreases the probability of the formation of a bubble at an adjacent nucleation site.

Chekanov (1977) presented the results of his experiment in the form of a plot of shape parameter ν as a function of dimensionless separation distance $S/\overline{D}_b$. From the results of his experiment, Chekanov (1977) concluded that for dimensionless separation distances $S/\overline{D}_b < 3$, the formation of a bubble at one nucleation site promoted the formation of a bubble at the other nucleation site whereas for dimensionless separation distances $S/\overline{D}_b > 3$, the formation of a bubble at one nucleation site inhibited the formation of a bubble at the other nucleation site. Chekanov (1977) was convinced that bubble formation at either nucleation site affected the formation of a bubble at the adjacent nucleation site, and postulated that the mechanism of interaction was acoustic propagation and hydrodynamic mixing, although he gave no further explanation of the interaction mechanism.

The theory advanced by Chekanov (1977) was used by Calka (1984) in his research investigation to analyze his experimental results. The elapsed time τ between the formation of a bubble at the more active nucleation site relative to the formation of a bubble at the less active nucleation site was determined by a computer, and the distributions obtained were fitted with the gamma distribution. Calka and Judd (1985) presented the variation of shape parameter ν determined from the results of Calka's (1984) experiment as a function of dimensionless separation distance $S/\overline{D}_b$ and observed that for dimensionless separation distances $S/\overline{D}_b < 1$, the formation of a bubble at the more active nucleation site promoted the formation of a bubble at the less active nucleation site, while for dimensionless separation distances $1 < S/\overline{D}_b < 3$, the formation of a bubble at the more active nucleation site inhibited the formation of a bubble at the less active nucleation site. For dimensionless separation distances $S/\overline{D}_b > 3$, there was no interaction between the events occurring at adjacent nucleation sites. In keeping with Chekanov (1977), Calka and Judd (1985) also concluded that the formation of bubbles at adjacent nucleation sites were related events.

The reason for the difference in the results of the two experimental investigations is not known. It is possible that the discrepancy in the results is due to differences in the temperature distributions in the heating surface inasmuch as Chekanov (1977) used a thin metallic heating surface and Calka and Judd (1985) used a glass heating surface. However, the difference is more likely attributable to the fact that Chekanov (1977) did not actually fit his data with the gamma distribution but calculated the shape parameter using the method of moments whereas Calka (1984) fitted his data with the gamma distribution using a computer routine (GAMFIT). The results are consistent, however, in identifying regions of dimensionless separation distance in which promotion and inhibition were found to occur in the formation of bubbles at adjacent sites.

Knowles (1985) also investigated the phenomenon of nucleation site interaction and employed the same analysis procedure advanced by Chekanov (1977) and used by Calka (1984). The only difference in the experiments performed by Calka (1984) and Knowles (1985) was the fact that different specimens of the same type of glass boiling surface were used. Furthermore, the results of Knowles' (1985) experiment were presented in the same way as the results of Calka's (1984) experiment. Therefore, while Knowles (1985) agreed with Judd and Calka (1985) that promotion occurred for dimensionless separation distances $S/\overline{D}_b < 1$, it was somewhat unexpected that he found that there was no interaction between bubbles forming at adjacent nucleation sites for dimensionless separation distances $S/\overline{D}_b > 1$, where Calka and Judd (1985) had found that inhibition occurred.

In attempting to rationalize the results of the two investi-

Nomenclature

A_T = heat transfer surface area
$\overline{D}_b$ = average bubble departure diameter
N/A_T = active nucleation site density
$p(\tau)$ = probability of occurrence
P_{sat} = saturation pressure
q/A_T = surface heat flux
S = separation distance
T_{sat} = saturation temperature
Γ = gamma function
ν = shape parameter
τ = elapsed time

gations, Judd (1988) proposed that the apparent difference was attributable to the boiling surfaces that had been used. Calka's (1984) surface was well aged, and as a consequence, the number of potentially active nucleation sites on Calka's (1984) surface was twice that on Knowles' (1985) surface, which was relatively new. The implication is that the distances separating a pair of nucleation sites would be considerably different on the two surfaces such that the ability of a bubble forming at one of the nucleation sites to cover an adjacent nucleation site and deposit the nucleus required for the formation of a bubble or to displace the nucleus that might already have been deposited would be different. Judd (1988) postulated that because of the differences in site density, bubbles forming at sites on Calka's (1984) boiling surface would have had a higher probability of promoting or inhibiting the formation of bubbles at adjacent nucleation sites than would have been the case on Knowles' (1985) surface, thereby causing the observed difference in nucleation site interaction.

Research Investigation

Using the same apparatus used by Calka (1984) and Knowles (1985), the present research investigation undertook to study nucleation site interaction by investigating changes in the relationship between the shape parameter ν and the dimensionless separation distance $S/\overline{D}_b$ in response to changes in the separation distance between nucleation sites S and the size of the bubbles at departure $\overline{D}_b$. The boiling surface was assumed to be represented by a population of randomly located nucleation sites, which were capable of forming bubbles continually within a much larger population of potentially active nucleation sites that could only form a single bubble upon receipt of the requisite vapor nucleus. The thrust of the research was to determine how the behavior of pairs of nucleation sites changed as the ability of the bubbles forming at a dominant nucleation site to activate/deactivate the adjacent nucleation site changed. Experiments were performed in which different values of $S/\overline{D}_b$ were generated by varying saturation pressure P_{sat} and heat flux q/A_T. In one set of experiments, active site density N/A_T was held constant while average bubble departure size $\overline{D}_b$ was varied and in the other set of experiments, average bubble departure size $\overline{D}_b$ was held constant while active site density N/A_T was varied. The experiments were contrived to test the validity of site activation/deactivation as the mechanism responsible for nucleation site interaction.

Experimental Apparatus

The boiling vessel, the central component of the experimental apparatus, was a vacuum tight cylindrical container made of stainless steel, which facilitated the mounting of a transparent glass heater surface in its baseplate. The upper surface of the glass was coated with a thin layer of stannic oxide, which allowed electric current to be conducted, thereby generating heat at the glass/liquid interface. As shown in Fig. 1, the dimensions of the surface at which heat was generated were 50 mm × 33 mm. The coating on the glass heater surface was supplied with electric power by a Kepco direct current power supply and it was assumed that the heat was generated uniformly over the surface. Bubbles formed in the dichloromethane in contact with the glass surface as a result of the generation of heat. Near the top of the vessel, the dichloromethane vapor was condensed back into the liquid phase by cold water passing through condenser coils located under the coverplate.

The bubble departure size was established by maintaining the pressure in the vessel below atmospheric pressure. An Edwards rotary vacuum pump drew air out of the boiling vessel in order that the pressure could be maintained at levels below atmospheric pressure by continually bleeding air into it. By

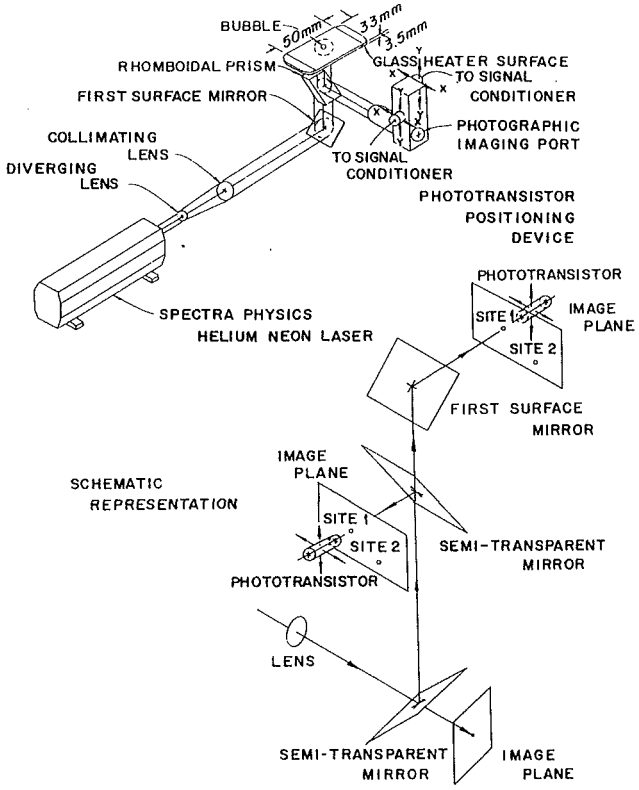

Fig. 1 Schematic representation of the research apparatus

monitoring a mercury manometer and adjusting the bleed valve, the pressure inside the vessel could be maintained at any specified value for long periods of time.

Four chromel-constantan thermocouples were used to measure the temperatures in the boiling vessel. Three of the four thermocouples were located in the liquid in the boiling vessel to measure the bulk liquid temperature. The fourth thermocouple was epoxied to the underside of the glass surface to measure the temperature of the glass heater surface. The signals from the thermocouples were read with a Rubicon-Honeywell potentiometer and/or recorded by a Minneapolis-Honeywell recorder.

To study the formation of bubbles at the nucleation sites on the upper surface of the glass, a laser was used as a light source to provide illumination for the stannic oxide coated surface. A Spectrophysics helium–neon laser (model 125A), which was capable of producing a 2-mm-dia 50 mW beam of monochromatic coherent light at a wavelength of 632.8 nm, was used. A collimator expanded the 2-mm-dia beam emitted by the laser to the required 20 mm diameter. Optical prisms and mirrors were employed to position the laser light on the glass heater surface and to guide the reflected beam to the phototransistor positioning device. A Soligar 105 mm objective lens focused on the stannic oxide coated surface produced an image that contained all the information pertaining to bubble formation on the glass heater surface at an image plane behind the objective lens. A semitransparent mirror directed half the laser beam to two other image planes for analysis purposes.

The procedure for determining the time elapsed between the formation of bubbles at two adjacent nucleation sites was dependent upon the analysis of the variation of light intensity that occurred as the bubbles formed on the heater surface. The variation in light intensity produced by the formation of a single bubble on the heater surface changed too rapidly to be followed by the human eye, but a succession of bubble formations at a particular nucleation site could be detected by studying the image of the glass heater surface through a viewfinder. The approximate locations of the active nucleation sites

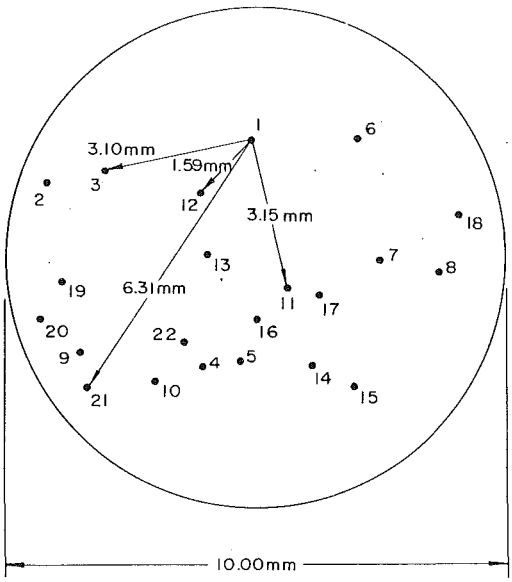

Fig. 2 Location of the nucleation sites on the boiling surface

on the heater surface were determined in both image planes in this way. Replacement of the viewfinders by phototransistors resulted in the generation of voltage signals, which corresponded to the variation in light intensity at the pair of nucleation sites at which interaction was being investigated. Fine resolution of the location of the nucleation sites was obtained by moving the phototransistors on their respective X–Y stages until the optimum voltage signal originating at each of the two adjacent nucleation sites had been obtained. The voltage signals were processed by a signal conditioner that reduced the high-frequency noise and generated an automatic offset, which eliminated the component of the voltage signals corresponding to the background laser light. After the voltage signals had been conditioned, they were processed by a Declab 11/03 minicomputer in order to determine the elapsed time interval.

Experimental Uncertainty

As outlined above, the thrust of the present research investigation is to investigate the interaction of the bubble formation processes occurring at adjacent nucleation sites by studying the changes in the relationship between the shape parameter ν of the gamma distribution that best fitted the measured values of the time elapsed between the formation of bubbles at adjacent sites τ and the dimensionless separation distance $S/\overline{D}_b$, where the quantities comprising the dimensionless separation distance were established by varying the saturation pressure P_{sat} and the heat flux q/A_T independently. Accordingly, the uncertainty associated with these parameters is an important consideration in judging the relevance of the inferences drawn from the results.

The uncertainty in the readings of the voltmeter and ammeter are ± 0.5 V and ± 0.05 A, respectively. Typical measurements are 40 V and 1.5 A so that as a result, the uncertainty in the generation of heat in the stannic oxide layer is on the order of ± 3.5 percent. In addition, under the most adverse conditions, the heat lost by convection to the air space below the glass heater surface is approximately 0.4 W and the heat conducted through the rubber gasket to the base of the boiling vessel is approximately 1.2 W. These uncertainties combined with those associated with the measurement of the length and width of the heated surface result in an estimated uncertainty of ± 6.5 percent in the determination of heat flux q/A_T. The uncertainty associated with reading the mercury manometer, including the small fluctuations in the pressure being measured, does not exceed ± 5 mm of Hg, so that the maximum uncertainty associated with the measurement of the smallest value of saturation pressure P_{sat} used in the investigation is of the order of ± 1.3 percent.

The location of the nucleation sites X, Y and the maximum diameter of the bubbles D_b forming there was determined by analyzing photographic images of the boiling phenomena occurring on the glass heater surface. The ability to identify the point in the photographic image at which the bubbles were originating or to judge the maximum diameter to which a bubble had grown at departure establishes the uncertainty associated with these dimensional measurements. It is estimated that the uncertainty in determining the location of the nucleation site in either direction or locating the edge of a bubble is approximately ± 0.05 mm, so that the corresponding uncertainty associated with the smallest separation distance S is on the order of ± 0.15 mm and the uncertainty associated with the smallest bubble departure diameter $\overline{D}_b$ is on the order of ± 0.10 mm. As a consequence, the uncertainty associated with the smallest value of $S/\overline{D}_b \approx 0.5$ is as large as ± 20 percent but the uncertainty associated with the remainder of the values of $S/\overline{D}_b$ is considerably less.

The uncertainty associated with the determination of the elapsed time τ between the formation of bubbles at adjacent sites using the Schmitt triggers in the Declab 11/03 minicomputer is ± 2 μs, which is insignificant insofar as the analysis of the results of the experimental investigation is concerned. The uncertainty associated with the value of the shape parameter ν obtained by fitting the measured values of elapsed time τ is not as easy to estimate because the values were determined by a computer optimization routine. However, the values of ν arising from more than 15 experiments performed with pairs of sites separated by so great a distance that it is reasonable to assume that there had been no interaction deviated from unity by ± 0.10 or less, which is indicative of the uncertainty in the determination of ν.

Experimental Results

Figure 2 depicts the distribution of 22 nucleation sites within a 10.00-mm-dia circle in the central portion of the field of view. The numbered dots in the illustration identify the locations at which bubbles were observed to originate, which correspond to the nucleation sites on the glass heater surface. It should be understood that Fig. 2 identifies all the nucleation sites at which bubbles were observed to originate and that only a fraction of these nucleation sites would be active under any particular combination of saturation pressure P_{sat} and heat flux q/A_T. Site 1, which was a particularly active nucleation site, was deemed to be the dominant site in this region of the field of view. The experiments described below investigate how bubbles forming at site 1 affect the subsequent formation of bubbles at sites 3, 11, 12, and 21.

Other than the distance separating the sites, the conditions under which the results reported in Figs. 3 and 4 were obtained are identical. Figure 3 is a composite of three histograms, which present the elapsed time intervals measured between the formation of bubbles at sites 1 and 12 for which the separation distance $S = 1.59$ mm at constant nucleation site density $N/A_T = 1.35 \times 10^5$ sites/m^2 and three different bubble departure diameters $\overline{D}_b = 1.80$, 2.00, and 2.50 mm. All the distributions have shape coefficient values ν greater than unity associated with them inasmuch as the distance separating the sites is relatively small. As a consequence, it is not surprising that bubble formation at site 1 would have a promotive effect on bubble formation at site 12. It is evident that bubble departure diameter $\overline{D}_b$ is instrumental in determining how the bubble formation at the dominant site affects bubble formation at the adjacent site.

Figure 4 is a composite of three histograms, which present

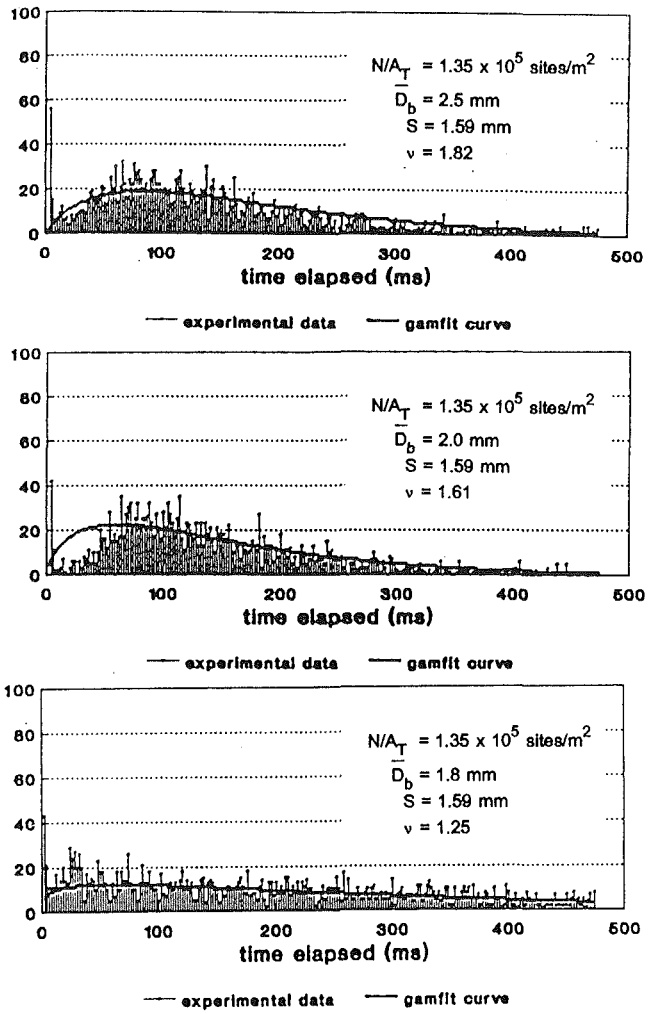

Fig. 3 Distribution of the elapsed time between the appearance of a bubble at site 1 and the subsequent appearance of a bubble at site 12 for $N/A_T = 1.35 \times 10^5$ sites/m^2 and $\overline{D}_b$ = 1.8, 2.0, and 2.5 mm

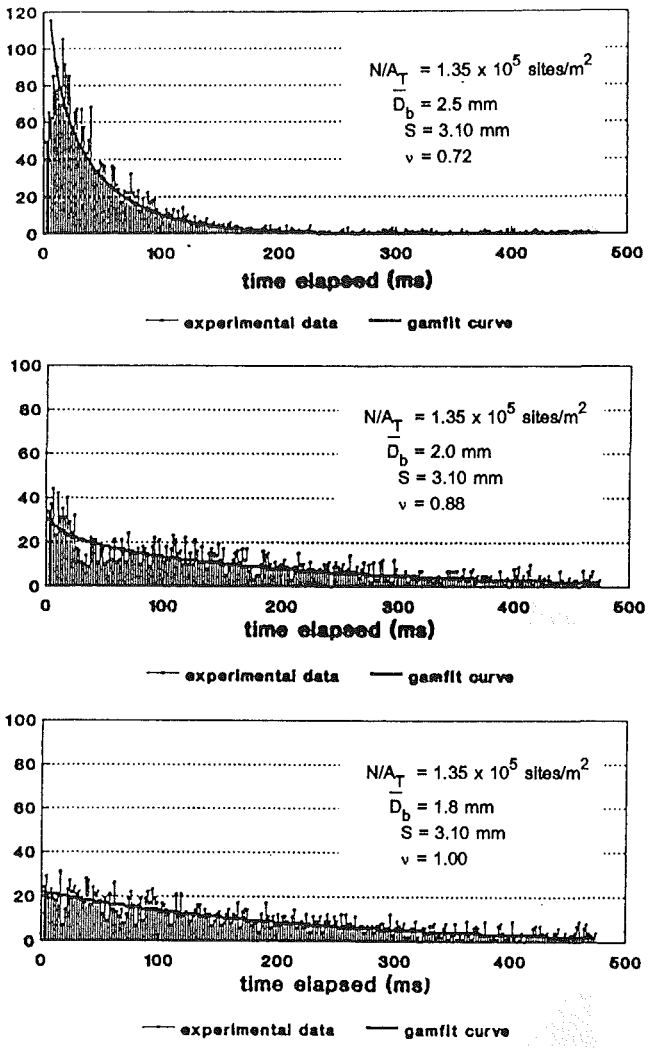

Fig. 4 Distribution of the elapsed time between the appearance of a bubble at site 1 and the subsequent appearance of a bubble at site 3 for $N/A_T = 1.35 \times 10^5$ sites/m^2 and $\overline{D}_b$ = 1.8, 2.0 and 2.5 mm

the elapsed time intervals measured between the formation of bubbles at sites 1 and 3 at constant nucleation site density $N/A_T = 1.35 \times 10^5$ sites/m^2 and three different bubble departure diameters $\overline{D}_b$ = 1.8, 2.0, and 2.5 mm. The distance separating the sites S = 3.10 mm and therefore the dimensionless separation distances $S/\overline{D}_b$ are within the range in which Calka's (1984) and Knowles' (1985) experiments disagreed. From inspection of the histograms, it is evident that the shape of the histograms changes. The shape factor ν = 0.72 corresponding to $\overline{D}_b$ = 2.5 mm is consistent with that reported by Calka and Judd (1985), while the shape factor ν = 1.00 corresponding to $\overline{D}_b$ = 1.80 mm is consistent with that reported by Knowles (1985). It would appear that both separation distance S and bubble departure diameter $\overline{D}_b$ are instrumental in determining what sort of effect bubble formation at the dominant site will have upon bubble formation at the adjacent site and that dimensionless separation distance $S/\overline{D}_b$ is not the determining factor.

In Fig. 5, two histograms presenting the elapsed time intervals measured between the formation of bubbles at sites 1 and 11 are shown. These histograms were obtained at constant bubble departure diameter $\overline{D}_b$ = 2.5 mm for two different values of active site density $N/A_T = 0.80$ and 1.35×10^5 sites/m^2. The distance separating the two sites S = 3.15 mm is almost identical to that separating sites 1 and 3 and while the values of ν presented in Figs. 4 and 5 agree when $N/A_T = 1.35 \times 10^5$ sites/m^2, they do not agree when $N/A_T = 0.80 \times 10^5$ sites/m^2. In addition to bubble departure diameter $\overline{D}_b$ and separation distance S, active site density N/A_T has a role to play in the process of bubble formation at adjacent nucleation sites.

In Fig. 6, two histograms presenting the elapsed time intervals measured between the formation of bubbles at sites 1 and 21, which are separated by S = 6.31 mm, are shown. The histograms were obtained at constant bubble departure diameter $\overline{D}_b$ = 2.5 mm for two different values of active site density $N/A_T = 0.80 \times 10^5$ and 1.35×10^5 sites/m^2. Both of the shape factor values ν = 0.95 and 1.10 are essentially equal to unity, implying that the data follow the exponential distribution. Obviously, the distance separating the sites is so large and there are so many sites intervening between them that there is no correlation between the events occurring at sites 1 and 21.

Discussion

The results obtained in the present investigation are compared with those obtained by Calka (1984) and Knowles (1985) in Figs. 7 and 8, respectively. Histograms very similar to those obtained by Calka (1984) were obtained at active site density $N/A_T = 1.35 \times 10^5$ sites/m^2 and bubble departure diameter $\overline{D}_b$ = 2.5 mm. The trend in the variation of shape parameter

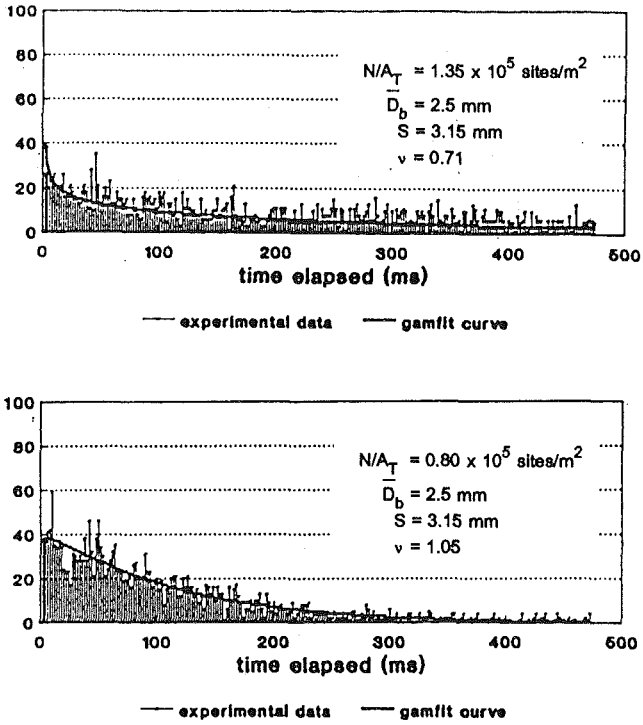

Fig. 5 Distribution of the elapsed time between the appearance of a bubble at site 1 and the subsequent appearance of a bubble at site 11 for $\bar{D}_b$ = 2.5 mm and N/A_T = 0.80 × 10^5 and 1.35 × 10^5 sites/m^2

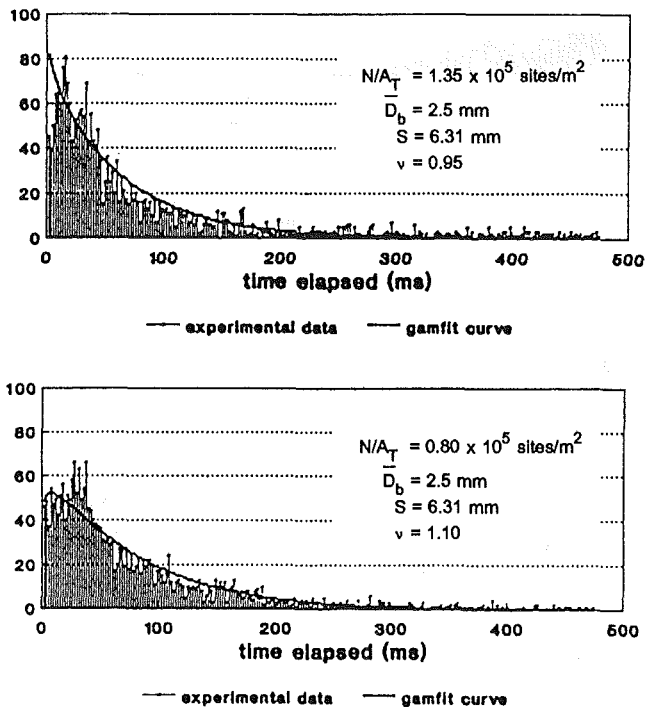

Fig. 6 Distribution of the elapsed time between the appearance of a bubble at site 1 and the subsequent appearance of a bubble at site 21 for $\bar{D}_b$ = 2.5 mm and N/A_T = 0.80 × 10^5 and 1.35 × 10^5 sites/m^2

ν with dimensionless separation difference $S/\bar{D}_b$ obtained by plotting the values resulting from the analysis of the histograms obtained at each of the sites surrounding site 1 can be seen to be identical to that presented by Calka (1984) in Fig. 7. Similarly, histograms very much like those obtained by Knowles (1985) were obtained at active site density N/A_T = 1.35 ×

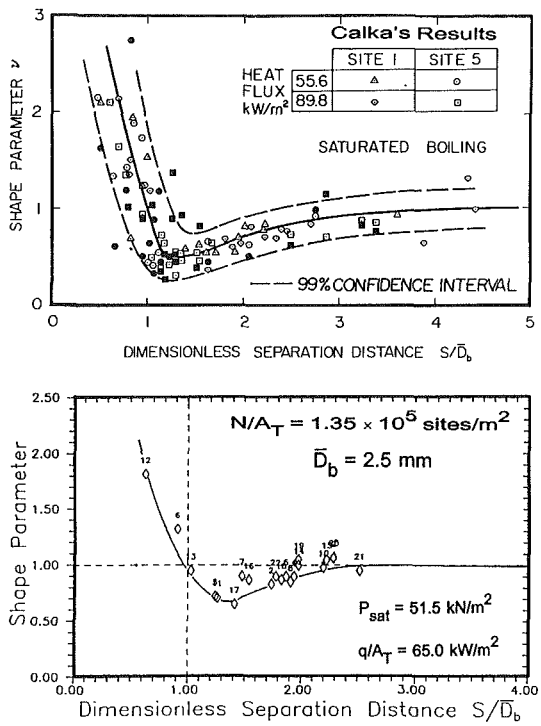

Fig. 7 Comparison of Calka's experimental results with those obtained in the present experiment for N/A_T = 1.35 × 10^5 sites/m^2 and $\bar{D}_b$ = 2.5 mm

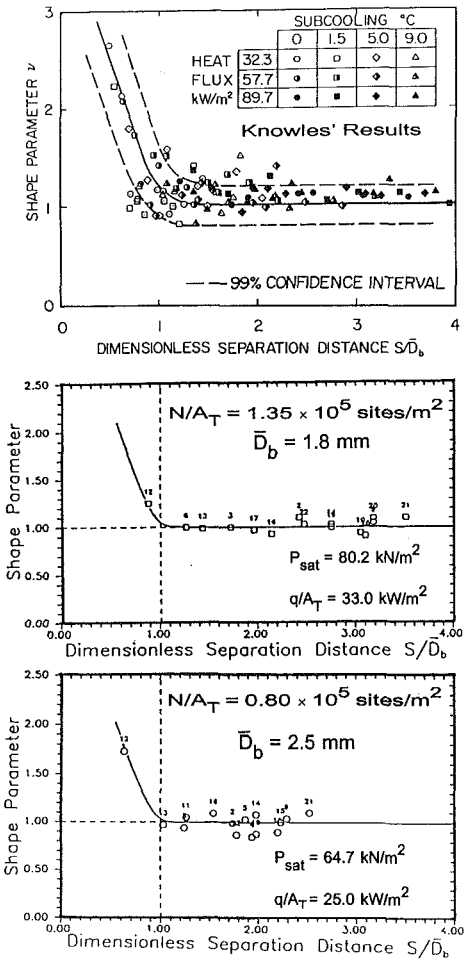

Fig. 8 Comparison of Knowles' experimental results with those obtained in the present experiment for N/A_T = 1.35 × 10^5 sites/m^2 and $\bar{D}_b$ = 1.8 mm and N/A_T = 0.80 × 10^5 sites/m^2 and $\bar{D}_b$ = 2.5 mm

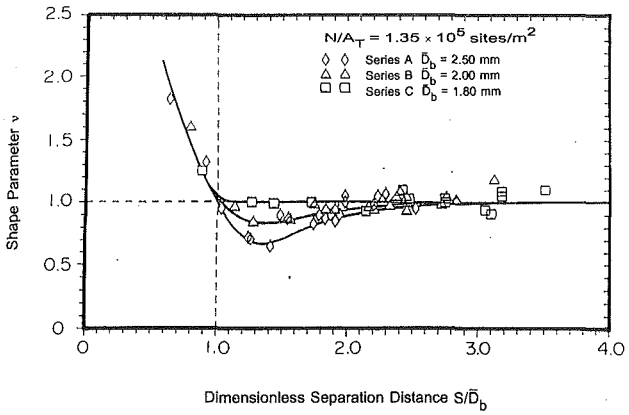

Fig. 9 Variation of shape parameter ν with dimensionless separation distance $S/\bar{D}_b$ for $N/A_T = 1.35 \times 10^5$ sites/m^2 and $\bar{D}_b = 1.8$, 2.0, and 2.5 mm

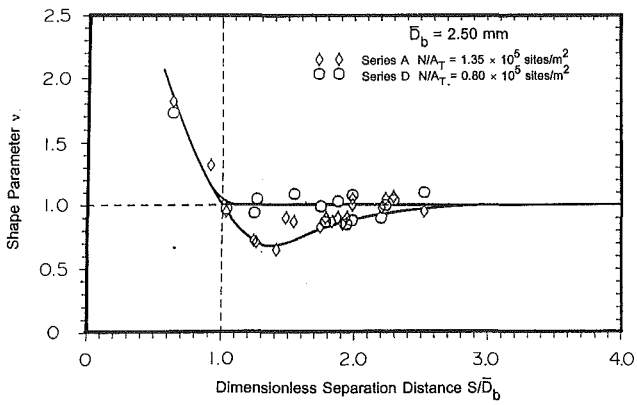

Fig. 10 Variation of shape parameter ν with dimensionless separation distance $S/\bar{D}_b$ for $\bar{D}_b = 2.5$ mm and $N/A_T = 0.80 \times 10^5$ and 1.35×10^5 sites/m^2

10^5 sites/m^2 and bubble departure diameter $\bar{D}_b = 1.8$ mm as well as active site density $N/A_T = 0.80 \times 10^5$ sites/m^2 and bubble departure diameter $\bar{D}_b = 2.50$ mm. Figure 8 displays the similarity between the variation of shape factor ν with dimensionless separation distance $S/\bar{D}_b$ obtained from these experiments with that presented by Knowles (1985). The results presented in Figs. 7 and 8 indicate how different combinations of active site density N/A_T and bubble departure size $\bar{D}_b$ change the interaction of bubbles forming at adjacent nucleation sites.

The results presented in Fig. 9 show how the variation between shape parameter ν and dimensionless separation distance $S/\bar{D}_b$ is affected by variation in bubble departure size $\bar{D}_b$ when the active site density N/A_T is held constant. The curves plotted in the figure show the same promotive effect $\nu > 1$ in the region $S/\bar{D}_b < 1$ and indicate how the inhibitive effect $\nu < 1$, which is evident in the region $1 < S/\bar{D}_b < 3$ when $\bar{D}_b = 2.5$ mm, vanishes when $\bar{D}_b = 1.8$ mm. The results presented in Fig. 10 show how the variation between shape parameter ν and dimensionless separation distance $S/\bar{D}_b$ is affected by variation in active site density N/A_T when the bubble departure size $\bar{D}_b$ is held constant. The curves plotted in the figure also show the same promotive effect $\nu > 1$ in the region $S/\bar{D}_b < 1$ and indicate how the inhibitive effect $\nu < 1$, which is evident in the region $1 < S/\bar{D}_b < 3$ when $N/A_T = 1.35 \times 10^5$ sites/m^2 vanishes when $N/A_T = 0.80 \times 10^5$ sites/m^2. All the trends present in Fig. 9 are present in Fig. 10 as well. Not unexpectedly, ν approaches unity when $S/\bar{D}_b > 3$ in both figures.

All the effects discussed above are consistent and confirm that nucleation site activation/deactivation is instrumental in determining how a bubble forming at a nucleation site influences the nucleation of the subsequent bubble at an adjacent nucleation site. The explanation advanced by Judd (1988), that the nucleation cavity must contain a vapor nucleus and that there must be sufficient energy in the vicinity of the nucleation site to establish the conditions that will upset the thermodynamic equilibrium that is preventing a bubble from forming, is essentially correct. Both conditions must be satisfied. The way in which events occurring at adjacent nucleation sites interact is determined by the way in which the conditions are satisfied.

If the geometry of a cavity is such that it cannot capture and hold a small amount of vapor each time a bubble forms at it, then bubble formation can only occur if a vapor nucleus is deposited by another bubble forming at an adjacent site in the course of growing and covering it. Then, when sufficient energy becomes available in the vicinity of the nucleation site to upset the thermodynamic equilibrium which is preventing bubble nucleation, a single bubble will be formed, unless the nucleus is displaced in the interim. Larger bubbles are more capable of covering the nucleation sites surrounding them than smaller bubbles and this is the explanation of the promotive effect that was commented upon in Fig. 3. In all three of the histograms $S/\bar{D}_b < 1$, so that it is reasonable to conclude that there would be a high probability of larger than average bubbles forming at site 1 covering site 12 and providing the nucleus that would enable a bubble to form at it. As a consequence, a promotive type of interaction was observed.

Situations occur where other potentially active sites, which themselves have a high probability of being activated, exist between the dominant site and the adjacent site under investigation; this is the explanation of the inhibitive effect that was commented upon in Fig. 4. When $\bar{D}_b = 2.5$ mm, the high probability of a bubble forming at site 1 resulting in the formation of a bubble at site 12 would lead to interference with bubble formation at site 3, because a bubble growing at site 12 is very capable of covering site 3 and depositing a nucleus in the nucleation cavity or displacing any nucleus that it might contain. When $\bar{D}_b = 1.8$ mm, the probability of a bubble formation at site 1 resulting in the formation of a bubble at site 12 is itself reduced to the point where the events occurring at site 1 and site 3 appear to be independent.

At a particular saturation pressure P_{sat}, the heat flux q/A_T establishes the conditions under which a nucleus in a nucleation cavity will begin to develop into a bubble and determines the length of time required before there will be sufficient energy in the vicinity of the nucleation site for the process to repeat itself. This is the reason that the shape parameter $\nu = 0.71$ at $N/A_T = 1.35 \times 10^5$ sites/m^2 corresponding to $P_{sat} = 51.5$ kN/m^2 and $q/A_T = 65.0$ kW/m^2 was observed to change to $\nu = 1.05$ at $N/A_T = 0.80 \times 10^5$ sites/m^2 corresponding to $P_{sat} = 64.7$ kN/m^2 and $q/A_T = 25.0$ kW/m^2 in Fig. 5. When the availability of energy diminishes, the events occurring at adjacent sites appear to be more and more independent.

Nucleation site activation/deactivation is likely to be more significant than energy availability in determining whether or not bubble nucleation will be influenced by bubble formation at an adjacent nucleation site. While it is undeniable that irregularities in surface temperature distribution do exist as pointed out by Kenning (1992), the surface quenching mechanism that is responsible for these irregularities is confined to the area within $S/\bar{D}_b \approx 1$, and would not affect the surface temperature at distances great enough to have any effect on what happens at the majority of the surrounding nucleation sites where the results of the present investigation show that bubble nucleation is inhibited by bubble formation at an adjacent site.

Concluding Remarks

The experimental investigation reported herein confirms that

site activation/deactivation is the mechanism responsible for nucleation site interaction. The formation of bubbles at adjacent nucleation sites would be independent events except for the circumstances that permit the formation of bubbles at one nucleation site to influence the subsequent formation of bubbles at another nucleation site. When a nucleation site that is unable to capture vapor nuclei lies within the area influenced by a continually active nucleation site that can deposit nuclei in it, bubbles will form at the adjacent nucleation site more frequently than would otherwise be the case. This type of interaction, which was observed to occur when $S/\overline{D}_b < 1$, is said to be "promotive." When a nucleation site that is unable to capture vapor nuclei lies within the area influenced by an intervening nucleation site capable of depositing/displacing nuclei in it that is itself under the influence of a continually active nucleation site, bubbles will form at the adjacent nucleation site less frequently than would otherwise be the case. This type of interaction, which was observed to occur when $1 < S/\overline{D}_b < 3$, is said to be "inhibitive." When bubble formation at one nucleation site is in no way influenced by bubble formation at another nucleation site, the events are said to be "independent." This type of interaction was observed to occur when $S/\overline{D}_b > 3$.

The ultimate goal of nucleate boiling heat transfer research is to be able to predict boiling heat transfer rates without recourse to empiricism. Much effort has been devoted toward achieving this goal but only recently have attempts been made to understand the physics underlying the phenomenon and to incorporate surface characteristics. If the underlying mechanisms were better understood, it would be possible to predict the rate of boiling heat transfer a priori and to design and manufacture boiling heat transfer surfaces to specification. More importantly, the ability to predict boiling heat transfer rates reliably would permit the performance of boiling heat transfer surfaces to be optimized.

A probabilistic approach to predicting boiling heat transfer rates that incorporates surface characteristics is still a long way off. However, it should be possible to predict the number of bubbles formed per unit area per unit time for specified boiling conditions if the number of nucleation sites randomly distributed over a heat transfer surface and the relationships describing the probability of bubble nucleation occurring at each of the nucleation sites are known. This aspect of the research is currently being investigated by performing Monte Carlo simulations of boiling experiments that have already been performed in which the gamma distribution is being used to predict the time elapsed between bubble formations at pairs of nucleation sites. Confidence in the approach will be established if the results of these simulations compare favorably with the measured results.

References

Bankoff, S. G., 1957, "Ebullition From Solid Surfaces in the Absence of Pre-existing Gaseous Phase," *AIChE Journal*, Vol. 3, pp. 735–740.

Bankoff, S. G., 1958, "Entrapment of Gas in the Spreading of Liquid Over a Rough Surface," *AIChE Journal*, Vol. 4, pp. 24–26.

Calka, A., 1984, "Some Aspects of the Interaction Among Nucleation Sites During Saturated Nucleate Boiling," M.Eng. Thesis, Mechanical Engineering Department, McMaster University, Hamilton, Ontario, Canada.

Calka, A., and Judd, R. L., 1985, "Some Aspects of the Interaction Among Nucleation Sites During Saturated Nucleate Boiling," *International Journal of Heat Mass Transfer*, Vol. 28, No. 12, pp. 2331–2342.

Chekanov, V. V., 1977, "Interaction of Centers in Nucleate Boiling," *Teplofizika Vysokikh Temperatur*, Vol. 15, No. 1, pp. 121–128.

Clark, H. B., Strenge, P. S., and Westwater, J. W., 1959, "Active Sites for Nucleate Boiling," *Chemical Engineering Progress Symposium Series*, Vol. 55, No. 29, pp. 103–110.

Cole, R., 1974, "Boiling Nucleation," *Advances in Heat Transfer*, Academic Press, Vol. 10, pp. 85–166.

Corty, C., and Foust, A. S., 1955, "Surface Variables in Nucleate Boiling," *Chemical Engineering Progress Symposium Series*, Vol. 51, No. 17, pp. 1–12.

Eddington, R. I., and Kenning, D. B. R., 1978, "The Prediction of Flow Boiling Bubble Populations From Gas Bubble Nucleation Experiments," *Proceedings of the 6th International Heat Transfer Conference*, Toronto, Vol. 1, pp. 275–279.

Griffith, P., and Wallis, J., 1960, "The Role of Surface Conditions in Nucleate Boiling," *Chemical Engineering Progress Symposium Series*, Vol. 56, No. 30, pp. 49–63.

Han, C. Y., and Griffith, P., 1965, "The Mechanism of Heat Transfer in Nucleate Boiling—Part I, Bubble Initiation, Growth and Departure," *International Journal of Heat and Mass Transfer*, Vol. 8, pp. 887–904.

Hsu, Y. Y., 1962, "On the Size Range of Active Nucleation Cavities on a Heating Surface," ASME JOURNAL OF HEAT TRANSFER, Vol. 84, pp. 207–216.

Judd, R. L., and Hwang, K. S., 1976, "A Comprehensive Model for Nucleate Pool Boiling Heat Transfer Including Microlayer Evaporation," ASME JOURNAL OF HEAT TRANSFER, Vol. 98, pp. 623–629.

Judd, R. L., and Lavdas, C. H., 1980, "The Nature of Nucleation Site Interaction," ASME JOURNAL OF HEAT TRANSFER, Vol. 102, No. 3, pp. 461–464.

Judd, R. L., 1988, "On Nucleation Site Interaction," ASME JOURNAL OF HEAT TRANSFER, Vol. 110, pp. 475–478.

Kenning, D. B. R., 1992, "Wall Temperature Patterns in Nucleate Boiling," *International Journal of Heat and Mass Transfer*, Vol. 35, No. 1, pp. 73–85.

Knowles, S., 1985, "Interaction Between Bubble Emission at Adjacent Nucleation Sites," unpublished research, Mechanical Engineering Department, McMaster University.

M. W. Wambsganss
Argonne National Laboratory,
Materials and Components Technology
Division,
Argonne, IL 60439

D. M. France
University of Illinois at Chicago
Department of Mechanical Engineering,
M/C 251,
Chicago, IL 60680

J. A. Jendrzejczyk

T. N. Tran

Argonne National Laboratory,
Materials and Components Technology
Division,
Argonne, IL 60439

Boiling Heat Transfer in a Horizontal Small-Diameter Tube

Results of a study on boiling heat transfer of refrigerant R-113 in a small-diameter (2.92 mm) tube are reported. Local heat transfer coefficients are measured for a range of heat flux (8.8–90.75 kW/m^2), mass flux (50–300 kg/m^{2}s), and equilibrium mass quality (0–0.9). The measured coefficients are used to evaluate 10 different heat transfer correlations, some of which have been developed specifically for refrigerants. High heat fluxes and low mass fluxes are inherent in small channels, and this combination results in high boiling numbers. In addition, based on a flow pattern map developed from adiabatic experiments with air–water mixtures, it has been shown that small-diameter channels produce a slug flow pattern over a large range of parameters when compared with larger-diameter channels. The effects of high boiling number and slug flow pattern lead to domination by a nucleation mechanism. As a result, the two-phase correlations that predicted this dominance also predicted the data the best when they properly modeled the physical parameters. The correlation of Lazarek and Black (1982) predicted the data very well. It is also shown that a simple form, suggested by Stephan and Abdelsalam (1980) for nucleate pool boiling, correlates the data equally well; both correlations are within a mean deviation of less than 13 percent. Results are applicable to boiling in compact heat exchangers.

Introduction

Compact heat exchangers in several different configurations have recently received attention for boiling heat transfer applications. V. P. Carey and co-workers have studied a variety of finned or otherwise enhanced passages; for example, Mandrusiak et al. (1988) considered offset strip fins and Xu et al. (1988) investigated ribbed surface enhancements. The channels considered in these studies had hydraulic diameters of 5 mm. Various compact heat exchanger channels have also been studied by Robertson and Wadekar (1988) and Robertson (1979), who, respectively, considered perforated finned channels and boiling in serrated finned channels. Typical hydraulic diameters of the channels in these studies were 2.4 mm.

A third group of extensive studies of two-phase heat transfer in compact heat exchangers was conducted by J. W. Westwater et al. (Haralumpus et al., 1975; Westwater, 1986). Design methods and predictions of heat transfer coefficients for evaporation and condensation were reviewed by Westwater (1986), and a commercial heat exchanger of the plate-fin type was tested by Haralampus et al. (1975).

Compact heat exchangers, as in the studies cited above, are typically designed with noncircular flow passages and involve multichannel arrangements. Flow maldistribution is inherent in such multichannel configurations. To circumvent the potential for flow maldistribution, a single channel was selected for the subject study. Furthermore, the channel cross-sectional geometry was chosen to be circular, in part, because there is very limited information on flow boiling in small circular channels, but also because data on a circular tube would provide a reference study upon which to base studies of more complex cross-sectional geometries. Damianides and Westwater (1988) took the first step in this approach and studied the two-phase flow patterns that occur in round tubes with diameters of 1–5 mm; however, they reported no studies of the heat transfer of these tubes.

The objectives of the investigation reported here were to measure forced convective-boiling heat transfer in a small-diameter tube, in the size range of the tubes used by Damianides and Westwater (1988), to identify characteristics which were different from those of larger tubes, and to determine the accuracy of the state-of-the-art heat transfer correlations for the small tube situation.

To accomplish these objectives, experiments were performed in a horizontal round-tube test channel, 2.92 mm in inside diameter, with Refrigerant-113 (R-113) as the boiling fluid. Ten heat transfer correlations from the engineering literature as well as other flow boiling data with R-113 were used to assess the characteristics of the 2.92 mm tube data.

Selection of Correlations and Data

Results of a recent study of boiling R-113 in horizontal tubes were reported by Reid et al. (1987). Tubes of two diameters, 8.71 mm and 10.92 mm, were used in that study. There was some overlap in mass flux and heat flux with the present study, and the data provide a useful comparison. Reid et al. (1987) identified six boiling flow heat transfer correlations for comparison with their data. These commonly used correlations include five that were developed from refrigerant data bases and the Chen (1966) correlation, whose format was followed by many others. In evaluating these correlations against their data, Reid et al. (1987) concluded that no single correlation predicted the data over the entire range of experimental parameters, although several were in reasonable agreement.

Another study, in which R-113 was the boiling fluid and which is closely related to the present investigation, was reported by Lazarek and Black (1982). Their study, motivated by the need to develop improved methods for electronic cooling, focused on evaporation of R-113 in a vertical tube with a diameter of 3.15 mm. The flow direction was both up and down (in a U-shaped test section), which is different from the present case, but where the channel diameter was closest to that of this study.

The R-113 flow boiling data of the present investigation, obtained with a 2.92-mm round tube, were compared with the R-113 results of Reid et al. (1987) and those of Lazarek and Black (1982). The use of the same refrigerant in all cases eliminated the fluid variable from the comparisons.

Saturated flow boiling data upstream of the critical heat flux (CHF) have been correlated according to a superposition prin-

Contributed by the Heat Transfer Division for publication in the JOURNAL OF HEAT TRANSFER. Manuscript received by the Heat Transfer Division June 1992; revision received March 1993. Keywords: Boiling, Evaporation, Multiphase Flows. Associate Technical Editor: L. C. Witte.

ciple since the idea was first introduced by Chen (1966). The physical mechanisms of bubble nucleation in a liquid on a heated surface and forced convection of the liquid have been modeled by many researchers. Either mechanism can dominate the heat transfer process, depending on other parameters. Correlation equations generally model either or both mechanisms. The correlation equations chosen for comparison with the present data were developed, for the most part, from refrigerant data bases; some have appeared frequently in the engineering literature, some are relatively new. The original Chen (1966) correlation was included with some form of the other five equations considered by Reid et al. (1987), as was the correlation proposed by Lazarek and Black (1982), the data base of which was closest to the data from the present study. The recent correlation of Jung and Radermacher (1991) was included because it was developed from a data base of numerous refrigerants. In addition, the recent correlation of Steiner and Taborek (1992) was evaluated because of its asymptotic behavior and its extensive data base. Finally, a simplified correlation of data by Stephan and Abdelsalam (1980) was included because other correlations based on this work were used by both Jung and Radermacher (1991) and Steiner and Taborek (1992).

Experimental Apparatus and Test Channel

The heat transfer test apparatus is shown schematically in Fig. 1. It is a closed-loop system that includes a gear pump with variable speed drive, a set of rotameters, a preheater, condenser, accumulator, and sight-glasses. The bladder-type accumulator allows for stable control of system pressure. The sizes of the rotameters (RM in Fig. 1) were chosen to cover a large range of flow rates, from below 50 to over 2500 kg/m^{2}s, and calibrated with a weighing-technique-with-stop-watch. The estimated uncertainty in measurement of flow rate was ±3 percent. Provisions were made to measure temperature and pressure at various locations, as indicated by T and P, respectively, in Fig. 1.

The test channel is shown schematically in Fig. 2. It is a stainless steel (Type 304) tube, with a heated length of 368 mm, and outside and inside diameters of 4.75 mm and 2.92 mm, respectively. Inlet pressure (p_{in}) is measured with a piezoresistive-type transducer, and differential pressure across the channel (Dp) is measured with a strain-gage-type transducer. The pressure transducers were calibrated against a known standard. The estimated uncertainty in the pressure measurements was ±5 percent. The temperature of the liquid at the inlet to the test channel (T_{in}) was measured with a chromel-constantan wall thermocouple, placed 38.1 mm upstream from the start of the heated length; the bulk temperature of the fluid at the outlet (T_{out}) was measured with an in-stream, chromel-constantan-sheathed thermocouple probe, positioned at the exit from the heated length. The probe is inserted into the channel from the end through a specially fabricated tee. The

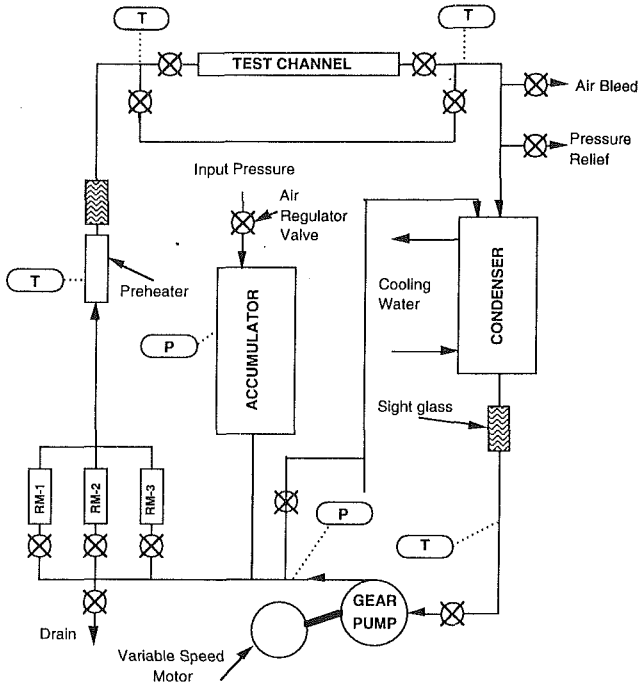

Fig. 1 Schematic diagram of heat transfer test apparatus

Nomenclature

A = channel flow area, m^2
B_o = boiling number = q''/Gi_{fg}
bd = bubble departure diameter, m
c_p = specific heat of fluid, J/kg·°C
D = tube inside diameter, m
D_o = tube outside diameter, m
Dp = differential pressure, kPa
E = electric voltage input, V
Fr = Froude number = $G^2/\rho^2 gD$
G = mass flux, kg/m^{2}s
g = acceleration of gravity = 9.81 m/s^2
h = local heat transfer coefficient, W/m^2°C; Eq. (1)
I = electric current through test channel, A
i_{fg} = latent heat of evaporation, J/kg
k = thermal conductivity, W/m°C
k_{ss} = thermal conductivity of channel material, W/m·°C
L_H = heated length, m
L_{sc} = subcooled length, m; Eq. (7)
M = molecular weight (Steiner and Taborek correlation, Table 1)
Nu = Nusselt number
P = pressure, Pa
Δp_{sat} = $p_{sat}(T_w) - p_{sat}(T_{sat})$
P_{cr} = critical pressure
P_r = reduced pressure = P/P_{cr}
Pr = Prandtl number
q'' = input heat flux, W/m^2
q''_E = electric power input, W/m^2 Eq. (5)
q_T = heat transfer rate, W
q''_T = input heat flux calculated from enthalpy increase of fluid over heated length, W/m^2; Eq. (2)
R_a = surface roughness (Steiner and Taborek Correlation, Table 1)
Re = Reynolds number = GD/μ
T = temperature, °C
T_{sat} = saturation temperature, °C
T'_{sat} = saturation temperature at start of bulk boiling, °C; Eq. (6)
ΔT_{sat} = $T_w - T_{sat}$
T'_w = temperature of tube outer wall, °C
X_{tt} = Martinelli parameter
x = equilibrium mass quality; Eq. (10)
z = distance along channel, m
η = heat loss factor; Eq. (4)
μ = viscosity, kg/m·s
ρ = mass density, kg/m^3
σ = surface tension, N/m

Subscripts

conv = convection
g, G = gas or vapor
in = test section inlet
l, L = liquid
NB = nucleate boiling
out = test section outlet
pool = pool boiling
sat = saturation
ss = stainless steel
TP = two-phase condition
w = tube wall at the I.D.
z = at location z along channel length

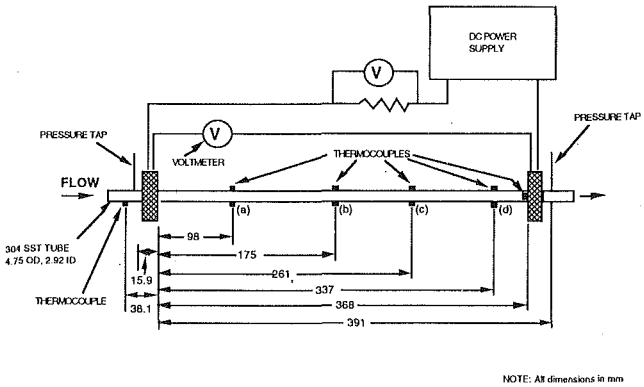

Fig. 2 Test channel, showing locations of thermocouples and pressure taps

Table 1 Experimental runs

G (kg/m^2s)	q''_T (kW/m^2)	Psat (kPa)	G (kg/m^2s)	q''_T (kW/m^2)	Psat (kPa)
50	8.8	151	200	27.0	134
	10.1	130		27.0	134
	10.1	151		41.8	136
	14.2	126		61.9	130
	16.5	124			
100	16.3	154	242	18.4	143
	16.4	127		25.3	158
	21.5	152		46.3	160
	25.5	152		55.4	160
	30.0	125		74.9	132
150	34.8	143	300	44.7	148
	44.4	152		63.3	151
				90.8	135

base of the probe is in the tee approximately 100 mm from the heated length. It is estimated that the temperature measurements were accurate to within $\pm 0.2°C$.

As illustrated in Fig. 2, the test channel was uniformly heated by passing direct electrical current through the channel wall. The temperature of the outside wall was measured at four locations along the channel length (98, 175, 261, and 337 mm from the start of the heated length at the inlet, corresponding to L/D = 34, 60, 89, and 115, respectively) with four pairs of chromel-constantan thermocouples oriented to measure temperature at the top and bottom of the channel and attached to the surface with electrically insulating, thermally conductive epoxy. Total electrical power supplied to the test channel was determined from a measurement of the overall voltage E across the channel and the current I, as determined from the measured voltage across a calibrated resistance installed in series with the test channel.

Measurements were recorded with a Hewlett-Packard (HP) data acquisition system (DAS) consisting of an HP Vectra microcomputer and a Model 3421A Data Acquisition/Control Unit. After steady state was achieved, based on analog recordings of stream and wall temperatures, all of the sensor output voltages were read by the DAS 30 times and averaged. The process took ≈ 3 min. The results were changed to engineering units and stored on computer disk for future processing.

Testing Procedure and Data Reduction

Single-Phase Heat Transfer. Single-phase tests were performed at mass fluxes ranging from 50 to 2200 kg/m^2s, which included a Reynolds-number range up to 8700, from laminar to turbulent flow. The local heat transfer coefficient, at position z along the length of the tube, is defined as

$$h_z = \frac{q''_T}{(T_{wz} - T_z)}. \tag{1}$$

In Eq. (1), the input heat flux q''_T was obtained from the enthalpy increase of the fluid over the heated length as

$$q''_T = \frac{(GAc_p)(T_{\text{out}} - T_{in})}{\pi D L_H}. \tag{2}$$

For a given mass velocity, outside-wall temperatures were obtained at four axial positions along the length of the test channel, as indicated in Fig. 2. Temperatures from the top and bottom of the channel were then averaged to give an average outside-wall temperature T'_{wz} at each axial position z. Inside-wall temperatures were calculated, accounting for heat generation within and conduction through the wall, as

$$T_{wz} = T'_{wz} + \left(\frac{q_T}{4\pi k_{ss} L_H}\right)\left[\frac{\xi(1 - \ln \xi) - 1)}{1 - \xi}\right], \tag{3}$$

where $\xi = (D_o/D)^2$. The corresponding bulk fluid temperature T_f at each axial position z was determined by interpolation, assuming a linear temperature gradient in the bulk fluid over the heated length.

Only data from measurements in the turbulent regime were considered in validating the test setup. This precluded the need for a mixing device that otherwise would be required to eliminate temperature profile effects, and to assure an accurate temperature measurement. The measured single-phase heat transfer coefficients approach the Petukhov–Popov correlation (Petukhov, 1970) at higher Reynolds numbers where the deviation was within 5 percent. This good agreement served to establish the validity of the measurements and data-reduction method.

Heat loss from the test channel, including end losses, under flow conditions was determined as the ratio of the heat flux determined from the liquid enthalpy change (Eq. (2)) divided by the heat flux calculated from the electric power input,

$$\eta = \frac{q''_T}{q''_E}, \tag{4}$$

where

$$q''_E = \frac{EI}{\pi D L_H}. \tag{5}$$

The heat loss factor η was determined as a function of wall temperature from single-phase tests, and it was subsequently used to determine the input heat flux for flow boiling experiments. (η was ≈ 0.89 for most of the tests.)

Flow Boiling Heat Transfer. The experimental runs are summarized in Table 1. Flow boiling tests were performed at selected values of mass velocity of 50, 100, 150, 200, 242, and 300 kg/m^2s. A preheater was used to vary the inlet temperature between ≈ 20 and 50°C. The fluid entered the test section as subcooled liquid in all tests. The saturation pressure at the outlet ranged from 124 to 160 kPa. The electric power to the test section was set in a particular test to achieve a desired outlet quality or to maintain a prescribed heat flux. The experimental heat flux ranged from 8.8 to 90.75 kW/m^2.

In the data analysis, thermal equilibrium of the vapor and liquid phases was assumed along the entire length of the channel. The length of the subcooled inlet region was determined by iteration from the equation

$$L_{sc} = \frac{GAc_p(T'_{\text{sat}} - T_{in})}{\pi D q''_T}, \tag{6}$$

and a single-phase liquid pressure-drop calculation for P at T'_{sat}. The fluid exited the test section with a quality of <1 in all tests, and the saturation pressure at the exit from the heated length was calculated from the bulk fluid temperature measured there. Linear interpolation was used to determine the fluid saturation pressure at the four measurement locations

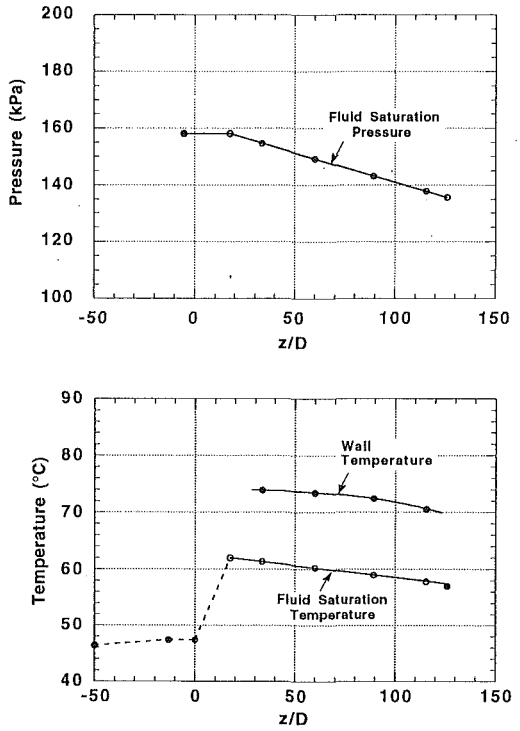

Fig. 3 Typical result illustrating calculation scheme: G = 200 kg/m^{2}s, q''_T = 41.8 kW/m^2: • measured, ○ calculated

along the test channel, after which the fluid saturation temperatures were determined. The total test section pressure drop was small (generally <40 kPa) so that this pressure linearization procedure introduced very little temperature error. Results from a typical boiling test, illustrating the calculational scheme, are shown in Fig. 3.

With knowledge of the input heat flux, inside-wall temperatures and corresponding bulk fluid temperatures, local heat transfer coefficients were calculated from Eq. (1). The mass qualities x at measurement locations z were calculated from heat balances based on q''_T as follows:

$$x(z)=\frac{\pi D(z-L_{sc})q''_T}{AGi_{fg}}. \tag{7}$$

Results and Analysis

Flow boiling data were obtained for a mass quality range from 0 to ≈ 0.9, and the heat transfer coefficients ranged from ≈ 1000 to 6500 W/m^{2}s. These results agree qualitatively with the measurements of Reid et al. (1987) for the evaporation of R-113 in smooth tubes 8.71 and 10.92 mm in diameter.

The bulk boiling region of the test section can be dominated by either the nucleate or convective two-phase component, or both components can contribute to the heat transfer. All three conditions have been found by various experimenters under various system parameters. The present small-channel data were considered carefully to determine the dominant mechanisms. All of the data are shown in Fig. 4, where mass flux is constant in each part of the figure. It is clear that the heat transfer coefficient is a function of heat flux over most of the quality region. This result indicates the nucleate boiling mechanism.

The knowledge of two-phase flow patterns is often important in interpreting and correlating data. Thus, flow pattern identification is included in Fig. 4. The transition boundaries were obtained from the flow pattern map developed by Damianides and Westwater (1988) for a 3-mm-dia tube, and based on adiabatic tests with air–water mixtures. It is recognized that the fluid properties of air/water mixtures are different from Freon vapor/liquid mixtures, and that surface tension, as well as vapor/liquid density ratio, can be expected to influence flow patterns. However, the channel geometry studied by Damianides and Westwater was quite similar to the present case, and comparison of the present data with reported flow patterns is instructive. Typically, for refrigerants flowing in evaporator tubes, qualities above ≈ 0.2 produce void fractions above 0.8. In larger diameter channels, the flow pattern is usually annular up to CHF, and the convective heat transfer mechanism dominates (Jung and Radermacher, 1991; Reid et al., 1987; Carey et al., 1992). However, the flow patterns indicated in Fig. 4 show that, for the small-diameter channel of this study, the predominant flow regime is slug flow.

The flow patterns of Wambsganss et al. (1991, 1992) in small rectangular channels were similar to those of Damianides and Westwater (1988) in small-diameter tubes. Application of the flow pattern maps to predict quality at the transition to annular flow indicated that annular flow generally did not start until qualities of 0.6 to 0.8. This condition is postulated to be a direct consequence of the small channel dimension that allows the crest of a wave on a liquid film to reach the opposite channel wall, producing a slug of liquid in a situation that would produce stratified or annular flow in a larger channel. The majority of the boiling data from the small-diameter tubes used in the present study also fall into the plug and slug pattern regions, with only a few measurements falling into the annular or wave flow pattern regions. The thick-liquid regions of slug flow are more likely to support nucleation than the thin-liquid films of annular flow. In fact, the data of this study show dominance of the nucleation mechanism by virtue of the heat flux dependence and mass flux independence of the data (see Figs. 4 and 5). Thus, two-phase flow patterns peculiar to small channels support the nucleation dominance observed in the data, as do the high boiling numbers of the data to be discussed subsequently.

Evaporation Heat Transfer Correlations

Reid et al. (1987) identified six in-tube evaporation heat transfer correlations, five of which are commonly associated with refrigerants: Chaddock–Brunemann [see Reid et al. (1987)], Pujol–Stenning (1969), Shah (1976), Kandlikar (1983), and Gungor–Winterton (1986). Reid et al. (1987) evaluated these five correlations and the Chen correlation (Chen, 1966), using data they obtained from evaporation of R-113 (the refrigerant used in this study) in tubes 8.71 and 10.92 mm in diameter. They concluded that several of the correlations showed reasonable agreement with the data at qualities >0.2. The mean deviations of the Gungor–Winterton (1986), Chaddock–Brunemann [see Reid et al. (1987)], and Kandlikar (1983) correlations from the 8.71-mm-tube data were 9.6, 12.6, and 13.5 percent, respectively. These six correlations were also compared with small-tube data of the present study. However, the original Gungor–Winterton (1986) correlation used by Reid et al. (1987) was replaced by a newer version by Liu and Winterton (1988), and the original Kandlikar correlation (1983) was replaced by the latest version (Kandlikar, 1990). These correlations, as well as other correlations that were evaluated in this study, are given in Table 2. Results are presented in Figs. 6–11 and Table 3, where statistical comparison of the correlations, based on mean deviation and percentage of data points predicted within ± 20 percent, is also given.

The Chen (1966) correlation was the first to use the superposition principle of nucleate and convection-dominated heat transfer. Used with boiling water, it was included here because of its wide use and as a benchmark. The results of all of the data of the present study are compared with this correlation in Fig. 6. There is considerable scatter in the plot, but the predictions are well centered in the data.

The predictions of the correlations of both Chaddock and

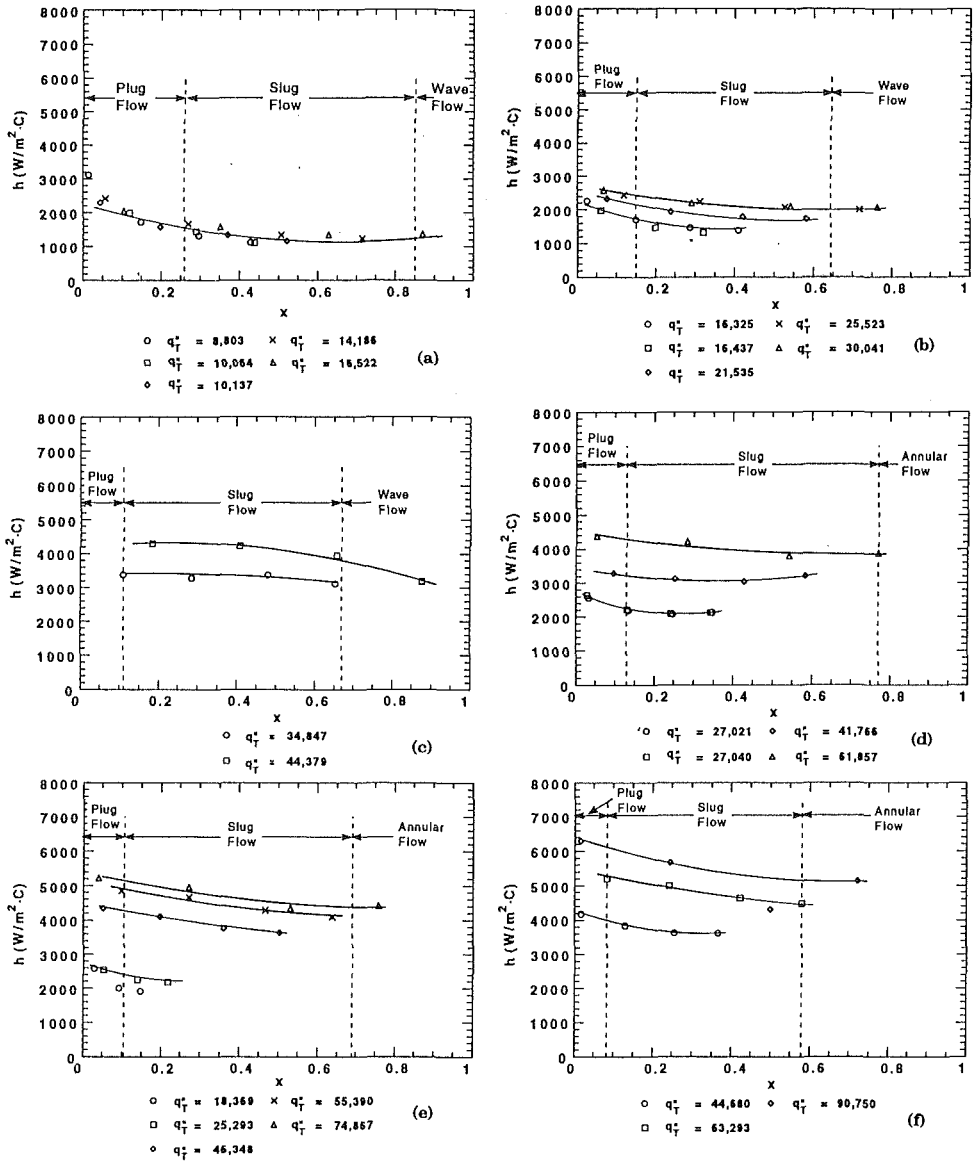

Fig. 4 Heat transfer coefficients at constant mass fluxes of: (*a*) G = 50 kg/m^{2}s, (*b*) G = 100 kg/m^{2}s, (*c*) G = 150 kg/m^{2}s, (*d*) G = 200 kg/m^{2}s, (*e*) G = 242 kg/m^{2}s, and (*f*) G = 300 kg/m^{2}s; q_T'' = W/m^2

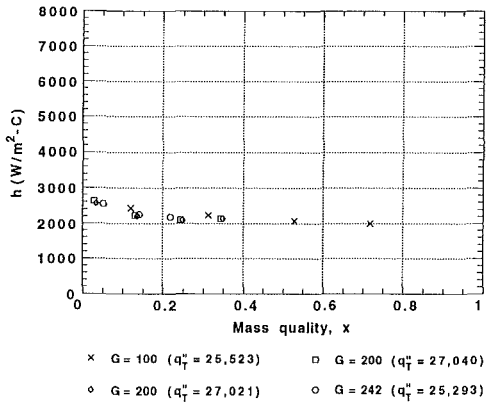

Fig. 5 Heat transfer coefficients at constant heat flux; q_T'' = W/m^2, G = kg/m^2

Brunemann [see Reid et al. (1987)] and Pujol and Stenning (1969) significantly underpredicted the data, with the Chaddock and Brunemann correlation the better performing of the two, as shown in Table 3.

The Shah (1976) correlation involved the use of graphs given in that reference, although in a later publication, Shah (1982), curves were fit to the graphs. The predictions of the Shah (1976) correlation are compared with the present data in Fig. 7. The results are similar to the Chen (1966) correlation of Fig. 6, where the predictions are centered in the data; however, there is considerable scatter, albeit less than in the Chen predictions (see Table 3).

Winterton and his colleagues presented three correlations in the literature: the initial correlation (Gungor and Winterton, 1986) was used by Reid et al. (1987) in evaluating their large-tube R-113 data. The correlation was revised in 1987 (Gungor and Winterton, 1987) and again in 1988 (Liu and Winterton, 1988). The most recent correlation (Liu and Winterton, 1988) was used in this investigation, and although the mean deviation is good (see Table 3), the data were consistently underpredicted (see Fig. 8).

The Kandlikar (1990) correlation had a mean deviation slightly greater than that of the Liu and Winterton (1988) correlation (see Table 3). However, as shown in Fig. 8, in contrast to the Liu and Winterton correlation it mostly overpredicted the data.

Three other correlations were evaluated with the present data: Lazarek and Black (1982), Jung et al. (1989, 1991), and

Table 2 Heat transfer correlations as applicable to experimental data of this study

Source	Correlation
Chen (1966)	$h_{TP} = h_{conv} + h_{NB}$ which is equivalent to $h_{TP} = Fh_\ell + Sh_{pool}$ where, $F = 2.35\left(\frac{1.}{X_{tt}} + 0.213\right)^{0.736}$, for $\frac{1}{X_{tt}} > 0.1$ $h_{pool} = 0.00122\left(\frac{k_\ell^{0.79} c_{p\ell}^{0.45} \rho_\ell^{0.49}}{\sigma^{0.5} \mu_\ell^{0.29} i_{fg}^{0.24} \rho_g^{0.24}}\right) \Delta T_{sat}^{0.24} \Delta p_{sat}^{0.75}$ $S = \left(1 + 0.12 Re_{TP}^{1.14}\right)^{-1}$, for $Re_{TP} < 32.5$ $Re_{TP} = \frac{G(1-x)D}{\mu_\ell}(F^{1.25})(10^{-4})$
Chaddock and Brunemann (1967)	$h_{TP} = 1.91\left[\left(Bo \times 10^4\right) + 1.5\left(\frac{1}{X_{tt}}\right)^{0.67}\right]^{0.6} h_\ell$
Pujol and Stenning (1969)	$h_{TP} = 4.0\left(\frac{1}{X_{tt}}\right)^{0.37} h_\ell$
Shah (1976)	$h_{TP} = \psi h_\ell$ $Fr_\ell > 0.04$, $Bo > 0.25 \times 10^{-4}$ ψ: From chart [Shah (1982)]
Liu and Winterton (1988)	$h_{TP} = [(Eh_\ell)^2 + (Sh_{pool})^2]^{1/2}$ where, $h_{pool} = 55\left(\frac{P}{P_{cr}}\right)^{0.12}\left[-\log_{10}\left(\frac{P}{P_{cr}}\right)\right]^{-0.55} m^{-0.5} q''^{0.67}$ $E = \left[1 + (x) Pr_\ell \left(\frac{\rho_\ell}{\rho_g} - 1\right)\right]^{0.35}$ $S = \left[1 + 0.055 E^{0.1} (Re_\ell)^{0.16}\right]^{-1}$
Jung and Radermacher (1989)	$h_{TP} = h_{NB} + h_{conv}$ $h_{TP} = Nh_{sa} + F_p h_\ell$ where $h_{sa} = 207 \frac{k_\ell}{(bd)}\left[\frac{q''(bd)}{k_\ell T_{sat}}\right]^{0.745}\left(\frac{\rho_g}{\rho_\ell}\right)^{0.581} Pr_\ell^{0.533}$ $(bd) = 0.146\beta\left[\frac{2\sigma}{g(\rho_\ell - \rho_g)}\right]^{0.5}$, $\beta = 35°$ $N = \begin{cases} 4048\, X_{tt}^{1.22} B_o^{1.13}, & \text{for } X_{tt} < 1 \\ 2.0 - 0.1 X_{tt}^{-0.28} B_o^{-0.33}, & \text{for } 1 < X_{tt} \le 5 \end{cases}$ $F_p = 2.37\left(0.29 + \frac{1}{X_{tt}}\right)^{0.85}$ $T_{sat} = °K$
Steiner and Taborek (1992)	$h_{TP} = \left[(h_{NB})^n + (h_{conv})^n\right]^{1/n}$ which is equivalent to $h_{TP} = \left[(h_{NB,o} F_{NBf})^n + (h_L F_{TP})^n\right]^{1/n}$ where $n = 3$

Table 2 (Cont'd)

Source	Correlation
	$F_{TP} = \left[(1-x)^{1.5} + 1.9(x)^{0.6}\left(\frac{\rho_\ell}{\rho_g}\right)^{0.35}\right]^{1.1}$, for $x \le 0.6$ and $F_{TP} = \left\{\left[(1-x)^{1.5} + 1.9(x)^{0.6}(1-x)^{0.01}\left(\frac{\rho_\ell}{\rho_g}\right)^{0.35}\right]^{-2.2} + \left[\left(\frac{h_G}{h_L}\right)(x)^{0.01}\left(1 + 8(1-x)^{0.7}\left(\frac{\rho_\ell}{\rho_g}\right)^{0.67}\right)\right]^{-2}\right\}^{-0.5}$, for $x > 0.6$ $h_{NB,o} = 2180$ W/m^{2}K, for R-113 $F_{NBf} = f(\dot{m}, x) F_{pf}\left(\frac{q''}{q''_{of}}\right)^{nf(P_r)} F(D) F(R_a) F(M)$ $f(\dot{m},x) = 1$ (for vertical flow nucleate boiling) $q''_{of} = 20{,}000$ W/m^2 $F_{pf} = \left[2.816(P_r)^{0.45}\left(3.4 + \frac{1.7}{1-(P_r)^7}\right)(P_r)^{0.37}\right]$, for $P_r \le 0.95$ $nf(P_r) = 0.8 - (0.1)\exp(1.75\, P_r)$, for all fluids except cryogenics $F(D) = \left(\frac{D}{d_o}\right)^{-0.4}$, where $d_o = 0.01$m $F(R_a) = \left(\frac{R_a}{R_{a,o}}\right)^{0.133} = 1$ $F(M) = 0.377 + 0.119\,\dot{m}(M) + 2.8427 \times 10^{-5}(M)^2$
Stephan and Abdelsalam (1980)	$h_{TP} = C_4\, q''^{0.745}$ $C_4 = 1.2$ for R-113, and P in the range 140-180 kPa
Lazarek and Black (1982)	$h_{TP} = 30 Re_L^{0.857} Bo^{0.714}\left(\frac{k_\ell}{D}\right)$
Kandlikar (1990)	$h_{TP} = \left[D_1(Co)^{D_2}(25 Fr_\ell)^{D_5} + D_3(Bo)^{D_4} 25(Fr_\ell)^{D_6}(F_{f\ell})\right] h_\ell$ where, Constant: For Co < 0.65 / For Co > 0.65 D_1: 1.136 / 0.6683 D_2: −0.9 / −0.2 D_3: 667.2 / 1058 D_4: 0.7 / 0.7 $D_5 = D_6 = 0$, for $Fr_\ell > 0.04$ $Co = \left(\frac{1-x}{x}\right)^{0.8}\left(\frac{\rho_g}{\rho_\ell}\right)^{0.5}$ $F_{f\ell} = 1.3$, for R-113 $Fr_\ell = \frac{G^2}{\rho_\ell^2 g D}$

[a]In the above correlations the following definitions are used:

Dittus-Boelter correlation for single-phase heat transfer:

$$h_\ell = 0.023\left(\frac{k_\ell}{D}\right)(Re_\ell)^{0.8}(Pr_\ell)^{0.4};$$

$$h_L = 0.023\left(\frac{k_\ell}{D}\right)(Re_L)^{0.8}(Pr_\ell)^{0.4};$$

$$h_G = 0.023\left(\frac{k_G}{D}\right)(Re_G)^{0.8}(Pr_g)^{0.4}$$

Table 2 (Cont'd)

Source	Correlation
Boiling number:	$Bo = \frac{q''}{G i_{fg}}$
Martinelli parameter:	$X_{tt} = \left(\frac{1-x}{x}\right)^{0.9}\left(\frac{\rho_g}{\rho_\ell}\right)^{0.5}\left(\frac{\mu_\ell}{\mu_g}\right)^{0.1}$
Reynolds number:	$Re_\ell = \frac{G(1-x)D}{\mu_\ell}$; $Re_L = \frac{GD}{\mu_\ell}$; $Re_G = \frac{GD}{\mu_g}$
Prandtl number:	$Pr_\ell = \frac{c_{p\ell}\mu_\ell}{k_\ell}$; $Pr_g = \frac{c_{pg}\mu_g}{k_g}$

All fluid properties are based on saturation temperature.

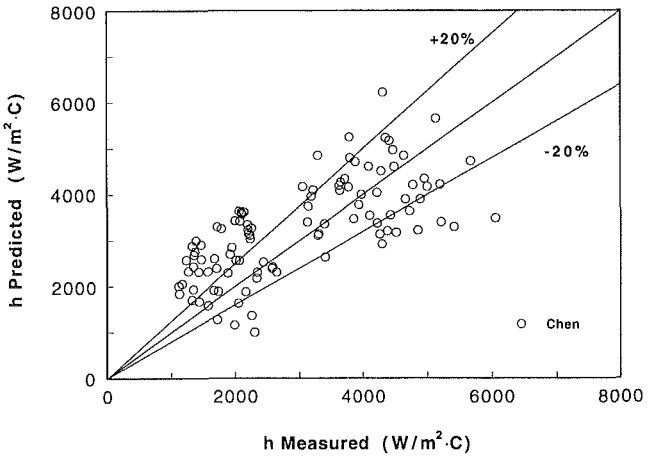

Fig. 6 Comparison of measured heat transfer coefficients with predictions of Chen correlation (1966)

Steiner and Taborek (1992). Each has a feature that suggested its inclusion in the present evaluation.

The correlation of Lazarek and Black (1982) was used in this study because the data base for it, viz., the boiling of R-113 inside of 3.1-mm-dia tubes, was the closest we found to the present experiments. The experiments of Lazarek and Black (1982) were different from the present study in that they used a vertically oriented test section with both upflow and downflow occurring simultaneously in different sections connected by a curved connecting section. The heat transfer correlation that was developed for these data is given in Table 2, and predictions are compared to the present data in Fig. 9. With a mean deviation of 12.7 percent (Table 3), the results are the best of all the correlations considered. As shown in Fig. 9, there is some larger error at low heat transfer coefficients that correspond to low qualities, but 85 percent of the data are correlated within ±20 percent (Table 3), and the predictions are well centered among the data.

Jung et al. (1989, 1991) recently developed a correlation specifically for refrigerants boiling in a relatively large (9-mm-dia) tube; the authors reported a mean deviation of 7.2 percent from their experimental data obtained with R-22, R-12, R-152a,and R-114. The correlation in Table 2 that is attributed to Jung and Radermacher (1991) was interpreted in this study from the work of Stephan and Abdelsalam (1980) and is not exactly as given by Jung and Radermacher (1989). In Fig. 10,

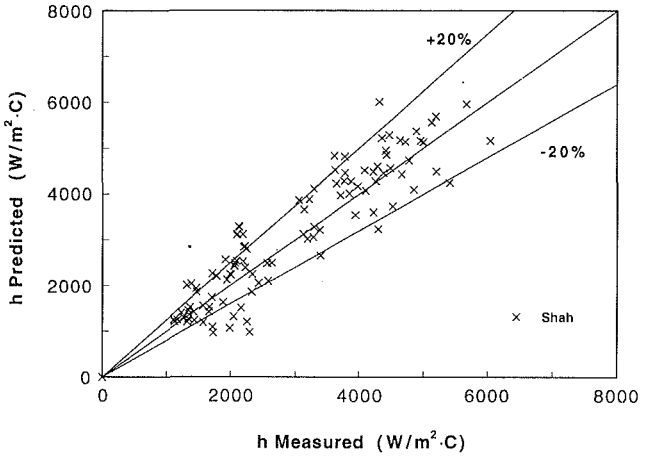

Fig. 7 Comparison of measured heat transfer coefficients with predictions of Shah correlation (1976)

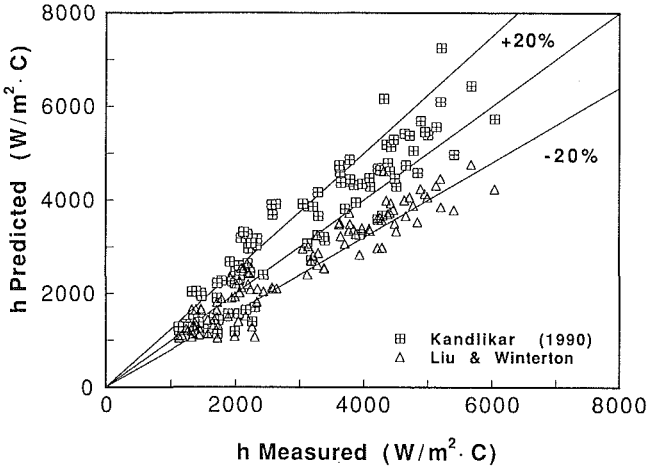

Fig. 8 Comparison of measured heat transfer coefficients with predictions of Kandlikar (1990) and Liu and Winterton (1988) correlations

Table 3 Statistical comparison of correlations

Correlation	Mean Deviation[a] (Percent)	Percentage of Data in ±20% range
Lazarek & Black (1982)	12.7	84.8
Stephan and Abdelsalam (1980)	12.9	83.8
Liu & Winterton (1988)	15.5	74.3
Jung & Radermacher (1991)	16.0	75.2
Shah (1976)	17.6	68.6
Kandlikar (1990)	19.7	63.8
Chaddock & Brunemann (1967)	24.0	50.5
Chen (1966)	36.0	41.9
Pujol & Stenning (1969)	53.0	6.7

[a]Mean deviation $= \frac{1}{N}\sum\frac{|h_{meas.} - h_{pred.}|}{h_{meas.}} \times 100\%$

the correlation is evaluated against the present data. The correlation shows good agreement with the data except for a few measurements, which are all at low quality. Seventy-five percent of the data fall within ±20 percent of predictions.

A new correlation that was considered for application to the present data is a new treatment from Steiner and Taborek (1992). This correlation was developed from a data base of over 12,000 measurements. It was developed along the superposition principle of Chen (1966), but it added the Churchill

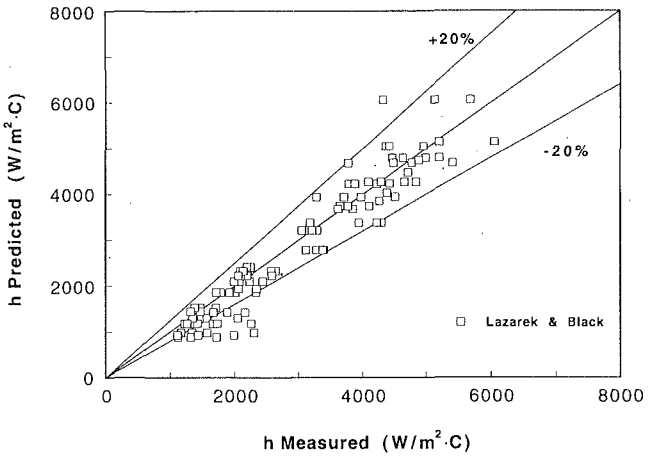

Fig. 9 Comparison of measured heat transfer coefficients with predictions of Lazarek and Black correlation (1982)

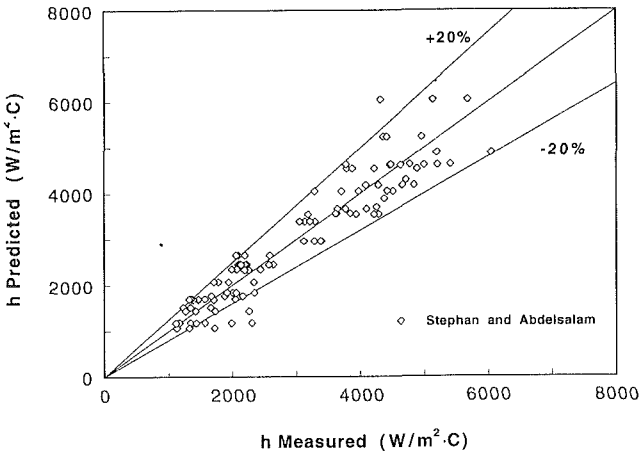

Fig. 11 Comparison of measured heat transfer coefficients with predictions of simplified Stephan and Abdelsalam correlation (1980)

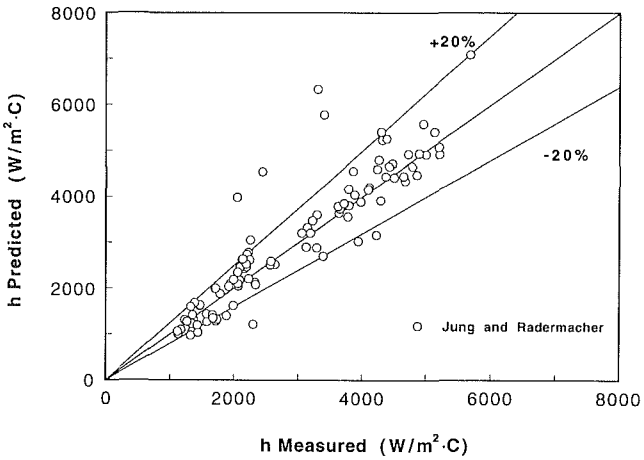

Fig. 10 Comparison of measured heat transfer coefficients with predictions of Jung and Radermacher correlation (1989)

(1974) technique for introducing the proper asymptotic predictions well into the nucleation- or convection-dominated heat transfer regimes. Although the correlation was developed for vertical-flow boiling in large diameter tubes, it was applied to the horizontal data of this study. The parameter that accounts for differences between nucleate-pool boiling and nucleation-dominant-flow boiling was much too large, and the correlation overpredicted the present data by a factor of approximately three.

The final correlation that was tried is the simplified correlation of Stephan and Abdelsalam (1980). As can be determined from Table 2, the correlation is a function of only the heat flux and a parameter, dependent on pressure, which is a constant for a particular fluid. Data predicted from this correlation are given in Fig. 11, where the correlation can be seen to be well-centered in the data, with a mean deviation of 12.9 percent and 83.8 percent of the predicted data points within ±20 percent (see Table 3).

Discussion

Evaluation of the applicability of existing correlations and/or the development of new correlations for heat transfer require a knowledge of whether or not a nucleate boiling mechanism or a convective mechanism is dominating a particular quality range or length of the heat transfer channel. To avoid unacceptably high pressure drops in compact heat exchangers, the small channel cross section leads to low mass fluxes with Reynolds numbers typically in the laminar regime for the subcooled liquid. Relatively short channel lengths lead to high heat flux to produce superheated vapor. This combination of high heat flux and low mass flux results in high boiling numbers for small channels. All of the boiling numbers of the tests in this study were relatively high, ranging from 5×10^{-4} to 25×10^{-4}. This parameter played a key role in interpeting the differences and predictions of the various correlations that were tested. In this regard, it should be noted that Steiner and Taborek (1992) also reported success in using the boiling number as a measure of the nucleate-boiling contribution to a flow boiling situation.

Lazarek and Black (1982) obtained heat transfer data over the entire range of qualities, up to CHF. They concluded that, in their experiments, nucleation was the dominant heat transfer mechanism controlling the wall heat transfer process in all tests. This conclusion was based on the observed strong dependence of heat transfer coefficients on heat flux with negligible influence of quality. Pujol and Stenning (1969) showed that, as the boiling number increases, the transition quality, from nucleation dominated to convection dominated boiling, also increases. Following the work of Pujol and Stenning (1969), Lazarek and Black (1982) suggested that the occurrence of nucleation-dominated heat transfer all the way to CHF could be attributed to the high (above 5×10^{-4}) boiling numbers of their data.

The high boiling numbers and slug-flow pattern of the data of this study are typical of what can be expected in boiling of refrigerants in compact heat exchangers with similar-size channels, as previously discussed. The resulting dominance of the nucleation mechanism in such systems is likely to be best correlated by models that accentuate the nucleation heat transfer component or use it exclusively. In attempting to verify this condition, all of the correlations considered in this study were carefully examined to determine the relative contributions of the nucleation and convective terms to the present data, all of which exhibit nucleation domination. It was found that, in general, those correlations that predicted the data best were dominated by the nucleation term. The converse was also found to be true; correlations that predicted the data poorly had large convective boiling terms.

The Chen (1966) correlation showed considerable spread, compared with the present data (see Fig. 6). It was found that the nucleation and convection components of the heat transfer were predicted to be of roughly equal magnitudes for most of the data. This condition is contrary to the data, and the spread in the predictions is a consequence.

The Shah (1976) correlation uses a basic nondimensionali-

zation typical of many correlations. As pointed out by Steiner and Taborek (1992), use of a convective heat transfer coefficient to nondimensionalize the nucleation contribution to heat transfer is not in agreement with the physics of the situation. The heat transfer coefficient h_l includes both mass flux and quality effects that are inappropriate in this regime. However, the Shah correlation has a mass flux effect in the boiling number of the nucleation heat transfer model. The mass flux from the boiling number and the convection coefficient used for nondimensionalization purposes produce a net small mass flux effect of $G^{0.3}$. The fact that there is no separate convection term in the Shah correlation makes it appropriate for the data of this study. The result is that the correlation predicts the data reasonably well, although there is some scatter, as seen in Fig. 7.

The correlations of both Chaddock and Brunemann [see Reid et al. (1987)] and Pujol and Stenning (1969) are nondimensionalized with a convective heat transfer coefficient. The mass flux effects in both correlations are larger than in the Shah (1976) correlation, and the data predictions are not good, as shown in Table 3.

In the correlation of Kandlikar (1990), which is also nondimensionalized by h_l, separate terms represent nucleation and convection contributions to the heat transfer. These terms are of comparable magnitude at higher qualities, with a mass flux effect in both terms giving rise to the deviation from the data shown in Table 3.

The latest correlation from Winterton (Liu and Winterton, 1988) is similar to the Steiner and Taborek (1992) correlation in the sense that it is based on the correct asymptotes for the Chen (1966) correlation form. Because there are two terms in this correlation, one for nucleation and one for convection, the relative magnitudes must be improved to predict the present data satisfactorily, which, despite a relatively small mean deviation of 15.5 percent, are consistently underpredicted by this correlation in its present form.

The correlation of Lazarek and Black (1982) contains only a nucleation term, because that was the data base from which it was derived. The mass flux appears both in a Reynolds number and in the boiling number such that the net effect is $G^{0.14}$. This minimal mass flux effect, coupled with no explicit convective term in the correlation, was consistent with the data of this investigation. In Fig. 9, this correlation is shown to predict the present data best of all the correlations tested. It also suggests that the 3-mm tube diameter is small enough for surface tension forces to dominate gravitational forces, inasmuch as the Lazarek and Black (1982) correlation, developed for vertical tubes (upflow and downflow), predicts the present horizontal-tube data so well.

The correlation of Jung and Radermacher (1989) is of the Chen (1966) type with two terms. Based on their study of 13 different refrigerants, they concluded that, in the quality range >20 percent, nucleate boiling is predicted to be fully suppressed for all refrigerants, indicated by the fact that the heat transfer coefficient increases with quality. Thus, most of the data base for this correlation was in the convection-dominated region at qualities above 0.2. However, the very good comparison of the correlation with the present data, shown in Fig. 10, is a result of the predicted dominance of the nucleate boiling term. This term was adopted from the general work of Stephan and Abdelsalam (1980), whose work also included simpler but fluid-specific correlations for nucleate boiling heat transfer.

The Stephan and Abdelsalam correlation listed in Table 2 is for R-113 and the pressure range of the present data. The correlation has a heat flux and no mass flux dependence (for the natural convection boiling situation of Stephan and Abdelsalam, 1980), and it predicts the data of this study very well, as shown in Fig. 11. This comparison supports the nucleate-boiling domination trend of the data, as do all other comparisons of this study where improved data prediction accompanies a prediction of nucleate boiling as the dominant heat transfer mechanism.

The Steiner and Taborek (1992) work is based on a combination of the superposition model with an interesting technique (Churchill, 1974) that produces the proper asymptotes to the data. Although the correlation is based on a very large data base, the spread of predictions from the present data is due to a reasonably large predicted convective term. (Arbitrarily decreasing the factor $f(\dot{m}, x)$ in Table 2 to 0.37 produced data predictions with a mean deviation of 17.5 percent, and 67 percent of the data were predicted within an accuracy of ± 20 percent.)

Conclusions

The results of this study showed that the local heat transfer coefficient for evaporation of R-113 in a small-diameter, horizontal tube is a strong function of heat flux, and only weakly dependent on mass flux and mass quality. Qualitatively, the values measured for heat transfer coefficients in this study were in good agreement with the measurements of Reid et al. (1987) at relatively high boiling numbers, in the range of 3×10^{-4} to 6×10^{-4}, giving rise to large regions of nucleation-dominant flow.

The flow pattern map of Damianides and Westwater (1988) for a 3-mm-dia tube was superimposed on the heat transfer data of this study. Although the map was developed from air–water data it indicated that most of the present data were in the plug and slug flow regions. The implication is that nucleation in the thick-liquid layers of these regions was not suppressed. The slug flow pattern regime occurs over a much larger parameter range with refrigerants in small-diameter channels compared with large channels, and the heat transfer trends show a dominance of the nucleation mechanism.

The dominance of the nucleation mechanism in the present data was also attributed to the high boiling number of the data. As a result, two-phase heat transfer correlations that predicted this dominance also predicted the data well if they also properly modeled the physical parameters. The correlation of Lazarek and Black (1982) predicted the data very well; mean deviations were ≈ 13 percent and >80 percent of the data were predicted within ± 20 percent. The simplified correlation of Stephan and Abdelsalam (1980) also predicted the data very well where heat flux, not mass flux, was the controlling parameter. In a similar manner, the recent correlation of Jung and Radermacher (1989), based on data of many refrigerants in large diameter tubes, predicted the present data well (with the exception of very low qualities) because of the dominance of the nucleation term.

In general, the small-tube boiling heat transfer coefficient exhibited the characteristics and trends found in larger tubes when nucleation was the dominant heat transfer mechanism. Compact heat exchanger designs used with refrigerants can lead to high boiling numbers and slug flow patterns similar to those of this study. This situation, in turn, leads to nucleation-dominant heat transfer in small-diameter round channels. This is the opposite of the predominantly convective-dominated heat transfer of conventional refrigeration evaporators using large diameter tubes (see for example, Jung and Radermacher, 1989).

Acknowledgments

This work was supported by the U.S. Department of Energy, Office of Conservation and Renewable Energy, under Contract No. W-31-109-Eng-38.

The authors thank Mr. R. K. Smith for his contributions in fabricating the test apparatus and flow channel and performing

the experiments, and Ms. Joyce Stephens for preparing the figures and the overall manuscript for publication. They also thank Mr. Claude Jourdain (University of Illinois at Chicago) for his contributions in the initial evaluation of the in-tube evaporation correlations.

References

ASHRAE, 1989, *Fundamentals*, American Society of Heating, Refrigerating and Air-Conditioning Engineers, Inc., Atlanta, GA.

Carey, V. P., Tervo, P., and Shullenberger, K., 1992, "Partial Dryout in Enhanced Evaporator Tubes and Its Impact on Heat Transfer Performance," SAE Technical Paper 920551.

Chen, J. C., 1966, "A Correlation for Boiling Heat Transfer to Saturated Fluids in Convective Flow," *I & EC Process Des. and Development*, Vol. 5, (3), pp. 322–329.

Churchill, S. W., 1974, *The Interpretation and Use of Rate Data*, Hemisphere Publishing Corp., New York.

Damianides, C. A., and Westwater, J. W., 1988, "Two-Phase Flow Patterns in a Compact Heat Exhanger and in Small Tubes," *Proc. 2nd U.K. National Conf. on Heat Transfer*, Glasgow, Scotland, Vol. II, 1257–1268.

Gungor, K. E., and Winterton, R. H. S., 1986, "A General Correlation for Flow Boiling in Tubes and Annuli," *Int. J. Heat Mass Transfer*, Vol. 29 (3), pp. 351–358.

Gungor, K. E., and Winterton, R. H. S., 1987, "Simplified General Correlation for Saturated Flow Boiling and Comparisons of Correlations With Data," *Chem. Eng. Res. Des.*, Vol. 65, pp. 148–156.

Haralampus, P., Gresham, R. D., and Westwater, J. W., 1975, "Boiling of Liquids in a Compact Plate-Fin Heat Exchanger," *Int. J. Heat Mass Transfer*, Vol. 18, pp. 37–42.

Jung, D. S., McLinden, M., Radermacher, R., and Didion, D., 1989, "A Study of Flow Boiling Heat Transfer With Refrigerant Mixtures," *Int. J. Heat Mass Transfer*, Vol. 32 (9), pp. 1751–1764.

Jung, D. S., and Radermacher, R., 1991, "Prediction of Heat Transfer Coefficient of Various Refrigerants During Evaporation," *ASHRAE Transactions*, Vol. 97, Pt. 2.

Kandlikar, S. S., 1983, "An Improved Correlation for Predicting Two-Phase Flow Boiling Heat Transfer Coefficient in Horizontal and Vertical Tubes," *Heat Exchangers for Two-Phase Flow Applications*, ASME, New York, pp. 3–10.

Kandlikar, S. S., 1990, "A General Correlation for Saturated Two-Phase Flow Boiling Heat Transfer Inside Horizontal and Vertical Tubes," ASME JOURNAL OF HEAT TRANSFER, Vol. 112, pp. 219–228.

Lazarek, G. M., and Black, S. H., 1982, "Evaporative Heat Transfer, Pressure Drop and Critical Heat Flux in a Small Vertical Tube With R-113," *Int. J. Heat Mass Transfer*, Vol. 25, (7), pp. 945–960.

Liu, Z., and Winterton, R. H. S., 1988, "Wet Wall Flow Boiling Correlation With Explicit Nuclear Term," presented at the 5th Miami Int. Symp. on Multiphase Transport and Particulate Phenomena.

Mandrusiak, G. D., Carey, V. P., and Xu, X., 1988, "An Experimental Study of Convective Boiling in a Partially Heated Horizontal Channel With Offset Strip Fins," ASME JOURNAL OF HEAT TRANSFER, Vol. 110, pp. 229–236.

Petukhov, B. S., 1970, "Heat Transfer and Friction in Turbulent Pipe Flow With Variable Physical Properties," *Advances in Heat Transfer*, J. P. Hartnett and T. F. Irvine, Jr., eds., Academic Press, New York, pp. 503–564.

Pujol, L., and Stenning, A. H., 1969, "Effects of Flow Directions on the Boiling Heat Transfer Coefficients in Vertical Tubes," *Co-current Gas-Liquid Flow*, E. R. Rhodes and D. S. Scott, eds., Plenum Press, New York, pp. 401–453.

Reid, R. S., Pate, M. B., and Bergles, A. E., 1987, "Evaporation of Refrigerant 113 Flowing Inside Smooth Tubes," ASME Paper No. 87-HT-51.

Robertson, J. M., 1979, "Boiling Heat Transfer With Liquid Nitrogen in Brazed-Aluminum Plate-Fin Heat Exchangers," *AIChE Symposium Series*, Vol. 75 (189), pp. 151–164.

Robertson, J. M., and Wadekar, V. V., 1988, "Boiling Characteristics of Cyclohexane in Vertical Upflow in Perforated Plate-Fin Passages," *Heat Transfer—Houston 1988*, AIChE Symposium Series, Vol. 84, (263), pp. 120–125.

Shah, M. M., 1976, "A New Correlation for Heat Transfer During Boiling Flow Through Pipes," *ASHRAE Transactions*, Vol. 82, (2), pp. 66–68.

Shah, M. M., 1982, "Chart Correlation for Saturated Boiling Heat Transfer: Equations and Further Study," *ASHRAE Trans.*, Vol. 88, pp. 185–196.

Steiner, D., and Taborek, J., 1992, "Flow Boiling Heat Transfer in Vertical Tubes Correlated by an Asymptotic Model," *Heat Transfer Eng.*, Vol. 13(2), pp. 43–69.

Stephan, K., and Abdelsalam, M., 1980, "Heat Transfer Correlations for Natural Convection Boiling," *Int. J. Heat Mass Transfer*, Vol. 23, pp. 73–87.

Wambsganss, M. W., Jendrzejczyk, J. A., and France, D. M., 1991, "Two-Phase Flow Patterns and Transitions in a Small, Horizontal, Rectangular Channel," *Int. J. Multiphase Flow*, Vol. 17(3), pp. 327–342.

Wambsganss, M. W., Jendrzejczyk, J. A., and France, D. M., 1992, "Two-Phase Flow and Pressure Drop in Flow Passages of Compact Heat Exchangers," SAE Technical Paper 920550.

Westwater, J. W., 1986, "Compact Heat Exchangers With Phase Change," *Heat Transfer 1986*, Proc. 8th Int. Heat Transfer Conf., San Francisco, Vol. 1, pp. 269–278.

Xu, X., Mandrusiak, G. D., and Carey, V. P., 1988, "Convective Boiling and Two-Phase Flow in a Partially Heated Horizontal Channel With Cross-Ribbed Walls," *Particulate Phenomena and Multiphase Transport*, Vol. 2, T. N. Veziroglu, ed., Hemisphere Publishing Corp., New York.

Orientation Effects on Critical Heat Flux From Discrete, In-Line Heat Sources in a Flow Channel

C. O. Gersey
Graduate Student.

I. Mudawar
Professor and Director.

Boiling and Two-Phase Flow Laboratory,
School of Mechanical Engineering,
Purdue University,
West Lafayette, IN 47907

The effects of flow orientation on critical heat flux (CHF) were investigated on a series of nine in-line simulated microelectronic chips in Fluorinert FC-72. The chips were subjected to coolant in upflow, downflow, or horizontal flow with the chips on the top or bottom walls of the channel with respect to gravity. Changes in angle of orientation affected CHF for velocities below 200 cm/s, with some chips reaching CHF at heat fluxes below the pool boiling and flooding-induced CHF values. Increased subcooling was found to dampen this adverse effect of orientation slightly. Critical heat flux was overwhelmingly caused by localized dryout of the chip surface. However, during the low velocity downflow tests, low CHF values were measured because of liquid blockage by vapor counterflow and vapor stagnation in the channel. At the horizontal orientation with downward-facing chips, vapor/liquid stratification also yielded low CHF values. Previously derived correlations for water and long, continuous heaters had limited success in predicting CHF for the present discontinuous heater configuration. Because orientation has a profound effect on the hydrodynamics of two-phase flow and, consequently, on CHF for small inlet velocities, downflow angles should be avoided, or when other constraints force the usage of downflow angles, the inlet liquid velocity should be sufficiently large.

Introduction

With the continuing trend of miniaturization of electronic components in chips, power dissipation from the chip is expected to continue to increase during the present and next decades. As a result, a need has arisen in the electrical packaging industry for new cooling schemes capable of dissipating heat from densely packaged, high-heat-flux systems. Direct immersion cooling in a dielectric fluid with nucleate boiling on the chip surface holds the promise of dissipating high heat fluxes while maintaining the chip at an acceptable operating temperature. However, as in any boiling system, the nucleate boiling regime is limited by the critical heat flux (CHF). Exceeding this heat flux limit causes a vapor blanket to form on the boiling surface, severely decreasing the heat transfer coefficient, which, in turn, causes the surface temperature to increase greatly and the component to fail. Predicting CHF has, therefore, become of paramount importance to the electronic packaging industry before direct immersion cooling with phase change can be utilized.

The nuclear industry has extensively studied CHF, but nuclear simulation systems do not accurately represent electrical components, such as circuit boards, with many small independent heat sources. This forced researchers in recent years to undertake new efforts specifically tailored to the needs of the electronic industry. Attention in these efforts has been focused on determining CHF from a small isolated heat source in pool (Nakayama et al., 1984; Park and Bergles, 1988; Mudawar and Anderson, 1989a, b; Park et al., 1990) and forced-convection boiling (Lee and Simon, 1989; Maddox and Mudawar, 1989; Mudawar and Maddox, 1989, 1990; Samant and Simon, 1989). Mudawar and Maddox (1989) investigated CHF on a single flush-mounted, 12.7 mm × 12.7 mm chip in vertical upflow of FC-72. Critical heat flux was observed to be a result of localized vapor blanketing on the chip surface. They constructed a semi-empirical CHF model from their data according to the following equation:

$$q_m^{**} = \frac{\dfrac{q_m''}{\rho_g U h_{fg}}}{\left(\dfrac{\rho_f}{\rho_g}\right)^{15/23}\left(\dfrac{L}{D_h}\right)^{1/23}\left(1+\dfrac{c_{pf}\Delta T_{sub}}{h_{fg}}\right)^{7/23}\left(1+0.021\,\dfrac{\rho_f}{\rho_g}\dfrac{c_{pf}\Delta T_{sub}}{h_{fg}}\right)^{16/23}} = 0.161\ (\mathrm{We})^{-8/23}. \quad (1)$$

Mudawar and Maddox also observed a change in the slope of their CHF data marking transition between low- and high-velocity CHF regimes. Low-velocity CHF was initiated by the propagation of a fairly continuous vapor blanket, which originated from the downstream edge of the chip. High-velocity CHF was characterized by the merging of smaller patches of vapor on the chip surface.

Only a few studies are available in the literature on CHF from simulated multichip arrays in forced-convection boiling (McGillis et al., 1991; Willingham et al., 1991; Willingham and Mudawar, 1992a, b). McGillis et al. (1991) found that Eq. (1) accurately predicted CHF for their flush-mounted, ten-element array in vertical upflow of R-113. Typically, the last chip in the array attained CHF first, and McGillis et al. used a calculated local subcooling for that chip in utilizing Eq. (1). Invariably, the heat sources in previous studies have been oriented either vertically or horizontally. So far, little attention has been focused on the detailed effects of orientation on forced-convection CHF from simulated microelectronic chips.

Contributed by the Heat Transfer Division for publication in the JOURNAL OF HEAT TRANSFER. Manuscript received by the Heat Transfer Division December 1992; revision received March 1993. Keywords: Boiling, Phase-Change Phenomena, Thermal Packaging. Associate Technical Editor: T. W. Simon.

Many researchers have tested the effect of surface orientation in pool boiling (Class et al., 1960; Githinji and Sabersky, 1963; Marcus and Dropkin, 1963; Chen, 1978; Nishikawa et al., 1983; Kumar et al., 1990) and forced-convection boiling (Simoneau and Simon, 1966; Bartolini et al., 1983; Mishima and Nishihara, 1985; Mishima et al., 1985; Bibeau and Salcudean, 1990) for various experimental configurations unrelated to electronic cooling; however, a full accounting of the orientation effect throughout a 360 deg circle on CHF with an array of discrete heat sources during flow boiling has never been made. This has important implications for design engineers since a thermal analysis is typically performed after the electronic package has been designed. Understanding the g-field effect on boiling performance will aid, perhaps, in formulating constraints on the chip orientation at the onset of the design process as well as providing some guidance in predicting the g-field effect in nonterrestrial environments such as microgravity and vehicular acceleration induced. Beside electronics, heat removal from small sources with varying orientations is also encountered in other applications such as laser devices, x-ray machines, and power supplies.

In the pool boiling studies reviewed, an increase in the nucleate boiling heat transfer coefficient was observed as the surface was rotated away from both horizontal positions (Class et al., 1960; Githinji and Sabersky, 1963; Marcus and Dropkin, 1963; Chen, 1978; Kumar et al., 1990). However, Nishikawa et al. (1983) observed little effect of orientation at high heat fluxes. Critical heat flux decreased severely when the heated surface was oriented in the horizontal, downward-facing position due to vapor accumulation, which kept liquid from reaching the heated surface.

Flow Boiling Orientation Studies

Because of the large density difference between the vapor and liquid phases, two-phase instabilities can occur during low-velocity forced-convection boiling involving downflow. During stable downflow, the vapor bubbles are entrained in the liquid flow forming a two-phase mixture. One type of unstable downflow is characterized by the vapor and the liquid moving in opposite directions because the buoyancy force acting on the vapor is greater than the drag force exerted by the liquid. Changes in vapor motion, from countercurrent at low liquid velocities to cocurrent at high liquid velocities, were observed during the forced-convection boiling of nitrogen in a vertical channel subjected to downflow (Simoneau and Simon, 1966). The liquid nitrogen velocity was varied between 25.9 and 106.7 cm/s for both upflow and downflow, and CHF was observed to be lower for downflow as compared to upflow tests at the same liquid velocity. The difference between upflow and downflow CHF decreased with increasing liquid velocity due to the diminishing effect of buoyancy. In a review article, Gambill (1968) noted that, in some of his previous work with boiling in a vertical channel at very low velocities, the CHF values for downflow were several times smaller than for upflow. The lowest downflow CHF value was measured when the liquid velocity was equal to the bubble rise velocity in the channel.

Mishima et al. (1985) studied the effect of upflow and downflow on CHF in a 6-mm tube in a soft flow loop design, where the flow rate was controlled through a bypass line and a throttle valve upstream of the tube. Downflow CHF values were lower than their upflow counterparts. In addition, the flow rate in downflow tests vacillated around the mean value at a high frequency as the heat flux was increased. A few minutes before CHF, the mean flow rate decreased purportedly as a result of the compressibility of the vapor in the flow loop. No adjustment was made to the flow rate, and CHF ensued. In order to investigate the effects of a compressible volume on flow rate and hence, CHF, a plenum with a volume of 1077 cm^3 was added upstream of the tube. The stagnation of vapor in the tube was found to contribute to a premature CHF in downflow tests. Critical heat flux for all of the downflow conditions tended toward the flooding-induced CHF value as flow rate was decreased to zero.

Mishima and Nishihara (1985) studied similar low-velocity effects of upflow and downflow on CHF in a 2.4 mm × 40 mm rectangular channel. The channel was heated on either one or two of the 40-mm sides, and flow throttling was performed upstream of the test section (soft system). Several flow regimes were observed for low inlet liquid velocities. At extremely small flow rates, CHF was triggered by flooding in downflow. Similarly, for upflow conditions, flooding was observed to cause CHF at small flow rates as the vapor kept liquid from flowing backward into the test section and rewetting the heated surface. Annular flow appeared in the downstream portion of the channel as the flow rate was in-

Nomenclature

A_{he} = heated area (900 mm^2 for the present study)
A_x = channel flow area
c_{pf} = specific heat of liquid
D_h = channel hydraulic diameter $= 4A_x/P_{wet}$
D_{he} = equivalent heated channel diameter $= 4A_x/P_{he}$
g = gravitational acceleration
G = mass velocity
G^* = nondimensional mass velocity $= G/[\rho_g g(\rho_f - \rho_g)\lambda]^{0.5}$
Δh_i = subcooled liquid enthalpy at inlet $= c_{pf}\Delta T_{sub}$
h_{fg} = latent heat of vaporization
k_f = thermal conductivity of liquid
L = chip length in flow direction (10 mm)
L_{he} = heated length (90 mm for the present study)
P = pressure
P_{he} = heated perimeter of channel (10 mm for the present study)
P_{wet} = wetted perimeter of channel
q'' = wall heat flux
q^* = nondimensional heat flux $= q''/[h_{fg}(\rho_g g(\rho_f - \rho_g)\lambda)^{0.5}]$
q''_m = critical heat flux
q^{**}_m = nondimensional critical heat flux defined in Eq. (1)
t = time
T = temperature
ΔT_{sub} = inlet subcooling $= T_{sat} - T_{f,in}$
U = mean inlet liquid velocity
We = Weber number $= (\rho_f U^2 L)/\sigma$
x_e = thermodynamic equilibrium quality
λ = length scale of the Taylor instability $= (\sigma/g(\rho_f - \rho_g))^{0.5}$
ρ = density
σ = surface tension
θ = orientation angle measured from the vertical position

Subscripts

ca = churn turbulent to annular flow transition
f = liquid
F = flooding-induced CHF correlation
g = vapor
H = H-regime CHF correlation, Table 2
HP = HP-regime CHF correlation, Table 2
in = inlet to multichip module
K = Katto and Kurata small L_{he}/D_{he} CHF correlation, Table 2
MM = Mudawar and Maddox CHF correlation, Table 2
pb = pool boiling CHF correlation, Table 2
sat = saturated
$x0$ = corresponding to $x_e = 0$
$x1$ = corresponding to $x_e = 1$

creased for upflow conditions; CHF for these conditions increased with increasing flow rate. As the flow rate was increased for downflow, the bubbles became motionless in the channel as the drag force of the incoming liquid equaled the buoyancy force acting on the bubble; as a result, CHF occurred at an even lower heat flux than for flooding. Bubbles became entrained in the liquid flow with a further increase in flow rate above the stagnation value, and CHF increased. For highly subcooled flow and relatively high flow rates, CHF was observed to occur at the transition between the churn-turbulent and annular flow regimes for upflow and at a liquid thermodynamic quality of zero for downflow. However, because of flooding and bubble stagnation, CHF in a forced-convection boiling system subjected to a small downflow liquid velocity may be considerably lower than CHF in pool boiling.

It is apparent from the findings of Mudawar and Maddox (1989), Mishima et al. (1985), and Mishima and Nishihara (1985) that CHF may result from a number of possible flow and heat transfer induced phenomena. The focus of this paper is to examine these various forms of CHF and assess the applicability of existing CHF correlations to forced-convection boiling from an array of discrete heat sources at different surface orientations.

The flush-mounted multichip module design was chosen to simulate a series of computer chips because this basic design allowed insight into the fundamental understanding of orientation effects without complications arising from variable chip designs. Currently the literature contains orientation studies on systems with heated walls and not on small discrete heat sources typical of a computer. The present study serves to enlighten design engineers to orientation effects in two-phase cooling while serving as a basis for future comparison with studies performed on actual circuit boards with complicated geometries.

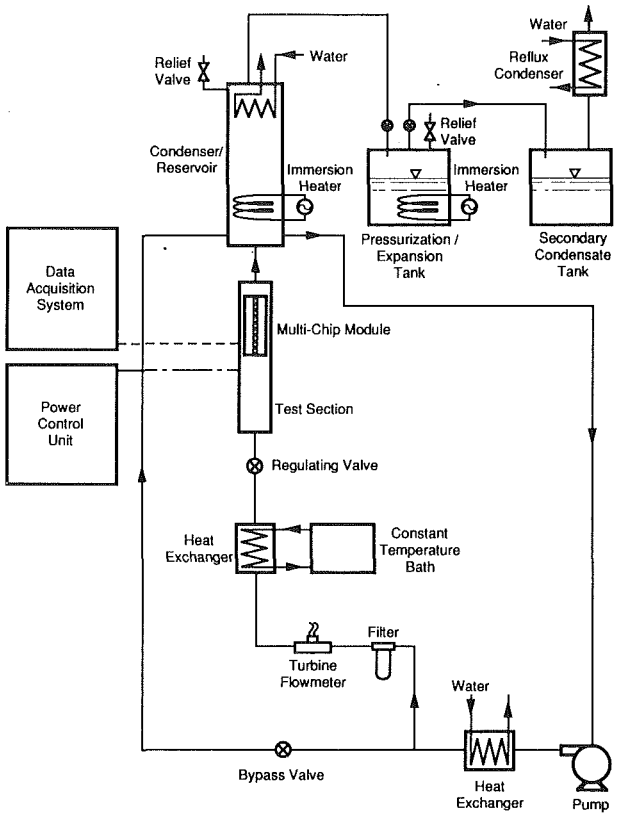

Fig. 1 Flow loop

Experimental Apparatus

A two-phase flow loop, shown in Fig. 1, circulated and conditioned the FC-72 fluid to the desired inlet flow velocity, temperature, and pressure. Liquid was forced through the loop by a magnetically coupled, centrifugal pump. Only a fraction of the total flow entered the test section while the rest was routed around the test section through a bypass line. Flow rate in the test section was controlled by two regulating valves and measured by one of two turbine flowmeters. Fluid temperature at the inlet to the test section was maintained by two heat exchangers. After leaving the test section, the fluid entered a condenser/reservoir where it recombined with the fluid from the bypass line. FC-72, a product of 3M Company, is derived from hydrocarbon compounds by replacing all of the hydrogen atoms bonded to carbon atoms with fluorine atoms.

The test section, Fig. 2(*a*), was comprised of the flow channel, upstream and downstream reservoirs, and multichip module. A support frame allowed the entire test section to rotate in 45-deg increments. A honeycomb section in the upstream reservoir served to straighten the flow and break up any large turbulent eddies. The upstream reservoir converged the flow to the channel dimensions of 20.0 mm wide by 5.0 mm high, and the flow was hydrodynamically developed in the remainder of the channel before it reached the chips. The most upstream edge of the first chip was 524.5 mm from the upstream reservoir. The rest of the chips were positioned linearly downstream of the first chip at a pitch of 20.0 mm. As shown in Fig. 2(*a*), the most upstream chip was referred to as Chip 1, and the remaining chips were sequentially assigned numbers up to nine. Three exit ports were machined in the downstream reservoir of the test section to eliminate the possibility of vapor trapping at different test section orientations.

A Lexan window housed the pressure taps, and served as the top cover for the channel. The multichip module with the flush-mounted chips formed the opposite wall at the location of the chips. Absolute and differential pressure measurements were made at Chip 1 and between Chips 1 and 9, respectively. In order to prevent air leaks into the system, the pressure in the condenser/reservoir was kept slightly above atmospheric. This caused the pressure at Chip 1 to be 1.36 bar (20 psia), which was maintained for all of the experiments. Also shown in Fig. 1, are a submerged water-cooled condenser and two immersion heaters located in the condenser/reservoir, which, along with a pressurization/expansion tank, maintained a stable system pressure within $\pm$ 0.0103 bar ($\pm$0.15 psi). The pressure at Chip 1, 1.36 bar, was taken to be the reference saturation pressure for the entire multichip array, and inlet subcooling was then calculated as the difference between the corresponding saturation temperature and the fluid temperature in the upstream reservoir. The fluid temperature in the upstream reservoir was within 0.2°C from the temperature measured by a thermocouple probe introduced into the flow at Chip 1 through the Lexan window, so liquid temperature in all the experiments was measured only in the upstream reservoir to avoid disrupting the flow in the channel by the thermocouple probe.

Figure 3 illustrates the nomenclature used to define the angle of orientation. The 0-deg reference was taken to be the vertical position with the fluid flow opposing gravity (upflow). The angle increases from 0 as the test section rotates in both directions with positive angles referring to orientations in which the chip surfaces were upward facing with respect to gravity, and negative angles to orientations in which the chip surfaces were downward facing.

The simulated chips, Fig. 2(*b*), were machined from oxygen-free copper such that the chip surface in contact with the fluid measured 10.0 mm $\times$ 10.0 mm. A thick-film resistor was silver soldered to the underside of the copper block. Three chromel-

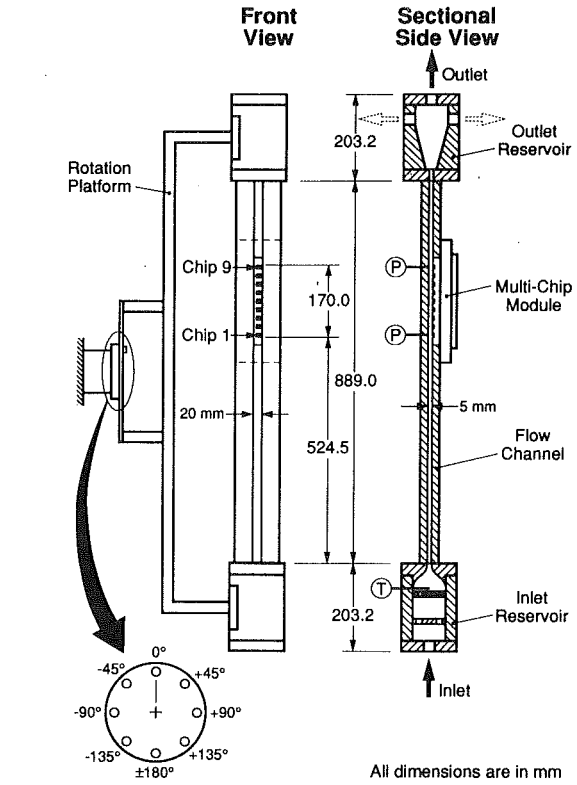

(a)

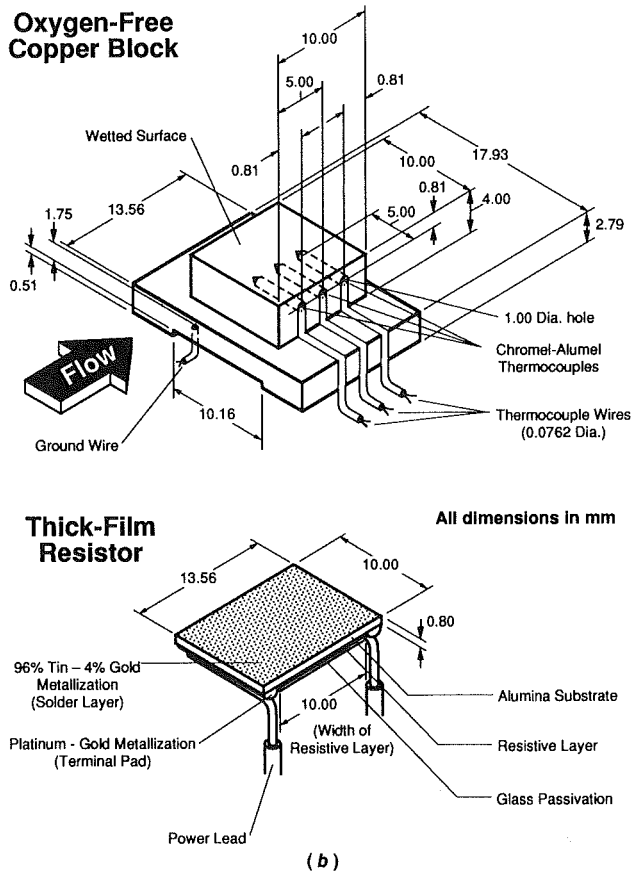

(b)

Fig. 2 Schematic of (*a*) test section and (*b*) simulated microelectronic chip

alumel thermocouples were inserted below the boiling surface and aligned along the chip centerline. One-dimensional heat conduction was used to calculate the surface temperature above

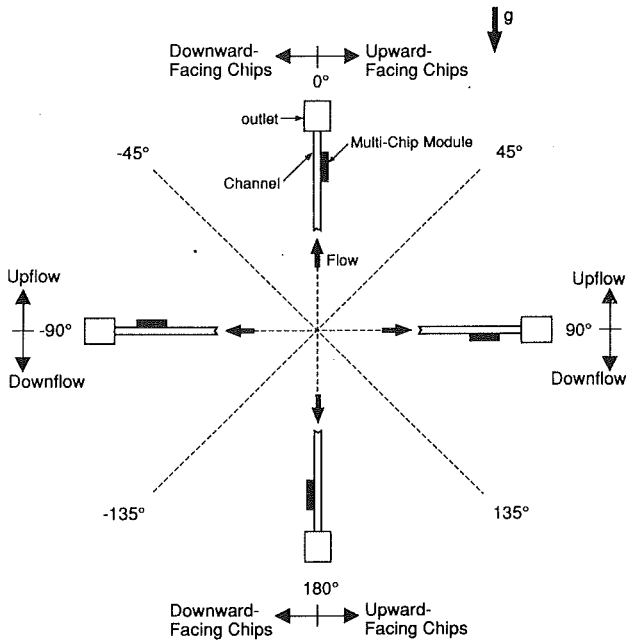

Fig. 3 Nomenclature for the angle of orientation

each of the three thermocouples, and a weighted average of the three surface temperatures set the mean surface temperature. The uniformity of the surface heat flux can be inferred from the closeness of the three thermocouple readings to each other except immediately preceding both the incipience of nucleate boiling and CHF where the streamwise temperature gradient across the chip was at most 1°C. A parallel electrical circuit powered the nine thick-film resistors. Nine variable resistors were installed in series with each chip and adjusted so that each thick-film resistor dissipated the same power. With the voltage across each chip being the same, one voltage transducer and nine current transducers were used to calculate the power dissipation of each chip. In order to save the thick-film resistor from burnout, the data acquisition system independently shut off the electric power input to each chip once that chip had reached CHF.

The chip surfaces were blasted with a water–particulate slurry prior to each set of experiments. The particles had an average size of 10 μm and served to create a uniform surface texture on each chip. Each time the system was started, the flow loop was deaerated by heating the fluid to its saturation temperature and allowing the vapor and air mixture to escape into the condensate tank. From the condensate tank, the vapor/air mixture entered a condenser where the vapor condensed and returned to the tank while the air escaped to the atmosphere. After deaerating for twenty minutes, the valve between the pressurization/expansion and condensate tanks was closed. Utilizing a gas chromatographic technique, Danielson et al. (1987) found that the air concentration in similar Fluorinerts was less than 1 percent by volume after only three minutes of deaeration; hence, a deaeration time of twenty minutes was chosen to deaerate the larger system sufficiently. The procedure for obtaining the data consisted of rotating the test section to the desired angle and then taking all of the data over the desired velocity and subcooling ranges. The standard daily procedure was to start with a particular subcooling and vary the velocity. Repeatability data were taken daily and checked with previous data obtained at the prescribed angle. Most of the CHF data were repeatable to ± 2.5 percent. The downflow orientations with low velocities had more scatter; however, almost all of those tests were repeatable within ±5 percent. On occasion, the channel was oriented to a previously tested angle, and repeatability checks were also performed.

Table 1 Experimental uncertainty

Experimental Reading	Maximum Experimental Uncertainty ± % of value	Experimental Uncertainty Estimation
Thermocouple	3.64	Manufacturer, Calibration
Heat Flux (voltage and current transducers)	7.5 at 5.7 W/cm^2 3.3 at 30.0 W/cm^2 1.6 at 120. W/cm^2	Calibration
Flowmeter ($U \leq 75$ cm/s)	1.0	Manufacturer
Flowmeter ($U > 75$ cm/s)	2.68	Manufacturer
Absolute Pressure	0.75	Manufacturer
Differential Pressure	8.0	Manufacturer

A data point was taken after the entire system attained steady state. Most of the time, steady state was reached when all the chip temperatures and the upstream reservoir temperature had 20 consecutive readings with a standard deviation of less than 0.1°C. At some orientations, the chip temperature during low-velocity test oscillated by as much as ±1.5°C at heat fluxes close to CHF. In these instances, steady state was assumed to occur when the oscillations became steady and repeatable over several sets of temperature readings. Near CHF, the heat flux increments were decreased to 0.5 W/cm^2 to ensure that CHF was not reached prematurely. A large and rapid increase in the chip temperature always signaled the attainment of CHF. Critical heat flux was approximated as the last stable heat flux plus one half of the last power increment.

The maximum percent uncertainty associated with each experimental reading is given in Table 1. Propagation of error (Moffat, 1988) was utilized, where appropriate, in calculating these uncertainties. The one-dimensional heat conduction adjustment introduced an additional uncertainty of at most ± 0.1°C in the chip surface temperature. Heat losses from the chips were minimized by constructing the multichip module from G-7 fiberglass. A two-dimensional numerical analysis was performed on a cross-sectional slice of the multichip module in order to estimate the heat losses from the chips. Heat transfer coefficients for the free convection between the backside of the multichip module and ambient air and the single-phase forced convection between the G-7 substrate and the fluid were calculated from classical correlations. The boiling heat transfer coefficient from the chip surface was adjusted until the predicted temperature at the location of the chip thermocouple agreed with the measured value. The estimated value was always within 3 percent of that based on zero heat loss. The analysis was extended to three dimensions by accounting for losses through the other transverse sides of the chip. This extension assumed that the heat flux from the chip to the substrate was the same in the three dimensions as it was in the two-dimensional model. Contact resistance between the chip and substrate was assumed to be negligible. The largest heat loss for all experiments was calculated to be 3 percent. In light of the small heat losses, the chip heat flux was taken to be the power dissipated by the thick-film resistor.

Results and Discussion

Critical heat flux data were taken using FC-72 for each of the nine chips at eight orientations spaced 45 deg apart. At each orientation, the flow velocity was varied between 13 and 400 cm/s for subcoolings of 3, 14, 25, and 36°C and an inlet pressure of 1.36 bar. Data for the 0-deg orientation were examined by Willingham and Mudawar (1992b), and the effects of orientation on the single-phase and nucleate boiling regimes were reported earlier by Gersey and Mudawar (1992).

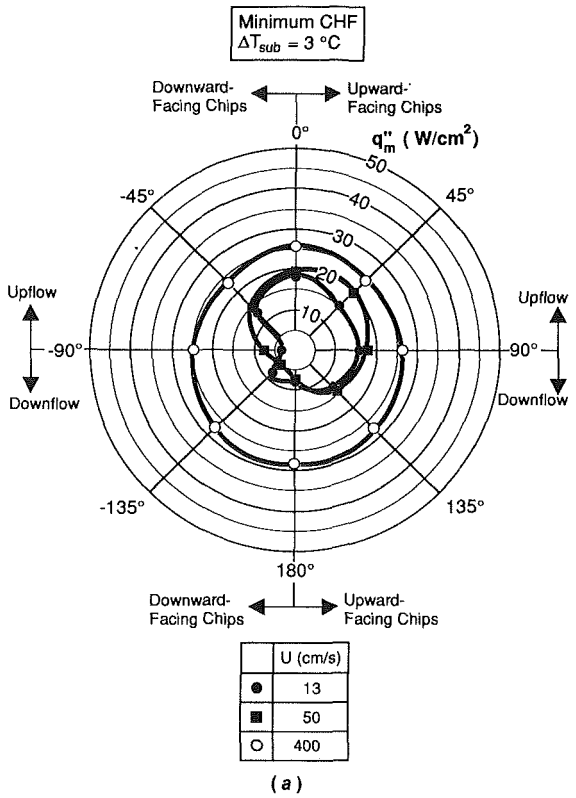

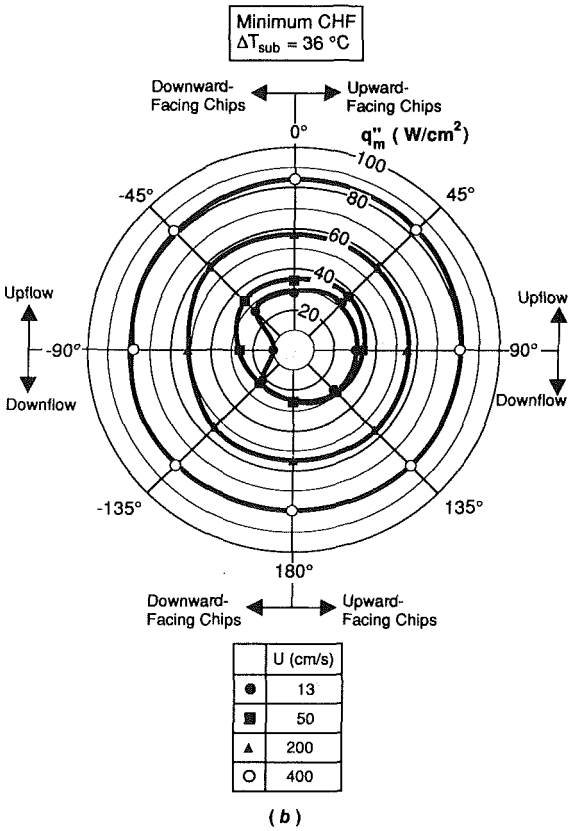

Fig. 4 Polar representation of the velocity effect on the minimum critical heat flux in the multichip array at an inlet subcooling of (a) 3°C and (b) 36°C

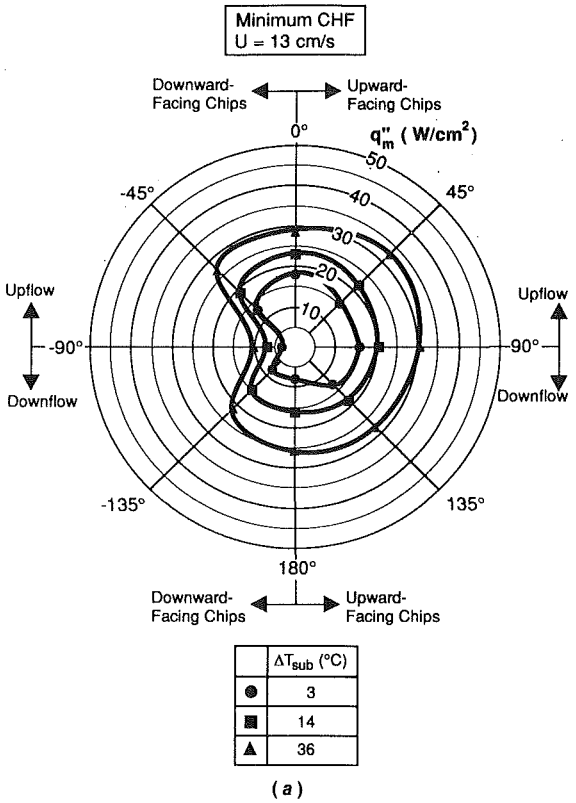

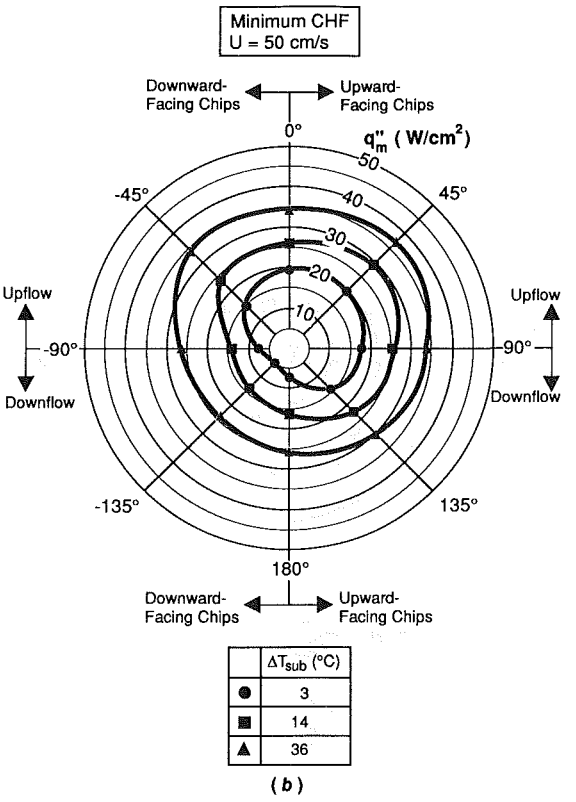

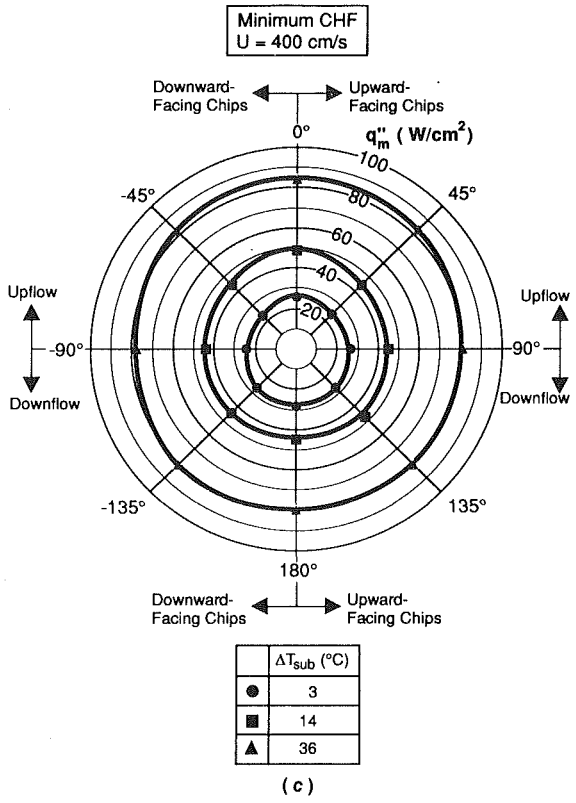

Fig. 5 Polar representation of the subcooling effect on the minimum critical heat flux in the multichip array at an inlet velocity of (*a*) 13 cm/s, (*b*) 50 cm/s, and (*c*) 400 cm/s

Minimum Critical Heat Flux in the Multichip Array. Prior to CHF, the liquid and vapor flow characteristics in the channel and at the chip surface were observed to fall into four categories:

1 Local dryout of the chip surface
2 Stratification of liquid and vapor
3 Vapor stagnation in the channel
4 Vapor counterflow causing liquid blockage

Localized dryout, similar to that observed by Mudawar and Maddox (1989), was responsible for an overwhelming majority of the CHF's. But during the downflow tests in the low velocity region, CHF was dependent on the relative motion of the liquid and vapor. Figures 4(*a*) and 4(*b*) show the effect of velocity on the minimum CHF in the multichip module in polar form. The minimum CHF is the heat flux at which the first chip, not necessarily Chip 1, reached CHF during each test. Since damage will occur to an electronic system once any chip reaches CHF, the minimum CHF value can be thought of as the prevailing design constraint. Except for the low-velocity tests at the downflow orientations, CHF generally increased with increasing inlet liquid velocity. At $\theta = -90$ deg, the vapor was observed to separate from the liquid in the channel and form stratified flow at $U = 13$ cm/s. The absence of liquid contact on the downstream chips promoted an extremely low CHF. Increases in liquid velocity were observed to retard the phase stratification and increase CHF. When the test section was oriented at $\theta = -135$ deg, CHF was actually higher for the near-saturated test at $U = 13$ cm/s as compared to $U = 25$ and 50 cm/s because the vapor moved counter to the liquid flow producing a large degree of mixing around the chips. At 25 cm/s, the vapor stagnated in the channel restricting liquid from contacting the chip surface causing a low CHF. By $U = 50$ cm/s, the drag force of the liquid became large enough to entrain the vapor; critical heat flux then increased with increasing velocity.

Figure 4(*a*) shows at $\theta = 180$ deg, the CHF values are approximately equal at both $U = 13$ cm/s (vapor counterflow) and 50 cm/s (cocurrent flow); however, the CHF values were much lower at the intermediate velocity of $U = 25$ cm/s as a result of vapor stagnation. Because the chips were upward facing at the 135-deg orientation, the stagnant bubbles pre-

dominantly rested on the Lexan window. Large-scale flow rate fluctuations prior to CHF, like those observed by Mishima et al. (1985), were never observed during the present experiments. As shown in Fig. 4(*a*), the effect of orientation on CHF became negligible for near-saturated flow for velocities greater than 200 cm/s as localized dryout was responsible for CHF for all orientations.

Lowering the inlet liquid temperature slightly dampened the effect of orientation on CHF as shown in Fig. 4(*b*). The CHF values were, again, noticeably lower at $\theta = 180$, -135, and -90 deg compared to the 0-deg reference for the low velocities. Typically, in highly subcooled flow, vapor completely condensed downstream of the chip, except at $\theta = -90$ deg, where the vapor and liquid separated, and thus, vapor could not readily condense. Vapor stagnation was still observed to lower CHF at $U = 25$ cm/s for these highly subcooled tests.

The effect of subcooling on the minimum CHF is highlighted in Figs. 5(*a*), 5(*b*), and 5(*c*) for inlet velocities of 13, 50, and 400 cm/s, respectively. The dampening of the effect of orientation on CHF with subcooled flow for downward-facing chips in downflow, $\theta = -90$, -135, and 180 deg, is further evident by comparing the angular dependence of the near-saturated and highly subcooled data in Figs. 5(*a*) and (*b*). As mentioned earlier, increasing the subcooling caused the disparity between the CHF values for upflow and downflow angles to lessen. Unlike the $U = 13$ cm/s test at $\theta = -90$ deg, vapor and liquid did not separate and remained in contact with all of the chip surfaces at $U = 50$ cm/s, and consequently, the CHF values do not show as sharp of a decrease at $\theta = -90$ deg in Fig. 5(*b*) as they do in Fig. 5(*a*). Figure 5(*c*) shows that the effect of orientation is negligible for $U = 400$ cm/s at all subcoolings. Visually, no angular dependence in boiling characteristics was observed in the channel for velocities greater than 200 cm/s with near-saturated conditions and greater than 150 cm/s with highly subcooled flow.

Critical Heat Flux Results for Individual Chips. As CHF was attained on a chip, the electrical power to that chip was shut off, and the experiment continued until all of the chips reached CHF. This facilitated the recording of the minimum CHF for the multichip array as well as a CHF value for each individual chip. Although the fluid conditions change in the channel as heaters are turned off, the continuation of the tests until all chips reached CHF elucidate important trends concerning the order of CHF occurrence in a multiheat source module. The CHF values for Chips 1, 4, and 9 are plotted versus inlet velocity for near-saturated flow in Figs. 6(*a*), 6(*b*), and 6(*c*), respectively. The relatively tight grouping of the data for the upflow angles and the spread in the data from the downflow angles shown in the earlier polar plots are evident in all three figures. The CHF values from the downflow, downward-facing chips are also clearly shown to be lower than the rest of the orientations. The lowest CHF values for Chip 1 and 4 occurred at $\theta = -135$ deg and $U = 25$ cm/s as a result of vapor bubble stagnation over the chip surface. In contrast, the lowest CHF value for Chip 9 occurred at $\theta = -90$ deg and $U = 13$ cm/s because of the local dryout caused by the vapor/liquid stratification.

In the midvelocity range, $U = 125$ to 200 cm/s, Chip 1 experienced a decrease in CHF for the near-saturated tests at all orientations. This decrease was repeatable, and since the other chips did not experience similar decreases, the anomalous behavior of Chip 1 in this velocity range was not investigated further. The transition between the low- and high-velocity CHF regimes, observed by Mudawar and Maddox (1989), are denoted on Figs. 6(*a*), 6(*b*), and 6(*c*). In the high-velocity CHF regime, the CHF data from all of the chips in the present study showed less scatter as the effect of orientation became negligible.

Figures 7(*a*), 7(*b*), and 7(*c*) show the CHF values for Chips

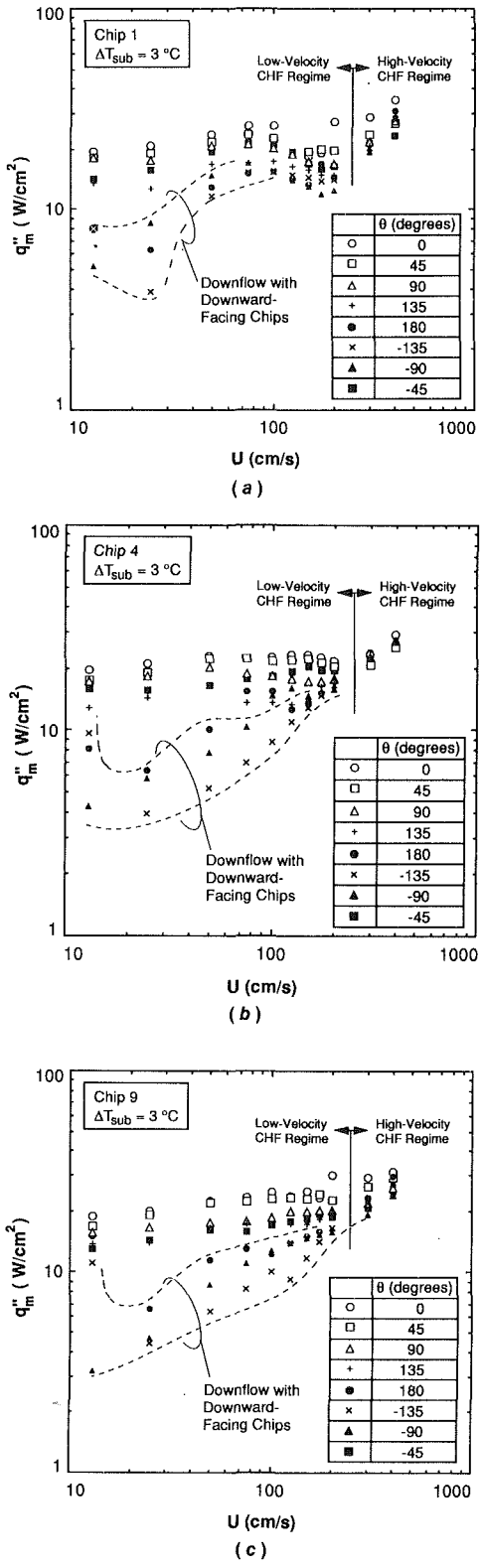

Fig. 6 Velocity effect on the critical heat flux for (*a*) Chip 1, (*b*) Chip 4, and (*c*) Chip 9 for an inlet subcooling of 3°C

1, 4, and 9, respectively, at an inlet subcooling of 25°C. As discussed earlier, increased subcooling dampened the effect of orientation. A substantial decrease in CHF for downward-facing chips with downflow is still evident from the data as well as the relative closeness of the upflow data. The effect of orientation also appears to become negligible at the transition between the low- and high-velocity CHF regimes that occurs

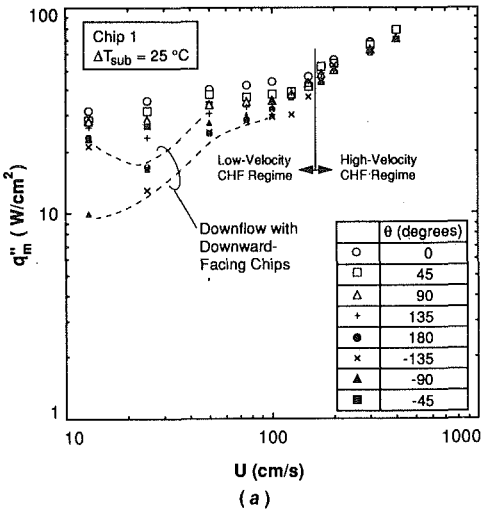

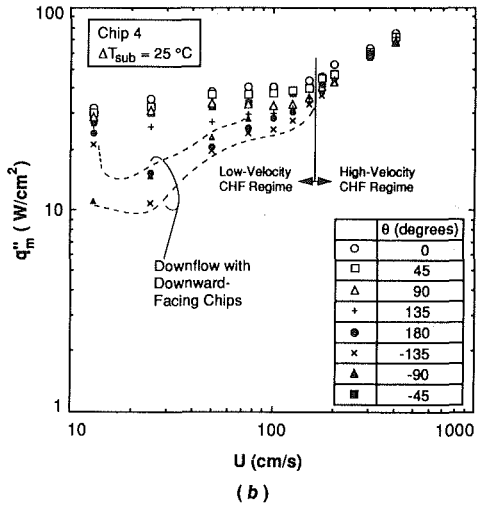

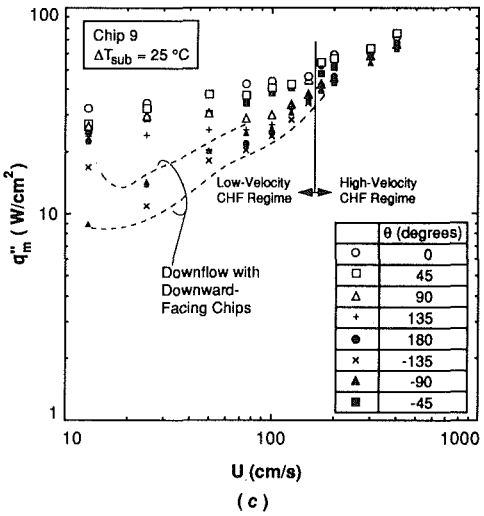

Fig. 7 Velocity effect on the critical heat flux for (*a*) Chip 1, (*b*) Chip 4, and (*c*) Chip 9 for an inlet subcooling of 25°C

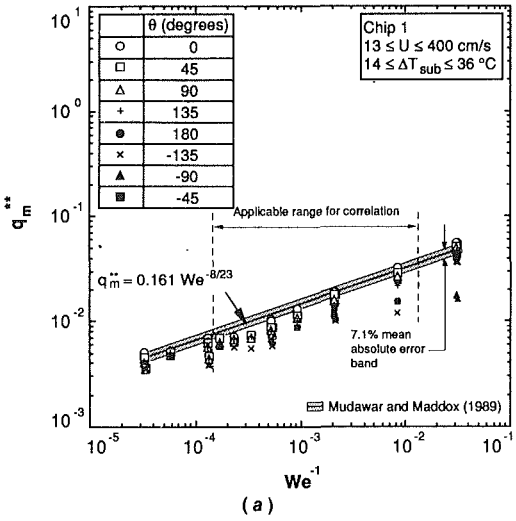

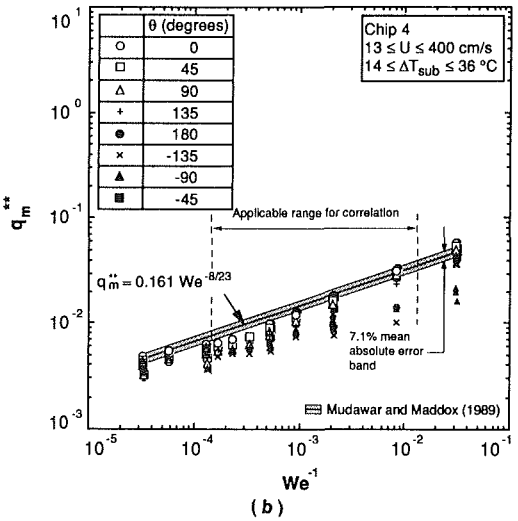

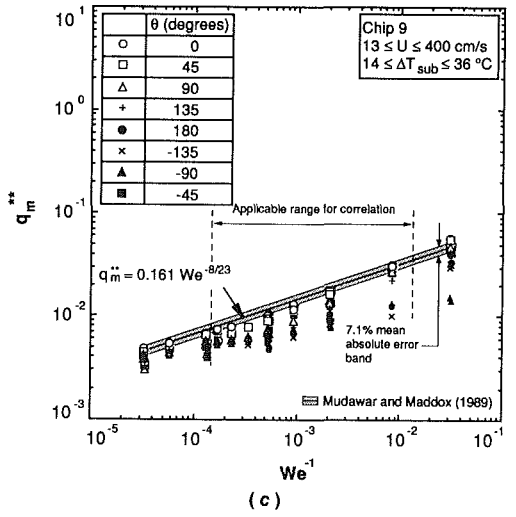

Fig. 8 Comparison of the nondimensional critical heat flux for (*a*) Chip 1, (*b*) Chip 4, and (*c*) Chip 9 with the Mudawar and Maddox (1989) correlation

at a lower inlet velocity for highly subcooled flow. Again, at these highly subcooled conditions, the effect of orientation on CHF became negligible for velocities greater than 150 cm/s.

The order in which the chips attained CHF was recorded. In general, the trends were similar to those reported by Willingham and Mudawar (1992b). That is, the most-upstream chips tended to reach CHF first during the near-saturated tests as the large degree of mixing and increased local fluid velocity caused by the void fraction appeared to enhance the heat transfer from the downstream chips. During the highly subcooled tests, the most-downstream chips tended to reach CHF first

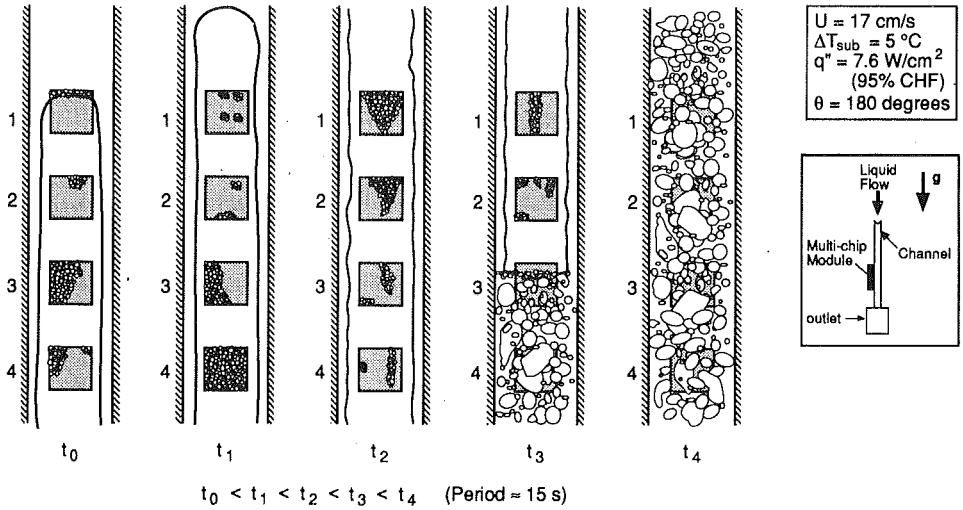

Fig. 9 Illustration of the periodic countercurrent formation of an elongated bubble

because of the streamwise warming of the fluid near the chips. There were some exceptions at low velocities as the test section was rotated from the upflow orientation. In the horizontal orientations ($\theta = \pm 90$ deg), the downstream chips reached CHF first during the near-saturated tests because of local liquid dryout. During the downflow tests at low velocities, both the upstream and the downstream chips tended to reach CHF first because of the vapor counterflow.

The relative spread in the CHF values for the nine chips during a particular experiment highlights the degree to which the presence of the multiple chips affected the individual CHF values. By defining a CHF bandwidth as the difference between the CHF values from the first and last chip to reach CHF (highest and lowest CHF values) divided by the average CHF value, Gersey and Mudawar (1992) found that CHF bandwidth was considerably less for upflow tests as compared to the corresponding downflow tests. For example, at $\Delta T_{sub} = 3°C$, upflow CHF bandwidth values ranged from 8.5 to 25.1 percent while the downflow values were between 12.8 and 49.2 percent. Critical heat flux bandwidth values were lower in the high-velocity CHF regime as compared to the low-velocity CHF regime. Increased liquid subcooling also served to decrease the CHF bandwidth.

Inlet subcooling was used to characterize the test conditions for all of the chips because no standard method exists for calculating a local streamwise subcooling along the multichip module. During the upflow tests, vapor did not spread out across the entire cross section of the channel, thus negating the usefulness of a mixing-cup temperature approximation. Although in downflow tests the vapor spread out across the channel, vapor stagnation and counterflow presented a further complication in calculating a local fluid temperature. The reader should consult the paper by Willingham and Mudawar (1992a) for analytical methods of calculating the streamwise increase in void faction.

Critical Heat Flux Limits

Critical Heat Flux Due to Local Dryout Caused by Intense Vapor Effusion. The ability to predict CHF is important to the design of a direct immersion electronic cooling system. To this end, several researchers have proposed empirical and semi-empirical equations in an effort to correlate CHF data. Figures 8(*a*), 8(*b*), and 8(*c*) compare the CHF values from Chips 1, 4, and 9 with the semi-empirical Mudawar and Maddox correlation (Mudawar and Maddox, 1989) for a single chip in subcooled upflow. Property data for FC-72 were obtained from the manufacturer (3M Company, 1986). Many of the upflow data fall within the error bounds of the correlation while the downflow data, especially at low velocities, are overpredicted by the correlation. Localized dryout was observed to be the cause of CHF for all of the upflow tests and the downflow tests at high velocities. These are the same tests that showed an insensitivity to orientation. This suggests that the Mudawar and Maddox correlation can be used to predict CHF for both upflow orientations and downflow orientations when the effect of orientation is negligible.

Critical Heat Flux Due to Stratification ($\theta \approx -90$ deg). As mentioned earlier, the vapor and liquid phases were observed to separate when the channel was oriented at $\theta = -90$ deg causing dryout on the surfaces of the downstream chips. The vapor and liquid also separated at $\theta = 90$ deg, but the liquid remained in contact with the surfaces of the chips because the chips were upward facing. Phase stratification was only observed at the lowest velocity tested, 13 cm/s, although the CHF values were still less than for the upflow conditions for velocities up to 150 to 200 cm/s. Because the vapor phase can possess a much larger velocity than the liquid when the phases are separated (Dukler and Taitel, 1986), the large velocity difference between the two phases could lead to interfacial waviness, density oscillations, and eventually to plug flow. This may actually aid in chip wetting at $\theta = -90$ deg but at the expense of undesirable flow instabilities.

Critical Heat Flux Due to Vapor Counterflow in Downflow ($\theta \approx 135$, -135, and 180 deg). At the lowest velocity, $U = 13$ cm/s, vapor bubbles coalesced into an elongated bubble, which moved counter to the liquid flow. This movement apparently increased the liquid contact with the chip surface because the CHF values when counterflow was present were higher than the tests at $U = 25$ cm/s where vapor stagnation occurred. As the inlet downflow velocity was reduced to zero, Mishima et al. (1985) and Mishima and Nishihara (1985) observed that flooding was responsible for CHF. The flow rates in the present study were large enough that flooding did not occur, but the large elongated bubbles that formed in the channel served to limit the replenishment of liquid to the chip surface in a manner similar to that of flooding. Figure 9 illustrates the development of an elongated bubble at $U = 17$ cm/s and $\theta = 180$ deg. In a periodic fashion, the elongated bubble formed and hovered over the chips before moving counter to the liquid flow. While the bubble moved up the channel, it condensed such that only a small amount of vapor was observed to enter the upstream reservoir of the test section. As the bubble condensed and decreased in size, its movement became erratic, at times flowing

cocurrent and countercurrent to the liquid. Also, a large degree of mixing occurred around the chips before the formation of the next elongated bubble. Boiling was observed at the leading edge of the elongated bubble at the upstream portion of Chip 1, and intense boiling was observed to take place sporadically on the chip surfaces highlighting the existence of a thin liquid film beneath the elongated bubble. Between the periods of intense boiling, the chip surfaces became momentarily dry. Critical heat flux occurred when the chip surfaces remained dry for a prolonged duration.

Critical Heat Flux Due to Bubble Stagnation ($\theta \approx 135$, -135, and 180 deg). During the low inlet velocity experiments at orientations of 135, 180 and -135 deg, vapor bubbles stagnated in the channel. At $\theta = -135$ and 180 deg, where the chips were downward facing, the stagnant bubbles starved the chips of liquid causing a large decrease in CHF compared to the 0-deg reference as shown in Figs. 6(*a*)–6(*c*) and 7(*a*)–7(*c*). However, at $\theta = 135$ deg where the chips were upward facing, the stagnant bubbles accumulated on the Lexan window permitting liquid to continually contact the chip surfaces; CHF values for this orientation were lower than for the 0-deg reference but not by as much as the downward-facing chips. Additional experiments were performed at $\theta = 180$ deg with near-saturated flow to determine the range of inlet velocities where bubble stagnation occurs. Flow visualization revealed that, for $U = 13$ to 31 cm/s, vapor tended to collect over the chips and form an elongated bubble typical of slug flow. Below $U = 25$ cm/s, the elongated bubbles occasionally moved in the channel counter to the liquid motion and eventually condensed inside the channel. For velocities above 25 cm/s, the elongated bubbles were observed to move in the same direction as the fluid and exit the channel. Very little bubble movement was observed at $U \approx 25$ cm/s, and as a result, CHF was lowest at this velocity with the 135, 180 and -135 deg orientations.

Since vapor stagnation has been shown to decrease CHF, predicting the downflow velocity at which bubble stagnation occurs is of vital importance. By equating the buoyancy force and the drag force on the bubble, an initial estimate of the stagnation velocity can be made. Because of its simplicity, the stagnation velocity (terminal velocity) for spherical and elongated bubbles in quiescent liquid has been extensively studied in infinite media (Haramathy, 1960; Wallis, 1974; Ishii and Zuber, 1979), and in a confining system of circular tubes and rectangular channels (Uno and Kintner, 1956; Harmathy, 1960; Davidson and Harrison, 1963; Collins, 1965; Wallis, 1969). Most of the previously derived correlations require knowledge of the bubble size in order to calculate a hydraulic bubble diameter, thus some estimate of vapor volume would be needed in order to utilize the correlations successfully.

When the volume of vapor in the bubble is increased, the bubble either grows in size or breaks into smaller bubbles, depending upon the ability of surface tension to resist interfacial instabilities. When flow boundaries restrict the bubble, the bubble may grow into an elongated bubble typical of slug flow such as the bubbles observed in the present study. The thin film-like flow around the elongated bubble produces a different stagnation velocity than that for a spherical or cap bubble. Many researchers have studied the stagnation velocity tests with elongated bubbles moving in vertical tubes and rectangular channels with no net liquid flow (Dumitrescu, 1943; Davies and Taylor, 1950; Haramathy, 1960; White and Beardmore, 1962; Brown, 1965; Zukoski, 1966; Stewart and Davidson, 1967). From their correlations, it is evident that the stagnation velocity is a function of the channel hydraulic diameter and liquid properties. For the most part, the analytic and empirical correlations agreed with each other. Most of the correlations predict a stagnation velocity (terminal velocity) of about 10 cm/s for FC-72 rising in quiescent fluid. Zukoski (1966) also tested orientations other than vertical and found that a maximum bubble rise velocity in quiescent liquid exists near the 45-deg orientation. Zukoski also had success in collapsing terminal velocity data for air in both acetone and water using a surface tension parameter, $4\sigma/(\rho_f - \rho_g)gD_h^2$.

The bubble velocity is also affected by the liquid velocity when a net liquid flow exists in the system, increasing when the liquid flow opposes gravity (upflow) and decreasing when the liquid flows with gravity (downflow). In upflow, the bubble velocity was found to be a function of the superficial liquid and vapor velocities and the terminal bubble velocity (Griffith and Wallis, 1961; Nicklin et al., 1962; Zuber and Findlay, 1965). This suggests that, in the absence of very high void fractions (total liquid dryout), upflow enhances vapor exit from the system, thus benefiting heat transfer. Although Griffith and Wallis (1961) did not correlate their downflow data, they observed that, for some downflow velocities, the shape and upward velocity of the vapor bubbles were erratic. Nicklin et al. (1962) recorded data with liquid downflow; however, the large degree of data scatter precluded their ability to correlate the data. They reported that elongated bubbles stagnated in their system at approximately 15 cm/s. Mishima and Nishihara (1985) observed bubble stagnation over an inlet mass velocity range of 150 to 200 kg/m^{2}s which, for water, amounts to a stagnation velocity of approximately 15 to 20 cm/s. Mishima and Nishihara proposed an empirical correlation based on the drift flux model for the stagnation velocity in downflow. Their method predicts a stagnation velocity of 9.15 cm/s for the present study. Bubble stagnation was also reported at a downflow inlet velocity of 26 cm/s during the boiling of water in a centrally heated annular system (Bibeau and Salcudean, 1990). Although the stagnation velocity was not investigated, Bartolini et al. (1983) observed a much higher void fraction of water vapor in the annulus at a downflow velocity of 20 cm/s. Because of the differences in thermophysical properties between fluids, a direct comparison of the stagnation velocities between experiments may not be accurate, rather some type of nondimensionalization, like that of Zukoski's (1966), may need to be employed.

Nevertheless, the previous studies illustrate that relative vapor movement, particularly stagnation, occurs at low downflow velocities. It is apparent that all the previous studies seem to point to a critical downflow velocity range between 10 and 30 cm/s, where stagnation most likely will occur and should be avoided. This range agrees well with the observed stagnation inlet velocity range of 13–31 cm/s. Downflow velocities below stagnation also pose flow stability problems even though CHF may actually increase. The erratic, up and down movement of the elongated bubble in the present study highlights the presence of undesirable, albeit small, flow oscillations. At extremely small inlet velocities, CHF could potentially become lower and unpredictable when this flow oscillations is coupled with the large void fraction in the vicinity of the heat sources. These flow oscillations could also pose problems in a multichannel (e.g., parallel flow into several modules) where pressure and density waves could momentarily redistribute the flow into the parallel channels, thereby decreasing the inlet liquid flow rate. In light of the unpredicatable nature of vapor movement at low downflow velocities, sufficiently large velocities should be utilized to ensure cocurrent vapor flow.

Critical Heat Flux Envelope. A polar representation of the four CHF regimes is shown in Fig. 10 for an inlet subcooling of 3°C; however, similar trends were observed for highly subcooled flow. The figure is meant as an illustration and does not suggest that the boundaries between CHF regimes are well defined and absolute. Stratification occurred at low velocities for angles near $\theta = -90$ deg while vapor counterflow was responsible for CHF for the rest of the downflow orientations. If lower downflow velocities were tested, perhaps flooding would have been observed to initiate CHF. For slightly higher

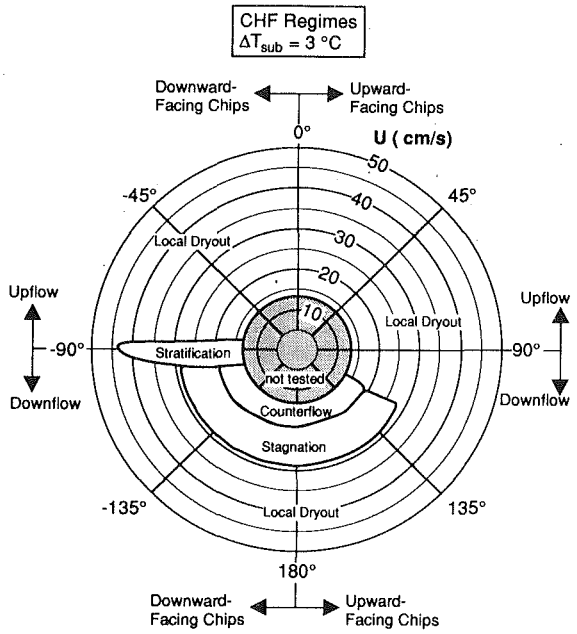

Fig. 10 Polar representation of the critical heat flux regimes at an inlet subcooling of 3°C

velocities, CHF was a result of vapor stagnation. Critical heat flux for the rest of the downflow experiments and all of the upflow experiments was caused by localized dryout of the chip surface.

In order to compare the CHF results of the present study with previous studies, the minimum CHF data at $\theta = 0$, 135, 180, and -135 deg are shown in Figs. 11(*a*) and 11(*b*) for inlet subcoolings of 3 and 25°C, respectively, using the nondimensional parameters suggested by Mishima and Ishii (1982) and Mishima and Nishihara (1985). Although the data for $\theta = \pm 135$ deg do not correspond to vertical downflow, they are included because visual observations suggest that the hydrodynamic and thermal mechanisms in the channel are similar to those at $\theta = 180$ deg. The CHF correlations listed in Table 2 are included in Figs. 11(*a*) and 11(*b*) for comparison with the data. Table 2 includes correlations for the following:

1 Pool boiling: reference
2 Flooding: limiting condition
3 $x_e = 0$ and $x_e = 1$: net vapor generation and liquid dryout, respectively
4 Transition from churn turbulent to annular flow
5 H-regime, HP-regime (Katto, 1981), and small L_{he}/D_{he} ratio (Katto and Kurata, 1980) correlations: CHF envelope for long, continuous heaters
6 Mudawar and Maddox (1989): localized dryout of the chip surface

As shown in Fig. 11(*a*) for near-saturated flow, the CHF values for the 0-deg reference were for the most part above the flooding and pool boiling limits while the downflow values were predominantly below both limits. This illustrates that the stratification, vapor counterflow, and vapor stagnation regimes can cause a lower CHF than for flooding. Forced-convection CHF can be lower than pool boiling CHF because the liquid flow confines the vapor near the chip surface, thus inhibiting liquid replenishment. Even though most of the CHF data fell below the $x_e = 0$ line, a large void fraction was observed in the channel for the near-saturated tests; thus, the flow was far from thermal equilibrium. Perhaps boiling on small discrete heat sources does not provide the same degree of mixing as experiments with a continuous heated wall because of vapor condensation between the heat sources. As a result, local void fractions at the heater were higher than the equilibrium assumptions would predict.

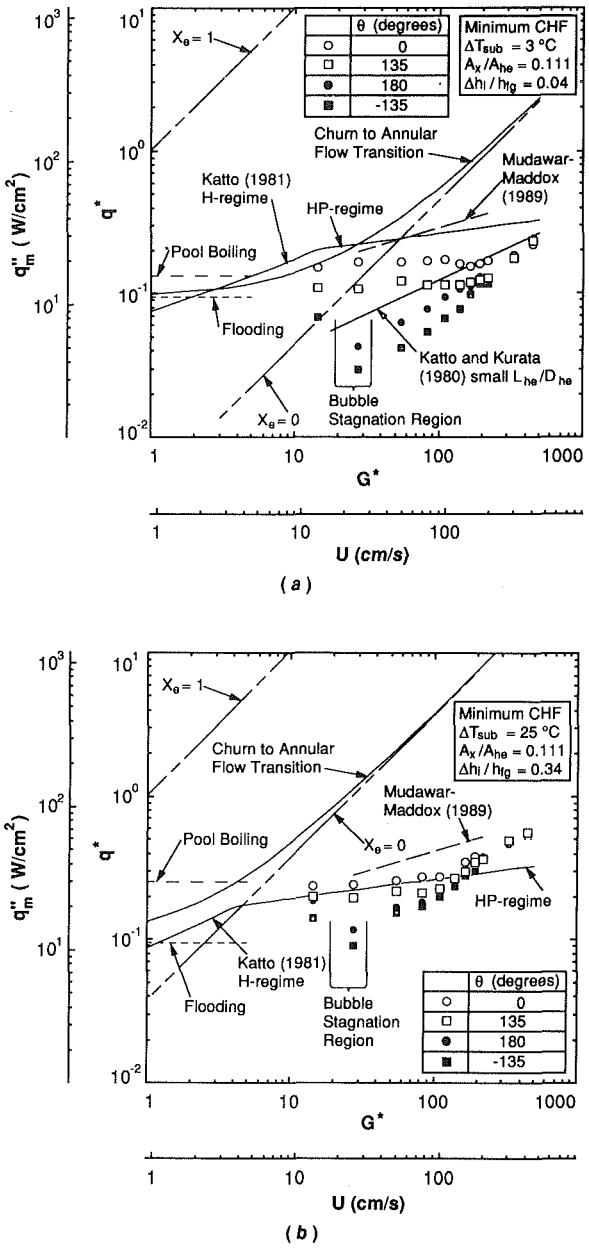

Fig. 11 Comparison of the minimum critical heat flux with previous correlations for inlet subcoolings of (*a*) 3°C and (*b*) 25°C

The Mudawar and Maddox correlation (Mudawar and Maddox, 1989) sets the upper heat flux limit of CHF associated with local dryout of the chip surface, and the minimum CHF data are overpredicted by the correlation. As shown in Figs. 8(*a*), 8(*b*), and 8(*c*), CHF for many of the chips was successfully predicted by the Mudawar and Maddox correlation. These values were, in many cases, larger than the minimum CHF, which did not necessarily occur at the same chip for all of the conditions. The empirical correlations of Katto (1981) were developed for rectangular channels continuously heated from one or two sides also appear to form an upper limit. Katto and Kurata (1980) proposed that their empirical CHF correlation for saturated parallel jet flow on a submerged heater could also be utilized in a heated annulus and other systems with small L_{he}/D_{he} ratios. As shown in Fig. 11(*a*), the correlation intersects the data at high velocities, but fails to predict either the upflow or downflow data at low velocities.

Figure 11(*b*) shows almost all of the highly subcooled data are above the flooding limit. Although vapor stratification,

Table 2 Correlations for Fig. 11

Reference	Correlation	Equation	Notes
Wallis (1969)	Flooding	$q_F^* = C^2 \frac{A_x}{A_{he}} \left(\frac{D_h^2\, g\, (\rho_f - \rho_g)}{\sigma}\right)^{1/4} \left[1 + \left(\frac{\rho_g}{\rho_f}\right)^{1/4}\right]^{-2}$	$C = 0.725$ Wallis (1969) $C = 0.6\left(\frac{L_{he}}{D_h}\right)^{0.05}$ for fluids with different ρ_g/ρ_f ratios (Nejat, 1981)
Zuber et al. (1961)	Pool Boiling	$q_{pb}^* = 0.131 \left(\frac{\rho_f + \rho_g}{\rho_f}\right)^{1/2} \left(1 + 5.3 \frac{\sqrt{k_f \rho_f c_{pf}}}{\rho_g h_{fg}} \left(\frac{g\, \sigma (\rho_f - \rho_g)}{\rho_g^2}\right)^{1/8} \left(\frac{g\, (\rho_f - \rho_g)}{\sigma}\right)^{1/4} \Delta T_{sub}\right)$	Derived for an infinite horizontal plate
	$x_e = 0.0$	$q_{x0}^* = \frac{A_x}{A_{he}} \frac{\Delta h_i}{h_{fg}} G^*$	Energy balance
	$x_e = 1.0$	$q_{x1}^* = \frac{A_x}{A_{he}} \left(1 + \frac{\Delta h_i}{h_{fg}}\right) G^*$	Energy balance
Mishima and Ishii (1982)	Churn Turbulent to Annular Flow Transition	$q_{ca}^* = q_F^* + q_{x0}^*$	Also observed by Mishima and Nishihara (1985)
Katto (1981)	H-Regime	$q_H^* = \frac{0.15}{1 + 0.0077 \frac{L_{he}}{D_{he}}} \left(\frac{\rho_g}{\rho_f}\right)^{0.133} \left(1 + k \frac{\Delta h_i}{h_{fg}}\right) \left(\frac{\rho_f \lambda}{L_{he} \rho_g}\right)^{1/3} (G^*)^{1/3}$, where $k = \frac{5}{9}\left(0.0308 + \frac{D_{he}}{L_{he}}\right) \left(\frac{\rho_g}{\rho_f}\right)^{-0.133} \left(\frac{\rho_f \lambda}{L_{he} \rho_g}\right)^{-1/3} (G^*)^{2/3}$	Made for water in a rectangular channel heated on one or two sides for $20 \le L_{he}/D_{he} \le 500$
	HP-Regime	$q_{HP}^* = \frac{0.26}{1 + 0.0077 \frac{L_{he}}{D_{he}}} \left(\frac{\rho_g}{\rho_f}\right)^{0.133} \left(\frac{\rho_f \lambda}{L_{he} \rho_g}\right)^{0.433} \left(\frac{L_{he}}{D_{he}}\right)^{0.171} (G^*)^{0.134}$	
Katto and Kurata (1980)		$q_K^* = 0.186 \left(\frac{\rho_g}{\rho_f}\right)^{0.559} \left(\frac{\rho_f \lambda}{L_{he} \rho_g}\right)^{0.264} (G^*)^{0.472}$	Correlates saturated water and R-113 data for parallel jet of water over a submersed heater Shown to work for annuli with small L_{he}/D_{he} ratios
Mudawar and Maddox (1989)	Local Dryout	$q_{MM}^* = 0.161\, G^*\, We^{-8/23} \left(\frac{\rho_f}{\rho_g}\right)^{-8/23} \left(\frac{L}{D_h}\right)^{1/23} \left(1 + \frac{c_{pf} \Delta T_{sub}}{h_{fg}}\right)^{7/23} \left(1 + 0.021 \frac{\rho_f c_{pf} \Delta T_{sub}}{\rho_g h_{fg}}\right)^{16/23}$	Developed for an isolated heat source in a rectangular channel with FC-72

counterflow, and stagnation caused a substantial decrease in CHF for the downflow tests, the CHF values associated with these regimes were not below the flooding value like the corresponding near-saturated tests. Some of the 0-deg data and all of the low-velocity downflow data are below the pool boiling limit. Figure 11(*b*) shows that the Mudawar and Maddox correlation is once again an upper limit for CHF. The correlations of Katto (1981) intersect the low velocity upflow data but fail to predict the rest of the data.

Conclusions

The effect of flow orientation on CHF of FC-72 from a linear array of nine, in-line simulated microelectronic chips was investigated. The following conclusions are drawn:

1 Orientation had a negligible effect on CHF for inlet fluid velocities greater than 200 cm/s for near-saturated flow and 150 cm/s for highly subcooled flow. Below these velocities, upflow orientations yielded higher CHF values as compared to downflow and horizontal flow with downward-facing chips.

2 Critical heat flux was the result of localized dryout on the chip surface for the upflow tests and the downflow tests with relatively high flow rates. During the low-velocity tests, CHF values were smaller for downflow and horizontal, downward-facing chip tests because of liquid blockage by vapor counterflow, vapor stagnation, and stratification in the channel.

3 Critical heat flux values measured for downward-facing chips subjected to downflow ($\theta = 180$ and -135 deg) and downward-facing chips with horizontal flow ($\theta = -90$ deg) were as low as 18 percent of their respective vertical upflow values.

4 The inlet liquid velocity that caused the vapor to stagnate in the channel was measured to be around 25 cm/s at $\theta = 180$ deg. The measured stagnation velocity agreed with previous studies, which found the stagnation velocity to be a function of the bubble terminal rise velocity in quiescent liquid and the velocity of incoming liquid. Because of the considerable effect of downflow on CHF, it is recommended that forced-convection cooling systems avoid downflow or use a sufficiently large inlet liquid velocity to overcome the orientation effects.

5 In comparing the present data to previously derived CHF correlations, CHF values for near-saturated downflow were found smaller than the heat fluxes corresponding to pool boiling and flooding-induced CHF. Critical heat fluxes for highly subcooled flow were all greater than the flooding value, but, again, many of the low velocity tests were below pool boiling. The Mudawar and Maddox (1989) correlation for local dryout on an isolated chip in vertical upflow provided an upper limit for the measured CHF values.

Acknowledgments

Support of this work by a grant from the Industrial Chemical Products Division of 3M is gratefully acknowledged.

References

3M Company, 1986, "Product Manual: Fluorinert Electronic Liquids," Industrial Chemical Products Division, 3M Center, St. Paul, MN.

Bartolini, R., Gugliemini, G., and Nannei, E., 1983, "Experimental Study on Nucleate Boiling of Water in Vertical Upflow and Downflow," *International Journal of Multiphase Flow*, Vol. 9, pp. 161–165.

Bibeau, E. L., and Salcudean, M., 1990, "The Effect of Flow Direction on Void Growth at Low Velocities and Low Pressure," *International Communications in Heat and Mass Transfer*, Vol. 17, pp. 19–25.

Brown, R. A. S., 1965, "The Mechanics of Large Gas Bubbles in Tubes: I. Bubble Velocities in Stagnant Liquids," *The Canadian Journal of Chemical Engineering*, Vol. 43, pp. 217–223.

Chen, L. T., 1978, "Heat Transfer to Pool-Boiling Freon From Inclined Heating Plate," *Letters in Heat and Mass Transfer*, Vol. 5, pp. 111–120.

Class, C. R., DeHaan, J. R., Piccone, M., and Cost, R. B., 1960, "Boiling Heat Transfer to Liquid Hydrogen From Flat Surfaces," *Advances in Cryogenic Engineering*, K. D. Timmerhaus, ed., Vol. 5, Plenum Press, New York, pp. 254–261.

Collins, R., 1965, "A Simple Model of the Plane Gas Bubble in a Finite Liquid," *Journal of Fluid Mechanics*, Vol. 22, pp. 763–771.

Danielson, R. D., Tousignant, L., and Bar-Cohen, A., 1987, "Saturated Pool Boiling Characteristics of Commercially Available Perfluorinated Inert Liquids," *Proceedings of the 1987 ASME/JSME Thermal Engineering Joint Conference*, P. J. Marto and I. Tanasawa, ed., Vol. 3, Honolulu, HI, pp. 419–430.

Davidson, J. F., and Harrison, D., 1963, *Fluidised Particles*, Cambridge University Press, Cambridge, United Kingdom.

Davies, R. M., and Taylor, G. I., 1950, "The Mechanics of Large Bubbles

Rising Through Extended Liquids and Through Liquids in Tubes," *Proceedings of the Royal Society of London Series A*, Vol. 200, pp. 375–390.

Dukler, A. E., and Taitel, Y., 1986, "Flow Pattern Transitions in Gas-Liquid Systems: Measurement and Modeling," *Multiphase Science and Technology*, G. F. Hewitt, J. M. Delhaye, and N. Zuber, ed., Vol. 2, Hemisphere Publishing Corp., New York, pp. 1–94.

Dumitrescu, D. T., 1943, "Stromung an einer Luftblase im senkrechten Rohr," *Zeitschrift für Angewandte Mathematik und Mechanik*, Vol. 23, pp. 139–149.

Gambill, W. R., 1968, "Burnout in Boiling Heat Transfer—Part II: Subcooled Forced-Convection Systems," *Nuclear Safety*, Vol. 9, pp. 467–480.

Gersey, C. O., and Mudawar, I., 1992, "Effects of Orientation on Critical Heat Flux From Chip Arrays During Flow Boiling," ASME *Journal of Electronic Packaging*, Vol. 114, pp. 290–299.

Githinji, P. M., and Sabersky, R. H., 1963, "Some Effects of the Orientation of the Heating Surface in Nucleate Boiling," ASME JOURNAL OF HEAT TRANSFER, Vol. 85, p. 379.

Griffith, P., and Wallis, G. B., 1961, "Two-Phase Slug Flow," ASME JOURNAL OF HEAT TRANSFER, Vol. 83, pp. 307–320.

Haramathy, T. Z., 1960, "Velocity of Large Drops and Bubbles in Media of Infinite or Restricted Extent," *AIChE Journal*, Vol. 6, pp. 281–288.

Ishii, M., and Zuber, N., 1979, "Drag Coefficient and Relative Velocity in Bubbly, Droplet, or Particulate Flows," *AIChE Journal*, Vol. 25, pp. 843–855.

Katto, Y., and Kurata, C., 1980, "Critical Heat Flux of Saturated Convective Boiling on Uniformly Heated Plates in a Parallel Flow," *International Journal of Multiphase Flow*, Vol. 6, pp. 575–582.

Katto, Y., 1981, "General Features of CHF of Forced Convection Boiling in Uniformly Heated Rectangular Channels," *International Journal of Heat and Mass Transfer*, Vol. 24, pp. 1413–1419.

Kumar, V., Prasad, M., Verma, M. K., and Garg, N. S., 1990, "Effect of Inclination on Pool Boiling Heat Transfer From a Flat Plate," *Indian Chemical Engineer*, Vol. 32, pp. 61–64.

Lee, T. Y., and Simon, T. W., 1989, "Critical Heat Flux in Forced Convection Boiling From Small Regions," *Heat Transfer in High Energy/High Heat Flux Applications*, R. J. Goldstein, L. C. Chow, and E. E. Anderson, eds., ASME HTD-Vol. 119, pp. 1–7.

Maddox, D. E., and Mudawar, I., 1989, "Single and Two-Phase Convective Heat Transfer From Smooth and Enhanced Microelectronic Heat Sources in a Rectangular Channel," ASME JOURNAL OF HEAT TRANSFER, Vol. 111, pp. 1045–1052.

Marcus, B. D., and Dropkin, D., 1963, "The Effect of Surface Configuration on Nucleate Boiling Heat Transfer," *International Journal of Heat and Mass Transfer*, Vol. 6, pp. 863–867.

McGillis, W. R., Carey, V. P., and Strom, B. D., 1991, "Geometry Effects on Critical Heat Flux for Subcooled Convective Boiling From an Array of Heated Elements," ASME JOURNAL OF HEAT TRANSFER, Vol. 113, pp. 463–471.

Mishima, K., and Ishii, M., 1982, "Critical Heat Flux Experiments Under Low Flow Conditions in a Vertical Annulus," ANL 82-6, Argonne National Laboratory Report.

Mishima, K., and Nishihara, H., 1985, "The Effect of Flow Direction and Magnitude on CHF for Low Pressure Water in Thin Rectangular Channels," *Nuclear Engineering and Design*, Vol. 86, pp. 165–181.

Mishima, K., Nishihara, H., and Michiyoshi, I., 1985, "Boiling Burnout and Flow Instabilities for Water Flowing in a Round Tube Under Atmospheric Pressure," *International Journal of Heat and Mass Transfer*, Vol. 28, pp. 1115–1129.

Moffat, R. J., 1988, "Describing the Uncertainties in Experimental Results," *Experimental Thermal and Fluid Science*, Vol. 1, pp. 3–17.

Mudawar, I., and Anderson, T. M., 1989a, "High Flux Electronic Cooling by Means of Pool Boiling—Part 1: Parametric Investigation of the Effects of Coolant Variation, Pressurization, Subcooling, and Surface Augmentation," *Heat Transfer in Electronics 1989*, R. K. Shah, ed., ASME HTD-Vol. 111, pp. 25–34.

Mudawar, I., and Anderson, T. M., 1989b, "High Flux Electronic Cooling by Means of Pool Boiling—Part 2: Optimization of Enhanced Surface Geometry," *Heat Transfer in Electronics 1989*, R. K. Shah, ed., ASME HTD-Vol. 111, pp. 35–49.

Mudawar, I., and Maddox, D. E., 1989, "Critical Heat Flux in Subcooled Flow Boiling of Fluorocarbon Liquid on a Simulated Electronic Chip in a Vertical Rectangular Channel," *International Journal of Heat and Mass Transfer*, Vol. 32, pp. 379–394.

Mudawar, I., and Maddox, D. E., 1990, "Enhancement of Critical Heat Flux From High Power Microelectronic Heat Sources in a Flow Channel," ASME *Journal of Electronic Packaging*, Vol. 112, pp. 241–248.

Nakayama, W., Nakjima, T., and Hirasawa, S., 1984, "Heat Sink Studs Having Enhanced Boiling Surfaces for Cooling of Microelectronic Components," ASME Paper No. 84-WA/HT-89.

Nejat, Z., 1981, "Effect of Density Ratio on Critical Heat Flux in Closed End Vertical Tubes," *International Journal of Multiphase Flow*, Vol. 7, pp. 321–327.

Nicklin, D. J., Wilkes, J. O., and Davidson, J. F., 1962, "Two-Phase Flow in Vertical Tubes," *Transactions of the Institution of Chemical Engineers*, Vol. 40, pp. 61–68.

Nishikawa, K., Fujita, Y., Uchida, S., and Ohta, H., 1983, "Effect of Heating Surface Orientation on Nucleate Boiling Heat Transfer," *Proceedings of the ASME-JSME Thermal Engineering Joint Conference 1983*, Y. Mori and W. J. Yang, eds., Vol. 1, Honolulu, HI, pp. 129–136.

Park, K. A., and Bergles, A. E., 1988, "Effects of Size of Simulated Microelectronic Chips on Boiling and Critical Heat Flux," ASME JOURNAL OF HEAT TRANSFER, Vol. 110, pp. 728–734.

Park, K. A., Bergles, A. E., and Danielson, R. D., 1990, "Boiling Heat Transfer Characteristics of Simulated Microelectronic Chips With Fluorinert Liquids," *Heat Transfer in Electronic and Microelectronic Equipment*, A. E. Bergles, ed., Hemisphere Publishing Corp., New York, pp. 573–588.

Samant, K. R., and Simon, T. W., 1989, "Heat Transfer From a Small Heated Region to R-113 and FC-72," ASME JOURNAL OF HEAT TRANSFER, Vol. 111, pp. 1053–1059.

Simoneau, R. J., and Simon, F. F., 1966, "A Visual Study of Velocity and Buoyancy Effects on Boiling Nitrogen," NASA, TN D-3354.

Stewart, P. S. B., and Davidson, J. F., 1967, "Slug Flow in Fluidised Beds," *Powder Technology*, Vol. 1, pp. 61–80.

Uno, S., and Kintner, R. C., 1956, "Effect of Wall Proximity on the Rate of Rise of Single Air Bubbles in a Quiescent Liquid," *AIChE Journal*, Vol. 2, pp. 420–425.

Wallis, G. B., 1969, *One-Dimensional Two-Phase Flow*, McGraw-Hill, New York.

Wallis, G. B., 1974, "The Terminal Speed of Single Drops or Bubbles in an Infinite Medium," *International Journal of Multiphase Flow*, Vol. 1, pp. 491–511.

White, E. T., and Beardmore, R. H., 1962, "The Velocity of Rise of Single Cylindrical Air Bubbles Through Liquids Contained in Vertical Tubes," *Chemical Engineering Science*, Vol. 17, pp. 351–361.

Willingham, T. C., Gersey, C. O., and Mudawar, I., 1991, "Forced Convective Boiling From an Array of In-Line Heat Sources in a Flow Channel," *Proceedings of the ASME-JSME Thermal Engineering Joint Conference 1991*, J. R. Lloyd and Y. Kurosaki, eds., Vol. 2, Reno, NV, pp. 365–374.

Willingham, T. C., and Mudawar, I., 1992a, "Channel Height Effects on Forced-Convection Boiling and Critical Heat Flux From a Linear Array of Discrete Heat Sources," *International Journal of Heat and Mass Transfer*, Vol. 35, pp. 1865–1880.

Willingham, T. C., and Mudawar, I., 1992b, "Forced-Convection Boiling and Critical Heat Flux From a Linear Array of Discrete Heat Sources," *International Journal of Heat and Mass Transfer*, Vol. 35, pp. 2879–2890.

Zuber, N., and Findlay, J. A., 1965, "Average Volumetric Concentration in Two-Phase Flow Systems," ASME JOURNAL OF HEAT TRANSFER, Vol. 87, pp. 453–468.

Zuber, N., Tribus, M., and Westwater, J. W., 1961, "The Hydrodynamic Crisis in Pool Boiling of Saturated and Subcooled Liquids," *International Developments in Heat Transfer: Proceedings of the 1961–62 International Heat Transfer Conference*, Boulder, CO, pp. 230–236.

Zukoski, E. E., 1966, "Influence of Viscosity, Surface Tension, and Inclination Angle on Motion of Long Bubbles in Closed Tubes," *Journal of Fluid Mechanics*, Vol. 25, pp. 821–837.

M. R. Duignan
Westinghouse Savannah River Company,
Savannah River Technology Center,
Aiken, SC 29802
Mem. ASME

G. A. Greene
Brookhaven National Laboratory,
Department of Nuclear Energy,
Upton, NY 11973
Mem. ASME

T. F. Irvine, Jr.
State University of New York
at Stony Brook,
Department of Mechanical Engineering,
Stony Brook, NY 11794
Fellow ASME

The Effect of Surface Gas Injection on Film Boiling Heat Transfer

A database was developed for heat transfer from a horizontal plate with film boiling and gas jetting occurring simultaneously, in a pool of water maintained at its saturation temperature. The effect of passing nitrogen through established film boiling is to increase the heat transfer from that surface. At the highest measured superficial gas velocity, approximately 8.5 cm/s, and for a constant surface temperature, the heat transfer increases by a factor of two over the heat transfer with no enhancement by gas flux. Further, as the superficial gas velocity approaches zero, the data approach the stable film boiling asymptote. A model was developed to correlate the database. The result is an equation that represents better than 90 percent of all the measured data within ±15 percent bounds.

Introduction

An issue of paramount concern in assessing the consequences of severe accidents in nuclear reactors is the coolability of molten core debris by an overlying water pool while the core debris is attacking a concrete substrate (molten core–concrete interaction or MCCI). If the boiling heat transfer from the molten core debris to the overlying water pool is greater than the heat generated by nuclear decay and chemical reactions in the core debris, the debris may be substantially cooled or even rendered solid. Under such circumstances, the core–concrete interaction may be halted and the accident may be arrested. If, on the other hand, the boiling heat transfer from the core debris to the overlying water pool is insufficient to remove the decay and chemical reaction heat from the core debris, the debris would remain molten. The MCCI would continue to ablate the concrete basemat and structures and to add noncondensable and flammable gases and volatile fission products to the atmosphere of the reactor containment. Should the containment pressure boundary be breached by these and other loads imposed upon it, these airborne radioactive fission products could be released to the environment. The issue of coolability of core debris as it attacks the concrete, and consequently the reliability of debris coolability evaluations and calculations of MCCI, are dominated by and depend upon the phenomenon of boiling at large superheats over a molten, heat-generating pool that is being sparged by a noncondensable gas from below, which passes through the boiling interface.

In some instances the top surface of the pool would be molten, in which case the boiling would be liquid–liquid boiling enhanced by gas flux from below with the possibility of intermittent stratified steam explosions between the core melt and the water. In other cases, presumed to be later in time from the conditions just discussed, the pool of core debris may become crusted at its top surface, presenting a solid boiling surface with discrete holes through which the MCCI gases would be blown. Steam explosions have not been observed to occur from this configuration, i.e., water over a crusted pool of core debris with gas injection.

It was the objective of this work to investigate the latter case, boiling at large superheats over a solid surface with discrete gas injection sites for application to modeling of molten core debris coolability during severe accident conditions in nuclear reactors. In this paper we will discuss the design and operation of the facility that was developed to perform these experiments on saturated film boiling over an upward facing surface with gas injection through discrete injection sites. The effect of a gas flux on the film boiling heat transfer will be discussed, as well as the trends in the data with respect to classical flat-plate film boiling (i.e., zero gas flux). A model was developed in order to correlate the experimental data, which is useful for gas-flux enhancement of film boiling on a horizontal flat surface for application to molten core-concrete interaction modeling.

Experimental Apparatus

Overview. The purpose of the experiment was to determine the effect on film boiling heat transfer from a horizontal, flat cylindrical disk when a noncondensible nonreactive gas, 99.996 percent pure nitrogen, was passed through the vapor film. An overall schematic of the experimental apparatus is shown in Fig. 1.

Heat was sent through the heat transfer surface into the overlying pool of water by means of a flexible electric heater. The pool of water was contained in a cylindrical quartz tube, which sat directly above the stainless-steel heat transfer surface, and the pool was maintained at atmospheric pressure and the saturation temperature. Measurement of the heat flux to the pool was made by measuring the plate temperature gradient with thermocouples embedded in the heat transfer plate and by measuring the mass flux of liquid water as it condensed in the condensing system.

Finally, the pertinent data were read by a data acquisition system to facilitate precise and accurate information. A description of the components of the experimental apparatus follows.

Test Pool. The experimental test pool had to be made from a material that would tolerate the highest temperature that the heat transfer plate would experience, approximately 1000 K, and also allow visual observation of the phenomena. The first of these characteristics could have been met by many materials, but the second was very limiting. The material chosen was quartz, which met both requirements. Furthermore, quartz has a small coefficient of linear expansion, so that the volumetric expansion of the pool, which occurred from room temperature to the maximum operating temperature, did not cause the seals at the top and the bottom of the pool to leak, Fig. 1. Moreover,

Contributed by the Heat Transfer Division and presented at the 28th National Heat Transfer Conference, San Diego, California, August 6–9, 1992. Manuscript received by the Heat Transfer Division August 1992; revision received March 1993. Keywords: Augmentation and Enhancement, Boiling, Multiphase Flows. Associate Technical Editor: L. C. Witte.

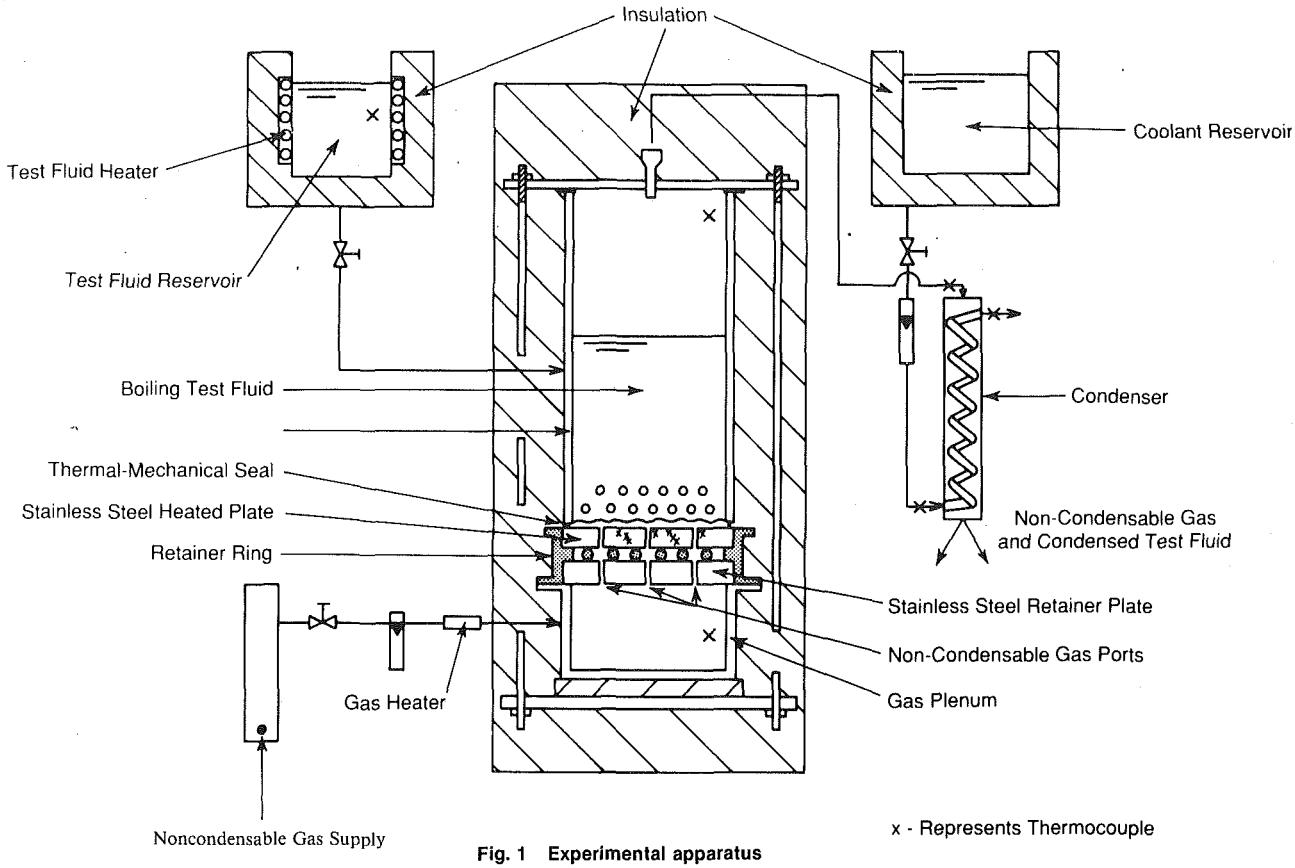

Fig. 1 Experimental apparatus

the pool wall had to withstand the thermal shock that took place each time the experiment was started.

The cylindrical liquid container stood approximately 25 cm high and had an inside diameter of 10.16 cm, with a wall thickness of 0.3 cm. At a height of 8 cm from the bottom of the pool there was an entrance port for the entry of makeup fluid. A stainless-steel tube was fitted through the port, which directed the incoming test fluid to a height of about 2 cm above the heat transfer plate.

The quartz pool was sealed at its top by a stainless-steel plate and a Teflon gasket. The plate was fitted with an exit tube, which led to the condensing system. The top plate secured the quartz tube to the heat transfer plate by means of four bolts. The bottom of the pool was sealed by a Durabla heat-resistant gasket, which had a thickness of approximately 0.04 cm and an inside diameter of 10.32 cm. This thickness is about ten times larger then the expected thickness of the vapor film previously observed in film boiling (Berenson, 1961). It was hoped that after film boiling started, the vapor–liquid boundary would be as close as physically possible to the inside bottom edge of the quartz pool wall. Being on the bottom edge of the wall would assure a minimum surface area for the boundary, so that the more efficient mechanism of heat release, nucleate boiling, could be minimized. Furthermore, the inside diameter of the gasket was made to be approximately 0.16 cm larger than the inside diameter of the pool wall so that it would be recessed back from the wall, thus eliminating a surface area over which nucleate boiling could occur. To clarify, a small gap was created between the bottom of the quartz pool wall and the heat transfer surface so that when film boiling started the vapor–liquid boundary coincided with the bottom edge of the quartz wall, thereby minimizing the surface upon which nucleate boiling could occur.

The side wall and the top of the test pool were covered with

Nomenclature

c_p = specific heat capacity
D = diameter of heating surface
D_l = Laplace reference length
g = acceleration of gravity
Gr = Grashof number
h = heat transfer coefficient
h_{fg} = latent heat
h_{fg}^* = modified latent heat
Ja = Jacob number = $c_{p_f} \Delta T_{SAT}/h_{fg}$
Ja* = modified Jacob number (defined for Eq. (5))
j_g = superficial gas velocity
k = thermal conductivity
Nu = Nusselt number
Pr = Prandtl number
q = heat flux
T = temperature
ΔT_{SAT} = superheat = $T_{SURF} - T_{SAT}$
β, β_I, β_{II} = coefficients
ϵ = surface emittance
λ = Taylor wavelength
μ = dynamic viscosity
ν = kinematic viscosity
ρ = density
σ = surface tension
σ_{SB} = Stefan–Boltzmann constant

Subscripts

d = most dangerous two-dimensional theoretical wavelength
f = film
FB = film boiling
g = gas
l = liquid
SAT = saturation
SURF = surface

guard heaters to ensure that there would be no subcooling between the wall and the pool. This precaution was taken so that measurements of the heat flux during film boiling by the condensing system would be as accurate as possible. The temperature of the pool wall was maintained close to the saturation temperature of water by monitoring the thermocouples placed between the pool wall and guard heaters.

Heat Transfer Surface—Thermal Features. From the thermocouples embedded in the heat transfer plate, both the surface temperature of the plate (by extrapolation), and the heat flux through the plate (by conduction) were determined. Figure 2 shows the top view of the heat transfer plate, which includes the gas holes and the placement of thermocouples. Also, Fig. 3 shows a schematic of an inside slice of the heat transfer plate with some material descriptions and pertinent dimensions. This schematic view shows how the thermocouples, gas orifices, and heating coil were arranged within the plate.

In making the heat transfer plate, two very important problems had to be addressed: (1) Would the flexible coil, used to heat the plate, create the necessary uniform temperature on the upper surface of the plate, since the coil was only in contact with the bottom of the plate at discrete locations (see Fig. 3)? (2) Would the thermocouples, implanted in the plate to measure the upper-surface temperature and the heat flux through that plate, give accurate readings? Both questions were answered analytically before constructing the experimental apparatus. The following is a summary of the analyses done to answer these questions and the details can be found from Duignan (1989).

It was determined from a conservative estimate that the distance between successive contacts of the coil on the plate should be approximately equal to the thickness of the heat transfer plate. This intercoil distance would give the upper heat transfer surface a uniform temperature from one-coil contact to the next, as long as the same amount of heat was released at each point of contact. Since the filament of the heating coil had a diameter of approximately 3.2 mm and the heat transfer plate had a thickness of 6.35 mm, the chosen separation between coils left a gap of approximately a one-coil diameter between successive coils. This gap was enough for the thermocouples and gas holes in the plate assembly to pass through.

For accurate temperature readings, it was important to consider how and where the thermocouples were to be located in the heat transfer plate. Because of the physical limitations in making very long, thin thermocouple wells through the stainless-steel heat transfer plate, the thermocouple leads, which extend immediately from the thermocouple bead, could not be placed radially though the heat transfer plate. Orientation of the leads along the radii would have been preferred, as then they would closely follow the isotherms in the plate. A less desirable orientation chosen was to have the leads exit the plate along a vertical axis; see Fig. 3. Placed vertically through the plate, the leads were exposed to the maximum temperature gradient in the plate, and, as such, could be an avenue for a differing heat flow than the one in the heat transfer plate. From the analysis, it was found that for the highest experimental plate temperature, approximately 1000 K, the thermocouple reading would differ by approximately 0.65 K from the true local temperature. This temperature difference is relatively insignificant since the absolute temperatures used in this experiment were greater by three orders of magnitude. Therefore, the chosen orientation of the thermocouples was deemed acceptable for the experiment.

The last important concern about the thermocouples in the heat transfer plate was an accurate knowledge of their location from the top of the plate surface. The measured surface-to-thermocouple distance for each plate thermocouple is a summation of: (1) the distance from the top of the plate to the bottom of the thermocouple well, (2) from the well bottom to the top of the thermocouple bead, and, finally, (3) the radius of the bead itself. These dimensions were measured to within ± 0.02 mm and the distance from the bottom of the thermocouple well to the midpoint of the thermocouple bead [i.e., (2) + (3)] was the same for all thermocouples: an average of 0.25 mm for the twelve thermocouples. Of course, distance (1) was different for each of the twelve thermocouple and varied from 0.47 mm, closest to the upper-plate surface, to 5.09 mm, farthest from the upper-plate surface.

With the knowledge of the thermocouples' locations and how much their readings differed from the true plate temperatures, both the surface temperature of the plate and the heat

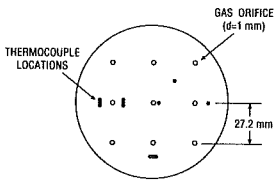

Fig. 2 Top surface of the heat transfer plate

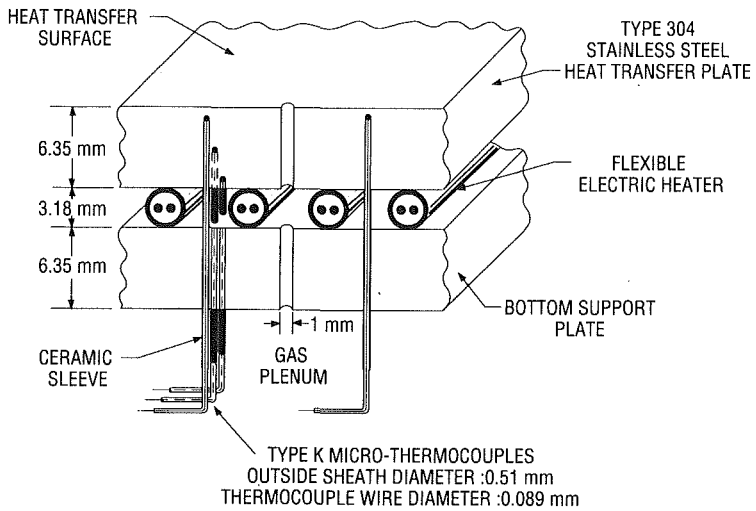

Fig. 3 Heat transfer plate and heater assembly

flow through the plate could be measured once the implanted thermocouples were calibrated. A calibration showed that the "true" thermocouple temperature differed from those obtained from tabulated EMF values, published by the National Institute of Standards and Technology (NIST), by not more than 1.5 K over the range of experimental temperatures. Note, "true" means a reading obtained from a platinum resistance thermometer, which had an accuracy of better than 0.01 K. Because of the high plate temperature common in the film boiling of water, above 500 K, this 1.5 K maximum temperature difference was considered insignificant, and therefore the NIST tabular values were applied directly to determine the thermocouple temperature from its voltage output.

Heat Transfer Surface—Physical Features. A heat transfer surface with discrete holes (rather than a porous surface) was thought to model the top of a solidified core-debris pool with gas injection because of observations from other MCCI experiments (e.g., Blose et al., 1987). As illustrated in Fig. 2 the heat transfer surface had nine 1-mm drilled holes through which nitrogen was injected into the overlying pool. The holes were drilled in a square geometry with the closest center-to-center hole spacing being 27.2 mm. This interhole distance was chosen to be equal to the "most dangerous" wavelength, $\lambda_d = 2\pi[3\sigma/(g(\rho_l - \rho_f))]^{1/2}$, first mentioned by Bellman and Pennington (1954), which is based on the Taylor (1950) instability theory. The actual configuration of the gas holes conform to the bubble release pattern described by Sernas et al. (1973) and observed by Duignan et al. (1989). The objective of this investigation was to develop a gas-flux enhanced film boiling model primarily for application to MCCI conditions. As a result, the hole spacing was chosen to correspond to the conventional assumptions made in MCCI analyses, i.e., the gas bubbling sites are separated from each other by the Taylor instability wavelength, which is nearly the same for both gas film bubbling and stable film boiling.

The chosen center-to-center hole spacing is also important with respect to the effect that bubbles have on the local heat transfer from the surface. Bard and Leonard (1967) showed that the effect of bubbling from a single orifice on the local heat transfer decreases inversely with the distance from the orifice. They noted that for distances along the surface greater than 10 mm from the center of the orifice of 1 mm or less in diameter, the heat transfer was not affected by the presence of the bubble. Therefore, if the bubbling sites are located far enough away from each other (referred to as "sparsely" located sites), the main contribution to the surface heat transfer is due to the movement of the fluid on that surface by natural convection and by the stirring action caused by the bubbles. For a more detailed discussion of the interhole spacing, the reader is directed to Duignan et al. (1990).

The heat transfer plate itself was a circular flat disk made of 304 stainless steel, 6.35 mm thick, and polished to minimize thermal radiation. The size of the surface, 101.6 mm diameter, was considered "large" with respect to film boiling. Kesselring et al. (1967) showed that when the smallest horizontal dimension of a flat heat transfer surface is less than approximately $2\lambda_d$, the film boiling heat transfer becomes a function of the surface geometry, similar to that experienced when changing the diameter of a tube heater (Lienhard and Wong, 1964). Klimenko (1981) also noted the importance of the size of the heat transfer surface and proposed that when the surface dimension D is greater than $2.8\lambda_d$, the surface is considered "large" and any further increase in size will not affect the heat transfer. Since λ_d is equal to 27.2 mm for water (at the surface superheats of concern) the surface, $D = 101.6$ mm, was considered to be large by both criteria.

Condenser System. Besides calculating the heat conduction through the heat transfer plate, another means used to obtain the heat flux was by measuring the mass of water vapor leaving the boiling chamber. This was done by condensing the vapor and measuring the rate at which water left the system. After eliminating the sources of superheating and subcooling water in the test pool, this mass flux measurement became the most accurate and primary means of measuring the heat flux. Moreover, the assessment of heat flux based on the collected condensate was inherently more stable than the method of heat conduction. Small changes in the temperature of the heat transfer plate led to large changes in the axial temperature gradient through the plate, and hence, large fluctuations in the inferred heat flux by conduction.

Figure 1 shows a schematic of the condenser system. Care was taken to make sure that the condensers completely condensed all the water vapor, while not significantly increasing the pressure in the boiling chamber, which would have changed the saturation temperature of the water. The pressure in the test pool was periodically measured and found to be approximately 5 cm of H_2O above atmospheric pressure, not enough to change significantly the saturation temperature from the value at atmospheric pressure. Total condensation was checked by measuring the temperature of the exiting mixture of nitrogen, water vapor, and water to determine that it was below the saturation temperature.

The only other concern in the mass flux measurements was the loss of water that left the condensing system with the nitrogen. To this end, the water vapor contained in the saturated nitrogen gas leaving the condenser was taken into account. Furthermore, the escaping nitrogen was checked to see if it was transporting water droplets. It was found that no perceptible water, in the form of liquid, left with the gas below superficial gas velocities of approximately 10 cm/s.

Gas Flow System. The noncondensible gas-flow system shown in Fig. 1 consisted of a gas supply reservoir, a pressurized metering system, and an in-line gas heater. The in-line gas heater ensured that gas entering the experimental apparatus was approximately at the temperature of the heat transfer plate. Even though the heat capacity of the nitrogen is insignificant with respect to the stainless-steel apparatus or the water in the bubbling pool, its entering the system at the temperature of the plate ensured that no local cooling would occur around the jet holes, which might have created instabilities.

The gas flow rate was measured by a rotameter, which was metered at 0.276 MPa above atmospheric pressure to ensure a smooth flow through the meter. To maintain approximately the same pressure drop across all the jet holes in the heat transfer plate, a gas plenum was used, which also included a thermocouple to monitor the temperature of the incoming gas.

Data Acquisition System. The system was controlled by interactive software, which received transfer parameters from the experimenter and scanned data channels upon command. The twelve thermocouples of the heat transfer plate were read sequentially at 0.1 second intervals during one minute. The one-minute interval gave 50 temperature values for each thermocouple, which were averaged to specify the plate temperature. All thermocouple outputs were measured by a programmable digital voltmeter with a resolution of 1 μV, and the thermocouple scanning time was 1 millisecond per channel.

Results and Discussion

The primary goal was to develop a database for gas-flux-enhanced film boiling. To that end, this section presents the data on the heat flux and then the correlation of those data to a model. These results are for water pools greater than 10 cm in height.

Database on Gas-Flux-Enhanced Film Boiling. Figure 4 shows the actual measured heat flux (also referred to as the

total heat flux) as a function of the superficial gas velocity (the total volumetric gas flux divided by the heat transfer surface area) with surface superheat as the parameter. The figure depicts the experimental data, which can be found in Duignan (1989).

The maximum measurement uncertainties for the surface superheat, surface heat transfer, and superficial gas velocity were determined to be 2 K, 1 kW/m^2, and 0.4 cm/s, respectively. These uncertainties were determined by considering both the random and bias errors and using the Law of Propagation of Errors (Duignan, 1989). To observe the reproducibility of the data, note that each symbol in Fig. 4 represents an average of several test runs made under the same conditions and that the deviations among each series of runs, which were averaged, lie within the symbols on the figure. That is, the average deviation from any value on the figure was 0.9 kW/m^2, with the maximum deviation being 2.6 kW/m^2.

The ranges of the data shown in Fig. 4 for both the surface superheat, ΔT_{SAT}, and superficial gas velocity, j_g, were not arbitrarily chosen, but were set by the physical limitations of the experimental apparatus and the phenomena being measured. For the lowest superheats, 159 K and 211 K, the data do not extend over the entire range of j_g. At the lower superheats, care had to be taken not to fall out of film boiling because of the proximity to the minimum film boiling point (MFB). For water at atmospheric pressure, Hosler and Westwater (1962) measured the MFB to be at a surface superheat of 158 K; Nishikawa et al. (1966) observed $\Delta T_{min} \sim 110$ K. One criterion by Poniewski (1987) for film boiling postulates that when the surface temperature is below the liquid critical temperature, and above that at the MFB, a small percentage of liquid still touches the heat transfer surface (for water: $T_{CRITICAL} \sim 647$ K or $\Delta T_{SAT} \sim 274$ K). With the introduction of gas jets from the surface, the physical situation becomes more unstable and possibly leads to a higher percentage of liquid touching the surface. At a constant heat flux, increasing the amount of liquid–solid contacts will eventually cause a spontaneous shift from film boiling to transition boiling and, finally, to nucleate boiling. In other words, it appears that the required surface superheat at the MFB increases with increasing j_g because of the increased instability caused by the jets. For surface superheats of 159 K, 211 K, and 271 K, film boiling could not be maintained for approximately $j_g > 1$ cm/s, $j_g > 4$ cm/s, and $j_g > 10.5$ cm/s, respectively. Experimentally, film boiling was known to exist after reaching a steady-state plate temperature because of the characteristic large bubbles (~20 mm) being formed on the plate, which slowly and calmly left the surface. The measured high surface temperature and low heat flux as compared to nucleate boiling was further evidence that the film boiling regime had been reached.

Another physical limitation was the surface superheat. Accurate heat transfer measurements could not be made for surface superheats greater than approximately 650°C because of the presence of nucleate boiling on the boiling pool wall. Care was taken to minimize any nucleate boiling by external cooling around the base of the test pool, but when the surface temperature of the heat transfer plate rose above 650°C, its occurrence was unavoidable. Also of concern at high temperatures was the oxidation of the heat transfer surface that occurred during the several hours needed for each experimental run. Below a surface temperature of about 650°C, the plate surface was minimally oxidized and could be cleaned off by careful polishing. This ensured that the plate-to-thermocouple distances were negligibly affected; thus, accurate temperature extrapolations could be made.

The last limitation was for superficial gas velocities above 9 cm/s. At about $j_g = 9$ or 10 cm/s, nitrogen flowed through the condensing system at a rate that caused droplets of water to be carried through the system with the gas, and consequently, were not captured in the collection system. To measure the data as accurately as possible, most measurements were made for superficial gas velocities under 8.5 cm/s.

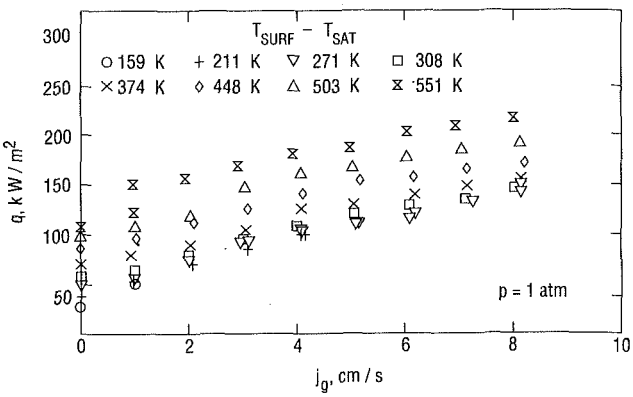

Fig. 4 Gas flux enhanced film boiling data for water

Figure 4 also includes the measured heat-flux values with no gas emerging from the heat transfer plate. These values were obtained from a previous investigation with a similar experimental apparatus (Duignan et al., 1991). For the present experimental apparatus the lowest superficial gas velocity that could be sustained was approximately 0.6 cm/s. Below this velocity some of the gas jets stopped bubbling and a further reduction in the gas flow would have caused back-flooding into the gas plenum through the 1-mm-dia jet holes.

Figure 4 shows that the noncondensable gas enhances the heat flux from the heat transfer surface, at all superheats. Unfortunately, the trend of this heat flux increase is not evident over the range of gas velocities measured. It appears that the slope of the data decreases with increasing superficial gas velocity, leading to a possible conclusion that the heat flux reaches an asymptotic value at large gas velocities. The fact that the heat flux becomes a weak function of the gas velocity is consistent with pool bubbling (Duignan et al., 1990). Even so, there is no basis for extrapolating the observed trend of the data beyond the range of gas velocities actually tested, since a flow regime transition from bubbly flow to churn-turbulent flow is expected for a superficial gas velocity of approximately 10 cm/s. That is, the range of these data is useful for the bubbly flow regime, but further data would be needed for information in the churn-turbulent flow regime.

Correlation of Experimental Data to the Model. To facilitate the use of the experimental database, a model was developed to correlate the data. As a starting point to the model development, an asymptote of enhanced-film-boiling heat transfer by gas injection was studied (i.e., stable film boiling, which exists when no gas injection emerges from the heat transfer surface). A model exists for film boiling on horizontal flat surfaces, which is based on the thermodynamic considerations of Bromley (1948) and the hydrodynamic considerations of Berenson (1961), i.e.,

$$q_{FB}(j_g = 0) = h_{FB}(j_g = 0)\Delta T_{SAT} = \beta \left[\frac{k_f^3 g \rho_f (\rho_l - \rho_f) h_{fg}^*}{\mu_f \Delta T_{SAT} D_l} \right]^{1/4} \Delta T_{SAT} \quad (1)$$

where

β = coefficient to be determined by correlation
h_{fg}^* = $h_{fg}(1 + 0.5\ \mathrm{Ja})$ = modified latent heat
D_l = $[\sigma/(g(\rho_l - \rho_f))]^{1/2}$ = Laplace reference length

Berenson (1962) correlated his heat transfer data with Eq. (1), and determined the coefficient to be 0.425, which he stated was within ± 10 percent of his experimental data. This accuracy has been shown to be true by other studies (e.g., Nishikawa

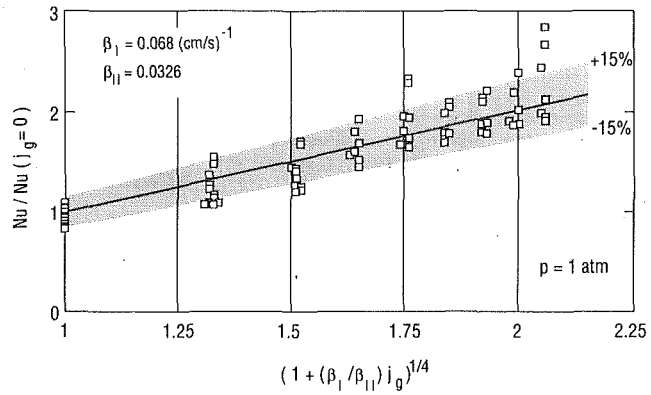

Fig. 5 Correlation of experimental data

et al., 1965; Ramilison and Lienhard, 1987, near the minimum film boiling point). It must be pointed out that Eq. (1) does not include the effect of thermal radiation from a heat transfer surface. To include radiation, Bromley (1948) proposed the following model:

$$q = \left(\frac{q_{FB}^4}{q}\right)^{1/3} + q_{RADIATION} \tag{2}$$

He further suggested that heat transfer by thermal radiation could be determined by using a parallel plate model, i.e.,

$$q_{RADIATION} = \sigma_{SB} \frac{1}{\left[\frac{1}{\epsilon_{SURF}} + \frac{1}{\epsilon_l} - 1\right]} (T_{SURF}^4 - T_{SAT}^4) \tag{3}$$

An analysis by Sparrow (1964) determined Eqs. (2) and (3) to represent the contribution of radiation to the film boiling heat transfer accurately. With respect to the radiative participation of water vapor in the vapor film, he concluded that the emissivity of steam at atmospheric pressure on the heat transfer is completely negligible (less than 0.01), because of the thin film typical of film boiling (~0.25 to 0.50 mm).

In summary, Eq. (2) can be used to determine the total heat transfer for film boiling from a flat horizontal surface to an overlying liquid pool at its saturation temperature, which would include the effect of radiation.

A model was developed (Duignan, 1989) that expanded upon Eq. (1) to include the effect of local gas injection on the global film boiling heat transfer rate. This model used the superficial gas injection velocity as an independent modeling variable. The basis for this assumption lies in the observation from nonboiling, bubbling heat transfer tests that when the gas injection was observed in transition from bubbling to jetting, no discernible change was measured in the surface heat transfer coefficient (Duignan et al., 1990). This was taken as substantiation that the controlling velocity is the superficial velocity, not the local injection velocity. It was proposed that the entrained mass from the vapor film reduces the film thickness between the heat transfer surface and the overlying liquid pool, from that which would exist in stable film boiling. This reduced thickness means less resistance to the flow of heat, therefore more liquid is transformed into vapor. The result of the modeling is

$$q_{FB} = h_{FB}\Delta T_{SAT} = (\beta_I j_g + \beta_{II})^{1/4} \times \left[\frac{k_f^3 g \rho_f (\rho_l - \rho_f) h_{fg}^*}{\mu_f \Delta T_{SAT} D_l}\right]^{1/4} \Delta T_{SAT} \tag{4}$$

The magnitude β_{II} was set to 0.0326, so that Eq. (4) reduces to Eq. (1) when the superficial gas velocity, j_g, is zero, i.e., $0.0326 = (0.425)^4$.

Note that the coefficient of Eq. (4), $(\beta_I j_g + \beta_{II})^{1/4}$, is dimensionless since the terms in the brackets together form the dimensions of h^4. This fact can be seen directly by grouping the nondimensional terms, i.e.,

$$Nu_f = (\beta_I j_g + \beta_{II})^{1/4} \left[\frac{Gr\ Pr}{Ja^*}\right]_f^{1/4} \tag{5}$$

where

Nu_f = $h_{FB} D_l / k_f$ = Nusselt number
Gr = $D_l^3 g[(\rho_l/\rho_f) - 1]/\nu_f^2$ = Grashof number
Pr = $\mu_f c_{p_f} / k_f$ = Prandtl number
Ja^* = $c_{p_f} \Delta T_{SAT} / h_{fg}^*$ = modified Jacob number

That is, while β_{II} is dimensionless, so is the group $\beta_I j_g$ with β_I taking on the reciprocal dimensions of j_g. Normalizing Eq. (4) to the Berenson equation, i.e., at $j_g = 0$, for the same superheat gives a convenient form for correlation:

$$\frac{Nu_f(j_g)}{Nu_f(j_g=0)} = \frac{h_{FB}}{h_{FB}(j_g=0)} = \frac{q_{FB}}{q_{FB}(j_g=0)} = \left(1 + \frac{\beta_I j_g}{\beta_{II}}\right)^{1/4} \tag{6}$$

Before determining β_I from correlation with the data, the measured heat flux shown in Fig. 4 had to be reduced by the heat flux due to radiation using Eq. (2). As in the Berenson relation, Eq. (1), Eq. (4) does not include the effect of thermal radiation. (Sources for the properties shown in Eq. (1) and the radiative properties in Eq. (3) are cited by Duignan (1989); for the vapor-liquid interface of water, ϵ_l was assumed to remain constant at 0.96. The emittance of the heat transfer plate was assumed to be that of a polished surface and a function of temperature. At the lowest surface superheat $\epsilon_{SURF} \sim 0.11$ and at the highest $\epsilon_{SURF} \sim 0.27$.)

Figure 5 contains dimensionless quantities, so that any consistent dimensional quantity can be used for β_I and j_g. Moreover, as shown in Fig. 4, the dimensions (cm/s) are used for j_g because of their common use in the literature. The coefficient β_I was determined by correlating the data so that the sum of the squared differences between the model and the data was minimized. The result is:

$$\beta_I = 0.068\ (cm/s)^{-1}$$

and β_I has a standard deviation of 0.005 $(cm/s)^{-1}$ and for a 99 percent confidence level has a range of (0.053 $(cm/s)^{-1}$, 0.083 $(cm/s)^{-1}$). To reiterate, this correlation was based on all the measured data after subtracting the radiation contribution to the total heat flux.

The resulting uncertainties in the heat transfer coefficients and the superficial gas velocities were found to be bounded by ±1 percent and ±17 percent, respectively. Bounds of ±15 percent on the best-fit correlation to the dimensionless data encompass 90 percent of the experimental data, as presented in Fig. 5. Based on the similar fluctuations of the heat flux data around $Nu/Nu(j_g=0) = h_{FB}/h_{FB}(j_g=0) = q_{FB}/q_{FB}(j_g=0) = 1$, also seen in Fig. 5, to the widely accepted Berenson (1961) model, then Eq. (4) adequately represents the experimental data when radiation is negligible or when the radiation heat transfer component is removed from the total heat flux.

Conclusions

1 Over the range of superficial gas velocities used, the effect of the gas jetting on the film boiling was to increase the surface heat transfer, at a constant surface superheat. This increase is approximately twofold as compared to heat transfer without gas jetting at a superficial gas velocity of 8.5 cm/s.

2 The heat transfer is increased by gas jetting at all the surface superheats observed.

3 When the surface superheat is close to the minimum film-boiling point, the introduction of the gas jets tends to cause

the film to collapse to nucleate boiling, unless the surface temperature is increased. This finding suggests that the required minimum film boiling superheat may increase with an increase in superficial gas velocity.

4 The model, Eq. (4), is applicable to the case of film boiling with gas jetting from "sparsely" located jet holes for water with an uncertainty of ± 15 percent.

It is generally concluded that when there is a surface over which film boiling occurs and from which gas jets emerge, the actual heat transfer from that surface can only be accurately ascertained when including the effects of those jets. Equation (4) is a useful approximation to the enhancement of film boiling heat transfer caused by jetting.

References

Bard, Y., and Leonard, E. F., 1967, "Heat Transfer in Simulated Boiling," *Int. J. Heat Mass Transfer*, Vol. 10, pp. 1727–1734.

Bellman, R., and Pennington, R. H., 1954, "Effects of Surface Tension and Viscosity on Taylor Instability," *Quart. J. Appl. Math.*, Vol. 12, pp. 151–162.

Berenson, P. J., 1961, "Film-Boiling Heat Transfer From a Horizontal Surface," ASME JOURNAL OF HEAT TRANSFER, Vol. 83, pp. 351–358.

Berenson, P. J., 1962, "Experiments on Pool-Boiling Heat Transfer," *Int. J. Heat Mass Transfer*, Vol. 5, pp. 985–999.

Blose, R. E., Gronager, J. E., Suo-Anttila, A. J., and Brockmann, J. E., 1987, "SWISS: Sustained Heated Metallic Melt/Concrete Interactions With Overlying Water Pools," NUREG/CR-4727, Sandia National Laboratories, NM.

Bromley, L. A., 1948, "Heat Transfer in Stable Film Boiling," Ph.D. Thesis, Department of Chemistry, University of California, Berkeley, CA.

Duignan, M. R., 1989, "Enhanced Convective and Film Boiling Heat Transfer by Surface Gas Injection," Ph.D. Thesis, Dept. of Mechanical Engineering, State University of New York at Stony Brook, NY.

Duignan, M. R., Greene, G. A., and Irvine, T. F., Jr., 1989, "Measurements of the Film Boiling Bubble Parameters on a Horizontal Plate," *Int. Comm. Heat Mass Transfer*, Vol. 16, pp. 355–366.

Duignan, M. R., Greene, G. A., and Irvine, T. F., Jr., 1990, "Heat Transfer From a Horizontal Bubbling Surface to an Overlying Water Pool," *Chem. Eng. Comm.*, Vol. 87, pp. 185–194.

Duignan, M. R., Greene, G. A., and Irvine, T. F., Jr., 1991, "Film Boiling Heat Transfer to Large Superheats From a Horizontal Flat Surface," ASME JOURNAL OF HEAT TRANSFER, Vol. 113, pp. 266–268.

Hosler, E. R., and Westwater, J. W., 1962, "Filming Boiling on a Horizontal Plate," *ARS Journal*, Vol. 32, pp. 553–558.

Kesselring, R. C., Rosche, P. H., and Bankoff, S. G., 1967, "Transition and Film Boiling From Horizontal Strips," *AIChE Journal*, Vol. 13, pp. 669–675.

Klimenko, V. V., 1981, "Film Boiling on a Horizontal Plate—New Correlation," *Int. J. Heat Mass Transfer*, Vol. 24, pp. 69–79.

Lienhard, J. H., and Wong, P. T. Y., 1964, "The Dominant Unstable Wavelength and Minimum Heat Flux During Film Boiling on a Horizontal Cylinder," ASME JOURNAL OF HEAT TRANSFER, Vol. 86, pp. 220–226.

Nishikawa, K., Hasegawa, S., Iwabuchi, T., and Miyabara, Y., 1965, "Characteristics of Transition Boiling on the Horizontal Plate," Technol. Reports Kyushu Univ., Vol. 38, pp. 306–310.

Nishikawa, K., Hasegawa, S., Kitayama, N., and Sakamoto, T., 1966, "The Effect of Heating Surface Conditions on the Transition Boiling—The Investigation of Transition Boiling (2nd Report)," Technol. Reports Kyushu Univ., Vol. 38, pp. 399–404.

Poniewski, M., 1987, "Dissipative Model of Film Boiling Crisis," *Int. J. Heat Mass Transfer*, Vol. 30, pp. 1847–1857.

Ramilison, J. M., and Lienhard, J. H., 1987, "Transition Boiling Heat Transfer and the Film Transition Regime," ASME JOURNAL OF HEAT TRANSFER, Vol. 109, pp. 746–752.

Sernas, V., Lienhard, J. H., and Dhir, V. K., 1973, "The Taylor Wave Configuration During Boiling From a Flat Plate," *Int. J. Heat Mass Transfer*, Vol. 16, pp. 1820–1821.

Sparrow, E. M., 1964, "The Effect of Radiation on Film Boiling Heat Transfer," *Int. J. Heat Mass Transfer*, Vol. 7, pp. 229–237.

Taylor, G. I., 1950, "The Instability of Liquid Surfaces When Accelerated in a Direction Perpendicular to Their Plane," *Proc. Roy. Soc.*, Ser. A (London), Vol. 201, pp. 192–196.

A Correlational Approach to Turbulent Saturated Film Boiling

T. Y. Chu
Severe Accident Phenomenology Department,
Sandia National Laboratories,
Albuquerque, NM 87185

A correlation method for saturated film boiling is proposed. The correlation is based on the analogy between film boiling and natural convection. As in the case of natural convection, the turbulent film boiling correlation takes the form of a Nusselt number versus the Rayleigh number power law, $Nu_B \propto Ra_B^{1/3}$. The proposed correlation shows very good agreement with current data for film boiling of water from vertical surfaces. The general applicability of the correlation is established by comparisons with film boiling data from R-113 and cryogenic fluids.

Introduction

Of all the boiling regimes, film boiling is the most amenable to analysis. The classical approach is boundary layer analysis pioneered by Bromley (1950). A summary of advances in film boiling up to 1975 can be found from Kalinin et al. (1975). The proceedings from the recent Santa Barbara conference on pool and external flow boiling (Dhir and Bergles, 1992) contain papers dealing with current issues as well as examples of current methods of analysis in film boiling. The present paper takes a slightly different approach in the analysis of film boiling. Conceptually, film boiling is still viewed from the point of boundary layer transport, but an analogy is used to derive the film boiling correlation.

It has long been recognized that film condensation and film boiling are analogous phenomena. Bromley's analysis (1950) of laminar film boiling is essentially an application of Nusselt's analysis (1916) of film condensation. In a paper on laminar film condensation Dhir and Lienhard (1971) showed explicitly, under the assumption of thin film analysis, that film condensation results can be applied directly to film boiling for a variety of axisymmetric surfaces. In a study of single-phase natural convection, Raithby and Hollands (1978) further pointed out that natural convection correlations can be readily applied to film condensation. Physically all three phenomena, natural convection, film condensation, and film boiling, involve film flow driven by a body force acting along the contour of a surface. The principal mode of heat transfer in the thin film is conduction (excluding the case of film boiling with elevated wall temperature). In the case of natural convection, buoyancy is the result of different densities caused by temperature differences between the surface and the bulk fluid. In the case of film boiling and film condensation, the body force is due to the density difference between phases. The present work attempts to examine the third leg of the natural convection/film condensation/film boiling triangle by proposing an analogy between natural convection and film boiling. The purpose is to establish a correlation for turbulent film boiling using existing correlations for turbulent natural convection.

The proposed analogy is not entirely new conceptually; Y. P. Chang (1957, 1959) in two classical papers on boiling first proposed the analogy between boiling and natural convection in a theoretical analysis of boiling. Frederking and Clark (1963) made the observation that their data for the film boiling heat transfer coefficients of spheres in liquid nitrogen could be correlated in a form similar to turbulent natural convection where the heat transfer coefficient was independent of the size of the sphere. However, this analogy has never been developed sufficiently, perhaps partly for lack of sufficient experimental data, to result in useful engineering correlations.

Contributed by the Heat Transfer Division for publication in the JOURNAL OF HEAT TRANSFER. Manuscript received by the Heat Transfer Division September 1992; revision received April 1993. Keywords: Boiling. Associate Technical Editor: L. C. Witte.

The present analysis is motivated by recent data on boiling from vertical surfaces in water (Bui and Dhir, 1985) and in helium (Nishio and Chandratilleke, 1989) where the heat transfer coefficient was found to be constant beyond a short distance from the leading edge. This behavior is exactly analogous to turbulent natural convection. The proposed analogy is examined using tabulated data of Bui (1984; Bui and Dhir, 1985) of film boiling on vertical surfaces in water and the natural convection correlations developed by Raithby and Hollands (1985).

Analysis

Laminar. Bromley's (1950) classical analysis of laminar film boiling from vertical isothermal surfaces shows that the Nusselt number based on distance from the leading edge (bottom of the surface) can be expressed as

$$\mathrm{Nu}_B^l = 0.5 \left[\frac{g\rho_v(\rho_l - \rho_v)h_{fg}'}{\mu_v \Delta T k_v} Z^3 \right]^{1/4} \tag{1}$$

where Nu_B^l is the Nusselt number based on Z, the distance from the leading edge, g, is the gravitational constant, ρ_v and ρ_l are the densities of vapor and liquid respectively, h_{fg}' is the sensible heat corrected effective latent heat, μ_v is the vapor viscosity, ΔT is the surface superheat, and k_v is the thermal conductivity of vapor. The properties are evaluated using the average of the surface temperature and the saturation temperature.

The expression in the bracket can be defined as the boiling Rayleigh number

$$\mathrm{Ra}_B = \mathrm{Gr}_B \mathrm{PR}_B \tag{2}$$

where Gr_B, the boiling Grashof number, is defined as

$$\mathrm{Gr}_B = \frac{g\left(\frac{\rho_l - \rho_v}{\rho_v}\right)}{(\mu_v/\rho_v)^2} Z^3 \tag{3}$$

and Pr_B, the boiling Prandtl number, is defined as

$$\mathrm{Pr}_B = \frac{\mu_v \cdot h_{fg}'/\Delta T}{k_v} \tag{4}$$

a Prandtl number with c_p replaced by $h_{fg}'/\Delta T$. The correlation can then be written as a power law:

$$\mathrm{Nu}_B^l = 0.5\ \mathrm{Ra}_B^{1/4} \tag{5}$$

As pointed out by Bui and Dhir (1985), more sophisticated analyses for laminar film boiling exist; however, for near-atmospheric pressures, the heat transfer rates predicted from these studies are close to Bromley's result.

The laminar film boiling correlation cast in the $\mathrm{Nu} = C\mathrm{Ra}^n$ form is directly analogous to the well-known correlation for laminar natural convection (Raithby and Hollands, 1985):

$$\mathrm{Nu}_c^l = C_l\,\mathrm{Ra}_c^{1/4} \tag{6}$$

where the natural convection Rayleigh number is defined as:

$$\mathrm{Ra}_c = \frac{g\beta\Delta T}{(\mu/\rho)^2} Z^3 \cdot \mathrm{Pr} \tag{7}$$

The parameter C_l is a function of Prandtl number,

$$C_l = \frac{0.503}{\left[1+\left(\frac{0.492}{\mathrm{Pr}}\right)^{9/16}\right]^{4/9}} \tag{8}$$

It is useful to examine the term h_{fg}', the sensible heat corrected latent heat in light of the analogy. For the present purpose the term will be given a general definition in terms of the Jacob number, $\mathrm{Ja} = c_p\Delta T/h_{fg}$:

$$h_{fg}' = h_{fg}\,[1 + F(\mathrm{Ja})\mathrm{Ja}] \tag{9}$$

and Pr_B can then be written as

$$\mathrm{Pr}_B = \mathrm{Pr}\left[\frac{1+F(\mathrm{Ja})\cdot\mathrm{Ja}}{\mathrm{Ja}}\right] \tag{10}$$

Typically the function $F(\mathrm{Ja})$ takes a constant value; 0.5 is one of the generally accepted values for the case where Ja is relative small compared to unity. For film boiling the value of superheat can be very large and Ja can be very large compared to unity. Taking the limiting case of a very large Jacob number, it can be argued that the problem might be more like a natural convection problem and the boiling Prandtl number, Pr_B, should approach the real Prandtl number, Pr; the boiling Rayleigh number, Ra_B, should have a form approaching the natural convection Rayleigh number, Ra_c.

Therefore, the function $F(\mathrm{Ja})$ should satisfy the following constraints:

$$F(\mathrm{Ja}) = \frac{1}{2} \qquad \mathrm{Ja} \ll 1$$

$$F(\mathrm{Ja}) = 1;\quad \mathrm{Pr}_B = \mathrm{Pr} \qquad \mathrm{Ja} \gg 1 \tag{11}$$

A simple function that satisfies the constraints is

$$F(\mathrm{Ja}) = \left[1 - \left(\frac{1}{2}\right)\cdot\exp(-\mathrm{Ja})\right] \tag{12}$$

This definition is adapted for the present analysis.

The heat transfer coefficient predicted by Bromley's analysis (1950) was found to be in good agreement with experiments for surfaces of small dimensions. For large surfaces (larger than a few centimeters), Bromley's correlation (1950) was found to underpredict experimental results. Some investigators (Hsu and Westwater, 1960; Suryanarayana and Merte, 1972) postulated that the increase of heat transfer might be due to the flow in the vapor film becoming turbulent. Turbulent boundary layer analyses were used by these investigators to model film boiling. Increased heat transfer was achieved; however, the prediction still did not agree with experimental results. In the present approach, the difficulties and uncertainties of turbulent boundary layer analysis are sidestepped by deriving the film boiling correction by analogy with natural convection.

Turbulent. The general correlation of turbulent natural convection from vertical isothermal surface as given by Raithby and Hollands (1985) is:

$$\mathrm{Nu}_c^t = C_t\cdot[\mathrm{Ra}_c]^{1/3} \tag{13}$$

where C_t is again a function of Prandtl number,

$$C_t = \frac{0.13\cdot\mathrm{Pr}^{0.22}}{[1+0.61\cdot\mathrm{Pr}^{0.81}]^{0.42}} \tag{14}$$

To apply the turbulent natural convection correlation to turbulent film boiling, it is postulated that for a given Rayleigh number the functional relationship between the value of the Nusselt number given by the turbulent correlation and the value of the Nusselt number given by the laminar correlation is unchanged for natural convection and film boiling. The Nusselt number for turbulent film boiling can thus be written as

$$\mathrm{Nu}_B^t = C_t\cdot\left(\frac{0.5}{C_l}\right)^{4/3}\cdot\mathrm{Ra}_B^{1/3} \tag{15}$$

For convenience, the coefficient group is renamed as $C_{B,t}$

$$C_{B,t} = C_t\cdot\left(\frac{0.5}{C_l}\right)^{4/3} \tag{16}$$

The turbulent film boiling correlation is then written as

$$\mathrm{Nu}_B^t = C_{B,t}\cdot\mathrm{Ra}_B^{1/3} \tag{17}$$

The data of Bui (1984) and Bui and Dhir (1985) are used to test the postulated analogy. The data were obtained from a copper surface measuring 6.3×10.3 cm high. The copper surface is the exposed surface of a copper block heated by cartridge heaters. Steady-state film boiling heat transfer coefficients were measured at locations 8, 26, 52, and 77 mm from the leading edge. The superheat of the test surface above saturation varied from 116 to 440 K.

In applying the analogy it is necessary to define the values of C_l and C_t. One possibility is to evaluate the constants using the Prandtl number for steam. For the temperature range of interest the Prandtl number is taken as 1.0 and C_l and C_t take on values of 0.4 and 0.106, respectively. The resulting film boiling correlation is

$$\mathrm{Nu}_B^t = 0.143\cdot\mathrm{Ra}_B^{1/3} \quad \text{Derived} \tag{18}$$

The best fit through the data of Bui and Dhir (1985) is

$$\mathrm{Nu}_B^t = 0.142\cdot\mathrm{Ra}_B^{1/3} \quad \text{Best Fit} \tag{19}$$

The fit is essentially in exact agreement with the derived correlation, thus supporting the premise for the analogy. The

Nomenclature

c_p = specific heat at constant pressure
g = gravitational constant
Gr_B = boiling Grashof number $= g\left(\frac{\rho_l-\rho_v}{\rho_v}\right)\frac{Z^3}{(\mu_v/\rho_v)^2}$
h = heat transfer
h_{fg}' = sensible heat corrected effective latent heat
Ja = Jacob number
k_v = thermal conductivity of steam
Nu = Nusselt number $= h_z/k_v$
Pr = Prandtl number
Pr_B = boiling Prandtl number $= \frac{\mu_v\cdot h_{fg}/\Delta T}{k_v}$
Ra_B = boiling Rayleigh number $= \mathrm{Gr}_B\cdot\mathrm{Pr}_B$
Ra_c = natural convection Rayleigh number
Z = distance from the leading edge
β = volumetric thermal expansion coefficient
ΔT = surface superheat
μ = viscosity
ρ = density
ϕ = angle of inclination (ϕ = 180, downward-facing horizontal)

Subscripts and Superscripts

B = boiling
c = convection
l = laminar, liquid
t = turbulent
v = vapor

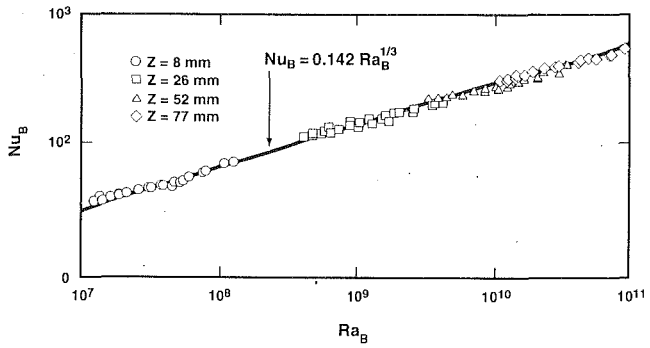

Fig. 1 Comparison between the constant Prandtl number model and the data of Bui and Dhir (1985) for film boiling from vertical surfaces

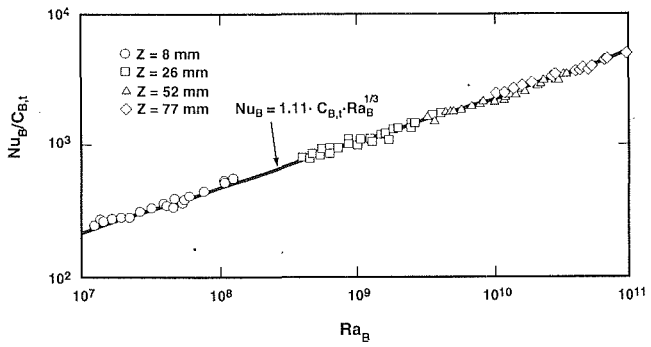

Fig. 3 Comparison between the variable Prandtl number model and the data of Bui and Dhir (1985) for film boiling from vertical surfaces

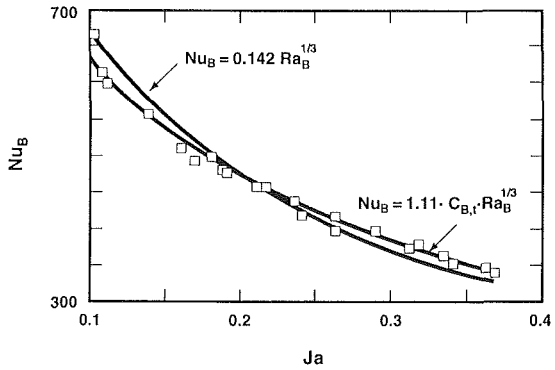

Fig. 2 Film boiling Nusselt number versus Jacob number, Bui and Dhir (1985) data, Z = 77 mm

comparison between the Bui and Dhir data (1985; Bui, 1984) and the correlation is shown in Fig. 1. The standard deviation of the data from the correlation is 5.5 percent. This accuracy for the correlation of heat transfer data can be considered to be reasonable.

However, a close examination of the comparison reveals that for each data set corresponding to a specific distance from the leading edge the trend of the data reflects a power law with an exponent less than 1/3. This discrepancy is further illustrated in Fig. 2 where the Nusselt number is plotted against the Jacob number for the location 77 mm from the leading edge. It is obvious that the shape of the correction is not correct. One way to modify the shape of the correlation is to note that the Prandtl number of steam may not be the correct variable for evaluating the constants C_l and C_t. An alternative would be to use the boiling Prandtl number, Pr_B, as defined in Eq. (4). In this case the values of C_l and C_t become functions of the surface superheat.

The best-fit correlation to the Bui and Dhir data based on the boiling Prandtl number is

$$Nu'_B = 1.11 \cdot C_{B,t} \cdot Ra_B^{1/3} \quad \text{Best Fit} \tag{20}$$

A proportional constant of 1.11 was needed to fit the data. This constant can be interpreted as accounting for systematic differences between natural convection and film boiling. As shown in Figs. 2 and 3, with the boiling Prandtl number the correlation gives an improved fit to the experimental data. The standard deviation of the data from the fit is 4.0 percent.

There are no experimental data that can be used to determine specifically the transition Rayleigh number for turbulent film boiling. An estimate can be obtained by finding the intersection of the Bromley laminar film boiling correlation and the turbulent film boiling correlation (Eq. (18)). The approximate transition Rayleigh number is found to be 3.6×10^6. Of course, it is really more appropriate to speak of a transition region. If data were available an overall correlation from laminar to turbulent film boiling with a smooth transition between the two can probably be constructed using the method first outlined by Churchill and Usagi (1972).

The present model can be extended to the classical case of boiling from an upward-facing surface if it is assumed that the ratio of Nusselt numbers of a vertical surface and a horizontal surface is the same for natural convection and film boiling. From the correlation given by Raithby and Hollands (1985) for turbulent natural convection from horizontal upward-facing surfaces, the correlation for film boiling from such a surface is derived from Eq. (18):

$$Nu_B = 0.188 Ra_B^{1/3} \tag{21}$$

The above expression has the same form as that derived by Klimenko and Shelepen (1982) using the Reynolds analogy, except the proportional constant is 0.169. Recent experiments by Duignan (Duignan et al., 1989; Duignan, 1989) in water give a value of 0.214 for the proportional constant; the difference with the present model is less than 15 percent.

Application of Model to Other Fluids

The correlation is tested against film boiling data in nitrogen (Kuriyama, 1987; Nishio et al., 1991; Suryanarayana and Merte, 1972), R-113 (Liaw and Dhir, 1986), and helium (Nishio and Chandratilleke, 1989) as shown in Figs. 4, 5, and 6. The term h'_B is calculated from Eq. (19), and $h'_B(Pr_B)$ is calculated from Eq. (20). Good agreement is achieved for all fluids except for helium where significant deviations (15 percent) are observed for superheats larger than 20 K. The latent heat for helium is relatively small; at a superheat of 20 K the Jacob number is 5.1. There really are not enough data to determine if the difference points to a deficiency in the correlation or the helium data. It is possible to coax the correlation to fit the helium data if an effective latent heat due to Greitzer and Abernathy (1972), $h'_{fg,GA} = h_{fg}(1 + 0.98Ja + 0.045Ja^2)$, is used (see Fig. 6). The quadratic term only becomes significant for helium with large superheats, otherwise the expression gives essentially the same correlation as the h'_{fg} expression in the present work. Therefore, adapting $h'_{fg,GA}$ in the present correlation will essentially correlate all the data considered. However, there is really no justification to do so.

Also shown in Figs. 4–6 are comparisons with the models of Greitzer and Abernathy (1972), Anderson (1976), Nishio and Chandratilleke (1989), and Nishio et al. (1991). All the models are different versions of what Nishio et al. (1991) termed the laminar-vapor-film-unit (LVFU) model. The model is based on an observed regular bubble pattern traveling up the surface during film boiling. Film boiling is modeled as a series of laminar films whose developments are interrupted by a regular bubble pattern. Therefore, essentially the effective length scale for the application of a Bromley-like laminar analysis is the distance defined by the bubble pattern. The main difference among the models is the way stability theory is applied to

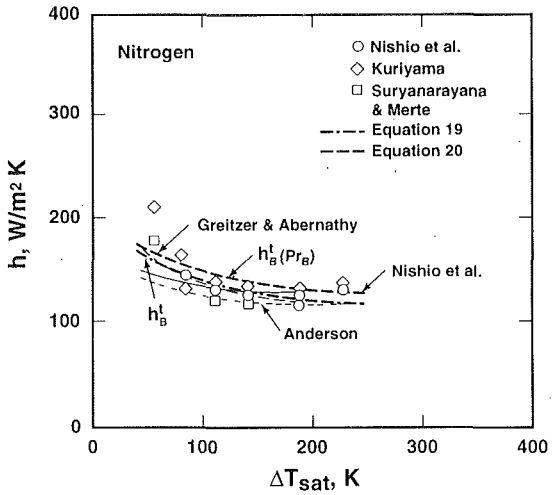

Fig. 4 Comparison between the present model and film boiling data in nitrogen on vertical surfaces

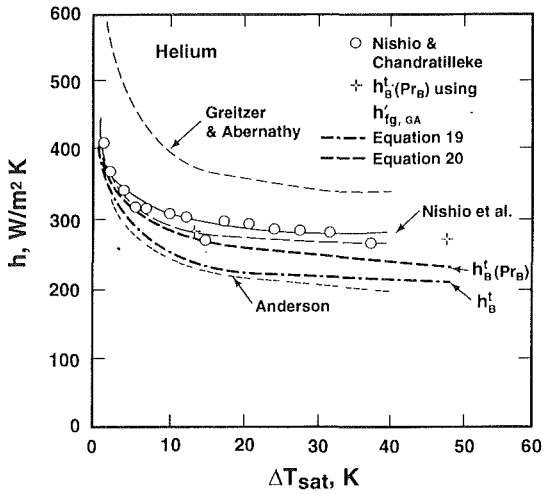

Fig. 6 Comparison between the present model and film boiling data in helium on vertical surfaces

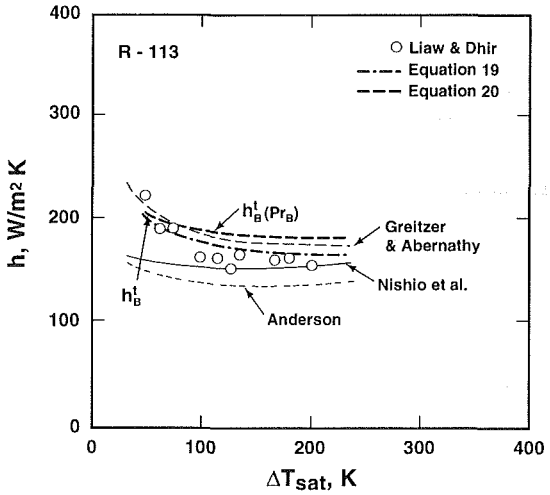

Fig. 5 Comparison between the present model and film boiling data in R-113 on vertical surfaces

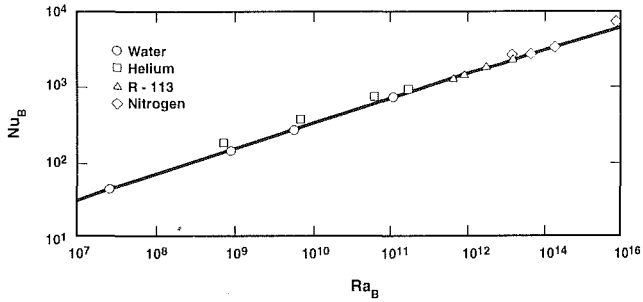

Fig. 7 General comparison of the present correlation and film boiling data for vertical surfaces

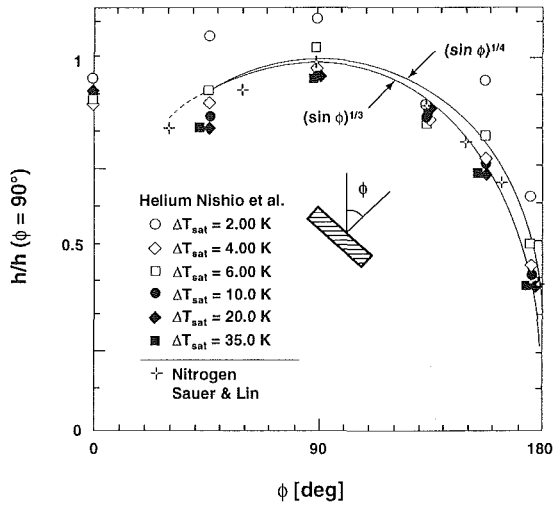

Fig. 8 Film boiling heat transfer coefficient as a function of inclination angle—comparisons of laminar film boiling model, turbulent film boiling model, and data

determine the characteristic length of the bubble pattern. The model results are directly reproduced (rather than recalculated) from published plots. The Nishio et al. (1991) model is probably the best among LVFU models. The Nishio et al. (1991) model performs better than the present model for helium at high superheat but it is 15 percent too low for the water data. The Nishio et al. (1991) model also fails to reproduce the upturn of heat transfer coefficient for small superheats for all fluids except helium. As an overall comparison, it can be seen that none of the models have the wide applicability of the present turbulent model.

At the present time there are no experimental data confirming that the film boiling boundary layer is laminar or turbulent. Therefore, one can make the observation that the existence of a regular bubble pattern over the surface does not exclude the possible existence of a turbulent film boiling boundary layer.

A general comparison of all the data is shown in Fig. 7. The figure is constructed using four representative data points from each fluid. The correlation is in good agreement with all the data spanning seven decades of Rayleigh numbers. The best fit through all the data plotted gives a constant of 0.148 instead of 0.142 for water. The difference is probably the same order of magnitude as scaling the nitrogen, R-113, and helium data from published plots.

Application of Model to Inclined Surfaces

The model can be extended to correlate film boiling data from inclined surfaces. In analogy with natural convection the Nusselt number for a downward-facing inclined surface is obtained by multiplying the Nusselt number for a vertical surface by $\sin^{1/3}\phi$:

$$Nu_{B,\phi} = Nu_{B,(\phi=90°)} \cdot \sin^{1/3}\phi \qquad (22)$$

The above correlation cannot be used for the case of a downward-facing horizontal surface, where $\phi = 0$ deg.

This $\sin^{1/3}\phi$ law is compared with the data of Nishio and Chandratilleke (1989) in helium and the data of Sauer and Lin (1974) in nitrogen in Fig. 8. For the Nishio and Chandratilleke data (1989), the heat transfer coefficients are normalized using the vertical value calculated from the Nishio LVFU models. Similarly, the Sauer and Lin data (1974) are normalized by the experimental value obtained for the vertical orientation. Also shown is a $\sin^{1/4}\phi$ curve, corresponding to a laminar boundary layer or a LVFU model. The data are really not accurate enough to differentiate the two power laws. However, the $\sin^{1/3}\phi$ law certainly gives a reasonable representation of the dependence of the heat transfer coefficient on inclination for downward-facing inclined surfaces ($\phi > 90$ deg). No quantitative examination is made for data corresponding to upward-facing inclined surfaces ($\phi < 90$ deg). However, it is interesting to observe that the trend of the data is similar to the data for detached flow in turbulent natural convection (Raithby and Hollands, 1985).

Concluding Observations

The present analysis shows the existence of an analogy between film boiling and natural convection. A direct application of the analogy for vertical surfaces produced a correlation that shows very good agreement with data in water as well as in nitrogen, helium, and R-113. An extension of the correlation to inclined surfaces also shows fair agreement with existing data. In view of the success of the analogy for vertical surfaces, it would be a natural extension to examine the application of the analogy to other geometries.

Acknowledgments

This work was performed at Sandia National Laboratories and supported by the U.S. Department of Energy under Contract No. DE-AC04-76DP00789.

References

Anderson, J. G. M., 1976, "Low-Flow Film Boiling Heat Transfer on Vertical Surfaces. Part 1: Theoretical Model," *Solar and Nuclear Heat Transfer*, A.I.Ch.E. Symposium Series, Vol. 164, No. 73, p. 2.

Bromley, L. A., 1950, "Heat Transfer in Stable Film Boiling," *Chemical Engineering Progress*, Vol. 46, No. 5, p. 221.

Bui, T. D., 1984, "Film and Transition Boiling Heat Transfer on Vertical Surfaces," Ph.D. Dissertation, University of California, Los Angeles, CA.

Bui, T. D., and V. K. Dhir, 1985, "Film Boiling Heat Transfer on an Isothermal Vertical Surface," ASME JOURNAL OF HEAT TRANSFER, Vol. 107, p. 764.

Chang, Y. P., 1957, "A Theoretical Analysis of Heat Transfer in Natural Convection and Boiling," ASME JOURNAL OF HEAT TRANSFER, Vol. 79, p. 1501.

Chang, Y. P. 1959, "Wave Theory of Heat Transfer in Film Boiling," ASME JOURNAL OF HEAT TRANSFER, Vol. 81, p. 1.

Churchill, S. W., and Usagi, R., 1972, "A General Expression for the Correlation of Rates of Transfer and Other Phenomena," *AIChE Journal*, Vol. 18, No. 6.

Dhir, V., and Lienhard, J., 1971, "Laminar Film Condensation on Plane and Axisymmetric Bodies in Nonuniform Gravity," ASME JOURNAL OF HEAT TRANSFER, Vol. 93, p. 1.

Dhir, V. K., and Bergles, A. E., eds., 1992, *Pool and External Flow Boiling*, Proceedings of the Engineering Foundation Conference on Pool and External Flow Boiling, Santa Barbara, CA, Mar. 22–27.

Duignan, M. R., et al., 1989, "Film Boiling Heat Transfer to Large Superheats From a Horizontal Flat Surface," ASME JOURNAL OF HEAT TRANSFER, Vol. 111, p. 266.

Duignan, M. R., 1989, "Enhanced Convection and Film Boiling Heat Transfer by Surface Gas Injection," Ph.D. Dissertation, State University of New York at Stony Brook, NY.

Frederking, T. H. K., and Clark, J. A., 1963, "Natural Convection Film Boiling on a Sphere," *Advances in Cryogenic Engineering*, Vol. VIII, p. 502.

Greitzer, E. M., and Abernathy, F. H., 1972, "Film Boiling on Vertical Surfaces," *Int. J. Heat Mass Transfer*, Vol. XV, p. 475.

Hsu, Y. Y., and Westwater, J. W., 1960, "Approximate Theory for Film Boiling on Vertical Surfaces," *Chem. Engr. Progr. Symp. Ser.*, Vol. 56, No. 30, p. 15.

Kalinin, E. K., Berlin, I. I., and Kostyuk, V. V., 1975, "Film-Boiling Heat Transfer," *Advances in Heat Transfer*, Vol. II, T. F. Irvine and J. P. Hartnett, eds., Academic Press, NY, pp. 51–197.

Klimenko, V. V., and Shelepen, A. G., 1982, "Film Boiling on a Horizontal Plate—A Supplementary Communication," *Int. J. Heat Mass Transfer*, Vol. XXV, No. 10, p. 1611.

Kuriyama, T., 1987, "Saturated Film-Boiling Heat Transfer on Vertical Surfaces," M. Eng. Thesis, University of Tokyo, Japan.

Liaw, S., and Dhir, V. K., 1986, "Effect of Surface Wettability on Transition Boiling Heat Transfer From a Vertical Surface," *Proceedings of 8th International Heat Transfer Conference*, Vol. 4, p. 2031.

Nishio, S., and Chandratilleke, G. R., 1989, "Steady-State Pool Boiling Heat Transfer to Saturated Liquid Helium at Atmospheric Pressure," *JSME International Journal, II*, Vol. 32, No. 4, p. 39.

Nishio, S., Chandratilleke, G. R., and Ozu, T., 1991, "Natural-Convection Film-Boiling Heat Transfer (Saturated Film Boiling With Long Vapor Film)," *JSME International Journal, II*, Vol. 34, No. 2, p. 202.

Nusselt, W., 1916, "Die Operflachenkondensation des Wasserdampfes," *Z. Ver. Deutsch. Ing.*, Vol. 60, p. 541.

Raithby, G. D., and Hollands, K. G. T., 1978, "Analysis of Heat Transfer by Natural Convection (or Film Condensation) for Three Dimensional Flows," *Proceedings ASME/JSME Thermal Engineering*, Vol. II, p. 275.

Raithby, G. D., and Hollands, K. G. T., 1985, *Handbook of Heat Transfer Fundamentals*, 2nd ed., Rohsenow, Hartnett, and Ganic, eds., McGraw-Hill, New York, p. 6–1.

Sauer, H. J., and Lin, S. C., 1974, "Effect of Inclination on Film Boiling," *Proceedings of the 5th International Heat Transfer Conference*, Tokyo, Japan, Vol. 3, p. 110.

Suryanarayana, N. V., and Merte, H., 1972, "Film Boiling on Vertical Surfaces," ASME JOURNAL OF HEAT TRANSFER, Vol. 94, p. 377.

Diffusion Layer Theory for Turbulent Vapor Condensation With Noncondensable Gases

P. F. Peterson

V. E. Schrock

T. Kageyama

Department of Nuclear Engineering,
University of California,
Berkeley, CA 94720

In turbulent condensation with noncondensable gas, a thin noncondensable layer accumulates and generates a diffusional resistance to condensation and sensible heat transfer. By expressing the driving potential for mass transfer as a difference in saturation temperatures and using appropriate thermodynamic relationships, here an effective "condensation" thermal conductivity is derived. With this formulation, experimental results for vertical tubes and plates demonstrate that condensation obeys the heat and mass transfer analogy, when condensation and sensible heat transfer are considered simultaneously. The sum of the condensation and sensible heat transfer coefficients becomes infinite at small gas concentrations, and approaches the sensible heat transfer coefficient at large concentrations. The "condensation" thermal conductivity is easily applied to engineering analysis, and the theory further demonstrates that condensation on large vertical surfaces is independent of the surface height.

Introduction

Noncondensable gases are well known for degrading condensation heat transfer in a variety of condensing geometries. Predicting this degradation is crucial to the design of new systems for safer, passive containment cooling for next-generation nuclear power reactors, as well as other applications. In condensation the liquid is effectively impermeable to the noncondensable species, so noncondensable gas accumulates next to the liquid/vapor interface. A balance occurs between the bulk convection of noncondensable gas toward the surface and the diffusion of noncondensable gas from the interface. The balance between convection and diffusion results in a logarithmic gas concentration distribution near the interface. Colburn and Hougen (1934) first proposed the theory that condensation mass transport is controlled by diffusion across a thin layer, or film, with the driving potential across the film given by the difference in the bulk and interface gas partial pressures, divided by the log mean gas partial pressure ratio. As the ambient gas concentration approaches zero, the resistance to condensation becomes negligible, the limit one expects.

This work examines two significant classes of condensation problems. For forced convection, extensive experiments were performed inside a vertical tube, providing detailed measurements of multidimensional noncondensable gas distributions. For natural convection, large vertical surfaces were studied. Using the proper formulation of the condensation and sensible heat transfer coefficients, standard heat transfer correlations were found to predict the experimental heat flux measurements accurately. Interestingly, the role of sensible heat transfer was found to be substantial at higher gas concentration, a result credited to mist formation in the saturated vapor/gas mixture. With experiments and analysis Mori and Hijikata (1973) found augmentation by a factor of two due to mist formation.

On vertical surfaces, concentration and temperature gradients develop next to the surface, creating a natural convection boundary layer and augmenting the condensation and sensible heat transfer rate. In the case of laminar boundary layers, Sparrow and Lin (1964) and others have developed analytical treatments, as summarized by Peterson (1992). However, for typical surfaces over 0.25 m in height, buoyancy forces are normally sufficient to generate turbulent flow. Traditionally, for vertical surfaces, nuclear applications have used an empirical curve fit of heat transfer coefficient data versus the gas-to-steam weight ratio measured by Uchida et al. (1965). Recently Kataoka et al. (1991) reconfirmed these results in a 4.2-m-high apparatus, showing that the condensation heat transfer coefficient follows that measured by Uchida et al. closely when plotted versus the steam-to-gas weight ratio. Dehbi et al. (1991) performed additional experiments for condensation on the outside of a vertical tube with both air and helium present.

Akers et al. (1960) applied the film model to predict condensation rates on vertical tubes and small vertical surfaces at lower Rayleigh numbers. Corradini (1984) applied a film model to predict the experimental data of Uchida et al. (1965) and Tagami (1965) for vertical surfaces. Subsequently Kim and Corradini (1990) improved the Corradini model by adopting the mass transfer coefficient recommended by Bird et al. (1960) for film problems, with the recommended correction factor for wall suction. Kim and Corradini report extensive investigations of film waviness effects and two-dimensional modeling.

Film models of the Colburn–Hougen type can be cumbersome in practice, requiring extensive iterations to match the condensation mass flux to heat transport through the condensate film and external thermal resistances, as outlined by Collier (1981). The complexity of film models has prompted researchers like Henderson and Marchello (1969) to correlate condensation data as the ratio of the experimental heat transfer coefficient, defined as $q_t''/(T_b^s - T_w)$, to the Nusselt solution for pure vapor. This simplified method was employed successfully by Vierow and Schrock (1991) to model condensation in a natural circulation loop.

Physically, however, condensation is best described by the resistances of the condensate film and noncondensable/vapor mixture placed in series. In the present paper a condensation heat transfer coefficient is defined based on the difference between the interface temperature and bulk saturation (dew point) temperature, as done by Corradini (1984) and Kim and Corradini (1990). Then to maintain simplicity, a "condensation" thermal conductivity is derived from thermodynamics and the fundamental solution for mass transport in diffusion layers with noncondensables. The resulting condensation ther-

Contributed by the Heat Transfer Division and presented at the National Heat Transfer Conference, San Diego, California, August 1992. Manuscript received by the Heat Transfer Division March 1992; revision received February 1993. Keywords: Condensation, Multiphase Flows, Phase-Change Phenomena. Associate Technical Editor: L. C. Witte.

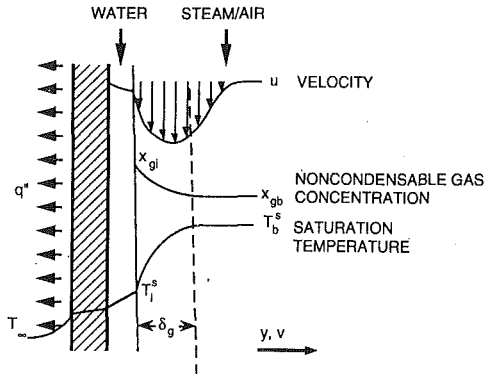

Fig. 1 Schematic diagram of noncondensable diffusion layer on a vertical plate

mal conductivity varies from zero at large gas concentrations to infinity at zero gas concentration. When combined with the sensible heat transfer contribution, for fully developed flow excellent prediction of experimental data is obtained with standard heat transfer correlations, over the full range of gas concentrations. Care should be taken in entrance regions, however, as temperature inversions and other phenomena cause large departures from fully developed behavior (Vierow and Schrock, 1991).

The significant advantage of the condensation thermal conductivity formulation is as follows. Because the condensation heat transfer coefficient is defined based on temperatures, in application it can be combined in parallel with the sensible heat transfer coefficient and in series with the film and wall resistances to determine the overall resistance to heat transfer. Further, use of this formulation to reduce experimental data has demonstrated the significant influence of sensible heat transfer and mist formation.

Diffusion Layer Theory Development

Figure 1 shows typical noncondensable gas mole fraction and temperature profiles for free convection condensation on vertical surfaces, where the gas-species molecular weight is greater than the vapor-species molecular weight. Noncondensable gas accumulates at the liquid/vapor interface, reducing the interface saturation temperature T_i^s below the bulk mixture saturation temperature T_b^s. The difference between the interface temperature T_i^s and the cooling medium temperature T_∞ governs the total heat flux q_t'' through the wall. The heat flux through the film and wall must equal the sum of the flux of latent heat q_c'' and the sensible heat q_s'' through the vapor to the liquid/vapor interface,

$$h_w(T_i^s - T_\infty) = q_t'' = q_c'' + q_s'' = -h_{fg}cM_v\tilde{v}_i + k_v\left(\frac{\partial T}{\partial y}\right)_i \quad (1)$$

where h_w is an effective heat transfer coefficient combining the condensate film, wall, and external thermal resistances, h_{fg} the latent heat, c the total molar density, M_v the molecular weight of the vapor species, k_v the vapor/gas mixture thermal conductivity, and y the coordinate normal to the surface. For higher temperatures, as may occur with hydrogen combustion, an additional term for radiation is required. The average molar velocity away from the interface, $\tilde{v}_i$, is related to the noncondensable gas mole fraction x_g by Fick's law,

$$cv_{gi} = cx_{gi}\tilde{v}_i - cD\frac{\partial x_g}{\partial y} \quad (2)$$

where D is the mass diffusion coefficient. The interface is impermeable to the noncondensable gas, so the absolute gas species velocity at the interface equals zero, $v_{gi} = 0$, and the condensation velocity is

$$\tilde{v}_i = \left(D\frac{1}{x_g}\frac{\partial x_g}{\partial y}\right)_i = \left(D\frac{\partial}{\partial y}\ln\,(x_g)\right)_i \quad (3)$$

The gradient of $\ln\,(x_g)$ at the interface can be related to the interface and bulk gas concentrations, x_{gi} and x_{gb}, by considering an effective thickness of the diffusion layer δ_g, shown in Fig. 1, where the thickness δ_g is defined through the relationship

$$\tilde{v}_i = \frac{D}{\delta_g}(\ln\,(x_{gb}) - \ln\,(x_{gi})) \quad (4)$$

It is useful to define a log mean mole fraction as

$$x_{\text{avg}} = \frac{x_b - x_i}{\ln\,(x_b/x_i)} \quad (5)$$

Under this definition, $x_b < x_{\text{avg}} < x_i$, and the condensation velocity can be written as

$$\tilde{v}_i = \frac{D}{x_{g,\text{avg}}\delta_g}(x_{gb} - x_{gi}) \quad (6)$$

Assuming ideal gas behavior, the mole fractions can be expressed as

$$\tilde{v}_i = \frac{D}{P_i x_{g,\text{avg}}\delta_g}(P_{vi} - P_{vb}) \quad (7)$$

where P_{vi} and P_{vb} are the partial pressures of the vapor at the

Nomenclature

c = molar density
c_p = constant pressure specific heat
d = diameter
D = mass diffusivity
Gr = Grashof number, Eq. (20)
h = heat transfer coefficient
h_{fg} = latent heat of vaporization
k = thermal conductivity
L = vertical length of surface
M = molecular weight
Nu = Nusselt number = h_sL/k_s
P = absolute pressure
q'' = heat flux
R = universal gas constant
Pr = Prandtl number = $c_p\mu/k_s$
Ra = Rayleigh number = GrSc or GrPr
Re = Reynolds number = $\rho vd/\mu$
Sc = Schmidt number = $\mu/\rho D$
Sh = Sherwood number = h_cL/k_c
T = absolute temperature
v = velocity
$\tilde{v}$ = molar average velocity
v_{fg} = difference between vapor and liquid specific volumes
x = mole fraction
x_{avg} = average mole fraction, Eq. (5)
y = coordinate normal to interface
δ = diffusion layer thickness
ϕ = gas/vapor log mean concentration ratio, Eq. (11)

Subscripts

b = bulk
c = condensation
g = noncondensable gas species
i = liquid/vapor interface
s = sensible heat
t = total
v = vapor species
w = wall, film, and external resistance
wb = wet bulb
∞ = bulk cooling medium

Superscript

s = saturation

interface and in the bulk fluid, respectively, and P_t is the total pressure.

The difference of partial pressures in Eq. (7) is not convenient for heat transfer calculations. If the difference is expressed in terms of saturation temperatures, then the wall, film, sensible, and condensation heat transfer coefficients can be combined. A modified Clausius–Clapeyron equation, where v_{fg} is an appropriate mean value in the boundary layer, provides a relationship between saturation pressures of Eq. (7) and the saturation temperatures at the interface and in the bulk, T_i^s and T_b^s. Using $\Delta P/\Delta T^s = h_{fg}/Tv_{fg}$ and the approximation $v_{fg} = \mathrm{R}T_{\mathrm{avg}}/M_v x_{v,\mathrm{avg}} P_t$, where the log mean vapor concentration $x_{v,\mathrm{avg}}$ is defined by Eq. (5), the molar condensation velocity is

$$\tilde{v}_i = \frac{Dh_{fg}M_v x_{v,\mathrm{avg}}}{RT_{avg}^2 x_{g,\mathrm{avg}}\delta_g}\,(T_i^s - T_b^s) \tag{8}$$

where R is the universal gas constant and $T_{\mathrm{avg}} = (T_i^s + T_b^s)/2$ the average temperature in the diffusion layer. For water vapor Eq. (8) gives velocity values within 3 percent of Eq. (7).

The Sherwood number relates the effective diffusion layer thickness δ_g to the characteristic system dimension L. Combining Eqs. (1), (3), and (8) and replacing the molar density c using the ideal gas law gives

$$\mathrm{Sh}_L = \frac{L}{\delta_g} = \left(\frac{q_c''}{T_b^s - T_i^s}\right) L\phi \left(\frac{R^2 T_{\mathrm{avg}}^3}{h_{fg}^2 P_t M_v^2 D}\right) \tag{9}$$

The first term on the right side is readily recognized as a condensation heat transfer coefficient. The saturation temperatures determine the driving potential for the condensation heat transfer coefficient h_c, such that

$$h_c = \frac{q_c''}{T_b^s - T_i^s} \tag{10}$$

The third term of Eq. (9) is the gas/vapor log mean concentration ratio, given by

$$\phi = \frac{x_{g,\mathrm{avg}}}{x_{v,\mathrm{avg}}} = -\frac{\ln[(1-x_{gb})/(1-x_{gi})]}{\ln[x_{gb}/x_{gi}]} \tag{11}$$

Uchida et al. (1965) used the gas-to-steam weight ratio to correlate condensation data for a vertical plane. The gas-to-steam weight ratio can be expressed as $\phi M_g/M_v$, providing a theoretical basis for their empirical observations on the effects of gas concentration.

Combined, the third and last terms of Eq. (9) have the inverse units of thermal conductivity, and can be viewed as an inverse *effective condensation thermal conductivity*, $1/k_c$. Because the mass diffusion coefficient varies inversely with pressure and with approximately the square of temperature (Bird et al., 1960), the effective condensation thermal conductivity can be written

$$k_c = \frac{1}{\phi T_{\mathrm{avg}}}\left(\frac{h_{fg}^2 P_o M_v^2 D_o}{R^2 T_o^2}\right) \tag{12}$$

where diffusion coefficient D is given in terms of the value D_o at a reference temperature T_o and pressure P_o.

The condensation thermal conductivity k_c increases as the gas/vapor log mean concentration ratio ϕ decreases. As required, the condensation thermal conductivity rapidly becomes infinite when the gas concentration reaches zero, and approaches zero as the gas concentration approaches unity. Furthermore, the condensation thermal conductivity is only weakly dependent upon pressure (as is the sensible thermal conductivity for gases), although it decreases as the average temperature T_{avg} increases. The Sherwood number for condensation now takes a simple form,

$$\mathrm{Sh}_L = \frac{h_c L}{k_c} \tag{13}$$

Equation (1) for the heat flux can be written as

$$h_w(T_i^s - T_\infty) = q_c'' + q_s'' = h_c(T_b^s - T_i^s) + h_s(T_b - T_i^s) \tag{14}$$

where h_c is the condensing heat transfer coefficient given by Eq. (10), and h_s the sensible heat transfer coefficient. Note that the driving potential for the condensing heat transfer coefficient depends on the bulk saturation temperature T_b^s, as this saturation temperature gives the driving potential for mass transfer. The driving potential for sensible heat transfer is the actual bulk temperature T_b, which allows for superheated vapor conditions.

When the bulk mixture is saturated, the condensation and sensible heat transfer coefficients can be combined into a total heat transfer coefficient, $h_t = h_c + h_s$. The total heat transfer coefficient, which can be measured experimentally, takes the correct limiting behavior with gas concentration. For small gas concentrations, $\phi \ll 1$, the condensation heat transfer coefficient dominates over the sensible heat transfer coefficient, which remains approximately constant with gas concentration. For large gas concentrations $\phi \gg 1$ and $h_t \to h_s$, as condensation becomes negligible.

Because the condensation mass transfer has been expressed in terms of a temperature difference, in engineering applications the heat transfer resistances can be summed in Eq. (14) to eliminate the interface temperature, giving the total heat flux as

$$q_t'' = \frac{h_c(T_b^s - T_\infty) + h_s(T_b - T_\infty)}{1 + \dfrac{h_c + h_s}{h_w}} \tag{15}$$

With an appropriate correlation for the Sherwood number and initial guess for the interface gas concentration, this formulation can be applied iteratively, converging to the correct heat flux and gas/vapor log mean concentration ratio ϕ in 2–10 iterations. Because ϕ depends on the average of the interface and bulk concentrations, while standard solutions depend on the difference between the concentrations, this solution technique is less sensitive to the initial guess for the interface concentration. Further, the solution is simple compared to iteratively matching the mass flux calculated from the difference between the interface and bulk concentrations, to the sum of sensible heat transport to the interface and conduction away through the liquid film.

Condensation in Vertical Tubes

Turbulent heat transfer in tubes is commonly correlated in the form

$$\mathrm{Nu}_d = C\mathrm{Re}_d^{0.8}\mathrm{Pr}^n \tag{16}$$

where $\mathrm{Nu}_d = hd/k$ is the Nusselt number, $\mathrm{Re} = \rho v d/\mu$ the Reynolds number, $\mathrm{Pr} = \mu c_p/k$ the Prandtl number, v the mass-averaged bulk velocity, d the pipe diameter, and μ the viscosity. The coefficients are commonly given the values $C = 0.023$ and $n = 0.35$.

In the experiments performed here, the gas/vapor mixture was saturated, so that $T_b = T_b^s$. Using Eq. (16), the condensation and sensible heat transfer coefficients can be expressed as $h_c = C_c(k_c/d)\mathrm{Re}_d^{0.8}\mathrm{Sc}^{0.35}$ and $h_s = C_s(k_s/d)\mathrm{Re}_d^{0.8}\mathrm{Pr}^{0.35}$. Inserting these into Eq. (14), a total Nusselt number can be defined in terms of experimentally measurable quantities,

$$\mathrm{Nu}_{dt} = \frac{q_t'' d/(T_b^s - t_t^s)}{k_c + \dfrac{C_s}{C_c}\left(\dfrac{\mathrm{Pr}}{\mathrm{Sc}}\right)^{0.35}} = C_c\mathrm{Re}_d^{0.8}\mathrm{Sc}^{0.35} \tag{17}$$

where the Schmidt number is $\mathrm{Sc} = \mu/\rho D$ and separate constants C_c and C_s are provided for the condensation and sensible heat transfer coefficients.

The local Nusselt number predicted by Eq. (17) was compared with values measured in an apparatus equipped with a

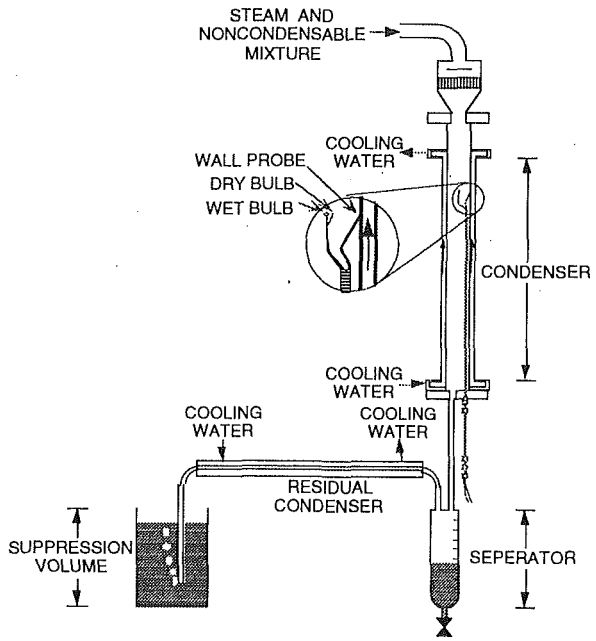

Fig. 2 Schematic of experimental apparatus for condensation in vertical tubes

traversing miniature wet-bulb probe. Kageyama (1992) provides a detailed description of the device and the error analysis. The local gas concentration comes from the total pressure and the saturation pressure determined from the wet-bulb temperature, $x_g = 1 - P^s_{wb}/P_t$, as described by Peterson and Tien (1987). With the apparatus and probe, shown in Fig. 2, radial and axial gas concentration measurements could be made throughout the condensing test section.

The test section consisted of a 41.3-mm-i.d., 4.76-mm-wall pyrex glass tube with an inlet honeycomb flow straightening section. Water circulated in the annulus between the inner and outer glass tubes to cool the 1.0-m-long condenser section. Measurements were made in locations at least $L/D > 10$ down the tube, to insure that the local heat transfer and turbulence were close to fully developed. The wall heat flux was determined from temperature measurements on both sides of the glass wall. Because the temperature difference across the glass was large (>30°C), error in the heat flux measurement was under 3 percent. The transducer used to measure the total pressure was calibrated by measuring the temperature of pure, saturated steam with the wet-bulb probe. This direct calibration for total pressure allowed gas concentrations to be measured with the wet-bulb probe with an accuracy of 1.5 percent.

The steam flow rate was determined within 1.5 percent by volumetric measurements of the condensate flow rate. The gas flow rate was determined within 2.0 percent using volumetric measurements, capturing the gas in a submerged vessel over a measured time period. The bulk gas concentration was estimated from a mass balance accounting for the upstream condensation rate. Transport properties were evaluated at the arithmetic mean of the bulk and interface temperatures and gas concentrations, using the mixture property values summarized calculated using the mixture property evaluation methods recommended by Reid et al. (1988) (Wilke's method for viscosity, Mason and Saxena modification for thermal conductivity, and mole fraction weighting for specific heat).

In the tests, the dominant source of experimental error was the evaluation of the gas/vapor log mean concentration ratio ϕ. For turbulent flow with smaller gas concentrations, the difference between the bulk and interface concentrations becomes small. The ratio ϕ then becomes very sensitive to absolute errors in the interface temperature measurement. The interface temperature was estimated from wall temperature

Table 1 Typical percentage change in Nusselt number from a ±0.3°C change in interface temperature for turbulent flow

x_{gb}	0.033	0.068	0.223	0.309
$\Delta T_i = 0.3$	+79.7	+25.1	+11.3	+4.3
$\Delta T_i = -0.3$	−26.7	−15.4	−9.0	−3.9

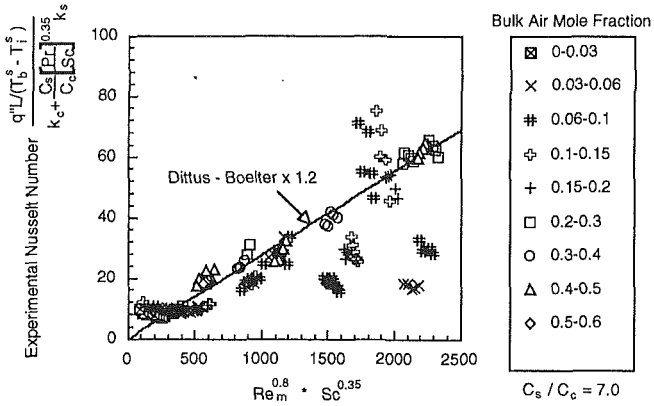

Fig. 3 Experimentally measured Nusselt number for condensation in vertical tubes; primary data scatter occurs at low gas concentrations

measurements made with a thermocouple pressed against the inside wall. Due to conduction along the leads, the measured temperature fell between the actual wall and interface temperatures. Measurements made with pure steam, where the interface temperature equals the saturation temperature, showed that the interface temperature was consistently 0.4 to 0.7°C higher than the measured wall temperature. Thus the measured wall temperature was increased by 0.3 to 0.7°C, depending on heat flux, giving the interface temperature with an estimated accuracy of ±0.3°C. As shown in Table 1 for typical turbulent flow measurements, the resulting error in the measured Nusselt number was large for small bulk gas concentrations, but the error dropped quickly as the bulk gas concentration increased. The accuracy was better for laminar flow, because the larger condensation resistance resulted in larger differences between the interface and bulk concentrations. This behavior is reflected in the experimental data, which scatters widely for smaller gas concentrations in turbulent flow, but converges nicely otherwise.

Figure 3 compares experimentally measured Nusselt numbers with the product $Re_d^{0.8}Sc^{0.35}$. Relatively wide scatter is observed for turbulent flow ($Re_d^{0.8}Sc^{0.35} > 370$) with bulk gas mole fractions less than 0.2, as expected due to the uncertainty in measuring the interface temperature. For $x_{gb} > 0.2$ and $Re_d > 10{,}000$ excellent agreement is obtained using $C_c = 1.2 \times 0.023 = 0.0276$ and $C_s/C_c = 7.0$, giving a standard deviation of 4.7 percent. For $Re_d > 2000$ and $x_{gb} > 0.2$, the agreement still gives a standard deviation of 13.2 percent, showing that the correlation can be applied in the transition region. The factor 1.2 multiplying the standard Dittus-Boelter coefficient is attributed to the effects of surface roughness due to film waviness, and to suction due to condensation. The augmentation of the sensible heat transfer factor C_s by an additional factor of 7.0 is attributed to mist formation as discussed in more detail for vertical plates. Also interesting is the fact that the Nusselt number approaches a constant value of 8.7 for laminar vapor flow with standard deviation 12 percent, in contrast to the constant value 4.364 obtained analytically for laminar constant heat flux heat transfer in tubes (here the high thermal resistance of the glass resulted in a relatively uniform condensation rate, mimicking constant heat flux behavior).

Condensation on Vertical Surfaces

With natural convection condensation on vertical surfaces, both temperature and concentration gradients contribute to

the density difference between the fluid at the surface and the ambient fluid. Assuming ideal gas behavior, the Rayleigh number for mass transfer under natural convection can be expressed as

$$\mathrm{Ra}_{Lc}=\mathrm{Gr}_L\mathrm{Sc}=\frac{gL^3}{\mu D}(\rho_i-\rho_b)=\frac{gL^3\rho_{vo}}{\mu D}\left\{\frac{T_o}{T_i}\left[1+x_{gi}\left(\frac{M_g}{M_v}-1\right)\right]-\frac{T_o}{T_b}\left[1+x_{gb}\left(\frac{M_g}{M_v}-1\right)\right]\right\} \quad (18)$$

where ρ_{vo} is the density of pure vapor at the total pressure P_t and a reference temperature T_o, and M_g and M_v are the molecular weights of the gas and vapor species. The average mixture viscosity μ is evaluated at the arithmetic mean of the interface and bulk temperatures and concentrations, using Wilke's method (Reid et al., 1988).

For the range of Rayleigh number values $10^9 < \mathrm{Ra}_L < 10^{13}$, which is typical for condensation on surfaces greater than 0.5 m in height, for heat transfer Warner and Arpaci (1968) give

$$\mathrm{Nu}_L=C(\mathrm{Ra}_{Ls})^{1/3}=C(\mathrm{Gr}_{Ls}\mathrm{Pr})^{1/3} \quad (19)$$

where they recommend $C = 0.10$. In this high Rayleigh number, turbulent regime, the Nusselt number increases linearly with the surface height L. As shown later the mass transfer can be treated analogously to heat transfer (using $\mathrm{Sh}_L = \mathrm{Nu}_L$ and $\mathrm{Ra}_{Lc} = \mathrm{Ra}_{Ls}\mathrm{Sc}/\mathrm{Pr}$), and thus the condensation heat transfer coefficient is independent of the surface height in this turbulent regime, a result justifying extrapolation of smaller scale experiments to full-scale containment modeling. Dehbi et al. (1991) found experimental evidence of the independence from surface height.

Kataoka et al. (1991) performed extensive condensation experiments on the 4.2-m-high wall of a water-wall simulator, obtaining Rayleigh numbers ranging from $9 \times 10^{10} < \mathrm{Ra}_{Lc} < 1 \times 10^{12}$. They measured the initial gas pressure, total pressure, and bulk and wall temperatures. The heat flux through the wall was measured with thermocouples on either side of the wall. Here the total Nusselt number calculated from the data of Kataoka et al. is compared with the Rayleigh number to the 1/3 power, where the Nusselt number is

$$\mathrm{Nu}_{Lt}=\frac{q_t'' L/(T_b^s-T_i^s)}{k_c+\frac{C_s}{C_c}\left(\frac{\mathrm{Pr}}{\mathrm{Sc}}\right)^{0.33}k_s}=C_c(\mathrm{Ra}_{Lc})^{0.33}=C_c(\mathrm{Gr}_{Lc}\mathrm{Sc})^{0.33} \quad (20)$$

and separate scaling coefficients C_c and C_s are provided for the condensation and sensible heat transfer coefficients. Here the effect of the condensate film resistance is neglected, as calculations for laminar films show it to be less than 5 percent of the total resistance. The bulk gas concentration x_{gb} was calculated from the total pressure, bulk temperature, and initial pressure, assuming ideal gas behavior. The interface concentration was calculated from the saturation pressured based on the wall temperature and total pressure.

Figure 4 shows a comparison of the total Nusselt number (Eq. (20)) and condensation Rayleigh number from the data of Kataoka et al. Using the standard scaling coefficient $C_c = 0.10$ for condensation and a larger value $C_s = 0.7$ for sensible heat transfer, the ratio of the experimental total heat transfer coefficient to the predicted value scatters by a maximum of 7 percent, with a standard deviation of 4.0 percent. Figure 5 shows the relative contributions of condensation and sensible heat transfer as the average gas concentration changes. As the gas concentration becomes small, $\phi \to 0$, the condensation heat transfer coefficient becomes large. For gas mole average ratios $\phi > 6$ (bulk mole fraction $x_{gb} > 0.8$) sensible heat transfer begins to contribute more than half of the total heat transfer.

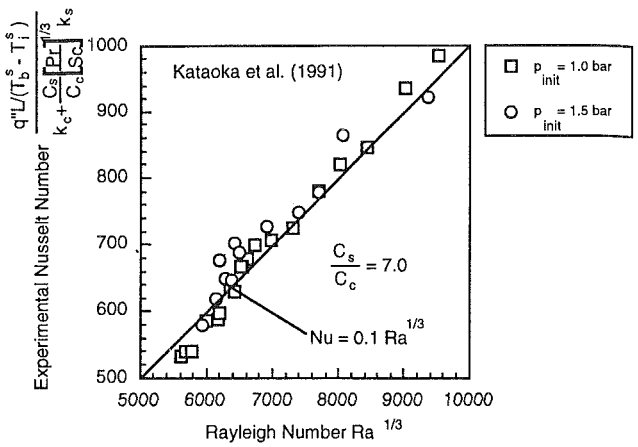

Fig. 4 Comparison of calculated total heat transfer coefficient with data of Kataoka et al. (1991)

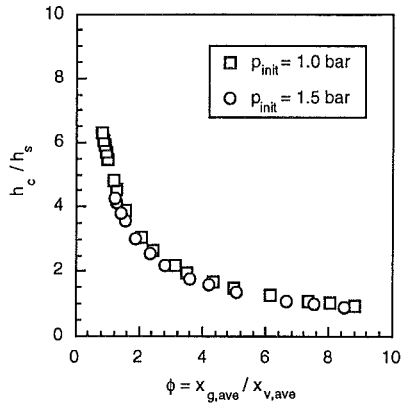

Fig. 5 Relative contributions of condensation and sensible heat transfer as a function of average gas concentration

The scaling coefficient for condensation, $C_c = 0.10$, matches the value found for heat transfer (Warner and Arpaci, 1968). However, the sensible heat scaling coefficient is larger, $C_s/C_c = 7.0$, almost an order of magnitude greater than that found for dry sensible heat transfer. This effect is attributed to mist formation, which substantially increases the effective specific heat c_p and thus the ratio $\mathrm{Pr}/\mathrm{Sc} = \rho c_p D/k_s$ in Eq. (20). A C_s/C_c ratio greater than unity corrects for the augmented specific heat. Mist formation has been observed experimentally by Mori and Hijikata (1973) during condensation of steam on vertical surfaces. Applying an integral boundary layer technique, they showed that mist formation augmented the total heat transfer by up to a factor of 2, requiring an even larger factor if the augmentation is credited to the sensible heat transfer contribution. Dehbi et al. (1991) visually observed gas mixture layer movement in their experiments, noting a drifting motion toward the wall that would imply the presence of mist. No data are available, but it would be expected that C_s/C_c would approach unity as the gas–vapor mixture becomes superheated.

Uchida et al. (1965) performed a series of experiments on a 0.3-m-high by 0.14-m-wide plate. Tagami (1965) performed experiments with vertical cylinders 0.3 and 0.9 m in height and 0.64 m in diameter inside a 3.3-m-ID, 6-m-high, 42-m^3-volume containment. The surfaces were cooled to maintain at a constant temperature of 322 K. The experiments covered a Rayleigh number range from $1 \times 10^7 < \mathrm{Ra}_{Lc} < 6 \times 10^{10}$. The vessels were filled with an initial quantity of air, nitrogen, or argon, and then steam was introduced. By increasing the steam flow rate in increments, the total pressure was increased, reducing the bulk gas concentration. The inlet and outlet cooling water, condensing surface, and vapor bulk temperatures were

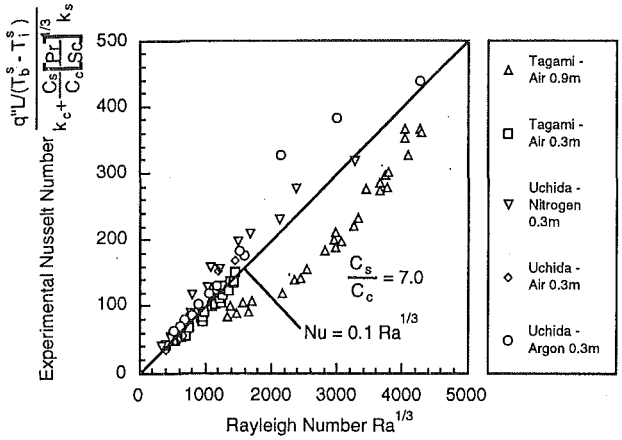

Fig. 6 Comparison of calculated total heat transfer coefficient with data of Uchida et al. (1965) and Tagami (1965)

measured to determine the heat flux and overall heat transfer coefficient, but unfortunately only graphic results for the heat transfer coefficient versus bulk gas mass ratio were presented, so the vapor temperature and (for Uchida et al.) total pressure must be inferred by assuming saturated conditions and ideal gas behavior, with an initial gas pressure of 1.0 bar.

Figure 6 compares Nusselt numbers versus Rayleigh numbers from data measured by Uchida et al. (1965) and Tagami (1965). Agreement is good, except for the data of Tagami for the 0.9-m-high cylinder. The ratio of the experimental total heat transfer coefficient to the predicted value scatters by a maximum of 46 percent, with a standard deviation of 23 percent. The transition to turbulence is known to occur between $10^8 < Ra_L < 10^{10}$, and the correlation form $Ra_L^{1/3}$ is often used down to 10^8. Here this form was found to work well for $Ra_L > 10^7$.

Conclusions

Beginning with the fundamental mass transfer equations and boundary conditions for condensation with noncondensable gases, an effective "condensation thermal conductivity," Eq. (12), was derived. With this simple parameter, combined sensible and condensation heat transfer can be predicted using the standard forms for heat transfer correlations.

For turbulent forced convection heat transfer ($Re_d > 2000$) from saturated vapor/gas mixtures in vertical tubes, the total heat transfer coefficient can be calculated using Eq. (17) with $C_c = 0.0276$ and $C_s/C_c = 7.0$. For laminar flow ($Re_d < 2000$) the Nusselt number is constant and equals 8.7. For turbulent natural convection heat transfer ($Ra_{Lc} > 10^7$) from saturated vapor/gas mixtures onto vertical flat plates and cylinders, the total heat transfer coefficient can be calculated using Eq. (20) with $C_c = 0.10$ and $C_s/C_c = 7.0$. As the vapor/gas mixture becomes superheated, C_s/C_c can be expected to drop toward unity as mist formation is reduced. For conservative design, $C_s/C_c = 1.0$ should be used for all cases.

Acknowledgments

The support of the National Science Foundation under Presidential Young Investigator grant No. CTS-9057258 is sincerely appreciated.

References

Akers, W. W., Davis, S. H., and Crawford, J. E., 1960, "Condensation of a Vapour in the Presence of Non-condensing Gas," *Chem. Engng. Prog. Symp. Series*, No. 30, Vol. 56, pp. 139–144.

Bird, R. B., Stewart, W. E., and Lightfoot, E. N., 1960, *Transport Phenomena*, Wiley, New York, pp. 511, 658–671.

Colburn, A. P., and Hougen, O. A., 1934, "Design of Cooler Condensers for Mixtures of Vapours With Non-condensing Gases," *Ind. Engng. Chem.*, Vol. 26, No. 11, pp. 1178–1182.

Collier, J. G., 1981, *Convective Boiling and Condensation*, 2nd ed., McGraw-Hill, New York, pp. 323–328.

Corradini, M. L., 1984, "Turbulent Condensation on a Cold Wall in the Presence of a Noncondensable Gas," *Nuclear Technology*, Vol. 64, pp. 186–195.

Dehbi, A. A., Golay, M. W., and Kazimi, M. S., 1991,"The Effects of Noncondensable Gases on Steam Condensation Under Turbulent Natural Convection Conditions," Report No. MIT-ANP-TR-004, Massachusetts Institute of Technology, Cambridge, MA.

Henderson, C. L., and Marchello, J. M., 1969, "Film Condensation in the Presence of a Noncondensable Gas," ASME JOURNAL OF HEAT TRANSFER, Vol. 91, pp. 447–450.

Kageyama, T., 1992, "Application of Diffusion Layer Theory to Vertical Downflow Condensation Heat Transfer," Master's Thesis, Dept. of Nuclear Engineering, University of California, Berkeley.

Kataoka, Y., Fukui, T., Hatamiya, S., Nakao, T., Naitoh, M., and Sumida, I., 1991, "Experimental Study on Convection Heat Transfer Along a Vertical Flat Plate Between Different Temperature Pools," *ANS Proceedings*, National Heat Transfer Conference, Vol. 5, pp. 99–106.

Kim, M. H., and Corradini, M. L., 1990, "Modeling of Condensation Heat Transfer," *Nuclear Engineering and Design*, Vol. 118, pp. 193–212.

Mori, Y., and Hijikata, K., 1973, "Free Convective Condensation Heat Transfer With Noncondensable Gas on a Vertical Surface," *International Journal of Heat and Mass Transfer*, Vol. 16, pp. 2229–2240.

Peterson, P. F., and Tien, C. L., 1987, "A Miniature Wet-Bulb Technique for Measuring Gas Concentrations in Condensing or Evaporating Systems," *Experimental Heat Transfer*, Vol. 1, pp. 1–15.

Peterson, P. F., 1992, "Species-Controlled Condensation in Enclosures," *Annual Review of Heat Transfer*, C. L. Tien, ed., Hemisphere, New York, pp. 247–295.

Reid, R. C., Prausnitz, J. M., and Poling, B. E., 1988, *The Properties of Gases and Liquids*, McGraw-Hill, New York, pp. 121, 407, 531.

Sparrow, E. M., and Lin, S. H., 1964, "Condensation Heat Transfer in the Presence of Noncondensable Gas," ASME JOURNAL OF HEAT TRANSFER, Vol. 86, pp. 430–436.

Tagami,T., 1965, "Interim Report on Safety Assessments and Facilities Establishment Project for June 1965," No. 1, Japanese Atomic Energy Research Agency, unpublished work (see Corradini, 1984).

Uchida, H., Oyama, A., and Togo,Y., 1965, "Evaluation of Post-incident Cooling Systems of Light-Water Power Reactors," *Proceedings of the Third International Conference on the Peaceful Uses of Atomic Energy*, Geneva, Aug. 31–Sept. 9, 1964, Vol. 13, United Nations, New York, pp. 93–104.

Vierow, K. M., and Schrock, V. E., 1991, "Condensation in a Natural Circulation Loop With Noncondensable Gases: Part I—Heat Transfer," *Proc. Intl. Conf. on Multiphase Flows*, Tsukuba,Japan, Sept., pp. 183–186.

Warner, C. Y., and Arpaci, V. S., 1968,"An Experimental Investigation of Turbulent Natural Convection in Air at Low Pressure Along a Vertical Heated Flat Plate," *International Journal of Heat and Mass Transfer*, Vol. 11, p. 397.

A Spectral Line-Based Weighted-Sum-of-Gray-Gases Model for Arbitrary RTE Solvers

M. K. Denison

B. W. Webb

Department of Mechanical Engineering,
Brigham Young University,
Provo, UT 84602

This paper presents an approach for generating weighted-sum-of-gray gases (WSGG) models directly from the line-by-line spectra of H_2O. Emphasis is placed on obtaining detailed spectral division among the gray gases. Thus, for a given model spectrum, the gray gas weights are determined as blackbody fractional functions for specific subline spectral regions at all temperatures. The model allows the absorption coefficient to be the basic radiative property rather than a transmissivity or band absorptance, etc., and can be used with any arbitrary solution method for the Radiative Transfer Equation (RTE). A single absorption cross section spectrum is assumed over the entire spatial domain in order to fix the subline spectral regions associated with a single spectral calculation. The error associated with this assumption is evaluated by comparison with line-by-line benchmarks for problems of nonisothermal and nonhomogeneous media.

Introduction

Radiative heat transfer in gases has important applications from combustion systems to modeling atmospheric processes. Modeling radiative heat transfer with participating media is more difficult with gases than other participating media such as suspended particulates because of the strong spectral variations of the radiative properties (i.e., the absorption coefficient, κ_η). The radiative properties of polydisperse particulates such as soot vary slowly with frequency or wavelength. Gases, on the other hand, emit and absorb electromagnetic radiation only at frequencies where the corresponding photon energies match the quantum changes in energy of the gas molecules. This gives rise to many narrow lines in the absorption spectra of gases. Radiative heat transfer calculations must be carried out at each wavelength of the spectrum followed by an integration over all wavelengths to obtain the total heat transfer rates. For media with slowly varying radiative properties, this is often done numerically by dividing the spectrum into bands where the properties over a given band are assumed uniform. The governing Radiative Transfer Equation (RTE) is solved for each band and the total heat transfer is found by simply summing the results over all the bands. Such an approach for gases is computationally expensive since the spectral range where the infrared radiant energy lies involves many thousands of spectral lines.

Current engineering models for gas radiative properties found in the literature are based on spectral averaging either over many lines contained in entire rotation-vibration bands (wide band models) (Edwards, 1976), or over relatively fewer lines (narrow band models) (Ludwig et al., 1973; Goody, 1964). This averaging has been required to make spectral calculations tractable. The Beer–Lambert Law does not hold when using an absorption coefficient that has been spectrally averaged over many lines (Edwards, 1981). Therefore, the wide band and narrow band models are based on spectrally averaging an emissivity (or absorptivity or transmissivity), which introduces the need to specify a path length. This introduces additional approximations for complex multidimensional fields since an obvious choice of path length may not exist. Applying these band models to fields with nonuniform temperature and/or composition requires the Curtis–Godson (Godson, 1953) or a similar approximation where the nonuniform gas along the line of sight is replaced by an "equivalent" uniform gas.

Several differential methods for the approximate solution of the RTE are available, such as spherical harmonics (Mengüç and Viskanta, 1985, 1986), discrete ordinates (Carlson and Lathrop, 1968; Jamaluddin and Smith, 1988a, 1988b), and moment methods (DeMarco and Lockwood, 1975; Lockwood and Shah, 1978). These differential methods provide a numerical solution of the RTE in its most fundamental form written in terms of the absorption coefficient. Therefore, when using these arbitrary solution methods along with a wide band or narrow band model for gas radiation analysis, an absorption coefficient must be extracted from an emissivity or transmissivity from the Beer–Lambert relation, as has been done by Fiveland and Jamaluddin (1991). Alternatively, the RTE must be written in terms of a transmissivity differentiated with respect to distance along a line of sight (Goody, 1964; Kim et al., 1991). The latter approach alters the form of the RTE and has been demonstrated only with relatively simple geometries. The absorption coefficient for gases can be specified locally and used directly in the RTE without specification of a path length. However, this necessitates either computationally intensive line-by-line calculations or some other more efficient means of performing spectral calculations using the absorption coefficient as the basic radiative property (in lieu of a transmissivity or band absorptance).

One means of performing spectral calculations of gas radiative transfer more efficiently is the k-distribution method (Goody and Yung, 1989; Arking and Grossman, 1972; Domoto, 1974). The essence of the method is to replace a spectral integration over the wave number with an integration over the absorption coefficient. The method requires that the Planck distribution function and scattering properties be treated as constant over a spectral band of interest. A spectrally dependent parameter (such as flux or divergence) is determined for each specific value of the absorption coefficient. The spectral mean for the band is determined by an integration over absorption coefficient weighted by the distribution function for the band (or an integration over the cumulative distribution function). Nonhomogeneous media are handled via the correlated k-distribution (c-k) method (Goody and Yung, 1989; Goody et al., 1989; Lacis and Oinas, 1991). To obtain total heat transfer rates using these k-distribution methods an in-

Contributed by the Heat Transfer Division for publication in the JOURNAL OF HEAT TRANSFER. Manuscript received by the Heat Transfer Division August 1992; revision received April 1993. Keywords: Combustion, High Temperature Phenomena, Radiation. Associate Technical Editor: R. O. Buckius.

tegration must be carried out for each band to account for the variation of the Planck distribution followed by a quadrature over the bands.

The weighted-sum-of-gray-gases (WSGG) models first introduced by Hottel and Sarofim (1967) have been convenient for expressing total gas emissivity of a given path length and have been used in zone method analysis. The total emissivity of the WSGG model is expressed as

$$\epsilon = \sum_j a_j (1 - e^{-\kappa_j L}) \tag{1}$$

where κ_j are the discrete gray gas absorption coefficients, L is the path length, and a_j are the associated weights, which are a function of temperature. These weights, including the weight for spectral windows ($\kappa = 0$), sum to unity. Two interpretations of Eq. (1) are discussed by Hottel and Sarofim (1967). The first is a physical interpretation where a_j may be considered to be the fraction of the blackbody energy in the spectral regions where the effective absorption coefficient is κ_j. In the second interpretation a_j and κ_j are simply numbers that give the best "fit" to emissivity data. In previous work the absorption coefficients and weights have been determined by minimizing the error between total emissivities from engineering gas property models and the emissivity given by Eq. (1) (Smith et al., 1982; Coppalle and Vervisch, 1983). The emissivity data used in these references have been generated from Edwards' wide band model (1976).

Modest (1991) has shown the weighted-sum-of-gray-gases model to be applicable to the general RTE assuming spatially independent absorption coefficients and weights. For gases, this implies an isothermal medium of uniform concentration. It was demonstrated that the total heat transfer rates can be accurately determined by summing solutions of the following RTEs, one for each jth gray gas:

$$\frac{dI_j}{ds} = \kappa_j \left(a_j \frac{\sigma T^4}{\pi} - I_j \right) \tag{2}$$

Here, I_j, κ_j, and a_j are the intensity, absorption coefficient, and corresponding weight associated with the jth gray gas. Modest arrived at Eq. (2) by introducing the WSGG model expression for the absorptivity [similar to Eq. (1)] into the integral solution of the RTE. The derivation involves three restrictions: (1) The boundaries are black, (2) the medium is nonscattering, and (3) a_j and κ_j are not allowed to depend on position along a given line of sight.

Song and Viskanta (1986) have developed a similar model called a spectral group model where, in addition to determining the absorption coefficients and weights that best fit the emissivity from a wide band model, they determined the total spectral width of each gray gas (spectral group) absorption coefficient within each wide band.

Equation (1) may be considered a quadrature over the absorption coefficient similar to the k-distribution method. However, in the context of the physical interpretation, a_j is a blackbody fractional function for subline regions over the entire spectrum and is not limited to a sufficiently narrow band where the Planck function may be considered constant (as with the k-distribution method). The WSGG approach presented here for obtaining total heat transfer rates requires only a single quadrature over the absorption cross section (i.e., one integration for the entire spectrum). In contrast, the k-distribution method requires an integration for each band.

In this paper, a WSGG model is developed via construction of a detailed histogram representation of the line-by-line spectrum of H_2O in accordance with the physical interpretation of Eq. (1) (Hottel and Sarofim, 1967). The WSGG model developed here is referred to as a spectral line-based weighted-sum-of-gray-gases model (SLWSGG). The Air Force Geophysics Laboratory's high-resolution transmission molecular absorption data base (Rothman et al., 1992) (known under the acronym HITRAN) is used. The emphasis of this work is not in obtaining expressions for emissivity as in previous work, but rather in obtaining a detailed spectral division among the gray gases. By representing the spectrum with a small number of absorption cross sections, a spectral integration over wave number is replaced by a quadrature over absorption cross section, similar to the k-distribution method. The resulting model spectra can then be used to determine the gray gas weights, a_j, as blackbody fractional functions at all temperatures for use in arbitrary solution methods of the RTE. Hence, the weights and absorption coefficients need not be independent of spatial position as per the third restriction of Modest. Nevertheless, the model presented involves an approximation for nonhomogeneous media, as will be shown.

Model Formulation

The Weighted-Sum-of-Gray-Gases RTE. The radiative transfer equation for a nonscattering medium is written

$$\frac{dI_\eta}{ds} = \kappa_\eta (I_{b\eta} - I_\eta) \tag{3}$$

where I_η is the spectral intensity at wave number η, s is the distance along a given line of sight, $I_{b\eta}$ is the blackbody intensity, and κ_η is the spectral absorption coefficient. Equation (2) can be obtained in a straightforward manner by a spectral integration of Eq. (3) over an idealized histogram model spec-

Nomenclature

a_j = WSGG weight of the jth gray gas
C_{abs} = absorption cross-sectional area
f = differencing factor used in the discrete ordinates method
I = radiation intensity
I_b = blackbody radiation intensity
$I_{b\eta}$ = spectral blackbody radiation intensity
I_j = spectrally integrated radiation intensity associated with the jth gray gas
I_η = spectral radiation intensity
L = path length
q = net total radiative flux
q_j^- = incident radiative flux of the jth gray gas
s = distance along a given line of sight
S_i = integrated line strength or line intensity of ith line
T = temperature
x = spatial distance
γ_i = half-width of the ith line
ϵ = total emissivity
η = wave number
κ = absorption coefficient
μ = direction cosine

Subscripts and Superscripts

b = blackbody
e = of the control volume face east of the node p
i = model histogram segment number or line number
j = of the jth gray gas
l = of the lth discrete ordinate, or the lower limit of integration
p = control volume node
s = supplemental
u = upper limit of integration
w = of the control volume face west of the node p, or wall quantity
η = spectral

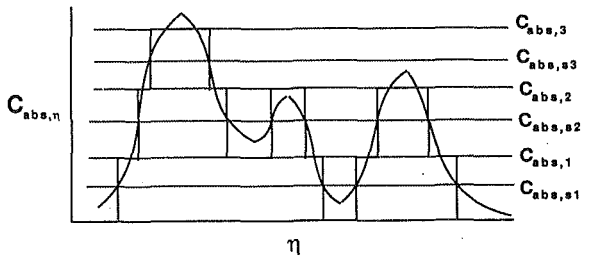

Fig. 1 SLWSGG model spectrum for a few absorption lines constructed from the actual line-by-line spectrum

trum. The focus of the derivation here is not Eq. (1), as in Modest's (1991) development, but the idealized spectrum from which Eq. (1) [and Eq. (2)] may be obtained. A histogram model spectrum representing the actual line-by-line spectrum may be constructed with the actual spectrum used as a template. The idealized spectrum would involve only a relatively few discrete values of the absorption cross section. Such a histogram representation with three absorption cross section values is shown in Fig. 1 for a few absorption lines at high resolution. The supplemental absorption cross sections denoted with the subscript s shown in the figure serve to define the histogram boundary locations.

Integrating Eq. (3) in a discontinuous fashion over all spectral regions associated with the jth discrete absorption coefficient gives

$$\sum_i \int_{\Delta\eta_{i,j}} \frac{dI_\eta}{ds}\, d\eta = \sum_i \int_{\Delta\eta_{i,j}} \kappa_\eta (I_{b\eta} - I_\eta)\, d\eta \tag{4}$$

The subscripts i and j denote the ith histogram segment of the jth absorption coefficient (or the absorption coefficient of the jth gray gas). The summation and integration can be brought inside the derivative on the left side of Eq. (4) by applying the Leibnitz rule. Equation (4) becomes

$$\frac{d}{ds}\left[\sum_i \int_{\Delta\eta_{i,j}} I_\eta d\eta\right] = \frac{dI_j}{ds} = \sum_i \int_{\Delta\eta_{i,j}} \kappa_\eta (I_{b\eta} - I_\eta)\, d\eta + \sum_i I_\eta(\eta_{u,i,j}) \frac{d\eta_{u,i,j}}{ds} - \sum_i I_\eta(\eta_{l,i,j}) \frac{d\eta_{l,i,j}}{ds} \tag{5}$$

where I_j is the integrated intensity of the radiant energy contained in the spectral regions associated with the jth gray gas. The subscripts l and u denote the lower and upper wave number limits of integration of the ith histogram segment, respectively. The many additional terms involving $d\eta_{u,i,j}/ds$ and $d\eta_{l,i,j}/ds$ arise for nonisothermal and/or nonhomogeneous media because the line intensities and line half-widths thus vary with position, along with the corresponding model histogram boundaries. This renders the analysis complicated, especially for multidimensional media. They also alter the form of the RTE so that standard solvers cannot be used without including an additional source/sink term. Therefore, in order to use arbitrary solution methods of the RTE, one must either fix the histogram boundaries throughout the problem domain so that these terms vanish, or one must simply neglect them. It must be emphasized that when applying the absorption coefficients and weights, determined in previous work (Smith et al., 1982; Coppalle and Vervisch, 1983; Taylor and Foster, 1974), to problems of nonuniform temperature and/or composition without knowledge of the detailed spectral division between the gray gases, these Leibnitz terms are not likely to be zero. This may be especially true when the fit has been made with emissivities over a range of temperature and/or species partial pressure, since the line-integrated intensities are known to be dependent on temperature and the line half-widths are dependent on temperature, total pressure, and species partial pressure. (However, the coefficients from previous work still provide an accurate evaluation of total emissivity for uniform media, since the Leibnitz terms would vanish under those conditions.) In Modest's derivation of Eq. (2) the absorption coefficients and weights are not allowed to depend on spatial position. The question to be answered is whether more error is incurred by neglecting the Leibnitz terms, or by holding the spectral histogram boundaries fixed by using the same model spectrum, determined at some mean temperature and composition, throughout the problem domain. This question will be examined in what follows. In the present development, the histogram boundaries are held fixed, and the Leibnitz terms are therefore zero. Since these boundaries are fixed, the gray gas weights are blackbody fractional functions for many fixed subline regions of the spectrum.

In physical terms, a model is desired that will allow the solution of the radiative transfer simultaneously at thousands of subline regions in the spectrum by assuming the radiative properties are identical at each of the spectral regions. This may be done by using a single spectrum of the absorption cross section over the entire spatial domain. In a real gas, the absorption cross sections at many spectral locations that are identical at one condition (temperature, pressure, and species concentrations) may diverge at a different condition, incurring error in the assumption of a single spectrum. The errors incurred by assuming a single spectrum will be studied in a later section.

Assuming the histogram spectrum is an accurate representation as far as the total heat transfer rates are concerned, the absorption coefficient can be taken outside the integral and summation of the right-hand side of Eq. (5), since in the ideal spectrum, κ_η is uniform over each histogram segment and equivalent for all histogram segments of the jth gray gas. The subscript, j, replaces the symbol, η, to denote the jth gray gas.

$$\frac{dI_j}{ds} = \kappa_j \left(\sum_i \int_{\Delta\eta_{i,j}} I_{b\eta} d\eta - \sum_i \int_{\Delta\eta_{i,j}} I_\eta d\eta \right) \tag{6}$$

Note that the summation over all histogram segments represents a spectral integration:

$$I_{bj} = a_j(T)\, \frac{\sigma T^4}{\pi} = \sum_i \int_{\Delta\eta_{i,j}} I_{b\eta} d\eta \tag{7}$$

$$I_j = \sum_i \int_{\Delta\eta_{i,j}} I_\eta d\eta \tag{8}$$

Inserting Eqs. (7) and (8) into Eq. (6), the RTE associated with the jth gray gas is obtained as Eq. (2). Once Eq. (2) is solved for each gray gas, the total intensity field is found simply as

$$I = \sum_j I_j \tag{9}$$

It should be noted that Eq. (2) can be extended to two and three-dimensional problems as well as one-dimensional problems such as those to be discussed in a later section.

Equation (7) defines the weights, a_j, as blackbody fractional functions for specific fixed subline regions in the spectrum based on a single model histogram spectrum. As an approximation for nonhomogeneous media, Eq. (7) also defines the weights based on the local temperature and the model histogram spectrum of the absorption cross section assumed for the entire spatial domain. The errors associated with this approximation are to be characterized as part of this study.

Model Spectrum Construction. Construction of the model histogram spectrum is carried out by minimizing an error between the histogram model spectrum and the actual line-by-line spectrum. The error function adopted is similar to that used in previous work (Smith et al., 1982; Coppalle and Vervisch, 1983; Taylor and Foster, 1974). This error is based on

the deviation of emissivities determined from the line-by-line data and those predicted by Eq. (1). In contrast to previous work, the gray gas weights are determined at one temperature and not fit *a priori* with a polynomial expression. The error function minimized is expressed as

$$\text{error} = \sum_{L} \left(1 - \frac{\epsilon_L}{\epsilon_{\text{true},L}}\right)^2 \tag{10}$$

where the emissivity, ϵ_L, is determined from Eq. (1) with path length L. The "true" emissivities are evaluated by a line-by-line integration of the spectral-line data. In this study, the summation in Eq. (10) is over path length only and not over temperature or even partial pressure path length as was done by Smith et al. (1982). Since the actual line-integrated intensities are dependent on temperature, and line half-widths are dependent on temperature, total pressure, and species partial pressure, the detailed histogram representation of the high resolution spectrum is also dependent on these variables. Therefore, a model histogram absorption cross section spectrum is generated at a single temperature, total pressure, and species partial pressure, and is imposed over the entire domain. The path lengths used in the summation of Eq. (10) are those that bracket the range of lengths for the problem at hand. For the one-dimensional problems analyzed, the path length is dependent on the zenith angle and, depending on the angular discretization, can vary over several orders of magnitude. Generally, a range of lengths spanning five decades was used in the optimization. It was found that sufficient accuracy was obtained by using two path lengths for each decade. Although Eq. (10) is based on fitting emissivities, the primary emphasis of this work is not to obtain expressions for emissivities, but rather to obtain absorption coefficients and corresponding weights for use in the standard RTE.

Other dimensional error functions were attempted that involved an integration of the absolute value of the deviation of absorption cross section of the model spectrum from the actual spectrum. However, these error functions, which did not involve path lengths, yielded unsatisfactory results.

The independent variables of the error function are the gray gas absorption cross-sectional areas and a supplemental set of absorption cross sections, which serve to determine the histogram boundaries, which in turn determine the weights via Eq. (7). The detailed spectral division is illustrated in Fig. 1 for three gray gases. The absorption cross-sectional areas are denoted in the figure by C_{abs1}, C_{abs2}, and C_{abs3}. The supplemental absorption cross-sectional areas are denoted by $C_{\text{abs,s1}}$, $C_{\text{abs,s2}}$, and $C_{\text{abs,s3}}$. The intersection points of these supplemental absorption cross sections with the actual spectrum define the locations of the histogram boundaries.

When using Eq. (10) for the error minimization, a great computational savings can be achieved by first determining the weights directly in the minimization procedure, followed by adjustment of the supplemental absorption cross sections to match the weights via Eq. (7). Therefore, the weights become the independent variables in lieu of the supplemental absorption cross sections in the minimization procedure. In this manner closed-form expressions of the error gradient can be obtained by simple differentiation of Eq. (10). The conjugate gradient method (Strang, 1986) was adopted for minimization of Eq. (10).

Once the model histogram boundaries have been determined from the minimization procedure, the weights a_j (T) for a given model spectrum are determined at all temperatures from Eq. (7).

Computation time for the model spectrum construction varied depending on the temperature at which the actual spectrum was generated. Typical run times were between 15 and 60 minutes on an HP 750 workstation.

Line-by-Line Data. At atmospheric conditions the single line shape is described by the Lorentz profile due to molecular collision or pressure broadening (Goody, 1964). Including the overlap contribution of neighboring lines, the absorption cross section is written as

$$C_{\text{abs},\eta} = \sum_i \frac{S_i}{\pi} \frac{\gamma_i}{(\eta - \eta_i)^2 + \gamma_i^2} \tag{11}$$

where, for the ith line, S_i is the integrated line intensity or strength, γ_i is the half-width, and η_i is the line location. As in previous work, the summation of Eq. (11) includes only neighboring lines for which the contribution to $C_{\text{abs},\eta}$ is significant. All spectral lines were included that were within 25 cm^{-1} on either side of the wave number of interest, η. The model histogram construction as well as the benchmark analyses (to be described shortly) in this work were carried out over the spectral range from 0 to 23,000 cm^{-1} (the entire range of the HITRAN database).

The line location, line intensity, and air-broadened half-width data are taken from the 1991 version of the HITRAN database (Rothman et al., 1992). The database includes only a limited amount of self-broadened half-width data. Since these data are available for only some of the lines, and information on the variation of the self-broadened half-width with temperature is not in the database, the expressions found in the NASA gas radiation handbook (Ludwig et al., 1973) are used.

The use of the HITRAN database has one disadvantage addressed by Hartman et al. (1984). The data were assembled at room temperature and lines insignificant at room temperature that are not in the database become significant and must be accounted for at combustion temperatures. These are the so-called "hot bands." Higher vibration and rotational levels must be considered. The vast majority of the lines in the current database are associated with transitions from the ground vibration energy level, quantum number 000 (lines of cold bands). There are a limited number of lines with transitions from the 010, 020, 100, and 001 lower vibration quantum levels. The same procedure as used by Hartman et al. (1984) is followed here to generate the hot lines (lines associated with transitions from a nonground vibration level) from cold lines. To summarize briefly, a hot line location of a given rotation and vibration transition is estimated from a cold line with the same rotation transition by assuming the rotational energies of the hot and cold line are the same (neglecting vibration-rotation coupling). A hot line intensity can be estimated from a cold line of the same rotation transition in a likewise manner by taking the ratio of the expressions for line intensity and canceling the rotational dependencies. The half-widths for a cold line and hot line with the same rotation transition are assumed the same. This was used both in the generation of benchmark predictions and in construction of the histograms for the model presented here.

It should be stated that the rotational levels for hot lines generated in this manner only include the levels that already exist in the database. The cutoff criterion for lines in the database is quite low [approximately 10^{-27} cm/molec. (Rothman et al., 1992)] for application with the large paths associated with atmospheric transmission. Therefore, the error of insufficient rotational levels is felt to be small for the path lengths considered for this study.

SLWSGG Model Spectrum. Figure 2(*a*) shows a model histogram spectrum with three gray gases generated from an H_2O spectrum at 1000 K with 100 percent H_2O concentration at one atmosphere pressure. The various bands of H_2O are seen to be represented in this model spectrum, although only three discrete absorption coefficients are needed for spectral calculations. At higher resolution in Fig. 2(*b*) is the model spectrum plotted against the actual line-by-line spectrum over a small portion of the spectrum. It should be noted that the SLWSGG model spectra are generated in terms of gray gas

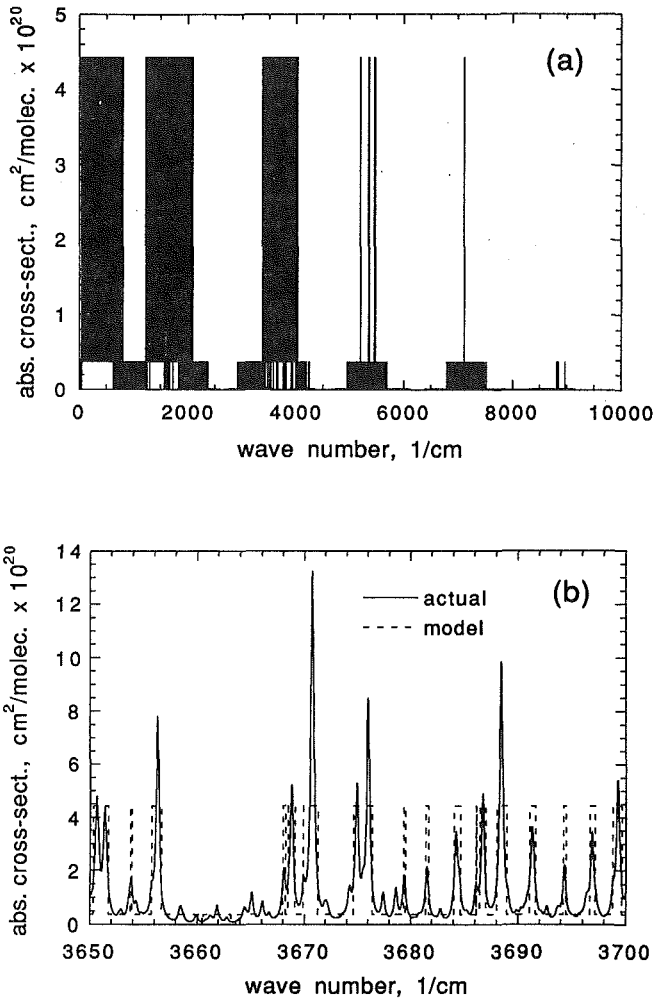

Fig. 2 SLWSGG model spectrum for H_2O at 1000 K and 100 percent H_2O

absorption cross-sectional areas. The local gray gas absorption coefficients are therefore calculated as the product of the absorption cross sections and the local molecular number density determined from an equation of state such as the ideal gas law.

Solution of the RTE. In this work a simple discrete ordinates method is used applicable to a gray analysis first developed by Carlson and Lathrop (1968) for solving a similar governing equation for neutron transport. The finite difference discrete ordinates equation used in these one-dimensional analyses with no scattering is written

$$I_{p,l}=\frac{\mu_l(1+f)I_{w,l}+\kappa_p I_{b,p}\Delta x}{\mu_l(1+f)+\kappa_p\Delta x} \tag{12}$$

where $I_{p,l}$ is the intensity in the lth direction at the spatial node p, μ_l is the lth direction cosine, $I_{w,l}$ is the intensity of the control volume cell face west of point p, Δx is the control volume width, and f is a differencing factor between 0 and 1. For simplicity the j subscript, denoting spectral, has been dropped in Eq. (12) and I_b would be the weighted blackbody intensity for the jth gray gas given by Eq. (7). The factor f determines the east cell face intensity, $I_{e,l}$ as

$$I_{e,l}=(1+f)I_{p,l}-fI_{w,l} \tag{13}$$

In this work "one-sided" differencing ($f=0$) was used. This eliminated a slight oscillation noticed in the solutions of problems with large temperature gradients. The intensities were updated iteratively using Eqs. (12) and (13) until the intensities ceased to change. The spatial grid in the calculations reported here has a resolution of between 40 and 120 grid points depending on the optical thickness of the medium for the particular problem. The flux divergence near a cold wall was found to be most sensitive to grid refinement.

For one-dimensional geometry, an even-order Gauss quadrature set is used for the discrete ordinates. A quadrature order of 20 was chosen. This is the same order used by Kim et al. (1991) who reported no significant improvement in adopting higher orders. Solutions of the RTE using the resulting SLWSGG model were nearly instantaneous.

Benchmark Predictions. Benchmark predictions for the problems presented in the next section were generated by solving for the intensity field using the detailed line-by-line data. Each of these computer runs involved between 80,000 and 200,000 spectral calculations. For each benchmark the actual spectrum was divided into 10 spectral regions between each pair of adjacent local maxima (perceptible lines), and a solution was carried out using the average absorption coefficient in each subline region. An increase in spectral resolution to 50 spectral calculations between adjacent local maxima showed no appreciable difference in the solution. For the cases of a nonisothermal medium or medium of nonuniform gas composition, the spectrum at the highest temperature or lowest H_2O concentration, which therefore had the greatest number of local maxima, was used as the basis for the spectral division just outlined. Each subline spectral region was held fixed throughout the spatial domain and the absorption coefficient was allowed to vary by determining the average absorption coefficient over the same subline region but from the spectrum at the local temperature and H_2O concentration. The uncertainties associated with the benchmark predictions associated with the discrete ordinates solutions and generated spectrum are estimated at 5 percent.

Results and Discussion

To test the model approach described, four different problems with simple one-dimensional geometry are analyzed. A broad range of problems has been studied in an attempt to draw general conclusions on the errors associated with the proposed model. Although the one-dimensional geometry was chosen to test the model, it can be extended to two and three dimensions. The cases considered are: (1) an isothermal homogeneous medium, (2) a nonisothermal medium, (3) a medium of nonuniform composition, and (4) nonblack gray reflecting walls. In all these problems H_2O vapor between two infinite parallel walls is considered. Two of the problems are taken from a recent paper by Kim et al. (1991) who formulated a discrete ordinates solution method for use with the narrow and wide band models. The problems of Kim et al. were chosen to compare predictions from the model presented here with results using these well-known gas property models, which provide a transmissivity or band absorptance as the basic radiative property. It should be emphasized that comparisons with the results from previously proposed band models is not intended to demonstrate the superiority of one model over another, since different spectroscopic and experimental databases are used making an objective comparison difficult. The line-by-line benchmarks generated as part of this study serve as a measure of the accuracy of the model proposed here since the same database is used. All problems are at 1 atm pressure.

Isothermal, Homogeneous Medium. In the first problem the two walls are black and held at 0 K. The intervening medium is filled with 100 percent H_2O at a uniform temperature of 1000 K. The wall spacing is 1 m. Figure 3(*a*) shows the divergence of the radiative flux (the radiative source) predicted by the current SLWSGG H_2O property model for two, three, and

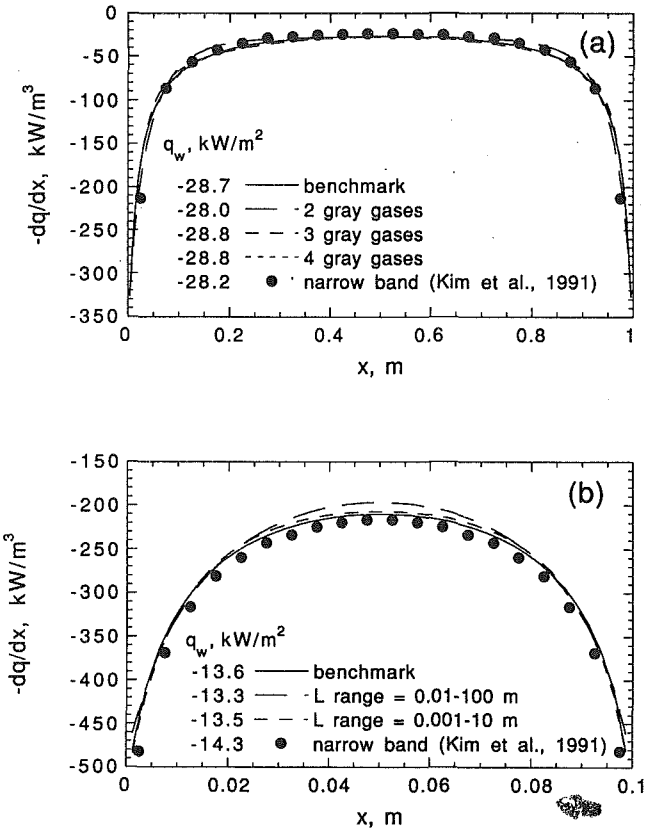

Fig. 3 Radiative source and net wall flux for a uniform 1000 K pure H_2O medium: (*a*) $L = 1.0$ m, and (*b*) $L = 0.1$ m

four gray gases. Also shown is the benchmark from the line-by-line calculation and the prediction reported by Kim et al. (1991) in their narrow band formulation. Although Kim et al. performed wide band model calculations as well, only the narrow band results are shown, since the wide band results generally agreed well with their narrow band predictions. The predicted net wall fluxes are shown in the legend of Fig. 3(*a*). All predictions show good agreement with the benchmark with the three and four gray gas SLWSGG results showing excellent agreement. The previously reported narrow band results agree well with the other predictions shown. The same trends are noted in the predicted net wall flux.

Figure 3(*b*) shows the results for the same problem as Fig. 3(*a*) but with the length between the walls reduced to 0.1 m. Three gray gas SLWSGG results are shown with the model spectra generated by minimizing Eq. (10) over the two different path length ranges given in the legend. The length range 0.01–100 m is the same used for the SLWSGG prediction in Fig. 3(*a*). As expected, better agreement is achieved when the length range more closely corresponds to that of the given problem. The narrow band model predicts the wall flux higher than the benchmark, whereas the SLWSGG results are slightly lower than the benchmark.

Nonisothermal Medium. A nonisothermal medium is considered with the following cosine temperature variation:

$$T = T_{av} + \frac{\Delta T}{2} \cos(\pi x/L) \tag{14}$$

This temperature profile provides a systematic departure from an isothermal medium by increasing the temperature variation, ΔT. T_{av} is taken at 1000 K and the H_2O mole fraction is 0.1 (90 percent air). The walls are 2 m apart and black at the temperatures of $T_{av} \pm \Delta T/2$. Predictions were generated for a ΔT of 100 K, 500 K, and 1000 K. Figures 4(*a*), 4(*b*), and 4(*c*)

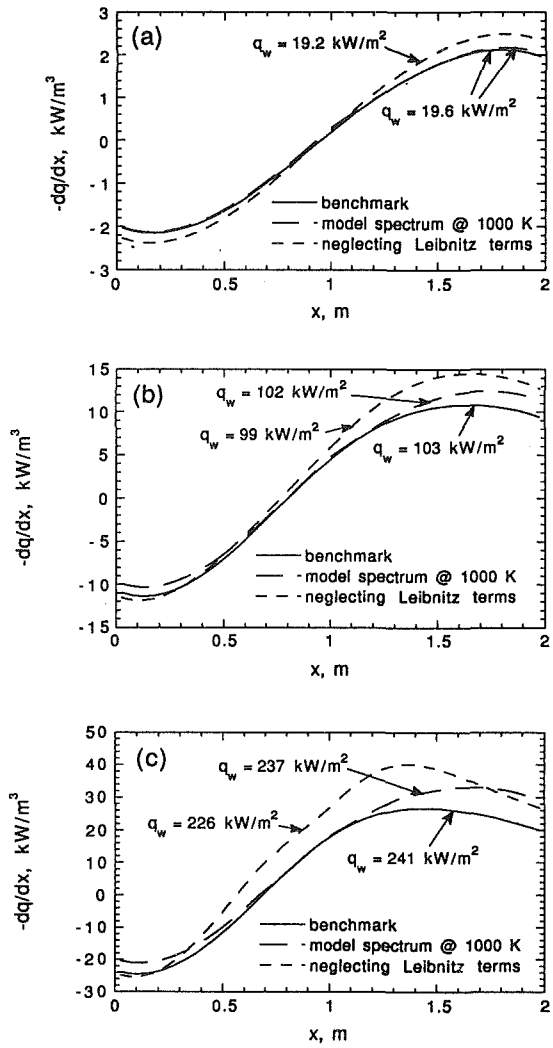

Fig. 4 Radiative source and net cold wall flux for the cosine temperature distribution for: (*a*) $\Delta T = 100$ K, (*b*) $\Delta T = 500$ K, and (*c*) $\Delta T = 1000$ K

show the radiative flux divergence profiles for the three ΔT as predicted by the SLWSGG model predictions compared with the line-by-line benchmarks. The net fluxes at the colder wall are also shown in the figures. The SLWSGG predictions are based on a three gray gas absorption cross section model spectrum generated with 10 percent H_2O at 1000 K, which is the mean temperature of the medium. This model spectrum was used throughout the spatial domain so that the Leibnitz terms of Eq. (5) vanish. The gray gas weights, a_j, were calculated using Eq. (7) at the local temperature, but with the same histogram boundaries of the single model spectrum. The error in the divergence is greatest in the cold region of the medium where there is an overprediction in the absorption. This is due to the assumption that a single absorption cross section spectrum may represent the entire domain. The real gas is less absorbing in the cold regions since the real gas contains less "hot" absorption lines than the model spectrum at 1000 K. The maximum error in the cold region is 1 or 2 percent for a ΔT of 100 K but increases to about 20 and 40 percent for the 500 K and 1000 K temperature variations, respectively. The SLWSGG underpredicts the radiative heat loss in the hotter region by a maximum of 1, 9, and 15 percent for ΔT of 100, 500, and 1000 K, respectively. The errors in the hot region are significantly less than those in the cold. The radiative flux predictions are in error of less than 2 percent by assuming a single spectrum. In summary, the use of a single absorption cross section spectrum can lead to significant errors in the

radiative divergence in cold regions below approximately 700 K for temperature differences greater than 500 K.

Also shown in Figs. 4(*a*) through 4(*c*) are the predictions obtained by neglecting the Leibnitz summation terms of Eq. (5) (while allowing the spectral histogram boundaries to vary with location in the domain). For these predictions, the absorption cross sections and weights were determined from absorption spectra generated at eight temperatures between 500 and 1500 K. At each temperature, Eq. (10) was minimized to obtain an optimum set of weights and absorption cross sections. Cubic splines were fit to these data for use in the discrete ordinates algorithm. Thus the local absorption coefficients and weights at each spatial position were, in effect, based on a spectrum at the local temperature without regard to the spectral location of subline regions associated with each gray gas (or each spectral calculation). While this approach is somewhat artificial, the net effect is to allow the spectral histogram boundaries to float, resulting in nonvanishing Leibnitz terms, which were then neglected. The result is generally an error in the overall prediction of the net radiative source term that is worse than the error associated with assuming that a single absorption cross section spectrum prevails over the entire domain. By using this approach, a single spectral calculation involves subline regions that are different at each spatial position, yielding the errors shown. By assuming a single spectrum, the many subline regions involved are the same for each spatial position.

Medium of Nonuniform Composition. The third problem presented is a uniform temperature field of 1000 K but with the concentration of H_2O given by a parabolic profile also analyzed by Kim et al. (1991). The concentration varies from zero at the walls to a maximum at the center. The other gas present is air. Predictions were generated for three values of the peak H_2O concentration at the center, 15, 45, and 100 percent. For a medium at uniform temperature but varying gas concentration the spectral line half-widths vary locally in the domain. Therefore, for the benchmark solution, the line half-widths were allowed to vary continuously throughout the domain by calculating them as needed using the expressions found from Ludwig et al. (1973) except that the HITRAN line-by-line air-broadened half-widths were used in place of the single value at a given temperature found from Ludwig et al. for all lines. Three gray gas SLWSGG results, calculated from a single spectrum generated at 1000 K and at the mean H_2O concentration, are shown in Figs. 5(*a*), 5(*b*), and 5(*c*), along with narrow band results of Kim et al. (1991).

Figure 5 also shows the prediction associated with neglecting the Leibnitz terms of Eq. (5). For these predictions, the absorption cross sections and weights were determined from absorption spectra generated at six H_2O concentrations between 5 and 100 percent. At each concentration, Eq. (10) was minimized to obtain an optimum set of weights and absorption cross sections. These cross sections and weights were fit with cubic splines. The weights were therefore found to depend on spatial position via the concentration. Hence, the histogram boundaries were again allowed to float. H_2O is known to be a strong self-broadener. The lines are very narrow at the walls from air-broadening, with some lines as narrow as 0.005 cm^{-1}, in contrast to the self-resonant half-width of 0.12 cm^{-1} at the center (Ludwig et al., 1973).

A physical explanation for the predicted **W**-shaped flux divergence profile of Fig. 5(*c*) is given by Kim et al. (1991). As shown in Figs. 5(*b*) and 5(*c*), the SLWSGG model predicts the peak radiative loss to occur closer to the walls than that of the benchmark. This is because the histogram boundaries are fixed throughout the domain and are unable to model as accurately the effect of the strong variation of line half-width across the domain. Nevertheless, the error is generally less than 15 percent and the prediction is closer to the benchmark than the prediction obtained from neglecting the Leibnitz terms. The models do however, correctly describe the qualitative behavior of this problem, as shown in the comparison with the benchmark. The predicted net wall fluxes are also shown in the legend of Fig. 5. The SLWSGG predicted wall flux shows better agreement than the prediction neglecting the Leibnitz terms.

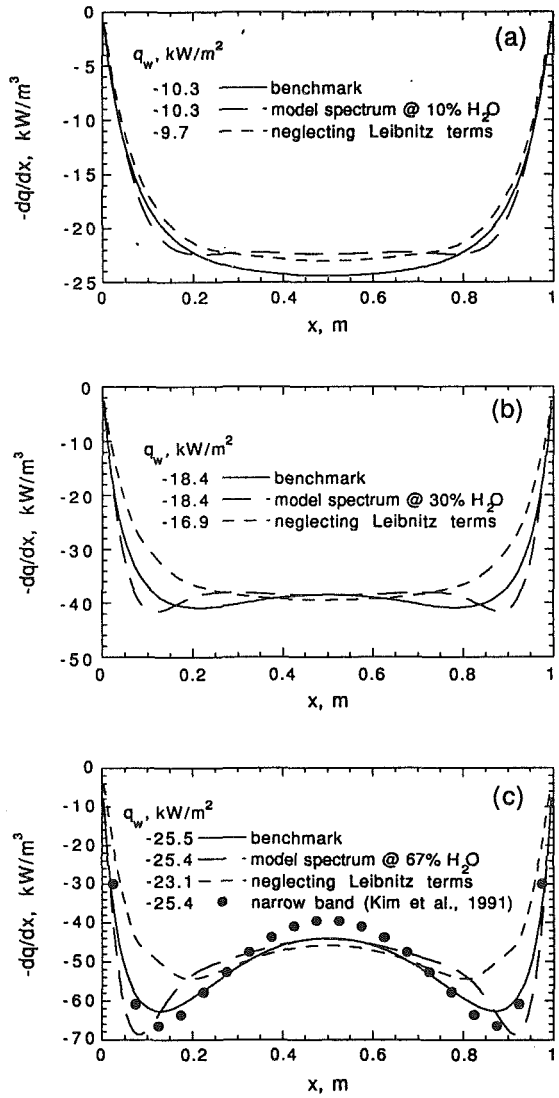

Fig. 5 Radiative source and net wall flux for the parabolic H_2O concentration profile and uniform temperature profile for a peak H_2O concentration of: (*a*) 15 percent, (*b*) 45 percent, (*c*) 100 percent

Nonblack Boundaries. All of the problems dealt with thus far have featured wall boundaries that are black, a restriction required by the development of Modest (1991). In the present development Eq. (2) has been derived independent of boundary conditions. Therefore, nonblack (but gray) boundary conditions are easily handled based on the histogram model spectrum. For the radiant energy in the subline spectral regions of the jth gray gas, a diffuse gray boundary condition, for example, with wall emittance, ϵ_w, is written for the boundary at $x=0$ as

$$I_{wj}^{+} = [\epsilon_w a_j(T_w)\sigma T_w^4 + (1-\epsilon_w)q_j^{-}]/\pi \tag{15}$$

where

$$q_j^{-} = \int_0^{2\pi}\int_{-1}^{0} I_j \mu d\mu d\phi \tag{16}$$

and where q_j^{-} is the incident radiant flux at the bottom wall

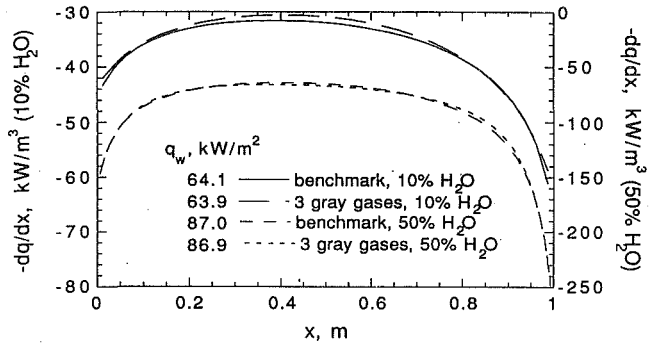

Fig. 6 Predicted radiative source and net wall flux for a uniform 10 and 50 percent H_2O medium at 1500 K with nonblack boundaries. $T_{w,x=0} = 1200$ K. $T_{w,x=1.0\ m} = 600$ K. $\epsilon_w = 0.6$

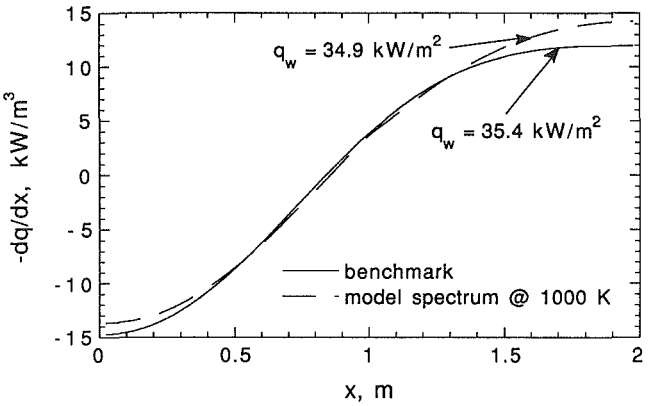

Fig. 7 Radiative source and net cold wall flux for the cosine temperature distribution of Fig. 4(*b*) with $\epsilon_w = 0.5$

of the radiant energy in the spectral regions of the jth gray gas. To demonstrate this, two problems with reflective boundaries are considered. In the first, the medium is isothermal at 1500 K. Two H_2O concentrations, 10 and 50 percent, are considered. The walls are gray with a wall emissivity of 0.6. The two wall temperatures are 1200 K at $x = 0$ and 600 K at $x = 1.0$ m. Figure 6 shows the benchmark prediction compared with that of the SLWSGG model for three gray gases. Good agreement between the SLWSGG and the benchmark predictions is demonstrated in both the radiative flux divergence and the predicted net wall flux at the colder wall.

The final problem is identical to the problem of Fig. 4(*b*) except that the walls are assigned an emissivity of 0.5. Figure 7 shows the results of the benchmark and the SLWSGG model for three gray gases. Again, the use of a single absorption cross section spectrum resulted in a 17 percent overprediction of the absorption in the cold region and an 8 percent underprediction in the radiative loss in the hot region. The error in the net radiative flux at the colder wall is less than 2 percent. The presence of reflective boundaries did not significantly change the relative errors as compared to the similar problem with black boundaries.

Conclusions and Recommendations

This paper has presented an approach for constructing WSGG models from the line-by-line spectra, thereby obtaining a detailed spectral division among the gray gases. The absorption coefficient (in lieu of a transmissivity or band absorptance) is the modeled radiative property permitting arbitrary solution methods for the RTE. This is especially important in multidimensional situations, where the specification of an appropriate path length is difficult. The model is based on detailed line-by-line spectral information, but requires only three to four spectral integrations.

High accuracy was demonstrated for isothermal media of uniform composition. In the nonisothermal media studied, the use of a single absorption cross section spectrum over the entire spatial domain in order to fix the subline spectral regions associated with a single spectral calculation resulted in an overprediction of the absorption, which worsened with increasing spatial temperature variation. In the high-temperature regions an underprediction of the radiative heat loss was noted. The errors in the high-temperature regions were significantly less than those of the colder regions. The use of a single spectrum in a medium of a large spatial variation in the H_2O concentration resulted in errors of the radiative flux divergence due to significant self-broadening. Errors in the net wall radiative flux were less than a few percent. Nevertheless, generally a greater error resulted in using optimum absorption cross sections and weights determined locally without regard to the spectral location of the subline regions of each gray gas.

Recommendations for future work include investigating ways to allow the gray gas absorption cross sections to vary locally in order to reduce errors associated with assuming a single model spectrum. Further work may also include generating model spectra over a range of temperatures and species partial pressures followed by fitting correlations from the resulting gray gas absorption cross sections and corresponding weights of the spectra for use in general codes. Also, knowledge of the histogram boundary locations will allow the model to be easily used with more than one gas specie (i.e., H_2O and CO_2) in arbitrary proportions throughout the computation domain, as well as with nongray particulates and nongray wall boundaries.

Acknowledgments

This work was supported by the Advanced Combustion Engineering Research Center (ACERC). ACERC is sponsored by the National Science Foundation, the State of Utah, the U.S. Department of Energy, and a number of industrial participants.

References

Arking, A., and Grossman, K., 1972, "The Influence of Line Shape and Band Structure on Temperatures in Planetary Atmospheres," *Journal of Atmospheric Science*, Vol. 29, p. 937.

Carlson, B. G., and Lathrop, K. D., 1968, "Transport Theory—The Method of Discrete Ordinates," *Computing Methods in Reactor Physics*, H. Greenspan, C. N. Kelber, and D. Okrent, eds., Gordon and Breach, New York, pp. 166–266.

Coppalle, A., and Vervisch, P., 1983, "The Total Emissivities of High-Temperature Flames," *Combustion and Flame*, Vol. 49, pp. 101–108.

DeMarco, A. G., and Lockwood, F. C., 1975, "A New Flux Model for the Calculation of Radiation in Furnaces," *La Rivisita dei Combustible*, Vol. 22, pp. 184–193.

Domoto, G. A., 1974, "Frequency Integration for Radiative Transfer Problems Involving Homogeneous Non-gray Gases: The Inverse Transmission Function," *Journal of Quantitative Spectroscopy and Radiative Transfer*, Vol. 14, p. 935.

Edwards, D. K., 1976, "Molecular Gas Band Radiation," *Advances in Heat Transfer*, Vol. 12, Academic Press, New York, pp. 115–193.

Edwards, D. K., 1981, *Radiation Heat Transfer Notes*, Hemisphere Publishing Corp., Washington-New York.

Fiveland, W. A., and Jamaluddin, A. S., 1991, "Three-Dimensional Spectral Radiative Heat Transfer Solution by the Discrete-Ordinates Method," *AIAA Journal of Thermophysics and Heat Transfer*, Vol. 5, No. 3, pp. 335–339.

Godson, W. L., 1953, "The Evaluation of Infrared Radiation Fluxes Due to Atmospheric Water Vapor," *Quarterly Journal of Royal Meteorological Society*, Vol. 79, pp. 367–379.

Goody, R. M., 1964, *Atmospheric Radiation*, Clarendon Press, Oxford, United Kingdom.

Goody, R., West, R., Chen, L., and Chrisp, D., 1989, "The Correlated-*k* Method for Radiation Calculations in Nonhomogeneous Atmospheres," *Journal of Quantitative Spectroscopy and Radiative Transfer*, Vol. 42, pp. 539–550.

Goody, R. M., and Yung, Y. L., 1989, *Atmospheric Radiation*, 2nd ed., Oxford, United Kingdom.

Hartman, J. M., Levi di Leon, R., and Taine, J., 1984, "Line-by-Line and

Narrow-Band Statistical Model Calculations for H_2O," *Journal of Quantitative Spectroscopy and Radiative Transfer*, Vol. 32, No. 2, pp. 119–127.

Hottel, H. C., and Sarofim, A. F., 1967, *Radiative Transfer*, McGraw-Hill, New York.

Jamaluddin, A. S., and Smith, P. J., 1988a, "Predicting Radiative Transfer in Rectangular Enclosures Using the Discrete Ordinates Method," *Combustion Science and Technology*, Vol. 59, pp. 321–340.

Jamaluddin, A. S., and Smith, P. J., 1988b, "Predicting Radiative Transfer in Axisymmetric Cylindrical Enclosures Using the Discrete Ordinates Method," *Combustion Science and Technology*, Vol. 62, pp. 173–186.

Kim, T. K., Menart, J. A., and Lee, H. S., 1991, "Nongray Radiative Gas Analyses Using the S-N Discrete Ordinates Method," ASME JOURNAL OF HEAT TRANSFER, Vol. 113, pp. 946–952.

Lacis, A. A., and Oinas, V., 1991, "A Description of the Correlated *k* Distribution Method for Modeling Nongray Gaseous Absorption, Thermal Emission, and Multiple Scattering in Vertically Inhomogeneous Atmospheres," *Journal of Geophysical Research*, Vol. 96, pp. 9027–9063.

Lockwood, F. C., and Shah, N. G., 1978, "Evaluation of an Efficient Radiation Flux Model for Furnace Prediction Procedures," in: *Heat Transfer—1978*, Hemisphere, Washington, DC, Vol. 2, pp. 33–40.

Ludwig, C. B., Malkmus, W., Reardon, J. E., and Thompson, J. A. L., 1973, *Handbook of Infrared Radiation From Combustion Gases*, NASA SP-3080, Scientific and Technical Information Office, Washington, DC.

Mengüç, M. P., and Viskanta R., 1985, "Radiative Transfer in Three-Dimensional Rectangular Enclosures Containing Inhomogeneous, Anisotropically Scattering Media," *Journal of Quantitative Spectroscopy and Radiative Transfer*, Vol. 33, No. 6, pp. 533–549.

Mengüç, M. P., and Viskanta R., 1986, "Radiative Transfer in Axisymmetric, Finite Cylindrical Enclosures," ASME JOURNAL OF HEAT TRANSFER, Vol. 108, pp. 271–276.

Modest, M. F., 1991, "The Weighted-Sum-of-Gray-Gases Model for Arbitrary Solution Methods in Radiative Transfer," ASME JOURNAL OF HEAT TRANSFER, Vol. 113, pp. 650–656.

Rothman, L. S., Gamache, R. R., Tipping, R. H., Rinsland, C. P., Smith, M. A. H., Chris Benner, D., Malathy Devi, V., Flaud, J. M., Camy-Peyret, C., Perrin, A., Goldman, A., Massie, S. T., and Brown, L. R., 1992, "The HITRAN Molecular Database: Editions of 1991 and 1992," *Journal of Quantitative Spectroscopy and Radiative Transfer*, Vol. 48, No. 5/6, pp. 469–507.

Smith, T. F., Shen, Z. F., and Friedman, J. N., 1982, "Evaluation of Coefficients for the Weighted Sum of Gray Gases Model," ASME JOURNAL OF HEAT TRANSFER, Vol. 104, pp. 602–608.

Song, T. H., and Viskanta, R., 1986, "Development and Application of a Spectral-Group Model to Radiation Heat Transfer," ASME Paper No. 86-WA/HT-36.

Strang, G., 1986, *Introduction to Applied Mathematics*, Wellesley-Cambridge Press, Wellesley, MA.

Taylor, P. B., and Foster, P. J., 1974, "The Total Emissivities of Luminous and Nonluminous Flames," *International Journal of Heat and Mass Transfer*, Vol. 17, pp. 1591–1605.

Measurements of the Thermal Radiative Properties of Liquid Uranium

M. A. Havstad

W. McLean II

Lawrence Livermore National Laboratory,
Livermore, CA 94550

S. A. Self
Stanford University,
Stanford, CA 94305

Measurements of the thermal radiative properties of liquid uranium have been made using an instrument with two optical systems, one for measuring the complex index of refraction by ellipsometry, the other for measuring the normal spectral emissivity by direct comparison to an integral blackbody cavity. The measurements cover the wavelength range 0.4–10 μm with sample temperatures between 1410 and 1630 K. Two 5-KeV ion sputter guns and an Auger spectrometer produce and verify, in situ, atomically pure sample surfaces. Good agreement between the two methods is observed for the normal spectral emissivity, which varies with wavelength in a manner typical of transition metals. The two components of the complex index of refraction—the index of refraction and the extinction coefficient—increase with wavelength, from ~3 at 0.4 μm to ~20 at 9.5 μm. Both components of polarized reflectivity are shown for visible to infrared wavelengths.

Introduction

The thermal radiative properties of the surfaces of various metals at high temperature, both below and above the melting point, are of importance to a wide range of research and development activities, including laser isotope separation, laser welding, metal refining, electron-beam processing, and vacuum-arc remelting. These properties, namely the reflectivity, emissivity, and absorptivity, influence the energy balance and heat transfer in such applications and thereby determine performance and economic viability. Thermal radiative properties are often vital input data for heat transfer computations performed during development of a process. For example, the development of laser isotope separators requires extensive use of the directional and spectral reflectivity of liquid metals for system design. The accuracy of the input data determines the results of calculations that provide the understanding needed to make design changes and successfully complete development. The properties of uranium in particular have only rarely been measured, and then only over limited parameter ranges (Burgess and Waltenberg, 1915; Hole and Wright, 1939; Lemmon, 1957; Baker et al., 1963; Rauh, 1956; Faldt and Nilsson, 1980; Weaver, 1980).

Accurate information is required on the three surface radiative properties as a function of wavelength, temperature, and angle relative to the surface normal. Interest in the high-temperature processes noted above led to the choice of 0.4–10 μm as the wavelength measurement range of interest. This range makes the results more generally useful than is typical, and can be reasonably accommodated with calcium fluoride (CaF_2) or reflective optics. Since the melting point of uranium is 1406 K, the temperature range of interest here is 900–1630 K. The full angular range from $\theta = 0$ deg (normal to the surface) to 90 deg (grazing incidence) was also studied. The tendency of the radiative property literature to be restricted to normal emission and near-normal reflection makes much of the data of limited value. In nearly all applications, off-normal and even oblique radiant properties can have a considerable impact on the results.

In many prior studies of thermal radiative properties, insufficient attention has been paid to the surface condition. In the few instance where surfaces have been well characterized and controlled, the measurements have been made over narrow parameter ranges or only at low temperature. Furthermore, studies of liquid metals are relatively rare and most often have been made in inadequate vacuum environment. Very low pressures [$\sim 10^{-9}$ Torr, i.e., ultrahigh vacuum (UHV)] are necessary in studies of molten metals because liquid metal surfaces are often highly reactive. A review of the reported work in this area leads to very low confidence in the results (because of the large scatter in the data) to the point where results from various workers rarely agree within their stated uncertainty limits. Estimates of surface contamination based on the reported system pressures often indicate a high probability of significant surface impurities.

The present work is distinguished from prior efforts by the use of surface analytic tools for control and measurement of surface composition, and by the use of two independent optical systems for the reduction and measurement of systematic errors. The surface science tools are the vacuum system (base pressure $\sim 5 \times 10^{-10}$ Torr), an Auger Spectrometer for detection of surface composition, and two ion-sputter guns for removing surface contamination in situ. One optical system measures complex index of refraction using a spectral ellipsometer, and the other measures normal spectral emissivity using an integral blackbody technique.

To our knowledge, the results given here are the first measurements of the complex index of refraction of liquid uranium.

Theoretical Background

Relations for the reflectivity of surfaces as a function of angle of incidence, material properties, and polarization follow from Maxwell's equations and the boundary conditions for continuity of electric and magnetic field across an interface (Jackson, 1975).

Thermal radiative properties are related to the square of the amplitude reflection coefficients, the intensity reflection coefficients, which are given by the Fresnel equations. These equations are commonly used in heat transfer because they give the fraction of incident energy reflected for each component of polarization. For a wave in vacuum incident on a planar surface of an isotropic material with complex index of refraction n, k:

Contributed by the Heat Transfer Division for publication in the JOURNAL OF HEAT TRANSFER. Manuscript received by the Heat Transfer Division November 1992; revision received April 1993. Keywords: Liquid Metals, Radiation, Thermophysical Properties. Associate Technical Editor: R. O. Buckius.

$$\rho_{\lambda,p} \equiv r^2_{\lambda,p}(\lambda, \theta) = \frac{a^2 + b^2 - 2a \sin\theta \tan\theta + \sin^2\theta \tan^2\theta}{a^2 + b^2 + 2a \sin\theta \tan\theta + \sin^2\theta \tan^2\theta} r^2_{\lambda,s}$$

$$\rho_{\lambda,s} \equiv r^2_{\lambda,s}(\lambda, \theta) = \frac{a^2 + b^2 - 2a \cos\theta + \cos^2\theta}{a^2 + b^2 + 2a \cos\theta + \cos^2\theta}$$

where

$$2a^2 = [(n^2 - k^2 - \sin^2\theta)^2 + 4n^2k^2]^{1/2} + (n^2 - k^2 - \sin^2\theta)$$

and

$$2b^2 = [(n^2 - k^2 - \sin^2\theta)^2 + 4n^2k^2]^{1/2} - (n^2 - k^2 - \sin^2\theta). \quad (1)$$

Since any polarized incident light can be represented by a linear combination of perpendicular and parallel polarized incident beams, the Fresnel equations give a complete description of surface reflectivity from smooth isotropic materials. The wavelength dependence indicated in the relations is a consequence of the dependence of n and k on wavelength. Because the complex index also depends on temperature, the polarized reflectivities depend on temperature, although this dependence is not indicated by the notation. The assumption of a planar reflection interface and an isotropic material leads to a dependence of ρ on θ only (the polar angle) in the results for polarized reflectivity. Many real materials are not isotropic so that a full description of their properties also involves the azimuthal angle.

In this work, direct measurements of normal spectral emissivity and ellipsometric measurements of the complex index of refraction form a redundant set, because the complex index of refraction can be used to compute the normal spectral emissivity:

$$\epsilon_{\lambda,n} = \frac{4n}{(n+1)^2 + k^2}. \quad (2)$$

The ellipsometric method used here was developed simultaneously by Beattie and Conn and Hodgson in 1955. Because it does not employ the narrow band wave plates common in many ellipsometers, this method is readily applied over the broad spectral regions of interest to heat transfer.

With the method of Beattie and Conn (1955), a beam of arbitrary polarization passes through a linear polarizer and reflects off the material of interest. This first linear polarizer, called the polarizer, is rotatable with rotation axis coincident with the beam axis. After reflection the beam passes through a second polarizer, referred to as the analyzer, which is also rotatable about an axis coincident with the axis of the reflected beam. The linearly polarized beam becomes an elliptically polarized beam after reflection from the sample surface, and the intensity variation of the radiation transmitted by the analyzer can yield the salient parameters of the polarization ellipse of the reflected radiation (Clarke and Grainger, 1971).

Using $\hat{\rho}$ for the ratio of the amplitude reflection coefficients r_p and r_s gives:

$$I = c_1 E^2 r_s^2 \left[\sin^2\psi_N \sin^2\psi_A + \hat{\rho}^2 \cos^2\psi_N \cos^2\psi_A + \frac{1}{2}\hat{\rho} \sin(2\psi_N) \sin(2\psi_A)\cos\Delta \right] \quad (3)$$

where

ψ_A is the azimuth of the analyzer

ψ_N is the azimuth of the polarizer

$\Delta = \delta_p - \delta_s$, the relative phase shift between the two components of polarization on reflection

$$\tan\psi = \hat{\rho} = \frac{|r_p|}{|r_s|}. \quad (4)$$

The derivation of the complex index of refraction from ψ and Δ measurements (Price, 1948; Sokolov, 1967) combines Snell's law, the Fresnel equations, and the definitions of ψ and Δ given above:

$$\epsilon/\epsilon_o = (n^2 - k^2) = \sin^2\theta \times \left\{ 1 + \tan^2\theta \left[\frac{\cos^2 2\psi - \sin^2 2\psi \sin^2\Delta}{(1 + \sin 2\psi \cos\Delta)^2} \right] \right\}$$

$$(\epsilon'/\epsilon_o) = 2nk = 2 \sin^2\theta \tan^2\theta \left[\frac{\cos 2\psi \sin 2\psi \sin\Delta}{(1 + \sin 2\psi \cos\Delta)^2} \right] \quad (5)$$

with

$$\tan\psi = |r_p|/|r_s|$$

and

$$\theta = \text{angle of incidence}$$

and

$$\Delta = \text{relative phase shift on reflection.} \quad (6)$$

These equations relate ψ and Δ to two formulations for the optical constants of solids, the complex refractive index, n and k, and the complex dielectric function, ϵ/ϵ_o and ϵ'/ϵ_o. Here ϵ_o denotes the permittivity of free space. The refractive index

Nomenclature

a, b = terms in the Fresnel equations
a_0, a_1, a_2, a_3 = constants in polynomial fits
c_1 = constant
E = electric field vector
I = intensity
I_o = reference intensity in ellipsometric technique
I_1, I_2, I_3, I_4 = measured variables in ellipsometric technique
k = extinction coefficient
n = index of refraction
r_e = direct current resistivity
r = amplitude reflection coefficient
T = temperature
V = voltage
Δ = relative phase shift on reflection
δ = phase angle, skin depth
ϵ = emissivity
θ = angle
λ = wavelength
ρ = intensity reflection coefficient
$\hat{\rho}$ = ratio of amplitude reflection coefficients
$\tilde{\rho}$ = average of polarized reflectivities
ψ = angle used in ellipsometry
ψ_A = azimuth of analyzer in ellipsometry
ψ_N = azimuth of polarizer in ellipsometry
ϵ = real part of complex dielectric function
ϵ' = imaginary part of complex dielectric function
ϵ_o = permittivity of free space

Subscripts

A = analyzer of ellipsometer
b = blackbody
c = cavity
n = normal
N = polarizer of ellipsometer
o = free-space value
p = parallel component
s = perpendicular component
sam = sample
scat = scattered

form is convenient for radiant property studies, while the dielectric function is commonly used with studies of the solid state.

The dependence of the intensity at the detector on the azimuths of the polarizer and analyzer was given above in Eq. (3). With the polarizer fixed at 45 deg (relative to the plane of incidence) ψ is determined by the ratio of the intensities at two azimuths of the analyzer, namely 0 and 90 deg. Thus, from Eq. (3) one obtains:

$$I_1 \equiv I(\psi_N = 45 \text{ deg}, \psi_A = 90 \text{ deg}) = I_o \sin^2(45 \text{ deg}) = \frac{I_o}{2} \quad (7)$$

$$I_2 \equiv I(\psi_N = 45 \text{ deg}, \psi_A = 0 \text{ deg}) = I_o \hat{\rho}^2 \cos^2 45 \text{ deg} = \frac{I_o}{2} \hat{\rho}^2 \quad (8)$$

where $I_o = I(\psi_N = 90 \text{ deg}, \psi_A = 90 \text{ deg})$.

From the ratio of Eqs. (7) and (8) one obtains:

$$\hat{\rho}(\theta) = \tan \psi = \sqrt{I_2/I_1}. \quad (9)$$

Two more intensity readings are taken with the analyzer at ± 45 deg (relative to the plane of incidence) with the polarizer position unchanged. These readings give:

$$I_3 \equiv I(\psi_N = 45 \text{ deg}, \psi_A = 45 \text{ deg}) = I_o(1 + \hat{\rho}^2 + 2\hat{\rho} \cos \Delta)/4. \quad (10)$$

$$I_4 \equiv I(\psi_N = 45 \text{ deg}, \psi_A = -45 \text{ deg}) = I_o(1 + \hat{\rho}^2 - 2\hat{\rho} \cos \Delta)/4. \quad (11)$$

In principle, either I_3 or I_4 can be used separately with I_1 and I_2 to obtain the phase shift, Δ. However, when the reflectivity is high, as it is for metals at long wavelengths, Δ is sensitive to small measurement errors. Using a combination of Eqs. (10) and (11) reduces this sensitivity:

$$\cos \Delta = \left\{\frac{1}{2}\left(\hat{\rho} + \frac{1}{\hat{\rho}}\right)\right\}\left\{\frac{I_3 - I_4}{I_3 + I_4}\right\}. \quad (12)$$

The use of Eq. (12) still presents problems in the classical long wavelength limit for conductors, $\hat{\rho} \to 1$ and $\Delta \to 0$, where all methods become insensitive. However, the method of Beattie and Conn allows one to go to longer wavelengths than methods that do not use both phase shift and amplitude attenuation on reflection (Havstad and Self, 1993).

Experimental Setup

The Vacuum System. The stainless steel UHV chamber uses all-metal seals. Optical access is provided by CaF_2 windows. A turbomolecular pump and an ion pump yield an ultimate pressure of $\sim 3 \times 10^{-10}$ Torr after bakeout. With liquid uranium samples in the chamber at 1500 K, the pressure is typically $\sim 4 \times 10^{-9}$ Torr. Other features of the vacuum system are described by Havstad et al. (1993b).

Samples are translated a distance of ~ 100 mm between the two instrumentation positions, one for optics and the other for surface science, by a mechanical feedthrough, which allows three translational degrees of freedom and two axes of tilt. Unlubricated sapphire ball bearings and micrometers allow precise positioning in the UHV environment.

The Auger spectrometer and one of the two ion guns have a common focus at what is termed the surface science position in the vacuum chamber. The spectrometer determines sample composition in the top 10–20 Å of the surface, and is ideal for studies of liquid metals because impurities tend to float to the top upon melting. Hence, once the surface is cleaned by ion sputtering, the sample is cleaned down to all depths of significance to the wavelength range of interest. (Skin depth, δ, is directly proportional to extinction coefficient and inversely proportional to wavelength.) With transmissive samples, optical depths are much greater and other methods might be required. Atomic composition is typically known to a precision of 5 percent or less with this instrument. Examples of Auger spectra for both clean and "dirty" samples (with quantitative analysis) are given by Havstad (1991).

A second ion gun, the emissivity optical system, and the ellipsometer have a common focus at the optics position. The ion guns are capable of a current density of 280 mA/cm^2 with a beam diameter of 2 mm, and 80 mA/cm^2 at full-width-at-half-maximum (FWHM) with a beam diameter of 12 mm. During typical operation, the chamber is filled to $\sim 5 \times 10^{-5}$ Torr of argon purified by a zirconia getter. For solid samples, short periods of sputtering remove surface contaminants, typically oxygen and carbon; with reactive liquid metals, such as uranium, two weeks or more of sputtering and remelting may be required to fully remove impurities from the surface. Sputter yields, rates, and techniques are described by Musket et al. (1982). Typically, tens of angstroms per minute, or hundreds of monolayers per hour, are removed by these methods.

Tungsten crucibles (~ 12-mm diameter and ~ 6-mm height) fit over a heater assembly: a molybdenum case that contains a tungsten-resistive element embedded in alumina. For a dissipation rate of 50 W, the samples reach 1270–1370 K. A broad, shallow hole in the bottom of the crucible accepts the molybdenum heater case, and a narrow deep hole on the top serves as the integral blackbody cavity (2.54-mm diameter and 5.08-depth). For the study of liquids, the crucible's molten pool was sometimes as shallow as 1 mm because unwanted impurities and sample volume are directly related. Constraints on crucible design were extensive and are described in a separate report (Havstad, 1992). Tungsten was selected because it gave a relatively flat pool and held liquid uranium, which is corrosive, for 10 to 30 hours.

Crucible design influences measurement error in two ways. First, any temperature difference between the blackbody and the sample leads to error in measurements of normal spectral emissivity. These errors are strongly dependent on wavelength (as given by the Planck function). For a well-designed crucible, errors are small because the cavity and the sample are well connected thermally. Second, errors in measurements of normal spectral emissivity are directly proportional to $(1 - \epsilon_c)$, where ϵ_c is the cavity emissivity. This is the extent that cavity emissivity is not ideal. These errors are strongly dependent on the depth-to-diameter ratio, h/D, of the cavity (here $h/D = 2$).

Both these sources of measurement error are influenced by three-dimensional conductive effects (which are themselves coupled to thermal radiative exchange in and out of the cavity). Finite element analysis of these effects (described by Havstad, 1992) predicted (1) temperature differences on the order of 6 K between the sample and the cavity (for a sample temperature of 1400 K), and (2) thermal gradients, nonisothermal and nonblack cavity emission combine to give measurement errors, which vary from 7 percent at 0.6 μm to 2 percent at 9.5 μm. These predictions were conservative; the discrepancy between the normal spectral emissivity determined by the direct measurements and the values deduced from the ellipsometric measurements were generally even smaller.

Sample temperature was indicated by two systems. A tungsten–rhenium thermocouple was placed in a hole in the crucible wall beside the blackbody cavity. Conductive connection to the crucible was poor with this arrangement, but errors could be quantified by comparison to the known sample melting temperature. Furthermore, none of the data reduction involves knowledge of the sample temperature. This is a principal advantage of integral blackbody techniques, such as those used here. Moreover, spectral emissivities, normal or otherwise, are often weakly dependent on temperature. It is only when spectral data are integrated over wavelength, with a temperature chosen for the Planck function weighting, that strong temperature dependence arises.

A pyrometer, sighting into the blackbody cavity via a folding

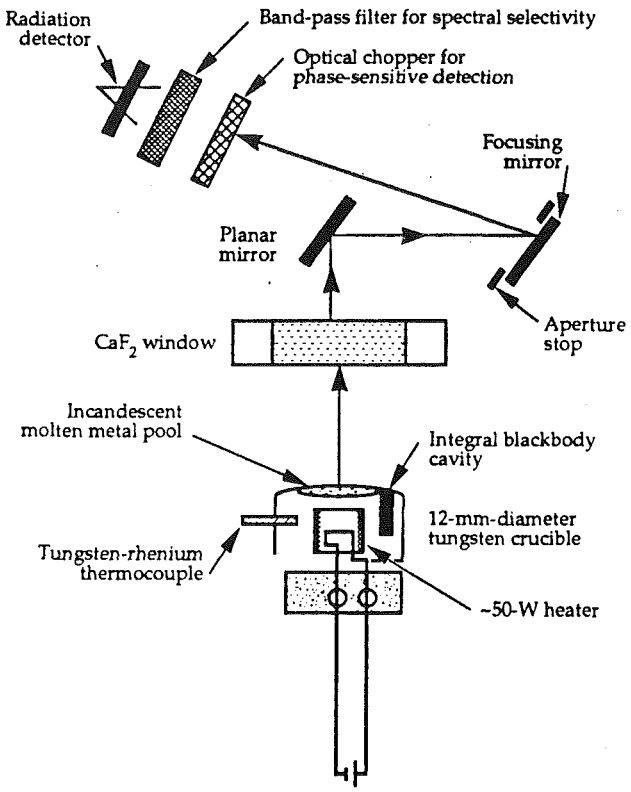

Fig. 1 Schematic of the apparatus for measurements of normal spectral emissivity

mirror of the normal emissivity system, was the second system for temperature measurement. As with the thermocouple, the sample phase change provided an estimate of the systematic error.

The Normal Spectral Emissivity Apparatus. Normal spectral emissivity was measured with an integral blackbody technique, shown schematically in Fig. 1 (specifications are given by Havstad, 1991). Thermal radiation emitted by the cavity or the sample into a small solid angle (beam half-angle = 1.24 deg) centered about the normal direction exits the vacuum system through a CaF_2 window. A planar mirror ~75 mm above the window folds the emission into a focusing mirror, which images the sample at the detector. Between this last mirror and the detector there is an optical chopper, band-pass filters for spectral selectivity, and a final aperture (directly in front of the detector). The entire top surface of the crucible (including both the sample and the exit face of the cavity) was imaged at the plane of this last field stop so that by lateral motion of the sample, radiation from either the sample or the blackbody could be selected by the aperture. The diameter of this aperture was 1.5 mm and the cavity diameter was 2.54 mm. Since the image and object distances were nearly equal in this optical system, the cavity image easily overfilled the aperture.

Direct comparison of the sample and cavity emissions, with an approximate correction for the contribution due to scattered light, is given by:

$$\epsilon_{n,\lambda}(\lambda, T) = \frac{V_{\text{sam}} - V_{\text{scat}}}{V_b - V_{\text{scat}}}. \tag{13}$$

Inclusion of the scattered term originated with Larrabee (1959) and was analyzed in detail by Latyev et al. (1969). The scattered light signal in this work was obtained by placing an aquadag (carbon suspension paint) coated card at the CaF_2 window there the emitted light exits the vacuum chamber. This approach neglects the scattered light introduced by the window itself, but includes other sources and somewhat overrepresents them because the card is flat rather than a cavity.

The Ellipsometric System. The need for a spectrally broadbanded method with good sensitivity from the visible to 10 μm dictated that the measurement technique consider both phase shift and amplitude attenuation—i.e., spectral ellipsometry (Havstad and Self, 1993). The method of Beattie and Conn, or a variant of it, was required. The original technique of Beattie and Conn was selected for the present work for its simplicity and precision.

The ellipsometer is shown schematically in Fig. 2 (specifications are given by Havstad, 1991). Since the wavelength range of interest here was not well covered by existing radiation sources, a new type was developed using a carbon composite filament (Havstad et al., 1993a).

Two types of polarizer were used. Calcite ($CaCO_3$) polarizers, which have an excellent extinction ratio (10^{-5} or better) were used from 0.4–2.3 μm. Wire grid polarizers were used from 2.3–10 μm since calcite is absorbing beyond 2.3 μm. Transmission losses and chromatic effects from the various CaF_2 elements prevented work beyond 10 μm.

The emissitivity and ellipsometric measurement systems employed the same detector and signal processing equipment. Both systems had optical choppers and a lock-in amplifier for reducing noise and, in the case of ellipsometry, for eliminating sample emission. Chopping frequencies of 700 and 300 Hz were typical with the ellipsometric and emissivity measurements, respectively.

Results

The normal spectral emissivity of liquid uranium at 1410 K is given in Fig. 3. The direct measurements of normal spectral emissivity are represented by squares, and the ellipsometric results by triangles. The curves shown are least-squares fits (of the following form) to the results from each of the two independent measurement systems.

$$\epsilon_n(\lambda) = a_0 + \frac{1}{a_1\lambda^2 + a_2\lambda + a_3}. \tag{14}$$

Coefficients for a single curve fit of the form of Eq. (14) to all of the data are given in Table 1.

Differences between the two curve fits indicate the magnitude of systematic errors. Errors are small over the 0.8–3.5 μm range, where both measurement systems have good signal-to-noise ratio and the ellipsometric system has good sensitivity. Outside of this range larger errors were expected from sensitivity considerations (Havstad and Self, 1993). The impact of discrepancies at the long wavelengths (beyond 3.5 μm) between the two sets of results is not severe for the principal applications that motivated this work: the peak in the Planck function for material at the melting point of uranium (1406 K) is at 2.06 μm and 62 percent of blackbody emission from a surface at 1406 K is below 3.5 μm. With the spectral dependence of the emissivity included (because the emissivity decreases strongly with wavelength) even a 20 percent uncertainty in the normal spectral emissivity at wavelengths greater than 3.5 μm involves a small fraction of the emitted energy in the whole spectrum. In summary, the small systematic errors indicated by Fig. 3 indicate that confidence is warranted in the results given here for normal spectral emissivity.

Random errors are indicated by the magnitude of the deviations of the measured results from the curve fits shown. The standard deviation of the data from the curve fit to the ellipsometric and direct measurements are 6.78 and 6.77 percent, respectively.

The difference between the results from the two measurement methods provides an unbiased estimate of error. If both techniques were free of both random and systematic error, the

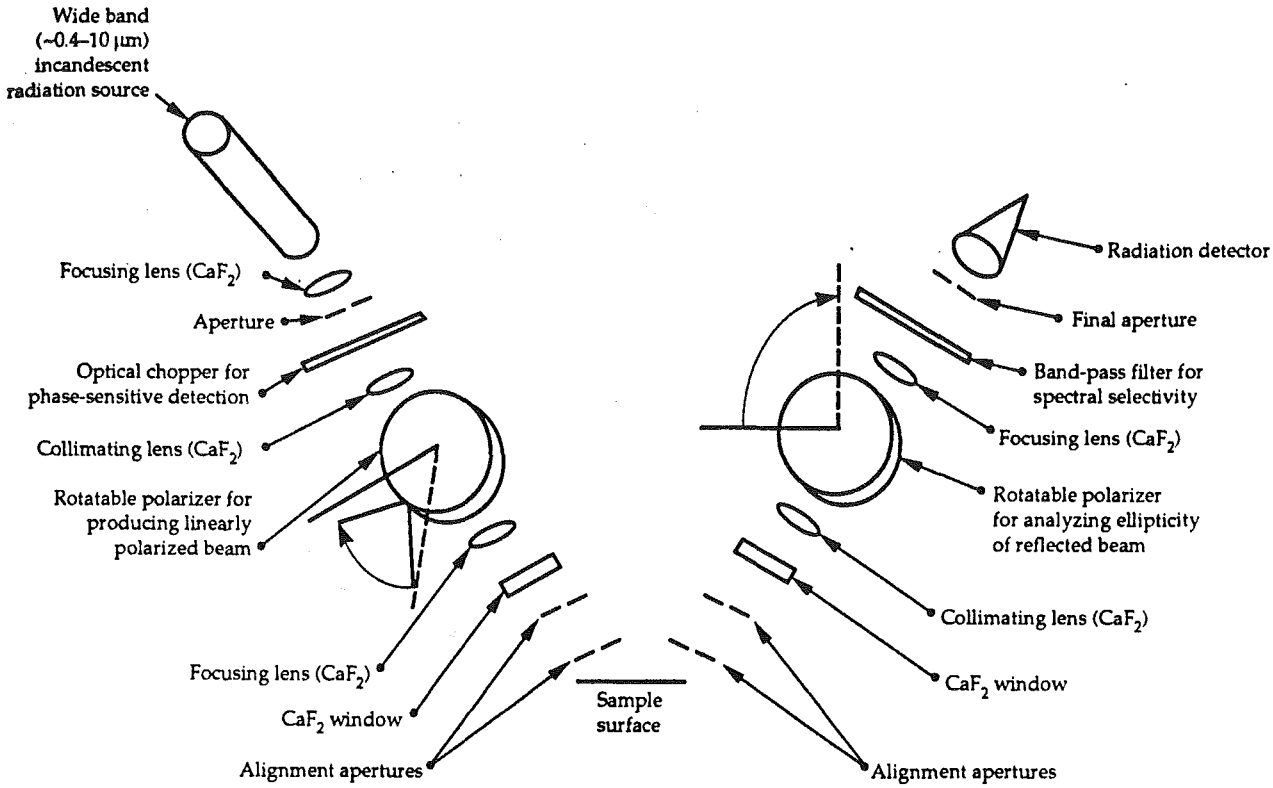

Fig. 2 Schematic of the ellipsometry measurement system (distances, sizes, and focal lengths are given by Havstad, 1991)

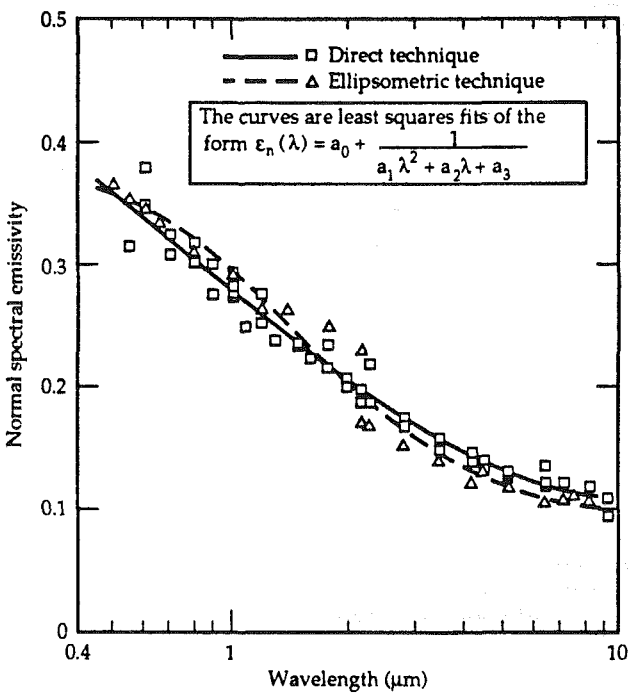

Fig. 3 The normal spectral emissivity of liquid uranium at 1410 K

Table 1 Coefficients for the curve fit to the normal spectral emissivity of liquid uranium as a function of wavelength (1410–1630 K), for $0.4 \leq \lambda \leq 10$ μm

Coefficient	Value
a_0	0.0793
a_1	0.254
a_2	2.50
a_3	2.42

Wavelength must be given in μm. The curve fit is of the form:

$$\varepsilon_n(\lambda) = a_0 + \frac{1}{a_1\lambda^2 + a_2\lambda + a_3}$$

two sets of results would coincide. The extent to which they disagree indicates the magnitude of the combination of both types of error. An error analysis by propagation of estimated uncertainties would involve subjective estimates and does not treat systematic error. The error shown here is an unbiased rendering of total error. Further discussion of errors is given by Havstad (1991).

The discontinuity in the results from the ellipsometric technique coincides with the change from calcite polarizers to wire grids (at 2 μm). The error is due to inaccurate rotational positioning of the polarizer and analyzer reference locations, and varies among the data sets (one set for each sample temperature between 1410 and 1630 K). When all sets are plotted together (Fig. 4), some systematic error can still be observed, but it is clear that the normal spectral emissivity lies very close to the region defined by the two curve fits.

The optical constants of liquid uranium from the visible to 8.5 μm are given in Figs. 5 and 6. The figures include data obtained at visible and infrared wavelengths for sample temperatures of 1410, 1480, and 1630 K, in addition to four sets of infrared measurements (2.8–8.5 μm) at temperatures ranging from 1430 to 1560 K. The scatter in the results in the long-wavelength region, which is as large or larger than the temperature dependence of the optical constants, is due to: (1) the combination of optical effects (discussed by Havstad et al., 1993b) that produce declining signal-to-noise ratio, and (2) declining measurement sensitivity with wavelength (discussed by Havstad and Self, 1993). The decrease in transmission of

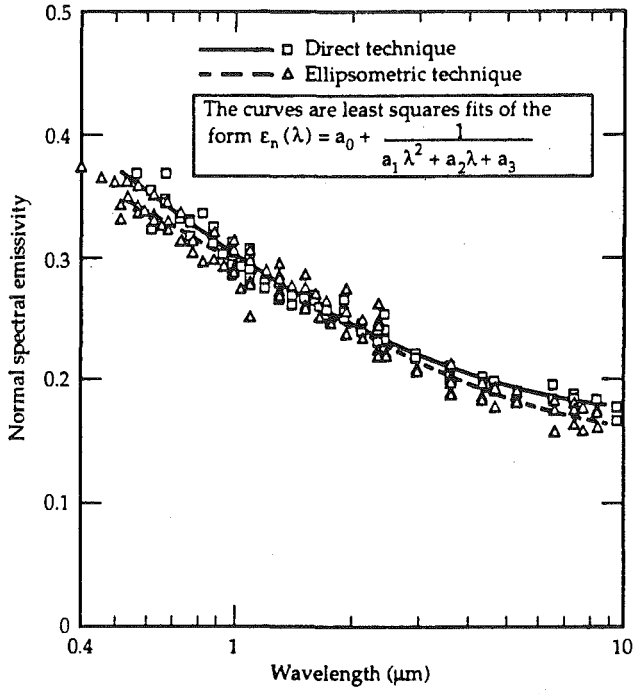

Fig. 4 The normal spectral emissivity of liquid uranium between 1410 and 1630 K

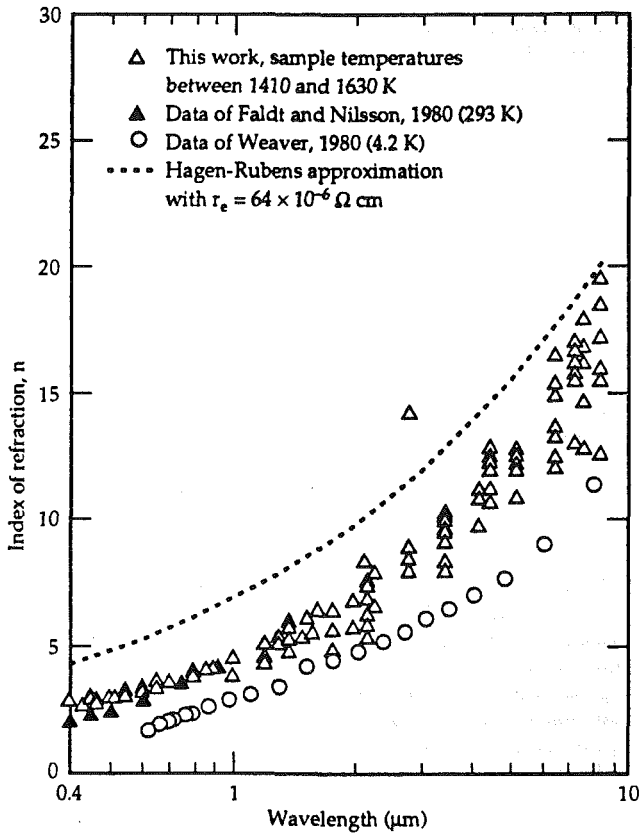

Fig. 5 The index of refraction of molten uranium

the CaF_2 optics beyond ~8 μm is particularly strong. The results of Faldt and Nilsson (1980) and Weaver (1980) are given, but their sample temperatures are so much lower that comparisons are of limited value.

The figures also show the result of applying the Hagen-Rubens formula for n and k:

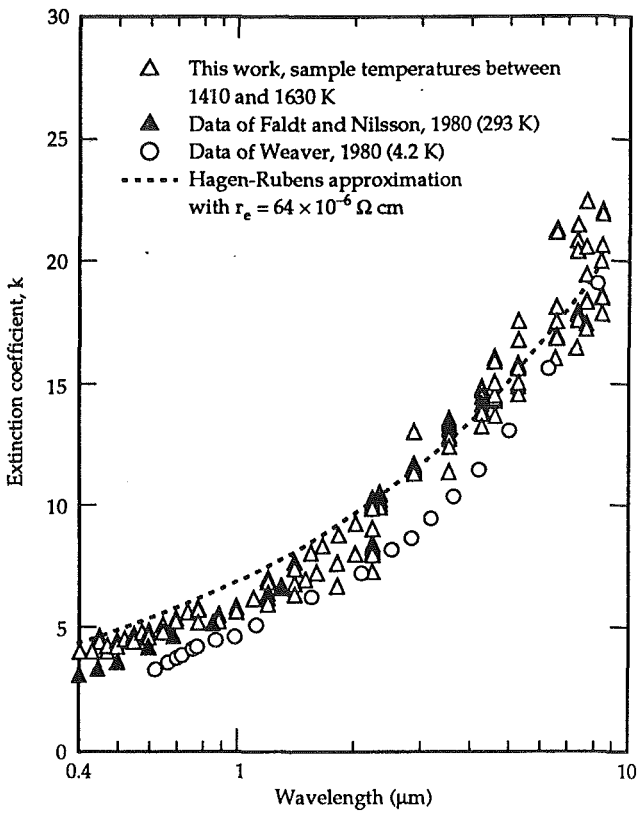

Fig. 6 The extinction coefficient of molten uranium

Table 2 Coefficients for a polynomial fit to the optical constants of liquid uranium as a function of wavelength (1410-1630 K), for $0.4 \leq \lambda \leq 10$ μm

n		k	
Coefficient	Value	Coefficient	Value
a_0	1.8939	a_0	2.6899
a_1	2.4832	a_1	3.4656
a_2	-0.08715	a_2	-0.17047

Wavelength must be given in μm. The curve fit is of the form:

n or $k = a_0 + a_1\lambda + a_2\lambda^2$

$$n = k = \sqrt{\frac{0.003\lambda_0}{r_e}}. \quad (15)$$

Agreement is good for k but poor for n. For Hagen-Rubens to apply, the measured values of n and k must approach equality and show agreement with Eq. (15) (a likelihood beyond 10 μm). Coefficients for polynomial fits to the data for both components of the complex index of refraction are given in Table 2.

The variation of n, k, and normal spectral emissivity with wavelength is similar to that reported for other transition metals such as tungsten. Normal spectral emissivity declines from the visible through the near infrared. At 8-10 μm and beyond, emissivity changes very slowly and remains at levels much greater than observed for clean, polished, noble metals such as platinum and gold. The components of the complex index of uranium in the visible range are comparable to those of more highly reflective metals, but as wavelength increases the noble metals display a much more rapid increase in each component and a convergence toward equality of the two com-

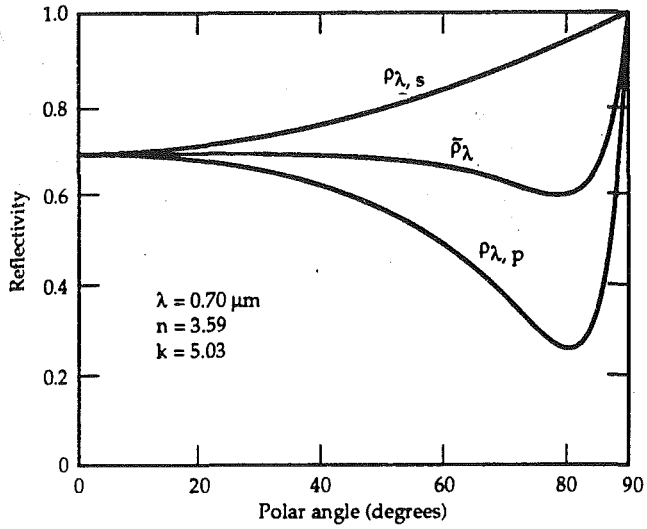

Fig. 7(*a*) The reflectivity of liquid uranium at 0.70 μm (1410 < T < 1630 K)

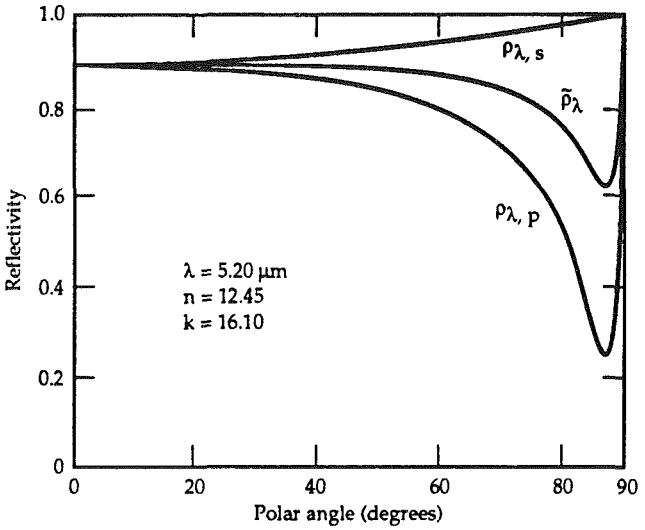

Fig. 7(*b*) The reflectivity of liquid uranium at 5.20 μm (1410 < T < 1630 K)

ponents at shorter wavelengths (but still beyond 10 μm in either case).

The failure of transition metals to satisfy the classical relations generated by Hagen–Rubens or the free-electron model (of Drude) has historically led to the use of combined free and bound oscillator type models (originally tried on tungsten by Roberts, 1955). This work involves fitting four or more parameters to the data. Subsequent studies of the electronic structure of transition metals (e.g., Kirillova et al., 1975) have shown that interband (i.e., bound) transitions set in at very low photon energies (~0.1–0.3 eV) so that there is no practical spectral region from which to derive the unbound parameters. The interband processes vary in type, strength, energy, and number so as to make simple oscillator models inadequate.

From the components of the complex refractive index (n and k) shown above and the Fresnel equations, the complete variation of the thermal radiative properties with wavelength and angle can be displayed. Figures 7(a) and 7(b) give the directional spectral reflectivity as a function of angle for liquid uranium for two wavelengths, 0.70 and 5.20 μm. (Values of n and k were computed from the polynomials given in Table 2.) Reflectivity increases toward unity as wavelength increases

Table 3 Coefficients for a polynomial fit to the total hemispherical emissivity of liquid uranium as a function of temperature (for 800 ≤ T < 1600 K)

Coefficient	Value
a_0	0.065
a_1	1.025e-4
a_2	-1.25e-8

Temperature must be given in degrees kelvin. The curve fit is of the form:

$$\varepsilon_{h,t} = a_0 + a_1 T + a_2 T^2$$

and the pseudo-Brewster angle (where the parallel component of reflectivity has a minimum) tends toward 90 deg. Both these trends are typical for conductors (either in the solid or the liquid state); with metals of higher electrical conductivity both high reflectivity and pseudo-Brewster angles near grazing occur at shorter wavelengths.

A polynomial fit for the total hemispherical emissivity (computed from the given polynomials for n and k) is given in Table 3. The variation with temperature is entirely due to the Planck function weighting within the integral.

Conclusions

The data for the normal spectral emissivity of molten uranium determined by two methods displayed good agreement over the entire spectral range of interest. The Hagen–Rubens relation does not apply for uranium at the wavelengths treated here because k remains significantly greater than n, even at 9 μm.

The variation with wavelength of the components of the complex index of refraction has been given by two polynomial curve fits. Any of the three thermal radiative properties, absorptivity, emissivity, and reflectivity, can be computed from these fits and then used in heat transfer calculations. Strong minima in the parallel component of reflectivity occur for angles of incidence greater than 80 deg, with positions of the minima moving toward grazing incidence with increasing wavelength.

All measurements were made on pure and smooth surfaces of liquid uranium metal. Ion sputtering and Auger spectroscopy were applied in situ to produce and verify the presence of oxide-free surfaces.

This work was performed under the auspices of the U.S. Department of Energy by Lawrence Livermore National Laboratory under contract No. W-7405-Eng-48.

References

Baker, L., Jr., Mouradian, E. M., and Bingle, J. D., 1963, "Determinations of the Total Emissivity of Polished and Oxidized Uranium Surfaces," *Nucl. Sci. Eng.*, Vol. 15, p. 218.

Beattie, J. R., 1955, "Optical Constants of Metals in the Infra-red—Experimental Methods," *Phil. Mag.*, Vol. 46, p. 235.

Beattie, J. R., and Conn, G. K. T., 1955, "Optical Constants of Metals in the Infra-Red—Principles of Measurement," *Phil. Mag.*, Vol. 46, p. 222.

Burgess, G. K., and Waltenberg, R. C., 1915, "The Emissivity of Metals and Oxides. II. Measurements With the Micropyrometer," *National Bureau of Standards Bulletin*, Vol. 11, p. 591.

Clarke, D., and Grainger, J. F., 1971, *Polarized Light and Optical Measurement*, Pergamon Press, Oxford, United Kingdom.

Faldt, A., and Nilsson, P. O., 1980, "Optical Properties of Uranium in the Range 0.6–25 eV," *J. Phys. F: Metal Phys.*, Vol. 10, p. 2573.

Havstad, M. A., 1991, "The Relative Properties and Optical Constants of Metals," Lawrence Livermore National Laboratory, Livermore, CA, UCRL-LR-107524.

Havstad, M. A., 1992, "Heat Transfer in a Liquid Metal Crucible With an Integral Blackbody Cavity," Lawrence Livermore National Laboratory, Livermore, CA, UCRL-LR-110322.

Havstad, M. A., Brown, J. D., Ebert, J. L., Maltby, J. D., and Self, S. A., 1993a, "A Simple Radiation Source for Both the Visible and the Infrared," *Infrared Phys.*, in press.

Havstad, M. A., McLean, W., II, and Self, S. A., 1993b, "Apparatus for the Measurement of the Optical Constants and Thermal Radiative Properties of Pure Liquid Metals From 0.4 to 10 μm," *Journal of Scientific Instruments*, accepted for publication.

Havstad, M. A., and Self, S. A., 1993, "Sensitivity Analyses of Measurement Methods for Optical Constants of Metals in the Spectral Range 0.4 to 10 μm," *International Journal of Thermophysics*, in press.

Hodgson, J. N., 1955, "The Infrared Properties of Some Metallic Films," *Proc. Phys. Soc.*, Vol. 9 (B), p. 593.

Hole, W. L., and Wright, R. W., 1939, "Emissive and Thermionic Characteristics of Uranium," *Phys. Rev.*, Vol. 56, p. 785.

Jackson, J. D., 1975, *Classical Electrodynamics*, 2nd ed., Wiley, New York.

Kirillova, M. M., Nomerovannaya, L. V., and Noskov, M. M., 1975, "Interband Optical Absorption and the Electronic Structure of 5d Metals," *Sov. Phys. Solid State*, Vol. 16, p. 1425.

Larrabee, R. D., 1959, "Spectral Emissivity of Tungsten," *J. Opt. Soc. Am.*, Vol. 49, p. 619.

Latyev, L. N., Chekhovskoi, V. Ya., and Shestakov, E. N., 1969, "Experimental Determination of Emissive Power of Tungsten in the Visible Region of the Spectrum in the Temperature Range 1200–2600 K," *High Temperatures—High Pressures*, Vol. 7, p. 610.

Lemmon, A. W., 1957, "The Reaction of Steam With Uranium and With Various Uranium-Niobium-Zirconium Alloys at High Temperatures," *Battelle Memorial Institute*, Vol. 1192, p. 1.

Musket, R. G., McLean, W., II, Colmenares, C. A., Makowiecki, D. M., and Siekhaus, W. J., 1982, "Preparation of Atomically Clean Surfaces of Selected Elements: A Review," *Applications of Surface Science*, Vol. 10, p. 143.

Price, D. J., 1948, "Note on the Calculation of Optical Constants," *Proc. Phys. Soc.*, Vol. 58, p. 704.

Rauh, E. G., 1956, "Work Function, Ionization Potential, and Emissivity of Uranium," Argonne National Laboratory, Lemont, IL, ANL-5534.

Roberts, S., 1959, "Optical Properties of Nickel and Tungsten and Their Interpretation According to Drude's Formula," *Phys. Rev.*, Vol. 114, p. 104.

Sokolov, A. V., 1967, *Optical Properties of Metals*, American Elsevier Publishing Company, New York.

Weaver, J. H., 1980, "Low-Energy Optical Absorption in a-U Metal," *J. Opt. Soc. Am.*, Vol. 70, p. 1030.

C. G. Malone

B. I. Choi

M. I. Flik

E. G. Cravalho

Department of Mechanical Engineering,
Massachusetts Institute of Technology,
Cambridge, MA 02139

Spectral Emissivity of Optically Anisotropic Solid Media

This work determines the spectral emissivity of a semi-infinite uniaxial medium in vacuum. If the optic axis is normal to the surface, then, for many materials and wavelengths, such as rutile between 10 and 25 μm, the directional and hemispherical spectral emissivities of the medium can be approximated, with an error of less than 10 percent, as those of an isotropic medium possessing the ordinary optical constants. In contrast, if the optic axis is parallel to the surface, the directional and hemispherical spectral emissivities can be predicted only by accounting for the optical anisotropy of the medium. Measurements of the directional emissivities of rutile crystals conform to the theoretical predictions.

Introduction

In an optically anisotropic material, the complex index of refraction $\bar{n}$ depends on the polarization of the propagating electromagnetic wave. Optically anisotropic materials include rutile (TiO_2), calcite ($CaCO_3$), quartz (SiO_2), and the new high-T_c superconducting compounds such as Y-Ba-Cu-O and Bi-Sr-Ca-Cu-O. Multiple quantum well devices exhibit optical anisotropy due to their layered structure. A birefringent medium is one in which the refractive index n varies with polarization. This term refers to the fact that, in general, a light ray incident on a birefringent material will result in two refracted rays, as illustrated in Fig. 1. The variation of the extinction coefficient, i.e., the imaginary part of $\bar{n}$, with polarization is called dichroism.

Materials exhibiting optical anisotropy have many applications in the field of optical electronics. These include polarizing crystals such as the Nicol prism, wire grid polarizers, Polaroid sheets, and optical window applications. Anisotropic layered media are used as high-performance polarization interference filters, waveguides, and multistage electro-optic modulators. The propagation of electromagnetic waves in optically anisotropic media has been investigated extensively, and was covered well by Born and Wolf (1980) and Ramachandran and Ramaseshan (1961). Yeh (1979) developed a general theory for plane-wave propagation in birefringent layered media.

This work addresses the spectral hemispherical emissivity, ϵ_λ, of an optically anisotropic medium. A systematic assessment of the influence of optical anisotropy on the directional emissivity is also performed. Hering and Smith (1968) determined analytically the hemispherical emissivity of an optically isotropic semi-infinite medium for a wide range of complex refractive indices but did not consider anisotropic media. The effect of anisotropy on the directional and hemispherical emissivity of a semi-infinite medium is considered for the two crystallographic orientations shown in Fig. 1: (001) where the optic axis is perpendicular to the interface, and (*hk*0) where the optic axis is parallel to the interface.

The new high-T_c superconducting copper-oxide materials exhibit a high degree of optical anisotropy. For example, the crystallographic *ab* plane in $YBa_2Cu_3O_7$ shows a metallic behavior whereas the material acts like a semiconductor along the *c* axis (Timusk and Tanner, 1989). Knowledge of the directional spectral emissivity of anisotropic media is required for establishing the feasibility of promising devices exploiting the high reflectance of high-T_c superconducting copper-oxide materials in the far-infrared spectral range, i.e., wavelengths longer than approximately 50 μm. High-reflectance applications include radiation shielding (Zeller, 1990) and the far-infrared Fabry–Perot resonator (Renk et al., 1990). The optimization of substrate temperature control in high-T_c superconducting thin-film processing systems demands an understanding of the hemispherical emittance of these materials (Flik et al., 1992).

Anisotropic Media

In an isotropic medium for monochromatic fields in the analytic representation, the complex electric field vector $\bar{\mathbf{E}}$ and the complex electric displacement vector $\bar{\mathbf{D}}$ are parallel and related by $\bar{\mathbf{D}} = \bar{\epsilon}\bar{\mathbf{E}}$ where $\bar{\epsilon}$ is the scalar complex dielectric function. In an anisotropic medium, $\bar{\mathbf{E}}$ and $\bar{\mathbf{D}}$ are not parallel and, thus, the dielectric function becomes a tensor. This work considers only materials that are magnetically isotropic and magnetically nondissipative, i.e., the magnetic permeability μ is a real scalar.

The succeeding discussion follows the treatment of Yeh (1988). In dichroic media with crystal structures of orthor-

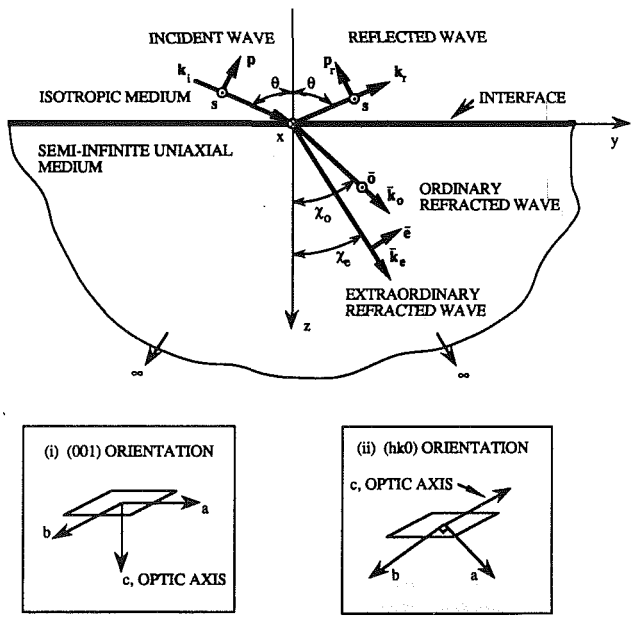

Fig. 1 Reflection and refraction at the interface between an isotropic and an anisotropic medium: (*i*) (001) orientation; (*ii*) (*hk*0) orientation

Contributed by the Heat Transfer Division and presented at the National Heat Transfer Conference, San Diego, California, August 9–12, 1992. Manuscript received by the Heat Transfer Division April 1992; revision received December 1992. Keywords: Radiation, Thermophysical Properties. Associate Technical Editor: R. O. Buckius.

hombic or higher symmetry, the complex dielectric function tensor is diagonalized if the coordinate axes are chosen such that they correspond with the crystallographic axes (Bohren and Huffman, 1983; Born and Wolf, 1980)

$$\bar{\epsilon} = \begin{pmatrix} \bar{\epsilon}_x & 0 & 0 \\ 0 & \bar{\epsilon}_y & 0 \\ 0 & 0 & \bar{\epsilon}_z \end{pmatrix} = \frac{\mu_0 \epsilon_0}{\mu} \begin{pmatrix} \bar{n}_x^2 & 0 & 0 \\ 0 & \bar{n}_y^2 & 0 \\ 0 & 0 & \bar{n}_z^2 \end{pmatrix} \tag{1}$$

where $\bar{\epsilon}_x$, $\bar{\epsilon}_y$, and $\bar{\epsilon}_z$ are the principal complex dielectric functions, $\bar{n}_x$, $\bar{n}_y$, and $\bar{n}_z$ are the principal complex refractive indices, and ϵ_0 is the electrical permittivity of free space. The principal dielectric axis system is the coordinate system that diagonalizes $\bar{\epsilon}$. The medium considered in the present analysis is classified optically as uniaxial. This means that the optical constants along two of the principal axes, x and y, are the same, i.e., $\bar{\epsilon}_x = \bar{\epsilon}_y$ and $\bar{n}_x = \bar{n}_y$. The optically uniaxial crystal structures are: tetragonal, hexagonal, and trigonal.

Maxwell's equations together with the material equations, $\bar{\mathbf{D}} = \bar{\epsilon}\bar{\mathbf{E}}$ and $\bar{\mathbf{B}} = \mu\bar{\mathbf{H}}$, are applied to a monochromatic plane wave propagating in an anisotropic medium to obtain

$$\bar{\mathbf{k}} \times (\bar{\mathbf{k}} \times \bar{\mathbf{E}}) + \omega^2 \mu \bar{\epsilon} \bar{\mathbf{E}} = 0 \tag{2}$$

In the principal dielectric axis system, for a given frequency and propagation direction $\tilde{s}$ the determinant of Eq. (2) may be viewed as a quadratic surface in $\bar{\mathbf{k}}$ space, which is called the normal surface. The normal surface of a uniaxial medium consists of two shells, a sphere, and an ellipsoid of revolution about the z axis, which intersect at two points on the z axis.

The determinant of Eq. (2) is zero for nontrivial solutions. Writing these solutions in terms of the direction cosines of the wave vector, $\tilde{s}_x$, $\tilde{s}_y$, $\tilde{s}_z$, one obtains Fresnel's equation of wave normals

$$\frac{\tilde{s}_x^2}{\bar{n}^2 - \bar{n}_x^2} + \frac{\tilde{s}_y^2}{\bar{n}^2 - \bar{n}_y^2} + \frac{\tilde{s}_z^2}{\bar{n}^2 - \bar{n}_z^2} = \frac{1}{\bar{n}^2} \tag{3}$$

where $\bar{n}^2 = (c_0/\omega)\bar{k}^2$. The directions of polarization of the electric field vector are given by

$$\begin{pmatrix} \dfrac{\tilde{s}_x}{\bar{n}^2 - \bar{n}_x^2} \\ \dfrac{\tilde{s}_y}{\bar{n}^2 - \bar{n}_y^2} \\ \dfrac{\tilde{s}_z}{\bar{n}^2 - \bar{n}_z^2} \end{pmatrix} \tag{4}$$

For an arbitrary propagation direction $\tilde{\mathbf{s}}$, Eq. (3) yields two values of $\bar{n}^2$, resulting in two possible directions of polarization, which are given by Eq. (4). In general, there are two propagation modes with different phase velocities along $\tilde{\mathbf{s}}$. In a uniaxial medium, these modes are called the ordinary and extraordinary waves.

Emissivity of Uniaxial Media

In order to predict the directional and hemispherical emissivity of a semi-infinite uniaxial medium, an expression for the directional-hemispherical spectral reflectivity $\rho_\lambda'(\theta, \varphi)$ must first be developed for all angles of incidence (θ, φ) of the hemisphere. It is assumed that the interface is optically smooth, i.e., that the standard deviation of the surface profile is much smaller than the wavelength of the electromagnetic waves in-

Nomenclature

$\bar{A}$ = incident wave complex electric vector amplitude, NC^{-1}
a, b, c = crystallographic axes
$\bar{B}$ = reflected wave complex electric vector amplitude, NC^{-1}
$\bar{C}$ = refracted wave complex electric vector amplitude, NC^{-1}
c_0 = speed of electromagnetic waves in vacuum, ms^{-1}
$\bar{\mathbf{D}}$ = complex electric displacement vector, Cm^{-2}
$\bar{\mathbf{E}}$ = complex electric field vector, NC^{-1}
$\bar{\mathbf{e}}$ = unit extraordinary complex electric field vector
$\bar{\mathbf{H}}$ = complex magnetic field vector, $Cm^{-1}s^{-1}$
h = Miller index
i = $(-1)^{1/2}$
$\bar{\mathbf{k}}$ = $(\omega/c_0)\bar{\mathbf{n}}\tilde{\mathbf{s}}$ = complex wave vector, m^{-1}
$\bar{k}$ = $(\omega/c_0)\bar{n}$ = complex wave number, m^{-1}
k = Miller index
$\bar{n}$ = complex refractive index $= n + i\kappa$
n = refractive index
n_i = refractive index of the medium of incidence
$\bar{\mathbf{o}}$ = unit ordinary complex electric field vector
$\mathbf{p}$ = unit transverse magnetic field vector
$\mathbf{r}$ = position vector, m
$\bar{r}$ = Fresnel reflection coefficient, complex
$\mathbf{S}$ = Poynting vector
$\tilde{\mathbf{s}}$ = unit plane wave propagation direction vector
$\mathbf{s}$ = unit transverse electric field vector
t = time, s
x, y, z = principal dielectric axes
$\mathbf{x}, \mathbf{y}, \mathbf{z}$ = unit vectors along principal dielectric axes
α_λ' = directional spectral absorptivity
γ_{pLO} = pth phonon longitudinal mode damping constant, $rad\ s^{-1}$
γ_{pTO} = pth phonon transverse mode damping constant, $rad\ s^{-1}$
δ = relative difference
$\bar{\epsilon}$ = complex dielectric function tensor, $C^2N^{-1}m^{-2}$
ϵ_λ = hemispherical spectral emissivity
ϵ_λ' = directional spectral emissivity
ϵ_0 = electrical permittivity of free space = 8.85×10^{-12} $C^2N^{-1}m^{-2}$
ϵ_∞ = high-frequency dielectric constant
θ = angle of incidence or emission measured from normal of surface, rad or deg
κ = extinction coefficient
λ = wavelength in vacuum, m
μ = magnetic permeability, $N\ s^2C^{-2}$
μ_0 = magnetic permeability of free space = $4\pi \times 10^{-7}$ $N\ s^2C^{-2}$
ρ_λ' = directional-hemispherical spectral reflectivity
φ = circumferential angle, rad
χ = refractance angle from surface normal, rad
Ω_{pLO} = pth phonon longitudinal mode oscillator frequency, $rad\ s^{-1}$
Ω_{pTO} = pth phonon transverse mode oscillator frequency, $rad\ s^{-1}$
ω = angular frequency, $rad\ s^{-1}$

Subscripts

e = extraordinary optical property
i = incident wave
o = ordinary optical property
p = transverse magnetic polarization, TM
r = reflected wave
s = transverse electric polarization, TE
x, y, z = principal dielectric axes
λ = spectral quantity

cident on the material. For a semi-infinite absorbing medium, the transmissivity is zero. Applying an energy balance at the interface gives the directional spectral absorptivity $\alpha'_\lambda(\theta, \varphi)$. Kirchhoff's law equates $\alpha'_\lambda(\theta, \varphi)$ with the directional spectral emissivity $\epsilon'_\lambda(\theta, \varphi)$. Integration of $\epsilon'_\lambda(\theta, \varphi)$ over all solid angles of the hemisphere yields ϵ_λ.

Wave Propagation. Consider the reflection and refraction of a monochromatic plane wave propagating in the yz plane at the interface between a nonabsorbing isotropic medium and a semi-infinite, absorbing uniaxial medium, as shown in Fig. 1. This analysis follows the general method outlined by Yeh (1988), adapted for both the (001) and the ($hk0$) orientations. In general, there will be two refracted waves, the ordinary and extraordinary, for an incident wave at an angle θ from the surface normal. At the boundary, the tangential components of all the wave vectors are equal and the sum of the tangential components of the incident and reflected $\overline{\mathbf{E}}$ and $\overline{\mathbf{H}}$ vectors equals the sum of the tangential components of the refracted $\overline{\mathbf{E}}$ and $\overline{\mathbf{H}}$ vectors.

The incident, reflected, and refracted electric field vectors are

$$\overline{\mathbf{E}}_i = (\overline{A}_s \mathbf{s} + \overline{A}_p \mathbf{p}) \exp[i(\mathbf{k}_i \cdot \mathbf{r} - \omega t)] \tag{5}$$

$$\overline{\mathbf{E}}_r = (\overline{B}_s \mathbf{s} + \overline{B}_p \mathbf{p}_r) \exp[i(\mathbf{k}_r \cdot \mathbf{r} - \omega t)] \tag{6}$$

$$\overline{\mathbf{E}}_{\text{refracted}} = \overline{C}_o \overline{\mathbf{o}} \exp[i(\overline{\mathbf{k}}_o \cdot \mathbf{r} - \omega t)] + \overline{C}_e \overline{\mathbf{e}} \exp[i(\overline{\mathbf{k}}_e \cdot \mathbf{r} - \omega t)] \tag{7}$$

where $\mathbf{k}_i = 0\,\mathbf{x} + k_i \sin\theta \mathbf{y} + k_i \cos\theta \mathbf{z}$ is the incident wave vector, $k_i = (\omega/c_0) n_i$ is the incident wave number, n_i is the refractive index of the incident medium, $\mathbf{k}_r = 0\,\mathbf{x} + k_i \sin\theta \mathbf{y} - k_i \cos\theta \mathbf{z}$ is the reflected wave vector; note that n_i, k_i, θ, $\mathbf{k}_i$, and $\mathbf{k}_r$ are real variables. Variables $\overline{\mathbf{k}}_\mathbf{o}$ and $\overline{\mathbf{k}}_\mathbf{e}$ are the ordinary and extraordinary complex wave vectors, respectively. The terms $\overline{A}_s$, $\overline{A}_p$, $\overline{B}_s$, $\overline{B}_p$, $\overline{C}_o$, and $\overline{C}_e$ are the complex electric field vector amplitudes of the different polarizations of the incident, reflected, and refracted waves, respectively. The vectors $\mathbf{s}$ and $\mathbf{p}$ are unit vectors in the direction of the electric field vectors of the incident wave where $\mathbf{s}$ is perpendicular to the plane of incidence and $\mathbf{p}$ is parallel to the plane of incidence. In Fig. 1, the plane of incidence is the yz plane and $\mathbf{s}$ in the $-\mathrm{x}$ direction. The vector $\mathbf{p}_r$ is a unit vector in the direction of the electric field vector of the reflected wave parallel to the plane of incidence. The vectors $\overline{\mathbf{o}}$ and $\overline{\mathbf{e}}$ are unit vectors parallel to the electric field vector of the ordinary and extraordinary wave vectors, respectively.

The corresponding complex magnetic field vectors are found from Faraday's law for a time-harmonic field

$$\overline{\mathbf{H}} = \frac{-i}{\omega\mu} \nabla \times \overline{\mathbf{E}} \tag{8}$$

The wave vectors $\overline{\mathbf{k}}_\mathbf{o}$ and $\overline{\mathbf{k}}_\mathbf{e}$ are determined as functions of θ and φ by applying to Eq. (3) the boundary condition that the components of the wave vectors tangent to the interface must be equal. The vectors $\overline{\mathbf{o}}$ and $\overline{\mathbf{e}}$ are evaluated using Eq. (4). Applying the boundary condition that requires continuity of the components of $\overline{\mathbf{E}}$ and $\overline{\mathbf{H}}$ tangent to the interface yields four equations. The unknowns $\overline{B}_s$, $\overline{B}_p$, $\overline{C}_o$, and $\overline{C}_e$ are found in terms of $\overline{A}_s$ and $\overline{A}_p$, providing the Fresnel reflection coefficients.

(001) Orientation. The Fresnel reflection coefficients for the (001) orientation, as a function of the angle of incidence θ are, for s- and p-polarized incidence waves, respectively

$$\bar{r}_{ss} = \frac{n_i \cos\theta - \sqrt{\overline{n}_o^2 - n_i^2 \sin^2\theta}}{n_i \cos\theta + \sqrt{\overline{n}_o^2 - n_i^2 \sin^2\theta}} \tag{9}$$

$$\bar{r}_{pp} = \frac{\overline{n}_o \overline{n}_e \cos\theta - n_i \sqrt{\overline{n}_e^2 - n_i^2 \sin^2\theta}}{\overline{n}_o \overline{n}_e \cos\theta + n_i \sqrt{\overline{n}_e^2 - n_i^2 \sin^2\theta}} \tag{10}$$

where for $\bar{r}_{ir}$ the first subscript refers to the incident wave and the second refers to the reflected wave, $\overline{n}_o$ is the complex refractive index of the crystallographic ab plane and $\overline{n}_e$ is the complex refractive index of the crystallographic c axis. For the (001) orientation, $\bar{r}_{sp} = \bar{r}_{ps} = 0$.

($hk0$) Orientation. The Fresnel reflection coefficients for the ($hk0$) orientation, as a function of the angle of incidence θ and circumferential angle φ, are

$$\bar{r}_{ss} = \frac{\overline{n}_{oz} \sin^2\varphi (n_z - \overline{n}_{oz}) (n_i^2 \overline{n}_{oz}^2 + \overline{n}_o^2 n_z \overline{n}_{ez}) + \overline{n}_o^2 \cos^2\varphi (n_z - \overline{n}_{ez}) (\overline{n}_o^2 n_z + n_i^2 \overline{n}_{oz})}{\overline{n}_{oz} \sin^2\varphi (n_z + \overline{n}_{oz}) (n_i^2 \overline{n}_{oz}^2 + \overline{n}_o^2 n_z \overline{n}_{ez}) + \overline{n}_o^2 \cos^2\varphi (n_z + \overline{n}_{ez}) (\overline{n}_o^2 n_z + n_i^2 \overline{n}_{oz})} \tag{11}$$

$$\bar{r}_{sp} = \frac{2 \overline{n}_o^2 n_i \overline{n}_{oz} n_z \cos\varphi \sin\varphi (\overline{n}_{oz} - \overline{n}_{ez})}{\overline{n}_{oz} \sin^2\varphi (n_z + \overline{n}_{oz}) (n_i^2 \overline{n}_{oz}^2 + \overline{n}_o^2 n_z \overline{n}_{ez}) + \overline{n}_o^2 \cos^2\varphi (n_z + \overline{n}_{ez}) (\overline{n}_o^2 n_z + n_i^2 \overline{n}_{oz})} \tag{12}$$

$$\bar{r}_{pp} = \frac{\overline{n}_{oz} \sin^2\varphi (n_z + \overline{n}_{oz}) (\overline{n}_o^2 n_z \overline{n}_{ez} - n_i^2 \overline{n}_{oz}^2) + \overline{n}_o^2 \cos^2\varphi (n_z + \overline{n}_{ez}) (\overline{n}_o^2 n_z - n_i^2 \overline{n}_{oz})}{\overline{n}_{oz} \sin^2\varphi (n_z + \overline{n}_{oz}) (n_i^2 \overline{n}_{oz}^2 + \overline{n}_o^2 n_z \overline{n}_{ez}) + \overline{n}_o^2 \cos^2\varphi (n_z + \overline{n}_{ez}) (\overline{n}_o^2 n_z + n_i^2 \overline{n}_{oz})} \tag{13}$$

$$\bar{r}_{ps} = \frac{2 \overline{n}_o^2 n_i \overline{n}_{oz} n_z \cos\varphi \sin\varphi (\overline{n}_{ez} - \overline{n}_{oz})}{\overline{n}_{oz} \sin^2\varphi (n_z + \overline{n}_{oz}) (n_i^2 \overline{n}_{oz}^2 + \overline{n}_o^2 n_z \overline{n}_{ez}) + \overline{n}_o^2 \cos^2\varphi (n_z + \overline{n}_{ez}) (\overline{n}_o^2 n_z + n_i^2 \overline{n}_{oz})} \tag{14}$$

where

$$n_z = n_i \cos\theta \tag{15}$$

$$\overline{n}_{oz} = \sqrt{\overline{n}_o^2 - n_i^2 \sin^2\theta} \tag{16}$$

$$\overline{n}_{ez} = \sqrt{\overline{n}_e^2 - n_i^2 \sin^2\theta \left(\cos^2\varphi + \frac{\overline{n}_e^2}{\overline{n}_o^2} \sin^2\varphi \right)} \tag{17}$$

For the ($hk0$) orientation, the plane of incidence is perpendicular to the optic axis for $\varphi = 0$ deg and $\varphi = 180$ deg and parallel to the optic axis for $\varphi = 90$ deg and $\varphi = 270$ deg.

The s and p wave directional-hemispherical spectral reflectivities are given by

$$\rho'_{s,\lambda}(\theta, \varphi) = |\bar{r}_{ss}|^2 + |\bar{r}_{sp}|^2 \tag{18}$$

$$\rho'_{p,\lambda}(\theta, \varphi) = |\bar{r}_{pp}|^2 + |\bar{r}_{ps}|^2 \tag{19}$$

The s and p wave directional spectral absorptivities, $\alpha'_{s,\lambda}(\theta, \varphi)$ and $\alpha'_{p,\lambda}(\theta, \varphi)$, are obtained by applying an energy balance at the interface of the nontransmitting semi-infinite medium for each polarization

$$\alpha'_{s,\lambda}(\theta, \varphi) = 1 - \rho'_{s,\lambda}(\theta, \varphi) \tag{20}$$

$$\alpha'_{p,\lambda}(\theta, \varphi) = 1 - \rho'_{p,\lambda}(\theta, \varphi) \tag{21}$$

Emissivity. Kirchhoff's law equates the directional spectral emissivity with the directional spectral absorptivity for a given state of polarization (Siegel and Howell, 1981)

$$\epsilon'_{s,\lambda}(\theta, \varphi) = \alpha'_{s,\lambda}(\theta, \varphi) \tag{22}$$

$$\epsilon'_{p,\lambda}(\theta, \varphi) = \alpha'_{p,\lambda}(\theta, \varphi) \tag{23}$$

Kirchhoff's original derivation was based on geometric optics and the Second Law of thermodynamics, and required that the body be in mutual equilibrium with blackbody radiation of the body's temperature. Reviewing theoretical results from

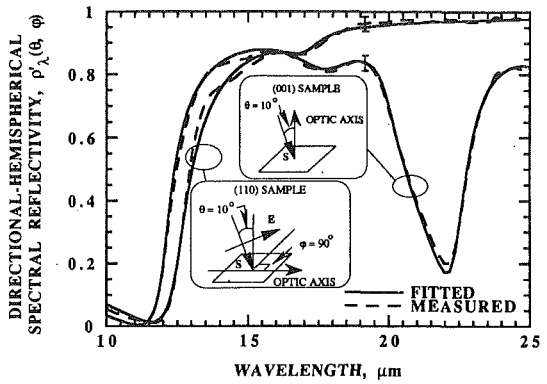

Fig. 2 Dispersion relation fit to the measured near-normal reflectivity of rutile

quantum mechanics, Baltes (1976) showed that Kirchhoff's law is valid independent of the radiation field surrounding the body, i.e., also in nonequilibrium, provided that the distribution of the material states of the body is the equilibrium distribution. This more general statement of Kirchhoff's law rests on the proper definitions of the radiative properties: emissivity must only account for spontaneous emission, while absorptivity considers the net effect of both induced absorption and induced emission. Only these definitions provide the quantities actually measured in an experiment. Hence, the emissivities predicted in the present work also hold for a freely radiating body, provided that its state is not too far removed from stable thermodynamic equilibrium. Ketelaar and Haas (1956) performed measurements of the infrared directional emissivity and reflectivity of calcite, a highly anisotropic material, in a nonequilibrium environment, providing experimental confirmation of the statement of Kirchhoff's law given above.

The radiation emitted by a body may be strongly polarized depending on the relative magnitudes of the s and p wave directional spectral emissivities. Sandus (1965) reviewed experimental and theoretical evidence of emission polarization.

To calculate the hemispherical spectral emissivity ϵ_λ, the arithmetic average of $\epsilon'_{s,\lambda}(\theta, \varphi)$ and $\epsilon'_{p,\lambda}(\theta, \varphi)$, $\epsilon'_\lambda(\theta, \varphi)$, is integrated over all solid angles in the hemisphere

$$\epsilon_\lambda = \frac{1}{2\pi} \int_{\varphi=0}^{2\pi} d\varphi \int_{\theta=0}^{\pi/2} d\theta \epsilon'_\lambda(\theta, \varphi) \sin 2\theta \qquad (24)$$

There is no φ-dependence for the (001) orientation because the xy plane is optically isotropic.

Measurements

In order to verify the analytical solution for the hemispherical emissivity, the reflectivity of rutile (TiO_2), a strongly anisotropic crystal, is measured using a Biorad FTS-60A Fourier-transform infrared (FT-IR) spectrometer for the wavelength region between 10 μm and 25 μm. The measurements are compared with the analytical results. The ratio of the spectral response of rutile to the spectral response of a gold reference mirror gives the directional-hemispherical spectral reflectivity. Zhang et al. (1992) gave a detailed description of the experimental system.

Two 12 mm × 12 mm × 1 mm rutile samples are investigated. One sample has a (001) orientation, with the optic axis perpendicular to the 12 mm × 12 mm surface, and the other has a (110) orientation, with the optic axis parallel to the 12 mm × 12 mm surface and aligned with an edge. The sample surfaces are optically smooth. The penetration depth in the investigated wavelength region is much less than the sample thickness (Spitzer et al., 1962; Gervais and Piriou, 1974). Reflectivity measurements are made at near-normal incidence,

Table 1 Oscillator frequencies, damping terms, and high-frequency dielectric constant for ordinary optical properties of (001) rutile sample

p	Ω_{pTO} (cm^{-1})	γ_{pTO} (cm^{-1})	Ω_{pLO} (cm^{-1})	γ_{pLO} (cm^{-1})
1	189	10	831	39
2	380	16.5	367	10
3	500	18.5	447	17.5
4	570	81.5	500	82

$\varepsilon_\infty = 6.0$

Table 2 Oscillator frequencies, damping terms, and high-frequency dielectric constant for extraordinary optical properties of (110) rutile sample

p	Ω_{pTO} (cm^{-1})	γ_{pTO} (cm^{-1})	Ω_{pLO} (cm^{-1})	γ_{pLO} (cm^{-1})
1	171	7	802	55
2	589	57	587	55

$\varepsilon_\infty = 7.8$

θ = 10 deg, and at incidence angles of θ = 30, 40, 50, 60, and 70 deg for the (001) sample. For the (110) sample, the reflectivity is measured at near-normal incidence for $\bar{\mathbf{E}}$ polarized both perpendicular and parallel to the optic axis and for unpolarized radiation at near-normal incidence with the plane of incidence parallel to the optic axis, φ = 90 deg. The relative photometric accuracy of the reflectivity measurements is estimated to be 3 percent. The reflectivity of the gold reference mirror is predicted to be 0.98 for 10 deg $\leq \theta \leq$ 60 deg, and 0.975 at θ = 70 deg from directional-hemispherical spectral reflectivity calculations made using the gold optical property data of Lynch and Hunter (1985).

Results and Discussion

Rutile Reflectivity Measurements. Figure 2 presents the near-normal directional-hemispherical reflectivity spectra for rutile. The rutile samples are opaque for wavelengths longer than 10 μm. The data are fitted using the four-parameter dispersion model described by Gervais and Piriou (1974). Tables 1 and 2 give the fitting parameters. The model gives the spectral complex dielectric function

$$\frac{\bar{\epsilon}}{\epsilon_0} = \epsilon_\infty \prod_p \frac{\Omega_{pLO}^2 - \omega^2 - i\gamma_{pLO}\omega}{\Omega_{pTO}^2 - \omega^2 - i\gamma_{pTO}\omega} \qquad (25)$$

where ω is the angular frequency, Ω_{pLO} and γ_{pLO} are the pth phonon longitudinal mode oscillator frequency and damping constant, respectively, Ω_{pTO} and γ_{pTO} are the pth phonon transverse mode oscillator frequency and damping constant, respectively, and ϵ_∞ is the high-frequency dielectric constant. The reflectance can be fitted more closely with this model than with the Lorentz model because it accounts for both the longitudinal and transverse vibration modes.

The fit to the (001) sample near-normal directional-hemispherical reflectivity yields the spectral ordinary complex refractive index and the fit to the (110) sample near-normal directional-hemispherical reflectivity with $\bar{\mathbf{E}}$ polarized along the optic axis gives the spectral extraordinary complex refractive index. Due to crystallographic symmetry, the near-normal reflectance spectra of the (001) sample and the (110) sample with $\bar{\mathbf{E}}$ polarized perpendicular to the optic axis are identical because both depend only on the ordinary refractive index. Experimental measurements of these two spectra displayed an

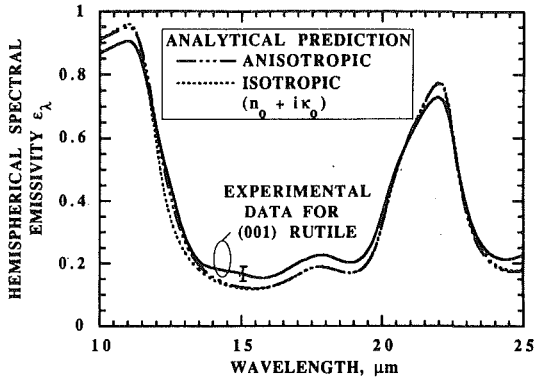

Fig. 3 Hemispherical spectral emissivity of (001) rutile

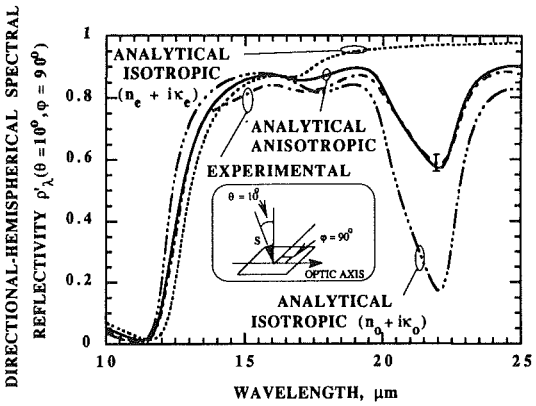

Fig. 4 Directional spectral reflectivity for (110) rutile, unpolarized incident radiation

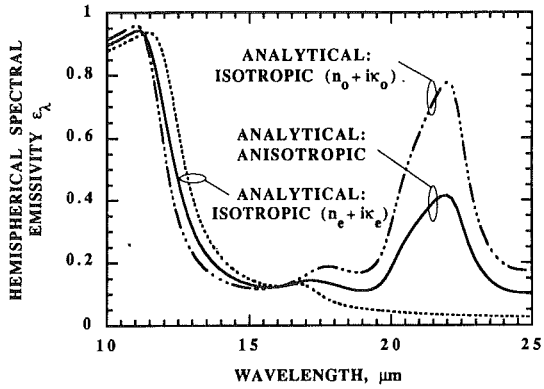

Fig. 5 Hemispherical spectral emissivity for (*hk*0) rutile

Table 3 Summary of the influence of optical anisotropy on the hemispherical emissivity of uniaxial media

Orientation				
(001)				(*hk*0)
$n_o < 1$ and $\kappa_o < 0.25$	$0.1 < n_o < 1$ and $\kappa_o > 0.25$ or $n_o \geq 1$			
	$\kappa_e < \kappa_o$		$\kappa_e \geq \kappa_o$	
	$n_e < 2$	$n_e > 2$		
Strong effect of anisotropy. ε_λ deviates from the isotropic $\varepsilon_\lambda(\bar{n}_o)$ by more than 10 %.	Strong effect of anisotropy. ε_λ deviates from the isotropic $\varepsilon_\lambda(\bar{n}_o)$ by as much as 35 %.	Moderate effect of anisotropy. ε_λ deviates from the isotropic $\varepsilon_\lambda(\bar{n}_o)$ by less than 10 %.	Anisotropy can be neglected. ε_λ deviates from the isotropic $\varepsilon_\lambda(\bar{n}_o)$ by less than 2 %.	Strong effect of anisotropy. ε_λ can be approximated by arithmetically averaging isotropic values based on ordinary and extraordinary optical constants.

agreement better than 2 percent. The parameters of Eq. (25) are varied until the fitted and measured reflectivities in Fig. 2 differ by no more than 5 percent. The reflectivity measurements compare well with those of Gervais and Piriou (1974). They did not measure the directional-hemispherical reflectivity for incidence angles greater than 7.5 deg.

The experimental hemispherical spectral emissivity for the (001) sample is approximated by integrating the (001) directional spectral emissivities measured at incidence angles of θ = 10, 30, 40, 50, 60, and 70 deg, using linear interpolation. The directional emissivity of θ = 0 deg is assumed to be the same as the measured quantity at θ = 10 deg and for θ = 90 deg, the directional emissivity is zero. Figure 3 compares the experimental hemispherical spectral emissivity with the values predicted analytically for both an anisotropic medium and an isotropic medium with the ordinary optical constants. The analytical result calculated for the anisotropic case is almost identical to that of the isotropic case. The agreement between the analytical and estimated experimental results is better than 7 percent.

Figure 4 displays the experimentally measured and analytically calculated directional-hemispherical spectral reflectivity for the (110) rutile sample. The plane of incidence contains the optic axis, φ = 90 deg, and the incidence angle θ = 10 deg. For comparison, $\rho'_\lambda(\theta, \varphi)$ is also calculated using isotropic ordinary and extraordinary optical constants. The experimental measurement of $\rho'_\lambda(\theta, \varphi)$ agrees with the analytical result that considers the optical anisotropy by better than 7 percent. The data in Fig. 4 are obtained with unpolarized incident radiation. Hence the reflectivity should be approximately equal to the arithmetic mean of the reflectivities for polarization along and perpendicular to the optic axis, respectively. This is corroborated by the data. For the prediction of the radiative properties of (110) rutile, the optical anisotropy must be considered.

Figure 5 shows the hemispherical emissivity of (*hk*0) rutile predicted analytically considering the optical anisotropy and, for comparison, that predicted assuming isotropy with the ordinary and extraordinary optical constants, respectively. The optical anisotropy strongly influences the hemispherical emissivity for this crystallographic orientation. The (*hk*0) hemispherical emissivity may be approximated by arithmetically averaging the isotropic ordinary and extraordinary hemispherical emissivities, $\epsilon_\lambda \approx 0.5[\epsilon_\lambda(\bar{n}_o) + \epsilon_\lambda(\bar{n}_e)]$.

General Uniaxial Materials. Table 3 summarizes the range of optical constants, n_e, n_o, κ_e, and κ_o, in which the anisotropy significantly influences the directional and hemispherical spectral emissivities.

Figures 6(*a*) and 6(*b*) present the difference between the predicted hemispherical spectral emissivity in vacuum for a semi-infinite uniaxial medium with a (001) crystallographic orientation and an isotropic medium possessing the ordinary optical constants in terms of the relative difference δ

$$\delta = \left(\frac{\epsilon_\lambda(\bar{n}_o, \bar{n}_e) - \epsilon_\lambda(\bar{n}_o)}{\epsilon_\lambda(\bar{n}_o)} \right) \tag{26}$$

The ordinary complex refractive index $\bar{n}_o$ is fixed at a particular value in each figure and the extraordinary refractive index n_e is varied between 1 and 4 for lines of constant extraordinary extinction coefficients κ_e. The ratios of the extraordinary to the ordinary extinction coefficient, κ_e/κ_o, are the same in each figure: κ_e/κ_o = 0.125, 0.5, 1, 1.5, and 5. The $\bar{n}_o$ values are chosen from the ordinary optical constant data for rutile in the spectral region of the phonon absorption band around 20 μm where the anisotropy of the optical constants is large. They are representative of the variation of the optical

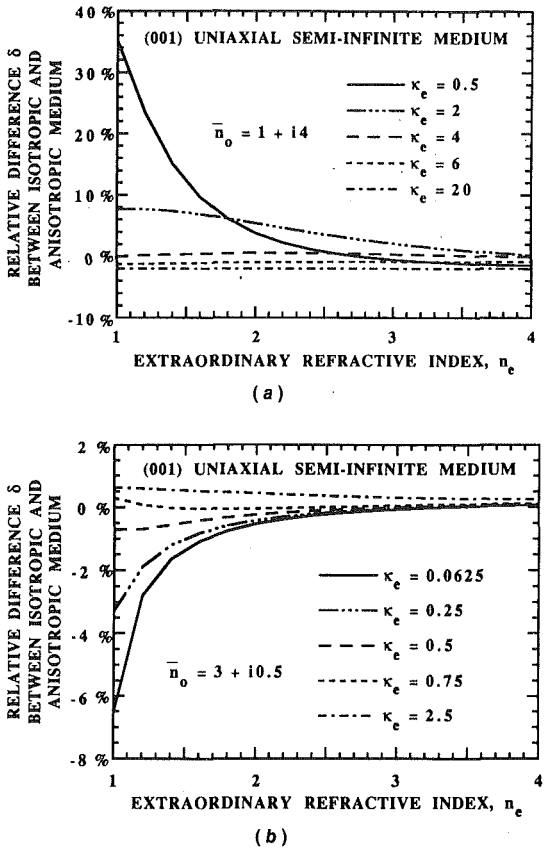

Fig. 6 Relative difference between the hemispherical spectral emissivity in vacuum of a (001) uniaxial semi-infinite medium and an isotropic medium possessing the ordinary optical constants of the uniaxial medium: (*a*) $\bar{n}_o = 1 + i4$; (*b*) $\bar{n}_o = 3 + i0.5$

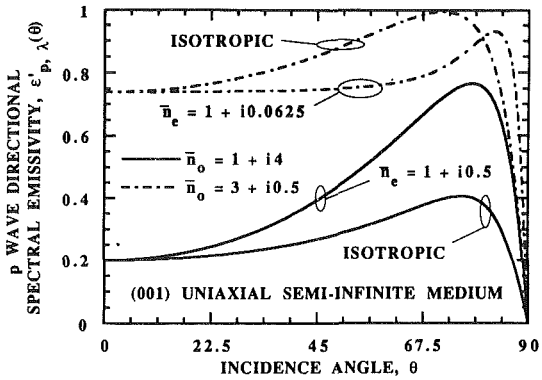

Fig. 7 Directional *p* wave spectral emissivity in vacuum of a (001) uniaxial semi-infinite medium and an isotropic medium possessing the ordinary optical constants of the uniaxial medium

constants in a typical phonon absorption band. In general, the principal axes of a uniaxial crystal have a different phonon structure. The optical anisotropy between the principal axes is usually maximized for wavelengths within a phonon absorption band. In Fig. 6(*a*), $\bar{n}_o = 1 + i4$, representing the optical constants for wavelengths slightly shorter than the resonance wavelength. In Fig. 6(*b*), $\bar{n}_o = 3 + i0.5$, representing the optical constants for wavelengths slightly longer than the resonance wavelength. The isotropic hemispherical spectral emissivities $\epsilon_\lambda(n_o, \kappa_o)$ are: $\epsilon_\lambda(1, 4) = 0.20838$ and $\epsilon_\lambda(3, 0.5) = 0.71347$.

For the (001) orientation, the ordinary refracted wave is independent of the variation of the optical anisotropy as it depends only on $\bar{n}_o$. The anisotropy influences only the extraordinary refracted wave, and the reflected and emitted *p* waves. The *s* wave directional spectral emissivity $\epsilon'_{s,\lambda}(\theta)$ is a function of $\bar{n}_o$ only. The variation in ϵ_λ due to the anisotropy is caused only by the variation in the *p* wave directional spectral emissivity $\epsilon'_{p,\lambda}(\theta)$. For a weakly absorbing semi-infinite medium, where the extinction coefficients are small but large enough such that the semi-infinite medium can be regarded as opaque, $\epsilon'_{p,\lambda}(\theta)$ increases with θ to near unity at the Brewster angle after which it decreases to zero at $\theta = 90$ deg. Similarly, for an absorbing medium, $\epsilon'_{p,\lambda}(\theta)$ passes through a maximum at a particular emission angle, referred to as a pseudo-Brewster angle (Klein and Furtak, 1986). At the pseudo-Brewster angle, $\rho'_{p,\lambda}(\theta)$ is minimized and, thus, $\epsilon'_{p,\lambda}(\theta)$ is maximized. The degree of anisotropy influences the pseudo-Brewster angle and magnitude of the maximum $\epsilon'_{p,\lambda}(\theta)$. Equation (24), which determines ϵ_λ from the integration of $\epsilon'_\lambda(\theta)$, contains the term $\sin 2\theta$ that is largest at $\theta = 45$ deg. Thus, ϵ_λ depends on the emission angle θ of the maximum $\epsilon'_{p,\lambda}(\theta)$.

It is evident from Figs. 6(*a*) and 6(*b*) that the influence of anisotropy on the hemispherical emissivity is negligible when $\kappa_e/\kappa_o \geq 1$ for all values of n_e. The ordinary optical constants strongly influence the predicted $\epsilon'_\lambda(\theta)$ and ϵ_λ. In this range, the extinction coefficient of the medium is effectively increased. As a result, the maximum value of $\epsilon'_{p,\lambda}(\theta)$ decreases slightly. For Fig. 6(*a*), the pseudo-Brewster angle remains essentially the same as that for the isotropic case and ϵ_λ is, at most, 2 percent less than the isotropic value. For Fig. 6(*b*), the pseudo-Brewster angle is reduced slightly when $\kappa_e/\kappa_o \geq 1$. The contribution of the maximum $\epsilon'_{p,\lambda}(\theta)$ to ϵ_λ increases and ϵ_λ exceeds the isotropic case by approximately 0.5 percent. In general, when $\kappa_e \geq \kappa_o$, ϵ_λ deviates from the isotropic ϵ_λ with the same $\bar{n}_o$ by no more than 2 percent.

Figures 6(*a*) and 6(*b*) indicate that for $\kappa_e/\kappa_o < 1$ and $n_e < 2$, the anisotropy influences ϵ_λ. The influence is particularly strong when $\kappa_e < 1$. For this optical constant range, the extraordinary refractance angle χ_e increases with respect to the isotropic refractance angle for any θ. The *c* axis component of the extraordinary electric field vector $\bar{\mathbf{e}}$ increases and, thus, the influence of anisotropy is strong. The anisotropic ϵ_λ varies from the isotropic ϵ_λ with the same $\bar{n}_o$ by as much as 35 percent.

Figure 7 illustrates the variation in $\epsilon'_{p,\lambda}(\theta)$ between a (001) medium in which $n_e = 1$ and $\kappa_e/\kappa_o = 0.125$ and a medium that is isotropic in $\bar{n}_o$ for the two $\bar{n}_o$ values from Fig. 6. In general, when $\kappa_e/\kappa_o < 1$ and $n_e < 2$, the pseudo-Brewster angle shifts to a larger θ and the maximum $\epsilon'_{p,\lambda}(\theta)$ changes with respect to the isotropic maximum. For $1 < \kappa_e < \kappa_o$, the change in $\epsilon'_{p,\lambda}(\theta)$ is relatively small. For $\bar{n}_o = 1 + i4$, Fig. 7 shows that the anisotropic $\epsilon'_{p,\lambda}(\theta)$ exceeds the isotropic value for all θ and the maximum increases sharply, causing the anisotropic ϵ_λ to exceed the isotropic value. When κ_e approaches zero, the peak narrows and the maximum $\epsilon'_{p,\lambda}(\theta)$ emission angle approaches 90 deg, resulting in the isotropic ϵ_λ exceeding the anisotropic value. This is evident in Fig. 7 for $\bar{n}_o = 3 + i0.5$ where a significant shift in the pseudo-Brewster angle peak is observed in the anisotropic material. Figure 6(*b*) shows that the isotropic ϵ_λ is greater than the anisotropic value for small values of κ_e.

Figures 6(*a*) and 6(*b*) show that the influence of anisotropy decreases for $n_e > 2$ and ϵ_λ is within 10 percent of the isotropic result for any κ_e/κ_o ratio. When n_e increases from unity, the maximum χ_e decreases for all κ_e/κ_o ratios. As a result, $\bar{\mathbf{e}}$ becomes increasingly aligned with the *ab* plane. Hence, $\epsilon'_{p,\lambda}(\theta)$ and ϵ_λ depend strongly on the ordinary optical constants. Increasing n_e from unity causes the variation between the anisotropic and isotropic pseudo-Brewster angle and maximum $\epsilon'_{p,\lambda}(\theta)$ to decrease rapidly. As a result, the variation between the isotropic and anisotropic ϵ_λ decreases.

The behavior of ϵ_λ and $\epsilon'_{p,\lambda}(\theta)$ exhibited in Figs. 6 and 7 holds for all values of $\bar{n}_o$ except where $n_o < 1$ and $\kappa_o < 0.25$. When

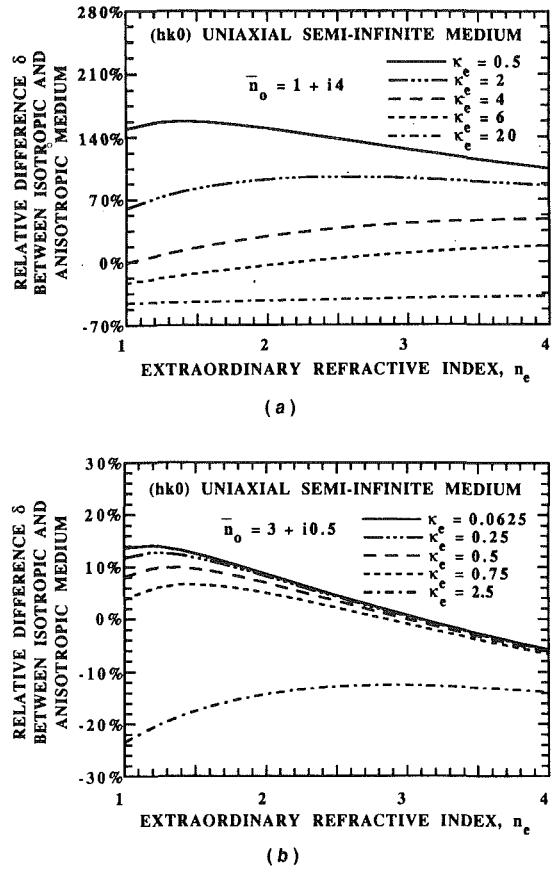

Fig. 8 Relative difference between the hemispherical spectral emissivity in vacuum of an (*hk*0) uniaxial semi-infinite medium and an isotropic medium possessing the ordinary optical constants of the uniaxial medium: (*a*) $\bar{n}_o = 1 + i4$; (*b*) $\bar{n}_o = 3 + i0.5$

$n_o < 1$ and $\kappa_o < 0.25$, the deviation of ϵ_λ from the isotropic value is greater than 10 percent for any value of $\bar{n}_e$. For weakly absorbing isotropic materials possessing a refractive index that is less than unity, a fraction of the energy incident from the surrounding medium undergoes total internal reflection. This dramatically reduces ϵ_λ as the amount of incident energy absorbed by the medium is reduced. An optical anisotropy strongly reduces the fraction of the incident energy that undergoes total internal reflection and, thus, there is a large difference between the isotropic and anisotropic ϵ_λ. When the extinction coefficient of an isotropic medium is increased from zero, total internal reflection no longer occurs. In the limiting case where n_o approaches zero, i.e., $n_o < 0.1$, the ordinary complex refractive index has an almost purely imaginary value and ϵ_λ for a medium that is isotropic in $\bar{n}_o$ goes to zero for any value of κ_o greater than zero. The influence of anisotropy is strong in the limiting case, except when n_e also approaches zero. For $0.1 < n_o < 1$ and $\kappa_o > 0.25$, total internal reflection does not occur and $\epsilon'_{p,\lambda}(\theta)$ and ϵ_λ behave in the same manner as Figs. 6 and 7.

Figures 8(*a*) and 8(*b*) show the relative difference between the predicted ϵ_λ in vacuum for a uniaxial medium with an (*hk*0) crystallographic orientation and an isotropic medium with the ordinary optical constants.

The influence of anisotropy on the radiative properties for the (*hk*0) orientation is considerable. Figures 8(*a*) and 8(*b*) show that there is no region of extraordinary optical constant values in which ϵ_λ may be accurately approximated by ϵ_λ for an isotropic medium with the ordinary optical constants. The (*hk*0) ϵ_λ may be accurately approximated, however, by the arithmetic average of ϵ_λ predicted for an isotropic medium with the ordinary optical constants, i.e., isotropic in $\bar{n}_o$, and with the extraordinary optical constants, i.e., isotropic in $\bar{n}_e$. The error introduced by this approximation is less than 5 percent for all optical constant values considered in Figs. 8(*a*) and 8(*b*).

For an (*hk*0) medium, optical anisotropy, in general, affects both the *s* and *p* wave directional spectral emissivities. For particular circumferential angles, the emitted *s* and *p* waves are uncoupled. Electromagnetic waves whose plane of emission, i.e., the plane containing the emission direction and the surface normal, is perpendicular to the optic axis, $\varphi = 0$ deg or $\varphi = 180$ deg, generate *s* wave directional spectral emissivities that are a function of $\bar{n}_e$ only and *p* wave directional spectral emissivities that are a function of $\bar{n}_o$ only. Waves whose plane of emission is parallel to the optic axis, $\varphi = 90$ deg or $\varphi = 270$ deg, generate *s* wave directional spectral emissivities that are a function of $\bar{n}_o$ only. For all other φ, $\epsilon'_{s,\lambda}(\theta, \varphi)$ and $\epsilon'_{p,\lambda}(\theta, \varphi)$ will be influenced by both $\bar{n}_o$ and $\bar{n}_e$.

Conclusions

1 The measured results for the directional-hemispherical reflectivity are in good agreement with that predicted from electromagnetic theory for the (001) and (110) crystallographic axis orientations of the tetragonal crystal rutile.

2 The directional spectral emissivity and the hemispherical spectral emissivity of a general uniaxial medium with a (001) orientation behave as follows, where n_o and n_e are the ordinary and extraordinary refractive indices, and κ_o and κ_e are the ordinary and extraordinary extinction coefficients, as summarized in Table 3:

(*a*) For $n_o < 1$ and $\kappa_o < 0.25$, the anisotropy considerably influences both radiative properties for all values of n_e, and κ_e. The deviation of ϵ_λ from a medium that is isotropic in $\bar{n}_o$ is greater than 10 percent.

(*b*) When $0.1 < n_o < 1$ and $\kappa_o > 0.25$ or when $n_o \geq 1$, the following conditions apply:

(*i*) For $\kappa_e \geq \kappa_o$, there is almost no difference between the anisotropic medium and isotropic medium with the same $\bar{n}_o$ regardless of the value of n_o, κ_o, n_e, and κ_e. The deviation in ϵ_λ is less than 2 percent.

(*ii*) For $\kappa_e < \kappa_o$, both emissivities deviate largely from the isotropic result for values of $n_e < 2$, i.e., ϵ_λ deviates by as much as 35 percent. For $n_e > 2$, the deviation in ϵ_λ is reduced to less than 10 percent.

3 Optical anisotropy strongly influences the directional spectral emissivity and the hemispherical spectral emissivity of a uniaxial medium with an (*hk*0) orientation. A good approximation for ϵ_λ is obtained from the arithmetic average of ϵ_λ calculated for an isotropic medium with the ordinary and with the extraordinary optical constants.

4 The results from this study will aid in the design of optoelectronic devices, such as multiple quantum well lasers, polarizers, and waveguides.

5 To determine precisely the directional emissivity of epitaxial high-T_c superconducting films, the *c* axis optical constants of these materials must be measured. The feasibility of ultrahigh far-infrared reflectance coatings depends on these parameters.

Acknowledgments

This work was supported by the National Science Foundation, grant No. CTS-9007765. C. G. M. acknowledges the support of the Natural Sciences and Engineering Research Council of Canada through a Postgraduate Scholarship. The cooperation of Z. M. Zhang in conducting the FT-IR reflectance measurements is appreciated.

References

Baltes, H. P., 1976, "On the Validity of Kirchhoff's Law of Heat Radiation for a Body in a Nonequilibrium Environment," *Prog. Opt.*, Vol. 13, pp. 1–25.

Bohren, C. F., and Huffman, D. R., 1983, *Absorption and Scattering of Light by Small Particles*, Wiley, New York, Chap. 9.

Born, M., and Wolf, E., 1980, *Principles of Optics*, 6th ed. (with corrections), Pergamon Press, Oxford, United Kingdom, Chap. 14.

Flik, M. I., Choi, B. I., Anderson, A. C., and Westerheim, A. C., 1992, "Thermal Analysis and Control for Sputtering Deposition of High-T_c Superconducting Films," ASME JOURNAL OF HEAT TRANSFER, Vol. 114, pp. 255–263.

Gervais, F., and Piriou, B., 1974, "Temperature Dependence of Transverse- and Longitudinal-Optic Modes in TiO_2," *Phys. Rev. B*, Vol. 10, pp. 1642–1654.

Hering, R. G., and Smith, T. F., 1968, "Surface Radiation Properties From Electromagnetic Theory," *Int. J. Heat Mass Transfer*, Vol. 11, pp. 1567–1571.

Ketelaar, J. A. A., and Haas, C., 1956, "Infrared Emission Spectrum of Calcite," *Physica*, Vol. 22, pp. 1283–1285.

Klein, M. V., and Furtak, T. E., 1986, *Optics*, 2nd ed., Wiley, New York, Chap. 9.

Lynch, D. W., and Hunter, W. R., 1985, "Comments on the Optical Constants of Metals and an Introduction to the Data for Several Metals," in: *Handbook of Optical Constants of Solids*, E. D. Palik, ed., Academic Press, Orlando, FL, pp. 275–367.

Ramachandran, G. N., and Ramaseshan, S., 1961, "Crystal Optics," in: *Handbuch der Physik*, Vol. 25/1, S. Flügge, ed., Springer-Verlag, Berlin, pp. 1–217.

Renk, K. F., Betz, J., Schützmann, J., Prückel, A., Brunner, B., and Lengfellner, H., 1990, "Use of High T_c Superconductors for Far-Infrared Fabry-Perot Resonators," *Appl. Phys. Lett.*, Vol. 57, pp. 2148–2149.

Sandus, O., 1965, "A Review of Emission Polarization," *Appl. Opt.*, Vol. 4, pp. 1634–1642.

Siegel, R., and Howell, J. R., 1981, *Thermal Radiation Heat Transfer*, 2nd ed., Hemisphere Publishing Corp., New York, Chaps. 3–5.

Spitzer, W. G., Miller, R. G., Kleinman, D. A., and Howarth, L. E., 1962, "Far Infrared Dielectric Dispersion in $BaTiO_2$, $SrTiO_3$, and TiO_2," *Phys. Rev.*, Vol. 126, pp. 1710–1721.

Timusk, T., and Tanner, D. B., 1989, "Infrared Properties of High-T_c Superconductors," in: *The Physical Properties of High-Temperature Superconductors I*, D. M. Ginsberg, ed., World Scientific Publishing Company, Singapore, pp. 389–407.

Yeh, P., 1979, "Electromagnetic Propagation in Birefringent Layered Media," *J. Opt. Soc. Am.*, Vol. 69, pp. 742–756.

Yeh, P., 1988, *Optical Waves in Layered Media*, Wiley, New York, Chap. 9.

Zeller, A. F., 1990, "High-T_c Superconductors as Thermal Radiation Shields," *Cryogenics*, Vol. 30, pp. 545–546.

Zhang, Z. M., Choi, B. I., Le, T. A., Flik, M. I., Siegal, M. P., and Phillips,, J. M., 1992, "Infrared Refractive Index of Thin $YBa_2Cu_3O_7$ Superconducting Films," ASME JOURNAL OF HEAT TRANSFER, Vol. 114, pp. 644–652.

Microscale Heat and Mass Transfer of Vascular and Intracellular Freezing in the Liver

J. C. Bischof
Massachusetts General Hospital,
Surgical Research Labs,
Charlestown, MA 02129

B. Rubinsky
University of California at Berkeley,
Department of Mechanical Engineering,
Berkeley, CA 94720

A set of heat and mass transfer equations is developed to predict vascular as well as intracellular ice formation during freezing in liver tissue. A modified Krogh unit with vascular and cellular compartments is used. In the model intracellular ice formation is predicted by a probability integral with functional dependence on cell compartment volume, temperature, and time. Finite difference computer simulations qualitatively predict the amount and location of vascular and intracellular ice, the temperature distribution in the tissue, and the position of the partial and total freezing interfaces at any time.

Introduction

Freezing is used extensively in medicine for both the destruction and preservation of biological tissue. These techniques are called cryosurgery and cryopreservation, respectively. The consequences of freezing, either destruction or preservation, are dependent on how and where ice forms. To control the results of a freezing protocol, it is important to have not only precise experimental information but also adequate mathematical models to predict the heat and mass transfer processes that occur during freezing. Mazur (1963) was the first to present theoretical work on the heat and mass transfer from individual cells at subfreezing temperatures. Many other investigators have followed his work. Most recently Toner et al. (1990) developed a model that predicts intracellular ice formation of individual cells under different freezing conditions. The present study couples cellular and vascular heat and mass transfer processes at the microscale level to predict freezing in the whole liver.

Other investigators have attempted to model freezing of whole tissues. The first analytical studies of freezing in cryosurgery were performed by Cooper and Trezek (1970, 1971, 1972). These studies helped predict the rate of the freezing interface growth around a surgical cryoprobe, and the associated temperature field. These studies were followed by that of Comini and del Guidice (1976) who attempted to predict the freezing behavior of a brain tumor with a finite element model. Rubinsky and Schitzer (1976) performed an analysis of a Stefan-like problem of phase change in tissue around a cryosurgical probe. They investigated the effects of blood perfusion and metabolic heat generation on the solution. Rubinsky and Cravalho (1984) developed a one-dimensional finite element model to predict cooling within organs during actual cryopreservation protocols. They were successful in developing a graphic scheme for prediction of the cooling rates at different locations and temperatures within the tissue for a given constant cooling rate on the boundary. Budman et al. (1986) described the temperature field around an embedded cryoprobe by both finite element and analytical methods. Bischof et al. (1992) presented an analytical study of temperature history and freezing interface location in freezing of tumorous lung during a cryosurgical protocol.

Most of the models of tissue freezing assume homogeneous thermal properties and no differentiation between cellular and extracellular space is made. Furthermore, no mass transfer during freezing between cells and vasculature is accounted for. However, the results of the experiments by Trump et al. (1964), Love (1966), and Rubinsky et al. (1987, 1990), on freezing of rat and mouse livers, demonstrate that mass transfer has a profound effect on the freezing process, and therefore must be accounted for to model freezing in liver tissue accurately.

Diller and Raymond (1990) used network thermodynamics to model mass transfer through a multicellular tissue during freezing. They show a differential osmotic response due to the spatial distribution of cells in a tissue. In particular an increase in the dehydration of surface cells directly in contact with extracellular ice, as compared to cells embedded in the interior of the tissue, is noted. This model is useful in determining the freezing response of tissues such as pancreatic islets. However, in the liver, extracellular or vascular ice forms directly outside of the hepatocytes so that all cells will respond as surface cells rather than showing the lag in dehydration associated with embedment in the tissue.

Recently a set of equations that describe the process of slow freezing in liver tissue incorporating the mass transfer between cells and the vasculature has been developed (Rubinsky and Pegg, 1988; Rubinsky, 1989). However, this work did not address the rapid freezing of liver tissue and the consequent intracellular nucleation. The purpose of this work is to expand the earlier coupled heat and mass transfer model of Rubinsky (1989) by modeling the vascular as well as the intracellular freezing in the liver by including the probability for intracellular ice formation in our calculations. The derived energy equations are then implemented on a computer using an Euler forward finite difference discretization and are used to study freezing in a semi-infinite domain. The numerical results are presented and qualitatively compared to previous experimental results from low temperature scanning electron microscopy (cryo-sem) work on the rat liver.

Analysis

The mathematical model in this study attempts to simulate the physical events observed in experiments with controlled freezing of the liver (Rubinsky et al., 1987, 1990). To make the model easier to understand, we will summarize the physical events we try to model.

The experiments suggest that ice forms first in the extracellular space, which in the liver is comprised of sinusoids. The ice propagates through the vasculature (sinusoids) in the general direction of the temperature gradients. As ice forms, solute is rejected, and the extracellular space becomes hypertonic. Water starts leaving the cells (hepatocytes) to freeze in the extracellular space. The water in the cells is supercooled. If

Contributed by the Heat Transfer Division and presented at the ASME Winter Annual Meeting, Anaheim, California, November 8–13, 1992. Manuscript received by the Heat Transfer Division July 1992; revision received January 1993. Keywords: Biotechnology, Cryogenics, Phase-Change Phenomena. Technical Editor: R. Viskanta.

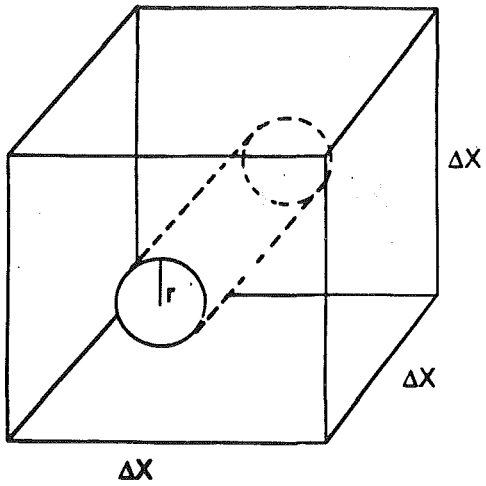

Fig. 1 Schematic drawing of the Krogh unit, the control volume for this analysis

the probability for intracellular ice formation is high enough, the water will freeze intracellularly. Otherwise the hepatocytes will dehydrate completely and the water will freeze extracellularly.

The equations modeling the process of freezing described above follow the work of Rubinsky (1989) and Rubinsky and Pegg (1988). The liver is represented by a large number of identical tissue/vascular structural units known as Krogh units (Krogh, 1919), and the governing equations are derived for an individual Krogh unit. A typical Krogh unit consists of a sinusoid (vascular space) surrounded by hepatocytes (cellular space) as shown in Fig. 1.

In order to model the freezing in the liver effectively, several assumptions and arguments were made. In the liver, water can travel from hepatocytes through fenestrations in the basement membrane of the blood vessel or through the endothelial cells, but we assume that the permeability to water of the interface between the blood vessel and the cells is dominated by the permeability of the hepatocytes, and that the interstitial tissue volume is negligible (Rubinsky and Pegg, 1988). In the mass transfer model it will be assumed that the water transfer occurs only across the boundary between the blood vessel lumen and the hepatocytes and not between adjacent cellular units or by diffusion along the vascular system, which is justified if the temperature difference between adjacent units is not large. The solute concentration in the extracellular space and in the intracellular space will be assumed uniform throughout the Krogh unit, and all the chemical species will be assumed to participate in this one lumped concentration.

The equations used in this model have been derived and presented before by Rubinsky (1989). The equations pertinent to this study are listed below as mass transfer and heat transfer equations.

Mass Transfer Equations. Fick's law predicts a volumetric flow of water from the cells into the extracellular space driven by the concentration difference between the vascular and cellular compartments during freezing:

$$j_v = p(C_v - C_c) \tag{1}$$

The geometry of the Krogh model, Fig. 1, defines the following quantities:

$$V = (\Delta x)^3$$
$$V_c = V - \pi r^2 \Delta x$$
$$S_v = 2\pi r \Delta x$$
$$r(x, 0) = r_o \quad \text{and} \quad r_{\max} = \left[\frac{\Delta x^3 - V_{ns})}{\pi \Delta x}\right]^{1/2} \tag{2}$$

These geometric constraints of the model allow the flux Eq. (1) to be written as:

$$j_v = (1/S_v) dV_c/dt = -dr(x, t)/dt \tag{3}$$

The concentration of the vascular and cellular compartments can be written as:

$$C_v = \frac{T_{phw} - T(x, t)}{1.86\,\sigma\,\nu}$$
$$C_c = C_{co}\frac{V_{co} - V_{ns}}{V_c(x, t) - V_{ns}} \tag{4}$$

which allows the cellular compartment volume change to be written as:

$$\frac{dV(x, t)}{dt} = pS_v\left[\frac{T(x, t) - T_{phw}}{1.86\,\sigma\,\nu} + C_{co}\frac{V_{co} - V_{ns}}{V_c(x, t) - V_{ns}}\right] \tag{5}$$

This leads to an equation describing the change of the radius of the vascular compartment, or Krogh cylinder, as a function of time and position from the cooling boundary.

Nomenclature

A = cross-sectional area, m^2
C = molar concentration, mole
c = specific heat, J/kg K
Fo = Fourier number
H = cooling rate, K/min
I = crystal nucleation frequency, number of nuclei/volume/s
j = volumetric flux, m/s
k = thermal conductivity, W/m K
L = latent heat of fusion, J/kg
m = molar concentration, mole
n = normal direction, m
N = Avogadro's number, number of particles/mole
p = permeability constant, m/s mole
P = probability of nucleation
q = heat flux = energy, W
r = radius of blood vessel in Krogh unit, m
R = gas constant, cal/mole K
S = surface area of blood vessel/Krogh unit, m^2
s = phase-change interface, m
T = temperature, K
t = time, s
V = volume, m^3
x = Krogh dimension, Cartesian coordinate, and direction of freezing, m
y = Cartesian coordinate, m
z = Cartesian coordinate, m
Δ = change/difference
Δt = time step in numerical formulation, s
Δx = grid size, m
α = constant in nucleation theory
β = constant in nucleation theory
η = viscosity, N s/m^2
σ = osmotic coefficient
ν = ionic dissociation coefficient
ρ = density, kg/m^3
ϕ = liquid-crystal interfacial tension, N/m

Subscripts

c = cellular compartment
f = frozen
i = ice
j = u or f
max = maximum
ns = nonsolvent
o = initial conditions
ph = phase transformation
u = unfrozen
v = vascular compartment
w = water

Table 1 Geometric, thermal, and mass transfer properties of the liver

Geometrical Data:	$r_o = 4.5\ \mu m$	$\Delta x = 22.0\ \mu m$	$V_{ns} = 0.3\ V_o$
Heat Transfer Data:	c (J/kg K)	k (W/m K)	ρ (kg/m³)
Water	4230	0.552	998.0
Ice	1230	2.25	921.0
Latent Heat L = 335,000 (J/kg)			
Mass Transfer Data:	$C_{vo} = 0.154$ (moles)	$p = 5 \times 10^{-7}$ (m/mole s)	
	$\sigma = 1$	$\upsilon = 2$	

$$\frac{dr(x,t)}{dt} = -p\left[\frac{T(x,t) - T_{phw}}{1.86\,\sigma\,\nu} + C_{co}\frac{(\Delta x)^3 - V_{ns} - \pi r_o^2 \Delta x}{(\Delta x)^3 - V_{ns} - \pi r(t)^2 \Delta x}\right] \quad (6)$$

Heat Transfer Equations. As in all derivations of the energy equation, an appropriate control volume must be selected to balance heat and mass transfer on. The control volume must have dimensions that ensure that thermodynamic properties are constant throughout it. Usually, this means that the control volume is arbitrarily or infinitesimally small. However, since liver tissue is nonhomogeneous, containing vascular and cellular spaces, the control volume must also have characteristic dimensions, which reflect the actual structure of the biological system. The natural choice of the control volume for the physical dimensions of the tissue is one Krogh unit, see Fig. 1 and Table 1. From scanning electron micrographs of normal rat liver (Motta et al., 1978), it was determined that the average distance between the middle of adjacent sinusoids was 22 μm, and the radius of the sinusoid was determined on average as 4.6 μm.

The problem here is that since the control volume is of finite dimensions, the differential form of the energy equation has limited resolution. The differential ∂x will equal the Δx of the Krogh unit, instead of being infinitesimal. This assumption is admissible if the thermal gradients are small relative to the Krogh dimensions. Thus, although the dimensions of the control volume limit the spatial resolution of the solution, continuity of the macroscopic thermodynamic properties of the tissue is ensured, and the differential form of the energy equation can be derived from the Krogh unit.

The complete energy equation derived for the Krogh unit control volume (Fig. 1) during freezing is:

$$\nabla(k\,\nabla T)\Delta x^3 - \rho c(\Delta x^3)\frac{\partial T}{\partial t} - \rho L j_v S_v \quad (7)$$

Since j_v and S_v have been defined in Eqs. (2) and (3), the energy equation can be written as:

$$\nabla(k\,\nabla T) = \rho c\frac{\partial T}{\partial t} - \frac{2\pi r \rho L}{\Delta x^2}\frac{dr}{dt} \quad (8)$$

The thermal properties in the unfrozen region are assumed to be those of water and in the frozen region the properties are assumed to be those of ice. However, in the partially frozen or mushy region where the mass transfer is taking place, the thermal properties are a function of the amount of ice and water present, which is in turn dependent on the size of the blood vessel radius.

$$k(r(x,t)) = \frac{((\Delta x^3) - \pi r(x,t)^2 \Delta x)k_w + \pi r(x,t)^2 k_i \Delta x}{\Delta x^3}$$
$$\rho c(r(x,t)) = \frac{((\Delta x^3) - \pi r(x,t)^2 \Delta x)\rho c_w + \pi r(x,t)^2 \rho c_i \Delta x}{\Delta x^3} \quad (9)$$

The averaging of thermal properties in this manner is typical of modeling freezing in porous materials, and will limit the resolution of the solution to one Krogh cylinder (Lunardini, 1981). To complete the formulation of the problem, the energy equation for the unfrozen and frozen regions is given as:

$$k_j\frac{\partial^2 T_j}{\partial x^2} = \rho c_j\frac{\partial T_j}{\partial t};\quad j = u \text{ or } f \quad (10)$$

where the unfrozen and frozen properties are those of water and ice respectively; see Table 1.

Intracellular Ice Formation. Equations (1)–(10) completely describe the process of freezing in the liver when no intracellular ice forms. The formation of intracellular ice has not been addressed in any of the previous models for freezing of tissue we have developed; therefore we wish to add this to the model here. A mathematical formulation was developed that evaluates the probability for intracellular ice formation. In supercooled water there are always fluctuations in structure, which give rise to rapid microscopic variations in such quantities as density, temperature, and pressure. These fluctuations are caused by the continual formation and disintegration of small embryos or nuclei of ice within the liquid phase. However, if an ice embryo larger than a certain critical size should form, it might be thermodynamically advantageous for it to continue to increase in size; in this case it would grow into a microscopic ice crystal (Barret et al., 1973). Turnbull has shown this to be a function of supercooling of the solution (Turnbull, 1969). To determine the intracellular supercooling ΔT, during the freezing of tissue, we can use the following equation (Rubinsky, 1989):

$$\Delta T = T_{phw} - T(x,t) - 1.86\,\sigma\nu\,C_v(x,t) \quad (11)$$

The intracellular supercooling ΔT can now be used to evaluate the probability for intracellular freezing. Several models are available to calculate the probability for intracellular ice formation. The most recent and probably the most accurate model of ice formation in single cells is based on heterogeneous nucleation theory (Toner et al., 1990). Turnbull has also derived an expression for the probability of homogeneous nucleation in a solution (Turnbull, 1969). Since there is no direct evidence of heterogeneous nucleation of ice in the cells of whole tissues, and since the approach taken here is generally valid regardless of the nucleation model used, we have chosen to work with the expression for homogeneous nucleation derived by Turnbull. The resistance of a liquid to nucleation, as measured by the undercooling necessary to overcome it, is much greater than its resistance to growth (Turnbull, 1969). Therefore, we will consider that if a nucleus forms, ice growth will also occur and fill the cell.

Turnbull presents an expression for homogeneous crystal nucleation frequency (Turnbull, 1969). It defines nucleation frequency, I, per volume, V, and time, t, as a function of viscosity, η, supercooling, $\Delta T = T_{ph} - T$, and temperature, T. The resulting equation is:

$$I(T) = \frac{k_\eta}{\eta(T)}\exp\left(\frac{-b\,\alpha^3\beta}{\frac{T}{T_{ph}}\left(\frac{\Delta T}{T_{ph}}\right)^2}\right) \quad (12)$$

$k\eta/\eta(T)$ is called the kinetic term, which accounts for the energy necessary for liquid atoms to diffuse to a critical nuclei, and $b\alpha^3\beta$ is the thermodynamic term because it represents an activation energy for the formation of a critical ice nucleus. The denominator of the exponent represents the driving force, or thermal energy available for the process (Toner et al., 1990; Barret et al., 1973). In Eq. (12), k_η is a dimensional constant specified by the model, b is a constant determined by the shape of the ice nucleus, and α and β are dimensionless parameters defined as follows:

Table 2 Constants and variables used in nucleation theory

Constants:	b = 16.755	
	$\alpha^3\beta = 0.4$	
	$k\eta = 10 \exp(22)$	$(N\,s/m^2)$
Variables:	$\eta(t) = 1800 + 891\,(273.15 - T(t))$	$(N\,s/m^2 \times 10^6)$

$$\alpha = \frac{(N\overline{V}^2)^{1/3}\phi}{\Delta H_m}, \quad \beta = \frac{\Delta H_m}{RT_m} \tag{13}$$

where N is Avogadro's number, ΔH_m is the molar heat of fusion, $\overline{V}$ is the molar volume of the crystal, R is the gas constant, and ϕ is the liquid-crystal interfacial tension (Turnbull, 1969). The values of the constants are taken from Coger et al. (1990) and are given in Table 2.

Integrating expression (13) over volume and time according to Holman and Gadja (1985) yields an expression for the probability of intracellular ice formation (Coger et al., 1990):

$$P(V(x, t), t) = \int_t \int_V I(T(x, t))\,dV\,dt \tag{14}$$

This integral has been evaluated for a case that is considered to be a high probability for intracellular ice formation. The integral was calculated for a fully hydrated tissue compartment of the Krogh unit, which is cooled to $-15°C$ from body temperature 37°C in 1 second. The result is a cooling rate over 3000°C/min, which according to Cosman et al. (1989), and according to experiments in rapidly frozen liver tissue (Rubinsky et al., 1987, 1990), consistently leads to intracellular ice formation. We have also found in experiments with liver tissue samples that this cooling rate consistently produces intracellular ice. By comparing the probability of intracellular ice formation in all the Krogh unit cellular spaces during partial freezing to this maximum probability we can determine whether intracellular ice formation should occur in a particular unit.

Boundary Conditions. To illustrate the thermophysical phenomena that occur during freezing of tissue and the technique of solving these problems, Eqs. (1)–(14) have been applied to the problem of freezing in a semi-infinite one-dimensional domain of liver tissue, depicted in Fig. 2. The following boundary and initial conditions are used. The tissue is originally at body temperature, 37°C.

$$T(x, 0) = 310\ \text{K} \tag{15}$$

The boundary of the tissue is exposed to either a constant cooling rate:

$$T(0, t) = 273\ \text{K} - H \cdot t \tag{16}$$

or a constant-temperature boundary condition, which, to model cryosurgery, is chosen to be that of liquid nitrogen:

$$T(0, t) = 77\ \text{K} \tag{17}$$

After freezing has begun in the tissue, boundary conditions between the unfrozen, partially frozen, and completely frozen regions in the tissue are necessary. The three regions are depicted schematically in Fig. 3. Between the unfrozen and partially frozen regions, the boundary condition is the initial freezing of the water in the blood vessel:

$$k(r)\frac{\partial T}{\partial x} - k_u \frac{\partial T}{\partial x} = \rho L \frac{\pi r_o^2}{(\Delta x)^2}\frac{\partial s}{\partial t} \quad \text{on } s(t) \quad \text{and} \quad T(s(t)) = T_{ph} \tag{18}$$

The propagation of an interface, s, between the unfrozen and mushy (partially frozen) regions is a function of the latent heat constraints on the volume of the node s, and the heat that passes through the node. The model first determines when a node has reached phase-change temperature, T_{ph}. We then

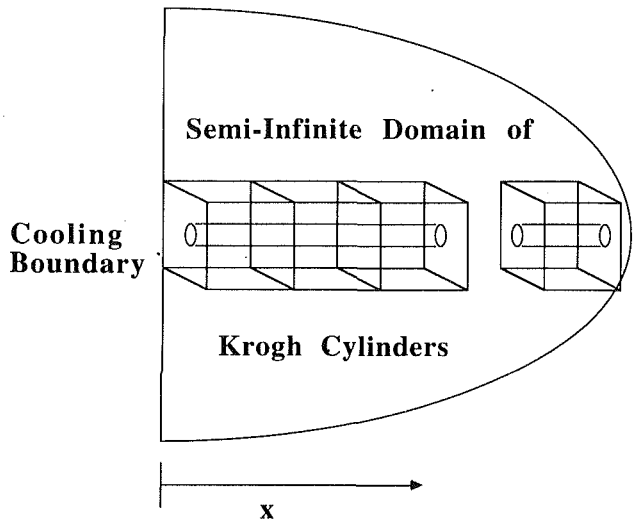

Fig. 2 Freezing configuration of semi-infinite tissue domain composed of Krogh units. Tissue is cooled from the boundary; freezing propagates in the x direction.

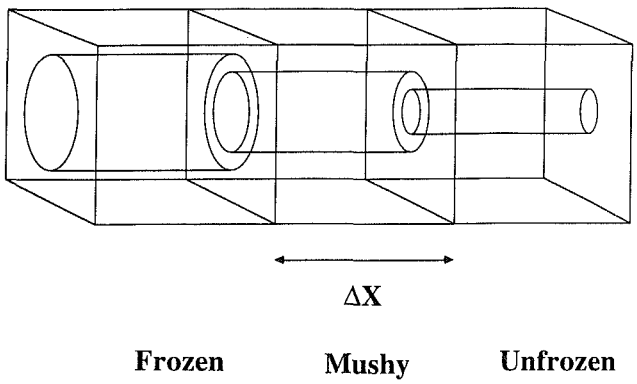

Fig. 3 Schematic of three regions during freezing: unfrozen, mushy or partially frozen, and completely frozen. The respective geometries of the three regions are indicated with increasing blood vessel diameter.

assume that phase change occurs in the vasculature first. Therefore, the amount of water that originally changes phase is the cylinder within the Krogh unit that represents the minimum capillary volume ($\pi r_o^2\,\Delta x$). The energy passing through the Krogh unit in the form of heat is summed until enough energy has passed through the node to allow change of phase. The interface then moves on to the next node, $s+1$. A discussion of this energy-summing algorithm on the frozen interface is presented by Lunardini (1981). Once the plasma in the blood vessel has frozen, the tissue unit changes from an unfrozen to a partially frozen region. Freezing of the node continues as the water transported from the cellular compartment into the vascular compartment changes phase even after the interface node, s, has moved on.

The second interface boundary condition, between the partially frozen and completely frozen regions, can be either geometric or thermodynamic. The geometric condition is when all the unbound cellular water is transported into the vasculature, where it freezes, and the cylinder reaches a maximum radius, at which time the tissue is effectively all frozen. The thermodynamic condition is met when the probability for intracellular ice nucleation exceeds the control value, at which point all unfrozen water in the cells changes phase.

Finite Difference Solution. The equations of heat and mass transfer (6), (8), (9), (10) as well as that for intracellular ice formation (14) were discretized along with boundary and initial

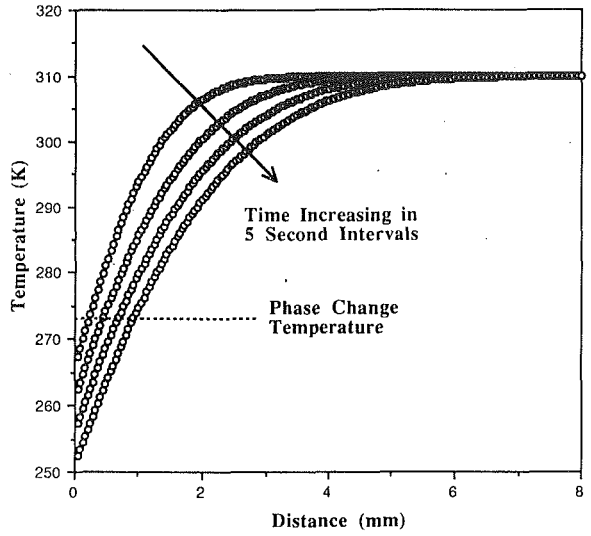

Fig. 4 Temperature profiles for tissue cooled at 60°C/min on the boundary

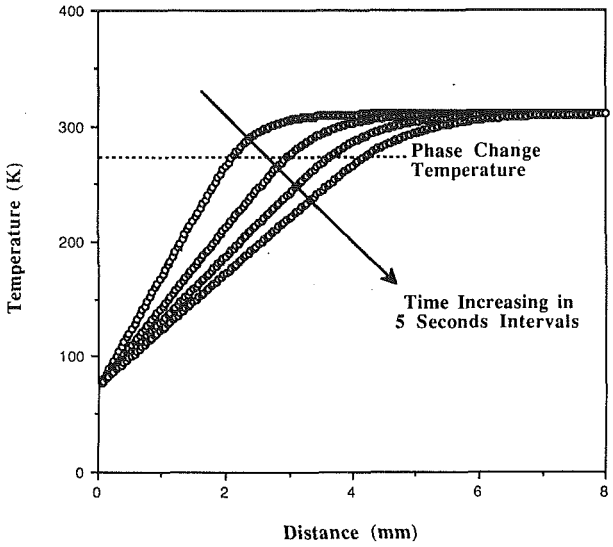

Fig. 6 Temperature profiles for tissue cooled by liquid nitrogen on the boundary

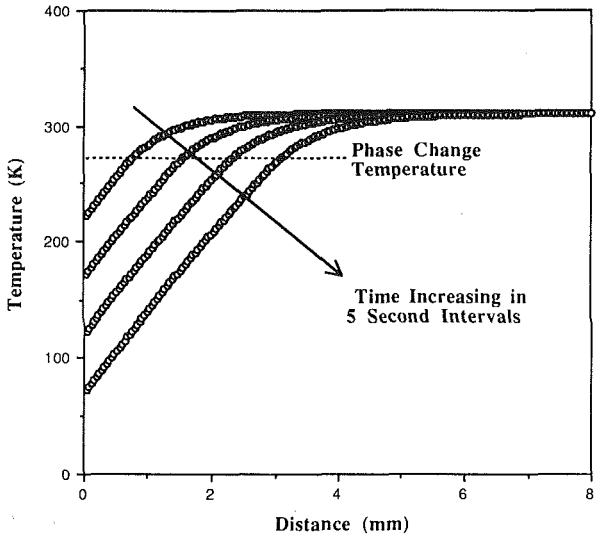

Fig. 5 Temperature profiles for tissue cooled at 600°C/min on the boundary

conditions (15)–(18) and solved using a one-dimensional finite difference Euler forward integration scheme. In order to insure convergence of the code, the time step was chosen in such a way to ensure that the Fourier number, $\mathrm{Fo} = [k(\Delta t)/\rho c(\Delta x)^2]$, in all regions including the mushy region did not exceed a value of 1/2. A sensitivity test was undertaken by successively halving the time step to ensure convergence of the code.

Comparison of our results to other phase-change solutions is hampered because other solutions do not include the effect of the mass transfer on phase change. With this limitation in mind the code was compared to the Stefan problem and to the plain conduction model (data not shown). The Stefan problem is an analytical solution to the propagation of the phase-change interface in a homogeneous medium where the liquid phase is originally at the change of phase temperature and then exposed on the boundary to a subphase change temperature. The plain conduction model assigns different thermal properties to the solid and liquid regions; however, no latent heat constraints are placed on the interface. The result of the comparison of our model to the Stefan model showed that the solid-liquid interface for the Stefan problem propagated slightly faster than the interface between the unfrozen/mushy region and significantly faster than the mushy/frozen region. This is to be expected since the mass transfer between the cellular and vascular compartments in our model should hold back the interface propagation. Furthermore, comparison to the plain conduction model showed that the solid/liquid interface with no latent heat constraints propagates significantly faster than the unfrozen/mushy or mushy/frozen interfaces of our model, where latent heat constraints exist. Therefore, accepting the limitations of these comparisons, our model is seen to give reasonable results.

Results

The numerical solution predicts the thermal history during freezing, the location of the partial and total freezing interfaces, and the amount of intracellular as well as vascular ice in the liver tissue. The thermal and physical properties used in the analysis are given in Table 1. The three regions of tissue—unfrozen, mushy or partially frozen, and completely frozen—are depicted schematically in Fig. 3. The regions are separated by two interfaces: the unfrozen/mushy interface separates unfrozen and partial freezing, and the mushy/frozen interface lies between partial freezing and completely frozen. The movement of the unfrozen/mushy interface is controlled by the freezing of the original dimensions of the vasculature and is expressed mathematically in boundary condition Eq. (18). The mushy/frozen interface is triggered by either a maximum vascular radius or the intracellular probability condition, which are both discussed in the boundary condition section.

Figure 4 depicts the temperature profiles for the liver when cooled at a constant rate of 60°C/min on the boundary. This corresponds to boundary condition (16) with $H = 1$°C/s. The x axis is the distance from the boundary into the tissue and the y axis is the temperature of the tissue in degrees Kelvin. The profiles are at 5 second intervals, and the phase-change temperature is shown on the graph for reference.

Figure 5 shows the temperature profiles in the liver when cooled at a constant rate of $H = 600$°C/min, or Eq. (16) with $H = 10$°C/s. The x axis is the distance from the boundary into the tissue and the y axis is the temperature of the tissue in degrees Kelvin. The profiles are at 5 second intervals, and the phase-change temperature is shown on the graph. The slopes are steeper than in the previous case, Fig. 4, indicating the faster rate of cooling applied here.

Figure 6 shows the temperature profiles for tissue exposed

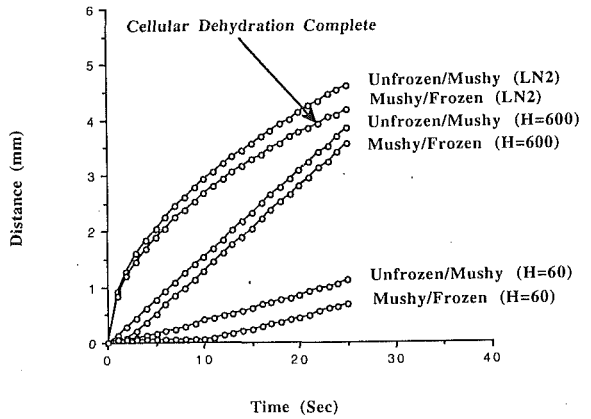

Fig. 7 Positions of unfrozen/mushy, and mushy/frozen interfaces as a function of time. Cases presented include cooling at 60°C/min, 600°C/min, and a constant liquid nitrogen cooling condition on the boundary. At 60°C/min all cells are completely dehydrated. At 600°C/min the tissue experiences some dehydration; however, all cells have intracellular ice. The liquid nitrogen cooling interfaces start with intracellular ice formation near the boundary, but dehydration proceeds until 4 mm into the tissue, cells become completely dehydrated as indicated

to a constant liquid nitrogen temperature boundary condition, Eq. (17). The profiles are separated by 5 second intervals and the phase-change temperature is marked for reference. The x axis is the location of the temperature profiles in the tissue in millimeters and the y axis is the temperature of the tissue in degrees Kelvin. The profile slopes start out steep; however, as time progresses, the profile slopes get shallower. The freezing rate is proportional to the thermal gradients, or slope of the temperature profiles; therefore the tissue nearest the boundary is exposed to the highest rates of freezing, and conversely the farther away from the boundary the tissue is located the slower is the cooling rate it experiences.

Figure 7 shows the interface position as a function of time for cooling on the boundary of the liver of 60°C/min, 600°C/min and for a liquid nitrogen cooled boundary. The x axis is the time in seconds since cooling began and the y axis is the distance the interface has progressed into the tissue. In all cases the unfrozen/mushy interface between the unfrozen and partially frozen regions is located farther into the tissue at any time than the mushy/frozen interface between the partially and totally frozen regions. At 60°C/min the cells are completely dehydrated. This means that at the time of complete solidification all the osmotically active cell water had been transported to the vasculature, leading to the maximum vascular radius. At 600°C/min there was uniform intracellular ice formation in the tissue. The fact that a distance between the partial and total freezing interfaces exists at any time, however, indicates that mass transfer is occurring, and therefore the cells are not totally hydrated when they change phase. These constraints translate into intracellular ice formation throughout the frozen area for the given cooling rate, 600°C/min.

For liquid nitrogen cooling on the boundary, the two interfaces unfrozen/mushy and mushy/frozen start together in Fig. 7. This indicates that freezing is originally so rapid that no partially frozen region forms. As expected the unfrozen/mushy interface progresses faster than the mushy/frozen interface. At any time, the difference in distance between the two interfaces is the physical extent of the partially frozen region. In this model mass transfer occurs only during freezing, and thus can only occur in the partially frozen region. It is not surprising, therefore, to notice that at a slower cooling rate away from the boundary, the partially frozen region is larger than near the liquid nitrogen cooled boundary. The extent of the partially frozen region is an indication of the mass transfer occurring; therefore, the farther away from the boundary one moves, the more mass transfer occurs. After sufficient mass transfer occurs, a certain point is reached where all the water has left the cells and resides in the vasculature. We monitored this with our program by tracking the size of the vascular radius and have indicated the point of total tissue dehydration on the figure at 4 mm into the tissue. Before this point the mushy/frozen interface, from partial to total freezing of the tissue, was exclusively triggered by the intracellular ice formation component of our code.

Discussion

The results show that slow freezing leads to extensive mass transfer into the vasculature leading to dehydration of the tissue and engorgement of the vasculature. In this case complete solidification of the mushy/frozen interface was triggered by the maximum vascular radius condition. Faster freezing on the other hand led to less dehydration of the tissue and more intracellular ice formation. In this case complete solidification of the mushy/frozen interface was triggered by the intracellular ice formation condition.

In Fig. 4, 60°C/min is the slowest rate of cooling investigated. The temperature profiles are shallow and the interfaces for this cooling rate, shown in Fig. 7, only reach approximately 0.5 mm into the tissue after twenty seconds of freezing. No intracellular ice forms in this case, and the distance between partial and total freezing interfaces at any time shows the region in the tissue experiencing mass transfer in response to freezing. Complete solidification was triggered by the maximum vascular radius condition.

For a cooling rate of 600°C/min, the temperature profile slopes, depicted in Fig. 5, are steeper than the previous case, Fig. 4. The partial and total freezing interfaces for 600°C/min, shown in Fig. 7, approach the 3 mm mark in the tissue after twenty seconds of freezing. Intracellular ice was predicted for tissue cooled at this rate; however, some mass transfer also occurred. As long as the partial and total freezing interfaces are separate, mass transfer will occur in the tissue. If the two interfaces are contiguous, then the tissue has no time to experience mass transfer, and the cell water is trapped entirely as intracellular ice. This is seen near the boundary of the liquid nitrogen cooled case discussed below.

The liquid nitrogen cooled tissue showed the fastest cooling of all cases near the boundary of the tissue. The temperature profiles in Fig. 6 show steep slopes from the constant temperature boundary of 77 K. The slopes get progressively shallower as time increases. The behavior of the slopes is different from the previous constant cooled cases since it is a constant temperature boundary condition. The partial and total freezing interfaces for this case, Fig. 7, show both intracellular ice near the boundary as well as total dehydration farther into the tissue. Near the boundary the partial and total freezing interfaces overlap, indicating that the freezing rate is so fast that mass transfer has no time to occur, trapping all cellular water as intracellular ice. The interfaces reach four millimeters in a twenty second time period, which is farther than any other case.

The model qualitatively predicts freezing behavior observed from a previous study of experimental cryosurgery on rat livers (Rubinsky et al., 1990). In the study, extensive intracellular ice was found in the tissue near the cooling boundary of the cryoprobe. Several millimeters away from the cooling boundary, however, large extracellular ice crystals indicated severe tissue dehydration and little intracellular ice. These results can be compared to the liquid nitrogen cooled interface results in Fig. 7 of this study. Near the cryoprobe or cooling boundary the partial and total freezing interfaces overlap, indicating that no mass transfer is occurring and therefore all the cell water solidifies intracellularly. Four millimeters into the tissue, however, our model predicts the complete dehydration of the tissue, which would correspond to all cell water being transported

into the vasculature thereby contributing to large extracellular ice crystals. Considering the simplifying assumptions used in this first-order model, it is encouraging that our results and the previous experiments are qualitatively comparable.

Conclusion

A mathematical model for freezing in the liver has been developed. This model is based on the mechanism of freezing in the liver from experimental evidence discussed earlier. The mechanism of freezing in the liver is such that freezing propagates first through the vasculature of the organ. The rejected solute in the vasculature increases the effective concentration of the vasculature setting up an osmotic gradient between it and the supercooled cells. This osmotic gradient then drives water out of the cells into the vasculature, where it freezes. Equations to model this mass transfer were developed and coupled to the energy equation.

The model is capable of qualitatively predicting the thermal history of the tissue, the location of the total and partial freezing interfaces, the amount and extent of intracellular ice formation, and dehydration of the tissue under arbitrary cooling conditions. This model represents progress toward the effective and accurate modeling of the freezing of biological tissue.

Acknowledgments

The authors gratefully acknowledge support by the Whitaker foundation. J.B. was also supported in part by an NIH traineeship grant.

References

Barret, C. R, Nix, W. D., and Tetelman, A. S., 1973, *The Principles of Engineering Materials*, Chap. 5, Prentice-Hall Co., Englewood Cliffs, NJ.

Bischof, J. C., Bastacky, J., and Rubinsky, B., 1992, "An Analytical Study of Cryosurgery in Lung," ASME *Journal of Biomechanical Engineering*, Vol. 114, pp. 467–472.

Budman, H., Schitzer, A., and Del Guidice, S., 1986, "Investigation of Temperature Fields Around Embedded Cryoprobes," ASME *Journal of Biomechanical Engineering*, Vol. 108, pp. 42–48.

Coger, R., Rubinsky, B., and Pegg, D. E., 1990, "Dependence of Probability of Vitrification on Time and Volume," *Cryo-Letters*, Vol. 11, No. 5, pp. 359–372.

Comini, G., and del Guidice, S., 1976, "Thermal Aspects of Cryosurgery," ASME JOURNAL OF HEAT TRANSFER, Vol. 98, pp. 543–549.

Cooper, T. E., and Trezek, G. J., 1970, "Analytical Prediction of the Temperature Field Emanating From a Cryogenic Surgical Cannula," *Cryobiology*, Vol. 7, pp. 71–90.

Cooper, T. E., and Trezek, G. J., 1971, "Rate of Lesion Growth Around Spherical and Cylindrical Cryoprobes," *Cryobiology*, Vol. 7, pp. 183–190.

Cooper, T. E., and Trezek, G. J., 1972, "On the Freezing of Tissue," ASME JOURNAL OF HEAT TRANSFER, Vol. 94, pp. 251–253.

Cosman, M. D., Toner, M., Kandel, J., and Cravalho, E. G., 1989, "An Integrated Cryomicroscopy System," *Cryo-Letters*, Vol. 10, pp. 17–38.

Diller, K. R., and Raymond, J. F., 1990, "Water Transport Through a Multicellular Tissue During Freezing: A Network Thermodynamic Modeling Analysis," *Cryo-Letters*, Vol. 11, pp. 151–162.

Holman, J., and Gadja, W., 1985, *Experimental Methods for Engineers*, Wiley, p. 213.

Krogh, A., 1919, "The Number and Distribution of Capillaries in Muscles With Calculation of Oxygen Pressure Heat Necessary for Supplying the Tissue," *J. Physiol.*, Vol. 52, p. 409.

Lunardini, V. J., 1981, *Heat Transfer in Cold Climates*, Chap. 4, Van Nostrand Rheinhold Co.

Love, R. M., 1966, "The Freezing of Animal Tissue," Chap. 7 in: *Cryobiology*, H. T. Meryman, ed., Academic Press, London.

Mazur, P., 1963, "Kinetics of Water Loss From Cells at Subzero Temperature and the Likelihood of Intracellular Freezing," *The Journal of General Physiology*, Vol. 47, pp. 347–369.

Motta, P., Muto, M., and Fijita, T., 1978, *The Liver: An Atlas of Scanning Electron Microscopy*, Igaku-Shoin, Tokyo.

Rubinsky, B., and Schitzer, A., 1976, "Analysis of a Stefan Like Problem in a Biological Tissue Around a Cryosurgical Probe," ASME JOURNAL OF HEAT TRANSFER, Vol. 98, pp. 514–519.

Rubinsky, B., and Cravalho, E. G., 1984, "An Anlytical Method to Evaluate Cooling Rates During Cryopreservation Protocols for Organs," *Cryobiology*, Vol. 21, pp. 303–320.

Rubinsky, B., Lee, C. Y., Bastacky, J., and Hayes, T. L., 1987, "The Mechanism of Freezing in Biological Tissue: The Liver," *Cryo-Letters*, Vol. 8, pp. 370–381.

Rubinsky, B., and Pegg, D. E., 1988, "A Mathematical Model for the Freezing Process in Biological Tissue," *Proc. R. Soc. London*, Vol. B234, pp. 343–358.

Rubinsky, B., 1989, "The Energy Equation for Freezing of Biological Tissue," ASME JOURNAL OF HEAT TRANSFER, Vol. 11, pp. 988–997.

Rubinsky, B., Lee, C. Y., Bastacky, J.., and Onik, G., 1990, "The Process of Freezing and the Mechanism of Damage During Hepatic Cryosurgery," *Cryobiology*, Vol. 27, pp. 85–97.

Toner, M., Cravalho, E. G., and Karel, M., 1990, "Thermodynamics and Kinetics of Intracellular Ice Formation During Freezing of Biological Cells," *J. Appl. Phys.*, Vol. 67(3).

Trump, B. F., Goldblatt, P. J., Griffin, C. C., Waravdekar, V. S., and Stowell, R. E., 1964, "Effects of Freezing and Thawing on the Ultrastructure of Mouse Hepatic Parenchymal Cells," *Laboratory Investigation*, Vol. 13(9), pp. 967–1002.

Turnbull, D. Y., 1969, "Under What Conditions Can a Glass Be Formed?" *Contemp. Phys.*, Vol. 10, pp. 473–488.

Flow and Morphological Conditions Associated With Unidirectional Solidification of Aqueous Ammonium Chloride

C. S. Magirl

F. P. Incropera

Heat Transfer Laboratory,
School of Mechanical Engineering,
Purdue University,
West Lafayette, IN 47907

Using a 27 percent aqueous ammonium chloride solution as a transparent analog, shadowgraph and dye injection techniques have been employed to observe flow and morphological conditions associated with unidirectional solidification (UDS) from below. Dendritic crystals, which initially form at the cold surface, reject lighter, solute deficient fluid, and the attendant instability is manifested by finger-type double-diffusive convection phenomena. As a two-phase (solid/liquid), or mushy, region grows from the bottom surface, vertical channels develop in the mushy region, and solutal plumes that emanate from the channels are characterized primarily by an ascending, oscillatory motion and secondarily by wisps of fluid, which detach and descend from bends in the plumes. In time, double-diffusive convection layers also form in the melt. From a numerical simulation of the process, it is concluded that the channels originate from perturbations at the liquid interface, which cause localized remelting and create conditions conducive to development of the channels.

Introduction

Free convection plays an important role in the freezing of many mixtures. For solidification of a simple binary alloy under off-eutectic conditions, the process can involve both solutal and thermal buoyancy, morphological instabilities in the growth of solid, and ultimately, large inhomogeneities and imperfections in the final product. Physical mechanisms associated with convection during solidification have been the focus of extensive research in such wide-ranging disciplines as oceanography, geology, and materials processing. The current study has been motivated by interests in materials processing, specifically as it relates to the static casting of binary alloys.

The need for high-strength, light-weight materials has long been associated with the development of high-performance gas turbine engines, where unidirectionally solidified (UDS) alloy turbine blades have shown markedly improved thermal creep behavior and strength. However, castings may often be characterized by unacceptable imperfections. If a mold is chilled at a side wall, the imperfections, known as A- and V-segregates, are manifested by slanted rods whose composition differs significantly from that of the original melt. If the mold is chilled from the bottom, the imperfections or segregates are manifested by long pencil-like regions, which are of unique composition and oriented parallel to the direction of gravity (Giamei and Kear, 1970). These imperfections reduce the strength of the cast and contribute to product failure.

As an off-eutectic binary alloy is solidified, regions of pure solid and liquid are separated by a two-phase mushy region, which is essentially a liquid-saturated, porous, crystalline structure. Working with aqueous ammonium chloride (NH_4Cl–H_2O), a popular low-temperature analog to metal alloys, McDonald and Hunt (1969) were the first to report the formation of A- and V-segregates in a side chill cast. In addition to freezing dendritically, the analog is transparent, thus allowing observation of convective fluid motion during solidification. Also using aqueous NH_4Cl, Copley et al. (1970) showed that, under certain conditions in a bottom chill cast, large vertical channels develop in the mushy region and become the source of freckle segregates in the final casting. If the initial concentration of NH_4Cl in the melt exceeds the eutectic concentration, solidification yields a mushy region in which the solid consists primarily of NH_4Cl and the interdendritic liquid is water-rich and hence compositionally lighter than the original melt. Lighter, interdendritic fluid ascends through the melt, and in the presence of a stable temperature gradient, conditions conducive to double-diffusive convection may be created (Turner, 1974; Chen and Turner, 1980).

From UDS experiments performed by chilling aqueous ammonium chloride from below, Sample and Hellawell (1982, 1984) concluded that channels nucleate from disturbances at the liquidus front and develop through downward propagation in the mushy region. Water-rich fluid emerged from the channels as plumes, which ascended into the melt. More recently, McCay et al. (1989) used Schlieren photography and particle tracking to study Rayleigh–Bénard type instabilities, which precede plume development, and Okumura et al. (1989) and Sarazin (1990) used shadowgraph techniques to reveal evolution of flow above the liquidus interface. Chen and Chen (1991) and Tait and Jaupart (1992) also used shadowgraph techniques to reveal the nature of salt fingering in the early stages of solidification and the development of plumes in subsequent stages. Although Chen and Chen restricted their experiments to a single composition (26 percent NH_4Cl), they did consider a range of cold wall temperatures ($-31.5°C < T < 11.9°C$). Through addition of small amounts of a polymerizing agent, Tait and Jaupart varied the viscosity of the melt and found the areal density of channels and the channel diameter to increase with decreasing and increasing viscosity, respectively.

Several attempts have recently been made to clarify the origins of channeling in the mushy zone by performing stability analyses and by analyzing coupled flow conditions in the mushy region and the melt. Linear (Nandapurkar et al., 1989) and nonlinear (Heinrich et al., 1989) stability analyses performed for a Pb–Sn system over a representative range of conditions revealed instabilities at the liquidus interface to be manifested by fingerlike, double-diffusive convection. These results were confirmed in a subsequent study (Nandapurkar et al., 1991),

Contributed by the Heat Transfer Division and presented at the ASME National Heat Transfer Conference, San Diego, California, August 9–12, 1992. Manuscript received by the Heat Transfer Division August 1992; revision received May 1993. Keywords: Double Diffusion Systems, Materials Processing and Manufacturing Processes, Phase-Change Phenomena. Technical Editor: R. Viskanta.

which revealed a strong interaction between advection in upper regions of the mushy zone and the overlying melt. However, the model prescribes a constant liquid volume fraction within the mushy zone and is only valid at the onset of convection.

In a numerical simulation of UDS for NH_4Cl–H_2O in a cylindrical mold, Neilson and Incropera (1991) solved the strongly coupled and nonlinear momentum, energy, and species equations that govern flow and thermosolutal conditions in the mushy and melt regions. Nucleation was predicted to be a consequence of perturbations in field variables at the liquidus front, which induced highly localized permeability variations that allowed liquid to emerge from the mushy zone in buoyant plumes. The plumes were sustained by the entrainment of liquid from the melt into the mushy region and by seepage through the mushy region into channels that propagated downward from the nucleation sites. Downward channel growth resulted from a freezing point depression caused by solute (H_2O)-rich fluid ascending within the channel. These conclusions are consistent with those obtained from a numerical solution of the coupled conservation equations for UDS of a Pb-Sn mixture (Felicelli et al., 1991). Channels were predicted to nucleate at the advancing solidification front (i.e., at dendrite tips) and in regions of upward flow between adjoining convection cells. The upflow consisted of solute-rich liquid, which depressed the local freezing point and retarded advancement of the growth front. Additionally, solute-enrichment caused local remelting of existing solid, and the net effect was downward development of the channels toward the bottom of the mushy zone. The calculations also revealed a pronounced accumulation of solute at the walls of the mold and hence a strong tendency for channels to form in this region.

The foregoing theoretical results are consistent with experimental findings for NH_4Cl–H_2O (Copley et al., 1970; Sample and Hellawell, 1984), namely that channels develop from the leading edge of the growth front. However, alternative interpretations of channel nucleation and development have been proposed. Subject to a constant growth front velocity, Fowler (1985) analyzed conditions *within* a mushy region induced by UDS from below and obtained a critical Rayleigh number for the onset of convection and channels. Worster (1992) differentiated between two modes of compositionally driven convection due to UDS from below. Using linear stability analysis, he revealed a *boundary layer mode*, which originates in a thin compositional boundary layer just above the liquidus interface, and a *mushy layer mode*, which originates from compositional buoyancy within the mushy zone. He concluded that the boundary layer mode yields weak recirculating flows in the melt above the mushy zone, but has virtually no influence on flow and solid fraction in the mushy zone. Conversely, the mushy layer mode induced convection in the mush, causing perturbations in the solid fraction, which can be precursors to channel formation. It was also argued that plumes emanating from the channels are not a direct consequence of fingerlike convection but, instead, constitute an independent convection mode. That is, although they may overlap, the boundary layer and mushy zone convection modes can be initiated independently. Tait and Jaupart (1992) also concluded that the onset of convection and channels in the mushy zone is determined by a local Rayleigh number criterion and is independent of buoyancy layer instabilities at the liquidus interface.

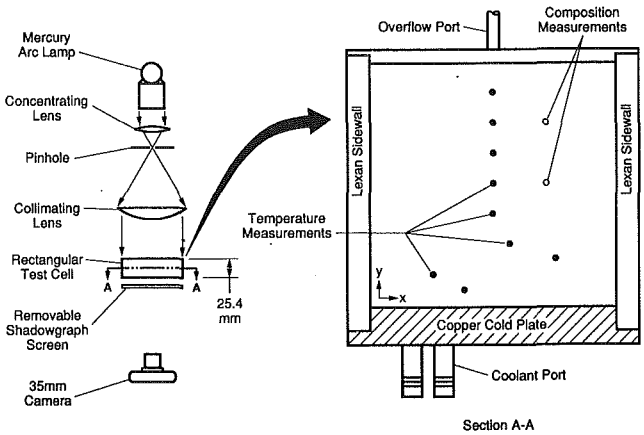

Fig. 1 Schematic of shadowgraph visualization optics and test section

The present study concerns UDS of NH_4Cl–H_2O from below, and its objectives are twofold. Experimentally, emphasis is placed on post-finger-to-plume transition phenomena, including special features of plume behavior and the evolution of double-diffusive convection cells. In addition, numerical simulation of the solidification process is used to clarify means by which channels nucleate and develop within the mushy zone.

Experimental Procedure

Because its liquidus temperature of 18.6°C is below room temperature, an aqueous solution of 27 percent NH_4Cl was chosen for all experiments, which were performed in a rectangular test cell, 101.6 mm wide by 101.6 mm high by 25.4 mm deep (Fig. 1). Its bottom wall was formed by a copper heat exchanger, while all other walls were made from a clear polycarbonate (Lexan). The lid to the test section contained a supply tube, through which the test section was filled before each experiment and fluid was slowly supplied during the experiment to compensate for solidification shrinkage.

The test section was chilled with a Neslab ULT-80DD constant temperature bath, and for most of the shadowgraph and particle tracking experiments, the bottom wall was maintained at -30°C. However, during dye injection experiments, the wall was maintained at -15°C to prevent dye injection ports from freezing shut. The increased chill temperature had little effect on the general pattern of flow conditions observed in

Nomenclature

c = specific heat
D = binary mass diffusivity
f = mass fraction
g = volume fraction or gravitational acceleration
h = mixture enthalpy
k = thermal conductivity
K = permeability
K_o = Blake-Kozeny permeability constant
P = pressure
t = time
T = temperature
u = x-direction mixture velocity component
v = y-directional mixture velocity component
$\mathbf{V}$ = velocity vector
x, y = rectangular coordinates
β_S = solute volumetric expansion coefficient
β_T = thermal volumetric expansion coefficient
μ = dynamic viscosity
ρ = mixture mass density
ψ = streamfunction
Δ = difference

Subscripts

e = eutectic
l = liquid
s = solid

Superscript

α = species designation

the melt. The test section was well insulated during experimentation, with the insulation briefly removed to photograph flow conditions.

In using the shadowgraph technique, a collimated beam of light was passed through the test section (Fig. 1) and deflection due to variations in refractive index were manifested as shadows on an imaging screen. Because of large temperature and composition differences in a solidifying salt system, the shadowgraph is well suited for identifying plumes and double-diffusive convection. It was also used to estimate the plume diameter by measuring the width of shadows cast on the shadowgraph screen. However, the shadowgraph is limited by virtue of providing a two-dimensional view of what are essentially three-dimensional phenomena. Hence, dye injection was also used to better resolve plume behavior and the evolution of double-diffusive convection cells.

To visualize flow patterns emanating from the mushy region, a dye solution of fluorescein disodium salt was injected into the mushy region. Before a particular experiment, four 16 gage hypodermic needles were strategically placed around the test section. To prevent crystallization in the needles, they were filled with a eutectic concentration (19.6 percent NH_4Cl) of solution colored with the fluorescein dye. Solidification was then begun and allowed to continue unimpeded until the mushy region had overgrown the needle locations and well-established channels and plumes had developed. The dyed eutectic was then slowly released into the dendritic structure and allowed to follow the flow of interdendritic fluid exiting the channels. Concurrently the dye was fluoresced with a source of black light.

Although the composition of fluid within a channel was not measured, it may be bracketed by acknowledging that mature channels extended throughout the mushy region (from the liquidus to the solidus fronts). With the numerical simulations of this study revealing seepage of interdentritic fluid into a channel from all depths of the mushy zone and assuming thermodynamic equilibrium in the zone, it follows that the composition of channel fluid must be in the range $0.196 \leq f_l^{NH_4Cl} \leq 0.270$. Hence, in choosing a eutectic composition for the injected dye solution, $f_l^{NH_4Cl} = 0.196$, some buoyancy was added to the fluid. However, to minimize the additional buoyancy, the imposed flow rate of the injected dye was approximately an order of magnitude less than that of the channel flow. From shadowgraph observations made before and after dye injection, characteristics of the plume and attendant flows in the melt were found to be unchanged.

Particle tracking was utilized to further reveal flow patterns within the melt. Pliolite particles, approximately 100 μm in size and having nearly the same density as the NH_4Cl solution, were illuminated with a thin sheet of white light from a mercury vapor lamp and were used for all particle tracking experiments. The displacement/time relationship of particles flowing in a plume was used to estimate plume velocities.

Temperature measurements in the test cell were made using type T (copper-constantan) thermocouples, calibrated to an accuracy of ± 0.05°C. The thermocouples were housed in 16 gage (1.59 mm) stainless steel probes, which were inserted through the side wall of the test section to minimize fin effects resulting from strong vertical thermal gradients in the melt. Nine probes were inserted at heights above the cold wall of $y = 6.35$, 12.7, 19.1, 25.4, 38.1, 50.8, 63.5, 76.2, and 88.9 mm (Fig. 1). The upper five thermocouples were placed on the test section midline, and the remaining thermocouples were positioned at staggered horizontal locations. In addition composition was determined at elevations of 50.8 and 76.2 mm in the melt (Fig. 1) by extracting small samples of fluid with a hypodermic needle and measuring the NH_4Cl concentration to ± 0.1 wt% with a refractometer.

Experiments involving temperature measurements, particle tracking, dye injection, and shadowgraphic visualization were performed separately, and repeatability from experiment to experiment was good.

Mathematical Model

The experimental system is modeled using a continuum theory of mixtures originally formulated by Bennon and Incropera (1987) and modified by Prescott et al. (1991). As applied in this study, the model assumes (*i*) laminar, two-dimensional flow in the melt and mushy regions, (*ii*) local thermodynamic equilibrium at phase interfaces, (*iii*) constant properties, including equivalence of the solid and liquid phase densities, (*iv*) applicability of the Boussinesq approximation, (*v*) isotropic permeability of the mushy region, (*vi*) negligible diffusion in the solid phase, and (*vii*) a solid crystalline structure, which is continuous and stationary. Equations governing conservation of mass, momentum, energy, and species are of the form

$$\frac{\partial}{\partial t}(\rho) + \nabla \cdot (\rho \mathbf{V}) = 0 \tag{1}$$

$$\frac{\partial}{\partial t}(\rho u) + \nabla \cdot (\rho \mathbf{V} u) = \nabla \cdot \left(\mu_l \frac{\rho}{\rho_l} \nabla u \right) - \frac{\mu_l \rho}{K \rho_l} u - \frac{\partial P}{\partial x} \tag{2}$$

$$\frac{\partial}{\partial t}(\rho v) + \nabla \cdot (\rho \mathbf{V} v) = \nabla \cdot \left(\mu_l \frac{\rho}{\rho_l} \nabla v \right) - \frac{\mu_l \rho}{K \rho_l} v - \frac{\partial P}{\partial y} + \rho_l g [\beta_T (T - T_e) + \beta_S (f_l^\alpha - f_{l,e}^\alpha)] \tag{3}$$

$$\frac{\partial}{\partial t}(\rho h) + \nabla \cdot (\rho \mathbf{V} h) = \nabla \cdot \left(\frac{k}{c_s} \nabla h \right) + \nabla \cdot \left[\frac{k}{c_s} \nabla (h_s - h) \right] - \nabla \cdot [\rho f_s (h_l - h_s) \mathbf{V}] \tag{4}$$

$$\frac{\partial}{\partial t}(\rho f^\alpha) + \nabla \cdot (\rho \mathbf{V} f^\alpha) = \nabla \cdot (\rho D \nabla f^\alpha) + \nabla \cdot [\rho D \nabla (f_l^\alpha - f^\alpha)] - \nabla \cdot [\rho f_s (f_l^\alpha - f_s^\alpha) \mathbf{V}] \tag{5}$$

The second term on the right-hand side of Eqs. (2) and (3) accounts for Darcy damping in the mushy region, while the last term of Eq. (3) accounts for thermal and solutal contributions to the buoyancy force. Mixture variables (ρ, $\mathbf{V}$, h, and f^α) may be expressed as weighted averages of values associated with the solid (s) and liquid (l) phases. The permeability of the mushy region is expressed by a Kozeny–Carman relation of the form (Asai and Muchi, 1977)

$$K = K_o \left[\frac{g_l^3}{(1 - g_l)^2} \right] \tag{6}$$

where the prescribed permeability coefficient of $K_o = 5.56 \times 10^{-12}$ m^2 corresponds to a representative dendrite arm spacing of 32 μm. The thermophysical properties of the NH_4Cl–H_2O system are provided elsewhere (Neilson and Incropera, 1991), as are closure relations based on use of the equilibrium phase diagram.

The continuum equations were solved using a control-volume-based finite-difference scheme originally implemented by Bennon and Incropera (1988). From comparative grid studies, a biased 102×66 grid was found to resolve many important features of the solidification process adequately and to provide good quantitative agreement with global quantities, such as heat rate and solid mass formation, obtained for the early stages of solidification with a finer grid. A time increment of 1 s was used in the marching solution.

Experimental Results

Within 15 seconds of applying coolant to the bottom heat

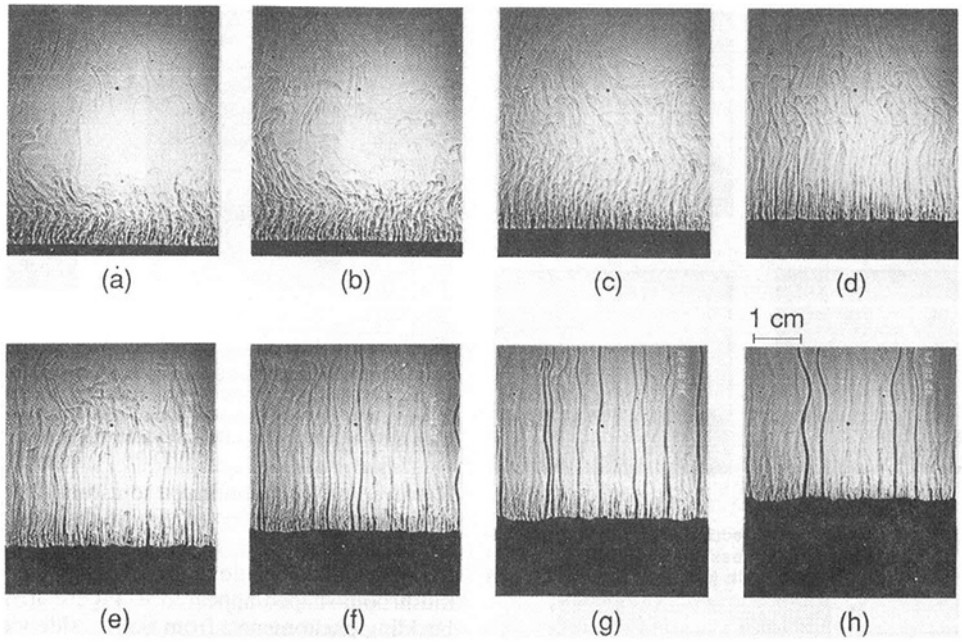

Fig. 2 Shadowgraph of early development of salt fingers and transformation into organized plumes: (*a*) 1.5, (*b*) 3, (*c*) 5, (*d*) 7.5, (*e*) 10, (*f*) 15, (*g*) 20, and (*h*) 25 min

exchanger, dendritic crystals began to form on the cold surface, and within another 20 seconds, the surface was covered with a crystalline mush about 4 mm thick. The crystalline structure was dendritic and tightly packed, and its rapid growth suggested the existence of substantial fluid undercooling. As crystals grew, they rejected lighter, water-rich fluid, and an attendant double-diffusive instability yielded ascending water-rich fingers of fluid adjacent to descending salt-rich fingers (Turner, 1974). Due to the large Lewis number of NH_4Cl–H_2O, the water-rich fingers retained their compositional identity and were clearly visible as they rose to the top of the test section.

The fingers strengthened and remained organized until, at approximately two minutes, the most vigorous fingers began to advect small crystals into the bulk liquid. It is not clear whether these crystals were small equiaxed dendrites that nucleated in the undercooled interdendritic fluid or whether they were fragmented dendrite arms resulting from remelting due to local compositional changes. In any case, at approximately five minutes, from 150 to 200 robust fingers were spewing discrete crystals into the melt just above the liquidus interface. The resulting slurry zone (a liquid region with free floating dendrite fragments) was approximately 5 mm thick. As small crystals were ejected by the salt fingers, some continued to ascend into the bulk liquid, where they melted, while most crystals migrated from the ascending water-rich fingers to adjacent, descending fingers. As the crystals descended, they rapidly grew such that their dendritic structure could be seen by the naked eye. The equiaxed crystals collected as rings around the mouths of the most vigorous salt fingers, and the liquidus interface became strewn with hillocks that surrounded each robust finger. As they grew, the rings of equiaxed crystals also rejected water-rich fluid, which augmented development of the associated fingers. However, within the equiaxed rings, the fingers had not yet begun to melt away noticeable holes in the mushy region. In fact, at $t \approx 15$ min, slurry formation had greatly diminished and the hillocks were overgrown by the advancing liquidus front. Of the 150 to 200 small fingers that existed originally, only a handful were sufficiently strengthened to subsequently become the source of plumes emanating from the mushy region.

Figure 2 shows the sequence by which transition from numerous salt fingers to a much smaller number of more robust plumes occurred. In general, neighboring fingers and plumes competed for the supply of water-rich, interdendritic fluid, and only the strongest fingers survived to become sources of channels. After strong fingers established themselves, small holes began to form in the mushy region immediately below these fingers. The holes were initially located in the weaker crystalline structure between primary dendrites, and as they developed, the associated plumes issuing from the mush strengthened. Over time the holes grew to a diameter of about 1.5 mm and became pathways for cold, water-rich fluid emerging from the mush and ascending to the top of the test section. In addition, large crystalline volcanos formed around the mouths of the robust channels (Fig. 3). While the plumes strengthened, fingers in regions between plumes weakened and continued to decline in number. The cold, water-rich fluid ascending from a channel was driven by strong solutal buoy-

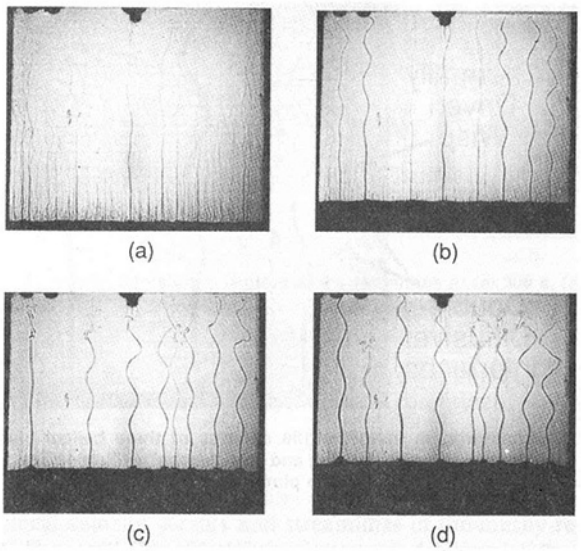

Fig. 3 Shadowgraph images in first hour showing the advancing liquidus front and development of plumes emanating from channels in the mushy region: (*a*) 15, (*b*) 30, (*c*) 45, and (*d*) 60 min

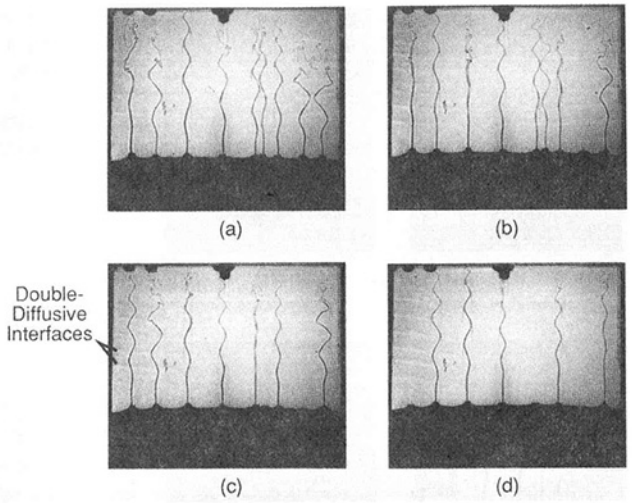

Fig. 4 Shadowgraph images during the second hour showing organization and strengthening of plumes, suppression of salt fingering, and double-diffusive convection within the melt: (*a*) 75, (*b*) 90, (*c*) 105, and (*d*) 120 min

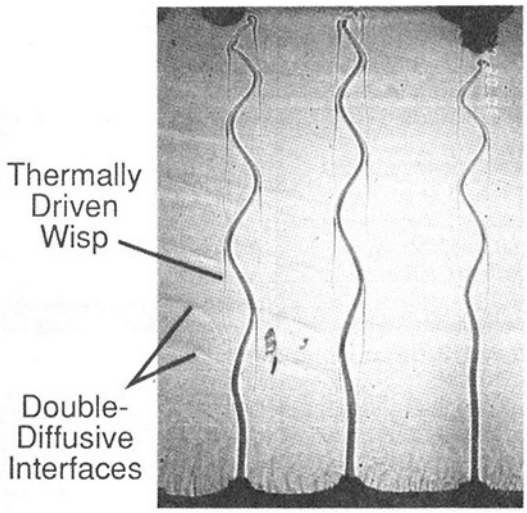

Fig. 5 Shadowgraph image at 106 minutes of three helical plumes showing double-diffusive layering and cold "wisps" of fluid falling from bends in the plume. Waves in the plume propagate upward

ancy forces, which were augmented through heat exchange with the surrounding melt. Due to the large Lewis number of NH_4Cl–H_2O, the plume maintained its solutal identity while gaining thermal buoyancy. In the later stages of the experiment, the plumes became the primary mechanism for convective transport of interdendritic fluid into the melt (Fig. 4). Manifestations of double-diffusive layering are indicated by the horizontal diffusive interfaces that appear in the figure.

The largest plume velocities were estimated to be approximately 10 mm/s, which corresponded to a Reynolds number, based on plume diameter, of approximately 10. As a plume strengthened, it developed a sinusoidal oscillation, which was initially confined to a two-dimensional vertical plane that bisected the axis of the originating channel. This plane of oscillation rotated very slowly around the channel axis and, with two-dimensional shadowgraphic imaging, created the illusion that the plume oscillation appeared and disappeared with time. The wavelength of the oscillations was approximately 15 mm, and the oscillation waves propagated upward at approximately 7.5 mm/s.

As a plume oscillated in its plane, fluid motion in the outer bends of the oscillation was retarded by viscous drag forces.

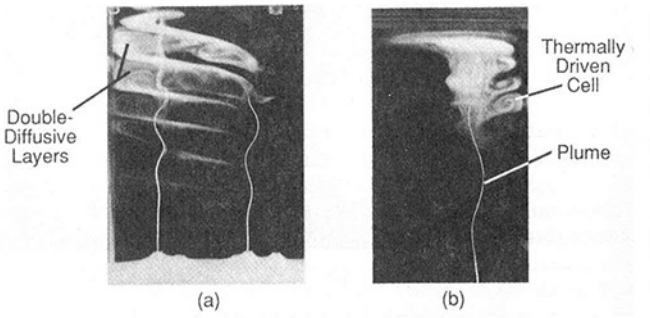

Fig. 6 Use of fluorescein dye to illustrate double-diffusive convection associated with ascending plumes in a UDS process: (*a*) pair of plumes on the left-hand side of the test section with associated double-diffusive layering and thermally driven wisps and (*b*) single plume on the right-hand side of the test section showing the thermally driven cells

However, as fluid continued to ascend from below the bend, it induced a bifurcation of flow in the bend causing the plume to fold onto itself. If viewed from a position perpendicular to the plane of oscillation, this plume buckling would have a mushroom-shaped appearance. Figure 4(*b*) shows this plume buckling phenomenon from both a side view (farthest plume on the right) and an end view (third plume from the left). Buckling flow phenomena are described in detail by Bejan (1989), and in a recent analysis of transverse instability for an axisymmetric plume (Yang, 1992), a sinuous, or *snake*, mode of instability was shown to be a precursor of buckling. Origins of the instability were first identified from a linear stability analysis of conditions at a vertical interface, across which changes in composition and temperature were imposed (Eltayeb and Loper, 1991). The change in composition induced a three-dimensional instability, which was enhanced by thermal diffusion and diminished by viscous effects. In this study, motion of the most vigorous plumes eventually became helical. A three-dimensional helical motion has also been reported by Stuebe and Hellawell (1992).

As salt-rich fluid adjacent to a plume is chilled, it descends as a sheath along the plume. However, when the plume begins to oscillate, the sheaths cannot traverse the plume bends, causing wisps of fluid to separate from the plume and to descend freely (Fig. 5).

About one hour into the experiment, slight double-diffusive convection layers began to develop in the bulk liquid. The layers were initially most pronounced at the side walls of the test section, where cold rising plumes generated a horizontal thermal gradient. Using fluorescein dye injection to track a plume, Figs. 6(*a*) and 6(*b*) show the characteristic double-diffusive layering behavior, which involved stacked, thermally driven convection cells separated by stable diffusive interfaces. In this case, the cells extend from the plume to the mold wall. Although they are strongest on the mold wall side of the plume, the cells surround the cold plume, essentially forming a tower of stacked, rolling tori. This condition was confirmed by particle tracking, which revealed cellular fluid motion surrounding a meandering plume. The cold plume thermally drives the cellular movement within each double-diffusive layer, and eventually, the double-diffusive layers extend across the entire width of the test section.

With increasing time, growth of the mushy zone reduced heat transfer to the chilled bottom, thereby reducing the solidification rate and the supply of water-rich interdendritic fluid to the channels. Hence, there was a progressive reduction in the number of plumes. When the supply of fluid flowing through a channel ceased, the channel quickly closed and became overgrown with crystals from the surrounding mush. At approximately two hours and thirty minutes into the experiment, only two weak plumes remained, and the double-diffusive layers became less distinct, with attendant weakening

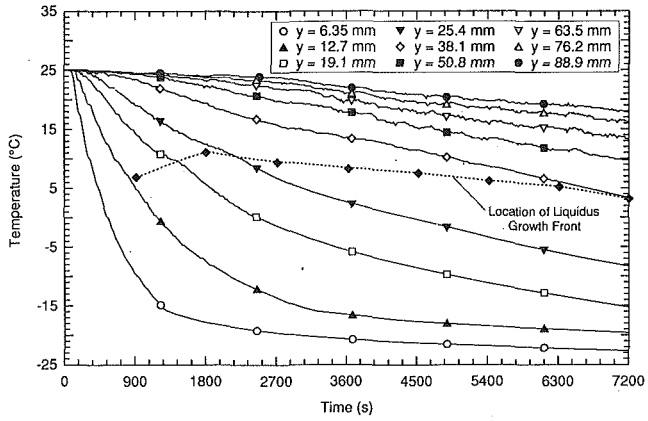

Fig. 7 Measured temperature histories at selected heights with superposition of temperature history for the liquidus growth front

of the convection cells. This behavior confirms the dependence of double-diffusive layering and cellular flow on the existence of strong plume motion.

Recorded temperature histories for the experiment are shown in Fig. 7. The results, which were highly repeatable, reveal a consistent decay in local temperatures, with the most pronounced decay occurring at the measurement location closest to the chill plate ($y = 6.35$ mm). As indicated previously, the chill plate was covered with a crystalline mush within 30 s, and because the chill temperature ($-30°C$) was well below the eutectic temperature ($-15.3°C$), there was almost concurrent formation of the fully solid (eutectic) layer. The liquidus and solidus fronts had advanced to the lowest probe location within approximately 120 and 1250 s, respectively, and a significant reduction in the slope of the temperature history occurred when the probe was overgrown by the solidus. Fingers and plumes produced random temperature fluctuations ($<0.5°C$) in the melt; however, as a probe was overgrown by the liquidus interface, temperature fluctuations were effectively suppressed by Darcy damping.

From knowledge of both the location of the liquidus front and the vertical temperature distribution as a function of time, it was possible to relate the temperature of the front to time. The results, which are shown in Fig. 7, reveal the significant constitutional undercooling that characterized the early stages of the experiment. At $t = 900$ s, for example, the actual front temperature of 7°C is well below the value of 17.3°C, which is obtained by using the measured composition ($f_l^{NH_4Cl} = 0.267$) with the equilibrium phase diagram. The inflection in the temperature history for $y = 19.1$ mm, which occurs at $t \approx 1250$ s, is therefore believed to be a manifestation of recalescence occurring at the growth front. With increasing time, the undercooling diminishes, and at $t = 7200$ s the actual liquidus temperature is virtually identical to the value obtained from use of the measured composition ($f_l^{NH_4Cl} = 0.238$) with the equilibrium phase diagram (3.7°C). This behavior is consistent with the findings of Tait and Jaupart (1992).

The progression of events associated with the early stages of solidification (from double-diffusive fingers to plumes to the onset of channels) has been reported by other investigators (Chen and Chen, 1991; Tait and Jaupart, 1992). However, questions remain concerning the mechanism by which the channels evolve. One interpretation (Sample and Hellawell, 1984; Neilson and Incropera, 1991; Felicelli et al., 1991) is that the channels nucleate at the liquidus interface as a result of perturbations induced during the transition from finger convection to plumes. Alternatively, it has been proposed that fingers and plumes are independent modes of convection and that channel formation is associated with the onset of convection in the mushy region (Worster, 1992; Tait and Jaupart, 1992). The experimental results of this study are consistent with those

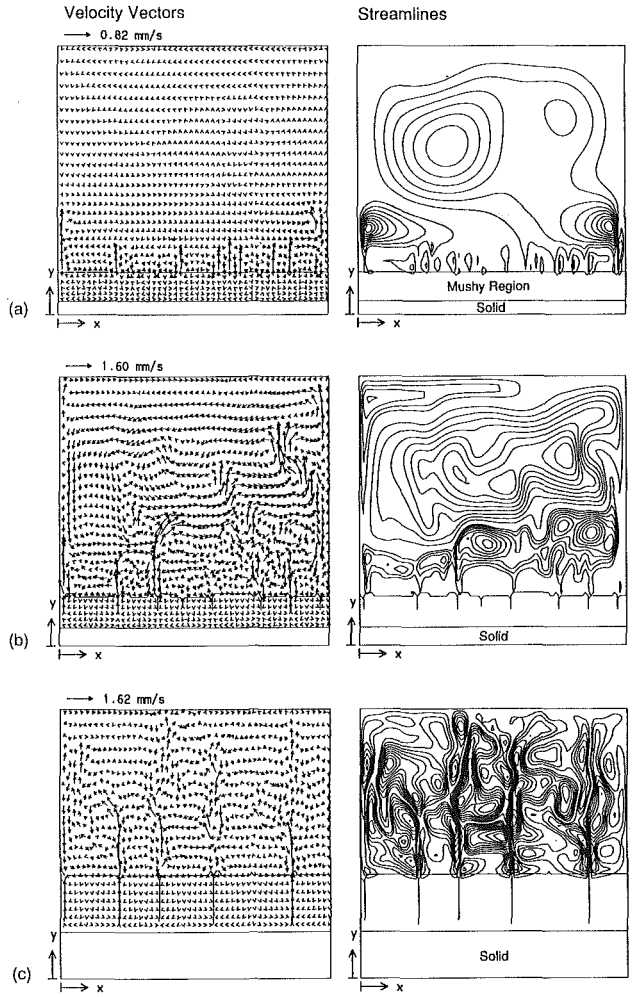

Fig. 8 Predicted velocity vectors and streamlines at (*a*) 300 s, (*b*) 600 s, and (*c*) 3600 s

of Sample and Hellawell (1984) and are supported by a numerical simulation of the experimental conditions.

Numerical Results

Results of the numerical simulation are represented in terms of local velocity vectors and streamlines in the mushy region and the melt. The first five minutes of the simulation were dominated by one-dimensional conduction, during which both the mushy and solid regions advanced into an essentially quiescent melt. However, as the mushy region developed, water-rich fluid was rejected, and at $t \approx 300$ s a boundary layer mode of compositional convection was induced along the liquidus front (Fig. 8*a*). The liquidus (and solidus) front locations were implicitly determined from knowledge of the local enthalpy and the use of equilibrium thermodynamic and phase relationships. Located at random sites along the liquidus front, ascending parcels of cold, water-rich fluid were adjoined by descending parcels of negatively buoyant, warmer, salt-rich fluid. Resulting from the same mechanism that produced finger convection during early stages of the experiment, the predictions represent the model's best attempt to simulate the double-diffusive convection phenomena. However, the control volumes of the prescribed grid were too large to fully resolve the small-scale transport associated with the fingers.

The stronger fingers provided sites for the nucleation of channels, and at $t = 600$ s eight channels were predicted to have formed in the mushy zone (Fig. 8*b*). The channels, whose width corresponded to the size of a control volume, ejected

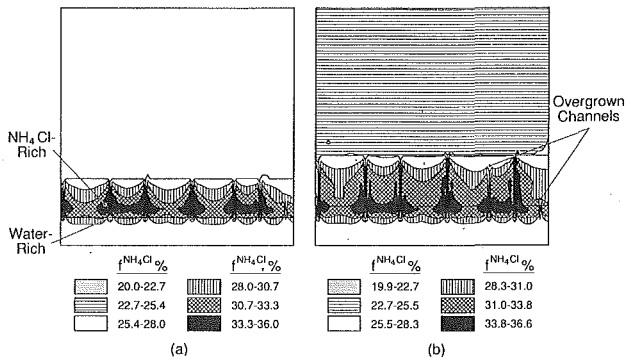

Fig. 9 Species macrosegregation plots at (*a*) 1800 s and (*b*) 3600 s

cold, water-rich plumes into the melt. With increasing time, the channels deepened, while the strength of the associated plumes increased, allowing the plumes to ascend to the top of the cavity. Flow within the mushy region was strongly influenced by the channels. Specifically, salt-rich fluid from the melt was drawn into the mushy region at locations removed from the channels, and once within the mush, the fluid became water-enriched as it was slowly entrained into the channels. However, the number of plumes decreased as the competition among channels to relieve the buoyancy potential of interdendritic fluid intensified. At $t = 3600$ s (Fig. 8*c*), the number of channels had decreased from eight to five, although channel penetration was approaching the solidus front and the plumes remained robust. The plumes exhibited oscillatory behavior similar to that observed experimentally, although the grid was too coarse to capture small-scale behavior, including double-diffusive convection effects. Throughout the simulation, temperature and composition gradients in the melt remained small.

The development of channels and strong plumes fostered the establishment of severe macrosegregation in the mush (Fig. 9). Macrosegregation is quantified in terms of the total mass fraction of NH_4Cl contained in a control volume, f^{NH_4Cl}, for which both maximum and minimum values were associated with a channel. That is, while the composition of fluid within a channel was nearly eutectic ($0.199 \lesssim f^{NH_4Cl} \lesssim 0.227$), a salt-rich sheath of crystals ($0.333 \lesssim f^{NH_4Cl} \lesssim 0.366$) formed around the channel. As near-nominal composition fluid was drawn into the mushy region by the channel entrainment process (Fig. 8*c*), it precipitated NH_4Cl on the dendritic array in an amount thermodynamically dependent on the temperature of the mush. The coldest region of the mush, the channel, promoted heavy solidification, eventually building NH_4Cl-rich segregates adjacent to the channel. The fluid, which eventually entered the channel, having been stripped of much of its salt, was a cold, but solutally light mixture, which ascended quickly to feed the plume. This entrainment process continued as the growth front advanced, and the channels were eventually filled with eutectic material forming freckle-type segregates in the resultant cast. During solidification, some channels ceased ejecting fluid, but their remnants can still be seen. Figure 9(*b*) shows two such channels on the right side of the cast, which have stopped developing and have been overgrown by the liquidus front.

As applied to the present problem, limitations of the model include use of a grid that is insufficiently small to capture finer details of the solidification process and the assumptions of two-dimensional flow, thermodynamic equilibrium, negligible solidification contraction, and a continuous, solid crystalline structure. However, despite the inability to obtain complete grid independence, this and other studies (Beckermann and Viskanta, 1988; Neilson and Incropera, 1991; Felicelli et al., 1991) have been able to predict many important features, including segregate formation. Moreover, in a recent extension of the model to include three-dimensional considerations (Neilson and Incropera, 1993), the actual pencil-like nature of the channels and plumes was predicted, again with the channels nucleating from convective instabilities at the liquidus front. The ability of the model to treat correctly the effects of non-equilibrium (constitutional undercooling), solidification contraction, or free floating crystals on the origins of channel formation has yet to be determined.

Conclusions

Shadowgraph, particle tracking, and dye injection techniques have been used to visualize flow conditions associated with unidirectional solidification of a 27 percent NH_4Cl–H_2O solution from below. Initial growth conditions were characterized by finger-type convection, which originated at the liquidus interface and was accompanied by advection of dendritic fragments into the melt. With increasing time, there was a transition from conditions characterized by a large number of weak fingers to a much smaller number of plumes emerging from channels that formed in the mushy region. The plumes were comprised of relatively large-scale, robust, and continuous fluid ejections driven by water-rich interdendritic fluid, which entered the channels. The channels tended to form at liquidus front locations characterized by large hillocks or elevations during the early salt finger stages. Flow phenomena that characterized later stages of the solidification process included the development of double-diffusive convection cells in the melt, planar and helical oscillations in the plumes, and wisps of fluid falling from bends in meandering plumes. A numerical simulation of the solidification process supported the conclusion that, at least for the conditions of this study, the plumes evolved from finger convection and that channels nucleate at the liquidus interface.

Acknowledgment

The authors are grateful to the U.S. Department of Energy for providing financial support of this work through Award Number DE-FG02-87ER 13759.

References

Asai, S., and Muchi, I., 1977, "Theoretical Analysis and Model Experiments on the Formation Mechanism of Channel-Type Segregation," *Trans. ISIJ*, Vol. 18, pp. 90–98.

Beckermann, C., and Viskanta, R., 1988, "Double-Diffusive Convection During Dendritic Solidification of a Binary Mixture," *PhysicoChemical Hydrodynamics*, Vol. 10, pp. 195–213.

Bejan, A., 1989, "Buckling Flows: A New Frontier in Fluid Mechanics," C. L. Tien, ed., *Annual Review of Heat Transfer and Fluid Mechanics*, Hemisphere, New York, pp. 262–300.

Bennon, W. D., and Incropera, F. P., 1987, "A Continuum Model for Momentum, Heat and Species Transport in Binary Solid-Liquid Phase Change, I: Model Formulation," *Int. J. Heat Mass Transfer*, Vol. 30, pp. 2161–2170.

Bennon, W. D., and Incropera, F. P., 1988, "Numerical Analysis of Binary Solid-Liquid Phase Change Using a Continuum Model," *Num. Heat Transfer*, Vol. 13, pp. 277–296.

Chen, C. F., and Turner, J. S., 1980, "Crystallization in a Double-Diffusive System," *J. Geophysical Research*, Vol. 85, pp. 2573–2593.

Chen, C. F., and Chen, F., 1991, "Experimental Study of Directional Solidification of Aqueous Ammonium Chloride Solution," *J. Fluid Mech.*, Vol. 227, pp. 567–586.

Copley, S. M., Giamei, A. F., Johnson, S. M., and Hornbecker, M. F., 1970, "The Origin of Freckles in Unidirectionally Solidified Castings," *Metall. Trans.*, Vol. 1, pp. 2193–2204.

Eltayeb, I. A., and Loper, D. E., 1991, "On the Stability of Vertical Double-Diffusive Interfaces. Part 1. A Single Plane Interface," *J. Fluid Mech.*, Vol. 228, pp. 149–181.

Felicelli, S. D., Heinrich, J. C., and Poirer, D. R., 1991, "Simulation of Freckles During Vertical Solidification of Binary Alloys," *Metall. Trans. B*, Vol. 22B, pp. 847–859.

Fowler, A. C., 1985, "The Formation of Freckles in Binary Alloys," *IMA J. Appl. Math.*, Vol. 35, pp. 159–174.

Gebhart, B., Jaluria, Y., Mahajan, R. L., and Sammakia, B., 1988, *Buoyancy-Induced Flows and Transport*, Hemisphere, New York.

Giamei, A. F., and Kear, B. H., 1970, "On the Nature of Freckles of Nickel Base Superalloys," *Metall. Trans.*, Vol. 1, pp. 2185–2192.

Heinrich, J. C., Felicelli, S., Nandapurkar, P., and Pourier, D. R., 1989,

"Thermosolutal Convection During Dendritic Solidification of Alloys, Part 2: Nonlinear Convection," *Metall. Trans.*, Vol. 20B, pp. 883–891.

McCay, T. D., McCay, M. H., Lowry, S. A., and Smith, L. M., 1989, "Convective Instabilities During Directional Solidification," *J. Thermophysics*, Vol. 3, No. 3, pp. 345–350.

McDonald, R. J., and Hunt, J. D., 1969, "Fluid Motion Through the Partially Solid Regions of a Casting and Its Importance in Understanding A Type Segregates," *Trans. AIME*, Vol. 245, pp. 1969–1993.

Nandapurkar, P., Pourier, D. R., Heinrich, J. D., and Felicelli, S., 1989, "Thermosolutal Convection During Dendritic Solidification of Alloys: Part 1. Linear Stability Analysis," *Metall. Trans.*, Vol. 20B, pp. 711–721.

Nandapurkar, P., Pourier, D. R., Heinrich, J. D., and Felicelli, S., 1991, "Momentum Equations for Dendritic Solidification," *Num. Heat Transfer*, Part A, Vol. 19, pp. 297–311.

Neilson, D. G., and Incropera, F. P., 1991, "Unidirectional Solidification of a Binary Alloy and the Effects of Induced Fluid Motion," *Int. J. Heat Mass Transfer*, Vol. 34, pp. 1717–1732.

Neilson, D. G., and Incropera, F. P., 1993, "Three-Dimensional Considerations of Unidirectional Solidification in a Binary Liquid," *Num. Heat Transfer*, Part A, Vol. 23, pp. 1–20.

Okumura, K., Kuwabara, M., Sassa, K., and Muchi, I., 1989, "Theoretical Analysis and Model Experiment on Thermosolutal Convection During Unidirectional Solidification in the Vertical Direction," *ISIJ*, Vol. 75, pp. 618–625.

Prescott, P. J., Incropera, F. P., and Bennon, W. D., 1991, "Modeling of Dendritic Solidification Systems: Reassessment of the Continuum Momentum Equation," *Int. J. Heat Mass Transfer*, Vol. 34, pp. 2351–2360.

Sample, A., and Hellawell, A., 1982, "The Effect of Mold Precession on Channel and Macro-segregation in Ammonium Chloride–Water Analog Castings," *Metall. Trans. B*, Vol. 13B, pp. 495–501.

Sample, A. K., and Hellawell, A., 1984, "The Mechanisms of Formation and Prevention of Channel Segregation During Alloy Solidification," *Metall. Trans. A*, Vol. 15A, pp. 2163–2173.

Sarazin, J. R., 1990, "Buoyancy-Driven Convection and Channel Segregation During Solidification in Metallic, Aqueous and Organic Systems," Ph.D. Dissertation, Michigan Technological University, Houghton, MI.

Stuebe, R. S., and Hellawell, A., 1992, "An Alternative Approach to Modeling the Grain Structure of Castings," ASME HTD-Vol. 218/AMD-Vol. 139, C. Beckermann et al., eds., pp. 73–81.

Tait, S., and Jaupart, C., 1992, "Compositional Convection in a Reactive Crystalline Mush and Melt Differentiation," *J. Geophys. Res.*, Vol. 97, B5, pp. 6735–6756.

Turner, J. S., 1974, "Double-Diffusive Phenomena," in: *Ann. Rev. Fluid Mech.*, M. Van Dyke, W. G. Vincenti, and J. V. Wehausen, eds., Vol. 6, pp. 37–56.

Worster, G., 1992, "Instabilities of the Liquid and Mushy Regions During Solidification of Alloys," *J. Fluid Mech.*, Vol. 237, pp. 649–669.

Yang, H. Q., 1992, "Buckling of a Thermal Plume," *Int. J. Heat Mass Transfer*, Vol. 35, pp. 1527–1532.

J. S. Lim
Senior Researcher,
Refrigeration and Air Conditioning Laboratory,
Samsung Electronics,
Suwon City, Kyungi-Do, Korea

A. J. Fowler

A. Bejan
J. A. Jones Professor of Mechanical Engineering.
Fellow ASME

Department of Mechanical Engineering and Materials Science,
Duke University,
Durham, NC 27708-0300

Spaces Filled With Fluid and Fibers Coated With a Phase-Change Material

Thermally active fabrics and insulations consist of fibers coated with phase-change materials and surrounded by air. This paper constructs a homogeneous porous medium model for melting and solidification in spaces filled with thermally active fibers. Three basic configurations are analyzed numerically: one-dimensional conduction, one-dimensional convection, and two-dimensional natural convection due to heating or cooling from the side. Concrete means for calculating the time of complete melting or solidification are reported as functions of the important dimensionless groups that govern each configuration. It is shown that the change of phase in a space filled with coated fibers and air differs fundamentally from the corresponding phenomena in a porous medium saturated with a phase-change material.

1 Objective

It has been shown recently that polyethylene glycols (polyols) can be bonded stably on fibrous materials. The resulting composite materials—the thermally active fabrics—exhibit reversible and reproducible energy storage and release properties (Vigo and Bruno, 1987, 1989; Bruno and Vigo, 1987). The energy storage and release is due to the high enthalpy (latent heat) of melting and crystallization of the polyols affixed to the fibers. Prior to this technological breakthrough, which simplifies the manufacturing, weaving, packing and washing of the fibers, phase-change materials had been used as fillers in hollow fibers (Vigo and Frost, 1982, 1983).

Thermally active fibers have several other attractive properties, for example, improved resistance to oily soiling, static charge, wear and piling,and significantly greater resiliency and hydrophilicity (Vigo and Bruno, 1989). This is why they are already used (e.g., the 1992 air conditioner model AY-C40F produced by Sharp Co.) or projected for use in a wide variety of applications in the apparel, insulation, air conditioning, aerospace, materials and chemical industries. Yet, the work that has been done until now is developmental in nature. It proved the feasibility of these applications, and unveiled the basic properties of the polyol coated fibers surrounded by air. To proceed from this level to industrial applications of many shapes and sizes (e.g., thermal control in buildings), one must possess a model with which to anticipate the performance of the material in the large-scale system.

The objective of this paper is to propose a fundamental model for heat transfer through a space filled with polyol-coated fibers surrounded by air. This is a model in which fibers *and* the phase-change material (polyol, liquid or solid) constitute the matrix, while air is the fluid that flows through the interstitial spaces. Of primary interest is the relation between the time of complete melting or solidification of the polyol coatings, and the various dimensions and the external parameters (e.g., flow configuration) of the space filled with fibers.

It is worth emphasizing that this model differs fundamentally from the one used already in studies of melting and solidification in saturated porous media (e.g., Kazmierczak et al., 1986, 1987, 1988; Beckermann and Viskanta, 1988; Kazmierczak and Poulikakos, 1988; Jany and Bejan, 1988). In the earlier studies the melted phase-change material was the only fluid present in the pores, therefore there was no flow through regions saturated with solid phase-change material. In the porous medium model for thermally active fibers, the fluid (air) flows through the entire matrix regardless of whether the polyol coatings are liquid or solid.

2 Model

When the layer of polyol-coated fibers is sufficiently thick and the air flow through the fibers sufficiently slow, the layer may be modeled as a homogeneous porous medium in which the air and the matrix (fibers and polyol) are in local thermal equilibrium. The pores are saturated with air, and the fibers are coated uniformly with polyol (solid or liquid). The effective properties of the equivalent homogeneous porous medium emerge after the volume averaging of the actual structure (air, fibers, polyol), and the conservation equations for mass, momentum, and energy (e.g., Cheng, 1978). Because of local thermal equilibrium, T represents the local temperature of the fiber and the air and polyol that immediately surrounds it. The composition of the homogeneous porous medium is described by the porosity ϕ (about 80 percent) and the fraction of the matrix occupied by polyol, ϵ (about 20 percent). This means that a unit volume is distributed in the following proportions: ϕ = air, $(1-\phi)$ = matrix (fibers and polyol), $(1-\phi)\,\epsilon$ = polyol, and $(1-\phi)(1-\epsilon)$ = fibers. The aggregate heat capacity of the porous medium is then

$$(\rho c)_m = \phi(\rho c_P)_a + (1-\phi)[\epsilon(\rho c)_p + (1-\epsilon)(\rho c)_f] \qquad (1)$$

in which the subscripts m, a, p, and f refer to the averaged porous medium, air, polyol, and fibers.

The thermal conductivity of the porous medium is k_m. The air flow through such fabrics is weak, therefore the effect of thermal dispersion is neglected. An order of magnitude estimate for the thermal conductivity k_m can be obtained by using the parallel conduction model, $k_m = \phi k_a + (1-\phi)k_f$, in which k_a (20°C air) = 0.026 W/m·K, ϕ = 0.8, $k_f \sim k_p$, and k_p (PEG 1000) = 0.187 W/m·K (Hansen and Washo, 1967). The result is $k_m \sim 0.06$ W/m·K, which is only a rough estimate because it is known that the parallel conduction model is most accurate when k_a and k_f (or k_p) are of the same order of magnitude (Nield and Bejan, 1992, pp. 22–23). In actual applications of

Contributed by the Heat Transfer Division for publication in the JOURNAL OF HEAT TRANSFER. Manuscript received by the Heat Transfer Division April 1992; revision received April 1993. Keywords: Phase-Change Phenomena, Porous Media, Thermal Energy Storage. Associate Technical Editor: C. E. Hickox, Jr.

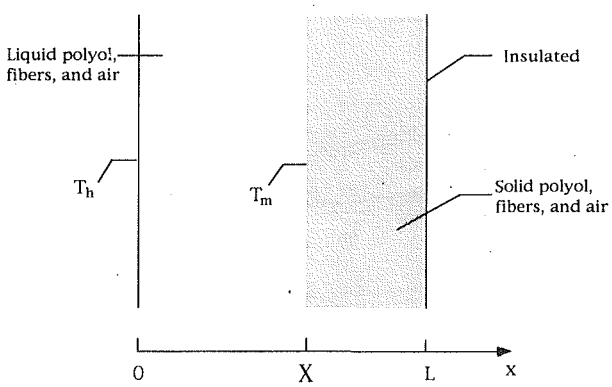

Fig. 1 One-dimensional layer of polyol-coated fibers and air

thermally active fibers the effective thermal conductivity k_m must be determined through direct measurement. It is further assumed that k_m is a constant, independent of T and whether the polyol is solid or liquid.

The volume-averaged energy conservation equation that corresponds to these assumptions is (e.g., Cheng, 1978; Bejan, 1984).

$$\sigma \frac{\partial T}{\partial t} + u \frac{\partial T}{\partial x} + v \frac{\partial T}{\partial y} = \alpha_m \left(\frac{\partial^2 T}{\partial x^2} + \frac{\partial^2 T}{\partial y^2} \right) \tag{2}$$

where (u, v) are the volume-averaged air velocity components, and σ and α are the heat capacity ratio and the thermal diffusivity of the porous medium,

$$\sigma = \frac{(\rho c)_m}{(\rho c_P)_a}, \quad \alpha_m = \frac{k_m}{(\rho c_P)_a} \tag{3}$$

The energy Eq. (2) refers to convection in the two-dimensional Cartesian system (x, y).

3 Melting by One-Dimensional Conduction

The simplest configuration in which the polyol has an effect on thermal behavior of the medium is shown in Fig. 1. The pores of the one-dimensional layer of thickness L are filled with stagnant air. The initial temperature of the layer is uniform (T_i) and lower than the polyol melting point (T_m). Beginning with the time $t = 0$, the temperature of the left side is maintained at a temperature (T_h) above the melting point. The right side is insulated. The heating that is administered through the left wall raises the temperature of the medium, and causes the gradual melting of the polyol. The melting front location, or the instantaneous thickness of the sublayer in which the polyol has melted is $X(t)$. Of primary interest is the time (t_{end}) when all the polyol of the L-thick layer has melted; this time interval is defined by

$$X(t_{\text{end}}) = L \tag{4}$$

The conservation of energy across the melting front requires

$$-k_m \left.\frac{\partial T}{\partial x}\right|_{x=X_-} + k_m \left.\frac{\partial T}{\partial x}\right|_{x=X_+} = (1-\phi)\epsilon\rho_p \lambda \frac{dX}{dt} \tag{5}$$

in which λ is the polyol latent heat of melting. The group $(1-\phi)\,\epsilon\rho_p$ represents the polyol density in the porous medium, i.e., kilograms of polyol per unit volume of porous medium. As noted in Fig. 1, the melting front temperature is T_m, in others words $T[X(t)] = T_m$. It is important to note that because the polyol coating is thin, and because of the local thermal equilibrium assumption (one local T value for air, polyol and fiber), there is no room in the model for a study of melting on each fiber, i.e., how the melting front propagates through the coating, into the fiber.

In order to increase the generality of the results, it is useful to nondimensionalize Eq. (5),

$$-\left.\frac{\partial \theta}{\partial \xi}\right|_{\xi=\tilde{x}_-} + \left.\frac{\partial \theta}{\partial \xi}\right|_{\xi=\tilde{x}_+} = S \frac{d\tilde{x}}{d\tau} \tag{6}$$

by using the notation

$$\tilde{x} = \frac{x}{L}, \quad \theta = \frac{T - T_i}{T_h - T_i} \tag{7}$$

$$M = \frac{X}{L}, \quad \tau = \frac{\alpha_m t}{\sigma L^2} \tag{8}$$

$$S = \frac{(1-\phi)\epsilon\rho_p\lambda}{(\rho c)_m (T_h - T_i)} \tag{9}$$

The new dimensionless group S plays a role similar to that of

Nomenclature

a_i = coefficients, Eq. (20)
c = specific heat
c_P = specific heat at constant pressure
g = gravitational acceleration
k_m = thermal conductivity
K = permeability
L = thickness of porous layer
M = dimensionless front location, Eq. (8)
$\overline{M}$ = average melting front position, Eq. (23)
Pe = Peclet number = uL/α
R = geometric aspect ratio = H/L
Ra = Rayleigh number, Eq. (19)
S = dimensionless group, Eq. (9)
t = time
t_{end} = time of complete melting or solidification
T = temperature
T_c = cold side temperature
T_h = warm side temperature
T_i = initial temperature
T_m = melting point
u, v = volume-averaged velocity components in the x and y directions
x, y = Cartesian coordinates
$\tilde{x}, \tilde{y}$ = dimensionless coordinates = x/L and y/H
X = front location, Figs. 1 and 5
α_m = thermal diffusivity of porous medium, Eq. (3)
β = coefficient of volumetric thermal expansion
ϵ = fraction of matrix volume occupied by polyol
θ = dimensionless temperature, Eqs. (7) and (14)
θ_m = dimensionless melting point, Eq. (13)
θ_m = dimensionless solidification point, Eq. (14)
λ = latent heat of melting and solidification
ν = kinematic viscosity of air
ξ = dimensionless horizontal position in computational space
ρ = density
σ = heat capacity ratio, Eq. (3)
τ = dimensionless time, Eq. (8)
τ_{end} = dimensionless time of complete melting and solidification, Eq. (8) with $t = t_{\text{end}}$
τ_H = dimensionless time, Eq. (18)
$\tau_{H,\text{end}}$ = dimensionless time of complete melting and solidification, Fig. 6
ϕ = porosity
ψ = streamfunction
$\tilde{\psi}$ = dimensionless streamfunction, Eq. (18)
$(\,)_a$ = air
$(\,)_f$ = fiber
$(\,)_m$ = porous medium
$(\,)_p$ = polyol

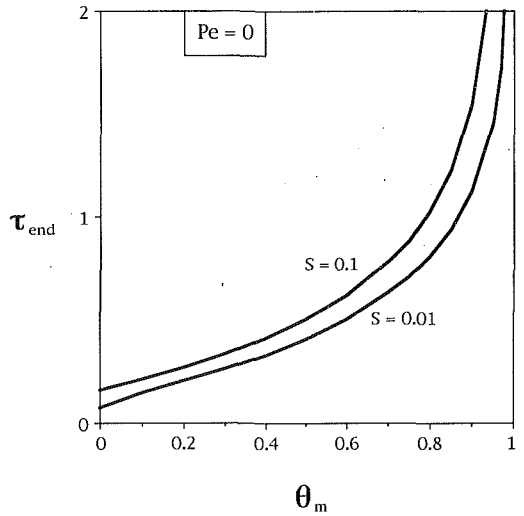

Fig. 2 The time needed to melt or solidify the entire layer (one-dimensional conduction)

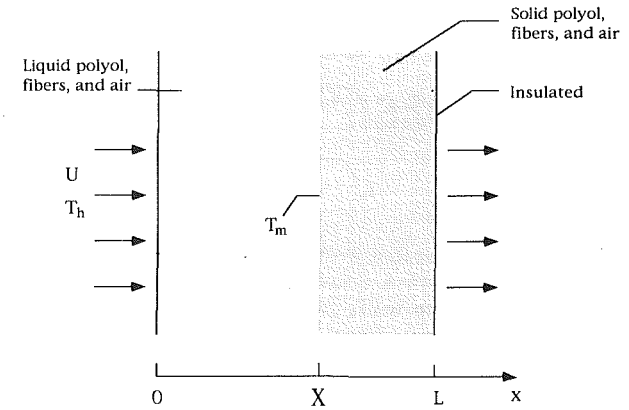

Fig. 3 Forced convection perpendicular to the one-dimensional layer

the inverse Stefan number in a medium consisting of only solid matrix and phase-change material. In the case of polyol-coated fibers, S falls in the range $0.01-0.1$. For example, if we consider the properties of cotton-polyester fibers coated with PEG 1000 (i.e., polyol with molecular weight 1000), we use T_h = 35°C, T_i = 0°C, λ = 10.9 kJ/kg, ρ_p = 1130 kg/m^3, ϕ = 0.8, ϵ = 0.2, $(\rho\, c_P)_a$ = 1.184 kJ/m^{3}K, $(\rho c)_p$ = 2.5 × 10^6 J/m^{3}K, $(\rho c)_f \sim (\rho c)_p$, and based on Eqs. (1) and (9) we obtain $(\rho c)_m \sim$ 0.45 × 10^6 J/m^{3}K, and $S \sim 0.03$. The corresponding calculation based on the properties of fiberglass coated with the polyol PEG 1450 yields $S \sim 0.023$.

In addition, to Eq. (6), the nondimensional problem statement for $M(\tau)$ and the time of complete melting, $M(\tau_{end})$ = 1, consists of

$$\frac{\partial\theta}{\partial\tau}=\frac{\partial^2\theta}{\partial\tilde{x}^2} \tag{10}$$

$$\theta(\tilde{x},\,0)=0,\quad \theta(M)=\theta_m \tag{11}$$

$$\theta(0,\,\tau)=1,\quad \left.\frac{\partial\theta}{\partial\tilde{x}}\right|_{\tilde{x}=1}=0 \tag{12}$$

The dimensionless parameter θ_m measures the position of the melting point T_m relative to the initial (low) and left-side (high) temperatures,

$$\theta_m=\frac{T_m-T_i}{T_h-T_i} \tag{13}$$

The problem statement, Eqs. (6), (10–(12), shows that the dimensionless complete melting time τ_{end} is a function of only two parameters, S and θ_m. This problem can be studied analytically based on classical methods (Carslaw and Jaeger, 1959); however, for the purpose of conserving space and showing the method that was used in the remainder of the paper, we proceed directly to the results. These were obtained numerically based on the explicit finite-differences method, using the grid step $\Delta\tilde{x}$ = 0.0025 and the time step $\Delta\tau$ = 3.125 × 10^{-5}. Grid refinement and time step refinement tests showed that the results are accurate within 2 percent. These tests are discussed further in the paragraph under Eq. (23).

Figure 2 shows the principal results of these calculations, namely, the time needed to melt all the polyol in the L-thick layer. The dimensionless time τ_{end} increases with both θ_m and S; however, the effect of the latter is weak in the range S = 0.01–0.1. The weakness of the effect of S on τ_{end} makes the calculation of the actual (dimensional) melting time t_{end} easier, because the S group accounts for several of the more complicated features of the fiber–polyol–air porous medium model. In other words, as a first approximation we can evaluate τ_{end} by first estimating θ_m, and then calculating the actual time t_{end} = $\tau_{end}\,\sigma L^2/\alpha$. For example, in an application where T_h = 35°C, T_i = 0°C and T_m = 28°C, we find that θ_m = 0.8, and from Fig. 2 that $\tau_{end} \sim 0.8$. Furthermore, if $k_m \sim 0.06$ W/m·K, $(\rho\, c_P)_a$ = 1.184 kJ/m^{3}K, $(\rho c)_m \sim$ 450 kJ/m^{3}K and L = 10 cm, we obtain $\sigma \sim 400$, $\alpha \sim 0.5$ cm^2/s and, finally, $t_{end} \sim$ 17 h.

4 Solidification by One-Dimensional Conduction

The analogous problem of solidification in a one-dimensional layer can be reduced to the same dimensionless statement as in Eqs. (6), (10)–(12), by replacing θ and θ_m with the new definitions

$$\theta=\frac{T_i-T}{T_i-T_c},\quad \theta_m=\frac{T_i-T_m}{T_i-T_c} \tag{14}$$

In these definitions T_c is the temperature of the cooled wall ($T_c<T_m<T_i$), i.e., the left-hand wall in Fig. 1. All the fibers are initially coated with liquid polyol at T_i, and the right-hand wall is insulated throughout the cooling and solidification process. The time t_{end} needed by the solidification front to traverse the entire layer can now be estimated based on Fig. 2 and the τ_{end} and S definitions (8) and (9).

5 Forced Convection Perpendicular to the Layer

The melting and solidification times are considerably shorter when the boundaries of the porous-layer are permeable, and air is forced to flow across the layer. In Fig. 3 we show this by considering the melting under the influence of warm (T_h) air of velocity u that penetrates the layer. The constant velocity u is the actual value outside the layer; if the changes experienced by the air density inside the layer are negligible, this value is the volume-averaged velocity of air in the porous medium (the average velocity in the pores is u/ϕ).

The new feature relative to the problems addressed in the preceding two sections is the $u\partial T/\partial x$ term, which is retained now in the energy Eq. (2), so that in place of Eq. (10) we obtain

$$\frac{\partial\theta}{\partial\tau}+\mathrm{Pe}\,\frac{\partial\theta}{\partial\tilde{x}}=\frac{\partial^2\theta}{\partial\tilde{x}^2} \tag{15}$$

The Peclet number is based on u and L, Pe = uL/α_m. For example, if $u \sim 1$ cm/s, $L \sim 10$ cm, and $\alpha \sim 0.5$ cm^2/s, the Peclet number is of order 20. The rest of the problem statement remains as stated in Eqs. (6) and (11), (12), which is why in section 3 we described in some detail the features of the melting process when there is no flow. The air flow does not have an

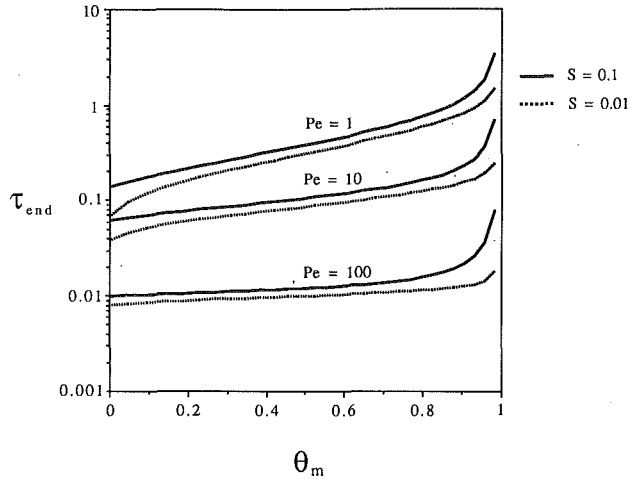

Fig. 4 The effect of transverse forced convection on the time needed to melt for or solidify the entire layer

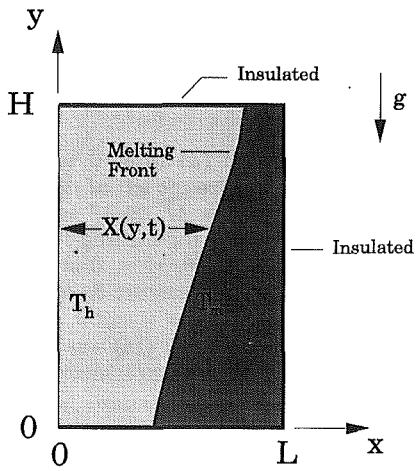

Fig. 5 Two-dimensional layer with natural convection due to heating from the side

effect on the two-phase front condition (6) because the air stream is single phase and its temperature varies continuously across the front. The adiabatic plane condition $\partial\theta/\partial\tilde{x} = 0$ at $\tilde{x} = 1$ [Eq. (12)] has been used by others as an outlet thermal boundary condition (e.g., Hlavacek and Votruba, 1977; Handa et al., 1983; Schmal et al., 1985; Gatica et al., 1989). It becomes more appropriate as the Peclet number increases, and is consistent with the assumption that the $\tilde{x} = 1$ wall is adiabatic in the absence of the u flow (Fig. 1).

The numerical results were obtained using the method described in section 3. These are presented in Fig. 4 as a sequence of three cases according to Peclet number. Worth noting is that Fig. 2 represents the Pe = 0 case in the same sequence. The range covered by τ_{end} in each of these frames shows that the melting time decreases appreciably as the transversal air velocity increases. For example, by repeating the numerical calculation that ended section 3, we find that when Pe ~ 10 the melting time reduces to $t_{end} \sim 2$ hours (compared with 17 hours in the case of no flow).

The effect of transverse forced convection on the overall solidification time of the layer can also be estimated using Fig. 4. In this case θ and θ_m are defined by Eqs. (14), as the cold air stream that crosses the $\tilde{x} = 0$ plane has the temperature T_c. The L-thick layer is originally at the temperature T_i, and all the fibers are coated with liquid polyol.

6 Natural Convection Within the Layer

Natural convection may be an important heat transfer mechanism in large-scale applications of polyol coated fibers, for example, in the walls of buildings. In this section and the next we shall determine under what conditions natural convection plays an important role, and to what extent the time of complete melting is influenced by natural convection.

The mass and momentum equations for the volume-averaged air flow are accounted for by the single equation (e.g., Nield and Bejan, 1992),

$$\frac{\partial^2\psi}{\partial x^2}+\frac{\partial^2\psi}{\partial y^2}=-\frac{Kg\beta}{\nu}\frac{\partial T}{\partial x} \tag{16}$$

in which ψ is the streamfunction ($u = \partial\psi/\partial y$, $v = -\partial\psi/\partial x$), and (u, v) are the volume-averaged velocity components of the air flow. Equation (16) is based on the Oberbeck–Boussinesq approximation and the Darcy flow model. It is assumed that the Reynolds numer based on pore size and volume-averaged velocity is of the order of 1 or smaller. The impermeable rectangular boundary indicated in Fig. 5 means that $\psi = 0$ at $x = 0, L$ and $y = 0, H$. The permeability K is treated as a constant; its value is not affected by the phase-change process because the polyol coating is thin and the porosity is high. The K value is controlled by the mix of air and fibers, and the size and shapes of the fibers.

In the beginning the fiber coatings are solidified completely and uniformly at the temperature T_i, which is below the polyol melting point T_m. The temperature of the left side is raised suddenly to the level T_h, which is higher than T_h. The remaining three boundaries are well insulated.

As the fiber coating melts, the melting front $X(y, t)$ migrates to the right as the time increases. The air flows both between fibers with liquid coatings and fibers with solid coatings. The only coupling between melting front position and the flow field is the temperature gradient that appears on the right-hand side of Eq. (16). The conservation of energy continues to be represented by Eq. (2). Replacing Eq. (5) is a new equation for the conservation of energy at the two-dimensional melting front,

$$-k_m\left.\frac{\partial T}{\partial x}\right|_{x=X_-}+k_m\left.\frac{\partial T}{\partial x}\right|_{x=X_+}$$
$$+\frac{\partial X}{\partial y}\left(k_m\left.\frac{\partial T}{\partial y}\right|_{x=X_-}-k_m\left.\frac{\partial T}{\partial y}\right|_{x=X_+}\right)=(1-\phi)\epsilon\rho_p\lambda\frac{\partial X}{\partial t} \tag{17}$$

The air flow spreads throughout the $L \times H$ porous medium, regardless of the instantaneous position of the melting front. This feature distinguishes the present phenomenon from the natural convection melting of a porous medium saturated with nothing but a phase-change material (e.g., Kazmierczak et al., 1986; Beckermann and Viskanta, 1988; Jany and Bejan, 1988). In the latter, the flow of liquid phase-change material is confined to only one side of the melting front. Another distinguishing feature of the present phenomenon is that the melted phase-change material (i.e., liquid polyol coatings) does not flow. The flow and the associated natural convection heat transfer are due solely to the air that fills the spaces between the coated fibers.

Numerical solutions were developed by using a dimensionless version of Eqs. (16), (2), and (17), with the dimensionless variables

$$\tilde{y}=\frac{y}{H},\quad \tau_H=\frac{\alpha_m t}{\sigma H^2},\quad \tilde{\psi}=\frac{\psi}{Kg\beta(T_h-T_i)H/\nu} \tag{18}$$

and $\tilde{x}$, θ, M, and S defined earlier in Eqs. (7)–(9). The new dimensionless time τ_H is based on H, so that the relation between it and τ of Eq. (8) is $\tau_H = \tau/(H/L)^2$.

The dimensionless groups that appear in the dimensionless governing equations (not listed, for brevity) are the geometric

aspect ratio (R) and the Darcy modified Rayleigh number for air (Ra),

$$R=\frac{H}{L}, \quad \mathrm{Ra}=\frac{Kg\beta(T_h-T_i)H}{\alpha_m\nu} \tag{19}$$

The boundary conditions are: (a) flow, $\tilde{\psi}=0$ at $\tilde{x}=0$, 1 and $\tilde{y}=0$, 1; (b) temperature to the left of the melting front, $\theta=1$ at $\tilde{x}=0$, $\theta=\theta_m$ at $\tilde{x}=M$, $\partial\theta/\partial\tilde{y}=0$ at $\tilde{y}=0$, 1; (c) temperature to the right of the melting front, $\theta=\theta_m$ at $\tilde{x}=M$, $\partial\theta/\partial\tilde{x}=0$ at $\tilde{x}=1$, $\partial\theta/\partial\tilde{y}=0$ at $\tilde{y}=0$, 1. The dimensionless melting front temperature θ_m is defined in Eq. (13). The initial conditions are $\tilde{\psi}=0$ and $\theta=0$ at $\tau_H=0$.

The dimensionless version of Eq. (16) was solved by using a combined finite-difference and spectral method. The streamfunction was represented by

$$\tilde{\psi}=\sum_{i=1}^{q} a_i(\tilde{y})\ \sin\ (i\pi\tilde{x}) \tag{20}$$

Substituting this $\tilde{\psi}$ expression into the dimensionless version of Eq. (16) yields

$$\frac{\partial^2 a_i}{\partial\tilde{y}^2}\sin\ (i\pi\tilde{x})-(Ri\pi)^2\,a_i\sin\ (i\pi\tilde{x})=-R\,\frac{\partial\theta}{\partial\tilde{x}} \tag{21}$$

Next, one can apply the orthogonality property of sin $(i\pi\tilde{x})$ to obtain q ordinary differential equations of the form

$$\frac{\partial^2 a_j}{\partial\tilde{y}^2}-(Rj\pi)^2 a_j=-2R\int_0^1\frac{\partial\theta}{\partial\tilde{x}}\sin\ (j\pi\tilde{x})\,d\tilde{x} \tag{22}$$

The boundary conditions for these equations follow from the requirement that $\tilde{\psi}$ must be zero on the top and bottom boundaries, hence $a_j(\tilde{y})=0$ at $\tilde{y}=0$, 1. The $\tilde{\psi}(\tilde{x},\tilde{y},\tau_H)$ field was obtained by solving Eqs. (22) using second-order accurate finite differences.

The advantages of this method are: (1) It is fairly fast, since it only requires tridiagonal matrix solvers, and (2) it gives a solution for the velocity field that is continuous in $\tilde{x}$. This is important because the energy equation needs to be solved in two domains (liquid coatings, and solid coatings) with horizontal widths that vary with $\tilde{y}$ and τ, and thus could not be solved with grid points that have fixed $\tilde{x}$ locations. To solve for the velocity field by using a method that is discrete in $\tilde{x}$ and $\tilde{y}$ one would have to abandon the simple (rectangular) domain in which the velocity problem occurs, in favor of the unsteady nonuniform grid that would be necessary in order to solve the energy equation. Having a velocity solution that is continuous in $\tilde{x}$ avoids this difficulty.

The energy equation was solved in both domains by using a shearing transformation to map each physical domain onto a unit square in computational space. The smoothness exhibited naturally by the melting front made a shearing transformation attractive. The transformed equations, which include terms accounting for the unsteadiness of the domain, were solved using finite differences and ADI. The mixed second derivative that arises as a result of the coordinate transformation was lagged by one complete time step, so that the ADI method was only first-order accurate in time. Second-order accurate finite differences were employed.

The initial condition, in which the domain to the left of the melting front does not exist, was approximated by starting the melting front arbitrarily close to $\tilde{x}=0$. Similarly the region to the right of the melting front was eliminated if the melting front at a given $\tilde{y}$ location approached arbitrarily close to $\tilde{x}=1$. Convergence tests showed that the results for the melting front position as a function of time were stable (unchanging) to better than 0.1 percent if the starting position was set at $\tilde{x}=0.001$, and the end position at $\tilde{x}=0.999$. Additional convergence tests showed that 41 grid points in the $\tilde{y}$ direction, and 41 grid points within each of the two $\tilde{x}$ domains were sufficient for an accuracy of better than 0.1 percent in $\overline{M}(\tau_H)$ and $\tau_{H,\mathrm{end}}$.

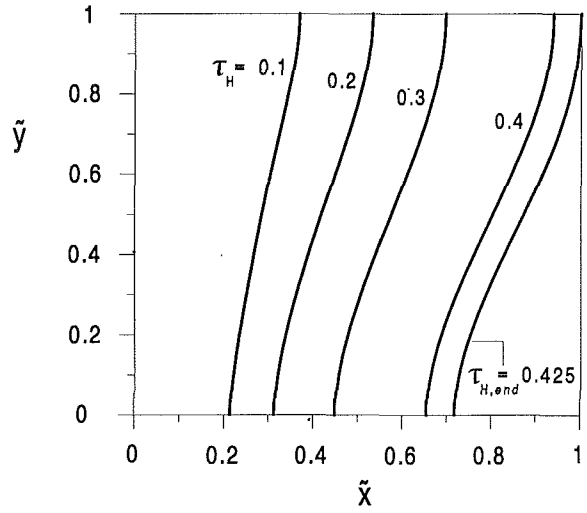

Fig. 6 The time evolution of the melting front, and the definition of the time of complete melting, $\tau_{H,\mathrm{end}}$ (Ra = 10, H/L = 1, S = 0.1, θ_m = 0.5)

Due to the small value of the latent heat parameter S, the most significant term that led to instability in the numerical method was the term that accounted for the unsteadiness of the domain, namely $(\xi/M)\cdot(\partial M/\partial\tau_H)\cdot(\partial\theta/\partial\xi)$, where ξ is the horizontal coordinate in the computational space ($0\le\xi\le1$ on the left side of the melting front, and a similar coordinate on the right side of the melting front). The time step was adjusted dynamically to keep this term smaller than a certain size. The maximum value for $[\partial M(\tilde{y},\tau_H)/\partial\tau_H]/M(\tilde{y},\tau_H)$, and the corresponding maximum in the region to the right of the melting front $[-\partial M(\tilde{y},\tau_H)/\partial\tau_H]/[1-M(\tilde{y},\tau_H)]$ were found. The τ_H step was set equal to the inverse of the largest of these terms times a user-determined fraction called FMF for short (FMF stands for "the front movement fraction"). Convergence tests showed that in most cases the value FMF = 1/200 was sufficient for 0.1 percent accuracy, but in some cases (e.g., when Ra < 5) the smaller value FMF = 1/400 was necessary. Tests also showed that retaining 15 terms in the expansion for $\tilde{\psi}$, Eq. (20), was sufficient for an accuracy better than 0.1 percent.

7 Numerical Results for Melting in the Presence of Natural Convection

The time-dependent flow and heat transfer modeled in the preceding section depend on four independent groups, Ra, H/L, S, and θ_m. This set shows that the phenomenon is more complex than natural convection in a porous medium saturated with a phase-change material, where there are only two groups, Ra and H/L, when the Stefan number is small (e.g., Jany and Bejan, 1988).

The effect of each of the four groups was investigated systematically by focusing on the main objective of this study, i.e., the calculation of the time of complete melting. The time $\tau_{H,\mathrm{end}}$ is defined in Fig. 6. The figure shows the evolution of the melting front in a square rectangular system, at a moderate Rayleigh number, and with a coating melting point halfway between the initial temperature and the temperature of the heated wall. The time of complete melting $\tau_{H,\mathrm{end}}$ is defined as the moment when the melting front first touches the insulated right-hand side of the system. In the particular case illustrated in Fig. 6, the melting front is more deformed and tilted than in a porous medium saturated with a phase-change material and at a similar Rayleigh number (examine Fig. 4 in Beckermann and Viskanta, 1988, or Fig. 10.3 in Nield and Bejan, 1992).

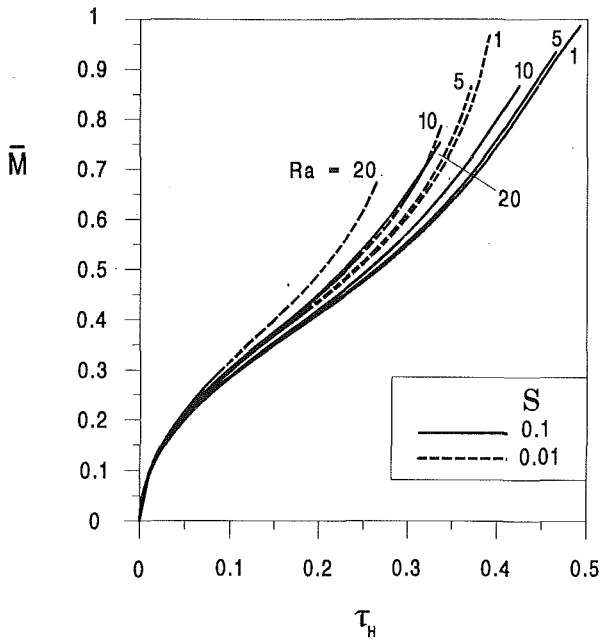

Fig. 7 The effect of the latent heat parameter S on the average melting front position and the time of complete melting ($H/L = 1$, $\theta_m = 0.5$)

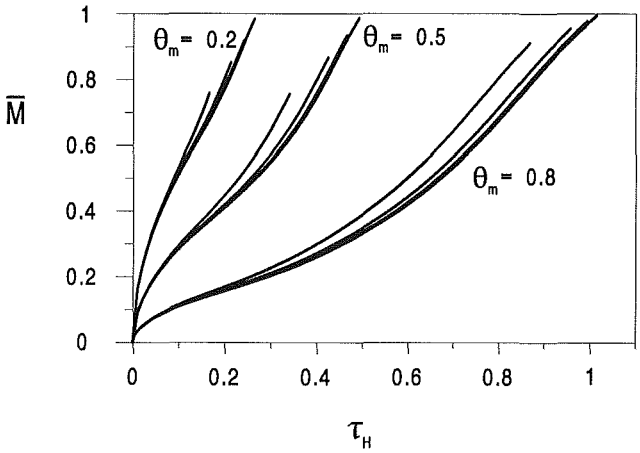

Fig. 8 The effect of the melting point parameter θ_m on the average melting front position and the time of complete melting ($H/L = 1$, $S = 0.1$)

Figures 7–9 illustrate the history of the average position of the melting front,

$$\overline{M}(\tau_H) = \int_0^1 M(\tilde{y}, \tau_H) d\tilde{y} \tag{23}$$

In each figure, the time of complete melting, $\tau_H = \tau_{H,\text{end}}$, is the point on the abscissa in line with the end of each $\overline{M}(\tau_H)$ curve. The inflection (S shape) of each curve is considerably more pronounced than in a porous medium saturated with a phase-change material (see, for example, Fig. 10.6 in Nield and Bejan, 1992).

The numerical work was based on an 81×81 grid for the liquid polyol region, and another 81×81 grid for the solid polyol region. The results obtained with these grids for $M(\tau)$ agreed within 0.1 percent with the corresponding results based on two 41 × 41 grids. The work was done on DEC 2000 workstations. Each computation required 4–6 hours.

The effect of the latent heat parameter S is documented in Fig. 7. A larger latent heat (i.e., larger S) means a longer time until the coating melts on the fibers located the farthest from the heated wall. The time of complete melting decreases sensibly as the Rayleigh number becomes greater than approximately 5.

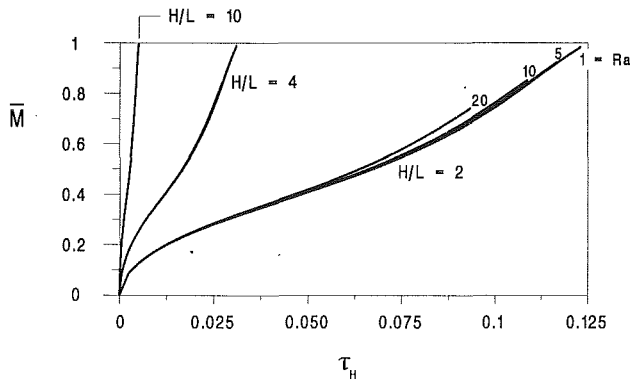

Fig. 9 The apparent effect of the geometric aspect ratio H/L, when $\overline{M}$ is plotted against τ_H

Figure 8 shows how $\overline{M}(\tau_H)$ and $\tau_{H,\text{end}}$ respond to changes in the dimensionless melting temperature θ_m. Three bundles of curves are shown, one bundle for each θ_m value. Each bundle contains four curves according to the Ra value (namely, 20, 10, 5, and 1, counting from the left). The θ_m effect is significant: The melting time increases steadily as θ_m increases, i.e., as the temperature difference $T_h - T_m$ becomes small. This trend agrees with what we saw in Figs. 2 and 4.

Figure 9 shows the effect of the geometric aspect ratio H/L. Three bundles of $\overline{M}(\tau_H)$ curves are shown, one bundle for each aspect ratio H/L. A fourth bundle, the one for $H/L = 1$, has been plotted in Fig. 7. Each bundle contains four curves that document the increase in the Rayleigh number from 1 to 20.

Expressed in terms of τ_H (i.e., in $\sigma H^2/\alpha_m$ units), the melting time $\tau_{H,\text{end}}$ decreases significantly as the aspect ratio H/L increases. This strong H/L effect is deceiving, for if $\tau = \alpha_m t/\sigma L^2$ is used instead of τ_H on the abscissa the three H/L bundles of curves fall almost on top of one another. In conclusion, at Rayleigh numbers smaller than 20 and aspect ratios greater than 1, the H/L effect is insignificant if $\overline{M}$ is plotted against τ. The universal bundle of curves that would result is nearly identical to the $H/L = 1$ bundle ($S = 1$, i.e., the solid lines) plotted in Fig. 7, where the abscissa parameter τ_H happens to be equal to τ.

The reason for the insignificant H/L effect on the melting time in increasingly taller spaces is that when Ra is small or moderate the heat transfer process becomes dominated by conduction in the horizontal direction. In the $H/L \to \infty$ and finite-Ra limit even the Ra effect becomes insignificant (note the tightening of the bundles as H/L increases in Fig. 9), and all the melting time estimates described in this section approach very closely the pure conduction results developed in Fig. 2.

8 Solidification in the Presence of Natural Convection

There is a perfect analogy between the problem of two-dimensional melting by natural convection, Fig. 5, and the problem of two-dimensional solidification by natural convection. In the latter, the $H \times L$ medium is initially isothermal and all the fibers are coated with liquid polyol, $T_i > T_m$. The temperature of one of the side walls is lowered suddenly to T_c, which is below the melting point. The remaining walls are insulated.

The air flow inhabits the entire $H \times L$ space, i.e., both sides of the solidification front. The movement of the solidification front is similar to that of Fig. 6; however, the shape of the

front is the mirror image of the shape shown in Fig. 6 (the "mirror" would be one of the horizontal boundaries). The time of complete solidification $\tau_{H,\text{end}}$ is defined in the same way, i.e., as the moment when the polyol coatings begin to solidify in the plane of the opposite (insulated) side wall. Figures 7–9 can be used to estimate the solidification time, provided θ_m is replaced now with the definition (14), and the air Rayleigh number Ra is defined by

$$\text{Ra} = \frac{Kg\beta(T_i - T_c)H}{\alpha_m \nu} \tag{24}$$

The existence of this analogy between melting and solidification is one more feature that distinguishes the present phenomena from the corresponding phenomena in a porous medium saturated with a phase-change material. In the latter such an analogy does not exist because the flow occurs on only one side of the phase-change interface (see, for example, Oosthuizen, 1988).

9 Conclusions

In this paper we have developed a homogeneous porous medium model for heat transfer through fibers coated with polyol and surrounded by air. We considered three basic heat transfer configurations, namely, one-dimensional conduction, one-dimensional forced convection, and two-dimensional natural convection. In each case, we identified the smallest number of important dimensionless groups, and their effect on system features such as the time of complete melting. The most important conclusions are the following:

1 In one-dimensional melting by conduction, Fig. 1, the dimensionless melting time τ_{end}, Eq. (8), depends on two numbers, the latent heat parameter S, Eq. (9), and the dimensionless melting temperature θ_m, Eq. (13). The function τ_{end} (S, θ_m) is displayed in Fig. 2.

2 In one-dimensional solidification by conduction, the solidification time can be estimated using Fig. 2 and the θ_m definition (14).

3 In one-dimensional melting by forced convection, Fig. 3, the dimensionless melting time τ_{end} depends on the Peclet number $\text{Pe} = uL/\alpha_m$, in addition to S and θ_m. The function $\tau_{\text{end}}(S, \theta_m, \text{Pe})$ is reported in Fig. 4.

4 The time of complete solidification by one-dimensional forced convection can be deduced from Fig. 4 by using the θ_m definition (14).

5 In melting by two-dimensional natural convection, Fig. 5, the important dimensionless groups are the air porous medium Rayleigh number Ra, Eq. (19), and the geometric aspect ratio H/L, in addition to S and θ_m. Graphic means for estimating the melting time as a function of S, θ_m, Ra, and H/L are presented in Figs. 7–9.

6 The time of solidification in the presence of two-dimensional natural convection can be estimated using Figs. 7–9, for which θ_m and Ra are defined in Eqs. (14) and (24).

7 For aspect ratios H/L of order 4 or greater, the results for two-dimensional natural convection are virtually identical to the results for one-dimensional conduction.

8 The phenomenon of natural convection phase change in the present medium (fibers coated with polyol and surrounded by air) differs fundamentally from melting and solidification in a porous medium saturated with a phase-change material.

Acknowledgments

This work was supported by the Electric Power Research Institute through contract No. RP 8006-4, and the Air Force Office of Scientific Research through contract No. F49620-92-J-0121.

References

Beckermann, C., and Viskanta, R., 1988, "Natural Convection Solid/Liquid Phase Change in Porous Media," *International Journal of Heat and Mass Transfer*, Vol. 31, pp. 35–46.

Bejan, A., 1984, *Convection Heat Transfer*, Wiley, New York, p. 353.

Bruno, J. S., and Vigo, T. L., 1987, "Thermally Active Fabrics Containing Polyethylene Glycols," *Journal of Coated Fabrics*, Vol. 16, pp. 264–274.

Carslaw, H. S., and Jaeger, J. C., 1959, *Conduction of Heat in Solids*, Oxford, Chap. 11.

Cheng, P., 1978, "Heat Transfer in Geothermal Systems," *Adv. Heat Transfer*, Vol. 14, pp. 1–105.

Gatica, J. E., Viljoen, H. J., and Hlavacek, V., 1989, "Interaction Between Chemical Reaction and Natural Convection in Porous Media," *Chemical Engineering Science*, Vol. 44, pp. 1853–1870.

Handa, T., Morita, M., Sugawa, O., Ishii, T., and Hayashi, K., 1983, "Computer Simulation of the Spontaneous Combusion of Coal Storage," *Fire Science and Technology*, Vol. 3, pp. 13–24.

Hansen, D., and Washo, B., 1967, "Molecular Weight and the Thermal Conductivity of High Polymers," *Kolloid-Zeitschrift und Zeitschrift für Polymere*, Vol. 210(2), pp. 111–112.

Hlavacek, V., and Votruba, J., 1977, "Steady-State Operation of Fixed-Bed Reactors and Monolithic Structures," *Chemical Reactor Theory, A Review*, L. Lapidus and N. R. Amundson, eds., Prentice-Hall, Englewood Cliffs, NJ, pp. 314–404.

Jany, P., and Bejan, A., 1988, "Scales of Melting in the Presence of Natural Convection in a Rectangular Cavity Filled With Porous Medium," ASME JOURNAL OF HEAT TRANSFER, Vol. 110, pp. 526–529.

Kazmierczak, M., Poulikakos, D., and Pop, I., 1986, "Melting From a Flat Plate Embedded in a Porous Medium in the Presence of Steady Natural Convection," *Numerical Heat Transfer*, Vol. 10, pp. 571–582.

Kazmierczak, M., Poulikakos, D., and Sadowski, D., 1987, "Melting of a Vertical Plate in Porous Medium Controlled by Forced Convection of a Dissimilar Fluid," *International Communications in Heat and Mass Transfer*, Vol. 14, pp. 507–517.

Kazmierczak, M., and Poulikakos, D., 1988, "Melting of an Ice Surface in a Porous Medium," *Journal of Thermophysics and Heat Transfer*, Vol. 2, pp. 352–358.

Kazmierczak, M., Sadowski, D., and Poulikakos, D., 1988, "Melting of a Solid in a Porous Medium Induced by Free Convection of a Warm Dissimilar Fluid," ASME JOURNAL OF HEAT TRANSFER, Vol. 110, pp. 520–523.

Nield, D. A., and Bejan, A., 1992, *Convection of Porous Media*, Springer-Verlag, New York, p. 212.

Oosthuizen, P. H., 1988, "The Effects of Free Convection on Steady-State Freezing in a Porous Medium-Filled Cavity," ASME HTD-Vol. 96, Vol. 1, pp. 321–327.

Schmal, D., Duyzer, J. H., and van Heuven, J., 1985, "A Model for the Spontaneous Heating of Coal," *Fuel*, Vol. 64, pp. 963–972.

Vigo, T. L., and Frost, C. E., 1982, "Temperature-Adaptive Hollow Fibers Containing Inorganic and Organic Phase Change Materials," *Thermal Analysis*, Proceedings of the Seventh International Conference on Thermal Analysis, Vol. 2, Wiley, New York, pp. 1286–1295.

Vigo, T. L., and Frost, C. M., 1983, "Temperature-Adaptable Hollow Fibers Containing Polyethylene Glycols," *Journal of Coated Fabrics*, Vol. 12, pp. 243–254.

Vigo, T. L., and Bruno, J. S., 1987, "Temperature-Adaptable Textiles Containing Durably Bound Polyethylene Glycols," *Textile Research Journal*, Vol. 57, pp. 427–429.

Vigo, T. L., and Bruno, J. S., 1989, "Improvement of Various Properties of Fiber Surfaces Containing Crosslinked Polyethylene Glycols," *Journal of Applied Polymer Science*, Vol. 37, pp. 371–379.

Journal of Heat Transfer

Technical Notes

This section contains shorter technical papers. These shorter papers will be subjected to the same review process as that for full papers.

Thermal Contact Conductance of a Moist Paper Handsheet/Metal Interface for Paper Drying Applications

M. C. Asensio,[1] J. Seyed-Yagoobi,[1] and L. S. Fletcher[1]

Nomenclature

BW = basis weight = (weight of air dry sheet/sheet area), g/m^2
h = heat transfer coefficient, W/m^{2}K
k = thermal conductivity, W/mK
MC = moisture content, dry basis = (weight of water/weight of dry fibers)
P = pressure, Pa
$\overline{R}^2$ = adjusted coefficient of determination
t = thickness of the material, m
$\overline{T}$ = average sheet temperature, °C
σ = standard deviation

Subscripts

eff = effective
i = interface
o, c = overall joint

Introduction

The most common paper drying system consists of a staggered array of 30 to 100 cylindrical cast-iron dryer drums. Paper is threaded around the dryer drums, which are internally heated by condensing steam, and conduction is the major mode of heat transfer to the paper sheet. One of the parameters affecting the overall drying rate is the thermal contact conductance between the cast iron dryer surface and the paper web. Yet few experimental data concerning the contact conductance between the dryer drum and paper web under various mill operating conditions have been published. Furthermore, there are very limited data available on contact conductance as a function of sheet moisture content.

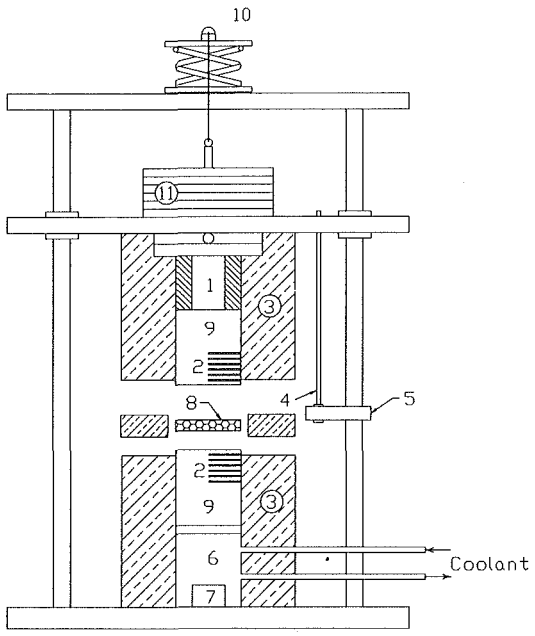

1 Electric Band Heater
2 Thermocouples
3 Insulation
4 LVDT Core
5 LVDT Coil
6 Cooling Section
7 Load Cell
8 Paper Sheet
9 Cast Iron Flux Meter
10 Scissor Jack
11 Weights

Fig. 1 Thermal contact conductance measurement apparatus

Most simulation models for conventional steam-heated dryer systems are based on energy and mass balances within the sheet. Therefore, an estimate of the heat input to the sheet across the paper web/cast iron dryer drum interface is needed for the entire dryer section. This paper is a continuation of a previous study by Seyed-Yagoobi et al. (1992a), which considered only bone-dry paper samples. Here, a correlation for the contact conductance as a function of handsheet moisture content is developed for incorporation into an existing paper drying simulation model (Seyed-Yagoobi et al., 1992b; Asensio and Seyed-Yagoobi, 1992).

Experimental Program

The details of the experimental contact conductance apparatus used to measure the overall joint conductance of a paper sample placed between two cast iron flux meters and the associated data analysis were given by Seyed-Yagoobi et al. (1992a) and Asensio (1992). The experimental apparatus, shown in Fig. 1, consists of two flux meters, a heat source and a heat

[1]Department of Mechanical Engineering, Texas A&M University, College Station, TX 77843-3123.

Contributed by the Heat Transfer Division of The American Society of Mechanical Engineers. Manuscript received by the Heat Transfer Division November 1992; revision received April 1993. Keywords: Conduction, Direct-Contact Heat Transfer, Measurement Techniques. Technical Editor: R. Viskanta.

sink, a temperature measurement system, a loading system, a paper sample thickness measurement system, and a mechanism for raising the top half of the assembly.

Handsheets were prepared with several different basis weights and moisture contents using a standard procedure (TAPPI, 1988). The desired moisture contents were achieved by drying the samples in a microwave oven prior to the experiments. Moisture loss from the sheets during each experiment was limited by transparent polyester film tape, 3M Scotch brand No. 850, wrapped around the outer edge of the paper gap between the two flux meters. The low vapor transmission rate (24.8 g $H_2O/m^2/24$ h at $-50°C \leq T \leq 177°C$) of the tape allowed the overall mass of moisture between the flux meters to remain fairly constant. During initial sheet warm-up, there was a redistribution of the moisture within the sheet due to the sheet temperature gradient. Once a steady-state condition had been achieved, the moisture content profile approached a steady-state case.

Steady-state measurements were recorded during each experiment, including elapsed time since load increase, applied load, handsheet thickness, sample density, and temperature profiles in the upper and lower flux meters. Calculated results included intercept temperatures and heat fluxes (for the upper and lower flux meters); average sample temperature and temperature drop across the sample; and overall joint conductance and uncertainty in overall joint conductance measurements. Flux meter temperature gradients, derived from a least-squares linear regression of six temperature measurements within each flux meter, were used to predict the upper and lower paper handsheet/metal interface temperatures. The temperature drop across the handsheet was considered to be the difference in the two interface temperatures while the average handsheet temperature was taken as their average. Heat fluxes through both meters were computed based on the flux meter thermal conductivity (previously calibrated) and the temperature gradient within each flux meter. The overall joint conductance between the two interfaces and interfacial handsheet was calculated by dividing the average heat flux (of the top and bottom flux meters) by the total temperature drop across the sheet. The uncertainty associated with any single overall joint conductance measurement was a function of the uncertainty in measurements of the temperature profile ($\pm 0.05°C$), thermocouple placement (2.54×10^{-4} mm), and thermal conductivity of the flux meters (0.50 W/mK). The uncertainty in the overall joint conductance measurements ranged from 4.70 to 4.77 percent and averaged 4.74 percent for all experimental data.

Results and Discussion

Unbleached Southern Pine handsheets composed of 80 percent softwood/20 percent hardwood with a water retention value of 1.92 was considered. Samples with basis weights of approximately 90, 150, and 300 g/m^2 and dry basis moisture contents of 5, 50, 100, and 150 percent were used in the experiments. The thickness variation per sample for all the samples used was less than 5 percent. Interface temperatures of approximately 130°C and 40°C were sustained throughout the course of an experiment, resulting in an average paper sample temperature of 85°C. Data analysis included development of a linear model to represent the experimental overall joint conductance data as a function of the dependent variables: pressure, sample basis weight, and thickness. The interface thermal contact conductance and the effective thermal conductivity of each handsheet were then simultaneously derived from this model.

The best-fit linear model of all overall joint conductance data was:

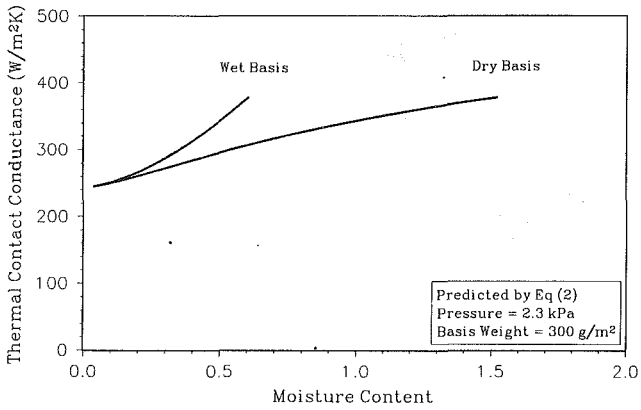

Fig. 2 Predicted effect of moisture content on the interface contact conductance for a paper/metal interface

$$h_{o,c} = 89.07 - 1.90\ln(P) + \frac{10259}{BW} + 12.95\left(\frac{MC}{1+MC}\right)^2 \ln(P) - \frac{9071.4}{BW}\left(\frac{MC}{1+MC}\right)^{5/4} + 170.11\left(\frac{MC}{1+MC}\right)^{3/2} - 27.09t - \frac{10218t}{BW} \quad (1)$$

where, based on the operating conditions of the experiments and the samples used, $0.68 < P \leq 328.81$ kPa, $84.0 \leq BW \leq 312.9$ g/m^2, 5 percent $\leq MC \leq 150$ percent, $0.27 \leq t \leq 2.23$ mm, $\bar{T} = 85°C$, $\sigma = 10.7$ W/m^{2}K (9 percent), and $\bar{R}^2 = 0.93$. The multiple regression of the overall joint conductance on handsheet thickness, basis weight, applied load, and moisture content contained regression estimators that were statistically significant at a 5 percent significance level. Furthermore, each model was corrected for multicollinearity among the variables and time-series autocorrelation between the observations.

The above model is primarily valid for the type of fibers used in the samples since the joint conductance is related to sample surface smoothness and density, which to some extent are dependent on fiber type and composition. However, in a similar study, an investigation was conducted to determine the effect of handsheet composition on the joint conductance by considering handsheets of four different compositions at the same basis weight. The results indicated that the handsheet composition had less effect on the joint conductance than what would be expected (Asensio et al., 1991).

Assuming equal contact conductance at the top and bottom interfaces, the predicted contact conductance values are equal to twice the overall joint conductance at a handsheet thickness of zero, or:

$$h_i = 178 - 3.8\ln(P) + \frac{20518}{BW} + 25.9\left(\frac{MC}{1+MC}\right)^2 \ln(P) - \frac{18142.8}{BW}\left(\frac{MC}{1+MC}\right)^{5/4} + 340.22\left(\frac{MC}{1+MC}\right)^{3/2} \quad (2)$$

The interface contact conductance predicted by Eq. (2) is shown in Fig. 2 as a function of moisture content for a sheet of 300 g/m^2 and an applied load of 2.3 kPa. Paper passed around conventional 1.52 m (5 ft) diameter dryer drums typically has a felt tension of 0.525 to 1.75 kN/m (3 to 10 lb/in.) of machine width, which results in an applied normal load of approximately 0.69 to 2.3 kPa (0.1 to 0.33 psi) on the web.

Although the top and bottom interfaces have different characteristics, prediction of interface contact conductances from measured values of overall joint conductance requires the as-

sumption of equal contact conductances at the two interfaces (Seyed-Yagoobi et al., 1992a). The top interface temperature is higher than the temperature of the bottom interface. The effect of temperature on contact conductance of handsheet samples has been previously investigated for average sheet temperatures of 68, 85, and 103°C, indicating that the contact conductance will increase with increasing temperature (Asensio et al., 1991).

In conjunction, though, the presence of moisture at the interface will also affect the contact conductance. A theoretical examination of the water and vapor diffusion within the sheet located between the two flux meters was performed (Asensio, 1992). Analysis of the heat and mass transfer occurring within the sheet indicated that a slight, nonuniform moisture content profile through the sheet thickness existed continuously during the steady-state period of each experiment. While the total amount of water contained between the two flux meters remained constant, the water within the sheet would diffuse to the top flux meter, evaporate and then condense on the bottom flux meter surface during the course of an experiment. Condensation was observed on the bottom flux meter following sheet removal for weighing. The amount of condensate was a function of the moisture content level of the sheet. Because the conductivity of water (0.673 W/mK at 85°C) is much greater than the conductivity of air (0.0306 W/mK at 85°C), the thin layer of condensate at the lower flux meter increased the heat transfer across the bottom interface. Therefore, under the experimental operating conditions, differences in temperature and moisture at the top and bottom interfaces may offset each other, allowing the contact conductance to be considered similar at the two interfaces.

Contact conductance will increase with increasing pressure, decreasing basis weight, and increasing moisture content levels. As the applied pressure increased, the handsheet/metal contact area increased, yielding increased heat transfer across the interface. At lower basis weights, the interfacial contact area increased due to smoother or more uniform sheet surfaces (observed visually) for the handsheet samples considered. The contact conductance was also enhanced by softer handsheet fibers at higher moisture levels since softer fibers provided a better effective contact area between the handsheet and flux meter surfaces. Differences in thermal softening of the handsheet fibers due to different interface temperatures were assumed to be negligible.

The predicted values of interface contact conductance are somewhat lower than some previously published contact coefficients summarized by Seyed-Yagoobi et al. (1992a). Differences can be attributed to the basis weight and composition of the paper under consideration as well as handsheet surface roughnesses greater than the asperity of paper sheets considered in other studies. Most contact conductance and paper thermal conductivity studies used actual machine paper samples collected either after the press section or at the end of the dryer section (Seyed-Yagoobi et al., 1992a).

The effective thermal conductivity of the handsheet samples can be determined as follows (Seyed-Yagoobi et al., 1992a):

$$k_{\text{eff}} = \left(\frac{1}{h_{o,c}} - \frac{2}{h_i}\right)^{-1} t \tag{3}$$

where $h_{o,c}$ and h_i are given by Eqs. (1) and (2). These predicted conductivity values for all the handsheets under consideration are shown as a function of handsheet density in Fig. 3, where the moist handsheet density has been calculated as the weight of the moist handsheet divided by sample area and moist handsheet thickness. For this study, increases in handsheet density were the result of decreases in sample thickness caused by increases in the applied load.

The predicted handsheet effective thermal conductivity ranges from 0.06 W/mK to 0.54 W/mK for sheet densities

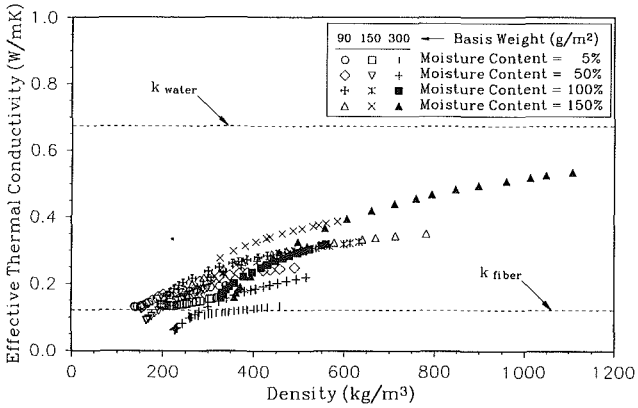

Fig. 3 Predicted effective thermal conductivity of moist unbleached Southern Pine handsheets

ranging from 137 kg/m^3 to 1108 kg/m^3 for all samples considered. A requirement during the development of the regression model for overall joint conductance was that the predicted conductivities lie between the conductivities of fiber (0.12 W/mK) and water (0.68 W/mK). The effective thermal conductivity of the paper samples increases with increasing handsheet density because of the decrease in air within and between the fibers of the handsheet. At a constant basis weight, the effective thermal conductivity of a moist handsheet increases slightly with increasing moisture content due to the greater conductivity of water. However, this smaller than expected contribution of moisture levels to thermal conductivity may be partially attributed to moisture condensation out of the sheet during the experiments. In addition, migration of liquid and vapor through the sheet coupled with evaporation near the hotter interface and condensation near the cooler interface could, in some instances, create a heat pipe effect within the sheet, yielding relatively high values of paper thermal conductivity.

Acknowledgments

This research was funded by an Award for Creativity in Engineering from the Division for Engineering Infrastructure Development, National Science Foundation. Additional support was provided by the Texas Drying Research Consortium, funded by the Energy Research Applications Program, Texas Higher Education Coordinating Board, and by the Beloit Corporation Research and Development Center.

References

Asensio, M. C., Seyed-Yagoobi, J., Ng, K. H., and Fletcher, L. S., 1991, *Thermal Contact Conductance of a Paper Handsheet/Metal Interface*, ME-CHTL-90-6698, Texas A&M University, College Station, TX.

Asensio, M. C., 1992, "Simulation of Paper Drying Systems With Incorporation of an Experimental Drum/Paper Thermal Contact Conductance Relationship," M.S. Thesis, Texas A&M University, College Station, TX.

Asensio, M. C., and Seyed-Yagoobi, J., 1992, "Further Analysis of Heat and Mass Transfer in a Paper Sheet During Drying," *Fundamentals of Heat Transfer in Porous Media*, ASME HTD-Vol. 193.

Seyed-Yagoobi, J., Ng, K. H., and Fletcher, L. S., 1992a, "Thermal Contact Conductance of a Bone-Dry Paper Handsheet/Metal Interface," ASME Journal of Heat Transfer, Vol. 114, pp. 326–330.

Seyed-Yagoobi, J., Bell, D. O., and Asensio, M. C., 1992b, "Heat and Mass Transfer in a Paper Sheet During Drying," ASME Journal of Heat Transfer, Vol. 114, pp. 538–541.

Technical Association of Pulp and Paper Industries (TAPPI), 1988, "Forming Handsheets for Physical Tests of Pulp," Procedure T 205, Atlanta, GA.

Thermal Analysis and Structural Modifications in an Electrical Card-to-Cold Plate Wedge Clamp

H. Kalman[1] and E. Berman[2]

Nomenclature

a = clamp surface length in contact with the electrical card
b = clamp surface length in contact with the cold plate
c = clamp thickness
e = clearance between clamp and cold plate
F = tension force acting on the screw
h = clamp width
h_c = thermal contact conductance of joint
k = thermal conductivity of the clamp material
K = mean length ratio of clamp parts
L = total clamp length
P = pressure
P_1, P_2, P_3 = contact pressure between clamp and cold plate, clamp and electrical card, parts of clamp
q'' = heat flux through the clamp
R_{th} = thermal resistance
S = shape factor
T = temperature
α = slope angle of contact surface between clamp parts
ΔT = temperature drop across the clamp

1 Introduction

In electrical packaging the heat is transferred from the source (the electrical device) to the sink (usually the environment) along different paths and by different heat transfer mechanisms. Due to the reduction of size and increased heat rates of electrical devices that have taken place during recent years, new technologies and mechanisms have been partially applied, such as immersion cooling, boiling, heat pumps, etc. Nevertheless, the main mechanism used for most electrical equipment is still a combination of conduction and natural or forced convection (due to its simplicity). In order to keep the devices at a reasonably low working temperature, the heat has to be removed to the surrounding as efficiently as possible. Most of the heat from the devices flows to the card's base (cold plate) through conduction strips and from there to the enclosure.

The relevance of reducing thermal resistance is to decrease the operating temperature of the devices, thereby increasing their reliability and enabling use of cheaper devices. Therefore, it is important to examine carefully the possibilities of reducing thermal resistance at every stage. In this paper the thermal performance of a typical wedge clamp is analyzed. This widely used clamp is shown in Fig. 1. The clamp is inserted into the gap between the card and the cold plate. By fastening the screw, the parts of the clamp are pushed in opposite directions due to the slope that lies between them and the card is fastened to the cold plate.

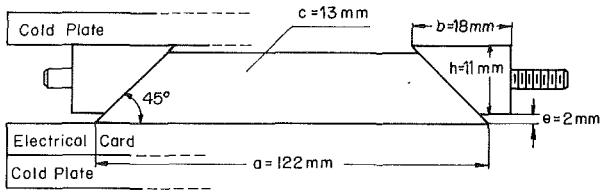

Fig. 1 Calmark's standard clamp with dimensions (Calmark Corporation, 1985)

Although most of the heat could be transferred from the card to the cold plate directly through the contact surface (on the other side of the clamp), at least some of it is transferred through the clamp. It is not easy to define the ratio of heat dissipation through the clamp to direct heat dissipation to the cold plate since it depends on many parameters and can be found only if a detailed analysis of the system is performed. Although the ratio is obviously less than one, the following analysis is useful.

The heat flows through the clamp from the long surface that is in contact with the card to the short surfaces that are in contact with the cold plate. A number of factors affect the thermal performance of the clamp: structural geometry (dimensions, slope angle, clearance between the card and the cold plate, etc.), thermal characteristics (thermal conductivity, dissipated heat rate, sink temperature, etc.), and contact resistance (surface roughness, fastening pressure, surface coating, etc.). Most of these factors will be considered later on.

2 The Basic Model

The analysis was carried out using ANSYS software (Joing, 1986) that can solve complicated one, two, and three-dimensional problems in strength of materials, fluid mechanics, and heat transfer by the finite element method. In order to simplify the actual case, the heat flow through the clamp was assumed to be two dimensional. It was further assumed:

1 The peripheral surfaces, except the contact surfaces with the card and the cold plate, are insulated.
2 The clamp is solid with no holes.
3 The thermal conductivity is constant.
4 All clamp parts are made of the same material.
5 The heat flux is constant on surface (a).
6 The cold plate is isothermal.

Different types of clamps, in respect to dimensions, materials and so on, are commercially available. The wedge clamp (card-lok) shown in Fig. 1 (Calmark Corporation, 1985) chosen for the analysis has the following dimensions: 11 mm width (h), length of the surface in contact with the card (a) is 122 mm, length of each of the surfaces in contact with the cold plate (b) is 18 mm, the thickness (c) is 13 mm, the slope angle between parts is 45 deg and the short parts (b) are shifted from the long part (a) by e = 2 mm. The conductivity of the clamp is k = 150 W/m°C, the heat rate coming from the card is 10 W, and the temperature of the cold plate is 50°C. This standard clamp is one of the largest available commercially and was chosen as the basic model for the analysis in order to achieve a higher temperature drop. However, the dimensions and the operating conditions of the basic model cannot possibly affect the nature of the analysis or the conclusions.

To analyze the clamp, described in Fig. 1, by ANSYS software, it was divided into six surfaces and about 600 elements. When dividing the clamp, care must be given to the continuity of the elements at the different surfaces. The analysis was done interactively, varying one of the influencing parameters while keeping the others constant. In this way, models of the clamp

[1]Pearlstone Center for Aeronautical Engineering Studies, Department of Mechanical Engineering, Ben-Gurion University of the Negev, Beer Sheva 84105, Israel.
[2]CAD/CAM/CAE Department, Computation Center, Ben-Gurion University of the Negev, Beer Sheva 84105, Israel.

Contributed by the Heat Transfer Division of THE AMERICAN SOCIETY OF MECHANICAL ENGINEERS. Manuscript received by the Heat Transfer Division July 1992; revision received April 1993. Keywords: Augmentation and Enhancement, Computer Codes, Conduction. Associate Technical Editor: L. S. Fletcher.

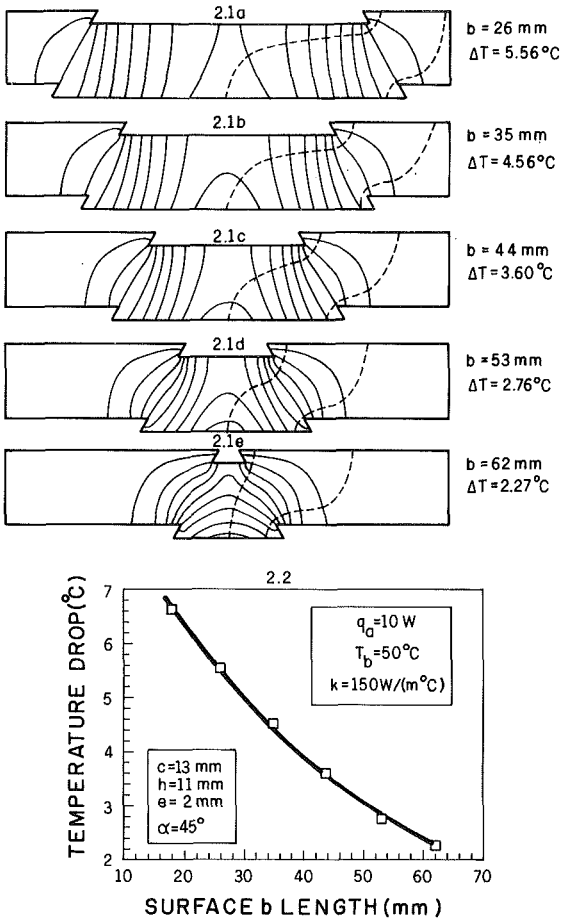

Fig. 2 The effect of the surface length connected to the cold plate on the temperature drop over the clamp

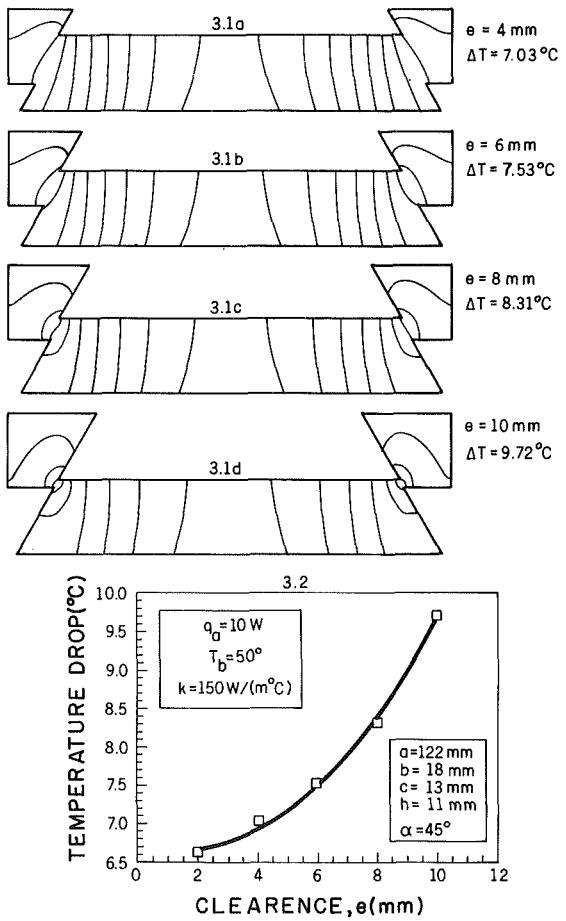

Fig. 3 The effect of the clearance between the clamp and the cold plate on the temperature drop

that deviate only by one parameter are defined so that the effect of this parameter can be examined.

The thermal contact resistance between parts of the clamp will be considered in a separate section. It was omitted here by assuming that the clamp is made of one piece.

3 Performance Analysis of the Clamp

Models of the clamp, each differing by one parameter, were defined based on the interactive method. In this section, the effects of the different parameters are examined. The linear dependence of the temperature drop on the heat flux (defined by models that are not shown here) can be described by the following equation:

$$\Delta T = q'' R_{th} \tag{1}$$

from which the thermal resistance of this clamp was calculated: 1.05×10^{-3} °C/W. The inverse dependence of the temperature drop on the thermal conductivity (previously observed in plots not shown here) can also be described by a common equation:

$$\Delta T = \frac{q'' S}{k} \tag{2}$$

where S is the shape factor (Holman, 1989) and equals 0.01 m. It should be emphasized that increase in heat flux is achieved by either increasing the heat rate coming from the card or by decreasing the clamp thickness.

Standard clamps adjust the contact surfaces so that the surface in contact with the card is always larger than the surfaces in contact with the cold-plate. Six models having the same constant parameters are shown in Fig. 1, except for the length of the surface in contact with the cold plate (b), which is increasing, and the length of the surface in contact with the card (a) is decreasing in order to keep the total clamp length constant. The lengths of (b) are 18, 26, 35, 44, 53, and 62 mm.

By running each model through the ANSYS software, the isotherms shown in Fig. 2.1 were obtained. The basic model is repeated several times and is shown only once in Fig. 4.1(c). For each of the models nine isotherms were plotted, except for the isotherm of the surface in contact with the cold plate. The temperature difference between each isotherm is 1/9 of the total temperature drop indicated beside each model on Fig. 2.1. The temperature difference between the coldest isotherm (the contact surfaces to the cold plate) and the nearest isotherm, and between the hottest point (the center of the contact surface to the card) and the nearest isotherm, is 1/18 of the total temperature drop.

The results of Fig. 2.1 are presented in Fig. 2.2 and show the decreases of the temperature drop as surface (b) increases. In all the models of Fig. 2.1, the heat rate to surface (a) was kept constant, and furthermore, as surface (a) decreased, the heat flux increased. Nevertheless the total temperature drop decreased. This phenomenon can be explained only because of the shortness of the heat-flow path.

To emphasize this phenomenon, two lines describing the heat-flow path were added to Fig. 2 (manually), one at the center of the surface and one at its edge. Between these lines, half of the heat rate (5 W) is transferred. It can be seen that the extreme line remains almost constant but the left line is

shortened. Therefore, the average path lines are shortened so that the thermal resistance as well as the temperature drop decrease. Figure 2 also shows that as surface (b) increased, growing areas at the edges are isothermal. Therefore, the shortness of the heat path is stabilized as can also be seen in Fig. 2.2.

In Fig. 3 the operating condition is examined, namely, the effect of the clearance between the clamp and the cold plate that should be bridged by moving away the parts of the clamp on the temperature drop over the clamp. As the clearance increases, surfaces (b) become more distant from surface (a), causing a heat transfer bottleneck at the constant surfaces of the clamp's parts. Figure 3.1 shows the isotherms of models with different clearances (2, 4, 6, 8, and 10 mm). In Fig. 3.1 (a) the isotherms are almost uniformly distributed, but as the clearance increases they become more concentrated at the contacts between the parts. The results of the temperature drop over the clamp of the models are presented in Fig. 3.2, demonstrating the increase of the temperature drop as the clearance increases.

Obviously the last models in Fig. 3.1 are exaggerated and not practical. Calmark, however, recommends applying clamps with clearance of 15–20 percent of the clamp's width, which in our case is about 2 mm. Nevertheless, Fig. 3 emphasizes the risk in temperature drop the designer takes where there is no minimum clearance.

In Fig. 4.1, eight models are shown in which the effect of the slope angle of the contact surface between the parts of the clamp on the temperature drop is examined. In all models, the length of surface (a) was kept constant, but surface (b) was decreased by increasing the slope angle. The results are presented in Fig. 4.2. It is clear from Fig. 4.2 that the temperature drop decreases sharply as the slope angle is reduced. The main reason for this phenomenon is obvious from Fig. 4.1. The heat flow paths become longer as the slope angle is increased. This is due to two reasons: the shortness of the surfaces (b) and the reduction of the contact surfaces between the parts of the clamp.

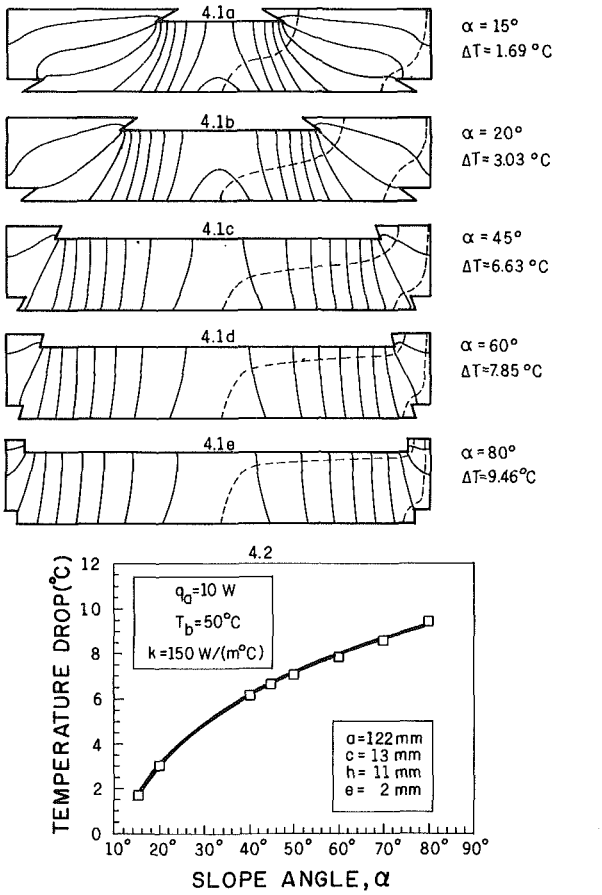

Fig. 4 The effect of the slope angle between the parts of the clamp on the temperature drop

4 Contact Resistance

This section takes into account the phenomenon of contact resistance that was omitted in the previous analysis. The main factors that affect contact resistance are: solid materials, fluid in the void space, surface roughness, and pressure between contacting surfaces. There are two more zones of contact resistance, which are beyond the scope of this paper: the contact of surface (a) with the electric card, and the contact of surfaces (b) with the cold plate. Increasing the contact pressure within the clamp can be achieved only by tightening the screw, which also increases the pressure between the clamp and the electric card or the cold plate.

Tightening the screw affects the three contact pressures differently. The contact pressure between the surfaces depends on the slope angle, the lengths of surfaces (a) and (b), etc. With simple force balance and geometry the contact pressures are defined as:

$$P_1 = \frac{2F\cot(\alpha)(K+1)}{Kc[L+2h\cot(\alpha)]} \tag{3}$$

$$P_2 = \frac{2F\cot(\alpha)(K+1)}{c[L+2h\cot(\alpha)]} \tag{4}$$

$$P_3 = \frac{F}{(h-e)c} \tag{5}$$

where P_1 and P_2 are the contact pressures of the clamp on the cold plate and the electric card, respectively, P_3 is the contact pressure between the parts of the clamp, F is the tension force on the screw, and K is the surface length ratio $2b/a$. The length L of the clamp is given for each specific system. A reasonable requirement concerning contact resistance is the presence of equal contact pressures, thus $P_1 = P_2 = P_3$. This requirement, derived from Eqs. (3)–(5), yields $K = 1$ and $\alpha < 45$ deg, which do not even approximate the given data on the analyzed clamp. Furthermore, substituting the given data on the analyzed clamp (including K and α) yields $P_1 \cong 0.5\,P_3$ and $P_2 \cong 0.15P_3$. The pressure between the parts of the clamp is the highest found in the system and therefore its contact resistance is the lowest. Nevertheless, the following analysis is concerned only with the effect of this contact resistance.

The thermal contact resistance between surfaces is affected mainly by solid properties, surface roughness, and contact pressure. Therefore, it can be reduced by increasing the pressure (tightening the screw), polishing the contact surfaces, and adding thermal grease between the parts. In order to examine the effect of contact resistance on the temperature drop, models in which a 1 μm thickness of various conductivities was inserted at the contact surfaces to simulate the contact resistance. The models and the isotherms are shown in Fig. 5.1 and the results in Fig. 5.2. The thermal resistance is determined in terms of h_c.

The models in Fig. 5.1 emphasize the behavior of the clamp due to changes in contact thermal resistance. Nine isotherms were plotted in each model. For the models with high thermal contact resistance only some of the isotherms appear on the plot. The rest are concentrated at the contact surface over which is the main temperature drop. The temperature drop over the clamp decreases as the contact resistance decreases until it is stabilized on the value of the temperature drop over a "one-piece" clamp having no contact resistance. The real

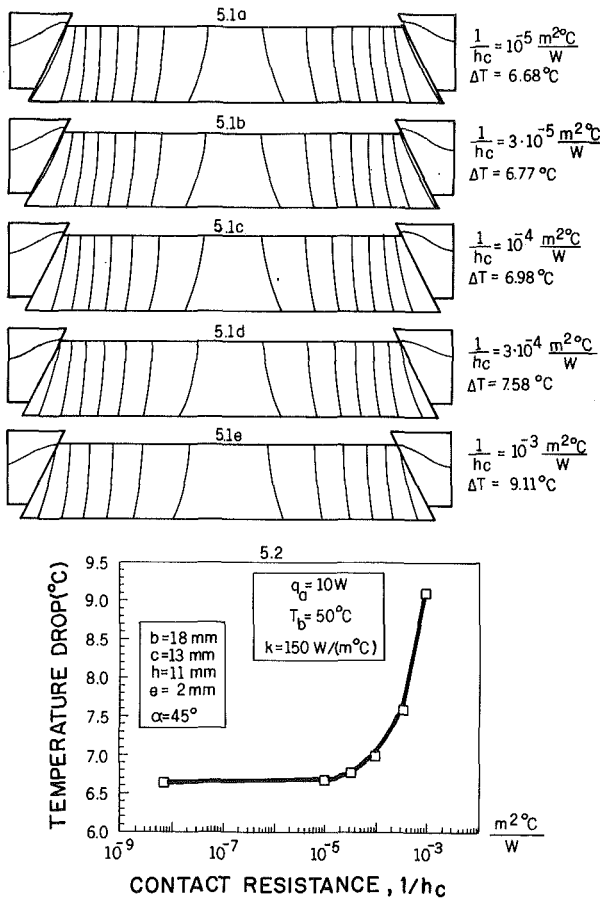

Fig. 5 The effect of thermal contact resistance between the parts of the clamp on the temperature drop

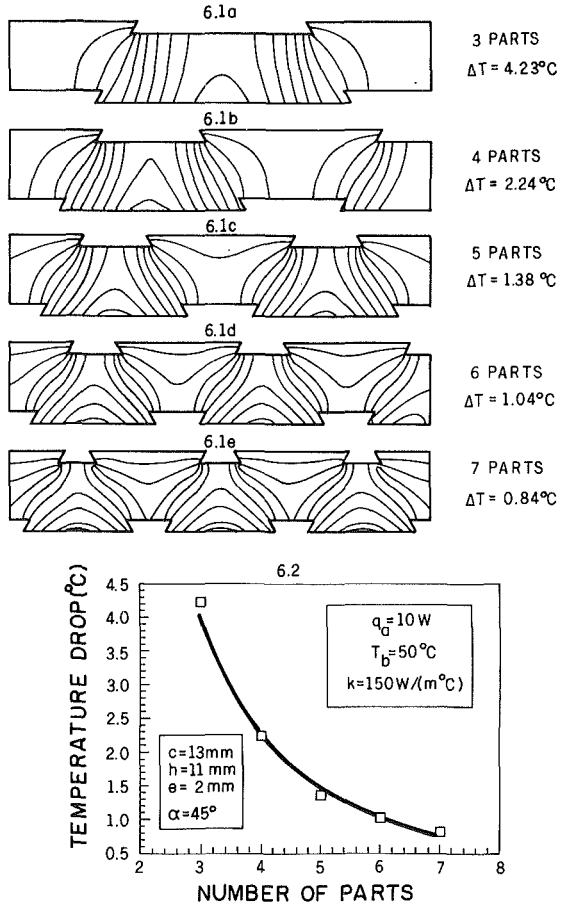

Fig. 6 The temperature drop of a multipart clamp

values of contact resistance in terms of $1/h_c$ appear from 10^{-5} to 10^{-3} $m^2°C/W$ for various surfaces contacting in air (Holman, 1989). Coating the surfaces with thermal grease can omit the need for high contact pressure or very smooth surfaces, as can be seen in Fig. 5.2. It should be emphasized that when contact resistance with the card and the cold plate are taken into account, the overall reduction of the temperature drop in Figs. 5 and 6 (later on) is expected to be less. This does not affect the basic behavior, however.

5 Structural Modifications

Numerous modifications can be made to reduce the temperature drop over the clamp to a minimum. All these modifications are described in the previous sections and can be divided into two categories: operational and structural. The operational modifications can be done by either decreasing gap (e), or coating the contact surfaces with thermal grease. Structural modifications all consist of shortening the heat flow path. This improvement can also be achieved by dividing the clamp into more than three parts.

The effect of a multipart clamp is examined in Fig. 6. It is assumed that thermal greases are used, and therefore the contact resistance in these models is negligible. To compare the models, the length of the clamp was kept constant. The lengths of the edge parts, at the middle height, were determined to be half of the center parts at the same position. Therefore, the three-part clamp shown in Fig. 1 is not the basic one; surface (a) is decreased while surface (b) is increased. These changes, however, were already examined in Fig. 2.

By reducing surface (a) from 122 mm to 83.6 mm and increasing surface (b) from 18 mm to 41.8 mm, the temperature drop decreases from 6.6°C to 4.2°C. Furthermore, the temperature drop over the clamp is reduced to 2.2°C by dividing it into four parts—100 percent improvement (relating to 4.2°C)—and 0.8°C for 7 parts—525 percent improvement. The significant thermal improvement is supported by one more benefit concerning design and production. By producing only two types of part (edge and center), varieties of lengths are achieved by combining three and more parts.

6 Conclusions

The behavior of a Calmark clamp was analyzed in this paper by ANSYS. One standard Calmark's clamp was chosen for the parametric study and analysis without loosing from the generality. The temperature drop over the clamp was chosen as a baseline for the performance of the clamp. It was shown that increasing the surface (b), decreasing the slope angle (α), decreasing the clearance (e), and reducing the contact resistance (by increasing the contact pressure or smoothing the contact surfaces), all reduce the temperature drop. It was shown without a doubt that the available structure of the clamp is far from being optimal and can be improved significantly. On the basis of the thermal analysis, a multipart clamp that can decrease the temperature drop more than five times has been suggested.

References

Calmark Corporation, 1985, Electronic Packaging Products.

Carslaw, H. S., and Jaeger, J. C., 1959, *Conduction of Heat in Solids*, Oxford Press, United Kingdom.

Holman, J. P., 1989, *Heat Transfer*, McGraw-Hill, New York.

Joing, F., 1986, User's Manual ANSYS.

A Scale Analysis Approach to the Correlation of Continuous Moving Sheet (Backward Boundary Layer) Forced Convective Heat Transfer

A. M. Jacobi[1]

Nomenclature

C_∞ = an order unity constant used in Eq. (7)
C_0 = an order unity constant used in Eq. (10)
h = local heat transfer coefficient, W m^{-2} K^{-1}
k = thermal conductivity of the fluid, W m^{-1} K^{-1}
Pr = Prandtl number = ν/α
Re_x = Reynolds number $U_s x/\nu$
T = temperature in the flow, K
U_s = moving surface velocity, ms^{-1}
u = flow velocity in the streamwise direction (x), ms^{-1}
v = flow velocity in the transverse direction (y), ms^{-1}
x = streamwise boundary layer coordinate (see Fig. 1), m
y = transverse boundary layer coordinate (see Fig. 1), m
α = thermal diffusivity, m^{2}s^{-1}
ΔT = temperature difference = $(T_s - T_\infty)$, K
δ_T = thermal boundary layer thickness, m
δ_V = velocity boundary layer thickness, m
ν = kinematic viscosity of the fluid, m^2 s^{-1}

Introduction

Continuous sheet heat transfer has many important applications; examples may be found in glass fiber production, metal extrusion, paper production, and roofing manufacturing. Notwithstanding considerable attention, there is no generally applicable correlation for backward boundary layer heat transfer.

The physical situation was recognized as a backward boundary layer by Sakiadis (1961), who analyzed the hydrodynamics. The thermal behavior was examined through an approximate integral analysis by Erickson et al. (1966), who found that for high Prandtl numbers, $\mathrm{Nu}_x/\sqrt{\mathrm{Pr}\,\mathrm{Re}_x} = 0.53$. Using a similarity transformation with a numerical approach, Tsou et al. (1967) explored the heat transfer behavior at Prandtl numbers of 0.7, 1.0, 10, and 100. Their numerical predictions for a constant temperature surface in laminar flow differed from those of Erickson et al. by nearly 30 percent at a Prandtl number of 0.7.

Conjugate convection and conduction for continuous moving cylinders and sheets has been studied (Chida and Katto, 1976), as have buoyancy effects on horizontal and vertical sheets (Chen and Strobel, 1980; Moutsoglou and Chen, 1980). The effects of a variable surface temperature and surface stretching were studied by Soundalgekar and Murty (1980), Grubka and Bobba (1985), and Jeng et al. (1986). Curve fits to numerical data, valid over a limited Prandtl number range, were provided by Ramachandran et al. (1987). These correlations, although useful for moderate Prandtl numbers, do not properly reflect the physics of the Pr effect, and are not applicable over the entire Pr range of interest.

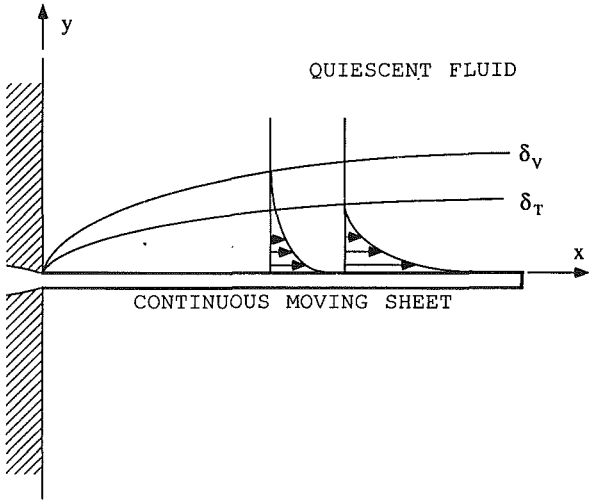

Fig. 1 A schematic showing the backward boundary layer flow, the coordinate system, and the relevant length scales for this physical situation

Recently, numerical studies including the effects of buoyancy, radiation, and conjugate conduction have been reported by Karwe and Jaluria (1988, 1991) and Kang et al. (1991). The effects of magnetic fields have been reported (Kumari et al., 1990; Murty, 1991), and so has the impact of a temperature-dependent viscosity (Pop et al., 1992). Experimental results for a conducting plate with opposing or assisting natural convection were recently reported by Karwe and Jaluria (1992).

There is considerable current interest in backward boundary layer behavior, due to its importance in manufacturing processes. The lack of a generally applicable predictive correlation is inconvenient, forcing the heat transfer engineer to resort to numerical techniques for heat transfer predictions. The purpose of this note is to propose a correlation with applicability for all Prandtl numbers, one that properly reflects the physics. The correlation was developed using the method of Churchill and Usagi (1972), a scale analysis, numerical solutions to the transformed boundary layer equations, and analytical solutions to the governing equations.

A Scale Analysis

The constant-property boundary layer equations take their usual form, except that the velocity boundary conditions are $u = 0$ as $y \to \infty$, and $u = U_s$ at $y = 0$. A scale analysis similar to the related work of Moutsoglou (1988) will be undertaken for the physical situation shown in Fig. 1. A scale analysis of the continuity equation shows (see Bejan, 1984):

$$\frac{v}{\delta_V} \sim \frac{U_s}{x} \tag{1}$$

Equation (1) with the momentum equation gives (Bejan, 1984):

$$\frac{U_s^2}{x} \sim \nu \frac{U_s}{\delta_v^2} \tag{2}$$

Heat transfer scaling may be determined by starting with the energy equation in integral form:

$$\frac{d}{dx}\int_0^{\delta_T} uT\,dy + (vT)_{\delta_T} = -\alpha \left.\frac{\partial T}{\partial y}\right|_{y=0} \tag{3}$$

First consider a limiting case of $\delta_V \gg \delta_T$, Eq. (3) with Eq. (1) yields:

[1]Department of Mechanical & Industrial Engineering, The University of Illinois at Urbana-Champaign, Urbana, IL 61801.

Contributed by the Heat Transfer Division of The American Society of Mechanical Engineers. Manuscript received by the Heat Transfer Division December 1992; revision received May 1993. Keywords: Forced Convection, Materials Processing and Manufacturing Processes, Moving Boundaries. Associate Technical Editor: Y. Jaluria.

$$\frac{\delta_T}{x} U_s \Delta T \sim \alpha \frac{\Delta T}{\delta_T} \tag{4}$$

Using Eq. (2) and rearranging, the boundary layer thicknesses are found to scale according to:

$$\frac{\delta_V}{\delta_T} \sim \sqrt{\mathrm{Pr}} \tag{5}$$

Equation (5) demonstrates that this case is obtained when $\sqrt{\mathrm{Pr}} \gg 1$. The Nusselt number,

$$\mathrm{Nu}_x = \frac{hx}{k} \sim \frac{k\Delta Tx}{\delta_T \Delta Tk} = \frac{x}{\delta_T} \tag{6}$$

may be rewritten using Eqs. (2) and (5) to show that:

$$\mathrm{Nu}_x|_{\mathrm{Pr}\to\infty} \sim \sqrt{\mathrm{Pr}\mathrm{Re}_x} \tag{7a}$$

or

$$\mathrm{Nu}_x|_{\mathrm{Pr}\to\infty} = C_\infty \sqrt{\mathrm{Pr}\mathrm{Re}_x} \tag{7b}$$

Equation (7) provides the Nusselt number scaling in a backward boundary layer at high Prandtl numbers, and if the order unity constant C_∞ was known it would provide the asymptotic Nu behavior. The scale analysis confirms the high Pr behavior predicted by Erickson et al. (1966); however, the constant determined later in this study differs from their value of 0.53.

For the other limiting case of $\delta_T \gg \delta_V$, the upper limit of integration on Eq. (3) should be δ_V since u is zero outside that boundary layer. Within the δ_T layer, v scales according to Eq. (1); therefore Eq. (3) gives:

$$\frac{\delta_V}{x} U_s \Delta T \sim \alpha \frac{\Delta T}{\delta_T} \tag{8}$$

Rearranging and using Eq. (2), the appropriate boundary layer scaling for this case is found:

$$\frac{\delta_V}{\delta_T} \sim \mathrm{Pr} \tag{9}$$

Equation (9) implies that this case is limited to $\mathrm{Pr} \ll 1$. Using the definition of the Nusselt number and Eqs. (2) and (9), the heat transfer scaling for the low Prandtl number case is:

$$\mathrm{Nu}_x|_{\mathrm{Pr}\to 0} \sim \sqrt{\mathrm{Re}_x}\mathrm{Pr} \tag{10a}$$

or

$$\mathrm{Nu}_x|_{\mathrm{Pr}\to 0} = C_0 \sqrt{\mathrm{Re}_x}\mathrm{Pr} \tag{10b}$$

The results given by Eqs. (7) and (10) are interesting in their contrast to the Blasius boundary layer behavior, where $\mathrm{Nu}_x|_{\mathrm{Pr}\to\infty} \sim \sqrt{\mathrm{Re}_x}\sqrt[3]{\mathrm{Pr}}$ and $\mathrm{Nu}_x|_{\mathrm{Pr}\to 0} \sim \sqrt{\mathrm{Pr}\mathrm{Re}_x}$ (Bejan, 1984). For the case of a high Pr backward boundary layer, the asymptotic behavior expressed by Eq. (7) shows that Nu scales with $\sqrt{\mathrm{Pr}}$, which is the same scaling found for the low Pr conventional boundary layer. This reflects the influence of similar physical mechanisms for the two cases: In the high Pr backward boundary layer the velocity boundary layer is so thick compared to the thermal boundary layer that within the entire thermal boundary layer the fluid is moving at the characteristic velocity, U_s. This behavior is open to the same interpretation given to the conventional low Pr boundary layer, where convection is into a uniform velocity flow. For the other case of a low Pr backward boundary layer, Nu scales directly with Pr, as shown in Eq. (10). Here, the velocity boundary layer is very thin compared to the thermal boundary layer, and conduction into the fluid is balanced by advection in the transverse direction. A thin (but finite) layer of fluid at the surface temperature of the plate is carried away by the flow, to be replaced by fluid from the surroundings. Advection balances conduction from the plate in the low Pr backward boundary layer in a manner not found in the conventional boundary layer.

To develop a correlation for backward boundary layer heat transfer, the constants associated with the asymptotes, C_∞ and C_0, must be known. An analytical approach may be taken to determine these constants.[2] Such an approach, however, does not provide results at intermediate values of the Prandtl number, and since intermediate values are needed to develop a correlation, a numerical study was undertaken.

A Numerical Analysis

Following the similarity approach of Tsou et al. (1967), the transformed boundary layer equations take the form:

$$f''' + 1/2\, f f'' = 0 \tag{11}$$

$$f'(0) = 1,\ f(0) = 0,\ \text{and}\ f'(\infty) = 0$$

and

$$\theta'' + 1/2\ \mathrm{Pr}\, f \theta' = 0 \tag{12}$$

$$\theta(0) = 1 \text{ and } \theta(\infty) = 0$$

where

$$f'(\eta) = \frac{u}{U_s},\ v = 1/2\sqrt{\nu U_s/x}\ (\eta f' - f),$$

$$\theta(\eta) = \frac{T - T_\infty}{T_w - T_\infty},\ \text{and}\ \eta = y\sqrt{U_s/\nu x}.$$

f is the dimensionless stream function, θ the dimensionless temperature, and η the similarity variable. Except for the boundary conditions on Eq. (11), this transformation is identical to the conventional similarity model of a laminar flat plate boundary layer.

Equations (11) and (12) were solved using a multiple shooting technique and a sixth-order Runge–Kutta–Verner method. The velocity solution was obtained from $\eta = 0$ to 10, then a sixth-order least-squares interpolating polynomial was used with the Runge–Kutta–Verner integration to obtain the temperature distribution. This implementation used the double precision IMSL mathematical library on a CONVEX C240 computer. The boundary condition tolerance was 10^{-12}, and the differential equation tolerance was set so that local errors produced a global error proportional to 10^{-6}.

The calculated velocity profiles agreed very well with those of Sakiadis (1961); the difference between the friction factor determined in this study and that due to Sakiadis was less than 0.007 percent. The numerical results for the temperature distribution, in terms of the Nusselt number, are summarized in Table 1, with other published results presented for comparison.

The numerical results of Table 1 are plotted in Fig. 2, where it is demonstrated that the scaling of Eqs. (7) and (10) is appropriate. This is verified by noting that as $\mathrm{Pr} \to 0$, the value of $\mathrm{Nu}_x/(\mathrm{Pr}\sqrt{\mathrm{Re}_x})$ approaches a constant; whereas for $\mathrm{Pr} \to \infty$, $\mathrm{Nu}_x/\sqrt{\mathrm{Pr}\mathrm{Re}_x}$ approaches a different constant. The numerical results give a value of 0.807 for C_0, and C_∞ is taken to be 0.545. The numerical results are also confirmed by the analytical results for the low and high Prandtl number limits.

Correlation Development

With C_0 and C_∞ determined, Eqs. (7) and (10) become:

$$\mathrm{Nu}_x|_{\mathrm{Pr}\to\infty} = 0.545\ \sqrt{\mathrm{Re}_x}\ \sqrt{\mathrm{Pr}} \tag{13}$$

$$\mathrm{Nu}_x|_{\mathrm{Pr}\to 0} = 0.807\ \sqrt{\mathrm{Re}_x}\ \mathrm{Pr} \tag{14}$$

[2]The low Pr case is pursued by integrating Eq. (12) twice, and noting that $f' \to 0$; it may be shown that for this situation $C_0 = f_\infty/2$, where $f_\infty = f(\eta \to \infty)$ may be taken from the numerical solutions of Sakiadis (1961). The high Pr solution may be found by noting that $u \to U_s$ in the differential form of the energy equation, and the error function solutions give $C_\infty = 1/\sqrt{\pi}$.

Table 1 Numerical results and a comparison to previously published data

Pr	$\frac{Nu_x}{\sqrt{Re_x}}$	$\frac{Nu_x}{\sqrt{Pr\,Re_x}}$	$\frac{Nu_x}{Pr\sqrt{Re_x}}$	$\frac{Nu_x}{\sqrt{Re_x}}$ from the literature
1.00 (10^{-4})	8.073 (10^{-5})	8.073 (10^{-3})	8.073 (10^{-1})	
1.00 (10^{-3})	8.067 (10^{-4})	2.551 (10^{-2})	8.067 (10^{-1})	
5.00 (10^{-3})	4.015 (10^{-3})	5.679 (10^{-2})	8.031 (10^{-1})	
1.00 (10^{-2})	7.986 (10^{-3})	7.986 (10^{-2})	7.986 (10^{-1})	
5.00 (10^{-2})	3.856 (10^{-2})	1.724 (10^{-1})	7.711 (10^{-1})	
1.00 (10^{-1})	7.484 (10^{-2})	2.366 (10^{-1})	7.484 (10^{-1})	
4.56 (10^{-1})	2.569 (10^{-1})	3.804 (10^{-1})	5.633 (10^{-1})	
5.00 (10^{-1})	2.749 (10^{-1})	3.888 (10^{-1})	5.499 (10^{-1})	
7.00 (10^{-1})	3.492 (10^{-1})	4.174 (10^{-1})	4.989 (10^{-1})	0.3492[1][3], 0.3508[2], 0.3493[4]
1.00 (10^{0})	4.438 (10^{-1})	4.438 (10^{-1})	4.438 (10^{-1})	0.4438[1]
2.00 (10^{0})	6.833 (10^{-1})	4.831 (10^{-1})	3.416 (10^{-1})	0.6831[2]
5.00 (10^{0})	1.154 (10^{0})	5.160 (10^{-1})	2.308 (10^{-1})	
7.00 (10^{0})	1.387 (10^{0})	5.241 (10^{-1})	1.981 (10^{-1})	1.387[3]
1.00 (10^{1})	1.679 (10^{0})	5.309 (10^{-1})	1.679 (10^{-1})	1.680[1][4], 1.681[2]
5.00 (10^{1})	3.854 (10^{0})	5.451 (10^{-1})	7.709 (10^{-2})	
1.00 (10^{2})	5.448 (10^{0})	5.448 (10^{-1})	5.448 (10^{-2})	5.545[1]

[1]Tsou, *et al.* (1967); [2]Soundalgekar and Murty (1980); [3]Moutsoglou and Chen (1980); [4]Jeng, *et al.* (1986)

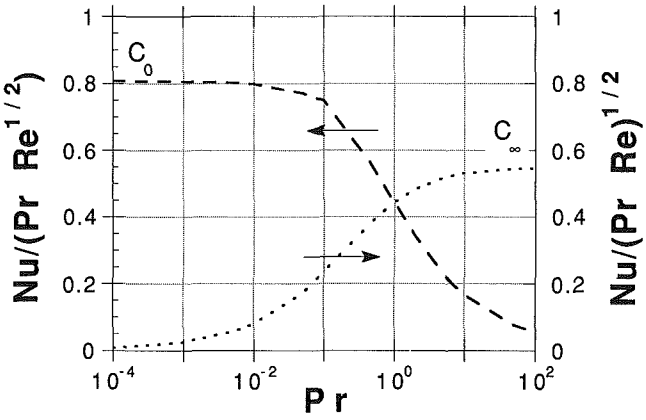

Fig. 2 Confirmation of the heat transfer scaling: As Pr decreases, Nu/(Pr $\sqrt{Re_x}$) approaches a constant, C_0. As Pr increases, Nu/$\sqrt{PrRe_x}$ approaches a constant, C_∞.

Applying the method of Churchill and Usagi (1972) yields the following correlation, with the parameter "n" to be determined from numerical or experimental results:

$$Nu_x = \frac{0.545\sqrt{PrRe_x}}{\left\{1+\left(\frac{0.545\sqrt{PrRe_x}}{0.807\ Pr\sqrt{Re_x}}\right)^n\right\}^{1/n}} \quad (15)$$

The value of n was selected, as suggested by Churchill and Usagi (1972), by evaluating Eq. (15) at the point where the limiting asymptotes are equal. The asymptotes cross at Pr = 0.456, and the numerical results are best matched using an integral value of $n = 2$. Thus,

$$Nu_x = \frac{0.545\sqrt{Re_x}\sqrt{Pr}}{\sqrt{1+0.456/Pr}} \quad (16)$$

Equation (16) and the two asymptotic limits, Eqs. (13) and (14), are plotted in Fig. 3, where a comparison to earlier studies is also shown. The figure confirms that both asymptotes are satisfied, and demonstrates agreement with earlier work. At Pr = 0.456, where the low and high Pr asymptotes cross, Eq. (16) predicts a value of Nu/$\sqrt{Re}$ that differs from that predicted by Eqs. (13) and (14) by 43 percent.

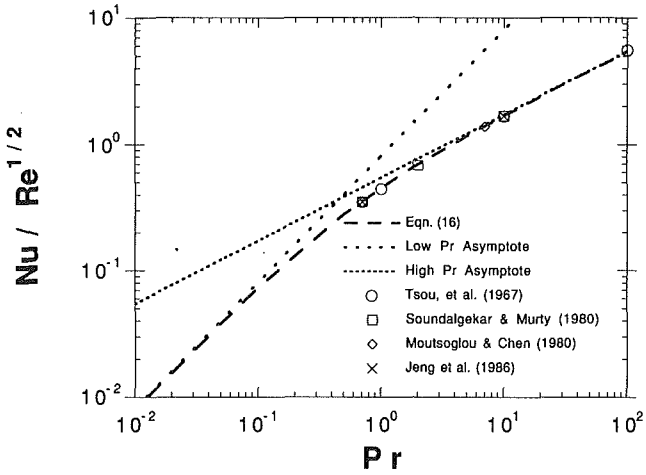

Fig. 3 Nu/$\sqrt{Re_x}$ behavior with the Prandtl number: The low and high Prandtl number asymptotes and the new general correlation are shown, along with a comparison to earlier studies.

Summary and Conclusions

While the friction factor of a backward boundary layer obeys the scaling law applicable for a Blasius boundary layer, the heat transfer behavior is markedly different. Apparently, heat transfer in the high Prandtl number backward boundary layer scales like low Prandtl number heat transfer in a Blasius boundary layer. Heat transfer in the low Prandtl number backward boundary layer, however, scales directly with the Prandtl number, a behavior not observed in either limit of the Blasius boundary layer flow.

In the high Prandtl number backward boundary layer, when the plate issues into the flow, it is as if a solid slab of fluid sticks to it. This slab is continuously applied at $x = 0$, and carried downstream while heat diffuses into it from the constant-temperature surface. For the low Prandtl number case, the plate issues into the flow and encounters near-slip conditions in velocity, but still entrains a finite mass flow. Diffusion, in this case, is balanced by advection of fluid into the thermal boundary layer at $y = \delta_T$.

This study provides the high and low Prandtl number asymptotic behavior of the Nusselt number, Eqs. (13) and (14), respectively. The high Pr results buttress an earlier study of Erickson et al. (1966), with an adjustment to the constant in their correlation. The low Pr limit has not previously appeared in the literature, but is important in establishing a general correlation. For common applications where the Prandtl number is near unity, the low Prandtl number asymptote is more important for the backward boundary layer than it is for a Blasius boundary layer. This is true because the backward boundary layer asymptotes cross at Pr = 0.456 (close to Pr = 1), in contrast to the Blasius boundary layer where they cross at Pr = 0.042.

The numerical results presented in Table 1 are supported by analytical arguments and previously published studies, but significantly extend the Prandtl number range of the available data. The numerical data and analytical results help establish the low and high Prandtl number asymptotes. The proposed correlation for heat transfer from a constant temperature con-

tinuous moving sheet, Eq. (16), spans the Prandtl number asymptotes, predicting within 2.5 percent the results of this study and any other study published to date. The correlation is valid for any Prandtl number, and properly reflects the physics of the Prandtl number effect. This correlation provides a useful tool to the heat transfer engineer.

Acknowledgments

The author would like to express his appreciation to the GAF Building Materials Corporation, Wayne, NJ, for their financial support of a related research project. The author also wishes to thank Prof. Clark Bullard for his comments and suggestions.

References

Bejan, A., 1984, *Convection Heat Transfer*, Wiley, New York.

Chen, T. S., and Strobel, F. A., 1980, "Buoyancy Effects in Boundary Layer Adjacent to a Continuous, Moving Horizontal Flat Plate," ASME JOURNAL OF HEAT TRANSFER, Vol. 102, pp. 170–172.

Chida, K., and Katto, Y., 1976, "Conjugate Heat Transfer of Continuously Moving Surfaces," *Int. J. Heat Mass Transfer*, Vol. 19, pp. 461–470.

Churchill, S. W., and Usagi, R., 1972, "A General Expression for the Correlation of Rates of Transfer and Other Phenomena," *AIChE Journal*, Vol. 18, pp. 1121–1128.

Erickson, L. E., Fan, L. T., and Cha, L. C., 1966, "The Cooling of a Moving Continuous Sheet," *AIChE, Chemical Engineering Progress Symposium Series*, Heat Transfer—Los Angeles, Vol. 62, pp. 157–165.

Grubka, L. J., and Bobba, K. M., 1985, "Heat Transfer Characteristics of a Continuous, Stretching Surface With Variable Temperature," ASME JOURNAL OF HEAT TRANSFER, Vol. 107, pp. 248–250.

Jeng, D. R., Chang, T. C. A., and De Witt, K. J., 1986, "Momentum and Heat Transfer on a Continuous Moving Sheet," ASME JOURNAL OF HEAT TRANSFER, Vol. 108, pp. 532–539.

Kang, B. H., Karwe, M. V., and Jaluria, Y., 1991, "Numerical Simulation of Conjugate Transport From a Continuous Moving Plate in Materials Processing," *Numerical Heat Transfer, Part A*, Vol. 19, pp. 151–176.

Karwe, M. V., and Jaluria, Y., 1988, "Fluid Flow and Mixed Convection Transport From a Moving Plate in Rolling and Extrusion Processes," ASME JOURNAL OF HEAT TRANSFER, Vol. 110, pp. 655–661.

Karwe, M. V., and Jaluria, Y., 1991, "Numerical Simulation of Thermal Transport Associated With a Continuously Moving Flat Sheet in Materials Processing," ASME JOURNAL OF HEAT TRANSFER, Vol. 113, pp. 612–619.

Karwe, M. V., and Jaluria, Y., 1992, "Experimental Investigation of Thermal Transport From a Heated Moving Plate," *Int. J. Heat Mass Transfer*, Vol. 35, pp. 493–511.

Kumari, M., Takhar, H. S., and Nath, G., 1990, "MHD Flow and Heat Transfer Over a Stretching Surface With Prescribed Wall Temperature or Heat Flux," *Wärme- und Stoffubertragung*, Vol. 25, pp. 331–336.

Lee, S. L., and Tsai, J. S., 1990, "Cooling of a Continuous Moving Sheet of Finite Thickness in the Presence of Natural Convection," *Int. J. Heat Mass Transfer*, Vol. 33, pp. 457–464.

Moutsoglou, A., 1988, "A Note on the Scale Analysis of Phase Change Problems," ASME JOURNAL OF HEAT TRANSFER, Vol. 110, pp. 523–526.

Moutsoglou, A., and Chen, T. S., 1980, "Buoyancy Effects in Boundary Layers on Inclined, Continuous, Moving Sheets," ASME JOURNAL OF HEAT TRANSFER, Vol. 102, pp. 371–373.

Murty, T. V. R., 1991, "Heat Transfer in Flow Past a Continuously Moving Semi-infinite Flat Plate in Transverse Magnetic Field With Heat Flux," *Wärme- und Stoffubertragung*, Vol. 26 pp. 149–151.

Pop, I., Gorla, R. S. R., and Rashidi, M., 1992, "The Effect of Variable Viscosity on Flow and Heat Transfer to a Continuous Moving Flat Plate," *Int. J. Engng. Sci.*, Vol. 30, pp. 1–6.

Ramachandran, N., Chen, T. S., and Armaly, B. F., 1987, "Correlations for Laminar Mixed Convection in Boundary Layers Adjacent to Horizontal, Continuous Moving Sheets," ASME JOURNAL OF HEAT TRANSFER, Vol. 109., pp. 1036–1039.

Sakiadis, B. C., 1961, "Boundary-Layer Behavior on Continuous Solid Surfaces: II. The Boundary Layer on a Continuous Flat Surface," *AIChE Journal*, Vol. 7, pp. 221–225.

Soundalgekar, V. M., and Murty, T. V. R., 1980, "Heat Transfer in Flow Past a Continuous Moving Plate With Variable Temperature," *Wärme- und Stoffubertragung*, Vol. 14, pp. 91–93.

Tsou, F. K., Sparrow, E. M., and Goldstein, R. J., 1967, "Flow and Heat Transfer in the Boundary Layer on a Continuous Moving Surface," *Int. J. Heat Mass Transfer*, Vol. 10, pp. 219–235.

Laminar Heat Transfer in the Thermal Entrance Regions of Concentric Annuli With Moving Heated Cores

T. Shigechi,[1] K. Araki,[1] and Y. Lee[2]

Nomenclature

a = $k/\rho c$ = thermal diffusivity
c = specific heat
D_h = $2(R_o - R_i)$ hydraulic diameter
f = friction factor
h = heat transfer coefficient
k = thermal conductivity
Nu = Nusselt number
p = pressure
Pr = Prandtl number
q_i = heat flux at the core wall
R = radius
Re = $\rho u_m D_h/\mu$ Reynolds number
T = temperature
U = core velocity
u = fluid velocity
x = axial coordinate
U^* = U/u_m relative velocity
X = $4(x/D_h)/\text{RePr}$ dimensionless axial coordinate
α = R_i/R_o radius ratio
ζ = $(r - R_i)/(R_o - R_i)$
ρ = density
μ = viscosity

Superscripts

(k) = refers to the four kinds of boundary conditions (k = 1, 2, 3, or 4)

Subscripts

b = bulk
crit = critical
d = developed
e = entrance or inlet
i = inner or core
ii = at the inner wall with the inner heated
m = mean or average
o = outer
oi = at the outer wall with the inner heated
th = thermal entrance

Constants

$$B = \frac{\alpha^2 - 1}{\ln \alpha}$$

$$B^* = \left[\frac{1 - \frac{1}{2}U^*}{1 - EU}\right] \cdot B$$

[1]Department of Mechanical Systems Engineering, Nagasaki University, Nagasaki, Japan, 852.

[2]Department of Mechanical Engineering, University of Ottawa, Ottawa, Canada, K1N 6N5.

Contributed by the Heat Transfer Division and presented at the ASME Winter Annual Meeting, Anaheim, California, November 8–13, 1992. Manuscript received by the Heat Transfer Division August 1992; revision received March 1993. Keywords: Forced Convection, Moving Boundaries, Transportation. Associate Technical Editor: J. H. Kim.

tinuous moving sheet, Eq. (16), spans the Prandtl number asymptotes, predicting within 2.5 percent the results of this study and any other study published to date. The correlation is valid for any Prandtl number, and properly reflects the physics of the Prandtl number effect. This correlation provides a useful tool to the heat transfer engineer.

Acknowledgments

The author would like to express his appreciation to the GAF Building Materials Corporation, Wayne, NJ, for their financial support of a related research project. The author also wishes to thank Prof. Clark Bullard for his comments and suggestions.

References

Bejan, A., 1984, *Convection Heat Transfer*, Wiley, New York.

Chen, T. S., and Strobel, F. A., 1980, "Buoyancy Effects in Boundary Layer Adjacent to a Continuous, Moving Horizontal Flat Plate," ASME JOURNAL OF HEAT TRANSFER, Vol. 102, pp. 170–172.

Chida, K., and Katto, Y., 1976, "Conjugate Heat Transfer of Continuously Moving Surfaces," *Int. J. Heat Mass Transfer*, Vol. 19, pp. 461–470.

Churchill, S. W., and Usagi, R., 1972, "A General Expression for the Correlation of Rates of Transfer and Other Phenomena," *AIChE Journal*, Vol. 18, pp. 1121–1128.

Erickson, L. E., Fan, L. T., and Cha, L. C., 1966, "The Cooling of a Moving Continuous Sheet," *AIChE, Chemical Engineering Progress Symposium Series*, Heat Transfer—Los Angeles, Vol. 62, pp. 157–165.

Grubka, L. J., and Bobba, K. M., 1985, "Heat Transfer Characteristics of a Continuous, Stretching Surface With Variable Temperature," ASME JOURNAL OF HEAT TRANSFER, Vol. 107, pp. 248–250.

Jeng, D. R., Chang, T. C. A., and De Witt, K. J., 1986, "Momentum and Heat Transfer on a Continuous Moving Sheet," ASME JOURNAL OF HEAT TRANSFER, Vol. 108, pp. 532–539.

Kang, B. H., Karwe, M. V., and Jaluria, Y., 1991, "Numerical Simulation of Conjugate Transport From a Continuous Moving Plate in Materials Processing," *Numerical Heat Transfer, Part A*, Vol. 19, pp. 151–176.

Karwe, M. V., and Jaluria, Y., 1988, "Fluid Flow and Mixed Convection Transport From a Moving Plate in Rolling and Extrusion Processes," ASME JOURNAL OF HEAT TRANSFER, Vol. 110, pp. 655–661.

Karwe, M. V., and Jaluria, Y., 1991, "Numerical Simulation of Thermal Transport Associated With a Continuously Moving Flat Sheet in Materials Processing," ASME JOURNAL OF HEAT TRANSFER, Vol. 113, pp. 612–619.

Karwe, M. V., and Jaluria, Y., 1992, "Experimental Investigation of Thermal Transport From a Heated Moving Plate," *Int. J. Heat Mass Transfer*, Vol. 35, pp. 493–511.

Kumari, M., Takhar, H. S., and Nath, G., 1990, "MHD Flow and Heat Transfer Over a Stretching Surface With Prescribed Wall Temperature or Heat Flux," *Wärme- und Stoffubertragung*, Vol. 25, pp. 331–336.

Lee, S. L., and Tsai, J. S., 1990, "Cooling of a Continuous Moving Sheet of Finite Thickness in the Presence of Natural Convection," *Int. J. Heat Mass Transfer*, Vol. 33, pp. 457–464.

Moutsoglou, A., 1988, "A Note on the Scale Analysis of Phase Change Problems," ASME JOURNAL OF HEAT TRANSFER, Vol. 110, pp. 523–526.

Moutsoglou, A., and Chen, T. S., 1980, "Buoyancy Effects in Boundary Layers on Inclined, Continuous, Moving Sheets," ASME JOURNAL OF HEAT TRANSFER, Vol. 102, pp. 371–373.

Murty, T. V. R., 1991, "Heat Transfer in Flow Past a Continuously Moving Semi-infinite Flat Plate in Transverse Magnetic Field With Heat Flux," *Wärme- und Stoffubertragung*, Vol. 26 pp. 149–151.

Pop, I., Gorla, R. S. R., and Rashidi, M., 1992, "The Effect of Variable Viscosity on Flow and Heat Transfer to a Continuous Moving Flat Plate," *Int. J. Engng. Sci.*, Vol. 30, pp. 1–6.

Ramachandran, N., Chen, T. S., and Armaly, B. F., 1987, "Correlations for Laminar Mixed Convection in Boundary Layers Adjacent to Horizontal, Continuous Moving Sheets," ASME JOURNAL OF HEAT TRANSFER, Vol. 109., pp. 1036–1039.

Sakiadis, B. C., 1961, "Boundary-Layer Behavior on Continuous Solid Surfaces: II. The Boundary Layer on a Continuous Flat Surface," *AIChE Journal*, Vol. 7, pp. 221–225.

Soundalgekar, V. M., and Murty, T. V. R., 1980, "Heat Transfer in Flow Past a Continuous Moving Plate With Variable Temperature," *Wärme- und Stoffubertragung*, Vol. 14, pp. 91–93.

Tsou, F. K., Sparrow, E. M., and Goldstein, R. J., 1967, "Flow and Heat Transfer in the Boundary Layer on a Continuous Moving Surface," *Int. J. Heat Mass Transfer*, Vol. 10, pp. 219–235.

Laminar Heat Transfer in the Thermal Entrance Regions of Concentric Annuli With Moving Heated Cores

T. Shigechi,[1] K. Araki,[1] and Y. Lee[2]

Nomenclature

a = $k/\rho c$ = thermal diffusivity
c = specific heat
D_h = $2(R_o - R_i)$ hydraulic diameter
f = friction factor
h = heat transfer coefficient
k = thermal conductivity
Nu = Nusselt number
p = pressure
Pr = Prandtl number
q_i = heat flux at the core wall
R = radius
Re = $\rho u_m D_h/\mu$ Reynolds number
T = temperature
U = core velocity
u = fluid velocity
x = axial coordinate
U^* = U/u_m relative velocity
X = $4(x/D_h)/\mathrm{RePr}$ dimensionless axial coordinate
α = R_i/R_o radius ratio
ζ = $(r - R_i)/(R_o - R_i)$
ρ = density
μ = viscosity

Superscripts

(k) = refers to the four kinds of boundary conditions (k = 1, 2, 3, or 4)

Subscripts

b = bulk
crit = critical
d = developed
e = entrance or inlet
i = inner or core
ii = at the inner wall with the inner heated
m = mean or average
o = outer
oi = at the outer wall with the inner heated
th = thermal entrance

Constants

$$B = \frac{\alpha^2 - 1}{\ln \alpha}$$

$$B^* = \left[\frac{1 - \frac{1}{2}U^*}{1 - EU}\right] \cdot B$$

[1]Department of Mechanical Systems Engineering, Nagasaki University, Nagasaki, Japan, 852.

[2]Department of Mechanical Engineering, University of Ottawa, Ottawa, Canada, K1N 6N5.

Contributed by the Heat Transfer Division and presented at the ASME Winter Annual Meeting, Anaheim, California, November 8–13, 1992. Manuscript received by the Heat Transfer Division August 1992; revision received March 1993. Keywords: Forced Convection, Moving Boundaries, Transportation. Associate Technical Editor: J. H. Kim.

$$M = 1 + \alpha^2 - B$$

$$E = \left[\frac{\alpha^2 - \frac{1}{2}B}{\alpha^2 - 1}\right]$$

Introduction

This is part of a continuing study on the fluid flow and heat transfer in a concentric annulus with a moving core of solid body or fluid. In our previous study, we presented the solutions on the problems of *fully developed turbulent* and *laminar* fluid flow and heat transfer in a concentric annulus with a moving core for conditions of constant heat fluxes at either wall (Shigechi et al., 1990; Shigechi and Lee, 1991; Lee and Shigechi, 1992). Problems involving fluid flow and heat transfer with a moving core of solid body or fluid in an annular geometry can be found in many manufacturing processes, such as extrusion, drawing and hot rolling, etc. In such processes, a hot cylindrical rod or plate continuously exchanges heat with the surrounding environment.

Another example that involves such fluid flow and heat transfer phenomena is a train traveling at high speed in a long tunnel, or an underground railway, where a significant amount of thermal energy may be transferred to or from the surroundings. The inverted annular film boiling that may occur during the emergency core cooling of nuclear fuel channels is another instance. For such cases, the fluid flow involved can be either *laminar* or *turbulent* flow and there seem to be few reliable predictions for momentum and heat transfer available in the literature.

The case of the laminar and turbulent flow and heat transfer in the *boundary layer* on a continuous moving surface was studied by Tsou et al. (1967).

In this paper, the heat transfer between a fully developed laminar fluid flow and a moving heated core of fluid or solid body in the thermal entrance region of a concentric annular geometry is studied analytically.

Using the finite difference method, the temperature profiles are obtained from the governing energy differential equations and heat transfer rates are calculated. The necessary boundary conditions are acquired from the heating boundary condition at the moving core wall surface.

Analysis

The assumptions used in the analysis are:

1 The fluid flow in the concentric annulus is incompressible, steady, and fully developed laminar.
2 The inner core tube is moving at a constant velocity, U.
3 Constant physical properties are exhibited.

Fluid Flow. The momentum equation for fully developed laminar flow is given as:

$$\frac{1}{r}\frac{\partial}{\partial r}\left(r\frac{\partial u}{\partial r}\right) = \frac{1}{\mu}\frac{dP}{dx} \tag{1}$$

together with the boundary conditions:

$$u = U \quad \text{at} \quad r = R_i; \qquad u = 0 \quad \text{at} \quad r = R_o$$

The fully developed velocity profiles are then obtained as:

$$u = \frac{2u_m}{M}[1 - EU^*][1 - (r/R_o)^2 + B^* \ln (r/R_o)] \tag{2}$$

where u_m is the average velocity, expressed from the usual definition as:

$$u_m = \frac{R_o^2}{4\mu}\left(-\frac{dp}{dx}\right)\frac{M}{2} + EU \tag{3}$$

Heat Transfer in the Thermal Entrance Region

Temperature Distributions. The energy equation is:

$$\frac{1}{r}\frac{\partial}{\partial r}\left(r\frac{\partial T^{(k)}}{\partial r}\right) = \frac{u}{a}\frac{\partial T^{(k)}}{\partial x} \tag{4}$$

where $k = 1, 2, 3,$ or 4 (the boundary conditions given below).

The concentric annulus can have many combinations of wall boundary conditions for surface temperature and heat flux. For the present case of the heating at the core tube only, we have the following four kinds of boundary condition for $x > 0$:

(1) The first kind:

$$T^{(1)} = T_i \quad \text{at} \quad r = R_i; \qquad T^{(1)} = T_e \quad \text{at} \quad r = R_o \tag{5}$$

(2) The second kind:

$$-k\frac{\partial T^{(2)}}{\partial r} = q_i \quad \text{at} \quad r = R_i; \qquad \frac{\partial T^{(2)}}{\partial r} = 0 \quad \text{at} \quad r = R_o \tag{6}$$

(3) The third kind:

$$T^{(3)} = T_i \quad \text{at} \quad r = R_i; \qquad \frac{\partial T^{(3)}}{\partial r} = 0 \quad \text{at} \quad r = R_o \tag{7}$$

(4) The fourth kind:

$$-k\frac{\partial T^{(4)}}{\partial r} = q_i \quad \text{at} \quad r = R_i; \qquad T^{(4)} = T_e \quad \text{at} \quad r = R_o \tag{8}$$

The condition at $x = 0$ is:

$$x = 0: \quad T^{(k)} = T_e \quad \text{for} \quad R_i \le r \le R_o \quad (k = 1, 2, 3, \text{ or } 4) \tag{9}$$

Heat Transfer. The Nusselt numbers are defined as:

$$\mathrm{Nu}_{ii}^{(k)} \equiv \frac{h_{ii}^{(k)} \cdot 2(R_0 - R_i)}{k} \quad \text{for } k = 1, 2, 3, \text{ or } 4 \tag{10}$$

$$\mathrm{Nu}_{oi}^{(k)} \equiv \frac{h_{oi}^{(k)} \cdot 2(R_o - R_i)}{k} \quad \text{for } k = 1 \text{ or } 4 \tag{11}$$

where the heat transfer coefficients are defined as:

$$h_{ii}^{(1),(3)} = \frac{-k\left.\frac{\partial T^{(1),(3)}}{\partial r}\right|_{R_i}}{[T_i^{(1),(3)} - T_b^{(1),(3)}]} \tag{12}$$

$$h_{ii}^{(2),(4)} = \frac{q_i}{[T_i^{(2),(4)} - T_b^{(2),(4)}]} \tag{13}$$

$$h_{oi}^{(1),(4)} = \frac{k\left.\frac{\partial T^{(1),(4)}}{\partial r}\right|_{R_o}}{[T_o^{(1),(4)} - T_b^{(1),(4)}]} \tag{14}$$

Thus, the various Nusselt numbers are calculated as:

$$\mathrm{Nu}_{ii}^{(1),(3)} = \frac{2(R_o - R_i)}{(T_i^{(1),(3)} - T_b^{(1),(3)})}\left[-\left.\frac{\partial T^{(1),(3)}}{\partial r}\right|_{R_i}\right] \tag{15}$$

$$\mathrm{Nu}_{ii}^{(2),(4)} = \frac{2(R_0 - R_i)}{(T_i^{(2),(4)} - T_b^{(2),(4)})}\left(\frac{q_i}{k}\right) \tag{16}$$

$$\mathrm{Nu}_{oi}^{(1),(4)} = \frac{2(R_o - R_i)}{(T_o^{(1),(4)} - T_b^{(1),(4)})}\left[+\left.\frac{\partial T^{(1),(4)}}{\partial r}\right|_{R_o}\right] \tag{17}$$

Numerical Calculation

In the calculation process, Eqs. (1)–(17) given above, including boundary and initial conditions, and the definitions are all expressed in dimensionless parameters.

The range of parameters considered are:

The radius ratio: $0 < \alpha \le 1$
The relative velocity: $0 \le U^* \le U^*_{\text{crit}}$

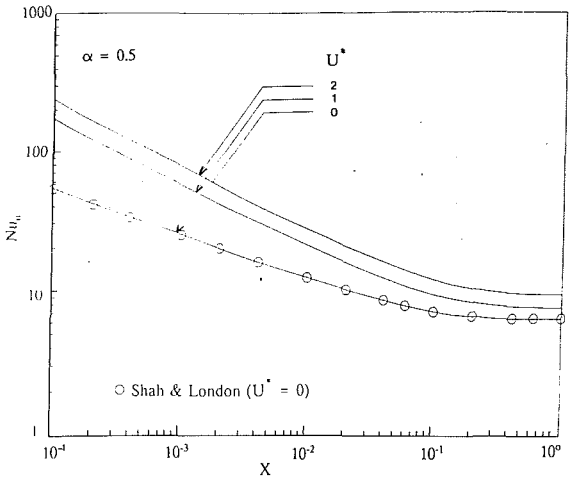

Fig. 1 Nusselt numbers (second kind)

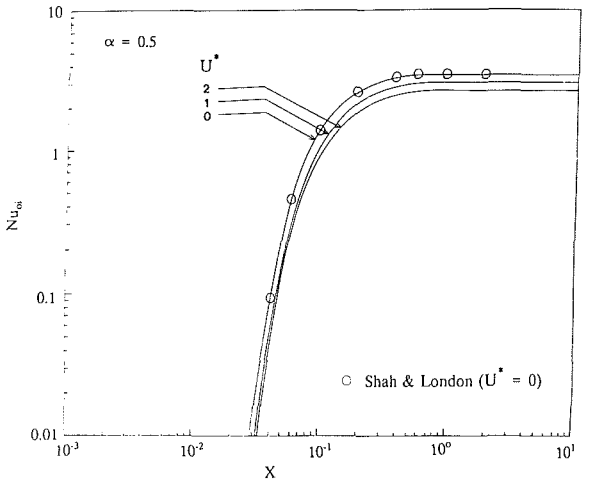

Fig. 2 Nusselt numbers (first kind)

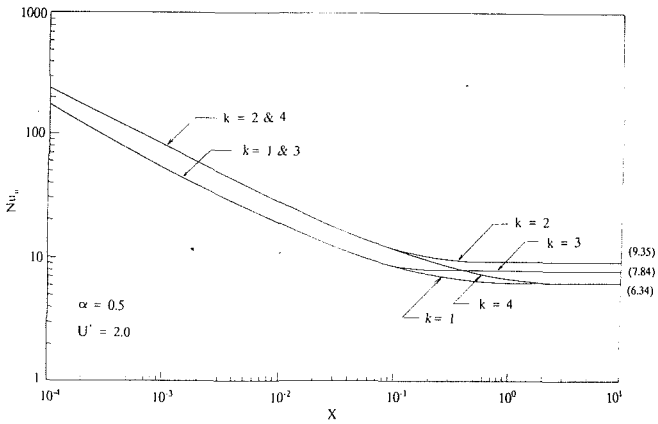

Fig. 3 Nusselt numbers, effect of boundary conditions

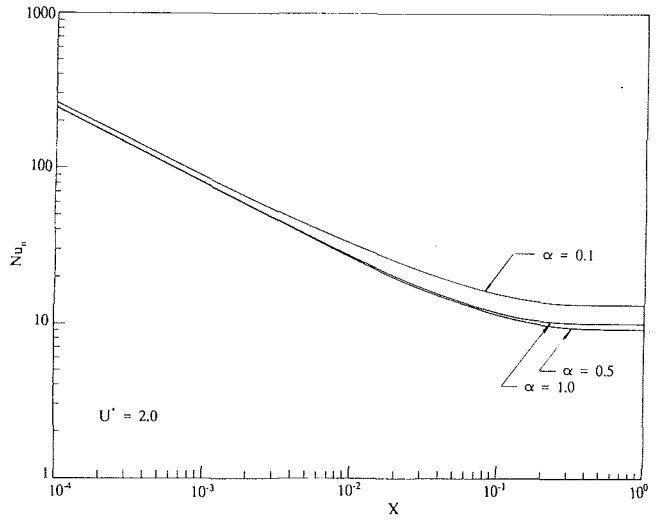

Fig. 4 Nusselt numbers, effect of radius ratio (second kind)

[The critical relative velocity, U^*_{crit}, is the value of U^* at $f = 0$, i.e., $(-dp/dx) = 0$. It is shown that $U^*_{crit} = 1/E$ (see Shigechi and Lee, 1991).] Therefore, the discussion of the results in this paper is confined to the fluid flow with $f \geq 0$ and $Re > 0$.

The calculation is carried out using the finite difference method (e.g., Conte and De Boor, 1972). For the range of X between 0 and 10^{-4}, the explicit method was employed from the comparison between the results of a previous study for the case of the stationary core (i.e., $U = 0$) (Shah and London, 1970) and the present results for the same condition. For the range of X greater than 10^{-4}, the implicit method was employed.

The mesh sizes in the axial direction, ΔX, used in the calculation ranged between 10^{-9} and 10^{-3}. The mesh sizes in the radial direction, $\Delta\zeta$, were between 1/200 and 1/800, depending on the value of the radius ratio, α.

The accuracy of the numerical calculation was estimated to be on the order of 10^{-3}.

Results and Discussion

Because of the restricted space of the paper, only a limited number of cases of the four kinds of fundamental boundary conditions will be discussed.

The effect of the relative velocity, U^*, on the Nusselt numbers, Nu_{ii}, defined by Eq. (10) at a given value of X for the second kind with $\alpha = 0.5$ is shown in Fig. 1. Similar figures to Fig. 1 also exhibit a comparable trend for the different boundary conditions, i.e., $k = 1$, 3, or 4. The effect of U^* on Nu_{oi}, defined by Eq. (11), for the first kind with $\alpha = 0.5$ is shown in Fig. 2.

Since there is no other result to compare for the case $U^* > 0$, the analytical results for the case of the stationary core, $U^* = 0$, from Shah and London (1970), is plotted in these figures. Even at a small value of X, it can be seen in the figures that the agreement is excellent. The comparison made between the analytical results of Lundberg et al. (1963) and Worsøe-Schmidt (1969) for the case of the stationary core, $U^* = 0$, and the present results also showed a similarly excellent agreement. These comparisons imply that the accuracy in the numerical calculation used in the present study is ascertained. The effect of the relative velocity of the heated core tube is to increase in the values of Nu_{ii} but to decrease Nu_{oi}, for given conditions of α and X. There is no experimental study on the problem in the open literature to compare with the results of the present study. Since this is an analytical study on a laminar flow, which is completely described by the Navier-Stokes equation, the experimental verification of the results is not so important as in the case of turbulent flow.

In Fig. 3, the effect of the boundary conditions, k, on Nu_{ii} for $\alpha = 0.5$ and $U^* = 2$ is illustrated. It is interesting to note that the values of Nu_{ii} for the first and third kinds, and the second and fourth kinds, are the same for the values of $X < 0.1$. The asymptotic value of the fourth kind converges to that of the first kind.

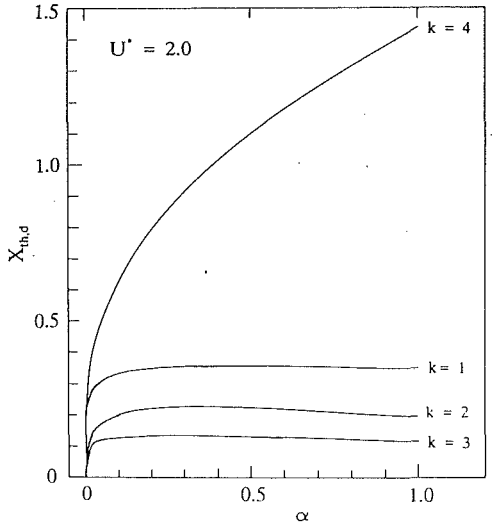

Fig. 5 Thermal entrance length

The effect of the radius ratio, α, on Nu_{ii} for the second kind with $U^* = 2$ is represented in Fig. 4. The effect seems to be rather small.

The generally accepted definition of the thermal entrance length, $X_{th,d}$, by analysis is that the distance required for the local heat transfer coefficient (or local Nusselt number) to approach to within 5 percent of the fully developed value, i.e., $(Nu_x/Nu_d) = 1.05$ (e.g., Sparrow et al., 1957). In this paper, the $X_{th,d}$ is based on this definition.

The values of $X_{th,d}$ corresponding to $(Nu_x/Nu_d) = 1.05$, as a function of α at $U^* = 2$ for all four kinds of boundary conditions, are plotted in Fig. 5 as an example. Again, a comparison was made between the results of Shah and London (1970) and those obtained from the present study for the case of $U^* = 0$ and for all four kinds of boundary condition and it was seen that the agreement was excellent. This confirms again that the present numerical calculation is correct. It can be observed in Fig. 5 that $X_{th,d}$ is usually less than 1.0 except for the case of the fourth kind of the boundary condition, $k = 4$. It was also noticed that while the value of $X_{th,d}$ for the case of $U^* = 0$ increases monotonously with increasing value of α, the value of $X_{th,d}$ for the case of $U^* > 0$ increases to its maximum value for a given U^*. The maximum value of $X_{th,d}$ increases with increasing value of U^* but with smaller value of α.

Concluding Remarks The present study showed that for equal conditions, increasing relative velocity was observed for the following changes:

(*i*) an increase in Nusselt numbers Nu_{ii} as Nu_{oi} decreases for all four cases.
(*ii*) an increase in the value of $X_{th,d}$ with a maximum at a given $U^* > 0$. The maximum value of $X_{th,d}$ increases with increasing value of U^* but with smaller values of α.

References

Conte, S. D., and De Boor, C., 1972, *Elementary Numerical Analysis*, 2nd ed., McGraw-Hill, New York.

Lee, Y., and Shigechi, T., 1992, "Heat Transfer in Concentric Annuli With Moving Cores—Fully Developed Turbulent Flow With Arbitrarily Prescribed Heat Flux," *Int. J. Heat Mass Transfer*, Vol. 35, pp. 3488–3493.

Lundberg, E. E., McCuen, P. A., and Reynolds, W. C., 1963, "Heat Transfer in Annular Passages. Hydrodynamically Developed Laminar Flow With Arbitrarily Prescribed Wall Temperatures or Heat Fluxes," *Int. J. Heat Mass Transfer*, Vol. 6, pp. 495–529.

Shah, R. K., and London, A. L. 1970, "Laminar Flow Forced Convection in Ducts," *Advances in Heat Transfer*, Supplement 1, Academic Press.

Shigechi, T., Kawae, N., and Lee, Y., 1990, "Turbulent Fluid Flow and Heat Transfer in Concentric Annuli With Moving Cores," *Int. J. Heat Mass Transfer*, Vol. 33, pp. 2029–2037.

Shigechi, T., and Lee, Y., 1991, "An Analysis on Fully Developed Laminar Fluid Flow and Heat Transfer in Concentric Annuli With Moving Cores," *Int. J. Heat Mass Transfer*, Vol. 34, pp. 2563–2601.

Sparrow, E. M., Hallman, T. M., and Siegel, R., 1957, "Turbulent Heat Transfer in the Thermal Entrance Region of a Pipe With Uniform Heat Flux," *Applied Science Research*, Vol. 7, pp. 39–52.

Tsou, F. K., Sparrow, E. M., and Goldstein, R. J., 1967, "Flow and Heat Transfer in the Boundary Layer on a Continuous Moving Surface," *Int. J. Heat Mass Transfer*, Vol. 10, pp. 219–235.

Worsøe-Schmidt, P. M., 1969, "Heat Transfer in the Thermal Entrance Region of Circular Tubes and Annular Passages With Fully Developed Laminar Flow," *Int. J. Heat Mass Transfer*, Vol. 10, pp. 541–551.

Calculation of Temperatures in a Single-Blow Regenerative Heat Exchanger Having Arbitrary Initial Solid and Entering Gas Temperatures

F. E. Romie[1]

Introduction

For a blow-down-type wind tunnel the admitted gas is often heated to a high temperature by passing it through an initially high temperature matrix (also referred to as a single-blow regenerator). The temperature of the gas entering the matrix can vary appreciably with time and, for reasons of economy, the initial matrix temperature is typically not uniform in the direction of gas flow. Following discharge the matrix is recharged by a high-temperature gas, which typically flows at a lower rate for a longer time than during matrix discharge.

The problem in both designing and using the matrix involves prediction of the temperature history of the gas leaving the matrix. This problem has been addressed by Larsen (1976) who used the Anzelius–Schumann functions (see following) to obtain the solution. Since Larsen's paper the computer has come into widespread use and the Anzelius–Schumann functions have been expanded (Romie, 1987) into a family of functions appropriate to the solution of the problem. The purpose of this note is to give an up-dated treatment of the solid and gas temperatures in the matrix.

The solution presented is exact for the idealized model defined both by Larsen and this note. Larsen indicated the method of solution but did not give an explicit solution for the matrix temperature that is required at the end of the blow period, in the absence of temperature measurements, to establish the matrix temperature distribution at beginning of the charge process. The use of the family of functions noted above eliminates two of the four convolution integrals that are required by Larsen's method to compute gas and matrix temperatures. The two eliminated integrals are replaced by sums, which are more rapidly evaluated using a computer.

The Differential Equations

The system analyzed is defined by the following idealiza-

[1]Palos Verdes Estates, CA 90274.

Contributed by the Heat Transfer Division of THE AMERICAN SOCIETY OF MECHANICAL ENGINEERS. Manuscript received by the Heat Transfer Division August 1992; revision received April 1993. Keywords: Heat Exchangers, Thermal Energy Storage, Transient and Unsteady Heat Transfer. Associate Technical Editor: W. A. Fiveland.

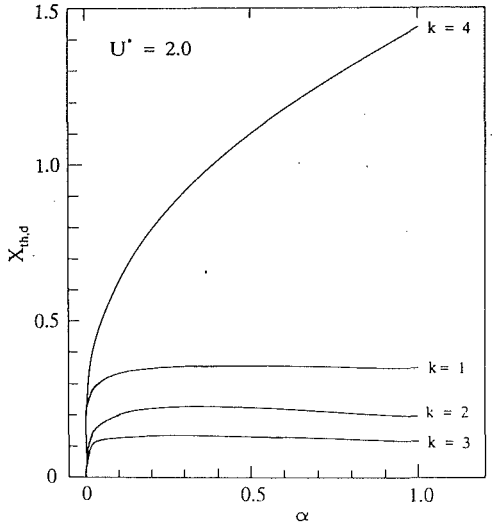

Fig. 5 Thermal entrance length

The effect of the radius ratio, α, on Nu_{ii} for the second kind with $U^* = 2$ is represented in Fig. 4. The effect seems to be rather small.

The generally accepted definition of the thermal entrance length, $X_{th,d}$, by analysis is that the distance required for the local heat transfer coefficient (or local Nusselt number) to approach to within 5 percent of the fully developed value, i.e., $(Nu_x/Nu_d) = 1.05$ (e.g., Sparrow et al., 1957). In this paper, the $X_{th,d}$ is based on this definition.

The values of $X_{th,d}$ corresponding to $(Nu_x/Nu_d) = 1.05$, as a function of α at $U^* = 2$ for all four kinds of boundary conditions, are plotted in Fig. 5 as an example. Again, a comparison was made between the results of Shah and London (1970) and those obtained from the present study for the case of $U^* = 0$ and for all four kinds of boundary condition and it was seen that the agreement was excellent. This confirms again that the present numerical calculation is correct. It can be observed in Fig. 5 that $X_{th,d}$ is usually less than 1.0 except for the case of the fourth kind of the boundary condition, $k = 4$. It was also noticed that while the value of $X_{th,d}$ for the case of $U^* = 0$ increases monotonously with increasing value of α, the value of $X_{th,d}$ for the case of $U^* > 0$ increases to its maximum value for a given U^*. The maximum value of $X_{th,d}$ increases with increasing value of U^* but with smaller value of α.

Concluding Remarks The present study showed that for equal conditions, increasing relative velocity was observed for the following changes:

(*i*) an increase in Nusselt numbers Nu_{ii} as Nu_{oi} decreases for all four cases.
(*ii*) an increase in the value of $X_{th,d}$ with a maximum at a given $U^* > 0$. The maximum value of $X_{th,d}$ increases with increasing value of U^* but with smaller values of α.

References

Conte, S. D., and De Boor, C., 1972, *Elementary Numerical Analysis*, 2nd ed., McGraw-Hill, New York.

Lee, Y., and Shigechi, T., 1992, "Heat Transfer in Concentric Annuli With Moving Cores—Fully Developed Turbulent Flow With Arbitrarily Prescribed Heat Flux," *Int. J. Heat Mass Transfer*, Vol. 35, pp. 3488–3493.

Lundberg, E. E., McCuen, P. A., and Reynolds, W. C., 1963, "Heat Transfer in Annular Passages. Hydrodynamically Developed Laminar Flow With Arbitrarily Prescribed Wall Temperatures or Heat Fluxes," *Int. J. Heat Mass Transfer*, Vol. 6, pp. 495–529.

Shah, R. K., and London, A. L. 1970, "Laminar Flow Forced Convection in Ducts," *Advances in Heat Transfer*, Supplement 1, Academic Press.

Shigechi, T., Kawae, N., and Lee, Y., 1990, "Turbulent Fluid Flow and Heat Transfer in Concentric Annuli With Moving Cores," *Int. J. Heat Mass Transfer*, Vol. 33, pp. 2029–2037.

Shigechi, T., and Lee, Y., 1991, "An Analysis on Fully Developed Laminar Fluid Flow and Heat Transfer in Concentric Annuli With Moving Cores," *Int. J. Heat Mass Transfer*, Vol. 34, pp. 2563–2601.

Sparrow, E. M., Hallman, T. M., and Siegel, R., 1957, "Turbulent Heat Transfer in the Thermal Entrance Region of a Pipe With Uniform Heat Flux," *Applied Science Research*, Vol. 7, pp. 39–52.

Tsou, F. K., Sparrow, E. M., and Goldstein, R. J., 1967, "Flow and Heat Transfer in the Boundary Layer on a Continuous Moving Surface," *Int. J. Heat Mass Transfer*, Vol. 10, pp. 219–235.

Worsøe-Schmidt, P. M., 1969, "Heat Transfer in the Thermal Entrance Region of Circular Tubes and Annular Passages With Fully Developed Laminar Flow," *Int. J. Heat Mass Transfer*, Vol. 10, pp. 541–551.

Calculation of Temperatures in a Single-Blow Regenerative Heat Exchanger Having Arbitrary Initial Solid and Entering Gas Temperatures

F. E. Romie[1]

Introduction

For a blow-down-type wind tunnel the admitted gas is often heated to a high temperature by passing it through an initially high temperature matrix (also referred to as a single-blow regenerator). The temperature of the gas entering the matrix can vary appreciably with time and, for reasons of economy, the initial matrix temperature is typically not uniform in the direction of gas flow. Following discharge the matrix is recharged by a high-temperature gas, which typically flows at a lower rate for a longer time than during matrix discharge.

The problem in both designing and using the matrix involves prediction of the temperature history of the gas leaving the matrix. This problem has been addressed by Larsen (1976) who used the Anzelius–Schumann functions (see following) to obtain the solution. Since Larsen's paper the computer has come into widespread use and the Anzelius–Schumann functions have been expanded (Romie, 1987) into a family of functions appropriate to the solution of the problem. The purpose of this note is to give an up-dated treatment of the solid and gas temperatures in the matrix.

The solution presented is exact for the idealized model defined both by Larsen and this note. Larsen indicated the method of solution but did not give an explicit solution for the matrix temperature that is required at the end of the blow period, in the absence of temperature measurements, to establish the matrix temperature distribution at beginning of the charge process. The use of the family of functions noted above eliminates two of the four convolution integrals that are required by Larsen's method to compute gas and matrix temperatures. The two eliminated integrals are replaced by sums, which are more rapidly evaluated using a computer.

The Differential Equations

The system analyzed is defined by the following idealiza-

[1]Palos Verdes Estates, CA 90274.

Contributed by the Heat Transfer Division of THE AMERICAN SOCIETY OF MECHANICAL ENGINEERS. Manuscript received by the Heat Transfer Division August 1992; revision received April 1993. Keywords: Heat Exchangers, Thermal Energy Storage, Transient and Unsteady Heat Transfer. Associate Technical Editor: W. A. Fiveland.

tions: (1) The thermal conductance hA, for transfer of heat between the fluid and matrix, the fluid capacitance rate, wc, and the matrix thermal capacitance, WC, are uniform and constant. (2) No heat is transferred by conduction or radiation in the matrix in the direction of fluid flow. (3) The matrix material offers no resistance to heat flow in the direction normal to fluid flow. (Biot's number must be very small.) (4) The ratio of the thermal capacitance of the contained fluid to the thermal capacitance of the containing matrix is negligibly small and is treated as zero. This latter idealization means, in effect, that the fluid must be a gas; that the transit time for a gas particle to flow through the matrix must be negligible compared to times of interest and that any effect of the gas resident in the matrix at initiation of flow is vanishingly small and can be ignored.

With these idealizations energy balances give two equations:

$$\frac{\partial T_g}{\partial(\Lambda y)} = T_m(x, y) - T_g(x, y) = -\frac{\partial T_m}{\partial(\Pi x)} \tag{1}$$

In these equations x $(=t/t_p)$ is the fractional completion of the flow period, t_p, and y is the fractional distance through the matrix of length L and is zero at the gas entrance plane. The matrix solid and gas temperatures are T_m (x, y) and T_g (x, y); $\Lambda = hA/wc$; $\Pi = hAt_p/WC$.

The initial matrix temperature distribution is given as an Nth degree polynomial of y:

$$T_m(0, y) = \sum_{n=0}^{N} A_n(\Lambda y)^n/n! \tag{2}$$

For any particular application the initial matrix temperature distribution must be known and the coefficients A_n can be evaluated using matrix algebra.

The temperature history of the entering gas is an arbitrary function of time:

$$T_g(x, 0) = \phi(\Pi x) \tag{3}$$

Functions Used

The Anzelius (1926)–Schumann (1929) functions, F_0 and G_0 (u, v), and their n-times successive integrals, $F_n(u, v)$, $G_n(u, v)$, with respect to the second argument are used to express the solution to the preceding equations. Some properties of the functions and methods of evaluation are given by Romie (1987). The functions satisfy two equations:

$$\frac{\partial G_n}{\partial v} = F_n(u, v) - G_n(u, v) = -\frac{\partial F_n}{\partial u} \tag{4}$$

For $n \geq 0$, $G_n(u, 0) = 0$ and $F_n(0, v) = v^n/n!$. Numerical values, $n = 0, 1, 2, \ldots$, can be found by evaluating three functions and then using two recurrence equations. The three functions are

$$F_{-1}(u, v) = \frac{\partial F_0(u, v)}{\partial v} = \exp(-u-v)(u/v)^{1/2} I_1(2\sqrt{uv}) \tag{5}$$

$$G_{-1}(u, v) = \frac{\partial G_0}{\partial v}(u, v) = \exp(-u-v) I_0(2\sqrt{uv}) \tag{6}$$

$$G_0(u, v) = \exp(-u-v) \sum_{1}^{\infty} (v/u)^{r/2} I_r(2\sqrt{uv}) \tag{7}$$

I_r is the modified Bessel function of the first kind, rth order, and u and v are positive. The two recurrence equations are

$$F_n(u, v) = G_n(u, v) + G_{n-1}(u, v), \pm \text{ integer } n \tag{8}$$

$$G_{n+1}(u, v) = \frac{1}{n+1}[(v-u-1-2n)G_n + (2v-n)G_{n-1} + vG_{n-2}], \quad n \geq 0 \tag{9}$$

Table 1 Three transform pairs

F(p)	f(v)
$\frac{e^{-\frac{up}{p+1}}}{p^{n+1}}$, $n \geq 0$	$F_n(u, v)$
$\frac{e^{-\frac{up}{p+1}}}{(p+1)p^{n+1}}$, $n \geq -1$	$G_n(u, v)$
$\frac{e^{-\frac{up}{p+1}}}{(p+1)^2}$	$\frac{v}{u}F_{-1}(u, v)$ $(=F_{-1}(v, u))$

Table 1 gives three Laplace transform pairs used in obtaining the solution. Note, from Eq. (6), that $G_{-1}(u, v) = G_{-1}(v, u)$ and, from Eq. (5), that $(v/u)F_{-1}(u, v) = F_{-1}(v, u)$.

Solution of Equations

Take the Laplace transform of Eqs. (1) with respect to Πx using s as the Laplace parameter and then find the Laplace transform of the resultant equations with respect to Λy using p as the Laplace parameter. The double transforms $T_m(s, p)$, $T_g(s, p)$ of $T_m(x, y)$, $T_g(x, y)$ can then be inverted first with respect to s and then, using Table 1, with respect to p. The algebra is straightforward and is not shown. The solutions for the matrix and gas temperatures are found to be

$$T_m(x, y) = \int_0^{\Pi x} G_{-1}(\Lambda y, \Pi x - \Pi x')\phi(\Pi x')d(\Pi x') + \sum_{n=0}^{N} A_n F_n(\Pi x, \Lambda y) \tag{10}$$

$$T_g(x, y) = \int_0^{\Pi x} F_{-1}(\Lambda y, \Pi x - \Pi x')\phi(\Pi x')d(\Pi x') + e^{-\Lambda y}\phi(\Pi x) + \sum_{n=0}^{N} A_n G_n(\Pi x, \Lambda y) \tag{11}$$

Numerical values of T_m and T_g can be found quite rapidly using a computer, particularly if the polynomial approximations for I_0 and I_1, given by Abramowitz and Stegun (1964) are used to evaluate G_{-1} and F_{-1} in the integrands of the two preceding equations.

Results and Discussion

Figures 1 and 2 give an example of the application of the solution with $\Lambda = 10$ and $\Pi = 5$. The initial matrix temperature, $T_m(0, y)$, is shown in Fig. 1 by the thicker line labeled $x = 0$. The imposed temperature history, $T_g(x, 0)$, of the entering gas is shown in Fig. 2 by the thinner line labeled $y = 0$. Specifically, for this example, $A_o = 300$, $A_1 = 1400$ and $A_2 = -14$ were used with Eq. (2) and, for Eq. (3) $T_g(x, 0) = 100 + 80\Pi x - 16(\Pi x)/2!$. Generally the coefficients A_n would be obtained from an initial matrix temperature distribution either measured or computed from a previously known

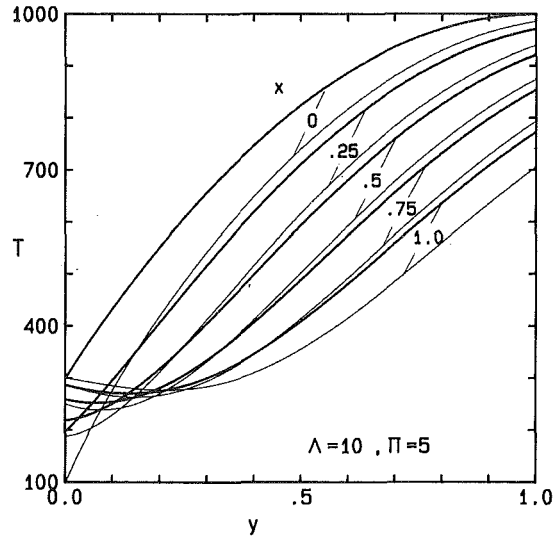

Fig. 1 Temperature distributions of matrix and gas (thin lines) at five times, x

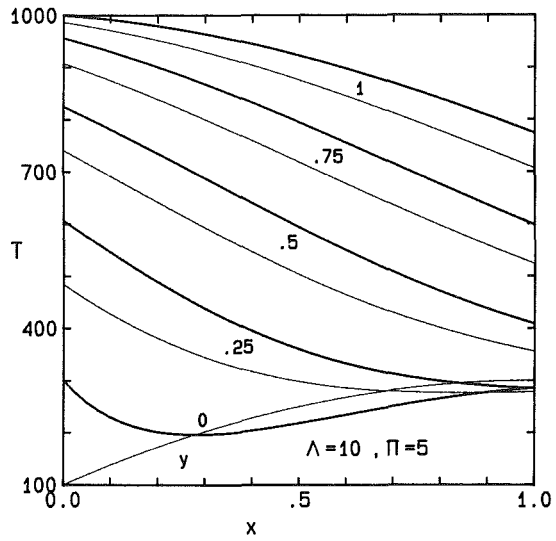

Fig. 2 Temperature histories of matrix and gas (thin lines) at five locations, y

distribution. The inlet gas temperature is, in general, the anticipated inlet gas temperature history (and would decrease with time for a matrix used with a blow-down wind tunnel).

Recharging the matrix with a hot gas is more efficient if the gas flows in the direction opposite to that during discharge because the hot gas then enters the high temperature end of the matrix. In this case y is zero at the other end of the matrix during recharge. Of course Π and Λ will, in general, be different from the values during discharge.

The temperature of the gas leaving the matrix during discharge should be effectively constant to simplify data interpretation. The exiting gas temperature will more nearly be constant as Λ is increased and Π/Λ is made small for discharge. For the charging process Π/Λ should be relatively large. From the parameter definitions, Π/Λ equals wct_p/WC, which can be recognized as the ratio of the thermal capacitance of the mass of gas passed through the matrix during the flow period to the thermal capacitance of the matrix. If parameters during discharge and charge are differentiated by the subscripts d and c then the preceding remarks indicate that $(wct_p)_d/(wct_p)_c$ should be less than unity, that $(wct_p)_d/WC$ should be small compared to unity, and Λ_d should be as large as feasible.

References

Abramowitz, M., and Stegun, I. A., 1964, "Handbook of Mathematical Functions," National Bureau of Standards, Gaithersburg, MD, p. 378.

Anzelius, A., 1926, "Über Erwärmung vermittles durchströmender Medien," *Zeitschrift fur Angewandte Mathematik und Mechanik*, Vol. 6, pp. 291–294.

Larsen, F. W., 1976, "Rapid Calculation of Temperature in a Regenerative Heat Exchanger Having Arbitrary Initial Solid and Entering Fluid Temperatures," *International Journal of Heat and Mass Transfer*, Vol. 10, pp. 149–168.

Romie, F. E., 1987, "Two Functions Used in the Analysis of Crossflow Exchangers, Regenerators and Related Equipment," ASME JOURNAL OF HEAT TRANSFER, Vol. 109. pp. 518–521.

Schumann, T. E. W., 1929, "Heat Transfer: A Liquid Flowing Through a Porous Prism," *Franklin Institute Journal*, Vol. 208, pp. 405–416.

Mixed Convection in a Spherical Enclosure

E. Arquis,[1] N. Richard,[1] J. P. Caltagirone,[1] O. Amiel,[2] and R. Salmon[2]

Nomenclature

a = thermal diffusivity
A = aspect ratio $= (L_x/D)$
B = aspect ratio $= (L_y/D)$
C = aspect ratio $= (L_z/D)$
d = in and outlet pipes internal diameter
D = sphere internal diameter
E = aspect ratio $= (l/D)$
F = aspect ratio $= (d/D)$
l = heating mantle extension in the x direction
L_x = total extension of the computational domain in the x direction
L_y = total extension of the computational domain in the y direction
L_z = total extension of the computational domain in the z direction
P = pressure
Pr = Prandtl number $= (\nu/a)$
Q = flow rate
Ra = Rayleigh number $= (g\beta\Delta TD^3/\nu a)$
Re = Reynolds number $= (VD/\nu)$
T = local temperature
T_I = inlet temperature
T_O = outlet temperature
T_S = sphere wall temperature
T_T = condensation tube wall temperature
V = local fluid velocity
x, y, z = Cartesian coordinates
β = fluid thermal expansion
γ = similarity parameter $= (\mathrm{Ra}/\mathrm{Re}^2\mathrm{Pr})$
λ = fluid thermal conductivity
ΔT = temperature difference $= (T_S - T_I)$
ν = kinematic viscosity

[1]Modélisation Avancée des Systémes Thermiques et Ecoulements Réels, ENSCPB, Université de Bordeaux I, 33405 Talence Cedex, France.

[2]Laboratoire de Chimie du Solide du C.N.R.S., Université de Bordeaux I, 33405 Talence Cedex, France.

Contributed by the Heat Transfer Division of THE AMERICAN SOCIETY OF MECHANICAL ENGINEERS. Manuscript received by the Heat Transfer Division August 1992; revision received March 1993. Keywords: Conjugate Heat Transfer, Mixed Convection, Modeling and Scaling. Associate Technical Editor: F. P. Incropera.

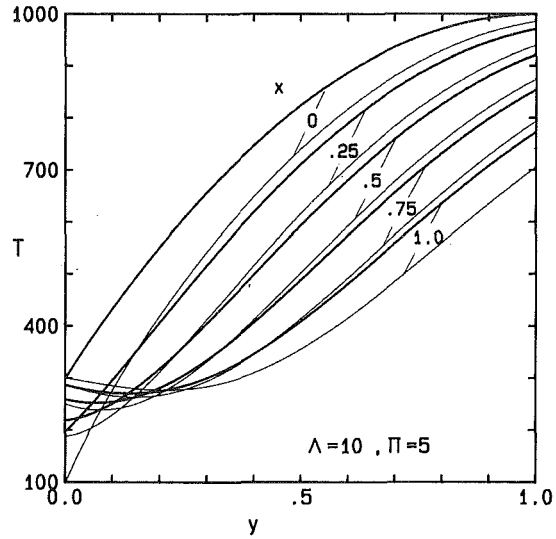

Fig. 1 Temperature distributions of matrix and gas (thin lines) at five times, x

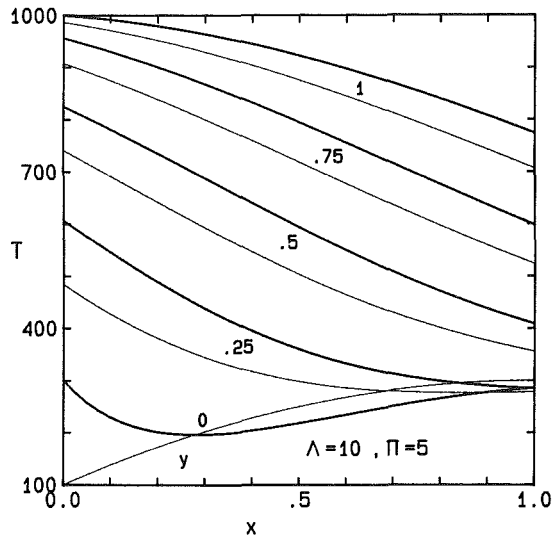

Fig. 2 Temperature histories of matrix and gas (thin lines) at five locations, y

distribution. The inlet gas temperature is, in general, the anticipated inlet gas temperature history (and would decrease with time for a matrix used with a blow-down wind tunnel).

Recharging the matrix with a hot gas is more efficient if the gas flows in the direction opposite to that during discharge because the hot gas then enters the high temperature end of the matrix. In this case y is zero at the other end of the matrix during recharge. Of course Π and Λ will, in general, be different from the values during discharge.

The temperature of the gas leaving the matrix during discharge should be effectively constant to simplify data interpretation. The exiting gas temperature will more nearly be constant as Λ is increased and Π/Λ is made small for discharge. For the charging process Π/Λ should be relatively large. From the parameter definitions, Π/Λ equals wct_p/WC, which can be recognized as the ratio of the thermal capacitance of the mass of gas passed through the matrix during the flow period to the thermal capacitance of the matrix. If parameters during discharge and charge are differentiated by the subscripts d and c then the preceding remarks indicate that $(wct_p)_d/(wct_p)_c$ should be less than unity, that $(wct_p)_d/WC$ should be small compared to unity, and Λ_d should be as large as feasible.

References

Abramowitz, M., and Stegun, I. A., 1964, "Handbook of Mathematical Functions," National Bureau of Standards, Gaithersburg, MD, p. 378.

Anzelius, A., 1926, "Über Erwärmung vermittles durchströmender Medien," *Zeitschrift fur Angewandte Mathematik und Mechanik*, Vol. 6, pp. 291–294.

Larsen, F. W., 1976, "Rapid Calculation of Temperature in a Regenerative Heat Exchanger Having Arbitrary Initial Solid and Entering Fluid Temperatures," *International Journal of Heat and Mass Transfer*, Vol. 10, pp. 149–168.

Romie, F. E., 1987, "Two Functions Used in the Analysis of Crossflow Exchangers, Regenerators and Related Equipment," ASME JOURNAL OF HEAT TRANSFER, Vol. 109. pp. 518–521.

Schumann, T. E. W., 1929, "Heat Transfer: A Liquid Flowing Through a Porous Prism," *Franklin Institute Journal*, Vol. 208, pp. 405–416.

Mixed Convection in a Spherical Enclosure

E. Arquis,[1] N. Richard,[1] J. P. Caltagirone,[1] O. Amiel,[2] and R. Salmon[2]

Nomenclature

a = thermal diffusivity
A = aspect ratio $= (L_x/D)$
B = aspect ratio $= (L_y/D)$
C = aspect ratio $= (L_z/D)$
d = in and outlet pipes internal diameter
D = sphere internal diameter
E = aspect ratio $= (l/D)$
F = aspect ratio $= (d/D)$
l = heating mantle extension in the x direction
L_x = total extension of the computational domain in the x direction
L_y = total extension of the computational domain in the y direction
L_z = total extension of the computational domain in the z direction
P = pressure
Pr = Prandtl number $= (\nu/a)$
Q = flow rate
Ra = Rayleigh number $= (g\beta\Delta TD^3/\nu a)$
Re = Reynolds number $= (VD/\nu)$
T = local temperature
T_I = inlet temperature
T_O = outlet temperature
T_S = sphere wall temperature
T_T = condensation tube wall temperature
V = local fluid velocity
x, y, z = Cartesian coordinates
β = fluid thermal expansion
γ = similarity parameter $= (\mathrm{Ra}/\mathrm{Re}^2\mathrm{Pr})$
λ = fluid thermal conductivity
ΔT = temperature difference $= (T_S - T_I)$
ν = kinematic viscosity

[1]Modélisation Avancée des Systémes Thermiques et Ecoulements Réels, ENSCPB, Université de Bordeaux I, 33405 Talence Cedex, France.

[2]Laboratoire de Chimie du Solide du C.N.R.S., Université de Bordeaux I, 33405 Talence Cedex, France.

Contributed by the Heat Transfer Division of THE AMERICAN SOCIETY OF MECHANICAL ENGINEERS. Manuscript received by the Heat Transfer Division August 1992; revision received March 1993. Keywords: Conjugate Heat Transfer, Mixed Convection, Modeling and Scaling. Associate Technical Editor: F. P. Incropera.

Introduction

Spherical volumes are commonly used in thermal and chemical engineering as mixing tanks or as preheating chambers for fluids. The main interest for operators during experimentation is to predict, starting from key parameters such as the fluid flow rate and the thermal conditions, the variations of the fluid outlet temperature when exiting this chamber. Although the conception and design of such apparatus are often empirical, there is a large interest in trying to determine the more efficient operating conditions by numerical modeling.

The present study was related to the hydrolysis reaction of liquid alkoxide droplets dispersed in a flowing fluid, which leads to the formation of solid particles of controlled size. The full experimental device, presented in Fig. 1, is constituted of three main sections: the injector (where a neutral gas flow nebulized the alkoxide solution), a spherical tank (where the alkoxide is evaporated), and finally the condensation tube (where the nucleation and the growth of alkoxide droplets take place). As these chemical processes are strongly related to the temperature, a precise study of the temperature distribution inside the tube was undertaken; it is reported in Amiel's thesis (1992). For this study, the inlet temperature of the tube (corresponding to the outlet temperature of the sphere) was required and motivated the present modeling of the mixed convection in the spherical tank.

As far as we are aware, only few papers are devoted to natural convection in spherical enclosures and none precisely to mixed convection. Heinrich and Pepper (1989) have studied the natural convection in a spherical cavity, the wall of which was vertically differentially heated. The problem in natural convection mostly studied in a spherical enclosure concerns an isothermal wall temperature, the fluid being heated by an uniform internal heat generation. Hardee (1974) and more recently Hutchins and Marschall (1989) have presented some computations for this configuration, assuming an axisymmetry and then reducing the numerical study to a two-dimensional problem.

Physical Modeling and Set of Equations

To manage the numerical modeling some assumptions have to be made. Firstly, the complex geometry of the injector was likened to a simple tube. The second assumption concerns the shape of the heating chamber. As it appears on Fig. 1 the chamber is not a perfect sphere. This geometric distortion has been neglected; the computational domain concerns only the idealized sphere with a part of the in and out pipes.

The flowing fluid was nitrogen containing liquid droplets; as their size was small and their concentration low the fluid was considered to be Newtonian.

From a thermal point of view, the gas is assumed to enter the sphere at the ambient temperature (T_I); the thermal fluctuations due to the expansion of the fluid and to the vaporization of the alcohol were thus neglected. The heating of the spherical domain wall was ensured by an electrical mantle; a uniform, constant temperature (T_S) is assumed on the wall covered by the mantle, while an ideal adiabatic condition is assumed on the outside. The temperature of the condensation tube wall (T_T) was maintained constant by a fluid circulating in a jacket. Because of the connection between the tube and the sphere we have to consider this thermal condition at the outlet of the spherical domain. Although the temperature difference inside the sphere is a priori large, we assumed that the classical Boussinesq approximation is valid.

According to the previous assumptions, the equations describing the phenomena are the continuity, momentum, and energy equations (here directly written in dimensionless form):

$$\text{div } \mathbf{V} = 0 \tag{1}$$

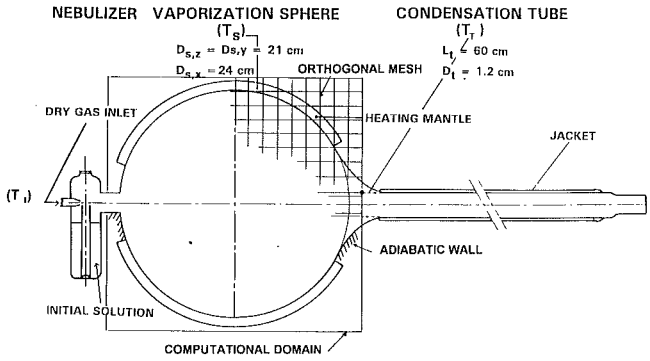

Fig. 1 Schematic of the experimental device and the computational domain

$$\text{div grad } \mathbf{V} - \text{Re } \mathbf{V} \text{ grad } \mathbf{V} + \text{Re grad } P + \text{Ra/(Re Pr) } T = 0 \tag{2}$$

$$\text{div (grad } \mathbf{T} - \text{(Re Pr) } \mathbf{V}T) = 0 \tag{3}$$

The dimensionless numbers are the Reynolds number (Re) based on the flow velocity in the tube, $\overline{V}$, the Rayleigh number (Ra) defined on the temperature difference between the sphere wall and inlet flow ($T_S - T_I$), the Prandtl number (Pr), and the aspect ratios A, B, C, E, F (defined in the nomenclature).

In order to lighten the computations, the flow as well as the temperature were assumed symmetric with respect to the vertical midplane.

Numerical Methodology

The conservation equations were discretized following a popular finite volume method in a primitive (P, V) formulation in association with a SIMPLER procedure. Despite the spherical geometry of the domain, a Cartesian discretization was used. We considered a cubic meshing of the domain including the spherical cavity and a part of the in- and outlets of the tube; the prescribed values of velocity (to ensure the impermeability and the no-slip conditions) and the temperature at the nodes outside the sphere were blocked by a penalization technique. This method is very simple to implement and very adaptive for complex geometry. Obviously there are some drawbacks. First of all the shape of a curvilinear boundary is not well rendered by a Cartesian mesh, especially for coarse grids. A second problem is related to the number of "useless" nodes, i.e., where the velocity is set equal to zero. Despite these disadvantages, we checked in treating some reference cases (natural convection inside a sphere, flow around a sphere, etc.) that the solutions were relatively accurate.

The computations were performed using a $32 \times 16 \times 32$ grid, respectively, in the X, Y, and Z directions. The mesh is regular, except in the axial region where it was adapted to describe more precisely the in and out tube sections. In order to obtain converging solutions the typical CPU time is very important; it could reach 10 hours on an Alliant VFX40 for the highest values of the parameters (Rayleigh and Reynolds numbers, respectively, up to 10^8 and 10^3).

Results and Discussion

Before performing computations in the real experimental conditions, we present a parametric study in order to define the respective influence of the Rayleigh number (in other words the temperature difference between wall and inlet) and the Reynolds number (i.e., the flow rate).

Some temperature profiles along the main X axis for different values of Ra and Re are reported in Fig. 2 (curves (a–f)). In order to estimate the dominant heat transfer mode, it

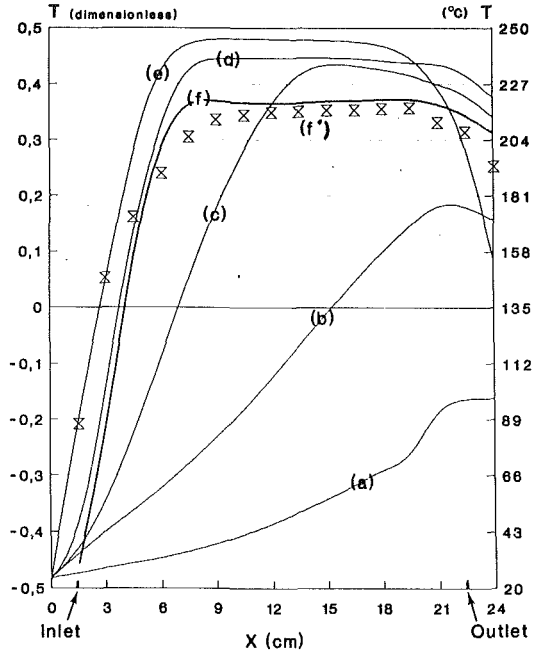

Fig. 2 Computed and experimental temperature distribution along the *X* axis for different values of Rayleigh-Reynolds numbers [Ra, Re]: (*a*) [10^6, 5×10^3], (*b*) [10^5, 10^3], (*c*) [10^6, 10^3], (*d*) [10^7, 10^3], (*e*) [10^5, 10^2], (*f*) [2×10^6, 5×10^3], (*f* ′) [2×10^6, 5×10^3] experimental

Table 1

Physical Parameters	
Sphere diameter	(D): 210 mm
Tube diameter	(d): 12 mm
Domain extension along x	(L_x): 239 mm
Domain extension along y	(L_y): 239 mm
Domain extension along z	(L_z): 239 mm
Heating mantle length	(l): 198 mm
Inflow temperature	(T_I): 20°C
Sphere wall temperature	(T_S): 250°C
Tube wall temperature	(T_T): 60°C
Flow rate	(q): 207 liter/h
Flow velocity ($q/(\Pi d^2/4)$)	(V): 0.5 m/s
Dimensionless Parameters	
Aspect ratio	A (L_x/D): 1.14
" "	B (L_y/D): 1.14
" "	C (L_z/D): 1.14
" "	E (l/D): 1.06
" "	F (d/D): 0.057
Reynolds number (VD/ν)	Re: 5×10^3
Rayleigh number ($g\beta(T_S - T_I)D^3/\mu a$)	Ra: 2×10^8
Prandtl number (ν/a)	Pr: 0.71

is usual in the case of mixed convection problems to introduce the grouping parameter, γ ($\gamma = \mathrm{Ra}/\mathrm{Re}^2\mathrm{Pr}$). For low γ' values (characteristic of a dominant forced convection) the temperature increases very slowly from the entrance to the exit of the spherical chamber, the maximal temperature being reached in the exit region. The rise in temperature is faster, the higher the value of γ, and in addition a local maximum is obtained. The curves corresponding to $\gamma = 10$ exhibit a large isothermal plateau in the major part of the flow axis. In this case, and active natural convection takes place inducing an intense mixing allowing a temperature homogenenization. A same value of γ can be obtained for different values of Rayleigh and Reynolds numbers. For example $\gamma = 10$ corresponds to $\mathrm{Ra} = 10^5$, $\mathrm{Re} = 10^2$, $\mathrm{Pr} = 1$, but also to $\mathrm{Ra} = 10^7$, $\mathrm{Re} = 10^3$, $\mathrm{Pr} = 1$ (curves *d* and *e*, respectively, in Fig. 2). As expected, the two temperature profiles are fairly identical, except in the outlet region. In conclusion, a relatively correct qualitative prediction of the thermal phenomena may be drawn from the value of the parameter $\mathrm{Ra}/\mathrm{Re}^2\mathrm{Pr}$. However, the precise determination of the exit gas temperature requires a full computation of the coupled hydrodynamic and thermal fields in the whole sphere.

From the geometric parameters and the operating conditions (reported in Table 1), the corresponding experimental dimensionless Reynolds and Rayleigh numbers were respectively 5×10^3 and 2×10^8 (so that γ is about 11.4).

The comparison between computed and experimental data turns only on the temperature along the inlet-to-outlet axis. This temperature was measured with a thermocouple placed in an alumina bore tube in axial translation from the outlet. Because of the thermal connection with outside, the temperature was not rigorously unperturbed. It should be stressed that during temperature measurements the condensation tube is removed.

The measured and predicted temperature distributions are presented in Fig. 2 (curves *f* ′ and *f*, respectively). A maximum temperature of about 219°C is experimentally reached at 8 cm from the entrance of the sphere and keeps the same value until 18 cm. This plateau is well predicted by the modeling, although the temperature calculated was 2°C higher. Moreover, some discrepancies in the temperature evolution were observed at both the entrance and the exit regions. These discrepancies may be firstly due to metrological errors (location of the thermocouple, thermal "bridges,". . .) or to some unjustified simplifications in modeling. More precisely the inflow was considered as a perfect one-dimensional jet, when the flow in the injector nozzle was very likely turbulent and three-dimensional. In this way, it is predictable that the real flow reaches the mixing temperature more quickly. In another part, assuming the chamber to a perfect sphere is not correct; the real shape is favorable to a reorganization of the flow in the outlet region (from a "loop" to a jet) probably causing a faster decrease in the temperature.

The modeling gives additional information and particularly the temperature field in the entire domain. As the velocity field is very complex and difficult to plot in such a three-dimensional configuration, the temperature has been used as a "tracer." In Fig. 3, the case where the natural convection is artificially deactivated (i.e., $\mathrm{Ra} = 0$) is compared to the real case ($\mathrm{Ra} = 2 \times 10^8$) by plotting the isotherms in the three main planes. For $\mathrm{Ra} = 0$ (Fig. 3*a*), the temperature field is perfectly axisymmetric in the *X* direction; a large closed convective cell develops around the cold jet, depicting the typical S-shaped isotherm deformation. In this case the velocity is so high that the heating of the fluid is not ensured so that the temperature increases linearwise from in to outlet reaching only 66°C at the exit of the sphere.

In presence of natural convection (Fig. 3*b*) the previous axisymmetry of the temperature field no longer exists. Immediately after entering the chamber, the cold flow deviates strongly toward the lower region of the spherical chamber. The major part of the sphere is filled with a large, three-dimensional convective loop, causing an active thermal homogenization: Note the vertical stratification in the (Y, Z) plane. The view in the (X, Y) plane, where few isothermal lines are drawn, confirms the isothermicity corresponding to the plateau evidenced in Fig. 2 (curve *f*).

Conclusions

Mixed convection driven flows in a spherical enclosure were investigated by a fully three-dimensional numerical modeling. The competition between natural and forced convection was studied through the analysis of the temperature distribution inside the sphere as a function of Rayleigh, Reynolds, and Prandtl numbers. The usual (in mixed convection) parameter γ ($\mathrm{Ra}/\mathrm{Re}^2\mathrm{Pr}$) allows a correct qualitative prediction of the phenomena but is not sufficient to define precisely the outlet temperature. When natural convection is predominant inside the sphere (high Rayleigh number, high γ value), the outlet

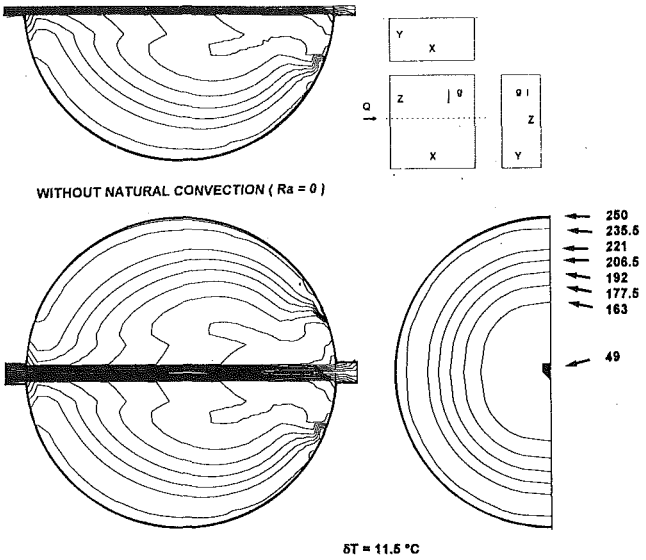

Fig. 3 Mixed convection in a spherical enclosure: isotherm lines ($\delta T = 11.5°C$) in three cutplanes ($Re = 5 \times 10^3$, $Pr = 0.71$): (*a*) without convection ($Ra = 0$); (*b*) with convection ($Ra = 2 \times 10^8$)

temperature seems independent of the Reynolds number (i.e., flow rate), so that the operating range of such a heating chamber is rather large. Simulated and measured temperature profiles are in relatively good agreement, even if the need of a better geometric description of the domain is pointed out.

References

Amiel, O., 1992, "Mécanismes de formation par voie aérosol de particules sphériques de taille contrôlée—Application à la préparation d'oxydes, caractérisation et comportement au frittage," Thesis No. 743, Université de Bordeaux, France.

Hardee, H. C., 1974, "Natural Convection in a Spherical Cavity With Uniform Internal Heat Generation," Internal Report, Sandia Labs, Albuquerque, NM.

Heinrich, J. C., and Pepper, D. W., 1989, "Flow Visualisation of Natural Convection in a Differentially Heated Sphere," ASME FEB-Vol. 85, pp. 135–141.

Hutchins, J., and Marschall, E., 1989, "Pseudosteady-State Natural Convection Heat Transfer Inside Spheres," *Int. J. Heat Mass Transfer*, Vol. 32, pp. 2047–2053.

On the Theoretical Prediction of Transient Heat Transfer Within a Rectangular Fluid-Saturated Porous Medium Enclosure

J. L. Lage[1]

Nomenclature

$A(\mathrm{Pr})$ = squared ratio of thermal and velocity layer thickness
α = thermal diffusivity
β = isobaric coefficient of thermal compressibility
δ = layer thickness
Da = Darcy number = K/H^2
F = inertia coefficient
ϕ = porosity
g = gravity acceleration in the vertical direction
H = enclosure height
J = viscosity ratio = μ_{eff}/μ_f
k = thermal conductivity
K = permeability
L = enclosure length
λ = volumetric specific heat = $(\rho c)_f/(\rho c)_m$
p, P = pressure, $P = \phi^2 H^2 (p + \rho_f g y)/(\rho_f \alpha_m^2)$
Pr = porous modified Prandtl number = ν_f/α_m
Ra = Rayleigh number = $g\beta H^3 (T_h - T_c)/(\nu_f \alpha_m)$
t, τ = time, $\tau = t/(H^2/\alpha_m)$
T, θ = temperature, $\theta = [T - (T_h + T_c)/2]/(T_h - T_c)$
u, U = horizontal velocity component, $U = u/(\alpha_m/H)$
v, V = vertical velocity component, $V = v/(\alpha_m/H)$
x, X = horizontal coordinate, $X = x/H$
y, Y = vertical coordinate, $Y = y/H$
μ = dynamic viscosity
ν = kinematic viscosity
ρ = density

Subscripts

c = cold
eff = effective
f = fluid
h = hot
m = porous medium (fluid and solid matrix)
θ = temperature

Introduction

Most of the existing studies on fluid flow and heat transfer within a fluid-saturated porous medium are based on the simplest flow model presented by Darcy (1856). Refined flow models are available from the literature such as the Forchheimer-extended Darcy model (Forchheimer, 1901) and the Brinkman-extended Darcy model (Brinkman, 1947). The most complex model for fluid flow within a porous medium is the generalized model presented by Vafai and Tien (1981).

Although the generalized model was introduced more than ten years ago, the theoretical heat transfer correlations found

[1]J. L. Embrey Assistant Professor, Mechanical Engineering Department, Southern Methodist University, Dallas, TX 75275-0335; Assoc. Mem. ASME.

Contributed by the Heat Transfer Division of THE AMERICAN SOCIETY OF MECHANICAL ENGINEERS. Manuscript received by the Heat Transfer Division September 1992; revision received April 1993. Keywords: Modeling and Scaling, Natural Convection, Porous Media. Associate Technical Editor: C. E. Hickox, Jr.

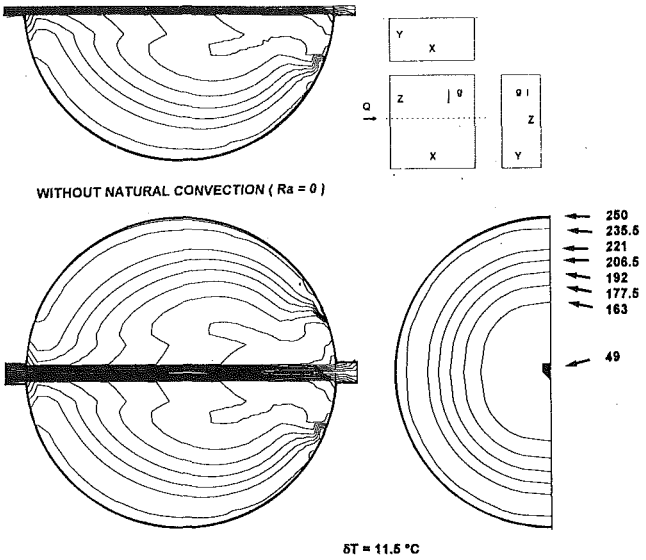

Fig. 3 Mixed convection in a spherical enclosure: isotherm lines ($\delta T = 11.5°C$) in three cutplanes ($Re = 5 \times 10^3$, $Pr = 0.71$): (*a*) without convection ($Ra = 0$); (*b*) with convection ($Ra = 2 \times 10^8$)

temperature seems independent of the Reynolds number (i.e., flow rate), so that the operating range of such a heating chamber is rather large. Simulated and measured temperature profiles are in relatively good agreement, even if the need of a better geometric description of the domain is pointed out.

References

Amiel, O., 1992, "Mécanismes de formation par voie aérosol de particules sphériques de taille contrôlée—Application à la préparation d'oxydes, caractérisation et comportement au frittage," Thesis No. 743, Université de Bordeaux, France.

Hardee, H. C., 1974, "Natural Convection in a Spherical Cavity With Uniform Internal Heat Generation," Internal Report, Sandia Labs, Albuquerque, NM.

Heinrich, J. C., and Pepper, D. W., 1989, "Flow Visualisation of Natural Convection in a Differentially Heated Sphere," ASME FEB-Vol. 85, pp. 135–141.

Hutchins, J., and Marschall, E., 1989, "Pseudosteady-State Natural Convection Heat Transfer Inside Spheres," *Int. J. Heat Mass Transfer*, Vol. 32, pp. 2047–2053.

On the Theoretical Prediction of Transient Heat Transfer Within a Rectangular Fluid-Saturated Porous Medium Enclosure

J. L. Lage[1]

Nomenclature

$A(\mathrm{Pr})$ = squared ratio of thermal and velocity layer thickness
α = thermal diffusivity
β = isobaric coefficient of thermal compressibility
δ = layer thickness
Da = Darcy number = K/H^2
F = inertia coefficient
ϕ = porosity
g = gravity acceleration in the vertical direction
H = enclosure height
J = viscosity ratio = μ_{eff}/μ_f
k = thermal conductivity
K = permeability
L = enclosure length
λ = volumetric specific heat = $(\rho c)_f/(\rho c)_m$
p, P = pressure, $P = \phi^2 H^2 (p + \rho_f g y)/(\rho_f \alpha_m^2)$
Pr = porous modified Prandtl number = ν_f/α_m
Ra = Rayleigh number = $g\beta H^3 (T_h - T_c)/(\nu_f \alpha_m)$
t, τ = time, $\tau = t/(H^2/\alpha_m)$
T, θ = temperature, $\theta = [T - (T_h + T_c)/2]/(T_h - T_c)$
u, U = horizontal velocity component, $U = u/(\alpha_m/H)$
v, V = vertical velocity component, $V = v/(\alpha_m/H)$
x, X = horizontal coordinate, $X = x/H$
y, Y = vertical coordinate, $Y = y/H$
μ = dynamic viscosity
ν = kinematic viscosity
ρ = density

Subscripts

c = cold
eff = effective
f = fluid
h = hot
m = porous medium (fluid and solid matrix)
θ = temperature

Introduction

Most of the existing studies on fluid flow and heat transfer within a fluid-saturated porous medium are based on the simplest flow model presented by Darcy (1856). Refined flow models are available from the literature such as the Forchheimer-extended Darcy model (Forchheimer, 1901) and the Brinkman-extended Darcy model (Brinkman, 1947). The most complex model for fluid flow within a porous medium is the generalized model presented by Vafai and Tien (1981).

Although the generalized model was introduced more than ten years ago, the theoretical heat transfer correlations found

[1]J. L. Embrey Assistant Professor, Mechanical Engineering Department, Southern Methodist University, Dallas, TX 75275-0335; Assoc. Mem. ASME.

Contributed by the Heat Transfer Division of THE AMERICAN SOCIETY OF MECHANICAL ENGINEERS. Manuscript received by the Heat Transfer Division September 1992; revision received April 1993. Keywords: Modeling and Scaling, Natural Convection, Porous Media. Associate Technical Editor: C. E. Hickox, Jr.

in the literature are for simpler flow models. For the simple Darcy flow within a cavity, heat transfer correlations were developed by Weber (1975) and Bejan (1979). The Forchheimer-extended Darcy model was tackled by Poulikakos and Bejan (1985) and by Poulikakos (1985). Heat transfer correlations for the Brinkman-extended Darcy model were presented by Tong and Subramanian (1985) using a Weber-type boundary layer analysis.

The fluid flow and heat transfer phenomena modeled by the general equations are governed by a large number of independent parameters. With this many degrees of freedom it is very difficult—if not impossible!—to find a unique empirical correlation based upon experimental or numerical results. In the present work, it is demonstrated, by using an extended new version of the method of scale analysis, that it is possible to obtain a unique heat transfer correlation valid for the entire spectrum covered by the general equations.

Theoretical Analysis

Consider the natural convection phenomenon within a fluid-saturated porous medium enclosure with impermeable walls, adiabatic top and bottom, and rectangular cross section of width L and height H. The general nondimensional set of equations that governs the transient fluid motion within the enclosure is (Hsu and Cheng, 1990),

$$\frac{\partial U}{\partial X}+\frac{\partial V}{\partial Y}=0 \tag{1}$$

$$\phi\frac{\partial U}{\partial \tau}+\mathbf{V}\cdot\nabla U=-\frac{\partial P}{\partial X}+\phi J\mathrm{Pr}\nabla^2 U-\frac{\phi^2 F}{\mathrm{Da}}|\mathbf{V}|U-\frac{\phi^2\mathrm{Pr}}{\mathrm{Da}}U \tag{2}$$

$$\phi\frac{\partial V}{\partial \tau}+\mathbf{V}\cdot\nabla V=-\frac{\partial P}{\partial Y}+\phi J\mathrm{Pr}\nabla^2 V-\frac{\phi^2 F}{\mathrm{Da}}|\mathbf{V}|V-\frac{\phi^2\mathrm{Pr}}{\mathrm{Da}}V+\phi^2\mathrm{RaPr}\theta \tag{3}$$

$$\frac{1}{\lambda}\frac{\partial\theta}{\partial\tau}+\mathbf{V}\cdot\nabla\theta=\nabla^2\theta \tag{4}$$

where $\mathbf{V}$ is the vector velocity with horizontal, U, and vertical, V, components.

Using the Ergun (1952) model, the nondimensional inertia coefficient can be written as: $F = 1.75\,(\mathrm{Da}/150\,\phi^3)^{1/2}$. Equations (1)–(4) have then six degrees of freedom, namely: medium porosity, ϕ, viscosity ratio, J, modified Prandtl number, $\mathrm{Pr} = \nu_f/\alpha_m$, Darcy number, $\mathrm{Da} = K/H^2$, Rayleigh number, $\mathrm{Ra} = g\beta H^3(T_h - T_c)/(\nu_f\alpha_m)$, and volumetric specific heat, $\lambda = (\rho c)_f/(\rho c)_m$. The parameter J, which accounts for the effective viscosity of the fluid saturated porous medium (Cheng, 1978), is equal to μ_{eff}/μ_f. Also influential upon the results is the aspect ratio of the rectangular enclosure, L/H.

The scaling of the general momentum equations is performed within a region occupied by the upward flow, limited by the hot (left) wall and the center of the enclosure. Cross differentiating Eqs. (2) and (3) to eliminate the pressure term, the resulting equation written in a scale form is

$$\phi\frac{V}{\tau}+V^2\sim-\phi J\mathrm{Pr}\frac{V}{\delta^2}-\frac{0.143\phi^{1/2}}{\mathrm{Da}^{1/2}}V^2-\frac{\phi^2\mathrm{Pr}}{\mathrm{Da}}V+\frac{\phi^2}{2}\mathrm{RaPr}\theta \tag{5}$$

where the nondimensional temperature scale, θ, is replaced by the value 0.5. Notice that in a strict scaling sense, setting $\theta \sim 1$ would not be incorrect. However, the value 0.5 *is* the correct scale, compatible with the selected region within which the present scale analysis is being developed. The importance of scaling consistently within a chosen region is emphasized by Bejan (1984).

The quadratic equation in V presented by Eq. (5) can be solved by first noting that the flow layer thickness, δ, correlates with the thermal layer thickness, δ_θ, as

$$\left(\frac{\delta_\theta}{\delta}\right)^2\sim A(\mathrm{Pr}) \tag{6}$$

where $A(\mathrm{Pr})$ for a porous medium is equivalent to 1 for $\mathrm{Pr}\geq 1$, or equivalent to Pr^{-1} for $\mathrm{Pr}\leq 1$. Equation (6) is the porous medium extension of a scale analysis result obtained for natural convection within a clear fluid enclosure introduced by Bejan (1984, p. 119); note that δ in here is equivalent to his δ_V, and Pr is equivalent to his fluid Pr. Equation (6) can be obtained, after some manipulation, from Eq. (5) and the scale for V obtained from energy Eq. (4), recognizing that δ and J scales are of order 1, and $\mathrm{Da}\leq 1$. Note that when $\mathrm{Pr}\to 0$ the flow tends to Darcy flow, or in other words, Eq. (5) will tend to become linear in V (this was pointed out by Nield and Bejan, 1992, p. 67, considering fluid Pr).

The scaling obtained from continuity Eq. (1), $V \sim U/\delta_\theta$, indicates that the convective terms of Eq. (4) have the same scale. Writing Eq. (4) in a scaling form, dropping the horizontal convective term and neglecting the vertical diffusion term (recall $\delta_\theta \leq 0.5 < 1$), the following expression is obtained for the thermal layer thickness scale:

$$\delta_\theta^2\sim\frac{1}{\left(\frac{1}{\lambda\tau}+V\right)} \tag{7}$$

Solving the quadric in V, Eq. (5), and discarding the negative root (remember that within the scaling region, close to the hot wall, the fluid moves upward, $V > 0$),

$$V\sim\frac{-\Pi+\left[\Pi^2+2\phi^2\mathrm{RaPr}\left(1+\phi JA(\mathrm{Pr})\mathrm{Pr}+\frac{0.143\,\phi^{1/2}}{\mathrm{Da}^{1/2}}\right)\right]^{1/2}}{2\left(1+\phi JA(\mathrm{Pr})\mathrm{Pr}+\frac{0.143\,\phi^{1/2}}{\mathrm{Da}^{1/2}}\right)} \tag{8}$$

where the parameter Π, which contains the time-dependent terms, is written as

$$\Pi=\frac{\phi}{\tau}+\frac{\phi^2\mathrm{Pr}}{\mathrm{Da}}+\frac{\phi JA(\mathrm{Pr})\mathrm{Pr}}{\lambda\tau} \tag{9}$$

The scale of the averaged nondimensional heat flux at the hot wall is defined by the Nusselt number, Nu_h,

$$\mathrm{Nu}_h=\frac{\bar{q}''_h L}{k_m(T_h-T_c)}=-\left(\frac{L}{H}\right)\int_0^1\left(\frac{\partial\theta}{\partial X}\right)_{X=0}dY\sim\frac{(L/H)}{2\delta_\theta} \tag{10}$$

Combining Eqs. (7), (8), and (10), the general scale for Nu_h becomes

$$\mathrm{Nu}_h\sim\frac{(L/H)}{2}\left\{\frac{1}{\lambda\tau}+\frac{-\Pi+\left[\Pi^2+2\phi^2\mathrm{RaPr}\left(1+\phi JA(\mathrm{Pr})\mathrm{Pr}+\frac{0.143\,\phi^{1/2}}{\mathrm{Da}^{1/2}}\right)\right]^{1/2}}{2\left(1+\phi JA(\mathrm{Pr})\mathrm{Pr}+\frac{0.143\,\phi^{1/2}}{\mathrm{Da}^{1/2}}\right)}\right\} \tag{11}$$

It is worth noting that Eq. (11) indeed reduces to the correct Nusselt scale for the steady-state Forchheimer regime (Nield and Bejan, 1992, p. 24), Nu_F, when the groups related to transient, convective inertia, Brinkman, and Darcy terms of Eq. (11) are set equal to zero,

$$Nu_F \sim 0.684\left(\frac{L}{H}\right)\phi^{3/8}Da^{1/8}(RaPr)^{1/4} \tag{12}$$

For clear fluid case at steady state, the groups relating to transient, Darcy, and Forchheimer terms of Eq. (11) are set equal to zero and $\phi = J = 1$. The resulting Nusselt number, Nu_{PF}, resembles the correlations introduced by Churchill and Chu (1975),

$$Nu_{CF} \sim 0.42\left(\frac{L}{H}\right)\left(\frac{RaPr}{(1+A(Pr)Pr)}\right)^{1/4} \tag{13}$$

Figure 1 presents some results from the general Eq. (11) for a square enclosure with Prandtl numbers equal to 1 (top) and 0.01 (bottom) and porosities 0.4 (continuous line) and 0.8 (dashed line). The change in inclination when the Rayleigh number is increased refers to the switch between the Darcy regime when $Nu_h \sim (Ra\ Da)^{1/2}$, and the Forchheimer regime when $Nu_h \sim (Ra\ Da)^{1/4}$.

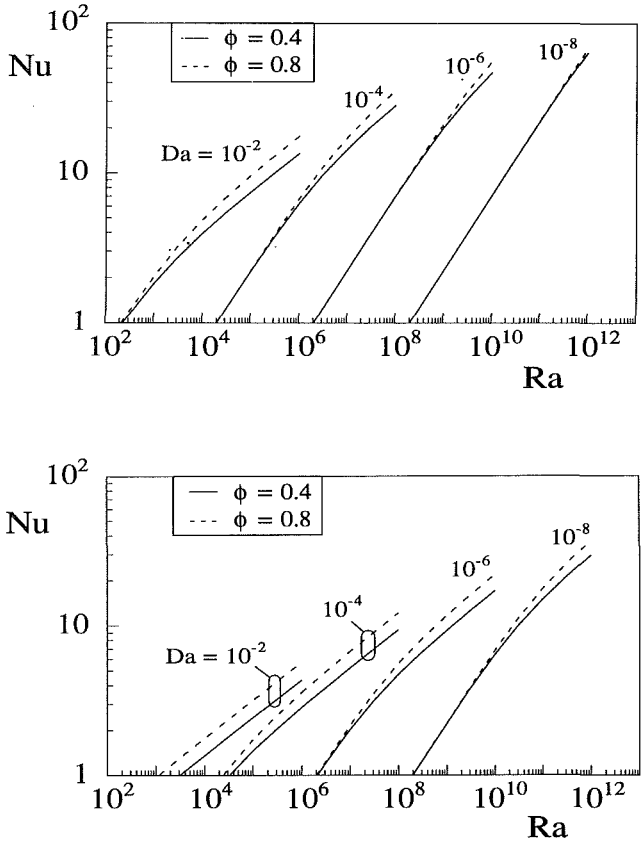

Fig. 1 Theoretical heat transfer results for Pr = 1 (top) and Pr = 0.01 (bottom)

Concluding Remarks

A unique general transient heat transfer correlation for natural convection flow within a rectangular porous medium enclosure heated from the sides is presented. Comparisons against some of the correlations shown in the literature for asymptotic regime show excellent agreement.

As a final comment, it is worth noting that the general heat transfer correlation, Eq. (11), has an extra pedagogical advantage: the identification of individual effects of general momentum equation terms. For instance, exclusion of transient and convective inertia terms from the general momentum equations, as suggested by Nield (1991), is easily implemented, resulting in a modified Nusselt number correlation,

$$Nu \sim \frac{(L/H)}{2}\left\{\frac{-\frac{Pr\,\phi^2}{Da}+\left[\frac{Pr^2\phi^4}{Da^2}+2\phi^2 RaPr\left(\phi JA(Pr)Pr+\frac{0.143\,\phi^{1/2}}{Da^{1/2}}\right)\right]^{1/2}}{2\left(\phi JA(Pr)Pr+\frac{0.143\,\delta^{1/2}}{Da^{1/2}}\right)}\right\}^{1/2} \tag{14}$$

Acknowledgments

Professor Lage acknowledges with gratitude the support from the School of Engineering and Applied Science of Southern Methodist University.

References

Bejan, A., 1979, "On the Boundary Layer Regime in a Vertical Enclosure Filled With a Porous Medium," *Lett. Heat and Mass Transfer*, Vol. 6, pp. 93–102.

Bejan, A., 1984, *Convection Heat Transfer*, Wiley, New York.

Brinkman, H. C., 1947, "A Calculation of the Viscous Force Exerted by a Flowing Fluid on a Dense Swarm of Particles," *Appl. Sci. Res.*, Vol. A1, pp. 27–34.

Cheng, P., 1978, "Heat Transfer in Geothermal Systems," *Advances in Heat Transfer*, Vol. 14, pp. 1–105.

Churchill, S. W., and Chu, H. H., 1975, "Correlating Equations for Laminar and Turbulent Free Convection From a Vertical Plate," *Int. J. Heat Mass Transfer*, Vol. 18, pp. 1323–1329.

Darcy, H., 1856, *Les Fontaines Publiques de la Ville de Dijon*, Victor Dalmond, Paris.

Ergun, S., 1952, "Fluid Flow Through Packed Columns," *Chem. Engng. Prog.*, Vol. 48, pp. 89–94.

Forchheimer, P., 1901, "Wasserbewegung durch Boden," *Z. Ver. D. Ing.*, Vol. 45, pp. 1782–1788.

Hsu, C. T., and Cheng, P., 1990, "Thermal Dispersion in a Porous Medium," *Int. J. Heat Mass Transfer*, Vol. 33, pp. 1587–1597.

Nield, D. A., 1991, "The Limitations of the Brinkman-Forchheimer Equation in Modeling Flow in a Saturated Porous Medium and at an Interface," *Int. J. Heat Fluid Flow*, Vol. 12, pp. 269–272.

Nield, D. A., and Bejan, A., 1992, *Convection in Porous Media*, Springer-Verlag, New York.

Poulikakos, D., 1985, "A Departure From the Darcy Model in Boundary Layer Natural Convection in a Vertical Porous Layer With Uniform Heat Flux From the Side," ASME JOURNAL OF HEAT TRANSFER, Vol. 107, pp. 716–720.

Poulikakos, D., and Bejan, A., 1985, "The Departure From Darcy-Flow in Natural Convection in a Vertical Porous Layer," *Phys. of Fluids*, Vol. 28, pp. 3477–3484.

Tong, T. W., and Subramanian, X. Y., 1985, "A Boundary Layer Analysis for Natural Convection in Porous Enclosure: Use of the Brinkman-Extended Darcy Model," *Int. J. Heat Mass Transfer*, Vol. 28, pp. 563–571.

Vafai, K., and Tien, C. L., 1981, "Boundary and Inertia Effects on Flow and Heat Transfer in Porous Media," *Int. J. Heat Mass Transfer*, Vol. 24, pp. 195–203.

Weber, J. W., 1975, "The Boundary Layer Regime for Convection in a Vertical Porous Layer," *Int. J. Heat Mass Transfer*, Vol. 18, pp. 569–573.

A Unified Examination of the Melting Process Within a Two-Dimensional Rectangular Cavity

C. P. Desai[1] and K. Vafai[2]

Nomenclature

A = aspect ratio of the cavity = Y/X
c_p = specific heat at constant pressure, J/kg-K
H = enthalpy, J/kg
T = temperature, °C
T_C = temperature of the cold wall, °C
T_H = temperature of the hot wall, °C
T_i = initial temperature of the solid, °C
T_l = temperature of the liquid, °C
T_m = fusion temperature, °C
T_s = temperature of the solid, °C
Θ_l = dimensionless liquid temperature = $(T_l - T_m)/(T_H - T_m)$
Θ_s = dimensionless solid temperature = $(T_s - T_m)/(T_m - T_C)$

Introduction

Phase change in metallurgical systems has received a great deal of research attention in the last 15 years (Sparrow et al., 1977; Gau and Viskanta, 1984; 1986; Brent et al., 1988; Viskanta, 1988). The difficulty involved in the numerical simulation of the phase-change problem is the need for tracking the position of the phase-change front as melting or solidification proceeds. Furthermore, at the phase-change front, interface conditions on temperature, velocity, and heat flux must be imposed. This poses some computational difficulties. To account for the position of the phase-change front properly (e.g., Sparrow et al., 1977; Webb and Viskanta, 1986), a transformed coordinate system resulting in a deformable grid distribution must be used. The enthalpy approach does not require a transformed coordinate system and constitutes another basic approach to the phase-change problem (Bonacina et al., 1973; Comini et al., 1974; Morgan et al., 1978; Voller et al., 1987).

Viskanta and co-workers (Gau and Viskanta, 1984, 1986; Webb and Viskanta, 1986; Beckermann and Viskanta, 1989) have done a considerable amount of pioneering experimental and numerical work to provide greater understanding of the melting of gallium in the presence of natural convection. The classical experiments that have already been performed in this area are those by Gau and Viskanta (1984, 1986) and Beckermann and Viskanta (1989). The pertinent numerical simulations that have been carried out and compared with some of these experimental results are those by Webb and Viskanta (1986), Brent et al. (1988), Beckermann and Viskanta (1989), Lacroix and Voller (1990), and Dantzig (1989). The experimental results have served very well their original purpose for providing insights into the general features of the melting process. However, due to the need for accurate predictions of the melting process, the development of well-defined and precise experimental techniques and results need to be reestablished, so as to ascertain the validity of new numerical schemes developed to solve phase-change problems. In the present work, we aim to establish and discuss the importance and the need for resolution of this issue.

All results presented in this work were obtained using a finite element formulation of the enthalpy approach (Bonacina et al., 1973; Comini et al., 1974; Morgan et al., 1978; Dantzig, 1989). The numerical scheme used here is based on the Galerkin-based weighted residual method of the finite element formulation. Results have been obtained for the conditions cited in the past (Gau and Viskanta, 1986; Brent et al., 1988; Beckermann and Viskanta, 1989; Webb and Viskanta, 1986; Lacroix and Voller, 1990) and rigorous detailed comparisons have been made between the present unified set of results and the previously obtained experimental and numerical results.

Analysis

The physical system considered here is a rectangular cavity containing solid metal at a uniform temperature T_i, which is lower than or equal to the melting point of the metal T_m. Melting begins as a result of the sudden elevation of the left vertical wall temperature to T_H where $T_H > T_m$. The equations governing this process are the Boussinesq forms of the continuity and momentum equations coupled with the energy equation in the liquid and the heat conduction equation in the solid. These equations were solved using the Galerkin-based weighted residual method (FIDAP, 1991).

The representation of discontinuities at the phase-change interface is an important feature in the modeling of phase-change problems. Four approaches, the SLOPE, SPATIAL, temporal INTEGRATION, and temporal NODAL methods were explored in this study. Essentially, the difference between these methods is the manner in which the enhanced specific heat is evaluated. The performance of the four approaches was evaluated by comparing against the analytical solution of the one-dimensional freezing problem of a pure material. It was established that the SPATIAL method, which is based on computing the specific heat using $C_p = (\nabla H \cdot \nabla H / \nabla T \cdot \nabla T)^{1/2}$ gives the best results among all the four methods for both low and high Stefan numbers. ∇H and ∇T are the gradients of enthalpy and temperature at the integration points. They are evaluated using the interpolation functions and the nodal values of these variables. This is to be expected because of the more accurate representation of the effective specific heat in the SPATIAL formulation.

An appropriate viscosity-temperature relationship (Gartling, 1980) is used in conjunction with the enthalpy-temperature curve to force the velocity to be zero in the solid phase. Also, the thermal conductivity is specified as a function of temperature to account for the different thermal conductivities of the solid and liquid phases. In each phase, however, all the thermophysical properties of the material are assumed to be constant.

Computations were made for the present problem (convection-driven gallium melting) using the SLOPE and SPATIAL approaches. For the SPATIAL method a zero mushy zone was used for the enthalpy-temperature curve, i.e., the latent heat jump was assumed to occur at the fusion temperature itself and not spread out over a range of temperatures. During the initial stages of the simulation using the SLOPE method, our numerical experimentation revealed that increasing the mushy zone from 0.38 to 0.8°C changed the results by only 1.1 percent. Our results based on the SLOPE method indicate that the melting rates obtained can be close to experimental results provided the mushy zone is selected judiciously through prior numerical experimentation. In obtaining the results, the time step size chosen was small enough (0.1–0.15 s) to ensure that the phase-change front does not jump across any of the ele-

[1]Graduate Research Assistant, Department of Mechanical Engineering, The Ohio State University, Columbus, OH.
[2]Professor, Department of Mechanical Engineering, The Ohio State University, Columbus, OH; Fellow ASME.

Contributed by the Heat Transfer Division of THE AMERICAN SOCIETY OF MECHANICAL ENGINEERS. Manuscript received by the Heat Transfer Division October 1992; revision received April 1993. Keywords: Materials Processing and Manufacturing Processes, Numerical Methods, Phase-Change Phenomena. Associate Technical Editor: J. H. Kim.

Table 1 The three cases considered in the present study

Case	Previous work	T_H	T_C	T_i	X	Y
(i)	Gau and Viskanta (1986) Brent et al. (1988)	38 °C	28.3 °C	28.3 °C	8.89 cm	6.35 cm
(ii)	Gau and Viskanta (1986) Webb and Viskanta (1986) Lacroix and Voller (1990)	38.3 °C	28.3 °C	28.3 °C	8.89 cm	4.45 cm
(iii)	Beckermann and Viskanta (1989)	39.98 °C	24.98 °C	29.78 °C	4.76 cm	4.76 cm

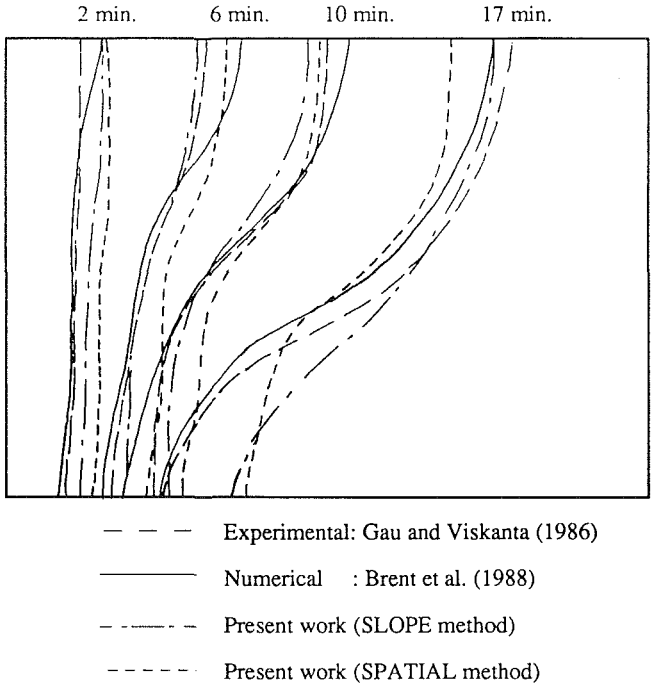

Fig. 1 Comparison of the melt front at t = 2, 6, 10, and 17 min (A = 0.714, T_H = 38°C)

ments. Thus the correct amount of latent heat was released in each element. This along with the use of a very fine mesh ensured higher accuracy of the results. The grid consisted of nine-noded quadrilateral elements with quadratic interpolation for the temperature and velocity fields. In each case, the correct grid size was arrived at by making *extensive* numerical runs so that the grid size independence was established. The system of algebraic equations resulting from the discretization of the governing equations was solved by using a Newton–Raphson iteration solver with a convergence criterion of 10^{-5}.

Results and Discussion

Three cases were considered here for comparison with previous studies. The conditions used to simulate the three cases along with the mesh size used in the present study are shown in Table 1. In each case, gallium was used as the working metal. Gallium properties listed by Brent et al. (1988) were used to ensure consistency in the analysis. The melting point of gallium is 29.78°C.

Figure 1 shows a comparison of the results at times 2, 6, 10, and 17 min for case (*i*). It can be seen that at early times (2 min) the results obtained using the finite element algorithm are in closer agreement with those of the experimental observations of Gau and Viskanta (1986). Overall, the numerical results show fairly good agreement with the experimental results and also with the numerical results of Brent et al. (1988).

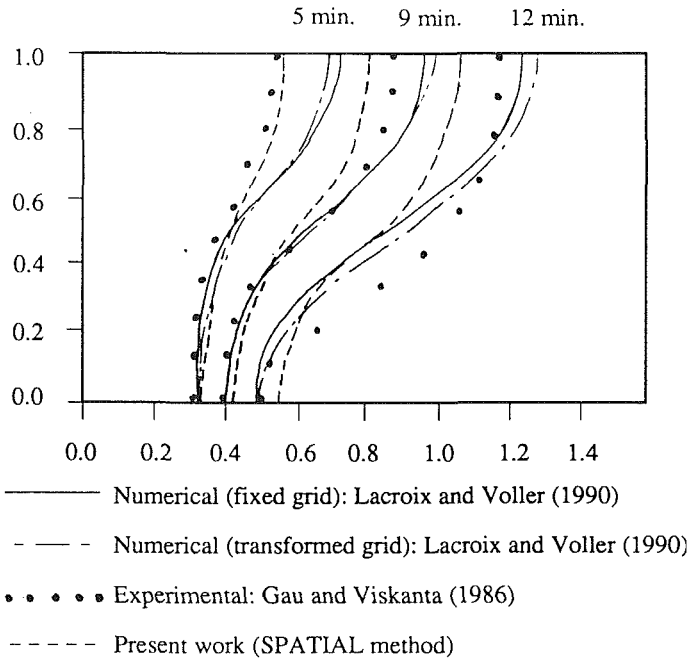

Fig. 2 Comparison of the melt front at t = 5, 8, and 12 min (A = 0.5, T_H = 38.3°C)

However, the present study substantially overpredicts the melting rate within the lower part of the cavity. To reconfirm that this was not caused by insufficient grid density, the results were obtained again after the grid size was halved. The grid distribution was also considerably refined near the walls of the cavity to resolve the steeper gradients near the walls. However, the results remained unchanged, reconfirming that grid independence had indeed been established.

Gau and Viskanta (1986) used the pour-out method to obtain the shape of the interface at different time steps. To obtain the position of the phase-change front at any instant, the experiment was carried out until that time. At that instant, the liquid metal was poured out and the position of the interface was determined. A new experiment was then started. The inaccuracies involved in the implementation of this method increase continuously as time progresses because more molten liquid needs to be drained out from the cavity. This is probably the reason why the experimental results show less molten metal at the bottom of the cavity and more near the top of the cavity than that predicted by the present work. As expected, this pattern becomes more pronounced at later times. It is anticipated that some of the molten metal in the bottom portion of the cavity solidifies and more solid melts at the top of the cavity during the drain-out process of the molten metal from the cavity.

Figure 2 shows the comparisons of the present work with previous experimental studies by Gau and Viskanta (1986) and the numerical studies of Lacroix and Voller (1990), i.e., case (*ii*) in the present study. Once again, the model used here does represent the melting process accurately at earlier times but shows a digression at later times, particularly in the lower part of the cavity. This is consistent with our earlier observations. It further confirms our previous arguments regarding the inadequacies associated with the pour-out method and need for the development of more well-defined and precise experimental techniques; results need to be re-established.

The numerical results of Webb and Viskanta (1986) substantially overpredict the melting rate. This is probably because the numerical model used by Webb and Viskanta (1986) does not account for conduction in the solid phase. Although sub-

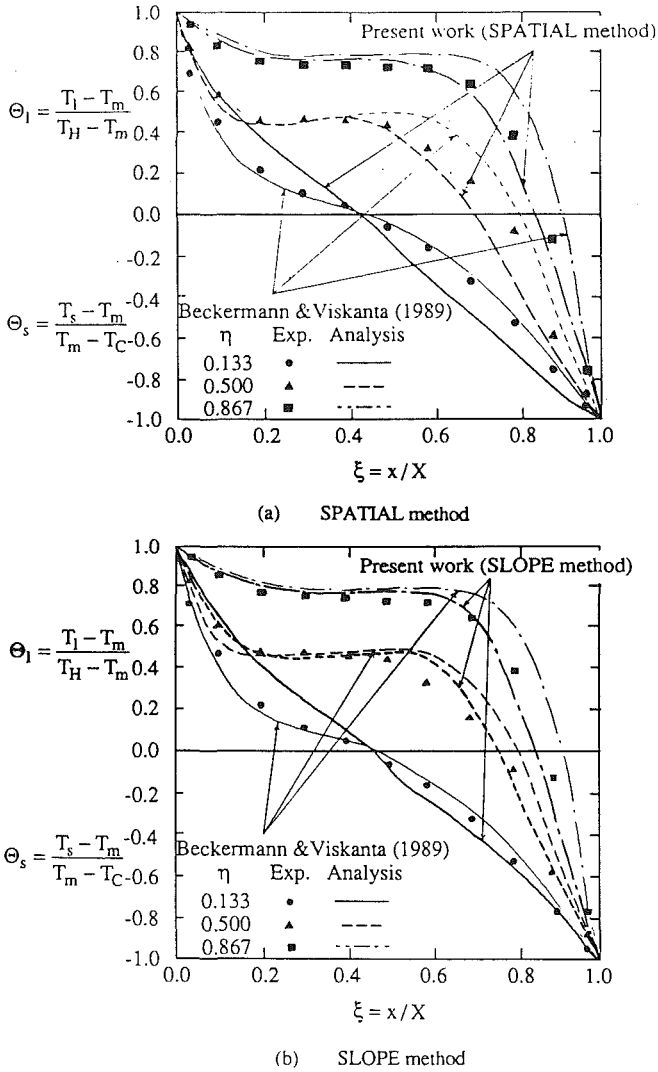

Fig. 3 Comparison of temperature profiles with results of Beckermann and Viskanta (1989) at t = 10 min

cooling is not substantial in this particular case, conduction is expected to impede the melting rate to some extent. The overprediction of the melting rate when compared with the experimental data can thus be anticipated using this model.

The effect of solid subcooling on the melting of gallium was studied experimentally as well as numerically by Beckermann and Viskanta (1989). The experimental results used in their study are more reliable than the experimental set-up used by Gau and Viskanta (1986). This is because of the more sophisticated techniques used in the experimental work of Beckermann and Viskanta (1989) as compared to the pour-out method used by Gau and Viskanta (1986). They found that solid subcooling significantly reduces the melting rate. Because the cold wall is kept at a temperature below the fusion temperature of the metal, the phase-change interface finally reaches a stationary position. Comparisons were made for a set of experimental data presented by Beckermann and Viskanta (1989), i.e., case (*iii*). Figure 3 shows the comparison between our results and those presented by Beckermann and Viskanta (1989) at t = 10 min. In this figure, η is the dimensionless y coordinate and ξ is the dimensionless x coordinate, i.e., $\eta = y/Y$ and $\xi = x/X$.

Conclusions

The gallium phase-change problem has been used in the past by other investigators for benchmarking their numerical schemes. But in all previous studies, the numerical schemes have been mainly tested only against a single set of experimental or numerical results. In the present study, several broad cases with different boundary and initial conditions and also different cavity dimensions were considered. One of the primary accomplishments in the present work is the assimilation of past studies by obtaining solutions to this problem by using a single robust algorithm, which was chosen after analyzing four different algorithms, subjected to a very extensive numerical analysis to ensure grid size and time step size independence as well as mushy zone thickness independence. Furthermore, the effect of the various approaches used to incorporate the enhanced specific heat was studied to ensure that the present results were accurate. Based on the results obtained, the need for developing well-defined and precise experimental techniques and results has been established. However, the observed discrepancies between some of the experimental and theoretical results could also be a result of several mathematical idealizations incorporated in the models being used to simulate the problem. In what follows some of these aspects that need to be clearly correlated between the experimental and numerical techniques in future investigations are presented.

(*i*) Heat exchangers have a finite heat capacity and hence, it is virtually impossible to impose a constant wall temperature instantaneously. This effect is even more prominent in the problem being considered here because of the high thermal conductivity of the liquid metal.

(*ii*) It may be necessary to incorporate the subcooling of the solid phase in all theoretical models (particularly when the theoretical results are compared with Gau and Viskanta's (1986) experiments) since the initial temperature of the solid during the experiments was not exactly the melting point of gallium. Subcooling of the solid phase has been considered in the present work. However, since definite data on the degree of subcooling are unknown, it is difficult to estimate the effect of this factor on the accuracy of the results.

(*iii*) Three-dimensional effects are probably present. Therefore, in future studies, either the experiments have to be devised such that the three-dimensional effects are minimized or a full three-dimensional analysis is necessary to simulate this problem correctly.

(*iv*) Another issue that requires more fundamental attention is the fact that the liquid metal may not wet the thermocouple junction. What gallium does to the thermocouple junction is yet to be determined.

Thus any future experimental work in this field should be aimed at attaining experimental conditions that can also be precisely simulated in theoretical models. The results presented and analyzed in this work thus establish the need for the development of combined numerical and experimental investigations in this area so as to ascertain the validity of new numerical schemes for solving phase-change problems.

References

Beckermann, C., and Viskanta, R., 1989, "Effect of Solid Subcooling on Natural Convection Melting of a Pure Metal," ASME JOURNAL OF HEAT TRANSFER, Vol. 11, pp. 416-424.

Bonacina, C., Comini, G., Fasano, A., and Primicerio, M., 1973, "Numerical Solution of Phase-Change Problems," *International Journal of Heat and Mass Transfer*, Vol. 16, pp. 1825-1832.

Brent, A. D., Voller, V. R., and Reid, K. J., 1988, "Enthalpy-Porosity Technique for Modeling Convection-Diffusion Phase Change: Application to the Melting of a Pure Metal," *Numerical Heat Transfer*, Vol. 13, pp. 297-318.

Comini, G., Del Guidice, S., Lewis, R. W., and Zienkiewicz, O. C., 1974, "Finite Element Solution of Non-linear Heat Conduction Problems With Special Reference to Phase Change," *International Journal for Numerical Methods in Engineering*, Vol. 8, pp. 613-624.

Dantzig, J. A., 1989, "Modeling Liquid-Solid Phase Changes With Melt Convection," *International Journal for Numerical Methods in Engineering*, Vol. 28, pp. 1769-1785.

FIDAP, 1991, *Theoretical Manual*, Fluid Dynamics International, Evanston, IL.

Gartling, D. K. 1980, "Finite Element Analysis of Convection Heat Transfer Problems in Phase Change," in: *Computer Methods in Fluids*, K. Morgan et al., eds., Pentech, London.

Gau, C., and Viskanta, R., 1984, "Melting and Solidification of a Metal System in a Rectangular Cavity," *International Journal of Heat and Mass Transfer*, Vol. 27, pp. 113–123.

Gau, C., and Viskanta, R., 1986, "Melting and Solidification of a Pure Metal on a Vertical Wall," ASME JOURNAL OF HEAT TRANSFER, Vol. 108, pp. 174–181.

Lacroix, M., and Voller, V. R., 1990, "Finite Difference Solutions of Solidification Phase Change Problems: Transformed Versus Fixed Grids," *Numerical Heat Transfer*, Part B, Vol. 17, pp. 25–41.

Morgan, K., Lewis, R. W., and Zienkiewicz, O. C., 1978, "An Improved Algorithm for Heat Conduction Problems With Phase Change," *International Journal of Numerical Methods in Engineering*, Vol. 12, pp. 1191–1195.

Sparrow, E. M., Patankar, S. V., and Ramadhyani, S., 1977, "Analysis of Melting in the Presence of Natural Convection in the Melt Region," ASME JOURNAL OF HEAT TRANSFER, Vol. 99, pp. 520–526.

Viskanta, R., 1988, "Heat Transfer During Melting and Solidification of Metals," ASME JOURNAL OF HEAT TRANSFER, Vol. 110, pp. 1205–1219.

Voller, V. R., Cross, M., and Markatos, N. C., 1987, "An Enthalpy Method for Convection/Diffusion Phase Change," *International Journal of Numerical Methods in Engineering*, Vol. 24, pp. 271–284.

Webb, B. W., and Viskanta, R., 1986, "Analysis of Heat Transfer During Melting of a Pure Metal From an Isothermal Vertical Wall," *Numerical Heat Transfer*, Vol. 9, pp. 539–558.

Ultrasonic Measurement of Solid–Liquid Interface for the Solidification of Water in a Rectangular Enclosure

M. W. McDonough[1] and A. Faghri[1]

Introduction

Solidification heat transfer has become an important area of research, with applications in latent heat thermal energy storage (LHTES). With the increasing cost of energy, the need for energy conservation, and the development of solar energy systems, the use of LHTES systems in residential, commercial, industrial, and aerospace applications has steadily increased. The dominant factor of experimental phase-change research is the location of the solid–liquid interface as a function of time. The experimental techniques used by previous investigators to measure the solid–liquid interface location during phase change can be divided into three categories: photographic, temperature measurement, and physical measurement. Each method only provides a "snapshot" of the interface location, that is, a frozen moment in time. With photographic techniques (Bathelt and Viskanta, 1980; Rieger and Beer, 1986; Webb et al., 1987), the test cell geometry is limited since the test cell must be designed to allow light rays parallel to the solid–liquid interface to pass through. Also, the choice of phase-change material (PCM) is limited since the PCM must possess specific optical properties. During experimentation, the photographic technique requires the removal of insulation from around the test cell, which is used to minimize the heat losses to the ambient. In order to maintain minimal ambient heat losses, the photographic technique can only be used at large time intervals, and thus only provide a limited quantity of experimental data.

With the physical measurement technique (Sparrow et al., 1981; Choi and Hong, 1990), the test cell geometry is also limited since the solidified or unmelted material has to be removed or physically probed. The major disadvantage of the physical measurement technique is that it is destructive in nature during the removal of the specimen from the test cell. Once the specimen has been removed, the test is concluded, thus requiring a large number of experimental runs to obtain a sufficient amount of data points.

The temperature measurement technique (Kalhori and Ramadhyani, 1985; Benard et al., 1986) is an intrusive method in which probes are placed in the test cell to detect the temperature at specific locations in the PCM. Unfortunately, the probes disrupt the fluid flow in all areas of the melted PCM and conduct heat throughout the PCM by acting as fins. Another disadvantage of this technique is that the solid–liquid interface can only be obtained at specific spatial locations in the test cell that correspond to the temperature probe locations.

The objectives of the present investigation of the solidification of water in an rectangular enclosure with isothermal end walls are: (1) to determine the solid–liquid interface position using a nonintrusive pulse-echo ultrasonic measurement technique during the solidification of water in a rectangular enclosure, (2) to investigate conduction-controlled and natural-convection-controlled solidification experimentally in a rectangular enclosure including flow visualization of the natural convection of water through its density inversion.

Experimental Methodology

The advantages of ultrasonic measurement over the previously used techniques are that the ultrasonic technique is nonintrusive and provides a means to measure the solid–liquid interface location continuously both temporally and spatially. Also, ultrasonic techniques are not restricted to particular test cell geometries.

Ultrasonic measurement technology has foundations in acoustics and has been widely used in nondestructive materials testing (Bray and Stanley, 1989) and in medical imaging (Hykes et al., 1985). The basis of ultrasonic measurement techniques is in propagation of mechanical vibrations in solid or liquid materials. In the present investigation, the ultrasonic technique commonly called the pulse-echo method (Krautkramer, 1977) has been used. The pulse-echo method is based on the fact that the propagation of a sound wave through a material is disturbed at a boundary of the material. If a boundary exists between materials of different acoustic properties, a sound wave will be partially reflected at the boundary and partially transmitted through the boundary into the other material. The intensity of the sound reflected or transmitted at a boundary (interface) is dependent on the acoustic properties of the two materials.

The location of the solid–liquid interface was determined by the pulse-echo ultrasonic technique. At the solid–liquid interface a boundary exists between two materials of different acoustic properties, ice and water, which will reflect a portion of a sound wave striking it. In the pulse-echo technique, a piezoelectric transducer is used to send and receive an ultrasonic pulse. When this pulse encounters a boundary, the sound wave is partially transmitted and partially reflected as shown schematically in Fig. 1. This reflected sound wave or echo is then received by the transducer. The time of flight in which the sound wave travels from the transducer to a boundary and is reflected back to the transducer is used to determine the distance traveled by the sound pulse.

Once a solidification test was complete, the stored ultrasonic signals were processed by a wave processing program. The

[1]Department of Mechanical and Materials Engineering, Wright State University, Dayton, OH 45435.

Contributed by the Heat Transfer Division of THE AMERICAN SOCIETY OF MECHANICAL ENGINEERS. Manuscript received by the Heat Transfer Division November 1992; revision received April 1993. Keywords: Instrumentation, Moving Boundaries, Phase-Change Phenomena. Associate Technical Editor: J. H. Kim.

Gartling, D. K. 1980, "Finite Element Analysis of Convection Heat Transfer Problems in Phase Change," in: *Computer Methods in Fluids*, K. Morgan et al., eds., Pentech, London.

Gau, C., and Viskanta, R., 1984, "Melting and Solidification of a Metal System in a Rectangular Cavity," *International Journal of Heat and Mass Transfer*, Vol. 27, pp. 113–123.

Gau, C., and Viskanta, R., 1986, "Melting and Solidification of a Pure Metal on a Vertical Wall," ASME JOURNAL OF HEAT TRANSFER, Vol. 108, pp. 174–181.

Lacroix, M., and Voller, V. R., 1990, "Finite Difference Solutions of Solidification Phase Change Problems: Transformed Versus Fixed Grids," *Numerical Heat Transfer*, Part B, Vol. 17, pp. 25–41.

Morgan, K., Lewis, R. W., and Zienkiewicz, O. C., 1978, "An Improved Algorithm for Heat Conduction Problems With Phase Change," *International Journal of Numerical Methods in Engineering*, Vol. 12, pp. 1191–1195.

Sparrow, E. M., Patankar, S. V., and Ramadhyani, S., 1977, "Analysis of Melting in the Presence of Natural Convection in the Melt Region," ASME JOURNAL OF HEAT TRANSFER, Vol. 99, pp. 520–526.

Viskanta, R., 1988, "Heat Transfer During Melting and Solidification of Metals," ASME JOURNAL OF HEAT TRANSFER, Vol. 110, pp. 1205–1219.

Voller, V. R., Cross, M., and Markatos, N. C., 1987, "An Enthalpy Method for Convection/Diffusion Phase Change," *International Journal of Numerical Methods in Engineering*, Vol. 24, pp. 271–284.

Webb, B. W., and Viskanta, R., 1986, "Analysis of Heat Transfer During Melting of a Pure Metal From an Isothermal Vertical Wall," *Numerical Heat Transfer*, Vol. 9, pp. 539–558.

Ultrasonic Measurement of Solid–Liquid Interface for the Solidification of Water in a Rectangular Enclosure

M. W. McDonough[1] and A. Faghri[1]

Introduction

Solidification heat transfer has become an important area of research, with applications in latent heat thermal energy storage (LHTES). With the increasing cost of energy, the need for energy conservation, and the development of solar energy systems, the use of LHTES systems in residential, commercial, industrial, and aerospace applications has steadily increased. The dominant factor of experimental phase-change research is the location of the solid–liquid interface as a function of time. The experimental techniques used by previous investigators to measure the solid–liquid interface location during phase change can be divided into three categories: photographic, temperature measurement, and physical measurement. Each method only provides a "snapshot" of the interface location, that is, a frozen moment in time. With photographic techniques (Bathelt and Viskanta, 1980; Rieger and Beer, 1986; Webb et al., 1987), the test cell geometry is limited since the test cell must be designed to allow light rays parallel to the solid–liquid interface to pass through. Also, the choice of phase-change material (PCM) is limited since the PCM must possess specific optical properties. During experimentation, the photographic technique requires the removal of insulation from around the test cell, which is used to minimize the heat losses to the ambient. In order to maintain minimal ambient heat losses, the photographic technique can only be used at large time intervals, and thus only provide a limited quantity of experimental data.

With the physical measurement technique (Sparrow et al., 1981; Choi and Hong, 1990), the test cell geometry is also limited since the solidified or unmelted material has to be removed or physically probed. The major disadvantage of the physical measurement technique is that it is destructive in nature during the removal of the specimen from the test cell. Once the specimen has been removed, the test is concluded, thus requiring a large number of experimental runs to obtain a sufficient amount of data points.

The temperature measurement technique (Kalhori and Ramadhyani, 1985; Benard et al., 1986) is an intrusive method in which probes are placed in the test cell to detect the temperature at specific locations in the PCM. Unfortunately, the probes disrupt the fluid flow in all areas of the melted PCM and conduct heat throughout the PCM by acting as fins. Another disadvantage of this technique is that the solid–liquid interface can only be obtained at specific spatial locations in the test cell that correspond to the temperature probe locations.

The objectives of the present investigation of the solidification of water in an rectangular enclosure with isothermal end walls are: (1) to determine the solid–liquid interface position using a nonintrusive pulse-echo ultrasonic measurement technique during the solidification of water in a rectangular enclosure, (2) to investigate conduction-controlled and natural-convection-controlled solidification experimentally in a rectangular enclosure including flow visualization of the natural convection of water through its density inversion.

Experimental Methodology

The advantages of ultrasonic measurement over the previously used techniques are that the ultrasonic technique is nonintrusive and provides a means to measure the solid–liquid interface location continuously both temporally and spatially. Also, ultrasonic techniques are not restricted to particular test cell geometries.

Ultrasonic measurement technology has foundations in acoustics and has been widely used in nondestructive materials testing (Bray and Stanley, 1989) and in medical imaging (Hykes et al., 1985). The basis of ultrasonic measurement techniques is in propagation of mechanical vibrations in solid or liquid materials. In the present investigation, the ultrasonic technique commonly called the pulse-echo method (Krautkramer, 1977) has been used. The pulse-echo method is based on the fact that the propagation of a sound wave through a material is disturbed at a boundary of the material. If a boundary exists between materials of different acoustic properties, a sound wave will be partially reflected at the boundary and partially transmitted through the boundary into the other material. The intensity of the sound reflected or transmitted at a boundary (interface) is dependent on the acoustic properties of the two materials.

The location of the solid–liquid interface was determined by the pulse-echo ultrasonic technique. At the solid–liquid interface a boundary exists between two materials of different acoustic properties, ice and water, which will reflect a portion of a sound wave striking it. In the pulse-echo technique, a piezoelectric transducer is used to send and receive an ultrasonic pulse. When this pulse encounters a boundary, the sound wave is partially transmitted and partially reflected as shown schematically in Fig. 1. This reflected sound wave or echo is then received by the transducer. The time of flight in which the sound wave travels from the transducer to a boundary and is reflected back to the transducer is used to determine the distance traveled by the sound pulse.

Once a solidification test was complete, the stored ultrasonic signals were processed by a wave processing program. The

[1]Department of Mechanical and Materials Engineering, Wright State University, Dayton, OH 45435.

Contributed by the Heat Transfer Division of THE AMERICAN SOCIETY OF MECHANICAL ENGINEERS. Manuscript received by the Heat Transfer Division November 1992; revision received April 1993. Keywords: Instrumentation, Moving Boundaries, Phase-Change Phenomena. Associate Technical Editor: J. H. Kim.

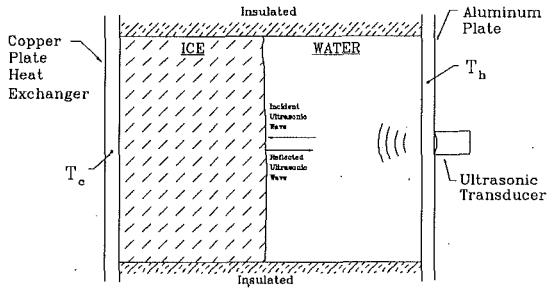

Fig. 1 Schematic of test cell and the implementation of the pulse-echo ultrasonic measurement technique

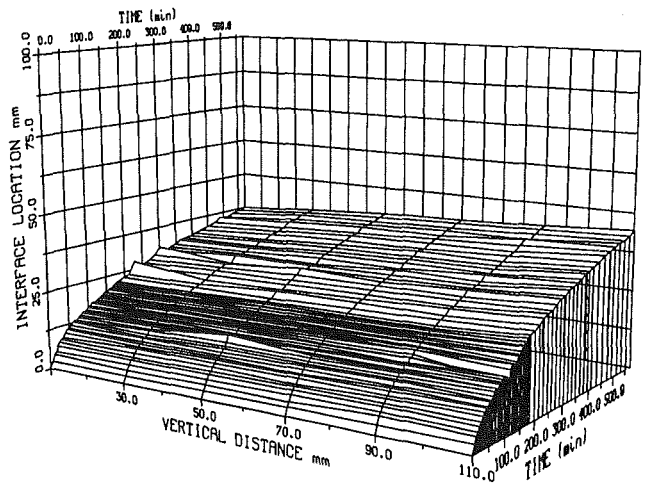

(a) Case 1, Conduction–Controlled

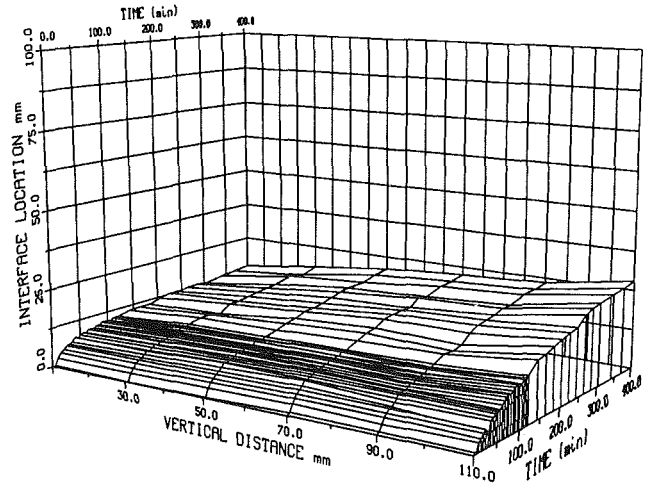

(b) Case 5, Natural–Convection–Controlled

Fig. 2 Ultrasonically measured interface locations as a function of time for a cold wall temperature of $T_c = -5°C$, and with $T_i = 0°C$ for Case 1 and $T_i = 5°C$ for Case 5

wave processing program determined the solid–liquid interface location from the digitized signal by the difference between the time of flight of a reference signal (no solidification) and the time of flight of a data signal (solidification). The accuracy in the ultrasonic measurement technique was determined to be ± 0.5 mm using the methods outlined by Miller (1989). This accuracy can be improved by using an oscilloscope with a higher sampling frequency. A complete discussion of the experimental setup and error analysis is given by McDonough (1992).

Eight experimental cases were conducted. The first four cases

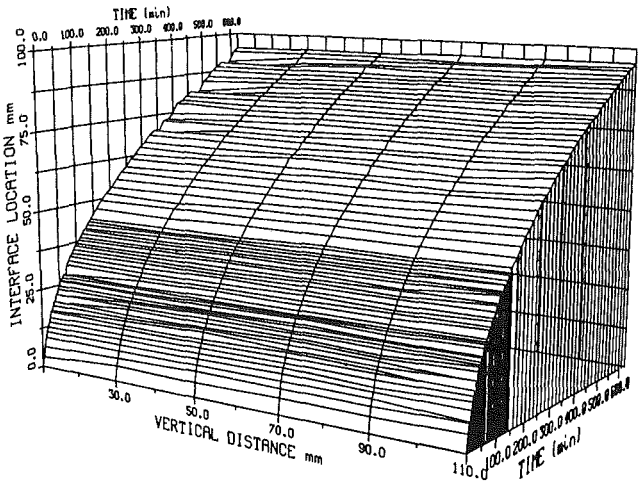

(a) Case 4, Conduction–Controlled

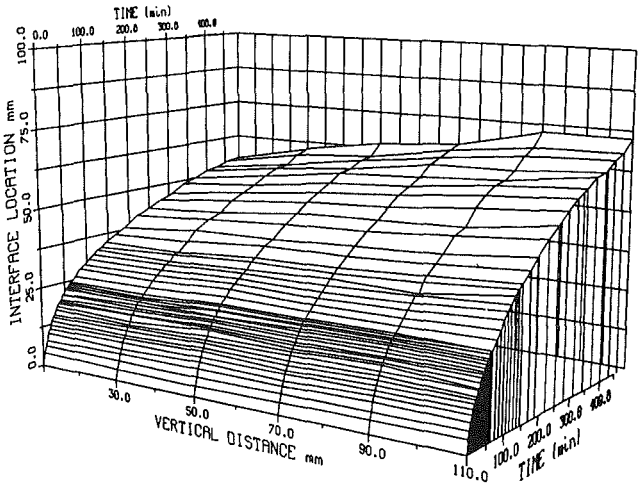

(b) Case 8, Natural–Convection–Controlled

Fig. 3 Ultrasonically measured interface locations as a function of time for a cold wall temperature of $T_c = -20°C$, and with $T_i = 0°C$ for Case 4 and $T_i = 5°C$ for Case 8

were with cold wall temperatures of -5, -10, -15, and $-20°C$, respectively, and an initial water temperature of 0°C and the hot wall held at 0°C for conduction-controlled solidification. Cases 5–8 were with cold wall temperatures of -5, -10, -15, and $-20°C$, respectively, and an initial water temperature of 5°C and a hot wall held at 5°C for natural-convection-controlled solidification.

Results and Discussion

Ultrasonic measurements of the solid–liquid interface locations were taken at six vertical locations, 10, 30, 50, 70, 90, and 110 mm from the bottom and in the vertical center plane of the test cell. These six ultrasonic measurements were taken at either three or five minute intervals during the first two hours of solidification, then at 10 to 30 minute intervals for the remainder of each test. The ultrasonic measurements of the solid–liquid interface were plotted as a function of time and vertical distance from the bottom of the test cell as shown in Figs. 2 and 3. These plots show the interface position from the cold wall as a function of time and represent the actual ultrasonic measurement data and no extrapolation beyond data points or interpolation between data points was employed to extend or smooth the surface.

The interface locations as a function of time for Cases 1 and 4 are presented in Figs. 2(*a*) and 3(*a*). The common trend

in each figure is a nearly uniform solid thickness, which indicates that conduction was the dominant heat transfer mechanism. During the early periods, the rapid growth of the solid was due to the high heat flux achieved across the thin solid. With a decrease in the cold wall temperature from $-5°C$ for Case 1 (Fig. 2(*a*)) to $-20°C$ for Case 4 (Fig. 3(*a*)), the duration of this early period became longer due to the increase in the temperature difference across the solid. For each case, the early period of solidification was characterized by a rough solid–liquid interface texture, which was caused by entrapped air, not removed by the degassing process. As solidification progressed, the interface texture changed to a smoother texture, which indicated that fluid motion was present at the interface. The transition from a rough to a smooth interface began at the bottom of the test cell and then gradually moved up the interface. The point in time during solidification at which the majority of the interface became smooth was later in the solidification process as the cold wall temperature was decreased for each case. In Case 1 with a $-5°C$ cold wall temperature the majority of the interface (the lower 100 mm) was smooth after 90 min. In Case 4 with a $-20°C$ cold wall temperature, the lower 100 mm of the interface was smooth after 180 minutes. The transition from a smooth to a rough interface texture has been shown to indicate the transition from natural-convection-controlled freezing to conduction-controlled freezing (Sparrow et al., 1981).

After this interface texture transition, the solid thickness became vertically nonuniform with a thinner solid thickness at the bottom of the test cell. The deviation from a perfectly vertical interface was most evident in Case 1. The difference between the interface locations at 110 mm and 10 mm vertical locations was 7.2 mm at 570 min. For Cases 2, 3, and 4 with cold wall temperatures of -10, -15, and $-20°C$ respectively, the deviation from a vertical interface decreased. The difference between the interface locations at 110 mm and 10 mm for Case 2 at 540 min was 4 mm, for Case 3 at 600 min was 4 mm, and for Case 4 at 600 min was 1 mm.

In Cases 5–8, the initial water temperature was $5°C$ and the hot wall temperature was maintained at $5°C$, which is above the fusion temperature. In these cases, natural convection significantly influences the solidification process. The interface location as a function of time for Cases 5 and 8 are presented in Figs. 2(*b*) and 3(*b*). During the early period of solidification, the influence of natural convection was weak and the solidification process was dominated by conduction. The early period of solidification was characterized by the uniform growth of the solid. The duration of the conduction-dominated period increased as the cold wall temperature was lowered for each case. For Case 5, Fig. 2(*b*), the duration of the conduction-dominated period was the shortest with a solid thickness difference of 2 mm at 60 min between the top and bottom of the test cell. For Case 8, Fig. 3(*b*), the duration of the conduction controlled period was approximately 75 min with a solid thickness difference of 2 mm. After this early period, the influence of natural convection began to dominate and the solid thickness was not vertically uniform.

The vertically nonuniform solid thickness, with a smaller thickness at the bottom of the enclosure than at the top, was due to a clockwise flow cell in which water heated at the hot wall flows to the bottom of the enclosure, and then up the solid–liquid interface where it is cooled before it freezes. As solidification progressed, the solid thickness became more vertically nonuniform as the influence of natural convection became more dominant. For each natural convection case, the shape of the interface after 300 min was similar, with a solid thickness difference between the bottom and top of the enclosure of 12 mm. This similarity of the interface shapes indicates that during the later period of solidification, the effect of natural convection was the same for each case and was independent of the cold wall temperature.

In Cases 5–8 with the initial and hot wall temperatures at $5°C$, the water in the enclosure was cooled through its density maximum during solidification. Since the density–temperature relation of water is nonlinear with a maximum at $3.98°C$, the transient behavior of the natural convection in the enclosure influenced the solidification process. The buoyancy-induced convection of water cooled through its density maximum has been shown to produce both single and bicellular flow patterns, which are dependant on the temperature gradient through the water (Vasseur et al., 1983; Braga and Viskanta, 1992). Flow visualization experiments were performed to investigate the transient natural convection of water being cooled through its density maximum. A thymol blue pH indicator technique was employed to visualize the low-velocity flow in the rectangular enclosure. This technique consists of placing two electrodes in a solution of 0.01 percent by weight of thymol blue and water that has been titrated to the end-point (Baker, 1966). By imposing a 1.25 to 3.0 V voltage difference between the electrodes, the fluid next to the positive electrode changes color to a deep blue and is then carried away by the fluid flow. The flow visualization experiments were conducted with the water in the test cell initially at a $5°C$ uniform temperature. At $t > 0$ the cold wall was held at $0°C$ and the hot wall maintained at $5°C$. These conditions were chosen so that the natural convection occurring during the flow visualization experiments would simulate the solidification experiments. The qualitative results of the flow visualization experiments are discussed here with respect to the transient convection during solidification.

The transient behavior of the convective flow in the enclosure was characterized by the movement of a flow cell across the enclosure. During the initial stage of cooling, buoyancy-induced downward flow occurred at the cold wall as the water near the cold wall was cooled to the density maximum. Once the water near the cold wall was cooled below the density maximum, the buoyancy-induced flow changed to an upward flow pattern, which created two opposing flow cells at approximately 15 min, as shown in Fig. 4(*a*). After 90 min of cooling, the flow pattern in the enclosure was bicellular, with a dominant clockwise flow cell at the cold wall encompassing 2/3 of the enclosure, and a weaker counterclockwise flow cell at the hot wall, as shown in Fig. 4(*b*). As cooling proceeded, the clockwise flow cell enlarged until it encompassed the entire enclosure after 150 min of cooling except at the bottom of the hot wall where a small counterclockwise flow cell existed as shown in Fig. 4(*c*).

The capabilities and the limitations of the ultrasonic measurement technique are shown by Fig. 3, in which the interface locations as a function of time and vertical distance are shown for Cases 4 and 8, respectively. Both cases have a $-20°C$ cold wall temperature, with Case 4 being conduction-controlled and Case 8 being natural-convection-controlled. In Fig. 3(*a*), the ice has a uniform thickness along the vertical distance axis, which is characteristic of conduction-controlled solidification. Figure 3(*a*) contains 408 separate ultrasonic measurement data points at 6 different vertical locations taken over a 10 hour period. In Fig. 3(*b*), the ice thickness is uniform during the early stages of solidification, and then becomes nonuniform at later stages with the ice thickness greater at the top of the test cell. The angled interface is due to natural convection producing a clockwise flow cell in which water heated at the hot wall flows to the bottom of the enclosure, and then up the solid–liquid interface where it is cooled before it freezes. As the angle of the interface increases, the ultrasonic signal sent by the transducer is reflected downwardly due to the angle of the interface as seen in Fig. 3(*b*). Once the interface angle becomes large enough, the ultrasonic signal is totally reflected away from the transducer. In Case 8 this limit was reached after 8 h of solidification with an 8 deg angle in the interface from the vertical. This was a limitation on the ultrasonic instrumentation used in the present investigation, since only one

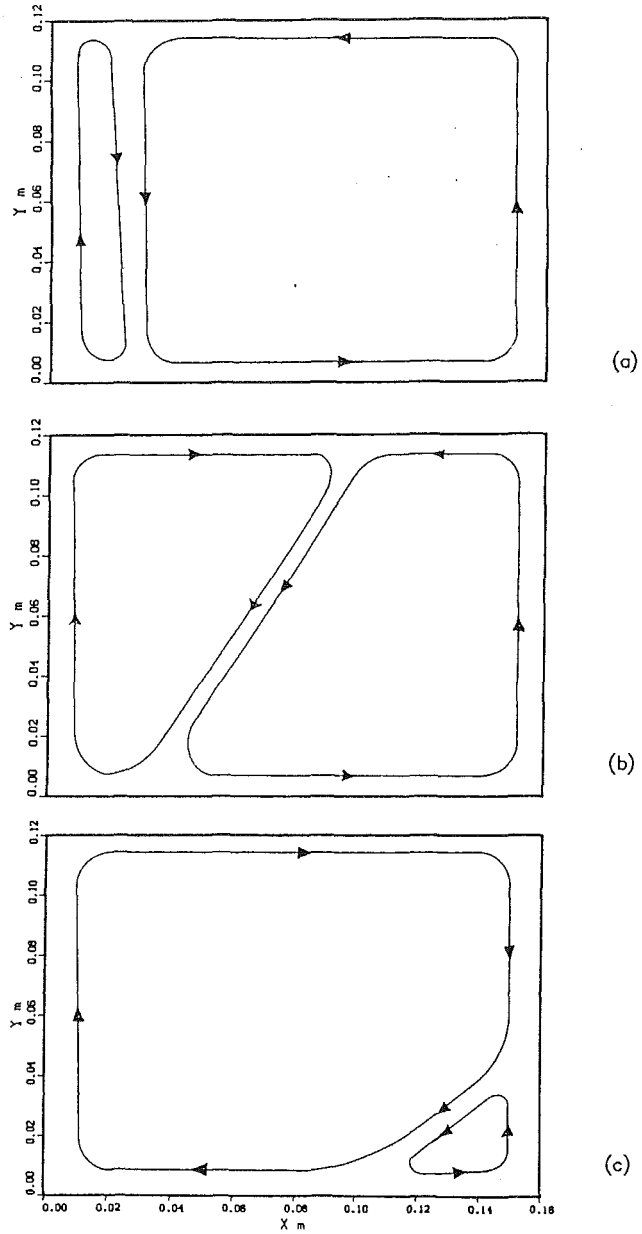

Fig. 4 Transient natural convection flow pattern in rectangular enclosure: (*a*) at t = 15 min; (*b*) at t = 90 min; (*c*) at t > 150 min

transducer was used to send and receive the ultrasonic signal. For ultrasonic measurement of a solid-liquid interface with an angle greater than 8 deg, an array of transducers could be used, so that the refracted signal from one transducer would be received by another.

References

Baker, D. J., 1966, "A Technique for Precise Measurement of Small Fluid Velocities," *J. Fluid Mech.*, Vol. 26, Pt. 3, p. 573.

Bathelt, A. G., and Viskanta, R., 1980, "Heat Transfer at the Solid-Liquid Interface During Melting From a Horizontal Cylinder," *Int. J. Heat Mass Transfer*, Vol. 23, p. 1493.

Benard, G., Gobin, D., and Zanoli, A., 1986, "Moving Boundary Problem: Heat Conduction in Solid Phase During Melting by Natural Convection in the Liquid," *Int. J. Heat Mass Transfer*, Vol. 29, No. 11, p. 1669.

Braga, S. L., and Viskanta, R., 1992, "Transient Natural Convection of Water Near Its Density Extremum in a Rectangular Cavity," *Int. J. Heat Mass Transfer*, Vol. 35, No. 4, p. 861.

Bray, D. E., and Stanley, R. K., 1989, *Nondestructive Evaluation*, McGraw-Hill, New York.

Choi, K. J., and Hong, J. S., 1990, "Experimental Studies of Melting Phenomena From a Constant Heat Flux Vertical Plate," *Experimental Heat Transfer*, Vol. 3, p. 49.

Hykes, D., Hedrick, W. R., and Starchman, D. E., 1985, *Ultrasound Physics and Instrumentation*, Churchill Livingstone, New York.

Kalhori, B., and Ramadhyani, S., 1985, "Studies on Heat Transfer From a Vertical Cylinder, With or Without Fins, Embedded in a Solid Phase Change Medium," ASME JOURNAL OF HEAT TRANSFER, Vol. 107, p. 44.

Krautkramer, J., 1977, *Ultrasonic Testing of Materials*, Springer-Verlag, New York.

Lide, D. R., 1991, *CRC Handbook of Chemistry and Physics*, CRC Press, Boca Raton, FL.

McDonough, M., 1992, "Solidification and Natural Convection in Enclosures," Master's Thesis, Wright State University, Dayton, OH.

Miller, R. W., 1989, *Flow Measurement Engineering Handbook*, 2nd ed., McGraw-Hill, New York.

Rieger, H., and Beer, H., 1986, "The Melting Process of Ice Inside a Horizontal Cylinder: Effects of Density Anomaly," ASME JOURNAL OF HEAT TRANSFER, Vol. 108, p. 166.

Sparrow, E. M., Ramsey, J. W., and Harris, J. S., 1981, "The Transition From Natural-Convection-Controlled Freezing to Conduction-Controlled Freezing," ASME JOURNAL OF HEAT TRANSFER, Vol. 103, p. 7.

Vasseur, P., Robillard, L., and Chandra Shekar, B., 1983, "Natural Convection Heat Transfer Within a Horizontal Cylindrical Annulus With Density Inversion Effects," ASME JOURNAL OF HEAT TRANSFER, Vol. 105, p. 117.

Webb, B. W., Moallemi, M. K., and Viskanta, R., 1987, "Experiments on Melting of Unfixed Ice in a Horizontal Cylindrical Capsule," ASME JOURNAL OF HEAT TRANSFER, Vol. 109, p. 454.

Shrinkage Formation During the Solidification Process in an Open Rectangular Cavity

C.-J. Kim[1,2] and S. T. Ro[1]

Nomenclature

AR = $H/(2W)$ = aspect ratio
h_{sf} = latent heat
H = height
m_s = solid mass
Pr = Prandtl number
Ra = Rayleigh number = $g\beta(T_0 - T_f)W^3/\nu\alpha_L$
S_h = superheating parameter = $c_L(T_0 - T_f)/h_{sf}$
Ste = Stefan number = $c_s(T_f - T_w)/h_{sf}$
t = time
T_0 = initial liquid temperature
T_f = fusion temperature
T_w = wall temperature
W = half-width of the cavity
ξ, η = transformed coordinates

Superscripts

$+$ = dimensionless
$\hat{}$ = interface

Subscripts

L = liquid
r = solid-to-liquid property ratio
S = solid
w = wall

[1]Department of Mechanical Engineering, Seoul National University, Seoul 151-742, Korea.

[2]Postdoctoral fellow.

Contributed by the Heat Transfer Division of THE AMERICAN SOCIETY OF MECHANICAL ENGINEERS. Manuscript received by the Heat Transfer Division January 1993; revision received April 1993. Keywords: Moving Boundaries, Phase-Change Phenomenon, Thermal Energy Storage. Associate Technical Editor: A. Faghri.

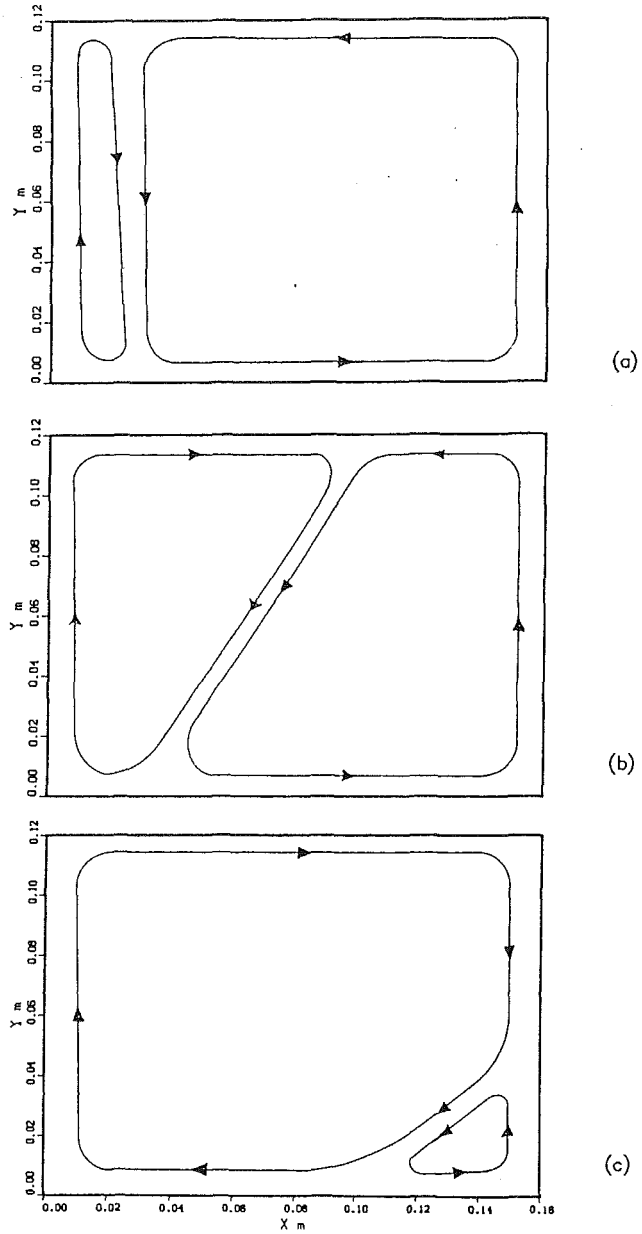

Fig. 4 Transient natural convection flow pattern in rectangular enclosure: (*a*) at t = 15 min; (*b*) at t = 90 min; (*c*) at t > 150 min

transducer was used to send and receive the ultrasonic signal. For ultrasonic measurement of a solid-liquid interface with an angle greater than 8 deg, an array of transducers could be used, so that the refracted signal from one transducer would be received by another.

References

Baker, D. J., 1966, "A Technique for Precise Measurement of Small Fluid Velocities," *J. Fluid Mech.*, Vol. 26, Pt. 3, p. 573.

Bathelt, A. G., and Viskanta, R., 1980, "Heat Transfer at the Solid-Liquid Interface During Melting From a Horizontal Cylinder," *Int. J. Heat Mass Transfer*, Vol. 23, p. 1493.

Benard, G., Gobin, D., and Zanoli, A., 1986, "Moving Boundary Problem: Heat Conduction in Solid Phase During Melting by Natural Convection in the Liquid," *Int. J. Heat Mass Transfer*, Vol. 29, No. 11, p. 1669.

Braga, S. L., and Viskanta, R., 1992, "Transient Natural Convection of Water Near Its Density Extremum in a Rectangular Cavity," *Int. J. Heat Mass Transfer*, Vol. 35, No. 4, p. 861.

Bray, D. E., and Stanley, R. K., 1989, *Nondestructive Evaluation*, McGraw-Hill, New York.

Choi, K. J., and Hong, J. S., 1990, "Experimental Studies of Melting Phenomena From a Constant Heat Flux Vertical Plate," *Experimental Heat Transfer*, Vol. 3, p. 49.

Hykes, D., Hedrick, W. R., and Starchman, D. E., 1985, *Ultrasound Physics and Instrumentation*, Churchill Livingstone, New York.

Kalhori, B., and Ramadhyani, S., 1985, "Studies on Heat Transfer From a Vertical Cylinder, With or Without Fins, Embedded in a Solid Phase Change Medium," ASME JOURNAL OF HEAT TRANSFER, Vol. 107, p. 44.

Krautkramer, J., 1977, *Ultrasonic Testing of Materials*, Springer-Verlag, New York.

Lide, D. R., 1991, *CRC Handbook of Chemistry and Physics*, CRC Press, Boca Raton, FL.

McDonough, M., 1992, "Solidification and Natural Convection in Enclosures," Master's Thesis, Wright State University, Dayton, OH.

Miller, R. W., 1989, *Flow Measurement Engineering Handbook*, 2nd ed., McGraw-Hill, New York.

Rieger, H., and Beer, H., 1986, "The Melting Process of Ice Inside a Horizontal Cylinder: Effects of Density Anomaly," ASME JOURNAL OF HEAT TRANSFER, Vol. 108, p. 166.

Sparrow, E. M., Ramsey, J. W., and Harris, J. S., 1981, "The Transition From Natural-Convection-Controlled Freezing to Conduction-Controlled Freezing," ASME JOURNAL OF HEAT TRANSFER, Vol. 103, p. 7.

Vasseur, P., Robillard, L., and Chandra Shekar, B., 1983, "Natural Convection Heat Transfer Within a Horizontal Cylindrical Annulus With Density Inversion Effects," ASME JOURNAL OF HEAT TRANSFER, Vol. 105, p. 117.

Webb, B. W., Moallemi, M. K., and Viskanta, R., 1987, "Experiments on Melting of Unfixed Ice in a Horizontal Cylindrical Capsule," ASME JOURNAL OF HEAT TRANSFER, Vol. 109, p. 454.

Shrinkage Formation During the Solidification Process in an Open Rectangular Cavity

C.-J. Kim[1,2] and S. T. Ro[1]

Nomenclature

AR = $H/(2W)$ = aspect ratio
h_{sf} = latent heat
H = height
m_s = solid mass
Pr = Prandtl number
Ra = Rayleigh number = $g\beta(T_0 - T_f)W^3/\nu\alpha_L$
S_h = superheating parameter = $c_L(T_0 - T_f)/h_{sf}$
Ste = Stefan number = $c_s(T_f - T_w)/h_{sf}$
t = time
T_0 = initial liquid temperature
T_f = fusion temperature
T_w = wall temperature
W = half-width of the cavity
ξ, η = transformed coordinates

Superscripts

$+$ = dimensionless
$\hat{}$ = interface

Subscripts

L = liquid
r = solid-to-liquid property ratio
S = solid
w = wall

[1]Department of Mechanical Engineering, Seoul National University, Seoul 151-742, Korea.

[2]Postdoctoral fellow.

Contributed by the Heat Transfer Division of THE AMERICAN SOCIETY OF MECHANICAL ENGINEERS. Manuscript received by the Heat Transfer Division January 1993; revision received April 1993. Keywords: Moving Boundaries, Phase-Change Phenomenon, Thermal Energy Storage. Associate Technical Editor: A. Faghri.

Introduction

For most substances with a few exceptions, the change of phase from liquid to solid normally accompanies the reduction in volume. The volume contraction upon solidification has been of practical interest in many areas of applications. For an instance of foundry operation, risers are used to compensate the volume contraction. Understanding how and where the volume contraction takes place during the solidification process constitutes a basic step for the proper control of the product quality such as reducing casting defects (Flemings, 1974). The effect of density change upon solidification has been investigated in a number of researches; the major concerns were varied from the shrinkage pattern (Shamsundar and Sparrow, 1976; Ho and Viskanta, 1983), the shrinkage-induced flow (Chiang and Tsai, 1992) to the porosity formation (Kubo and Pehlke, 1986).

As for the solidification of liquids in rectangular cavities, which is to be studied herein, various aspects of research activities are reviewed by Viskanta (1983). However, a survey of literature indicates that the fluid flow has rarely been included in the analysis of the shrinkage formation during such static casting processes, probably due to the difficulty in handling two moving boundaries: the solid/liquid interface and the contracting solid surface. The motivation of this study is to present a first-principle-based analysis of solidification with volume contraction by accounting for the fluid motion in the liquid as well as the conduction in the solid, and thus to enhance our understanding of the process.

Analysis

Figure 1 shows an example of the shrinkage pattern during the solidification of *n*-octadecane, initially at a uniform temperature $T_0 (> T_f)$, charged in an open-top rectangular cavity with isothermally cooled walls (at a fixed temperature of $T_w < T_f$). Due to the volume contraction upon freezing and the gravity, the solid top surface slopes continuously down to the edge of the liquid free surface, as is schematically shown in Fig. 1. Several assumptions are adopted for the analysis: the two-dimensional and symmetric process; the Newtonian and Boussinesq liquid; the laminar flow; constant thermophysical properties; no encaptured void inside the liquid; and a horizontal liquid free surface.

The general conservation equation written as

$$\frac{\partial}{\partial t}(\rho\phi)+\frac{\partial}{\partial x}\left(\rho u\phi-\Gamma\frac{\partial\phi}{\partial x}\right)+\frac{\partial}{\partial y}\left(\rho v\phi-\Gamma\frac{\partial\phi}{\partial y}\right)=S(x, y) \quad (1)$$

is to be solved in the solid and liquid domains, respectively, and Table 1 summarizes the dimensionless governing equations in both the phases. It can be recognized that the process of interest is characterized by Ste, S_h, Ra, and $AR = H/(2W)$. The actual computation is effected via the coordinate transformation [$x = x(\xi, \eta, t)$ and $y = y(\xi, \eta, t)$] in order to handle the moving domains whose shape and size vary with time. Figure 2 illustrates the mapping obtained by using an algebraic transformation suggested by Oberkampf (Crank, 1984). In particular, an imaginary hole of radius $0.001W$ is punched out at the top corner point (see Fig. 1) to eliminate any singularity (it was found that using a smaller radius of 10^{-4} W produces insignificant differences in the solutions).

Both at the symmetry line and at the top surface, the adiabatic condition is used for the temperature field (the top of the cavity indeed remains in direct contact with the air, the thermal conductivity of which is much smaller than *n*-octadecane). The constant temperature condition is used along the cavity wall. For the velocity field, the conditions of the impermeable surface and zero-shear are applied to the symmetry line and the liquid free surface. The downward velocity of the free surface is determined from the mass conservation over the liquid phase [for details, see Kim and Kaviany (1992)].

The interfacial conditions are the continuity of temperature, the conservation of the mass and energy fluxes crossing the interface, and the motionless solid. Further in-depth discussion on the interfacial boundary conditions is available elsewhere (Kim and Kaviany, 1992; Kim et al., 1993) and hence is not repeated here.

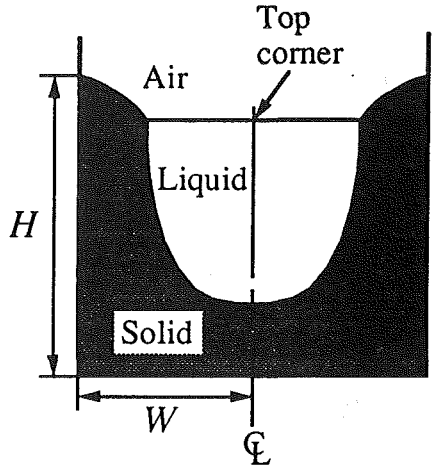

Fig. 1 Schematic diagram describing the shrinkage formation in an open rectangular cavity

Table 1 Variables in the conservation equation. Here, $\rho_r = \rho_s/\rho_L$, $c_r = c_s/c_L$, $k_r = k_s/k_L$. The density, time, length, velocity, pressure and enthalpy† are nondimensionalized by ρ_L, $W^2\nu^{-1}$, W, νW^{-1}, $\rho_L\nu^2W^{-2}$ and $c_L(T_f - T_w)$, respectively.

Phase	ρ^+	ϕ^+	Γ^+	S^+
Solid	ρ_r	1	0	0
		θ_s	$\frac{1}{\mathrm{Pr}}\frac{k_r}{c_r}$	0
Liquid	1	1	0	0
		u^+	1	$-\frac{\partial p^+}{\partial x^+}$
		v^+	1	$-\frac{\partial p^+}{\partial y^+}+\frac{\mathrm{Ra}\cdot\mathrm{Ste}}{\mathrm{Pr}\cdot c_r\cdot S_h}\left(\theta_L-\frac{c_r}{\mathrm{Ste}}\right)$
		θ_L	$\frac{1}{\mathrm{Pr}}$	0

†$h_L = c_L(T - T_f) + h_{sf}$, $h_s = c_s(T - T_f)$.

Solution Procedure

For the *n*-octadecane, the dimensionless properties given by Pr = 53.84, $\rho_r = 1.11$, $c_r = 0.86$, and $k_r = 2.48$ are used for computation. The contracting solid surface is identified by utilizing the overall mass conservation, as was treated by Kim et al. (1993). Since the procedure elaborated there is applicable to the present problem with a minor modification, further discussion is omitted here. For the computation, a nonuniform 31×49 grid system is employed in the solid and liquid phases, respectively. Computation is initiated by imposing a thin solid crust of thickness $0.01W$ and by prescribing a linear temperature profile inside the solid layer. The movement of the interface is controlled by using a variable time step in such a way that the phase thicknesses in the constant η direction do change within 0.5 percent each time step. The global conservations of the mass and the energy are checked each time and prove to be valid to within 0.03 and 0.5 percent, respectively.

Results and Discussion

Computation is mainly performed with Ste = 0.148, S_h = 0.010, Ra = 1.35 × 10^6, and AR = 0.5, 1.0. Figure 3 shows sequential contour plots to exhibit the timewise progression of the streamline and the isotherm distributions. The flow is upward along the symmetry line and downward adjacent to the interface. Near the completion of solidification [Fig. 3(*c*)], it can be seen that besides a circulating flow, a bunch of streamlines start at the liquid free surface and terminate at the interface. This is in fact established by the suction at the interface and this sort of density-change-induced fluid motion was also reported recently (Kim et al., 1993). The isotherms intersect orthogonally with the adiabatic lines, as expected. It is further noted that the isotherms are stably stratified in the liquid core region, and that natural convection survives to the last moment, however, with a negligible intensity [e.g., Fig. 3(*c*) illustrates the strength of the circulating flow relative to the weak suction flow]. Also evidenced is that the liquid cools down very quickly and becomes nearly saturated. These results conform to the experimental observation that the initial superheat affects the heat transfer only at early times and its effect is notably small (Ho and Viskanta, 1983).

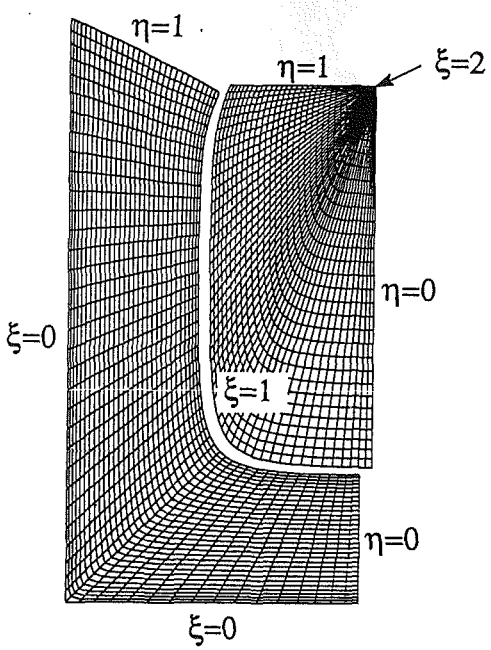

Fig. 2 The mesh configurations for both the solid and liquid phase at an intermediate stage of solidification

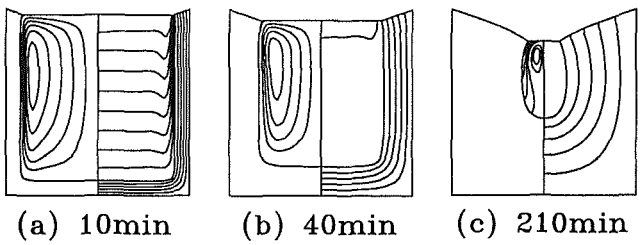

Fig. 3 Contour plots for streamlines (left) and isotherms (right) for the case of AR = 1. The isotherms are drawn by an increment of 0.2(T_f − T_w) in the solid and of 0.1(T_o − T_f) in the liquid.

The migration pattern of the interface is depicted in Fig. 4 where two different density ratios (ρ_r = 1.11 and 1.17) are considered. It is noted that the predicted interface positions in general disagree with the experimental data except at small times. In the case of AR = 1, the prediction is found to be mostly behind the experiment, whereas the prediction at late melting is overestimated in the case of AR = 0.5. Such a discrepancy might be partly due to the heat loss from the material to the ambient, and partly due to the existence of the "whiskerlike" structure in the vicinity of the interface (cf. Ho and Viskanta, 1983). Interestingly, the predicted shrinkage surface falls nicely onto the experiment curve particularly for ρ_r = 1.17, although the solid-to-liquid density ratio of *n*-octadecane is not expected to be so large over the temperature range considered. The present results reveal that the interface movement except near the edge of the free surface is insensitive to the magnitude of the density ratio.

For an optimum design of casting, of first-order significance is how the solidification rate relies on the magnitude of the aspect ratio of the casting. The degree of solidification is quantified in terms of

$$f^* \equiv \frac{m_s}{m_{\text{total}}} \cdot \frac{H/W}{1+H/W} = \frac{m_s}{2(W+H)} (\rho_L W)^{-1} \qquad (2)$$

which represents the amount of the frozen mass (normalized by $\rho_L W$) per unit cooling area. Figure 5 displays the variation of f^* with the dimensionless time t^+Ste/Pr for the cases of AR = 0.5, 1, and 2. It can be seen that all the corresponding curves initially follow a single trajectory (due to the one-dimensional behavior at early freezing) and then branch into individual ones. For the range examined, inspection reveals that the higher the cavity aspect ratio, the more mass is solid-

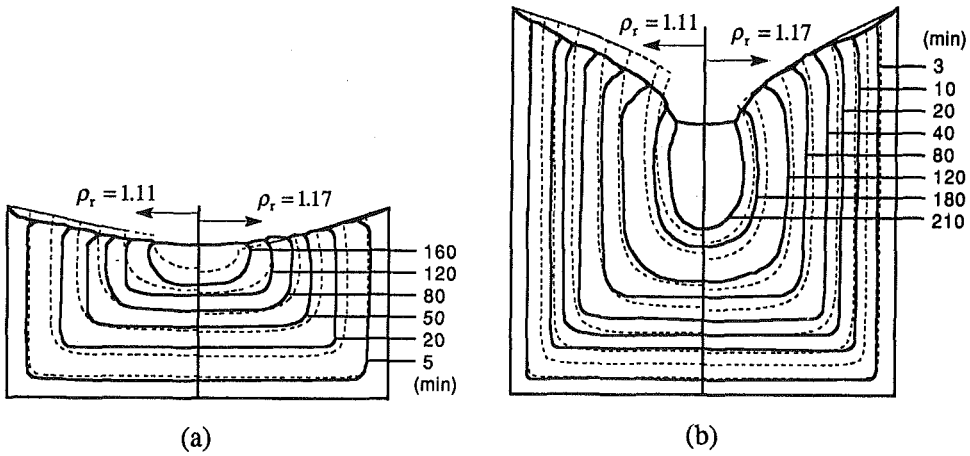

Fig. 4 The loci of the interfaces corresponding to several preselected times: (*a*) AR = 0.5 and (*b*) AR = 1. The experimental data (Ho and Viskanta, 1983) are marked by solid lines and the present predictions by dotted lines.

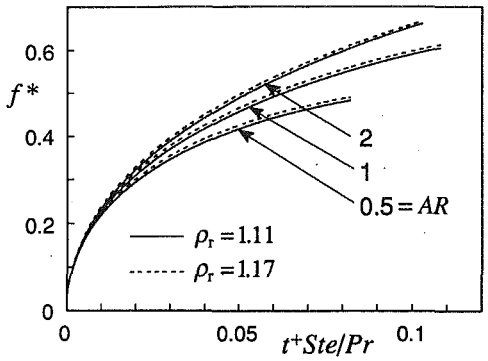

Fig. 5 The timewise variation of the nondimensional frozen mass per unit cooling area for Ste = 0.148, S_h = 0.010, Ra = 1.35 × 10^6, and three different aspect ratios

ified per unit cooling area at a given time. Further examination of Fig. 5 shows that solidification with a larger density difference proceeds a little faster.

Concluding Remarks

The shrinkage formation during isothermal solidification of pure *n*-octadecane in an open-top cavity was studied by considering the buoyancy and shrinkage-driven flow. The results clearly showed that the contraction of the solid surface was mostly dependent on the magnitude of the density difference. The previous experimental observations were reaffirmed that the superheat in the liquid dissipated quickly and hence the heat transfer was little affected by convection. The influence of the density difference on the interface movement was confined only to the region near the edge of the liquid free surface. It was found that the higher the aspect ratio of the cavity and the density difference between phases, the larger was the frozen mass per unit cooling area. It is likely that during the solidification process the volume contraction plays a more important role than the convection and should be taken into consideration to gain better insight into the solidification behavior.

Acknowledgments

This work was supported by the Turbo and Power Machinery Research Center at Seoul National University, for which the authors are grateful.

References

Chiang, K. C., and Tsai, H. L., 1992, "Shrinkage-Induced Fluid Flow and Domain Change in Two-Dimensional Alloy Solidification," *International Journal of Heat and Mass Transfer*, Vol. 35, pp. 1763–1770.

Crank, J., 1984, *Free and Moving Boundary Problems*, Clarendon Press, Oxford, UK.

Flemings, M.C., 1974, *Solidification Processing*, McGraw-Hill, New York.

Ho, C. J., and Viskanta, R., 1983, "Experimental Study of Solidification Heat Transfer in an Open Rectangular Cavity," ASME JOURNAL OF HEAT TRANSFER, Vol. 105, pp. 671–673.

Kim, C.-J., and Kaviany, M., 1992, "A Numerical Method for Phase-Change Problems With Convection and Diffusion," *International Journal of Heat and Mass Transfer*, Vol. 35, pp. 457–467.

Kim, C.-J., Ro, S. T., Lee, J. S., and Kim, M. G., 1993, "Two-Dimensional Freezing of Water Filled Between Vertical Concentric Tubes Involving Density Anomaly and Volume Expansion," *International Journal of Heat and Mass Transfer*, Vol. 36, pp. 2647–2656.

Kubo, K., and Pehlke, R. D., 1985, "Mathematical Modeling of Porosity Formation in Solidification," *Metallurgical Transactions*, Vol. 16B, pp. 359–365.

Shamsundar, N., and Sparrow, E. M., 1976, "Effect of Density Change on Multidimensional Conduction Phase Change," ASME JOURNAL OF HEAT TRANSFER, Vol. 98, pp. 550–557.

Viskanta, R., 1983, "Phase-Change Heat Transfer," *Solar Heat Storage: Latent Heat Materials*, G. A. Lane, ed., CRC Press, Boca Raton, FL.

Journal of Heat Transfer

Discussion

Two-Dimensional Transient Solutions for Crossflow Heat Exchangers With Neither Gas Mixed[1] and Transient Temperature Fields in Crossflow Heat Exchangers With Finite Wall Capacitance[2]

F. E. Romie.[3] Spiga and Spiga use exponential functions and the modified Bessel functions I_0 and I_1 to express the Green's functions used to find the exchanger responses to variations of fluid inlet temperatures. The purpose of this discussion is to show that the closely related Anzelius–Schumann functions, $F_0(u, v)$ and $G_0(u, v)$ and their n-times successive integrals, $F_n(u, v)$, $G_n(u, v)$ with respect to the second argument (Romie, 1987) are well suited to expression of the Green's functions.

The three basic functions are

$$F_{-1}(u, v) = \frac{\partial F_0(u, v)}{\partial v} = \exp(-u-v)(u/v)^{1/2} I_1(2\sqrt{uv})$$

$$G_{-1}(u, v) = \frac{\partial G_0(u, v)}{\partial v} = \exp(-u-v) I_0(2\sqrt{uv})$$

$$G_0(u, v) = \int_0^v G_{-1}(u, v')dv'$$

Two recurrence equations permit finding $F_n(u, v)$ $(n \geq 0)$ and $G_n(u, v)$ $(n > 0)$ in terms of these three functions. In particular, $F_0(u, v) = G_0(u, v) + G_{-1}(u, v)$ and $F_1(u, v) = (v - u)\, G_0(u, v) + v(F_{-1} + G_{-1})$.

For gas-to-gas ($V_a = V_b = 0$) crossflow exchangers the Green's functions derived by Spiga and Spiga (1987) can be written in an especially simple form using the $F_n - G_n$ functions:

$$T_a^G(x, y, t) = \delta(t)e^{-x} + F_{-1}(x, t)F_0(Rt, y)$$
$$T_b^G(x, y, t) = G_{-1}(x, t)G_0(Rt, y)$$
$$T_w^G(x, y, t) = G_{-1}(x, t)F_0(Rt, y)$$
$$\overline{T}_a^G(t) = \delta(t)e^{-N_a} + F_{-1}(N_a, t)F_1(Rt, N_b)/N_b$$
$$\overline{T}_b^G(t) = (1 - F_0(N_a, t))G_0(Rt, N_b)/N_a$$

In this case the only integration required is that for G_0 for which rapid algorithms are indicated in the reference cited.

For liquid-to-liquid exchangers ($V_a \neq 0$ and $V_b \neq 0$) the Green's functions derived by Spiga and Spiga (1988) can be written in the following form. (The variables θ and η, $\theta \equiv t - V_a x$ and $\eta \equiv \theta - V_b y'/R$, are introduced here for brevity of notation.)

$$T_a^G(x, y, t) = \delta(\theta)e^{-x} + U(\theta)\left\{e^{-R\theta}F_{-1}(x, \theta) + \int_0^{y^*} F_{-1}(x, \eta)F_{-1}(R\eta, y')dy'\right\}$$

$$T_b^G(x, y, t) = U(\theta)\int_0^{y^*} G_{-1}(x, \eta)G_{-1}(R\eta, y')dy', \qquad y^* = \min(y, R\theta/V_b)$$

$$T_w^G(x, y, t) = U(\theta)\left\{e^{-R\theta}G_{-1}(x, \theta) + \int_0^{y^*} G_{-1}(x, \eta)F_{-1}(R\eta, y')dy'\right\}$$

$$\overline{T}_b^G(t) = \frac{1}{N_a}\int_0^{N_a} T_b^G(x, N_b, t)dx \quad \text{and}$$

$$\overline{T}_a^G(t) = \frac{1}{N_b}\int_0^{N_b} T_a^G(N_a, y, t)dy$$

In this case the integrals must be evaluated numerically because η contains the variable of integration, y'. Thus the advantage of the $F_n - G_n$ functions is limited to conciseness of expression of the Green's functions when $V_a \neq 0$ and $V_b \neq 0$. Use of the polynomial approximations for I_0 and I_1, given by Abramowitz and Stegun (1964), gives rapid evaluation of F_{-1} and G_{-1}.

References

Abramowitz, M., and Stegun, I. A., 1964, *Handbook of Mathematical Functions*, National Bureau of Standards, p. 378.

Romie, F. E., 1987, "Two Functions Used in the Analysis of Crossflow Exchangers, Regenerators, and Related Equipment," ASME JOURNAL OF HEAT TRANSFER, Vol. 109, pp. 519–521.

Authors' Closure

The comments of Dr. Romie do not modify our work, but rather put the results in a formally more compact and elegant form. We acknowledge with pleasure the ingenuity and care of Dr. Romie in properly establishing at an explicit level recurrence properties that were only implicit in our equations.

We feel grateful to him for the achieved improvement, and are happy to see that our articles have stimulated some interest.

[1]By G. Spiga and M. Spiga, published in the May 1987 issue of the ASME JOURNAL OF HEAT TRANSFER, Vol. 109, pp. 281–286.

[2]By M. Spiga and G. Spiga, published in the February 1988 issue of the ASME JOURNAL OF HEAT TRANSFER, Vol. 110, pp. 49–53.

[3]Palos Verdes Estates, CA 90274.

Surface Roughness and Its Effects on the Heat Transfer Mechanism of Spray Cooling[4]

R. Mesler.[5] These investigators have presented interesting results, which certainly reveal that surface roughness has an effect on the heat transfer in spray cooling. The exceptionally high heat fluxes that are achieved with spray cooling are remarkable. This discussion centers on two interpretations they make of their results. First, they only recognize heterogeneous nucleation as the source of nuclei for the nucleate boiling, which appears to account for the exceptionally high heat fluxes. Research has shown that another mechanism can operate to cause nucleation in liquid films, that is, secondary nucleation. Second, they postulate the existence of an ultrathin liquid film but provide no direct experimental support. An examination of the postulated ultrathin liquid film relative to their other observations reveals a contradiction that questions the suitability of the postulate.

First, the paper discusses only heterogeneous nucleation as the mechanism responsible for the onset of nucleation in their experiments, but research over the last 15 years has provided evidence for another mechanism that operates to produce nucleation in liquid films (Bergman and Mesler, 1981; Carroll and Mesler, 1981; Kim et al., 1983; Mesler and Mailen, 1977; Mesler, 1982; Udomboresuwan and Mesler, 1986). When liquid drops strike a liquid surface, they entrain gas or vapor bubbles. When the liquid is superheated these entrained bubbles serve as nuclei for more bubbles to grow. When nucleate boiling occurs in a liquid film, bubbles bursting from the film produce drops close to the liquid film. Some of the drops return to the film where they can entrain bubbles and thus produce a chain reaction. The bubbles bursting from the film thus sustain further nucleation. The process has been called secondary nucleation after the analogous process that produces nuclei in crystallization. By supplying a liquid film on a heated surface with a spray, as in the present study, abundant sources of nuclei are created that are independent of the surface temperature.

Their study includes results of a pool boiling experiment where it was observed that a surface temperature of about 105°C was necessary for the onset of nucleation. They observed that for spray-applied liquid films nucleation occurred at temperatures below this. This observation can be interpreted as an indication of nucleation initiated by drop-entrained bubbles.

Second, the authors do not examine a postulated ultrathin liquid film in light of all their other observations. These authors state in their conclusions that "For roughness greater than 1 μm, nucleation plays a major role in the heat transfer. However, for films of the order of 0.1 μm, heat is conducted through the (ultrathin liquid) film and evaporated on the surface." This implies that for a surface roughness less than 1 μm the spray-applied liquid film will be on the order of 0.1 μm thick. Apparently the basis for this statement is that it is conceivable that a postulated film 0.1 μm thick might exist on a polished surface with roughness less than 1 μm. The authors offer no direct evidence that a film of such a thickness exists. It appears significant that the portion of the heat flux versus surface temperature plots for surfaces polished with any of the abrasives studied look quite similar at surface temperatures above 100°C. The plots all level off at a high value for the heat flux but the value is higher the smoother the surface. The authors state, "Spray cooling of an ultrathin liquid film on a flat surface enhances heat removal by evaporation, nucleate boiling being enhanced by early bubble departure." This implies that nucleation occurred in the liquid film applied to the smoothest surface as well as in the films applied to the rougher surfaces. How can the authors be so sure that the mechanism for heat removal is so different for the smoothest surface at the high surface temperatures and high heat fluxes when the plot of heat flux versus surface temperature is so similar? How is it that nucleation is being enhanced by early bubble departure? Is this a new mechanism for nucleation?

It is useful to examine the suitability of the postulated ultrathin film by considering it with respect to the observation that an increase in liquid flow rate is accompanied by an increase in the heat flux. An increase in liquid flow rate must cause an increase in liquid film thickness. Yet an increase in film thickness should cause a decrease in the heat flux according to the logic applied elsewhere in the paper. There is therefore a contradiction that questions the suitability of the postulated ultrathin liquid film in explaining the situation. The logic applied here is the same logic as the authors use in arguing that the thinner film accounts for the increase in heat flux with an increase in air flow rate.

A couple of other comments would seem to be in order. The authors explain that heat removal can be enhanced by maximizing microlayer evaporation. However, they do not mention the crucial role of the liquid film in making this possible (Mesler, 1982). In a liquid film a bubble can escape very rapidly because the bubble needs only to break out of the film. Furthermore, the film very quickly re-establishes itself. Escape is so quick that the microlayer does not have time to dry out as when a bubble grows by itself in an abundance of liquid. In that case the microlayer drys out well before the bubble escapes, leaving the surface dry and delaying further microlayer evaporation until the bubble has departed and another bubble grows.

The investigators found that increasing either or both air flow rates and liquid flow rates increased the maximum values of heat flux. Increasing either the air flow rate or the liquid flow rate should act to supply more liquid to the film. It has been noted in previous research that taking additional steps to keep a surface wet with a liquid film increases the maximum heat flux (Mesler, 1982).

Spray applying a liquid film on a surface with a temperature above the saturation temperature of the liquid benefits heat transfer in two ways. First, droplets in the spray entrain bubbles to provide an abundant supply of bubble nuclei to sustain nucleate boiling in the film. Second, the film acts in concert with the nucleate boiling to promote microlayer evaporation where heat can be conducted from the surface to the vapor region through an extremely thin liquid film, the microlayer.

References

Bergman, T., and Mesler, R., 1981, "Bubble Nucleation Studies. Part I: Formation of Bubble Nuclei in Superheated Water by Bursting Bubbles," *AIChE Journal*, Vol. 27, pp. 851–853.

Carroll, K., and Mesler, R., 1981, "Bubble Nucleation Studies. Part II: Bubble Entrainment by Drop-Formed Vortex Rings," *AIChE Journal*, Vol. 27, pp. 853–856.

Kim, H-K., Fakeeha, A., and Mesler, R., 1983, "Nucleate Boiling in Flowing and Horizontal Liquid Films," ASME HTD- Vol. 23, pp. 61–65.

Mesler, R., and Mailen, G., 1977, "Nucleate Boiling in Thin Liquid Films," *AIChE Journal*, Vol. 23, pp. 954–957.

Mesler, R., 1982, "Research on Nucleate Boiling," *Chemical Engineering Education*, Fall, pp. 152–156.

Udomboresuwan, A., and Mesler, R., 1986, "The Enhancement of Nucleate Boiling by Foam," *Heat Transfer 1986*, Vol. 6, pp. 2939–2944.

Authors' Closure

The authors appreciate Professor Mesler's interest in our paper. We would like to respond by stating our current understanding on the heat transfer mechanisms in spray cooling.

The current knowledge of the thermophysics of spray cooling on surfaces is based on observations in experiments performed

[4]By M. R. Pais, L. C. Chow, and E. T. Mahefkey, published in the February 1992 issue of the ASME JOURNAL OF HEAT TRANSFER, Vol. 114, No. 1, pp. 211–219.

[5]Department of Chemical and Petroleum Engineering, University of Kansas, Lawrence, KS 66045-2223.

to drive heat transfer through conduction–convection at the surface is larger than that required for nucleation. In this case nucleation will predominate.

In conclusion the above observations indicate that several heat transfer mechanisms coexist and contribute significantly to the high heat fluxes dissipated during spray cooling. The studies performed so far have not had the capability to isolate and determine the individual contributions of the aforementioned mechanisms.

References

Berenson, P. J., 1962, "Experiments on Pool-Boiling Heat Transfer," *Int. J. Heat Mass Transfer*, Vol. 5, pp. 985–999.

Chandra, S., and Avedisian, C. T., 1991, "On the Collision of a Droplet With a Solid Surface," *Proc. R. Soc. Lond.*, Vol. XX, pp. 15–41.

Gopalen, B., and Mesler, V. R., 1990, "Surface Nucleate Boiling, Secondary Nucleation and Threshold Superheat," *AIAA/ASME Thermophysics and Heat Transfer Conf.*, ASME HTD-Vol. 136, pp. 7–12.

Gu, C. B., Su, G. S., Chow, L. C., and Pais, M. R., 1993, "Comparison of Spray and Jet Impingement Cooling," presented at the 29th ASME/AIChE Natl. Heat Transfer Conference, Atlanta, GA, Aug.

Hsu, Y. Y., 1962, "On the Size of Range of Active Nucleation Cavities on a Heating Surface," ASME JOURNAL OF HEAT TRANSFER, Vol. 84, p. 204.

Huang, Y. C., and Hammitt, F. G., 1972, "Hydrodynamic Phenomena During High-Speed Collision Between Liquid Droplet and Rigid Plane," *Proc. ASME Polyphase Flow Forum*, Vol. 1, pp. 9–10.

Kays, W. M., and Crawford, X. X., 1993, *Convective Heat and Mass Transfer*, 3rd ed., McGraw-Hill, New York.

Kenning, D. B. R., 1992, "Wall Temperature Patterns in Nucleate Boiling," *Int. J. Heat Mass Transfer*, Vol. 35, No. 1, pp. 73–85.

Longuet-Higgins, M. S., 1990, "An Analytical Model of Sound Production by Raindrops," *J. Fluid Mechanics*, Vol. 214, pp. 395–410.

Mesler, R., 1976, "A Mechanism Supported by Extensive Experimental Evidence to Explain High Heat Fluxes Observed During Nucleate Boiling," *AIChE J.*, Vol. 22, No. 2, pp. 246–252.

Mesler, R., and Bellows, W. S., 1988, "Explosive Boiling: a Chain Reaction Involving Secondary Nucleation," *Proc. ASME 1988 Natl. Heat Transfer Conf.*, ASME HTD-96, Vol. 2, pp. 487–491.

Pais, M. R., Chow, L. C., and Mahefkey, E. T., 1992, "Surface Roughness and Its Effects on the Heat Transfer Mechanism of Spray Cooling," ASME JOURNAL OF HEAT TRANSFER, Vol. 114, pp. 211–219.

Sehmbey, M. S., Pais, M. R., and Chow, L. C., 1992a, "Effect of Surface Material Characteristics and Surface Properties in Evaporative Spray Cooling," *J. Thermophysics and Heat Transfer*, Vol. 6, No. 3, pp. 505–512.

Sehmbey, M. S., Pais, M. R., and Chow, L. C., 1992b, "A Study of Diamond Laminated Surfaces in Evaporative Spray Cooling II," *Int. J. on the Science and Technology for Condensed Matter Films, Thin Solid Films*, Vol. 212, pp. 25–29.

Tilton, D. E., 1989, "Spray Cooling," PhD Dissertation, University of Kentucky, Lexington, KY.

Yang, J., Chow, L. C., and Pais, M. R., 1993a, "A Heat Transfer Correlation for Thin Liquid Film Cooling," presented at the 29th ASME/AIChE Natl. Heat Transfer Conference, Atlanta, GA, Aug.

Yang, J., Chow, L. C., and Pais, M. R., 1993b, "An Analytical Method to Determine the Liquid Film Thickness in Spray Cooling Using Secondary Gas Atomizing Nozzles," presented at the 29th ASME/AIChE Natl. Heat Transfer Conference, Atlanta, GA, Aug.

Yang, J., Chow, L. C., Pais, M. R., and Ito, A., 1993c, "Liquid Film Thickness and Topography Determination Using Fresnel Diffraction and Holography," *Experimental Heat Transfer*, Vol. 5, pp. 239–252.

Yang, J., Pais, M. R., and Chow, L. C., 1993d, "Critical Heat-Flux Limits in Secondary Gas Atomized Liquid Spray Cooling," *Experimental Heat Transfer*, Vol. 6, pp. 55–67.

Natural Convection With Radiation in a Cavity With Open Top End[6]

C. Balaji[7,9] and S. P. Venkateshan.[8,9]

The subject paper reports the results of a numerical study of natural convection and surface radiation in a cavity with open top end. The objective of the present discussion is to bring to focus certain deficiencies in the modeling of the equations by Lage et al. Because of these, conceptual errors have been committed in reporting the effect of surface radiation in the combined mode problem. The details of the problem geometry and coordinate system for the natural convection problem and the simultaneous natural convection and radiation problem are given, respectively, in Figs. 2 and 8 of the paper. A cursory look at the figures exposes certain deficiencies. For the convection problem the bottom wall has been assumed to be adiabatic while for the combined mode problem the bottom wall has been assumed to be at the temperature T_2, which is taken to be the same as the temperature of the right wall. Specification of the first and second type of boundary conditions for the bottom wall is mathematically inconsistent. This is all the more jarring, because while solving the combined mode problem, free convection results obtained in the absence of surface radiation along with an adiabatic bottom wall have been used. Temperature T_2 has been evaluated (for the right and bottom wall) assuming a balance between convection and radiation as shown in Fig. 8. This assumption, apart from causing errors, is fundamentally incorrect, and the authors fail to mention the very important fact that the question of convection from the right wall does not arise at all if the right wall does not receive heat radiatively from the left wall. As a consequence, a conceptual error has been made in reporting the effect of radiation; this point will be elaborated a little later.

The correct way of handling the combined mode problem would be to assume that the right wall and bottom wall are in convective and radiant balance ($q_{conv} + q_{rad} = 0$), i.e., the walls are truly adiabatic (Balaji and Venkateshan, 1993a). With this condition the convection equations along with the radiosity equations have to be simultaneously solved. This results in a temperature distribution on both the bottom and right side walls. The above procedure has been used and elaborate results have been obtained for the problem considered by Lage et al. and communicated elsewhere by the authors (Balaji and Venkateshan, 1993b).

The CPU time reported for the pure convection problem was 1500 CPU seconds for $Ra = 10^5$, on a supercomputer facility. However, even with the computationally more involved procedure of solving radiation and convection equations simultaneously for the same Rayleigh number, our calculations consumed only 750 CPU seconds on a Siemens system (5 MIPS) for nonblack walls and only 150 CPU seconds for black walls, with a finite volume algorithm for the flow equations and Hottel's method for radiation. Use of this procedure not only reduces the errors that will be made by using simpler models but is also consistent with the physics of the problem under consideration.

Finally, in the section on the results reporting the effect of radiation on the overall heat transfer, the definition that has been used for the effect of radiation is

$$\text{Enhancement due to radiation} = \frac{q_{conv(left)} + q_{rad(left)}}{q_{conv(left)} + q_{conv(right)}} \quad (1)$$

where $q_{rad(left)}$ is given as the sum of the radiative heat transfer from the left wall to wall 2 and the left wall to the ambient. It will now be shown that Eq. (1) is actually incorrect. If one considers the actual physics of the problem, the left wall, being an isothermal heat source, heats the right and bottom walls radiatively to a temperature above the ambient temperature. This gives rise to the development of boundary layers on the right and bottom walls and they lose heat convectively to the air. Under equilibrium the net radiation received by these walls, i.e., bottom and right walls, balances the convection heat transfer away from the two walls and there is no net heat transfer from the right and bottom walls. Thus, in the problem with no radiation ($\epsilon = 0$) the heat loss from the system is $q_{conv(left)}$ only.

Hence Eq. (1) should be modified as

[6]By J. L. Lage, J. S. Lim, and A. Bejan, published in the May 1992 issue of the JOURNAL OF HEAT TRANSFER, Vol. 114, No. 2, pp. 479–486.

[7]Research Scholar.

[8]Professor.

[9]Heat Transfer Thermal Power Lab, Department of Mechanical Engineering, Indian Institute of Technology, Madras 600 036 India.

$$\text{Enhancement due to radiation} = \frac{q_{\text{conv(left)}} + q_{\text{rad(left)}}}{q_{\text{conv(left)}}} \quad (2)$$

At this point it needs to be emphasized that because of the predominantly boundary layer type of flow the convective heat flux from the left wall itself is relatively insensitive to radiation and remains more or less constant within the limits of numerical accuracy.

If one uses Eq. (1), spuriously low values of the enhancement factor would be obtained and this actually underplays the influence of radiation. The definition (2) is more meaningful because of the simple reason that when radiation is not there $q_{\text{conv(right)}}$ is also not there and hence the denominator that has been used in Eq. (1) is incorrect. We take an example from Lage et al. The results obtained with Eq. (1) have been plotted in Fig. 11 of their paper. Typically when $T_1 = 100°C$, $T_\infty = 25°C$, $L/H = 0.25$, and $\epsilon_1 = \epsilon_2 = 0.6$, the right wall temperature is around 56°C, as given in Fig. 10. Under these conditions Eq. (1) gives a value of 1.12 as the enhancement due to radiation. However, under these conditions, from the results reported in their paper the convection heat transfer from the right wall is 33 percent of the convective heat transfer from the left. Hence, Eq. (2) will give an enhancement factor of 1.49 and this is the actual effect of radiation. This directly disproves the statement of Lage et al. that ". . .in the temperature range considered in the example, the radiation contribution to the overall heat transfer rate is overshadowed by natural convection. . .". In fact radiation could contribute 50 percent of the total heat transfer as proved earlier by taking a simple example. Hence it is concluded that the interaction between radiation and convection is indeed strong.

References

Balaji, C., and Venkateshan, S. P., 1993a, "Interaction of Surface Radiation with Free Convection in a Square Cavity," *International Journal of Heat and Fluid Flow*, Butterworth, United Kingdom, in press.

Balaji, C., and Venkateshan, S. P., 1993b, "Interaction of Radiation With Free Convection in an Open Cavity," *AIAA Journal of Thermophysics and Heat Transfer*, submitted.

Authors' Closure

J. L. Lage,[10] J. S. Lim,[11] and A. Bejan.[12] We regret to say that the letter writers' observations add nothing to the comments we already included in many parts of our paper. It may be that these writers did not read our text carefully, or that they think that their forthcoming paper on the same problem will be received better if they publicize it ahead of time. To this point we will return in the last paragraph.

What the letter writers call "conceptual errors" are modeling decisions we made and discussed in detail, as part of a deliberate effort to construct the simplest model possible. We stated our objectives in Section 1, especially in the last three paragraphs. We set out to solve a real industrial problem (first paragraph, p. 479), not to calculate in the most accurate way possible the temperature distribution around an ash pit.

We recognized from the very beginning (p. 479) that "an alternative method that is well documented (e.g., Larson and Viskanta, 1976; Lauriat, 1980) consists of solving simultaneously the differential equations for natural convection and radiation, while the nonuniform temperature distribution of the three refractory surfaces is one of the unknowns." We discussed this further on p. 486. This alternative approach is apparently preferred by the letter writers. They are as free to choose their approach as we were when we chose ours. Their objectives are obviously not the same as ours.

Our decision to assign a single temperature (T_2) to the right wall and the bottom of the pit is one of the features of the simplest possible model. We analyzed the pluses and minuses of this decision in a long paragraph (see the bottom-left corner on p. 484); we did not hide it to be "discovered" now by the letter writers. We stated that the actual bottom wall acquires a temperature that varies between T_1 and T_2, and then we listed several *reasons* why we think our modeling decision "is a good *approximation*." To see the good approximations is not only an integral part of good engineering practice, but also the main mission of the *teaching* of engineering research.

Our estimate of the effect of radiation relative to a pure-convection model (Fig. 11) was meant to be qualitative, because it is impossible to separate the two mechanisms *after* they have been coupled in the radiation and convection model. The denominator in our ratio refers to a cavity in which *both* vertical walls are heated, as in the first part of our paper (the letter writers misunderstood our definition). We agree that there may be other ratios that can be looked at. The important point is that the letter writers' estimate (49 percent) agrees with our estimate (12 percent) in a qualitative sense, i.e., in that the dominant mechanism is natural convection. To attack this qualitative conclusion, as they have done, is to split hairs.

By the way, the best place to study the effect of radiation in an enclosure with natural convection is by looking at the *simplest* enclosure geometry, not at the open pit considered in our paper. That simplest geometry may be the square enclosure heated and cooled from the side: It makes a nice undergraduate textbook problem (Bejan, 1993), to which we direct the letter writers' attention.

In summary, we welcome Balaji and Venkateshan's interest in the problem we identified and solved, because it reminds us of what we felt: The problem is interesting. We would have thought, however, that a fairer way of commenting on our work would have been to submit the full-length paper (Balaji and Venkateshan, 1993b) to the JOURNAL OF HEAT TRANSFER, instead of a short letter. We question Professor Venkateshan's decision to (1) "criticize" our work in a letter to the original journal, and, simultaneously, (2) submit the long version of the same to a different journal.

Reference

Bejan, A., 1993, *Heat Transfer*, Wiley, New York, Project 10.3, pp. 573–574.

[10]J. L. Embrey Assistant Professor, Mechanical Engineering Department, Southern Methodist University, Dallas, TX 75275-0335.

[11]Senior Researcher, Samsung Electronics, Co., Refrigeration & Living R&D Center, 416, Maetan-3 Dong, Paldal-Gu, Suwon City, Korea.

[12]J. A. Jones Professor of Mechanical Engineering, Department of Mechanical Engineering and Materials Science, Duke University, Box 90300, Durham, NC 27708-0300.

$$\text{Enhancement due to radiation} = \frac{q_{\text{conv(left)}} + q_{\text{rad(left)}}}{q_{\text{conv(left)}}} \quad (2)$$

At this point it needs to be emphasized that because of the predominantly boundary layer type of flow the convective heat flux from the left wall itself is relatively insensitive to radiation and remains more or less constant within the limits of numerical accuracy.

If one uses Eq. (1), spuriously low values of the enhancement factor would be obtained and this actually underplays the influence of radiation. The definition (2) is more meaningful because of the simple reason that when radiation is not there $q_{\text{conv(right)}}$ is also not there and hence the denominator that has been used in Eq. (1) is incorrect. We take an example from Lage et al. The results obtained with Eq. (1) have been plotted in Fig. 11 of their paper. Typically when $T_1 = 100°C$, $T_\infty = 25°C$, $L/H = 0.25$, and $\epsilon_1 = \epsilon_2 = 0.6$, the right wall temperature is around 56°C, as given in Fig. 10. Under these conditions Eq. (1) gives a value of 1.12 as the enhancement due to radiation. However, under these conditions, from the results reported in their paper the convection heat transfer from the right wall is 33 percent of the convective heat transfer from the left. Hence, Eq. (2) will give an enhancement factor of 1.49 and this is the actual effect of radiation. This directly disproves the statement of Lage et al. that ". . .in the temperature range considered in the example, the radiation contribution to the overall heat transfer rate is overshadowed by natural convection. . .". In fact radiation could contribute 50 percent of the total heat transfer as proved earlier by taking a simple example. Hence it is concluded that the interaction between radiation and convection is indeed strong.

References

Balaji, C., and Venkateshan, S. P., 1993a, "Interaction of Surface Radiation with Free Convection in a Square Cavity," *International Journal of Heat and Fluid Flow*, Butterworth, United Kingdom, in press.

Balaji, C., and Venkateshan, S. P., 1993b, "Interaction of Radiation With Free Convection in an Open Cavity," *AIAA Journal of Thermophysics and Heat Transfer*, submitted.

Authors' Closure

J. L. Lage,[10] J. S. Lim,[11] and A. Bejan.[12] We regret to say that the letter writers' observations add nothing to the comments we already included in many parts of our paper. It may be that these writers did not read our text carefully, or that they think that their forthcoming paper on the same problem will be received better if they publicize it ahead of time. To this point we will return in the last paragraph.

What the letter writers call "conceptual errors" are modeling decisions we made and discussed in detail, as part of a deliberate effort to construct the simplest model possible. We stated our objectives in Section 1, especially in the last three paragraphs. We set out to solve a real industrial problem (first paragraph, p. 479), not to calculate in the most accurate way possible the temperature distribution around an ash pit.

We recognized from the very beginning (p. 479) that "an alternative method that is well documented (e.g., Larson and Viskanta, 1976; Lauriat, 1980) consists of solving simultaneously the differential equations for natural convection and radiation, while the nonuniform temperature distribution of the three refractory surfaces is one of the unknowns." We discussed this further on p. 486. This alternative approach is apparently preferred by the letter writers. They are as free to choose their approach as we were when we chose ours. Their objectives are obviously not the same as ours.

Our decision to assign a single temperature (T_2) to the right wall and the bottom of the pit is one of the features of the simplest possible model. We analyzed the pluses and minuses of this decision in a long paragraph (see the bottom-left corner on p. 484); we did not hide it to be "discovered" now by the letter writers. We stated that the actual bottom wall acquires a temperature that varies between T_1 and T_2, and then we listed several *reasons* why we think our modeling decision "is a good *approximation*." To see the good approximations is not only an integral part of good engineering practice, but also the main mission of the *teaching* of engineering research.

Our estimate of the effect of radiation relative to a pure-convection model (Fig. 11) was meant to be qualitative, because it is impossible to separate the two mechanisms *after* they have been coupled in the radiation and convection model. The denominator in our ratio refers to a cavity in which *both* vertical walls are heated, as in the first part of our paper (the letter writers misunderstood our definition). We agree that there may be other ratios that can be looked at. The important point is that the letter writers' estimate (49 percent) agrees with our estimate (12 percent) in a qualitative sense, i.e., in that the dominant mechanism is natural convection. To attack this qualitative conclusion, as they have done, is to split hairs.

By the way, the best place to study the effect of radiation in an enclosure with natural convection is by looking at the *simplest* enclosure geometry, not at the open pit considered in our paper. That simplest geometry may be the square enclosure heated and cooled from the side: It makes a nice undergraduate textbook problem (Bejan, 1993), to which we direct the letter writers' attention.

In summary, we welcome Balaji and Venkateshan's interest in the problem we identified and solved, because it reminds us of what we felt: The problem is interesting. We would have thought, however, that a fairer way of commenting on our work would have been to submit the full-length paper (Balaji and Venkateshan, 1993b) to the JOURNAL OF HEAT TRANSFER, instead of a short letter. We question Professor Venkateshan's decision to (1) "criticize" our work in a letter to the original journal, and, simultaneously, (2) submit the long version of the same to a different journal.

Reference

Bejan, A., 1993, *Heat Transfer*, Wiley, New York, Project 10.3, pp. 573–574.

[10]J. L. Embrey Assistant Professor, Mechanical Engineering Department, Southern Methodist University, Dallas, TX 75275-0335.

[11]Senior Researcher, Samsung Electronics, Co., Refrigeration & Living R&D Center, 416, Maetan-3 Dong, Paldal-Gu, Suwon City, Korea.

[12]J. A. Jones Professor of Mechanical Engineering, Department of Mechanical Engineering and Materials Science, Duke University, Box 90300, Durham, NC 27708-0300.